BİTLİS EREN ÜNİVERSİTESİ
FEN BİLİMLERİ DERGİSİ
Journal of Science

BİTLİS EREN ÜNİVERSİTESİ
FEN BİLİMLERİ DERGİSİ

Bitlis Eren University

Journal of Science

Bitlis Eren Üniversitesi Fen Bilimler Dergisi
Bitlis Eren University Journal of Science

ABOUT
BİTLİS EREN ÜNİVERSİTESİ FEN BİLİMLER DERGİSİ *(Bitlis Eren University Journal of Science)*

Papers in the fields of engineering and basic sciences are published in Bitlis Eren University Journal of Science. The publication language of the journal is English. Journal of Science has been publishing free and open access since 2012. Original research papers and technical notes on experimental and theoretical advances in engineering and basic sciences are included. The similarity rate of the studies submitted to the journal should not exceed 25%. Papers that do not comply with the spelling rules are sent back to the author for revision before being sent to the reviewers. In addition, if the revisions or requests from the editors to the authors are not answered within 15 days, the relevant articles are rejected. The papers sent to the journal for publication are evaluated by at least two reviewers. Reviewer suggestions are not requested from the authors. The Editorial Board of the Journal decides whether to accept the articles for publication, taking into account the reviewer reports (after the evaluations of at least two reviewers are received). Bitlis Eren University Journal of Science is published four times a year (March, June, September, and December). Our journal is indexed in the Journal List of Tübitak-ULAKBİM Engineering and Basic Sciences Database.

The Journal is currently indexed:

*   **TR DİZİN**

*   **ACADEMINDEX**

*   **SCILIT**

ETHICAL PRINCIPLES AND PUBLICATION POLICY

PUBLICATION ETHICS

While establishing the ethical duties and responsibilities below, as open access, guidelines and policies published by the Committee on Publication Ethics (COPE) were taken into account.

It is expected that the author(s) submitting a paper to Bitlis Eren University Journal of Science comply with ethical responsibilities and all stakeholders have the following ethical responsibilities within the scope of publication ethics.

ETHICAL RESPONSIBILITIES OF THE AUTHORS

The articles submitted by the author(s) are expected to be original. If the author(s) benefit from or use other articles, they are required to cite and/ or give reference completely and accurately. Those who do not contribute to the content intellectually in the creation of the article should not be specified as the author. If any article(s) submitted for publication have situations and relationships that may constitute a conflict of interest, this must be clearly stated. Raw data regarding their articles can be requested from the author(s) within the framework of the evaluation processes. In such a case, the author(s) should be ready to present the expected data and information to the editorial board and scientific committee. The author(s) should have a document showing that they have the right to use the data benefited, the necessary permissions for the research/analysis, or the consent of the experimented subjects. If the author(s) notices an inaccuracy or error in their published, early appearance or evaluation processes of their articles, he/she is obliged to cooperate with the editor in informing the journal editor or publisher, correcting the error or withdrawing the article. Authors cannot have their article in the application process of more than one journal at the same time. Each application can be started following the completion of the previous application. An article published in another journal cannot be sent to Bitlis Eren University Journal of Science. Changing the author responsibilities of an article whose evaluation process has begun (such as adding an author, changing the order of authors, removing an author) cannot be proposed.

ETHICAL DUTIES AND RESPONSIBILITIES OF EDITORS

General duties and responsibilities

Editors are responsible for every article published in Bitlis Eren University Journal of Science. Within the context of this responsibility, editors have the following roles and responsibilities:

- Making efforts to meet the information needs of readers and writers,
- Ensuring the continuous development of the journal,

• Conducting processes to improve the quality of articles published in the journal,

• Supporting freedom of thought,

• Ensuring academic integrity,

• Continuing business processes without compromising intellectual property rights and ethical standards,

• Showing openness and transparency in terms of publication on issues that require correction and explanation.

Relations with the Reader

Editors should make decisions by considering the knowledge, skills and experience expectations of all readers, researchers and practitioners. They should pay attention to the fact that the published articles contribute to the reader, researcher, practitioner and scientific literature and that they are original. In addition, editors are obliged to consider the feedback from readers, researchers and practitioners, and to provide explanatory and informative feedback.

Relations with Authors

The duties and responsibilities of the editors to the authors are as follows:

• Editors should make a positive or negatory decision based on the importance, original value, validity, clarity of the narrative, and the journal's goals and objectives.

• Articles that are suitable for the scope of publication should be taken to the preliminary evaluation stage unless they have serious problems.

• Editors should not ignore positive referee suggestions unless there is a serious problem with the article.

• New editors should not change the decisions made by the previous editor(s) for articles unless there is a serious problem.

• "Blind Reviewing and Evaluation Process" must be published and the editors must prevent deviations that may occur in the defined processes.

• Authors should be given feedback in an explanatory and informative way.

Relations with Referees

The editor;

• should assign the referees in accordance with the subject of the article.

• is responsible for providing the information and guides that the referees will need during the evaluation phase.

• has to consider whether there is a conflict of interest between the authors and the referees.

• should keep the identity of the referees confidential in the context of blinded refereeing.

• should encourage the referees to evaluate the article in an impartial, scientific and objective language.

• should determine practices and policies that increase the performance of referees.

• should take the necessary steps to dynamically update the referee pool.

• should avoid rude and unscientific reviews.

• should take steps to ensure that the referee pool is broad.

Relations with the Editorial Board

Editors should ensure that all editorial board members follow the processes in accordance with editorial policies and guidelines. The Editor should inform the members of the Editorial Board about the editorial policies and keep them informed of the developments. In addition, editors should;

• ensure that members of the Editorial Board evaluate the article impartially and independently.

• nominate new editorial board members who can contribute and are suitable.

• submit articles suitable for the expertise of the members of the Editorial Board for evaluation.

• interact with the Editorial Board regularly.

• hold regular meetings with the Editorial Board for the development of editorial policies and the journal.

Relations with the Journal Owner and Publisher

The relationship between the editors and the publisher is based on the principle of editorial independence. In accordance with the written contract between the editors and the publisher, all decisions taken by the editors are independent of the publisher and the journal owner.

Editorial and Blind Peer Review Processes

Editors; is obliged to apply the "Blind Refereeing and Evaluation Process" policies included in the journal's publication policies. In this context, the editors ensure that the fair, impartial and timely evaluation process of each article is completed.

Quality Assurance

Editors; are responsible for publishing every article published in the journal in accordance with journal publication policies and international standards.

Protection of Personal Data

Editors; are obliged to ensure the protection of personal data regarding the subjects or images included in the evaluated studies. They are responsible for rejecting the article unless the explicit consent of the individuals used in the studies is documented. In addition, editors are responsible for protecting the individual data of authors, referees and readers.

Ethics Committee, Human and Animal Rights

Editors are responsible for ensuring the protection of human and animal rights in the evaluated studies. Editors are responsible for refusing the article in the absence of ethical committee approval for the subjects used in the studies and permissions for experimental studies.

Precaution Against Possible Abuse and Misconduct

Editors are obliged to take precautions against possible abuse and misconduct. It is among the responsibilities of the editor to share the relevant findings, as well as to conduct a rigorous and objective investigation regarding the identification and evaluation of complaints regarding this situation.

Ensuring Academic Publication Integrity

Editors should ensure that judgments containing errors, inconsistencies or misdirection in studies are promptly corrected.

Protection of Intellectual Property Rights

Editors are obliged to protect the intellectual property rights of all published articles and to defend the rights of the journal and the author(s) in case of possible violations. In addition, the editors are obliged to take the necessary measures so that the contents of all published articles do not violate the intellectual property rights of other publications.

Constructivism and Openness to Discussion

Editors should;

• consider persuasive criticisms of the articles published in the Journal and should adopt a constructive attitude towards these criticisms.

• give the right of reply to the author(s) of the criticized articles.

• not ignore or exclude studies with negative results.

Complaints

Editors are responsible for carefully examining and responding to complaints from authors, referees or readers in an enlightening and explanatory manner.

Political and Commercial Concerns

The journal owner, publisher and no other political or commercial factors affect the editors' independent decision making.

Conflicts of Interest

The editors ensure that the publication process of the studies is completed independently and impartially, taking into account the conflicts of interest between the author(s), referees and other editors.

ETHICAL RESPONSIBILITIES OF REFEREES

Evaluation of all articles with "Blind Refereeing" directly affects the quality of the publication. This process provides confidence through an objective and independent evaluation of the publication. Bitlis Eren University Journal of Science evaluation process is carried out with the principle of double-blind refereeing. Referees cannot directly communicate with authors, evaluations and comments are transmitted through the journal management system. In this process, reviewer comments on evaluation forms and full texts are forwarded to the author(s) through the editor. In this context, it is expected that the referees who evaluate the articles for Bitlis Eren University Journal of Science have the following ethical responsibilities:

• Reviewers should agree to evaluate only articles related to their field of expertise.

• They should evaluate articles neutrally and confidentially.

• If the referees think that they are facing a conflict of interest during the evaluation process, they should refuse to review the article and inform the journal editor.

• In accordance with the principle of confidentiality, the referees should destroy the articles they have reviewed after the evaluation process. They can only use the final versions of the articles they have reviewed after they are published.

• Referees should make the evaluation objectively only in relation to the content of the article. They should not allow nationality, gender, religious beliefs, political beliefs and commercial concerns to influence the evaluation.

• Referees must do the evaluation in a constructive and courteous language. They should not make derogatory personal comments that include hostility, slander or insults.

• The referees must perform the article they accept to evaluate in the allotted time and in line with the above-mentioned ethical responsibilities.

ETHICAL RESPONSIBILITIES OF THE PUBLISHER

Bitlis Eren University Journal of Science Editors and Editorial Board act with the awareness of the following ethical responsibilities:

• The editors are responsible for all processes of the articles submitted to Bitlis Eren University Journal of Science. In this context, the decision makers are the editors, regardless of economic or political gains.

• Undertakes to create an independent editorial decision.

• Protects the property and copyright of every article published in Bitlis Eren University Journal of Science and undertakes to keep a record of each published copy.

• Takes precautions against all kinds of scientific abuse, citation fraud and plagiarism regarding the editors.

In Case of an Unethical Situation

If you encounter any unethical behavior or content other than the above-mentioned ethical responsibilities and content in the Bitlis Eren University Journal of Science, please don't hesitate to e-mail us.

JOURNAL POLICY

Open Access Policy

Bitlis Eren University Journal of Science, as a journal aware of the need for easy access to information in order to advance scientific studies, supports the initiative to make peer-reviewed journal literature open access in the Budapest Open Access Declaration and presents all published articles free of charge in an environment that anyone can read and download. According to this declaration open access means "its free availability on the public internet, permitting any users to read, download, copy, distribute, print, search, or link to the full texts of these articles, crawl them for indexing, pass them as data to software, or use them for any other lawful purpose, without financial, legal, or technical barriers other than those inseparable from gaining access to the internet itself." Considering the role of knowledge sharing in the advancement of science, open access is of great importance for researchers and readers. For this reason, the articles in this journal can be used as long as the author and original source are cited. No permissions from authors or publishers are required. Articles in this journal are available across search engines, websites, blogs, and other digital platforms.

Fee Policy

No fee is charged for publishing the article and conducting the article processes in the journal.

Evaluation Process

Articles submitted to the journal for publication are primarily subjected to editorial evaluation in terms of compliance with the purpose and scope of the journal, writing rules and the proposed draft. At this stage, articles that are not suitable for the purpose and scope of the journal are returned to the authors. Articles that do not comply with the spelling rules and draft formatting are returned to the authors to be corrected and reloaded.

All articles are expected to be original and unique articles that have not been published in any medium before. In the evaluation phase, articles are reviewed through the Ithenticate similarity scanning and plagiarism detection program. The similarity index value of the articles must be below 20%. Articles above this value are rejected without being evaluated.

Articles found appropriate in the editorial evaluation are directed to the relevant field editor according to their subjects.

The field editor starts the referee evaluation process of the article by determining two referees suitable for the subject and quality of the article.

The referees selected for the first step evaluation process are given a 30-day evaluation period. At the end of this period, the duties of the referees who do not complete their evaluation or upload the evaluation report are terminated and new referees are determined.

Articles that are not deemed suitable for publication according to the results of peer-review are returned to the authors. The authors are informed about the articles accepted for publication and they are published in the next issue.

Authors are given 30 days for the articles that the referees want to be corrected. During this period, necessary corrections should be made and the corrected article should be uploaded to the journal system. If this period granted to the authors is exceeded, the process of the article is terminated and must be uploaded as a new article from the beginning. In this case, the first step evaluation process is restarted. The corrected version uploaded in the given time is directed to the referee again if necessary and the second step referee process starts. If the referee hasn't wanted to see the corrected version of the article, the editor decides whether to publish it or not.

In the second step evaluation process, the corrections made by the authors are followed by the referees and the referees inform the editor of their final decisions about the article. Finally, the editor informs the authors about the publication process.

EDITOR'S NOTE

We are pleased to present the 14th issue of the Bitlis Eren Üniversitesi Fen Bilimler Dergisi (*Bitlis Eren University Journal of Science*), a peer-reviewed academic journal published four times a year. This issue features original and high-quality research articles from various fields of science and engineering. The interdisciplinary nature of the contributions reflects our commitment to promoting diverse perspectives and facilitating academic dialogue across scientific domains. We hope these works inspire new research ideas and provide valuable insights for our readers.

Our journal adheres strictly to scientific ethics and publication standards, supporting content that bridges multiple disciplines. All submitted manuscripts undergo a rigorous and impartial peer-review process to ensure scientific merit and relevance. As an open-access journal, we aim to make every article widely accessible to national and international scholars, fostering a more inclusive academic community. Our primary goal is to enhance the exchange of knowledge between fields and contribute meaningfully to the global body of scientific literature.

As an emerging academic platform, the Bitlis Eren Üniversitesi Fen Bilimler Dergisi (Bitlis Eren University Journal of Science) continues to grow with each issue. We sincerely thank our contributing authors, the reviewers for their meticulous evaluations, and our readers for their ongoing interest and encouragement. We look forward to sharing more innovative and impactful work with you in the upcoming issues.

Editor-in-Chief

CONTENTS

A MULTI-INPUT MULTI-OUTPUT ENERGY HARVESTING ARCHITECTURE FOR MICROBIAL FUEL CELL

Rıdvan UMAZ [1] iD

[1] *Bitlis Eren University, Department of Electrical-Electronics Engineering, Bitlis, Türkiye, rumaz@beu.edu.tr*

ABSTRACT

This paper presents an energy harvesting architecture that accommodates two microbial energy sources and delivers power supply synchronously to two loads. The proposed architecture enables the maximum power extraction from the first energy source, whereas the second source is disabled. However, once the first energy source is impaired (i.e., not working), the second energy source becomes the primary energy source in the architecture, and the first energy source is decoupled from the system. The measurement result of the proposed architecture, implemented with the off-the-shelf components and tested with two emulated MFCs, demonstrates a peak efficiency of 56.51%, which is the highest end-to-end efficiency among prior work. The proposed architecture can operate from a minimum input voltage of 0.3 V and simultaneously regulate two outputs to constant voltages of nearly 3.7 V and 5 V.

Keywords: Burst mode, Energy combiner, Energy harvesting, Energy scavenging, Microbial fuel cell, Multiple input, Multiple loads, Underwater electronic devices, Wireless sensor networks

1 INTRODUCTION

Microbial fuel cells (MFCs) are considered an emerging alternative energy source for underwater electronic devices (e.g., hydrophones) [1], [2]. MFCs have a significant potential to deploy in deep oceans, seas, lakes, and rivers in the harsh aquatic environment [2]-[5]. MFCs generate energy from biodegradable substrates through the metabolic activities of microorganisms in marine sediment [6]. Typically, MFCs contain two electrodes: an anode

buried in sediment and a cathode floating in water. Microbial activity in the marine sediment causes a potential difference between electrodes. Thus, MFCs generate electrical energy.

MFCs are generally not sufficient to directly drive electronic devices (e.g., sensors) since the voltage and power generated by MFCs are inherently at low levels [1]-[18]. Thus, an energy harvesting system that boosts the low voltage is needed along with a temporary storage element (e.g., supercapacitor) for accumulating the harvested energy over time to intermittently transfer to the load (i.e., burst mode operation). This type of load can be classified as a heavy load, which requires more power than the generated power by the energy source.

However, the energy available from a single microbial fuel cell might not be secured to power the load due to the issue of bioturbation by diverse aquatic organisms [3], [7], [11], [18]-[20]. In other words, the anode of the MFC can be impaired by either burrowing organism [7] or incomplete installation [5], [17], thereby allowing dissolved oxygen in water to contact the anode that becomes the cathode. Thus, the potential difference across the electrodes is eliminated, and the MFC becomes short-circuited without producing any useful voltage and power at the output. In order to increase the reliability of the microbial energy source, it is possible to construct the energy harvesting system with multiple MFCs [14], [17], [18], [20].

Prior work in multi-input energy harvesting systems for MFCs has involved combining the outputs of the individual power converters for each MFC to a common output capacitor and transferring its power to the load [13], [14], [17], [20]. However, these works have a large area overhead, resulting in complexity and large power losses. As a result, they have low overall efficiencies (e.g., $\leq 32.8\%$). To further improve the complexity and efficiency, adding the output voltages of the MFCs through switches to supply a single inductor power converter is proposed in prior work [18]. However, the work utilizes all MFCs at the same time; thus, all MFCs are not isolated from each other. Also, the MFC with the highest output voltage constrains the contributions from other MFCs. Thus, all MFCs do not exploit their best efficiencies, thereby degrading the overall efficiency. Also, these works do not consider the regulation of multiple output loads. Thus, there is a need for a more efficient architecture for multi-input energy harvesting systems with multi-output regulation.

This paper presents an energy harvesting architecture. The architecture handles energy from two emulated MFCs and provides efficient regulation of two output loads. One MFC is allowed merely to support the loads by the architecture, but the other MFC stays at the idle mode (i.e., not utilized). This leads to full isolation among MFCs. As a result, the overall

efficiency degradation is reduced or eliminated in the system. Once the first MFC is impaired, the architecture allows the second MFC to supply the loads. Thus, the energy path to the loads is maintained with the spare MFC, i.e., MFC 2. The architecture can start the operation from the minimum input voltage of 0.3 V and regulate two outputs to voltage levels of roughly 3.7 V and 5 V. The architecture implemented with discrete components, accomplishes a peak efficiency of 56.51%. As compared to prior multiple MFC works, the architecture achieves the highest end-to-end efficiency, supports multiple loads with regulated voltages, and secures full isolation between sources.

2   THE PROPOSED ARCHITECTURE

Figure 1 shows the top-level architecture of the proposed architecture, which consists of four power switches, a low voltage step-up converter (e.g., $V_{in} \geq 0.3$ V), a high voltage boost converter (e.g., $V_{dc} \leq 3.7$ V), and a temporary storage element (e.g., $C_{STOR}=235$ mF). The architecture does not require any precharge voltage to start the system operation; thus, the voltage in all capacitors is initially equal to zero.
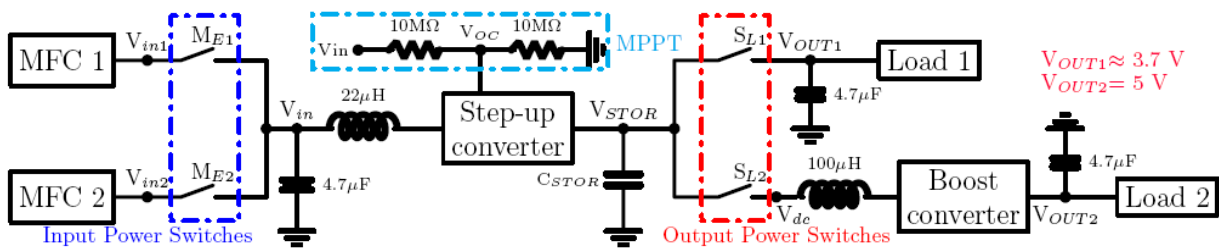
Figure 1. Block diagram of the proposed architecture.
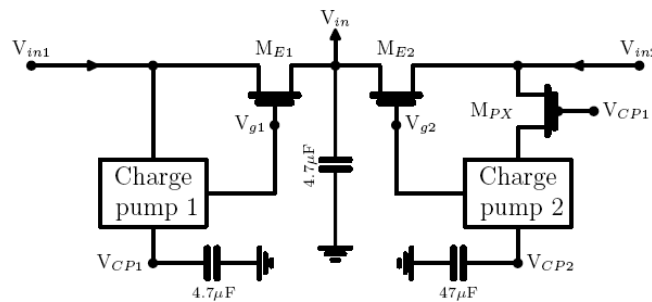
Figure 2. The input detecting circuit (IDC).

Two MFCs are enabled to provide voltage to their outputs (V_{in1}-V_{in2}), but input power switches (M_{E1}-M_{E2}) block these voltages to supply the V_{in} node. In order to allow the available power from the MFCs to transfer to the step-up converter, an input detecting circuit (IDC) is needed, as shown in Figure 2. The MFCs provide a power supply to charge pumps to charge

capacitors at the V_{CP1} and V_{CP2} nodes from 0 V. Once the V_{CP1} node reaches 0.4 V, the M_{PX} PMOS transistor turns off, which was on. Thus, the charge pump 2 is decoupled from the output of the MFC 2, V_{in2}, and the capacitor at the V_{CP2} node stops charging. As a result, the voltage at the V_{in2} node becomes the open-circuit voltage of the MFC 2. However, the MFC 1 keeps supplying the charge pump 1 to charge. Once the voltage at the V_{CP1} node reaches 2 V, the charge pump internally connects the V_{CP1} node to the V_{g1} node, which is the gate of the M_{E1} NMOS transistor. Consequently, the M_{E1} transistor turns on, and the energy available from the MFC 1 is transferred to the V_{in} node, which is isolated from the MFC 2. With the IDC, the energy sources are fully isolated from each other.

However, once the MFC 1 is impaired, the output V_{in1} drops to zero or an insufficient voltage level. Thus, the charge pump 1 stops to charge the capacitor at the V_{CP1}, and the capacitor voltage is not delivered internally to the V_{g1} node. As a result, the M_{E1} transistor shuts off, and the energy transfer from the MFC 1 to the step-up converter is cut-off. Meantime, due to the small value of the capacitor at the V_{CP1} node, the energy at the capacitor is consumed internally; consequently, it drops to nearly zero. This causes the M_{PX} transistor to switch on, and the MFC 2 starts to supply the charge pump 2. Once the capacitor at the V_{CP2} node charges to 2 V, the energy at the capacitor releases to the gate of the M_{E2} transistor. As a result, the transistor turns on, and the MFC 2 starts to provide a power supply to the converter. This is precisely what the IDC detects: the MFC 2 as the energy source once the MFC 1 is not functional to supply the converter.

The step-up converter receives power supply from the IDC output V_{in} to up-convert to higher voltage levels to charge a supercapacitor at the V_{STOR} node. When the V_{STOR} reaches 1.8 V, the converter internally enables the maximum power point tracking (MPPT), which drives the maximum power available from the MFC. The V_{OC} pin of the converter is placed at the output of the voltage divider of the V_{in} node in order to achieve the MPPT. After this voltage level (e.g., 1.8 V), the supercapacitor keeps charging at a faster rate. Once the V_{STOR} arrives at nearly 3.7 V, which is the maximum voltage level for the supercapacitor to charge in this study, the accumulated energy should be released to two output loads. Thus, there is a need for a circuit between the loads and the supercapacitor to manage the charge transfer.

Figure 3 shows the circuit used for controlling the outputs. Before the accumulated energy at the supercapacitor is transferred to the loads, the Nx transistor shuts on. This is because resistors of 1 and 6.7 MΩ placed between the V_{STOR} and V_{GL} nodes behave as a linear element to supply current to the gates of the S_{L1}, $S_{L2,}$ and Nx transistors. Thus, the diode between

the V_{x1} and the V_{x2} nodes is bypassed. The voltage at the V_{STOR} node goes across four diodes to charge the capacitor of 4.7 μF at the V_{cntrl} node. A comparator circuit is an interface between the V_{cntrl} and OUT nodes. The comparator circuit compares internally a divided version of the V_{cntrl} node with the internally generated reference voltage (V_{ref}).
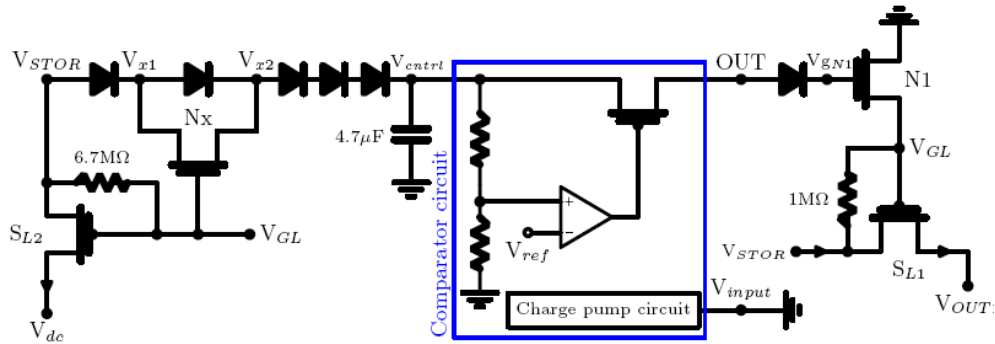
Figure 3. Output control circuit (OCC).

Once the V_{STOR} node is charged to nearly 3.7 V which drops over diodes to charge the capacitor at the V_{cntrl} node to 2 V, the comparator energizes the gate of the PMOS transistor. As a result, the PMOS switches on, which was cut-off, and the V_{cntrl} node is at the same potential as the OUT node. The OUT voltage goes across the diode to supply the gate of the N1 transistor (Vg_{N1}). In consequence, the N1 turns on, and the V_{GL} node drops to zero. Thus, the S_{L1}, S_{L2}, and Nx transistors turn on, on, and off, respectively. The stored energy is transferred to Load 1 and the V_{dc} node, and the diode between the V_{x1} and V_{x2} nodes becomes conducting. The load 1 receives a power supply with a voltage level of approximately 3.7 V.

Due to shutting off the Nx transistor, the voltage at the V_{cntrl} node undergoes a decrease with the amount equal to the voltage drop across the corresponding diode, and the V_{cntrl} voltage drops from 2 V to 1.5 V. Both load 1 and load 2 receive power supply from the supercapacitor. Thus, the supercapacitor starts discharging, and the capacitor at the V_{cntrl} node discharges as well. Once the V_{cntrl} voltage reduces to 1.44 V, the comparator circuit internally shuts off the internal PMOS. This step leads to the isolation between the V_{cntrl} and OUT nodes. As a result, the OUT voltage drops to zero, and the N1 transistor switches off, and the V_{GL} voltage shifts from 0V to nearly V_{STOR} voltage. This causes the S_{L1}, S_{L2}, and Nx transistors turns off, off and on, respectively. Therefore, the supercapacitor is disconnected from the loads and starts charging back to 3.7 V again. The same operation process will occur over time for the loads operating in burst mode. This is precisely what the control circuit carries out.

Once the supercapacitor transfers the energy to loads, the load 1 is at the voltage level of 3.7 V while load 2 is at 5 V. For load 1, there is no need for another stage to boost the voltage since the V_{OUT1} node is at the same potential as the V_{STOR} node. However, load 2 requires a second converter placed between the S_{L2} transistor and the V_{OUT2} node to step up the voltage from 3.7 V to 5 V. The output voltage levels of the proposed architecture can be adjusted by adding/subtracting more diodes to the output control circuit or rearranging the boost converter. Table 1 tabulates off-the-shelf components used in the architecture.

Table 1. List of discrete components used to construct the architecture.

Component	Name	Specifications
Input detecting circuit		
Charge pump	S-8880A20	min. input voltage=0.3 V
M_{E1} & M_{E2} NMOS	BSH103	$V_{GS(th)}$=0.4 V
M_{PX} PMOS	SI-3499DV	$V_{GS(th)}$=-0.35 V
Outputs control circuit		
Comparator circuit	S-8880A20	Input connected to gnd
N_X & N1 NMOS	SI-3460BDV	$V_{GS(th)}$=0.45 V
S_{L1} & S_{L2} PMOS	SI-3499DV	$V_{GS(th)}$=-0.35 V
Diodes	1N4007	Drop voltage
Converters		
Step-up converter	BQ25505	min. input voltage=0.1 V
Boost converter	L6920DB	min. input voltage=0.8 V
Supercapacitor	235mF	ESR=8Ω

3   MEASUREMENT RESULTS

The proposed architecture is implemented using off-the-shelf components. The experimental setup of the architecture is shown in Figure 4. The architecture harvests energy from two MFCs while regulating two different output voltage levels, which are nearly 3.7 V and 5 V. MFC can be electrically modelled as a voltage source in series with a resistance [12]. Voltage sources with series resistors are used to model the MFC 1 and MFC 2 for testing. The MFC 1 is emulated as a voltage source of 0.8 V in series with a resistor of 0.1 kΩ, and the MFC 2 is modeled as a 0.7 V input voltage in series with a 0.2 kΩ internal resistor.

Figure 5 shows the operation of the architecture from the initial time to several cycles. Two functional MFCs provide power supply to the architecture; however, the architecture receives energy from MFC 1, but MFC 2 is not allowed to support the architecture, and it becomes an open-circuit. The supercapacitor voltage (V_{STOR}) begins to rise from 0 V. Once the

V_{STOR} exceeds 1.8 V, the step-up converter triggers the MPPT accomplished by regulating the converter input as half of the open-circuit voltage of MFC 1. After that, it is obviously seen that the supercapacitor has charged at a faster rate than before. Once the V_{STOR} voltage gets to 3.7 V, both the S_{L1} and S_{L2} turn on, and both loads, thus, start receiving power supply. Once the MFC 1 is impaired ($V_{in1} \approx 0$), the backup source (i.e., the MFC 2) should deliver energy to the architecture to maintain the load operations. It can be seen from Figure 4 that the MFC 2 does not start immediately providing power to the architecture. This is because the voltage of the capacitor at the V_{CP1} in the IDC does not drop instantly to below the threshold voltage of the M_{PX} PMOS transistor. Once the V_{CP1} drops to the below the transistor threshold voltage, the transistor switches on and, consequently, the MFC 2 is allowed to supply the circuit. Thus, the voltage of the MFC 2 V_{in2} shifts from the open-circuit voltage to nearly half of the open-circuit voltage of the MFC 2, which is equal to the voltage at the V_{in}.

Figure 6 shows voltage waveforms at the V_{in1}, V_{in2}, V_{CP1}, and V_{CP2} nodes in Figure 2. Once the impairment occurs at MFC 1, the input voltage V_{in1} begins reducing to zero due to shutting off the M_{E1} transistor. Also, the charge pump 1 does not charge up, and the capacitor voltage V_{CP1} starts todrop. Once the capacitor voltage reaches roughly 0.35 V, the M_{PX} transistor turns on and the MFC 2 starts the operation of the charge pump 2 to charge the capacitor at the V_{CP2} node. As the V_{CP2} reaches 2 V, the M_{E2} transistor turns on, and MFC 2 is connected to the step-up converter. These results demonstrate that the energy path to the architecture is secured with the backup source (i.e., the MFC 2).
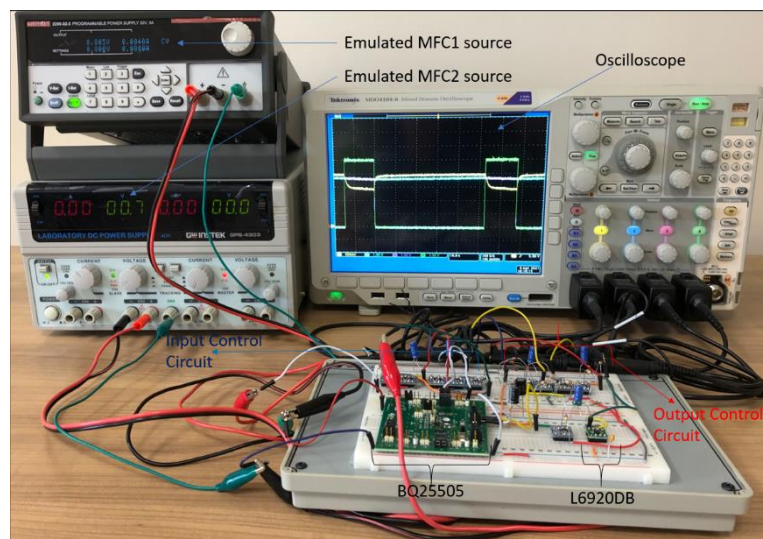
Figure 4. Experimental setup of the proposed architecture.
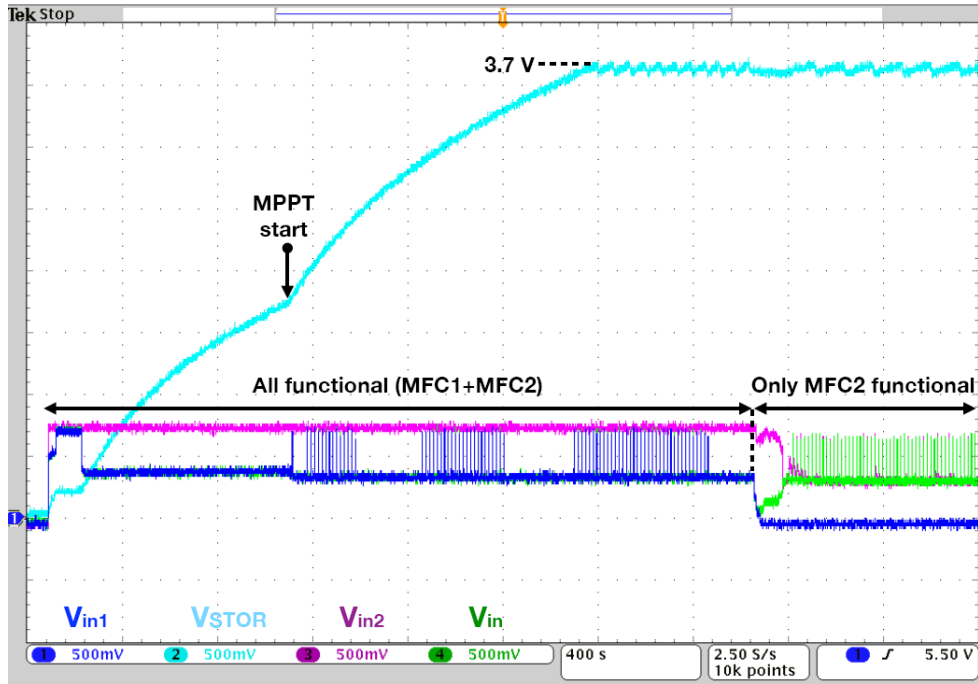
Figure 5. The operation from the initial time without impaired MFCs and once MFC 1 is impaired.
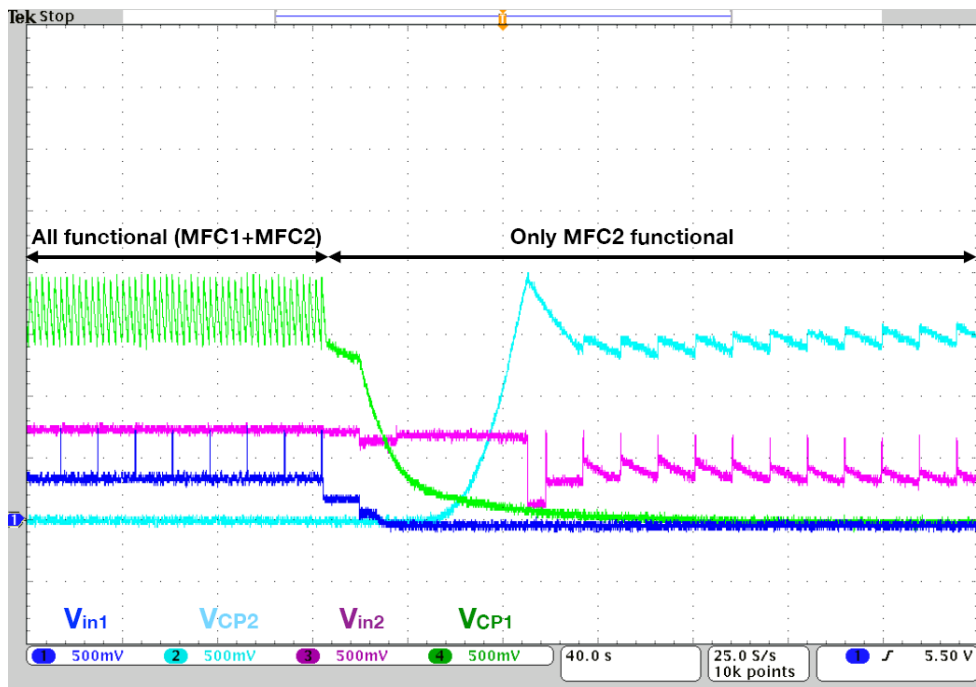
Figure 6. Voltage waveforms at the V_{in1}, V_{in2}, V_{CP1}, V_{CP2} nodes for the IDC once MFC 1 is impaired.

In order to verify the operation of the boost converter, voltage waveforms at the V_{dc}, V_{cntrl}, V_{GL}, and V_{OUT2} are monitored, as illustrated in Figure 7. Before the V_{cntrl} voltage arrives at 2 V, the voltages of the input (V_{dc}) and output of the boost converter are equal to zero. This is because output power switches (S_{L1}-S_{L2}) are kept being in off status by the resistors located

between the V_{STOR} and V_{GL} nodes. The resistors act as a short-circuit to energize the common gate of the transistors V_{GL} that is almost at the same potential as the V_{STOR} node. Once the V_{cntrl} voltage charges to 2 V, the common gate voltage V_{GL} drops to zero. Therefore, the S_{L2} transistor turns on, and consequently, the boost converter is bridged to the supercapacitor. Voltages of the input (V_{dc}) and output of the boost converter (V_{OUT2}) are 3.7 V and 5 V, respectively. Because of the heavy load, the supercapacitor at the V_{STOR} and the capacitor at the V_{cntrl} start discharging. Once the V_{cntrl} voltage drops to 1.44 V, the S_{L2} shuts off, and thus, the supercapacitor is disconnected from the boost converter. The V_{dc} and V_{OUT2} voltages drop to zero while the V_{GL} voltage increases from 0 V to the V_{STOR} voltage. The V_{cntrl} voltage starts rising up again, and the same process will be repeated over time.
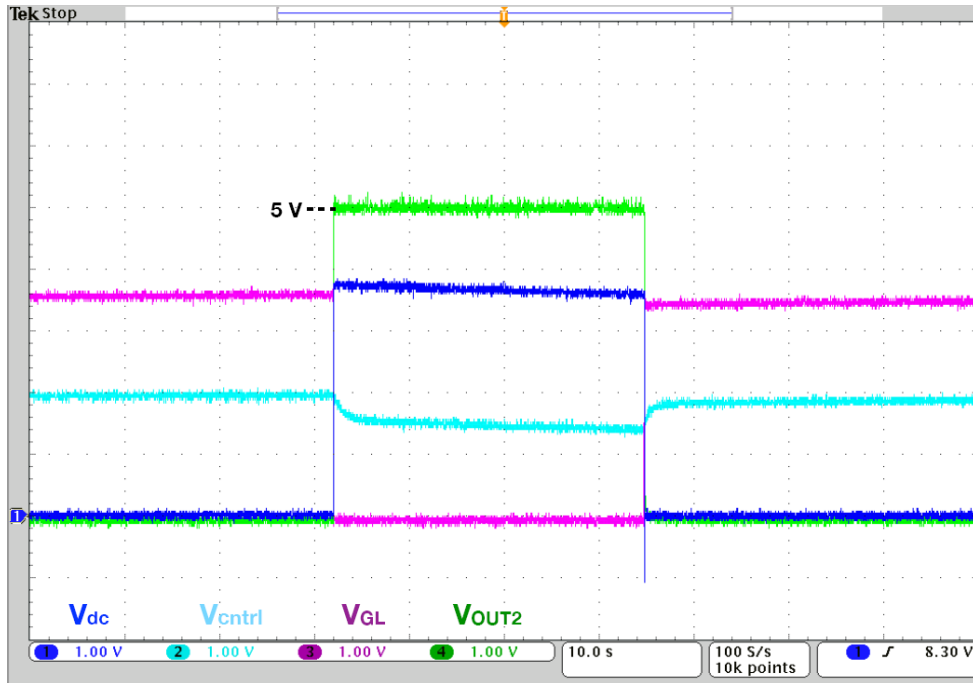
Figure 7. Voltage waveforms at the V_{cntrl}, V_{dc}, V_{GL}, V_{OUT2} nodes under a heavy load at the load 2.

Figure 8 indicates measured voltage waveforms for the proposed architecture operating in burst mode with various output power levels. The measured waveforms demonstrate that the architecture regulates two outputs at voltage levels of nearly 3.7 and 5 V.

Finally, the end-to-end efficiency of the proposed architecture that accommodates two loads operating in burst mode was measured. The efficiency is expressed as

$$\eta_{end} = \frac{\sum P_{load}}{P_{max}} \times \frac{t_{on}}{(t_{on} + t_{off})} = \frac{P_{out1} + P_{out2}}{P_{max}} \times \frac{t_{on}}{(t_{on} + t_{off})} \qquad (1)$$

where t_{ON} is the time duration for both active loads. t_{ON} times for both loads are the same. $(t_{ON}+t_{OFF})$ is the time between two power cycles received by the loads. P_{max} is the maximum power available from the functional MFC. Efficiency measurements indicated a peak efficiency of 56.51% with two outputs at $V_{OUT1}= 3.7$ V and $V_{OUT1}= 5$ V.

Table 2 shows the performance summary and comparison to prior work. The architecture is the first to regulate multiple outputs with multiple MFCs. Also, the architecture accomplishes the highest efficiency among prior art multi-input MFCs.
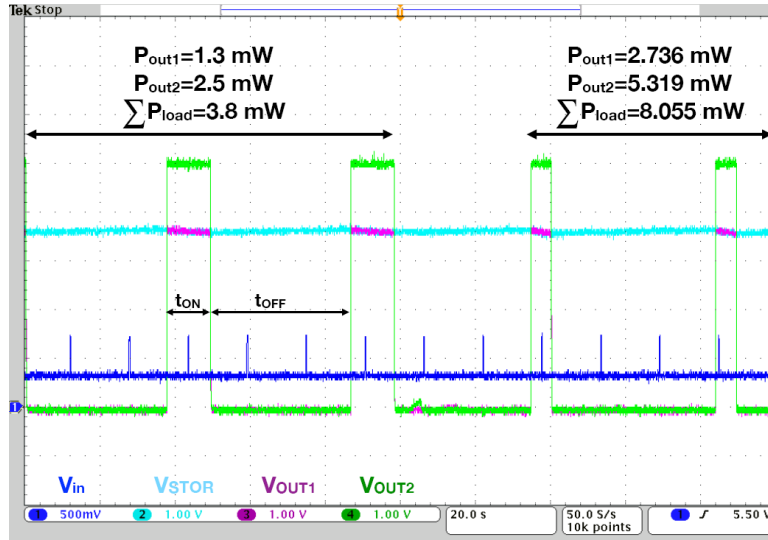
Figure 8. Measured voltage waveforms under varying heavy loads.

Table 2. Performance comparison of the proposed architecture to prior work for multiple MFCs.

Parameters	[14]	[17]	[18]	[20]	This work
Technology	Discrete	Discrete	Discrete	Discrete	Discrete
No of inputs	2	4	2	2	2
No of outputs	1	1	1	1	2
Architecture	2-stage 2-transfs+1-ind	1-stage 8-inds[*]	2-stage 2-inds	2-stage 2-caps[§]+1-ind	2-stage[±] 2-inds[±]
Output voltage (V)	5	0.4-1.6[‡]	3.3	3.3	3.7 & 5
Efficiency	26%[†] @Vin=0.44 V	32.8%[†]	42.16%	NA	56.51

[*] 4-inductors used for startup circuit. [§] First-stage includes two charge pumps. [±] Second load needs an addition boost converter. [‡] Not regulated. [†] Not end-to-end efficiency.

4   CONCLUSION

This article presented an energy harvesting architecture for multiple MFCs, implemented using off-the-shelf components. The architecture receives the energy from two MFCs while regulating two independent different power rails. The architecture decoupled one of the MFCs from the output load contribution by putting in the position of the backup in order to employ it once the other active MFC is impaired. The architecture used a second boost converter to regulate the second output to a higher voltage level (e.g., 5 V) than the first output (e.g., 3.7 V). The architecture achieves the peak efficiency of 56.51% due to the full isolation between MFCs, the optimum maximum power extraction from the energy source, and one converter at the load side. Measurement exhibited that the architecture achieves the highest peak efficiency with multiple outputs as compared to prior work.

Statement of Research and Publication Ethics

The study is complied with research and publication ethics.

Artificial Intelligence (AI) Contribution Statement

This manuscript was entirely written, edited, analyzed, and prepared without the assistance of any artificial intelligence (AI) tools. All content, including text, data analysis, and figures, was solely generated by the author.

REFERENCES

[1]   U. Karra, E. Muto, R. Umaz, M. Kölln, C. Santoro, L. Wang, and B. Li, "Performance evaluation of activated carbon-based electrodes with novel power management system for long-term benthic microbial fuel cells," *Int. J. Hydrogen Energy*, vol. 39, no. 36, pp. 21847–21856, 2014.

[2]   A. Meehan, H. Gao, and Z. Lewandowski, "Energy harvesting with microbial fuel cell and power management system," *IEEE Trans. Power Electron.*, vol. 26, no. 1, pp. 176–181, Jan. 2011.

[3]   R. Umaz and L. Wang, "Integrated power converter design for bioturbation resilience in multi-anode microbial fuel cells," *IET Circuits, Devices Syst.*, vol. 13, no. 8, pp. 1142–1151, 2019.

[4]   C. Donovan, A. Dewan, H. Peng, D. Heo, and H. Beyenal, "Power management system for a 2.5 W remote sensor powered by a sediment microbial fuel cell," *J. Power Sources*, vol. 196, no. 3, pp. 1171–1177, 2011.

[5]   I. Lee *et al.*, "System-on-mud: Ultra-low power oceanic sensing platform powered by small-scale benthic microbial fuel cells," *IEEE Trans. Circuits Syst. I: Reg. Papers*, vol. 62, no. 4, pp. 1126–1135, Apr. 2015.

[6]   B. Logan, *Microbial Fuel Cells*, Hoboken, NJ, USA: John Wiley & Sons, Inc., 2008.

[7]   R. Umaz, C. Garrett, F. Qian, B. Li, and L. Wang, "A power management system for multianode benthic microbial fuel cells," *IEEE Trans. Power Electron.*, vol. 32, no. 5, pp. 3562–3570, May 2017.

[8] E. Dallago, A. Lazzarini Barnabei, A. Liberale, G. Torelli, and G. Venchi, "A 300-mV low-power management system for energy harvesting applications," *IEEE Trans. Power Electron.*, vol. 31, no. 3, pp. 2273–2281, Mar. 2016.

[9] G. Huang, R. Umaz, U. Karra, B. Li, and L. Wang, "A biomass-based marine sediment energy harvesting system," in *Proc. Int. Symp. Low Power Electron. Design (ISLPED)*, Sept. 2013, pp. 359–364.

[10] P. K. Wu, J. C. Biffinger, L. A. Fitzgerald, and B. R. Ringeisen, "A low power DC/DC booster circuit design for microbial fuel cell," *Process Biochem.*, vol. 47, no. 11, pp. 1620–1626, 2012.

[11] F. Qian, R. Umaz, Y. Gong, B. Li, and L. Wang, "Design of a shared stage charge pump circuit for multi-anode microbial fuel cells," in *Proc. IEEE Int. Symp. Circuits Syst. (ISCAS)*, May 2016, pp. 213–216.

[12] J. D. Park and Z. Ren, "Hysteresis-controller-based energy harvesting scheme for microbial fuel cells with parallel operation capability," *IEEE Trans. Energy Convers.*, vol. 27, no. 3, pp. 715–724, Sept. 2012.

[13] R. Umaz and L. Wang, "An energy combiner design for multiple microbial energy harvesting sources," in *Proc. Great Lakes Symp. VLSI*, May 2017, pp. 443–446.

[14] J.-D. Park and S. Lee, "Single-transistor sub-1-V self-startup voltage boost energy harvesting system for microbial fuel cells," *J. Power Sources*, vol. 418, pp. 90–97, 2019.

[15] S. Carreon-Bautista, C. Erbay, A. Han, and E. Sanchez-Sinencio, "An inductorless DC-DC converter for an energy aware power management unit aimed at microbial fuel cell arrays," *IEEE J. Emerg. Sel. Topics Power Electron.*, vol. 3, no. 4, pp. 1109–1121, Dec. 2015.

[16] R. Umaz, "A power management system for microbial fuel cells with 53.02% peak end-to-end efficiency," *IEEE Trans. Circuits Syst. II: Express Briefs*, vol. 67, no. 11, pp. 2592–2596, Nov. 2020.

[17] N. Tang, W. Hong, T. Ewing, H. Beyenal, J. H. Kim, and D. Heo, "A self-sustainable power management system for reliable power scaling up of sediment microbial fuel cells," *IEEE Trans. Power Electron.*, vol. 30, no. 9, pp. 4626–4632, Sept. 2015.

[18] R. Umaz, "A single inductor self-startup energy combiner circuit with bioturbation resilience in multiple microbial fuel cells," *IEEE Trans. Circuits Syst. II: Express Briefs*, vol. 67, no. 12, pp. 3227–3231, Dec. 2020.

[19] U. Karra, G. Huang, R. Umaz, C. Tenaglier, L. Wang, and B. Li, "Stability characterization and modeling of robust distributed benthic microbial fuel cell (DBMFC) system," *Bioresour. Technol.*, vol. 144, pp. 477–484, 2013.

[20] R. Umaz and Y. Sahin, "An architecture for two ambient energy sources," in *Proc. Int. Conf. Power Electron. Appl. (ICPEA)*, 2019, pp. 1–6.

PERFORMANCE COMPARISONS OF THERMAL PROTECTION METHODS BASED ON THERMALLY ENHANCED PHASE CHANGE MATERIALS

Ahmet Can ÇAPAR[1] , **Ümit Nazlı TEMEL[2]***

[1] Turkish Electricity Transmission Corporation, Sivas, Türkiye

[2] Sivas Cumhuriyet University, Mechanical Engineering Department, Sivas, Türkiye

* Corresponding Author: untemel@cumhuriyet.edu.tr

ABSTRACT

This study focuses on phase change material-based passive thermal protection of electronic components that release heat for a period of time. Firstly, an investigation was carried out in terms of PCM thickness for thermal protection and it was determined that an 11 mm thickness was the appropriate PCM thickness. It was determined that the thermal conductivities in the solid phase could be improved by 35.9%, 119.2%, and 178.6%, respectively, if 1%, 3%, and 5% GNP were doped into the PCM. In the case of 1%, 3%, and 5% GNP doping, it was determined that the melting temperatures of PCM did not change, whereas the latent heat of melting decreased slightly depending on the GNP fraction. The deterioration in the latent melting heat for 5% GNP/RT-44 composite was measured as 5.4%. Then, the thermal protection performance of PCM, Fin/PCM, Nanoparticle/PCM, and Nanoparticle/Fin/PCM composites on an electronic component that releases heat for a period of time was compared in terms of maximum surface temperature and maximum surface temperature difference. The results indicated that the Nanoparticle/PCM thermal protection exhibited a performance improvement effect predominantly during sensible heat storage, whereas the Fin/PCM thermal protection demonstrated an improvement in performance during both sensible heat and latent heat storage. While all thermal protection methods were successful at 3 W heating power, only PCM thermal protection equipped with six fins (6F/PCM) was successful at 6W heating power. At 6 W heating power, maximum temperature and maximum temperature difference performances were improved by 15.3% and 45.2%, respectively, with 6F/PCM thermal protection compared to PCM thermal protection only. An increase in the GNP mass fraction above 3% has been demonstrated to have a detrimental effect on thermal protection. With 3% GNP/6F/PCM hybrid thermal protection, it was determined that the maximum temperature and maximum temperature difference performances have the potential to be improved by 22.3% and 53.4% compared to PCM thermal protection.

Keywords: PCM, Thermal protection, Fin, Nanoparticles, Hybrid thermal protection

ABBREVIATIONS

PCM	: Phase Change Material	**CNTs**	: Carbon Nano Tubes
GNP	: Graphene Nano Platelets	**BN**	: Boron Nitride
PW	: Paraffin Wax	**EG**	: Expanded Graphite
LA	: Lauric Acit	**FLG**	: Few Layer Graphene
MWCNTs	: Multi-Walled Carbon Tubes	**PEG**	: Polyethylene Glycol
S-MWCNTs	: Short MWCNTs	**DSC**	: Differential Scanning Calorimetry
L-MWCNTs	: Long MWCNTs	**DC**	: Direct Current
CNFs	: Carbon Nano Fiber	**SiC**	: Silicone Carbide

1   INTRODUCTION

Phase change materials (PCMs) have the potential to store thermal energy due to their high latent heat. The heat absorbed from a source is stored thermally as the PCM transitions to a higher energy state during the phase change process. Conversely, the PCM releases the stored thermal energy as it returns to a lower energy state during the reverse phase change. With this feature, PCMs have a wide range of applications such as energy storage in solar panels [1] and building walls [2], thermal protection of electronic devices [3], performance improvement of coolers [4], waste heat recovery [5] and blood and organ transplantation [6].

The thermal energy released by transient electronic devices during operation leads to an undesired temperature increase within the device. This temperature rise can cause the device to malfunction or operate inefficiently. Therefore, it is essential to thermally protect transient operating devices by effectively dissipating the thermal energy they generate for instance, during the transient operation of battery cells, it is crucial to maintain the maximum temperature below 50 °C and the maximum temperature difference below 5 °C. Failure to do so may result in issues such as explosion risks, capacity loss, short charge/discharge cycles, and accelerated aging of the battery cells. Passive thermal protection of transient electronic devices based on the use of PCM is seen as an innovative method because it is economical and does not involve moving mechanical systems such as pumps and fans. The effectiveness of this type of thermal protection depends on the rapid transfer of the heat released in electronic devices to the PCM. In other words, the PCM used must have a rapid thermal response. This outcome necessitates a high thermal conductivity for PCM. Conversely, the thermal conductivity of PCMs that are suitable for practical applications is relatively low. This is the most important obstacle to the use of PCMs in the thermal protection of electronic devices. To enable the use of PCMs for passive thermal protection, enhancing their heat transfer capabilities is essential. Efforts to

improve the thermal conductivity of PCMs can be grouped into three main categories. The first involves creating PCM/nanoparticle composites by incorporating nanoparticles with high thermal conductivity into the PCM. The second method uses thermal bridges, such as metal fins or pins, embedded in the PCM to enhance heat dissipation. The third approach entails forming shape-stable composites by impregnating PCM into the pores of highly porous materials. A comparative analysis of these thermal protection methods is presented in Table 1.

Table 1. Comparative literature studies.

Ref.	Composite	Proportion	Melting Temp. of PCM (ºC)	Latent Heat (J/g) PCM – PCM/Additive	Thermal Cond. (W/mK) or Enhancement (%) PCM – PCM/Additive	Load	T_{max} (ºC)	ΔT_{max} (ºC)
Chinnasamy et al. [7]	LA – LA/CuO, LA/Fe$_3$O$_4$, LA/SiC, LA/Al$_2$O$_3$	95%/5%	22.1	217 – 193.4, 185.3, 191.1, 185.3	0.4 – 52.2%, 9.8%, 17.9%, 29.1%	-	-	-
Temel et al. [8]	A82 – A82/ZnO, A82/TiO$_2$, A82/Al$_2$O$_3$, A82/MgO, A82/MWCNTs, A82/GNP	95%/5%	70.8	159 – 229, 147, 148, 139, 149, 150	0.31– 2.6%, 3.6%, 6.5%, 8.4%, 26.7%, 155%	-	-	-
Fan et al. [9]	PW – PW/S-MWCNTs, PW/L-MWCNTs, PW/CNFs, PW/GNPs	95%/5%	58.8	207 – 178, 177, 185, 187	0.263 – 23%, 17%, 16%, 166%	-	-	-
Goli et al. [10]	PW – PW/Hybride Graphene	80%/20%	-	-	0.25 – 45 (W/mK)	5A	43	13
Grosu et al. [11]	PW – PW/Cu-Mg-Zn	50%/50%	46.7	72.2 –	0.5 – 2.11 (W/mK)	2C	32.5	7.8
Zang et al. [12]	PW – PW/CNTs/BN	69%/1%/30%	52.5	150 – 60.7	0.24 – 0.69 (W/mK)	2C	52.8	-
Zou et al. [13]	PW – PW/Graph./MWCNTs/ EG		46.1	224.8– 178.5	0.38 – 5.1 (W/mK)	3C	44.6	0.8
Jiang et al. [14]	PW – PW/EG	70%/30%	42.9	275– 193	0.2 – 13.9 (W/mK)	5C	44	-
Chen et al. [15]	PW – PW/EG/FLG/GNP	88%/9%/1%/ 2%	54.5	210–179.5	0.28-0.74 (W/mK)	2C	48.9	2.1
Ma et al. [16]	Docasane – Docasane/Cu/EG	83.3%/2%/ 14.7%	43.9	205	1.18– 1.98 (W/mK)	2C	45.6	0.8
Xu et al. [17]	PW – PW/GNP/EG	76% /5%/19%	53.1	207 – 159.1	–	15W	60	-
Chen et al. [18]	PW – PW/SiC/EG	80%/10%/ 10%	45.5	155 – 122	0.28 – 4.09 (W/mK)	2C	39.3	7.8
Zhang et al. [19]	PW – PW/EG/Kaolin	80%/10% /10%	41.6	210.9– 165.2	0.40 – 7.5 (W/mK)	2C	40	3.5
Wang et al. [20]	PW – PW/Al foam	-	-	-	-	1C	26.1	-
Hussain et al. [21]	PW – PW/Nickel foam	-	-	-	0.2 – 1.16 (W/mK)	1.5C	41	0.8
Rao et al. [22]	PW – PW/Cu foam	-	37	180	0.2 – (W/mK)	5C	42	4.1
Dey et al. [23]	PEG – PEG/Al Fin	2 Fin	-	-	-	4C	34	0.8
Heyhat et al. [24]	n-Eicosane – n-Eicosane/Cu Fin	5 Fin	36.5	-	0.42 – (W/mK)	9.2 W	73	5
Moaveni et al. [25]	RT-44 – RT-44/Al Fin	4 Fin	41	270	0.2 – (W/mK)	4C	61	-
Wang et al. [26]	PW – PW/Al Fin	8 Fin	41	255	0.15 – (W/mK)	8W	52	-

In the literature, it has been shown that the low thermal conductivity of PCMs can be improved by doping metal/metal oxide nanoparticles at certain percentages. Chinnasamy et al. [7] reported enhancements in the thermal conductivity of PCM doped with 5% by mass of Al_2O_3, CuO, Fe_3O_4, and SiC nanoparticles as 29.1%, 52.2%, 9.8%, and 17.9%, respectively. In contrast, improvements in the thermal conductivity of PCMs doped with carbon-based nanoparticles have been reported to reach several-fold increases [8]. However, it is also known that the shape of the carbon-based nanoparticles plays a critical role in determining the effectiveness of the thermal conductivity improvement. Fan et al. [9] found that plate-shaped nanoparticles offer better improvements compared to tube- or thread-shaped nanoparticles. Similarly, Temel et al. [8] demonstrated that doping with 5% multi-walled carbon nanotubes resulted in a 26.7% increase in PCM thermal conductivity, while graphene nanoparticle doping at the same concentration achieved a remarkable 155% improvement.

In the literature, studies on the use of PCM/Nanoparticle composites for thermal protection purposes are generally focused on the thermal protection of batteries. When Table 1 is examined, the protection performances have been improved with thermally improved composites by doping different types of nanoparticles into paraffin type PCM. It is seen that the studies carried out in recent years are generally orientated towards the doping of more than one nanoparticle into paraffin as a hybrid. Zang et al. [12] doped carbon nanotubes (CNTs) and boron nitride (BN) within paraffin, Zou et al. [13] doped graphene (GNP), multi-walled carbon nanotubes (MWCNTs) and expanded graphite (EG) within paraffin, Chen et al. [18] doped EG and silicon carbide (SiC) in paraffin and investigated the thermal protection performances of the composite obtained by doping in terms of maximum temperature and maximum temperature difference. Similarly, Chen et al. [15] doped expanded graphite (EG), graphene nanoparticles (GNP) and few-layer graphene (FLG) hybrid nanoparticles into paraffin. They measured the maximum temperature and maximum temperature difference of the battery cell as 48.9 °C and 2.1 °C at 2C discharge rate. The most significant drawbacks of this approach are the high cost of nanoparticles and the adverse impact of enhanced liquid PCM viscosity following nanoparticle doping on heat transfer.

Another method discussed in the literature for the thermal protection of electronic components is the use of composites made by encapsulating PCM in the pores of porous structures with high thermal conductivity. Metal foams such as aluminium, nickel and copper are commonly used as base materials for this purpose. The thermal protection performance of these materials, which combine high thermal conductivity with heat storage capacity, is

summarised in Table 1. Wang et al. [20] reported that the maximum temperature for aluminum foam/paraffin composite was 26.1 $^{\circ}$C at 1C discharge rate. Similarly, Hussain et al. [21] reported that nickel foam/paraffin composite can maintain the maximum temperature at 41 $^{\circ}$C and the maximum temperature difference at 0.8 $^{\circ}$C at a discharge rate of 1.5C. Rao et al. [22] determined the maximum temperature and temperature difference of copper foam/paraffin composite as 42 $^{\circ}$C and 4.1 $^{\circ}$C, respectively, at a higher discharge rate of 5C. Based on the discharge rates, it is clear that aluminium and copper foams provide better thermal protection than nickel foam due to their superior thermal conductivity. While this method provides effective thermal protection, its utility is limited by the relatively small amount of PCM that can be encapsulated within the pores, which significantly reduces the duration of its effectiveness.

In another approach, metal inserts with high thermal conductivity, such as fins and pins, have been proposed to increase the heat transfer rate from the heat source to the inner regions of the phase change material (PCM). Nevertheless, the simplicity of implementation and the relatively low cost of this approach represent significant advantages. These studies were generally carried out to compare the number of fins, fin thickness, fin angle, fin length and heating direction. Hosseinizadeh et al. [27] determined that increasing the number of fins and fin length increases the thermal energy storage performance. In a study conducted by Acır et al. [28], the effects of the number of fins and fin thickness on PCM melting performance in a top-heated thermal energy storage unit were investigated. The results demonstrated that an increase in fin number has a positive effect on melting performance, whereas an increase in fin thickness has a negative effect. Tian et al. [29] conducted a numerical study to investigate the effects of materials such as aluminum, copper, and steel used as fins in an energy storage unit on melting. They determined that aluminum is the most suitable material in terms of Nusselt number, melting time, total stored energy, stored energy per mass, and cost per stored energy. Huang et al. [30] reported that increasing the number of fins in an energy storage unit makes the temperature distribution more homogeneous. When the studies on Fin/PCM thermal protection are examined in Table 1, it is seen that the effects of heat loads and number of fins are focused. Moaveni et al. [25] reported that the protection system with 4 aluminum fins equipped in RT-44 can keep the maximum temperature around 61 $^{\circ}$C at 4C discharge rate. Heyhat et al. [24] reported that 5 copper finned shielding systems equipped in n-Eicosane can maintain the maximum temperature and maximum temperature difference at 73 $^{\circ}$C and 5 $^{\circ}$C, respectively, under 9.2 W heat load. Wang et al. [26] showed that the paraffin protection system with 8 aluminum fins can reduce the maximum temperature up to 52 $^{\circ}$C under 8 W heat load. However,

it can be said that the use of fins causes an increase in weight and prevents natural convection currents according to the placement position.

A review of the above studies reveals that various techniques have been employed to enhance the thermal performance of PCMs. It is evident that these techniques provide performance improvements depending on the specific application. However, each technique has been studied under varying conditions, including nanoparticle type and concentration, fin material and quantity, and heating load. This lack of standardization has resulted in a gap in systematic comparisons of thermal protection performance. In addition, since it is not economical to use more than one nanoparticle as hybrid thermal protection in Nanoparticle/PCM thermal protection systems, there is a need to develop a lower cost hybrid thermal protection method. However, it can be said that there are not enough studies on the systematic comparison of these methods. Therefore, this study mainly involves comparing different thermal improvement methods of PCM-based thermal protection of a transient operating and heat-releasing electronic device scenario. In order to achieve this scenario, a vertical cylindrical resistance is encased in a PCM material, which serves as a thermal protection medium. As such, the experimental setup represents a battery cell that releases heat. The thermal response of the Resistance/PCM system with respect to time was measured in response to the heat released from the resistance. The objective of this study is to compare the thermal protection capabilities of PCM materials that have undergone fins and/or nanoparticle adding. For this purpose, the thermal responses of PCM with 3, 4 and 6 fins and PCM doped with 1%, 3% and 5% Graphene Nanoparticles (GNP) were analyzed. The study also investigated the performance and usability of a more economical Nanoparticle/Fin/PCM hybrid thermal protection.

2   MATERIAL AND METHOD

RT-44 organic phase change material (PCM) commercially available from Rubitherm (Germany) was used as thermal energy storage material. The transient electronic device was represented by a cylindrical resistance with a diameter of 0.018 m and a height of 0.065 m. Consequently, a representative battery cell is constructed, which is capable of releasing heat temporarily. To provide PCM-based thermal protection, the mentioned resistance was mounted on the axis of a larger diameter and 0.1 m high acrylic tube by screwing it from the bottom side (Figure 1). Thermocouples labeled T_1, T_2, and T_3, were brought into contact with the surface to measure the temperature at three different points along the resistor. Liquid PCM was poured

into the acrylic tube surrounding the resistance and left to solidify at room temperature to form the resistance-PCM system.
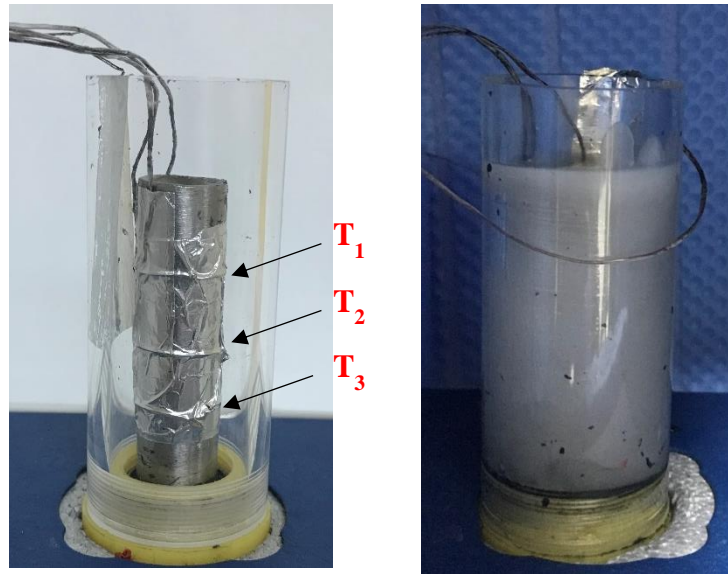
Figure 1. Resistance-PCM system.

Ping et al. [31] reported that the optimum fin thickness for thermal protection of li-ion battery cells in terms of maximum temperature and difference is 1 mm. Therefore, in this study, 1 mm thick aluminum fins were used to improve the thermal protection performance of PCM. The aluminum fins at the height of the resistance were tightly in contact with one end of the resistance, while the other end extended radially to the wall of the acrylic tube. As shown in Figure 2, different fin arrangements were realized as 3, 4 and 6 fins so that the angles between the fins were 120º (3 Fins - 3F), 90º (4 Fins - 4F) and 60º (6 Fins - 6F) respectively. Considering the studies in the literature, it is seen that variable fin numbers are used from 2 fins protection [23] to 8 fins protection [26]. Essentially, it is evident that increasing the number of fins will be effective in reducing the maximum temperature on the battery surface and achieving a more uniform temperature distribution. In their numerical study, Turkakar et al. [32] demonstrated that a 12-fin system at a 3C discharge rate maintained the average temperature on the battery surface 15 °C lower compared to the case without any thermal protection. However, the increase in the number of fins is restricted to situations where weight increase and reduction of the PCM amount are not desired. For example, for battery packs such as in this study, the increase in the number of fins should be limited due to the increase in weight. For this reason, 3, 4 and 6 fins were selected as the number of fins in this study. The resistance/Fin/PCM thermal protection system was formed by pouring the molten PCM into the acrylic tube and allowing it to solidify at room temperature.
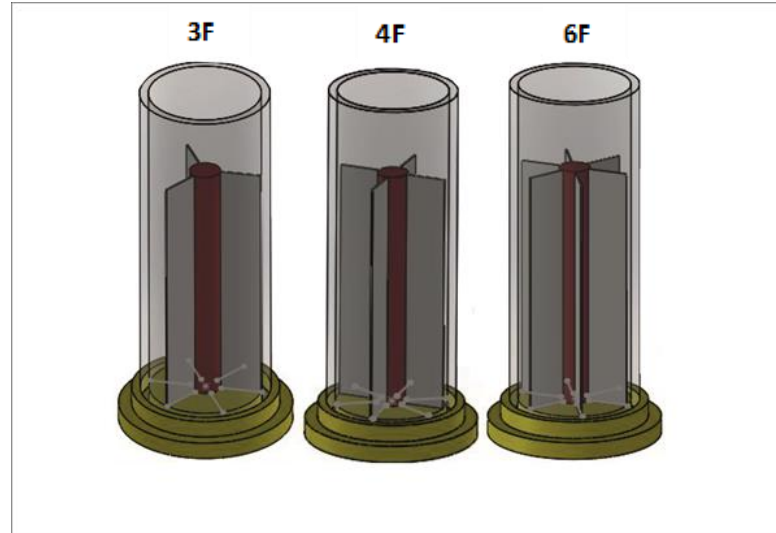
Figure 2. Fin arrangements with 3, 4 and 6 fins.

The other method used for thermal improvement in the study is the improvement of PCM low thermal conductivity with nanoparticle additives. For this purpose, plate-type GNP with high thermal conductivity and low density was used as an additive. GNP/PCM composites were synthesized by doping GNP at 1%, 3%, and 5% by mass into liquid PCM melted on a heater. The rationale for limiting the nanoparticle mass fraction to a maximum of 5% is based on the observation that an additional increase in PCM viscosity in the liquid state hurts heat transfer. The GNP nanoparticles in the PCM were mixed using a 750 W probe type ultrasonic mixer (Sonics & Materials INC, USA) for a period of 30 minutes. A mixing time of 30 minutes is sufficient to achieve a homogeneous dispersion of the nanoparticles in the PCM [33]. The resulting homogenous liquid GNP/PCM composites were poured into the region between the resistance and the tube and allowed to solidify at room temperature, thus forming a nanoparticle/PCM thermal protection system.

In this study, the thermal characterization of PCMs doped with GNP at 0% (only PCM), 1%, 3%, and 5% by mass was also obtained. For this purpose, the thermal conductivities of both PCM and GNP/PCM composites were measured using a KD2 Pro device (Decagon Devices Inc, USA) operating on the principle of transient linear heat source. Thermal conductivity measurements were carried out at different temperatures in an air conditioning cabinet (Jeiotech, South Korea) using samples prepared in accordance with the sensor inlet of the device. The accuracy of the KD2 Pro is ±0.02 W/mK for the range of 0.1-0.2 Wm/K and at least five measurements were taken for each sample and the average values were recorded with a standard deviation of 0.5%. Thermal properties such as melting temperature, latent heat of

melting was measured using a differential scanning calorimeter (DSC-60 Shimadzu Corporation, Japan). Mass-sensitive DSC samples were determined with an electronic weighing scale with an accuracy of 0.01 and samples were formed by confining them in a special container. In accordance with the expected melting temperature of the PCM used, the scan temperature range was set to 20 ºC - 60 ºC and the rate of climb was set to 2 ºC/min. The accuracy of the DSC device was 0.1 ºC and at least three measurements were performed for each sample and the average values were recorded with a standard deviation of 1%.

Thermal protection performance comparisons of differently enhanced PCMs were performed using the experimental setup shown in Figure 3. This setup consists of a DC power supply, data acquisition device, computer, air conditioning cabinet, and resistance-PCM system. The resistance-PCM systems with different thermal improvements were placed in an air conditioning cabinet and thermal response measurements were carried out under the same ambient conditions (20 ºC). The resistance was operated at 3 W and 6 W heating powers by using a DC power supply and adjusting the current to generate the heat-releasing source. Hemery et al. [34] reported that the heating powers of 0.14 W, 0.30 W, 1.30 W and 2.75 W for the resistance used as representative battery cell correspond to 0.5C, 1C, 2C and 3C discharge rates, respectively, for a real battery cell. In this case, it is clear that the selected heating powers will correspond to medium and extreme discharge rates.

Figure 3. Experimental setup used for thermal performance tests.

The temperature data at the measurement points shown in Figure 1 were measured instantaneously using J-type thermocouples. The temperature values were collected using a data logger device that measured the temperature every 30 seconds and recorded the data on a computer. The behavior of the temperatures obtained for each thermal protection method was compared with respect to time. Performance evaluations were conducted with consideration of specific criteria, including maximum temperature and maximum temperature difference. In the case of electronic components, the maximum temperature below 50 °C and the maximum temperature difference along the component below 5 °C were desired conditions.

3   RESULTS AND DISCUSSION

Temperature dependent thermal conductivity measurements for both the solid and liquid phases are shown in Figure 4. The thermal conductivity of the organic phase change material RT-44 was measured to be 0.387 W/mK at 10 °C. In the solid state, the thermal conductivity was measured to be 0.364 W/mK at 20 °C and 0.356 W/mK at 30 °C. This slight decrease in thermal conductivity can be attributed to the increase in molecular disorder with increasing temperature. At 40 °C the thermal conductivity could not be measured due to the inability of RT-44 to maintain a stable form. Upon transitioning to the liquid phase, disruptions in molecular order, such as the breakdown of lattice structures, result in a sharp decrease in thermal conductivity. The thermal conductivity values in the liquid state were recorded as 0.153 W/mK, 0.151 W/mK, and 0.148 W/mK at 50 °C, 60 °C, and 70 °C, respectively. This indicates a 59% reduction in thermal conductivity during the phase transition from solid to liquid for RT-44. A similar result was obtained in another study [35] for RT-64 with a reduction of around 41%.

The phenomenon of thermal conductivity is dependent upon the process of phonon scattering, which is in turn influenced by the lattice size and the vibrational frequency of the crystals in question. The low vibrational frequency of PCM results in a reduction in thermal conductivity, whereas the high vibrational frequency of GNP gives rise to an increase in thermal conductivity. Phonon scattering occurs along the GNP plane, rather than perpendicular to it [36]. It can thus be posited that the formation of network structures comprising the combination of GNP planes in PCM with low thermal conductivity will result in an enhancement of thermal conductivity. The formation of these network structures is directly proportional to the ratio of GNP doped into the PCM. For instance, the thermal conductivity of PCMs doped with 1%, 3%, and 5% GNP in the solid phase at 20 °C exhibited 35.9%, 119.2%, and 178.6% improvements, respectively. Similarly, enhancements of 18.5%, 55.6%, and 89.5% were observed in the

thermal conductivities of PCMs doped with 1%, 3%, and 5% GNP for the liquid phase at 50 °C, respectively. It can be reasonably assumed that similar improvements would be observed at other temperatures for both the solid and liquid phases. It was noted that the results were consistent with those reported in the literature. Kim et al. [37] achieved a 207% improvement in the solid state thermal conductivity of a 7% xGNP/PCM composite.
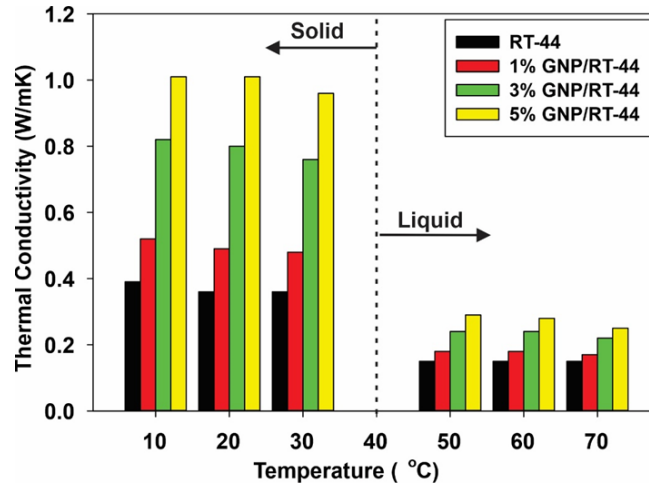
Figure 4. Thermal conductivity coefficients of RT-44 and GNP/RT-44 composites.

The DSC properties of RT-44 and GNP/RT-44 (1%, 3% and 5%) composites such as onset melting temperature (T_{om}), endset melting temperature (T_{em}), and melting latent heat (H_m) were determined by analyzing the endotherm curves given in Figure 5. The separation and junction points of these curves from the baseline give the onset melting temperature (T_{om}) and endset melting (T_{em}) temperatures, respectively. The area between the endotherm curve and the baseline is a measure of the melting latent heat of melt (H_m).
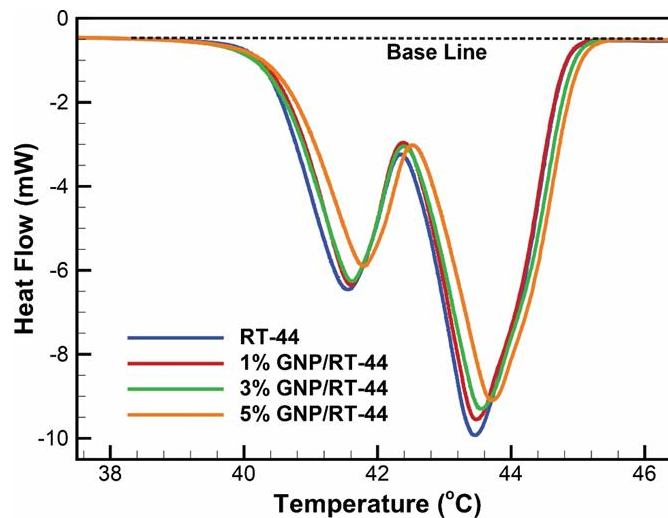
Figure 5. The endotherm curves of the RT-44 and GNP/RT-44 composites.

From the analysis of the endothermic curve for RT-44, the onset melting temperature (T_{om}) and endset melting temperature (T_{em}) were determined to be 40.36 °C and 44.73 °C, respectively, while the latent heat (H_m) was measured as 239.2 J/g. When 1%, 3% and 5% GNP is added to RT-44, T_{om} and T_{em} temperatures and H_m values are given quantitatively in Table 2. It is seen that GNP addition does not affect the melting onset and melting endset temperatures. On the other hand, it was determined that the latent heat of melting decreased depending on the amount of GNP addition. For example, the latent heat of melt for 5% GNP/RT-44 composite was measured as 226.3 J/g, which is a deterioration of 5.4% compared to RT-44. Essentially, this is an expected result due to the mixture of a material with high energy storage capability and a material with low energy storage capability. Similar results regarding the decreasing of the latent heat of melting with the addition of nanoparticles to the PCM have been reported in the literature. For example, Chen et al. [36], reported that when 5% GNP was added to paraffin with a latent heat of 144 J/g, the reduction in the latent heat of melting was approximately 16%. In this case, the partly lower latent heat of the paraffin employed may have resulted in a more pronounced reduction. However, the loss in latent heat is negligible in the face of the considerable improvement in thermal conductivity achieved with GNP doping.

Table 2. DSC properties of RT-44 and GNP/RT-44 composites.

Composite	T_{om} (°C)	T_{em}(°C)	H_m (J/g)
RT-44	40.26	44.73	239.2
1% GNP/RT-44	40.18	44.76	237.7
3% GNP/RT-44	40.11	44.81	235.4
5% GNP/RT-44	40.34	44.63	226.3

In the next phase of the study, performance tests were carried out to evaluate the effect of the PCM thickness of the PCM surrounding the resistance on the thermal protection. Acrylic tubes of three different diameters were used to create PCM thicknesses of 6 mm, 9 mm and 11 mm around the resistance.
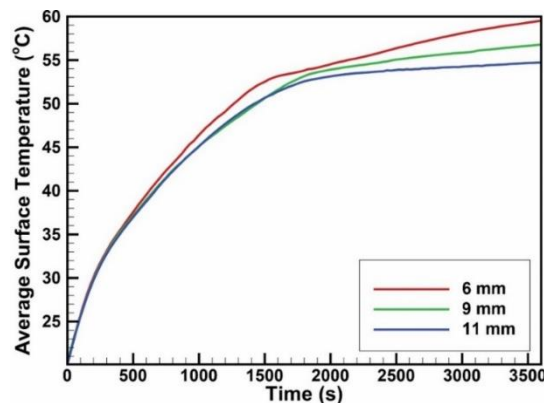
Figure 6. Variation of average surface temperature at different PCM thicknesses.

Figure 6 illustrates the variation in the mean surface temperature of the resistance over time for PCM thicknesses of 6, 9 and 11 mm. The reduction in temperature rise resulting from an increase in PCM thickness provides evidence that the thermal protection performance will be enhanced with greater PCM thickness. Below 40.26 °C, the temperature rise during sensible heat storage of PCM is almost independent of PCM thickness. Above 44.73 °C, it is determined that PCM thickness affects thermal protection as the PCM becomes liquid. The reason for this is that the conduction-dominant heat transfer mechanism (heat transfer is mostly by conduction) is effective in solid PCM and the convection-dominant (heat transfer is mostly by convection) heat transfer mechanism is effective in liquid PCM. It is seen that increasing the PCM thickness in a liquid state, where the convection-dominant heat transfer mechanism is effective, significantly reduces the temperature rise. In case of using 11 mm PCM thickness, the temperature remains almost constant from 1500th second. In other words, increasing the PCM thickness cannot have an extra effect. For this reason, it was deemed appropriate to use 11 mm as the optimum PCM thickness in the study. In their numerical study, Dincer et al. [38] concluded that the optimum PCM thickness around the li-ion cell is 9 mm in terms of maximum surface temperature.

Figure 7. Variation of Maximum Temperature and Maximum Temperature Difference with time for RT-44.

The thermal protection performance of 3 W and 6 W heat-emitting resistances with 11 mm thick RT-44 is evaluated in Figure 7, based on the criteria of maximum surface temperature and maximum surface temperature difference. The upper region of the resistance is the maximum and the lower region is the minimum temperature region. With the onset of phase change, a decrease in density occurs in the liquid state as the temperature rises. This situation allows the low density hot liquid to move upwards. In other words, buoyancy movements start with the exposure of the liquid to temperature increase. As a result of the continuous upward

movement of heat by buoyancy movements, a significant temperature difference occurs between the upper and lower region of the resistance. Due to the low thermal conductivity of RT-44 organic PCM, a rapid temperature increase occurs initially on the surface of the resistor due to the inability to transfer the heat released in the resistor to the inner region of the PCM. In other words, the principal mechanism of heat transfer in the resistance/RT-44 system is conduction.

At 3 W heating power, the maximum temperature was observed to reach 44.7 °C at the end of 3600 seconds. It can thus be stated that the phase change is still in its initial stage, as the melting endset temperature of RT-44 has not yet been reached. In such a case, it can be stated that the energy released from the heat source is fully stored by the PCM as sensible (heat storage based on temperature change) heat. The deceleration in temperature increases at 3 W heating power is attributable to the resistance/PCM system achieving thermal equilibrium with its surrounding environment. In terms of limiting the maximum temperature, it is a sufficient condition that the temperature value remains below 50 °C. The maximum surface temperature difference exhibited a similar behavior, with a maximum temperature difference of 5.8 °C at the end of 3600 seconds. Considering that the maximum surface temperature difference below 5 °C on the thermally protected component is the expected performance criterion, it can be said that RT-44 thermal protection alone is not sufficient.

The conduction-dominant heat transfer mechanism, initially effective at 6 W heating power, facilitates a faster temperature rise due to the low PCM thermal conductivity and high heating rate. In addition, the liquid layer formed around the heating source with the onset of phase change has two effects that support the temperature increase in the maximum temperature region. The first of these is the decrease in the conduction rate due to the lower thermal conductivity of the liquid RT-44 (approximately 0.150 W/mK). In other words, due to the low thermal conductivity in the liquid state, the slowing of the heat transfer in the radial direction to the PCM depths of conduction causes the temperature increase on the resistance surface. The second is the transfer of heat to the upper region of the resistance due to the effect of upward buoyancy currents that start with the increase in the liquid layer thickness sufficiently. As a result of the mentioned effects, the temperature increase in the upper region leads to the expansion of the liquid RT-44. The gradual weakening of heat conduction and the strengthening of buoyancy currents ensure that the dominant heat transfer mechanism returns to convection. The fact that the temperature remains almost constant in the maximum temperature region, especially from 1500 seconds onwards, is an indication of this. Similar findings have been

reported in the literature. Wang et al. [39] reported that when the PCM melting front intersects the upper region of the enclosure wall, the heating power on the resistor is balanced and the temperature remains constant as a result of the acceleration of convective heat transfer between the resistor and the enclosure wall. At 6 W heating power, the maximum surface temperature was measured as 58.8 °C at the end of 3600 seconds. Until the convection dominant heat transfer is effective, the maximum surface temperature difference increases continuously. So much so that the maximum surface temperature difference reaches up to 11 °C at 1618 seconds. From this moment on, the temperature difference slows down significantly because the maximum temperature zone in the upper region of the resistor remains approximately constant and the minimum temperature zone in the lower region of the resistance continues to increase. At the end of 3600 seconds, the maximum temperature difference was measured as 8.4 °C and it was determined that the power increase in the RT-44 thermal protection negatively affected the maximum surface temperature difference. It was determined that RT-44 thermal protection at 6 W heating power could not provide sufficient protection due to exceeding the maximum temperature and maximum temperature difference limit values (50 °C and 5 °C).
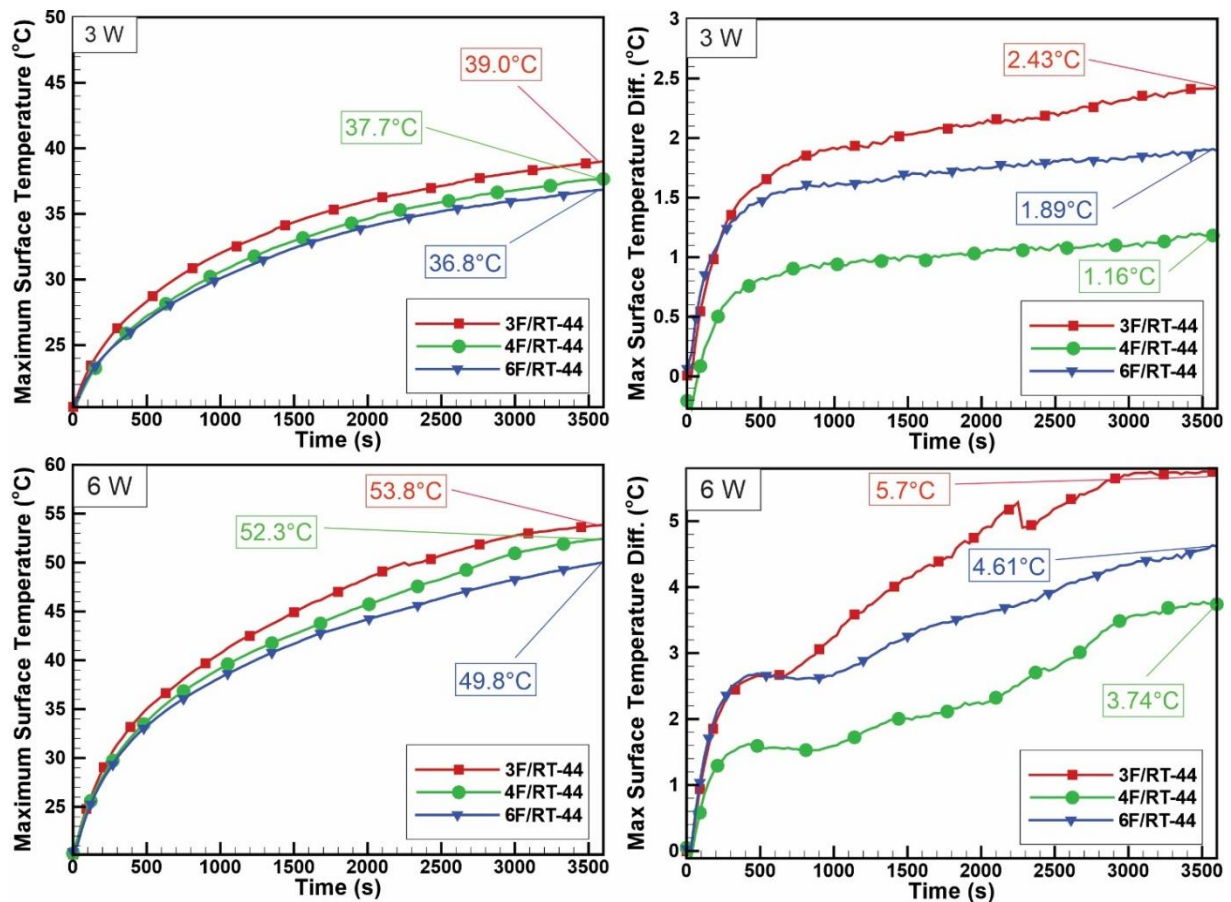
Figure 8. Variation of Maximum Temperature and Maximum Temperature Difference with time for Fins/RT-44 arrangements.

The thermal protection performances of the resistance/PCM system equipped with 3, 4, and 6 fins at 3 W and 6 W heating powers are evaluated in Figure 8 by considering the maximum surface temperature and maximum surface temperature difference criteria. At 3W heating power, it is observed that the time variation of the maximum temperature increase on the resistance slows down due to the increasing number of fins. In this case, it is clear that the heat released on the resistance is removed from the surface and transferred to the RT-44 by interacting with it in the radial direction along the fins. The aluminum fins with high thermal conductivity form thermal bridges for very fast heat transfer. Due to being below the RT-44 phase change temperature for 3600 seconds at 3 W heating power, the heat emitted from the resistance fin component is sensibly stored in the RT-44. At the end of 3600 seconds, the maximum temperature on the resistance in RT-44 thermal protection was 44.7 °C, while the maximum temperatures for the 3, 4 and 6 fins resistance system were measured as 39.0 °C, 37.7 °C and 36.8 °C, respectively. In this case, in terms of m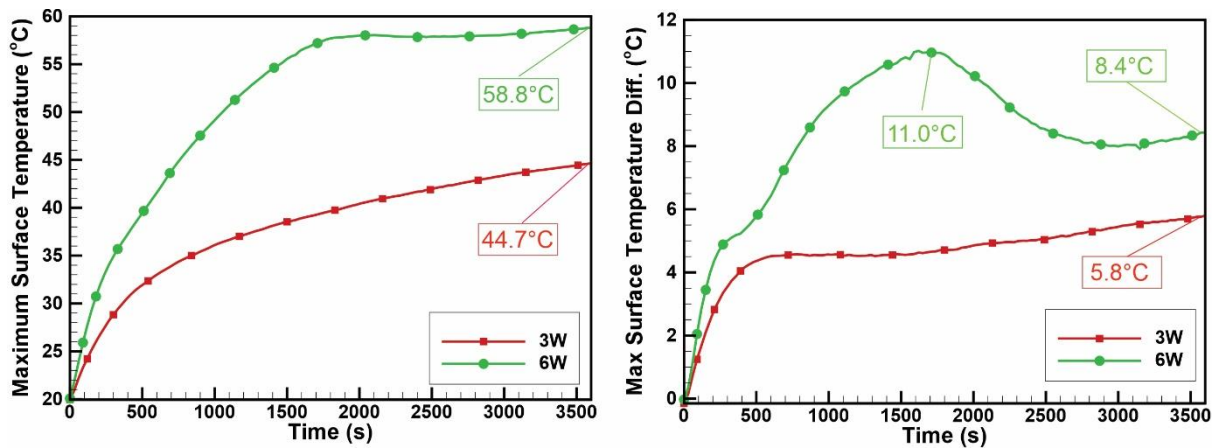aximum surface temperature, RT-44 thermal protection with 3, 4 and 6 fins provide 12.8%, 15.7% and 17.7% performance improvements respectively. In terms of maximum surface temperature difference, it is an optimal design criterion that the temperature difference on the thermally protected component is below 5 °C. It can be stated that the RT-44 thermal protections with 3, 4, and 6 fins have been effective in maintaining a maximum temperature difference below 5 °C. Additionally, the maximum surface temperature differences were found to be 2.4 °C, 1.2 °C and 1.9 °C for the 3, 4 and 6-fins/RT-44, respectively. Given that the maximum surface temperature difference for the RT-44 thermal protection system is 5.8 °C, the performance improvements of the 3, 4 and 6 fins/RT-44 system in comparison to the RT-44 thermal protection system are determined to be 58.6%, 79.3% and 67.2%, respectively.

At 6 W heating power, the deceleration in the maximum temperature increase depending on the number of fins is more pronounced. While the maximum temperature was 58.8 °C at the end of 3600 seconds in RT-44 thermal protection, the maximum temperatures in RT-44 thermal protection with 3, 4, and 6 fins were measured as 53.8 °C, 52.3 °C and 49.8 °C respectively. In other words, compared to RT-44, RT-44 thermal protection with 3, 4, and 6 fins provides 8.5%, 11.1%, and 15.3% performance improvement respectively. It was noted that the results obtained were compatible with those found in the literature. Wang et al.[39] found that the protection system with 4 copper fins at 6 W heating power reduced the maximum temperature by approximately 6 °C. On the other hand, in this study, the maximum temperature limitation was measured as 6.5 °C using aluminum fins under the same conditions. In terms of maximum

temperature difference, it is seen that the temperature difference has a continuously increasing trend. While the maximum surface temperature difference at the end of 3600 seconds in RT-44 thermal protection is 8.4 °C, the maximum surface temperature differences in RT-44 protection systems with 3, 4, and 6 fins are measured as 5.7 °C, 3.7 °C and 4.6 °C, respectively. In this case, it is determined that 3, 4, and 6 fins/RT-44 protections provide 32.1%, 56.0%, and 45.2% performance improvement, respectively, compared to RT-44 thermal protection.
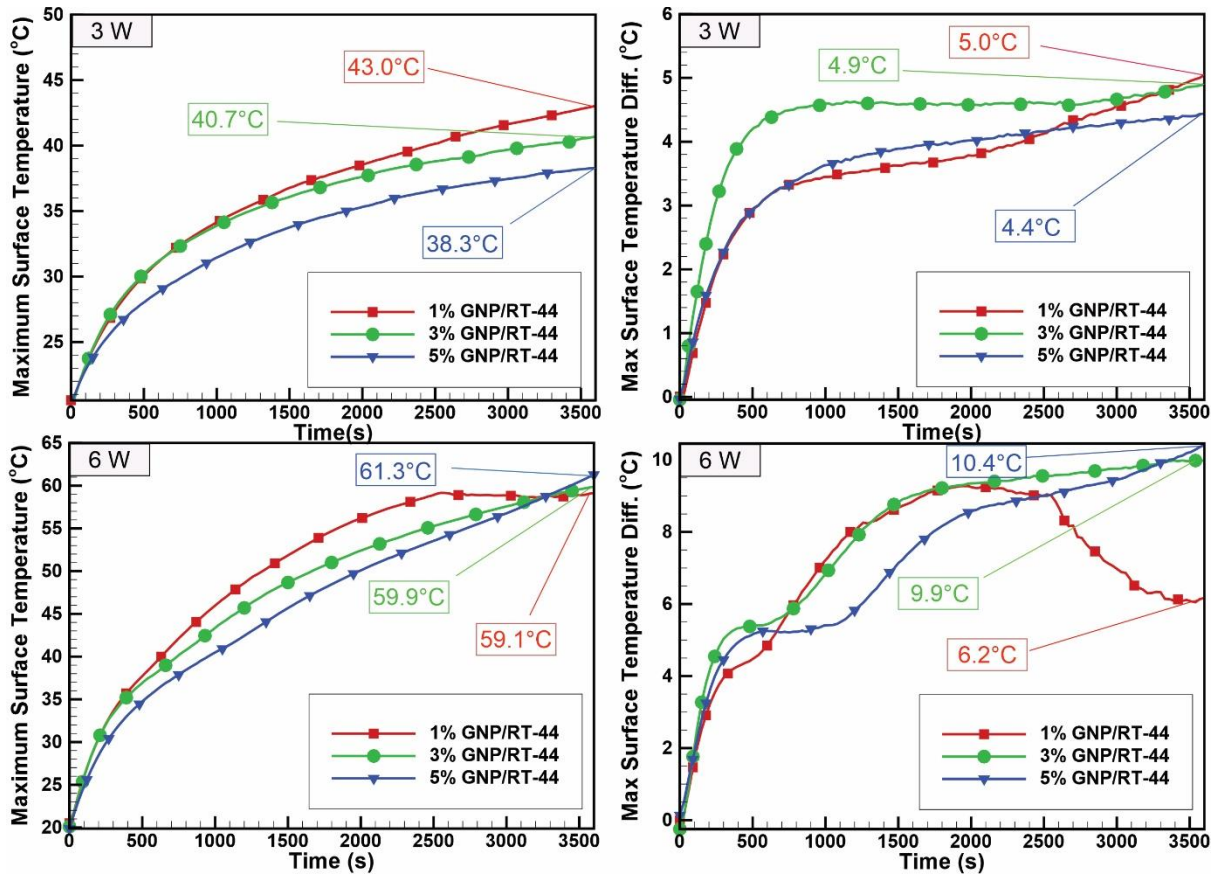
Figure 9. Variation of Maximum Temperature and Maximum Temperature Difference with time for GNP/RT-44 composites.

The thermal protection performances of RT-44 composites doped with 1%, 3%, and 5% GNP at 3 W and 6 W heating powers were evaluated in Figure 9 by considering the maximum surface temperature and maximum surface temperature difference criteria. At 3 W heating power, the rate of sensible heat storage of by RT-44 below the phase change temperature increases. For RT-44 composites doped with 1%, 3% and 5% GNP, the maximum surface temperatures at the end of 3600 seconds were measured as 43 °C, 40.7 °C and 38.3 °C, respectively. In other words, it was determined that the thermal protection performances of 1%, 3% and 5% GNP doped RT-44 composites were improved by 3.8%, 8.9% and 14.3% compared to RT-44 thermal protection in terms of limiting the maximum surface temperature. It is seen

that GNP nanoparticle doping in RT-44 has a decreasing effect on the maximum surface temperature difference. While the maximum surface temperature difference at the end of 3600 seconds for RT-44 thermal protection was 5.8 ^{o}C, the maximum surface temperature differences in RT-44 composites doped with 1%, 3% and 5% GNP nanoparticles were measured as 5.0 ^{o}C, 4.9 ^{o}C and 4.4 ^{o}C, respectively. It was determined that the maximum surface temperature difference performances compared to RT-44 were improved by 13.8%, 15.5% and 24.1% in 1% GNP/RT-44, 3% GNP/RT-44 and 5% GNP/RT-44 composites respectively.

It can be said that the results obtained are compatible with the results for GNP/PCM thermal protection in the literature. Temel et al.[40] reported that the maximum temperature of 7% GNP/RT-44 composite was limited to 47 ^{o}C as a result of 3600 seconds at 3.90 W heating power in a simulative battery pack. In this study, the maximum temperature was obtained as 38.3 ^{o}C with 5% GNP/RT-44 at 3 W heating power for the same period, while in the other study the maximum temperature was measured as 47 ^{o}C with 7% GNP/RT-44. This difference can be explained as follows; i) Higher heating power (3.90 W), ii) Contribution of neighboring cells to heating in battery pack, iii) 7% GNP/RT-44 composite suppresses natural convection movements more than 5% GNP/RT-44.

At 6 W heating power, the maximum temperature exhibits a lower temperature increase compared to RT-44 due to the thermal conductivity improvement effect provided by 1%, 3%, and 5% GNP doping by mass during conduction dominant heat transfer. For example, at the end of 1800 seconds, the maximum temperature on the resistance in RT-44 thermal protection was 57.68 ^{o}C, while the maximum temperatures for RT-44 composites doped with 1%, 3%, and 5% GNP were measured as 54.67 ^{o}C, 51.0 ^{o}C and 48.45 ^{o}C, respectively. In this case, at the end of 1800 seconds, it can be said that the thermal protection performances of 1% GNP/RT-44, 3% GNP/RT-44, and 5% GNP/RT-44 composites are 5.2%, 11.6%, and 16.0% better than RT-44, respectively. However, it is seen that the mentioned thermal protection improvement is lost with the transition to convection-dominated heat transfer. In fact, while the temperature increase remains constant from approximately 2000 seconds in RT-44, it remains constant after 2585 seconds in 1% GNP/RT-44. On the other hand, in RT-44 composites doped with 3% and 5% GNP, it is seen that there is no constant temperature change, on the contrary, the temperature continues to increase. The reason for this is that the viscosity increases as the GNP ratio doped into RT-44 increases. The inhibition of buoyancy-driven movements due to increased viscosity slows down the transfer of heat released on the resistance in the liquid phase where the convection dominant heat transfer mechanism is effective. In fact, during convection-

dominated heat transfer, heat transfer slows down because the positive effect of GNP addition above 3% on thermal conductivity is smaller than the negative effect due to the suppression of convection movements. In terms of maximum temperature protection, 3% GNP/RT-44 and 5% GNP/RT-44 composites perform worse than 1% GNP/RT-44 from 3292 and 3270 seconds respectively. At the end of 3600 seconds, the maximum temperature on the resistance in RT-44 thermal protection was 58.74 °C, while the maximum temperatures for RT-44 composites doped with 1%, 3%, and 5% GNP were measured as 59.13 °C, 59.88 °C and 61.27 °C, respectively. In this case, it can be said that the thermal protection performances of 1% GNP/RT-44, 3% GNP/RT-44 and 5% GNP/RT-44 composites deteriorated by 0.7%, 1.9% and 4.3% compared to RT-44 thermal protection. While the maximum surface temperature difference in RT-44 thermal protection at 6 W heating power was 8.4 °C, the maximum surface temperature differences for 1% GNP/RT-44, 3% GNP/RT-44 and 5% GNP/RT-44 composites were measured as 6.2 °C, 9.9 °C and 10.4 °C, respectively. In this case, in terms of maximum surface temperature difference, 1% GNP/RT-44 thermal protection shows 26.9% performance improvement compared to RT-44 thermal protection. On the contrary, 3% GNP/RT-44 and 5% GNP/RT-44 thermal protection show 17.9% and 23.8% worse performance respectively.

If convection-dominated heat transfer mechanism is dominant in RT-44 thermal protection, it is an advantage that the maximum temperature remains constant for a certain period of time. On the other hand, the increase in the temperature difference between the upper and lower region due to buoyancy currents is seen as a disadvantage. The addition of GNP in RT-44 has two effects on the thermal protection performance of the buoyancy currents due to the increase in viscosity. The fact that the amount of GNP doped into RT-44 causes an increase in viscosity in the liquid phase leads to the inhibition of natural convection movements. For this reason, the maximum surface temperature increases continuously when 3% and more GNP is added by mass. This means unfavorable performance in terms of maximum surface temperature. On the other hand, the addition of GNP also has the effect of reducing the maximum temperature difference. In addition to the drawback of increased viscosity, other drawbacks include nanoparticle production is still limited to laboratory scale, the high cost of nanoparticles, and their negative impact on living organisms. For these reasons, keeping the amount of GNP used small is a limiting criterion. Under these limitations, 1% GNP/6F/RT-44 and 3% GNP/6F/RT-44 thermal protection methods were also investigated as a hybrid thermal protection system based on the use of less GNP. However, it has been observed that there were no studies in the literature on the combined use of different protection systems. For this purpose,

maximum surface temperature and maximum surface temperature difference performance measurements of 1% GNP/6F/RT-44 and 3% GNP/6F/RT-44 hybrid thermal protection systems were performed and the results are given in Figure 10.
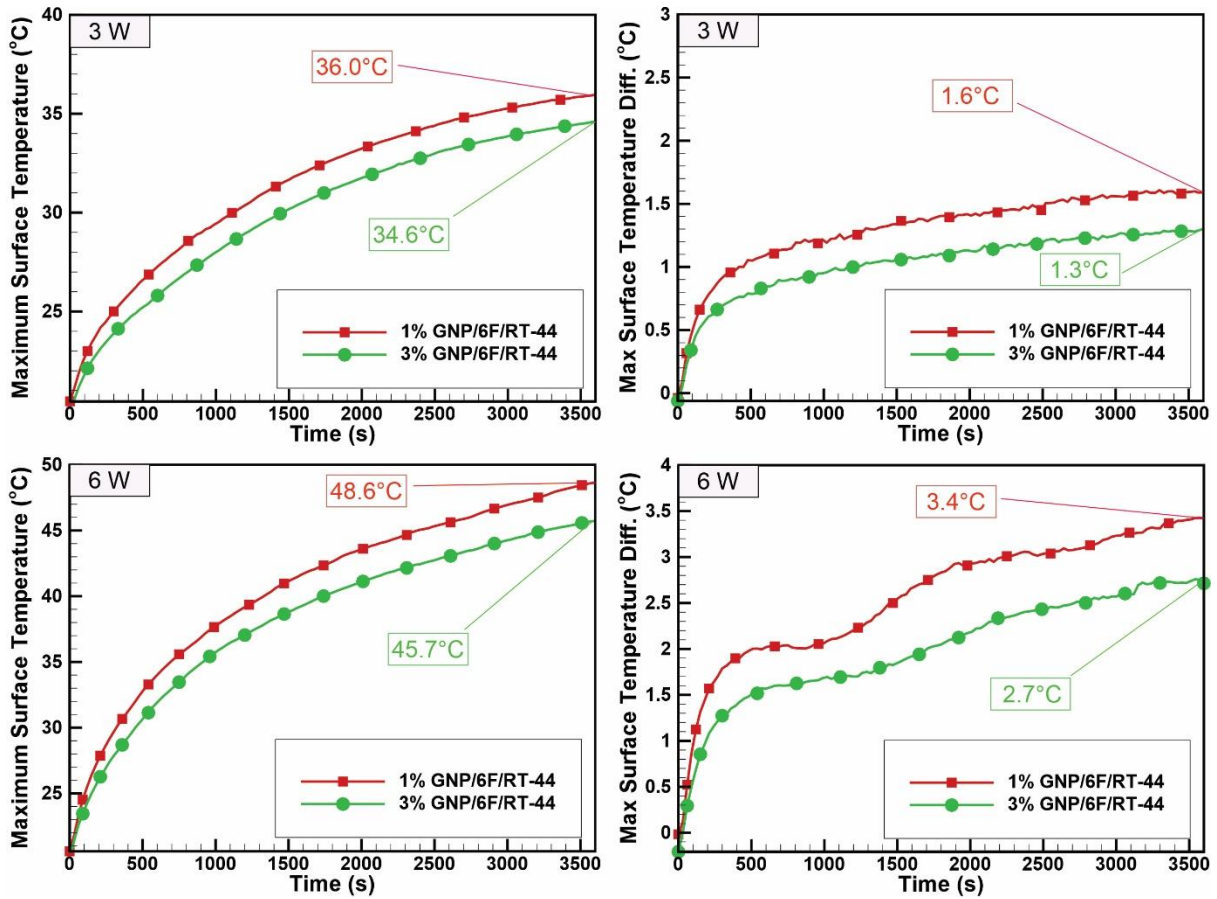
Figure 10. Variation of Maximum Temperature and Maximum Temperature Difference with respect to time for 1%GNP/6F/RT-44%, 3% GNP/6F/RT-44.

At the end of 3600 seconds at 3 W heating power, the maximum surface temperatures were 44.7 °C, 36.8 °C, 43.0 °C, and 40.7 °C for RT-44, 6F/RT-44, 1% GNP/RT-44 and 3% GNP/RT-44 thermal protections, respectively, while the maximum surface temperatures were 36 °C and 34.6 °C for 1% GNP/6F/RT-44 and 3% GNP/6F/RT-44 thermal protections, respectively. In this case, it was determined that the maximum surface temperature performances of 1% GNP/6F/RT-44 and 3% GNP/6F/RT-44 thermal protection could be improved by 19.5% and 22.6%, respectively, compared to RT-44 thermal protection. At the end of 3600 seconds at 3 W heating power, the maximum surface temperature differences were 5.8 °C, 1.9 °C, 5.0 °C and 4.9 °C for RT-44, 6F/RT-44, 1% GNP/RT-44 and 3% GNP/RT-44 thermal protections respectively, while the maximum surface temperature differences were 1.6 °C and 1.3 °C for 1% GNP/6F/RT-44 and 3% GNP/6F/RT-44 thermal protectors respectively. In other

words, compared to RT-44 thermal protection, 1% GNP/6F/RT-44 and 3% GNP/6F/RT-44 hybrid thermal protectors provide 72.4% and 77.6% performance improvement in terms of maximum surface temperature difference, respectively.

At the end of 3600 seconds at 6 W heating power, the maximum surface temperatures for 1% GNP/6F/RT-44 and 3% GNP/6F/RT-44 thermal protectors were measured as 48.6 ºC and 45.7 ºC, respectively. In this case, it was determined that 1% GNP/6F/RT-44 and 3% GNP/6F/RT-44 thermal protectors provided 17.3% and 22.3% improvement respectively compared to RT-44 thermal protection in terms of maximum surface temperature. At the end of 3600 seconds at 6 W heating power, the maximum surface temperature differences for 1% GNP/6F/RT-44 and 3% GNP/6F/RT-44 thermal protectors were measured as 3.4 ºC and 2.7 ºC, respectively. In other words, it was determined that 1% GNP/6F/RT-44 and 3% GNP/6F/RT-44 thermal protectors provided 41.4% and 53.4% improvement, respectively, compared to RT-44 thermal protection in terms of maximum surface temperature difference.

Table 3. Performance improvements over RT-44 thermal protection.

Composite	Max. Temp. Enhancement (%)	Max. Temp. Enhancement (%)	Max. Temp.Diff. Enhancement (%)	Max. Temp. Diff. Enhancement (%)
	3W	6W	3W	6W
RT-44	-	-	-	-
3F/RT-44	12.8	8.5	58.6	32.1
4F/RT-44	15.7	11.1	79.3	56.0
6F/RT-44	17.7	15.3	67.2	45.2
1% GNP/RT-44	3.8	-0.7	13.8	26.9
3% GNP/RT-44	8.9	-1.9	15.5	-17.9
5% GNP/RT-44	14.3	-4.3	24.1	-23.8
1% GNP/6F/RT-44	19.5	17.3	72.4	41.4
3% GNP/6F/RT-44	22.6	22.3	77.6	53.4

Table 3 summarizes the performance changes of all thermal protection methods with respect to RT-44 thermal protection. It has been determined that fin-added protections perform better than nanoparticle-added protections in terms of both maximum temperature and maximum temperature difference constraints. Nanoparticle-added protections are advantageous from the initial moment when heat conduction is dominant until the dominance of convection-dominated heat transfer, which is passed by the onset of buoyancy currents in the liquid phase. In the dominance of convection-dominant heat transfer, nanoparticle-protected thermal methods lose their advantages. With hybrid thermal protection systems, performance

improvements can be increased by 10%. It has been observed that the main contribution in hybrid thermal protection is provided by the fins and the fin/nanoparticle attachment does not create any synergistic effect. As a hybrid thermal protection system, it is determined that it is appropriate to limit the GNP mass fraction to a maximum of 3%. However, for longer protection times (>3600s), the GNP mass fraction should be kept low.

4   CONCLUSION AND SUGGESTIONS

Phase change material-based thermal protection of a heat-releasing system is compared in terms of PCM, fin/PCM, GNP/PCM, and fin/GNP/PCM composites and the results are given below.

- ✓ From the comparison of 6, 9, 11 mm PCM thicknesses in terms of maximum temperature criterion, it was concluded that 11 mm PCM thickness is the appropriate thickness.

- ✓ The thermal conductivities of GNP composites doped with 1%, 3% and 5% GNP were improved by 35.9%, 119.2% and 178.6%, respectively, in the solid phase. In the same case, the improvements obtained for the liquid phase were 18.5%, 55.6% and 89.5%, respectively.

- ✓ While the amount of GNP doped into RT-44 does not cause a significant change in melting temperatures, it causes a decrease in latent heat in proportion to the amount of GNP doped. For 5% GNP/RT-44 composite, this reduction is 5.4%.

- ✓ In RT-44 thermal protection, the maximum temperature and maximum temperature difference are 44.7 ℃ and 5.8 ℃ respectively in case of 3 W heat dissipation, while they are 58.8 ℃ and 8.4 ℃ respectively in the case of 6 W heat dissipation. In this case, considering that the maximum temperature and maximum temperature difference limit values are 50 ℃ and 5 ℃, RT-44 thermal protection alone is not sufficient.

- ✓ Fin/RT-44, GNP/RT-44, and Fin/GNP/RT-44 composites provide sufficient thermal protection in terms of keeping the maximum temperature below 50 ℃ and the maximum temperature difference below 5 ℃ for 3600 seconds at 3 W heating power.

- ✓ At the end of 3600 seconds at 6 W heating power, 3F/RT-44, 4F/RT-44, and 6F/RT-44 thermal protectors have 8.5%, 11.1%, and 15.3% improvement performance over RT-44 thermal protection in terms of maximum temperature restriction, respectively.

Similarly, 3F/RT-44, 4F/RT-44, and 6F/RT-44 thermal protectors have 32.1%, 56.0%, and 45.2% performance improvement over RT-44 thermal protection in terms of maximum temperature difference restriction, respectively.

✓ 6F/RT-44 thermal protection provides successful thermal protection by keeping the maximum temperature at 49.8 ℃ and the maximum temperature difference at 4.6 ℃ after 3600 seconds at 6 W heating power.

✓ The addition of 1%, 3%, and 5% GNP to RT-44 creates an advantage during sensible heat storage and a disadvantage during latent heat storage in terms of thermal protection.

✓ At the end of 3600 seconds at 6 W heating power, 1% GNP/RT-44, 3% GNP/RT-44 and 5% GNP/RT-44 thermal protectors show 0.7%, 1.9% and 4.3% worse performance than RT-44 thermal protection in terms of limiting the maximum temperature, respectively. In terms of limiting the maximum temperature difference compared to RT-444 thermal protection, 1% GNP/RT-44 has 26.9% performance improvement, 3% GNP/RT-44 and 5% GNP/RT-44 have 17.9% and 23.8% performance deterioration respectively.

✓ There is no synergistic effect in the Fin/GNP/RT-44 hybrid thermal protection and the main contribution to the thermal protection performance is provided by the fins.

✓ Fin/GNP/RT-44 hybrid thermal protections have usability when the GNP mass fraction is kept below 3%. At the end of 3600 seconds at 6 W heating power, 1% GNP/6F/RT-44, 3% GNP/6F/RT-44 thermal protections provide 17.3% and 22.3% performance improvement over RT-44 thermal protection in terms of limiting the maximum temperature, respectively. Similarly, 1% GNP/6F/RT-44 and, 3% GNP/6F/RT-44 thermal protections provide 41.4% and 53.4% performance improvement over RT-44 thermal protection in terms of limiting the maximum temperature difference.

The most important disadvantage of further increasing the number of fins is known as weight increase. However, the increase in the number of fins also causes a decrease in the amount of PCM. When the weight increase is ignored, the evaluation of the positive effects of increasing the number of fins (decrease in the amount of PCM) in terms of thermal protection performance criteria can be carried out as a subject of future study.

Conflict of Interest Statement

There is no conflict of interest between the authors.

Statement of Research and Publication Ethics

The study is complied with research and publication ethics.

Artificial Intelligence (AI) Contribution Statement

This manuscript was entirely written, edited, analyzed, and prepared without the assistance of any artificial intelligence (AI) tools. All content, including text, data analysis, and figures, was solely generated by the authors.

Contributions of the Authors

The experimental studies of this study were carried out by Ahmet Can Çapar and Ümit Nazlı Temel. Data analysis and interpretations, manuscript writing and editing were performed by Ümit Nazlı TEMEL.

REFERENCES

[1] A. E. Kabeel, A. Khalil, S. M. Shalaby, and M. E. Zayed, "Experimental investigation of thermal performance of flat and v-corrugated plate solar air heaters with and without PCM as thermal energy storage," *Energy Convers. Manag.*, vol. 113, pp. 264–272, 2016, doi: 10.1016/j.enconman.2016.01.068.

[2] P. Mihálka, C. Lai, S. Wang, and P. Matiaˇ, "Experimental investigation of the daily thermal performance of a mPCM honeycomb wallboard," vol. 159, pp. 419–425, 2018, doi: 10.1016/j.enbuild.2017.10.080.

[3] Y. Galazutdinova, S. Ushak, M. Farid, S. Al-Hallaj, and M. Grágeda, "Development of the inorganic composite phase change materials for passive thermal management of Li-ion batteries: Application," *J. Power Sources*, vol. 491, no. June 2020, 2021, doi: 10.1016/j.jpowsour.2021.229624.

[4] W. L. Cheng, B. J. Mei, Y. N. Liu, Y. H. Huang, and X. D. Yuan, "A novel household refrigerator with shape-stabilized PCM (Phase Change Material) heat storage condensers: An experimental investigation," *Energy*, vol. 36, no. 10, pp. 5797–5804, 2011, doi: 10.1016/j.energy.2011.08.050.

[5] K. Du, J. Calautit, P. Eames, and Y. Wu, "A state-of-the-art review of the application of phase change materials (PCM) in Mobilized-Thermal Energy Storage (M-TES) for recovering low-temperature industrial waste heat (IWH) for distributed heat supply," *Renew. Energy*, vol. 168, pp. 1040–1057, 2021, doi: 10.1016/j.renene.2020.12.057.

[6] D. Mondieig, F. Rajabalee, A. Laprie, H. A. J. Oonk, T. Calvet, and M. A. Cuevas-Diarte, "Protection of temperature sensitive biomedical products using molecular alloys as phase change material," *Transfus. Apher. Sci.*, vol. 28, no. 2, pp. 143–148, 2003, doi: 10.1016/S1473-0502(03)00016-8.

[7] V. Chinnasamy and H. Cho, "Thermophysical investigation of metallic nanocomposite phase change materials for indoor thermal management," *Int. J. Energy Res.*, vol. 46, no. 6, pp. 7626–7641, 2022, doi: 10.1002/er.7664.

[8] Ü. N. Temel and B. Y. Ç. İ. F. T. Ç. İ, "Determination of Thermal Properties of A82 Organic Phase Change Material Embedded with Different Type Nanoparticles List of Seymbols," pp. 75–85, 2018.

[9]   L. W. Fan *et al.*, "Effects of various carbon nanofillers on the thermal conductivity and energy storage properties of paraffin-based nanocomposite phase change materials," *Appl. Energy*, 2013, doi: 10.1016/j.apenergy.2013.04.043.

[10]   P. Goli, S. Legedza, A. Dhar, R. Salgado, J. Renteria, and A. A. Balandin, "Graphene-enhanced hybrid phase change materials for thermal management of Li-ion batteries," *J. Power Sources*, vol. 248, pp. 37–43, 2014, doi: 10.1016/j.jpowsour.2013.08.135.

[11]   Y. Grosu *et al.*, "Hierarchical macro-nanoporous metals for leakage-freeygrosu@cicenergigune.com high-thermal conductivity shape-stabilized phase change materials," *Appl. Energy*, vol. 269, no. April, p. 115088, 2020, doi: 10.1016/j.apenergy.2020.115088.

[12]   B. Zhang, Y. Zhang, K. Li, C. Ma, and B. Yuan, "Novel segregated-structure phase change materials with binary fillers and the application effect in battery thermal management," *J. Energy Storage*, vol. 54, no. June, p. 105336, 2022, doi: 10.1016/j.est.2022.105336.

[13]   D. Zou *et al.*, "Preparation of a novel composite phase change material (PCM) and its locally enhanced heat transfer for power battery module," *Energy Convers. Manag.*, vol. 180, no. September 2018, pp. 1196–1202, 2019, doi: 10.1016/j.enconman.2018.11.064.

[14]   G. Jiang, J. Huang, Y. Fu, M. Cao, and M. Liu, "Thermal optimization of composite phase change material/expanded graphite for Li-ion battery thermal management," *Appl. Therm. Eng.*, vol. 108, pp. 1119–1125, 2016, doi: 10.1016/j.applthermaleng.2016.07.197.

[15]   M. Chen *et al.*, "Experimental study on the hybrid carbon based phase change materials for thermal management performance of lithium-ion battery module," *Int. J. Energy Res.*, vol. 46, no. 12, pp. 17247–17261, 2022, doi: 10.1002/er.8388.

[16]   C. Ma, Y. Zhang, S. Hu, X. Liu, and S. He, "A copper nanoparticle enhanced phase change material with high thermal conductivity and latent heat for battery thermal management," *J. Loss Prev. Process Ind.*, vol. 78, no. January, p. 104814, 2022, doi: 10.1016/j.jlp.2022.104814.

[17]   T. Xu, Y. Li, J. Chen, H. Wu, X. Zhou, and Z. Zhang, "Improving thermal management of electronic apparatus with paraffin (PA)/expanded graphite (EG)/graphene (GN) composite material," *Appl. Therm. Eng.*, vol. 140, no. May, pp. 13–22, 2018, doi: 10.1016/j.applthermaleng.2018.05.060.

[18]   M. Chen *et al.*, "Preparation of thermally conductive composite phase change materials and its application in lithium-ion batteries thermal management," *J. Energy Storage*, vol. 52, no. PA, p. 104857, 2022, doi: 10.1016/j.est.2022.104857.

[19]   X. Zhang, C. Liu, and Z. Rao, "Experimental investigation on thermal management performance of electric vehicle power battery using composite phase change material," *J. Clean. Prod.*, vol. 201, pp. 916–924, 2018, doi: 10.1016/j.jclepro.2018.08.076.

[20]   Z. Wang, Z. Zhang, L. Jia, and L. Yang, "Paraffin and paraffin/aluminum foam composite phase change material heat storage experimental study based on thermal management of Li-ion battery," *Appl. Therm. Eng.*, vol. 78, pp. 428–436, 2015, doi: 10.1016/j.applthermaleng.2015.01.009.

[21]   A. Hussain, C. Y. Tso, and C. Y. H. Chao, "Experimental investigation of a passive thermal management system for high-powered lithium ion batteries using nickel foam-paraffin composite," *Energy*, vol. 115, pp. 209–218, 2016, doi: 10.1016/j.energy.2016.09.008.

[22]   Z. Rao, Y. Huo, X. Liu, and G. Zhang, "Experimental investigation of battery thermal management system for electric vehicle based on paraffin/copper foam," *J. Energy Inst.*, vol. 88, no. 3, pp. 241–246, 2015, doi: 10.1016/j.joei.2014.09.006.

[23]   H. Dey, S. Pati, P. R. Randive, and L. Baranyi, "Effect of finned networks on PCM based battery thermal management system for cylindrical Li-ion batteries," *Case Stud. Therm. Eng.*, vol. 59, no. May, p. 104572, 2024, doi: 10.1016/j.csite.2024.104572.

[24]   M. M. Heyhat, S. Mousavi, and M. Siavashi, "Battery thermal management with thermal energy storage composites of PCM, metal foam, fin and nanoparticle," *J. Energy Storage*, vol. 28, no. December 2019, 2020, doi: 10.1016/j.est.2020.101235.

[25]   A. Moaveni, M. Siavashi, and S. Mousavi, "Passive and hybrid battery thermal management system by cooling flow control, employing nano-PCM, fins, and metal foam," *Energy*, vol. 288, no. May 2023, p. 129809, 2024, doi: 10.1016/j.energy.2023.129809.

[26]   Z. Wang, H. Zhang, and X. Xia, "Experimental investigation on the thermal behavior of cylindrical battery with composite paraffin and fin structure," *Int. J. Heat Mass Transf.*, 2017, doi: 10.1016/j.ijheatmasstransfer.2017.02.057.

[27]   S. F. Hosseinizadeh, F. L. Tan, and S. M. Moosania, "Experimental and numerical studies on performance of PCM-based heat sink with different configurations of internal fins," *Appl. Therm. Eng.*, vol. 31, no. 17–18, pp. 3827–3838, 2011, doi: 10.1016/j.applthermaleng.2011.07.031.

[28]   A. Acır and M. Emin Canlı, "Investigation of fin application effects on melting time in a latent thermal energy storage system with phase change material (PCM)," *Appl. Therm. Eng.*, vol. 144, no. September, pp. 1071–1080, 2018, doi: 10.1016/j.applthermaleng.2018.09.013.

[29]   L. L. Tian, X. Liu, S. Chen, and Z. G. Shen, "Effect of fin material on PCM melting in a rectangular enclosure," *Appl. Therm. Eng.*, vol. 167, no. April 2019, 2020, doi: 10.1016/j.applthermaleng.2019.114764.

[30]   M. J. Huang, P. C. Eames, B. Norton, and N. J. Hewitt, "Natural convection in an internally finned phase change material heat sink for the thermal management of photovoltaics," *Sol. Energy Mater. Sol. Cells*, vol. 95, no. 7, pp. 1598–1603, 2011, doi: 10.1016/j.solmat.2011.01.008.

[31]   P. Ping, R. Peng, D. Kong, G. Chen, and J. Wen, "Investigation on thermal management performance of PCM-fin structure for Li-ion battery module in high-temperature environment," *Energy Convers. Manag.*, vol. 176, no. August, pp. 131–146, 2018, doi: 10.1016/j.enconman.2018.09.025.

[32]   G. Türkakar and İ. Hoş, "Numerical investigation of lithium-ion battery thermal management using fins embedded in phase change materials," *J. Fac. Eng. Archit. Gazi Univ.*, vol. 38, no. 2, pp. 1105–1116, 2023, doi: 10.17341/gazimmfd.762563.

[33]   F. Bahiraei, A. Fartaj, and G. A. Nazri, "Experimental and numerical investigation on the performance of carbon-based nanoenhanced phase change materials for thermal management applications," *Energy Convers. Manag.*, vol. 153, no. August, pp. 115–128, 2017, doi: 10.1016/j.enconman.2017.09.065.

[34]   C. V. Hémery, F. Pra, J. F. Robin, and P. Marty, "Experimental performances of a battery thermal management system using a phase change material," *J. Power Sources*, vol. 270, pp. 349–358, 2014, doi: 10.1016/j.jpowsour.2014.07.147.

[35]   U. Nazli, T. Kutlu, S. Murat, and P. Kerim, "Transient thermal response of phase change material embedded with graphene nanoplatelets in an energy storage unit," *J. Therm. Anal. Calorim.*, vol. 133, no. 2, pp. 907–918, 2018, doi: 10.1007/s10973-018-7161-7.

[36]   Y. J. Chen, D. D. Nguyen, M. Y. Shen, M. C. Yip, and N. H. Tai, "Thermal characterizations of the graphite nanosheets reinforced paraffin phase-change composites," *Compos. Part A Appl. Sci. Manuf.*, 2013, doi: 10.1016/j.compositesa.2012.08.010.

[37]   S. Kim and L. T. Drzal, "High latent heat storage and high thermal conductive phase change materials using exfoliated graphite nanoplatelets," *Sol. Energy Mater. Sol. Cells*, vol. 93, no. 1, pp. 136–142, 2009, doi: 10.1016/j.solmat.2008.09.010.

[38]   N. Javani, I. Dincer, G. F. Naterer, and B. S. Yilbas, "Heat transfer and thermal management with PCMs in a Li-ion battery cell for electric vehicles," *Int. J. Heat Mass Transf.*, vol. 72, pp. 690–703, 2014, doi: 10.1016/j.ijheatmasstransfer.2013.12.076.

[39]   Z. Wang, H. Zhang, and X. Xia, "Experimental investigation on the thermal behavior of cylindrical battery with composite paraffin and fin structure," *Int. J. Heat Mass Transf.*, vol. 109, pp. 958–970, 2017, doi: 10.1016/j.ijheatmasstransfer.2017.02.057.

[40]   U. N. Temel, "Passive thermal management of a simulated battery pack at different climate conditions," *Appl. Therm. Eng.*, vol. 158, no. May, p. 113796, 2019, doi: 10.1016/j.applthermaleng.2019.113796.

POTENTIAL, ECONOMIC, AND ENVIRONMENTAL EVALUATION OF BIOGAS ENERGY IN PROVINCES WHERE ANIMAL HUSBANDRY IS DEVELOPED IN TÜRKİYE

Yağmur ARIKAN YILDIZ[1]* iD, Mehmet GÜÇYETMEZ[1] iD

[1] Sivas University of Science and Technology, Department of Electrical-Electronic Engineering, Sivas, Türkiye

Corresponding Author: yagmur.arikanyildiz@sivas.edu.tr

ABSTRACT

The increase in demand for energy due to various reasons, such as population growth, quality of life, and industrial and technological developments, has increased the need for new alternative energy sources. In addition, fossil fuels, which are the most used sources to meet energy needs, have reserve problems and polluting effects on the environment. The import of natural gas, which is another important source, has a negative impact on national economies. These situations have led us to turn to clean alternative sources for energy needs. In this context, biomass energy represents a renewable energy source with untapped potential for further development. Biomass energy is generated by burning various organic wastes such as human waste, agricultural waste, or animal waste. Türkiye is a country rich in agriculture and animal husbandry. Therefore, in this study, provinces with rich potential in terms of animal husbandry in Türkiye have been investigated. The biomass energy that can be obtained from animal wastes in these provinces is calculated annually. If a facility is established in these provinces to obtain this energy, economic indicators have been calculated. Finally, the positive contributions of biogas energy to the environment have been determined with numerical indicators.

Keywords: Renewable energy, Biomass energy, Energy consumption, Environmental effects, Sustainability.

1   INTRODUCTION

Ensuring the reliability and sustainability of energy, making it affordable, decarbonizing the energy system, and achieving net zero emissions are the main goals of today's global energy system. For the future of the energy sector, the BP 2023 energy outlook and IEA 2023 World Energy Outlook reports emphasize the following points [1], [2]:

- ❖ In addition to population growth, industrial and technological developments, the global warming problem, various wars, and inflation problems experienced in large countries in recent years have emphasized the importance of a successful and permanent energy transition. It has been stated that even a possible minor interruption will lead to significant economic and social consequences for the nations' economies.

- ❖ It has also been stated that although the shares of coal, oil, and natural gas, which have a large share in meeting energy, demand in global energy supply, have decreased, this decrease is still not sufficient, and more work needs to be carried out.

- ❖ In addition, it has been stated that greenhouse gas emissions are still increasing even though countries committed to reduce greenhouse gas emissions in the Paris agreement in 2015. It is stated that the later steps are taken towards this, the bigger problems will arise.

Türkiye has the fastest-growing energy demand among OECD countries. It is also the second country in the world after China in terms of electricity and natural gas demand. Therefore, the above-mentioned objectives are very important in Türkiye's energy policy strategy, and the main items are diversifying energy resources, ensuring energy security, increasing the share of new and renewable energy in electricity generation, and considering environmental impacts [3].

Türkiye's electricity energy consumption was 326.3 TWh in 2023. According to the results of Türkiye's National Energy Plan, electricity consumption is expected to reach 380.2 TWh in 2025, 455.3 TWh in 2030, and 510.5 TWh in 2035. In 2023, 36.3% of our electricity generation was from coal, 21.4% from natural gas, 19.6% from hydroelectric power, 10.4% from wind, 5.7% from solar, 3.4% from geothermal, and 3.2% from other sources [4].

In Türkiye, significant investments have been made in the last decade to increase renewable energy sources such as hydro, wind, and solar energy, and the share of these sources in the installed capacity has increased. However, although it is potentially rich in biomass,

another important renewable energy source, it has not been able to fully utilize this resource. Figure 1 shows the installed capacity of biomass energy in Türkiye by years [5].
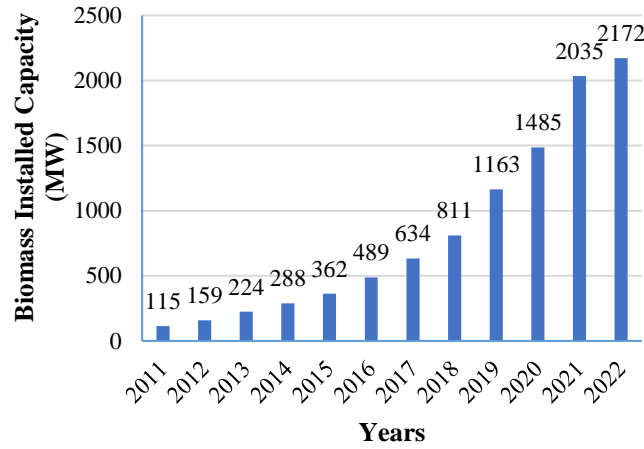
Figure 1. Biomass installed capacity in Türkiye by years.

Biomass studies have gained popularity, especially in recent years, since biomass energy is not used at the desired performance both globally and in Türkiye, is renewable, its cost is much lower than other systems, and resources are abundant. Some of the studies on this subject in the literature are as follows:

Iglinski et al. investigated the biogas potential that could be obtained from the biological fraction of cattle manure, pig manure, poultry, corn, and municipal waste for Poland and emphasized that biogas energy would provide continuous and uninterrupted energy, unlike wind and solar energy [6]. Abdeshahian et al. mentioned the development of livestock farming in Malaysia and calculated that a biogas potential of 4589.49 million m^3 year-1 could be produced from animal wastes annually and that this potential could generate 8.27×10^9 kWh year-1 of electricity [7]. Özer investigated the biogas potential of the region by using the resources of agriculture and animal husbandry in the Ardahan region and calculated that the energy obtained from biogas sources is 323 GWh per year [8]. Avcıoğlu et al. investigated the energy potential of agricultural biomass residues for Türkiye by using studies on the properties of agricultural biomass residues in many countries. They calculated the energy potential of agricultural biomass residues as 298,955 TJ for field crops and 65,491 TJ for horticultural crops [9]. Ramos-Squarez et al. researched the amount of fertilizer that could be produced from animals on farms in the Canary Islands and its biogas equivalent. It has been stated that this potential is equivalent to 0.68%-8.56% of the region's renewable energy production in 2016 [10]. Başcetincelik et al. discussed the evaluation of the use of agricultural wastes in Türkiye for electricity generation

and thermal energy, market difficulties, incentive elements, and strategic developments as a whole [11]. Karaca determined the potential of plant wastes in Türkiye in terms of quantity, mapping, and calculated their total calorific values. He also stated that with the use of these wastes, the amount of CO_2 would decrease by 30 Mt per year [12]. Karaca investigated the biogas potential that can be obtained from animal manure in Türkiye in his study and showed that the potential obtained from these wastes could meet 1.1% of Türkiye's annual energy consumption [13]. Jekayinfa et al. investigated biogas resources for Nigeria and calculated the biogas energy potential of different sources such as forest residues, agricultural residues, human and animal waste [14]. Ardebili investigated the potential for bioenergy from animal and agricultural waste in Iran and found that 62,808 GWh of energy could be produced annually, which corresponds to 27% of the country's electricity consumption. It was also stated that this value would reduce greenhouse gas emissions by 4.1 Mt of CO_2 per year [15]. Yaqob et al. mentioned the problems such as long power outages in Pakistan and examined a solution to this problem by using abundant wastes such as animal manure, poultry waste, sugarcane bagasse, and kitchen waste and converting them into biomass energy. As a result of their calculations, they stated that 59,536 GWh of electricity could be generated from these wastes per year, and this value could meet half of the country's electricity consumption [16]. Seyitoğlu and Avcıoğlu investigated the biogas potential of Çorum province by using the data on the number of cattle, ovine, and poultry in 2021. As a result of the calculations, they stated that it can generate 100.32 GWh of electricity, and this production will reduce 2608.06 tons of CO_2 emissions [17]. Mana et al. calculated the amount of animal manure that could be produced from animals on farms in the Canary Islands and stated that this manure was equivalent to 6.8 MWe equivalent installed power biogas potential [18]. Alnhoud et al. noted that the increase in livestock and chicken manure is a threat to public health in the AL-Mafraq region in northern Jordan and investigated the use of these manures as biogas energy. They concluded that 10.1×10^6 GJ of energy could be obtained annually from these manures, which could meet 5% of the population's electricity consumption [19]. Nehra and Jain investigated the biomass energy potential from animal manure for the Haryana region in India. They calculated that 106.11 GJ of heating value and 9.84 TWh of electrical power could be produced annually from this potential. They also stated that this value would reduce 2.56 Mt CO_2 emissions [20]. Akter et al. investigated the biomass potential of 25 different agricultural crops in Bangladesh and found that they have a biogas production capacity of 9,868 million m^3. They stated that this potential can meet 88% of the total electricity consumption of the country [21].

In this study, considering that Türkiye has a developed potential in the field of animal husbandry and does not fully use this potential, seven provinces that are rich in terms of the number of cattle, sheep, and poultry in 2023 have been determined. Depending on the number of animals in these provinces, manure amounts, methane values, and biogas energy potentials have been calculated for each province. The installed power values corresponding to these potentials and the values that meet the energy consumption of those provinces have been found. If there are relevant investments in the regions, these investments have been evaluated economically and the environmentally positive effects of these investments have been proven with numerical data.

2 BIOGAS AND BIOMASS ENERGY

Biogas is obtained from the biochemical fermentation and microbiological activity of various organic wastes under anaerobic conditions. The energy obtained from biogas is called biomass energy. Biomass sources are diverse as shown in Figure 2 [22]. The formation stages of biogas using resources and their explanations are given in Figure 3 [23]-[24].
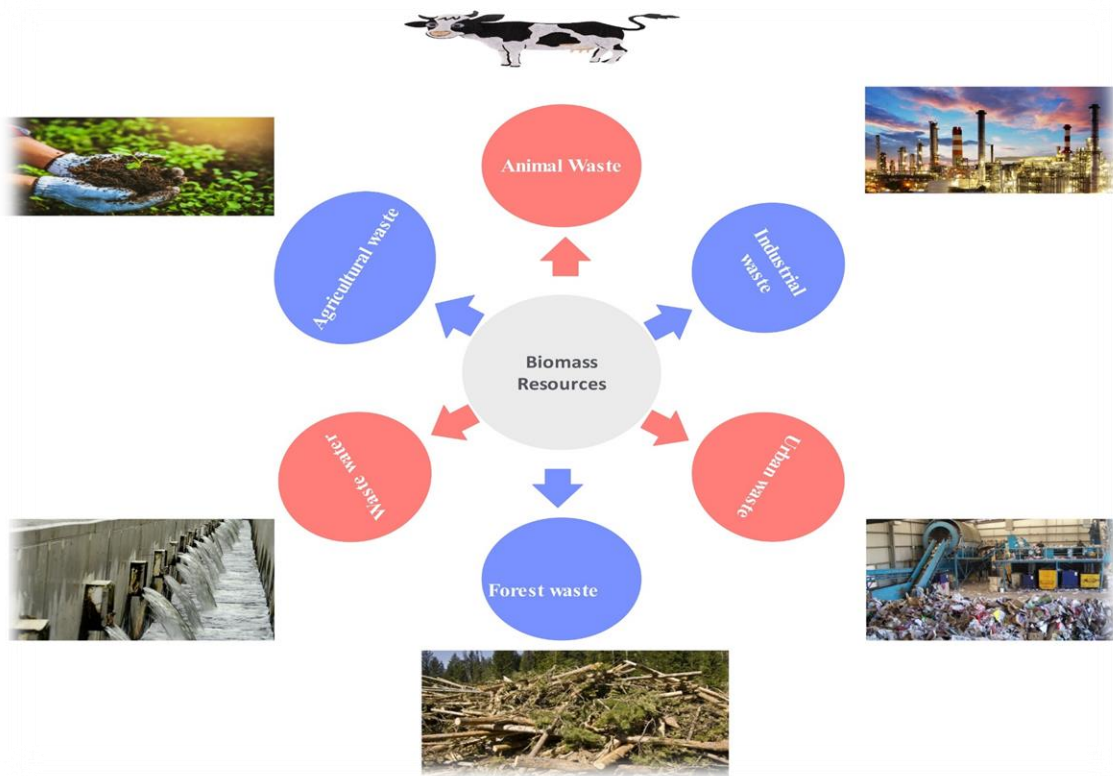
Figure 2. Biomass resources.
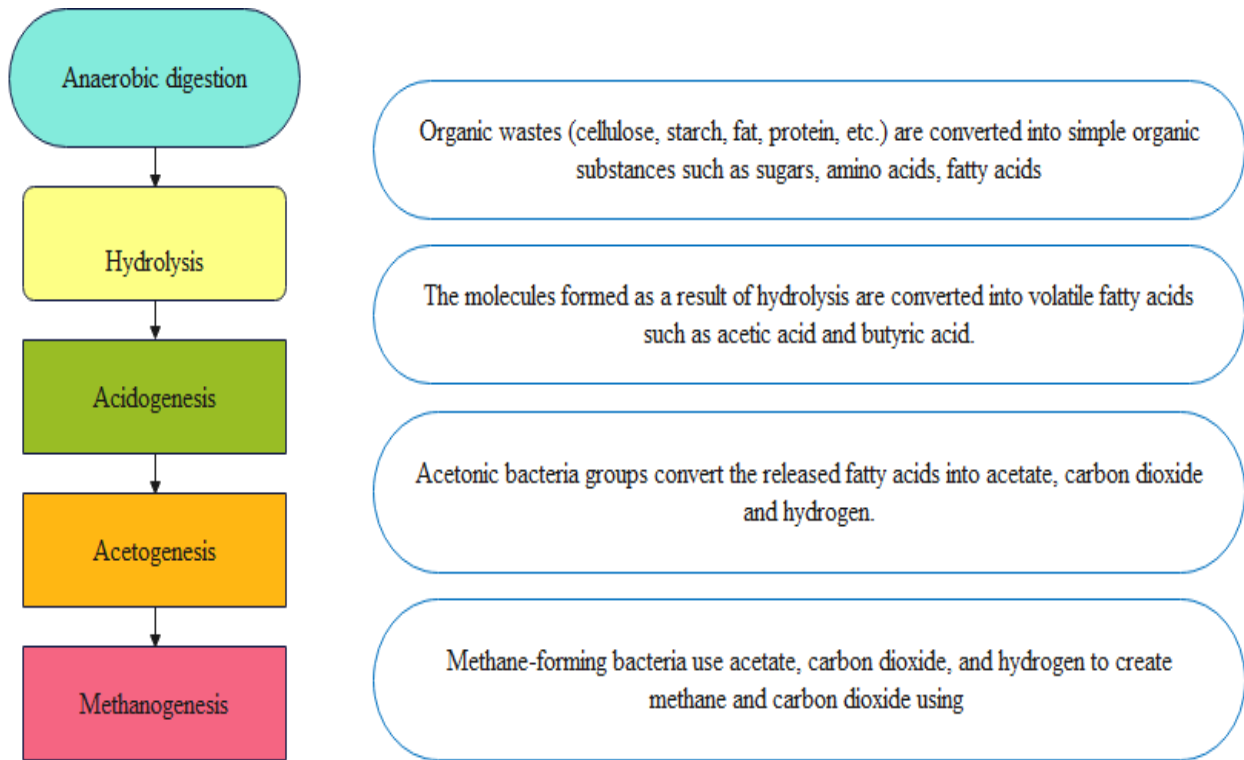
Figure 3. Formation stages of biogas.

The content of biogas, which is a colorless, odorless, lighter than air and gas mixture with high thermal value that burns with a bright blue flame, is given in Table 1. The composition of the gas varies according to factors, such as ambient temperature, water content, acidity, and type of residues [25].

Table 1. Composition content of biogas.

Components	Volume content (%)
Methane (CH_4)	40-70
Carbon dioxide (CO_2)	30-60
Hydrogen (H_2)	5-10
Nitrogen (N_2)	1-2
Water vapor (H_2O)	0.3
Hydrogen Sulphide (H_2S)	Small quantities

Although it depends on the components in terms of calorific value, one cubic meter of biogas has 5500-6000 kcal energy. When biogas is compared to other fuels; 1 m^3 of biogas is equivalent to 0.60 m^3 of natural gas, 0.70 liters of gasoline, 0.65 liters of diesel fuel, and 0.80 kg of coke [25]. From an electrical point of view, biogas is equal to 4.70 kWh of electrical energy [25], making this gas produced by burning various biomasses an important renewable energy source today.

3   MATERIAL AND METHOD

In this section, the data set and mathematical formulas regarding the production of biogas from animal waste and its energy, economic and environmental evaluation are presented.

3.1   Material

Türkiye has a favorable potential for animal husbandry due to its natural resources and ecological conditions, and the animal husbandry sector has an important place in the national economy. Therefore, the approach in this study is to prevent the harm of these wastes to the environment and to support meeting the increasing energy demand by converting these wastes into energy.

Accordingly, 7 provinces rich in large animals, small animals, and poultry have been identified in Türkiye for 2023. Another important feature of these provinces is that they are among the most populous provinces of the country and have high electricity consumption. These provinces are Konya, Erzurum, Ankara, İzmir, Diyarbakır, Balıkesir and Aydın. The number of large animals, small animals and poultry animals including chickens, turkeys and goose in these provinces in 2023 is given in Table 2 [26].

Table 2. The number of animals of provinces for 2023.

Province	Large Animals	Small Animals	Chicken (Laying hens)	Chicken (Broiler)	Goose	Turkey	Poultry Animals
Konya	928,335	3,059,048	10,702,230	209,200	18,976	32,093	10,962,449
Erzurum	696,321	877,869	141,859	0	14,669	8,184	164,712
Ankara	610,514	1,879,345	9,011,815	610,514	18,249	16,756	9,657,334
İzmir	816,337	813,211	5,230,818	12,241,010	3,748	210,972	17,686,578
Diyarbakır	580,335	2,070,682	533,880	270,400	20,542	87,658	912,480
Balıkesir	532,646	1,327,116	5,674,117	29,174,723	1,027	40,239	34,890,106
Aydın	491,087	363,364	858,308	2,397,250	3,312	5,403	3,264,273

3.2   Method

The following steps and relevant mathematical equations are used to calculate the biomass energy to be obtained from animal waste.

3.2.1 Determination of Biomass Energy Potential and Generation

Depending on the number of animals, the annual amount of wet manure that can be produced from large-small animals and laying hens chicken, broiler chicken, goose, and turkey can be found by using the Equations between 1 and 4, respectively [7]-[8], [27],[28].

$$T_{AWM\,(1)} = \frac{\sum_{i=1}^{N} q * 365}{1000} \tag{1}$$

$$T_{AWM\,(1)} = \frac{\sum_{i=1}^{N} q * 42}{1000} \tag{2}$$

$$T_{AWM\,(1)} = \frac{\sum_{i=1}^{N} q * 98}{1000} \tag{3}$$

$$T_{AWM\,(1)} = \frac{\sum_{i=1}^{N} q * 110}{1000} \tag{4}$$

where N, T_{AWM} and q represent the number of animals, total amount of annual wet manure (t year^{-1}) the average amount of manure per animal, respectively. Considering the animals' stay in the shelter, the amount of utilizable wet manure can be calculated from the total amount of fertilizer with the help of the Equation 5 [27].

$$T_{AUWM} = T_{AWM} * b_f \tag{5}$$

where T_{AUWM} is the total amount of utilizable wet manure per year (t year^{-1}) and b_f represents the benefit rate as a percentage. The proportion of solids in the utilizable wet manure (T_{sm}) obtained is found by using Equation 6, and the proportion of volatile solids in the solids (T_{vsm}) is found by using Equation 7 [27].

$$T_{sm} = T_{AUWM} * \eta_{sm} \tag{6}$$

$$T_{vsm} = T_{sm} * \eta_{vsm} \tag{7}$$

where η_{sm} and η_{vsm} are percentage for the proportion of solids in wet manure and the proportion of volatile solids in solid manure, respectively. The methane production of manure from (T_{CH4}) is calculated by multiplying the volatile solids content by the percentage of methane production (μ). The equation for this is shown in Equation 8 [7]-[8],[27].

$$T_{CH_4} = T_{vsm} * \mu \tag{8}$$

The energy potential that can be generated from methane gas (E_p) is calculated by multiplying the amount of methane and the energy equivalent of methane [7], [27].

$$E_p = T_{CH_4} * e_{CH4} \tag{9}$$

where e_{CH4} is the energy equivalent of 1 m^3 methane (kWh). The energy equivalent of methane is taken as 10 kWh. The electrical energy equivalent to be produced from methane is found with the help of Equation 10 [7]-[27].

$$E_g = T_{CH_4} * e_{CH4} \, \eta_c \tag{10}$$

where η_c is the electricity conversion coefficient. η_c value varies between 25% and 40% depending on the power generation plant. For this study, this value is taken as 35% [7]-[27]. The coefficients between Equations 5-8 have been determined as a result of literature reviews and market research, and the values used in the study are given in Table 3 [7]-[27].

Table 3. Coefficients related to equations.

Animal Type	q (kg)	b$_f$ (%)	η_{sm} (%)	η_{vsm} (%)	μ (%)
Large animals	29	90	15	83	25
Small animals	2.1	13	23	75	30
Chicken	0.16	70	19	75	35
Turkey	0.38	68	19.36	76	35
Goose	0.33	68	17.27	61.28	35

3.2.2 Performing Economic Analysis

The inputs that make up the costs of the biomass facility consist of items such as installation costs, operating costs, general maintenance and intermediate maintenance costs, commissioning costs of generators, personnel costs; and Equation 11 is used to calculate the total cost [29].

$$C_T = C_i + C_O + C_M + C_L + C_{GR} \tag{11}$$

where C_T, C_O, C_M, C_L, C_{GR} is the installation, operation, maintenance, labour, and generation reinstallation cost, respectively. The payback period defines how many years it will take to recover the initial investment amount. This value is calculated as follows [29]:

$$n = \frac{Capital\ investment}{net_{cash-i}} = \frac{C_i + C_O}{rev_{ees} - c_{oth}} \tag{12}$$

where n is the payback period (year), net_{cash-i} is the annual net cash inflow. rev_{ees} is the income obtained from the sale of electrical energy in that year, and c_{oth} is the sum of expenses such as maintenance and personnel expenses that may occur in that year.

3.2.3 Performing Emission Analysis

The biggest advantages that biomass energy can provide to the environment are collecting waste released into the environment through recycling, preventing sediment formation in the environment, and reducing greenhouse gas emissions, which are the biggest danger in terms of global warming. The amount of total greenhouse gas reduction with biomass energy generation is found with the help of Equation 13 [30].

$$T_{GHG-R} = E_g * \eta_{GHG} \tag{13}$$

where T_{GHG-R} is the total amount of greenhouse gas reduction (GHG), η_{GHG} is the greenhouse gas conversion coefficient. Another important perspective of GHG mitigation is the carbon market. The carbon market stands for carbon trading, where a carbon quota is equal to 1 ton of carbon dioxide. In basic practice, countries are given a specific carbon emission quota, which is expected to be shared equally among producers. If any producer exceeds its quota, it can buy it from another producer that already has a quota. In this way, a carbon trading market has emerged. Carbon markets are divided into two. These are called mandatory markets and voluntary markets. In voluntary markets, a ton of carbon is worth between 4.5-5.5 Euros/dollar, while in mandatory markets this value goes up to 80 Euros. In Türkiye, voluntary "Voluntary Carbon Markets" practices aiming to reduce carbon emissions have been ongoing since 2005. Accordingly, the market value of reducing 1 ton CO_2 (Mv) is found with the help of Equation 14.

$$M_V = T_{GHG-R} * p_{CO2} \tag{14}$$

where p_{co2} is the price of one ton of carbon. Also, the equivalencies of the GHG reduction achieved through energy from biomass in terms of gasoline, forest land, and recovered waste have been evaluated in the emission analysis. Reduction of 1 ton of CO_2 is approximately equivalent to 429.6 L of unconsumed gasoline ($N_{uncongasoline}$), 227.6 acres of carbon absorbing land ($N_{forestland}$) and 344.9 tons of recovered waste ($N_{recoveredwaste}$). Using these values, the relevant equations are given below [31].

$$N_{uncongasoline} = T_{GHG-R} * 429.6 \tag{15}$$

$$N_{forestland} = T_{GHG-R} * 227.6 \tag{16}$$

$$N_{recoveredwaste} = T_{GHG-R} * 344.9 \tag{17}$$

4   RESULTS AND DISCUSSION

The annual methane production amount, total energy potential, and annual energy production amounts that can be produced in these provinces have been calculated by using the number of animals in the provinces with developed animal husbandry in Türkiye (Table 1) and various mathematical equations and coefficients in section 3.2.1. The values found are summarized in Table 4.

The annual electricity production that can be obtained as a result of the use of animal manure in the regions is shown in Figure 4. Accordingly, the highest electricity production is realized in Konya province with 1,095.36 GWh, while the lowest electricity consumption is realized in Aydın province with 524.43 GWh.

Table 4. Total CH₄, energy potential and electricity generation values of provinces.

Province	Animal Type	T_{CH4} (km³ year⁻¹)	Ep (Gwh year⁻¹)	Eg (Gwh year⁻¹)
Konya	Large Animals	275,262.7	2,752.7	963.4
	Small animals	15,774.4	45.26	55.2
	Poultry	21,932.188	3.13	76.76
Erzurum	Large Animals	206,467.8	2,064.7	722.6
	Small animals	4,526.8	45.26	15.8
	Poultry	313.163	3.13	1.096
Ankara	Large Animals	181,024.9	1,810.2	633.6
	Small animals	9,691.1	96.91	33.9
	Poultry	18,556.7	185.57	64.95
İzmir	Large Animals	242,053.9	2,420.5	847.2
	Small animals	4,193.4	41.93	14.7
	Poultry	13,848.8	138.488	48.471
Diyarbakır	Large Animals	172,224.7	1,722.2	602.8
	Small animals	10,677.7	106.77	37.4
	Poultry	1,297.0	12.97	4.54
Balıkesir	Large Animals	157,936.1	1,579.4	552.8
	Small animals	6,843.4	68.43	23.9
	Poultry	18,473.37	184.73	64.66
Aydın	Large Animals	145,613.3	1,456.1	509.7
	Small animals	1,873.7	18.73	6.6
	Poultry	2,323.0	23.23	8.13
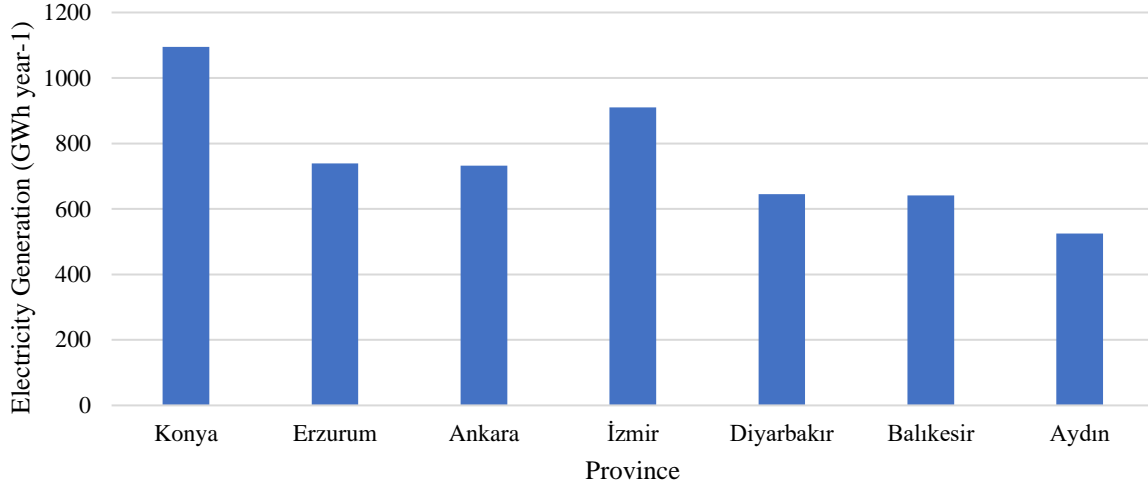
Figure 4. Electricity generation from biogas in provinces.

The graphical representation of the electricity generation values obtained according to animal species in the provinces is given in Figure 5. In addition to the fact that the majority of biomass energy production in the provinces is generally obtained from large animal wastes, poultry has a significant impact on biogas energy for Balıkesir province.

After calculating the amount of biogas energy production with animal manure, the total energy consumption of the regions and especially the electricity consumption of the households in the regions have been investigated. According to the 2023 report of the Energy Market Regulatory Authority [32], the total electricity consumption and residential electricity consumption values of these provinces in that year are given in Table 5. In addition, the percentages of the energy obtained from biogas covering these consumptions have also been calculated.

As seen in Table 5, biogas is an especially important energy source. Even in Erzurum alone, all of the household consumption can be met by biomass energy. Therefore, it would not be wrong to say that biomass energy will be one of the most important renewable energy sources for the provinces in the coming years if the potential of biogas is utilized.
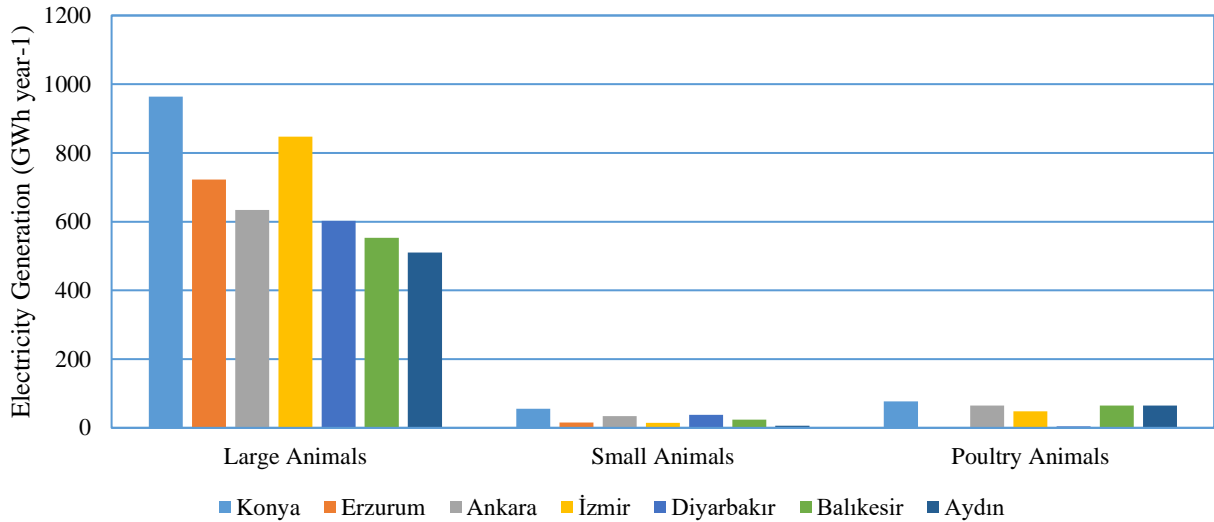
Figure 5. Electricity generation values from biogas by animal type in provinces.

Table 5. Percentages of production meeting consumption.

Province	Total electricity consumption (GWh)	Residential electricity consumption (GWh)	Covering total electricity consumption (%)	Covering residential electricity consumption (%)
Konya	8,031.271	1,598.422	13.63	68.52
Erzurum	964.453	395.556	76.67	100
Ankara	14,879.935	4,835.479	4.92	15.14
İzmir	16,422.049	4,627.856	5.54	19.67
Diyarbakır	3,137.268	1,070.959	20.55	60.20
Balıkesir	3,950.758	1,155.818	16.23	55.49
Aydın	3,098.515	1,167.488	16.93	44.92

After comparing energy generation values and consumption values, necessary calculations have been made to evaluate the investments economically in the case of investing in a biogas facility in these regions. Based on the fact that a year consists of 8,760 hours in these facilities, the installed power values that can be installed in the regions have been calculated by assuming that the facilities operate for approximately 8000 hours. Accordingly, an installed power potential of 137 MW in Konya, 92 MW in Erzurum, 91 MW in Ankara, 113 MW in Izmir, 81 MW in Diyarbakır, 80 MW in Balıkesir, and 67 MW in Aydın has been found.

Cost items of biogas facilities change from day to day. However, as a result of literature research and market research, it is generally accepted that the average cost of electrical output power per kW is 3,600 Euros [33]. The Euro-TL exchange rate has been taken as 35 TL, and capital investment has been calculated according to the installed capacities of the regions. Likewise, as of July 1, 2024, the electrical energy sales price of biomass in Türkiye is 2.9047 TL and the evening support is 0.4836 TL [34]. Considering the evening support, the annual

electricity returns of the investments have been calculated by taking the average electrical energy sales price as 3.00 TL. Since installed power values have been determined according to the amount of raw materials, the payback period for investments to be established for all provinces has been found to be five years. In case of any equity, this value will decrease further. If investments have a lifespan of approximately 25 years, the profitability rates to be achieved after five years are quite high. Therefore, it is recommended to make these investments in these provinces. The relevant results are listed in Table 6.

In analysing the contribution of energy from biomass to the environment, the amount of greenhouse gas reduction with the energy obtained from biomass in the provinces and its market value in the carbon markets have been calculated. As of January 1, 2024, the greenhouse gas conversion coefficient of the final electrical energy for Türkiye is determined as 0.689 t_CO_2-eq. per MWh [35]. In the calculation of the market value, 1 Euro has been accepted as 35 TL. In addition, the equivalents of unconsumed gasoline, forest land, and recycled waste of the annual greenhouse gas reduction for the provinces have been also calculated. The calculated values are listed in Table 7. As can be seen from the values in Table 7, while generating income with biomass energy, the environment is protected in many ways.

Table 6. The results of economic analysis.

Province	Installed power capacity (MW)	Capital investment (million TL)	Income electricity sales (million TL/year)	Payback period (year)
Konya	137	17,262	3,286.08	~5
Erzurum	92	11,592	2,218.5	~5
Ankara	91	11,466	2,197.4	~5
İzmir	113	14,238	2,731.11	~5
Diyarbakır	81	10,206	1,934.21	~5
Balıkesir	80	10,080	1,924.08	~5
Aydın	65	8,190	1,573.29	~5

Table 7. The results of emission analysis.

Province	E_g (GWhyear^{-1})	T_{GHG-R} (ktonyear^{-1})	M_v (millionTL year^{-1})	$N_{uncomgasoline}$ (kL/year)	$N_{forestland}$ (km²/year)	$N_{recoveredwaste}$ (Mtonyear^{-1})
Konya	1,095.36	754.70	118.86	324.22	171,769	260.3
Erzurum	739.496	509.51	80.25	218.89	115,964	175.73
Ankara	732.45	504.66	79.48	216.80	114,861	174.1
İzmir	910.371	627.25	98.79	269.47	142,762	216.3
Diyarbakır	644.739	444.23	69.96	190.84	101,107	153.2
Balıkesir	641.36	441.90	69.59	189.84	100,576	152.4
Aydın	524.43	361.33	56.91	155.23	82,238	124.6

5   CONCLUSION

In this paper, seven provinces in Türkiye where animal husbandry is developed have been identified, and biomass energy in these regions has been investigated. The numbers of large animals, small animals, and poultry in these provinces as of 2023 have been researched. Depending on the number of animals, the amount of fertilizer, methane amount, and biomass energy have been calculated annually. It has been observed that a minimum of 524.43 GWh and a maximum of 1095.36 GWh of electrical energy can be obtained in 7 provinces. In addition, the electricity generated has a coverage rate varying between 15.14% and 100% of household electricity consumption in the provinces. It has been numerically shown that if biomass energy-based facilities are built in the provinces, these facilities will pay back in five years without any equity capital, and since the investment period is 25 years, they will bring a substantial profit after five years. Finally, the positive effects of biomass energy on the environment have been investigated. It has been calculated that biomass energy will reduce greenhouse gas by a maximum of 754.7 ktons and a minimum of 361.33 ktons per year for the provinces, and this will provide extra profit to the investor due to carbon credits. It has also been emphasized that evaluating biomass energy is environmentally important by calculating the values of unconsumed gasoline, unused land, and recycled waste depending on greenhouse gas reduction values.

Conflict of Interest Statement

There is no conflict of interest between the authors.

Statement of Research and Publication Ethics

The study is complied with research and publication ethics.

Artificial Intelligence (AI) Contribution Statement

This manuscript was entirely written, edited, analyzed, and prepared without the assistance of any artificial intelligence (AI) tools. All content, including text, data analysis, and figures, was solely generated by the authors.

Contributions of the Authors

Yağmur Arıkan Yıldız worked on the data collection, analysis, and concept of the study.

Mehmet Güçyetmez contributed to the scope, integrity and writing of the study.

REFERENCES

[1] BP, *BP Energy Outlook 2023 edition*, Jul. 2023. [Online]. Available: https://www.bp.com/content/dam/bp/business-sites/en/global/corporate/pdfs/energy-economics/energy-outlook/bp-energy-outlook-2023.pdf. [Accessed: May 10, 2024].

[2] IEA, *World Energy Outlook 2023*, Oct. 24, 2023. [Online]. Available: https://www.iea.org/reports/world-energy-outlook-2023. [Accessed: May 10, 2024].

[3] Republic of Turkey Ministry of Foreign Affairs, "Turkey's International Energy Strategy," Jul. 2024. [Online]. Available: https://www.mfa.gov.tr/turkeys-energy-strategy.en.mfa. [Accessed: Jul. 10, 2024].

[4] Republic of Turkey Ministry of Energy and Natural Resources, "Energy." [Online]. Available: https://enerji.gov.tr/infobank-energy-electricity. [Accessed: Jun. 12, 2024].

[5] Republic of Turkey Ministry of Energy and Natural Sources, "Biomass." [Online]. Available: https://enerji.gov.tr/bilgi-merkezi-enerji-biyokutle-en. [Accessed: May 11, 2024].

[6] B. Iglinski, R. Buczkowski, A. Ingliska, M. Cichosz, G. Piechota, and W. Kujawski, "Agricultural biogas plants in Poland: Investment process, economic and environmental aspect, biogas potential," *Renewable and Sustainable Energy Reviews*, vol. 16, pp. 4890–4900, 2012.

[7] P. Abdeshahian, J. S. Lim, W. S. Ho, H. Hashim, and C. T. Lee, "Potential of biogas production from farm animal waste in Malaysia," *Renewable and Sustainable Energy Reviews*, vol. 60, pp. 714–723, 2016.

[8] B. Özer, "Biogas energy opportunity of Ardahan city of Turkey," *Energy*, vol. 139, pp. 1144–1152, 2017.

[9] A. O. Avcıoğlu, M. A. Dayıoğlu, and U. Türker, "Assessment of the energy potential of agricultural biomass residues in Turkey," *Renewable Energy*, vol. 138, pp. 610–619, 2018.

[10] J. L. Ramos-Suarez, A. Ritter, J. Gonzalez, and A. C. Mata Perez, "Biogas from animal manure: A sustainable energy opportunity in the Canary Islands," *Renewable and Sustainable Energy Reviews*, vol. 104, pp. 137–150, 2019.

[11] A. Bascetincelik, H. H. Ozturk, K. Ekinci, D. Kaya, M. Kacıra, and C. Karaca, "Strategy development and determination of barriers for thermal energy and electricity generation from agricultural biomass in Turkey," *Energy Exploration & Exploitation*, vol. 27, no. 4, pp. 277–294, 2009.

[12] C. Karaca, "Mapping of energy potential through annual crop residues in Turkey," *International Journal of Agricultural and Biological Engineering*, vol. 8, no. 2, pp. 104–109, 2015.

[13] C. Karaca, "Determination of biogas production potential from animal manure and GHG emission abatement in Turkey," vol. 11, no. 3, pp. 205–210, 2018.

[14] S. O. Jekayinfa, J. I. Orisaleye, and R. Pecenka, "An assessment of potential resources for biomass energy in Nigeria," *Resources*, vol. 9, no. 8, 2020.

[15] S. M. S. Ardebili, "Green electricity generation potential from biogas produced by anaerobic digestion of farm animal waste and agricultural residues in Iran," *Renewable Energy*, vol. 154, pp. 29–37, 2020.

[16] H. Yaqoob, Y. H. Teoh, Z. U. Din, N. U. Sabah, M. A. Jamil, M. A. Mujtaba, and A. Abid, "The potential of sustainable biogas production from biomass waste for power generation in Pakistan," *Journal of Cleaner Production*, vol. 307, 127250, 2021.

[17] S. S. Seyitoğlu and E. Avcıoğlu, "An investigation for the potential of biogas to be produced from animal waste in Çorum," *Gazi University Journal of Science Part C: Design and Technology*, vol. 9, no. 2, pp. 246–261, 2021.

[18] A. Mana, A. Allaouhi, K. Ouazzani, and A. Jamil, "Feasibility of agriculture biomass power generation in Morocco: Techno-economic analysis," *Journal of Cleaner Production*, vol. 295, 126293, 2021.

[19]   O. T. Alnhoud, A. M. AL-Harahsheh, M. S. Al-Harahsheh, and F. I. Irshaid, "Animal solid waste as a potential renewable biomass energy source: A case study of Jordan," *Biomass Conversion and Biorefinery*, vol. 13, pp. 6807–6816, 2023.

[20]   M. Nehra and S. Jain, "Estimation of renewable biogas energy potential from livestock manure: A case study of India," *Bioresource Technology Reports*, vol. 22, 101432, 2023.

[21]   Mst. M. Akter, I. Z. Surovy, N. Sultana, Md. O. Faruk, B. H. Gilroyed, L. Tijing, Md. Arman Didar-ul-Alam, H. K. Shon, S. Y. Nam, and M. M. Kabir, "Techno-economics and environmental aspects of agricultural biomass-based energy potential," *Applied Energy*, vol. 359, 122652, 2024.

[22]   H. Long, X. Li, H. Wang, and J. J. Wang, "Biomass resources and their bioenergy potential estimation: A review," *Renewable and Sustainable Energy Reviews*, vol. 26, pp. 344–352, 2013.

[23]   D. Mignogna, P. Ceci, C. Cafaro, G. Corazzi, and P. Avino, "Production of biogas and biomethane as renewable energy sources: A review," *Applied Sciences*, vol. 13, no. 18, 10219, 2023.

[24]   M. J. B. Kabeyi and O. A. Olanrejawu, "Biogas production and applications in the sustainable energy transition," *Journal of Energy*, 8750221, 2022.

[25]   A. Yılmaz, S. Ünvar, T. Koca, and A. Koçer, "Biogas production and statistical information of biogas production," *Technological Applied Sciences*, vol. 12, no. 4, pp. 218–232, 2017.

[26]   "Livestock production in Turkey by provinces." [Online]. Available: https://www.drdatastats.com/illere-gore-turkiyede-hayvancilik-canli-hayvan-sayilari/. [Accessed: Jun. 5, 2024].

[27]   H. Yağlı and Y. Koç, "Determination of biogas production potential from animal manure: A case calculation for Adana province," *Çukurova University Journal of the Faculty of Engineering and Architecture*, vol. 34, no. 3, pp. 35–48, 2019.

[28]   C. Karaca, "The biogas potential of animal manure and its GHG reduction effect in Konya province, Turkey," *Journal of Environmental Engineering and Landscape Management*, vol. 31, no. 4, pp. 232–239.

[29]   F. Masala, D. Groppi, B. Nastasi, G. Piras, and D. Garcia, "Techno-economic analysis of biogas production and use scenarios in a small island energy system," *Energy*, vol. 258, 124831, 2022.

[30]   World Bank, *State and Trends of Carbon Pricing 2024*. [Online]. Available: http://hdl.handle.net/10986/41544. [Accessed: Jun. 10, 2024].

[31]   Y. Arıkan, "A software design-based energy potential and economic analysis for investing in renewable energy systems," Master's Thesis, Kırıkkale University, 2014.

[32]   Republic of Türkiye Energy Market Regularity Authority, [Online]. Available: https://www.epdk.gov.tr/Detay/Icerik/3-0-24/elektrikyillik-sektor-raporu. [Accessed: Jun. 10, 2024].

[33]   Eastern Mediterranean Development Agency, "Feasibility report for establishing biogas facilities in Kahramanmaraş province," [Online]. Available: https://www.dogaka.gov.tr/assets/upload/dosyalar/19-4-kahramanmaras-ilinde-biyogaz-tesisleri-kurulmasina-yonelik-fizibilite-raporu.pdf.

[34]   "Current YEKDEM Prices." [Online]. Available: https://enerjiajansi.com.tr/yekdem-fiyatlari/. [Accessed: Jul. 10, 2024].

[35]   Republic of Türkiye Ministry of Environment, Urbanization and Climate Change, "Emission conversion coefficient 2024."

CREATING DATABASE WITH IMAGE PROCESSING METHODS FROM DENTAL X-RAY

Emre AVUÇLU [1] * , Fatih BAŞÇİFTÇİ [2]

¹ Aksaray University, Department of Software Engineering, Aksaray, Türkiye

² Selçuk University, Department of Computer Engineering, Konya, Türkiye

* Corresponding Author: emreavuclu@aksaray.edu.tr

ABSTRACT

The characteristic distinguishing features of a person define that person. With these characteristics, a person can be distinguished from other persons. Forensic sciences have to identify individuals in some cases. In identification, dental images are frequently used today, especially in age and gender determination procedures. In this study, a data base was created in which panoramic dental x-ray images could be used to identify people. By removing the borders from panoramic dental X-ray images, a total of 1313 dental images and 162 distinct tooth groups were generated. These images have undergone pre-processing to achieve improved results. Preprocessed images are saved in a folder. The preprocessed images are corrected with a novel and originally developed rotation algorithm. The application was developed in C # programming language.

Keywords: Dataset create, Computer programming, Panoramic graph, Image processing, X-ray images.

1 INTRODUCTION

Age estimation from teeth plays an important role in various fields. In forensic medicine, age estimation from teeth is an important tool, especially in identifying unidentified corpses. This method helps in cases such as determining the cause of death and finding missing persons. In anthropology, in the study of prehistoric human populations, age estimation from teeth provides information about the life span, health status and social structures of individuals [1].

In paleontology, examination of teeth is of critical importance in fossil findings, especially in determining the ages of early human species. In immigration and asylum, in some countries, age estimation from teeth can be used to determine the ages of immigrants and refugees without identity documents. This is especially important in terms of protecting children and correctly conducting legal processes. In orthodontics and dentistry, the developmental stages of teeth are used to monitor the growth and development processes of children. This helps in making appropriate orthodontic treatment plans. Age estimation from teeth is generally based on the growth, development and wear patterns of teeth [2]. The accuracy of identification methods can vary based on an individual's genetic and environmental factors. In forensic medicine, identification, which involves recognizing the characteristics of living or deceased individuals, is a critical concern. Identification may be necessary for various reasons, such as natural disasters, legal or forensic cases, with age determination being a vital component of this process [3-4]. Teeth are the structure that will be affected at the latest by external factors and physical factors. Teeth are also frequently found on the person after physical wear. Today, atlases are used in dental practice and forensic sciences for the prediction of age, showing the development and riding stages of the teeth. It is a method used in identification studies during mass disasters, particularly when there are numerous casualties [5]. The studies carried out to date in the forensic events show that the identification of the forensic sciences will remain a growing and popular field of occupation. Race, age, gender, physical properties are the identity parameters that the forensic sciences give priority [6]. They conducted various segmentation and identification procedures on dental X-ray images [7-9]. These analyses are an effective tool in identifying individuals and making correct decisions in social or legal situations. By using different methods of dental x-ray images [10-11], by measuring different areas of the tooth [12], by making measurements in young and pediatric teeth [13-17], age estimations for were made depending on the human skeletal size [18-19]. Avuçlu and Başçiftçi used artificial intelligence techniques to determine age and gender by preprocessing dental images [20-23].

In this study, the dental images acquired from panoramic dental x-rays were manually prepared. These images were first applied to image pre-processing. With these image processing techniques, a database was created to perform age and gender estimation from dental images. These images can be used not only to predict age and gender, but also to be used in other subjects such as classification, recognition and diagnosis in artificial intelligence techniques.

2   MATERIAL AND METHOD

In this study, the database consists of images obtained from the X-ray device shown in Figure 1.

Figure 1. Panoramic X-ray device.

Extracted tooth images are stored in the source folder. There are a number of procedures to create a database from dental images. The flow diagram showing the sequence of this operation is shown in Figure 2.
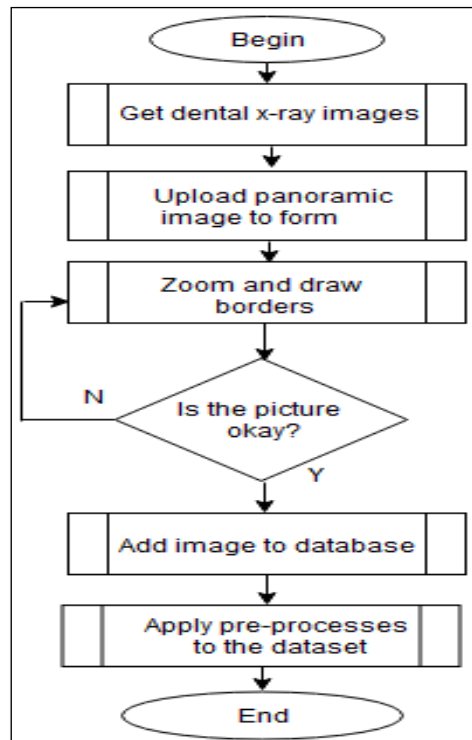
Figure 2. Flow diagram.

As shown in Figure 3., the teeth images are first applied to the methods. Thus, it is ensured that the images are of a certain standard quality. With otsu image thresholding method, tooth images are converted to binary form. The overall structure of the program is as shown in Figure 3.

```
┌─────────────────────────────┐
│  ┌───────────────────────┐  │
│  │    CREATE DATABASE     │  │
│  └───────────────────────┘  │
│             │               │
│             ▼               │
│  ┌───────────────────────┐  │
│  │     Gray Scaling       │  │
│  └───────────────────────┘  │
│             │               │
│             ▼               │
│  ┌───────────────────────┐  │
│  │   ForegroundEnhance    │  │
│  └───────────────────────┘  │
│             │               │
│             ▼               │
│  ┌───────────────────────┐  │
│  │        Median          │  │
│  └───────────────────────┘  │
│             │               │
│             ▼               │
│  ┌───────────────────────┐  │
│  │   OTSU-Thresholding    │  │
│  └───────────────────────┘  │
└─────────────────────────────┘
```
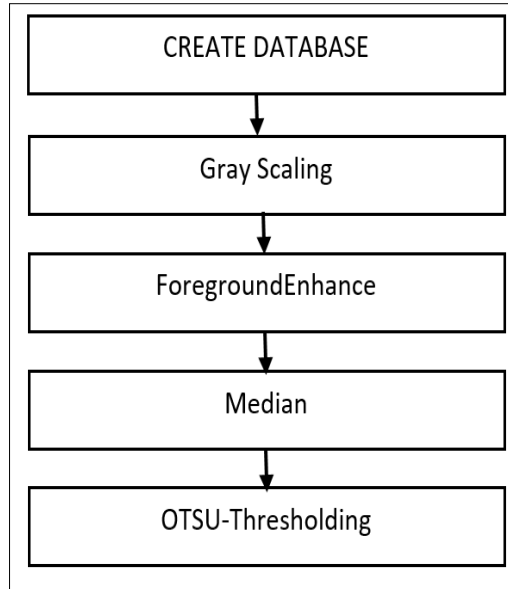
Figure 3. General Methodology.

Gray scale is a term used in image processing to describe a format that represents a color image as only black, white, and shades of gray in between. Such images are a single-channel format, where each pixel has only the light intensity.

Foreground enhance is a technique that aims to increase the visibility and distinctness of foreground objects or regions in an image. This process is used specifically to strengthen the differences between the background and the foreground in an image and to make foreground objects clearer.

Median filtering is a technique specifically designed to reduce noise. It is often preferred because it removes noise while preserving the edges.

Otsu Thresholding is an automatic binary image acquisition method used in image processing. This method is used to separate pixel values in an image into two classes (e.g., objects and background). Otsu Thresholding provides an effective solution, especially in cases where it is difficult to choose a specific threshold value.

2.1   Creating Dataset

Each of these recorded images was examined one by one and sturdy teeth were selected. When enumerating the teeth, the Universal Numbering System was used. Accordingly, the numbering of the teeth is as shown in Figure 4.

Figure 4. Dental Numbering System.

2.2   Zoom and Free Drawing Processes

The image zoom technique is used to accurately remove the boundaries of the tooth image. Zooming is the process of software incrementing an image at pixel dimensions. With the C # programming language, zooming, dimensioning and limiting operations on the tooth images can be performed. Digital zoom is used as in Figure 5.
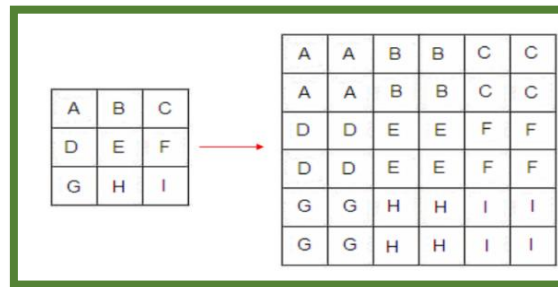
Figure 5. Zooming.

The user selects the tooth area. As shown in Figure 6, the click zones are marked with yellow circles. These sections can be adjusted later if needed. The chosen teeth are separated from the boundary regions.
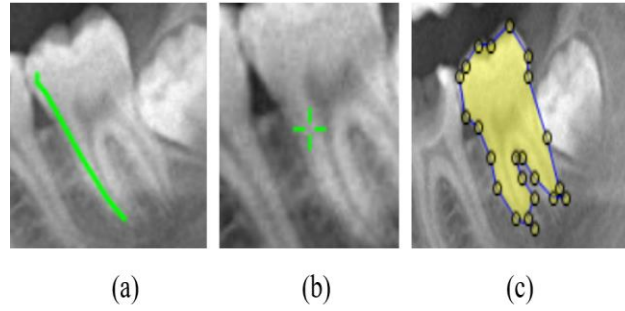
Figure 6. (a) Freehand drawing (b) Zooming (c) Editing and saving.

Figure 7 shows the parts of the tooth (a) and the teeth created by removing the boundaries in the database (b).
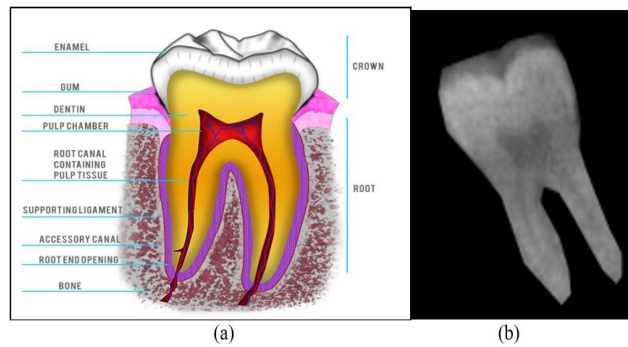
Figure 7. (a) Tooth sections (b) Drawing result.

The database creation process is recorded with the age, gender, number, and number of each tooth (AGE_GENDER_TOOTHNUMBER_COUNT.jpeg). As a result, for example, the 3nd tooth of 19 number for the males of 11 year old is saved as follows: 11_M_19_3. The tooth name of someone whose gender is female is kept as F instead of M. An example of this is shown in Figure 8, and a portion of this dataset appears.

0,10.5,F	0,10.5,F	0,10.5,F	0,10.5,F	0,10.5,F	0,10.5,F	0,10.5,F	0,10.5,F
1,10.5,M	1,10.5,M	1,10.5,M	1,10.5,M	1,10.5,M	1,10.5,M	1,10.5,M	1,10.5,M
2,10,F	2,10,F	2,10,F	2,10,F	2,10,F	2,10,F	2,10,F	2,10,F
3,10,M	3,10,M	3,10,M	3,10,M	3,10,M	3,10,M	3,10,M	3,10,M
4,11.5,F	4,11.5,F	4,11.5,F	4,11.5,F	4,11.5,F	4,11.5,F	4,11.5,F	4,11.5,F
5,11.5,M	5,11.5,M	5,11.5,M	5,11.5,M	5,11.5,M	5,11.5,M	5,11.5,M	5,11.5,M
6,11,F	6,11,F	6,11,F	6,11,F	6,11,F	6,11,F	6,11,F	6,11,F
7,11,M	7,11,M	7,11,M	7,11,M	7,11,M	7,11,M	7,11,M	7,11,M
8,12.5,F	8,12.5,F	8,12.5,F	8,12.5,F	8,12.5,F	8,12.5,F	8,12.5,F	8,12.5,F
9,12.5,M	9,12.5,M	9,12.5,M	9,12.5,M	9,12.5,M	9,12.5,M	9,12.5,M	9,12.5,M
10,12,F	10,12,F	10,12,F	10,12,F	10,12,F	10,12,F	10,12,F	10,12,F
11,12,M	11,12,M	11,12,M	11,12,M	11,12,M	11,12,M	11,12,M	11,12,M
12,13.5,F	12,13.5,F	12,13.5,F	12,13.5,F	12,13.5,F	12,13.5,F	12,13.5,F	12,13.5,F
13,13.5,M	13,13.5,M	13,13.5,M	13,13.5,M	13,13.5,M	13,13.5,M	13,13.5,M	13,13.5,M
14,13,F	14,13,F	14,13,F	14,13,F	14,13,F	14,13,F	14,13,F	14,13,F
15,13,M	15,13,M	15,13,M	15,13,M	15,13,M	15,13,M	15,13,M	15,13,M
16,14.5,F	16,14.5,F	16,14.5,F	16,14.5,F	16,14.5,F	16,14.5,F	16,14.5,F	16,14.5,F
17,14.5,M	17,14.5,M	17,14.5,M	17,14.5,M	17,14.5,M	17,14.5,M	17,14.5,M	17,14.5,M
18,14,F	18,14,F	18,14,F	18,14,F	18,14,F	18,14,F	18,14,F	18,14,F
19,14,M	19,14,M	19,14,M	19,14,M	19,14,M	19,14,M	19,14,M	19,14,M

Figure 8. Database view.

Figure 9 shows the number of teeth in the 4-21 age group. In addition, age, gender information of these teeth are also seen.

Age	Gender	Count	Age	Gender	Count	Age	Gender	Count
4	F	2	9.5	M	5	15.5	F	7
4	M	4	10	F	11	15.5	M	4
4.5	F	3	10	M	7	16	F	5
4.5	M	6	10.5	F	7	16	M	6
5	F	8	10.5	M	10	16.5	F	10
5	M	9	11	F	5	16.5	M	5
5.5	F	12	11	M	11	17	F	5
5.5	M	11	11.5	F	8	17	M	4
6	F	15	11.5	M	4	17.5	F	9
6	M	18	12	F	4	17.5	M	6
6.5	F	17	12	M	2	18	F	9
6.5	M	13	12.5	F	2	18	M	5
7	F	19	12.5	M	4	18.5	F	12
7	M	16	13	F	4	18.5	M	2
7.5	F	14	13	M	5	19	F	10
7.5	M	16	13.5	F	5	19	M	8
8	F	17	13.5	M	6	19.5	F	16
8	M	16	14	F	7	19.5	M	9
8.5	F	9	14	M	4	20	F	3
8.5	M	8	14.5	F	4	20	M	4
9	F	15	14.5	M	5	20.5	F	7
9	M	8	15	F	4	20.5	M	7
9.5	F	6	15	M	4	21	F	9

Figure 9. Age of 4-21 Dataset.

Figure 10 shows the number of teeth in the 21-63 age group.

Age	Gender	Count	Age	Gender	Count	Age	Gender	Count	Age	Gender	Count
21	M	8	28	M	12	35	M	7	42	M	2
21.5	F	13	28.5	F	11	35.5	F	5	42.5	F	9
21.5	M	7	28.5	M	7	35.5	M	3	42.5	M	10
22	F	7	29	F	5	36	F	12	43	F	2
22	M	8	29	M	11	36	M	5	43	M	3
22.5	F	12	29.5	F	15	36.5	F	10	43.5	F	8
22.5	M	13	29.5	M	7	36.5	M	9	43.5	M	8
23	F	6	30	F	5	37	F	7	44	F	2
23	M	5	30	M	3	37	M	2	44	M	3
23.5	F	10	30.5	F	7	37.5	F	11	44.5	F	5
23.5	M	5	30.5	M	11	37.5	M	6	44.5	M	5
24	F	11	31	F	6	38	F	6	45	M	3
24	M	7	31	M	6	38	M	7	45.5	F	8
24.5	F	8	31.5	F	6	38.5	F	7	45.5	M	4
24.5	M	7	31.5	M	10	38.5	M	9	46	F	10
25	F	5	32	F	5	39	F	4	46	M	5
25	M	7	32	M	6	39	M	3	47	F	9
25.5	F	11	32.5	F	9	39.5	F	6	47	M	7
25.5	M	8	32.5	M	10	39.5	M	9	48	F	9
26	F	6	33	F	6	40	F	6	49	M	5
26	M	8	33	M	4	40	M	6	50	M	5
26.5	F	7	33.5	F	5	40.5	F	4	51	M	7
26.5	M	11	33.5	M	9	40.5	M	3	52	F	5
27	F	13	34	F	3	41	F	7	52	M	7
27	M	4	34	M	6	41	M	4	57	M	5
27.5	F	7	34.5	F	4	41.5	F	5	60	M	5
27.5	M	6	34.5	M	10	41.5	M	7	63	M	5
28	F	8	35	F	5	42	F	3	-	-	-

Figure 10. Age of 21-63 Dataset.

2.3   Developed Method for Rotation

Teeth are automatically corrected for more accurate and standard results. The tooth rotation algorithm was developed as new and original.
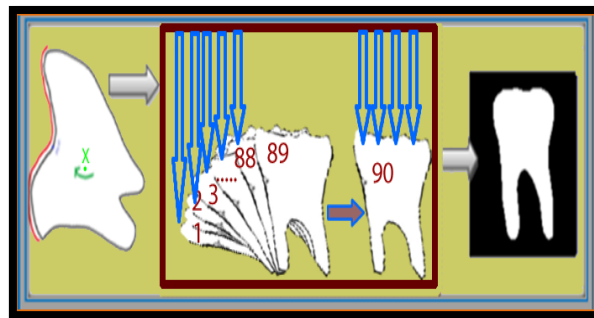
Figure 11. Tooth rotating.

In Figure 11, the tooth is rotated 180 degrees and the rotation is stopped when the total value on the Y axis during rotation is the smallest because the tooth is then in the most upright

position. In Figure 12, Algorithm-1 checks whether the tooth is in the correct position (perpendicular).

```
Algorithm-1: Fix Position
0:function private int fixPosition()
1:inputs: angle, result, tmpImage, calcTop.
2:outputs: angle.
3: Angle ← 0
4: Result ← int.MaxValue
5: tmpImage ← (Bitmap)this.imgTooth.Clone()
6:     for i = 1 to i <= 90 do
7:         calcTop ← calcPosValue(tmpImage)
8:         if (calcTop < result) then
9:             angle ← -i
10:            result ← calcTop
11:        end if
12:        tmpImage ← rotate(tmpImage, -1)
13:        new OtsuThreshold().ApplyInPlace(tmpImage)
14:    end for
15:imgTooth ← rotate(this.imgTooth, angle)
16:new OtsuThreshold().ApplyInPlace(this.imgTooth)
17: return angle
18:end function
```

Figure 12. Fix Position.

In Figure 13, Algorithm-2 is a sub-method of Algorithm-1 and controls the rotation process of the tooth.

```
Algorithm-2: Calculate Position Value
0:function private int calcPosValue(Bitmap img)
1:inputs: result, blobCounter, blobs, topEdge, bottomEdge.
2:outputs: angle.
3:     result ← 0
4:     blobCounter ← new BlobCounter()
5:     blobCounter.ProcessImage(img)
6:     blobs ← blobCounter.GetObjects(img, false)
7:     if (blobs.Length =1) then
8:      topEdge ← new List<IntPoint>()
9:      bottomEdge ← new List<IntPoint>()
10: blobCounter.GetBlobsTopAndBottomEdges(blobs[0], out topEdge, out bottomEdge)
11:        for i = 0 to i < topEdge.Count do
12:            result ← + topEdge[i].Y
13:        end for
14:     result ← / topEdge.Count
15:     result ← + topEdge.Count
16:     end if
17: return result
18:end function
```

Figure 13. Calculate Position Value.

As a result of this process the database is prepared and can be used for the desired study. Figure 14 shows a section from the database of 7-7.5 years old rotated tooth image.

Figure 14. A section from the database.

3   DISCUSSION

Dental images of the same age and gender group of 37,5_F_18_1 and 37,5_F_18_2 may differ as shown in Figure 15. This could be in any group of teeth. If the database is prepared in this way, then some test methods may have a higher error rate. Such images should not be added to the database.
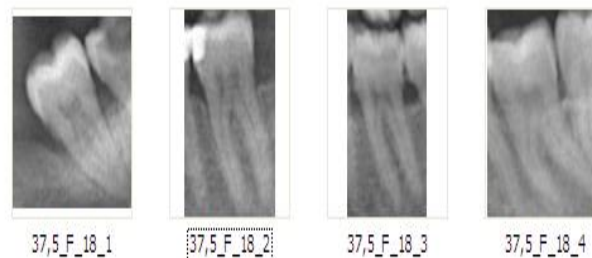
Figure 15. The same age but different looking teeth.

In real life, the size of people according to age can differ from theoretically. Morphological characteristics of the teeth in some dental groups etc. the information may be the same. In practice, such data may be encountered.

The group (A) shown in Figure 16 is generally in the small age group. Since the pulp is not completely closed at this age, it should be included in the tooth. Incorrect boundary removal (B) causes incorrect calculations. The result should be like (C) after the correct border extraction.
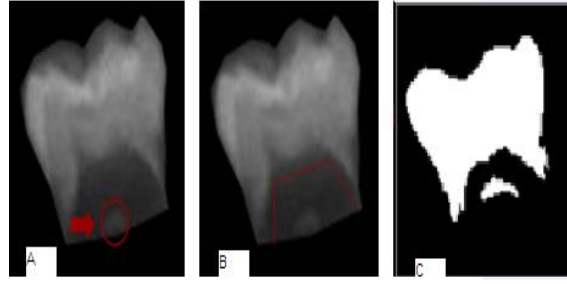
Figure 16. Preventing incorrect drawings.

In dentistry a mirror of a tooth has the same characteristics as itself. The teeth in the database in our study have the same properties as the mirror because they are rotated. Thus, the number of images in the dental database can be considered as 2630 images. The example mirror teeth shown in Figure 17 are shown.
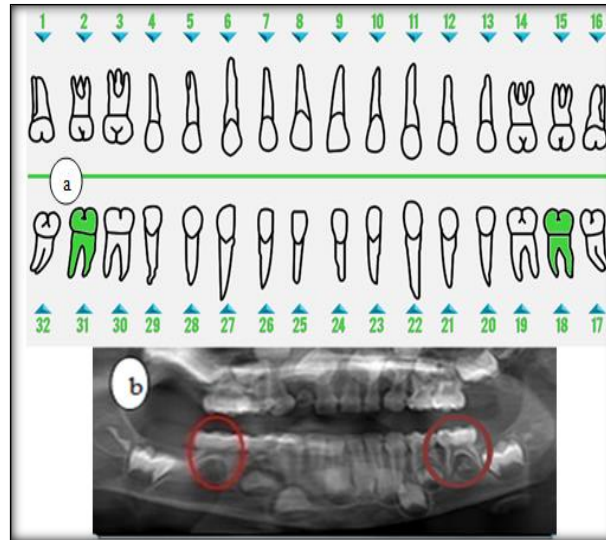
Figure 17. Mirror teeth.

If the image of the teeth in the database has an upright appearance, the application gives more accurate results. Even on images taken from the same x-ray machine, the density may be different. For this reason, this effect was tried to be eliminated by using pre-process methods in this study. This study presents an example of how to create a dataset. The preprocesses suggested in this study are only suggestions. Different preprocesses can be applied and datasets of different sizes can be created.

4   CONCLUSION AND SUGGESTIONS

In this study, a database was created by using x-ray images, using image processing methods, to perform age determination process and to be used in different fields. First,

panoramic x-ray images were obtained. In these images, 1313 (2626 teeth with a mirror) boundary image was removed and added to the database. The images were first preprocessed so that each image was kept to a certain standard of appearance. After preprocesses, images were corrected in the plane with a novel and originally developed rotation algorithm. The created database can be used to process fields such as classification, recognition, image processing. In future studies, these images can be subjected to some pre-processing and age and gender estimates can be made by conducting experimental studies with deep learning models.

Conflict of Interest Statement

There is no conflict of interest between the authors.

Statement of Research and Publication Ethics

The study is complied with research and publication ethics.

Artificial Intelligence (AI) Contribution Statement

This manuscript was entirely written, edited, analyzed, and prepared without the assistance of any artificial intelligence (AI) tools. All content, including text, data analysis, and figures, was solely generated by the authors.

Contributions of the Authors

Emre AVUÇLU: Conceptualization, Methodology, Software, Validation, Writing - review & editing, original draft.

Fatih BAŞÇİFTÇİ: Conceptualization, Methodology, Investigation, Writing - review.

REFERENCES

[1] A. Öcal Z, R. S. Bakıcı, O. Meral, Z. Öner, and S. Öner, "Adli Yaş Tahminine Yönelik Web of Science Veritabanında Yer Alan Araştırma Çalışmaların Bibliometrik Analizi," *Harran Üniversitesi Tıp Fakültesi Dergisi*, vol. 20, no. 3, pp. 618-624, 2023.

[2] P. S. Patel, A. R. Chaudhary, B. B. Dudhia, P. V. Bhatia, N. C. Soni, and Y. V. Jani, "Accuracy of two dental and one skeletal age estimation methods in 6-16 year old Gujarati children," *J. Forensic Dent. Sci.*, vol. 7, no. 1, pp. 18, 2015.

[3] S. Çöloğlu, "Adli Olgularda Kimlik Belirlemesi," in *Adli Tıp*, vol. 1, Z. Soysal and C. Çakalır, Eds. İstanbul Üniversitesi Basımevi ve Film Merkezi, İstanbul, 1999, pp. 73-92.

[4] A. Baransel Isır and H. E. Dülger, "1998-2005 yılları arasında Gaziantep Üniversitesi Adli Tıp Anabilim Dalında raporlandırılan yaş tayini olgularının irdelenmesi," *Türkiye Klinikleri Adli Tıp Dergisi*, vol. 4, no. 1, pp. 1-6, 2007.

[5]   Y. Zeyfeoğlu and İ. Hancı, "İnsanlarda Kimlik Tespiti," *Sürekli Tıp Eğitimi Dergisi*, vol. 10, pp. 375-377, 2001.

[6]   E. Ö. Aktaş, "Kostaların Sternal Uç Kemik Morfolojisinde Yaşa İlişkin Progressif değişikliklerin Kişinin Öldüğü Zamanki Yaşının Saptanmasında Kullanılabilirliği," Uzmanlık Tezi, Tıp Fakültesi, İzmir, 1997.

[7]   R. G. Birdal, E. Gumus, A. Sertbas, and I. S. Birdal, "Automated lesion detection in panoramic dental radiographs," *Oral Radiol*, vol. 32, pp. 111–118, 2016.

[8]   P. L. Lin, P. Y. Huang, P. W. Huang, H. C. Hsu, and C. C. Chen, "Teeth segmentation of dental periapical radiographs based on local singularity analysis," *Comput. Methods Progr. Biomed.*, vol. 113, pp. 433–445, 2014.

[9]   A. E. Rad, M. S. M. Rahim, R. Kumoi, and A. Norouzi, "Dental x-ray image segmentation and multiple feature extraction," in *Proc. 2nd World Conf. Innovation Comput. Sci.*, vol. 2, pp. 188-197, 2012.

[10]   J. I. Yun, J. Y. Lee, J. W. Chung, H. S. Kho, and Y. K. Kim, "Age estimation of Korean adults by occlusal tooth wear," *J. Forensic Sci.*, vol. 52, no. 3, pp. 678-683, 2007.

[11]   A. Cruz-Landeira, J. Linares-Argote, M. Martínez-Rodríguez, M. S. Rodríguez-Calvo, X. L. Otero, and L. Concheiro, "Dental age estimation in Spanish and Venezuelan children: Comparison of Demirjian and Chaillet's scores," *Int. J. Legal Med.*, vol. 124, no. 2, pp. 105, 2009.

[12]   R. Cameriere and L. Ferrante, "Age estimation in children by measurement of carpals and epiphyses of radius and ulna and open apices in teeth: a pilot study," *Forensic Sci. Int.*, vol. 174, pp. 60–63, 2008.

[13]   R. Cameriere, A. Giuliodori, M. Zampi, I. Galic, M. Cingolani, and F. Pagliara, "Age estimation in children and young adolescents for forensic purposes using fourth cervical vertebra (C4)," *Int. J. Legal Med.*, vol. 129, pp. 347–355, 2015.

[14]   M. Nystrom, L. Peck, E. Kleemola-Kujala, M. Evalahti, and M. Kataja, "Age estimation in small children: reference values based on counts of deciduous teeth in Finns," *Forensic Sci. Int.*, vol. 110, pp. 179–188, 2000.

[15]   R. Cameriere, D. De Angelis, L. Ferrante, F. Scarpino, and M. Cingolani, "Age estimation in children by measurement of open apices in teeth: a European formula," *Int. J. Legal Med.*, vol. 121, pp. 449–453, 2007.

[16]   E. Paewinsky, H. Pfeier, and B. Brinkmann, "Quantification of secondary dentine formation from orthopantomograms–a contribution to forensic age estimation methods in adults," *Int. J. Legal Med.*, vol. 119, pp. 27–30, 2005.

[17]   Y. C. Guo, C. X. Yan, X. W. Lin, H. Zhou, J. P. Li, and F. Pan, "Age estimation in northern Chinese children by measurement of open apices in tooth roots," *Int. J. Legal Med.*, vol. 129, pp. 179–186, 2015.

[18]   S. Schmidt, U. Baumann, R. Schulz, W. Reisinger, and A. Schmeling, "Study of age dependence of epiphyseal ossification of the hand skeleton," *Int. J. Legal Med.*, vol. 122, pp. 51–54, 2008.

[19]   H. M. Garvin, N. V. Passalacqua, N. M. Uhl, D. R. Gipson, R. S. Overbury, and L. L. Cabo, "Developments in forensic anthropology: age-at-death estimation," in *A Companion to Forensic Anthropology*, J. Wiley & Sons, Ltd, 2012, pp. 202–223.

BIOSORPTION OF OXYTETRACYCLINE FROM AQUEOUS SOLUTIONS BY PINE TREE WASTE CONES *(PINUS NIGRA ARN.)*

Talip TURNA [1]

[1] *Dicle University, Department of Parks and Garden Plants, Diyarbakır, Türkiye, talipturna@gmail.com*

ABSTRACT

Removal of Oxytetracycline (OTC), which is in the antibiotic group with toxicological effects for aquatic ecosystems, is very important due to its negative effects on flora and fauna. Adsorption process, which is one of the most effective methods for removing pharmaceutical pollutants, is an economical and environmentally friendly method. For this reason, in this study, biosorbent obtained from pine tree (*Pinus nigra* Arn.) waste cone powder (*Pn*-wcp), which is a low-cost and easily available waste material, was used. The results obtained from the batch adsorption experiments were tested with 4 different kinetic and isotherm models and various error functions were used to determine the most appropriate model. In order to optimize the variables in the adsorption system, contact time and initial OTC concentration factors were investigated. In addition, fourier transform infrared spectroscopy (FTIR), scanning electron microscope (SEM) and energy dispersive X-ray (EDX) images of raw and OTC-loaded *Pn*-wcp were examined. In this study, the most appropriate kinetic model was determined as Pseudo second order (PSO) with 0.999 R^2 value and Freundlich isotherm model with 0.998 R^2 value. In addition, the maximum adsorption capacity (q_{max}) was calculated as 67.51 mgOTC/g*Pn*-wcp. The results show that *Pn*-wcp is a sustainable environmentally friendly biosorbent for OTC removal.

Keywords: Adsorption, Oxytetracycline, Pinus nigra Arn, Kinetics, Isotherm.

1   INTRODUCTION

Antibiotics are used to control bacterial infections in humans and agriculture [1]. With the development of aquaculture and animal husbandry in the world, the use of oxytetracycline (OTC), a type of antibiotic, has increased excessively [2]. Only a small amount of tetracyclines used in treatment can be metabolized or absorbed by humans and animal [3]. Residues of these antibiotics reach the recipient environment and accumulate there, and this accumulation can lead to the emergence of resistant strains with antibiotic resistance [4], [5]. For this reason, antibiotics pose a potential threat to human health through biomagnification and drinking water use [6]. Antibiotics with toxicological properties for flora and fauna are frequently detected in surface waters because conventional wastewater treatment processes cannot adequately remove many of them [7]. Studies have detected OTC as the most abundant antibiotic in two large rivers in the Pearl River System in China, with concentrations of up to 2030 ng/L in water and 2100 ng/g in sediment [8]. The presence of antibiotics that have the potential to reach the recipient environment creates problems due to their possible potential effects on the ecosystem. For these reasons, their elimination is of great importance The development and use of useful water treatment technologies are essential for the removal of these drugs, which have ecotoxicological properties and cause antibiotic resistance in aquatic ecosystems [9] Different removal methods are used for OTC removal from aquatic environments. Various treatment processes such as aerobic systems [10], ozonation [11], electrochemical processes [12], UV degradation [13], adsorption [14], [15] have been frequently applied for OTC removal. Among the alternative methods for OTC removal, the adsorption process is used intensively due to its effectiveness, cheapness, environmental friendliness, and less toxicity [16]. Recently, researchers have been interested in producing low-cost and effective new biosorbents, especially from by-products or waste products obtained from industrial or agricultural processes [17].

In this study, waste pine cones were used to investigate OTC biosorption from aqueous solutions in a batch system. Also 4 different kinetic and isotherm models were tested and various error functions were used to determine the best-fit model. Additionally, pH, contact time and initial OTC concentration factors were investigated to optimize the variables in the adsorption system. Furthermore, FTIR and SEM-EDX images of raw and OTC-loaded pine cone biosorbent were investigated. The results indicate that the biosorbent obtained from waste pine cones is an environmentally sustainable material for OTC removal from aqueous solutions.

2   MATERIAL AND METHOD

2.1   Chemicals

In experimental studies, Pan Trivalent injection solution (Zoetis, Türkiye) was used as OTC source. 1 mL of the solution is equivalent to 30 mg Oxytetracycline hydrochloride. 0.1 M NaOH and 0.1 M H_2SO_4 were used to adjust the pH during the adsorption process.

2.2   Preparation of *Pn-wcp*

The pine cones used in the study were obtained from the area given in the location details (37.910665-40.275318) of Dicle University Campus (Diyarbakır/Türkiye). Pine cones that had fallen under the trees were collected seasonally. The pine cones were first washed with tap water 3 times to remove impurities (mostly leaves and sand), then passed through pure water and dried in sunlight. The dried pine cones were first broken with a pestle and then ground in a laboratory mill. After the process, they were passed through 75-micron sieves and stored for use in experiments.

2.3   Adsorption studies

Adsorption studies were carried out at 25±2 ^{0}C and 200 rpm in an orbital shaker (Heidolp, Unimax1010, Germany). Batch adsorption experiments were carried out in the pH range of 3-10 and especially concentrated at pH 5.0 ±0.5, where OTC has a maximum water solubility [18]. In the wavelength scan, the abs value of the OTC solution with a concentration of 6.6 mg/L and a pH value of 5 was measured as 0.226. The full wavelength scan is presented in Figure 1. OTC stock solution with a concentration of 1000 mg/L was prepared and necessary dilutions were made from the obtained solution to create a calibration curve on a UV-Vis spectrophotometer (Hach DR6000, Germany).

When creating the calibration curve of OTC, necessary dilutions were made from the stock solution. 50 mg/L intermediate stock mixture was obtained, and 2/3 ratios were prepared from 9 different solutions until the ratios reached 2.055 mg/L and the calibration curve was obtained in the spectrophotometer. The equation is *y = 0.0291x + 0.0087 (R^2:0.999)*. The absorbance of the OTC solution was carried out with a UV-Vis spectrophotometer at a maximum wavelength of 354 nm to determine the concentration [19]. In a study where OTC removal was performed with activated carbon, it was reported that OTC measurement with UV-Vis peaked in the pH range of 3.68-8.57 and at wavelengths of 354-366 nm [20].
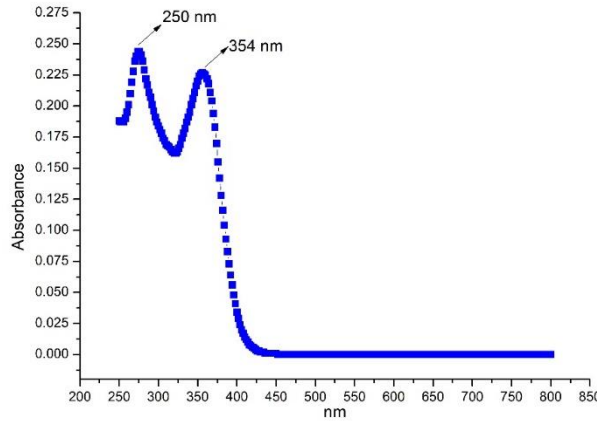
Figure 1. Wavelength scanning results of 6.6 mg/L OTC solution.

MS-Excel program was used in the model calculations of the study and graphics were created with Origin Pro 8.5. Additionally, equations 1 and 2 were used to evaluate the results obtained in each experiment.

$$R(\%) = \frac{C_0 - C_e}{C_0} \times 100 \qquad (1)$$

$$q_e = \frac{(C_0 - C_e) \times V}{m} \qquad (2)$$

Here, *R* represents the % removal efficiency, C_0 (mg/L) is the initial OTC concentration, C_e (mg/L) is the equilibrium concentration of OTC, q_e is the equilibrium adsorption capacity, *V* (L) is the volume of OTC solution, and *m* (g) is the amount of *Pn*-wcp.

2.4 Impact of environmental factors

The effect of time and initial concentration on the adsorption of OTC molecules onto *Pn*-wcp was tried to be determined. In order to determine the effect of time, 50 mL of OTC solution with an initial concentration of 75 mg/L was taken and 50 mg *Pn*-wcp was added to it. In the experiment carried out at room temperature and pH 5.0 ±0.5, samples were taken at certain time intervals and OTC concentrations were measured. On the other hand, in order to determine the effect of initial OTC concentration on adsorption, OTC solutions were added to 7 different tubes with volumes of 10 mL under the same conditions, with initial concentrations ranging from 10.13 to 116.76 mg/L.

2.5 Kinetic and isotherm studies

For kinetic studies, a 50 mL solution with a concentration of 50 mg/L was prepared from the stock OTC solution. 50 mg of *Pn*-wcp was added to the solution and samples were taken

with a 0.45-micron syringe filter at certain times in the orbital shaker and the concentration was found at the specified wavelengths in the UV-Vis spectrophotometer.

For isotherm studies, experiments were carried out by adding 10 mg of *Pn*-wcp to each of 7 different falcon tubes with a volume of 10 mL, with initial OTC concentrations ranging from 10.13 to 116.76 mg/L. Pseudo first order (PFO), PSO, Intra-particle diffusion and Elovich models were used for kinetic models and interpreted with Freundlich, Langmuir, Temkin and Dubinin-Radushkevich models for isotherm models. The equations used are presented in Table 1.

Table 1. Kinetic and isotherm models used in OTC adsorption on Pn-wcp.

	Model	Equation	References
Kinetic models	PFO	$q_t = q_e(1 - e^{-k_1 t})$	[21]
	PSO	$q_t = \dfrac{q_e^2 k_2 t}{1 + q_e k_2 t}$	[21]
	Intra-particle diffusion	$q_t = K_{id} t^{1/2} + C$	[22]
	Elovich	$q_t = \beta \ln(\alpha\beta t)$	[22]
Isotherm models	Freundlich	$q_e = K_F C_e^{1/n}$	[23]
	Langmuir	$q_e = \dfrac{q_{max} K_L C_e}{1 + K_L C_e} \quad R_L = \dfrac{1}{1 + a_L C_e}$	[23]
	Temkin	$q_e = B \ln(A_T C_e) \quad B = \dfrac{RT}{b_T}$	[24]
	Dubinin-Radushkevich	$q_e = q_s e^{-k_D \varepsilon^2}$	[24]

The terms q_t and q_e specified in the table indicate the amount of OTC removed per unit *Pn*-wcp (mg/g) at a time t and under equilibrium, respectively. The term k_1 (min^{-1}) indicates the PFO, the term k_2 (g/mg.min) indicates the PSO and K_{id} indicates the Intra-particle diffusion model constant. α (mg/g.min) indicates the Elovich initial adsorption rate and the term β (g/mg) indicates the desorption constant. In the section where isotherm models are explained, q_e (mg/g) indicates the amount of OTC adsorbed at equilibrium, C_e (mg/L) indicates the OTC concentration at equilibrium and q_{max} (mg/g) indicates the maximum adsorption capacity. K_f (mg/g) (L/mg) is the Freundlich constant $1/n$, n is the dimensionless constant and indicates the adsorption density. The terms K_L (L/mg) and a_L are the Langmuir constant. R_L represents the dispersion constant. In addition, B in the Temkin model represents the model constant, b_T

(J/mol) represents the heat of adsorption, T (K) represents the temperature, and R (8.314 J/molK) represents the universal gas constant. In the Dubinin-Radushkevich isotherm model, ε represents the Polanyi potential, and k_D represents the model constant.

2.6   Error functions

The use of error functions is extremely important in the evaluation of the adsorption process. Different error functions are usually used to minimize the error distribution between the adsorption experimental data and the isotherm correlations. In order to minimize the error distribution, it is achieved by finding the minimum value of certain error functions or by maximizing them, depending on the definition of the error function used. For this reason, it is very important to choose an error function in order to evaluate the most suitable isotherm that best explains the experimental equilibrium data [25]. The error functions and equations used in the study are presented in Table 2.

Table 2. The error functions and equations used in the study.

Function Definition	Equation	References
Error Sum of Squares (*SSE*)	$SSE = \sum (q_{e,cal} - q_{e,exp})^2$	
Sum of Absolute Errors (*SAE*)	$SAE = \sum_{i=1}^{n} \left\vert q_{e,exp} - q_{e,cal} \right\vert$	[26], [27]
Average relative errors (*ARE*)	$RAE = \dfrac{1}{n} \sum_{i=1}^{n} \left\vert \dfrac{q_{e,cal} - q_{e,exp}}{q_{e,exp}} \right\vert$	
Hybrid fractional error function (*HYBRID*)	$HYBRID = \dfrac{1}{N-P} \sum \left\vert \dfrac{q_{e,exp} - q_{e,cal}}{q_{e,exp}} \right\vert$	[27]
Marquardt's percent standard deviation (*MPSD*)	$MPSD = \sqrt{\dfrac{\sum \left\vert (q_{e,exp} - q_{e,cal})/q_{e,exp} \right\vert^2}{N-P}}$	[26]
Non-linear Chi-Square test (*X²*)	$X^2 = \sum \dfrac{(q_{e,exp} - q_{e,cal})^2}{q_{e,cal}}$	[26], [27]

In order to evaluate the adsorption results, different error function models were used to examine the kinetic models. Five error analysis methods were used to determine the kinetic model parameters in the study. These are Sum of Absolute Error (*SAE*), Marquart's percent standard deviation (*MPSD*), sum of squared errors (*SSE*), hybrid fractional error function (*HYBRID*), mean relative error (*ARE*) and Nonlinear Chi-Square (*X²*) error functions.

3 RESULTS AND DISCUSSION

3.1 Characterization results

3.1.1 FTIR results

FTIR spectra of raw *Pn*-wcp before the reaction and OTC-loaded *Pn*-wcp after the reaction are presented in Figure 2. Functional groups are seen between both cases.
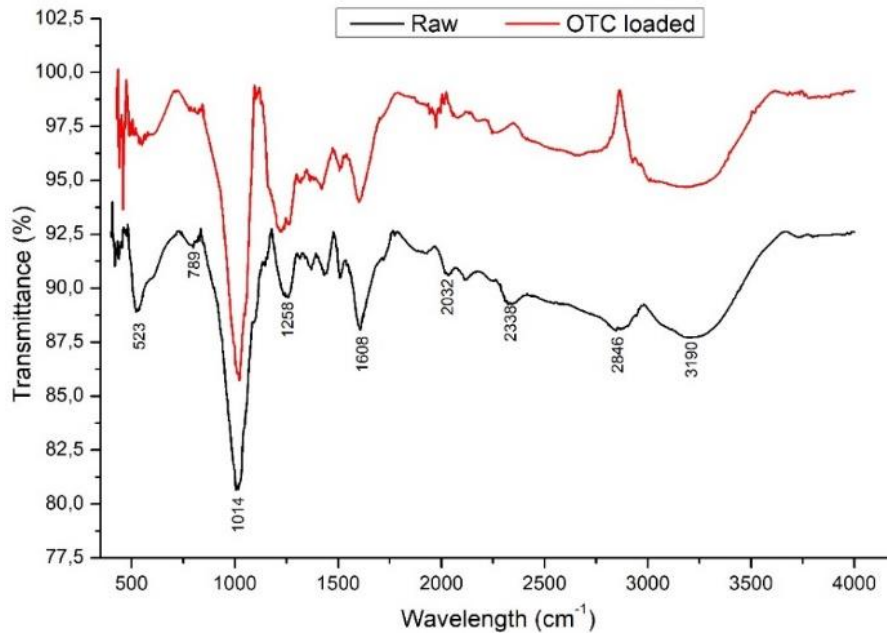
Figure 2. FTIR diagram of Pn-wcp before and after reaction.

In the spectrum of the raw adsorbent, characteristic absorption bands are observed at wavelengths of 523 cm^{-1}, 789 cm^{-1}, 1014 cm^{-1}, 1258 cm^{-1}, 1608 cm^{-1}, 2032 cm^{-1}, 2338 cm^{-1}, 2846 cm^{-1} and 3190 cm^{-1}. These bands indicate the presence of functional groups (such as hydroxyl, carbonyl, and carboxyl groups) on the surface of the adsorbent. Especially the bands around 1608 cm^{-1} indicate the C-O and C=C stretching, and therefore the presence of lignin, cellulose, and other organic components [28].

Aliphatic C–H stretching vibration is found as a very weak peak at 2846 cm^{-1}, while the asymmetric vibration of CH$_2$ group belonging to aliphatic cellulose vibration is seen at 3190 cm^{-1} [29], [30]. The bands between 523 and 1014 cm^{-1} represent –C–N– and –C–C– stretching, respectively [31]. After OTC adsorption, the obvious changes in the spectrum indicate that there is a chemical interaction on the surface of the adsorbent. Especially, the obvious changes in the regions of 1258 cm^{-1}, 1608 cm^{-1} and 2846 cm^{-1} may indicate that OTC interacts with the adsorbent surface and is probably held by hydrogen bonds or Van der Waals forces.

3.1.2 SEM and EDX results

The SEM imaging technique is an important tool for characterizing active sorptive surface areas and basic physical properties of biosorbent surfaces. It helps in morphological characterization by providing information about particle shape and size distribution. The surface morphology of *Pn*-wcp was imaged before and after adsorption and is presented in Figure 3. When Figure 3-a is examined, it is seen that *Pn*-wcp exhibits a rough, irregular, heterogeneous structure. This structure creates the necessary areas for the biosorption of OTC. In the image obtained after adsorption (Figure 3-b), the pores are partially filled, and the roughness is reduced.

The possible reason for this situation is that OTC molecules are adsorbed on the surface and pores. When the EDX graphs given in Figure 3 are examined, the changes after adsorption and the differences in element ratios support the successful adsorption of OTC molecules [32]. It can be said that especially oxygen groups play an active role in the process and are connected to the surface with the carbon-based structure of OTC.
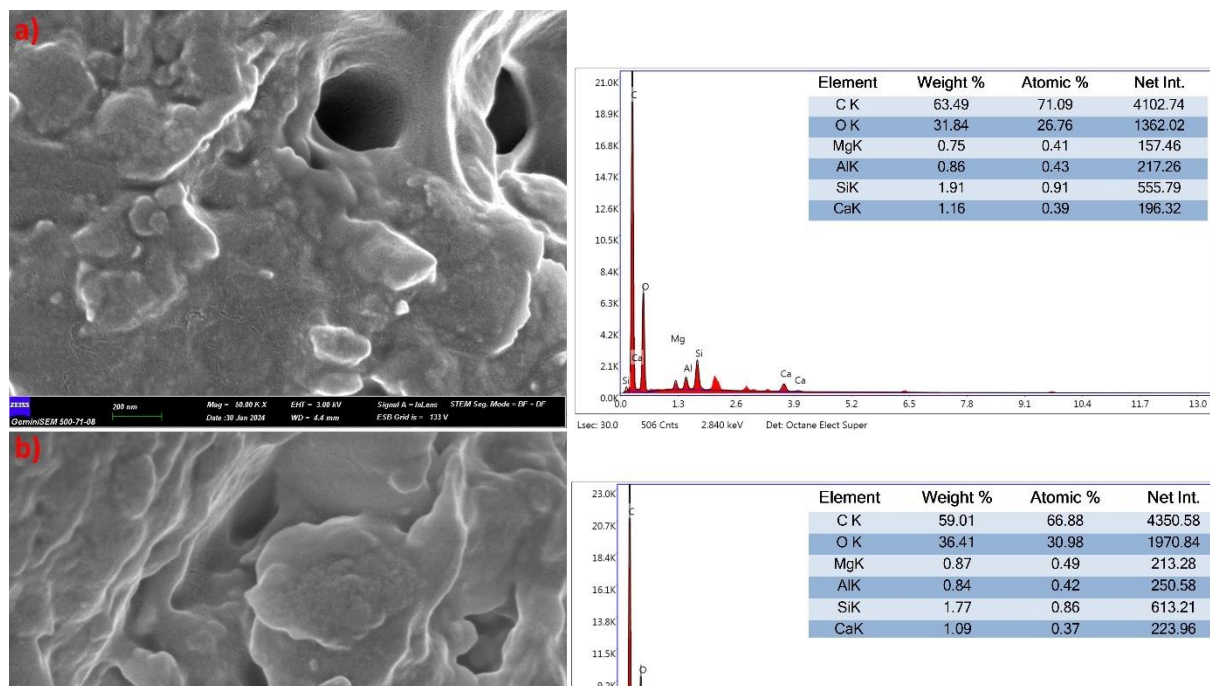
Figure 3. (a) SEM and EDX images of Pn-wcp before (b) and after reaction.

3.2   Adsorption Results

3.2.1 Effect of contact time on removal efficiency

The results obtained from the studies conducted to determine the effect of time on the adsorption of OTC molecules onto *Pn*-wcp particles are presented in Figure 4.
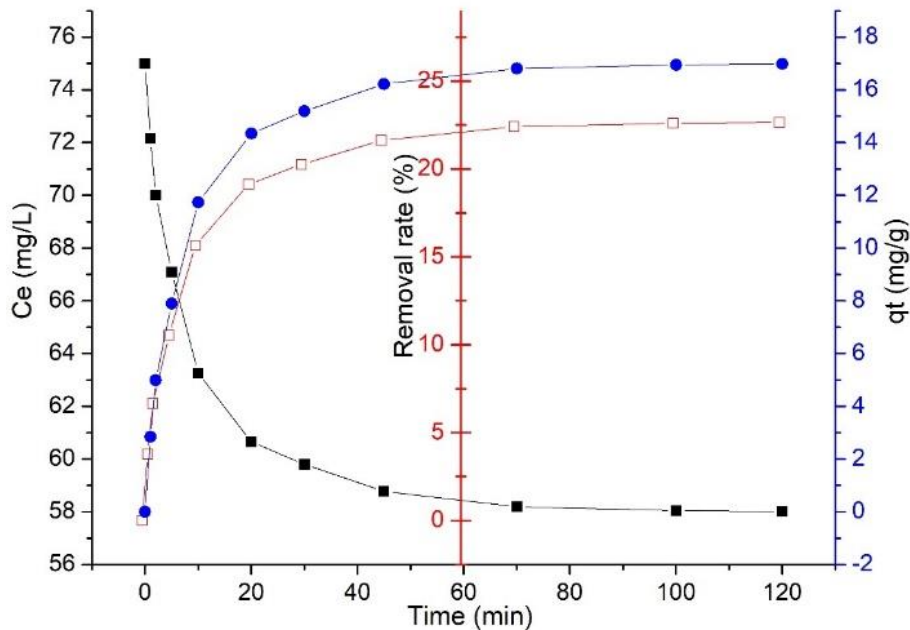
Figure 4. Effect of time on the adsorption of OTC molecules onto Pn-wcp particles.

According to Figure 4, the removal efficiency in the 1st minute was 3.8%, while it reached 10.5% in the 5th minute and 21.6% in the 45th minute, and the efficiency increase decreased in the following minutes. When the *qt* values were examined, it was determined as 2.85 mg/g in the 1st minute, 7.90 mg/g in the 5th minute and 16.22 mg/g in the 45th minute. Similarly, the increase rate slows down considerably in the following minutes. Accordingly, the removal efficiency increases with the increase in the contact time of OTC particles and OTC molecules on *Pn*-wcp. The results showed that there was a rapid adsorption in the first minutes, then it gradually increased with increasing contact time until equilibrium was reached. When Figure 4 is examined, the gradual increase that started rapidly slowed down for a certain period and then reached equilibrium. The probable reason for this is that the sorption areas become close to saturation [33].

3.2.2 Effect of initial concentration on removal efficiency

The results obtained from the experiments conducted to determine the effect of initial OTC concentration on the adsorption of OTC molecules onto *Pn*-wcp particles are presented in Figure 5.
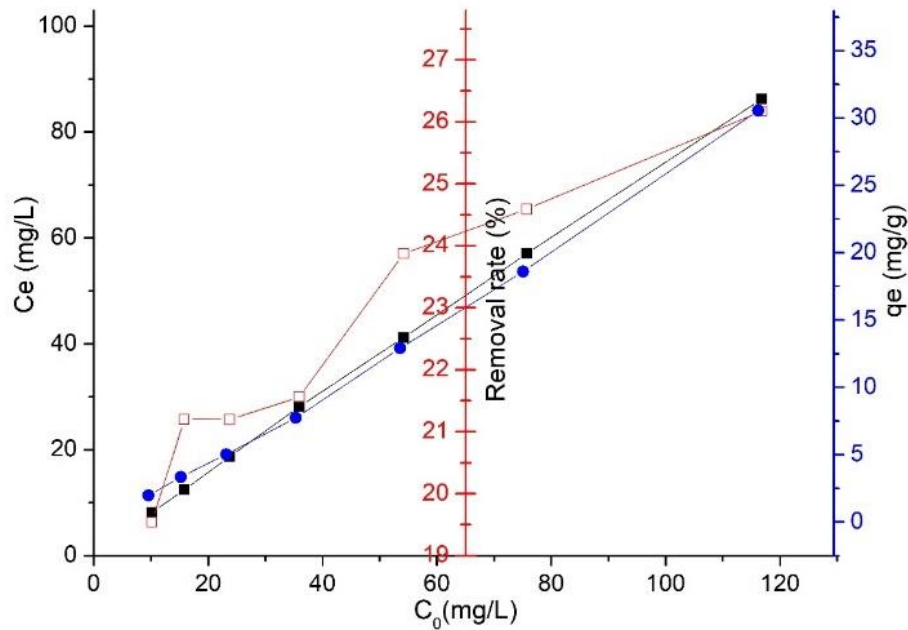
Figure 5. Effect of initial OTC concentration on the adsorption of OTC molecules onto Pn-wcp particles.

When Figure 5 is examined, when the initial OTC concentration is 10.13 mg/L, the removal efficiency is calculated as 19.55%, when the OTC concentration reaches 35.90 mg/L, the efficiency reaches 21.56%, and when the initial OTC concentration is 116.76 mg/L, the efficiency is calculated as 26.17%. When the removal efficiencies per unit adsorbent are examined, the initial OTC concentrations are calculated as 1.98, 7.74 and 30.56 mg/g at 10.16, 35.90 and 116.76 mg/L, respectively. Accordingly, the increase in the OTC change in the medium causes an increase in the adsorption capacity in the removal efficiency. When the literature is examined, it was reported that the removal efficiency increased with the increase in OTC concentration in the adsorption study of OTC hydrochloride on magnetic zeolite/Fe_3O_4 particles[34].

3.2.3 Adsorption kinetics

Adsorption kinetic models are very important for evaluating the performance of the adsorbent and investigating the adsorption mass transfer mechanisms [35]. In this study, the results obtained from 4 different kinetic models were compared with each other and presented in Table 3. In addition, the graphs obtained from the linearized forms of each model equation are also presented in Figure 6. The numerical values obtained in the laboratory environment during the adsorption of OTC molecules by *Pn*-wcp particles were tested with PFO, PSO, Elovich and Intra-particle diffusion models, respectively. In addition to these, the change graph comparing the numerical values obtained from the applied kinetic models with the amount of pollutant removed by the unit adsorbent (q_t) obtained in the experimental studies is given in Figure 7.

Table 3. Summary of the calculated kinetic models for the adsorption of OTC onto Pn-wcp.

Kinetic models	PFO	PSO	Elovich	Intra-Particle Diffusion
Parameters	$k_1 = 0.052$	$k_2 = 0.011$	$\beta = 0.317$	$k_i = 1.321$
		$q_e = 17.834$	$\alpha = 9.377$	$a = 5.295$
R^2	0.987	0.999	0.958	0.784
SSE	50.704	0.875	9.432	55.758
SAE	16.810	1.665	8.719	21.222
ARE	33.70	2.47	12.38	39.94
$HYBRID$	47.184	1.614	4.942	26.204
$MPSD$	0.993	0.960	0.970	0.987
X^2	6.746	0.102	0.797	8.394

When Table 3 is examined, the R^2 values of the PFO, Elovich and Intra-particle diffusion models were calculated as 0.987-0.958 and 0.784, respectively, while the R^2 value of the PSO model was calculated as 0.999. The evaluation of error functions in the selection of the most appropriate model is very important in terms of the accuracy of the result. The lower the error value obtained in the model, the better the performance of the estimated model [36]. When the SSE value, which is the sum of the squares of the difference between the amounts of pollutants removed per unit adsorbent ($q_{e,cal}$) obtained from the examined kinetic models and the results obtained from the adsorption process ($q_{e,exp}$), is examined, it is seen that the PSO kinetic model has the smallest value (0.875). Again, in the SAE value, which is the sum of the absolute value of the difference between the batch adsorption experimental results and the model results, the PSO kinetic model is the lowest with the value of (1.665).
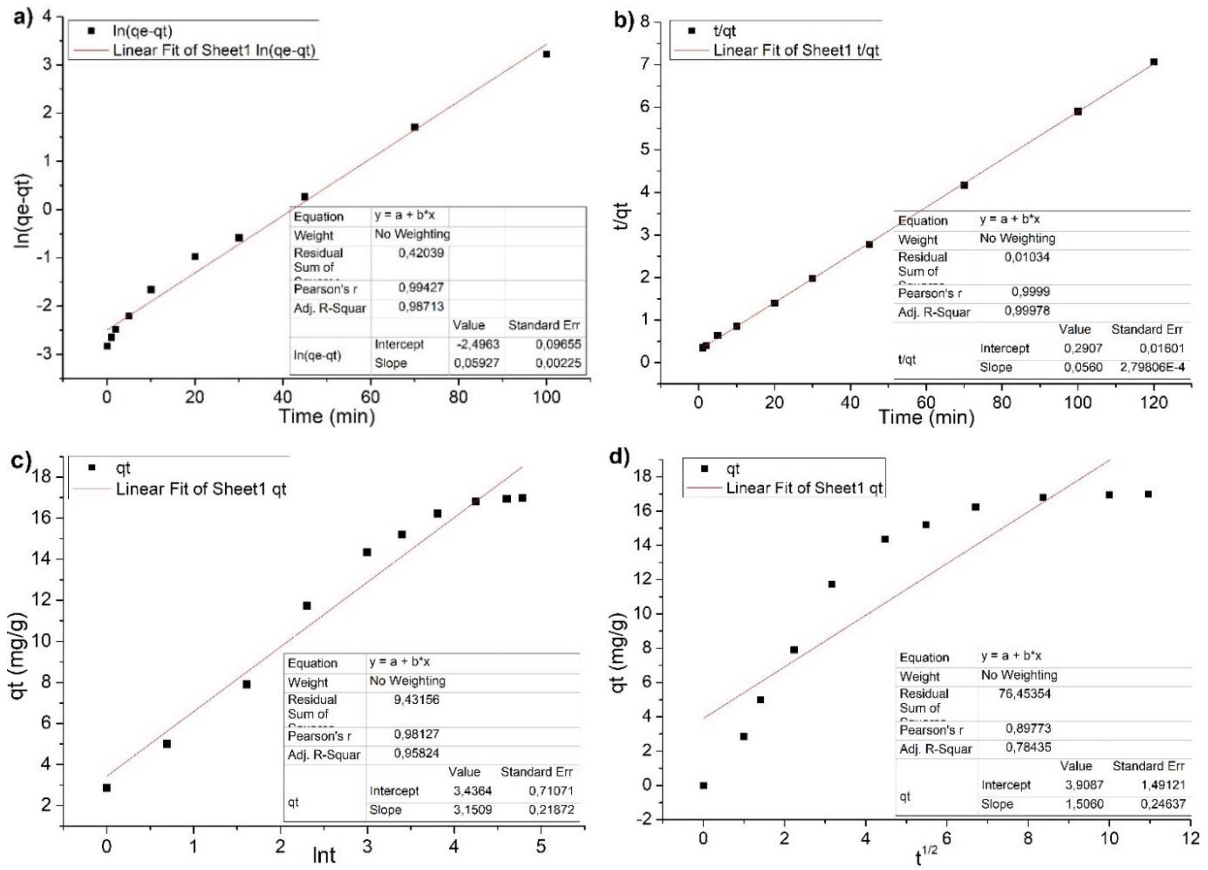
Figure 6. Regression curves, a) PFO, b) PSO, c) Elovich, d) Intra-Particle Diffusion.
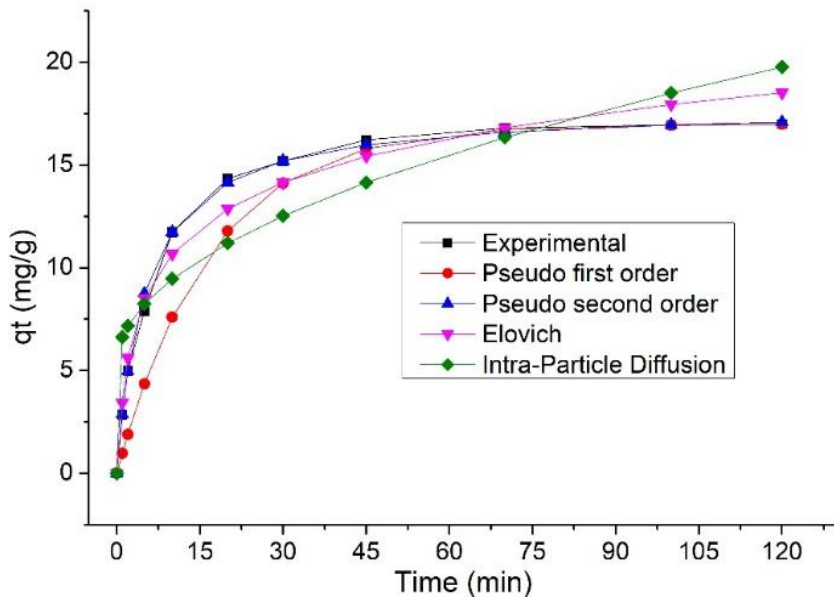
Figure 7. Graph of q_t values versus time.

When the *ARE* value obtained from the absolute value of the difference between the model and adsorption experiments divided by the experimental results is examined, it is understood that the PSO kinetic model is the lowest with the value of (2.47). In the *HYBRID* value obtained as a result of the $q_{e,cal}$ division of the *SSE* values, the lowest value is again in the PSO model with the value of (1.614) and in the *MPSD* value, which is the error calculation made regarding the geometric error distribution, (0.960).

When different literature studies were examined, it was stated that the PSO kinetic model was the model that best explained the process with the value of R^2: 0.999 in the study on OTC adsorption using pine cone biochar modified with MnO_2 [32]. Similarly, in the study on the removal of tetracycline from water with activator agents using activated carbon obtained from pine cones, it was reported that the PSO model was the model that best explained the adsorption process with the value of R^2: 0.994 [38]. In a different study, it was stated that the removal of tetracycline with pine cone biochar prepared by hydrothermal pretreatment with KOH solution was aimed, and the adsorption process was similarly suitable for the PSO model [39]. When the obtained R^2 values and error functions were evaluated together, it was seen that the PSO kinetic model was the most suitable model to explain the process among these 4 models.

3.2.4 Adsorption isotherms

The application of adsorption isotherms is very important to explain the interaction between the adsorbate and the adsorbent of any system. The parameters obtained from the modeling of isotherm results provide important information for the appropriate analysis and design of the adsorption system [40]. In this study, Freundlich, Langmuir, Temkin and Dubinin-Radushkevich isotherm models were used to interpret the data obtained from the experiments conducted for the adsorption of OTC molecules onto *Pn*-wcp particles. The results obtained from the models are presented in Table 4. In addition, the graphs obtained from the linear forms of each model are presented in Figure 8 (a), (b) (c) and (d). In addition, the comparison graph of qt values against C_e values, in which the isotherm models used are compared, is given in Figure 9.

Table 4. Summary of isotherm models calculated for the adsorption of OTC molecules onto Pn-wcp.

Isotherms	Freundlich	Langmuir	Temkin	Dubinin-Radushkevich
Parameters	$k_F = 0.176$	$k_L = 0.004$	$B_T = 0.216$	$k_D = 29.041$
	$1/n = 1.153$	$R_L = 0.8$	$k_T = 0.102$	$q_s = 14.354$
		$q_{max} = 67.512$		$E = 0.131$
R^2	0.998	0.917	0.831	0.682
SSE	0.752	266.363	88.122	332.334
SAE	1.605	27.367	21.668	31.770
ARE	3.3	31.1	75.1	58.3
HYBRID	0.07	31.07	23.34	14.74
MPSD	0.930	0.988	0.986	0.981
X^2	0.056	10.681	13.846	16.446

When Table 4 is examined, the R^2 values of the Langmuir, Temkin and Dubinin-Radushkevich models were calculated as (0.917), (0.831) and (0.682), respectively, while the R^2 value of the Freundlich model was found to be 0.998. In the evaluation made with error functions, when the *SSE, SAE, ARE, HYBRID, MPSD* and X^2 values were examined, they were calculated as (0.752), (1.605), (3.3), (0.07), (0.930) and (0.056), respectively. When similar literature studies were examined, the isotherm model in the study on the adsorption of quinolone antibiotics in water with activated carbon was defined as the Freundlich isotherm [41]. In the study carried out by Alnajrani and Alsager for the removal of antibiotics from aqueous environments, they reported that the Freundlich model with the highest R^2 values represented the process in the best way [42]. As a result, when both R^2 values and error functions are evaluated together in our study, it is seen that the adsorption of OTC molecules on *Pn*-wcp particles conforms to the Freundlich isotherm model.
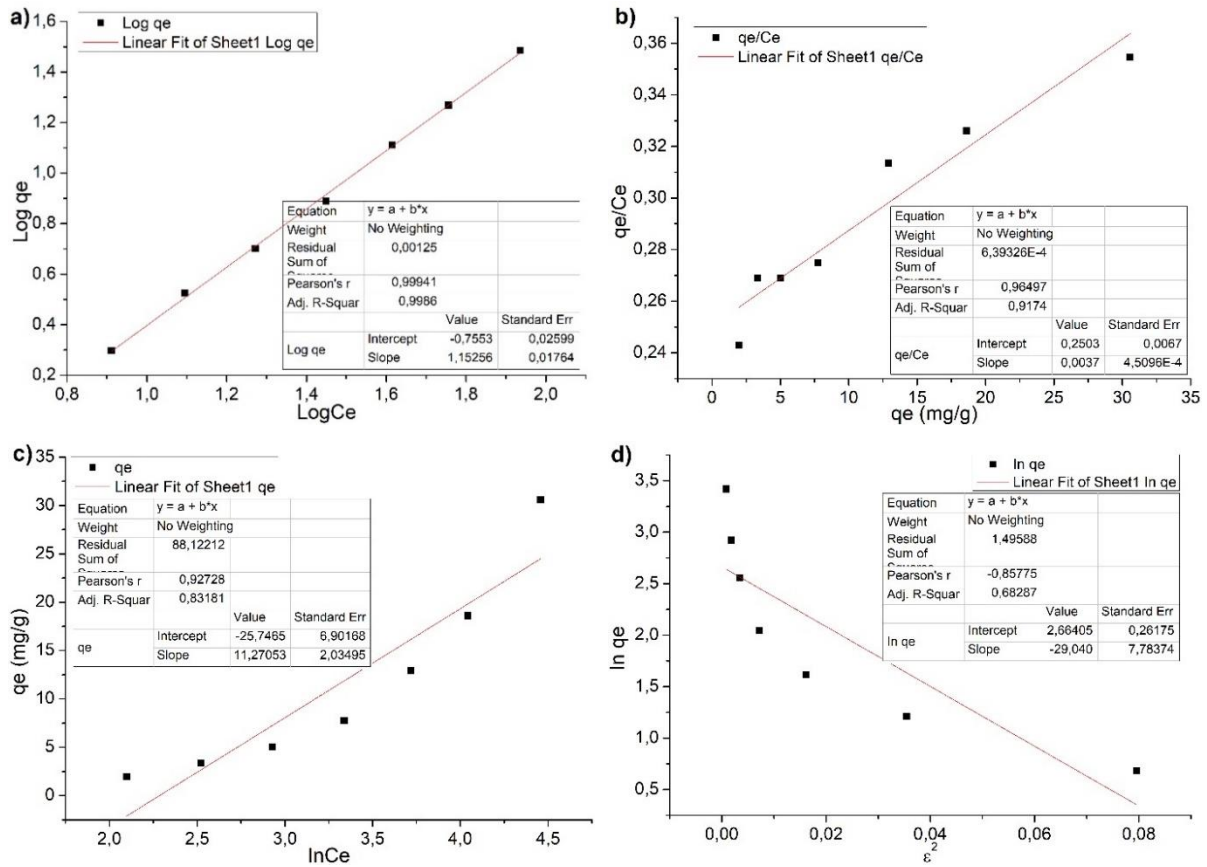
Figure 8. Regression curves (a) Freundlich, b) Langmuir, c) Temkin, d) Dubinin – Radushkevich.
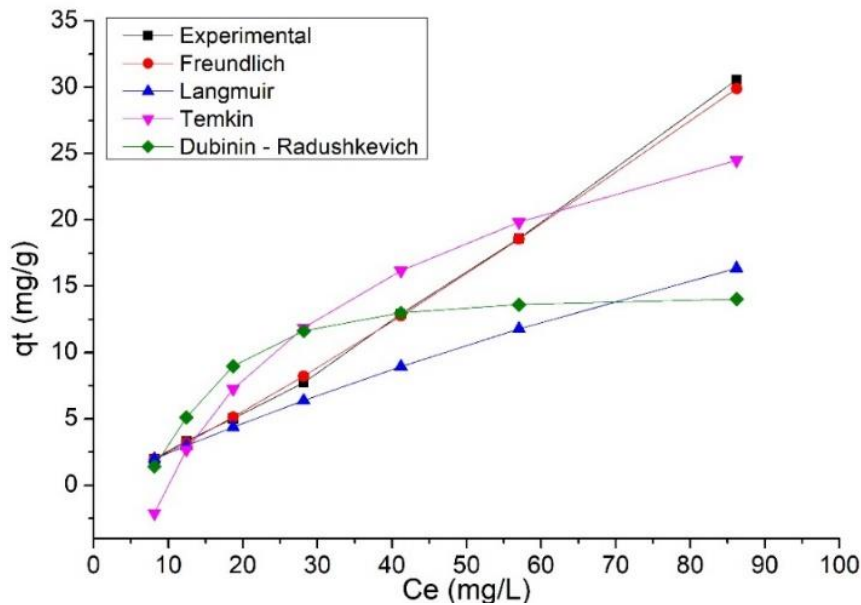
Figure 9. Graph of change of qt values against C_e values.

3.2.5 Comparison of the study and the results obtained with the literature.

When the studies in the literature (Table 5) are examined, the maximum adsorption capacity was determined as 90.9 mg/g in a study where OTC was removed from an aqueous solution with activated sludge. The maximum adsorption capacity was determined as 598 mg/g in a study where OTC was removed with activated carbon obtained from mesoporous lignin.

Table 5. Comparison of the obtained values with the literature.

Type of pollutant	Adsorbent origin	q_m (mg/g)	Reference
OTC	Activated sludge	90.9	[43]
OTC	Lignin-based carbon with mesoporous	598	[44]
OTC	Lanthanum modified magnetic humic acid	23.43	[45]
OTC	Hydroxyapatite	291.32	[33]
OTC	*Pn*-wcps	67.51	This study

The maximum adsorption capacity was determined as 23.43 mg/g in a similar study where OTC was removed with lanthanum modified magnetic humic acid. In another adsorption study where OTC was removed from an aqueous solution with hydroxyapatite, the maximum adsorption capacity was reported as 291.32 mg/g. In our study, the maximum adsorption capacity was found as 67.51 mg/g.

4   CONCLUSION AND SUGGESTIONS

In this research study, low-cost biosorbent obtained from waste pine cones was used for OTC removal from aqueous solutions in laboratory scale. 4 different kinetic and isotherm models were investigated in bulk adsorption studies. In addition, FTIR and SEM-EDX images were examined to investigate the morphological properties of raw and loaded *Pn*-wcps to support the adsorption mechanism. In the evaluation of the obtained results together with error tests, the most suitable kinetic and isotherm models were found to be PSO (R^2: 0.999) and Freundlich (R^2: 0.998), respectively. On the other hand, q_{max} was calculated as 67.51 mgOTC/g*Pn*-wcp. When the optimization studies carried out around pH 5.0 ±0.5 were evaluated, it was found that the gradual increase that started rapidly slowed down for a while and then reached equilibrium. In addition, the increase in OTC concentration in the medium caused an increase in removal efficiency and adsorption capacity. This study may be an example of different combination studies that can be applied in the removal of broad-spectrum OTC, which is used very intensively in the world, from aquatic environments in order to reduce the possible harmful effects on the environment after its use.

Statement of Research and Publication Ethics

The study is complied with research and publication ethics.

Artificial Intelligence (AI) Contribution Statement

This manuscript was entirely written, edited, analyzed, and prepared without the assistance of any artificial intelligence (AI) tools. All content, including text, data analysis, and figures, was solely generated by the author.

REFERENCES

[1]   R. Ding *et al.*, "Light-excited photoelectrons coupled with bio-photocatalysis enhanced the degradation efficiency of oxytetracycline," *Water Res*, vol. 143, pp. 589–598, Oct. 2018, doi: 10.1016/j.watres.2018.06.068.

[2]   Z. LI, W. QI, Y. FENG, Y. LIU, S. Ebrahim, and J. LONG, "Degradation mechanisms of oxytetracycline in the environment," *J Integr Agric*, vol. 18, no. 9, pp. 1953–1960, Sep. 2019, doi: 10.1016/S2095-3119(18)62121-5.

[3]   M. Karpov, B. Seiwert, V. Mordehay, T. Reemtsma, T. Polubesova, and B. Chefetz, "Transformation of oxytetracycline by redox-active Fe (III)- and Mn(IV)-containing minerals: Processes and mechanisms," *Water Res*, vol. 145, pp. 136–145, Nov. 2018, doi: 10.1016/j.watres.2018.08.015.

[4]   P. Gao, M. Munir, and I. Xagoraraki, "Correlation of tetracycline and sulfonamide antibiotics with corresponding resistance genes and resistant bacteria in a conventional municipal wastewater treatment plant," *Science of The Total Environment*, vol. 421–422, pp. 173–183, Apr. 2012, doi: 10.1016/j.scitotenv.2012.01.061.

[5]   H. Schmitt, K. Stoob, G. Hamscher, E. Smit, and W. Seinen, "Tetracyclines and Tetracycline Resistance in Agricultural Soils: Microcosm and Field Studies," *Microb Ecol*, vol. 51, no. 3, pp. 267–276, Apr. 2006, doi: 10.1007/s00248-006-9035-y.

[6]   L. M. Chiesa, M. Nobile, S. Panseri, and F. Arioli, "Suitability of feathers as control matrix for antimicrobial treatments detection compared to muscle and liver of broilers," *Food Control*, vol. 91, pp. 268–275, Sep. 2018, doi: 10.1016/j.foodcont.2018.04.002.

[7]   P. Gao, Y. Ding, H. Li, and I. Xagoraraki, "Occurrence of pharmaceuticals in a municipal wastewater treatment plant: Mass balance and removal processes," *Chemosphere*, vol. 88, no. 1, pp. 17–24, Jun. 2012, doi: 10.1016/j.chemosphere.2012.02.017.

[8]   F.-Z. Gao *et al.*, "The variations of antibiotics and antibiotic resistance genes in two subtropical large river basins of south China: Anthropogenic impacts and environmental risks," *Environmental Pollution*, vol. 312, p. 119978, Nov. 2022, doi: 10.1016/j.envpol.2022.119978.

[9]   M. Harja and G. Ciobanu, "Studies on adsorption of oxytetracycline from aqueous solutions onto hydroxyapatite," *Science of The Total Environment*, vol. 628–629, pp. 36–43, Jul. 2018, doi: 10.1016/j.scitotenv.2018.02.027.

[10]   X. Wang, J. Shen, J. Kang, X. Zhao, and Z. Chen, "Mechanism of oxytetracycline removal by aerobic granular sludge in SBR," *Water Res*, vol. 161, pp. 308–318, Sep. 2019, doi: 10.1016/j.watres.2019.06.014.

[11]   J.-A. Park, M. Pineda, M.-L. Peyot, and V. Yargeau, "Degradation of oxytetracycline and doxycycline by ozonation: Degradation pathways and toxicity assessment," *Science of The Total Environment*, vol. 856, p. 159076, Jan. 2023, doi: 10.1016/j.scitotenv.2022.159076.

[12]   W. Sun, Y. Sun, K. J. Shah, H. Zheng, and B. Ma, "Electrochemical degradation of oxytetracycline by Ti-Sn-Sb/γ-Al2O3 three-dimensional electrodes," *J Environ Manage*, vol. 241, pp. 22–31, Jul. 2019, doi: 10.1016/j.jenvman.2019.03.128.

[13] Y. Wang *et al.*, "Schwertmannite catalyze persulfate to remove oxytetracycline from wastewater under solar light or UV-254," *J Clean Prod*, vol. 364, p. 132572, Sep. 2022, doi: 10.1016/j.jclepro.2022.132572.

[14] A. Solmaz, M. Karta, T. Depci, T. Turna, and Z. A. Sari, "Preparation and characterization of activated carbons from Lemon Pulp for oxytetracycline removal," *Environ Monit Assess*, vol. 195, no. 7, p. 797, Jul. 2023, doi: 10.1007/s10661-023-11421-4.

[15] Y. Liu, N. Tan, B. Wang, and Y. Liu, "Stepwise adsorption-oxidation removal of oxytetracycline by Zn0-CNTs-Fe3O4 from aqueous solution," *Chemical Engineering Journal*, vol. 375, p. 121963, Nov. 2019, doi: 10.1016/j.cej.2019.121963.

[16] J. Zhou, F. Ma, H. Guo, and D. Su, "Activate hydrogen peroxide for efficient tetracycline degradation via a facile assembled carbon-based composite: Synergism of powdered activated carbon and ferroferric oxide nanocatalyst," *Appl Catal B*, vol. 269, p. 118784, Jul. 2020, doi: 10.1016/j.apcatb.2020.118784.

[17] M. B. Ahmed, J. L. Zhou, H. H. Ngo, and W. Guo, "Adsorptive removal of antibiotics from water and wastewater: Progress and challenges," *Science of The Total Environment*, vol. 532, pp. 112–126, Nov. 2015, doi: 10.1016/j.scitotenv.2015.05.130.

[18] Z. Li, H. Jiang, X. Wang, C. Wang, and X. Wei, "Effect of pH on Adsorption of Tetracycline Antibiotics on Graphene Oxide," *Int J Environ Res Public Health*, vol. 20, no. 3, p. 2448, Jan. 2023, doi: 10.3390/ijerph20032448.

[19] A. Kumar Subramani, P. Rani, P.-H. Wang, B.-Y. Chen, S. Mohan, and C.-T. Chang, "Performance assessment of the combined treatment for oxytetracycline antibiotics removal by sonocatalysis and degradation using Pseudomonas aeruginosa," *J Environ Chem Eng*, vol. 7, no. 4, p. 103215, Aug. 2019, doi: 10.1016/j.jece.2019.103215.

[20] M. Berger, J. Ford, and J. L. Goldfarb, "Modeling aqueous contaminant removal due to combined hydrolysis and adsorption: oxytetracycline in the presence of biomass-based activated carbons," *Sep Sci Technol*, vol. 54, no. 5, pp. 705–721, Mar. 2019, doi: 10.1080/01496395.2018.1520721.

[21] X. Guo and J. Wang, "A general kinetic model for adsorption: Theoretical analysis and modeling," *J Mol Liq*, vol. 288, p. 111100, Aug. 2019, doi: 10.1016/j.molliq.2019.111100.

[22] J. Wang and X. Guo, "Adsorption kinetic models: Physical meanings, applications, and solving methods," *J Hazard Mater*, vol. 390, p. 122156, May 2020, doi: 10.1016/j.jhazmat.2020.122156.

[23] M. Mozaffari Majd, V. Kordzadeh-Kermani, V. Ghalandari, A. Askari, and M. Sillanpää, "Adsorption isotherm models: A comprehensive and systematic review (2010−2020)," *Science of The Total Environment*, vol. 812, p. 151334, Mar. 2022, doi: 10.1016/j.scitotenv.2021.151334.

[24] J. Wang and X. Guo, "Adsorption isotherm models: Classification, physical meaning, application and solving method," *Chemosphere*, vol. 258, p. 127279, Nov. 2020, doi: 10.1016/j.chemosphere.2020.127279.

[25] S. M. Miraboutalebi, S. K. Nikouzad, M. Peydayesh, N. Allahgholi, L. Vafajoo, and G. McKay, "Methylene blue adsorption via maize silk powder: Kinetic, equilibrium, thermodynamic studies and residual error analysis," *Process Safety and Environmental Protection*, vol. 106, pp. 191–202, Feb. 2017, doi: 10.1016/j.psep.2017.01.010.

[26] H. Alrobei *et al.*, "Adsorption of anionic dye on eco-friendly synthesised reduced graphene oxide anchored with lanthanum aluminate: Isotherms, kinetics and statistical error analysis," *Ceram Int*, vol. 47, no. 7, pp. 10322–10331, Apr. 2021, doi: 10.1016/j.ceramint.2020.07.251.

[27] S. S. A. Alkurdi, R. A. Al-Juboori, J. Bundschuh, L. Bowtell, and A. Marchuk, "Inorganic arsenic species removal from water using bone char: A detailed study on adsorption kinetic and isotherm models using error functions analysis," *J Hazard Mater*, vol. 405, p. 124112, Mar. 2021, doi: 10.1016/j.jhazmat.2020.124112.

[28] I. L. A. Ouma, E. B. Naidoo, and A. E. Ofomaja, "Thermodynamic, kinetic and spectroscopic investigation of arsenite adsorption mechanism on pine cone-magnetite composite," *J Environ Chem Eng*, vol. 6, no. 4, pp. 5409–5419, Aug. 2018, doi: 10.1016/j.jece.2018.08.035.

[29] M. Momčilović, M. Purenović, A. Bojić, A. Zarubica, and M. Ranđelović, "Removal of lead(II) ions from aqueous solutions by adsorption onto pine cone activated carbon," *Desalination*, vol. 276, no. 1–3, pp. 53–59, Aug. 2011, doi: 10.1016/j.desal.2011.03.013.

[30]   N. S. Kumar, M. Asif, and M. I. Al-Hazzaa, "Adsorptive removal of phenolic compounds from aqueous solutions using pine cone biomass: kinetics and equilibrium studies," *Environmental Science and Pollution Research*, vol. 25, no. 22, pp. 21949–21960, Aug. 2018, doi: 10.1007/s11356-018-2315-5.

[31]   E. Malkoc, "Ni(II) removal from aqueous solutions using cone biomass of Thuja orientalis," *J Hazard Mater*, vol. 137, no. 2, pp. 899–908, Sep. 2006, doi: 10.1016/j.jhazmat.2006.03.004.

[32]   R. Zafar *et al.*, "Efficient and simultaneous removal of four antibiotics with silicone polymer adsorbent from aqueous solution," *Emerg Contam*, vol. 9, no. 4, p. 100258, Dec. 2023, doi: 10.1016/j.emcon.2023.100258.

[33]   M. Harja and G. Ciobanu, "Studies on adsorption of oxytetracycline from aqueous solutions onto hydroxyapatite," *Science of The Total Environment*, vol. 628–629, pp. 36–43, Jul. 2018, doi: 10.1016/j.scitotenv.2018.02.027.

[34]   G. Başkan, Ü. Açıkel, and M. Levent, "Investigation of adsorption properties of oxytetracycline hydrochloride on magnetic zeolite/Fe3O4 particles," *Advanced Powder Technology*, vol. 33, no. 6, p. 103600, Jun. 2022, doi: 10.1016/j.apt.2022.103600.

[35]   J. Wang and X. Guo, "Adsorption kinetic models: Physical meanings, applications, and solving methods," *J Hazard Mater*, vol. 390, p. 122156, May 2020, doi: 10.1016/j.jhazmat.2020.122156.

[36]   A. Terdputtakun, O. Arqueropanyo, P. Sooksamiti, S. Janhom, and W. Naksata, "Adsorption isotherm models and error analysis for single and binary adsorption of Cd(II) and Zn(II) using leonardite as adsorbent," *Environ Earth Sci*, vol. 76, no. 22, p. 777, Nov. 2017, doi: 10.1007/s12665-017-7110-y.

[37]   P. Bobde, A. K. Sharma, R. Kumar, S. Pal, J. K. Pandey, and S. Wadhwa, "Adsorptive removal of oxytetracycline using MnO2-engineered pine-cone biochar: thermodynamic and kinetic investigation and process optimization," *Environ Monit Assess*, vol. 195, no. 11, p. 1291, Nov. 2023, doi: 10.1007/s10661-023-11932-0.

[38]   S. O. Sanni, O. Oluokun, S. O. Akpotu, A. Pholosi, and V. E Pakade, "Removal of tetracycline from the aquatic environment using activated carbon: A comparative study of adsorption performance based on the activator agents," *Heliyon*, vol. 10, no. 14, p. e34637, Jul. 2024, doi: 10.1016/j.heliyon.2024.e34637.

[39]   S. Wang, L. Wu, L. Wang, J. Zhou, H. Ma, and D. Chen, "Hydrothermal Pretreatment of KOH for the Preparation of PAC and Its Adsorption on TC," *Materials*, vol. 16, no. 14, p. 4966, Jul. 2023, doi: 10.3390/ma16144966.

[40]   M. J. Ahmed, "Adsorption of quinolone, tetracycline, and penicillin antibiotics from aqueous solution using activated carbons: Review," *Environ Toxicol Pharmacol*, vol. 50, pp. 1–10, Mar. 2017, doi: 10.1016/j.etap.2017.01.004.

[41]   H. Fu *et al.*, "Activated carbon adsorption of quinolone antibiotics in water: Performance, mechanism, and modeling," *Journal of Environmental Sciences*, vol. 56, pp. 145–152, Jun. 2017, doi: 10.1016/j.jes.2016.09.010.

[42]   M. N. Alnajrani and O. A. Alsager, "Removal of Antibiotics from Water by Polymer of Intrinsic Microporosity: Isotherms, Kinetics, Thermodynamics, and Adsorption Mechanism," *Sci Rep*, vol. 10, no. 1, p. 794, Jan. 2020, doi: 10.1038/s41598-020-57616-4.

[43]   X. Song, D. Liu, G. Zhang, M. Frigon, X. Meng, and K. Li, "Adsorption mechanisms and the effect of oxytetracycline on activated sludge," *Bioresour Technol*, vol. 151, pp. 428–431, Jan. 2014, doi: 10.1016/j.biortech.2013.10.055.

[44]   H. Zhou *et al.*, "High capacity adsorption of oxytetracycline by lignin-based carbon with mesoporous structure: Adsorption behavior and mechanism," *Int J Biol Macromol*, vol. 234, p. 123689, Apr. 2023, doi: 10.1016/j.ijbiomac.2023.123689.

[45]   C. Yan, L. Fan, Y. Chen, and Y. Xiong, "Effective adsorption of oxytetracycline from aqueous solution by lanthanum modified magnetic humic acid," *Colloids Surf A Physicochem Eng Asp*, vol. 602, p. 125135, Oct. 2020, doi: 10.1016/j.colsurfa.2020.125135.

GEOMETRY OF TIMELIKE NORMAL SURFACES IN DE SITTER 3-SPACE

Ahmet SAZAK [1]

[1] *Muş Alparslan University, Varto Vocational School, Muş, Türkiye, a.sazak@alparslan.edu.tr*

ABSTRACT

In this paper, we characterize the normal surfaces of regular curves in de Sitter 3-space, which is a pseudosphere in 4-dimensional Minkowski space. The results obtained in terms of curvatures, which are the basic parameters of curves in differential geometry, have always been meaningful. Here we examine with the help of the given normal surface curvatures associated with a regular curve. First of all, we obtain the geometric components of the surface, such as fundamental forms and curvatures, in terms of the curvatures of the curve. Then, we examine the special conditions of this surface, such as minimalness and flatness. Finally, we obtain some new characterizations, theorems, and results with the help of the obtained equations.

Keywords: Normal surface, Weingarten surface, Minimal surface, Flat surface, de Sitter space

1   INTRODUCTION

The study of the geometry of surfaces associated with a curve by differential operations is a very convenient field of study for mathematics and some applied sciences. The surface associated with the curve results from the curvilinear or linear motion of a curve. In this study, the relationship between the Frenet elements and curvatures of the curve and mean, principal, and Gaussian curvatures of surface is established. As a result, surface characterizations obtained in terms of the curvatures of the curve yield meaningful results [1-11].

Some examples of surfaces associated with curves can be given as T (tangent), N (normal), and B (binormal) surfaces: Surfaces formed by the parallel movement of the curve to vector fields T, N, and B are named with these vector fields. The characteristics of these surfaces in different spaces have been widely studied. For some, see [5-7]. The normal surfaces that we will refer to in this study are formed by the transport of a curve in the vector field N direction. Let Y be the regular curve with unit speed parameter (s) and N be the (unit) normal vector field of Y. In this case, the normal surface associated with the Y is expressed by

$$\Psi(s, v) = Y + vN,$$

where v is the motion parameter [5].

Hyperbolic geometry in Minkowski space-time corresponds to the geometry of spherical space in Euclidean geometry. The place in differential geometry and mathematics of Euclidean and Minkowski spaces is undeniable [2], [4], [6-12], [14-17]. In addition, these spaces provide important geometrical explanations in other applied sciences, especially in physics. For centuries, spherical space served as the geometric foundation for Newtonian mechanics, but it fell short in explaining Einstein's theory of special relativity. At this point, Minkowski space-time and hyperbolic geometry come into play. Hyperbolic space geometry offers the geometric framework necessary for the explanation of special relativity. In our study, we characterize the surfaces in the de Sitter space

$$S_1^3 = \{X \in R_1^4; \ X \circ X = 1\},$$

from the hyperbolic space forms in *4D* Minkowski space R_1^4. Here, "∘" denotes the Lorentzian inner product [2].

In this article, we examine the normal surfaces of unit speed regular curves in S_1^3. After giving the necessary definitions, theorems, and formulas, we obtain the geometric components of the surface, such as fundamental forms, mean curvature, principal curvatures, and Gaussian curvature. With the help of these components, which we obtained in terms of the curvatures of the curve, we examine the characteristic conditions of the surface, such as being minimal, flat, and Weingarten surfaces. We obtain some theorems and corollaries from the equations we have obtained from here.

2   SURFACES AND TIMELIKE CURVES IN DE SITTER 3-SPACE

In this part, we introduce *4D* Minkowski space and its pseudo-sphere, the de Sitter space S_1^3. In addition, we give the basic theorems, definitions, and equations for the surface characterizations that we will examine in this space.

Lorentzian inner product "∘" defined in *4D* Minkowski space R_1^4 is given by

$$X \circ Y = -x_1 y_1 + x_2 y_2 + x_3 y_3 + x_4 y_4,$$

for any $X, Y \in R_1^4$. Vector product for any $X, Y, Z \in R_1^4$ is defined by

$$X \times Y \times Z = \begin{vmatrix} -e_1 & e_2 & e_3 & e_4 \\ x_1 & x_2 & x_3 & x_4 \\ y_1 & y_2 & y_3 & y_4 \\ z_1 & z_2 & z_3 & z_4 \end{vmatrix},$$

where $\{e_1, e_2, e_3, e_4\}$ is the canonical basis. The de-Sitter space S_1^3, which is a pseudo-sphere in R_1^4, is defined by [2]

$$S_1^3 = \{X \in R_1^4;\ X \circ X = 1\}.$$

Let Y be a unit speed reguler curve in S_1^3. If Y is a timelike curve, then the Serret-Frenet frame formulas and curvatures for the curve are given by [2]

$$\nabla_T T = \eta_1 N + Y$$

$$\nabla_T N = \eta_1 T + \eta_2 B$$

$$\nabla_T B = -\eta_2 N$$

and

$$\eta_1 = \|\nabla_T T - Y\|,$$

$$\eta_2 = -\frac{det(Y, \nabla_T Y, \nabla_T^2 Y, \nabla_T^3 Y)}{\eta_1^2}.$$

And also, let's remember the basic components for the characterization of surfaces. For any surface $\Psi(s, v)$ field of normal vectors and the first and second fundamental forms are respectively defined by the equations

$$n = \frac{\Psi_{\{s\}} \times \Psi_{\{v\}}}{\|\Psi_{\{s\}} \times \Psi_{\{v\}}\|}$$

where $\Psi_{\{v\}} = \frac{\partial \Psi}{\partial v}, \Psi_{\{s\}} = \frac{\partial \Psi}{\partial s}$, v parameterizes movement of curve Y, and

$$I = Ads^2 + 2Bdsdv + Cdv^2,$$

$$II = ads^2 + 2bdsdv + cdv^2,$$

where

$$A = \Psi_{\{s\}} \circ \Psi_{\{s\}}, B = \Psi_{\{s\}} \circ \Psi_{\{v\}}, C = \Psi_{\{v\}} \circ \Psi_{\{v\}},$$
$$a = \Psi_{\{ss\}} \circ n, \quad b = \Psi_{\{sv\}} \circ n, \quad c = \Psi_{\{vv\}} \circ n. \tag{1}$$

Also, Gaussian, mean, and principal curvatures K, H, and κ_1, κ_2 are defined as [3-7]:

$$K = \frac{ac - b^2}{AC - B^2}, \qquad H = \frac{Ac - 2Bb + Ca}{2\left(AC - B^2\right)}, \tag{2}$$

and

$$\kappa_1 = H + \sqrt{H^2 - K}, \quad \kappa_2 = H - \sqrt{H^2 - K}. \tag{3}$$

After giving these basic equations, we remind the following theorems to examine the cases where the normal surface is a minimal, flat, or Weingarten surface:

Definition 1. If the mean and Gaussian curvatures of a surface Ψ satisfy the equation

$$\left(\frac{\partial K}{\partial v}\right)\left(\frac{\partial H}{\partial s}\right) - \left(\frac{\partial H}{\partial v}\right)\left(\frac{\partial K}{\partial s}\right) = 0,$$

the surface Ψ is called Weingarten surface [11].

Theorem 2. A surface Ψ is a minimal surface if and only if its mean curvature is zero for all points of the surface [1].

Theorem 3. A surface Ψ is developable (flat) if and only if its Gaussian curvature is zero for all points of the surface [1].

3   TIMELIKE NORMAL SURFACES IN S_1^3

In this section, we characterize normal surfaces formed by timelike curves in S_1^3 with the help of reminders from previous sections.

Theorem 4. Let Ψ be the normal surface of a timelike curve Y with unit speed in S_1^3. Then, the first and second fundamental forms of surface Ψ are

$$I = ((v\eta_1)^2 + 2v\eta_1 + v^2\eta_2^2 + 1)ds^2 + dv^2,$$

$$II = \left(\frac{-\eta_1'\eta_2 v^2 - \eta_2' v - \eta_1 \eta_2' v^2}{\sqrt{(v\eta_1)^2 + 2v\eta_1 + v^2\eta_2^2 + 1}}\right) ds^2 + \left(\frac{-4\eta_2\eta_1 v - 2\eta_2}{\sqrt{(v\eta_1)^2 + 2v\eta_1 + v^2\eta_2^2 + 1}}\right) ds dv.$$

Proof. The normal surface of Y is given as

$$\Psi(s,v) = Y + vN.$$

Then, by partial derivatives of Ψ, we get

$$\Psi_{\{s\}} = (v\eta^1 + 1)T + \eta^2 vB,$$

$$\Psi_{\{ss\}} = (v\eta_1 + 1)Y + \eta_1'vT + (\eta_1 + v(\eta_1^2 - \eta_2^2))N + v\eta_2'B,$$

$$\Psi_{\{v\}} = N, \quad \Psi_{\{vv\}} = 0, \quad \Psi_{\{sv\}} = \eta_1 T + \eta_2 B,$$

where $\eta_1' = \frac{\partial \eta_1}{\partial s}$ and $\eta_2' = \frac{\partial \eta_2}{\partial s}$. From these equalities, field of unit normal vectors of Ψ is got as

$$n = \frac{\Psi_{\{s\}} \times \Psi_{\{v\}}}{\|\Psi_{\{s\}} \times \Psi_{\{v\}}\|} = \frac{-\eta_2 vT - (1 - v\eta_1)B}{\sqrt{(v\eta_1)^2 + 2v\eta_1 + v^2\eta_2^2 + 1}}$$

Also, from equalities (1), we obtain

$$A = (v\eta^1 + 1)^2 + v^2\eta^{22}, \quad B = C = c = 0,$$

$$a = \frac{-\eta_1'\eta_2 v^2 - \eta_2' v - \eta_1 \eta_2' v^2}{\sqrt{(v\eta_1)^2 + 2v\eta_1 + v^2\eta_2^2 + 1}}, \quad b = \frac{-2\eta_2\eta_1 v - \eta_2}{\sqrt{(v\eta_1)^2 + 2v\eta_1 + v^2\eta_2^2 + 1}} \tag{4}$$

Therefore, I and II for Ψ surface are calculated as

$$I = ((v\eta_1)^2 + 2v\eta_1 + v^2\eta_2^2 + 1)ds^2 + dv^2,$$

$$II = \left(\frac{-\eta_1'\eta_2 v^2 - \eta_2' v - \eta_1 \eta_2' v^2}{\sqrt{(v\eta_1)^2 + 2v\eta_1 + v^2\eta_2^2 + 1}}\right) ds^2 + \left(\frac{-4\eta_2\eta_1 v - 2\eta_2}{\sqrt{(v\eta_1)^2 + 2v\eta_1 + v^2\eta_2^2 + 1}}\right) ds dv.$$

Corollary 5. Let Ψ be the normal surface of a timelike curve Y with unit speed in S_1^3. Then, the mean H and Gaussian curvatures K of the surface Ψ are given by the following equations:

$$H = \frac{-\eta_1'\eta_2 v^2 - \eta_2' v - \eta_1 \eta_2' v^2}{2[(v\eta_1)^2 + 2v\eta_1 + v^2\eta_2^2 + 1]^{\frac{3}{2}}}, \tag{5}$$

$$K = \frac{-(2\eta_2\eta_1 v + \eta_2)^2}{[(v\eta_1)^2 + 2v\eta_1 + v^2\eta_2^2 + 1]^3}. \tag{6}$$

Proof. From equations (2) and (4), it's obtained

$$H = \frac{Ac - 2Bb + Ca}{2(AC - B^2)} = \frac{-\eta_1'\eta_2 v^2 - \eta_2' v - \eta_1\eta_2' v^2}{2[(v\eta_1)^2 + 2v\eta_1 + v^2\eta_2{}^2 + 1]^{3/2}},$$

$$K = \frac{ac - b^2}{AC - B^2} = \frac{-(2\eta_2\eta_1 v + \eta_2)^2}{[(v\eta_1)^2 + 2v\eta_1 + v^2\eta_2{}^2 + 1]^3}.$$

Theorem 6. Let Ψ be the normal surface of a timelike curve Y with unit speed in S_1^3. Then, the surface Ψ is minimal if and only if

$$\eta_1'\eta_2 v^2 = -\eta_2' v - \eta_1\eta_2' v^2.$$

Proof. Let Ψ be minimal surface. Then, from Theorem 2, $H = 0$. Hence, it's obtained $-\eta_1'\eta_2 v^2 - \eta_2' v - \eta_1\eta_2' v^2 = 0$. Conversely, let be $\eta_1'\eta_2 v^2 = -\eta_2' v - \eta_1\eta_2' v^2$. Then, $H = 0$. Therefore, Ψ is a minimal surface.

Theorem 7. Let Ψ be the normal surface of a timelike curve Y with unit speed in S_1^3. Then, the surface Ψ is flat if and only if

$$\eta_2 = 0 \ (\eta_1 \neq ((-1)/v))$$

or

$$\eta_1 = ((-1)/(2v)).$$

Proof. From Theorem 3 and Eq. (6), the proof is clear.

As a result of Theorem 6 and Theorem 7:

Corollary 8. Let Ψ be the normal surface of a timelike curve Y with unit speed in S_1^3. Then, the following results are obtained:

The surface Ψ is both minimal and flat if and only if the torsion of Y is zero for all points of the curve: $\eta_2 = 0 \ (\eta_1 \neq ((-1)/v))$,

Let curvature η_1 of Y be a constant. Then, the surface Ψ is a minimal surface if and only if the torsion η_2 is constant or $\eta_1 = -1/v \ (\eta_2 \neq 0)$.

Corollary 9. Let Ψ be the normal surface of a timelike curve Y with unit speed in S_1^3. In this case, principal curvatures for the surface Ψ are obtained as

$$\kappa_1 = [\sqrt{(\eta_1'\eta_2 v^2 + \eta_2' v + \eta_2'\eta_1 v^2)^2 + 4(2\eta_2\eta_1 v + \eta_2)^2} - \eta_2' v$$
$$-\eta_1'\eta_2 v^2 - \eta_2'\eta_1 v^2]/2[(v\eta_1)^2 + 2v\eta_1 + v^2\eta_2{}^2 + 1]^{3/2},$$

$$\kappa_2 = [-\sqrt{(\eta_1'\eta_2 v^2 + \eta_2'v + \eta_2'\eta_1 v^2)^2 + 4(2\eta_2\eta_1 v + \eta_2)^2} - \eta_2'v$$
$$-\eta_1'\eta_2 v^2 - \eta_2'\eta_1 v^2]/2[(v\eta_1)^2 + 2v\eta_1 + v^2\eta_2^2 + 1]^{3/2}.$$

Proof. From Eq. (3) and Corollary 5, the proof is clear.

As a result of Corollary 9:

Corollary 10. Let Ψ be the normal surface of a timelike curve Y with unit speed in S_1^3. If the curve Y has constant curvatures, principal curvatures for the surface Ψ are expressed by

$$\kappa_1 = \frac{2\eta_2\eta_1 v + \eta_2}{[(v\eta_1)^2 + 2v\eta_1 + v^2\eta_2^2 + 1]^{3/2}}$$

and

$$\kappa_2 = \frac{-2\eta_2\eta_1 v - \eta_2}{[(v\eta_1)^2 + 2v\eta_1 + v^2\eta_2^2 + 1]^{3/2}}.$$

Theorem 11. Let Ψ be normal surface of timelike curve Y with unit speed in S_1^3. If the equation

$$[2(-2v\eta_2\eta_1' - \eta_2'\eta_1 v - \eta_2' - \eta_1 v\eta_2')((v\eta_1)^2 + 2v\eta_1 + 1$$
$$+v^2\eta_2^2) - (6v\eta_2^2 + 6\eta_1^2 v + 6\eta_1)(-(\eta_1 v^2 + v)\eta_2'$$
$$-\eta_2 v^2\eta_1')][(6\eta_2 v\eta_1 + 3\eta_2)(2(\eta_1 v^2 + v)\eta_1' + 2v^2\eta_2\eta_2')$$
$$-2((v\eta_1)^2 + 2v\eta_1 + v^2\eta_2^2 + 1)(2v\eta_2\eta_1' - 2\eta_2'v\eta_1 - \eta_2')]$$
$$= [\eta_2(\eta_1 + v(4\eta_1^3 v + 5\eta_1^2 + 4\eta_1\eta_2^2 v + 3\eta_2^2))][4(v^2\eta_2^2$$
$$+(v\eta_1 + 1)^2)(v^2\eta_2\eta_1'' + 2v^2\eta_1'\eta_2' + \eta_2''v^2\eta_1 + \eta_2''v)$$
$$+6v(\eta_1' + v\eta_1\eta_1' + v\eta_2\eta_2')(v\eta_2\eta_1' + \eta_2'v\eta_1 + \eta_2')]$$

is satisfied, then surface Ψ is called Weingarten surface.

Proof. From Definition 1, if surface Ψ satisfy the equation

$$\left(\frac{\partial K}{\partial v}\right)\left(\frac{\partial H}{\partial s}\right) - \left(\frac{\partial H}{\partial v}\right)\left(\frac{\partial K}{\partial s}\right) = 0,$$

surface Ψ is a Weingarten surface. Partial derivatives of mean and Gaussian curvatures of surface Ψ are obtained as

$$\left(\frac{\partial H}{\partial v}\right) = \left(\frac{-3(2\eta_1(\eta_1 v + 1) + 2v\eta_2^2)(-\eta_2 v^2\eta_1' - v(\eta_1 v + 1)\eta_2')}{4((\eta_1 v + 1)^2 + v^2\eta_2^2)^{5/2}}\right)$$
$$+ \left(\frac{-2v\eta_2\eta_1' - \eta_1 v\eta_2' - (\eta_1 v + 1)\eta_2'}{2((\eta_1 v + 1)^2 + v^2\eta_2^2)^{3/2}}\right),$$

$$\left(\frac{\partial H}{\partial s}\right) = \left(\frac{-3(2v^2\eta_2\eta_2' + 2v\eta_1'(v\eta_1 + 1))(-v^2\eta_2\eta_1' - v\eta_2'(v\eta_1 + 1))}{4((\eta_1 v + 1)^2 + v^2\eta_2^2)^{5/2}}\right)$$
$$+ \left(\frac{-v^2\eta_2\eta_1'' - v^2\eta_1'\eta_2' - v^2\eta_1'\eta_2' - v\eta_2''(v\eta_1 + 1)}{2((\eta_1 v + 1)^2 + v^2\eta_2^2)^{3/2}}\right),$$

and

$$\left(\frac{\partial K}{\partial v}\right) = \left(\frac{2\eta_2^2(2\eta_1 v + 1)(4\eta_1^3 v^2 + 5\eta_1^2 v + 4\eta_1\eta_2^2 v^2 + \eta_1 + 3\eta_2^2 v)}{(\eta_1^2 v^2 + 2\eta_1 v + \eta_2^2 v^2 + 1)^4}\right),$$

$$\left(\frac{\partial K}{\partial s}\right) = \left(\frac{3\eta_2^2(2v\eta_1 + 1)^2(2v(v\eta_1 + 1)\eta_1' + 2v^2\eta_2\eta_2')}{(\eta_1^2 v^2 + 2\eta_1 v + \eta_2^2 v^2 + 1)^4}\right)$$
$$+ \left(\frac{2\eta_2(2v\eta_1 + 1)(2v\eta_2\eta_1' - (2v\eta_1 + 1)\eta_2')}{((v\eta_1 + 1)^2 + v^2\eta_2^2)^3}\right),$$

Hence, it's obtained

$$[2(-2v\eta_2\eta_1' - \eta_2'\eta_1 v - \eta_2' - \eta_1 v\eta_2')((v\eta_1)^2 + 2v\eta_1 + 1$$
$$+ v^2\eta_2^2) - (6v\eta_2^2 + 6\eta_1^2 v + 6\eta_1)(-(\eta_1 v^2 + v)\eta_2'$$
$$- \eta_2 v^2 \eta_1')][(6\eta_2 v\eta_1 + 3\eta_2)(2(\eta_1 v^2 + v)\eta_1' + 2v^2\eta_2\eta_2')$$
$$- 2((v\eta_1)^2 + 2v\eta_1 + v^2\eta_2^2 + 1)(2v\eta_2\eta_1' - 2\eta_2'v\eta_1 - \eta_2')]$$
$$= [\eta_2(\eta_1 + v(4\eta_1^3 v + 5\eta_1^2 + 4\eta_1\eta_2^2 v + 3\eta_2^2))][4(v^2\eta_2^2$$
$$+ (v\eta_1 + 1)^2)(v^2\eta_2\eta_1'' + 2v^2\eta_1'\eta_2' + \eta_2''v^2\eta_1 + \eta_2''v)$$
$$+ 6v(\eta_1' + v\eta_1\eta_1' + v\eta_2\eta_2')(v\eta_2\eta_1' + \eta_2'v\eta_1 + \eta_2')]$$

as a result of Theorem 6 and Theorem 11:

Corollary 12. Let Ψ be the normal surface of a timelike curve Y with unit speed in S_1^3. If the curve Y has constant curvatures, then the surface Ψ is both minimal and Weingarten surface.

Proof. Let be the curve Y has constant curvatures. From Eq. (5), $H = 0$. Hence, Ψ is minimal surface and also, from Theorem 11, Ψ is Weingarten surface.

Example

Consider the unit speed curve

$$Y(s) = (sinh(s), cosh(s), 0, 0).$$

Since

$$Y(s) \circ Y(s) = -sinh^2(s) + cosh^2(s) + 0 + 0 = 1$$

equality is satisfied, the curve is in S_1^3. Let's calculate the curvature and the torsion of curve Y. The first, second, and third derivatives of the curve are obtained as

$$Y'(s) = (cosh(s), sinh(s), 0,0),$$

$$Y''(s) = (sinh(s), cosh(s), 0,0)$$

and

$$Y'''(s) = (cosh(s), sinh(s), 0,0).$$

Also, unit vector fields T and N are obtained as

$$Y'(s) = T = (cosh(s), sinh(s), 0,0)$$

and

$$N = \frac{Y''(s)}{\|Y''(s)\|} = (sinh(s), cosh(s), 0,0)$$

Hence, the curvature is calculated as

$$\eta_1 = \nabla_T N \circ T = \sqrt{-sinh^2(s) + cosh^2(s)} = 1 .$$

Since the first, second, and third derivatives of the curve are linear, the determinant is zero. Then the torsion of the curve is obtained as

$$\eta_2 = -\frac{det(Y, Y', Y'', Y''')}{\eta_1{}^2} = 0 .$$

Therefore, η_1 and η_2 curvatures are constant. Let the normal surface of the curve be $\Psi(s, v) = Y + vN$

$$= \big((1 + v)sinh(s), (1 + v)cosh(s), 0,0\big).$$

Then, it's obtained

$$\Psi_{\{s\}} = \big((1 + v)cosh(s), (1 + v)sinh(s), 0,0\big),$$

$$\Psi_{\{ss\}} = \big((1 + v)sinh(s), (1 + v)cosh(s), 0,0\big),$$

$$\Psi_{\{v\}} = (sinh(s), cosh(s), 0,0),$$

$$\Psi_{\{vv\}} = 0, \quad \Psi_{\{sv\}} = (cosh(s), sinh(s), 0,0)$$

$n=0$ (Because $\Psi_{\{s\}}$ and $\Psi_{\{v\}}$ are linear.)

Then, $a = b = c = 0$. Hence $H = 0$. Therefore, from Definition 1 and Theorem 2, the surface Ψ is both minimal and Weingarten surface. Corollary 12 is verified.

4   CONCLUSION

Curvatures of a curve are the most basic characterization parameters. The results obtained in terms of these parameters have always been favorable. In this study, we have revealed the relationship between the normal surfaces of timelike curves and some special surfaces in Sitter space in 3D. Here we studied minimal, flat, and Weingarten surfaces. Minimizing a surface means minimizing the surface area. Minimal surfaces allow the solution of minimum field problems in physics. Similarly, flat surfaces offer convenient solutions in plane geometry and Weingarten surfaces in terms of establishing the surface curvature relationship. By obtaining the relationship of these surfaces with the normal surface in terms of the curvature and torsion of the curve, we have produced very plain and convenient results. For some main results, see Theorem 6, Theorem 7, Corollary 8, and Corollary 12. In addition, we think that our study will make a meaningful contribution to the literature, given that the subject of curves and surfaces is rarely studied in hyperbolic spaces, especially in 3-dimensional de Sitter space.

Statement of Research and Publication Ethics

The study is complied with research and publication ethics.

Artificial Intelligence (AI) Contribution Statement

This manuscript was entirely written, edited, analyzed, and prepared without the assistance of any artificial intelligence (AI) tools. All content, including text, data analysis, and figures, was solely generated by the author.

REFERENCES

[1]   M. Do Carmo, "Differential Geometry of Curves and Surfaces", *Prentice-Hall, Englewood Cliffs*, 1976.

[2]   T. Mert and B. Karlıga, "Timelike Surfaces With Constant Angle in de-Sitter Space S_1^3", *Cumhuriyet University Faculty of Science Science Journal*, vol. 37(1), pp. 1-11, 2016.

[3]   G.U. Kaymanli, S. Okur and C. Ekici, "The Ruled Surfaces Generated By Quasi Vectors", *IV. International Scientific and Vocational Studies Congress - Science and Health*, November 2019.

[4]   R. Lopez, "Differential geometry of curves and surfaces in Lorentz-Minkowski space", *Mini Course taught at IME-USP*, Brasil, 2008.

[5]   F. Sakai, "Weil divisors on normal surfaces", *Duke Mathematical Journal*, vol. 51(4), pp. 877-887, 1984.

[6]   T. Körpınar and A. Sazak, "Binormal Surfaces of Adjoint Curves in 3D Euclidean Space", *Journal of Polytechnic,* vol. 26(3), pp. 1141-1144, 2023.

[7]   T. Körpınar and A. Sazak, "Normal Surfaces Associated with Adjoint Curves in E3", *Bitlis Eren University Science Journal*, vol. 11(3), pp. 779-783, 2022.

[8]   I. Protrka, "Harmonic Evolutes of Timelike Ruled Surfaces in Minkowski Space", *18th Scientific-Professional Colloquium on Geometry and Graphics,* September, 2015.

[9]   I. Protrka, "The harmonic evolute of a helicoidal surfaces in Minkowski 3-space", *Proceedings of the Young Researcher Workshop on Differential Geometry in Minkowski Space*, Granada, Spain, pp. 133-142, 2017.

[10]   A. Sarıoglugil and A. Tutar, "On Ruled Surface in Euclidean Space E³", *Int. J. Contemp. Math. Sci.,* vol. 2(1), pp. 1-11, 2007.

[11]   Y. Ünlütürk and C. Ekici, "Parallel Surfaces of Spacelike Ruled Weingarten Surfaces in Minkowski 3-space", *New Trends in Mathematical Sciences*, vol. 1(1), pp. 85-92, 2013.

[12]   G.Y. Senturk and S. Yuce, "Characteristic properties of the ruled surface with Darboux frame in E³", *Kuwait J. Sci.*, vol. 42(2), pp. 14-33, 2015.

[13]   J.H. Choi and Y.H. Kim, "Associated curves of a Frenet curve and their applications", *Appl. Math. Comput.*, vol. 218(18), pp. 9116-9124, 2012.

[14]   T. Körpınar, M.T. Sarıaydın, and E. Turhan, "Associated curves according to Bishop frame in Euclidean 3-space", *Adv. Model. Optim.*, vol. 15(3), pp. 713-717, 2013.

[15]   N. Macit and M. Düldül, "Some new associated curves of a Frenet curve in E³ and E⁴", *Turkish J. Math.*, vol. 38, pp. 1023-1037, 2014.

[16]   S. Yılmaz, "Characterizations of some associated and special curves to type-2 Bishop frame in E³", *Kırklareli University J. Eng. Sci.*, vol. 1, pp. 66-77, 2015.

[17]   B. O'Neill, "Semi-Riemannıan Geometry with applications to relativity", *Academic Press*, *New York,* 1983.

PERFORMANCE BENCHMARKING OF CLASSICAL STATISTIC, MACHINE LEARNING, AND DEEP LEARNING TIME SERIES MODELS IN FORECASTING MEASLES CASES

Pınar CİHAN [1*] (iD), Özcan GÜLER [1] (iD)

[1] *Tekirdağ Namık Kemal University, Computer Engineering Department, Tekirdağ, Türkiye*

* *Corresponding Author: pkaya@nku.edu.tr*

ABSTRACT

In the globalizing world, the reduction in travel time has facilitated the spread of infectious diseases, particularly those transmitted through contact and respiratory secretions. Measles, a highly contagious disease easily transmitted via respiratory droplets, continues to be a significant public health threat. Despite being largely preventable through vaccination, the measles virus remains endemic in regions with low vaccination rates, impacting public health in countries receiving migrants from these areas. Accurate computer-aided forecasting of measles outbreaks can assist policymakers in making informed decisions to prevent the spread of the disease. This study compares the performance of different time series models, including classical statistical methods, machine learning, and deep learning techniques, in forecasting the number of measles cases. For performance evaluation, a comparative analysis was conducted on datasets from Benin, Cameroon, and Nigeria. The forecasting performance of the models— ARIMA, HW, LSTM, Greykite, Prophet, and XGBoost—was assessed using RMSE, MAPE, MAE, and MSLE evaluation metrics. The models were trained on the first 147 months of data from each dataset, with their forecasting performance evaluated over the subsequent 12 months. The study results reveal that the XGBoost model achieved the lowest MSLE in predicting measles cases for Benin (0.08) and Nigeria (0.69), while the LSTM model performed best for Cameroon with an MSLE of 0.67. Using the developed computer-aided system, the next six months of measles cases were forecasted for these countries. To our best knowledge, this study is one of the first to benchmark different time series models, using diverse datasets in forecasting measles cases. The findings suggest that artificial intelligence-based prediction systems can play a crucial role in preventing the spread of infectious diseases like measles and in developing effective health policies.

Keywords: Measles, Time series analysis, Machine learning, Deep learning, Benchmarking.

1   INTRODUCTION

Measles is a highly contagious viral infection. Despite the availability of a safe and effective vaccine, it remains a leading cause of childhood morbidity and mortality worldwide [1]. The virus spreads easily when an infected person breathes, coughs, or sneezes. Measles typically affects children but can impact individuals of all ages, particularly those with weakened immune systems. Symptoms include high fever, cough, runny nose, and a widespread rash. Measles-related deaths are predominantly seen in low-income countries, regions experiencing crises, areas with unmet basic needs, and where vaccination rates are insufficient. Even in countries claiming to have eliminated measles [2] or with low case numbers, imported cases from endemic regions continue to pose a significant infection risk.

Since there is no specific antiviral treatment for measles, widespread vaccination is the most effective preventive measure. The first dose of the measles-containing vaccine (MCV1) provides approximately 93% protection, while the second dose (MCV2) offers around 97% protection [3]. Achieving herd immunity requires at least 95% of the population to be vaccinated, with the remaining 5% protected indirectly through the prevention of disease spread among vaccinated individuals [4]. In 2022, approximately 83% of children worldwide received MCV1 and 74% received MCV2 before their first birthday [5]. In the African region, only 69% of children received a single dose, and 45% received two doses of the measles vaccine. These rates are below the World Health Organization (WHO) recommendations, suggesting that the disease will continue to persist in these regions and potentially affect countries with otherwise low measles incidence [6].

Computer-aided time series methods are employed to analyze temporal changes in datasets and predict future values. Recently, these methods have gained popularity, particularly for forecasting outbreaks like COVID-19 and Monkeypox. These tools have proven invaluable for predicting the course of outbreaks, analyzing disease spread and impact, and providing critical information for determining healthcare system capacities and planning intervention strategies. Similar technologies can be applied to predict the spread of infectious diseases like measles, facilitating the development of effective health policies and interventions.

In recent years, there has been an observed increase in measles cases, exacerbated by rising vaccine hesitancy [7]. This resurgence not only negatively impacts national economies but also increases mortality rates. To minimize these issues, computer-aided forecasting systems are crucial.

Accurate prediction of measles cases using these technologies is essential for disease prevention and control, as well as for maintaining public health and economic stability.

The accuracy and reliability of computer-aided forecasting systems depend on the careful selection of the model used. Therefore, this study tested six models with different methodologies: classical statistical models like Autoregressive Integrated Moving Average (ARIMA) and Holt-Winters (HW); deep learning models like Long Short-Term Memory (LSTM); and machine learning models such as Greykite, Prophet, and Extreme Gradient Boosting (XGBoost). The performance of these models was evaluated using metrics including Mean Absolute Percentage Error (MAPE), Root Mean Square Error (RMSE), Mean Absolute Error (MAE), and Mean Squared Logarithmic Error (MSLE). To generalize model performance, all models were tested across three different countries (Benin, Cameroon, and Nigeria). After identifying the most successful models, forecasts were made for measles case numbers over the next six months in these countries. The contributions of this paper are as follows:

- To compare the performance of classical statistic, machine learning, and deep learning time series models for computer-aided prediction of measles case numbers.
- To benchmark the performance of the models, Benin, Cameroon, and Nigeria measles datasets used.
- To identify the most successful model(s) in forecasting measles case numbers.
- To predict the next six months of measles case numbers for Benin, Cameroon, and Nigeria using the computer-based forecasting system developed with the most successful models.

2   RELATED STUDIES

Various models have been used in the literature for predicting measles case numbers and vaccination rates. Some of these studies are presented in Table 1. In the reviewed studies, some used a single model, while others compared the performance of multiple models. In studies with multiple models, the most successful model is indicated in bold. Additionally, different metrics were used to evaluate the models, and both the metrics used, and the results of the most successful metric are presented in the table. Examination of the studies presented in Table 1 reveals that only a limited number of time series models have been tested for their effectiveness.

Table 1. Various studies on measles epidemic.

Method(s)	Predict	Study area	Data Range	Metrics	Best Result	Forecast	Ref.
ANFIS	Monthly measles case	Twenty-eight EU members	01-2011 03-2018	RMSE MAPE MAE MSE NRMSE	MAPE= 136.486	✓	[8]
ANFIS GA Based RFNN	Monthly measles case	Ethiopia	01-2011 12-2017	RMSE MAPE MAE NMSE	MAPE= 200.25	✗	[9]
ARIMA Improved ARlMA	Monthly measles case Monthly birth Annual immigration	Baltimore New York USA	1939-1972 1946-1959 1820-1962	RMSE MSE MAE	MAE= 0.26 0.02 0.06	✗	[10]
SARIMA	Monthly measles case	India	01-1980 07-2017	RMSE MAE R²	MAE= 1329.29	✓	[11]
ARIMA combined Poisson regression	Monthly measles case	Kano (Nigeria)	1997-2012	RMSE MAPE R²	MAPE= 162.66	✗	[12]
ARIMA	Quarterly data of measles case Quarterly data of Measles Immunization	Obudu (Nigeria)	2000-2020	MAPE MAD MSD	MAPE= 301.88 206	✓	[13]
ARIMA	Monthly measles case	Bangladesh	01-2000 08-2009	-	-	✓	[14]
ARIMA SLR	Monthly measles case	UK Spain Italy France Germany All	10-2013 08-2018	MSE% MSE R	MSE%= 26.88 14.43 11.80 21.88 17.86 12.19	✗	[15]
ARIMA	Annual measles case	Philippines	2015-2019	-	-	✓	[16]
ARIMA	Annual measles case	Iran	1974-2021	-	-	✓	[17]
ARIMA GM GRNN	Monthly measles incidence rate	Shenyang (China)	01-2011 12-2017	SSE RMSE MAPE MAE	MAPE= 0.440	✗	[18]
ARIMA	Annoual Measles morbidity rate	Bulgaria	1921-2017	-	-	✗	[19]
ARIMA	Monthly measles vaccination coverage	Cabanatuan (Philippines)	01-2014 12-2018	RMSE Normalized BIC	RMSE= 73.86	✓	[20]
ANN	Annual measles vaccination rate	Nigeria	1984-2019	MSE MAE	MAE= 0.641	✓	[21]
ARIMA	Monthly measles case	Ashanti Region (Ghana)	01-2001 05-2012	MAE MSE	MAE= 28.11	✗	[22]

3   DATA SOURCE AND METHODOLOGY

The aim of this study is to develop a computer-aided system for accurate and reliable forecasting of measles case numbers. To generalize and evaluate the prediction performance of the system, the models were tested through benchmarking on datasets from different countries. In the study, monthly measles case numbers from Benin, Cameroon, and Nigeria between January 2011 and March 2024 were used, with data obtained from the World Health Organization (WHO) website [23]. The datasets for each country contain 159 months of data, with the first 147 months (92.5%) from January 2011 to March 2023 used for training the models, and the last 12 months (7.5%) from April 2023 to March 2024 used for testing the models' prediction performance. The computer-aided system developed with the most successful models was used to forecast measles case numbers for the next 6 months (April-September 2024) in these countries.

Figure 1 presents the measles case numbers and vaccination rates in Benin, Cameroon, and Nigeria. An examination of Figure 1 reveals that these countries exhibit low vaccination rates and high case numbers.
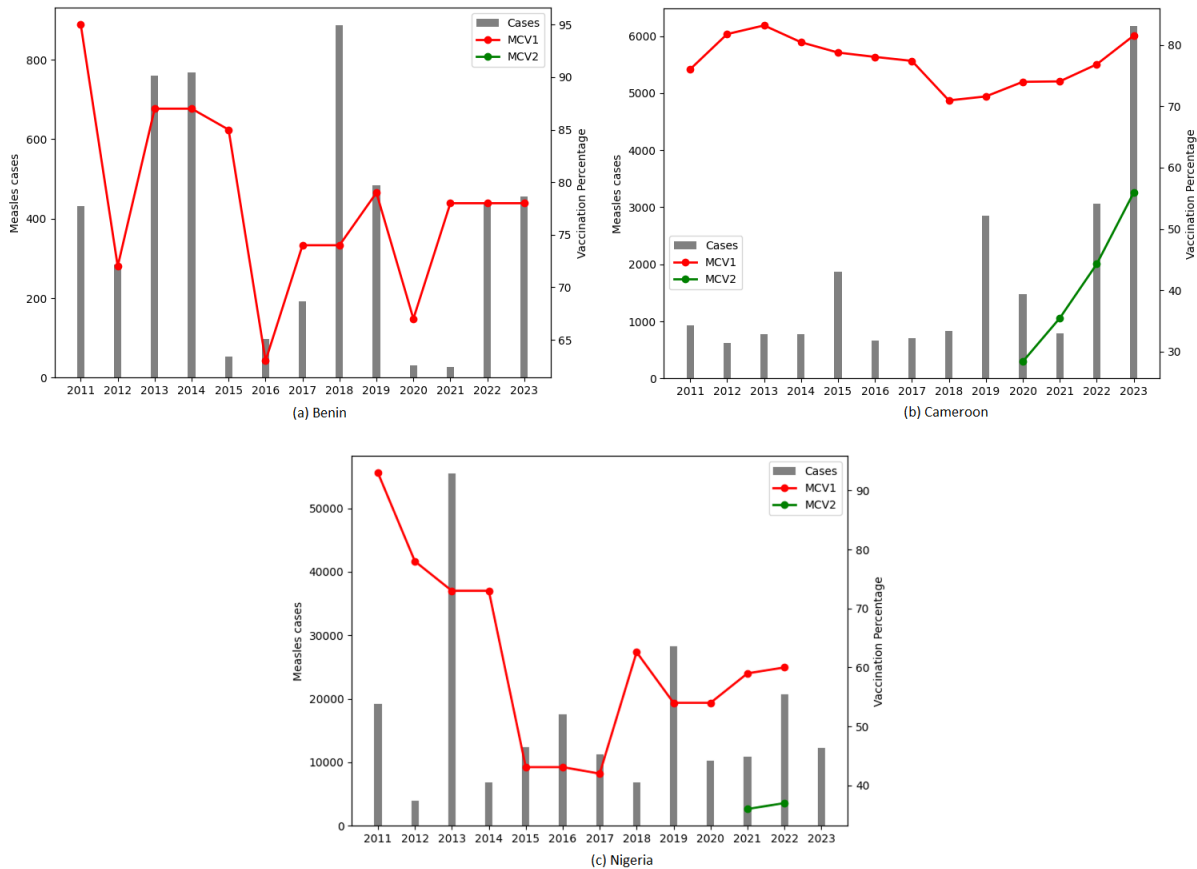
Figure 1. Number of measles cases and vaccination percentage from 2011 to 2023.

3.1   Used Time Series Forecasting Models

The performance of the forecasting models ARIMA and HW from classical statistics, LSTM from deep learning, and Greykite, Prophet, and XGBoost from machine learning has been compared. Brief descriptions of these models are provided below.

The ARIMA model is a classical statistical approach widely used in fields such as health [24-27], environment [28], and energy [29]. It assumes that the predicted value of a variable is generated from a linear equation of previous observations and random errors. The model is denoted as ARIMA (p,d,q), where (p) represents the autoregressive order, (d) is the number of differencing required to make the series stationary, and (q) denotes the moving average order.

Stationarity means the series is free from seasonal fluctuations; if the series is not stationary, it must be transformed before developing the forecasting model. A stationary series becomes an ARMA (p,q) model. For series with seasonal variations, the Seasonal AutoRegressive Integrated Moving Average (SARIMA) model is used, represented as SARIMA (p,d,q)(P,D,Q)s, where s is the seasonal period and P, D, and Q are seasonal autoregressive, seasonal differencing, and seasonal moving average terms.

During model parameterization, Autocorrelation Function (ACF) and Partial Autocorrelation Function (PACF) are utilized. ACF measures the relationship between current values and previous ones, while PACF represents the correlation coefficient between the variable and its time lag. Model selection involves calculating the Akaike Information Criterion (AIC) and Bayesian Information Criterion (BIC), with the smallest values typically indicating the best model for forecasting.

The Holt-Winters (HW) model is a classical statistical method that extends simple exponential smoothing by incorporating seasonality and trend components into the forecasting process. There are two methods based on seasonality: additive and multiplicative. The multiplicative method derives seasonality by multiplying it with the trend, while the additive method incorporates seasonality by adding it to the trend [30].

The Long Short-Term Memory (LSTM) model is a type of Recurrent Neural Network (RNN) designed for processing sequential data with temporal dependencies. RNNs often face the issue of vanishing gradients as training progresses backward over time, making it difficult for the

network to learn long-term dependencies. LSTM addresses this problem using memory cells and gating mechanisms, which help the network retain or forget information over time. The core concepts of LSTM are cell state and gating structure, where cell states can carry information and mitigate short-term memory effects. Each LSTM unit includes three types of gates to control the state of the cells, as shown in Figure 2 [31].
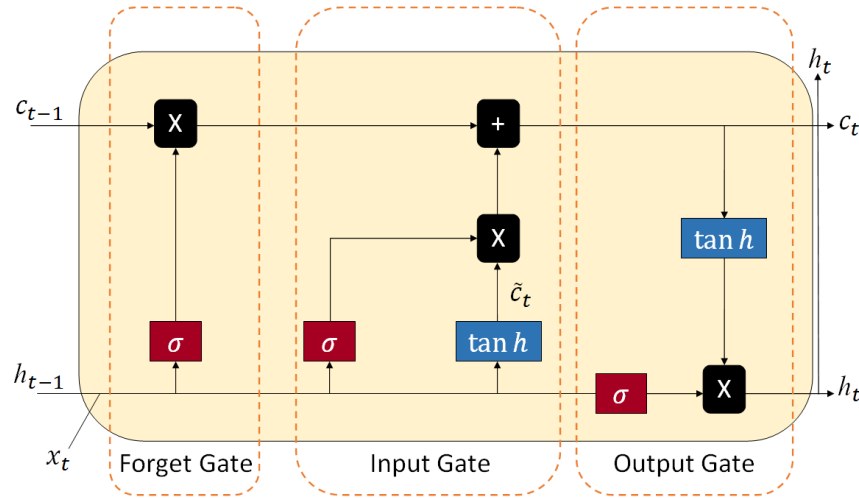
Figure 2. LSTM Architecture.

Here, the forget gate determines whether to keep or discard the information in the memory cell from the previous time step. It takes the previous hidden state and the current input as inputs, producing a forget gate vector that is element-wise multiplied with the current memory cell state. The resulting product is combined with the candidate values obtained from the input gate and candidate calculation to update the memory cell state c_t.

The input gate regulates the flow of new information into the memory cell. It determines which parts of the current input, and the previous hidden state are relevant and should be stored in the cell state. The input gate takes two inputs: the previous hidden state (h_{t-1}) and the current input (x_t). These inputs are combined and passed through a linear transformation to compute the input gate vector.

Candidate Value ($\tilde{c}_t$) contributes to updating the memory cell state in LSTM networks by generating new information from the current input and the previous hidden state.

Cell State (c_t) stores information over long time periods, allowing the LSTM to retain important information from previous time steps.

The output gate determines the new hidden state based on the updated memory cell, the previous hidden state, and the current input data. It decides which information from the updated memory cell should be output as the current hidden state (h_t). The output gate takes two inputs: the previous hidden state (h_{t-1}) and the current input (x_t) and uses these inputs to make this decision.

Output (h_t) can be used for prediction tasks or passed to subsequent layers in the neural network.

The Greykite model, a machine learning approach, offers a fast, accurate, and intuitive algorithm, making it suitable for large-scale interactive and automated forecasting. Greykite includes a simple modeling interface that facilitates data exploration and model tuning. This interface provides intuitive forecasts through its flagship algorithm, known as Silverkite [32].

The Prophet model, a machine learning method, relies on an additive approach that combines non-linear trends with annual, monthly, weekly, and daily seasonalities to forecast time series data. A well-constructed model not only aids in future predictions but also enables anomaly detection and missing value imputation [33]. Seasonal effects are modeled using Fourier series, allowing for accurate capture of periodic patterns across various time scales.

The Extreme Gradient Boosting (XGBoost) model is a scalable machine learning system for tree-based boosting methods. XGBoost is known as an optimized and distributed gradient boosting library. This algorithm efficiently analyzes the importance of all input features. The goal of XGBoost is to enhance performance by continuously creating new tree models and minimizing the objective function to improve existing models. By employing gradient reduction techniques, each new model corrects the errors of the previous one, leading to better results [34].

3.2   Validation Index

In this study, MAPE, RMSE, MAE, and MSLE metrics were used to assess the accuracy of models in predicting measles case numbers [8, 34-36]. These metrics allow for a comprehensive analysis of model accuracy by evaluating prediction performance from various perspectives. All these metrics are related to error, with lower values indicating higher prediction performance of the model [24].

The MAPE metric measures the average magnitude of errors as a percentage and is calculated as shown in Equation 1.

$$MAPE = \frac{100\%}{n} \sum_{t=1}^{n} \left| \frac{(actual_t - predicted_t)}{actual_t} \right| \tag{1}$$

The MAE is a regression metric that represents the average of the absolute differences between predicted values and actual values and is calculated as shown in Equation 2.

$$MAE = \frac{1}{n} \sum_{t=1}^{n} |actual_t - predicted_t| \tag{2}$$

The RMSE is a metric that provides the difference between the predicted values and the observed actual values and is calculated as shown in Equation 3.

$$RMSE = \sqrt{\frac{1}{n} \sum_{t=1}^{n} (actual_t - predicted_t)^2} \tag{3}$$

The MSLE measures the average squared difference between the natural logarithms of predicted and actual values. This metric provides more accurate results in cases where actual values are close to zero compared to MSE and is calculated as shown in Equation 4.

$$MSLE = \frac{1}{n} \sum_{1}^{n} (log(actual_t) - log(predicted_t))^2 \tag{4}$$

Here, n epresents the number of observations, $actual_t$ and $predicted_t$ represent the actual and predicted values at time t, respectively. $actual_t - predicted_t$ represents the error at time t.

4   EXPERIMENTAL EVALUATION AND RESULT ANALYSIS

Measles is a vaccine-preventable disease, but it can still have a significant impact, especially in developing countries. Factors such as limited vaccine access, natural disasters, wars, migration, and malnutrition can alter the disease's progression, leaving governments struggling. Computer-aided predictions of future measles case numbers can help authorities implement preventive measures. Therefore, comparing the performance of different models to determine the most accurate one for forecasting with minimal error is crucial.

To this end, the study compares the performance of ARIMA, HW, LSTM, Greykite, Prophet, and XGBoost models in predicting measles case numbers. To generalize the model performances, three different datasets from Benin, Cameroon, and Nigeria were used in the study. This approach allowed for a comprehensive evaluation of the models' effectiveness under different data conditions and the identification of the most successful prediction methods. Figure 3 shows the monthly measles case numbers for the countries used in the study and the time range of the training/testing datasets for the models.
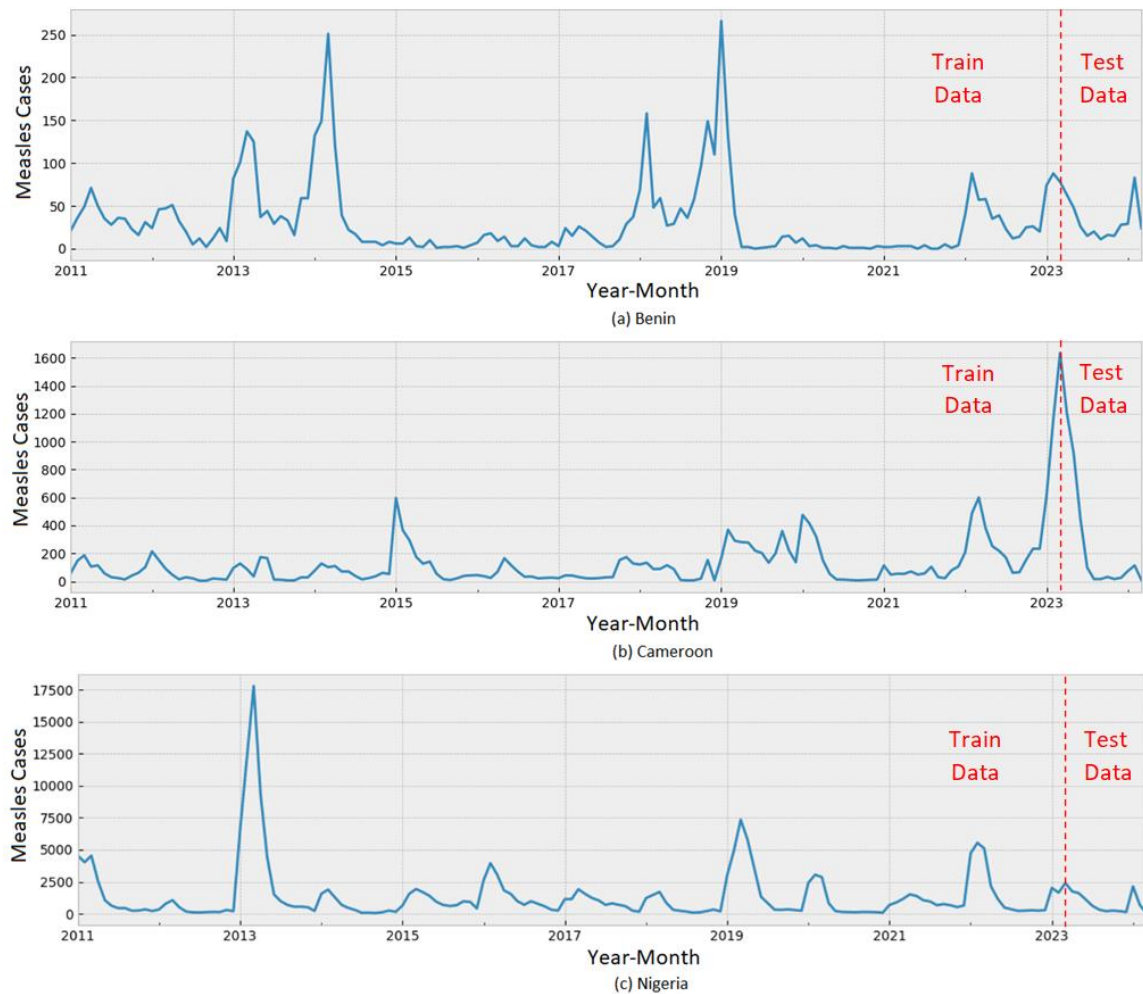
Figure 3. Graphs of monthly measles cases from January 2011 to March 2024.

As shown in Figure 3, the measles case numbers in Benin, Cameroon, and Nigeria vary between January 2011 and March 2024. Each country has a dataset of 159 months of data, with the first 147 months used for training the models and the last 12 months for testing their prediction performance. Benin reached its highest number of cases in 2014 (251 cases) and 2019 (266 cases).

In Cameroon, a significant increase was observed in 2023 (1,634 cases). Nigeria reported the highest number of measles cases in 2013 (17,797 cases).

The measles case numbers for the three countries have been archived in Excel format. The datasets were split into two parts: training and testing datasets. After completing the training phases of the models, predictions were made, and prediction errors for the test dataset were measured. A forecasting system was developed with the models having the lowest test errors, and the measles case numbers for the next six months were predicted for the three countries. All models used in the study were developed with Python 3.10.12, utilizing pandas, numpy, seaborn, and matplotlib libraries. The process followed in developing the computer-aided measles case prediction and forecasting system is presented in the flowchart in Figure 4.
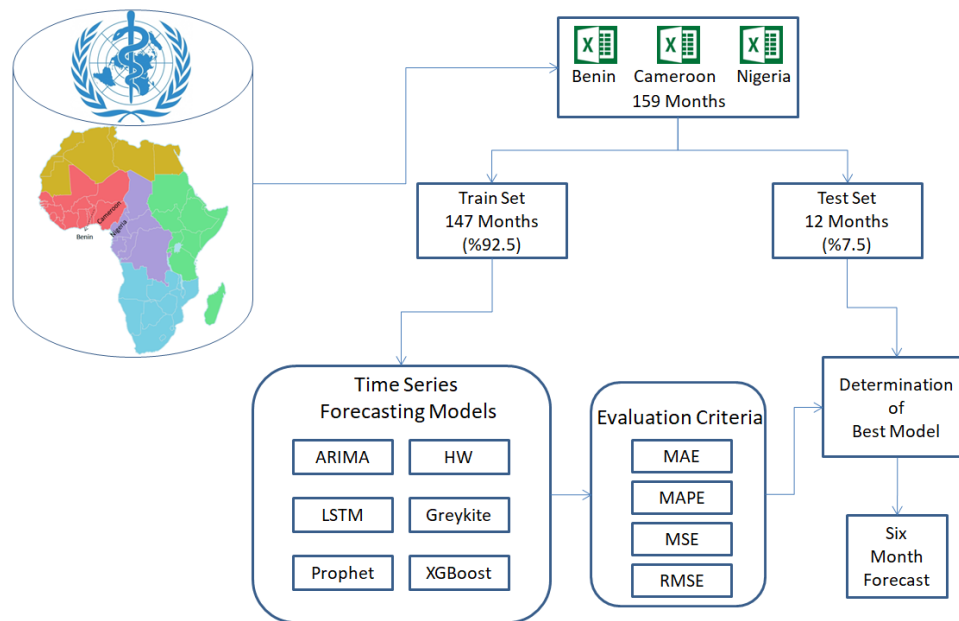
Figure 4. Flowchart for Measles Case Forecasting.

4.1 ARIMA Model Performance in Measles Case Prediction

For the ARIMA model, the time series must be stationary. Stationarity analysis is typically performed using the Augmented Dickey–Fuller (ADF) test. In the ADF test, the null hypothesis suggests that the series is non-stationary, while the alternative hypothesis suggests that the series is stationary. A 95% confidence level is used for reliable predictions, meaning the p-value should be less than 0.05. Additionally, the test statistic must be smaller than the critical value (5%). The ADF test results for the three countries are presented in Table 2.

Table 2. Augmented Dickey-Fuller test results by country.

Country	p-value	Test statistic	Critical value (5%)	Lags	Stationarity
Benin	0.03	-3.08	-2.58	12	Stationarity
Cameroon	0.00	-5.25	-2.88	1	Stationarity
Nigeria	0.00	-5.51	-2.88	4	Stationarity

The ADF test results indicate that the time series for the three countries are stationary, as the p-values are less than 0.05 and the test statistics are smaller than the corresponding critical values. To determine seasonality and model parameters, ACF and PACF plots were examined. Figure 5 shows the ACF and PACF plots for Benin, Cameroon, and Nigeria.
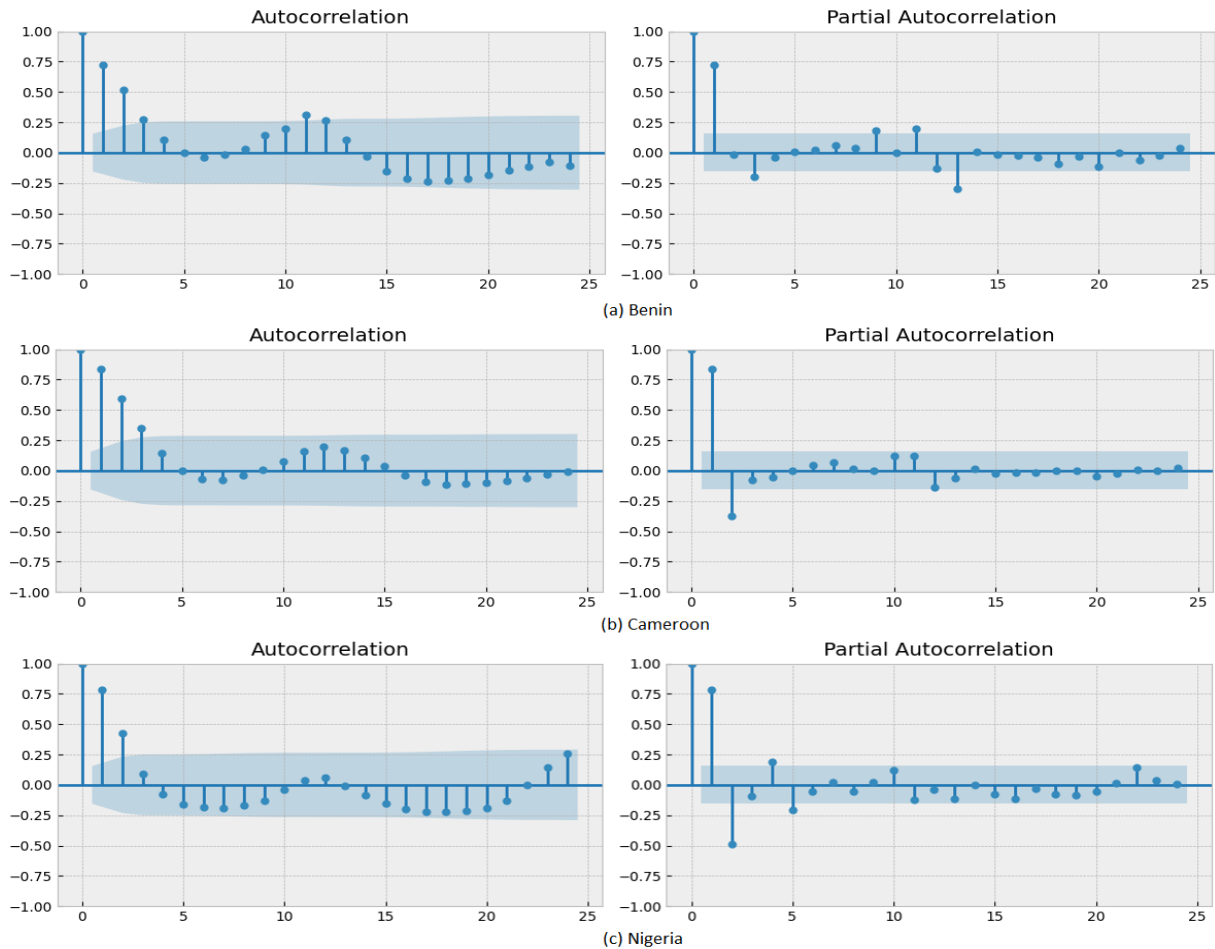
Figure 5. ACF and PACF plots of the original series

Figure 5 shows the ACF and PACF graphs, where the x-axis represents the lag number, indicating previous periods of the series. PACF helps determine the AR (p) parameter, while ACF helps determine the MA (q) parameter. Since the ADF test indicates that the series is stationary, the d parameter is zero. When ACF and PACF graphs are insufficient, the auto_arima function automatically determines the parameters by selecting the model with the lowest AIC/BIC values. Figure 5(a) shows a gradual decline in the ACF graph up to the 4th lag and significant changes in the PACF graph for the first 4 lags, leading to ARIMA (4, 0, 2) as the best model for Benin. Figure 5(b) indicates that for Cameroon, ARIMA (2, 0, 0) is the recommended model based on ACF and PACF graphs. Figure 5(c) shows regular increases and decreases in 12-month periods in the ACF graph, indicating seasonality. Using the auto_arima function, ARIMA (2,0,0)(2,0,1)12 was found to be the best model. Different ARIMA parameters were tested for measles prediction, and the results are presented in Tables 3, 4, and 5.

Table 3. Comparison of ARIMA models tested for Benin.

Model	RMSE	MAPE	MAE	MSLE	AIC	BIC
ARIMA (0,0,2)	19.44	63.90	15.21	0.32	1437	1449
ARIMA (1,0,0)	23.03	92.00	19.18	0.49	1426	1434
ARIMA (1,0,4)	19.16	64.70	14.36	0.33	1428	1449
ARIMA (1,0,5)	19.45	68.12	14.93	0.35	1430	1454
ARIMA (2,0,1)	23.30	93.21	19.43	0.50	1429	1444
ARIMA (2,0,3)	18.58	59.33	13.56	0.30	1428	1449
ARIMA (3,0,1)	18.50	57.66	13.23	0.29	1426	1444
ARIMA (3,0,4)	15.63	44.27	11.01	0.18	1428	1455
ARIMA (4,0,0)	18.46	57.42	13.21	0.29	1426	1444
ARIMA (4,0,2)	18.53	58.84	13.35	0.30	1427	1451
ARIMA (5,0,4)	21.06	78.69	16.48	0.42	1427	1460
ARIMA (5,0,5)	16.34	55.77	13.38	0.22	1424	1460

Table 4. Comparison of ARIMA models tested for Cameroon.

Model	RMSE	MAPE	MAE	MSLE	AIC	BIC
ARIMA (0,0,4)	113.33	367.43	99.70	2.04	1815	1833
ARIMA (1,0,0)	1266.01	4745.68	1222.59	11.53	1808	1817
ARIMA (1,0,4)	911.70	2918.16	863.19	8.98	1803	1824
ARIMA (1,0,5)	912.64	2809.30	844.90	8.74	1817	1832
ARIMA (2,0,0)	879.11	2983.65	846.41	9.10	1798	1810

Table 4 (continued). Comparison of ARIMA models tested for Cameroon.

Model	RMSE	MAPE	MAE	MSLE	AIC	BIC
ARIMA (2,0,1)	792.72	2435.41	737.93	8.06	1800	1815
ARIMA (3,0,3)	761.29	2274.21	695.73	7.68	1805	1829
ARIMA (3,0,4)	802.46	2523.28	741.60	8.11	1798	1825
ARIMA (4,0,0)	810.71	2286.23	723.35	7.63	1801	1818
ARIMA (4,0,3)	716.90	1971.96	633.80	6.95	1805	1832
ARIMA (5,0,2)	1094.91	3619.55	1045.90	10.13	1797	1824
ARIMA (5,0,4)	736.81	1617.82	588.15	5.58	1800	1833

Table 5. Comparison of SARIMA models tested for Nigeria.

Model	RMSE	MAPE	MAE	MSLE	AIC	BIC
ARIMA(0,0,0)(3,0,3)$_{12}$	491.79	742.00	376.91	1.80	2841	2865
ARIMA(0,0,0)(5,0,4)$_{12}$	487.38	705.59	443.20	2.12	2666	2699
ARIMA(0,0,1)(4,0,1)$_{12}$	517.53	790.04	454.15	2.15	2561	2585
ARIMA(0,0,1)(5,0,3)$_{12}$	410.08	195.51	362.57	1.08	2545	2578
ARIMA(0,0,5)(3,0,3)$_{12}$	518.33	782.82	430.77	2.21	2480	2519
ARIMA(1,0,0)(4,0,5)$_{12}$	519.44	805.15	451.65	2.29	2525	2561
ARIMA(1,0,1)(3,0,5)$_{12}$	585.44	926.99	526.95	2.52	2501	2537
ARIMA(2,0,0)(2,0,1)$_{12}$	1442.74	2907.46	882.48	3.58	2476	2497
ARIMA(2,0,0)(3,0,3)$_{12}$	636.26	784.55	606.33	2.49	2477	2507
ARIMA(2,0,0)(5,0,3)$_{12}$	508.54	878.30	417.61	2.23	2485	2521
ARIMA(3,0,0)(3,0,4)$_{12}$	526.96	906.35	447.37	2.28	2486	2521
ARIMA(3,0,0)(5,0,3)$_{12}$	778.53	1543.21	536.44	2.77	2487	2526

Based on the test results of different ARIMA models, the most successful models were determined as follows: ARIMA(3,0,4) with an MSLE of 0.18 for the Benin dataset, ARIMA(0,0,4) with an MSLE of 2.04 for the Cameroon dataset, and ARIMA(0,0,1)(5,0,3)12 with an MSLE of 1.08 for the Nigeria dataset.

The Ljung-Box test is used to statistically assess whether a time series shows autocorrelation at various lags. The p-value is compared to the critical value of the chi-squared distribution; if it is below the 0.05 significance level, the null hypothesis is rejected, indicating significant autocorrelation in the residuals and possible inadequacy of the model. If the p-value is above 0.05, the null hypothesis is accepted, suggesting the model is adequate. The choice of 12 lags considers the seasonality in the dataset and the length of the time series. The Ljung-Box test results for these models are presented in Table 6.

Table 6. Results of the Ljung-Box test for ARIMA models.

lags	P value			
	ARIMA (3,0,4)	**ARIMA (0,0,4)**	**ARIMA (0,0,1)(5,0,3)$_{12}$**	**ARIMA (0,0,5)(3,0,3)$_{12}$**
1	0.80	0.64	0	0.38
2	0.93	0.52	0	0.61
3	0.97	0.37	0	0.52
4	0.99	0.39	0	0.67
5	1.00	0.52	0	0.74
6	0.97	0.40	0	0.81
7	0.96	0.52	0	0.88
8	0.98	0.54	0	0.92
9	0.94	0.63	0	0.88
10	0.71	0.64	0	0.91
11	0.18	0.52	0	0.95
12	0.05	0.26	0	0.97

Although the most accurate model was ARIMA(0,0,1)(5,0,3)12, its p-value of 0 indicates statistically significant autocorrelations, making the model unsuitable for use. Ljung-Box tests were also conducted on other models to select the most accurate ones. According to the Ljung-Box test results for different ARIMA models: ARIMA(3,0,4) with an MSLE of 0.18 was found to be the best for the Benin dataset, ARIMA(0,0,4) with an MSLE of 2.04 for the Cameroon dataset, and ARIMA(0,0,5)(3,0,3)12 with an MSLE of 2.21 for the Nigeria dataset. The fit of these models was analyzed using Standardized Residuals, Histogram plus Estimated Density, Quantile-Quantile (Q-Q) plots, and Correlograms, with the results presented in Figure 6.

The Q-Q plot shows that the points mostly follow the red line in the center of the distribution but exhibit significant deviations in the tails. The histogram indicates that residuals are generally centered around zero but not perfectly symmetrical. For Benin, the histogram displays a distribution that is asymmetric around zero, whereas for Cameroon and Nigeria, residuals appear to be centered around zero. The normal distribution curve (N(0,1)) does not perfectly align with the histogram and Kernel Density Estimate (KDE), confirming the deviation from normality seen in the Q-Q plot. The Standardized Residual Plot shows that residuals are generally centered around zero and highlights times when the model failed to capture variability well. Sudden increases in 2014, 2018, and 2019 for Benin, 2015, 2020, and 2023 for Cameroon, and 2013 and 2016 for Nigeria indicate times when the model struggled to capture variability. The Correlogram (residual

ACF plot) shows that lags are within confidence limits, indicating that the models have effectively captured existing dependencies in the time series data.
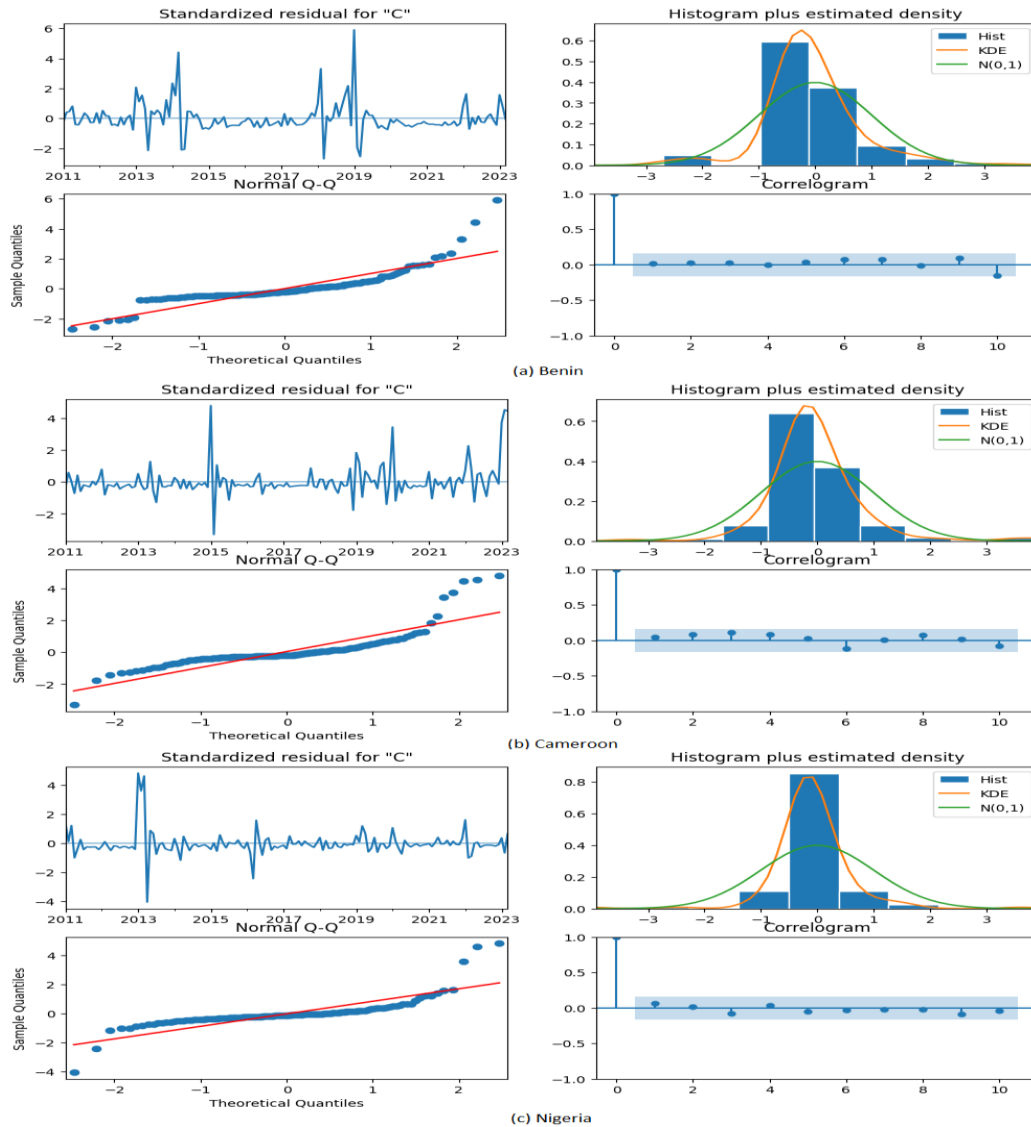
Figure 6. *Standardized Residual Plot, Quantile-Quantile plot, Histogram plus estimated density, Correlogram.*

4.2   Holt-Winters Model Performance in Measles Case Prediction

The Holt-Winters model is particularly useful for time series data that exhibit trends and seasonality. The parameters used in the development of this model for measles case prediction are presented in Table 7.

Table 7. The parameters and values of the Holt-Winters model.

Parameters	Benin	Cameroon	Nigeria
Trend	None	None	Additive
Seasonal	None	None	Multiplicative
seasonal_periods	0	0	12
initialization_method	Heuristic	Heuristic	Heuristic
use_boxcox	False	True	False
damped	False	False	False
smoothing_level	0.1	0.1	1
smoothing_trend	None	None	0.1
smoothing_seasonal	None	None	0.1

The developed model has been used to forecast measles case numbers for three different countries, with test performance results presented in Table 8.

Table 8. Test results of the Holt-Winters model by country.

Country	RMSE	MAPE	MAE	MSLE	AIC	BIC
Benin	22.42	92.38	20.32	0.47	1102	1108
Cameroon	386.45	730.15	298.26	3.92	1594	1555
Nigeria	704.88	92.99	488.64	1.60	2061	2109

4.3 LSTM Model Performance in Measles Case Prediction

To enhance the learning and prediction performance of the LSTM model, the MinMaxScaler function has been used. The model has been built using the Sequential function from the Keras library. The parameters and values used in developing the LSTM model for measles case forecasting are presented in Table 9.

Table 9. The parameters and values of the LSTM model.

Parameters	Benin	Cameroon	Nigeria
LSTM Layers/#neurons	2/128,64	2/128,64	1/128
Dense Layers/#neurons	2/25,1	2/25,1	2/25,1
Dropout	{0,0.2,0.4,0.6,0.8}	{0,0.2,0.4,0.8}	{0,0.2,0.4,0.8}
Optimizer	Adam	Adam	Adam
Activation Function	Relu	Relu	Relu
Learning rate	0.001	0.001	0.001
Validation split	0.2	0.2	0.2
Epoch	Min=10, Max=300	Min=10, Max=200	Min=35, Max=450
Batch size	Min=1, Max=64	Min=1, Max=64	Min=1, Max=128

The prediction performance of different LSTM models for measles case numbers across countries is presented in Tables 10-12.

Table 10. Comparison of LSTM models tested for Benin.

Model	Batch Size	Epoch	Dropout Rate	RMSE	MAPE	MAE	MSLE
LSTM$_1$	1	10	0	17.45	28.94	9.51	0.18
LSTM$_2$	1	10	0.2	17.00	27.25	9.23	0.14
LSTM$_3$	8	10	0.8	27.20	117.40	23.80	0.65
LSTM$_4$	8	30	0.6	19.39	36.64	13.42	0.17
LSTM$_5$	16	50	0.4	35.34	101.57	28.87	0.51
LSTM$_6$	16	150	0.2	18.69	50.52	13.74	0.25
LSTM$_7$	32	50	0.6	57.04	274.31	53.83	1.61
LSTM$_8$	32	200	0	45.27	86.48	31.46	0.70
LSTM$_9$	64	10	0.8	23.24	81.50	18.44	0.47
LSTM$_{10}$	64	300	0	28.24	71.05	20.31	0.76

Table 11. Comparison of LSTM models tested for Cameroon.

Model	Batch Size	Epoch	Dropout Rate	RMSE	MAPE	MAE	MSLE
LSTM$_1$	1	15	0	93.28	157.17	61.60	0.80
LSTM$_2$	1	20	0.8	196.51	393.39	151.63	1.94
LSTM$_3$	8	10	0	272.90	321.19	185.65	2.19
LSTM$_4$	8	50	0.4	43.65	103.58	36.68	0.67
LSTM$_5$	8	50	0.8	152.31	242.48	103.32	1.39
LSTM$_6$	16	15	0	283.49	351.91	194.52	2.43
LSTM$_7$	32	50	0.4	190.94	225.16	129.67	1.40
LSTM$_8$	32	200	0.2	277.11	378.88	192.03	2.25
LSTM$_9$	64	50	0.2	272.42	257.98	172.23	1.71
LSTM$_{10}$	64	200	0	220.71	163.28	151.07	1.04

Table 12. Comparison of LSTM models tested for Nigeria.

Model	Batch Size	Epoch	Dropout Rate	RMSE	MAPE	MAE	MSLE
LSTM$_1$	1	35	0	659.12	358.58	513.28	1.68
LSTM$_2$	1	40	0.8	673.86	564.08	520.88	1.97
LSTM$_3$	8	50	0.2	769.62	872.98	539.51	2.22
LSTM$_4$	8	100	0	696.96	328.80	558.17	1.65
LSTM$_5$	16	100	0.8	731.30	620.49	527.43	2.05
LSTM$_6$	16	150	0	714.73	569.83	496.66	1.94
LSTM$_7$	32	300	0.4	789.66	1110.48	611.50	2.41
LSTM$_8$	64	250	0.2	875.54	1212.50	638.06	2.47
LSTM$_9$	128	400	0.2	809.62	198.46	469.20	1.19
LSTM$_{10}$	128	450	0.2	789.17	157.36	462.33	1.06

4.4   Greykite Model Performance in Measles Case Prediction

The Greykite model is user-friendly and can be integrated with various predictors. The parameters and values used for developing the Greykite model for measles case number prediction are presented in Table 13.

Table 13. The parameters and values of the Greykite model.

Parameters	Benin	Cameroon	Nigeria
seasonality			
yearly_seasonality	None	None	-12
growth: growth_term	-	-	Quadratic
events:	Linear	None	None
holidays_to_model_separately	None	None	Auto
changepoints_dict: method	Auto	Auto	0.5
regularization_strength	0.5	0.5	11
potential_changepoint_n	5	1	0.1
no_changepoint_proportion_from_end	0.1	0.1	Auto
uncertainty: uncertainty_dict	Auto	Auto	elastic_net
fit_algorithm_dict :	quantile_regression	quantile_regression	ts
fit_algorithm	ts	ts	y
time_col	y	y	MS
value_col	MS	MS	12
freq	12	12	0.95
forecast_horizon	0.95	0.95	
coverage			

The Greykite model's measles case number prediction results for three different countries are presented in Table 14.

Table 14. Test results of the Greykite model by country.

Country	RMSE	MAPE	MAE	MSLE
Benin	23.22	38.60	14.62	0.36
Cameroon	422.43	177.01	226.15	2.36
Nigeria	858.00	1715.08	642.37	3.01

4.5 Prophet Model Performance in Measles Case Prediction

Prophet is known for its robust capability to model trends and seasonal components and for making reliable predictions even with missing data. The parameters and values used in the development of the Prophet model for measles case number prediction are presented in Table 15.

Table 15. The parameters and values of the Prophet model.

Parameters	Benin	Cameroon	Nigeria
seasonality_mode	Multiplicative	Multiplicative	Multiplicative
yearly_seasonality	False	False	True
growth	linear	flat	linear
changepoints	None	None	None
n_changepoints	5	5	0
changepoint_range	0.8	0	0
periods	12	12	12
freq	MS	MS	MS

The test results for measles case numbers across three different countries are presented in Table 16.

Table 16. Test results of the Prophet model by country.

Country	RMSE	MAPE	MAE	MSLE
Benin	23.69	40.89	15.26	0.37
Cameroon	404.36	374.67	244.87	2.84
Nigeria	826.52	1699.92	546.58	2.68

4.6 XGBoost Model Performance in Measles Case Prediction

XGBoost is commonly used for regression and classification problems and is also favored for time series forecasting. However, due to its lack of parameter adjustments for seasonality and trend, it is less frequently used compared to other time series models. The parameters and values used in developing the XGBoost model for measles case number forecasting are presented in Table 17.

Tablo 17. The parameters and values of the XGBoost model.

Parameters	Benin	Cameroon	Nigeria
n_estimators	17	17	17
max_depth	7	7	7
eta	Min=0.1, Max=1.6	Min=0.1, Max=1.9	Min=0.3, Max=2.7
subsample	Min=0.2, Max=1.8	Min=0.1, Max=0.9	Min=0.3, Max=0.6
colsample_bytree	Min=0, Max=1	Min=0, Max=1	Min=0, Max=1
early_stopping_rounds	20	20	20

The test results for measles case numbers across three different datasets, according to various XGBoost model parameters, are presented in Tables 18-20.

Table 18. Comparison of XGBoost models tested for Benin.

Model	eta	subsample	Colsample_bytree	RMSE	MAPE	MAE	MSLE
XG_1	0.1	0.2	0.5,0.6,0.7	14.58	50.45	12.86	0.2
XG_2	0.1	0.2	0.8,0.9	11.62	39.21	9.73	0.14
XG_3	0.1	0.3	0.8,0.9	11.40	41.26	10.10	0.14
XG_4	0.3	0.3	0.8,0.9	8.21	27.48	6.50	0.08
XG_5	0.3	0.4	0.8,0.9	16.53	72.33	14.70	0.32
XG_6	0.3	0.8	0,0.1,0.2,0.3,0.4	21.05	91.95	17.84	0.44
XG_7	1.1	0.4	0.8,0.9	9.00	28.06	6.70	0.09
XG_8	1.2	0.5	0.5,0.6,0.7	16.78	39.52	11.79	0.15
XG_9	1.3	0.7	0,0.1,0.2,0.3,0.4	12.83	35.25	10.79	0.16
XG_{10}	1.6	0.4	1	10.46	39.39	9.23	0.15

Table 19. Comparison of XGBoost models tested for Cameroon.

Model	eta	subsample	Colsample_bytree	RMSE	MAPE	MAE	MSLE
XG_1	0.1	0.1	0,0.1,0.2,0.3,0.4	388.96	573.39	275.18	3.42
XG_2	0.1	0.9	0.5,0.6,0.7	384.15	651.55	286.30	3.63
XG_3	0.2	0.1	0.1,0.2,0.3,0.4	383.81	701.75	297.27	3.80
XG_4	0.3	0.5	0.5,0.6,0.7,0.8,0.9,1	393.13	472.65	259.60	3.07
XG_5	0.6	0.3	0.5,0.6,0.7	385.17	570.63	274.34	3.32
XG_6	1.1	0.2	0.8,0.9	400.27	1122.73	357.23	5.06
XG_7	1.2	0.6	0.8,0.9,1	355.15	441.37	231.00	2.33
XG_8	1.7	0.9	1	965.07	3796.44	891.68	10.08
XG_9	1.8	0.6	0.8,0.9,1	341.94	477.23	226.52	2.15
XG_{10}	1.9	0.6	0.8,0.9,1	340.59	483.20	225.78	2.12

Table 20. Comparison of XGBoost models tested for Nigeria.

Model	eta	subsample	Colsample_bytree	RMSE	MAPE	MAE	MSLE
XG_1	0.3	0.4	1	715.20	1287.53	569.61	2.80
XG_2	0.8	0.4	1	576.57	715.81	392.06	1.89
XG_3	1.2	0.6	0,0.1,0.2,0.3,0.4	1119.47	2111.79	728.44	2.98
XG_4	1.2	0.4	0.8,0.9,1	594.26	177.51	421.99	1.03
XG_5	1.3	0.4	1	581.80	321.52	399.57	1.47
XG_6	1.4	0.4	1	457.39	84.44	289.22	0.69
XG_7	1.7	0.3	0,0.1,0.2,0.3,0.4	946.56	129.62	661.15	3.63
XG_8	1.7	0.4	1	592.97	952.18	396.08	1.96
XG_9	1.9	0.3	1	920.32	236.40	747.72	3.05
XG_{10}	2.7	0.3	0,0.1,0.2,0.3,0.4	3364.87	3732.18	3292.91	7.26

4.7 Comparison of the Most Successful Prediction Models by Country and Forecasting with the Best Models

Figure 7 shows the comparison of the most successful results from the test sets of the six time series models for the three countries.

Figure 7 shows that the most successful model for predicting measles case numbers in Benin and Nigeria is XGBoost, while for Cameroon, the best results were achieved with the LSTM model. Using these models, a system was developed to forecast the next 6 months of measles cases for the three countries. The actual, predicted, and forecasted results for Benin, Cameroon, and Nigeria are presented in Figures 8, 9, and 10, respectively.
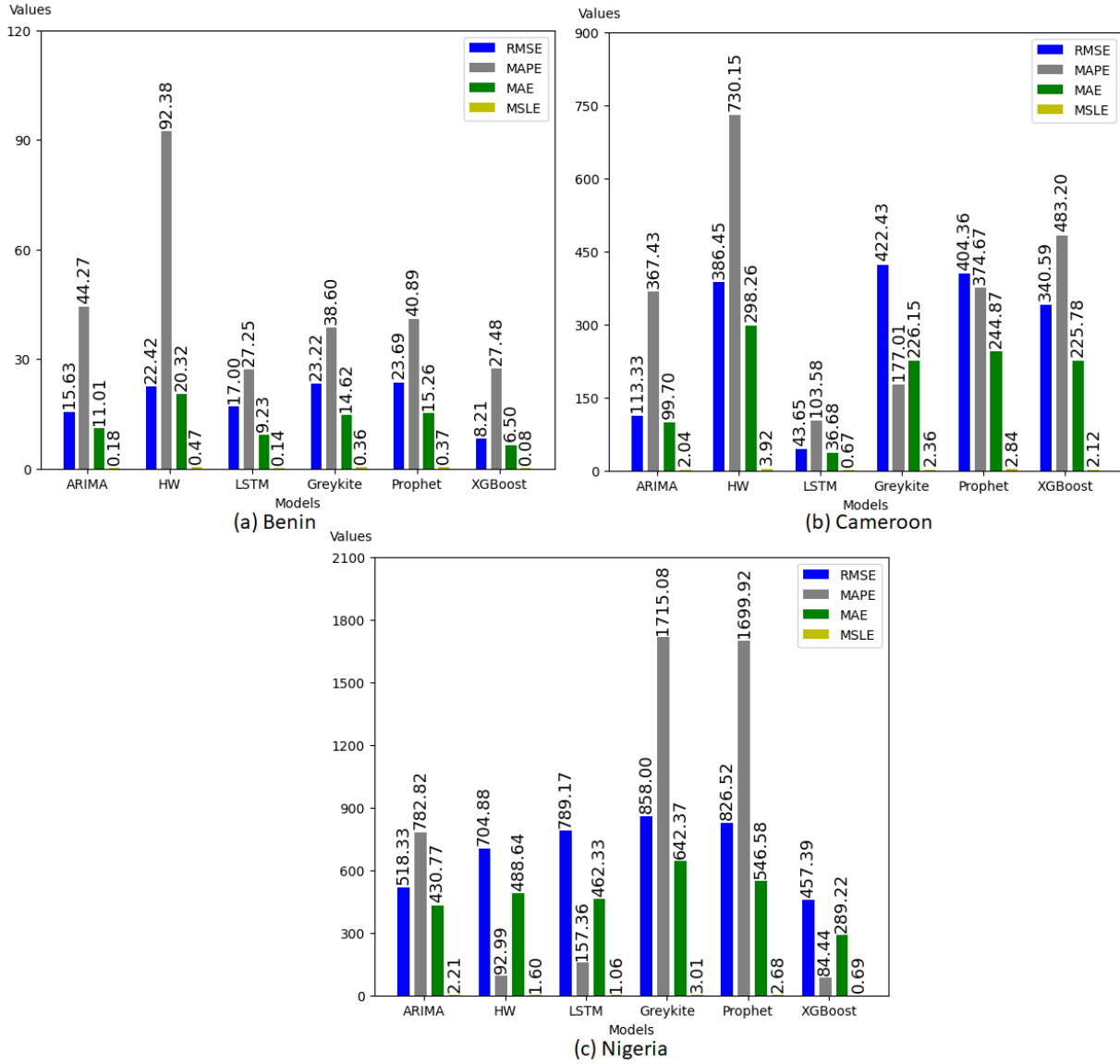
Figure 7. Comparison of models tested for each country.
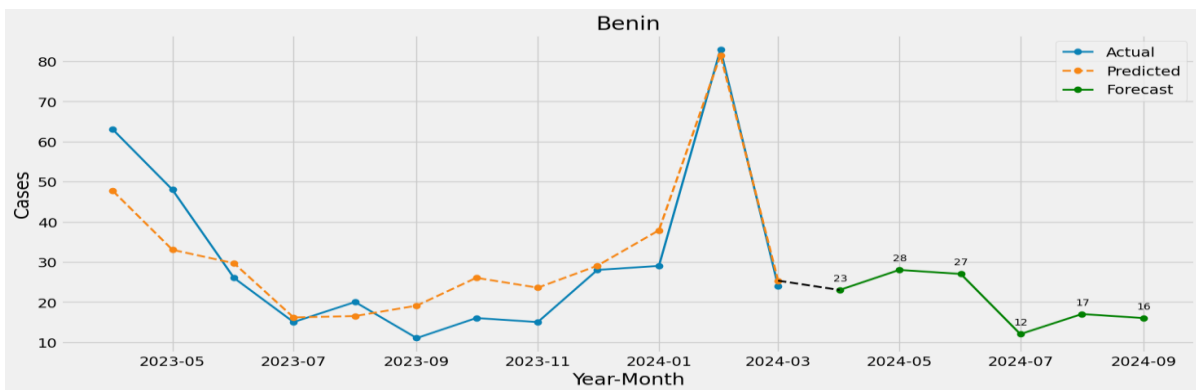
Figure 8. XGBoost Model Results for the Benin Dataset: Actual (Test), Predicted, and Forecast.
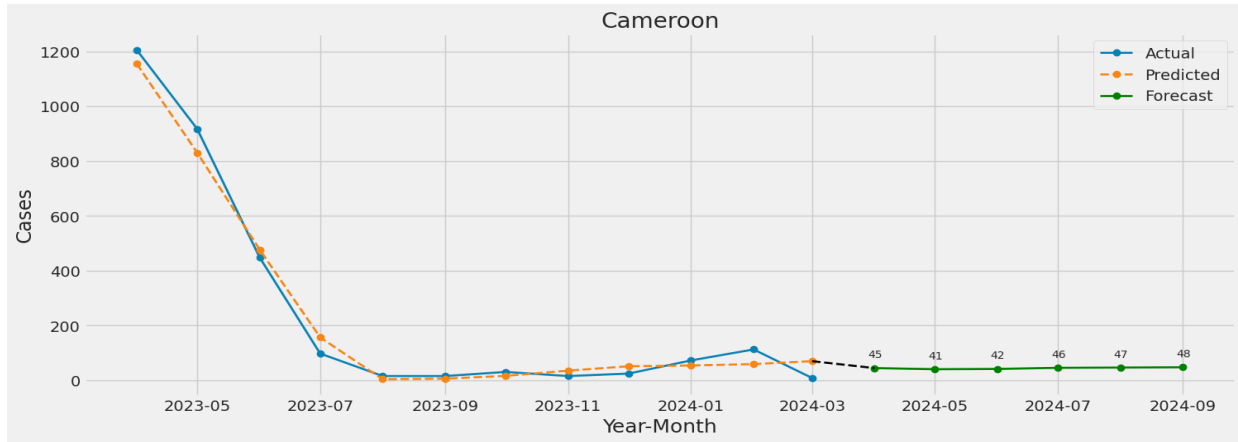
Figure 9. LSTM Model Results for the Cameroon Dataset: Actual (Test), Predicted, and Forecast.
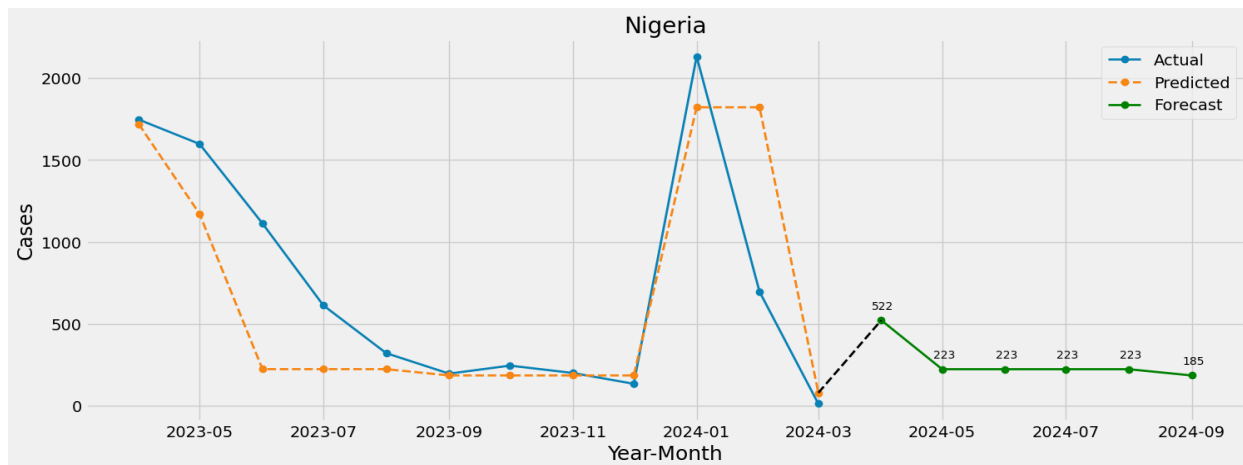
Figure 10. XGBoost Model Results for the Nigeria Dataset: Actual (Test), Predicted, and Forecast.

5   DISCUSSION

In recent years, the increase in measles cases can be attributed to factors such as the rise in social contact following the end of the COVID-19 pandemic, the growing prevalence of vaccine hesitancy, inadequate nutrition, population growth, and insufficient mass vaccination programs. Computer-aided forecasting of measles case numbers can facilitate early interventions, which can have positive effects on public health, national economies, and health systems. Additionally, computer-aided prediction systems, due to their low cost and the ability to provide useful and accurate results, allow for more effective planning of health policies and intervention strategies.

This study aims to develop an effective and reliable system for computer-aided prediction and forecasting of measles case numbers. To this end, the forecasting performance of different methodologies, including ARIMA, HW, LSTM, Greykite, Prophet, and XGBoost time series models, has been evaluated using benchmarking methods. This approach has allowed for the comparison of the prediction performance of various models, identifying the most effective and reliable forecasting methods, and ensuring more accurate and effective prediction of measles case numbers. To our best knowledge, this study is one of the first to benchmark different time series models, using diverse datasets in forecasting measles cases.

Previous studies on measles case prediction have used a limited number of models, and the performance comparisons of these models have been inadequate. Often, classical statistical models like ARIMA have been used. There has been no comprehensive comparison between classical statistical and artificial intelligence models for predicting measles case numbers. This study aims to fill this gap and provide a more detailed examination of the prediction performance of different methods. In doing so, it will highlight the advantages and limitations of various modeling techniques and provide insights into selecting the most suitable prediction methods.

As shown in Figure 3, one of the datasets used is seasonal, and considering that all data are complete, with abnormal increases and decreases in case numbers in both the short and long term (e.g., social interactions between countries, insufficient vaccination rates for various reasons, extraordinary situations like the COVID-19 pandemic, differences in birth rates and population density), different testing environments have been provided to find the most suitable model for these conditions.

In the study, the monthly case numbers in the countries under investigation showed occasional sudden increases and decreases, which reduced the accuracy of the models' predictions. On an annual basis, a decrease in total case numbers was observed across all countries, particularly in 2020 and 2021. Despite no significant increase in vaccination rates in 2019 and 2020, the reduction in close contact between people due to the COVID-19 pandemic affected measles case numbers. In the last two years, vaccination rates and total case numbers have remained stable in Benin, while in Cameroon, the vaccination rate increased, but the case numbers have doubled. In Nigeria, the number of cases has roughly halved. Models that could adapt to sudden changes in a short time have been XGBoost and LSTM.

Since the parameter values used in the XGBoost model vary for each dataset, finding the most suitable values for prediction takes time. The adjustment of the number of layers, neurons, and other parameters in the LSTM model changes the results for each dataset, making it more challenging to select suitable parameters compared to other models. While the training and testing process for the model takes an average of 1 minute, this duration does not exceed 20 seconds for other models. Considering these conditions, selecting the appropriate model and parameters requires a complex and lengthy process. In the ARIMA model, the number of suitable parameters can be reduced using ACF and PACF graphs or found quickly using the auto_arima function. Parameter adjustments for Prophet, Greykite, and HW models are easier compared to other models.

According to the study findings, artificial intelligence models XGBoost and LSTM have demonstrated superior performance for measles case number prediction compared to ARIMA and other frequently used models in the literature. However, determining suitable model parameters is a challenging process. This study recommends XGBoost and LSTM from artificial intelligence models for predicting measles case numbers. The development of an effective and reliable forecasting system will provide more accurate predictions for health authorities and policymakers, assisting in the development of early warning systems and intervention strategies. Additionally, this system will support more efficient resource management and have positive effects on public health.

6   CONCLUSIONS

In this article, a computer-aided system has been developed to forecast measles case numbers efficiently, cost-effectively, and reliably. To achieve optimal performance of the developed system, the prediction accuracy of various methodological models was tested, and these models were compared across three different country datasets. The test performance of the ARIMA, HW, LSTM, Greykite, Prophet, and XGBoost models was evaluated using RMSE, MAPE, MAE, and MSLE metrics. The results indicate that the XGBoost model performed better in the Benin (8.21 RMSE, 27.48 MAPE, 6.50 MAE, 0.08 MSLE) and Nigeria (457.39 RMSE, 84.44 MAPE, 289.22 MAE, 0.69 MSLE) datasets, while the LSTM model performed better in the Cameroon (43.65 RMSE, 103.58 MAPE, 36.68 MAE, 0.67 MSLE) dataset. The computer-aided system developed with these models forecasts measles case numbers for the next six months. For Benin,

no significant change in case numbers is expected in the first three months, followed by a projected halving in the subsequent month, with a slight increase and stabilization in the following month. In Nigeria, a 43-fold increase in case numbers is expected in the first month, followed by a reduction of more than half in the next month, with case numbers remaining stable for the next four months before a decrease in the final month. For Cameroon, a fourfold increase in case numbers is anticipated in the first month, with no significant changes expected in the subsequent months. Overall, this study demonstrates that artificial intelligence models outperform classical models. To our best knowledge, this study is one of the first to benchmark different time series models, using diverse datasets in forecasting measles cases. Additionally, the benchmarking study conducted to compare the performance of various models will guide future research and contribute to the development of effective forecasting tools.

Conflict of Interest

The authors have no competing interests to declare that are relevant to the content of this article.

Statement of Research and Publication Ethics

The study is complied with research and publication ethics.

Artificial Intelligence (AI) Contribution Statement

This manuscript was entirely written, edited, analyzed, and prepared without the assistance of any artificial intelligence (AI) tools. All content, including text, data analysis, and figures, was solely generated by the authors.

Author Contributions

PC and OG: Conceptualization, Writing – original draft preparation, Methodology, Validation, Software; Visualization, Writing – review and editing.

Data Availability

The dataset used in this study is obtained from the World Health Organization (WHO). The 'Distribution of measles cases by country and by month' dataset is available in Excel format and can be accessed at https://immunizationdata.who.int/global?topic=&location=

Code Availability

The code for the models developed in this study is available on GitHub at https://github.com/ozcanguler/Computer-Aided-Prediction-and-Forecasting-of-Measles-Case-Numbers.git.

REFERENCES

[1]   D.E. Griffin "Measles Vaccine," *Viral Immunology*, 31(2), 86-95, 2018. https://doi.org/10.1089/vim.2017.0143.

[2]   A. A. Minta, M. Ferrari, S. Antoni, A. Portnoy, A. Sbarra, B. Lambert, C. Hatcher, C. H. Hsu, L.L. Ho, C. Steulet, M. Gacic-Dobo, P.A. Rota, M.N. Mulders, A.S. Bose, W.P. Caro, P. O'Connor, N.S. Crowcroft "Progress Toward Measles Elimination — Worldwide, 2000–2022," US Department of Health and Human Services | Centers for Disease Control and Prevention | Morbidity and Mortality Weekly Report (MMWR), 72(46), 1262-1268, 2023. http://dx.doi.org/10.15585/mmwr.mm7246a3.

[3]   R. A. Bednarczyk, W. A. Orenstein, S. B. Omer "Estimating the Number of Measles-Susceptible Children and Adolescents in the United States Using Data From the National Immunization Survey–Teen (NIS-Teen)," *American Journal of Epidemiology*, 184(2), 148-156, 2016. https://doi.org/10.1093/aje/kwv320.

[4]   World Health Organization, "Measles vaccines: WHO position paper, April 2017 – Recommendations," *Vaccine*, 37(2), 219-222, 2019. https://doi.org/10.1016/j.vaccine.2017.07.066.

[5]   World Health Organization, "Measles", https://www.who.int/news-room/fact-sheets/detail/measles.

[6]   A.D. Mathis, K. Raines, N.B. Masters, T.D. Filardo, G. Kim, S.N. Crooke, B. Bankamp, P.A. Rota, D.E. Sugerman "Measles — United States, January 1, 2020–March 28, 2024," *Centers for Disease Control and Prevention Morbidity and Mortality Weekly Report*, 73(14), 295-300, 2024. https://doi.org/10.15585%2Fmmwr.mm7314a1.

[7]   A. Hussain, S. Ali, M. Ahmed, S. Hussain " The Anti-vaccination Movement: A Regression in Modern Medicine," *Cureus*, 10(7), 2018. https://doi.org/10.7759%2Fcureus.2919.

[8]   E. I. Iseri, K. Uyar, E. U. Ilhan "Forecasting Measles in the European Union Using the Adaptive Neuro-Fuzzy Inference System," *Cyprus Journal Of Medical Sciences*, 4, 34-37, 2019. http://dx.doi.org/10.5152/cjms.2019.611.

[9]   K. Uyar, U. Ilhan, E. I. Iseri, A. Ilhan "Forecasting Measles Cases in Ethiopia using Neuro-Fuzzy Systems," *International Symposium on Multidisciplinary Studies and Innovative Technologies (ISMSIT)*, 2019. https://doi.org/10.1109/ISMSIT.2019.8932882.

[10]   S. Mehrmolaei, M.R. Keyvanpour "Time series forecasting using improved ARIMA," *IEEE 2016 Artificial Intelligence and Robotics (IRANOPEN)*, 92-97, 2016. https://doi.org/10.1109/RIOS.2016.7529496.

[11]   H.S. Siddalingaiah, A. Chaudhuri, D. Chandrakala "Measles occurrence, vaccination coverages and malnutrition in India: correlations, trends, and projections by time series analysis," *International Journal of*

Community Medicine and Public Health, 5(1), 86-94, 2018. https://doi.org/10.18203/2394-6040.ijcmph20175532.

[12] A. Akinbobola, A. S. Hamisu "Predicting Measles Occurrence Using Some Weather Variables in Kano, North western Nigeria," *American Journal of Public Health Research*, 6(4), 195-202, 2018. http://dx.doi.org/10.12691/ajphr-6-4-4.

[13] C.E. Okorie, C.C. Ilomuanya, O.A. Bamigbala "Statistical Analysis On Impact Of Measles Among Children In Obudu Local Government Area Of Cross River State," *Journal Health And Technology*, 2(2), 2023. https://doi.org/10.47820/jht.v2i2.36.

[14] S. Sharmin, I. Rayhan "Modelling of Infectious Diseases for Providing Signalof Epidemics: A Measles Case Study in Bangladesh," *Journal of Health, Population and Nutrition*, 29(6), 567-573, 2011. https://doi.org/10.3329/jhpn.v29i6.9893.

[15] L. Samaras, M.A. Sicilia, E.G. Barriocanal "Predicting epidemics using search engine data: a comparative study on measles in the largest countries of Europe," *BMC Public Health*, 21(100), 157-168, 2021. https://doi.org/10.1186/s12889-020-10106-8.

[16] H. Talirongan, M.Y. Orong, F.J.B. Talirongan "Alleviating Vulnerabilities of the Possible Outbreaks of Measles: A Data Trend Analysis and Prediction of Possible Cases," *Mediterranean Journal of Basic and Applied Sciences (MJBAS),* 4(4), 129-135, 2020. http://doi.org/10.46382/MJBAS.2020.4405.

[17] Y. Alimohamadi, M. Sepandi "Forty-seven year trend of measles in Iran: An interrupted time series analysis," *Health Science Reports*, 6(2), 2023. https://doi.org/10.1002/hsr2.1139.

[18] E. Yang, D. Yan, Q. Xu, Z. Wang, S. Liu "Nonlinear combination forecasting of measles incidence in Shenyang based on General Regression Neural Network," *IEEE 2020 Chinese Control And Decision Conference (CCDC),* 3015-3020, 2020. https://doi.org/10.1109/CCDC49329.2020.9164712.

[19] R. Komitova, A. Kevorkyan, O. Boykinova, S. Krumova, M. Atanasova, R. Raycheva, Y. Stoilova, A. Kunchev "Difficulties in achieving and maintaining the goal of measles elimination in Bulgaria," *Revue d'Épidémiologie et de Santé Publique*, 67(3), 155-162, 2019. https://doi.org/10.1016/j.respe.2019.01.120.

[20] R.T. Alegado, G.M. Tumibay "Forecasting Measles Immunization Coverage Using ARIMA Model," *Journal of Computer and Communications*, 7(10), 157-168, 2019. https://doi.org/10.4236/jcc.2019.710015.

[21] T.C. Maradze, S.P. NYONI, T. NYONI "Modelling and Forecasting Immunization against Measles Disease in Nigeria Using Artificial Neural Networks (ANN)," *International Research Journal of Innovations in Engineering and Technology (IRJIET)*, 5(3), 571-575, 2021. https://doi.org/10.47001/IRJIET/2021.503097.

[22] K.A. Gyasi-Agyei, W.O. Denteh, A. Gyasi-Agyei "Analysis and Modeling of Prevalence of Measles in the Ashanti Region of Ghana," *British Journal of Mathematics & Computer Science*, 7(10), 209-225, 2013. https://doi.org/10.4236/jcc.2019.710015.

[23] World Health Organization, "Distribution of measles cases by country and by month". https://immunizationdata.who.int/global?topic=&location=,[Accessed at April 16, 2024].

[24] P. Cihan "Forecasting of Monkeypox Cases in the World Using the ARIMA Model," *European Journal of Science and Technology*, 46, 37-45, 2023. https://doi.org/10.31590/ejosat.1190981.

[25] P. Cihan "Forecasting fully vaccinated people against COVID-19 and examining future vaccination rate for herd immunity in the US, Asia, Europe, Africa, South America, and the World," *Applied Soft Computing*, 111, 2021. https://doi.org/10.1016%2Fj.asoc.2021.107708.

[26] P. Cihan "ARIMA-Based Forecasting of Total COVID-19 Cases in the USA and India," *Signal Processing and Communications Applications Conference (SIU)*, June 2021. https://doi.org/10.1109/SIU53274.2021.9477773.

[27] P. Cihan "The machine learning approach for predicting the number of intensivecare, intubated patients and death: The COVID-19 pandemic in Turkey," *Sigma Journal of Engineering and Natural Sciences*, 40(1), 85-94 2022. https://dx.doi.org/10.14744/sigma.2022.00007.

[28]   P. Cihan "Comparative Performance Analysis of Deep Learning, Classical, and Hybrid Time Series Models in Ecological Footprint Forecasting," *Applied Sciences*, 14(4), 2024. https://doi.org/10.3390/app14041479.

[29]   P. Cihan "Impact of the COVID-19 lockdowns on electricity and natural gas consumption in the different industrial zones and forecasting consumption amounts: Turkey case study," *International Journal of Electrical Power and Energy Systems*, 134, 2022. https://doi.org/10.1016%2Fj.ijepes.2021.107369.

[30]   C.P.D. Veiga, C.R.P.D. Veiga, A. Catapan, U. Tortato, W.V.D. Silva "Demand forecasting in food retail: a comparison between the HoltWinters and ARIMA models," *Wseas Transactions on Business and Economics*, 11, 608-614, 2014. https://wseas.com/journals/bae/2014/a085707-276.pdf.

[31]   F. Shahid, A. Zameer, M. Muneeb " Predictions for COVID-19 with deep learning models of LSTM, GRU and Bi-LSTM," *Chaos, Solitons & Fractals*, 140, 2020. https://doi.org/10.1016/j.chaos.2020.110212.

[32]   R. Hosseini, A. Chen, K. Yang, S. Patra, Y. Su, S.E.A. Orjany, S. Tang, P. Ahammad "Greykite: Deploying Flexible Forecasting at Scale at LinkedIn," *Proceedings of the 28th ACM SIGKDD Conference on Knowledge Discovery and Data Mining*, 3007-3017, 2022. https://doi.org/10.1145/3534678.3539165.

[33]   G. Battineni, N. Chintalapudi, F. Amenta "Forecasting of COVID-19 epidemic size in four high hitting nations (USA, Brazil, India and Russia) by Fb-Prophet machine learning model," *Applied Computing and Informatics*, 2020. https://doi.org/10.1108/ACI-09-2020-0059.

[34]   Z. Fang, S. Yang, C. Lv, S. An, W. Wu "Application of a data-driven XGBoost model for the prediction of COVID-19 in the USA: a time-series study," *BMJ Open*, 12(7), 2022. https://doi.org/10.1136/bmjopen-2021-056685.

[35]   P. Cihan "Fuzzy Rule-Based System for Predicting Daily Case in COVID-19 Outbreak," *2020 4th International Symposium on Multidisciplinary Studies and Innovative Technologies (ISMSIT),* November 2020. https://doi.org/10.1109/ISMSIT50672.2020.9254714.

[36]   O. Istaiteh, T. Owais, N. Al-Madi, S. Abu-Soud "Machine Learning Approaches for COVID-19 Forecasting," *2020 International Conference on Intelligent Data Science Technologies and Applications (IDSTA),* November 2020. https://doi.org/10.1109/IDSTA50958.2020.9264101.

ON THE GAS ADSORPTION & DESORPTION CHARACTERISTICS FOR SOME TURKISH LIGNITES IN TERMS OF COAL QUALITY PARAMETERS

Mehmet Bilen [1*] iD, Sait Kızgut [1] iD

[1] Zonguldak Bülent Ecevit University, Department of Mining Engineering, Zonguldak Türkiye

* Corresponding Author: mehmetubilen@yandex.com

ABSTRACT

Gas sorption capacity in coals is a well-researched topic, yet the complexity of experimental setups often limits detailed reporting. Understanding coal gas adsorption and seam gas content is essential for predicting and preventing mine gas outbursts and explosions. Therefore, characterizing coal samples based on their adsorption capacities is crucial. This study explores the adsorption of nitrogen, carbon dioxide, and methane across different coals and plots isotherms to assess the impact of gas type, pressure, and coal quality parameters. Results indicate that methane can adsorb even at low pressures in the Dursunbey sample, while higher pressures are required for carbon dioxide and nitrogen. The study also finds a strong correlation between Langmuir volume and ash percentage on an original basis, with nitrogen showing the highest correlation ($R^2 = 0.7$), followed by methane ($R^2 = 0.69$). Carbon dioxide, however, exhibits a weaker correlation ($R^2 = 0.44$).

Keywords: Adsorption-desorption, Coal, Proximate analysis, Lignite, Ash, Moisture, Methane

1   INTRODUCTION

The gases formed in the coals are first dissolved on the surfaces by adsorption and in cases where the gas pressure is high, they dissolve in the water in the structure of the coal and are trapped and accumulate in the pores and cracks. It can be said that adsorption is the most effective mechanism for gas accumulation in coal.

Determining the gas adsorption or gas holding capacity of coal is critical to the safe conduct of mining operations. Gas adsorption to coal directly affects the stability of underground mines, the release of harmful gases and the environmental impact of coal mining operations. By determining the gas adsorption characteristics of coals and understanding the importance of this issue, effective safety measures and sustainable mining practices will be easier and faster. The gases formed in coals are first adsorbed on the surfaces through adsorption. In cases where the gas pressure to which the coal is exposed is high, the gas dissolved in the water in the coal structure is trapped in the pores and cracks in the coal structure. Gases are found in coal beds as both adsorbed and free gases [1]. Gases can also be compressed in pore spaces, condensed as solid or liquid, dissolved in the coal structure or adsorbed on surfaces [2]. Coal contains gases, mostly methane, due to biogenic and thermogenic processes that occur during coalification [3], and as a result, these gases are stored in coal seams [4]. The water solubility of gases decreases with increasing temperature and increases with increasing pressure.

Pores are openings or voids of various shapes and sizes in the matrix of a coal. These voids are either closed and isolated from other pores or connected to other pores [5]. Pores are categorized into 3 groups according to their size [6] [7] [8].

-Micro pores (pores smaller than 2 nm in size in coals with carbon content between 85-91%),

-Transitional (meso) pores (pores between 2-50 nm in size in coals with carbon content between 75-84%),

-Macropores (pores larger than 50 nm in size in coals with carbon content below 75%).

Young coals have high moisture content and porosity. As the carbon content in coal increases, porosity decreases and reaches its lowest value around 85% carbon. The average porosity of lignite is between 27-35%. Coals with high porosity are more easily oxidized and emit more volatiles under temperature. The distribution of pores in a coal matrix, adsorbed gas molecules and the types of cracks in the coal are given in Figure 1 [5] [7].
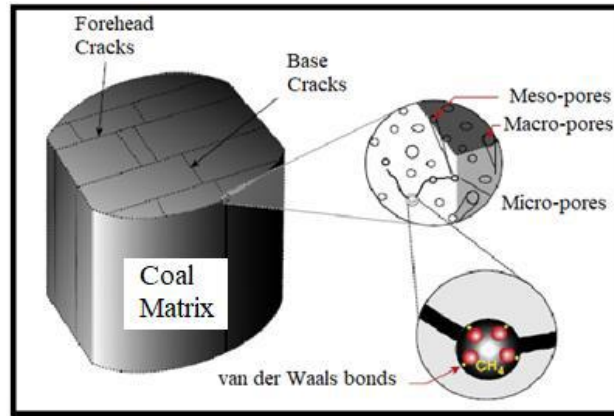
Figure 1. A cross-section of the clastic system and molecular internal structure of coal [7].

Gas adsorption on coal is influenced by the specific properties of the coal. Studies have confirmed that coal condition and coal type, as well as moisture content, ash yield, mineral content, and coal pore distribution have effects on adsorption. According to Perera et al. [9], gas adsorption in coal is determined by various factors, including the properties of the coal seam (such as composition, moisture content, temperature, and pressure) as well as the characteristics of the adsorbed gas. A detailed review of these studies showed that the degree of coal metamorphism [10], pressure [11], temperature [12], pore space, ash, moisture [13] and burial depth [14] greatly affect the coal-CH_4 adsorption process. Adsorption pressure contributes significantly to the gas adsorption process to coal, but the development of the adsorption process varies in the same pressure gradient [15]. In terms of CH_4 adsorption on coal under the influence of temperature, it is generally believed that the adsorption amount gradually decreases with the increase in temperature. Zhang et al. [16] confirmed through variable temperature adsorption experiments that the adsorption capacity of coal is inversely proportional to temperature. Charrière et al. [17] studied the sorption properties of bituminous coals for CO_2 and CH_4 in the temperature range of 283.15-333.15°K and found that increasing temperature shortens the time to reach sorption equilibrium [18]. Han vd. [19] investigated the adsorption properties of CO_2 and CH_4 on coal samples with six different particle sizes ranging from 0.063 to 3 mm and showed that the adsorption capacity of coal samples for single component gases weakens as the particle size increases [18].

Previous investigations, such as those by Florentin [20], have highlighted the dependency of adsorption-desorption characteristics on particle size, gas type, and temperature. In this study, proximate analyses and adsorption-desorption experiments were conducted on lignite samples to evaluate their gas retention properties. Langmuir isotherms and parameters were determined for CO_2, CH_4, and N_2, and their relationships with coal quality parameters

were analyzed to assess implications for methane recovery, coalbed methane extraction, and CO_2 sequestration.

2   MATERIAL AND METHOD

In the experimental studies, coal samples were collected from eight different enterprises in Türkiye, namely Saray, Dursunbey, Milas-Ekizköy, Yatağan, Çayırhan, Ilgın, Ermenek, and Gürmin-Merzifon, the locations of which are presented in Figure 2. These samples were subjected to detailed analysis to assess their properties. In terms of sample preparation, collected samples were crushed and screened to have samples under the sieve size of 18 mm, i.e. -18 mm. In order to be better clear in this context, samples analyzed in terms of the adsorption desorption experiments have %100 undersize fraction of 18 mm. In addition, samples have not been objected to any dehumidification process, i.e. they are not oven nor air dried. They are the run of mine samples from the mines collected from each location as mentioned in Figure 2.

Figure 2. Geolocation map showing the regions of the samples used in the study.

2.1   Proximate Analyzes

Proximate analyses of the coal samples were meticulously carried out following the guidelines of the relevant standards. These analyses included moisture content determination (ASTM D3173), ash content measurement (ASTM D3174), volatile matter determination (ASTM D3175), calculation of fixed carbon content, total sulfur content analysis (ASTM D3177), and calorific value assessment (ASTM D5865). Each parameter was evaluated with precision to ensure accurate characterization of the coal samples' physical and chemical properties, providing a comprehensive understanding of their quality and usability.

2.2 Adsorption and Desorption Experiments

Adsorption and desorption experiments were carried out in the schematic experimental setup given in Figure 3 (previously described in the study of Bilen [21] and Bilen and Kizgut [22].
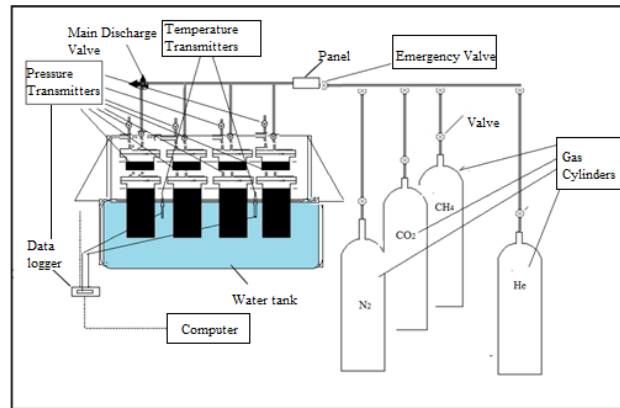
Figure 3. Schematized experimental set-up.

The temperature effect in the adsorption process is quite high, so two temperature sensors (Pt100) embedded in the water bath are supplied and connected to the analog converter. A visual of the laboratory where the adsorption and desorption experiments were carried out is presented in Figure 4.
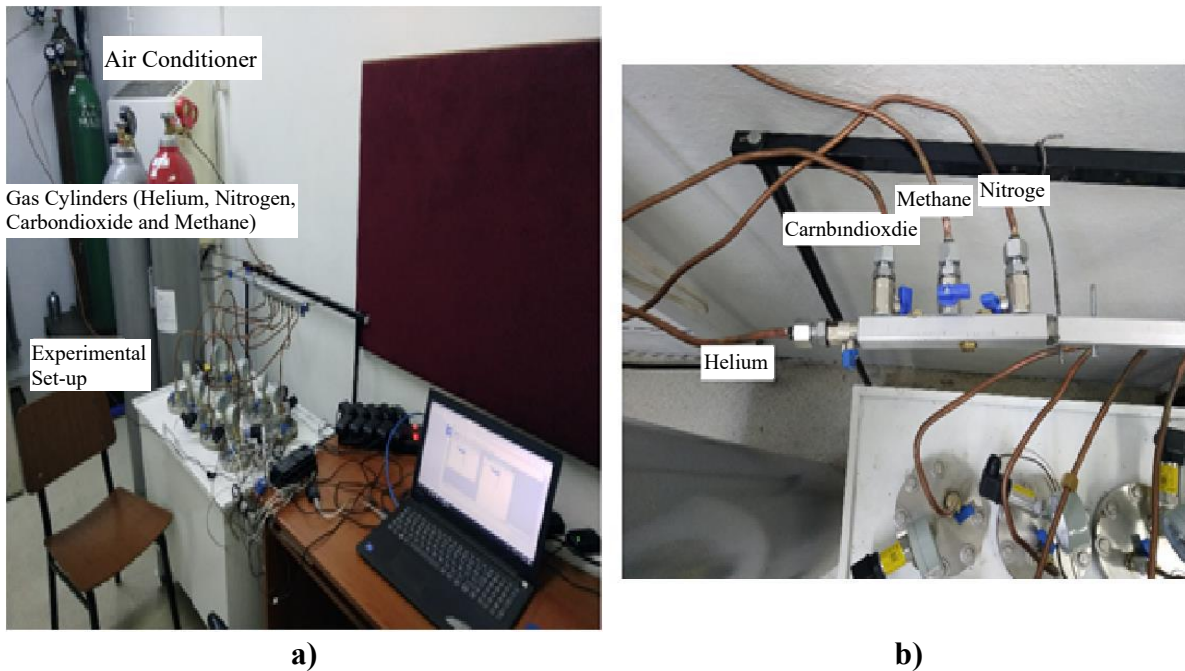
Figure 4. A visual of the laboratory where adsorption & desorption experiments were performed, (a) complete experimental set-up, (b) each gas connection and valves.

The adsorption-desorption experiments were conducted under controlled laboratory conditions, with temperature fluctuations maintained within ±0.5°C. Humidity was also monitored and controlled to prevent any unintended variations in coal moisture content. The calibration of the pressure sensors and gas flow meters was performed using standard calibration gases, ensuring accuracy in gas adsorption measurements.

The selection of a -18 mm sample size was based on industry-standard procedures for adsorption-desorption studies, ensuring uniformity in particle size distribution while preventing excessive fragmentation, which could alter surface area and pore structure. The constant temperature of 20°C was chosen to maintain consistency with previous studies and to reflect typical underground coal mine conditions where adsorption occurs.

3 RESULTS AND DISCUSSION

Proximate analysis results of lignite samples are given in Table 1 and Table 2. The experimentally obtained CH_4, CO_2 and N_2 gas adsorption & desorption graphs of the studied coal samples are given in Figure 5 - Figure 12.
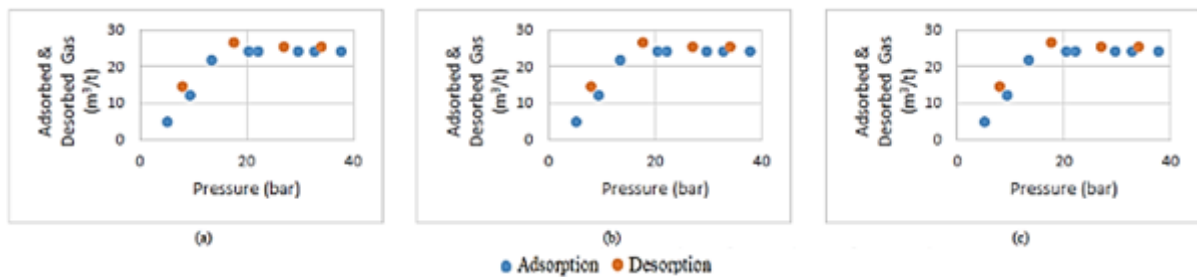
Figure 5. Experimentally obtained a) CO_2 b) CH_4, c) N_2 gas adsorption & desorption graphs of Çayırhan sample.
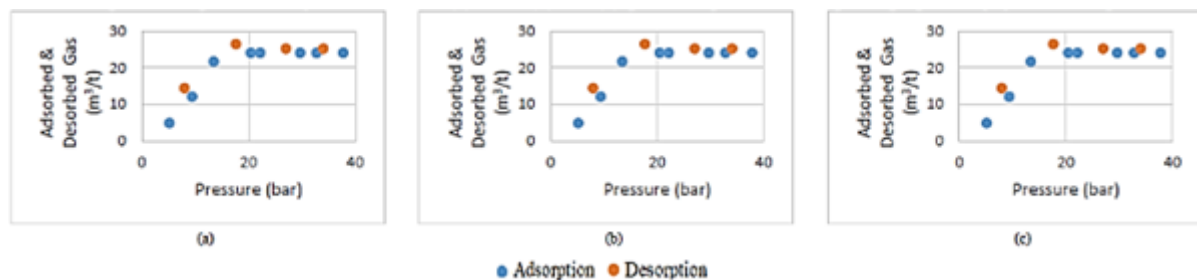
Figure 6. Experimentally obtained a) CO_2 b) CH_4, c) N_2 gas adsorption & desorption graphs of Dursunbey sample.
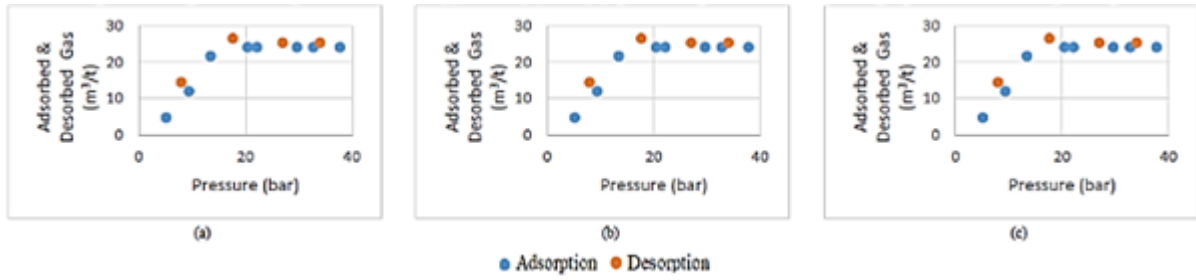
Figure 7. Experimentally obtained a) CO$_2$ b) CH$_4$, c) N$_2$ gas adsorption & desorption graphs of Ermenek sample.
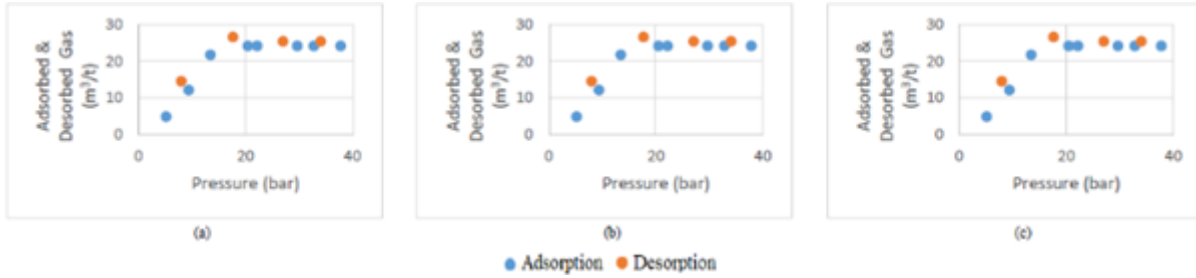
Figure 8. Experimentally obtained a) CO$_2$ b) CH$_4$, c) N$_2$ gas adsorption & desorption graphs of Gürmin-Merzifon sample.
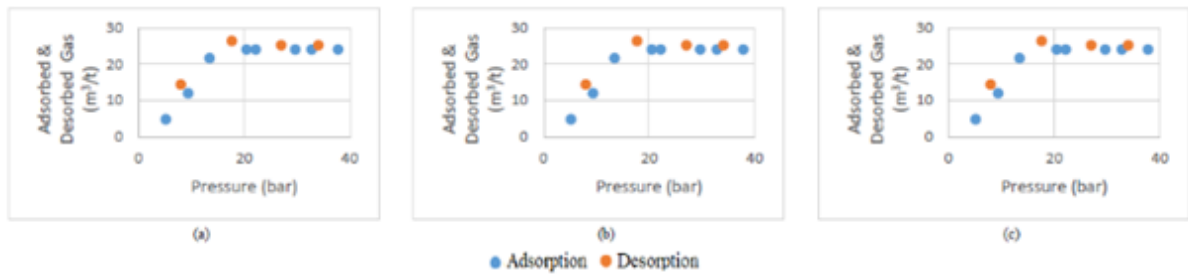
Figure 9. Experimentally obtained a) CO$_2$ b) CH$_4$, c) N$_2$ gas adsorption & desorption graphs of Ilgın sample.
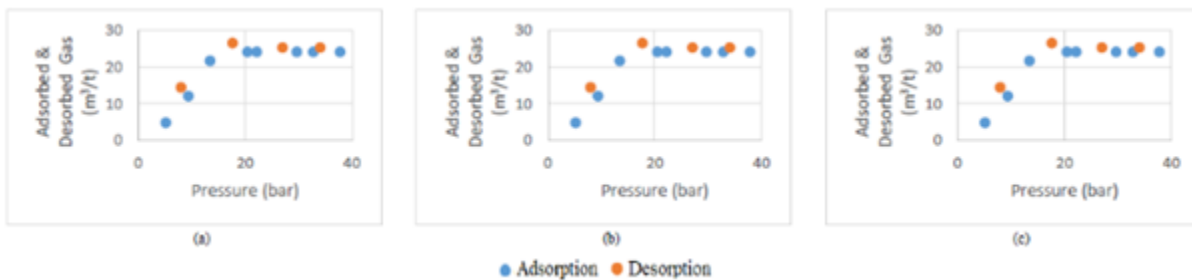
Figure 10. Experimentally obtained a) CO$_2$ b) CH$_4$, c) N$_2$ gas adsorption & desorption graphs of Milas Ekizköy sample.
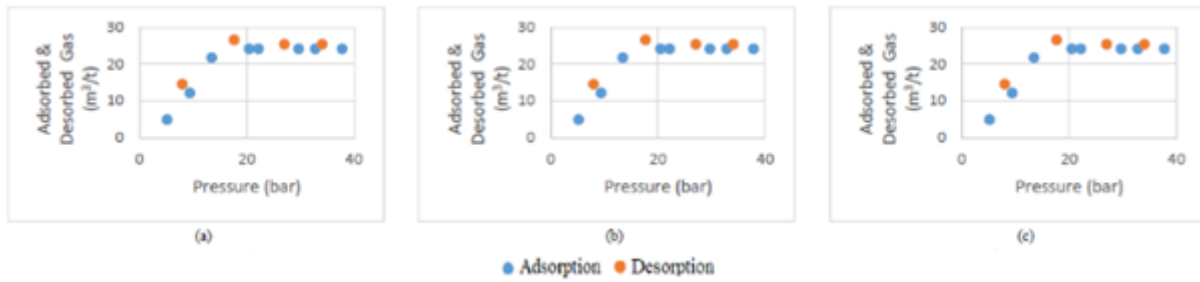
***Figure 11.** Experimentally obtained a) CO_2 b) CH_4, c) N_2 gas adsorption & desorption graphs of Saray sample.*
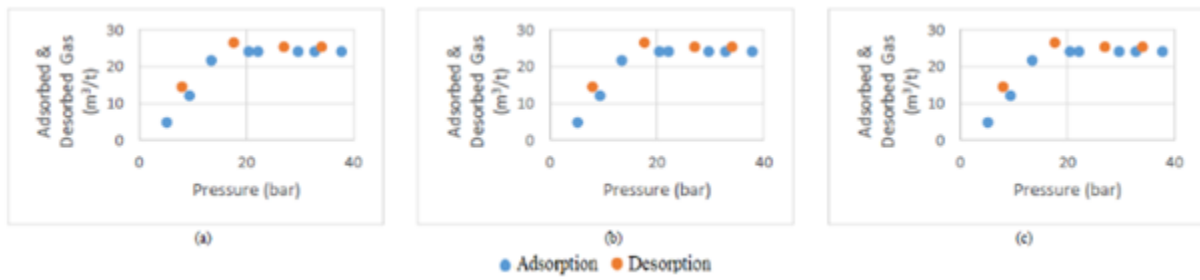
***Figure 12.** Experimentally obtained a) CO_2 b) CH_4, c) N_2 gas adsorption & desorption graphs of Yatağan sample.*

***Table 1.** Proximate analysis results of the Saray, Dursunbey, Milas-Ekizköy and Yatağan coded lignite samples.*

Analysis	Saray		Dursunbey		Milas-Ekizköy		Yatağan	
	Original Basis	Dry Basis	Original Basis	Dry Basis	Original Basis	Dry Basis	Original Basis	Dry Basis
Total Moisture (%)	43.52	-	8.76	-	30.92	-	26.32	-
Ash (%)	8.21	14.53	22.68	24.86	9.03	13.07	11.77	15.97
Volatile Matter (%)	27.09	47.96	33.02	36.19	34.89	50.51	38.78	52.63
Fixed Carbon (%)	21.19	37.51	35.54	38.95	25.16	36.42	23.14	31.40
Total Sulfur (%)	2.26	4.01	5.47	6.00	3.18	4.60	2.58	3.50
Upper Calorific Value (kcal/kg)	2936	5198	4731	5185	3614	5231	3657	4963
Lower Calorific Value (kcal/kg)	2801	4960	4551	4988	3438	4978	3466	4705

Table 2. Proximate analysis results of the lignite samples coded Çayırhan, Ilgın, Ermenek and Gürmin-Merzifon.

Analysis	Çayırhan		Ilgın		Ermenek		Gürmin-Merzifon	
	Original Basis	Dry Basis	Original Basis	Dry Basis	Original Basis	Dry Basis	Original Basis	Dry Basis
Total Moisture (%)	26.74	-	38.32	-	16.32	-	2.14	-
Ash (%)	19.52	26.64	23.91	38.77	22.07	26.37	44.06	45.02
Volatile Matter (%)	28.29	38.62	30.06	48.73	33.04	39.48	28.29	28.91
Fixed Carbon (%)	28.38	38.74	7.71	12.50	28.58	34.15	25.51	26.07
Total Sulfur (%)	3.41	4.66	3.48	5.65	3.86	4.61	2.65	2.71
Upper Calorific Value (kcal/kg)	3601	4915	2024	3282	3867	4621	3521	3598
Lower Calorific Value (kcal/kg)	3449	4708	1894	3071	3703	3703	3361	3435

3.1 Langmuir Isotherms and Langmuir Parameters

In this section, Langmuir isotherms were drawn on a coal sample using Equation 1 and Langmuir parameters were found. For this purpose, data obtained from adsorption experiments were used. Langmuir curves were not drawn due to the low number of pressure stages (4 pressure values, 8, 16, 24, 32 bar) for the desorption process. According to this equation, a linear line is obtained if P/V is plotted against P. The slope of the line gives 1/Vm and the point where it intersects the ordinate gives 1/(bVm).

$$\frac{P}{V} = \frac{P_L}{V_L} + \frac{P}{V_L} \tag{1}$$

where

P: Pressure , V: Volume , PL: Langmuir Pressure, VL: Langmuir Volume

In the context of Langmuir isotherms:

• Vm: This represents the maximum adsorption capacity of the material, which is the theoretical volume of gas that the coal sample can adsorb under ideal conditions when the adsorption sites are fully saturated. It is often referred to as the Langmuir volume VL in studies.

• bVm: This term combines the Langmuir volume (Vm) with the Langmuir affinity constant (b), which describes the strength of the interaction between the gas molecules and the adsorption sites on the coal surface. The parameter bbb is inversely proportional to the Langmuir pressure (PL) and is a measure of how easily the gas is adsorbed onto the coal. The term bVm thus reflects the product of the maximum adsorption capacity and the affinity constant, contributing to the adsorption equilibrium behavior. As an example, Langmuir linear curve of Çayırhan sample for nitrogen gas is given in Figure 13.
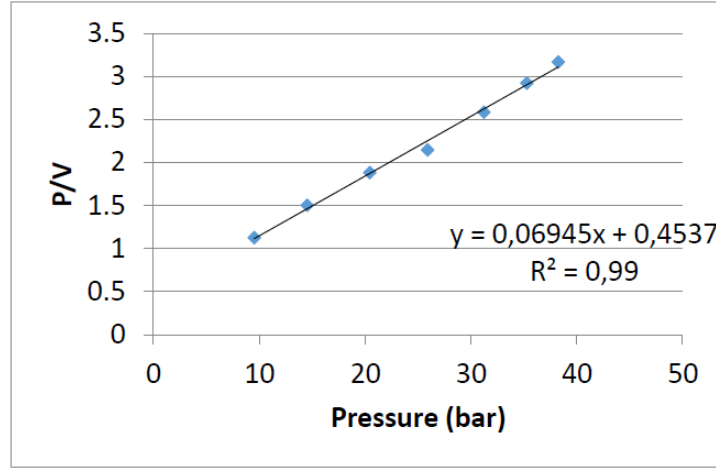
Figure 13. Çayırhan Example Langmuir Linear Curve (Nitrogen).

According to Figure 13, the slope (1/Vm) was found to be 0.0695 and the point intersecting the ordinate (1/bVm) was found to be 0.4537. Accordingly, the 1/b value was found as 6.534, while the b value was determined as 0.153. Accordingly, if 1/bVm is considered as PL/VL, and 1/Vm is considered as 1/VL, PL and VL are easily found. For the Çayırhan sample, the PL value was 6.53 bar and the VL value was 14.4 m³/t. Similarly, Langmuir parameters of nitrogen, carbon dioxide and methane gases of studied lignite samples were found and tabulated (Table 3).

Table 3. Langmuir Parameters, P_L and V_L.

Samples	Nitrogen		Carbondioxide		Methane	
	P_L (bar)	V_L (m³/t)	P_L (bar)	V_L (m³/t)	P_L (bar)	V_L (m³/t)
Çayırhan	6.53	14.40	9.21	31.47	8.76	21.48
Dursunbey	10.32	15.79	16.08	38.89	5.53	19.90
Ermenek	1.12	12.14	3.81	27.89	3.61	19.56
Gürmin-Merzifon	3.73	7.72	3.15	17.18	6.83	13.52
Ilgın	1.23	11.89	5.79	30.59	9.40	22.25
Milas-Ekizköy	2.86	14.39	4.81	28.96	4.14	20.88
Saray	4.21	16.02	11.54	38.54	16.42	27.17
Yatağan	2.80	13.53	4.45	28.53	6.34	20.73

When the Langmuir parameters obtained for nitrogen gas were examined, it was determined that the VL and PL values of the Dursunbey sample were the highest among all samples. This is also true for carbon dioxide gas. However, when Langmuir parameters of methane gas are examined, it is seen that the VL value of the Dursunbey sample is not the highest among the samples, while the Saray sample has the highest PL value and the Ilgın sample has the highest VL value. With a maximum adsorbing amount of approximately 20 m³/t (VL for methane gas), the pores of the Dursunbey sample with a volume of approximately 10 m3 per ton are filled with methane gas at 5.5 bar levels. This value is the lowest among the methane gas PL values after Ermenek and Milas Ekizköy samples. These values can be explained by the methane gas adsorption susceptibility of the samples (methane gas affinity). When the petrographical analysis results are examined, the vitrinite percentages of Dursunbey, Ermenek and Milas Ekizköy samples are 78% and above (Dursunbey 85%, Ermenek 78% and Milas Ekizköy 86%). Dursunbey, one of the examples, has come to the fore in recent years in our country as a place where methane gas-related accidents have occurred. The high methane adsorption capacity of this sample and the low PL (pressure equivalent to half the Langmuir volume) value, which is one of the Langmuir parameters, and the difference in PL and VL values for a single methane gas compared to other gases necessitate a separate evaluation of the Dursunbey sample regarding methane gas. The differences in the coal matrix (pore structure) of the aforementioned Dursunbey sample are also suitable for the methane gas adsorption process. It is thought that the coal matrix and the changes in the coal matrix by adsorption (swelling in the coal matrix) are effective in this process. Pillalamarry et al. [23] stated that they saw a negative correlation between diffusion coefficients and pressures at pressure values below 35 bar. This shows that the methane moves freely in the coal matrix with the pressure drop and the diffusion coefficient is high at low pressures. For the Dursunbey sample, the low methane gas PL value compared to the high nitrogen and carbon dioxide gas PL values shows that the diffusion coefficient is higher for this sample at low pressures. It can be said that for Ermenek coals with the lowest PL value (for methane gas), the diffusion coefficient of methane gas is high at low pressures. In our country, there have been accidents related to methane gas in the coals of the Ermenek basin in the past years, resulting in loss of life.

When the adsorption process and Langmuir parameters were examined carefully, different capacities were determined depending on the structural differences of the coals and the gas type, and different Langmuir pressure and volume values were determined as parameters. However, the point to be noted here is that the maximum amount of methane gas

adsorption of lignite samples varies between 13 and 23 m^3 per ton. This value was determined as the lowest in Gürmin Merzifon sample (13.52 m^3/t) and the highest in Ilgın sample (22.25 m^3/t). However, VL values alone are not sufficient for the evaluation of the methane gas adsorption of the samples. Samples with both high VL values and low PL values can be considered as examples that may cause problems in terms of methane gas. For example, Dursunbey Ermenek and Milas Milas– Ekizköy samples stand out in this sense as both their Langmuir pressures are low and their Langmuir volumes are around 20 m^3/t. Among the samples, it was determined that Saray sample had the highest PL and VL values in terms of methane gas. Although this indicates that methane gas is adsorbed at high pressures, the high Langmuir volume indicates that the Saray sample may be the subject of alternative studies such as underground coal gasification and obtaining methane from the coal bed, as well as traditional coal mining. When evaluated from this point of view, the replacement of carbon dioxide and methane seems possible for the Saray example compared to methane gas (low carbon dioxide gas PL value).

Gürmin Merzifon sample (VL=7.7 m^3/t) was determined as having the lowest nitrogen gas adsorption (in terms of VL value). The PL value of Gürmin Merzifon sample was determined as 3.7 bar. In terms of PL value, the lowest value was determined in the Ermenek sample. The PL and VL values for nitrogen gas in this example are 1.12 bar and 12.14 m^3/t, respectively. When nitrogen gas is considered, the Dursunbey sample has the highest PL value (10.32 bar), while the Saray sample has the highest VL (16.02 m^3/t). Considering the nitrogen adsorption values, the porosity of the samples can be commented on. Since the molecular diameter of nitrogen gas is 1.55 A°, when the adsorbed amount (on mole basis) is considered, correlations can be made between the porosity and the surface areas of the samples. It is understood that the surface areas of the Saray and Dursunbey samples, which have the highest Langmuir volume, are larger than the other samples. Likewise, it can be said that the structures of Dursunbey and Saray examples, which have more surface areas, are more porous than the other examples. Both surface area and porosity of Gürmin Merzifon sample are less than other samples.

The Saray sample exhibits the highest methane Langmuir parameters (PL = 16.42 bar and VL = 27.17 m³/t), along with significant nitrogen and carbon dioxide adsorption capacities (PL = 4.21 bar and VL = 16.02 m³/t for nitrogen; PL = 11.54 bar and VL = 38.54 m³/t for carbon dioxide), correlating with its high total moisture content (43.52%). In contrast, Gürmin-Merzifon has the lowest moisture content (2.14%), accompanied by the lowest methane

adsorption capacity (PL = 6.83 bar and VL = 13.52 m³/t) and relatively low values for nitrogen (PL = 3.73 bar and VL = 7.72 m³/t) and carbon dioxide (PL = 3.15 bar and VL = 17.18 m³/t). Meanwhile, Dursunbey stands out with the highest carbon dioxide adsorption parameters (PL = 16.08 bar and VL = 38.89 m³/t) and also shows notable adsorption for nitrogen (PL = 10.32 bar and VL = 15.79 m³/t) and methane (PL = 5.53 bar and VL = 19.90 m³/t), despite having the lowest moisture content among the samples (8.76%). On the other hand, Ilgın shows strong methane adsorption (PL = 9.40 bar and VL = 22.25 m³/t), while its nitrogen and carbon dioxide adsorption capacities are moderate (PL = 1.23 bar and VL = 11.89 m³/t for nitrogen; PL = 5.79 bar and VL = 30.59 m³/t for carbon dioxide). These results highlight the varying adsorption behaviors and moisture contents of the lignite samples.

When the parameters obtained for carbon dioxide gas adsorption were evaluated, the highest PL and VL values were determined for the Dursunbey sample (PL=16.1 bar and VL =38.9 m³/t). Similarly, the lowest PL and VL values for carbon dioxide gas were determined in the Gürmin Merzifon sample (PL=3.2 bar and VL =17.2 m³/t). Information can be obtained for applications such as carbon dioxide gas adsorption capacities and carbon dioxide storage. In this context, the example of Gurmin Merzifon is the example where carbon dioxide can be stored at the lowest pressures. Similarly, Dursunbey has the highest carbon dioxide adsorption capacity. The Dursunbey example is considered as an example that has the potential to be evaluated in terms of underground coal gasification, obtaining methane from coal beds and carbon dioxide storage.

The findings related to the Dursunbey sample indicate a significant risk associated with methane desorption under pressure drops. The high methane adsorption capacity (VL = 19.90 m³/t) and the relatively low Langmuir pressure (PL = 5.53 bar) suggest that methane is readily stored within the coal matrix but can also be rapidly released when pressure decreases. This characteristic increases the likelihood of sudden gas emissions, which is a critical hazard in underground coal mining. The history of methane-related incidents in the Dursunbey region aligns with these findings, emphasizing the necessity for proactive gas drainage and monitoring systems to mitigate the risk of outbursts. Additionally, the differences in Langmuir parameters among the studied samples highlight the role of coal matrix composition and porosity in governing methane desorption behavior, reinforcing the need for site-specific risk assessments in mining operations.

3.2 Interrelationships Between Langmuir Parameters and Coal Quality Parameters

In this section, the coal quality parameters and the Langmuir parameters obtained will be compared and the test results will be correlated.

In addition, possible relationships between the results of the proximate analysis of coal samples and Langmuir parameters were similarly investigated. The relationships between the results of the proximate analysis of the coal samples and the Langmuir parameters gave more significant (with higher correlation coefficient) results than the relationships between the analysis results on the dry basis and these parameters. In all data, coal ash and fixed carbon content are given according to the original basis. In this context, the most significant results were obtained for each sample and gas between Langmuir volume and ash. These relationships between Langmuir volumes and ash are given in Figure 14, Figure 15 and Figure 16.

Figure 14. Relationship between Langmuir parameter V_L (Nitrogen) and Ash (%, on original basis).

Figure 15. Relationship between Langmuir parameter V_L (Carbon Dioxide) and Ash (%, on original basis).
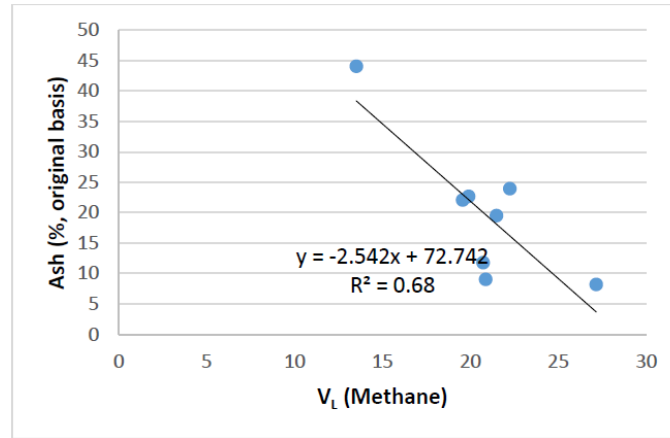
Figure 16. Relationship between Langmuir parameter V_L (Methane) and Ash (%, on original basis).

According to Figure 14-Figure 16, it was observed that Langmuir volumes increased as the ash percentages of the samples decreased. In particular, the relationship between the Langmuir volume results of nitrogen gas and ash has the highest correlation coefficient ($R^2=0.7$) observed in this context. Similarly, a similar correlation ($R^2=0.69$) was observed between Langmuir volumes of methane gas and ash. Another of these relationships, the Langmuir volume of carbon dioxide gas, did not show a significant relationship as expected, and a correlation of 0.44 ($R^2=0.44$) was observed between ash and Langmuir volume (VL).

Similarly, Langmuir pressure and proximate analysis results were compared, and here the relations of nitrogen gas with fixed carbon carbon dioxide and methane gas with total sulfur were relatively more significant (higher correlation coefficient) than other analysis results. has given. These aforementioned relationships are presented in Figure 17, Figure 18 and Figure 19, respectively.
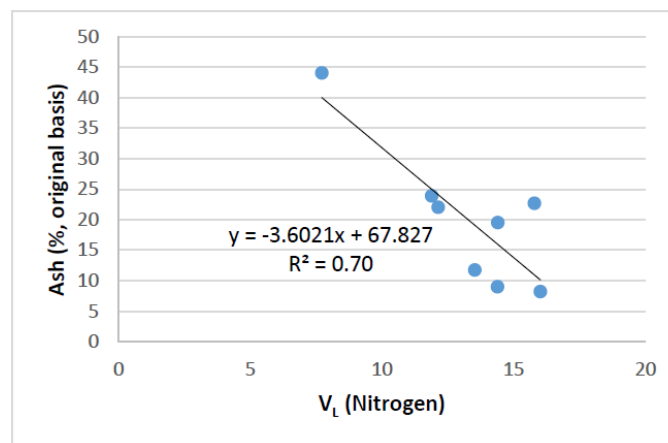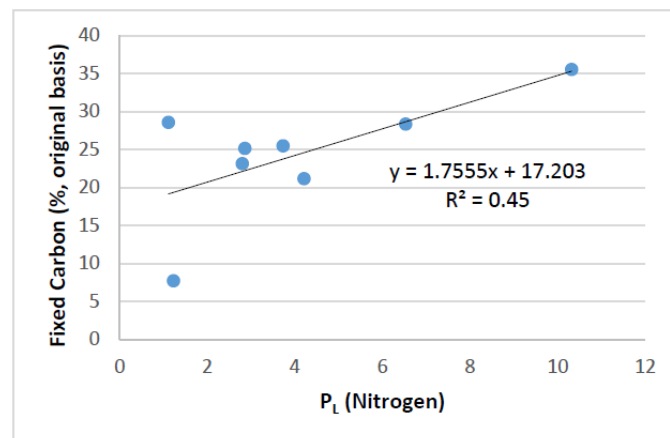

Figure 17. Relationship between Langmuir parameter PL (Nitrogen) and Fixed Carbon (%, on original basis).
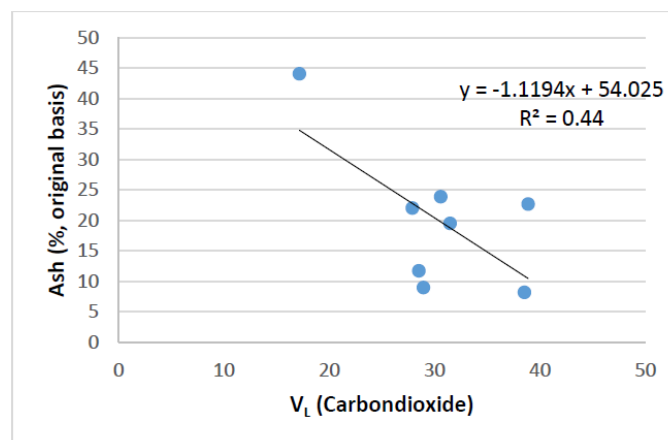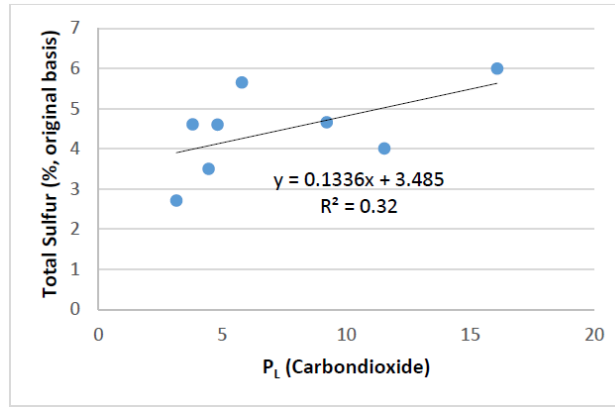
Figure 18. Relationship between Langmuir parameter PL (Carbon Dioxide) and Total Sulfur (%, on original basis).
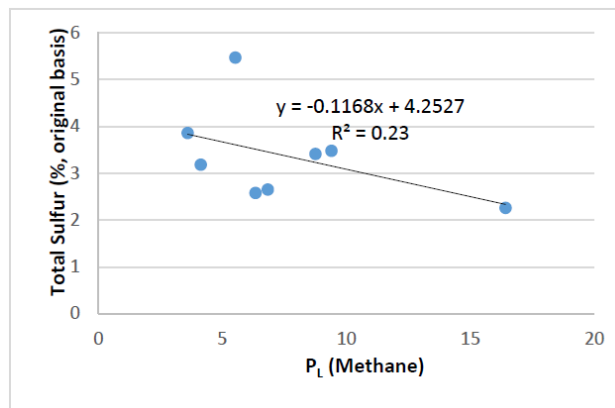
Figure 19. Relationship between Langmuir parameter PL (Methane) and Total Sulfur (%, on original basis).

In this context (Figure 17-Figure 19), the best relationship was observed between nitrogen gas Langmuir pressure and fixed carbon. An increase in Langmuir pressure (nitrogen) was observed as the fixed carbon values increased in the samples examined. The results obtained in this context, Duda et al. [24], a U-shaped relationship with fixed carbon has been evaluated by many researchers [25] [26] [27]. Therefore, it has been seen in the relatively results that the nonlinear (Figure 17) relationship with the carbon content is consistent with the literature and that the Langmuir pressure first decreases and then increases with the increase of the carbon content. When the gas adsorption amounts to the coals are evaluated (m^3/t), it has been observed that carbon dioxide gas has the highest, nitrogen gas the lowest and methane has values between them. In addition, the adsorption amounts of methane gas at different temperatures were compared in the literature [9] [28], but since the temperature was kept constant at 20 °C (293 °K) in this study, a comparison could not be made with the result stated in the literature. However, there was no need for experimental evidence in this sense, since it would not be difficult to predict that the amount of adsorption will decrease with (increasing)

temperature and that the gases attached to the pores will be released to the environment more with temperature. In the literature, ash percentages and carbon dioxide adsorbed volumes were compared and it was observed that increasing ash amount decreased the adsorbed amount of carbon dioxide gas. A similar relationship (Langmuir volumes and ash percentages) is given in Figure 14, Figure 15 and Figure 16. According to these relations given, Langmuir volumes (the volume of gas to be adsorbed at maximum pressure) were found to be high when ash was low and low when high. The Langmuir volume values of the coal samples with high ash content were determined as low, and the result was obtained which is in line with the literature. Again, a similar study was conducted on South Wales coals belonging to methane gas adsorption [29] [30]. In literature it was shown that high adsorbed volume (methane) when ash is 1.99% and low adsorbed volume (methane) when ash is 90.27%. In our samples, the maximum volumes of methane gas (VL) to be adsorbed significantly decrease with the increase in the amount of ash. This obtained relationship (Figure 16) has a correlation coefficient of 0.68 (R^2=0.68) and is considered to be significant when compared with the literature.

The presence or absence of these relationships will be decided more clearly by increasing the number of samples. However, differing associations and varying correlation coefficients in different gases will make it possible to make inferences about which parameters are effective in the gas adsorption desorption process to these coals.

4 CONCLUSION AND SUGGESTIONS

This study provides valuable insights into the adsorption and desorption characteristics of nitrogen, carbon dioxide, and methane in lignite samples, aligning with findings in the existing literature. The results indicate that carbon dioxide exhibits the highest adsorption and desorption capacity at all pressure levels, while methane surpasses nitrogen in adsorption capacity, except at low pressures. These findings emphasize the importance of understanding gas behavior in coal seams, particularly in relation to safety risks and resource utilization.

From an industrial perspective, the characterization of Langmuir parameters in the studied lignite samples offers practical implications for both methane management and carbon dioxide sequestration. The potential for methane recovery from coal seams presents an opportunity to enhance energy production while simultaneously reducing greenhouse gas emissions. At the same time, identifying coal seams with high CO_2 adsorption capacity supports sustainable carbon storage initiatives. These insights could inform industry stakeholders,

including mining companies and regulatory bodies, in optimizing gas drainage strategies and developing more effective safety protocols in underground mining operations.

To enhance workplace safety, mining companies should integrate site-specific gas monitoring systems that account for variations in methane desorption behavior, particularly in regions like Dursunbey, where low Langmuir pressure values indicate a higher risk of sudden methane release. Proactive gas drainage, ventilation improvements, and continuous monitoring should be prioritized to mitigate explosion hazards. Additionally, policymakers should consider the potential of lignite-based carbon sequestration projects in climate action plans, leveraging coal seams for long-term CO_2 storage.

For researchers, future studies should focus on refining the predictive modeling of gas adsorption and desorption under varying geological conditions. Expanding experimental datasets, incorporating petrographic analyses, and conducting field-scale trials will further validate the applicability of these findings in real-world mining environments. Moreover, interdisciplinary collaborations between mining engineers, geologists, and environmental scientists will be crucial in translating laboratory-scale insights into actionable strategies for sustainable resource management.

Ultimately, this study provides a foundation for both improving safety in coal mining and advancing cleaner energy initiatives. By integrating these findings into industrial practices and policy frameworks, the coal sector can move toward more efficient, sustainable, and safer resource extraction and utilization.

Acknowledgements

Conflict of Interest Statement

There is no conflict of interest between the authors.

Statement of Research and Publication Ethics

The study is complied with research and publication ethics.

Artificial Intelligence (AI) Contribution Statement

This manuscript was entirely written, edited, analyzed, and prepared without the assistance of any artificial intelligence (AI) tools. All content, including text, data analysis, and figures, was solely generated by the authors.

Contributions of the Authors

Mehmet Bilen: Writing - review & editing, Formal analysis, Investigation, Data curation

Sait Kizgut: Conceptualization, Methodology, Validation.

REFERENCES

[1]. L. Qi, X. Tang, Z. Wang and X. Peng, "Pore characterization of different types of coal from coal and gas outburst disaster sites using low temperature nitrogen adsorption approach". *International Journal of Mining Science and Technology*, 2017, 27(2), 371-377. http://dx.doi.org/10.1016/j.ijmst.2017.01.005

[2]. P.J. Crosdale, B.B. Beamish and M. Valix, "Coalbed methane sorption related to coal composition". *International Journal of Coal Geology,* 1998, 35(1-4), 147-158. https://doi.org/10.1016/S0166-5162(97)00015-3

[3]. R. Susilawati, J.S. Esterle, S.D. Golding and T.E. Mares, "Microbial methane potential for the South Sumatra Basin coal: Formation water screening and coal substrate bioavailability". *Energy Procedia*, 2015, 65, 282-291. https://doi.org/10.1016/j.egypro.2015.01.051

[4]. S. Harpalani and S. Ouyang, "A new laboratory technique to estimate gas diffusion characteristics of coal". 1999, U.S. Mine Ventilation Symposium. 4.

[5]. R.M. Flores, "Coal and coalbed gas: Fueling the future". First Edition. ISBN: 9780123969729, Elsevier, USA. 2014.

[6]. M. M. Dubinin, "The potential theory of adsorption of gas". *Chemical Reviews*, 1969, 60(13), 235-241.

[7]. O. Esen, "Investigation of Gas Content, Gas Adsorption Capacity and Gas Flow Properties of the Coal Seams in the Soma Coal Basin, Turkey. Ph.D. Dissertation. İstanbul Technical University, Graduate school of natural and applied science, 2021.

[8]. R.A. Schraufnagel and P.S. Schafer, "The Success of Coalbed Methane". Edited By: J. L. Saulsberry, P.S. Schafer, and R.A. Schraufnagel, A Guide To Coalbed Methane Reservoir Engineering (s. 343). 1996, Chicago, Illinois, U.S.A. Printed in the U.S.A. GRI: Gas Research Institute.

[9]. M.S.A. Perera, P.G. Ranjith, S.K. Choi, D. Airey and P. Weniger, "Estimation of Gas Adsorption Capacity in Coal: A review and an analytical study". *International Journal of Coal Preparation and Utilization.* 2012, 32(1), 25-55. https://doi.org/10.1080/19392699.2011.614298

[10]. A.S. Ranathunga, M.S.A. Perera, P.G. Ranjith, T.D. Rathnaweera and X.G. Zhang, "Effect of coal rank on CO_2 adsorption induced coal matrix swelling with different CO_2 properties and reservoir depths". *Energy & Fuel*s, 2017, 31(5), 5297-5305. https://doi.org/10.1021/acs.energyfuels.6b03321

[11]. B.V. Krooss, F. Van Bergen, Y. Gensterblum, N. Siemons, H.J.M. Pagnier and P. David, "High-pressure methane and carbon dioxide adsorption on dry and moisture-equilibrated Pennsylvanian coals". *International Journal of Coal Geology*, 2002, 51(2), 69-92. https://doi.org/10.1016/S0166-5162(02)00078-2

[12]. T.F. Rexer, M.J. Benham, A.C. Aplin and K.M. Thomas, "Methane adsorption on shale under simulated geological temperature and pressure conditions". *Energy & Fuels*, 2013, 27(6), 3099-3109. https://doi.org/10.1021/ef400381v

[13]. C.R. Clarkson, and R.M. Bustin, "Binary gas adsorption/desorption isotherms: effect of moisture and coal composition upon carbon dioxide selectivity over methane". *International Journal of Coal Geology*, 2000, 42(4), 241-271. https://doi.org/10.1016/S0166-5162(99)00032-4

[14]. X. Liu, D. Song, X. He, Z. Wang, M. Zeng, and K. Deng, "Nanopore structure of deep-burial coals explored by AFM." *Fuel*, 2019, 246, 9-17. https://doi.org/10.1016/j.fuel.2019.02.090

[15]. L. Xu, Z. Xinghua and C. Xiuzhi, "Study on adsorption capacity of coal based on low-temperature nitrogen absorption and high-pressure adsorption". *Safety in Coal Mines*, 2009, 40(5), 9-11.

[16]. Z.G. Zhang, D. Zhao, C.H. Zhang, Y. Chen and C. Tang, "Isothermal adsorption/desorption characteristics of soft coal at different temperatures". J Liaoning Tech University, 2021, 40, 510-7. https://doi.org/10.11956/j.%20issn.1008-0562.2021.06.005

[17]. D. Charrière, Z. Pokryszka, and P. Behra, "Effect of pressure and temperature on diffusion of CO_2 and CH_4 into coal from the Lorraine basin (France)". *International Journal of Coal Geology*, 2010, 81(4), 373-380. https://doi.org/10.1016/j.coal.2009.03.007

[18]. J. Jia, H. Song and P. Jia, "Molecular Simulation of Methane Adsorption Properties of Coal Samples with Different Coal Rank Superposition States". *ACS Omega*, 2023, 8(3), 3461-3469. https://doi.org/10.1021/acsomega.2c07471.

[19]. F. Han, A. Busch, B.M. Krooss, Z. Liu and J. Yang "CH_4 and CO_2 sorption isotherms and kinetics for different size fractions of two coals". *Fuel*, 2013, 108, 137-142. https://doi.org/10.1016/j.fuel.2011.12.014

[20]. R.M.M. "Florentin Characterisation of the parameters influencing the storage and drainage of gas". PhD thesis, The University of Wollongong School of Civil, Mining and Environmental Engineering, 2012, 320 s.

[21]. Bilen, M. "Investigation of gas retention and release properties in lignites". PhD thesis, Zonguldak Bülent Ecevit University). 2019. Retrieved from https://acikbilim.yok.gov.tr/bitstream/handle/20.500.12812/253331/yokAcikBilim_10278664.pdf?isAllowed=y&sequence=-1

[22]. M. Bilen, and S. Kizgut, "Investigation of gas adsorption and desorption characteristics for some Turkish lignites in terms of coal petrographic properties". *International Journal of Oil, Gas and Coal Technology*, 2023, 34(1), 68-95. https://doi.org/10.1504/IJOGCT.2023.133537

[23]. M. Pillalamarry, S. Harpalani and S. Liu, "Gas diffusion behavior of coal and its impact on production from coalbed methane reservoirs". *International Journal of Coal Geology*, 2011, 86(4), 342-348. https://doi.org/10.1016/j.coal.2011.03.007

[24]. J.M. Duda, J. Duda, A. Nodzenski and J. Lakatos, "Absorption and Adsorption of Methane and Carbon Dioxide in Hard Coal and Active Carbon". *Langmuir*, 2000, 16(12), 5458-5466. https://doi.org/10.1021/la991515a

[25]. M. Faiz, A. Saghaf, N. Sherwood and I. Wang, "The influence of petrological properties and burial history on coal seam methane reservoir characterisation, Sydney Basin, Australia". *International Journal of Coal Geology,* 2007, 70(1-3), 193-208. https://doi.org/10.1016/j.coal.2006.02.012

[26]. P.B. Hirsch, "X-ray scattering from coals. Proceedings of the Royal Society", London, 1954, 226, 143-169.

[27]. D.H. Moffat and K.E. Weale, "Sorption by coal of methane at high pressures". *Fuel*, 1955, 34, 449-462.

[28]. R.M. Bustin and C.R. Clarkson, "Geological controls on coal bed methane reservoir capacity and gas content". *International Journal of Coal Geology*, 1998, 38(1-2), 3-26. https://doi.org/10.1016/S0166-5162(98)00030-5

[29]. G.R.R. Barker-Read and S.A. Radchenko, "The relationshio between the pore structure of coal and gas dynamic behaviour of coal seams". Mining Science and Technology, 1989, 8, 109-131. https://doi.org/10.1016/S0167-9031(89)90521-5

[30]. M. Tshifhiwa, "Effects of carbon dioxide storage in coal on the physical and chemical properties of coal". (PhD Thesis). Faculty of Engineering and the Built Environment, University of the Witwatersrand. 2012.

THE AGRIVOLTAIC POTENTIAL OF TÜRKİYE

İbrahim KIRBAŞ [1]

[1] Burdur Mehmet Akif Ersoy University, Department of Electrical and Energy, Burdur, Türkiye,
ikirbas@mehmetakif.edu.tr

ABSTRACT

Agrivoltaic systems, also known as agrivoltaics, represent an innovative approach that combines agricultural activities with solar energy production on the same land. This concept emerged as a solution to the increasing demand for land for food production and the increasing demand for land for energy production. It is also a fact that greenhouse gas emissions will decrease with the increase in agrivoltaic systems and therefore with the increase in clean energy production. This study measures the agricultural potential of Türkiye by region using 1% of Türkiye's farmland, according to TUIK data. In two different PV systems modeled, single-array systems and single-axis tracking configurations will be used. It will also enable the traditional farming of crops (and potentially increase efficiency). The results of the study determined that 398 GWh of electricity would be produced in the single array system and 445 GWh in the single-axis tracking system. As a result of these results, not only can Türkiye meet all of its electrical energy needs in 2023, but also 20.7% and 34.8% more in single array and single-axis tracking systems, respectively, can be provided by agrivoltaics using only 1% of the existing agricultural lands. These results show that agrivoltaics can make a significant contribution to sustainable electricity production and provide the ability to reduce/purify greenhouse gas emissions associated with the Turkish energy production sector.

Keywords: Agrivoltaic, Türkiye, Photovoltaic, Agriculture, Solar energy, Renewable energy.

1   INTRODUCTION

Agrivoltaic, the practice of co-locating agricultural and solar energy systems, maximizes land use efficiency and sustainability, offering a dual-use approach where both food and energy can be produced simultaneously, leading to mutual benefits for agriculture and the

energy industry [1]-[3]. Research has shown that agrivoltaic systems can increase land productivity by up to 60-70% [2]. Agrivoltaics combines solar energy production with agricultural activities, creating a mutually beneficial relationship in which both food and energy production can occur simultaneously [4]. This dual-use approach not only optimizes land but also provides additional benefits, such as stabilizing crop production, reducing land occupation, and reducing greenhouse gas emissions [5]-[7].

Eastern Pyrenean region of France (2.2 MWp), Castelvetro Piacentino region of Italy (1.3 MWp) and Monticellid'Ongina region (3.2 MWp), Babberich of the Netherlands (2.7 MWp), Jodhpur of India in (105 kWp / Ground-mounted), in Austria (22 kWp / bifacial PV), in Aasen of Germany (4.1 MWp / bifacial PV) applications such as are available [5].

In addition, studies have highlighted the potential of agrivoltaics in various regions, including Europe [8], Canada [9], India [10] and the United States [11]. Agrivoltaic systems have been found to increase crop yields, increase economic productivity, and support the mainstream market for solar energy systems [12].

The integration of agrivoltaic systems involves installing solar panels on farmland to generate electricity while also allowing agricultural activities to be carried out under or around the panels [13]. This approach not only helps transition to renewable energy but also helps reduce land competition, irrigation requirements, and increase solar panel efficiency [14]. Agrivoltaics have the potential to increase land productivity and efficiency by offering a strategic way to combine solar energy production with agricultural production [15].

The integration of photovoltaics into agricultural frameworks such as greenhouses has emerged as a research focus to increase food production and renewable energy production [16]. Agrivoltaics not only contribute to meeting global commitments and increasing clean energy production but also offer employment opportunities, economic stability, and conservation of natural resources [10]. Additionally, the development of agrivoltaic standards, regulations, and incentives could accelerate the adoption of this technology over traditional PV systems [17].

As a result, agrivoltaics represents a strategic and innovative approach to sustainable land use that combines the benefits of agriculture and solar energy production. Leveraging the synergy between food and energy production, agrivoltaics has the potential to address the challenges of land competition and contribute to a more sustainable future. There are very few applications in the world regarding agrivoltaics. There is no application yet in our country.

2   MATERIAL AND METHOD

This study was carried out to determine the agrivoltaic potential in Türkiye by using 1% of the existing agricultural lands in Türkiye. It was thought that it should not be used in this area to ensure the protection of meadow and pasture lands. Excluding meadow and pasture lands from Türkiye's agricultural areas, the remaining agricultural lands are given in Table 1, and their distribution by region is shown in Figure 1. Calculations will be made using these fields.
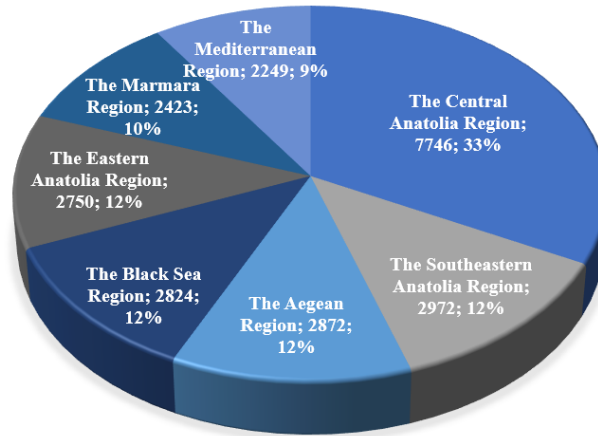
Figure 1. Distribution of Türkiye agricultural lands by regions in 2022 (Thousand Ha) [19].

Table 1. Agricultural areas of Türkiye (Thousand Ha) [18].

Years	Total agricultural area*	Cereals and other plant products area		Vegetable gardens area	Ornamental plants area	Fruits, beverages and spice plants area
		Cultivated area	Fallow			
2018	23180	15421	3513	784	5.2	3457
2019	23099	15398	3387	790	5.2	3519
2020	23145	15628	3173	779	5.4	3559
2021	23473	16062	3059	755	5	3591
2022	23865	16510	2960	718	6	3671

Meadow and pasture land are excluded in the total agricultural area calculation.

Türkiye has a significant solar energy potential due to its geographical location. According to the Türkiye Solar Energy Potential Atlas (GEPA) prepared by the Energy Ministry, the average annual total sunshine duration is 2741 hours, and the average annual total radiation value is calculated as 1527.46 kWh/m^2. The general potential view, monthly average global radiation distribution, and sunshine duration values in GEPA are shown in Figure 2. [20], [21].
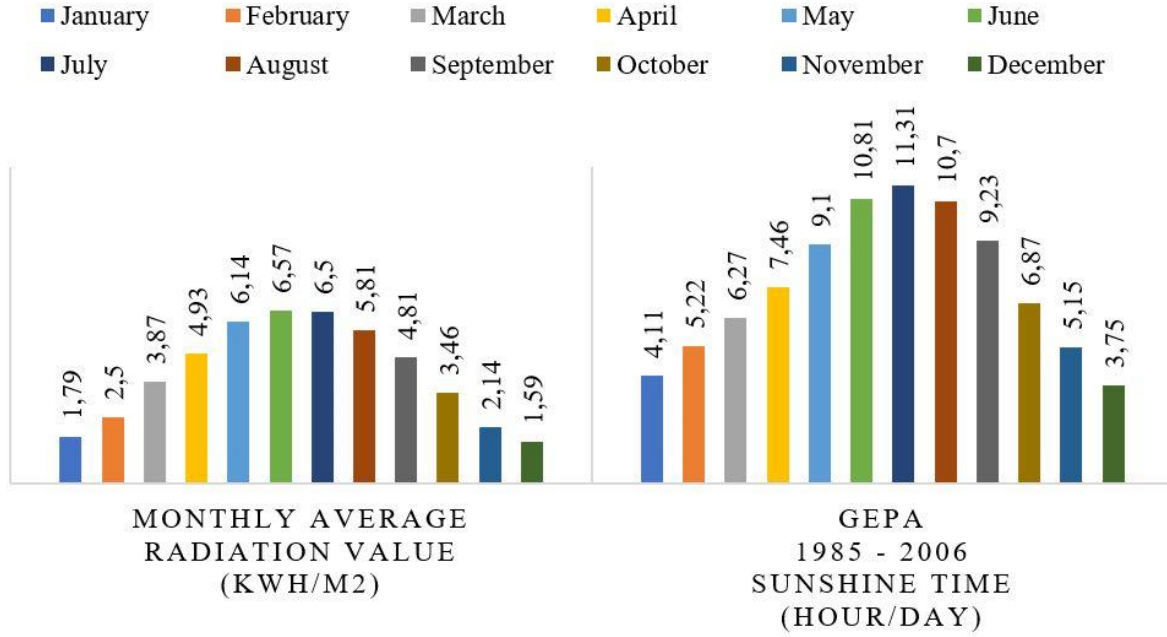
Figure 2. Average solar energy potential per month of Türkiye [21].

The distribution of Türkiye's annual total solar energy potential according to geographical regions is shown in Table 2 [21]. The region that receives the most solar energy in Türkiye is the Southeastern Anatolia Region, followed by the Mediterranean Region.

In the study, the appropriate location was determined for each region, taking into account the distribution of Solar Energy Potential according to regions given in Table 2. These accepted locations are marked on the map in Figure 3. Additionally, details for each region are given in Table 3. The PV section of the Agrivoltaic system to be designed uses Meteonorm 8.1 (2005-2013) climate values of these locations (Table 3).

Table 2. Distribution of Türkiye's annual total solar energy potential by geographical regions.

Area	Sunshine Time (hour/year)	Total Solar Energy (kWh/m²-year)
The Southeastern Anatolia	2993	1460
The Mediterranean	2956	1390
The Eastern Anatolia	2664	1365
The Central Anatolia	2628	1314
The Aegean	2738	1304
The Marmara	2409	1168
The Black Sea	1971	1120
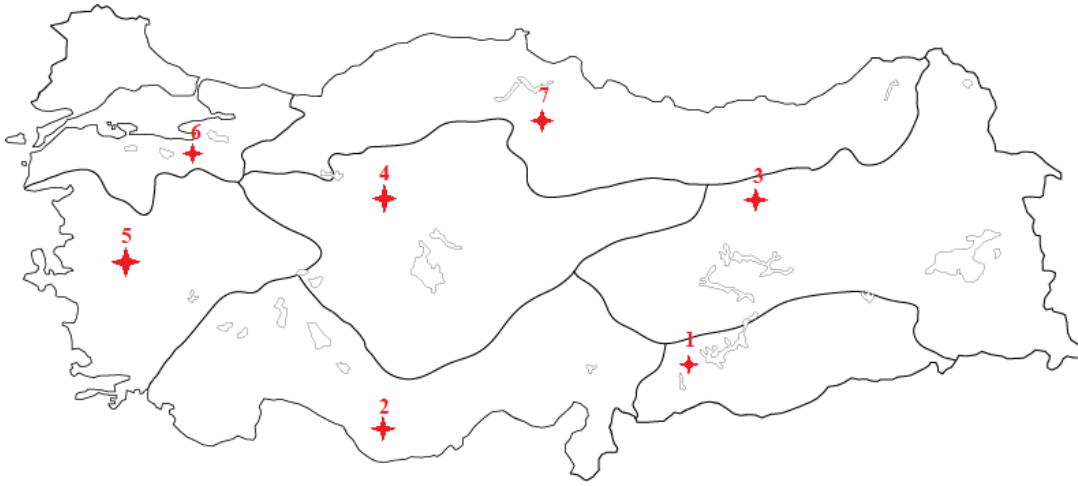
Figure 3. Geographical regions of Türkiye [22].

Table 3. Geographical locations of the Agrivoltaic systems to be designed.

	Geographic Region	Selected Region		Meteonorm Solar Energy (kWh/m²-year)
		City / District / Location	Latitude, longitude, altitude	
1	The Southeastern Anatolia	Gaziantep / Nizip / Çanakçı	37.12ºN, 37.72ºE, 729m	1904.2
2	The Mediterranean	Mersin / Anamur / Kılıç	36.24ºN, 32.77ºE, 769m	1848.9
3	The Eastern Anatolia	Erzincan / Kemah / Kömürköy	39.65ºN, 39.02ºE, 1075m	1819.1
4	The Central Anatolia	Ankara / Sincan / Temelli	39.75ºN, 32.33ºE, 792m	1702.9
5	The Aegean	Manisa / Kula	38.56ºN, 28.66ºE, 860m	1745.3
6	The Marmara	Bursa / Osmangazi / Tuzaklı	40.11ºN, 28.99ºE, 888m	1563.0
7	The Black Sea	Amasya / Merzifon / Aksungur	40.91ºN, 35.51ºE, 885m	1496.2

As the area of interest of this study, 1% of agricultural land was calculated for each region in Türkiye. For the configuration of PV systems on this land, it was designed to be installed on an area of 20m X 500m = 10000 m²/1 Hectare (1 Ha). The production amount of the agrivoltaic PV system to be installed on an area of 1 Ha was calculated with the PVsyst 7.4 program. The PV production of that region was determined by the proportion of the area corresponding to 1% of the agricultural area calculated for each region. Then, the annual energy production and total agrivoltaic potential for Türkiye was determined. PVsyst 7.4 program and Meteonorm 8.1 climate data, which is a sub-module of this program, were used to determine solar energy electricity production.

The majority of solar power plants installed on land are built permanently. At the same time, efficiency studies aimed at increasing energy production have also come to the fore in recent days. Increasing production efficiency can only be achieved by increasing the radiation intensity falling on the panel. As long as sunlight falls on the modules at a right angle, production is maximized. This is possible with a system that tracks the sun and ensures that the

sun's rays are constantly received vertically. In this study, two different agrivoltaic systems, one of which is a single array as a PV system and consists of a single-axis tracking system to increase efficiency, were taken into consideration for analysis. 50 arrays were placed for 500m, with the distance between arrays being 10m. In the PVsyst analysis, it was determined that a 10m distance was sufficient for shading tests. Shading loss tests were carried out separately for each region, and as a result, the shadowing on the panel for a distance of 10m occurred before 9.00 am and after 5.00 pm. This is an expected situation that does not have a negative impact on the efficiency of the PV system. In addition, the distance between single array PV system arrays in System-1 is 10m, which provides easy access to agricultural lands as well as ease of use of agricultural machines. A single-axis tracking (horizontal, 0° inclined, East-West axis tracking) system was designed as System-2. On the electricity side, single-axis tracking systems are used to obtain maximum solar energy per unit area. Having a distance of 10m between the arrays also gave suitable shading results for System-2. System-2 also offers an option for vertical orientation of the panels so that farmers can work on agricultural lands.

The array spacing on the piece of land was determined separately for both systems, ensuring sufficient distance for the mobility of the agricultural equipment and taking into account the distances between the panels shading each other. Once the array spacing was determined, the total number of panels in an area was determined using the number of single array and single-axis tracking arrays. As a result of all these assumptions and designs, for an area of 1 Ha (10000 m^2), in System-1, there are 50 arrays of Panasonic brand AE14-H550-VHC-10B modules with 4x9=36 panels in each array, a total of 1800 pieces. In System-2, there are 36 Panasonic brand AE14-H550-VHC-10B modules in each array. Again, a total of 1800 panels were used in 50 series. As an inverter, 8 units of the SUN2000-100KTL-M1 brand inverter from Huawei Technology were used, calculated according to the system's needs. The panel placement on the land is given in Figure 4, and the technical specifications of the panel and inverter used in the system are given in Table 4.
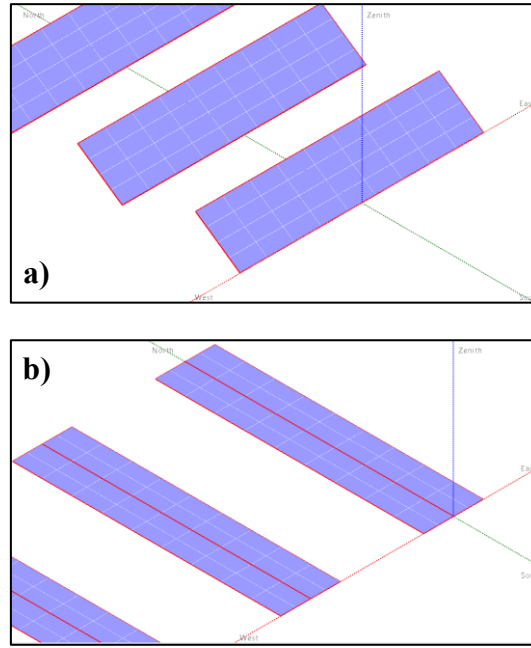
Figure 4. Panel layout (a) System-1, (b) System-2.

Table 4. Features of system components.

PV Modul	Technical Specifications
Modul (Panasonic)	AE14-H550-VHC-10B
Prod. Since	2024
Modul power	550 Wp
Modul size (WxL)	1.133 x 2.278 m^2
Open circuit voltage (Voc)	50.3 V
Max. Power voltage (Vmpp)	42.1 V
Short-circuit current (Isc)	13.65 A
Max. power point current (Impp)	13.06 A
İnverter	Technical Specifications
İnverter (Huawei)	SUN2000-100KTL-M1-480 Vac
Prod. Since	2021
Max. Efficiency	98.8%
MPPT Operating Voltage Range	200 V ~ 1000 V
Max. Input Voltage	1100 V
Maximum AC Power (Pmax AC)	110 kWac
Maximum AC current (Imax AC)	134 A

3   RESULTS AND DISCUSSION

3.1   The Southeastern Anatolia Region

The Southeastern Anatolia Region is the region with the greatest potential in terms of solar energy potential and sunshine duration. In this region, in the Nizip District of Gaziantep Province, Çanakcı district, 37.12ºN, 37.72ºE, 729m, was located closest to the region's sunshine

potential average. The total agricultural area of the Southeastern Anatolia Region is 2972000 Ha, and the results of the calculations regarding the electrical energy production to be obtained from the agrivoltaic system to be established on an area of 29720 Ha, corresponding to 1% of this area, are given in Table 5.

Table 5. The Southeastern Anatolia Region agrivoltaic potential for 1% of agricultural land.

	Single Array (GWh/year)	Single-Axis Tracking (GWh/year)
Unit area (10000 m^2 = 1 Ha)	1.825	2.218
1% agricultural area (29720 Ha)	54239	65919

3.2 The Mediterranean Region

Agrivoltaic system for the Mediterranean region was planned Kılıç location, located at 36.24ºN, 32.77ºE at an altitude of 769m, within the borders of Anamur District of Mersin province. The values obtained are given in Table 6 by the implementation of PVsyst program calculations to 1% of the area's agricultural area size of 2249000 Ha.

Table 6. The Mediterranean Region agrivoltaic potential for 1% of agricultural land.

	Single Array (GWh/year)	Single-Axis Tracking (GWh/year)
Unit area (10000 m^2 = 1 Ha)	1.746	1.917
1% agricultural area (22490 Ha)	39268	43114

3.3 The Eastern Anatolia Region

The Eastern Anatolia Region is mountainous and has a higher elevation than other regions. For this region, it is planned to establish an agrivoltaic system at 39.65ºN, 39.02ºE, and 1075m altitude within the borders of the village called Kömürköy in Kemah District of Erzincan province. The Eastern Anatolia Region has an agricultural land of 2750000 Ha. In most of this land are cultivated cereal products such as barley and wheat, which are resistant to cold and arid climate conditions. In addition, legumes, sugar beets, fruits, and vegetables are also grown. The annual electrical energy to be provided by an agrivoltaic system that can be established on 1 Ha land in the region called Kömürköy has been determined for both a single

array and solar tracking system power plant. The energy to be provided from 1% of the agricultural lands in the Eastern Anatolia region is given in Table 7 as a result of the calculations.

Table 7. The Eastern Anatolia Region agrivoltaic potential for 1% of agricultural land.

	Single Array (GWh/year)	Single-Axis Tracking (GWh/year)
Unit area (10000 m^2 = 1 Ha)	1.821	2.005
1% agricultural area (27500 Ha)	50077	55137

When Table 2 of the Distribution of Annual Total Solar Energy Potential by Regions is examined, the Eastern Anatolia Region ranks 3rd. However, as a result of the calculations, it produces more than the Mediterranean Region, which ranks 2nd. This situation is thought to be due to the fact that the altitude of the region chosen for agrivoltaic system planned to be established in the region is 1075m. As the ambient temperature decreases with increasing altitude, panel temperature will also decrease. Thus, panel efficiency will increase.

3.4   The Central Anatolia Region

The Central Anatolia Region is the largest region of Türkiye, both in surface area and the size of agricultural lands. It has an agricultural area of 7746000 Ha. In these areas, a wide variety of agricultural products are grown, primarily wheat and barley. For the agrivoltaic system to be established, this region, a location with an altitude of 39.75ºN, 32.33ºE, 792m Temelli, within the borders of the Sincan district of Ankara province, was chosen. The values of the electricity production to be obtained from 1% of the agricultural land, based on the agrivoltaic system to be established for 1 Ha of land and the production of this system, are given in Table 8.

Table 8. The Central Anatolia Region agrivoltaic potential for 1% of agricultural land.

	Single Array (GWh/year)	Single-Axis Tracking (GWh/year)
Unit area (10000 m2 = 1 Ha)	1.671	1.840
1% agricultural area (77460 Ha)	129435	142526

3.5   The Aegean Region

A location within the borders of Manisa province was determined for the Aegean region, which forms the western coast of Türkiye. The production amounts obtained from the PVsyst program of an agrivoltaic system to be built on a 1 Ha area at 38.56ºN, 28.66ºE, and 860m altitude in Kula district of Manisa province are shown in Table 9.

Table 9. The Aegean Region agrivoltaic potential for 1% of agricultural land.

	Single Array (GWh/year)	Single-Axis Tracking (GWh/year)
Unit area (10000 m² = 1 Ha)	1.686	1.855
1% agricultural area (28720 Ha)	48422	53276

3.6   The Marmara Region

For the agrivoltaic system planned to be established in the Marmara Region, a location at 40.11ºN, 28.99ºE and 888m altitude in the Tuzaklı village of Osmangazi district of Bursa province was chosen. Electricity production estimates to be obtained from the single array system and single-axis tracking system for the region are given in Table 10.

Table 10. The Marmara Region agrivoltaic potential for 1% of agricultural land.

	Single Array (GWh/year)	Single-Axis Tracking (GWh/year)
Unit area (10000 m² = 1 Ha)	1.496	1.651
1% agricultural area (24230 Ha)	36248	40004

3.7   The Black Sea Region

The Black Sea Region, which has the lowest data on sunshine potential and sunshine duration, ranks 3rd in terms of agricultural lands. The region with high rainfall has high mountain ranges running parallel to the coastline. The majority of agricultural areas are formed on tea and hazelnuts on the slopes of this mountain range. There are various plains in the western and central parts and traditional agriculture can be done. For the calculations to be made for the Black Sea region, a location of 40.91ºN, 35.51ºE and 885m altitude was determined in Aksungur village of Merzifon district of Amasya province. The results are given in Table 11.

Table 11. The Black Sea Region agrivoltaic potential for 1% of agricultural land.

	Single Array (GWh/year)	Single-Axis Tracking (GWh/year)
Unit area (10000 m^2 = 1 Ha)	1.455	1.607
1% agricultural area (28240 Ha)	41089	45382

As a result of calculations separately for each region, the amount of electricity production to be obtained by applying agrivoltaic systems to 1% of Türkiye's agricultural lands is given in Table 12.

Table 12. Agrivoltaic potential of Türkiye for 1% of agricultural land.

Area	Single Array (GWh/year)	Single-Axis Tracking (GWh/year)
The Southeastern Anatolia	54239	65919
The Mediterranean	39268	43114
The Eastern Anatolia	50077	55137
The Central Anatolia	129435	142526
The Aegean	48422	53276
The Marmara	36248	40004
The Black Sea	41089	45382
Total	398778	445358

The amount of electricity production to be obtained by applying agrivoltaic systems to 1% of Türkiye's agricultural lands was calculated in single array and single axis tracking systems at 398778 GWh and 445358 GWh, respectively. In the data of the Ministry of Energy and Natural Resources of the Republic of Türkiye, Türkiye's electrical energy consumption was reported as 330300 GWh in 2023. With these results, the electrical energy obtained from agrivoltaic systems covers Türkiye's consumption by 120.7% in the single array system and 134.8% in the single-axis tracking system. Contribution to the country's economy can be made by selling excess electrical energy produced from agrivoltaics, which has the potential to meet all of Türkiye's electricity needs in the first years. In addition, it is inevitable that the energy need will increase with the increasing population. The excess energy produced can be used to meet the increasing energy demand in the coming years. Thus, problems arising from energy increase and most importantly, foreign dependency in energy will be prevented in the coming years.

4   CONCLUSION AND SUGGESTIONS

This study estimated the agrivoltaic potential in Türkiye using agricultural areas 1% with single array and single-axis tracking system configurations for PV modules. Only 1% of Türkiye's agricultural lands can meet all of the country's total electricity needs. In fact, it has the potential to generate excess electricity, with 20.7% in the single array system and 34.8% in the single-axis tracking system. Overproduced electricity can be sold or used in other areas within the country. The number of electric vehicles in transportation is expected to increase day by day. Agrivoltaics can supply production for use in electric vehicle charging to decarbonize transportation in Türkiye. Finally, it could help Türkiye eliminate its dependence on fossil fuels.

Türkiye has many varieties of agricultural products that can be grown in full shade and semi-shade environments. Various studies have proven that growing these products under agrivoltaic systems contributes to increased product productivity. It has been reported that production losses due to panel heating decrease and system efficiency increases in solar power plants installed on agricultural lands. Agrivoltaics, which is an agriculture-energy system gains can be achieved in both directions.

It is very difficult to reserve 1% of agricultural lands for agrivoltaics and to implement power plants on a single land. This will lead to the establishment of power plants at various scales depending on land suitability and to increase the number of power plants. Although it may seem like a limitation at first glance, increasing the number of power plants and spreading them to different locations will reduce some problems, especially transmission and distribution losses.

When we evaluate agrivoltaics with all these results, agrivoltaic technology reveals a significant potential for Türkiye's efforts to produce renewable energy and reduce greenhouse gases.

Our country legally restricts the installation of solar power on agricultural lands that do not qualify as marginal agricultural land. It has been determined by various studies that agrivoltaic systems do not harm agricultural lands and increase crop yield when appropriate designs are made. Additionally, energy production is also carried out. Considering all these positive aspects, legal regulations can pave the way for the installation of agrivoltaic systems on agricultural lands. A great contribution will be made to Türkiye reaching its green energy target.

Conflict of Interest Statement

There is no conflict of interest between the authors.

Statement of Research and Publication Ethics

The authors declare that all the rules required to be followed within the scope of "Higher Education Institutions Scientific Research and Publication Ethics Directive" have been complied with in all processes of the article, that BEU Journal of Science and the editorial board have no responsibility for any ethical violations that may be encountered, and that this study has not been evaluated in any academic publication environment other than BEU Journal of Science.

Artificial Intelligence (AI) Contribution Statement

This manuscript was entirely written, edited, analyzed, and prepared without the assistance of any artificial intelligence (AI) tools. All content, including text, data analysis, and figures, was solely generated by the author.

REFERENCES

[1]   E. Warmann, "Agrivoltaic system design tools for managing trade-offs between energy production, crop productivity and water consumption," *Environmental Research Letters,* vol. 19(3), pp. 034046, 2024.

[2]   K. Sharpe, B. Heins, E. Buchanan, and M. Reese, "Evaluation of solar photovoltaic systems to shade cows in a pasture-based dairy herd," *Journal of Dairy Science*, vol. 104(3), pp. 2794-2806, 2021.

[3]   H. Dinesh, and J. Pearce, "The potential of agrivoltaic systems," *Renewable and Sustainable Energy Reviews,* vol. 54, pp. 299-308, 2016.

[4]   E. Adeh, J. Selker, and C. Higgins, "Remarkable agrivoltaic influence on soil moisture, micrometeorology and water-use efficiency," *Plos One,* vol. 13(11), pp. e0203256, 2018.

[5]   İ. Kırbaş, (2023). "Agrivoltaik Sistemler ve Tarım Alanlarının Hibrit Kullanımı," *Uluslararası Mühendislik Tasarım ve Teknoloji Dergisi,* vol. 5 (1-2) pp. 9-19, 2023.

[6]   A. Pascaris, "Examining existing policy to inform a comprehensive legal framework for agrivoltaics in the U.S." *Energy Policy,* vol. 159, pp. 112620, 2021.

[7]   J. Zheng, S. Meng, X. Zhang, H. Zhao, X. Ning, F. Chen, A.A.A. Omer, J. Ingenhoff, and W. Liu, "Increasing the comprehensive economic benefits of farmland with even-lighting agrivoltaic systems," *Plos One,* vol. 16(7), pp. e0254482, 2021.

[8]   K. Niazi, and M. Victoria, "Comparative analysis of photovoltaic configurations for agrivoltaic systems in Europe," *Progress in Photovoltaics Research and Applications,* vol. 31(11), pp. 1101-1113, 2023.

[9]   J. Pearce, "Agrivoltaics in Ontario Canada: promise and policy," *Sustainability,* vol. 14(5), pp. 3037, 2022.

[10]   R. Mahto, D. Sharma, R. John, and C. Putcha, "Agrivoltaics: a climate-smart agriculture approach for Indian farmers," *Land,* vol. 10(11), pp. 1277, 2021.

[11]   J. Macknick, H. Hartmann, G. Barron-Gafford, B. Beatty, R. Burton, C. Seok-Choi, … and L. Walston, "The 5 cs of agrivoltaic success factors in the United States: lessons from the inspire research study," *Technical Report,* 2022.

[12]   A. C. Andrew, C. W. Higgins, M. A. Smallman, M. Graham, and S. Ates, "Herbage yield, lamb growth and foraging behavior in agrivoltaic production system," *Frontiers in Sustainable Food Systems,* vol. 5, pp. 659175, 2021.

[13]   T. Sekiyama, and A. Nagashima, "Solar sharing for both food and clean energy production: performance of agrivoltaic systems for corn, a typical shade-intolerant crop," *Environments,* vol. 6(6), pp. 65, 2019.

[14]   L. Shepard, C. Higgins, and K. Proctor, "Agrivoltaics: modeling the relative importance of longwave radiation from solar panels," *Plos One,* vol. 17(10), pp. e0273119, 2022.

[15]   A. Pascaris, C. Schelly, and J. Pearce, "A first investigation of agriculture sector perspectives on the opportunities and barriers for agrivoltaics," *Agronomy*, vol. 10(12), pp. 1885, 2020.

[16]   M. Haroon, and M. Janjua, "High-throughput designing and investigation of d–a−π–a-type donor materials for potential application in greenhouse-integrated solar cells," *Energy & Fuels,* vol. 35(15), pp. 12461-12472, 2021.

[17]   U. Jamil, and J. Pearce, "Energy policy for agrivoltaics in Alberta Canada," *Preprints,* 2022100405, 2022.

[18]   TUIK, "Türkiye'nin Tarım Alanları," [Online]. Available: https://data.tuik.gov.tr/Kategori/GetKategori?p=Tarim-111 [Accessed: 30.03.2024].

[19]   Türkiye Bankalar Birliği (TBB), 2022 Tarım Sektörü Raporu, Haziran 2023, [Online]. Available:https://www.tbb.org.tr/Content/Upload/Dokuman/8960/Tarim_Sektor_Raporu_130723.pdf [Accessed: 03.04.2024].

[20]   İ. Kırbaş, B. Aydoğan, and A. Uyumaz, "Hava Isıtmalı Güneş Kollektörlerin'de Güneş Takip Mekanizması Kullanımı," *Burdur Mehmet Akif Ersoy Üniversitesi Fen Bilimleri Enstitüsü Dergisi,* vol. 2(2), pp. 74-84, 2011.

[21]   Elektrik İşleri Genel Müdürlüğü (EİGM), (2024). [Online]. Available: https://enerji.gov.tr/eigm-yenilenebilir-enerji-kaynaklar-gunes [Accessed: 05.04.2024].

[22]   URL-1, [Online]. Available: http://cografyaharita.com/turkiye-dilsiz-haritalari.html [Accessed: 05.04.2024].

IMPROVING TEXT-TO-SQL CONVERSION FOR LOW-RESOURCE LANGUAGES USING LARGE LANGUAGE MODELS

Emir Öztürk [1] (iD)

[1] *Trakya University, Computer Engineering Department, Edirne, Türkiye, emirozturk@trakya.edu.tr*

ABSTRACT

Accurate text-to-SQL conversion remains a challenge, particularly for low-resource languages like Turkish. This study explores the effectiveness of large language models (LLMs) in translating Turkish natural language queries into SQL, introducing a two-stage fine-tuning approach to enhance performance. Three widely used LLMs Llama2, Llama3, and Phi3 are fine-tuned under two different training strategies, direct SQL fine-tuning and sequential fine-tuning, where models are first trained on Turkish instruction data before SQL fine-tuning. A total of six model configurations are evaluated using execution accuracy and logical form accuracy. The results indicate that Phi3 models outperform both Llama-based models and previously reported methods, achieving execution accuracy of up to 99.95% and logical form accuracy of 99.95%, exceeding the best scores in the literature by 5–10%. The study highlights the effectiveness of instruction-based fine-tuning in improving SQL query generation. It provides a detailed comparison of Llama-based and Phi-based models in text-to-SQL tasks, introduces a structured fine-tuning methodology designed for low-resource languages, and presents empirical evidence demonstrating the positive impact of strategic data augmentation on model performance. These findings contribute to the advancement of natural language interfaces for databases, particularly in languages with limited NLP resources. The scripts and models used during the training and testing phases of the study are publicly available at https://github.com/emirozturk/TT2SQL.

Keywords: Llama2, Llama3, Nl to Sql, Phi3, Turkish text to sql.

1 INTRODUCTION

The application of large language models (LLMs) has significantly expanded across various fields, including tasks such as classification, detection, and clustering [1], [2], [3]. One specific area of interest is translating natural language text into SQL queries, a task known as

text-to-SQL [4]. Generally, text-to-SQL algorithms involve converting natural language statements into SQL queries to retrieve the desired data from a database [5], [6], [7].

The main challenges in text-to-SQL tasks include handling the complexity and variability of natural language, managing different database schemas, and ensuring the accuracy and efficiency of the generated SQL queries. These challenges are further amplified when dealing with languages other than English, due to differences in syntax, semantics, and available resources. The complexity arises from the need to correctly interpreting the user's intent, which can be expressed in diverse ways, and accurately map it to a corresponding SQL query that adheres to the structure and constraints of the target database. Variability in natural language includes different ways to ask the same question, use of synonyms, and varying sentence structures. When this task extends to other languages, additional layers of complexity such as idiomatic expressions, grammatical structures, and specific linguistic characteristics further challenge the model's capabilities.

LLMs have revolutionized numerous natural language processing (NLP) tasks due to their advanced reasoning and contextual understanding capabilities. Their application in the text-to-SQL domain is particularly noteworthy because it involves understanding the semantics of natural language queries and converting them into structured SQL queries executable by a database. This task requires not only linguistic competence but also an understanding of database schemas and the ability to translate complex logical constructs into correct and efficient SQL code.

Before the use of language models, various methods were employed for text-to-SQL conversion. [8] proposed DialSQL, a dialogue-based framework leveraging human interaction to improve the accuracy of text-to-SQL models. [9] introduced IRNet, a neural approach decomposing the text-to-SQL generation process into three phases: schema linking, intermediate representation generation, and SQL inference. [10] focused on using graph neural networks (GNNs) to represent the database schema structure, enhancing the semantic parser's schema understanding. [11] presented execution guidance, a method utilizing SQL semantics by executing partially generated queries during decoding to filter out invalid candidates. [12] proposed INCSQL, a sequence-to-action parsing approach incrementally filling SQL query slots, exploring non-deterministic oracles to account for multiple correct SQL queries.

Following the success of generative models in reasoning and accurate response generation, these models were also applied to the text-to-SQL domain [13]. Generative models,

with their advanced language understanding and generation capabilities, have proven particularly effective in dealing with the complexities of text-to-SQL tasks. Their ability to generate diverse and contextually appropriate responses makes them suitable for handling the nuances of natural language queries and converting them into precise SQL statements.

While most research has been conducted in English, there have been studies in other languages as well. [14] conducted a pilot study for Chinese SQL semantic parsing by creating the CSpider dataset, translating English questions from the Spider dataset into Chinese, and experimenting with word-based and character-based encoders. [15] introduced the first large-scale text-to-SQL semantic parsing dataset for Vietnamese, extending and evaluating two strong semantic parsing baselines, EditSQL and IRNet, on their dataset and exploring various configurations to improve performance. [16] introduced TableQA, a large-scale Chinese text-to-SQL dataset focusing on table-aware SQL generation, proposing two table-aware approaches to address entity linking and answerability challenges. [17] developed a framework for cross-lingual text-to-SQL semantic parsing that translates non-English utterances into SQL queries based on an English schema, evaluating their method on Chinese, Vietnamese, Farsi, and Hindi using the XSPIDER and XKAGGLE-DBQA datasets. [18] proposed REX, a framework for cross-lingual text-to-SQL semantic parsing leveraging English translations to bridge the language gap for non-English utterances, demonstrating REX's performance on Chinese and Vietnamese datasets.

The aim of these studies is to perform text-to-SQL conversions in low-resource languages with limited data. Researchers have created datasets and adapted existing models to these languages, addressing their unique challenges. These efforts contribute to extending semantic parsing research to languages other than English, increasing linguistic diversity in this field. Besides low-resource languages, there have also been multilingual studies. In [19], text-to-SQL operations were conducted in English, Portuguese, Spanish, and French. However, none of these studies included the Turkish language.

To conduct these studies and make comparisons, common datasets consisting of text and corresponding SQL queries are essential. Many datasets have been provided and their contents reviewed for this purpose [20]. For English, the Spider dataset has become the standard for benchmarking [21]. Multilingual datasets are crucial for developing and evaluating models that can work across different languages. Therefore, the Spider dataset has been translated or manually labeled in other languages [14], [22], [23], [24]. Additionally, a multilingual version of the Spider dataset has been made available for multilingual studies [25]. Besides Spider,

other text-to-SQL datasets in different languages have also been provided [15], [18]. However, for Turkish, the lack of a dedicated dataset has been a significant barrier.

Although text-to-SQL conversion has been explored in various languages, there has been a notable absence of such models and datasets for the Turkish language. To address this gap, [28] introduced TUR2SQL, the first publicly available cross-domain Turkish text-to-SQL dataset. This dataset comprises pairs of natural language statements and their corresponding SQL queries, facilitating objective comparison and evaluation of text-to-SQL models for Turkish, similar to the Spider dataset for English. The authors also conducted experiments using SQLNet [27] and ChatGPT on TUR2SQL, demonstrating the feasibility of text-to-SQL conversion in Turkish and providing baseline performance for future research.

In this study, the goal is to perform unguided text-to-SQL conversion using the TUR2SQL dataset and six fine-tuned language models.

The limited availability of Turkish models and datasets, coupled with the relatively few studies conducted in this area, has highlighted a significant gap in current research. Existing datasets often fall short in fully capturing the unique structural and semantic nuances of the Turkish language, which results in suboptimal outcomes. To further improve these results, this study employs training with Turkish-specific datasets before training with sql dataset to enhance the reasoning capacity of the models in Turkish. This approach aims to enable a more accurate understanding of Turkish linguistic intricacies, ultimately leading to the generation of more precise and reliable SQL queries.

For this process, in the initial phase, these language models are fine-tuned with TUR2SQL, and results are obtained. In the subsequent phase, to enable the models to better understand Turkish instructions, the models are first trained with a Turkish instruction dataset [28] and then fine-tuned with the TUR2SQL dataset.

The contributions of this study are as follows:

- Given that Turkish is a low-resource language and there are no specialized models trained on Turkish text-to-SQL tasks prior to this study, training multiple models capable of generating SQL from Turkish text and making these models publicly available introduces a significant novelty.

- To enhance the model's performance, the LLaMA and Phi models are first trained on a Turkish instruction dataset before being fine-tuned on SQL data. Consequently, Turkish LLaMA and Phi models for instructions are developed. Although the

primary goal of the study is not to develop a Turkish language model, these models have also been made publicly available.

- The study provides a comparative analysis by examining the EX and LF results obtained from other low-resource or multilingual studies. Despite differences in datasets and languages, this analysis evaluates the acceptability and robustness of the model's performance.

The second section of the study provides detailed information about the dataset, models, and training process. The third section presents the experimental results. The analysis includes a comparison with previous studies to highlight the advancements made in text-to-SQL conversion for Turkish. The final section presents the conclusions and discusses the implications of the results.

2 MATERIAL AND METHOD

The Tur2SQL dataset includes a metadata file containing tables and their IDs, as well as natural language instructions for querying these tables and the corresponding SQL queries. Additionally, for guided training, the dataset includes fields within the JSON files indicating the indices of keywords such as SELECT and COUNT. An example of a record in the Tur2SQL dataset is shown in Figure 1.

```json
{
  "question": "Çiftliklerin koyun sayılarını getir.",
  "query_tok": [
    "SELECT",
    "koyun_sayisi"
  ],
  "table_id": "100046",
  "sql": {
    "agg": 0,
    "sel": 5,
    "conds": []
  },
  "phase": 1,
  "query": "SELECT koyun_sayisi",
  "question_tok": [
    "Çiftliklerin",
    "koyun",
    "sayılarını",
    "getir",
    "."
  ]
}
```

Figure 1. An example record in Tur2SQL dataset.

Upon examining the dataset example, it is noted that the keyword "FROM" is not present. Instead, the dataset uses a variable `table\_id` to indicate which table the query is

directed at. The `table\_id` values are also provided with names instead of ids in the database file used for result calculation. For the training stage, the IDs are first matched with the table names in the database. Subsequently, the relevant table name is appended with the "FROM" clause before the WHERE clause if present, or at the end of the query otherwise. The processed data is then used for training and testing. The steps for preparing the training data are illustrated in Figure 2.
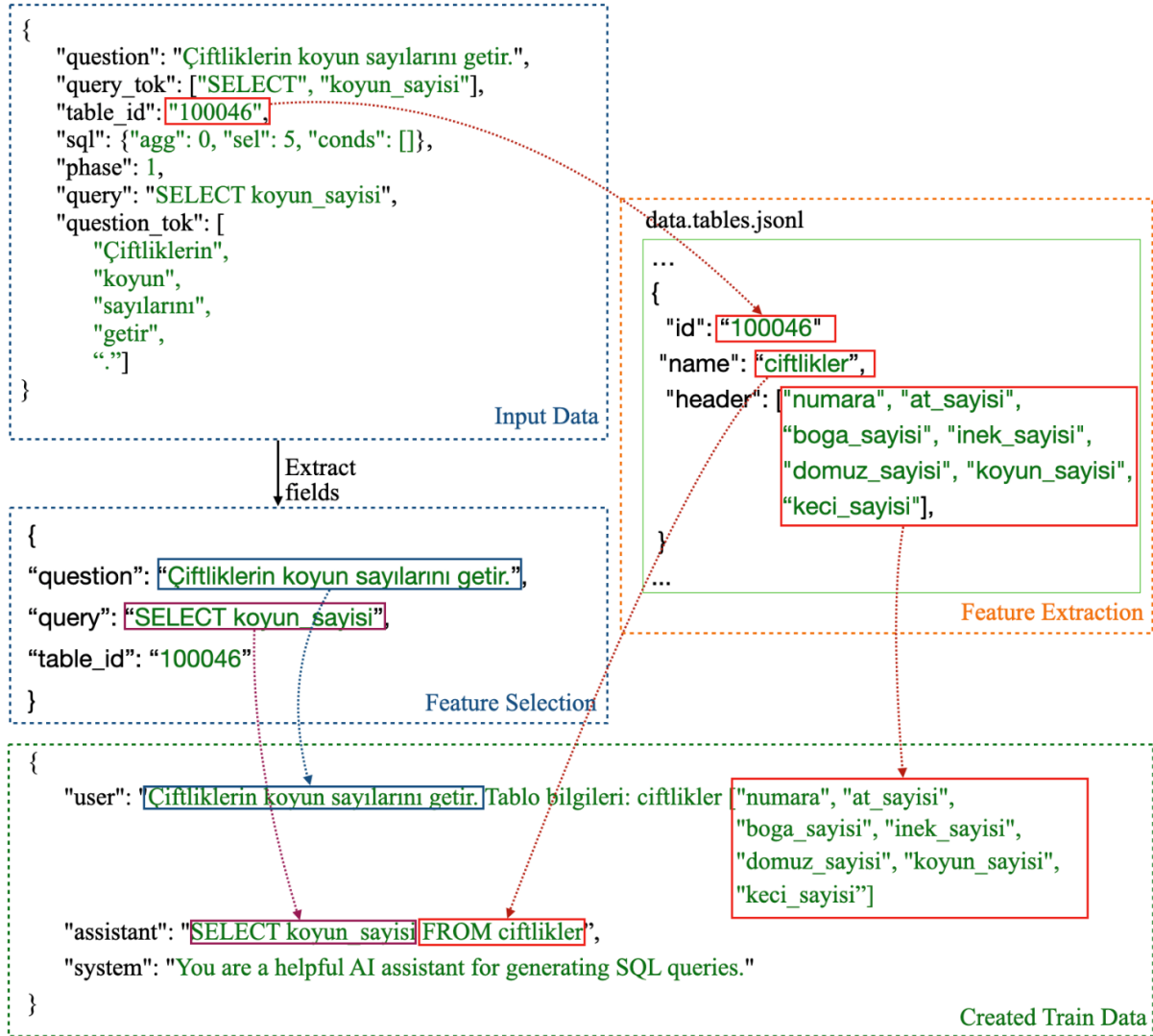
Figure 2. Preprocessing steps of training data.

As seen in Figure 2, a JSON file containing records with three key fields is provided to the models for training. Among these fields, the system field defines the nature of the response that the LLM model will generate. The system instruction acts as a guideline for the model's responses, nudging the AI to prioritize user satisfaction, offer assistance, and avoid generating harmful or offensive content. The user field contains the desired natural language text for the

query and information about the table from which the query is requested. In Figure 2, the example sentence means "Retrieve the number of sheep on the farms" and the "Tablo bilgileri" field shows the table information. The assistant field contains the response that needs to be generated based on the requested query.

In this study, since unguided training is being conducted, the indices of the keywords are not used. Only the natural language request text and the SQL query are utilized. The dataset is divided into three different files: train, dev, and test. The train and dev files are used for training, while the test file is used for evaluating the results. This approach focuses on leveraging the natural language requests to train models without explicit guidance, which can help in developing models that generalize better to unseen queries.

For training the dataset, the following models are used: "meta-llama/Llama-2-7b-chat-hf" [29], "meta-llama/Meta-Llama-3-8B-Instruct" [30], and "microsoft/Phi-3-mini-4k-instruct" [31]. As these models do not inherently support the Turkish language, two approaches are taken for model training. Initially, the models are trained with the Tur2SQL dataset, and the test results are obtained. The resulting models are named Llama2-7b-chat-SQL, Llama3-8b-instruct-SQL, and Phi3-mini-4k-instruct-SQL. Since the SQL queries' length does not exceed a certain number of tokens, the input and output token numbers are reduced in the models to improve training and test performance. This token reduction helps to optimize memory usage and training time, ensuring efficient handling of the dataset without compromising model accuracy.

In the second phase, to improve the models' understanding of the table name context or better interpret the desired instructions, the models are first trained with Turkish instruction dataset which can generate Turkish responses to Turkish inputs. Subsequently, in the second phase, these models are further fine-tuned with the Tur2SQL dataset to obtain new performance results. The resulting models are named as Llama2-7b-chat-Turkish-SQL, Llama3-8b-instruct-Turkish-SQL, and Phi3-mini-4k-instruct-Turkish-SQL. This two-step approach aims to enhance the models' understanding of Turkish syntax and semantics before fine-tuning them specifically for text-to-SQL tasks, thereby improving their overall performance and accuracy.

A general schema of the model training stages is illustrated in Figure 3.
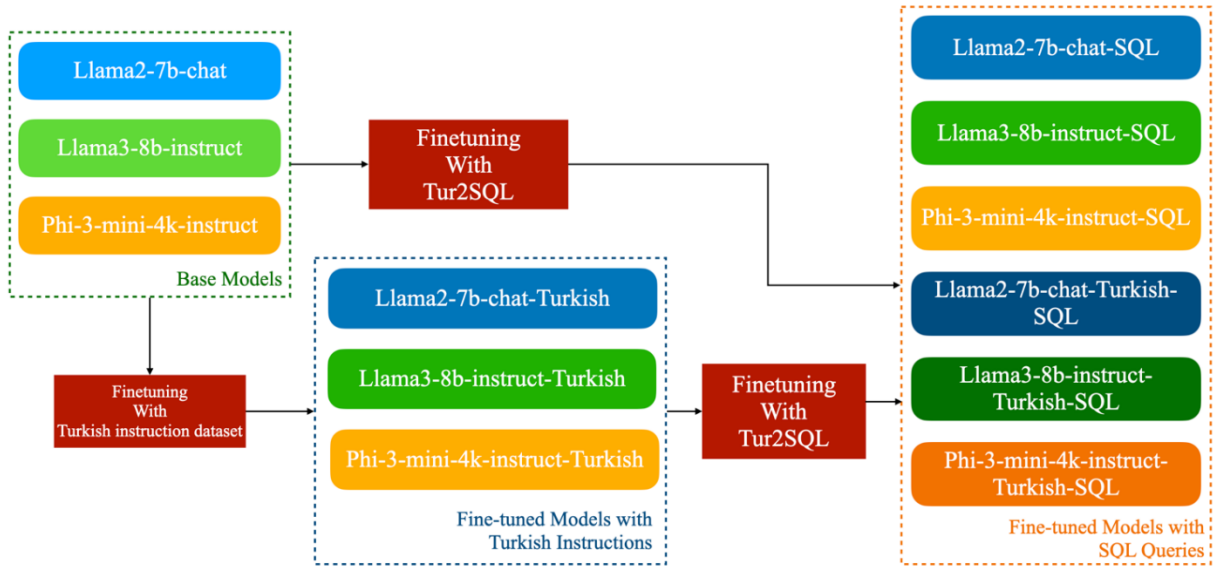
Figure 3. Overall model fine-tuning stages.

For training SuperAdapters library on Github is used. Since the datasets used were preprocessed and structurally presented, no additional preprocessing was performed in the study, except for converting them into a prompt format suitable for the given languages. During the fine-tuning phase, LoRa and PEFT were used, with the learning rate set to 0.00025. Adam was used as the optimizer, and different target modules were trained for each model. Training is conducted for 50 steps for each dataset. Training is stopped when the loss values of the training and test datasets converged and their changes minimized. As a result of the training phase, six models are obtained. These models and their train and validation loss values on step 50 are presented in Table 1 and training and validation loss graphs are given in Figure 4. The training process involves iterating over the data multiple times (steps), adjusting the model parameters to minimize the difference (loss) between the predicted SQL queries and the actual queries in the dataset. The loss values indicate how well the model is learning to perform the task, with lower values signifying better performance.

Table 1. Train and validation losses of fine-tuned models for 50 steps.

Model	Train Loss	Validation Loss
Llama2-7b-chat-SQL	0.0001	0.00008
Llama2-7b-chat-Turkish-SQL	0.0001	0.00010
Llama3-8b-instruct-SQL	0.0001	0.00004
Llama3-8b-instruct-Turkish-SQL	0.0001	0.00005
Phi3-mini-4k-instruct-SQL	0.0001	0.00009
Phi3-mini-4k-önstruct-Turkish-SQL	0.0001	0.00051
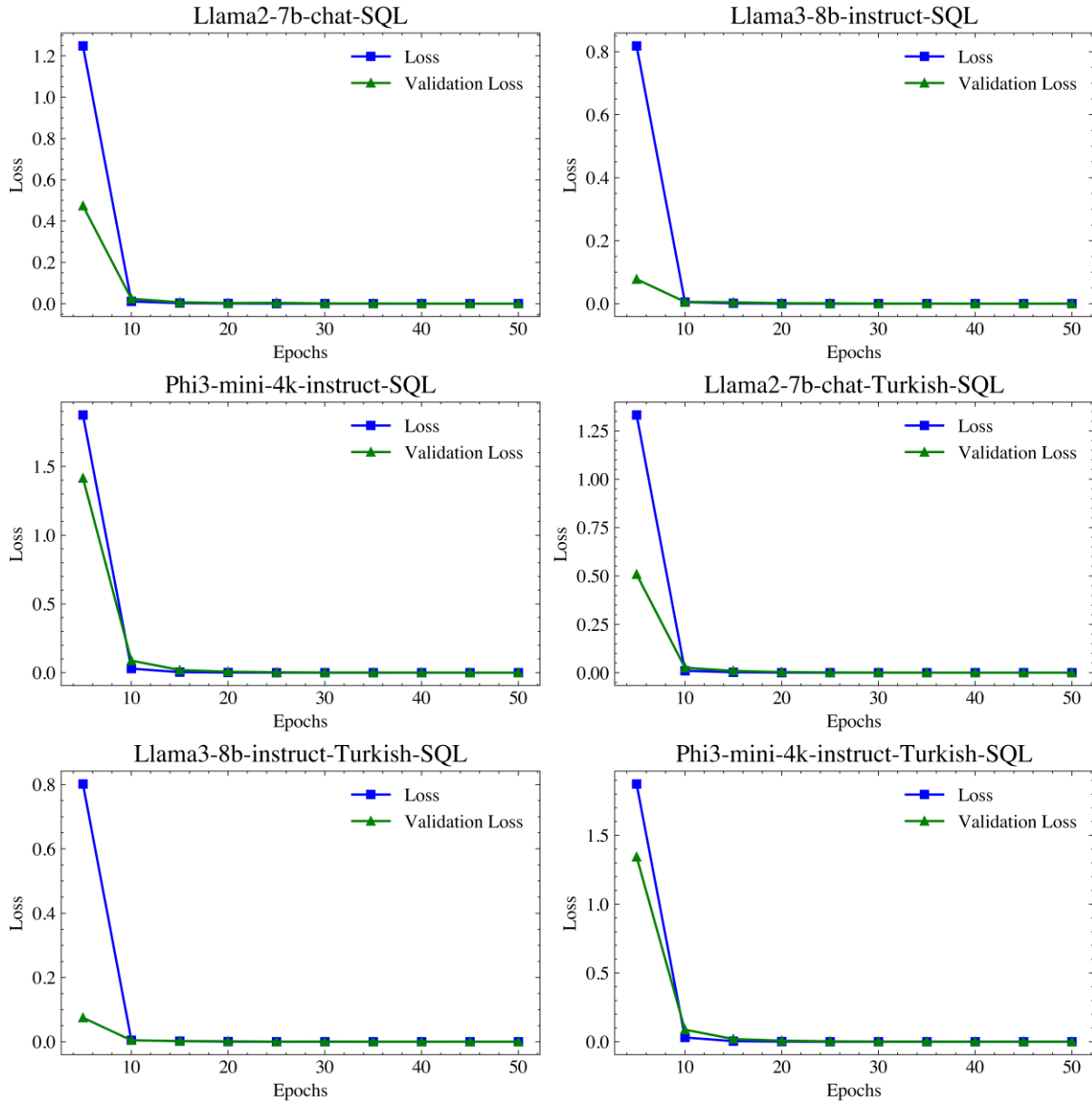
Figure 4. Training and validation loss graphs.

As seen in Table 1 and Fig 4, the train and validation loss values progress steadily without any signs of overfitting. The validation data, like the training data, also showed a reduction in the loss value.

3   RESULTS AND DISCUSSION

For performance evaluation of the test data, the ground truth SQL queries, referred to as gold SQL, are compared with the SQL queries predicted by the model. These comparisons are measured by execution accuracy (EX) and logical form accuracy (LF), as reported in the literature [32], [33]. Execution accuracy compares the generated query and the ground truth

171

query in terms of their results, typically by executing both queries on the same database and comparing their outputs. Logical form accuracy focuses on exact string matching between synthesized and ground truth queries but penalizes correct results without exact string matches [34]. In this study, to facilitate comparison with the results obtained in [26], the execution accuracy and logical form accuracy results of the models are obtained. The test file of the Tur2SQL dataset is used to obtain the results.

Each model uses specific prompt formats during the training and testing phases. These formats contain certain special tags and at the end of training, and the outputs require preprocessing. The LLaMA2 models generate outputs between </s> tags and produce tokens up to the maximum token limit specified. In contrast, the LLaMA3 models generate the <|eot_id|> tag up to the maximum token limit at the end of production. The Phi models, however, produce outputs directly without including any special tags. Consequently, it is necessary to process these tags for each model before calculating EX and LF results. The outputs generated by the models and their cleaned versions are presented in Table 2.

Table 2. Models and examples of predictions and cleaned predictions.

Model	Prediction	Cleaned Prediction
Llama2-7b-chat-SQL	SELECT *max(numara)* FROM *sehirler*</s></s>2. SELECT *count(numara)* FROM *kategori* </s> SELECT *count(num*	SELECT *max(numara)* FROM *sehirler*
Llama2-7b-chat-Turkish-SQL	SELECT *max(numara)* FROM *sehirler* </s></s>2. SELECT *count(numara)* FROM kategori </s> SELECT *count(num*	SELECT *max(numara)* FROM *sehirler*
Llama3-8b-instruct-SQL	SELECT *max(numara)* FROM *sehirler*<|eot_id|> <|eot_id|><|eot_id|><|eot_id|><|eot_id|><|eot_id|> <|start_header_id|><|eot_id|><|eot_id|><|eot_id|> <|eot_id|><|eot_id|><|end_header_id|><|eot_id|>	SELECT *max(numara)* FROM *sehirler*
Llama3-8b-instruct-Turkish-SQL	SELECT *max(numara)* FROM *sehirler* <|eot_id|> <|eot_id|><|eot_id|><|eot_id|><|eot_id|> <|eot_id|> <|start_header_id|> <|start_header_id|><|eot_id|> <|eot_id|><|eot_id|><|eot_id|><|start_header_id|> <|eot_id|>	SELECT *max(numara)* FROM *sehirler*
Phi3-mini-4k-instruct-SQL	SELECT *max(numara)* FROM *sehirler*	-
Phi3-mini-4k-instruct-Turkish-SQL	SELECT *max(numara)* FROM *sehirler*	-

As shown in Table 2, for LLaMA2 models, it is sufficient to take the portion of the output before the first </s> tag to obtain the cleaned result. Similarly, for LLaMA3 models, the portion of the output before the first <|eot_id|> tag is taken as the produced result. For Phi models, there was no need for a splitter.

The execution accuracy and logical form accuracy values of the trained models are presented in Table 3.

Table 3. Execution and Logical Form Accuracy results.

Model	Dev		Test	
	EX	LF	EX	LF
Llama2-7b-chat-SQL	85.95	85.31	85.89	85.29
Llama2-7b-chat-Turkish-SQL	89.15	85.04	86.03	85.01
Llama3-8b-instruct-SQL	93.25	93.25	92.96	92.73
Llama3-8b-instruct-Turkish-SQL	92.40	92.65	93.84	92.83
Phi3-mini-4k-instruct-SQL	99.72	99.42	99.81	99.81
Phi3-mini-4k-instruct-Turkish-SQL	99.96	99.95	**99.95**	**99.95**
SQLNet	-	-	40.19	39.03
ChatGPT	-	-	98.38	86.72

Table 3 presents the results of six different models trained in this study, as well as the results from SQLNet and ChatGPT previously tested in the TUR2SQL study. The latter two results did not involve any fine-tuning procedures. When examining the execution accuracy results, it is evident that the Phi models achieved the best performance, while the LLaMA models produced results comparable to ChatGPT. Additionally, as demonstrated by the results, training with the Turkish dataset improved execution accuracy for every model, since the instruction dataset helped the models learn the context of the natural language questions more effectively. Considering that the Phi models are smaller versions, it is expected that they would perform significantly better on the existing SQL dataset. The LLaMA models, being more generalized models, did not converge as effectively on the dataset as the Phi models. In terms of logical form accuracy, all models except for the LLaMA2 models achieved better results than ChatGPT. The LLaMA2 models, also, produced results very close to ChatGPT with only a 1\% difference. It is clear that in resource-constrained scenarios, the Phi models would be more suitable for use. Each model trained with the [28] dataset showed an average performance improvement of 1\% for the LLaMA models.

Despite the results provided by [26] for untrained SQLNet and ChatGPT models, there are no other trained models available for comparison. Execution accuracy and exact match accuracy values of other methods published in the literature are given in Table 4.

Table 4. Execution and Logical Form Accuracy results of studies conducted on Spider dataset.

Model	Dev		Test	
	LF	EX	LF	EX
Coarse2Fine	72.9	79.2	71.7	78.4
IncSQL	76.1	82.5	75.5	81.6
SQLova	81.6	87.2	80.7	86.2
X-SQL	83.8	89.5	83.3	88.7
HydraNet	83.6	89.1	83.8	89.2
IE-SQL	84.6	88.7	84.6	88.8
BRIDGE	86.2	91.7	85.7	91.1
SDSQL	86.0	91.8	85.6	91.4
SeaD	84.0	90.2	84.7	90.1

Table 4 presents the performance of various models on English datasets from existing literature. It is seen that the top-performing models on English datasets to achieve around 80-90\% execution accuracy and logical form accuracy. For instance, the BRIDGE model, which is one of the top performers in the literature, achieves 91.7\% execution accuracy and 86.2\% logical form accuracy on the test set. Therefore, the results from our Turkish dataset, where models trained achieve 85-99\% execution and logical form accuracy, are particularly acceptable.

Table 5 provides examples of the errors made by the models and the situations that classified as errors, which led to decreases in EX or LF values.

Table 5. Models and examples of false predictions.

Model	Query	Cleaned Prediction
Llama2-7b-chat-SQL	SELECT *tip* FROM *suruculer* WHERE *kod = 20202020*	SELECT *tip* FROM suruculer WHERE *kod = 20203020*
Llama2-7b-chat-Turkish-SQL	SELECT *alan* FROM *sehirler* WHERE *nufus = 15000000*	SELECT *alan* FROM sehirler WHERE *nufus = 1500*
Llama3-8b-instruct-SQL	SELECT *kalkis_tarihi* FROM *ucuslar* WHERE *kalkis_tarihi* = \	SELECT *kalkis_tarihi* FROM ucuslar WHERE *kalkis_tarihi* = \
Llama3-8b-instruct-Turkish-SQL	SELECT *kalkis_tarihi* FROM *ucuslar* WHERE *kalkis_tarihi* = \	SELECT *kalkis_tarihi* FROM ucuslar WHERE *kalkis_tarihi* = \
Phi3-mini-4k-instruct-SQL	SELECT *max(numara)* FROM *kopruler*	SELECT *max(uzunluk)* FROM *kopruler*
Phi3-mini-4k-instruct-Turkish-SQL	SELECT *cikis_tarihi* FROM *sarkilar*	SELECT *cikis_tarihi* FROM *sarkilar* WHERE *cikis_tarihi* = şarkı tablosu içerisinde bulunan çıkış tarihlerini ekrana\

As shown in Table 5, all models produced a response to the given queries. All of the generated responses also produced correct SQL queries. Only the Phi3 model generated natural language texts at the end of the SQL query. Upon examination, it was generally found that the outputs contained errors due to typographical errors in the numbers or within the text. For example, in the first query example, the value 20202020 was generated as 20203020, and because it did not produce the correct result, it was classified as incorrect. However, it can be observed that the query would work if this typographical error were corrected. It was observed that, with a few exceptions, all outputs from the models had errors of this nature.

Since query construction is a text generation process, it does not involve reasoning, and therefore, common errors are mostly related to matching numbers and dates. Additionally, errors such as generating redundant data are encountered. To correct these errors in the query generation system, solutions should focus on detecting the endpoint of the query and identifying inconsistencies in values like dates and numbers within the query, ensuring they are corrected based on internal consistency checks.

4 CONCLUSION AND SUGGESTIONS

In this study, text-to-SQL task for the Turkish language, considered a low-resource language, is performed using open-source models. To accomplish this, three different models are trained following two different approaches, and a reliable dataset presented in the literature is used for training.

The results of this study illustrate the significant advancements in text-to-SQL performance achieved through the use of large language models (LLMs) in the context of the Turkish language. All the models exhibit same or better performance compared to models given in the literature, with the Phi3 models achieving the highest execution accuracy and logical form accuracy values.

4.1 Comparative Performance Analysis

Furthermore, the study reveals that all trained models outperform SQLNet, with models except the Phi-3 models closely matching ChatGPT's success. This indicates the substantial benefits of LLMs in handling text-to-SQL tasks, even in languages with limited resources. The Phi-3 models, although not as complex as the LLaMA models, surpass all methods, suggesting their potential utility in resource-constrained environments. The reason of this is the restricted

availability of datasets for Turkish, which is classified as a low-resource language. The success of the Phi-3 models demonstrates that effective text-to-SQL processing can be achieved with low resource usage. Thus, by selecting Phi-3 models, acceptable production success can be ensured with minimal resource consumption.

4.2   Impact of Turkish Instruction Data

The integration of Turkish instruction data in model training has significantly improved SQL query generation accuracy. This improvement is attributed to the enhanced understanding of natural language question contexts facilitated by the instruction dataset. On average, the pre-training with the Turkish instruction dataset resulted in a performance gain across all models. This step helped the models better grasp the linguistic nuances and typical query structures in Turkish, thereby improving their ability to generate accurate SQL queries from natural language inputs. The instruction-tuning phase effectively fine-tuned the models to handle Turkish-specific syntactic and semantic patterns, which are crucial for accurate text-to-SQL conversion.

Results highlights the transformative impact of LLMs on text-to-SQL tasks, particularly in low-resource languages like Turkish. The findings underscore the value of leveraging large, instruction-tuned models to achieve high accuracy in SQL query generation, paving the way for more effective and accessible natural language interfaces to databases. Additionally, the study demonstrates that even in the absence of extensive resources, strategic use of instruction data and careful model training can bridge the performance gap, enabling high-accuracy applications in diverse linguistic contexts.

4.3   Future Work

In future, further optimization of model architecture and training procedures could potentially enhance performance even further. Additionally, the creation or acquisition of a larger dataset will provide sufficient data to meet the requirements of models with more parameters. By fulfilling the data needs of these models, subsequent training endeavors can lead to the development of a significantly more generalized text-to-SQL model for the Turkish language. Also, investigating the combination of LLMs with other techniques, such as data augmentation and transfer learning, may also yield valuable insights and improvements.

Conflict of Interest Statement

There is no conflict of interest between the authors.

Statement of Research and Publication Ethics

The study is complied with research and publication ethics.

Artificial Intelligence (AI) Contribution Statement

This manuscript was entirely written, edited, analyzed, and prepared without the assistance of any artificial intelligence (AI) tools. All content, including text, data analysis, and figures, was solely generated by the author.

REFERENCES

[1] K. Mohamad and K. M. Karaoğlan, "Enhancing Deep Learning-Based Sentiment Analysis Using Static and Contextual Language Models," *Bitlis Eren Üniversitesi Fen Bilimleri Dergisi*, vol. 12, no. 3, pp. 712–724, 2023.

[2] K. M. Karaoğlan, "Novel approaches for fake news detection based on attention-based deep multiple-instance learning using contextualized neural language models," *Neurocomputing*, vol. 602, p. 128263, 2024.

[3] K. M. Karaoglan and O. Findik, "Enhancing Aspect Category Detection Through Hybridised Contextualised Neural Language Models: A Case Study In Multi-Label Text Classification," *Comput J*, p. bxae004, 2024.

[4] D. Gao *et al.*, "Text-to-SQL Empowered by Large Language Models: A Benchmark Evaluation", *arXiv preprint arXiv:2308.15363*, 2023.

[5] A. Kumar, P. Nagarkar, P. Nalhe, ve S. Vijayakumar, "Deep Learning Driven Natural Language Text-to-SQL Query Conversion: A Survey", *arXiv preprint arXiv:2208.04415*, 2022.

[6] C. Wang, A. Cheung, ve R. Bodik, "Synthesizing Highly Expressive SQL Queries from Input-Output Examples", içinde *Proceedings of the 38th ACM SIGPLAN Conference on Programming Language Design and Implementation*, 2017, ss. 452-466.

[7] A. Giordani ve A. Moschitti, "Translating Questions to SQL Queries with Generative Parsers Discriminatively Reranked", içinde *Proceedings of COLING 2012: Posters*, 2012, ss. 401-410.

[8] I. Gür, S. Yavuz, Y. Su, ve X. Yan, "DialSQL: Dialogue Based Structured Query Generation", içinde *Proceedings of the 56th Annual Meeting of the Association for Computational Linguistics (Volume 1: Long Papers)*, 2018, ss. 1339-1349.

[9] J. Guo *et al.*, "Towards Complex Text-to-SQL in Cross-Domain Database with Intermediate Representation", *arXiv preprint arXiv:1905.08205*, 2019.

[10] B. Bogin, M. Gardner, ve J. Berant, "Representing Schema Structure with Graph Neural Networks for Text-to-SQL Parsing", *arXiv preprint arXiv:1905.06241*, 2019.

[11] C. Wang *et al.*, "Robust Text-to-SQL Generation with Execution-Guided Decoding", *arXiv preprint arXiv:1807.03100*, 2018.

[12] T. Shi, K. Tatwawadi, K. Chakrabarti, Y. Mao, O. Polozov, ve W. Chen, "InCSQL: Training Incremental Text-to-SQL Parsers with Non-Deterministic Oracles", *arXiv preprint arXiv:1809.05054*, 2018.

[13] A. Liu, X. Hu, L. Wen, ve P. Yu, "A Comprehensive Evaluation of ChatGPT's Zero-Shot Text-to-SQL Capability", *arXiv preprint arXiv:2303.13547*, 2023.

[14] Q. Min, Y. Shi, ve Y. Zhang, "A Pilot Study for Chinese SQL Semantic Parsing", *arXiv preprint arXiv:1909.13293*, 2019.

[15] A. T. Nguyen, M. H. Dao, ve D. Q. Nguyen, "A Pilot Study of Text-to-SQL Semantic Parsing for Vietnamese", *arXiv preprint arXiv:2010.01891*, 2020.

[16]   S. Ningyuan, Y. Xuefeng, ve L. Yunfeng, "TableQA: A Large-Scale Chinese Text-to-SQL Dataset for Table-Aware SQL Generation". 2020. Erişim adresi: https://arxiv.org/abs/2006.01234

[17]   P. Shi, R. Zhang, H. Bai, ve J. Lin, "XRICL: Cross-Lingual Retrieval-Augmented In-Context Learning for Cross-Lingual Text-to-SQL Semantic Parsing", *arXiv preprint arXiv:2210.13693*, 2022.

[18]   P. Shi *et al.*, "Cross-Lingual Text-to-SQL Semantic Parsing with Representation Mixup", içinde *Findings of the Association for Computational Linguistics: EMNLP 2022*, 2022, ss. 5296-5306.

[19]   M. A. Jose ve F. G. Cozman, "A Multilingual Translator to SQL with Database Schema Pruning to Improve Self-Attention", *International Journal of Information Technology*, c. 15, sy 6, ss. 3015-3023, 2023.

[20]   N. Deng, Y. Chen, ve Y. Zhang, "Recent Advances in Text-to-SQL: A Survey of What We Have and What We Expect", *arXiv preprint arXiv:2208.10099*, 2022.

[21]   T. Yu *et al.*, "Spider: A Large-Scale Human-Labeled Dataset for Complex and Cross-Domain Semantic Parsing and Text-to-SQL Task", *arXiv preprint arXiv:1809.08887*, 2018.

[22]   A. Heakl, Y. Mohamed, ve A. B. Zaky, "AraSpider: Democratizing Arabic-to-SQL", *arXiv preprint arXiv:2402.07448*, 2024.

[23]   D. Bakshandaeva, O. Somov, E. Dmitrieva, V. Davydova, ve E. Tutubalina, "PAUQ: Text-to-SQL in Russian", içinde *Findings of the Association for Computational Linguistics: EMNLP 2022*, 2022, ss. 2355-2376.

[24]   O. Somov ve E. Tutubalina, "Shifted PAUQ: Distribution Shift in Text-to-SQL", içinde *Proceedings of the 1st GenBench Workshop on (Benchmarking) Generalisation in NLP*, 2023, ss. 214-220.

[25]   L. Dou *et al.*, "MultiSpider: Towards Benchmarking Multilingual Text-to-SQL Semantic Parsing", içinde *Proceedings of the AAAI Conference on Artificial Intelligence*, 2023, ss. 12745-12753.

[26]   A. B. Kanburoğlu ve F. B. Tek, "TUR2SQL: A Cross-Domain Turkish Dataset For Text-to-SQL", içinde *2023 8th International Conference on Computer Science and Engineering (UBMK)*, IEEE, 2023, ss. 206-211.

[27]   X. Xu, C. Liu, ve D. Song, "SQLNet: Generating Structured Queries from Natural Language without Reinforcement Learning", *arXiv preprint arXiv:1711.04436*, 2017.

[28]   T. Kurtuluş, "turkish_73k_instruct_extended", *HuggingFace Dataset Repository*. HuggingFace.co, 2024. Erişim adresi: https://huggingface.co/datasets/tolgadev/turkish_73k_instruct_extended

[29]   H. Touvron *et al.*, "LLaMA 2: Open Foundation and Fine-Tuned Chat Models", *arXiv preprint arXiv:2307.09288*, 2023.

[30]   AI@Meta, "LLaMA 3 Model Card", 2024. Erişim adresi: https://github.com/meta-llama/llama3/blob/main/MODEL_CARD.md

[31]   M. Abdin *et al.*, "Phi-3 Technical Report: A Highly Capable Language Model Locally on Your Phone", *arXiv preprint arXiv:2404.14219*, 2024.

[32]   B. Qin *et al.*, "A Survey on Text-to-SQL Parsing: Concepts, Methods, and Future Directions", *arXiv preprint arXiv:2208.13629*, 2022.

[33]   V. Zhong, C. Xiong, ve R. Socher, "Seq2SQL: Generating Structured Queries from Natural Language Using Reinforcement Learning", *arXiv preprint arXiv:1709.00103*, 2017.

[34]   A. B. Kanburoğlu ve F. B. Tek, "Text-to-SQL: A Methodical Review of Challenges and Models", *Turkish Journal of Electrical Engineering and Computer Sciences*, c. 32, sy 3, ss. 403-419, 2024.

OBJECT TRACKING USING LIDAR DATA FILTERED BY MINIMIZED KALMAN FILTER ON TURTLEBOT3 MOBILE ROBOT

Kotiba ALDIBS[1] [iD], **Oğuz MISIR [1*]** [iD]

[1] Bursa Technical University, Department of Mechatronics Engineering, Bursa, Türkiye

* Corresponding Author: oguz.misir@btu.edu.tr

ABSTRACT

The development of autonomous vehicles requires high accuracy and precision in sensor data for effective interaction with the environment and execution of functions. Processing this data with efficient algorithms positively influences vehicle decision-making. In this study, the TurtleBot3 platform, an ideal simulation model for autonomous vehicles, is used to detect and track nearby objects in the sub-system Robotic Operating System (ROS) Noetic environment. The lidar sensor data from this platform is refined using interpolation and a minimized Kalman filter to remove noise and irregularities. This approach provides clearer and more reliable measurement data, resulting in more stable and fine-tuned responses in the vehicle's motion planning. Compared to the general Kalman filter theory, this method offers faster implementation without relying on the exact error tolerance of the sensor to provide acceptable results.

Keywords: Mobile Robot, Autonomous, Kalman filter, Object tracking.

1 INTRODUCTION

As technology advances, research into mobile robots and autonomous vehicles is becoming increasingly important. Systems capable of performing various functions without human intervention, sensing environmental factors, and processing this information to make decisions have become quite common [1]. Among the systems developed are mobile robots used in logistics, service robotics, cleaning, industrial applications, and healthcare. These robots, which vary according to their purpose, are commonly known as Automated Guided

Vehicles (AGVs) or Autonomous Mobile Robots (AMRs) [2], [3]. While AGVs perform strip tracking by interacting with a magnetic field, AMRs perceive their environment through sensors and apply mapping and navigation processes through algorithms and methods [4]. The basic task for both AMRs and AGVs is to plan a route to a desired destination while avoiding collisions with obstacles in their environment [5]. AMRs typically use lidar sensors for mapping and obstacle detection. While the lidar sensors used are typically 2D, 3D lidar sensors are also used to obtain more geometric information about the environment [6]. In mobile robot applications, lidar is often preferred for simultaneous localization and mapping (SLAM) applications [7]. Researchers have been developing navigation and path planning methods using SLAM for a long time [8]. Lidar is also used in mobile robot applications to detect both dynamic and static obstacles [9], [10]. In environments where mobile robots operate, the objects encountered can be either stationary or moving.

These objects can serve as obstacles or be designated as targets to be followed. Object detection and position estimation are critical requirements for safe path and motion planning in mobile robot navigation [11]. In indoor environments, SLAM applications based on lidar data have developed methods that produce successful results in navigation and path planning. However, the inability to fully detect dynamic changes in the environment and its surroundings can limit the navigation of mobile robots [12], [13]. Lidar data can not only map the environment but also collect data to detect dynamic objects, allowing mobile robots to better understand their environment [14]. The development of these methods provides an opportunity to avoid additional costly requirements, but it requires processing through algorithms tailored to the application using lidar data. In addition, lidar data must be filtered prior to processing due to potential measurement errors inherent in electronic devices [15].

In this study, a 2D lidar-based dynamic object detection and tracking method has been developed that is capable of identifying objects of any class and geometry in a model-independent manner. Information obtained from lidar sensors in real-world conditions can lead to erroneous measurements due to reflections and noise, so the proposed method employs an interpolation-based process on the distance data from the lidar sensor to minimize these erroneous measurements, introducing a new approach that minimizes the noise of lidar data by reducing the reliance on Kalman filters. To implement this method, the Turtlebot3 Waffle pi version development platform was used, which is ideal for such problems and research. This platform also supports Robotic Operating Systems (ROS), which are used for environmental data processing for mobile robots, autonomous navigation, and mapping [16]. We made it

compatible with a developed method using ROS, enabling its application on both the real TurtleBot3 platform and the Gazebo robot simulator. Our method aims to minimize the Kalman filter, thereby reducing the noise in the real data obtained from the TurtleBot3's lidar sensor. We have also developed an approach to address this issue in the Gazebo simulator environment. We took measurements at different distances and conditions to enable the mobile robot to detect and track objects regardless of their geometry. We processed these measurements using the defined method to ensure appropriate filtering. The results showed successful results both in real conditions and in simulation environments.

2   RELATED WORKS

Researchers address tasks such as object recognition and tracking in mobile robot applications and develop different solution algorithms. In the object recognition method developed in [17], a trained CNN structure was used and implemented in the Gazebo environment. This study provided the robot with the ability to interpret the objects it encounters; however, the mode of operation was limited by the camera angle and the classes within the training set. Similarly, [18] used cameras, but at a more advanced level. Instead of mere object recognition, the study focused on real-time object detection by slicing the video data from the camera into frames and evaluating them. Algorithms capable of discriminating objects were used to feed a Kalman filter model with changes in the object's position across frames. The result was a system capable of predicting the next object position. In another study, we observe a low-cost model for human tracking. The measurement and detection device used in this model is a low-cost laser scanner [19].

This study focused on the identification and tracking of human footprints using an algorithm based on footprint detection in lidar data. According to this algorithm, the midpoint between two different footprints was designated as the target point, and the model showed good success results. An important feature of the model is its ability to track a single person without confusion, even when multiple people are present in the tracking area. In addition, the footprints of different people vary on the lidar data, and the distance between footsteps changes when walking. Special adjustments can be made for such cases. In [20], a Kalman filter was used to deal with irregularities in the readings of electronic measurement devices. Specifically, a fixed Kalman gain was used to analyze differences between the signal curves at the input and output of the filter, effectively mitigating irregularities in the sensor data. The study reported promising results in correcting measurement irregularities using this method.

3   APPROACH SYSTEM OVERVIEW

The scheme of the developed method for the detection of dynamic objects using 2D Lidar is shown in Figure 1. In the method, the distance information perceived by the lidar on the mobile robot is sometimes inaccurately or incompletely assigned due to noise and reflections on the real environment platform; therefore, the sensor data read from the real TurtleBot3 and the simulator environment may differ. In order to deal with these differences, two approaches have been taken in this study due to problems arising from different sensor structures between the physical system and the simulation environment, which involve the integration of different algorithms. In this study, the TurtleBot3 Waffle Pi platform manufactured by Robotis uses a 360-degree lidar (LDS-2) to measure distances to physical obstacles, with software components based on ROS (Robot Operating System) in Linux Ubuntu 20.04.

We chose to use ROS1 Noetic for this platform, which is compatible with both ROS1 and ROS2 versions. Besides the physical environment, the Gazebo software will be used for the virtual environment. As mentioned before, the readings of virtual and physical sensors may differ, and the sensor resolution may change too. In the physical platform, the linear velocity of the robot ranges from 0 to 0.26 m/s and the angular velocity from 0 to 1.82 rad/s, and the lidar sensor resolution is defined as 1 degree [16]. For the virtual platform, the properties are the same with a lower tolerance and higher confidence about the resolution of the lidar data. Robotis provides a ready-made system for TurtleBot3, and this software is primarily designed for the basic functions of the robot. Therefore, any additional applications require a ROS package and control from an external master.
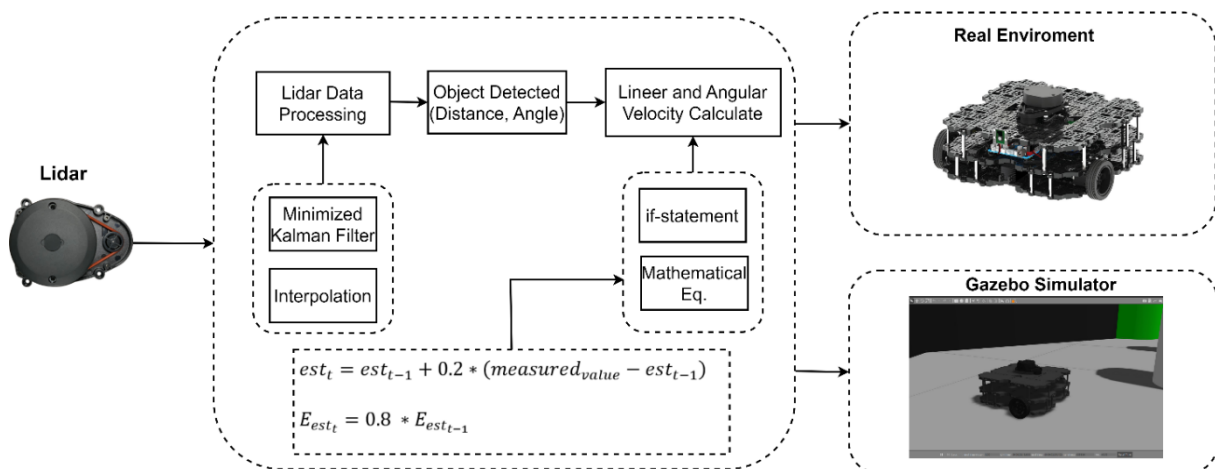

$$est_t = est_{t-1} + 0.2 * (measured_{value} - est_{t-1})$$

$$E_{est_t} = 0.8 * E_{est_{t-1}}$$

Figure 1. Method developed to detect dynamic objects using 2D Lidar.

In object tracking, the accuracy of the angle and distance information obtained from the lidar sensor is critical. During our research on the TurtleBot3 physical platform using the LDS-2 lidar sensor, we identified instances where distance measurements resulted in erroneous "zero" values due to reflections or incorrect readings. To avoid this problem, we compared the index numbers of erroneous distance measurements from the lidar sensor with neighboring index values and implemented an interpolation to mitigate these erroneous measurements. For the proposed method in the simulation environment, unlike the physical system, the distance information from the lidar sensor did not have zero values due to reflections, and the angles of the detected distances were sequentially synchronized. Therefore, there was no need for solutions to eliminate zeros in the simulation environment, allowing direct focus on the object detection method using the lidar.

3.1   Minimized Kalman Filter

Since Rudolf Kalman introduced the Kalman filter theory, it has been at the forefront of advanced research. Designed to overcome uncertainties in predicting the final state of a variable during its monitoring and measurement, this model fundamentally involves predicting a new value in place of the measured value, using the equations of the Kalman model [21], [22]. There exist improved and generalized versions with common equation variables. Equation (1) shows the Kalman Gain (KG), calculated based on parameters of the prediction error and the measurement error. KG is used in predicting the current value. Equation (2) expresses the current predicted value (est_t), which is obtained by adding the product of the KG coefficient and the difference between the measured value and the previous predicted value to the previous predicted value. Equation (3) calculates the prediction error (E_{est_t}) [20], [21], [23], [24], [25].

$$KG = \frac{E_{est}}{E_{est} + E_{measurement}} \tag{1}$$

$$est_t = est_{t-1} + KG * (measured - est_{t-1}) \tag{2}$$

$$E_{est_t} = (1 - KG) * E_{est_{t-1}} \tag{3}$$

So basically, the traditional Kalman filter could be defined with these three equations. The term est_{t-1} denotes the previous predicted value, while est_t denotes the current predicted value. E_{est} denotes the current prediction error, while $E_{measurement}$ denotes the measurement error. In the Kalman model, the relationship (measurement - old estimate) continuously facilitates new value predictions. Subsequently, the Kalman Gain (KG) coefficient is updated

and tends toward zero, allowing the predicted value to continuously converge to the actual value [20]. Figure 2 shows an example that graphically illustrates the prediction of the Kalman filter. Assuming a measurement of a value at 95 degrees with measurement errors in the range [-6, +6], an initial estimation error of -5 and an initial estimated value of 90 are chosen for consideration. This data is used to demonstrate how convergence to the true value occurs within 10 iterations.
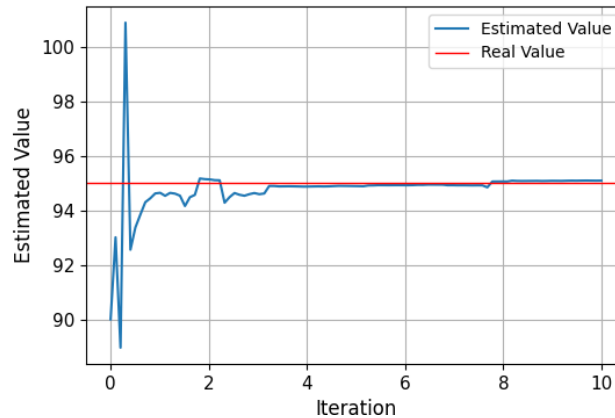
Figure 2. Comparison of actual and Kalman filter prediction graphs.

Considering the physical environment and the accuracy level of the LDS-2 lidar, the goal is to smooth the robot's responses. The response of the robot is highly dependent on the distance to the nearest object, so this parameter is prioritized. The measured distance from the lidar data is sometimes set to zero and at other times varies due to measurement tolerances. In such cases, instead of relying on the measured minimum, estimation is used to reduce the sensitivity to fluctuations. To produce an estimate at any time t, the previous predicted value is required; if this value is not available, it is initialized to the current measured value to start the algorithm. Figure 3 shows both the normal Kalman filter and the improved minimized Kalman filter in comparison.

The smoothing aims to achieve independence from the values of the estimation and measurement errors, as indicated by the Kalman Gain (KG) coefficient in equation (1), which depends on the ratio of the prediction and measurement errors. To achieve this, the change in estimated values is kept constant relative to the difference between the current measured state and the previous state values, thus ensuring continuous convergence of the estimated value to the measured value. Therefore, as expressed in equation (4), the KG coefficient is kept constant. Through experimentation, this value was determined to be 0.2 to suit the robot model. Equation (5) expresses the difference between the current estimated value and the previous value. If

incorrect measurement errors occur, they are absorbed by the improved Kalman filter without causing abrupt responses.
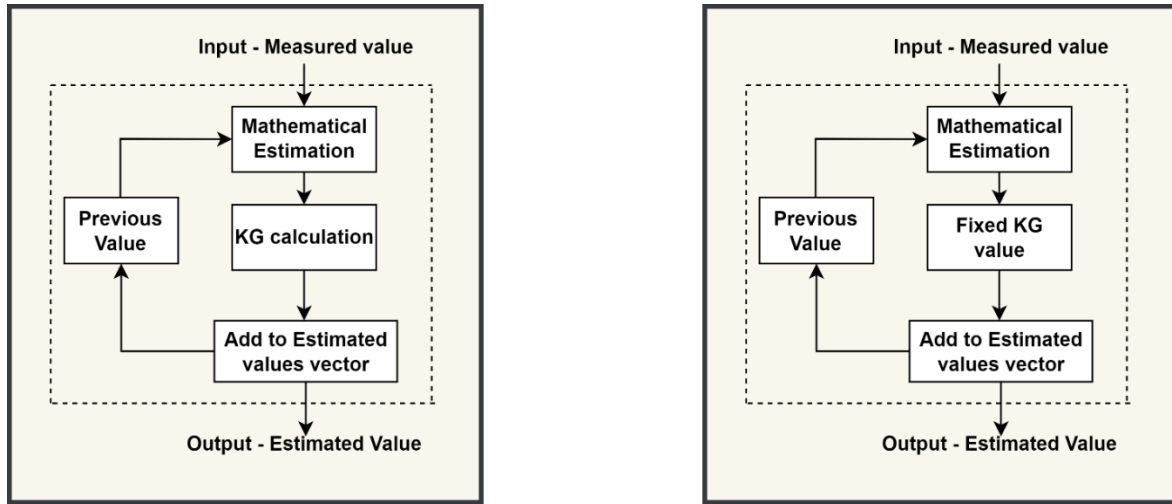
(a) Kalman Filter   (b) Minimized Kalman Filter

Figure 3. *Kalman Filter and Minimized Kalman Filter Diagram.*

$$KG = \frac{\Delta est}{measured\ value - est_{t-1}} \tag{4}$$

$$\Delta est = est_t - est_{t-1} \tag{5}$$

When the KG value is fixed, the relationship between the measurement error and the estimation error is also fixed to a constant value. This means that each position update of the object depends on the influence of the previous estimated state and 20% of the change in the measured value, thus achieving smoother responses, which lead our modifications on equations (2) and (3) to produce the following (6) and (7) equations.

$$est_t = est_{t-1} + 0.2 * (measured - est_{t-1}) \tag{6}$$

$$E_{est_t} = 0.8 * E_{est_{t-1}} \tag{7}$$

During the movement of the mobile robot, there are sometimes inappropriate responses such as sudden changes in speed and direction. The causes of this problem include abrupt transitions caused by simple if-else statements, sudden changes in distance from the lidar sensors, and measurement errors. To solve these problems, we propose variable velocity and angular velocity coefficients that can absorb sudden changes in linear and angular velocity. We can achieve changes in linear velocity through a mathematical function where the variable is the position angle of the object. Since the angle values range from 0 to 180 degrees, we can

map them to the range [0, 1], which is called the mapped_theta variable, so that the output of this function is in the range [0, 1]. In other words, using this coefficient, we can scale the speed value as a percentage of the maximum speed value. So, our linear velocity changing rules can be listed as follows: (1) maximum when the angle of the object is less than 30 degrees; (2) decreases exponentially after 30 degrees; and (3) tapers to zero near 90 degrees. The appropriate mathematical function that combines these three points is expressed in equation (8), which uses the mapped_theta as its independent variable. Here, $kv(\theta)$ refers to the linear velocity controller, and θ represents the mapped_theta. In addition, the graph of this function is shown in Figure 4.

$$kv(\theta) = \frac{1}{1 + 0.2 * e^{(20*(\theta - 0.167))}} \tag{8}$$
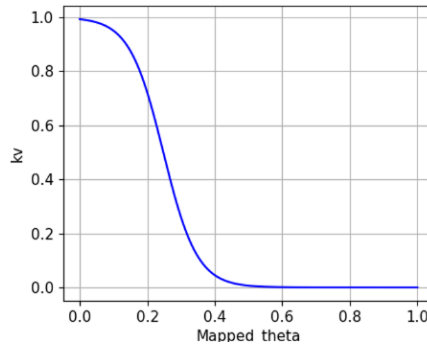
Figure 4. kv function.

According to this graph, the coefficient kv begins a rapid descent when the mapped_theta variable reaches 0.167 (corresponding to a 30-degree angle). At a value of 0.34, corresponding to a 60-degree angle of the object, the coefficient becomes 0.15 when multiplied by the maximum speed, giving a value of 15%. As mapped_theta approaches 0.5, or as the object angle approaches 90 degrees, the output speed converges to zero. This satisfies these criteria and provides a nonlinear change in linear velocity. Using this method, we can control the angular velocity. However, as the object angle decreases, we need a function where the angular velocity value also decreases-a reverse version of the linear velocity criteria. The function used for the change in angular velocity is expressed in equation (9). Here, $kw(\theta)$ corresponds to the angular velocity coefficient change.

$$kw(\theta) = \frac{1}{1 + e^{(-15*(mapped_{theta} - 0.334))}} \tag{9}$$

Figure 5 displays the graph of the function that handles the change in angular velocity. As the object's angle approaches zero, it ensures that the angular velocity converges to zero. In addition, a function was obtained that non-linearly increases the angular velocity as the object angle exceeds 30 degrees.
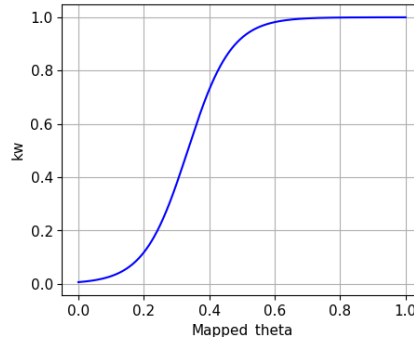
Figure 5. kw function.

3.2 Proposed Approach for The Virtual (Gazebo) Environment

Lidar data was used to implement object tracking using the Gazebo simulator as the simulation environment. Gazebo includes the Turtlebot3 robot model, which is equipped with sensors and actuators similar to the physical hardware. To run this method in the Gazebo simulator environment, a turtle_world environment was used. To obtain lidar data, a data subscription was performed on the "/scan" topic within a ROS package node, allowing access to the transmitted data. The content of the data was examined using the "/rostopic info" command to identify and utilize parameters critical to the mobile robot. Figure 6 illustrates the subscribed topics within the Gazebo environment.
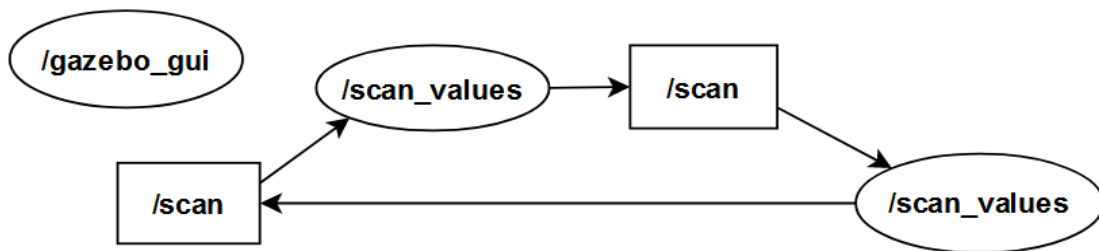
Figure 6. Data flow in the Gazebo environment.

Figure 7 shows the object detection method diagram for the Gazebo environment. It shows the process where the nearest detected lidar distance data and its index are identified from the "/scan" scan data obtained with the help of ROS. To guide or move the mobile robot to the nearest object, this process is facilitated by themes defined by ROS. The control of linear

and angular velocities is transferred to the right and left motors of the mobile robot using the Twist function. We ensured successful navigation of the mobile robot to the detected object based on specified angle and distance tolerances.
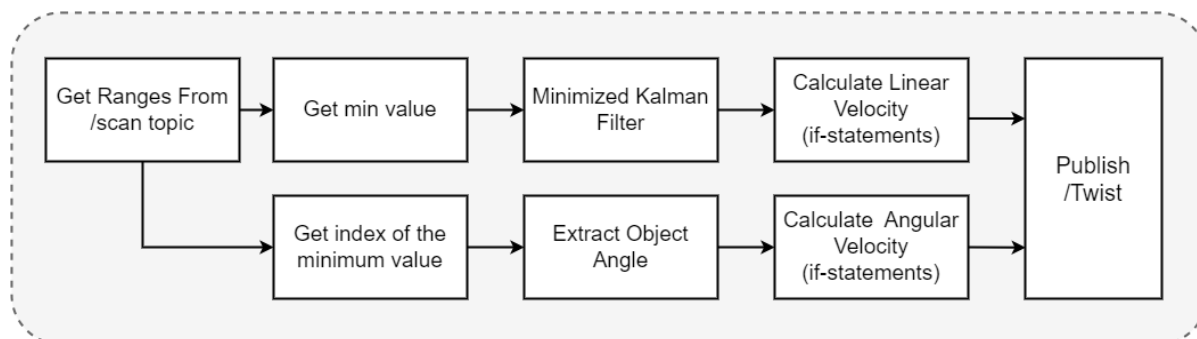
Figure 7. Developed object detection algorithm for virtual environment.

The pseudo code expressed in virtual_env1 for calculating linear and angular velocities can be explained in terms of multiple steps. According to this code, the closest vector distance data is determined from the lidar sensor. Then the index number of the closest distance is extracted, which allows the relative angle of the closest distance with respect to the robot to be calculated. To orient the robot to the object based on the calculated angle and distance, the angular difference between the robot's heading angle and the angle of the detected object is calculated. If this angular difference is within +/- 8 degrees, the angular velocity is set to 0 to minimize oscillations during orientation. If the angular difference is -90 or 90 degrees, indicating that the object is directly to the left or right, the angular velocity is set to maximum in the opposite direction of the object. At the same time, if the distance to the object is less than 0.35 units, the linear velocity is set to 0, causing the robot to stop. Conversely, if the distance is greater than 0.35 units, the linear velocity is maximized, allowing the robot to search for or track the object. A notable drawback of this method is the use of numerous if-else structures. In a simplified way, in the following Algorithm 1. table a summary of the operations in the form of codes.

Algorithm 1. Coded representation of the algorithm's flow.

```
           Virtual-Env-1
 1: Subscribe /scan
 2: Subscribe /Twist
 3: Get /scan
 4: lidar_min_range ← min(laserData.ranges)
 5: lidar_min_ranges_angle ← detect_angle(lidar_min_range)
 6: angle_diff ← heading_angle − lidar_min_ranges_angle
 7: if −8 ≤ angle_diff ≤ 8 then
 8:     angular_vel ← 0
 9: else if angle_diff < −90 then
10:     angular_vel ← max
11: else if angle_diff > 90 then
12:     angular_vel ← −max
13: end if
14: if lidar_min_range < 0.35 then
15:     linear_vel ← 0
16: else
17:     linear_vel ← max
18: end if
```

3.3   Proposed Approach for The Physical Environment

Unlike the virtual environment, the mobile robot in the physical environment has a different number of topics, as shown in Figure 8. These topics are used to share sensor information and monitor changes in the hardware. The noise generated by the Lidar sensor has resulted in some distances being assigned a value of "0" and in the detection of sudden noisy distance values during measurements.

Figure 9 outlines the solutions to these problems, with the steps summarized as follows: first, the indices of the zeros were identified. Since these are not fixed indices, new values were assigned by interpolating between the real values before and after the zeros. To detect the nearest object, the nearest distance from the noise-filtered data is used as a reference. The index of this nearest distance is also used to calculate the angle of the object. To avoid errors in the measured minimum values, an estimation is made using the proposed minimized Kalman filter. This method also helps to avoid sudden speed changes and wrong turns. To navigate to the object at the determined angle and distance, the linear and angular velocities are calculated. These velocities are then sent to the motors using the '/Twist' publisher.

Figure 10 shows the comparison between the raw lidar data containing zeros and erroneous measurements and the data after the interpolation process. It is evident that the values initially assigned as zero ("0") have been absorbed after interpolation.
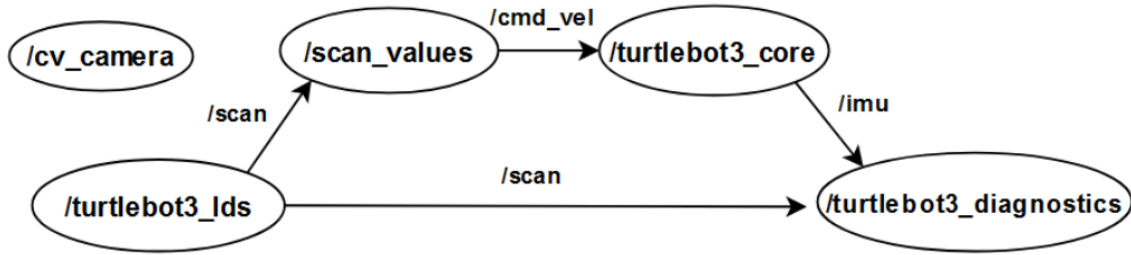
Figure 8. Data flow in Turtlebot3 Waffle Pi.
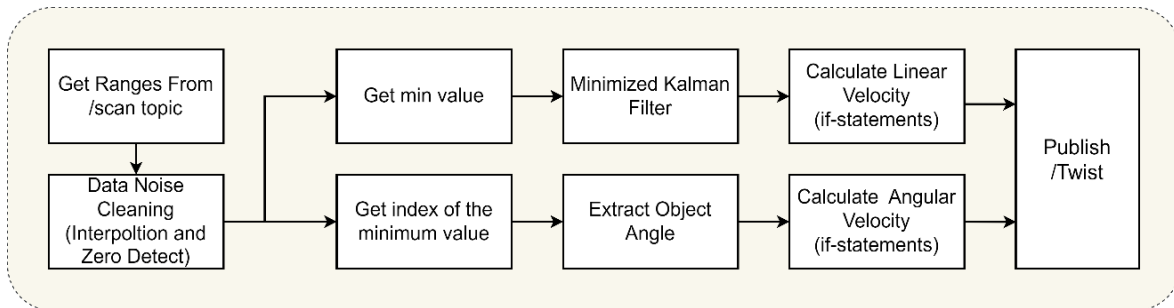
Figure 9. Developed object detection algorithm for physical environment.
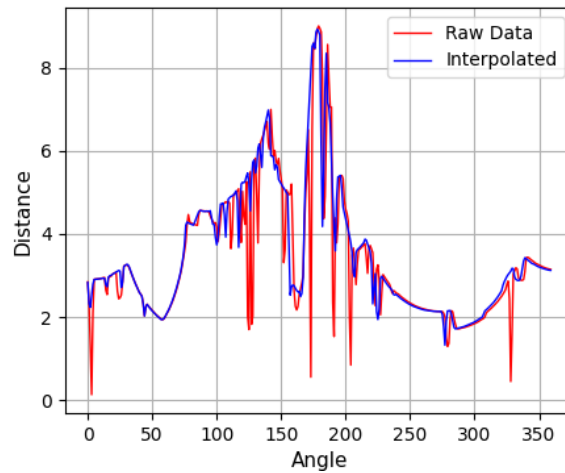
Figure 10. The impact of interpolation on raw lidar data.

4   EXPERIMENTAL RESULTS

In this study, an improved Kalman filter-based method for the detection and tracking of dynamic objects using 2D Lidar is proposed. The proposed method provides different solutions for simulated and physical Turtlebot3 environments. Applications have been developed for detecting objects at different distances and angles both in the physical environment and on the

Turtlebot3 platform. Furthermore, the developed minimized Kalman filter method addresses how improvements were made to noisy raw lidar data.

4.1   Results for Physical Turtlebot3 Environment

The physical environment experiments used the Waffle Pi version of the Turtlebot3. In the first experiment, objects placed at angles of 30, 60, and 90 degrees were detected, and their angles relative to the Turtlebot3 were determined. Figure 11 shows objects placed at angles of 30, 60, and 90 degrees relative to the Turtlebot3.

In the experiments conducted, objects placed at a distance of less than 1 meter were analyzed for velocity variations using two different methods. Figure 12 (a) shows the velocity variations based on different angles using a simple if-else structure. Similarly, Figure 12 (b) shows the velocity variations obtained using the proposed method aimed at smoothing changes based on different angle values.
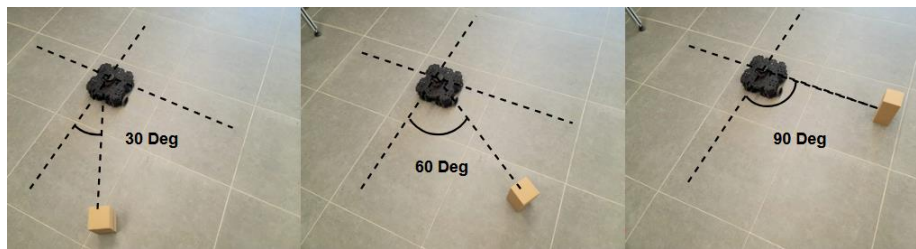
Figure 11. Detection of objects placed at different angle positions.
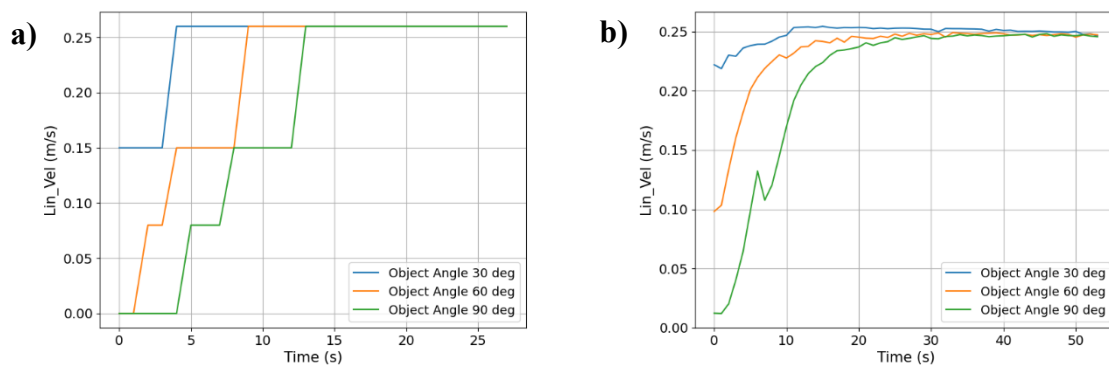
Figure 12. Velocity responses of Robot speed relative to object placed at different angles for physical environment. a) Linear velocity changes using if-else conditions, b) Linear Velocity changes using math equations.

The velocity responses to objects placed at different angles using a simple if-else structure show abrupt changes, resulting in the robot's jerky movements. As shown in Figure 12(a), the velocity changes are characterized by high accelerations. To reduce these high

accelerations, the proposed method uses exponential equations depending on the acceleration coefficients, as shown in Figure 12(b). Acceleration rates are reduced in steps of 30 degrees, resulting in smoother velocity changes. To verify the object detection based on the minimum detected distance, measurements were taken for three different distances in front of the robot as shown in Figure 13, by defining three distances of 35 cm, 65 cm, and 95 cm, in this test we used a static and fixed object in order to observe the efficiency of the designed filter.
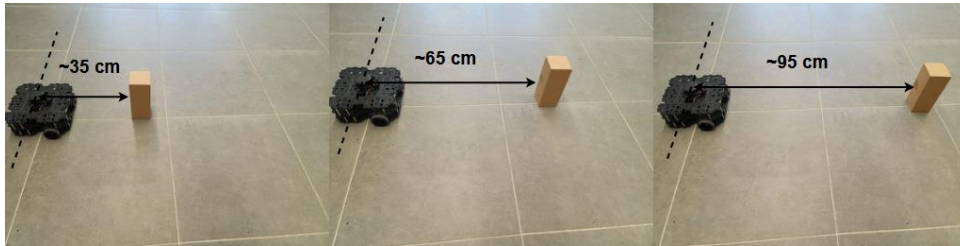
Figure 13. Distance measurement application of object at different distances.

As a result, the effects of changes in the minimum distance are shown in Figures 14 (a) and (b), comparing the outputs of noisy data and the proposed minimized Kalman filter. According to the comparative results obtained based on variations in different distances, it can be seen that the object distances obtained with the minimized Kalman filter are denoised compared to the raw lidar data. It is observed that the use of the minimized Kalman filter reduces sudden accelerations and abrupt oscillations caused by noisy data during object tracking by the mobile robot
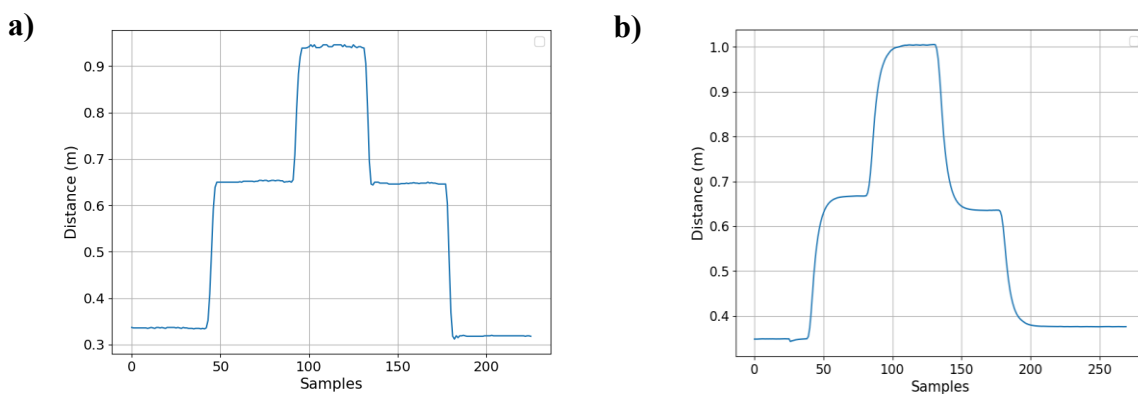
Figure 14. Object detection distances based on raw and minimized Kalman filtered data for the physical environment. a) Object distance detection based on raw lidar data b) Object detection distance obtained by using minimized Kalman filter on lidar data.

In addition, the distance of a stationary object was monitored over a period of time, and comparative data including raw lidar data, data processed through the Kalman filter, and data processed through the enhanced minimized filter are shown in Figure 15. This collection includes lidar data obtained from a stationary object at a given distance. According to the results obtained, the data processed through the developed minimized Kalman filter shows a better absorption of fluctuations compared to both the noisy raw data and the general Kalman filter.
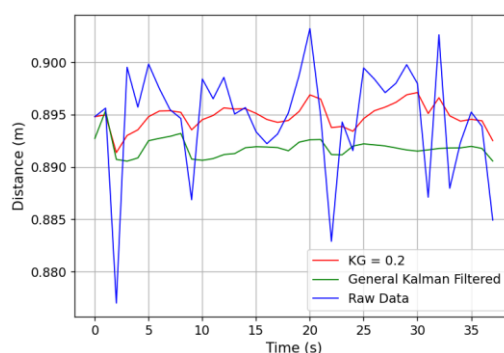
Figure 15. Comparison of raw lidar data, data passed through the general Kalman filter, and data passed through the minimized Kalman filter.

4.2   Results for Gazebo Environment

Experiments conducted in the Gazebo environment involve examining changes in velocity by placing different objects at different angles and fixed distances, similar to those in the physical environment. Unlike the real environment, the virtual environment is free of zeros. Therefore, we wanted to observe the accuracy of our method in both virtual and physical environments. The experiments conducted in the Gazebo environment are shown in Figure 16.

The speed variation of the object placed at 30, 60, and 90 degrees in the virtual environment is shown in Figure 17, as specified in the method, showing both the speed variations based on the simple if-else structure and those adjusted using exponential speed coefficients. According to the results obtained, smoother speed transitions were observed in the virtual environment due to the absence of physical environment noise.
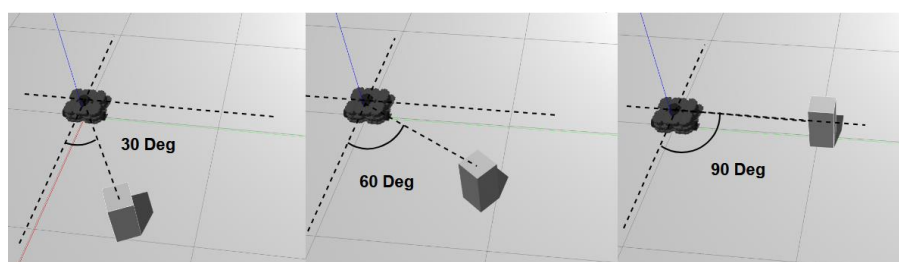
Figure 16. Experiment on object distance with angles of 30, 60, and 90 degrees in the Gazebo environment.
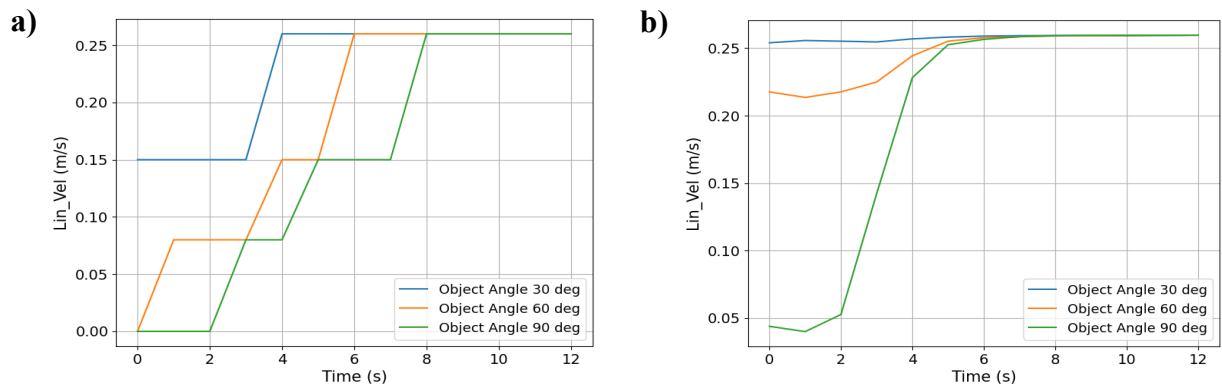
Figure 17. Robot speed responses according to object placed at different angles for virtual environment. a) linear speed changing using if-else conditions for virtual environment b) linear velocity changing using mathematical equations for virtual environment.

Figure 18 illustrates experiments conducted in the virtual gazebo environment with objects placed at different fixed distances. This experiment focuses on the distances perceived by the lidar for objects placed at 3 different distances.
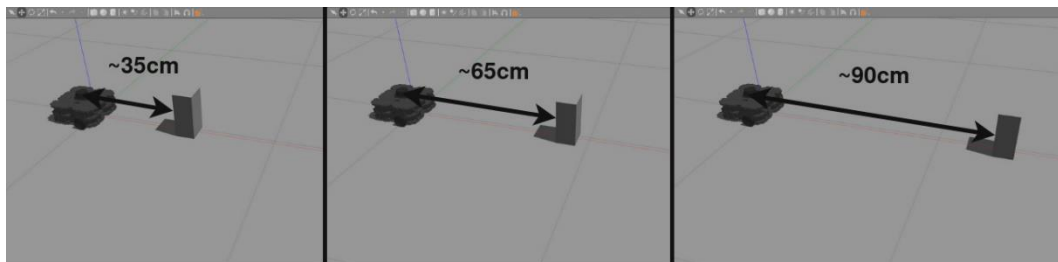
Figure 18. Experiment applied for different fixed distances for the virtual environment.

Figure 19 shows the closest object distances obtained from lidar data with and without application of the minimized Kalman filter in the virtual environment at 3 different distances. In the results with the minimized Kalman filter applied, the distance measurement transitions are smoother compared to the unfiltered lidar data in the virtual environment, where the lidar data is free from noise-induced sudden distance transitions.
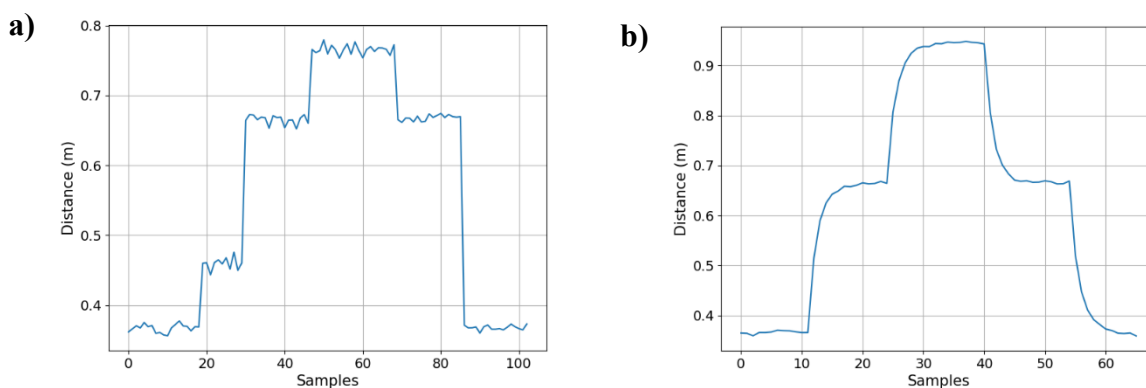
Figure 19. Object detection distances based on raw and minimized filtered data in the gazebo environment. a) Object distance detection based on raw lidar data b) Object detection distance obtained by using minimized Kalman filter on lidar data.

5   CONCLUSION

This paper proposes a method based on an extended Kalman filter for tracking objects without specifying geometries and shapes, so it is focused on enhancing the quality of lidar data intended for use in autonomous mobile robots; however, as an examples, a 35x20x20 cm box and observer legs have been used in different tests. Real-world lidar data often produce erroneous measurements due to reflections and noise. To mitigate these inaccuracies, a minimized Kalman filter methodology incorporating interpolation and Kalman filtering techniques has been developed. The proposed method is adaptable to both the Turtlebot3 physical robot and the Gazebo simulation environment, presenting two different approaches. Experimental trials for object tracking have been conducted using both the physical Turtlebot3 and the Gazebo environment. Instead of a simple control mechanism where linear and angular velocities change based on the perceived angle and distance of the object, the study uses well-tuned mathematical functions with intervals and breakpoints to achieve smoother velocity transitions. In addition, the minimized Kalman filter was observed to protect against sudden jumps in measurements and to mitigate state noise during discrete-time measurements. Object detection and tracking are performed using lidar information, and future work will focus on improving object classification using new lidar data, considering both computational performance and object tracking accuracy.

Acknowledgment

Conflict of Interest Statement

There is no conflict of interest between the authors.

Statement of Research and Publication Ethics

The study is complied with research and publication ethics.

Artificial Intelligence (AI) Contribution Statement

This manuscript was entirely written, edited, analyzed, and prepared without the assistance of any artificial intelligence (AI) tools. All content, including text, data analysis, and figures, was solely generated by the authors.

Contributions of the Authors

Conceptualization, K.A. and O.M.; methodology, O.M. and K:A.; software, K.A.; validation, O.M. and K.A.; supervision, O.M.

REFERENCES

[1]   M. A. K. Niloy *et al.*, "Critical Design and Control Issues of Indoor Autonomous Mobile Robots: A Review," *IEEE Access*, vol. 9, pp. 35338–35370, 2021, doi: 10.1109/ACCESS.2021.3062557.

[2]   Z. Bai, H. Pang, Z. He, B. Zhao, and T. Wang, "Path Planning of Autonomous Mobile Robot in Comprehensive Unknown Environment Using Deep Reinforcement Learning," *IEEE Internet Things J*, Jun. 2024, doi: 10.1109/JIOT.2024.3379361.

[3]   F. Li, J. Cheng, Z. Mao, Y. Wang, and P. Feng, "Enhancing Safety and Efficiency in Automated Container Terminals: Route Planning for Hazardous Material AGV Using LSTM Neural Network and Deep Q-Network," *Journal of Intelligent and Connected Vehicles*, vol. 7, no. 1, pp. 64–77, Mar. 2024, doi: 10.26599/JICV.2023.9210041.

[4]   A. Bhargava, M. Suhaib, and A. S. Singholi, "A review of recent advances, techniques, and control algorithms for automated guided vehicle systems," Jul. 01, 2024, *Springer Science and Business Media Deutschland GmbH*. doi: 10.1007/s40430-024-04896-w.

[5]   E. A. Oyekanlu *et al.*, "A review of recent advances in automated guided vehicle technologies: Integration challenges and research areas for 5G-based smart manufacturing applications," 2020, *Institute of Electrical and Electronics Engineers Inc.* doi: 10.1109/ACCESS.2020.3035729.

[6]   H. Kim, H. Kim, S. Lee, and H. Lee, "Autonomous Exploration in a Cluttered Environment for a Mobile Robot With 2D-Map Segmentation and Object Detection," *IEEE Robot Autom Lett*, vol. 7, no. 3, pp. 6343–6350, Jul. 2022, doi: 10.1109/LRA.2022.3171069.

[7]   H. Dong, C. Y. Weng, C. Guo, H. Yu, and I. M. Chen, "Real-Time Avoidance Strategy of Dynamic Obstacles via Half Model-Free Detection and Tracking with 2D Lidar for Mobile Robots," *IEEE/ASME Transactions on Mechatronics*, vol. 26, no. 4, pp. 2215–2225, Aug. 2021, doi: 10.1109/TMECH.2020.3034982.

[8]   Z. Xu, J. Y. Wu, and Q. L. Liu, "Research on mobile robot indoor positioning mapping based on front-end and back-end optimization," *Journal of Mechanical Science and Technology*, vol. 38, no. 5, pp. 2555–2561, May 2024, doi: 10.1007/s12206-024-0434-0.

[9]   Y. Chen, B. Pervan, and M. Spenko, "Quantifying the Risk of Unmapped Associations for Mobile Robot Localization Safety," *IEEE Transactions on Robotics*, 2024, doi: 10.1109/TRO.2024.3401093.

[10]   O. Misir and L. Gökrem, "Dynamic interactive self organizing aggregation method in swarm robots," *BioSystems*, vol. 207, Sep. 2021, doi: 10.1016/j.biosystems.2021.104451.

[11]   X. Li, L. Wang, Y. An, Q. L. Huang, Y. H. Cui, and H. S. Hu, "Dynamic path planning of mobile robots using adaptive dynamic programming," *Expert Syst Appl*, vol. 235, Jan. 2024, doi: 10.1016/j.eswa.2023.121112.

[12]   F. Li, C. Fu, D. Sun, J. Li, and J. Wang, "SD-SLAM: A Semantic SLAM Approach for Dynamic Scenes Based on LiDAR Point Clouds," *Big Data Research*, p. 100463, May 2024, doi: 10.1016/j.bdr.2024.100463.

[13]   V. Vaquero, E. Repiso, and A. Sanfeliu, "Robust and real-time detection and tracking of moving objects with minimum 2d lidar information to advance autonomous cargo handling in ports," *Sensors (Switzerland)*, vol. 19, no. 1, 2019, doi: 10.3390/s19010107.

[14]   Z. Liu *et al.*, "Positive and Negative Obstacles Detection Based on Dual-LiDAR in Field Environments," *IEEE Robot Autom Lett*, 2024, doi: 10.1109/LRA.2024.3414256.

[15]   H. Zhang, R. Xiao, J. Li, C. Yan, and H. Tang, "A High-Precision LiDAR-Inertial Odometry via Invariant Extended Kalman Filtering and Efficient Surfel Mapping," *IEEE Trans Instrum Meas*, vol. 73, pp. 1–11, 2024, doi: 10.1109/TIM.2024.3382751.

[16]   Robotis, "Turtlebot3," *https://emanual.robotis.com/docs/en/platform/turtlebot3/overview/*.

[17]   C. Nandkumar, P. Shukla, and V. Varma, "Simulation of Indoor Localization and Navigation of Turtlebot 3 using Real Time Object Detection," in *Proceedings of IEEE International Conference on Disruptive Technologies for Multi-Disciplinary Research and Applications, CENTCON 2021*, Institute of Electrical and Electronics Engineers Inc., 2021, pp. 222–227. doi: 10.1109/CENTCON52345.2021.9687937.

[18]   P. R. Gunjal, B. R. Gunjal, H. A. Shinde, S. M. Vanam, and S. S. Aher, "Moving object tracking using kalman filter," in *2018 International Conference On Advances in Communication and Computing Technology (ICACCT)*, IEEE, 2018, pp. 544–547.

[19]   Y. Ge and W. Li, "Human following of mobile robot with a low-cost laser scanner," in *2019 IEEE International Conference on Systems, Man and Cybernetics (SMC)*, IEEE, 2019, pp. 3987–3992.

[20]   Z. Khan, H. Bugti, and A. S. Bugti, "Single dimensional generalized kalman filter," in *2018 International Conference on Computing, Electronic and Electrical Engineering (ICE Cube)*, IEEE, 2018, pp. 1–5.

[21]   D. Simon, "Kalman filtering," *Embedded systems programming*, vol. 14, no. 6, pp. 72–79, 2001.

[22]   H. Liu *et al.*, "Uncertainty-Aware UWB/LiDAR/INS Tightly Coupled Fusion Pose Estimation via Filtering Approach," *IEEE Sens J*, vol. 24, no. 7, 2024, doi: 10.1109/JSEN.2024.3362741ˆx.

[23]   Q. Li, R. Li, K. Ji, and W. Dai, "Kalman filter and its application," in *Proceedings - 8th International Conference on Intelligent Networks and Intelligent Systems, ICINIS 2015*, Institute of Electrical and Electronics Engineers Inc., Aug. 2016, pp. 74–77. doi: 10.1109/ICINIS.2015.35.

[24]   G. Welch and G. Bishop, "An introduction to the Kalman filter," 1995.

[25]   H. T. Madan, V. Akram, S. Reddy, K. N. Mohan Gowda, and L. D. Uday Kumar, "An Error-State Extended Kalman Filter Based State Estimation and Localization Algorithm for Autonomous Systems," in *International Conference on Smart Systems for Applications in Electrical Sciences, ICSSES 2023*, Institute of Electrical and Electronics Engineers Inc., 2023. doi: 10.1109/ICSSES58299.2023.10199535.

BIOMEDICAL IMAGE SUPER-RESOLUTION USING SRGAN: ENHANCING DIAGNOSTIC ACCURACY

Zübeyr Güngür [1*] (iD), İbrahim Ayaz [2] (iD), Vedat Tümen [1] (iD)

[1] *Bitlis Eren University, Computer Engineering, Bitlis, Türkiye*

[2] *Bitlis Eren University, Department of Computer Technologies, Bitlis, Türkiye*

* Corresponding Author: zubeyr1313@gmail.com

ABSTRACT

The super-resolution method, which has gained significant popularity today, aims to obtain high-resolution images from low-resolution ones, enhancing image quality and making details clearer. This technique allows for more detailed analysis of images, providing significant advantages in medical imaging, restoration of old photographs, and the analysis of security cameras. In medical imaging, super-resolution contributes to more accurate diagnosis of diseases by clarifying low-resolution MRI, CT, and ultrasound images. Similarly, in the restoration of old photographs, improving blurred visuals allows for the preservation and renewal of historically significant images. In the field of security, enhancing images obtained from low-resolution surveillance cameras makes it easier to identify suspects and allows for a more detailed analysis of events, playing a critical role in solving crimes. In recent years, deep learning-based approaches have made significant progress in the field of super-resolution. Notably, Convolutional Neural Networks (CNN) have achieved great success in solving these problems. However, one of the most remarkable developments in super-resolution is the SRGAN model, based on Generative Adversarial Networks (GAN). SRGAN has surpassed traditional methods by more effectively improving image quality. In this study, the SRGAN model was trained on three different biomedical datasets, achieving PSNR values of 31 and SSIM values of up to 94%. These results demonstrate the potential of super-resolution in enhancing biomedical imaging, offering clearer images for more accurate disease diagnosis, thereby improving the precision of medical analyses. Moreover, given that these developments can also be applied in fields such as security and restoration, the importance of super-resolution techniques across different disciplines is increasingly recognized.

Keywords: Generative adversarial networks, SRGAN, Biomedical.

1   INTRODUCTION

Super-resolution (SR) is a method of obtaining high-resolution images from one or more low-resolution versions of the same image. High-resolution images provide more detail and clarity, thereby increasing the accuracy of image analysis and classification [1]. SR technology has become increasingly important with rapid advancements in digital image processing and analysis. This technology enhances the quality and details of low-resolution images, producing high-resolution results. One of the most common problems encountered in digital images is the loss of detail and blurriness [2]. SR can address these issues by producing sharper and higher-quality images.

SR is often used to improve the quality of old or low-quality images. This technology enhances the clarity of images, providing detailed and high-quality visuals [3]. Particularly in the restoration of historically significant old photographs, SR has made a significant difference. Using SR techniques, details lost in old, low-resolution, and degraded images can be recovered, adapting the image to modern digital standards [4]. For example, enhancing and restoring the details of nostalgic and historically valuable images significantly increases visual quality, allowing these photographs to be used more effectively in modern digital formats.

One of the important application areas of SR is the medical field. In medical imaging techniques, SR enhances the resolution of images, helping doctors make more accurate diagnoses. Particularly in imaging techniques such as magnetic resonance (MR), computed tomography (CT), and ultrasound, high-resolution images allow doctors to analyze diseases in more detail [5]. The early detection of cancer cells or abnormal tissues becomes easier with SR technology, enabling the creation of more effective treatment plans for patients. Diseases identified early, especially in serious conditions like cancer, can be treated before they progress, thanks to SR.

SR also has a significant impact in the field of security and surveillance. Images obtained from security cameras are often low-resolution, and the lack of detail can result in the loss of critical information. SR technology enhances the clarity of these images, enabling the identification of suspects and the detailed analysis of events [6]. This allows security forces to intervene more effectively in incidents. Additionally, using SR technology, surveillance systems in cities can be made more efficient, and clearer results can be obtained in detecting security issues.

Super-resolution can be implemented using two main methods: Single Image Super-Resolution (SISR) and Multi-Image Super-Resolution (MISR). SISR aims to obtain a high-resolution image from a single low-resolution image [7]. This technique is often applied using deep learning models, particularly Convolutional Neural Networks (CNNs). Deep learning analyzes the features of low-resolution images and generates a high-resolution prediction. MISR, on the other hand, uses multiple low-resolution images of the same scene captured from different angles or at different times to produce a high-resolution image [8]. This method benefits from the redundancy of information across images, resulting in higher-quality outcomes.

In recent years, significant progress has been made in deep learning-based super-resolution (SR) research. Particularly, CNN-based models have demonstrated great success in addressing SR problems. CNNs are known for their strong performance in image processing and analysis and provide innovative solutions in the SR domain [9, 10]. One of the first major breakthroughs in super-resolution was the SRCNN (Super-Resolution Convolutional Neural Network) model developed by Dong et al. (2015). SRCNN uses a three-layer CNN to create high-resolution versions of low-resolution images. This model first scales a low-resolution image to a higher resolution and then performs feature extraction and reconstruction on this image [11].

After the success of SRCNN, Kim et al. introduced a deeper model called VDSR (Very Deep Super-Resolution Network). VDSR is a 20-layer deep neural network and leverages the power of deep learning to predict high-resolution versions of low-resolution images [12]. Lim et al. developed the Enhanced Deep Super-Resolution (EDSR) model, which significantly improved SR performance. EDSR uses a structure similar to VDSR but enhances performance with several key improvements [13]. The RDN (Residual Dense Network) model developed by Zhang et al. represents a new approach to SR problems and has been effective in improving resolution [14].

In deep learning-based SR research, the sharpening of blurred images has also been an important area of study in the literature. For example, Xu et al. have conducted important research in this area using deep convolutional networks to sharpen blurred images. These studies reduce blurry areas through sharpening filters, allowing fine details in the image to be emphasized [15]. Reducing random noise in digital images is important for improving image quality. Zhang et al. introduced a deep learning model called DnCNN that effectively reduces

image noise. Additionally, contrast enhancement techniques highlight the difference between light and dark areas in the image, resulting in clearer and more vibrant visuals [16].

In this study, three different biomedical datasets—skin cancer, retina fundus, and blood cell cancer—were trained with the SRGAN model [17], and the model's performance was evaluated using PSNR and SSIM metrics. The results show that for the skin cancer dataset, the model achieved a PSNR of 31.11 and an SSIM of 85.74%; for the retina fundus dataset, a PSNR of 30.75 and an SSIM of 94.83%; and for the blood cell cancer dataset, a PSNR of 33.65 and an SSIM of 88.38%. These results demonstrate the effectiveness of SR in enhancing the quality of medical images for analysis.

2 MATERIAL AND METHOD

This study uses three different datasets from global sources: the Skin Cancer dataset from the International Skin Imaging Collaboration (ISIC) [18], the Blood Cell Cancer dataset from Taleqani Hospital in Tehran, Iran [19] , and the Retina Fundus dataset from the Papageorgiou Hospital at Aristotle University of Thessaloniki [20].

2.1 Skin Cancer Dataset

From the databases of the International Skin Imaging Collaboration (ISIC), a total of 2,357 images of malignant and benign oncological diseases were obtained. These images were initially classified according to the ISIC classification and divided into equal numbers for all subsets, excluding melanomas and moles, which were slightly more prevalent. Figure 1 shows some example images from the skin cancer dataset.
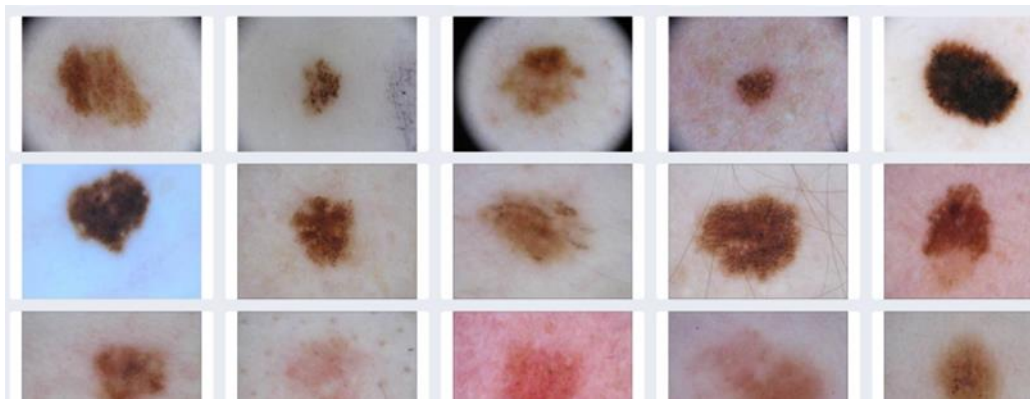
Figure 1. Skin cancer dataset sample images.

As seen in Figure 1, the dataset consists of images related to various skin lesions or moles. Irregularities in shape, color, and patterns can be observed among these lesions, which are crucial for the detection of cancerous cells [21]. The distribution of color, asymmetry, border characteristics, and size differences in the lesions are used to diagnose the disease.

2.2   Blood Cell Cancer Dataset

The accurate diagnosis of Acute Lymphoblastic Leukemia (ALL), a highly common form of cancer, often requires invasive, expensive, and time-consuming diagnostic tests [22]. Peripheral blood smear (PBS) images play a critical role in the initial screening of ALL by differentiating cancerous cells from non-cancerous cases. Manual examination of these PBS images by laboratory users is prone to diagnostic errors due to the non-specific nature of ALL's symptoms. This dataset consists of 3,242 PBS images from 89 patients suspected of having ALL, which were prepared and stained by skilled laboratory personnel. These images are divided into two classes: benign (non-cancerous) and malignant, with malignant ALL further categorized into three subtypes: Early Pre-B, Pre-B, and Pro-B ALL. All images were captured using a Zeiss camera with a 100x magnification microscope and saved as JPG files. Figure 2 shows the blood cell cancer dataset.
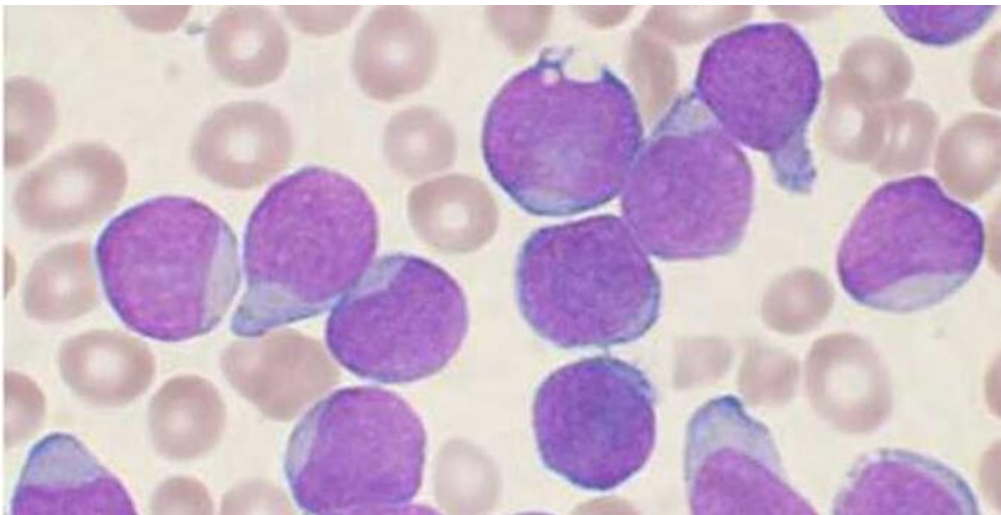
Figure 2. Blood cell cancer dataset sample images.

In Figure 2, it can be observed that cancerous blood cells are larger and have a purplish color compared to healthy blood cells. Leukemia is characterized by the uncontrolled proliferation of abnormal white blood cells in the blood and bone marrow, replacing normal cells and weakening the body's ability to fight infections and impairing other essential functions.

2.3   Retina Fundus Veri Seti

This dataset consists of 129 retinal images forming 134 image pairs, which are divided into three categories based on their features. The images were captured using a Nidek AFC-210 fundus camera with a 45° field of view. The data was collected from 39 patients at the Papageorgiou Hospital in Thessaloniki, Greece. Figure 3 shows the retina fundus dataset.
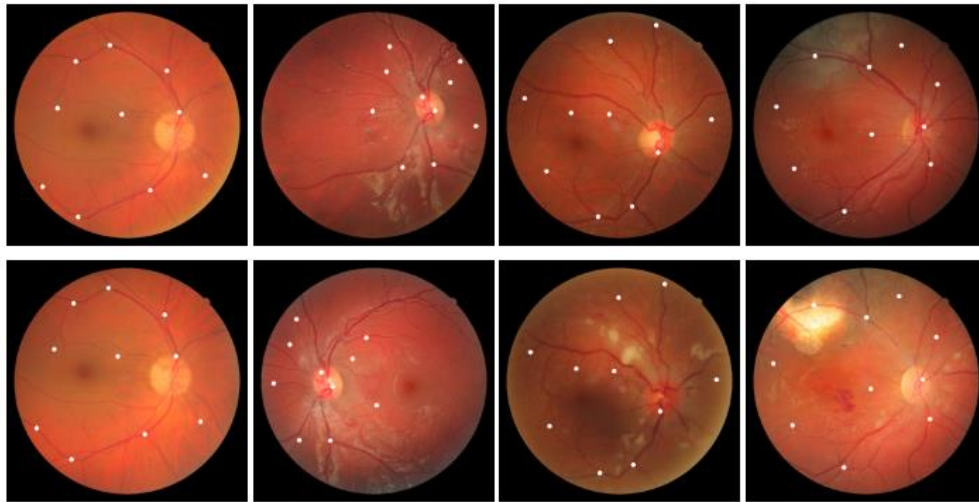
Figure 3. Retina fundus dataset sample images.

In Figure 3, the optic nerve, blood vessels, and retina surface can be seen. The optic nerve's center is usually a bright spot, and blood vessels radiate outward from this point. To diagnose eye diseases, the structure of the retinal vessels, abnormalities around the optic disc, hemorrhages, and areas such as the macula are examined. The white spots in the images are markings used to identify problem areas in the eye. Fundus images are often used to diagnose conditions such as diabetic retinopathy, where hemorrhages, cotton wool spots, and other vascular changes are significant features.

2.4   Generative Adversarial Networks

Generative Adversarial Networks (GANs) are an unsupervised deep learning framework proposed by Goodfellow et al. [23]. The framework consists of two networks: a generator (G) and a discriminator (D), optimized to minimize a two-player minimax game where the generator learns to deceive the discriminator, and the discriminator learns to protect itself from being deceived. As explained by Goodfellow and his colleagues, "The generator model can be likened to a team of counterfeiters trying to produce fake money, while the discriminator model resembles the police attempting to detect the counterfeit money" [24].

During GAN training, the generator receives a random noise vector as input and produces an output distribution PG. The discriminator is then trained to distinguish between PG and the real data distribution PData. Simultaneously, the generator is trained to learn how to deceive the discriminator. In theory, PG should converge towards PData as the discriminator becomes unable to differentiate between the generated and real samples, resulting in an ideal generator model capable of producing data following the real data distribution.

While GANs are a powerful framework, they often face stability issues, where competing networks rarely converge. Variations of the framework that use different loss functions, such as Wasserstein GANs (WGANs) [25], have been developed to improve training stability. Unlike the original GAN framework, WGANs minimize the Earth Mover's Distance and impose a gradient penalty in the loss function to constrain the discriminator's gradient norm relative to its input.

2.5   Super Resolution Generative Adversarial Networks

Super Resolution Generative Adversarial Networks (SRGAN), SRGAN is a method that uses generative adversarial networks (GANs) to produce photorealistic super-resolution (SR) images with high scaling factors. While traditional SR approaches focus on minimizing pixel-based error metrics (e.g., Mean Squared Error – MSE), SRGAN adopts an innovative perceptual loss function to produce images of a quality closer to human perception [26]. This loss function takes advantage of a discriminator network trained to distinguish between real and super-resolved images. SRGAN uses a deep residual network (ResNet) architecture and applies a VGG loss that measures the Euclidean distance between feature maps obtained from the VGG19 network. The SRGAN architecture is shown in Figure 4.
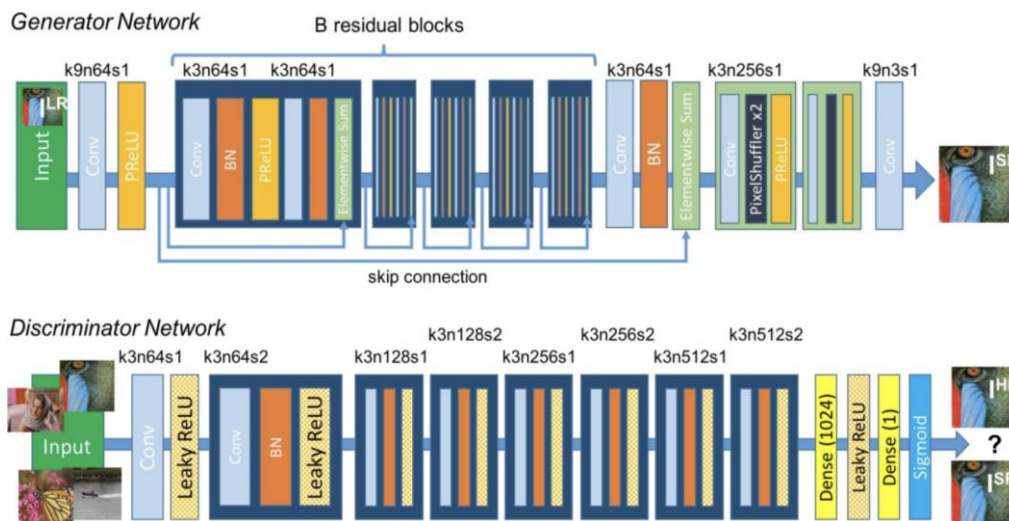
Figure 4. SRGAN Architecture.

Extensive experiments have shown that SRGAN sets a new standard for PSNR and Structural Similarity Index (SSIM) metrics on three publicly available datasets. Additionally, the quality of SR images produced by SRGAN has significantly outperformed other state-of-the-art methods, according to the results of the Mean Opinion Score (MOS) test [27]. This study demonstrates the potential of GANs in enhancing perceptual quality in the field of super-resolution.

2.6 Peak Signal-to-Noise Ratio

Peak Signal-to-Noise Ratio (PSNR) is a signal processing metric used to compare a processed signal to its original source. This comparison allows us to measure how faithfully the processed signal retains the qualities of the original, as well as to identify any noise or distortions introduced during processing [28]. PSNR directly represents the relationship between a signal before and after the degradation process. Equations 1 and 2 show these relationships.

$$PSNR = 20\,log_{10}\frac{MAX_1^2}{MSE} \tag{1}$$

$$MSE = \frac{1}{mn}\sum_{i=0}^{m=1}\sum_{j=0}^{n=1}[(i,j)-K(i,j)]^2 \tag{2}$$

MAX is the highest possible value of the signal. In the case of an 8-bit grayscale image, AX=255, and $PSNR$ is inversely proportional to MSE (Mean Square Error), as shown in Equation (1). The final value $PSNR$ is given in decibels. PSNR is inversely proportional to MSE (Mean Squared Error), and the final value of PSNR is expressed in decibels. PSNR is commonly used to evaluate the quality of image or video signals based on the MSE relative to the source image. However, it has also been used as an analytical measure for segmentation algorithm assessments [29]. However, it has also been used as an analytical measure for segmentation algorithm assessments [30]. In the case of multi-threshold algorithms, it has been used to determine the number of thresholds in addition to their value [31].

2.6.1 Structural Similarity Index

The Structural Similarity Index (SSIM) is a metric used to evaluate the quality of digital images based on their structural integrity. SSIM was developed based on the perceptual characteristics of the Human Visual System (HVS) and, unlike traditional methods, compares the structural information of images to assess the level of degradation [32].

SSIM evaluates quality by focusing on the degradation of a scene's structural information. SSIM consists of three components: luminance, contrast, and structure. Luminance compares the average brightness values of two images; contrast is calculated based on the variance of the images; and structure is compared by calculating the covariance of the two images. The SSIM value is calculated as shown in Equation (3).

$$SSIM(x,y) = \frac{(2\mu x\mu y + C_1)(2\sigma xy + C_2)}{(\mu x_2 + \mu y_2 + C_1)(\sigma x_2 + \sigma y_2 + C_2)} \tag{3}$$

Where μx and μy are the mean brightness values of the original and distorted images, σx_2 and σy_2 are their variances, and σxy is the covariance between the two images. C_1 and C_1 are constants added for stability in the calculations.

3   RESULTS AND DISCUSSION

The PSNR and SSIM performance graphs for the skin cancer dataset after training the SRGAN model are presented in Figure 5. It is clear that during training, the PSNR value exceeds 30, which represents an ideal level for image quality [33]. Additionally, the SSIM value surpasses 85%, indicating that the generated images maintain a high level of structural integrity.
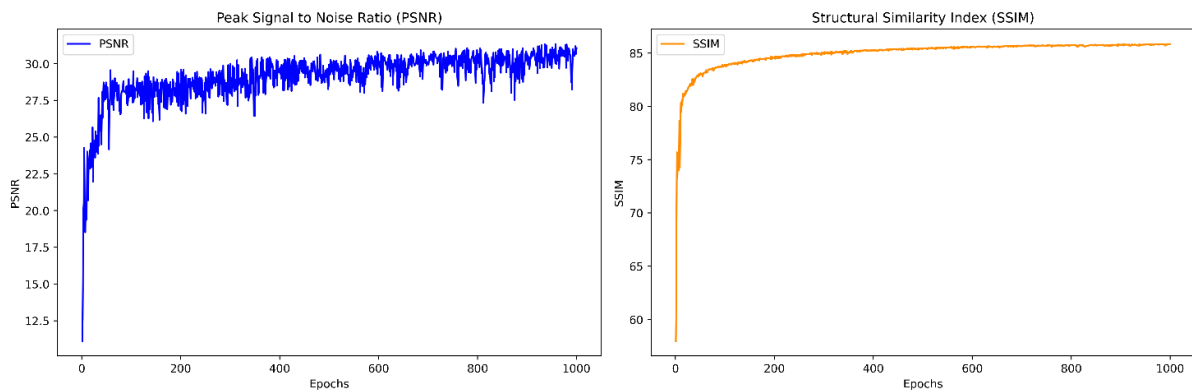
Figure 5. PSNR and SSIM Performance Graph for the Skin Cancer Dataset.

The PSNR and SSIM performance graphs for the retina fundus dataset are shown in Figure 6. During training, the PSNR value increases above 30, which is considered an excellent level for image quality [34]. Furthermore, the SSIM value approaches 95%, signifying that the generated images have a high structural resemblance to the originals.
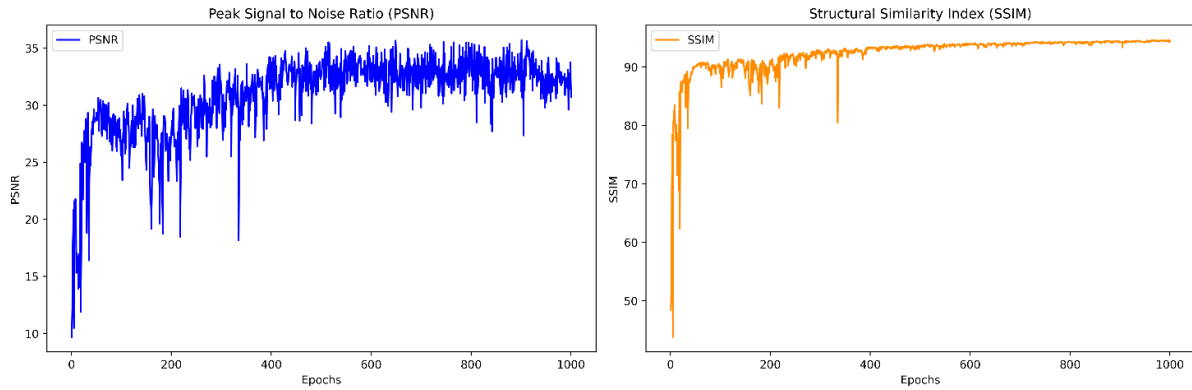
Figure 6. PSNR and SSIM Performance Graph for the Retina Fundus Dataset.

For the blood cell cancer dataset, the PSNR and SSIM performance graphs are shown in Figure 7. As illustrated, the PSNR value approaches 31 during training, and a final value of 30.97 is achieved after 1000 iterations. Additionally, the SSIM performance value of 88.18% demonstrates the structural integrity of the generated images.
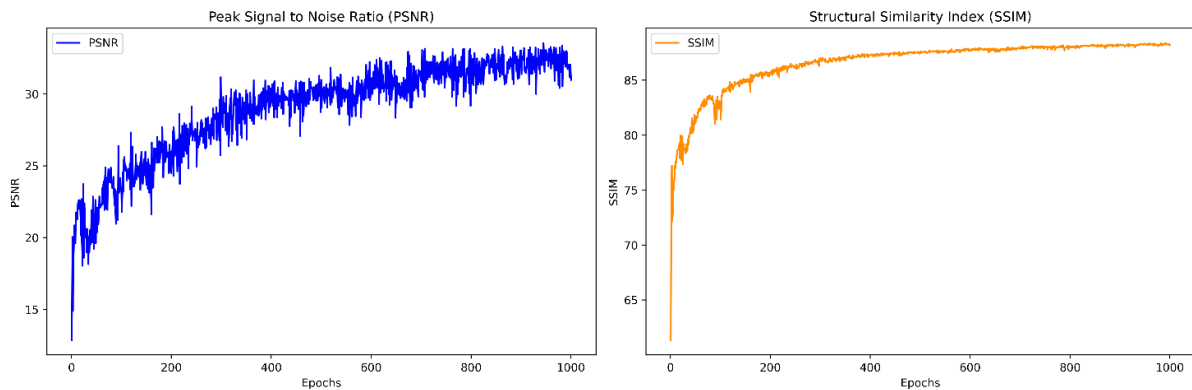
Figure 7. PSNR and SSIM Performance Graph for the Blood Cell Cancer Dataset.

The results for the SRGAN model's performance on different medical image datasets are presented in Table 1.

Table 1. Dataset Performance Values.

Datasets	PSNR	SSIM	MAE
Skin Cancer	31.06	85.84%	1.11%
Retina Fundus	30.71	94.30%	1.80%
Blood Cell Cancer	30.97	88.18%	1.51%

For the skin cancer dataset, the PSNR value of 31.06 indicates that the image quality is quite good. The SSIM value of 85.84% shows that the images have been reconstructed with high structural accuracy, while the Mean Absolute Error (MAE) value of 1.11% indicates a meager error rate. For the retina fundus dataset, the PSNR value of 30.71 represents good image

quality, and the SSIM value of 94.30% indicates an exceptionally high structural similarity to the original images. The MAE value of 1.8% shows that the model made very few errors with this dataset. Finally, for the blood cell cancer dataset, the PSNR value of 30.97 demonstrates the highest performance, indicating superior image quality compared to the other datasets. The SSIM value of 88.18% confirms the model's strong structural accuracy, and the MAE value of 1.51% indicates a low error rate. These results show that the SRGAN model can be successfully applied to different medical image datasets and effectively produces high-resolution images.

4   CONCLUSION AND SUGGESTIONS

In this study, the performance of the SRGAN model on different medical image datasets was evaluated. The results demonstrate that the model achieves successful outcomes on medical images, producing high-resolution images. Specifically, the analyses on the skin cancer, retina fundus, and blood cell cancer datasets reveal the model's overall success. Figure 8 shows the LR: Low Resolution and SR: Super Resolution images obtained as a result of the study conducted on three different original skin cancer images.
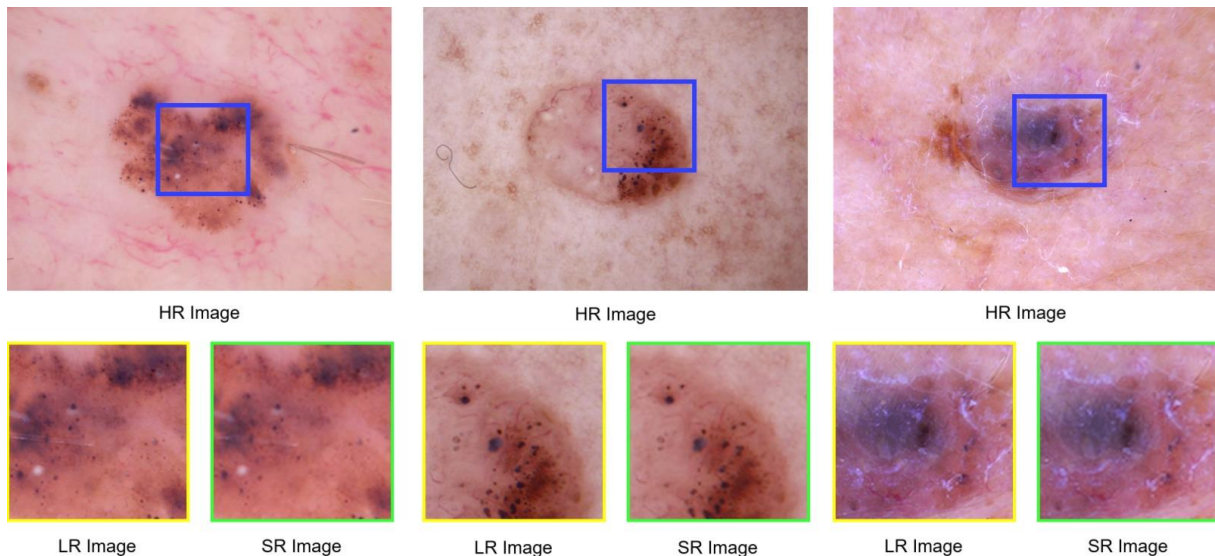
Figure 8. LR and SR results of different images in the skin cancer dataset.

For the skin cancer dataset, the PSNR value of 31.06 indicates that the image quality is quite high, which is crucial for medical diagnoses. A PSNR value above 30 suggests that the model is performing effectively. The SSIM value of 85.84% indicates that the structural integrity of the images has been preserved. The MAE value of 1.11% represents a low error rate. Figure 9 shows the LR and SR images obtained as a result of the study conducted on three different original retina fundus images.
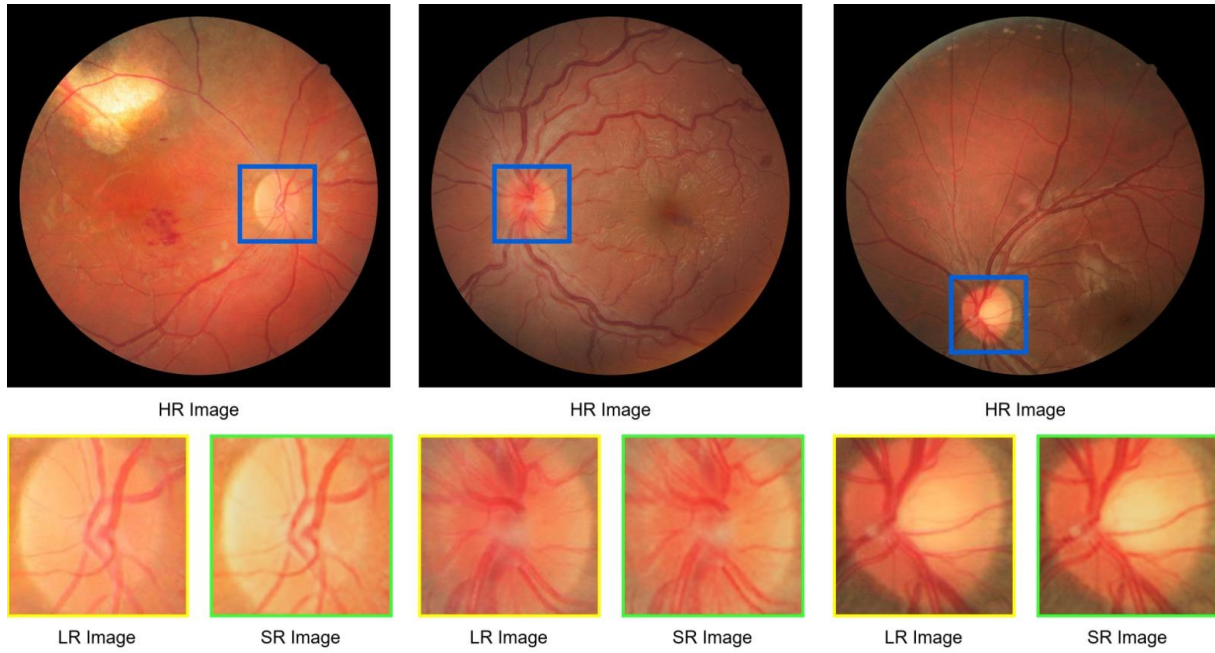
Figure 9. LR and SR results of different images in the retina fundus dataset.

For the retina fundus dataset, the PSNR value of 30.71 confirms that the image quality is high. The SSIM value of 94.30% shows a very close structural resemblance between the original and generated images. The low MAE value of 1.8% indicates that the model made very few errors on these images, suggesting that it can be applied in sensitive areas like retinal imaging. Figure 10 shows the LR and SR images obtained as a result of the study conducted on three different original blood cell cancer images.
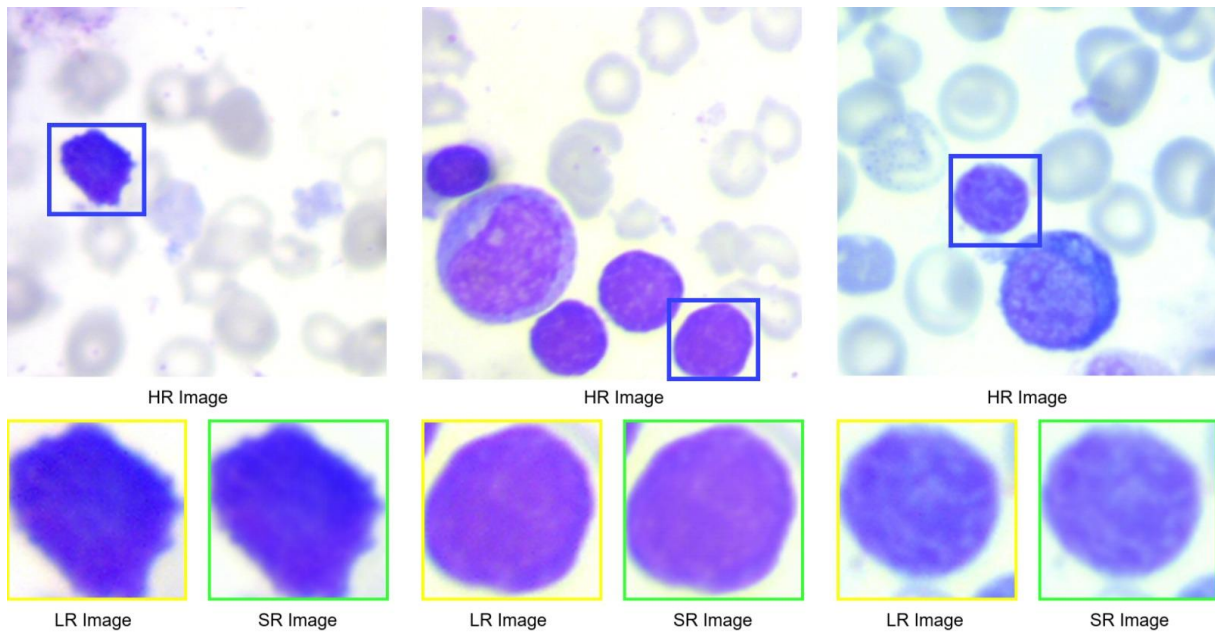
Figure 10. LR and SR results of different images in the blood cell cancer dataset.

Finally, the blood cell cancer dataset achieved the highest PSNR value of 30.97, demonstrating the best performance. The SSIM value of 88.18% confirms the model's success in maintaining structural accuracy, while the MAE value of 1.51% reflects a low error rate.

Overall, the SRGAN model has proven to generate successful results across different medical datasets. These findings indicate that the model holds great potential for medical image processing applications.

Conflict of Interest Statement

There is no conflict of interest between the authors.

Statement of Research and Publication Ethics

The study is complied with research and publication ethics.

Artificial Intelligence (AI) Contribution Statement

This manuscript was entirely written, edited, analyzed, and prepared without the assistance of any artificial intelligence (AI) tools. All content, including text, data analysis, and figures, was solely generated by the authors.

Contributions of the Authors

Zübeyr Güngür: Formal analysis; investigation; methodology; software; writing original draft; writing, review and editing.

İbrahim Ayaz: Methodology, resources, software, validation, visualization, writing original draft, writing, review and editing.

Vedat Tümen: Conceptualization, supervision, data curation, formal analysis, investigation, methodology, project administration, software, writing, review and editing.

REFERENCES

[1]   P. Chopade and P. Patil, "Image super resolution scheme based on wavelet transform and its performance analysis," in *International Conference on Computing, Communication & Automation*, 2015, pp. 1182-1186: IEEE.

[2]   L. Yue, H. Shen, J. Li, Q. Yuan, H. Zhang, and L. Zhang, "Image super-resolution: The techniques, applications, and future," *Signal processing,* vol. 128, pp. 389-408, 2016.

[3]   X. Hou, T. Liu, S. Wang, and L. Zhang, "Image Quality Improve by Super Resolution Generative Adversarial Networks," in *2021 2nd International Conference on Intelligent Computing and Human-Computer Interaction (ICHCI)*, 2021, pp. 117-121: IEEE.

[4]   J. Yang and T. Huang, "Image super-resolution: Historical overview and future challenges," in *Super-resolution imaging*: CRC Press, 2017, pp. 1-34.

[5]   G. Zamzmi, S. Rajaraman, and S. Antani, "Accelerating super-resolution and visual task analysis in medical images," *Applied Sciences,* vol. 10, no. 12, p. 4282, 2020.

[6]   A. Aakerberg, K. Nasrollahi, and T. B. Moeslund, "Real-world super-resolution of face-images from surveillance cameras," *IET Image Processing,* vol. 16, no. 2, pp. 442-452, 2022.

[7]   T. An, X. Zhang, C. Huo, B. Xue, L. Wang, and C. Pan, "TR-MISR: Multiimage super-resolution based on feature fusion with transformers," *IEEE Journal of Selected Topics in Applied Earth Observations and Remote Sensing,* vol. 15, pp. 1373-1388, 2022.

[8]   F. Salvetti, V. Mazzia, A. Khaliq, and M. Chiaberge, "Multi-image super resolution of remotely sensed images using residual attention deep neural networks," *Remote Sensing,* vol. 12, no. 14, p. 2207, 2020.

[9]   S. M. A. Bashir, Y. Wang, M. Khan, and Y. Niu, "A comprehensive review of deep learning-based single image super-resolution," *PeerJ Computer Science,* vol. 7, p. e621, 2021.

[10]   P. Wang, B. Bayram, and E. Sertel, "A comprehensive review on deep learning based remote sensing image super-resolution methods," *Earth-Science Reviews,* vol. 232, p. 104110, 2022.

[11]   C. Dong, C. C. Loy, K. He, and X. Tang, "Image super-resolution using deep convolutional networks," *IEEE transactions on pattern analysis and machine intelligence,* vol. 38, no. 2, pp. 295-307, 2015.

[12]   J. Kim, J. K. Lee, and K. M. Lee, "Accurate image super-resolution using very deep convolutional networks," in *Proceedings of the IEEE conference on computer vision and pattern recognition*, 2016, pp. 1646-1654.

[13]   B. Lim, S. Son, H. Kim, S. Nah, and K. Mu Lee, "Enhanced deep residual networks for single image super-resolution," in *Proceedings of the IEEE conference on computer vision and pattern recognition workshops*, 2017, pp. 136-144.

[14]   Y. Zhang, Y. Tian, Y. Kong, B. Zhong, and Y. Fu, "Residual dense network for image super-resolution," in *Proceedings of the IEEE conference on computer vision and pattern recognition*, 2018, pp. 2472-2481.

[15]   L. Xu, J. S. Ren, C. Liu, and J. Jia, "Deep convolutional neural network for image deconvolution," *Advances in neural information processing systems,* vol. 27, 2014.

[16]   K. Zhang, W. Zuo, Y. Chen, D. Meng, and L. Zhang, "Beyond a gaussian denoiser: Residual learning of deep cnn for image denoising," *IEEE transactions on image processing,* vol. 26, no. 7, pp. 3142-3155, 2017.

[17]   T. Y. Timothy, D. Ma, J. Cole, M. J. Ju, M. F. Beg, and M. V. Sarunic, "Spectral bandwidth recovery of optical coherence tomography images using deep learning," in *2021 12th International Symposium on Image and Signal Processing and Analysis (ISPA)*, 2021, pp. 67-71: IEEE.

[18]   (10.10.2024). *The International Skin Imaging Collaboration*. Available: https://www.isic-archive.com/

[19]   M. G. Mehrad Aria, Davood Bashash, Hassan Abolghasemi, and F. A. a. A. Hossein, "Acute Lymphoblastic Leukemia (ALL) image datase," ed, 2021.

[20]   C. Hernandez-Matas, X. Zabulis, A. Triantafyllou, P. Anyfanti, S. Douma, and A. A. Argyros, "FIRE: fundus image registration dataset," *Modeling and Artificial Intelligence in Ophthalmology,* vol. 1, no. 4, pp. 16-28, 2017.

[21]   R. Krithiga and P. Geetha, "Breast cancer detection, segmentation and classification on histopathology images analysis: a systematic review," *Archives of Computational Methods in Engineering,* vol. 28, no. 4, pp. 2607-2619, 2021.

[22]   C. Mondal *et al.*, "Ensemble of convolutional neural networks to diagnose acute lymphoblastic leukemia from microscopic images," *Informatics in Medicine Unlocked,* vol. 27, p. 100794, 2021.

[23]   I. Goodfellow *et al.*, "Generative adversarial nets," *Advances in neural information processing systems,* vol. 27, 2014.

[24] I. Goodfellow *et al.*, "Generative adversarial networks," *Communications of the ACM,* vol. 63, no. 11, pp. 139-144, 2020.

[25] M. Arjovsky, S. Chintala, and L. Bottou, "Wasserstein generative adversarial networks," in *International conference on machine learning*, 2017, pp. 214-223: PMLR.

[26] C. Ledig *et al.*, "Photo-realistic single image super-resolution using a generative adversarial network," in *Proceedings of the IEEE conference on computer vision and pattern recognition*, 2017, pp. 4681-4690.

[27] X. Zhu, L. Zhang, L. Zhang, X. Liu, Y. Shen, and S. Zhao, "GAN-Based Image Super-Resolution with a Novel Quality Loss," *Mathematical Problems in Engineering,* vol. 2020, no. 1, p. 5217429, 2020.

[28] J. Korhonen and J. You, "Peak signal-to-noise ratio revisited: Is simple beautiful?," in *2012 Fourth international workshop on quality of multimedia experience*, 2012, pp. 37-38: IEEE.

[29] Y.-K. Chen, F.-C. Cheng, and P. Tsai, "A gray-level clustering reduction algorithm with the least PSNR," *Expert Systems with Applications,* vol. 38, no. 8, pp. 10183-10187, 2011.

[30] M.-H. Horng and R.-J. Liou, "Multilevel minimum cross entropy threshold selection based on the firefly algorithm," *Expert Systems with Applications,* vol. 38, no. 12, pp. 14805-14811, 2011.

[31] S. Arora, J. Acharya, A. Verma, and P. K. Panigrahi, "Multilevel thresholding for image segmentation through a fast statistical recursive algorithm," *Pattern Recognition Letters,* vol. 29, no. 2, pp. 119-125, 2008.

[32] Z. Wang, A. C. Bovik, H. R. Sheikh, and E. P. Simoncelli, "Image quality assessment: from error visibility to structural similarity," *IEEE transactions on image processing,* vol. 13, no. 4, pp. 600-612, 2004.

[33] D. R. I. M. Setiadi, "PSNR vs SSIM: imperceptibility quality assessment for image steganography," *Multimedia Tools and Applications,* vol. 80, no. 6, pp. 8423-8444, 2021.

[34] U. Sara, M. Akter, and M. S. Uddin, "Image quality assessment through FSIM, SSIM, MSE and PSNR—a comparative study," *Journal of Computer and Communications,* vol. 7, no. 3, pp. 8-18, 2019.

EFFECT OF VENLAFAXINE AND VITAMIN C ON SOME BIOCHEMICAL PARAMETERS OF SACCHAROMYCES CEREVISIAE (NRRLY-12632)

Meltem ÇAKMAK [1] , Dursun ÖZER [1*] , **Fikret KARATAŞ [2*]** , Sinan SAYDAM [2]

[1] *Fırat University, Department of Chemical Engineering, Elazığ, Türkiye*

[2] *Fırat University, Department of Chemistry, Elazığ, Türkiye*

* Corresponding Author: *cakmak_meltem@hotmail.com*

ABSTRACT

In this study, *Saccharomyces cerevisiae* (NRLLY-12632) was grown in Yeast Extract–Peptone–Dextrose (YPD) medium containing different concentrations of venlafaxine, (RS)-1-[2-dimethylamino-1-(4-methoxyphenyl)-ethyl] cyclohexanol. To counteract the effect of venlafaxine, vitamin C were added to the growth medium of *Saccharomyces cerevisiae* (*S. cerevisiae)*. Then the antioxidant enzymes activities and stress biomarkers were investigated through the use of spectrophotometric methods and HPLC technique, respectively. Addition of venlafaxine in to growth medium of *S. cerevisiae*, significantly increased the superoxide dismutase (SOD), catalase (CAT), glutathione peroxidase (GSH-Px), glutathione reductase (GSH-Rd) and peroxidase (POD) activities ($p < 0.05$). On the other hand, activities of CAT, GSH-Px, GSH-Rd and POD enzymes were decreased significantly in all vitamin C concentrations added to the growth medium containing venlafaxine ($p < 0.05$). SOD activities were found to be significantly decreased at 50 and 75 ppm vitamin C concentrations ($p < 0.05$). While total protein amount decreased at all venlafaxine concentrations, on the other hand amount of advanced oxidized proteins (AOP) increased significantly ($p < 0.05$). Vitamin C at 25, 50 and 75 ppm concentrations with venlafaxine led to increase the total protein amount and decreased the AOP concentration ($p < 0.05$). The amount of reduced glutathione (GSH) decreased in all venlafaxine concentrations while the amounts of oxidized glutathione (GSSG), malondialdehyde (MDA) and 4-hydroxynonenal (4-HNE) increased ($p < 0.05$). With the addition 25, 50 and 75 ppm vitamin C to the growth medium containing venlafaxine while leading to decrease the amount of GSSG, MDA and 4-HNE, the amount of GSH increased significantly ($p < 0.05$). From these findings, it can be said that the negative effect of venlafaxine on the biochemical parameters of *S. cerevisiae* is reduced by the addition of vitamin C to the medium.

Keywords: *S. cerevisiae*, Venlafaxine, Vitamin C, Antioxidant enzymes, Stress biomarkers.

1   INTRODUCTION

The term microorganism is used to describe many living things in a broad framework, including bacteria, yeast, fungi and algae. Yeasts are eukaryotic, unicellular microorganisms that reproduce by budding. Yeasts are composed of high protein, lipid, polysaccharide and nucleic acids as a cellular composition [1]. *S. cerevisiae* is commonly used in scientific studies for similarities to human genome. Yeasts are used in many industries due to their high reproduction in a short time and low cost by using cheap renewable food sources [2].

Depression is the most common complex psychiatric disorder worldwide, causing severe dysfunction in patients [3]. Depression is characterized by feelings of worthlessness, anxiety, guilt, hopelessness, suicidal ideation, loss of appetite, weight changes, constipation, agitation, and other somatic symptoms. In addition to its chronicity, depression causes significant work and social losses, resulting in negativities in current activities [4]. The most common treatment method for depression is the use of antidepressant drugs. Antidepressants are usually administered for a long time and in some cases in combination with other antidepressants [5]. It has been reported that in patients using antidepressants, normal metabolism is disrupted due to the side effects of drugs, abnormal signals reach the cell, and oxidative stress occurs as a result [6]. Antidepressants might cause oxidative stress by affecting cell metabolism, and the resulting free radicals in cell membrane, proteins, amino acids, vitamins. Determining the damage to the cells is of great importance in terms of preventing this damage [3]. Vitamin C, which is effective in the release of some hormones in the event of stress in living organism, has a strong antioxidant effect [7]. It is stated that vitamin C effectively protects DNA, proteins and lipids against oxidative damage due to its ability to actively capture reactive oxygen and nitrogen species [8].

All organisms, eukaryotic or prokaryotic, have developed complex cellular defense mechanisms to protect their cell and organ systems against the harmful effects of Reactive Oxygen Species (ROS) and other reactive species [9]. These mechanisms, which are generally referred to as antioxidant systems, contain various components of endogenous and exogenous origin, realized by enzymatic and non-enzymatic means, and have a radical scavenging effect, repair radical-induced damage and prevent mutations [10]. The most important of the enzymes that play a role in the antioxidant system are SOD, CAT, POD, GSH-Px and GSH-Rd, as well as non-enzymatic is GSH [11]. It was reported by Adwas et al. [12] that the antioxidant enzyme activity is important due to oxidative stress. In order to maintain its normal functioning, the

amount of protein must be kept at a constant level. Changes that may occur in the total amount of protein may be the harbinger of some diseases. Therefore, analysis of total protein is important. Free radicals formed as a result of different stress factors cause oxidation in proteins. Proteins damaged by oxidation are called advanced AOP. Protein oxidation can occur directly with reactive oxygen species or indirectly with secondary products of oxidative stress [13,14]. If there is no stress factor present in the cell, glutathione is in form GSH, in the event of stress glutathione is converted to GSSG by the action of the GSH-Px enzyme. Conversion of GSSG to GSH is important in terms of preventing free radical damage [15]. While GSSG is an indicator of oxidative stress, it also inhibits protein synthesis, GSH has many physiological functions like preventing the harmful effect of drugs [16]. Radicalic compounds cause lipid peroxidation of fatty acids in cell membranes. Lipid peroxides transform into compounds such as MDA and 4-HNE, which are indicative of lipid peroxidation [17]. In this work, *S. cerevisiae* was chosen for having at least 23% common genes to humans [18].

The aim of this study is to determine the effect of venlafaxine, one of the widely used antidepressants, on antioxidant enzymes and stress biomarkers in metabolism of *S. cerevisiae*. Additionally, investigating the effect of vitamin C on antioxidant enzymes and stress biomarkers that will be affected by antidepressants containing growth medium of *S. cerevisiae*.

2 MATERIAL AND METHOD

2.1 Material

S. cerevisiae (NRRLY-12632) used in this study was obtained from Fırat University, Department of Chemical Engineering, Biotechnology Laboratory. *S. cerevisiae* produced in yeast peptone dextrose (YPD) broth (10.0 g peptone, 5.0 g yeast extract, 10.0 g Dextrose per liter) was used. Solutions of 1000 ppm venlafaxine chloride and 500 ppm vitamin C were prepared freshly and used. The microorganism was produced in 250 mL flasks containing 50 mL nutrient medium. Experiments were carried out by forming the following groups for the study.

1. Control group: Microorganisms were grown by inoculating *S. cerevisiae* in the YPD medium.

2. Venlafaxine group: Microorganisms were grown by adding venlafaxine stock solution at desired concentrations (100 - 500 ppm) to the control.

3. Vitamin C group: Microorganisms were produced by adding vitamin C at the desired concentration (10-75 ppm) to the venlafaxine group.

The medium was incubated on an orbital shaker for 72 hours at 150 rpm at 30 °C. The concentration of *S. cerevisiae* was determined by measuring the absorbance at 600 nm with a spectrophotometer. After centrifugation of the medium containing the microorganism at 8000 rpm at 10 ºC for 10 minutes, the supernatant was removed, and the microorganism was washed twice with distilled water for further analysis [19].

2.2   Methods

Total protein analysis, Glutathione peroxidase, Glutathione reductase, Catalase and Peroxidase enzyme activities were performed by UV-Visible spectrophotometer according to the methods applied by İbrahim et al. [20], Superoxide dismutase activity was determined using the pyrogallol autoxidation method [21] and AOP determination was made according to the method developed by Witko-Sarsat et al. [22] by using by UV-Visible spectrophotometer. GSH, GSSG and MDA were analyzed using a Utisil-XB-C-8 column, using mobile phase as 50 mM $NaClO_4$ at pH: 4 in 0.1 % H_3PO_4 solution and 4-HNE were determinated on ODS-2 column by HPLC according to İbrahim et al. [20]. The HPLC chromatogram of GSH, GSSG and MDA is given in figure 1.
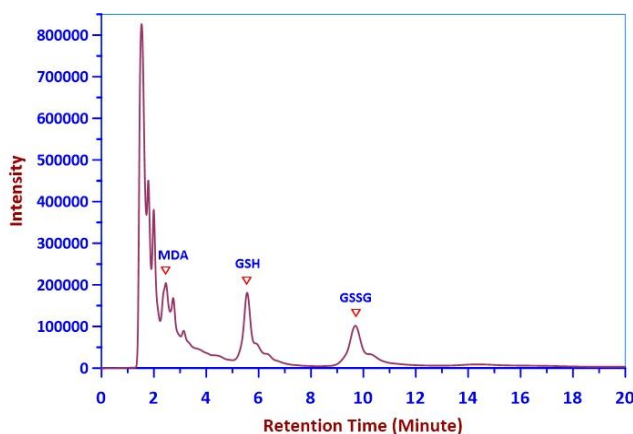
Figure 1. HPLC chromatogram of GSH, GSSG and MDA.

2.3   Statistical Analysis

All measurements were triplicated, and Mean ± Standard Deviation was determined. The results were subjected to one-way ANOVA by SPSS 26.0 for Windows. Differences between the group's means were analyzed for significance using the Tukey HSD test. The level

of statistical significance was expressed as $p<0.05$. The superscripts in the table columns are indicated as an if the effect of antidepressants compared to the control group is statistically significant ($p<0.05$), b if the effect of vitamin C in growth medium containing antidepressants is statistically significant ($p<0.05$), and c if it is not statistically significant ($p>0.05$).

3   RESULTS AND DISCUSSION

Antioxidant enzyme activities, total and oxidized protein and stress biomarkers concentrations determined in *S. cerevisiae* for different experimental groups are given in Table 1-3, respectively.

Table 1. Enzymes activities of SOD, CAT, GSH-Px, and GSH-Rd in S. cerevisiae produced in a nutrient medium.

Application	SOD (U g^{-1} dw)	CAT (U g^{-1} dw)	GSH-Px (U g^{-1} dw)	GSH-Rd (U g^{-1} dw)
Control	211.25±5.00	250.38±5.37	27.57±0.59	36.37±0.77
Ven-1	231.64±4.50 [a]	300.66±5.80 [a]	50.59±1.06 [a]	48.22±1.07 [a]
Ven-2	240.79±5.23 [a]	349.27±5.96 [a]	72.12±1.17 [a]	55.73±1.10 [a]
Ven-3	250.98±5.28 [a]	383.99±6.00 [a]	87.75±1.33 [a]	62.67±1.07 [a]
Ven-4	257.36±5.37 [a]	418.72±6.38 [a]	96.08±1.46 [a]	67.00±1.16 [a]
Ven-5	262.70±5.56 [a]	435.40±6.10 [a]	103.40±1.55 [a]	73.15±1.14 [a]
Ven-1+C10	225.48±4.93 [c]	287.64±4.70 [c]	46.86±0.88 [b]	44.10±0.93 [b]
Ven-1+C25	220.95±4.88 [c]	273.24±4.06 [b]	40.61±0.81 [b]	40.34±0.88 [b]
Ven-1+C50	216.14±4.23 [b]	255.69±3.77 [b]	35.87±0.73 [b]	36.94±0.75 [b]
Ven-1+C75	212.41±4.74 [b]	247.16±3.54 [b]	30.74±0.70 [b]	34.48±0.73 [b]
Ven-2+C10	233.58±4.97 [c]	332.15±3.49 [b]	66.95±1.07 [b]	50.56±1.02 [b]
Ven-2+C25	227.17±4.87 [c]	309.19±3.36 [b]	60.59±0.87 [b]	47.37±0.93 [b]
Ven-2+C50	222.38±4.73 [b]	289.47±2.93 [b]	54.15±0.83 [b]	43.72±0.81 [b]
Ven-2+C75	218.10±4.66 [b]	272.52±2.52 [b]	48.61±0.81 [b]	40.85±0.71 [b]
Ven-3+C10	244.84±4.81 [c]	363.44±3.64 [b]	78.71±1.29 [b]	56.41±1.04 [b]
Ven-3+C25	237.79±4.74 [c]	342.14±3.48 [b]	70.72±1.16 [b]	51.92±0.88 [b]
Ven-3+C50	233.06±4.66 [b]	313.48±3.04 [b]	61.89±1.11 [b]	47.21±0.74 [b]
Ven-3+C75	227.57±4.59 [b]	290.68±2.90 [b]	53.03±1.04 [b]	41.77±0.64 [b]
Ven-4+C10	249.89±4.85 [c]	397.99±3.42 [b]	85.33±1.28 [b]	62.47±0.96 [b]
Ven-4+C25	242.54±4.70 [c]	374.67±3.60 [b]	74.12±1.13 [b]	54.69±0.89 [b]
Ven-4+C50	236.45±4.58 [b]	345.04±3.96 [b]	65.29±1.07 [b]	49.90±0.81 [b]
Ven-4+C75	230.53±4.36 [b]	320.08±3.50 [b]	57.75±0.87 [b]	45.73±0.74 [b]
Ven-5+C10	255.25±4.11 [c]	417.16±3.76 [b]	94.90±1.42 [b]	67.25±0.99 [b]
Ven-5+C25	249.54±4.02 [c]	395.28±3.54 [b]	83.67±1.33 [b]	60.90±0.91 [b]
Ven-5+C50	242.88±4.06 [b]	373.88±3.40 [b]	73.05±1.25 [b]	56.86±0.84 [b]
Ven-5+C75	236.10±3.81 [b]	343.90±3.48 [b]	64.10±1.16 [b]	49.15±0.78 [b]

Ven-1: 100 ppm Venlafaxine, Ven-2: 200 ppm Venlafaxine, Ven-3: 300 ppm Venlafaxine, Ven-4: 400 ppm Venlafaxine, Ven-5: 500 ppm Venlafaxine, C10: 10 ppm Vitamin C, C25: 25 ppm Vitamin C, C50: 50 ppm Vitamin C, C75: 75 ppm Vitamin C.

Table 2. Peroxidase Activity, Total protein and Advanced Oxidized Protein.

Application	POD (U g⁻¹ dw)	Total Prot. (mg g⁻¹ dw)	AOP (µmol Cloramine T g⁻¹ dw)
Control	55.63±0.97	72.76±1.46	6.75±0.12
Ven-1	80.20±1.45 [a]	65.92±0.87 [a]	8.50±0.15 [a]
Ven-2	100.55±1.80 [a]	59.38±1.06 [a]	10.10±0.19 [a]
Ven-3	110.91±1.77 [a]	54.50±1.02 [a]	11.95±0.20 [a]
Ven-4	117.54±1.82 [a]	51.14±0.96 [a]	13.10±0.21 [a]
Ven-5	124.40±1.98 [a]	48.85±0.84 [a]	14.25±0.20 [a]
Ven-1+C10	72.40±1.16 [b]	67.24±1.15 [c]	7.90±0.13 [b]
Ven-1+C25	65.51±1.13 [b]	69.30±0.82 [b]	7.41±0.11 [b]
Ven-1+C50	59.66±1.09 [b]	70.24±1.31 [b]	7.00±0.10 [b]
Ven-1+C75	56.16±1.02 [b]	72.58±1.42 [b]	6.70±0.07 [b]
Ven-2+C10	89.65±1.19 [b]	61.47±0.90 [c]	9.15±0.16 [b]
Ven-2+C25	78.21±1.10 [b]	63.78±0.96 [b]	8.53±0.15 [b]
Ven-2+C50	69.05±0.93 [b]	65.31±1.00 [b]	8.00±0.11 [b]
Ven-2+C75	60.69±0.87 [b]	67.58±1.08 [b]	7.35±0.09 [b]
Ven-3+C10	97.38±1.49 [b]	57.52±0.95 [b]	10.90±0.14 [b]
Ven-3+C25	84.59±1.17 [b]	59.78±0.98 [b]	9.76±0.12 [b]
Ven-3+C50	75.67±1.04 [b]	63.04±0.99 [b]	8.92±0.10 [b]
Ven-3+C75	67.58±0.96 [b]	65.90±1.02 [b]	8.52±0.12 [b]
Ven-4+C10	106.97±1.46 [b]	53.73±0.73 [c]	12.25±0.17 [b]
Ven-4+C25	93.47±1.45 [b]	56.87±0.88 [b]	11.54±0.15[b]
Ven-4+C50	82.85±1.04 [b]	59.15±1.02 [b]	10.95±0.13 [b]
Ven-4+C75	70.06±1.02 [b]	62.84±1.10 [b]	9.95±0.12 [b]
Ven-5+C10	109.60±1.86 [b]	51.00±0.87 [c]	13.60±0.12 [b]
Ven-5+C25	96.48±1.64 [b]	53.10±0.89 [b]	12.75±0.13 [b]
Ven-5+C50	84.80±1.62 [b]	55.90±0.93 [b]	11.50±0.15 [b]
Ven-5+C75	74.10±1.31 [b]	59.50±1.00 [b]	10.74±0.10 [b]

Ven-1: 100 ppm Venlafaxine, Ven-2: 200 ppm Venlafaxine, Ven-3: 300 ppm Venlafaxine, Ven-4: 400 ppm Venlafaxine, Ven-5: 500 ppm Venlafaxine, C10: 10 ppm Vitamin C, C25: 25 ppm Vitamin C, C50: 50 ppm Vitamin C, C75: 75 ppm Vitamin C

The effects of vitamin C on the oxidative DNA damage and mutagenesis were investigated by Nikolic et al. [23] using *S. cerevisiae* and *Escherichia coli* microorganisms, and they reported that vitamin C had a reducing effect on oxidative stress. Due to this feature of vitamin C, 10 - 75 ppm vitamin C was added to the medium containing venlafaxine.

SOD, CAT, GSH-Px, GSH-Rd and POD are very important for restoring the oxidative balance, which is disrupted as a result of metabolic events in the cell by external factors. It was determined that *S. cerevisiae*, which was stressed by adding different concentrations of venlafaxine to the medium, increased the SOD and CAT activities. Whereas vitamin C added to the medium containing venlafaxine decreased these enzyme activities depending on its concentration ($p < 0.05$) (Table 1).

The SOD enzyme converts the superoxide radical anion to the less toxic hydrogen peroxide (H_2O_2) and oxygen. CAT in an important enzyme in cellular detoxification converts

H_2O_2 into water and oxygen. Another function of catalase, which is considered as a hemoprotein is present in all animal cells and aerobic microorganisms and contributes to the cell's defense system [24, 25].

In the study investigating the effect of *S. cerevisiae* against S-nitroso glutathione-induced stress, it was reported that SOD and CAT enzyme activities increased [26]. It was determined that GSH-Px and GSH-Rd activities of *S. cerevisiae* increased due to the oxidative stress caused by venlafaxine added to the medium. while vitamin C added to the medium containing venlafaxine decreased GSH-Px and GSH-Rd activities ($p<0.05$) (Table 1). According to the results of a study carried out stress caused by cadmium on *Rhizobium leguminosarum*, they reported the increased activities of GSH-Rd and GSH Px [27]. It has been reported that GSH-Rd and GSH-Px enzyme activities increased in *S. cerevisiae* cells grown in $KMnO_4$-containing medium [28].

Table 3. Concentrations of stress biomarkers in S. cerevisiae produced in a nutrient medium.

Application	GSH ($\mu g\ g^{-1}\ dw$)	GSSG ($\mu g\ g^{-1}\ dw$)	MDA ($\mu g\ g^{-1}\ dw$)	4-HNE ($\mu g\ g^{-1}\ dw$)	GSH/GSSG
Control	2950±20.30	245±2.18	8.20±0.13	4.10±0.06	12
Ven-1	2860±13.34 [a]	285±2.03 [a]	9.00±0.13 a [a]	4.60±0.05 [a]	10
Ven-2	2700±17.98 [a]	320±2.09 [a]	9.75±0.14 [a]	5.20±0.06 [a]	8.44
Ven-3	2630±18.27 [a]	360±2.20 [a]	10.30±0.14 [a]	5.90±0.08 [a]	7.31
Ven-4	2550±17.40 [a]	405±2.32 [a]	11.00±0.15 [a]	6.50±0.09 [a]	6.30
Ven-5	2480±16.70 [a]	460±2.32 [a]	11.68±0.15 [a]	7.10±0.09 [a]	5.40
Ven-1+C10	2880±18.56 [c]	273±2.03 [b]	8.75±0.12 [c]	4.52±0.06 [c]	10.55
Ven-1+C25	2907±12.76 [b]	260±1.97 [b]	8.55±0.12 [b]	4.41±0.05 [b]	11.17
Ven-1+C50	2930±17.98 [b]	253±1.86 [b]	8.40±0.11 [b]	4.36±0.05 [b]	11.58
Ven-1+C75	2955±18.27 [b]	246±1.86 [b]	8.10±0.10 [b]	4.22±0.05 [b]	12.00
Ven-2+C10	2760±16.82 [c]	305±1.91 [b]	9.45±0.12 [c]	5.12±0006 [c]	9.05
Ven-2+C25	2805±17.11 [b]	290±1.86 [b]	9.15±0.11 [b]	4.98±0.06 [b]	9.67
Ven-2+C50	2855±17.40 [b]	273±1.80 [b]	8.76±0.10 [b]	4.88±0.05 [b]	10.46
Ven-2+C75	2910±17.69 [b]	259±1.71 [b]	8.35±0.09 [b]	4.72±0.05 [b]	11.24
Ven-3+C10	2695±16.24 [b]	345±1.80 [b]	9.90±0.12[c]	5.75±0.07 [c]	7.81
Ven-3+C25	2750±15.08 [b]	330±1.74 [b]	9.50±0.12 [b]	5.62±0.06 [b]	8.33
Ven-3+C50	2810±15.20 [b]	315±1.68 [b]	9.15±0.11 [b]	5.48±0.06 [b]	8.92
Ven-3+C75	2880±15.02 [b]	292±1.51 [b]	8.70±0.10 [b]	5.34±0.06 [b]	9.86
Ven-4+C10	2605±14.50 [c]	348±2.03 [b]	10.40±0.13 [b]	6.36±0.08 [c]	7.49
Ven-4+C25	2660±14.50 [b]	331±1.97 [b]	9.95±0.12 [b]	6.15±0.06 [b]	8.04
Ven-4+C50	2705±14.21 [b]	316±1.86 [b]	9.54±0.12 [b]	5.90±0.06 [b]	8.56
Ven-4+C75	2770±14.50 [b]	298±1.74 [b]	8.90±.0.10 [b]	5.72±0.06 [b]	9.30
Ven-5+C10	2525±13.34 [c]	445±2.20 [b]	11.05±0.13 [b]	6.95±0.08 [c]	5.67
Ven-5+C25	2590±13.92 [b]	430±2.09 [b]	10.60±0.12 [b]	6.80±0.07 [b]	6.02
Ven-5+C50	2645±14.21 [b]	413±2.00 [b]	10.00±0.12 [b]	6.62±0.06 [b]	6.40
Ven-5+C75	2700±14.50 [b]	390±1.97 [b]	9.40±0.11 [b]	6.45±0.06 [b]	6.92

Ven-1: 100 ppm Venlafaxine, Ven-2: 200 ppm Venlafaxine, Ven-3: 300 ppm Venlafaxine, Ven-4: 400 ppm Venlafaxine, Ven-5: 500 ppm Venlafaxine, C10: 10 ppm Vitamin C, C25: 25 ppm Vitamin C, C50: 50 ppm Vitamin C, C75: 75 ppm Vitamin C.

Peroxidase activity is used as a stress marker by many researchers. Studies conducted on many plant species, it has been emphasized that peroxidase activity increases rapidly as a result of the plant's uptake of heavy metals [29]. In a similar way in our studies, it was observed that POD enzyme activity increased ($p<0.05$) due to oxidative stress caused by venlafaxine, while vitamin C added to the same medium caused a decrease in POD activity ($p<0.05$) (Table 2). It has been reported that there is a significant increase in POD activity of *Bacillus subtilis* and *Pseudomonas putida* bacteria under heavy metal stress [30]. It is very important to preserve the protein structure for the continuation of the functions in the cells. Proteins are highly sensitive to oxidative damage, and cellular metabolism is negatively affected when their structures are disrupted [31]. It was observed that the amount of total protein decreased and the amount of AOP increased as the increasing concentrations of venlafaxine added to the broth of *S. cerevisiae* ($p<0.05$). It was determined that vitamin C added to venlafaxine-containing media increased the total protein and decreased the amount of oxidized protein ($p<0.05$) (Table 2). It was determined that carbon tetrachloride (CCl_4) added to the nutrient medium decreased the total protein amount in *S. cerevisiae*, while clove plant extract added as an antioxidant significantly increased the total protein amount [32]. It has been reported that the amount of AOP increases at the end of the 6th and 9th hours in *S. cerevisiae*, which is stressed by applying a magnetic field [33].

GSH is especially important for the transport of amino acids keeping the sulfhydryl groups in proteins in a reduced state and acting as a coenzyme in some enzymatic reactions [34]. GSH and GSSG are important indicators of cellular redox status and organismal health. Therefore, reduced glutathione ratio to oxidized glutathione is also known as a stress indicator [35].

Our results showed that while amount of GSH decreased. GSSG increased due to the oxidative stress caused by the addition of venlafaxine to the medium. It was seen that the amount of GSH increased and the amount of GSSG decreased with the addition of vitamin C to media containing venlafaxine. While the ratio of GSH/GSSG, decreased depending on the concentration of venlafaxine. addition of vitamin C to medium caused to increase this ratio, due to antioxidant properties of vitamin C (Table 3). It has been reported that cadmium addition to the growth medium increases the amount of GSSG while decreasing the amount of GSH in *Citrobacter Freundii*, and this situation is reversed with the addition of vitamin C to the medium [20]. As a result of lipid peroxidation, MDA and 4-HNE, which are considered stress biomarkers, are formed [17]. It was observed that the amount of MDA and 4-HNE increased

depending on the concentration of venlafaxine added to the *S. cerevisiae* medium, on the other hand, the amount of MDA and 4-HNE decreased with the addition of vitamin C to the same medium (Table 3). It has been reported that heavy metals applied to the *S. cerevisiae* medium increase the amount of GSSG and MDA, while decreasing the GSH/GSSG ratio and the amount of GSH [36].

Vitamin C is a good singlet oxygen scavenger that neutralizes ROS, reduces oxidative stress [37]. It can be concluded that other antioxidant systems are less affected by oxidative stress due to the antioxidant effect of vitamin C.

4 CONCLUSION AND SUGGESTIONS

With the increase of venlafaxine concentration added to YPD medium, it was observed that antioxidant enzyme activities, the amounts of GSSG, AOP, MDA, 4-HNE increased, while the amount of GSH and total protein decreased.

Similarly, with the increase of vitamin C concentration in the growth medium of *S. cerevisiae*, reduced the negative effects of venlafaxine on all the measured parameters.

Conflict of Interest Statement

There is no conflict of interest between the authors.

Statement of Research and Publication Ethics

The study is complied with research and publication ethics.

Artificial Intelligence (AI) Contribution Statement

This manuscript was entirely written, edited, analyzed, and prepared without the assistance of any artificial intelligence (AI) tools. All content, including text, data analysis, and figures, was solely generated by the authors.

Contributions of the Authors

Meltem Çakmak: Resources, Methodology, Research, Formal analysis, **Dursun Özer**: Data curation, Conceptualization, Writing – original draft, Visualization, Validation, **Fikret Karataş**: Data curation, Conceptualization, Writing – original draft, Visualization, Validation, **Sinan Saydam**: Writing – review & editing, Visualization.

REFERENCES

[1] A. M. Gil-rodriguez, A. V. Carrascosa, T. Requena, "Yeasts in foods and beverages: *In vitro* characterisation of probiotic traits"*, LWT-Food Science and Technology,* vol. 64, no. 2, pp. 1156–1162. December, 2015. doi: 10.1016/j.lwt.2015.07.042.

[2] H. Albergaria, N. Arneborg, "Dominance of *Saccharomyces cerevisiae* in alcoholic fermentation processes: role of physiological fitness and microbial interactions"*, Applied Microbiology and Biotechnology,* vol. 100, no. 5, pp. 2035–2046, 2016. https://doi.org/10.1007/s00253-015-7255-0.

[3] H. J. Möller, I. Bitter, J. Bobes, K. Fountoulakis, C. Höschl, S. Kasper, "Position statement of the European Psychiatric Association (EPA) on the value of antidepressants in the treatment of unipolar depression", *European Psychiatry*, vol. 27, no. 2, pp. 114-128. February, 2012, https://doi.org/10.1016/j.eurpsy.2011.08.002.

[4] R. Gadassi, N. Mor, "Confusing acceptance and mere politeness: Depression and sensitivity to Duchenne smiles", *Journal of Behavior Therapy and Experimental Psychiatry,* vol. 50, pp. 8-14, March, 2016. doi: 10.1016/j.jbtep.2015.04.007.

[5] M. Çetin, C. Açıkel, "Meta-analizler ışığında: bütün antidepresanlar aynı mıdır?", *Klinik Psikofarmakoloji Bülteni*, vol. 19, no. 2, pp. 87-92. 2009. www.psikofarmakoloji.org.

[6] E. Birben, U. M. Sahiner, C. Sackesen, S. Erzurum, O. Kalayci, "Oxidative stress and antioxidant defense", *World Allergy Organization Journal,* vol. 5, no. 1, pp. 9-19, January, 2012. doi: 10.1097/WOX.0b013e3182439613.

[7] S. J. Devaki, R. L. Raveendran, "Vitamin C: sources, functions, sensing and analysis"*, INTECH,* pp. 1-20. *Agust,* 2017. doi: 10.5772/intechopen.70162.

[8] C. Paciolla, S. Fortunato, N. Dipierro, A. Paradiso, S. De Leonardis, L. Mastropasqua, M. C. De Pinto, "Vitamin C in plants: from functions to biofortification", *Antioxidants,* vol. 8, no. 11, pp. 519, October, 2019. https://doi.org/10.3390/antiox8110519.

[9] Y. M. Janssen-Heininger, B. T. Mossman, N. H. Heintz, H. J. Forman, B. Kalyanaraman, T. Finkel, A. van der Vliet, "Redox-based regulation of signal transduction: principles, Pitfalls, and promises", *Free Radical Biology and Medicine*, vol. 45, no. 1, pp. 1-17, Jule 2008. doi: 10.1016/j.freeradbiomed.2008.03.011.

[10] O. M. Ighodaro, O. A. Akinloye, "First line defence antioxidants-superoxide dismutase (SOD), catalase (CAT) and glutathione peroxidase (GPX): Their fundamental role in the entire antioxidant defence grid", *Alexandria Journal of Medicine,* vol. 54, pp. 287–293, 2018. https://doi.org/10.1016/j.ajme.2017.09.001

[11] H. Sies, "Oxidative stress: eustress and distress in redox homeostasis, In Stress: physiology, biochemistry and pathology, *Handbook of Stress Series,* vol. 3, pp. 153-163. 2019. doi.org/10.1016/B978-0-12-813146-6.00013-8.

[12] A. A. Adwas, A. S. I. Elsayed, A. E. Azab, F. A. Quwaydir, "Oxidative stress and antioxidant mechanisms in human body", *Journal of Applied Biotechnology & Bioengineering, vol. 6*, no. 1, pp. 43-47, February, 2019. doi: 10.15406/jabb.2019.06.00173.

[13] E. Shacter, "Quantification and significance of protein oxidation in biological samples", *Drug Metabolism Reviews,* vol. 32, no. 3-4, pp. 307-326. Aug-Nov; 2000. doi: 10.1081/dmr-100102336.

[14] E. R. Stadtman, R. L. Levine, "Free radical-mediated oxidation of free amino acids and amino acid residues in proteins"*, Amino Acids,* vol. 25, no. 3-4, pp. 207-218, January, 2004. doi: 10.1007/s00726-003-0011-2.

[15] S. S. Gill, N. A. Anjum, M. Hasanuzzaman, R. Gill, D. K. Trivedi, I. Ahmad, N. Tuteja, "Glutathione and glutathione reductase: a boon in disguise for plant abiotic stress defense operations"*, Plant Physiology and Biochemistry*, vol. 70, pp. 204-212, September, 2013. https://doi.org/10.1016/j.plaphy.2013.05.032.

[16] D. Mendoza-Cózatl, H. Loza-Tavera, A. Hernández-Navarro, R. Moreno-Sánchez, "Sulfur assimilation and glutathione metabolism under cadmium stress in yeast, photosynthetic protists and plants", *FEMS Microbiology Reviews, v*ol. 29, no. 4, pp. 653–671, 2005. doi: 10.1016/j.femsre.2004.09.004.

[17] S. Gaweł, M. Wardas, E. Niedworok, P. Wardas, "Malondialdehyde as lipid peroxidation marker, *Wiadomości Lekarskie,* vol. 57, no. 9-10, pp. 453-455, February, 2004. PMID: 15765761.

[18] G. Cazzanelli, F. Pereira, S. Alves, R. Francisco, L. Azevedo, P. Dias Carvalho, A. Almeida, M. Côrte-Real, M. J. Oliveira, C. Lucas, M. J. Sousa, A. Preto, "The yeast *Saccharomyces cerevisiae* as a model for

understanding RAS proteins and their role in human tumorigenesis", *Cells,* vol. 7, no. 2, pp. 1-35, February, 2018. doi: 10.3390/cells7020014.

[19] M. Çakmak, D. Özer, F. Karataş, S. Saydam, "Effect of venlafaxine on the vitamins contents of *Saccharomyces cerevisiae* (NRRLY-12632)", *Journal of Advanced Research in Natural and Applied Sciences,* vol. 10, no. 1, pp. 218-227, 2024. https://doi.org/10.28979/jarnas.1397331.

[20] M. S. Ibrahim, M. Çakmak, D. Özer, F. Karatas, S. Saydam, "Effect of cadmium and vitamin C on *Citrobacter Freundii's* antioxidant enzymes and stress markers", *Afyon Kocatepe University Journal of Sciences and Engineering,* vol. 22, pp. 23-3*2,* 2022. https://doi.org/10.35414/akufemubid.1007756.

[21] Y. I. Sun, L. W. Oberley, Y. Li, *"*A simple method for clinical assay of superoxide dismutase", *Clinical Chemistry,* vol. 34, no. 3, pp. 497-500, March, 1988. PMID: 3349599.

[22] V. Witko-Sarsat, M. Friedlander, C. Capeillère-Blandin, T. Nguyen-Khoa, A. T. Nguyen, J. Zingraff, P. Lungers, B. Descamps-Latscha, "Advanced oxidation protein products as a novel marker of oxidative stress in uremia", *Kidney International,* vol. *49, no. 5, pp.* 1304-1313, May, 1996. doi: 10.1038/ki.1996.186.

[23] B. Nikolic, J. Stanojevic, B. Vukovic-Gacic, D. Simic, J. Knezevic-Vukcevic, "The effects of vitamin C on oxidative DNA damage and mutagenesis", *Food Technology and Biotechnology*, vol. 44, no. 4, pp. 449–456, October, 2006. ISSN 1330-9862.

[24] E. Çöteli, F. Karataş, "Krom III klorür tuzuna maruz kalan mayalara C vitamini katılarak mayaların antioksidan enzimlerine etkisinin araştırılması", *Gümüşhane Üniversitesi Fen Bilimleri Dergisi,* vol. 11, no. 4, pp. 1071-1081, 2021. https://doi.org/10.17714/gumusfenbil.909183.

[25] L. Sheng, X. Zheng, H. Tong, S. Liu, J. Du, Q. Liu, "Purification and characterization of cytosolic isoenzyme III of Cu. Zn-superoxide dismutase from tobacco leaves", *Plant Science,* vol. 167, no. 6, pp. 1235-1241, December, 2004. https://doi.org/10.1016/j.plantsci.2004.06.022.

[26] O. V. Lushchak, V. I. Lushchak, "Catalase modifies yeast *Saccharomyces cerevisiae* response towards S-nitrosoglutathione-induced stress", *Redox Report*, Vol. *13, no. 6, pp.* 283-291, 2008. doi: 10.1179/135100008X309037.

[27] S. C. Corticeiro, A. I. G. Lima, E. M. d. A. P. Figueira, "The importance of glutathione in oxidative status of Rhizobium leguminosarum biovar viciae under Cd exposure", *Enzyme and Microbial Technology,* vol. 40, no. 1, pp. 132-137, December, 2006. doi: 10.1016/j.enzmictec.2005.10.053.

[28] H. Chen, X. Cao, N. Zhu, L. Jiang, X. Zhang, Q. He, P. Wei, "A stepwise control strategy for glutathione synthesis in *Saccharomyces cerevisiae* based on oxidative stress and energy metabolism", *World Journal of Microbiology and Biotechnology,* vol. 36, no.8, pp. 1-10, July, 2020. doi: 10.1007/s11274-020-02895-2.

[29] A. Chaoui, B. Jarrar, E. E. Ferjani, "Effects of cadmium and copper on peroxidase. NADH oxidase and IAA oxidase activities in cell wall, soluble and microsomal membrane fractions of pea roots", *Journal of Plant Physiology,* vol. 161, no. 11, pp.1225-1234, November, 2004. https://doi.org/10.1016/j.jplph.2004.02.002.

[30] K. A. Hussein, J. H. Joo, "Heavy metal resistance of bacteria and its impact on the production of antioxidant enzymes", *African Journal of Microbiology Research,* vol. 7, no. 20, pp. 2288-2296, May, 2013. doi: 10.5897/AJMR12.1764.

[31] S. Reeg, T. Grune, "Protein oxidation in aging: does it play a role in aging progression?" *Antioxidants & Redox Signaling,* vol. 23, no. 3, pp. 239-255, July, 2015. doi: 10.1089/ars.2014.6062.

[32] S. Beyaz, "*Saccharomyces cerevisiae*'de Karbon Tetraklorür (CCl₄) ile oluşturulan oksidatif hasara karşı karanfil (*Syzygium aromaticum* L.) ekstraktının koruyucu etkilerinin glutatyon. malondialdehit ve total protein düzeyleri ile araştırılması", *Journal of the Institute of Science and Technology*, vol. 12, no. 2, pp. 597-608, 2022. https://doi.org/10.21597/jist.1057451

[33] A. Kthiri, S. Hidouri, T. Wiem, R. Jeridi, D. Sheehan, A. Landouls, "Biochemical and biomolecular effects induced by a static magnetic field in *Saccharomyces cerevisiae*: Evidence for oxidative stress", *Plos one,* vol. 14, no. 1, pp. e0209843. January, 2019. doi: 10.1371/journal.pone.0209843.

[34] B. A. Arrick, C. F. Nathan, "Glutathione metabolism as a determinant of therapeutic efficacy: a review", *Cancer Research,* vol. 44, no. 10, pp. 4224-4232, Octaber, 1984. PMID: 6380705.

[35] N. H. P. Cnubben, I. M. C. M. Rietjens, H. Wortelboer, J. Van Zanden, P. J. Van Bladeren, "The interplay of glutathione-related processes in antioxidant defense", *Environmental Toxicology and Pharmacology,* vol. 10, no. pp. 141-152, September, 2001. doi: 10.1016/s1382-6689(01)00077-1.

[36] O. A. Kireçci, "Mn, Cd, Fe ve Mg Metallerinin *Saccharomyces cerevisiae* mayasında antioksidan enzim aktiviteleri üzerine etkisi", *Kahramanmaraş Sütçü İmam Üniversitesi Tarım ve Doğa Dergisi,* vol. 21, no. 4, pp. 520-528, 2018. https://doi.org/10.18016/ksudobil.359165.

[37] K. S. El-Gendy, N. M. Aly, F. H. Mahmoud, A. Kenawy, A. K. H. El-Sebae, "The role of vitamin C as antioxidant in protection of oxidative stress induced by imidacloprid"*, Food and Chemical Toxicology,* vol. 48, no. 1, pp. 215-221, January, 2010. doi: 10.1016/j.fct.2009.10.003.

A PRELIMINARY EXPERIMENTAL STUDY ON THE COMPARISON OF CONCRETE STRENGTH TESTS AND BOHME ABRASION TEST FOR BASALT AGGREGATE CONCRETE

Esra TUGRUL TUNC [1] iD

[1] *Fırat University, Civil Engineering Department, Elazığ, Türkiye, esratugrul@firat.edu.tr*

ABSTRACT

It is very important to determine whether the strength of concrete structures, especially under the effect of earthquakes, is sufficient to prevent loss of property and life. In this context; the tests required for the concrete to be used in the structure should determine the most suitable concrete properties for the intended use of the structures. With the present study, by utilizing basalt aggregate in concrete production, both concrete strengths will be increased and economic contribution will be provided since its reserves are abundant. In addition to the concrete compressive strength and concrete splitting tensile strength tests performed on structural concrete for the building of earthquake-resistant structures, alternative strength tests should also be tested to determine the mechanical properties of concrete with the developments in concrete production and application technologies. One of them is the Bohme abrasion strength test, which is performed to determine the resistance to abrasion. In the present study, concrete compressive strength, concrete splitting tensile strength, and Bohme abrasion strength tests were performed experimentally for a series of conventional concrete specimens produced using basalt aggregate. Relatively high concrete strength values were obtained for the tested concrete specimens. It was observed that the concrete compressive strength value and concrete splitting tensile strength value increased in direct proportion to each other, while the Bohme abrasion loss value decreased with a high determination coefficient. Thus, it indicates that the concrete strength increases with decreasing Bohme abrasion loss value.

Keywords:	Bohme abrasion strength, Compressive strength, Splitting tensile strength, Basalt aggregate, Earthquake.

1   INTRODUCTION

Since Türkiye is located in a geography surrounded by the Eurasian, African, and Arabian active fault plates that can produce earthquakes, it has been exposed to many destructive earthquakes throughout history and is still at earthquake risk [1]. When the earthquakes that occurred in Türkiye in the last century are analyzed; it is seen that 16 destructive earthquakes above magnitude 7.0 occurred (Figure 1). Especially after the earthquakes in recent years, it has been determined that there have been many losses of life and property, and many structures were severely damaged [2], [3].

As a result of the investigations made as a result of the earthquakes experienced; it was concluded that the damaged or collapsed structures were mostly produced from poor-quality concrete [4], [5]. Thus, there is a need for more research on the production of concrete, which has a great impact on the durability of structures. In addition, it has become essential to design sustainable and economical concrete production by performing concrete strength tests more meticulously and ensuring that the mix content and mix ratios are optimum for the purpose. For this reason, it is of great importance to investigate the effect of aggregates, which constitute a large part of the content of concrete, on concrete strength. In this context; in order to increase the strength of concrete produced with traditional aggregates, there is a lack of literature and practice in literature and practice on the production of concrete that can be produced with higher strength aggregates with Türkiye's own resources. It is known that the existing building stocks worldwide generally consist of reinforced concrete structures and Türkiye has a high ratio of concrete production. In the present study, basalt aggregates, which are known to have higher strength than other aggregates, were tested for a series of basalt concrete specimens produced. Since it is known that basalt aggregate reserves in our country are quite high, it is thought that it will be economical to use it in concrete production [6].
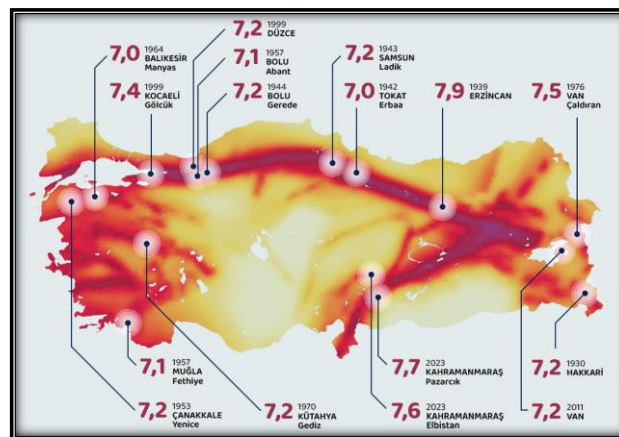
Figure 1. Türkiye earthquake map [7].

Concrete is the most common building material required for the construction of reinforced concrete structures, which is formed by combining aggregate materials such as gravel and sand with a binder material such as cement. The annual consumption of concrete in the world is estimated to be quite high, at around 6 billion m3 [8]. Concrete aggregate is defined as the unbroken or crushed grains of natural or artificial material that are mixed with the binding material consisting of cement and water mixture in concrete production. The diameter of concrete aggregate used in construction concrete is generally less than 63 mm [9].

Concrete aggregate has the largest volume and mass among concrete components. Aggregates are very important for the properties of concrete, as they usually account for about 60-80% of the total volume of concrete. Aggregate is not only an economical filling material for concrete but also an important component that increases the durability, abrasion resistance, and bearing capacity of concrete. In addition, it is possible to say that the physical and mechanical properties of concrete are largely influenced by the aggregate properties used. In this context, the physical and mechanical properties of the tested concrete aggregate directly determine the quality of the concrete [10].

Concrete producers should definitely evaluate the quality and economic conditions when choosing aggregate. Necessary tests of the aggregate to be used in concrete production should be carried out and especially 7-28 day compressive strengths of hardened concrete specimens containing the tested aggregate should be measured. In general, concrete aggregate should be hard, durable, void-free, and resistant to abrasion [11]. Experiments such as sieve analysis, specific gravity, and water absorption should be performed on concrete aggregates to have an idea about aggregate quality. In our country, concrete aggregates are required to comply with the TS 706 EN 12620 +A1 standard [12].

It is known that limestone aggregate is widely used in traditional concrete. However, basalt aggregate can also be preferred for more durable concrete production. Because basalt is a hard, dense volcanic rock that can be found in many regions of the world. Previously used only in architectural applications and pavements, basalt has recently been used in concrete production as crushed basalt aggregate. Basalt aggregate concrete, which is generally ideal for highway and airport pavements, is also known to have high abrasion resistance and high compressive strength. It has been determined that the specific gravity of basalt aggregate is higher than that of limestone aggregate used in traditional concrete production, while its abrasion loss and water absorption value are lower [13], [14].

Concrete used as pavement in road superstructure is subject to abrasion due to friction in bridge abutments and dams exposed to water flow. The abrasion resistance of concrete varies depending on the strength characteristics of the concrete, the internal structure of the concrete, the construction of the concrete surface, and the test method used. It is known that the most common test to determine the abrasion resistance of concrete is the Bohme (Dorry Device) Test [15], [16], [17].

For the Bohme abrasion test, firstly, concrete specimens with standard dimensions and a certain water-to-cement ratio are manufactured and left to cure for a certain period of time. After the weights of the cured specimens are measured with a precision balance, they are abraded in the Bohme abrasion device at the specified time and speed. After the abrasion process, the weights of the specimens are measured again. Based on the weight loss and the change in the dimensions of the specimen, the volume change is calculated. Using the data obtained, the abrasion resistance of the concrete is determined. The values obtained as a result of the Bohme abrasion test are an important parameter showing the resistance of concrete against abrasion. These values are used for the comparison of different concrete mixtures, material selection, and quality control. The bohme abrasion test is performed according to national and international standards such as TS 699. These standards contain detailed information on the conduct of the test, the equipment used, specimen preparation, and evaluation of the results. In conclusion; the Bohme abrasion test is an important method used to determine the resistance of building materials such as concrete against abrasion. Thanks to this test, structures are ensured to be longer lasting and safer [18], [19].

In a study [20] investigating the abrasion resistance of natural building blocks under different loads between 100 N and 500 N, the widely used Bohme abrasion tester was used to determine the abrasion properties. It was concluded that abrasion loss was an important factor depending on the load on the tested natural building blocks. In another study [21], the wide wheel abrasion test and Bohme abrasion test were performed to determine the abrasion loss of 21 different building stones from the Denizli province of Türkiye and it was determined that the findings obtained from these test methods were very close to each other. In another study [22], it was stated that the effect of aggregate properties on mechanical properties such as wear and strength is very important depending on the intended use.

Concrete's abrasion resistance primarily depends on the aggregate it contains, as aggregates typically comprise a larger portion of the material than cement [23]. The aggregate's properties, including specific gravity, hardness, and void ratio, influence its abrasion resistance.

Certain aggregates, like glass, schist, marly limestone, and coarse mineralized stones, are susceptible to abrasion. To enhance concrete's abrasion resistance, using hard, abrasion-resistant aggregates is crucial. The availability and mechanical properties of aggregates are key factors to consider in concrete production. Abrasion resistance is a significant parameter in evaluating aggregate suitability for concrete applications [24].

Various tests have been employed in the literature to assess the abrasion resistance of concrete aggregates [23, 25]. In a previous study [26], marble powder and sand were partially replaced with different proportions (10-90% by volume) and subjected to the Bohme surface abrasion test on 28-day specimens. The results indicated a correlation between abrasion resistance and compressive and splitting tensile strengths, key indicators of concrete strength. The optimal mixture contained 40% marble dust. Another study [27] applied the Bohme abrasion test to tile mosaic floor coverings reinforced with steel fiber. Abrasion resistance was evaluated using volume and average surface abrasion values, with results of 9.3 ± 0.3 cm^3/cm^2.

In the present study; primarily the aim is to test concrete strength experimentally. In this context; concrete compressive strength, concrete splitting tensile strength, and concrete Bohme abrasion value of a series of concrete specimens containing basalt aggregate produced in the present laboratory were measured experimentally. It is known that the basic tests determining concrete quality are compressive strength and splitting tensile strength tests [28], [29]. With this study, the relationship between the Bohme abrasion value of concrete and concrete strength is revealed and it is determined that the Bohme abrasion value is a test that can be evaluated in determining concrete properties and quality [30], [31]. Thus, the studies to be carried out on the subject, it is aimed to evaluate and disseminate the Bohme abrasion test, which is seen to be a great deficiency in the literature, together with the existing destructive strength tests.

Since a large amount of concrete is used in the construction of buildings, the durability of the structure against a possible earthquake is directly related to the durability of concrete. Concrete strength is directly related to the aggregate properties. In the present study, concrete compressive strength, concrete splitting tensile strength and Bohme abrasion tests were performed experimentally on a series of basalt aggregate concrete specimens. The aim of the present study is to compare the related strength and abrasion tests for basalt aggregate concrete and to determine the relationship between them. For this purpose, within the scope of the present study, the relationship between the change in Bohme abrasion loss and concrete strength was experimentally investigated.

2   MATERIAL AND METHOD

2.1   Experimental Materials

Basalt aggregate from ready-mixed concrete companies in Elazığ province of Türkiye was used in the present study (Figure 2). Specific gravity, unit weight, and water absorption rate values of aggregate mixtures with the largest grain diameter of 31.5 mm are presented in Table 1 [32].
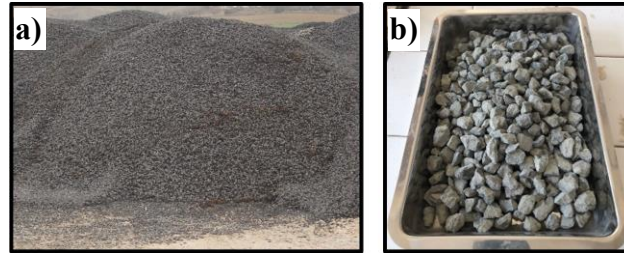
Figure 2. View of tested basalt aggregate in the present study: a) view from the aggregate quarry, b) view from the laboratory.

Table 1. Specific gravity, unit weight, and water absorption ratio values of tested basalt aggregate.

G_{coarse}	G_{fine}	W_{coarse}	W_{fine}	A_{coarse}	A_{fine}
2.87	2.83	1.87	1.85	0.7	1.4

In Table 1; G_{coarse}: coarse basalt aggregate specific gravity, G_{fine}: fine basalt aggregate specific gravity, W_{coarse}: coarse basalt aggregate unit weight, W_{fine}: fine basalt aggregate unit weight, A_{coarse}: coarse basalt aggregate water absorption rate and A_{fine}: fine basalt aggregate water absorption rate.

The granulometry curve of the aggregate mixture to be used in the concrete mix design calculation according to TS 802 is given in Figure 3. The best compactness was achieved with the curve graph of the mixture falling into the A-B region (except 16.0 mm and 0.125 mm).
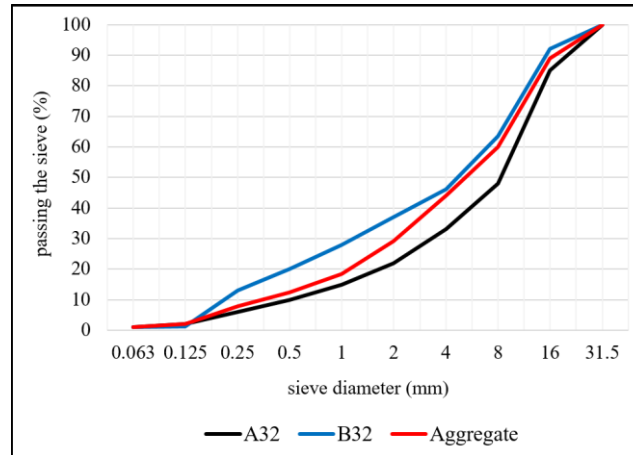
Figure 3. Granulometry of the mixture basalt aggregate prepared according to TS 802.

The cement used in the present experimental studies is CEM I 42.5 N Portland cement produced in Elazığ Cement Factory. The physical and chemical properties of this cement type are presented in detail in Table 2.

Table 2. Physical and chemical properties of the cement used in the present study.

physical properties	test results
specific gravity (gr/cm^3)	3.03
setting start (min.)	155
setting end (min.)	210
finesse (cm^2/gr)	3490
chemical composition	mass percent
SiO_2 (%)	21.12
Al_2O_3 (%)	5.62
Fe_2O_3 (%)	3.24
CaO (%)	62.94
Cl^-	0.0044
insoluble residue	0.64
glow loss	3.52

2.2 Concrete Compressive Strength Test

The compressive strength test was carried out in accordance with TS EN 12390-3 standard [33] and concrete cube specimens with dimensions of 150×150×150 mm were tested to determine the strength. At the end of the 28-day curing period, the related concrete cube specimens removed from the curing pool were subjected to uniaxial compression test in the laboratory environment and their compressive strength was determined. A compressive press with a capacity of 2000 kN was used for the said test and at the end of the test, the compressive strength value was taken on the computer screen (Figure 4a). The specimens placed in the

device were loaded at a constant speed of 6.8 MPa/sec, the fracture loads were determined and the compressive strengths were calculated by Equation (1).

$$f_c = \frac{P}{A} \qquad (1)$$

In Eq. (1); f_c= represents the compressive strength value (MPa), P= represents the maximum load (N) that causes the specimen to fracture and A= represents the cross-sectional area (mm^2) of the specimen perpendicular to the direction of load application.

2.3   Concrete Splitting Tensile Strength Test

Similar to the compressive strength test, at the end of the 28-day curing period, tensile strength at splitting test was performed on the tested concrete cube specimens with dimensions of 150×150×150×150 mm in accordance with TS EN 12390-6 standard [34] (Figure 4b). The specimens placed in the device were loaded at a constant speed of 1.05 MPa/sec, the fracture loads were determined and the splitting tensile strength was calculated by Eq. (2). For each series, 3 control specimens were tested and the strength results were evaluated as the arithmetic average of these three specimens.

$$f_t = \frac{2\,P}{\pi\,D^2} \qquad (2)$$

In Eq. (3); f_t= represents the splitting tensile strength value (MPa), P= represents the compressive load (N) causing fracture and D= represents the size of the cube specimen (mm).

2.4   Bohme Abrasion Test

Surface abrasion tests of basalt aggregate concrete specimens were determined on 71×71×71 mm cube specimens cured in water for 28 days in accordance with TS 699 and TS EN 14157 standards [35], [36]. In order to determine the unit volume weights of the specimens, the specimens were weighed in air and water-saturated state and dried in an oven at 105±5 °C for 24 hours. The oven-dried samples were placed on the abrasive disc, the abrasive surface was coated with 20 g ± 0.5 g corundum powder, and a load of 294±3 N was applied to the sample (Figure 4c). The surface of the disk, which was rotated 22 turns, was carefully cleaned at the end of the process and the same process was repeated by rotating the sample 90° on the same surface. This process was repeated 16 times for 3 specimens from each series. At the end of the experiment, the volumetric wear loss of the specimens was calculated by Eq. (3).

$$\Delta V = \frac{\Delta m}{\rho_r} \tag{3}$$

In Eq. (3); ΔV: represents the volume loss after 16 cycles (cm^3), Δm: represents the mass loss after 16 cycles (g), and ρ_r = sample unit volume weight (g/cm^3).

With the help of the above calculations, the total volume loss occurring in the sample is calculated. In addition, the volume loss can be calculated with the help of the total shortening that occurs in the thickness of the specimen. Since the base area of the specimen is approximately 50 cm^2 (71×71 mm), all results should be based on this base area [32]. Tested water-to-cement ratios and tested aggregate-to-cement ratios of the series of concrete specimens produced are presented in Table 3.
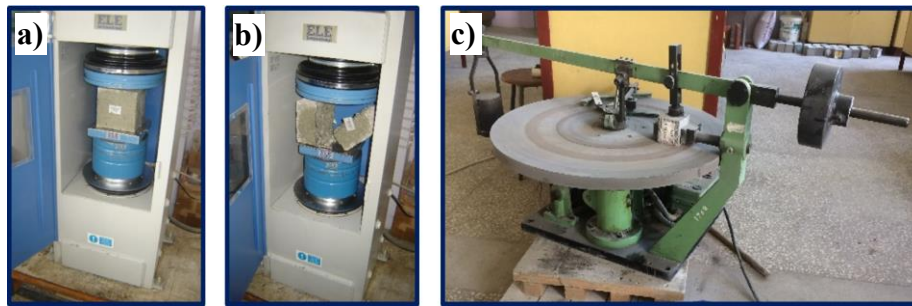
Figure 4. a) compressive strength test, b) splitting tensile strength test, c) Bohme abrasion strength test.

Table 3. Ranges of parameters for tested basalt aggregate concrete specimens.

W/C	A/C
0.20-0.25-0.30-0.35-0.40	2.0-2.1-2.2-2.3-2.4-2.5

3   RESULTS AND DISCUSSION

In the present study, a series of strength tests were carried out on a total of 30 concrete mix series by evaluating different water-to-cement ratios (W/C= 0.20, 0.25, 0.30, 0.35 and 0.40) and different basalt aggregate to cement ratios (A/C= 2.0, 2.1, 2.2, 2.3, 2.4 and 2.5) on a series of concrete specimens with basalt aggregate tested. The experimental strength tests performed on these specimens are the concrete compressive strength test, also known as destructive concrete strength tests, the tensile strength test in splitting, and Bohme abrasion test. Figure 5 shows the variation of concrete compressive strength values (f_c), concrete splitting tensile strength values (f_t), and Bohme abrasion strength values (BA) of the tested specimens with water to cement ratio (W/C). Accordingly, it was observed that the tested f_c values varied between

23.6 MPa and 46.2 MPa, f_t values varied between 2.3 MPa and 5.2 MPa, and *BA* values varied between 6.8 cm^3/50cm^2 and 24.1 cm^3/50cm^2. Table 4 presents the concrete compressive strength (f_c), concrete splitting tensile strength (f_t), and Bohme abrasion (*BA*) values of the concrete for the tested water-to-cement ratio (*W/C*) and aggregate-to-cement ratio (*A/C*) separately.

Table 4. Experimental test parameters and the strength results of tested concrete specimens.

W/C	A/C	f_c	f_t	BA
0.20	2.0	46.2	5.0	12.2
0.20	2.1	47.9	5.2	10.8
0.20	2.2	48.5	5.3	9.2
0.20	2.3	50.1	5.5	8.0
0.20	2.4	51.2	5.6	7.2
0.20	2.5	52.3	5.8	6.8
0.25	2.0	40.9	4.5	15.1
0.25	2.1	41.6	4.6	14.5
0.25	2.2	42.8	4.7	13.8
0.25	2.3	44.1	4.9	12.9
0.25	2.4	45.2	5.0	12.4
0.25	2.5	46.7	5.1	11.9
0.30	2.0	36.8	3.8	17.5
0.30	2.1	37.5	4.0	16.6
0.30	2.2	39.1	4.2	16.0
0.30	2.3	39.9	4.3	15.3
0.30	2.4	40.8	4.5	14.8
0.30	2.5	42.3	4.7	13.9
0.35	2.0	30.9	3.2	20.6
0.35	2.1	31.6	3.3	20.0
0.35	2.2	32.9	3.4	19.1
0.35	2.3	34.1	3.6	18.4
0.35	2.4	35.6	3.7	17.8
0.35	2.5	37.2	3.9	16.9
0.40	2.0	23.6	2.3	24.1
0.40	2.1	25.1	2.5	23.5
0.40	2.2	27.2	2.7	22.6
0.40	2.3	28.0	2.8	22.0
0.40	2.4	28.8	2.9	21.5
0.40	2.5	29.6	3.1	20.9

3.1 Variation of Concrete Strength Values with Water to Cement Ratio for Tested Specimens

Figure 5 shows the variation of concrete compressive strength values (f_c), concrete splitting tensile strength values (f_t), and Bohme abrasion values (BA) of tested basalt aggregate concrete specimens with water-to-cement ratio (W/C). The lowest f_c value (f_c= 23.6 MPa) and the lowest f_t value (f_t= 2.3 MPa) were measured for the highest water-to-cement ratio (W/C= 0.40) and the lowest aggregate-to-cement ratio (A/C=2.0) tested. The highest f_c value (f_c= 46.2 MPa) and the highest f_t value (f_t= 5.2 MPa) were measured for the lowest water-to-cement ratio (W/C= 0.20) and the highest aggregate-to-cement ratio (A/C= 2.5) tested. The lowest BA value (BA= 6.8 cm^3/50cm^2) was measured for the highest tested water-to-cement ratio (W/C= 0.40) and the lowest aggregate-to-cement ratio (A/C= 2.0).

The highest BA value (BA= 24.1 cm^3/50cm^2) was measured for the lowest tested water-to-cement ratio (W/C= 0.20) and the highest aggregate-to-cement ratio (A/C= 2.5). With the increase in water-to-cement ratio from W/C= 0.20 to W/C= 0.40; an average decrease of approximately 42% in f_c values, an average decrease of approximately 47% in f_t values, and an average increase of approximately 2.4 times in BA values were calculated. The coefficient of determination of the equation developed for the variation of f_c values with W/C was calculated as $R^2 \approx 0.93$. The coefficient of determination of the equation developed for the variation of f_t values with W/C was calculated as $R^2 \approx 0.91$. The coefficient of determination of the equation developed for the variation of BA values with W/C was calculated as $R^2 \approx 0.93$. This indicates that the variation of the values of the relevant strength indicators (f_c, f_t, and BA) with W/C was formulated with a near-perfect fit.
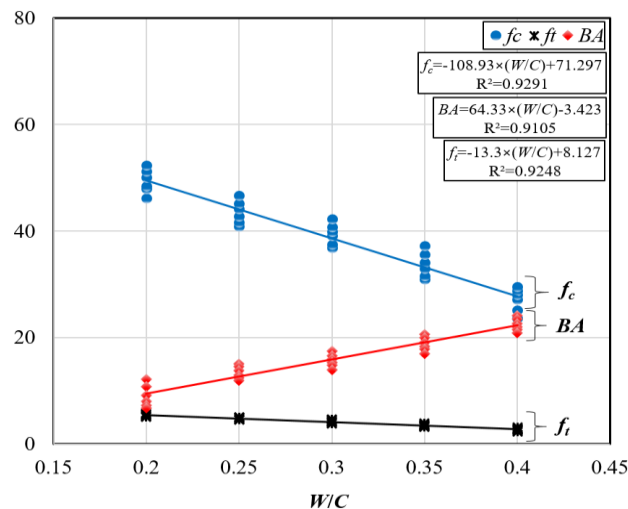
Figure 5. Variation of concrete strength values and Bohme abrasion strength values of the tested specimens with water-to-cement ratio.

3.2   Variation of Concrete Strength Values with Aggregate to Cement Ratio for Tested Specimens

Figure 6 shows the variation of concrete compressive strength values (f_c), concrete splitting tensile strength values (f_t), and Bohme abrasion values (BA) of tested basalt aggregate concrete specimens with aggregate-to-cement ratio (A/C). With the increase in aggregate to cement ratio from A/C= 2.0 to A/C= 2.5, an average increase in f_c values of approximately 13% for W/C= 0.20, an average increase of approximately 14% for W/C= 0.25, an average increase of approximately 15% for W/C= 0.30, an average increase of approximately 20% for W/C= 0.35 and an average increase of approximately 25% for W/C= 0.40 were calculated. Thus, it is possible to say that the percentage change of the f_c value with A/C increases as the W/C value increases. When the findings of all tested specimens were evaluated, it was calculated that there was a total average increase of approximately 17% in f_c values with the increase from A/C= 2.0 to A/C= 2.5. With the increase in aggregate to cement ratio from A/C= 2.0 to A/C= 2.5; it was calculated that there was an average increase of approximately 16% for W/C= 0.20, an average increase of approximately 13% for W/C= 0.25, an average increase of approximately 24% for W/C= 0.30, an average increase of approximately 22% for W/C= 0.35 and an average increase of approximately 35% for W/C= 0.40 in ft values. When the findings of all tested specimens were evaluated, it was calculated that there was a total average increase of approximately 22% in f_t values with an increase from A/C= 2.0 to A/C= 2.5. With the increase in aggregate to cement ratio from A/C= 2.0 to A/C= 2.5; approximately 44% decrease in BA values for W/C= 0.20, approximately 22% decrease for W/C= 0.25, approximately 21% decrease for W/C= 0.30, approximately 18% decrease for W/C= 0.35, approximately 13% decrease for W/C= 0.40 were calculated. Thus, it is possible to say that the percentage of change of BA value with A/C decreases as the W/C value increases. When the findings of all tested specimens were evaluated, it was calculated that with the increase from A/C= 2.0 to A/C= 2.5; there was a total average decrease of approximately 24% in BA values.
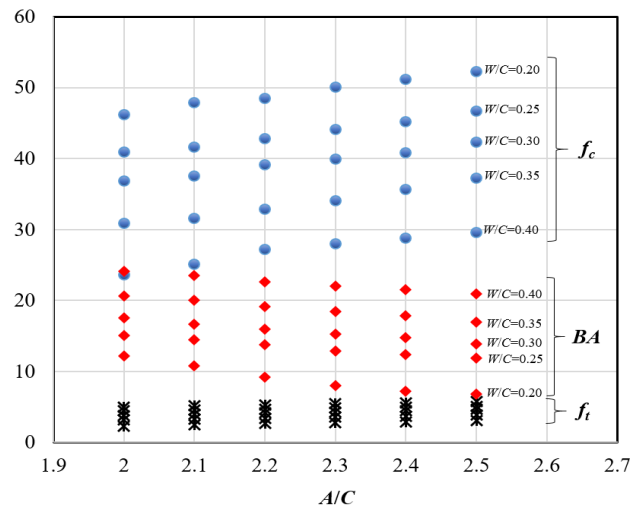
Figure 6. Variation of concrete strength values and Bohme abrasion values of the tested specimens with aggregate-to-cement ratio.

3.3 Variation of Compressive Strength Values with Splitting Tensile Strength Values for Tested Specimens

Figure 7 shows the variation of concrete compressive strength values (f_c) of the tested specimens with concrete splitting tensile strength values (f_t). Accordingly, f_c values ranged between 23.6 MPa and 52.3 MPa and f_t values ranged between 2.3 MPa and 5.8 MPa. It is observed that f_c values increase linearly with f_t. The correlation coefficient $R^2= 0.9963$ was calculated for the linear equation developed for the estimation of f_c depending on f_t. Accordingly, it is possible to say that the agreement is very close to perfect (Figure 7). Equation (4) was developed to calculate the concrete compressive strength value from the concrete splitting tensile strength value of the tested concrete specimens.

$$f_c = 8.157 \times f_t + 4.875 \tag{4}$$
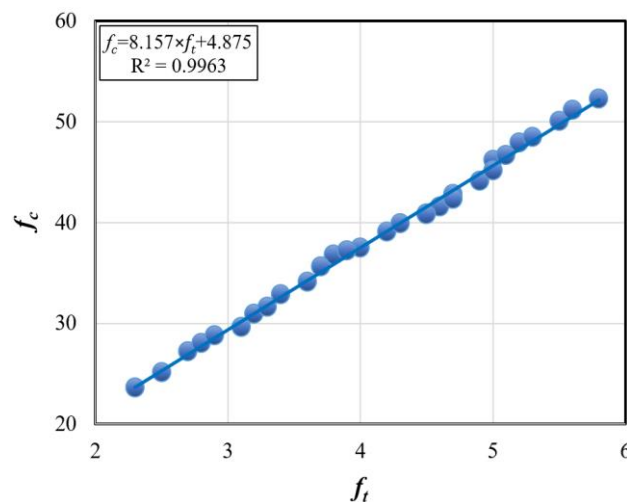
Figure 7. Variation of measured fc values with measured ft values of the tested specimens.

3.4 Variation of Bohme Abrasion Strength Values with Compressive Strength Values for Tested Specimens

Figure 8 shows the variation of concrete Bohme abrasion values (BA) with concrete compressive strength values (f_c) for the tested specimens. Accordingly, f_c values ranged between 23.6 MPa and 52.3 MPa, and BA values ranged between 6.8 cm^3/50cm^2 and 24.1 cm^3/50cm^2. It was observed that BA values decreased linearly with f_c values. The correlation coefficient R^2= 0.988 was calculated for the linear equation developed for the estimation of BA depending on f_c. Accordingly, it is possible to say that the agreement is very close to perfect (Figure 8). Equation (5) was developed to calculate the concrete Bohme abrasion value from the concrete compressive strength value of the tested concrete specimens.

$$BA = 0.59 \times f_c + 38.78 \tag{5}$$
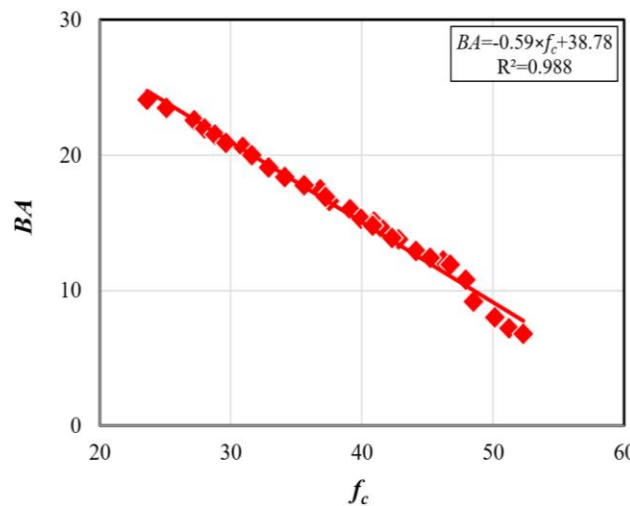
Figure 8. Variation of measured BA values with measured fc values of the tested specimens.

3.5 Variation of Bohme Abrasion Strength Values with Splitting Tensile Strength Values for Tested Specimens

Figure 9 shows the variation of concrete Bohme abrasion values (BA) with concrete splitting tensile strength values (f_t) for the tested specimens. Accordingly, f_t values ranged between 2.3 MPa and 5.8 MPa, and BA values ranged between 6.8 cm^3/50cm^2 and 24.1 cm^3/50cm^2. It was observed that BA values decreased linearly with f_t values. The correlation coefficient R^2= 0.9817 was calculated for the linear equation developed for the estimation of BA depending on ft. Accordingly, it is possible to say that the agreement is very close to perfect (Figure 9). The low Bohme abrasion loss value (BA) indicates that the abrasion resistance is high. Concrete with high abrasion resistance will also have high compressive strength and high

splitting tensile strength. Equation (6) was developed to calculate the concrete Bohme abrasion value from the concrete splitting tensile strength value of the tested concrete specimens.

$$BA = -4.83 \times f_t + 35.86 \tag{6}$$
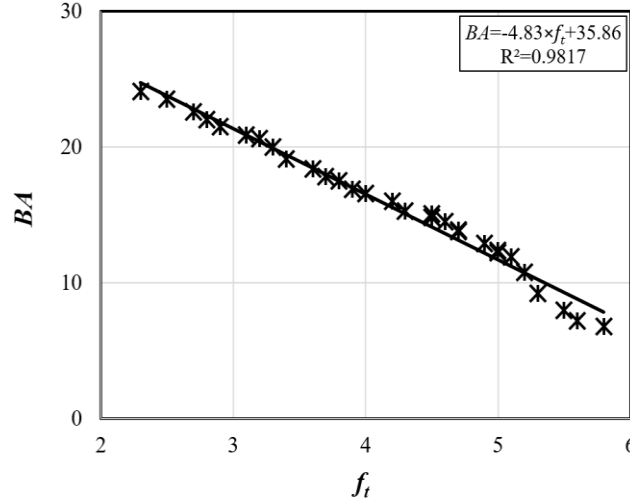
Figure 9. Variation of measured BA values with measured ft values of the tested specimens.

4   CONCLUSION AND SUGGESTIONS

The main results obtained from the present study, which experimentally investigated the relationship between concrete compressive strength, concrete splitting tensile strength, and Böhme abrasion strength, which are the test methods determining concrete strength for basalt aggregate concrete, are summarized below.

➢ Since reinforced concrete structures are composed of concrete, the mechanical properties of concrete should be investigated in detail for resistance against possible earthquakes.

➢ In the present experimental study; f_c values of the tested specimens ranged from 23.6 MPA to 46.2 MPa, f_t values ranged from 2.3 MPa to 5.2 MPa, and *BA* values ranged from 6.8 cm^3/50cm^2 to 24.1 cm^3/50cm^2.

➢ The lowest f_c and f_t values were measured for the highest water-to-cement ratio and the lowest aggregate-to-cement ratio tested. The highest f_c and f_t values were measured for the lowest water-to-cement ratio and the highest aggregate-to-cement ratio tested.

➢ The lowest *BA* value was measured for the highest water-to-cement ratio and the lowest aggregate-to-cement ratio tested. The highest *BA* value was measured for the lowest water-to-cement ratio and the highest aggregate-to-cement ratio tested.

➢ With the increase of the water-to-cement ratio from W/C=0.20 to W/C=0.40; approximately average 42% decrease in f_c values, approximately average 47% decrease in f_t values and approximately average 2.4 times increase in BA values were calculated.

➢ The coefficient of determination of the equation developed for the variation of f_c values with W/C was calculated as $R^2 \approx 0.93$. The coefficient of determination of the equation developed for the variation of f_t values with W/C was calculated as $R^2 \approx 0.91$. The coefficient of determination of the developed equation for the variation of BA values with W/C is calculated as $R^2 \approx 0.93$.

➢ It is concluded that the values of the concrete strength findings (f_c, f_t, and BA) investigated experimentally in the present study are correlated with the W/C and A/C dimensionless parameters with a near-perfect agreement.

➢ It is suggested that the present study be further developed by applying destructive and non-destructive strength test methods on concrete specimens produced with other aggregates and different mix contents specific to the region.

Statement of Research and Publication Ethics

The study is complied with research and publication ethics.

Artificial Intelligence (AI) Contribution Statement

This manuscript was entirely written, edited, analyzed, and prepared without the assistance of any artificial intelligence (AI) tools. All content, including text, data analysis, and figures, was solely generated by the author.

REFERENCES

[1]   K. Gokkaya, "Geographic analysis of earthquake damage in Türkiye between 1900 and 2012. Geomatics," *Natural Hazards and Risk*, vol. 7, no. 6, pp. 1948-1961, April 2016. doi: 10.1080/19475705.2016.1171259

[2]   W. Y. Kam, S. Pampanin, K. Elwood, "Seismic performance of reinforced concrete buildings in the 22 February Christchurch (Lyttleton) earthquake," *Bulletin of the New Zealand Society for Earthquake Engineering*, vol. 44, no. 4, pp. 239-278, December 2011.

[3]   E. Sayın, B. Yon, O. Onat, M. Gor, M. E. Oncu, E. Tugrul Tunc, ... Y. Calayır Y, "24 January 2020 Sivrice-Elazığ, Türkiye earthquake: geotechnical evaluation and performance of structures," *Bulletin of Earthquake Engineering*, vol. 19, pp. 657-684, January 2021. doi: 10.1007/s10518-020-01018-4.

[4]   A. Dogangun, "Performance of reinforced concrete buildings during the May 1, 2003 Bingöl Earthquake in Türkiye," *Engineering Structures*, vol. 26, no. 6, pp. 841-856, May 2004. doi: 10.1016/j.engstruct.2004.02.005.

[5]   A. H. Akca, O. Sahin, K. Koc, Y. Aygörmez, "Mechanical and microstructural investigations on concrete of the collapsed buildings after Kahramanmaraş earthquakes," *Engineering Science and Technology, an International Journal*, vol. 56, no. 101784, August 2024. doi: 10.1016/j.jestch.2024.101784.

[6]   E. Tugrul Tunc, "Strength and Durability of Superplasticizer Concrete Based on Different Component Parameters: An Experimental and Statistical Study," *Arabian Journal for Science and Engineering*, pp. 1-16, April 2024. doi: 10.1007/s13369-024-08985-9.

[7]   https://bilimgenc.tubitak.gov.tr/turkiyede-son-yuzyilda-gerceklesen-buyuk-depremler

[8]   P. K. Mehta, P. Monteiro, "Concrete: microstructure, properties, and materials" (*No Title*), 2006.

[9]   http://www.agub.org.tr

[10]   E. Tugrul Tunc, K. E. Alyamac, "A preliminary estimation method of Los Angeles abrasion value of concrete aggregates," *Construction and Building Materials*, vol. 222, pp. 437-446, October 2019. doi: 10.1016/j.conbuildmat.2019.06.176.

[11]   M. Bustillo Revuelta, "Properties and Testing," *In The Basics of Aggregates, Cham: Springer International Publishing*, pp. 21-52, February 2024. doi: 10.1007/978-3-031-42961-3_2.

[12]   "Beton agregaları," *Türk Standartları Enstitüsü*, TS 706 EN 12620+A1, 2009 (in Turkish).

[13]   E. Tugrul Tunc, "Effects of basalt aggregates on concrete properties," *Qualitative Studies*, vol. 13, no. 2, pp. 68-79, April 2018. doi: 10.12739/NWSA.2018.13.2.E0043.

[14]   C. Ingrao, A. L. Giudice, C. Tricase, C. Mbohwa, R. Rana, "The use of basalt aggregates in the production of concrete for the prefabrication industry: Environmental impact assessment, interpretation and improvement," *Journal of Cleaner Production*, vol. 75, pp. 195-204, July 2014. 10.1016/j.jclepro.2014.04.002

[15]   C. Yalcinkaya, J. Sznajder, A. Beglarigale, O. Sancakoglu, H. Yazici, "Abrasion resistance of reactive powder concrete: The influence of water-to-cement ratio and steel micro-fibers," *Advanced Materials Letters*, vol. 5 no. 6, pp. 345-351, 2014. doi: 10.5185/amlett.2014.amwc.1021.

[16]   C. Kara, S. Yazıcıoğlu, "Effects of Marble Duster Waste and Silica Fume to Carbonation of Concrete," *Bitlis Eren University Graduate Institute Journal*, vol. 5, no. 2, pp. 191-202, August 2016. doi: 10.17798/bitlisfen.282253.

[17]   İ. Çobanoğlu, S. B. Çelik, "Assessments on the usability of Wide Wheel (Capon) test as reference abrasion test method for building stones," *Construction and Building Materials*, vol. 151, pp. 319-330, October 2017. doi: 10.1016/j.conbuildmat.2017.06.045.

[18]   F. Bayram, "Data mining techniques for the prediction of Bohme surface abrasion rates from rock properties," *Journal of Testing and Evaluation*, vol. 48, no. 1, pp. 323-332, January 2020. doi: 10.1520/JTE20190130.

[19]   L. Bodnárová, R. Hela, L. Osuská, M. Ťažký, "Effect of Type of Aggregate on Abrasion Resistance of Concrete," *In Materials Science Forum*, vol. 987, pp. 39-43, April 2020. doi: 10.4028/www.scientific.net/MSF.987.39.

[20]   Z. Karaca, A. H. Deliormanli, H. Elci, C. Pamukcu, "Effect of freeze–thaw process on the abrasion loss value of Stones," *International Journal of Rock Mechanics & Mining Sciences*, vol. 47, no. 7, pp. 1207-1211, October 2010. doi: 10.1016/j.ijrmms.2010.07.003.

[21]   İ. Çobanoğlu, S. Çelik, D. Alkaya, "Correlation between "wide Wheel abrasion (capon)" and "Bohme abrasion" test results for some carbonate rocks," *Scientific Research and Essays*, vol. 5, no. 22, pp. 3398-3404, November 2010.

[22]   B. Ç. Sefer, "Investigation of Abrasion Resistance of Carbonate Rocks by Wide Wheel Abrasion Test," *Fırat University Journal of Engineering Science*, vol. 30, no. 1, pp. 303-310. March 2018.

[23]   E. Tugrul Tunc, K. E. Alyamac, "Determination of the relationship between the Los Angeles abrasion values of aggregates and concrete strength using the Response Surface Methodology," *Construction and Building Materials*, vol. 260, no. 119850, November 2020. doi: 10.1016/j.conbuildmat.2020.119850.

[24]   P. Poitevin, "Limestone aggregate concrete, usefulness and durability," *Cement and Concrete Composites*, vol. 21, no. 2, pp. 89-97, April 1999. doi: 10.1016/S0958-9465(98)00047-X.

[25]   E. T. Tunç, K. E. Alyamaç, "The Effect of Aggregate Type on Los Angeles Abrasion Loss for Different Test Parameters," *Fırat University Journal of Engineering Science*, vol. 32, no. 1, pp. 1-10, March 2020. doi: 10.35234/fumbd.569198. (in Turkish).

[26]   K. E. Alyamaç, A. B. Aydin, "Concrete properties containing fine aggregate marble powder," *KSCE Journal of Civil Engineering*, vol. 19, no. 7, pp. 2208-2216, February 2015. doi: 10.1007/s12205-015-0327-y.

[27]   K.E. Alyamaç, R. İnce, "Çelik lifli karo mozaik döşeme kaplama plakalarının fiziksel ve mekanik özelliklerinin belirlenmesi," *BAÜ FBE Dergisi*, vol. 1, pp. 31-45, 2008. (in Turkish).

[28]   A. Alyaseen, A. Poddar, N. Kumar, P. Sihag, D. Lee, T. Singh, "Assessing the compressive and splitting tensile strength of self-compacting recycled coarse aggregate concrete using machine learning and statistical techniques," *Materials Today Communications*, 38:107970, 2024. doi: 10.1016/j.mtcomm.2023.107970.

[29]   F. Almohammed, M.S. Thakur, D. Lee, R. Kumar, T. Singh, "Flexural and split tensile strength of concrete with basalt fiber: An experimental and computational analysis." *Construction and Building Materials*, 414:134936, 2024. doi: 10.1016/j.conbuildmat.2024.134936.

[30]   A. Teymen, "Assessment of Bohme surface abrasion resistance of natural stones by simple and nonlinear multiple regression methods." *Construction and Building Materials*, 411:134195, 2024. doi: 10.1016/j.conbuildmat.2023.134195.

[31]   E. Köken, "Development of Comprehensive Predictive Models for Evaluating Böhme Abrasion Value (BAV) of Dimension Stones Using Non-Destructive Testing Methods." *Applied Sciences*, 15(1):60, 2025. doi: 10.3390/app15010060.

[32]   E. Tuğrul, "The investigation of abrasion resistance of aggregates under different conditions," Fırat University, Master Thesis, 2015. (in Turkish).

[33]   TS EN 12390-3 (2010) Testing hardened concrete – Part 3: Compressive Strength of Test Specimens. Turkish Standards Institutions Ankara. (in Turkish).

[34]   TS EN 12390-6 (2010) Testing Hardened Concrete – Part 6: Tensile Splitting Strength of Test Specimens. Turkish Standards Institutions Ankara. (in Turkish).

[35]   TS 699, 2009, Nokta Yükü Dayanım İndeksi Deneyi, Türk Standartları Enstitüsü, Ankara. (in Turkish).

[36]   TS EN 14157, 2005, Aşınma direncinin tayini – Böhme, Türk Standartları Enstitüsü, Ankara. (in Turkish).

STRUCTURAL ANALYSIS OF DIFFERENT HINGE POSITIONS ON THE MECHANICAL BEHAVIOR OF A WOODEN DOOR SYSTEM USING ANSYS

Yasin Furkan GÖRGÜLÜ [1] *, Rahim MERDAN [2]

[1] *Isparta University of Applied Sciences, Department of Machinery and Metal Technologies, Isparta, Türkiye*

[2] *Isparta University of Applied Sciences, Design Department, Isparta, Türkiye*

*** Corresponding Author:** yasingorgulu@isparta.edu.tr*

ABSTRACT

This study investigates the effect of different hinge configurations on the mechanical performance of a wooden door system using finite element analysis. Two configurations were evaluated: one where the middle hinge was positioned closer to the upper hinge, and the other where it was centrally positioned. The results show that the maximum von Mises stress for the upper hinge configuration reached 75.614 MPa, while the centrally placed hinge configuration exhibited a slightly higher stress of 78.809 MPa. However, the central hinge placement provided more uniform stress and strain distribution across the door. Deformation values were also significant, with a maximum deformation of 0.0213 mm observed for the centrally positioned hinge, offering better load distribution compared to the upper hinge configuration. These findings suggest that the central hinge placement enhances the mechanical stability and lifespan of the door by reducing localized stress concentrations. The study highlights the importance of hinge positioning in optimizing the structural integrity of wooden door systems.

Keywords: Deformation and strain distribution, FEA, Hinge positioning, Von Mises stress, Wooden door.

1   INTRODUCTION

Wooden doors are commonly used as interior doors in residential buildings. These doors are typically referred to as swing doors and are attached to the frame using hinges, which allow the door to pivot open and closed [1]. The mechanical performance of door systems, particularly

those constructed from wood, is heavily influenced by the positioning and configuration of hinges. Hinges act as critical load-bearing elements that transfer forces between the door and its frame. As a result, their placement directly impacts the structural integrity and durability of the entire system. Previous research in the field has largely focused on automotive and furniture doors, demonstrating that hinge configuration plays a crucial role in mitigating stress concentrations and minimizing deformation. Wooden doors, unlike their metal or composite counterparts, present unique mechanical challenges due to the anisotropic and heterogeneous properties of wood. These characteristics result in material behaviors that vary depending on the grain direction, significantly influencing how loads are distributed and absorbed. In the context of hinge positioning, these properties can exacerbate localized stress and strain concentrations, particularly in improperly positioned hinges. Such effects can lead to accelerated material fatigue and reduced durability of the door system. Addressing these challenges requires an in-depth evaluation of hinge configurations to optimize load sharing and minimize the adverse effects of wood's material properties. This study aims to investigate these aspects, providing insights into optimal hinge placement strategies for wooden doors.

Research into hinge configurations for automotive applications has shown that finite element analysis (FEA) can be effectively employed to optimize the placement and design of door hinges. Studies have indicated that optimizing the hinge layout significantly improves load distribution, thereby enhancing the door's mechanical strength. For instance, Liu et al. (2021) conducted a comprehensive study on vehicle door hinges using FEA to investigate vibration control and structural stability, underscoring the importance of hinge positioning in reducing stress concentrations under dynamic conditions [2]. Similar findings were reported by Erol and Özgül (2019), who explored the correlation between simulation and experimental results for door hinges subjected to regulatory tests. The study confirmed that optimal hinge configurations improve the load-bearing capacity of door systems [3]. Bayrak et al. (2025) conducted a finite element assessment of torsion springs in hinges, demonstrating the importance of accurate modeling and experimental validation in improving fatigue life and ensuring the durability of hinge components [4]. Bekah (2004) utilized finite element analysis to predict fatigue life in door hinge systems under uni-axial and multi-axial loading, identifying critical points of crack initiation and optimizing hinge design to enhance durability [5]. Meyer et al. (2023) developed novel test methods for the mechanical characterization of flexure hinges under large deformations, providing insights into stiffness properties crucial for designing compliant mechanisms [6]. Hwang et al. (2021) investigated the flexural anisotropy of rift-sawn softwood

boards caused by end-grain orientation, revealing superior flexibility and deformation mechanisms beneficial for curved wooden applications [7].

In the context of furniture doors, a study by Zhongshan Four Seas Furniture Ltd. demonstrated the benefits of optimized hinge placement for wooden doors using ANSYS for FEA. This research revealed that doors with carefully positioned hinges exhibit reduced deformation and stress, even when subjected to high loads [8]. These findings highlight the importance of optimizing hinge configurations, not only for metal doors but also for wooden structures, where mechanical properties such as anisotropy and inhomogeneity can exacerbate stress concentrations if not properly accounted for.

In light of these findings, the present study employs ANSYS Structural Analysis to assess the impact of different hinge positions on the mechanical performance of a wooden door system. A complete pre-assembled press door set, including the frame, leaf, and trim, typically weighs around 35 kg. However, for the purposes of this study, only the weight of the door leaf itself has been considered, as the frame and trim do not contribute directly to the mechanical performance evaluated in this analysis. Two configurations are considered: one with the middle hinge placed centrally, and another with the middle hinge positioned closer to the upper hinge. The results of this analysis will contribute to a better understanding of the influence of hinge placement on stress and strain distributions, providing a basis for optimizing door design to enhance structural integrity and prolong service life.

2   MATERIAL AND METHOD

2.1   Wooden Door and Frame

The finite element analysis was conducted with several key assumptions to simplify the model and ensure computational efficiency. Firstly, the wooden material of the door was treated as isotropic, which does not fully capture the anisotropic nature of wood. While wood exhibits varying mechanical properties along its grain direction, isotropy was assumed to standardize the material behavior and simplify the simulation. This assumption may lead to an underestimation of strain concentrations along specific grain orientations. Secondly, rigid connections were applied at the contact points between the hinges and the door/frame. This simplification does not account for minor relative motions or deformations at the connections, which could slightly influence the stress distribution in real-world scenarios. Despite these limitations, these assumptions are commonly used in preliminary finite element models to

balance accuracy with computational feasibility. The door and frame were modeled using oak wood, a material selected for its widely recognized structural properties in door systems. Oak wood is characterized by its high density, strength, and stiffness, making it a suitable material for load-bearing components in door assemblies [9]. The material properties for oak were sourced from ANSYS's material library, the mechanical properties were applied in the analysis, and demonstrated in table 1.

Table 1. Mechanical properties of oak wood and structural steel used in the finite element analysis of the door system [10].

Material	Density (kg/m^3)	Young's Modulus (GPa)	Poisson's Ratio
Oak Wood	935.7	22.7	0.3742
Structural Steel	7850	200	0.3

These values were chosen based on the general mechanical properties of oak wood, which has been well-documented for its durability and resistance to deformation under compression and bending loads. The hinges and all associated fastening elements, including bolts, were modeled using structural steel. Structural steel was selected for its superior tensile strength and durability, particularly in applications involving load transfer through mechanical connections. The material properties for structural steel, also sourced from ANSYS's material library (Table 1.).

The wooden door and frame geometries were designed with precise dimensions to reflect real-world door systems. The door's dimensions were 2000 mm in height, 790 mm in width, and 42 mm in thickness. The frame was modeled with an external height of 2140 mm, a width of 942.5 mm, and a thickness of 260 mm (detailed in Figure 1.(a)). The selected dimensions align closely with the TS 825 standard, which defines typical door measurements for interior applications in Türkiye [11]. Both the frame and door were designed as solid models, and the hinge positions were adjusted according to two configurations. In this study, two hinge configurations were examined to assess their impact on the mechanical performance of a wooden door system. The first configuration placed the middle hinge closer to the upper hinge (Figure 1.(c)), concentrating the load toward the top of the door. The second configuration positioned the middle hinge centrally, aiming to distribute the load more evenly across the entire door (Figure 1.(b)). These two setups were analyzed using finite element analysis to compare their effects on stress, strain, and deformation, providing insights into the benefits and limitations of each configuration for enhancing the structural integrity and durability of the door system.
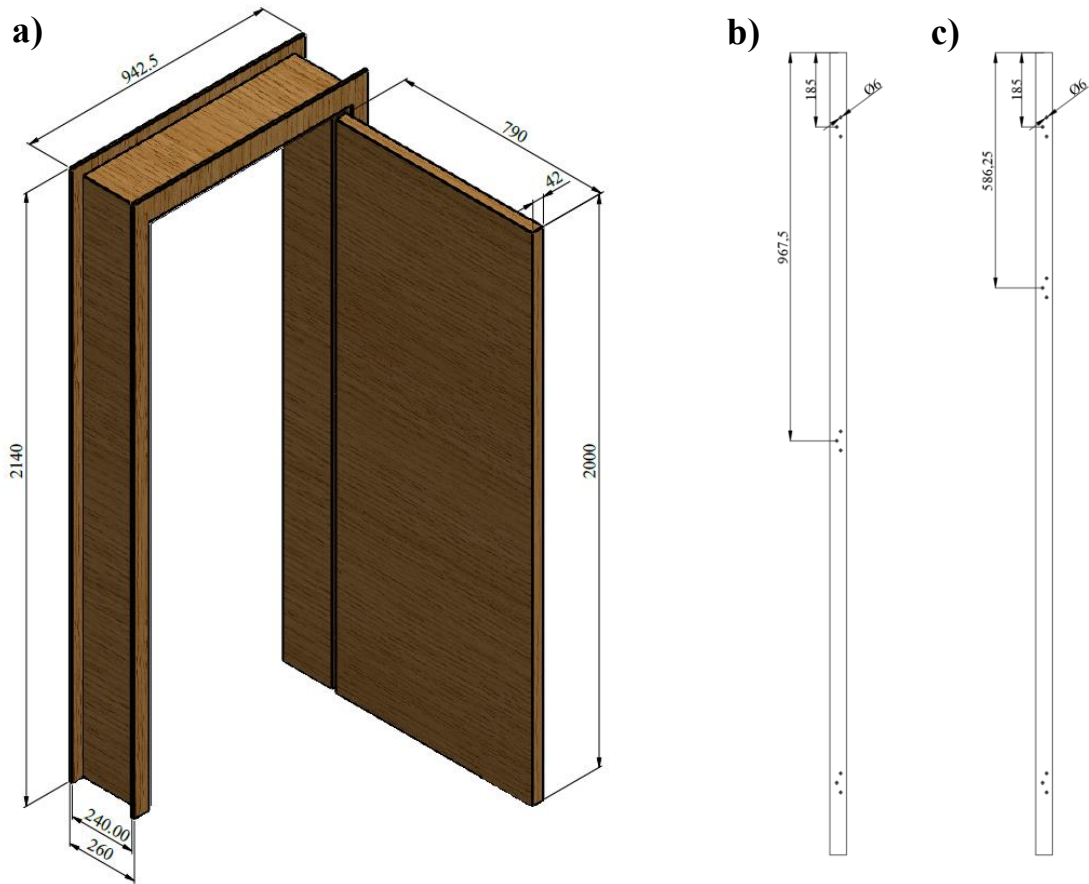
Figure 1. Dimensional schematic of the wooden door system, showing the full assembly and hinge placements. (a) Overall dimensions of the door and frame assembly, (b) hinge placement with the middle hinge centrally positioned, and (c) hinge placement with the middle hinge closer to the upper hinge.

2.2 Finite Element Modeling

Finite element analysis (FEA) was performed using ANSYS Workbench 2022. A 3D solid model of the door, frame, hinges, and bolts was created. The system was meshed using tetrahedral elements, which were generated by ANSYS Meshing tool. The finite element model for the door system was created with 2,761,628 nodes and 1,895,191 elements, utilizing a tetrahedral mesh to accurately capture the complex geometry around the hinges and bolts. The average skewness of the mesh was 0.25033, which falls into the very good range (0.25–0.50), indicating minimal distortion and reliable element quality. The average orthogonal quality was 0.76953, placing it in the very good range (0.70–0.95), further ensuring the mesh's suitability for detailed stress and strain analysis. This high-quality mesh allowed for accurate and reliable simulation results in the finite element analysis [12], [13], [14], [15].
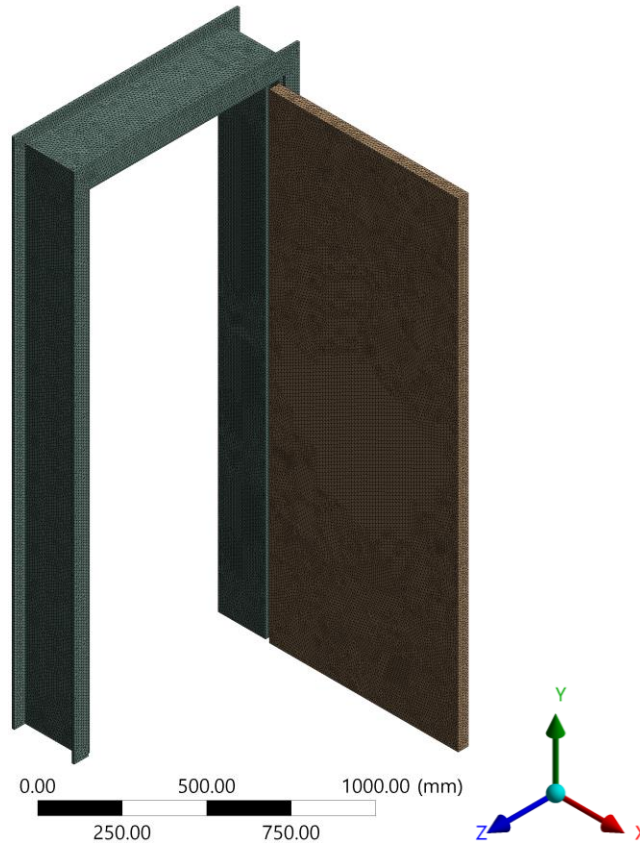
Figure 2. Mesh structure of the door system. The average skewness (0.25033) and orthogonal quality (0.76953) indicate a high-quality mesh suitable for accurate stress and strain analysis.

The analysis was conducted under standard earth gravity conditions (9.81 m/s²), with no additional external forces applied to the system. To simulate the real-world attachment of the door frame to the surrounding structure, the regions where the door frame contacts the wall were modeled using fixed support boundary conditions. This ensured that the frame remained stationary during the analysis, accurately reflecting its role in bearing the load transferred through the door and hinges. The contact interactions between the door, hinges, and bolts were modeled as bonded contacts, simulating a rigid connection where no relative movement or separation occurs between these components. This approach provides a realistic representation of the mechanical connections within the door system, ensuring accurate stress, strain, and deformation results in the finite element analysis. The analysis was conducted using a static structural analysis in ANSYS. The solver was set to account for large deflections, and non-linear material behavior was included to capture any plastic deformation in the hinges and bolts. The results focused on deformation, strain, and von Mises stress across the system for both hinge configurations. Key results were extracted from the simulation, including total deformation (mm), strain (mm/mm), and von Mises stress (MPa). These results were used to

compare the mechanical behavior of the two hinge configurations. Stress and strain contours were plotted to visually represent areas of high deformation and potential failure points.

For isotropic materials, the relationship between stress and strain is governed by Hooke's Law. In the case of linear elasticity, this is represented by the following equation:

$$\sigma = E.\varepsilon \tag{1}$$

where:

σ is the stress (Pa or MPa)

E is the Young's Modulus (Pa or GPa)

ε is the strain

This equation applies to the linear elastic range of both oak wood and structural steel used in the analysis. In structural analysis, the von Mises stress is used to predict yielding of ductile materials. It's calculated using the following equation:

$$\sigma_v = \sqrt{\frac{1}{2}[(\sigma_1 - \sigma_2)^2 + (\sigma_2 - \sigma_3)^2 + (\sigma_3 - \sigma_1)^2]} \tag{2}$$

where:

σ_v is the von Mises Stress (Pa or MPa)

σ_1, σ_2, σ_3 are the principal stresses in the system

This criterion was used to assess whether the structural steel components (hinges and bolts) remain within the elastic limit during the loading conditions.

The total deformation δ in a body under load can be expressed as a function of applied force F, length L, cross-sectional area A, and Young's Modulus E:

$$\delta = \frac{F.L}{A.E} \tag{3}$$

This equation helps in understanding the relationship between the applied forces and the resulting deformation in the door and frame, considering the material properties of oak wood.

Strain (ε is defined as the ratio of change in length ΔL to the original length L_0

$$\varepsilon = \frac{\Delta L}{L_0} \tag{4}$$

Strain is a dimensionless quantity that was calculated for various components in the system to assess how the door and hinges deformed under load.

3   RESULTS AND DISCUSSION

The FEA results presented in Figure 3. illustrate the deformation contours for two different hinge configurations of a wooden door system. The figure is organized into two rows and four columns, where each column represents a different set of components analyzed within the system. The first row corresponds to the case where the middle hinge is positioned closer to the upper hinge, while the second row represents the configuration where the middle hinge is centrally located.

The first contour plot on the left shows the deformation distribution for the entire door system, including the door, frame, hinges, and bolts. The maximum deformation in this configuration is observed at approximately 0.0237 mm, which occurs at the free end of the door. The deformations are relatively more concentrated at the top corner of the door, reflecting the hinge position's influence on the door's structural response. The second plot focuses on the door's deformation only, excluding the frame and other components. The highest deformation reaches 0.0237 mm, again concentrated at the top corner. This distribution suggests that the door's upper part experiences the most significant deformation, potentially due to the closer proximity of the middle hinge to the upper hinge, reducing the support near the center of the door. The third contour plot shows the deformation of the door frame alone. The frame experiences a maximum deformation of 0.00076 mm, indicating minimal displacement, which suggests that the frame structure remains rigid and unaffected by the hinge position. The final plot in this row presents the deformation of the hinges and bolts. The maximum deformation in this configuration is 0.00929 mm, indicating some deformation within the connecting elements but not significant enough to affect the overall assembly's integrity.

In the second row, where the middle hinge is centrally located, the total assembly deformation is again analyzed. The maximum deformation remains at 0.0213 mm. Compared to the first configuration, the overall deformation is slightly reduced, suggesting that central hinge positioning may improve the load distribution across the door. The deformation of the door alone shows a similar pattern to the first configuration, with a maximum of 0.0213 mm. However, the stress distribution appears more uniform compared to the closer hinge configuration, indicating that the central hinge may provide better load balance. The door frame deformation remains minimal, with a maximum of 0.00089 mm. This value is slightly higher than in the first configuration, but still negligible, reinforcing the structural rigidity of the frame. The deformation in the hinges and bolts is again highlighted, with a maximum deformation of

0.00858 mm. This is slightly lower than in the first configuration, suggesting that the central positioning of the hinge reduces the stress on the connecting elements.

A comparison between the two hinge configurations reveals that the middle hinge's position significantly affects the deformation patterns within the door system. When the middle hinge is positioned closer to the upper hinge, the deformation is more concentrated at the top of the door, leading to higher stress concentrations in that area. In contrast, when the middle hinge is centrally positioned, the deformation is more evenly distributed, reducing the overall stress on the door and its components. This suggests that a central hinge position may provide better mechanical performance by improving load distribution and reducing localized stress concentrations.
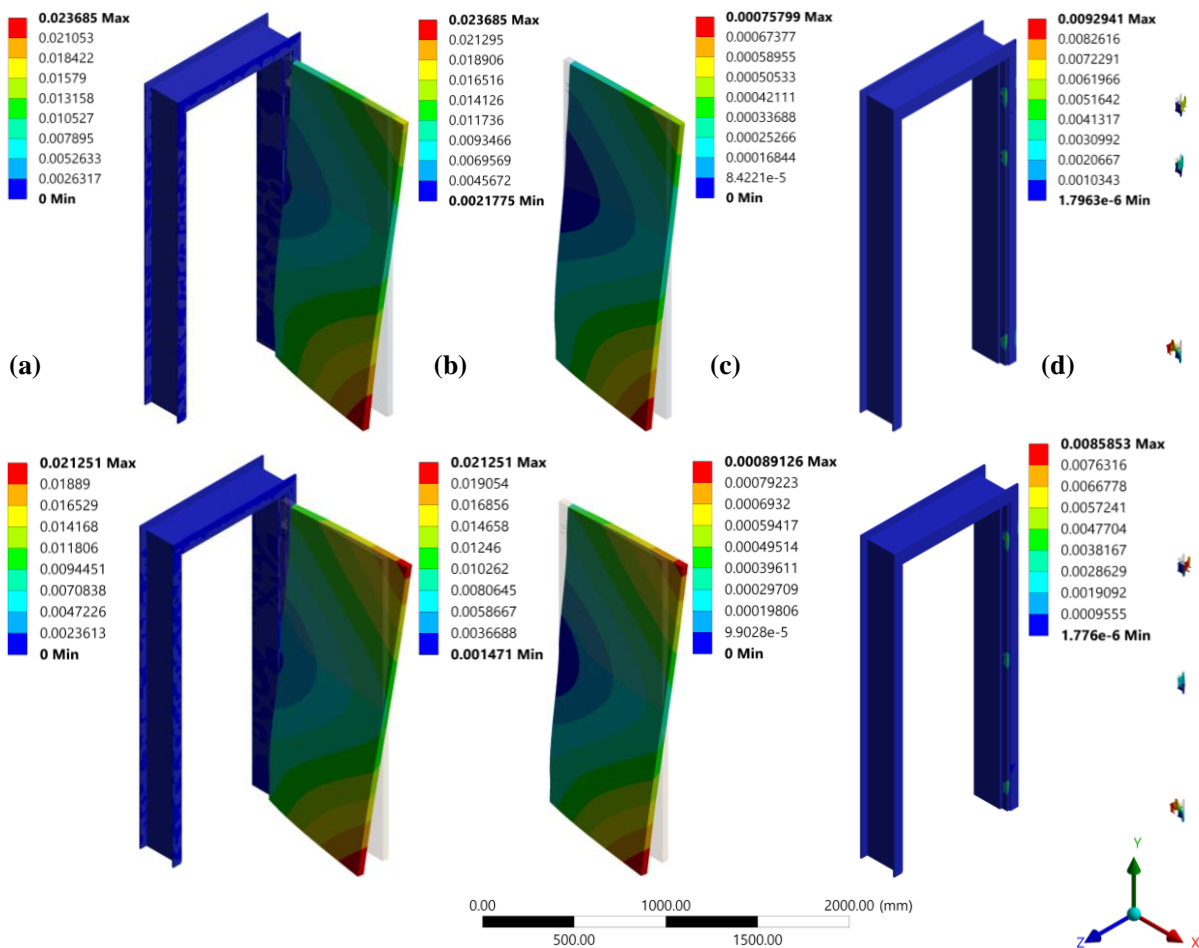
Figure 3. Deformation contours (mm) for two hinge configurations of a wooden door system. The first row illustrates the configuration with the middle hinge closer to the upper hinge, while the second row shows the middle hinge centrally located. The columns display (a) the total assembly, (b) the door, (c) the frame, and (d) the hinges and bolts. The centrally placed hinge results in more uniform deformation, while the upper hinge configuration shows higher localized deformation near the upper part of the door.

The results shown in Figure 4 depict the strain distributions (in mm/mm) for the two different hinge configurations of a wooden door system. The first row represents the configuration where the middle hinge is positioned closer to the upper hinge, while the second row corresponds to the configuration with the middle hinge centrally located. Each column highlights the strain contours of different components of the door system, providing insights into how hinge positioning influences the strain distribution across the assembly.

The strain distribution for the entire door system, including the door, frame, hinges, and bolts, is shown in the first contour plot. The maximum strain observed is approximately 0.00046277 mm/mm, with strain concentration localized at the door edges, particularly near the upper hinge area. This indicates that positioning the middle hinge closer to the upper hinge leads to higher localized strain in the upper part of the door. The second plot isolates the strain distribution within the door itself. The maximum strain is 0.0002309 mm/mm, and the strain is primarily concentrated near the upper corner of the door, corresponding to the location of the upper hinge. This suggests that the closer proximity of the middle hinge to the upper hinge leads to less even strain distribution, with a greater focus near the top. The third contour plot shows the strain distribution in the door frame. The maximum strain here is significantly lower, at 0.00010039 mm/mm, indicating that the frame experiences minimal strain, reinforcing its structural rigidity. However, the strain is still somewhat concentrated in areas close to the hinges. In the final plot, the strain within the hinges and bolts is displayed, with a maximum strain of 0.00046277 mm/mm. This suggests moderate strain accumulation in the connecting elements, though it remains within a low range. The higher strain around the upper hinge reflects the positioning's impact on the overall assembly. The total strain distribution for the system when the middle hinge is centrally positioned reveals a maximum strain of 0.00048654 mm/mm, slightly higher than in the first configuration. The strain appears more uniformly distributed across the door, indicating a more balanced load distribution due to the central positioning of the hinge. The door's strain in this configuration shows a maximum value of 0.00024153 mm/mm, and the strain is more evenly distributed compared to the first configuration. This suggests that the central hinge provides better support, leading to a more uniform strain profile across the door's surface. The frame strain remains minimal, with a maximum strain of 0.00010435 mm/mm. This is slightly higher than the first configuration but still indicates that the frame is largely unaffected by hinge positioning, retaining its rigidity. The strain in the hinges and bolts in this configuration has a maximum value of 0.00048654 mm/mm, indicating a more distributed strain compared to the first configuration. This suggests

that placing the middle hinge centrally reduces localized strain, improving the load distribution across the connecting elements.

The strain analysis reveals that the middle hinge's position has a significant effect on the strain distribution within the door system. When the middle hinge is placed closer to the upper hinge, higher strain concentrations are observed in the upper part of the door, potentially leading to increased wear in that area. In contrast, when the middle hinge is centrally positioned, the strain is more evenly distributed, reducing localized stress and improving the overall mechanical performance of the system. These findings suggest that central hinge positioning may enhance the long-term durability of wooden door systems by minimizing strain concentrations.
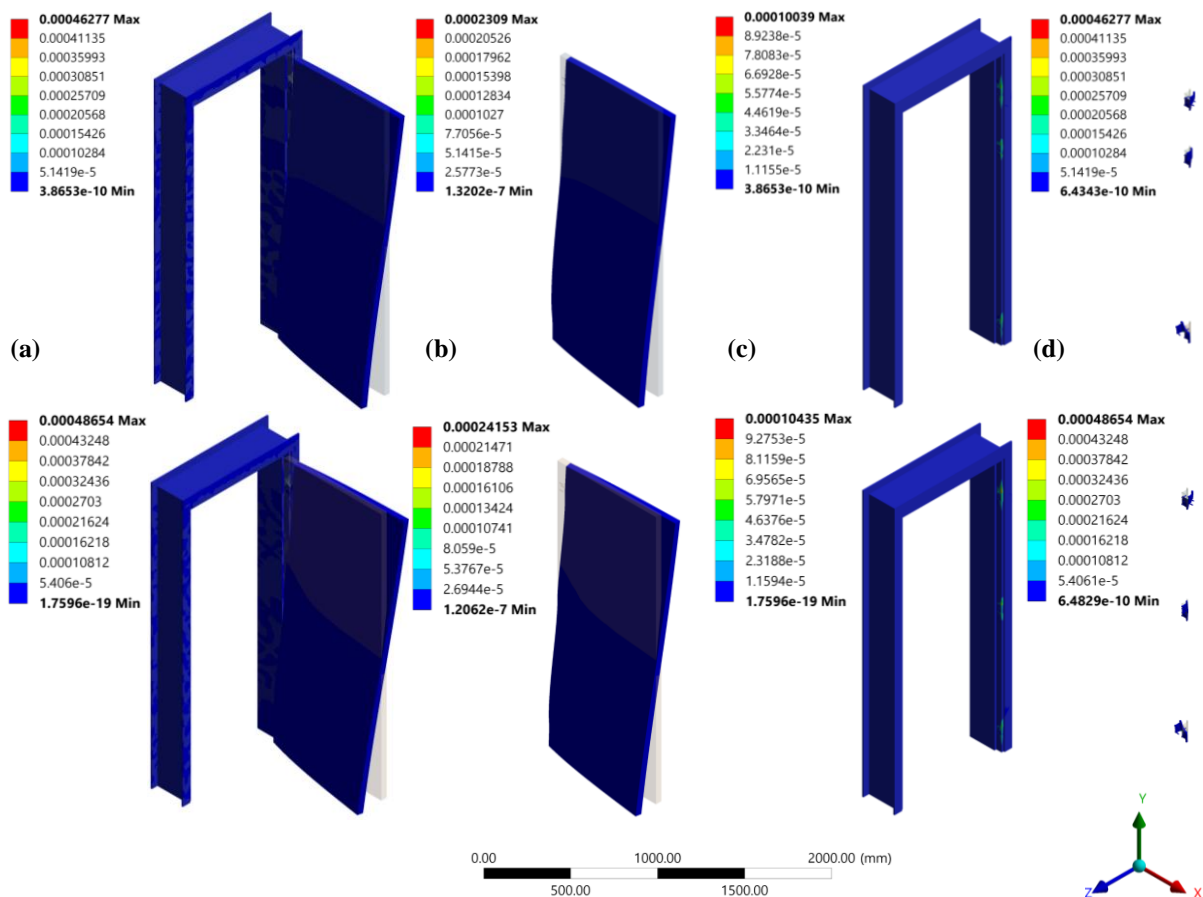
Figure 4. Strain contours (mm/mm) for two hinge configurations of a wooden door system. The first row shows the middle hinge positioned closer to the upper hinge, and the second row shows the middle hinge centrally located. The columns represent (a) the total assembly, (b) the door, (c) the frame, and (d) the hinges and bolts. Central hinge placement significantly reduces strain concentrations compared to the upper hinge configuration.

The stress contours (in MPa) shown in Figure 5 offer an in-depth look into the stress distribution across different parts of the wooden door system for two hinge configurations. The figure consists of two rows and four columns, with the first row representing the configuration where the middle hinge is closer to the upper hinge, and the second row showing the middle hinge in a central position. Each column corresponds to different components of the system, highlighting their stress responses under loading.

The first contour plot in the top-left corner shows the stress distribution for the entire door system, including the door, frame, hinges, and bolts. The maximum von Mises stress is 75.614 MPa, and it is concentrated near the upper section of the door, particularly around the hinges and frame connections. This concentration indicates that the closer positioning of the middle hinge to the upper hinge results in higher stress in these areas. The second plot focuses solely on the door's stress distribution. The maximum stress value here is 2.264 MPa, and it is concentrated near the upper corner of the door. The stress is more localized, likely because the middle hinge being closer to the upper hinge limits load transfer across the entire door, causing higher stress in the upper region. The third plot shows the stress distribution within the door frame, with a maximum stress of 75.614 MPa. The frame experiences significant stress near the hinge attachments, especially at the top. This high stress concentration indicates that the frame bears most of the load when the middle hinge is positioned near the top. The final plot in the first row highlights the stress in the hinges and bolts. The maximum stress is 4.8867 MPa, and it is primarily located around the connections between the hinges and the frame. This stress concentration near the upper hinge suggests that this configuration places considerable stress on the upper joint components.

In the second row, where the middle hinge is centrally located, the overall stress distribution for the door system shows a maximum stress of 78.809 MPa. This is slightly higher than the first configuration, but the stress appears more evenly distributed across the door, frame, and hinges, suggesting better load sharing across the system. The door alone experiences a maximum stress of 2.0502 MPa in this configuration, slightly lower than in the previous setup. The stress distribution is also more uniform, indicating that the central hinge allows for better stress management along the length of the door. The frame shows a maximum stress of 78.809 MPa, similar to the first configuration. However, the stress concentration is more distributed along the frame, particularly around the middle hinge area, which reduces the peak stress near the upper part of the frame. The final plot focuses on the stress within the hinges and bolts, with a maximum stress of 5.0971 MPa. This stress is concentrated near the middle and upper hinges,

indicating that the central hinge configuration distributes the load more evenly across all the connecting elements, resulting in a more balanced stress profile.

The stress analysis highlights significant differences between the two hinge configurations. When the middle hinge is positioned closer to the upper hinge, stress concentrations occur in the upper region of both the door and frame, with higher stress in the bolts and hinges as well. In contrast, when the middle hinge is centrally located, the stress is more evenly distributed across the door and frame, and the overall system experiences better load sharing. This suggests that the central hinge configuration is more effective in reducing localized stress concentrations, which may improve the durability and performance of the door system.
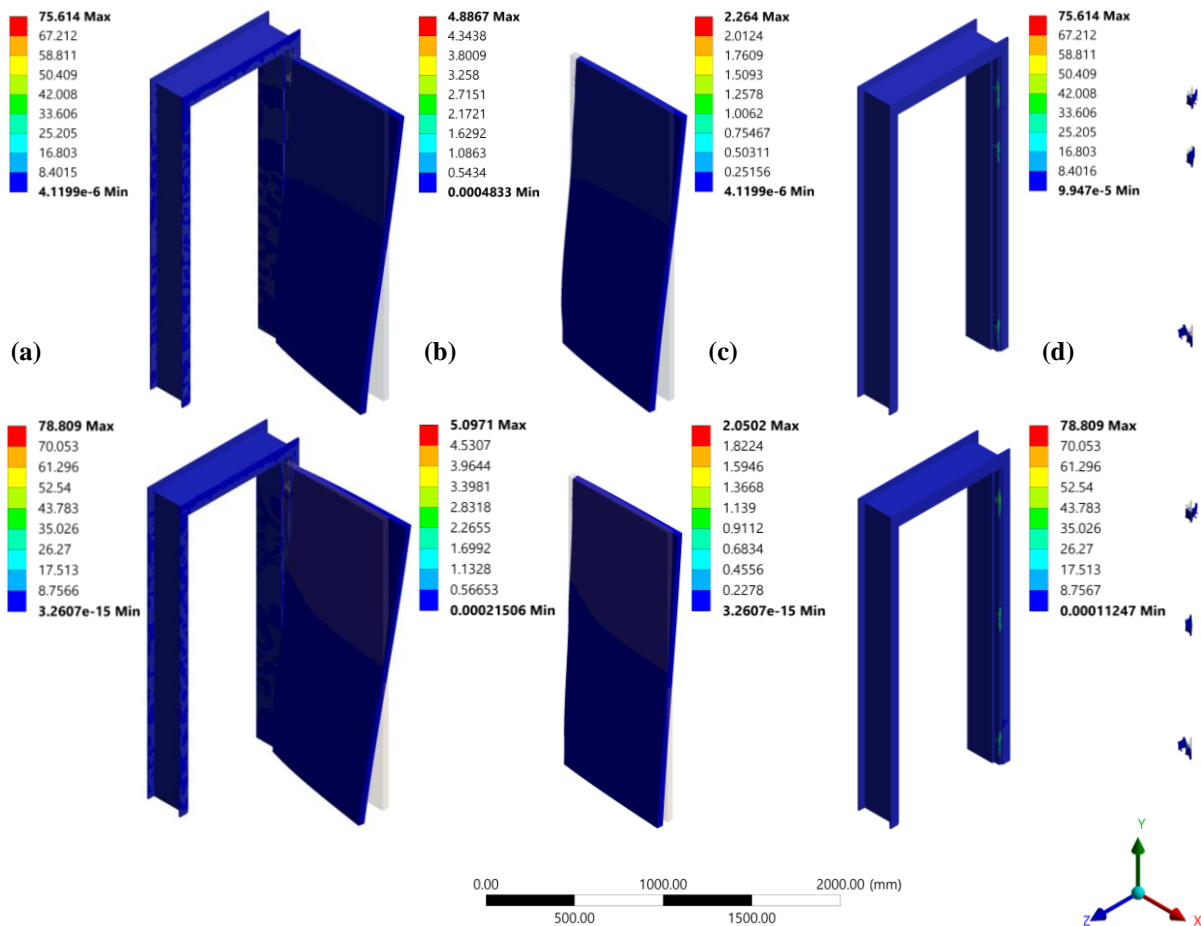
Figure 5. Von Mises stress contours (MPa) for two hinge configurations of a wooden door system. The first row shows the middle hinge positioned closer to the upper hinge, and the second row shows the hinge centrally located. The columns represent (a) the total assembly, (b) the door, (c) the frame, and (d) the hinges and bolts. The upper hinge configuration exhibits higher stress concentrations at the top of the door, whereas the central hinge configuration provides a more balanced stress distribution.

The results of this study, which analyzed different hinge configurations in a wooden door system, show distinct differences in the mechanical behavior of the system. These findings align with similar research on door hinges, particularly regarding the effects of deformation, stress, and strain distribution.

The configuration where the middle hinge was placed closer to the upper hinge showed more localized deformation near the top section of the door. This result is consistent with the findings of Zhou et al. (2012), who observed that improper hinge placement can lead to increased deformation at hinge attachment points, especially when hinges are placed too close to one another. Their study demonstrated that multiple hinge placements could help distribute loads more effectively and reduce overall deformation [8], [16]. A similar outcome was observed in Seker et al. (2021), who studied cabinet doors and found that deformation increased significantly when hinge distribution was not optimized, particularly in two-hinge systems [16]. The centrally placed hinge configuration in the current study resulted in more uniform deformation, confirming that well-spaced hinge placement improves load distribution and structural integrity.

Strain analysis further supports the benefits of central hinge placement, as this configuration exhibited lower strain values compared to the upper hinge placement. Studies by Seker et al. and Zhou et al. (2012) also highlighted that optimal hinge positioning reduces strain concentrations, particularly in high-load areas. Seker et al. noted that uneven hinge distribution in cabinet doors leads to higher strain and greater material fatigue over time, while Zhou et al. demonstrated similar strain behavior in their research on furniture doors [8], [16]. The current study's findings echo these results, showing that central hinge placement promotes a more even distribution of strain across the door's length, reducing the risk of localized strain-induced damage. The results presented in this study are based on static loading conditions, which represent typical operational forces applied to wooden doors. However, in real-world applications, doors may experience dynamic or variable loading, such as impacts, cyclic forces from repeated use, or wind loads. Dynamic loading could introduce additional stress and strain variations, potentially amplifying localized stress concentrations, especially near hinge attachment points. Furthermore, cyclic loading might accelerate material fatigue, particularly in wooden doors with anisotropic properties. Future studies could address these aspects by incorporating time-dependent (dynamic) analyses or fatigue simulations to provide a more comprehensive understanding of the door system's performance under variable loading conditions.

The stress distribution analysis further highlighted that placing the middle hinge closer to the upper hinge resulted in higher stress concentrations at the top of the door and the frame, which could increase the risk of localized failure over time. Erol and Özgül (2019) reported similar behavior in automotive doors, where closely spaced hinges led to stress peaks under operational loads [3]. The central hinge configuration, on the other hand, showed a more balanced stress distribution across the door and frame, which could improve the long-term durability of the door system by reducing the likelihood of material failure. This finding is in line with the work of Isobe and Sato (2023), who found that reducing stress concentrations, especially during seismic events, can significantly improve door performance and longevity [17].

4   CONCLUSION

The finite element analysis of the wooden door system with varying hinge configurations has revealed significant insights into how hinge positioning affects the door's mechanical performance. The key findings of the study are summarized below:

- The configuration with the middle hinge closer to the upper hinge exhibited a maximum von Mises stress of 75.614 MPa in the frame, while the centrally placed hinge configuration showed a slightly higher stress of 78.809 MPa. Despite this, the central configuration provided more balanced load distribution.

- The centrally positioned hinge configuration resulted in a maximum deformation of 0.0213 mm, with a more uniform deformation profile compared to the upper hinge configuration, where deformation was localized near the upper part of the door.

- The central hinge placement significantly reduced localized stress and strain concentrations, suggesting improved structural integrity and prolonged service life for the door system.

- From a practical perspective, centrally placed hinges are recommended for high-use environments, such as residential and commercial settings, where durability and load balance are critical.

- For larger or heavier doors, designers may consider using additional hinges to further enhance load distribution.

This study serves as a practical reference for optimizing hinge placement in wooden door systems, offering insights into how minor adjustments in design can lead to significant improvements in mechanical performance. Future research could explore additional variables such as material properties, hinge stiffness, and dynamic loading conditions to refine the findings and apply them to a wider range of door designs and materials.

Conflict of Interest Statement

There is no conflict of interest between the authors.

Statement of Research and Publication Ethics

The study is complied with research and publication ethics.

Artificial Intelligence (AI) Contribution Statement

Artificial intelligence (AI) tools, including language models, were used solely for language editing, grammar corrections, and improving the fluency of the manuscript. No AI tools were involved in the generation of original content, data analysis, or interpretation of results.

Contributions of the Authors

Yasin Furkan GÖRGÜLÜ: Conceptualization, Data curation, Formal analysis, Funding acquisition, Investigation, Methodology, Project administration, Resources, Software, Supervision, Validation, Visualization, Writing – original draft, Writing – review & editing.

Rahim MERDAN: Conceptualization, Methodology, Writing – original draft.

REFERENCES

[1]   M. Binan, *Ahşap Kapılar ve Metal Tamamlayıcı Elemanlar*. YEM Yayınları, 2000.

[2]   M. I. Hadi, M. R. M. Akramin, and M. S. Shaari, "Finite Element Analysis of Automotive Door Hinge," 2023, pp. 3–11. doi: 10.1007/978-981-19-1457-7_1.

[3]   O. Erol and H. G. Özgül, "Determining simulation parameters of prototype door hinge for correlation between simulation and experimental results in united nations economic commission for europe regulation no: 11 tests," *Designs*, vol. 3, no. 1, pp. 1–20, 2019, doi: 10.3390/designs3010017.

[4]   R. Bayrak, H. Kenan, U. Coşkun, and N. Güzeltepe, "Finite Element Assessment and Fatigue Life Improvement of the Torsion Spring in Hinge," *J. Fail. Anal. Prev.*, Jan. 2025, doi: 10.1007/s11668-024-02085-4.

[5] S. Bekah, "Fatigue life prediction in a door hinge system under uni-axial and multi-axial loading conditions," Ryerson University, 2004. [Online]. Available: http://proquest.umi.com/pqdweb?did=932420431&Fmt=7&clientId=36097&RQT=309&VName=PQD

[6] P. Meyer, J. Finder, and C. Hühne, "Test Methods for the Mechanical Characterization of Flexure Hinges," *Exp. Mech.*, vol. 63, no. 7, pp. 1203–1222, Sep. 2023, doi: 10.1007/s11340-023-00982-7.

[7] S.-W. Hwang, H. Isoda, T. Nakagawa, and J. Sugiyama, "Flexural anisotropy of rift-sawn softwood boards induced by the end-grain orientation," *J. Wood Sci.*, vol. 67, no. 1, p. 14, Dec. 2021, doi: 10.1186/s10086-021-01946-y.

[8] J. Zhou, C. Hu, S. Hu, H. Yun, and G. Jiang, "Optimization of Hinge Configuration of Furniture Doors Using Finite Element Analysis," *BioResources*, vol. 7, no. 4, pp. 5809–5816, Oct. 2012, doi: 10.15376/biores.7.4.5809-5816.

[9] M. H. Ramage *et al.*, "The wood from the trees: The use of timber in construction," *Renew. Sustain. Energy Rev.*, vol. 68, pp. 333–359, Feb. 2017, doi: 10.1016/j.rser.2016.09.107.

[10] M. Ashby, "Material property data for engineering materials," 2021.

[11] TSE, "TS 825." Accessed: Jan. 15, 2025. [Online]. Available: https://intweb.tse.org.tr/standard/standard/Standard.aspx?08111805111510805110411911010405504710 510212008811104311310407309909811109911408611411704809098

[12] Y. F. Gorgulu, "Thermal efficiency evaluation in shell-and-tube heat exchangers: A CFD-based parametric study," *Proc. Inst. Mech. Eng. Part E J. Process Mech. Eng.*, 2024, doi: 10.1177/09544089241262481.

[13] M. Aydin and Y. F. Gorgulu, "Structural Investigation of Wood-Inspired Cell Wall Geometries Using Additive Manufacturing: Compression Testing and Finite Element Analysis Validation," *BioResources*, vol. 19, no. 4, pp. 7493–7512, 2024, doi: biores.19.4.7493-7512.

[14] Ansys Inc. and A. Inc., "Introduction to Ansys Meshing." Ansys Inc., pp. L5-16, 2011. [Online]. Available: file:///C:/Users/Furkan/AppData/Local/Mendeley Ltd./Mendeley Desktop/Downloaded/Ansys Inc. - 2011 - Introduction to Ansys Meshing.pptx

[15] Ansys Inc., "Mesh Quality And Advanced Topics Ansys Workbench 16.0," 2015.

[16] S. Seker, E. S. Erdinler, and Y. Z. Erdil, "A study on hinges and cabinet doors," in *Proceedings of the XXXth International online conference Research for Furniture Industry*, 2022, pp. 125–135. doi: 10.17306/mk.978-83-67112-51-2.11.

[17] D. Isobe and K. Sato, "Numerical investigation on mechanical behavior of door systems during seismic excitation," *J. Build. Eng.*, vol. 68, no. September 2022, p. 106129, Jun. 2023, doi: 10.1016/j.jobe.2023.106129.

COMPARISON OF NUMERICAL METHODS FOR THE KUBA OSCILLATOR

Gülşen ORUCOVA BÜYÜKÖZ [1*] 🆔, Tuğçem PARTAL [2] 🆔, Mustafa BAYRAM [3] 🆔

[1] *Necmettin Erbakan University, Department of Mathematics and Computer Science, Konya, Türkiye*

[2] *Recep Tayyip Erdoğan University, Department of Computer Engineering, Rize, Türkiye*

[3] *Biruni University, Department of Computer Engineering, İstanbul, Türkiye*

* Corresponding Author: gorucova@erbakan.edu.tr

ABSTRACT

In this study, numerical solutions of stochastic differential equation (SDE) systems have been analyzed and three different numerical methods used for solving these systems, the Milstein method, the Simplified Second-Order Taylor Scheme, and the Stochastic Runge-Kutta (SRK) method, have been compared. The Kubo oscillator model has been considered and the stochastic dynamics of this model have been solved using numerical methods. Initially, the general structure of SDEs is introduced, and the theoretical foundations of the methods used for solving these systems are explained.

In the study, the stochastic model of the Kubo oscillator was solved numerically using the Milstein method, the Simplified Second-Order Taylor Scheme, and the SRK method. The results obtained were compared with exact solutions. In the numerical computations, the accuracy of all three methods is analyzed for different discretization counts and the results were supported by graphs and error tables. The comparisons revealed that the Simplified Second-Order Taylor Scheme provided more accurate solutions compared to the Milstein method. It is observed that the Taylor method and the SRK 2-stage method gave close results. Additionally, it was observed that increasing the number of discretizations brought both methods closer to the exact solution.

Keywords: Stochastic differential equation systems, Numerical approximations, Kubo oscillator.

1   INTRODUCTION

Stochastic differential equations (SDEs) are mathematical tools developed and widely used to model the effects of uncertainty in various fields. These equations are employed in disciplines such as physics, biology, engineering, and economics to understand how systems respond to random variables. For instance, SDEs can enhance the realism of modeling changes in population dynamics in biological systems under uncertainty [1]. Similarly, in finance, effective risk management approaches have been developed by modeling market fluctuations using SDEs [2].

The Kubo oscillator is a well-known model used to study uncertainties and random effects when modeling with stochastic differential equations [3]. This model is particularly suitable for evaluating the dynamics of stochastic processes and the performance of various numerical methods applied to these processes.

The Kubo oscillator is a cornerstone model in stochastic dynamics, blending deterministic behavior with random fluctuations to describe systems influenced by noise. Initially introduced by Kubo to model spectral diffusion and line broadening in nuclear magnetic resonance (NMR), it has since evolved into a versatile tool used across various scientific and engineering disciplines [4]. The oscillator's dynamics, governed by the interplay between a damping term and stochastic forcing, enable it to capture the complexity of processes ranging from molecular interactions in fluctuating environments [5].

The Kubo oscillator, a fundamental example of a stochastic Hamiltonian system, is a subject of extensive study for the purpose of comprehending the interplay between deterministic Hamiltonian dynamics and stochastic noise. Its structural characteristics offer insights into the influence of random fluctuations on physical and mathematical systems, thus establishing it as a pivotal model in the field of stochastic dynamics [6].

In addition, the Kubo oscillator effectively models systems affected by high-frequency oscillations and multiplicative noise, making it a cornerstone in the study of stochastic dynamics [7].

The Milstein method is frequently used for solving stochastic differential equations and provides higher accuracy as an extension of the Euler-Maruyama method [8]. This method is especially preferred for reducing the error rate in stochastic models. On the other hand, the Simplified Second-Order Taylor Scheme aims to provide more precise solutions by considering higher-order terms of stochastic equations [9].

The fact that analytical solutions for SDEs are often not feasible increases the importance of numerical solution methods. In fields such as biology and ecology, modeling using these equations provides essential insights into understanding the impact of uncertainties in the real world [10]. However, in such modeling, ensuring accuracy and optimizing computational costs are equally important. Comparing numerical approaches in terms of computational complexity and accuracy is therefore essential [11].

Previous studies on the Kubo oscillator have shown that this model effectively represents the dynamics of stochastic oscillations and provides a suitable foundation for testing numerical methods. Fox, Roy, and Yu (1987) demonstrated that different simulation algorithms, including those for white and colored noise, can be effectively tested using the Kubo oscillator, and that the use of colored noise significantly enhances the accuracy of the numerical solutions compared to white noise simulations, reducing spurious decays in the oscillator amplitude [12].

In this study, the Milstein method, the Simplified Second-Order Taylor Scheme and Stochastic Runge-Kutta method are applied to the Kubo oscillator model, and the obtained numerical results are compared with exact solutions. Additionally, different discretization strategies are used to analyze the accuracy and computational efficiency of both methods.

In conclusion, this study aims to compare the performance of three different numerical methods used for SDEs within the context of the Kubo oscillator model. This comparison highlights the advantages and disadvantages of these methods, providing valuable insights into determining the most suitable method for solving SDEs.

2   MATERIAL AND METHOD

2.1   Systems of Stochastic Differential Equations

Systems of stochastic differential equations are used for vector-valued states or high-order stochastic differential equations. The general form of a d-dimensional stochastic differential equation is described by [9] as following:

$$dX_t = f(t, X_t)dt + g(t, X_t)dW_t \tag{1}$$

where $W = \{W_t, t \geq 0\}$ Wiener process is m-dimensional and its components $W_t^1, W_t^2, ..., W_t^m$ are independent Wiener processes with respect to a common family of $\sigma -$ algebras $\{A_t, t \geq 0\}$, d-dimensional vector function is $f: [0, T] \times \mathbb{R}^d \to \mathbb{R}^d$ and $d \times m$-matrix function is $g: [0, T] \times \mathbb{R}^d \to \mathbb{R}^{d \times m}$. Stochastic integral equation form of (1) is

$$X_t = X_{t_0} + \int_{t_0}^{t} f(r, X_r)dr + \int_{t_0}^{t} g(r, X_r)dW_r \qquad (2)$$

i.th component of (2) is

$$X_t^i = X_{t_0}^i + \int_{t_0}^{t} f^i(r, X_r)dr + \sum_{k=1}^{m} \int_{t_0}^{t} g^{i,k}(r, X_r)dW_r^k \qquad (3)$$

where $i = 1,2, \dots, d$.

The existence and uniqueness for strong solutions of (1) are proven in [9]. There is a relation between the Ito stochastic differential equation and the Stratonovich stochastic differential equation as follows: X_t solution of (1) is also a solution of the Stratonovich differential equation as;

$$dX_t = \bar{f}(t, X_t)dt + g(t, X_t)odW_t \qquad (4)$$

where

$$\bar{f}^i(t, X_t) = f^i(t, X_t) - h^i(t, X_t) \qquad (5)$$

and

$$h^i(t, X_t) = \frac{1}{2} \sum_{n=1}^{d} \sum_{k=1}^{m} g^{n,k}(t, X_t) \frac{\partial g^{i,k}}{\partial x_n}(t, X_t) \qquad (6)$$

for $i = 1,2, \dots, d$.

The general form of d-dimensional linear stochastic differential equations is

$$dX_t = [F(t)X_t + f(t)]dt + \sum_{l=1}^{m} [G^l(t)X_t + g^l(t)]\, dW_t^l \qquad (7)$$

where $F(t), G^1(t), G^2(t), \dots, G^m(t)$ are $d \times d$-matrix function and $f(t), g^1(t), g^2(t), \dots, g^m(t)$ are d-dimensional vector functions. Solution of (7) is

$$X_t = \Psi_{t,t_0} \left\{ X_{t_0} + \int_{t_0}^{t} \Psi_{r,t_o}^{-1} \left(f(r) - \sum_{l=1}^{m} G^l(r)g^l(r) \right) dr + \sum_{l=1}^{m} \int_{t_0}^{t} \Psi_{r,t_0}^{-1} g^l(r)dW_r^l \right\} \qquad (8)$$

where Ψ_{t,t_0} is $d \times d$-fundamental matrix which satisfying $\Psi_{t_0,t_0} = I$ and the homogeneous matrix stochastic differential equation

$$dΨ_{t,t_0} = F(t)Ψ_{t,t_0}dt + \sum_{l=1}^{m} G^l(t)\,Ψ_{t,t_0}dW_t^l \tag{9}$$

Because the systems of linear stochastic differential equations cannot be solved analytically. Therefore, we need numerical solutions which are given in [10], [13], [14].

2.2 Numerical Methods for Stochastic Differential Equations

We use in our study three numerical methods named with the Milstein method, the Simplified order 2 Taylor scheme, and the SRK method.

2.2.1 Milstein Method

The Milstein method is a numerical method used to approximate solutions to stochastic differential equations (SDEs). It is particularly well-known for achieving strong order 1 convergence under certain conditions, making it more accurate than the other simple methods (which has strong order 0.5). The Milstein scheme has the following recurrence formula for d-dimensional stochastic differential equations when $m = 1$. i.th component of the Milstein scheme for (1) given in [8] as

$$X_{k+1}^i = X_k^i + f^i(t, X_t)Δt + g^i(t, X_t)ΔW_k + \frac{1}{2}\left(\sum_{n=1}^{d} g^n \frac{\partial g^i}{\partial x^n}(t, X_t)\right)[(ΔW_k)^2 - Δt] \tag{10}$$

where

$$ΔW_k = W_{t_{k+1}} - W_{t_k}, \qquad i = 1,2,\dots,d, \qquad k = 1,2,\dots,N\,.$$

2.2.2 Simplified Order 2 Taylor Scheme

The Simplified Second-Order Taylor Scheme provides significant advantages in solving stochastic differential equations (SDEs) by incorporating higher-order terms that improve accuracy and reduce errors. Unlike first-order methods such as Euler-Maruyama, which have a strong convergence rate of $\left(O(Δt^{1/2})\right)$ or the Milstein Method, which has a strong convergence rate of $\left(O(Δt)\right)$, the Second-order scheme achieves a faster convergence rate of $\left(O(Δt^2)\right)$. This improvement allows for more precise approximations, especially in systems with nonlinear dynamics and significant stochastic influences. By accounting for higher-order interactions, the method effectively captures the interplay between deterministic and stochastic components,

ensuring a more faithful representation of the system's behavior. Additionally, this scheme mitigates accumulated errors in long-term simulations, enhancing stability and reliability over time [9].

In the d-dimensional case, the i.th component of the Simplified Order 2 Taylor scheme for (1) is given in [15] as follows:

$$
X_{k+1}^i = X_k^i + \sum_{l=1}^m g^{i,l} \Delta W_k^l + f^i \Delta t + \frac{1}{2} \sum_{p,l=1}^m \left(\sum_{n=1}^d g^{n,p} \frac{\partial g^{i,l}}{\partial x^n} \right) \left(\Delta W_k^p \Delta W_k^l + U_{pl,k} \right)
$$

$$
+ \frac{1}{2} \sum_{l=1}^m \left(\sum_{j=1}^d g^{j,l} \frac{\partial f^i}{\partial x^j} + \frac{\partial g^{i,l}}{\partial t} + \sum_{j=1}^d f^j \frac{\partial g^{i,l}}{\partial x^j} + \frac{1}{2} \sum_{n,j=1}^d h^{n,j} \frac{\partial^2 g^{i,l}}{\partial x^n \partial x^j} \right) \Delta t \Delta W_k^l \qquad (11)
$$

$$
+ \frac{1}{2} \left(\frac{\partial f^i}{\partial t} + \sum_{n=1}^d f^n \frac{\partial f^i}{\partial x^n} + \frac{1}{2} \sum_{n,j=1}^d h^{n,j} \frac{\partial^2 f^i}{\partial x^n \partial x^j} \right) (\Delta t)^2
$$

where $k = 1,2, \dots, N$ and $U_{pl,k}$,$p, l = 1,2, \dots, m$ are independent two-point distributed random variables with

$$
P\left(U_{pl,k} = \Delta\right) = \frac{1}{2} = P\left(U_{pl,k} = -\Delta\right) \quad \text{if } l < p
$$

$$
U_{pp,k} = -\Delta
$$

$$
U_{pl,k} = -U_{lp,k} \quad \text{if } l > p
$$

2.2.3 Two Stage Stochastic Runge-Kutta Method

The scheme of the Stochastic Runge-Kutta (SRK) method for a system of stochastic differential equations according to the $s-$stage ($s \geq 1$) is as follows [15]:

$$
X_{k+1} = X_k + \sum_{j=1}^s \alpha_j f\left(t_k + \mu_j \Delta t, \eta_j\right) \Delta t + \sum_{j=1}^s \beta_j g\left(t_k + \mu_j \Delta t, \eta_j\right) \Delta W_k \qquad (12)
$$

where $k = 1,2, \dots, N$ and $\mu_1 = 0, \eta_1 = X_k$ for $j = 1,2, \dots s$

$$
\eta_j = X_k + \sum_{l=1}^{j-1} \lambda_{jl} f(t_k + \mu_l \Delta t, \eta_l) \Delta t + \sum_{l=1}^{j-1} \gamma_{jl} g(t_k + \mu_l \Delta t, \eta_l) \Delta W_k
$$

and α_j, β_j are to provide $\sum_{j=1}^s \alpha_j = \sum_{j=1}^s \beta_j = 1$.

The coefficients occurring in (12) can be displayed by generalising Butcher arrays;

$$
\begin{array}{c|cccc|cccc}
\mu_2 & \lambda_{21} & & & & \gamma_{21} & & & \\
\mu_3 & \lambda_{31} & \lambda_{32} & & & \gamma_{31} & \gamma_{32} & & \\
\vdots & \vdots & \vdots & \ddots & & \vdots & \vdots & \ddots & \\
\mu_s & \lambda_{s1} & \lambda_{s2} & \cdots & \lambda_{s,s-1} & \gamma_{s1} & \gamma_{s2} & \cdots & \gamma_{s,s-1} \\
\hline
 & \alpha_1 & \alpha_2 & \cdots & \alpha_{s-1} & \alpha_s & \beta_1 & \beta_2 & \cdots & \beta_{s-1} & \beta_s
\end{array}
$$

In our study, the SRK method for 2-stage is used and coefficients are taken from [16]

$$
\begin{array}{c|c|c}
1 & 1 & 1 \\
\hline
 & \frac{1}{2} \quad \frac{1}{2} & \frac{1}{2} \quad \frac{1}{2}
\end{array}
$$

The algorithms of the Milstein, the Simplified Order 2 Taylor, and the SRK methods are given in Figure 1.

Our aim in this paper is to compare these numerical methods. We compare the exact solution with numerical solutions that we obtain using the MATLAB program. We aim to demonstrate the errors between the exact solution and each numerical solution. We support our work with graph and error tables.
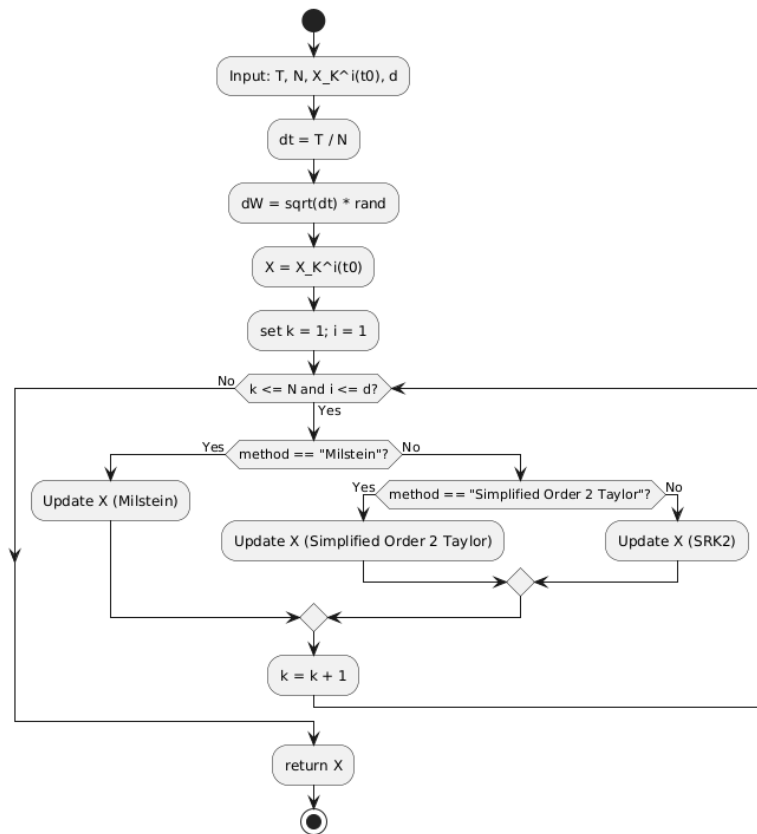
Figure 1. Flowchart of the Milstein, the Simplified Order 2 Taylor, and the SRK methods.

3   NUMERICAL EXPERIMENTS AND RESULTS

Consider the Kubo oscillator in our study. This oscillator is used in many works to demonstrate the efficiency of numerical methods. The general form of the Kubo oscillator, which is given in [1], is

$$\begin{pmatrix} dX_t^1 \\ dX_t^2 \end{pmatrix} = \begin{pmatrix} 0 & -\alpha \\ \alpha & 0 \end{pmatrix}\begin{pmatrix} X_t^1 \\ X_t^2 \end{pmatrix} dt + \begin{pmatrix} 0 & -\gamma \\ \gamma & 0 \end{pmatrix}\begin{pmatrix} X_t^1 \\ X_t^2 \end{pmatrix} o dW_t \tag{13}$$

with $X_0^1 = x^1, X_0^2 = x^2$ where α , γ are real and $t \in [0, T]$. For initial values $X_0^1 = 1$, $X_0^2 = 0$, the exact solution of (13) is

$$X_t^1 = \cos(\alpha t + \gamma W_t) \tag{14}$$

$$X_t^2 = \sin(\alpha t + \gamma W_t)$$

Coefficients $\alpha = 2, \gamma = 0.3$ and exact solutions are taken from [3] (David Cohen who used these coefficients for testing his method) and initial values are $X_0^1 = 1, X_0^2 = 0$, $T = 10$. Using (5) and (6) formulas we obtain Ito stochastic differential equation system for (13) as follow;

$$dX_t^1 = \left(-2X_t^2 - \frac{(0.3)^2}{2} X_t^1\right) dt - 0.3 X_t^2 dW_t \tag{15}$$

$$dX_t^2 = \left(2X_t^1 - \frac{(0.3)^2}{2} X_t^2\right) dt + 0.3 X_t^1 dW_t$$

where $d = 2, m = 1$.

We solve numerically (15), using the Milstein scheme (10) for $X_0^1 = 1, X_0^2 = 0, T = 10$ and $N = 10000$ discretization by the MATLAB program. There is numerical approximation and an exact solution in the same graph in Figure 2. In this figure, the exact solution is plotted with a red line, and the Milstein approximation is plotted with a blue line. As seen in Figure 2, the approximate solution and the exact solution are very close to each other.
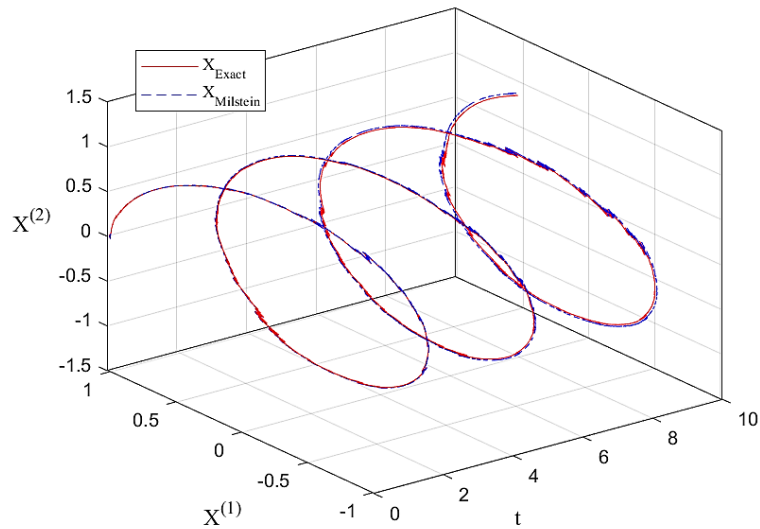
***Figure 2. The exact solution with the Milstein Approximation of the Kubo Oscillator for
N = 10000, T=10, α = 2, γ = 0.3.***

Analogously, using the simplified order 2 Taylor scheme (11) for solving (15), we obtain Figure 3, where the exact solution is plotted with a red line and the Simplified Order 2 Taylor Scheme approximation is plotted with a blue line. It is seen that the solutions are very close.
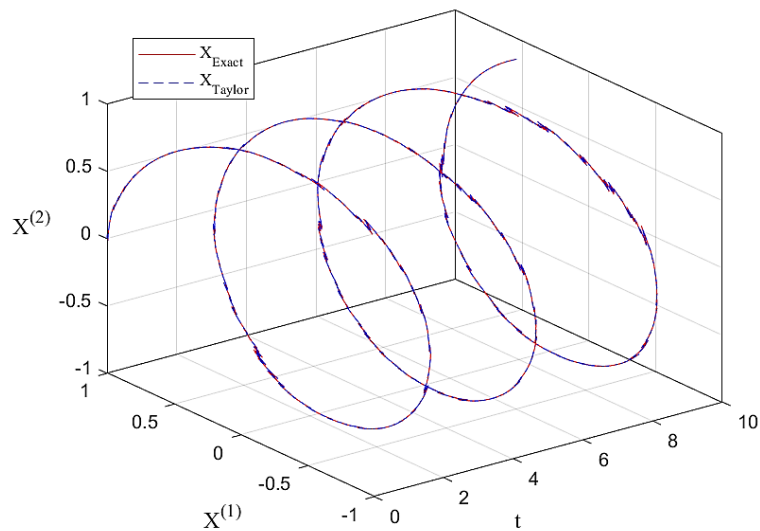
***Figure 3. The exact solution and the Simplified 2 order Taylor Approximation of the Kubo
Oscillator for N = 10000, T=10, α = 2, γ = 0.3.***

In addition, using the SRK method for 2-stage solving (15), we obtain Figure 4, where the exact solution is plotted with a red line and the SRK approximation is plotted with a blue line.
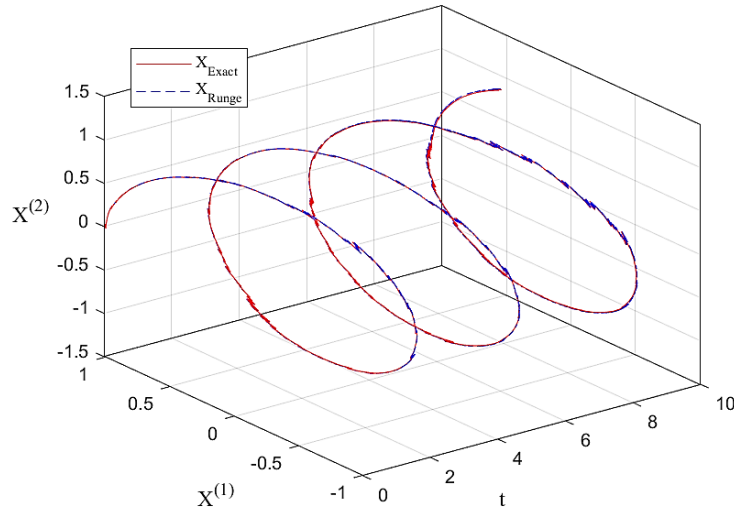
Figure 4. The exact solution and the SRK for 2-Stage Approximation of the Kubo Oscillator for $N = 10000$, T=10, $\alpha = 2, \gamma = 0.3$.

For efficiency both approximations are given in the same graph in Figure 5. There the exact solution is plotted with a red line, the Milstein approximation is plotted with a green line, the simplified order 2 Taylor scheme approximation is plotted with a blue line, and the SRK approximation is plotted with a magenta line.
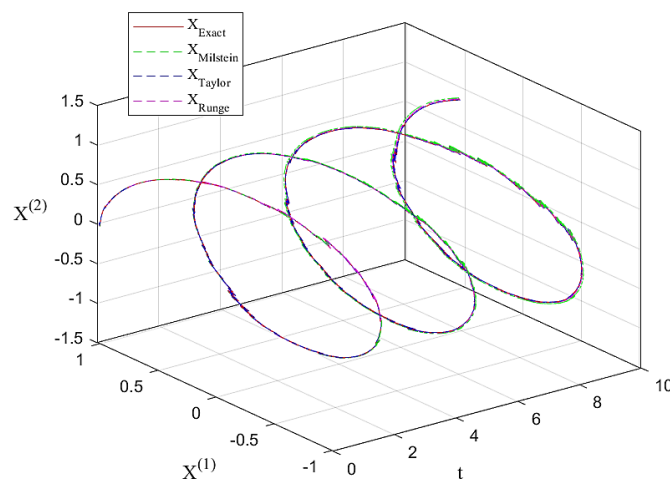
Figure 5. The exact solution with the Milstein Approximation Simplified 2 Order Taylor Approximation and the SRK Approximation of the Kubo Oscillator for $N = 10000$, T=10, $\alpha = 2, \gamma = 0.3$.

To compare the solutions obtained by the Milstein, the Simplified 2 Order Taylor methods, and the SRK methods, the mean absolute error and mean relative error were calculated. For different N discretizations, there are the mean absolute errors (MAE) obtained with the Milstein Simplified 2 Order Taylor and SRK methods using following scheme;

$$MAE = \frac{1}{N} \sum_{k=1}^{N} |X_k - \tilde{X}_k| \qquad (16)$$

where X_k and $\tilde{X}_k$ represent the exact and approximate solutions, respectively, in iteration k.

Table 1. *Mean absolute errors of the Milstein, Simplified 2 Ordet Taylor and SRK methods for different discretizations.*

N	Milstein Method		Simplified 2 Order Taylor Method		SRK Method for 2-Stage	
	X_t^1	X_t^2	X_t^1	X_t^2	X_t^1	X_t^2
10^4	0.0059	0.0057	0.0036	0.0035	0.00357	0.00362
10^5	6.8179e-04	7.6157e-04	1.6650e-04	2.0252e-04	1.6650e-04	2.0252e-04
10^6	6.6710e-05	7.5789e-05	6.5196e-05	7.2913e-05	6.5197e-05	7.2911e-05

Table 1 shows the mean absolute errors of the three methods for different N discretizations. It is observed that the solutions obtained by the Simplified 2 Order Taylor method are more effective than the solutions obtained by the Milstein method. Runge-kutta 2-stage and Simplified 2 Order Taylor solutions are close to each other.

In addition, for different N discretizations, there are the mean relative errors (MRE) obtained with the three methods using the following scheme:

$$MRE = \frac{1}{N} \sum_{k=1}^{N} \left| \frac{X_k - \tilde{X}_k}{X_k} \right| \qquad (17)$$

where X_k and $\tilde{X}_k$ represent the exact and approximate solutions, respectively, in iteration k.

Table 2. *Mean relative errors of the Milstein, Simplified 2 Ordet Taylor and SRK method for different discretizations.*

N	Milstein Method		Simplified 2 Order Taylor Method		SRK Method for 2-Stage	
	X_t^1	X_t^2	X_t^1	X_t^2	X_t^1	X_t^2
10^4	2.0440e-05	9.4782e-06	2.1132e-08	7.7765e-09	2.1135e-08	7.7769e-09
10^5	3.4300e-07	1.1335e-06	5.4836e-10	1.6983e-09	5.4839e-10	1.6988e-09
10^6	1.8974e-09	1.4597e-09	2.1355e-12	1.5529e-12	2.1357e-12	1.5531e-12

Table 2 shows the mean relative errors of the three methods for different N discretizations. It can be seen that the solutions obtained with the simplified 2 Ordet Taylor method are better than the solutions obtained with the Milstein method.

4 RESULTS AND DISCUSSION

In this paper we compare the Milstein scheme and the Simplified 2 Order Taylor scheme for the Kubo oscillator. For each scheme we show the approximate solution and the exact solution. We also calculate the mean absolute error and the mean relative error between the numerical solutions and the exact solution. According to our results, we can say that the numerical solution obtained from the Simplified 2 Order Taylor scheme is closer to the exact solution than the numerical solution obtained from the Milstein method. From the error table, we can say that the numerical solutions get closer to the exact solution as the number of discretizations increases for each numerical scheme. It is also observed that the mean relative error is smaller than the mean absolute error for both methods. The reason is that Simplified 2 Order Taylor's strong convergence order is greater than Milstein's strong convergence order. The errors obtained from the SRK 2-stage and Simplified 2 Order Taylor solutions are lower than the Milstein solution. The Taylor and SRK 2-stage solutions are very close to each other.

Conflict of Interest Statement

There is no conflict of interest between the authors.

Statement of Research and Publication Ethics

The study is complied with research and publication ethics.

Artificial Intelligence (AI) Contribution Statement

This manuscript was entirely written, edited, analyzed, and prepared without the assistance of any artificial intelligence (AI) tools. All content, including text, data analysis, and figures, was solely generated by the authors.

Contributions of the Authors

Gülşen Orucova Büyüköz: Conceptualization, Methodology, Formal Analysis, Writing – Original Draft, Writing – Review & Editing.

Tuğçem Partal: Methodology, Software, Validation, Data Curation, Writing – Review & Editing.

Mustafa Bayram: Supervision, Project Administration, Resources, Writing – Review & Editing.

REFERENCES

[1]   X. Mao, *Stochastic Differential Equations and Applications*, 2nd ed. Elsevier, 2007.

[2]   F. Black and M. Scholes, "The Pricing of Options and Corporate Liabilities," *Journal of Political Economy*, vol. 81, no. 3, pp. 637-654, 1973.

[3]   D. Cohen, "On The Numerical Discretisation of Stochastic Oscillators," *Mathematics and Computers in Simulation*, vol. 82, no. 8, pp. 1478-1495, 2012.

[4]   R. Kubo, "Stochastic Liouville equations", *J. Math. Phys*. 4, 174–183, 1963.

[5]   B. J. Berne, R. Pecora, *Dynamic Light Scattering: With Applications to Chemistry, Biology, and Physics*, Wiley-Interscience, 1976.

[6]   C. Xupeng & W. Lijin, "Learning stochastic Hamiltonian systems via neural network and numerical quadrature formulae", *Journal of University of Chinese Academy of Sciences*, 74.

[7]   D. Segal, "Vibrational relaxation in the Kubo oscillator: Stochastic pumping of heat.", *The Journal of chemical physics* 130.13, 2009.

[8]   G. N. Milstein, "Approximate Integration of Stochastic Differential Equations," *Theory of Probability & Its Applications*, vol. 19, no. 3, pp. 557-562, 1975.

[9]   P. E. Kloeden and E. Platen, *Numerical Solution of Stochastic Differential Equations*, Berlin, Heidelberg: Springer, 1992.

[10]   E. Allen, *Modeling with Itô Stochastic Differential Equations*, vol. 22. Springer Science & Business Media, 2007.

[11]   D. J. Higham, "An Algorithmic Introduction to Numerical Simulation of Stochastic Differential Equations," *SIAM Review*, vol. 43, no. 3, pp. 525-546, 2001.

[12]   R. F. Fox, R. Roy, and A. W. Yu, "Tests of Numerical Simulation Algorithms for the Kubo Oscillator," *Journal of Statistical Physics*, vol. 47, pp. 477-487, 1987.

[13]   B. Øksendal, *Stochastic Differential Equations*, Berlin, Heidelberg: Springer, 2003.

[14]   A. Friedman, *Stochastic Differential Equations and Applications*, Berlin, Heidelberg: Springer, 1975.

[15]   A. Tocino and R. Ardanuy, "Runge–Kutta Methods for Numerical Solution of Stochastic Differential Equations," *Journal of Computational and Applied Mathematics*, vol. 138, no. 2, pp. 219-241, 2002.

[16]   Baylan, E., (2014). Simulating Stochastic Differential Equations Using Ito-Taylor Schemes, Master's Thesis, METU, Ankara. 3(1):37-51.

A HYDROPHILLIC DEEP EUTECTIC SOLVENT ASSISTED MAGNETIC COLLOIDAL GEL BASED DISPERSIVE SOLID PHASE MICROEXTRACTION METHOD FOR PRECONCENTRATION OF BROWN HT (E155)

Figen EREK [1] (iD)

[1] *Dicle University, Department of Chemistry, Diyarbakir, Türkiye, figen.erek@dicle.edu.tr*

ABSTRACT

A hydrophillic deep eutectic solvent assisted magnetic colloidal gel based dispersive solid phase microextraction method (MCG-dSPME) was developed for the pre-concentration of Brown HT (E155) before its spectrophotometric analysis. Magnetic colloidal gel was obtained from Fe_3O_4@XAD-7 nanoparticles and phenol/choline chloride (2:1) (hyrophillic deep eutectic solvent (DES). For the optimization of the developed method, several parameters such as pH, amount of Fe_3O_4@XAD-7 nanoparticles in the colloidal gel, volume of colloidal gel, type of desorption solvent, vortex time (for adsorption and desorption), sample volume were investigated. After determining the optimum conditions, the linear range, limit of detection (LOD), enhencament factor (EF), preconcentration factor (PF), relative standard deviation (RSD %) of the method were calculated. Then, addition/recovery test and intraday-interday test were applied for the accuracy and the precision, respectively. The matrix effect study was examined for the selectivity of the method. The linear range, LOD, RSD %, EF, and PF values of the method were found to be 0.05-0.75 mgL^{-1}, 0.016. mgL^{-1}, 3.8%, 51 and 25, respectively. The study was found to be no interference method with high accuracy and precision. In this study, according to our literature research, since there are very few studies on the determination of Brown HT, it was aimed to develop an up-to-date, economical, non-invasive, environmentally friendly and simple method for this dye.

Keywords: Magnetic colloidal gel, Dispersive solid phase microextraction method, Preconcentration, Spectrophotometric determination, Brown HT.

1 INTRODUCTION

Food coloring agents can be used to restore the original appearance of food in cases where the color of the food is affected by processing, storage, packaging and distribution, and

its visual acceptability is damaged, to make the food more visually attractive, and to give color to colorless food [1].

Brown HT (E 155, IC: 20285), whose chemical name is disodium 4,4'-(2,4-dihydroxy-5-hydroxymethyl-1,3-phenylene bis-azo) di- (naphthalene-1-sulfonate), (CAS No: 4553 -89-3) is a bis azo group food colorant. The molecular weight of this dye, which has the closed formula $C_{27}H_{18}N_4Na_2O_9S_2$, is 652.56 g/mol. This food colorant dissolves well in water and methanol[2]. The chemical structure of the dye is shown in Figure 1.
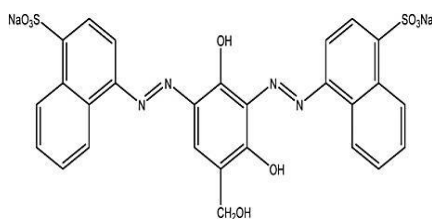
Figure 1. Chemical structure of Brown HT.

The maximum daily acceptable intake of Brown HT is 1.5 mg / kg-bw. Studies on mice with the dye have shown that it or its metabolites are absorbed in limited amounts and approximately 90% of this is excreted in the feces. It has also been observed that it accumulates in the lymph nodes and kidneys of mice [3].

According to the Turkish Food Codex, the maximum amount of Brown HT in foodstuffs/beverages is 50 mgkg^{-1} or mgL^{-1} [1]. According to European Parliament and Council Directive 94/36/EC, the maximum usage levels in foodstuffs and beverages are 500 mgkg^{-1} and 200 mgL^{-1}, respectively [3].

Brown HT is widely used as an additive in the food industry in soft drinks, flour, chocolate sauces, puddings, creams, candies and cookies[2-3]. Brown HT has been reported to be toxic to human at high concentrations. Because it has high water solubility, it can easily spread into the environment with industrial waste and harm animals. Like other azo dyes, Brown HT is also known as ecotoxic due to its harmful effects on the environment and public health. Therefore, the analysis of this dye is very important. Sensitive, accurate and reliable methods are needed for the analysis of this dye[4-8]. However, in our literature research, analysis methods for the determination of this dye are quite few]. Cloud point extraction-scanometry (CPE-scanometry) [9], UV-Vis spectrophotometer [10] and high-performance liquid chromatography/diode array detection (HPLC/DAD) [2], the cyclic voltammetry (CV) [11] methods are among the studies in the literature for the quantitative analysis of Brown HT.

Magnetic solid phase microextraction methods, unlike classical solid phase extraction methods, apply more miniature extraction processes. Smaller amounts of magnetic adsorbents and low volumes of extraction solvents are used. The advantage of magnetic adsorbents is that they can be easily removed from the solution with an external magnet. In magnetic dispersive solid phase microextraction methods, magnetic solid adsorbent is dispersed in the sample matrix to increase extraction efficiency [12-13]. In magnetic colloidal gel-based microextraction methods, the magnetic adsorbent is dispersed in a carrier liquid phase. This carrier liquid phase can be deep eutectic solvents, ionic liquids. It is thought that the sorbent obtained by mixing this material is better extracted since its association with the analyte increases [14].

Since the methods developed for the analysis of this dye are few in the literature, the main purpose of this study is to develop a sensitive, accurate and reliable method. In this study, magnetic amberlite XAD-7 nanoparticle was synthesized and characterized by TEM and FT-IR. A hydrophilic deep eutectic solvent (phenol/choline chloride, 2:1) based colloidal gel was created with magnetic amberlite XAD-7 nanoparticles. With the created colloidal gel, solid phase microextraction method was developed for the pre-concentration and separation of Brown HT. In the developed method, various parameters such as pH, composition of magnetic gel, type of desorption solvent, vortex time (for adsorption and desorption), sample volume were investigated. Then, the method was validated. Finally, the developed method was successfully applied to real samples.

2 MATERIALS AND METHOD

2.1 Apparatus

The spectra were recorded by a Carry 100 Bio UV-visible model double beam spectrophotometer, attached with 10.0 mm quartz cells was used for the absorbance measurements. A vortex (Velp brand) was used to facilitate the adsorption and desorption of Brown HT. A neodymium magnet with a strong magnetic field was used to remove nanoparticles from the solution. Infrared spectra of Fe_3O_4-XAD-7 and Fe_3O_4-XAD-7/DES were taken from an Agilent brand Cary 63 FT-IR model devices. The homogenous dispersion of the Fe_3O_4@XAD-7 nanoparticle in colloidal gel was investigated by Hitachi HT-7700 transmission electron microscope.

2.2   Reagents and Solutions

Choline chloride was taken from Glentham Life Sciences Ltd. (Corsham, United Kingdom). Phenol, Iron (III) chloride hexahydrate ($FeCl_3.6H_2O$), Iron (II) chloride tetrahydrate ($FeCl_2.4H_2O$), Amberlite XAD-7, ammonia, acetonitrile, acetone, ethanol, methanol, and Brown HT were obtained from Sigma-Aldrich (St. Louis, MO, USA). Stock solutions of 100 μg/mL of Brown HT prepared by dissolving distilled water in a 100 mL calibrated flask. Norateks (Istanbul, Turkey) brand buffer solutions were used for pH adjustments.

2.3   Preparation of DES, Fe₃O₄@ XAD-7 and Magnetic Colloidal Gel

For DES, choline chloride and phenol are mixed in 1:2 ratio in a capped conical flask. The mixture is stirred until it becomes clear. The transparent solution is left at room temperature [15].

Amberlite XAD-7 was added to a solution containing 1.0 M ($mol.L^{-1}$) Fe^{3+} and 2.0 M Fe^{2+} in 2.0 M HCl medium(1:2). After this mixture was stirred for 5 minutes, 1.0 M ammonia solution was slowly added until the solution turns to black. After the magnetic nanoparticles were formed, they were collected at the bottom of the conical flask with a neodymium magnet and the aqueous phase was removed and then the nanoparticles were washed with pure water and ethyl alcohol. The washed nanoparticles were then dried at 80 °C [15].

1.0 mL of DES and 60.0 mg of Fe_3O_4-XAD-7 magnetic nanoparticles were vortexed thoroughly in a tube until a homogenous black gel was obtained and then sonicated [15].

2.4   Real Sample Procedure

A real sample (chocolate souce) was taken from market in Diyarbakir, Türkiye. The appropriate amount of chocolate souce sample was weighed in the erlenmeyer. It was dissolved in 30 mL of water and transferred to volumetric flask. Then, the solution was diluted to 50 mL with pure water. The developed method was applied to 0.1 mL of this solution.

2.5   Analytical Procedure

20 mL of 0.5 mgL^{-1} Brown HT model solution was prepared at pH 4. Then, 0.4 mL of magnetic colloidal gel was added to the model solution. The solution was then vortexed for 10 minutes. The magnetic nanoparticles dispersed by vortexing were collected with a magnet and the water phase was decanted. Then, 0.8 mL of ammoniacal acetonitrile was added to the

nanoparticles loaded with the analyte. After vortexing this solution for 8 minutes, nanoparticles were collected on one side of the tube with the help of a magnet and the aqueous phase was removed. Then, the absorbance of the model solution was measured.

2.6 Carachterization of Fe_3O_4@XAD-7 and Fe_3O_4@XAD-7/DES

The structures of DES, Fe_3O_4@XAD-7 and Fe_3O_4@XAD-7/DES were characterized by Fourier transform infrared spectroscopy (FT-IR). As shown in Figure 2 (a), in the IR spectrum obtained for DES, the OH group of choline chloride and phenol in DES gives a broad band at 3000-3400 cm^{-1}, which meets the expectation. As shown in Figure 2 (b), the peak between 2850-3000 cm^{-1} for Fe_3O_4@XAD-7 can be related to the stretching vibration of the aliphatic C-H group in the structure of XAD-7. The broad peak at 500-600 cm^{-1} can be related to the Fe-O bond in the spectrum of the composite. As shown in Figure 2 (c), the broad peak between 3000-3400 cm^{-1} in the spectrum of Fe_3O_4@XAD–7/DES can be related to the O-H stretching vibration in the structure of both phenol and choline chloride in DES.

The shape of Fe_3O_4@XAD-7 and its distribution in DES in colloidal gel were investigated by transformation electron microscopy (TEM) analysis. As shown in Figure 3(a and b), it was observed(image of DES), DES beads are dispersed in the form of an emulsion.

3 RESULTS AND DISCUSSIONS

3.1 Effect of pH

pH is one of the most important parameters in the sorption of analyte onto the adsorbent. The increase or decrease of proton in the solution medium increases or decreases the affinity of the analyte to the adsorbent [16]. In order to determine the effect of pH on the recovery of Brown HT, the range of pH 2-8 was investigated. It is observed that the affinity of Brown HT to the adsorbent is high only at pH 4, from the acidic region to the basic region (pH 8). As shown in Figure 4, in this study, the sorption of Brown HT to nanoparticles was at maximum level at pH 4, the highest recovery was obtained at pH 4. Therefore, in the following experiments, the pH of the solutions was adjusted to 4.
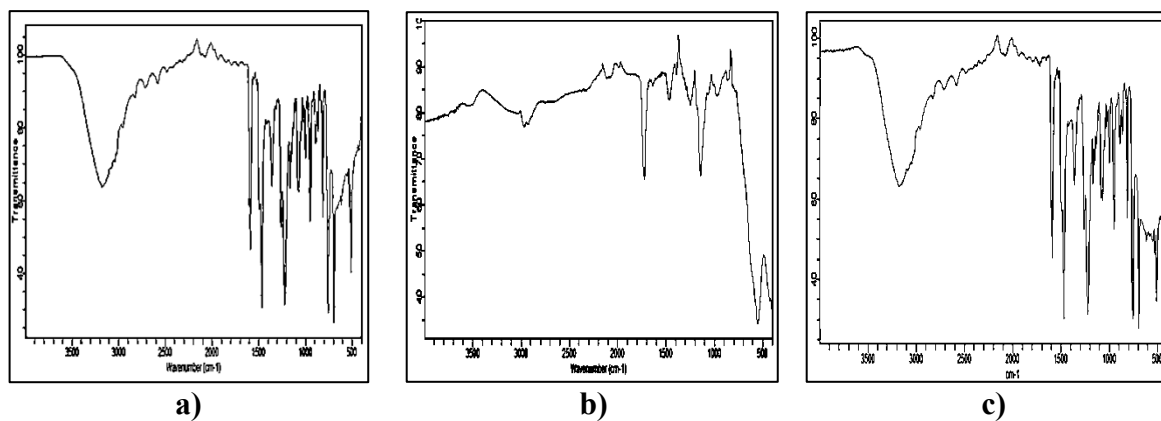
Figre 2. a) FT-IR spectrum of DES, b)Fe₃O₄@XAD-7 c) and Fe₃O₄@XAD-7/DES.
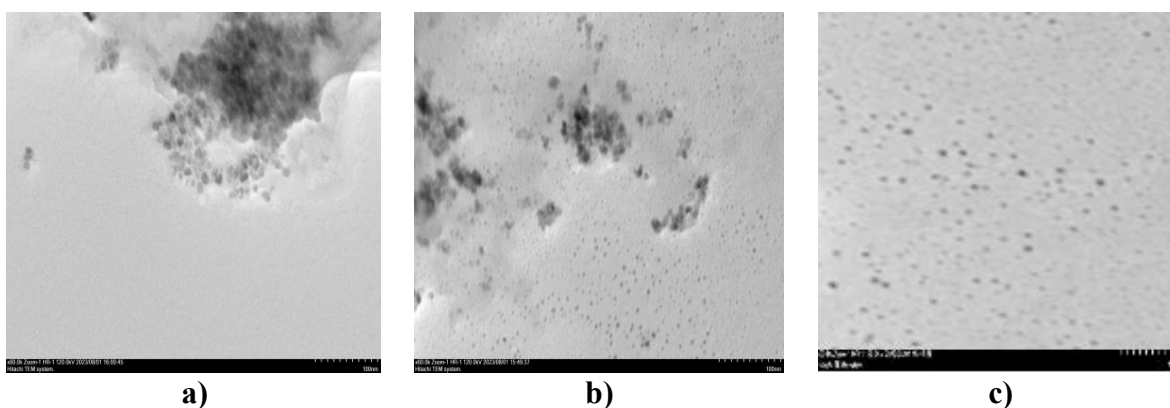
Figure 3. a) TEM images of Fe3O4@XAD-7 b) and Fe3O4@XAD-7/DES c) DES.
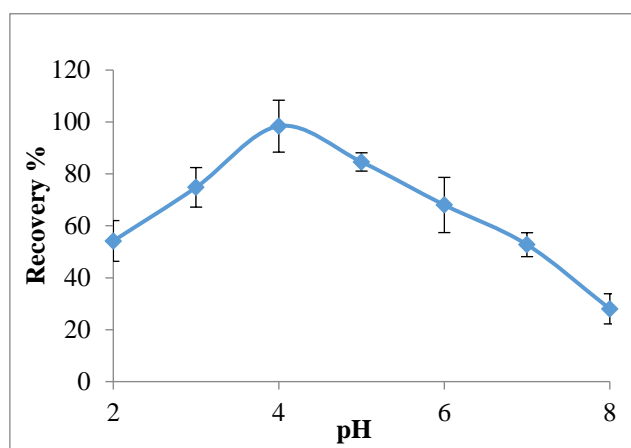
Figure 4. The effect of pH.

3.2   The Composition of Magnetic Colloidal Gel and Its Volume

In order to determine the optimum amount of nanoparticles in 1.0 mL of DES, the range of 20-80 mg was examined. The results obtained are presented in Figure 5. According to these results, the optimum amount of nanoparticles in 1.0 mL of DES should be 60 mg for the colloidal gel composition where the highest recovery is obtained. At values below 60 mg, the

recovery of Brown HT is quite low because the amount of nanoparticles is insufficient. Above 60 mg, there were no major changes in the recovery percentages.

After determining the composition of the colloidal gel, the volume of gel to be added to the solutions containing Brown HT must be determined. For this purpose, 100-600 µL of gel was added to the solutions. The results obtained are presented in Figure 6. According to these results, the optimum volume of gel to be added to the solutions is 400 µL. It was observed that the recovery of Brown HT increased continuously in the range of 100-400 µL of colloidal gel, and there were no major changes after 400 µL.
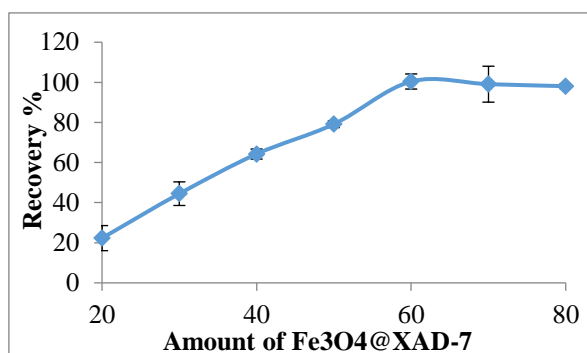
Figure 5. The effect of amount of Fe3O4@XAD-7.
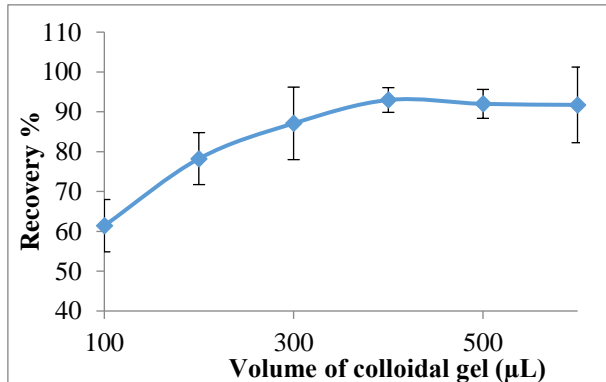
Figure 6. Effect of volume of colloidal gel.

3.3 Effect of Solvent Type

In this experiment, methanol, ethanol, acetonitrile, acetone and 0.1 M ammonia solutions of these solvents were used to investigate whether Brown HT completely passes into the solvent by reducing its interaction with the sorbent. As seen in Figure 7, it was determined that ammoniacal acetonitrile reduced the interaction between the sorbent and the analyte, thus recovering the analyte with high efficiency. Therefore, the best solvent was determined to be 0.1 M ammonia acetonitrile.
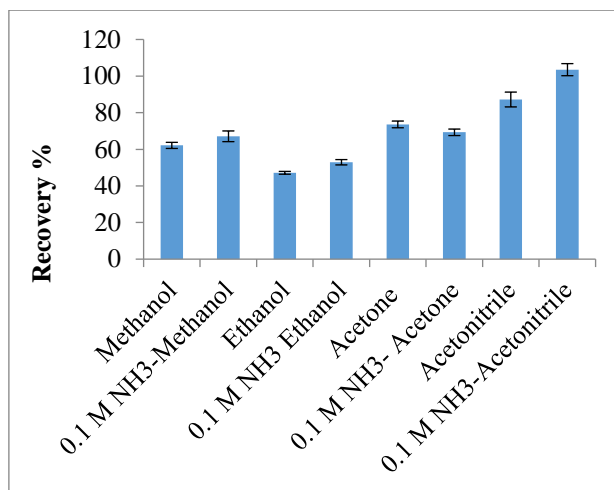
Figure 7. The effect of desorption solvent type.

3.4   Effect of Vortex Time

Vortex duration is a very important parameter in extraction studies. While it is important to increase the interaction between the analyte and the adsorbent in the adsorption process, it is important to increase the interaction between the extraction solvent and the analyte in the desorption process [17-18].

In the vortexing time study, Brown HT was investigated between 5-20 minutes for nanoparticle adsorption and 3-15 minutes for its desorption into ammonia acetonitrile solvent. It was determined that the most effective vortexing time in increasing the interaction between the nanoparticle and the analyte was 10 minutes, and the most effective vortexing time in transferring the analyte to the ammonia acetonitrile solvent was 8 minutes.
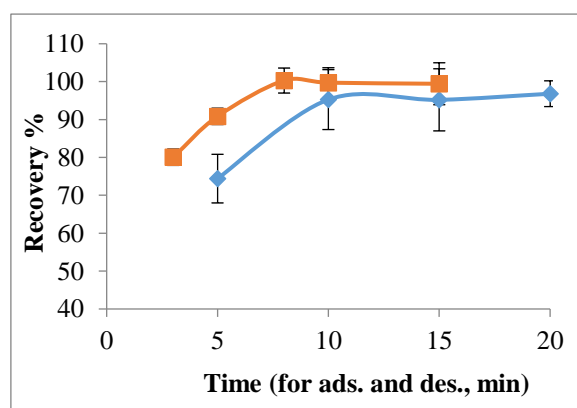
Figure 8. The effect of vortex time.

3.5   Sample Volume

To determine the highest sample volume at which the highest recovery was obtained, model solutions containing 0.5 mg.L^{-1} Brown HT between 10-50 mL were examined. 10 mL and 20 mL were also mixed with 0.8 mL of ammoniacal acetonitrile, which is a high desorption solvent. The optimum sample volume was found to be 20 mL and the preconcentration factor was 25. All the results obtained are shown in Table 1.

Table 1. The effect of sample volume to extraction efficiency.

Sample volume (mL)	Recovery %
10	97.03
20	97.13
30	91.05
40	90.06
50	84.43

3.6   Matrix Effect

Under the determined optimum conditions, the selectivity of the sorbent to Brown HT was tested by matrix effect. For this purpose, the effects of ions abundant in drinking water and a commonly used food dye (amaranth) on the adsorption of Brown HT onto the sorbent were investigated. As seen in Table 2, As seen in Table 3, we can say that the selected ions and dye have no effect on the adsorption of Brown HT onto the sorbent at the concentrations examined in the matrix. With these results, we can say that the sensitivity of the method is high.

Table 2. The effect of interfering species to extraction efficiency.

Interfering species	Concentration (mgL^{-1})	Recovery %
K^+	3000	97
Mg^{2+}	250	97
Fe^{3+}	3	93
Cl^-	3000	97
Amaranth	0.5	99

3.7   Analytical Parameters of the Developed Method

According to the ICH-Q2 [19] validation procedures, the linear working range, detection and determination limits of the method were determined. Then, in the accuracy study, the analyte addition/recovery test was applied to real samples. Matrix effect study was applied for the selectivity of the method.

After determining the optimum condition of each parameter, the analytical performance of the method under these conditions was examined. First, it was determined in which working range of the method the relationship between the absorbance and concentration of Brown HT was linear. This range was determined to be 0.05-0.75 mg L^{-1} under optimum conditions. The correlation equation in this concentration range is A= 1.2354C-0.0127, with a correlation coefficient of 0.9962 (C: Brown HT Concentration (mgL^{-1}); A: Absorbance of Brown HT). In the method, limit of detection and quantification (LOD and LOQ) were calculated 0.016 mgL^{-1} and 0.052 mgL^{-1}, respectively. EF and PF of developed method were found to be 51, and 25, respectively. The analytical data of the method are given in Table 3.

LOD was calculated with the formula 3s_b/m where s_b and m are the standard deviation of the blank solution and the slope of the calibration curve, respectively. LOQ was calculated as 10 times s_b/m. EF was calculated by dividing the slopes of the calibration curves obtained before and after the preconcentration method. The RSD% of the developed method was calculated with the results obtained from 10 measurements of the lowest concentration in the working range [12].

Table 3. Analytical performance of the developed microextraction.

Parameters	Values
Linear equation	*A= 1.2354C -0.0127
R^2	0.9963
Linear range (mgL^{-1})	0.05-0.75
LOD (3 s/m) (mgL^{-1})	0.016
LOQ (10 s/m) (mgL^{-1})	0.052
RSD %	3.8
EF	51
PF	25

*C:Concantration of Brown HT (mgL^{-1}), A: Absorbance of Brown HT

3.8   Applying the Procedure to Real Samples

To determine the accuracy of the method, the analyt addition/recovery test was applied to real samples. For this purpose, Analyte was added to the chocolate sauce samples at 3 different concentrations to form 3 parallel solutions [15]. The developed method was applied to these prepared solutions. Then, the recoveries of Brown HT in the solutions were calculated. All the results obtained are shown in Table 4. The total Brown HT content in the sample is presented in Table 5. The developed method was successfully applied to chocolate sauce as a

real sample and the result found was below the maximum level of 50 mg.kg^{-1} determined by the Turkish Food Codex [20].

For the precision of the method, repeatability (intraday) and intermediate precision (interday) tests were applied to 3 parallel solutions of the analyte at 2 different concentrations. For intraday study, the method was applied to the solutions at 3 different times in one day, and in the interday study, the method was applied to the solutions on 3 different consecutive days.

The results of intraday and interday studies were evaluated by calculating RSD% (Table 6). While RSDs % were in the range of 1.2-2.4% in the intraday study, RSDs % were in the range of 4.3-6.1% in the interday study. According to the ICH-Q2 evaluation, precision results are evaluated with % RSDs. Accordingly, if the RSDs % are below 10, the precision of the method can be considered high.

Table 4. Application of the procedure to real samples(N=3).

Sample	Added, mgL^{-1}	Found, mgL^{-1}	Recovery %
	0.10	0.28	98±2
Chocolate sauce	0.25	0.443	104±3
	0.50	0.678	99±5

Table 5. Content of Brown HT in the chocolate sauce(N=3).

mg.kg^{-1}±1.4

Table 6. The repeatability (intraday) and intermediate precision (interday) of the method, N=3.

		Intraday			Interday		
	Added (mgL^{-1})	Found (mgL^{-1})	Recovery %	RSD %	Found (mgL^{-1})	Recoveryy %	RSD %
	-	0.21	-	1.2	0.19	-	4.3
Chocolate sauce	0.2	0.42	105	2.4	0.41	110	6.1
	0.4	0.59	95	1.8	0.60	103	4.4

3.9 The Comparison Between the Developed Method and Other Techniques Reported in the Literature

According to our research, there are very few studies in the literature on the determination of Brown HT. The LOD of the method we developed is quite low compared to the Cloud Point Extraction method in Table 7, while the PF is high. The linear range is quite wide compared to the DES based microextraction method developed with UV-Vis spectrophotometer.

The advantage of this study is that it provides an up-to-date, simple, environmentally friendly, sensitive and accurate method due to the scarcity of studies on the determination of Brown HT. Magnetic nanoparticles were easily removed from the medium with an external magnet.

Therefore, no extra process was required to remove the particles. It will shed light on this dye to researchers with an up-to-date method.

Tablo 7. The comparison between the suggested method and other techniques reported in the literature.

Method	Enstrument	Real Sample	LOD (mgL^{-1})	PF	Linear Range (mgL^{-1})	Ref.
Direct differential pulse polarography	Saturated calomel electrode	Orange, lime, blackcurrant drinks	-	-	0-45.5	[21]
Cloud point extraction	Scanometry	Water	0.04	19.05	0.06–2.60	[9]
Deep eutectic solvent based microextraction	UV-Vis	Cake, two different urines, two different water	0.23	37.5	0.23–1.04	[10]
MCG- dSPME	UV-Vis	Chocolate sauce	0.016	25	0.05-0.75	This work

*UV-Vis: Ultraviyole spectrophotometry; MCG-dSPME: magnetic colloidal gel based dispersive solid phase microextraction

4 CONCLUSION

A new magnetic colloidal gel based dispersive solid phase microextraction method (MCG-dSPME) was developed for the preconcentration of Brown HT. This colloidal gel was obtained by mixing Fe_3O_4@XAD-7 and DES (choline chloride/phenol; 1/2). In this developed method, LOD, PF, EF values were calculated as 0.016 mg L^{-1}, 25, 51, respectively. The working range of Brown HT was found as 0.05-0.75 mg L^{-1} in this method. The linear range of our method is wide, LOD is low, selectivity, accuracy and precision are high. The low LOD and

high selectivity, EF and PF of our method enable the determination of Brown HT, even at trace levels, in many complex matrices.

The developed method was successfully applied to chocolate sauce as a real sample and the result found was below the maximum level of 50 mg.kg^{-1} determined by the Turkish Food Codex [20].

Studies on the determination of this dye are quite few in the literature. The magnetic colloidal gel based dispersive solid phase microextraction method developed for the determination of Brown HT has great importance in this respect.

Statement of Research and Publication Ethics

The study is complied with research and publication ethics.

Artificial Intelligence (AI) Contribution Statement

This manuscript was entirely written, edited, analyzed, and prepared without the assistance of any artificial intelligence (AI) tools. All content, including text, data analysis, and figures, was solely generated by the authors.

REFERENCES

[1]   Turkish Food Codex Regulation, "*Turkish Food Codex Food Additives Regulation*," 2013. [Online]. Available: https://faolex.fao.org/docs/pdf/tur152534.pdf. (Accessed: Oct. 28, 2024).

[2]   M. N. Hong, H. J. Suh, O. H. Lee, H. S. Chun, and C. Lee, "Improved analytical method of synthetic food colour additive, Brown HT by high-performance liquid chromatography," *J. Int. Sci. Publ. Agric. Food*, vol. 2, pp. 68–75, Jun. 2014.

[3]   European Food Safety Authority, "Scientific Opinion on the re-evaluation of Brown HT (E 155) as a food additive, EFSA Panel on Food Additives and Nutrient Sources (ANS)," *EFSA J.*, vol. 8, pp. 1–31, Sept. 2010.

[4]   A. E. Lawen, O. O. Hazha, A. O. Nigar, and H. S. Jabbar, "A novel fluorescence probe using Brown HT precursor carbon dots for highly selective and ultrasensitive quantitation of potassium ion in some staple food samples," *Food Chem.*, vol. 467, Mar. 2025, Art. no. 142341.

[5]   F. Karimi *et al.*, "Advancement in electrochemical strategies for quantification of Brown HT and Carmoisine (Acid Red 14) from Azo Dyestuff class," *Food Chem. Toxicol.*, vol. 165, Apr. 2022, Art. no. 113075.

[6]   A. C. Sezgin and S. Ayyıldız, "A research on the colorants used in snack foods consumed by children," *Int. J. Soc. Res.*, vol. 11, no. 18, pp. 877–913, Jun. 2019.

[7]   M. Corona-Bautista, A. Picos-Benítez, D. Villaseñor-Basulto, E. Bandala, and J. M. Peralta-Hernández, "Discoloration of azo dye Brown HT using different advanced oxidation processes," *Chemosphere*, vol. 267, Dec. 2021, Art. no. 129234.

[8]   Y. Tang *et al.*, "Electrochemical oxidative degradation of X-6G dye by boron-doped diamond anodes: Effect of operating parameters," *Chemosphere*, vol. 258, Nov. 2020, Art. no. 127368.

[9]   A. Shokrollahi and S. Ahmadi, "Determination of trace amounts of Brown HT as a food dye by a CPE-scanometry method," *J. Taibah Univ. Sci.*, vol. 11, pp. 196–204, Apr. 2018.

[10]   M. Soylak, S. Deryol, and F. Uzcan, "A new green microextraction method for traces Brown HT (E155) by using deep eutectic solvents prior to its spectrophotometric determination," *Int. J. Environ. Anal. Chem.*, vol. 101, pp. 1437–1447, Oct. 2021.

[11]   B. Tutunaru, A. Samide, C. Neamțu, and I. Prunaru, "Electrochemical and thermal stability of Chocolate Brown HT food additive," *Chem. Ind. Chem. Eng. Q.*, vol. 25, pp. 89–96, Aug. 2019.

[12]   X. Zheng *et al.*, "Determination of triazine herbicides from water, tea, and juice samples using magnetic dispersive micro-solid phase extraction and magnetic dispersive liquid-liquid microextraction with HPLC," *Food Chem.*, vol. 468, Mar. 2025, Art. no. 142430.

[13]   S. Agatonovic-Kustrin, V. Gegechkori, T. Kobakhidze, and D. Morton, "Solid-phase microextraction techniques and application in food and horticultural crops," *Molecules*, vol. 28, Sept. 2023, Art. no. 6880.

[14]   M. Shirani, M. Faraji, H. R. Nodeh, B. Akbari-adergani, and S. Sepahi, "An efficient deep eutectic magnetic nano gel for rapid ultrasound-assisted dispersive μ-solid phase extraction of residue of tetracyclines in food samples," *J. Food Sci. Technol.*, vol. 60, pp. 2802–2812, Aug. 2023.

[15]   F. Erek, M. F. Lanjwani, and M. Tuzen, "A sensitive determination of Brilliant Blue FCF in some food samples using hydrophilic deep eutectic solvent-assisted magnetic nano gel-based dispersive solid phase microextraction prior to spectrophotometric analysis," *Food Chem.*, vol. 453, Sept. 2024, Art. no. 139632.

[16]   H. van Doorn, C. B. Grabanski, D. J. Miller, and S. B. Hawthorne, "Solid-phase microextraction with pH adjustment for the determination of aromatic acids and bases in water," *J. Chromatogr. A*, vol. 829, pp. 223–233, Dec. 1998.

[17]   M. Ghaedi *et al.*, "Activated carbon and multiwalled carbon nanotubes as efficient adsorbents for removal of arsenazo (III) and methyl red from waste water," *Toxicol. Environ. Chem.*, vol. 93, pp. 438–449, Dec. 2010.

[18]   M. Rezaei, H. R. Rajabi, N. Bavarsad-Esfandiari, A. Shokrollahi, and I. Setayeshfar, "Vortex-assisted dispersive micro-solid phase extraction based on nanostructured imprinted polymer: A comparison study between spectrophotometric and solution scanometric techniques," *J. Chromatogr. B*, vol. 1199, Apr. 2022, Art. no. 123262.

[19]   ICH-Q2, International Conference on Harmonisation of Technical Requirements for Registration of Pharmaceuticals for Human Use, "Validation of Analytical Procedures: Text and Methodology Q2 (R1)," 2005. [Online]. Available: https://www.fda.gov/media/152208/download. (Accessed: Oct. 23, 2024).

[20]   Turkish Food Codex Regulation, "Amendment to the Communiqué on Colorants Used in Foods," 2007. [Online]. Available: https://www.etuder.org.tr/wp-content/uploads/etudermevzuatlar/tebligler/renklendiriciler_tebligi.pdf. (Accessed: Oct. 29, 2024).

[21]   A. Fogg and K. Yoo, "Direct differential-pulse polarographic determination of mixtures of food colouring matters, chocolate brown HT, tartrazine and Green S," *Analyst*, vol. 104, pp. 1087–1090, Apr. 1979.

EVALUATING VISION TRANSFORMER MODELS FOR BREAST CANCER DETECTION IN MAMMOGRAPHIC IMAGING

Uğur DEMIROĞLU [1] (iD), **Bilal ŞENOL** [2] [*] (iD)

[1] *Kahramanmaraş İstiklal University, Software Engineering Department, Kahramanmaraş, Türkiye*

[2] *Aksaray University, Software Engineering Department, Aksaray, Türkiye*

*** Corresponding Author:** ugurdemiroglu@istiklal.edu.tr*

ABSTRACT

Breast cancer is a leading cause of mortality among women, with early detection being crucial for effective treatment. Mammographic analysis, particularly the identification and classification of breast masses, plays a crucial role in early diagnosis. Recent advancements in deep learning, particularly Vision Transformers (ViTs), have shown significant potential in image classification tasks across various domains, including medical imaging. This study evaluates the performance of different Vision Transformer (ViT) models—specifically, base-16, small-16, and tiny-16—on a dataset of breast mammography images with masses. We perform a comparative analysis of these ViT models to determine their effectiveness in classifying mammographic images. By leveraging the self-attention mechanism of ViTs, our approach addresses the challenges posed by complex mammographic textures and low contrast in medical imaging. The experimental results provide insights into the strengths and limitations of each ViT model configuration, contributing to an informed selection of architectures for breast mass classification tasks in mammography. This research underscores the potential of ViTs in enhancing diagnostic accuracy and serves as a benchmark for future exploration of transformer-based architectures in the field of medical image classification.

Keywords: Breast mammography with masses, Image classification, Vision transformers, base-16, small-16, tiny-16.

1   INTRODUCTION

Cancer is a leading cause of death worldwide; one in two people diagnosed with cancer will require treatment, and early detection is the best method of preventing the progression of

the disease to a later stage. More than one million cases of breast cancer are diagnosed each year, and despite increased survival rates, it remains the leading cause of death among women [1]. The small size of malignant masses has been shown to correlate with treatment success, making early diagnosis treatments such as mammography critical for improved long-term survival and quality of life [2]. Historically, most women would not become aware of their cancer until later stages of tumorigenesis due to the delayed onset of symptoms or would actively avoid detection as societal attitudes were against early mastectomy [3]. Current cancer detection guidelines have begun to promote public health education on their necessity; with increased awareness of need comes the resources to support potential candidates. A significant portion of individuals fail to access treatment due to systemic inability to pay for or seek care, a symptom of false patient belief or clinician default that mammography results in frequent benign biopsy and consequently low patient satisfaction [4]. Despite these informational hurdles, mammography remains our gold standard in breast screening, potentially changing long-term prognoses with easy attainability today. The accessibility of mammography has risked malignant tumor diagnosis, allowing those under poverty to live with progressive disease until care is both useful and affordable. The message of our work is not to catalog a list of diagnoses lost to accessibility, but instead to reinforce the idea that education on available services can potentially lead to lifestyle changes that drastically improve public health. Recommending yearly checks, even with breast self-exams, can increase the 5-year survival rate by 94% for early detection of tumor outgrowth and subsequent apoptosis [5]. Our increasing knowledge base on heterogenic carriers and specific risks, coupled with decreased test invasiveness, could ensure increased preventive lifestyle changes. Early cancer detection guidelines aimed at potentially affected groups of the general public could encourage preventive lifestyle changes in those on the brink, who cannot or choose not to earn access to screening [6].

Breast cancer is a major cause of mortality worldwide. To survive, affected individuals must receive timely treatment. Early diagnosis is also associated with reduced treatment toxicity and healthcare costs. Because breast-focused physical examination alone often fails to detect small lesions early on, imaging technologies have been utilized in cancer screening. Among these techniques, mammography has the strongest supporting evidence [7]. Mammography was first adopted for convenient use in healthcare screening in the 1960s. Both the sensitivity and specificity of the imaging machines have gradually improved. Rates of interval cancers and those detected beyond the screen-detected tumor have also marginally decreased. Widespread

mammographic screening has thus been adopted in many countries in some form [8]. Because mammography is performed in a private area and may have a variety of outcomes, it might be intimidating. It is essential to have a basic idea of what mammography entails and how it should be performed before attending your appointed days [9]. Traditional mammography machines help discover breast cancer as they employ a functioning X-ray system that allows them to detect abnormalities in the breast, such as tumors, before the patient or doctor notices them. Understanding what takes place when you receive a mammogram can help you make an informed decision about your breast health with the information you have. Inform your doctor if you have breast implants or have been diagnosed with breast cancer [10].

Mammography is an imaging technique focused on breast composition to screen for breast cancer and is widely considered the gold standard in the investigation for detecting early breast cancer, in addition to its important role in diagnostic evaluation [11]. Breast tomosynthesis is essentially an advanced type of mammography that creates three-dimensional images of the breast from a two-dimensional radiograph image. The purpose of mammography is to provide detailed images of the breast by passing a very low dose of radiation through the tissue. Mammography can detect tumors that are not easily felt. It can also identify some non-cancerous abnormalities, which surgeons may review to know if biopsies are required in the future [12]. A screening mammogram is part of regular healthcare. This test is designed to detect early signs of breast cancer in women who do not display clinical symptoms or signs of breast disease. Diagnostic mammography, on the other hand, is used to investigate tissue changes that were detected as a result of a screening mammography or not, or following clinical and/or self-exam detection [13]. Recently, computer-aided techniques developed to classify mammogram images gained a significant place in machine learning world. There can be found numerous methods proposed in this regard. This paper implements the Vision Transformers (ViTs) for this issue.

Deep learning has made a breakthrough in many fields, especially in computer vision, where convolutional networks have played a major role. Recent years have shown a shift from traditional convolutional networks to transformer-based approaches, mostly in language processing, as they have outperformed benchmark datasets [14]. ViTs have shown the ability to capture spatial information effectively, replacing convolutional networks. Vision Transformers have shown the ability to capture spatial information effectively, replacing convolutional networks. The extensive analysis of Vision Transformer models and their workings will help us improve the performance of such transformer-based models further [15]. Traditional

Convolutional Neural Networks (CNNs) have shown impressive results in a variety of tasks, from image classification to object segmentation. CNNs are popular in image classification tasks because they are translationally invariant and have a compact representation of the input image at each layer. For instance, classical networks for image classification may capture intricate hierarchical relationships, but they are entirely dependent on convolutional and max-pool layers, which limit the size of the receptive field. Large images are difficult to process, leading to an increased number of layers and parameters, which may result in computational inefficiency. Large stride values lose a lot of local features [16]. The transformer architecture is a multi-head self-attention mechanism with various layers. Interest in the transformer has increased with respect to computer vision applications' best pre-trained model. However, the transformer architecture is completely image-agnostic, which means it can stitch data of any kind [17]. More information about the architecture is provided in the further sections.

Mammogram image classification is one of the predominant approaches to detect breast cancer. The classification is either performed within different categories of tumors or between different types of tumors. In our study, we have differentiated the mammogram images of a general mammogram dataset into three classes: benign, malignant, and normal. In the modern era, any model requires several types of enhancements to classify a complex real-life dataset with high accuracy and minimal time complexity. Therefore, one of the state-of-the-art models suffers from this drawback. Thus, in our study, we have performed a comparative analysis between various models.

ViTs have recently gained attention in medical image analysis, offering an alternative to traditional CNNs by capturing long-range dependencies through self-attention mechanisms. Studies have demonstrated that ViTs can achieve performance comparable to or even surpassing that of CNNs in breast cancer detection tasks, as evidenced by research applying ViTs to classify breast ultrasound images with promising results [18]. However, CNNs remain prevalent in medical imaging due to their efficiency and strong inductive biases, which are advantageous for learning spatial hierarchies in complex medical datasets [19]. To leverage the strengths of both architectures, hybrid models that combine CNN-based feature extraction with transformer-based self-attention have been proposed. These hybrid approaches have been applied in various studies, such as one that integrated a convolutional backbone with transformer layers to enhance feature representation in histopathological images [20]. Another study proposed a token-mixer hybrid architecture, demonstrating improved diagnostic accuracy in breast cancer classification by effectively balancing local and global feature extraction [21]. Additionally, recent

investigations have explored novel training strategies and data augmentation techniques that further boost the performance of hybrid models in medical image classification tasks [22]. Overall, the integration of transformer-based architectures with traditional CNNs not only enhances diagnostic performance but also provides a flexible framework that can adapt to different imaging modalities and clinical requirements, marking a significant step forward in the evolution of automated breast cancer detection systems.

Recent advancements in ViT models have significantly enhanced breast cancer detection in medical imaging. For instance, a study introduced a ViT-based transfer learning method for breast mass classification, achieving an impressive area under the curve (AUC) of 1.0 on both ultrasound and mammogram datasets, thereby outperforming traditional CNN-based approaches [23]. Another innovative approach, the TokenMixer hybrid architecture, combines CNNs and ViTs to improve feature extraction and classification accuracy in histopathological image analysis, effectively balancing local and global feature representations [24]. Additionally, the NHS has launched the world's largest trial of AI for breast cancer diagnosis, aiming to expedite detection by using AI to analyze a significant portion of mammograms, potentially reducing the workload on radiologists and decreasing patient wait times [25]. These developments underscore the potential of ViT-based models and AI integration in enhancing the accuracy and efficiency of breast cancer diagnostics.

The article contributes significantly to the literature by providing a comprehensive evaluation of ViT models for breast cancer detection in mammographic imaging. Unlike traditional CNNs, which rely on local receptive fields, the study highlights the effectiveness of ViTs in capturing long-range dependencies and complex patterns in mammographic textures through self-attention mechanisms. By assessing three different ViT configurations—Base-16, Small-16, and Tiny-16—the research offers a comparative analysis of model performance, considering factors such as accuracy, computational efficiency, and training time. The findings indicate that while the Small-16 model achieves the highest accuracy, the Tiny-16 model provides a computationally efficient alternative with moderate performance. This study underscores the importance of selecting appropriate model architectures based on computational resources and diagnostic accuracy requirements. Furthermore, by leveraging a publicly available mammographic dataset and implementing a standardized preprocessing pipeline—including resizing, normalization, and Contrast Limited Adaptive Histogram Equalization (CLAHE)—the study ensures reproducibility and robustness in medical image classification. The research also contributes to the broader understanding of transformer-based

architectures in medical imaging, positioning ViTs as a viable alternative to CNNs for automated breast cancer diagnosis. This work serves as a benchmark for future studies, encouraging further exploration of ViTs and hybrid deep learning approaches to enhance diagnostic accuracy in medical applications.

This paper implements a comprehensive analysis of the classification structure of ViTs. The three sub-models in the ViTs architecture which are the base-16, small-16 and tiny-16 models have been separately considered for classifying mammographs. Thus, a detailed analysis of ViTs and its sub-models are discussed. In the paper next section presents the dataset and the third section gives information about the ViTs. The case study is shown in the fourth section and the last section includes the conclusions.

2 THE DATASET OF MAMMOGRAPHY

The *Breast Mammography Images with Masses* dataset, available through the Digital Object Identifier (DOI) 10.17632/ywsbh3ndr8.2, is an essential asset for professionals and researchers focused on medical imaging, breast cancer detection, and computer-aided diagnostic systems [26]. This comprehensive dataset comprises mammographic images that contain masses, which are critical indicators in assessing the likelihood of breast cancer. The images provide high-resolution visual information that supports the differentiation between benign and malignant masses, enhancing diagnostic accuracy. Each image in the dataset is carefully labeled and categorized, supporting diverse research applications such as mass detection, segmentation, and classification. This thorough annotation allows researchers to utilize the dataset effectively in machine learning contexts, where high-quality labeled data is essential for training algorithms designed to identify early-stage breast cancer. Such annotated data proves particularly valuable for developing and testing deep learning models in diagnostic radiology, where advancements in automated mass detection and classification can make a substantial impact on early diagnosis and patient outcomes. Figure 1 contains sample images from the dataset.
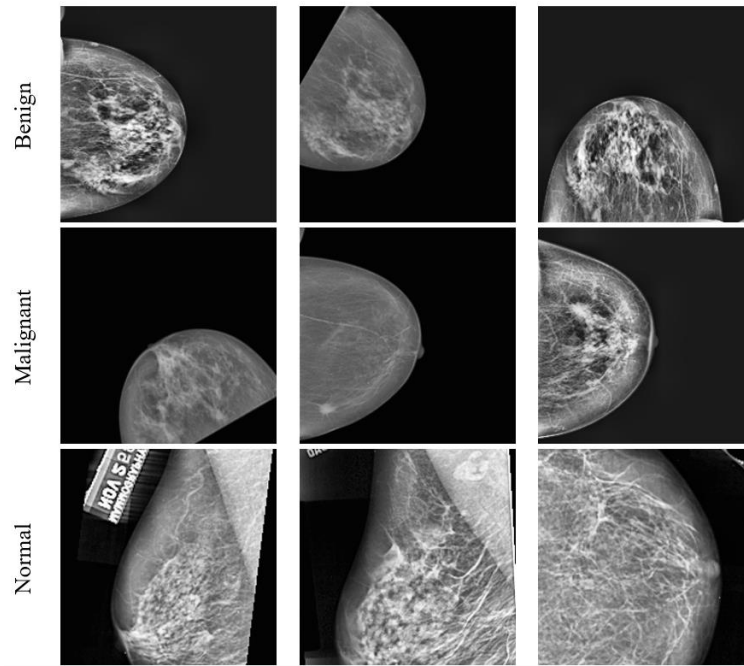
Figure 1. Sample images from the dataset.

The dataset is freely accessible for public use, making it a critical resource for both academic and industry researchers committed to advancing breast cancer detection and diagnosis technologies. Its availability allows a broad community of researchers to contribute to the development of new methodologies and models, ultimately aiding the early detection and treatment of breast cancer.

The dataset is a structured collection designed for cancer detection and classification, containing approximately 625MB of data across 26,602 images. These images are divided into three main categories—benign, malignant, and normal—organized in subfolders corresponding to each class. Specifically, the dataset includes 10,866 images labeled as benign, 13,710 as malignant, and 2,026 as normal. Each image is 8 bits deep, primarily in PNG format, with a minimum resolution of 227x227 pixels, providing adequate detail for analysis. The PNG format used for these images supports clear labeling of each sample as benign, malignant, or normal, which is essential for training machine learning models. In addition, the dataset is publicly licensed, making it widely accessible and frequently utilized in medicine, oncology research, and computer vision applications. This open access allows researchers and developers uninterrupted downloading and use, supporting diverse initiatives in medical imaging. For deep learning model development, the dataset underwent further enhancements. After being resized to standardized dimensions, the images were enhanced using CLAHE, a technique that improves image contrast by adjusting local histogram intensities. This preprocessing step

enhances image quality, making it suitable for machine learning applications where subtle differences in tissue appearance are critical for model accuracy. The processed dataset thus serves as a valuable foundation for developing, testing, and refining deep learning models focused on breast cancer detection and classification. While this dataset provides high-resolution images with well-annotated benign, malignant, and normal cases, we acknowledge the importance of assessing its applicability across different populations. The dataset primarily consists of images collected under specific clinical conditions, which may not fully represent the diversity of real-world patient populations, including variations in age, ethnicity, breast density, and imaging protocols. Additionally, potential sources of error in the dataset could arise from factors such as label inaccuracies, imaging artifacts, or biases introduced during data collection and annotation. For example, mammograms from different devices and institutions may exhibit variations in contrast and noise, which could impact model generalization. Moreover, the presence of class imbalances—such as fewer normal cases compared to benign and malignant ones—could affect classification performance. Addressing these limitations would require additional validation on diverse, multi-institutional datasets and collaboration with clinicians to assess model reliability in real-world scenarios. Future work could also incorporate domain adaptation techniques and bias mitigation strategies to improve the robustness and fairness of ViT-based models across different populations.

It would be useful to give brief information about some existing studies using the dataset. The mammography dataset comprising INbreast, MIAS, and DDSM has been extensively utilized in various studies to enhance breast cancer detection and diagnosis through advanced machine learning techniques. For instance, a study by Al-Antari et al. developed a fully integrated computer-aided diagnosis (CAD) system employing deep learning models, achieving an overall classification accuracy of 95.64% on the INbreast dataset [27]. Similarly, Li et al. proposed a method combining deep learning with an extreme learning machine, resulting in accuracies of 97.19% on DDSM, 98.13% on MIAS, and 98.26% on INbreast datasets [28]. Another notable approach by Falconí et al. utilized transfer learning on NasNet Mobile and fine-tuned VGG models to classify mammogram images according to the BI-RADS scale, achieving an accuracy of 90.9% on the INbreast dataset [29]. These studies underscore the efficacy of integrating deep learning methodologies with traditional machine learning models to improve the accuracy and reliability of breast cancer diagnostics using the INbreast, MIAS, and DDSM datasets.

3   THE VISION TRANSFORMERS

Vision transformers (ViTs) are a revolutionary development in computer vision that have the potential to replace traditional convolutional neural networks (CNNs) as the backbone of various vision tasks. CNNs process visual data in blocks, and at each layer, more abstract representations that capture spatial hierarchies are generated [30]. The modern architectures employ average pooling in the last layers to produce task-specific outputs. For example, if an image is being classified, the final average pooling layer is replaced by a classification head, and if the task at hand is object detection, the final average pooling layer is omitted altogether. Overall, the functions of CNNs are very different from global attention-based vision transformers. Thus, while the architectural details may differ, the overall task outputs are still closely related to each other for CNNs [31]. ViTs, on the other hand, decompose the input images into fixed-sized patches that are fed into conventional transformer blocks, which is a self-attention-based deep learning architecture. This decomposition allows the end-to-end training of large transformers acting on very large image datasets by ensuring a linear scaling in complexity with respect to the size of the images independent of dataset size [32]. All of the self-attention mechanisms in the transformer allow the model to perform efficient deduplication of work in processing pixel interactions because each operation is not applied between every possible pair of pixels. Rather, operations are applied across groups of patches, and information between the groups is incorporated sparsely from some operations across particular patches in each group. This allows for a more controlled and modular learning process that operates at the level of entire patches while leveraging information from different parts of the visual input [33].

The self-attention mechanism is the cornerstone of vision transformers, allowing them to weigh different local parts of the image differently without losing any global information. The weighted mean of this local information is then calculated to obtain the image representation. The self-attention mechanism calculates attention scores that describe the similarity of the query feature against the key feature for all positions in the input space. [34] The attention score is calculated by taking the softmax of a scaled dot-product score, defined as the matrix multiplication (after scaling element-wise) between the query and key [35]. These attention scores specify the distribution of relative importance of signals from different positions. The output of the final self-attention layer is then calculated as a weighted sum of the value features, where each value is weighted by the normalized attention score [36]. The self-attention mechanism introduces the representation of each position to be influenced by the context surrounding the position. In a more global scope, self-attention leads to potential

relationships between every position, and in turn makes it difficult for any position to contain the same amount of information [37].

Unlike conventional computer vision project names that consist of the phrase "smaller," these project names instead describe the scale of the vision and vision model, similar to a hardware platform descriptor. We utilize this descriptor to emphasize that there are three variations of the model that cater to different hardware platforms while maintaining a consistent vision size. The vision part of the model is linear by complexity [38]. The "Base-16" refers to a model with a standard complexity structure that conventionally achieves a balance between size and speed. The "Small-16" and "Tiny-16" variations project the complexities and outputs to 64 and 32 respectively, making them cheaper and more accessible. Keeping the vision part models constant between Base-16, Small-16, and Tiny-16 allows us to test the different models under similar settings [39].

General workflow of ViTs is shows in figure 2 [40]. The Vision Transformer (ViT) workflow draws inspiration from the transformer architecture, which has shown great success in natural language processing. By applying transformers to image processing, Vision Transformers follow a specific sequence of steps to analyze image data and generate highly precise outcomes in computer vision tasks. Let's take a closer look at the detailed breakdown of the Vision Transformer workflow.

Image Preprocessing

Vision Transformers necessitate fixed input dimensions, which means that all images must be resized to a consistent size, such as 224x224 pixels for ViT. Following resizing, the image is split into a grid of set-size patches, with each patch flattened into a 1D vector. For example, a 224x224 image can be divided into 16x16 patches, resulting in a 14x14 grid, with each patch containing 256 pixels.
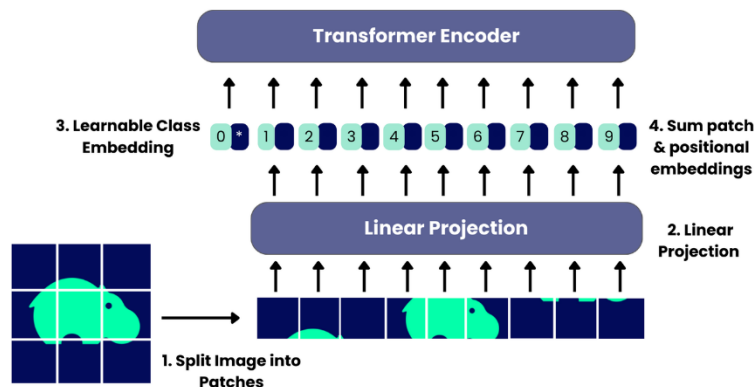
Figure 2. General workflow of ViTs.

These flattened patches are then passed through a linear projection to map them to a higher-dimensional space, such as 768 dimensions, ensuring that the model has a consistent feature size irrespective of the original patch size. The resulting vectors, one for each patch, are known as patch embeddings [41].

Positional Encoding

In contrast to CNNs, transformers do not naturally grasp spatial information, which is why positional encoding is included in each patch embedding. This encoding is crucial for helping the transformer comprehend the spatial connections between patches. Positional encodings commonly consist of learned or sinusoidal values that contribute specific position-related details to each patch embedding, thereby preserving the image's spatial arrangement within the sequence. [42, 43].

Input Embedding Construction

Following the incorporation of patch embedding and positional encoding, there is an output of a series of vectors, each of which represents a patch with position-aware details. A "class token" is also included at the beginning of the sequence, serving a similar purpose to the [CLS] token in NLP transformers. This class token is intended to consolidate information from all patches for use in classification tasks [44].

Transformer Encoder

The sequence of embeddings undergoes several layers of transformer encoders. Each layer includes: Multi-Head Self-Attention (MHSA), where each embedding interacts with others to capture global relationships; Layer Normalization to stabilize and speed up training; a Feed-Forward Network (FFN) with a ReLU activation that processes each embedding independently; and Residual Connections to help gradients flow through the model. This sequence is iterated across all transformer encoder layers, gradually learning complex relationships across patches [45].

Classification Head (or Task-Specific Head)

Upon completion of the encoder layers, the ultimate form of the class token serves as the representation of the image. In classification activities, this representation is processed

through an MLP head, generating class probabilities for each category through softmax. This head is adaptable for other tasks like segmentation or object detection [46].

Training and Optimization

Vision Transformers are usually trained for classification tasks using cross-entropy loss, adjusting parameters through backpropagation and gradient descent. Pretraining on extensive datasets such as ImageNet can improve the ViT model's ability to perform well on related tasks. Fine-tuning the model on a specific dataset, like medical images, can also improve its performance by making it more adaptable to domain-specific characteristics [47].

Inference

In the process of inference, the image goes through identical preprocessing procedures such as resizing, patch extraction, patch embedding, and positional encoding. The representation of the ultimate class token is employed for classification, enabling the model to anticipate the category of fresh, unobserved images [48].

Vision Transformers offer a more organic approach to capturing overall connections across an entire image as opposed to CNNs, which are limited by local receptive fields. They show efficient scalability with larger datasets, making them suitable for extensive image datasets. In contrast to CNNs, Vision Transformers do not impose a rigid hierarchical feature structure, enabling more adaptable feature learning [49].

4   THE CLASSIFICATION STUDY

The Breast Mammography dataset was methodically divided to optimize model training, validation, and testing phases, with 80% of the images dedicated to training, 10% set aside for validation, and the remaining 10% reserved for testing. This split was chosen to provide a balanced approach that maximizes training data while ensuring ample samples for unbiased validation and evaluation. To prepare the images for deep learning model input, each image was resized to a uniform dimension of 384x384 pixels with three color channels (RGB). This resizing ensures that all images share a consistent structure, which is essential for convolutional neural networks that rely on uniform input shapes for accurate learning. Additionally, the choice to process the images as color (RGB) images, rather than grayscale, preserves critical color details that could aid in distinguishing between benign, malignant, and

normal tissue types. Normalization was applied to each image, adjusting pixel values to a standardized range, typically between 0 and 1, or to a distribution centered around zero. This step is critical as it minimizes variations across the dataset, enabling the network to focus on important visual features rather than being affected by differing brightness or contrast levels. Such preprocessing ensures that the model can learn effectively from the images without bias introduced by inconsistent pixel intensities. This preprocessing pipeline—including resizing, color preservation, and normalization—was applied identically to images used in both training and testing. This approach guarantees that the model encounters images of identical quality and format during training and evaluation, reducing any risk of performance discrepancies due to preprocessing differences. Overall, this careful preparation of the Breast Mammography dataset supports robust and reliable model training, validation, and testing, fostering a more accurate classification performance across breast tissue image categories. The training parameters are selected as follows. **MiniBatchSize** =12, **MaxEpochs** =5, **IterationsPerEpoch** =443, **ObservationsTrain**=1773 and **Iterations**=8865. This study utilized the base, small, and tiny ViT models with their default parameters. No particular hyperparameter modification was conducted to improve performance, as our emphasis was on examining the influence of the default models on the dataset. The ViT models used in this study were trained using a standardized set of hyperparameters to optimize performance while maintaining computational efficiency. The models utilized a patch size of 16×16 pixels, with input images resized to 384×384 pixels. Training was conducted using the Adam optimizer with an initial learning rate of 1e-4 and a weight decay of 0.01. Each model was trained for five epochs with a batch size of 12, processing 443 iterations per epoch, totaling 8,865 iterations. The loss function employed was cross-entropy loss, and images were normalized to a [0,1] range to enhance model stability. The activation function used was Gaussian Error Linear Unit (GELU), and dropout was set at 0.1 to prevent overfitting. The transformer architecture varied across models, with the Base model featuring 12 multi-head self-attention heads, 12 transformer encoder layers, a hidden dimension of 768, and a feed-forward network dimension of 3072. The Small model had 6 attention heads, 8 encoder layers, a hidden dimension of 384, and a feed-forward network dimension of 1536, while the Tiny model was the most compact, with 3 attention heads, 4 encoder layers, a hidden dimension of 192, and a feed-forward network dimension of 768. Positional encoding was learnable across all models. These hyperparameters were carefully selected to balance accuracy and efficiency, with the Small model achieving the highest classification performance, while the Tiny model offered a computationally efficient alternative with moderate accuracy.

In training the network, the *Adam* (Adaptive Moment Estimation) algorithm was applied as an optimization solver for deep learning. This optimizer was selected for its adaptive learning rate capability, which efficiently handles dynamic learning rates and accelerates convergence during training. The training process was executed on a GPU using parallel computing, with 16 parallel workers operating concurrently to maximize processing efficiency and reduce training time. Key training parameters are as follows:

Initial Learning Rate: Set at 1e-4 to provide a stable starting point that adjusts adaptively during training, facilitating consistent model updates.

Shuffle: Data shuffling was configured to occur at every epoch, ensuring that the training data is randomly reordered with each cycle to enhance generalization and minimize overfitting.

Execution Environment: Configured for parallel processing, utilizing the GPU's multi-threading capabilities for optimized computation.

This configuration was designed to support efficient, stable, and resource-effective training, as detailed in the computational setup, and provided the necessary foundation for robust model convergence.

The computational setup, detailed in Table 1, illustrates the hardware specifications and the configuration that enabled efficient and stable training. The optimized environment supported a faster convergence rate, enhancing model performance while ensuring consistent resource utilization throughout the learning process.

Table 1. Hardware specifications of the computer used in this study.

Processor	12th Gen Intel(R) CoreTM i9-12900F 2.40 GHz
Cores, Processors	16, 24
Installed RAM	64.0 GB (63.7 GB usable)
GPU	NVIDIA RTX A4000
DirectX version	12 (FL 12.1)
GPU Memory	47.9 GB (16.0 GB Dedicated, 31.9 GB Shared)

The Vision Transformers (ViT) models employed in this study consist of the following configurations:

1. **Base-16-ImageNet-384**: This base-sized model contains 86.8 million parameters, with a patch size of 16 pixels, and is fine-tuned on the ImageNet 2012 dataset. It processes images at a resolution of 384x384 pixels, making it suitable for capturing complex features in larger images.

2. **Small-16-ImageNet-384**: This smaller model includes 22.1 million parameters, also with a patch size of 16, and is fine-tuned on the ImageNet 2012 dataset at the same resolution of 384x384 pixels. It provides a balance between model size and computational efficiency, enabling effective feature extraction with lower resource requirements.

3. **Tiny-16-ImageNet-384**: The smallest of the three models, this configuration has 5.7 million parameters and a patch size of 16. It is similarly fine-tuned on the ImageNet 2012 dataset with an image resolution of 384x384 pixels. This model is optimized for scenarios with limited computational resources while still leveraging the benefits of the ViT architecture.

Each of these ViT models, fine-tuned with ImageNet 2012 data, offers unique trade-offs in terms of parameter count and processing capacity, making them adaptable to various resource constraints and performance needs in image classification tasks.

In the study, the dataset was divided into three subsets: 80% for training, 10% for validation, and 10% for testing. These groups were separated before training began, ensuring that they consisted of independent images.

The training and testing performance graphs, along with the computed values for the base, small, and tiny ViT models, are presented below. Figure 3 shows the training visualities for the base model.
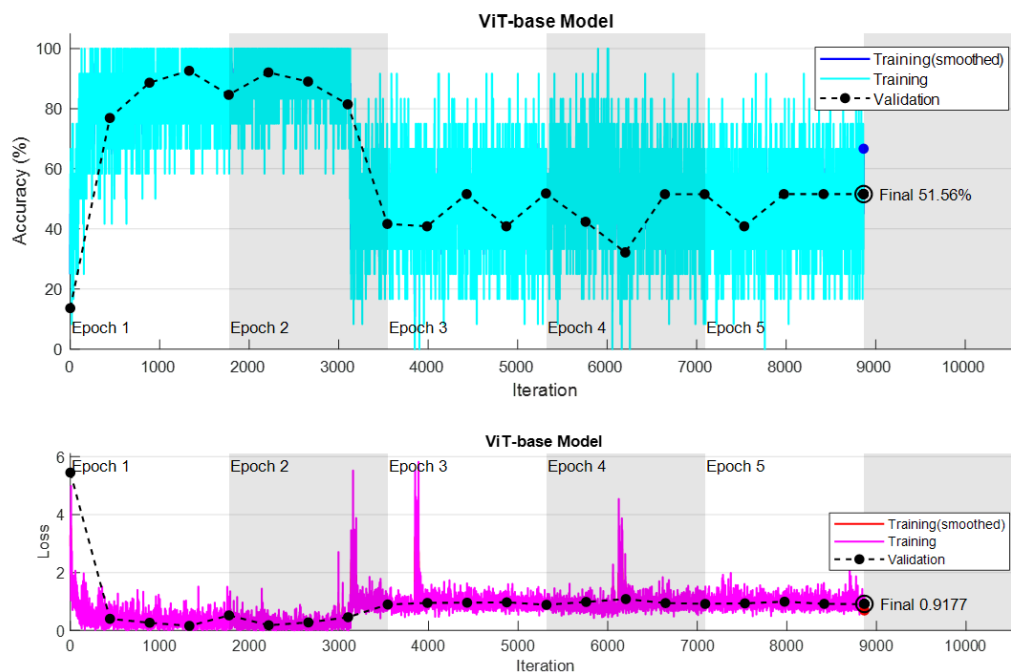
Figure 3. Training process of the base model.

The test performance parameters of the ViT base model—Accuracy, Error, Recall, Specificity, Precision, F1-Score, Geometric Mean Precision Recall (G-Measure PR), Geometric Mean Sensitivity Specificity (G-Measure SS), and Matthews Correlation Coefficient (MCC)—are presented in the table below.

Table 2. Performance metrics for the base model.

Accuracy	Error	Recall	Specificity	Precision	F1-Score	G-Measure PR	G-Measure SS	MCC
83.9534	16.0466	87.4203	89.5156	88.4118	87.4151	87.6649	88.0407	71.9342

The training visualities for the small model are illustrated in Figure 4. The test performance metrics of the model are listed in Table 3.

Table 3. Performance metrics for the small model.

Accuracy	Error	Recall	Specificity	Precision	F1-Score	G-Measure PR	G-Measure SS	MCC
87.9369	12.0631	91.1346	92.4234	91.1982	91.1647	91.1656	91.7628	78.5135
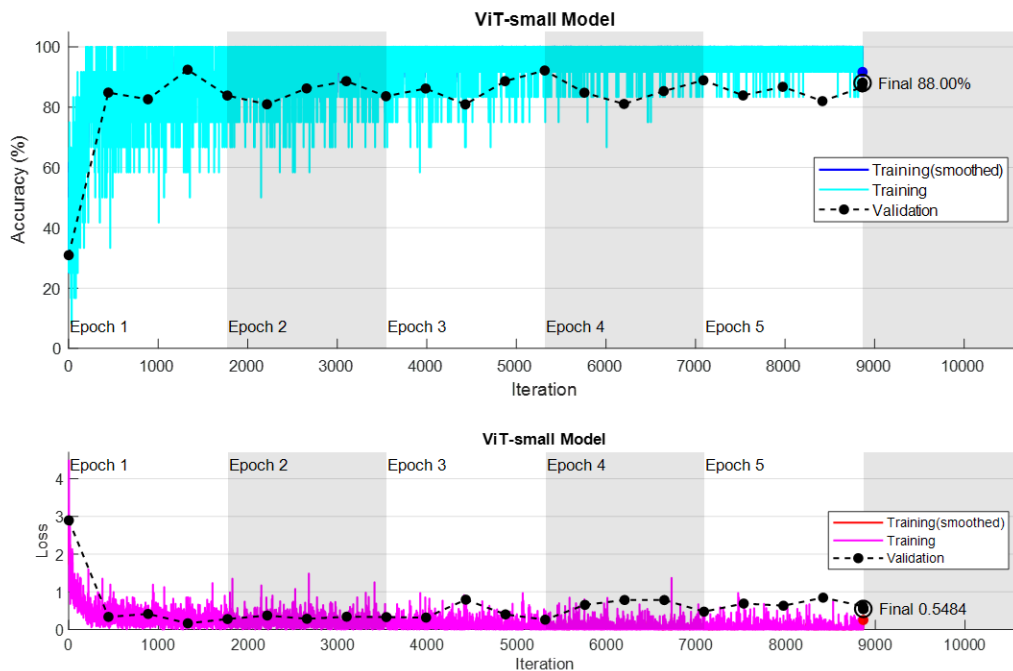
Figure 4. Training process of the small model.

Finally, the training of the tiny model is visualized in Figure 5. The test performance parameters of the model can be seen in Table 4.
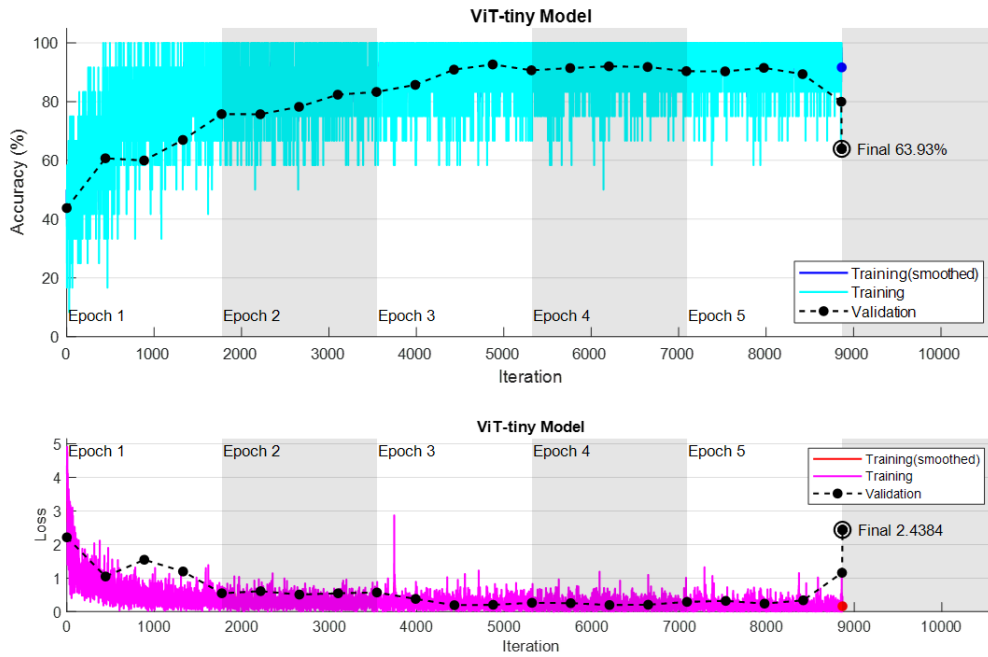
Figure 5. Training process of the tiny model.

Table 4. Performance metrics for the tiny model.

Accuracy	Error	Recall	Specificity	Precision	F1-Score	G-Measure PR	G-Measure SS	MCC
81.5859	18.4141	86.3841	88.3812	86.4489	86.3963	86.4064	87.3136	67.1630

For all three ViT model types, training was conducted using the same parameters on the 80% training dataset, while validation was performed independently using the 10% validation dataset. Testing was carried out after training was completed using a separate and independent 10% test data.

As a result of the training process, the test accuracies for each model type are as follows:

- **Base model**: Accuracy = 0.8395

- **Small model**: Accuracy = 0.8794

- **Tiny model**: Accuracy = 0.8159

These results indicate that the accuracy rates vary according to the model size, with the small model achieving the highest accuracy, while the tiny model achieved the lowest.

The training durations for each model are as follows:

- **Base Model**: Training completed in 32 hours 37 minutes 40 seconds.

- **Small Model**: Training completed in 3 hours 12 minutes 39 seconds.

- **Tiny Model**: Training completed in 1 hour 47 minutes 1 second.

These training times demonstrate a significant reduction in duration as the model size decreases. However, there is also a noticeable trade-off in accuracy, with the smaller models taking less time but showing some differences in accuracy. This highlights the impact of model size on both accuracy and training time. Confusion matrixes showing the training accuracies obtained for three models are given in figure 6.
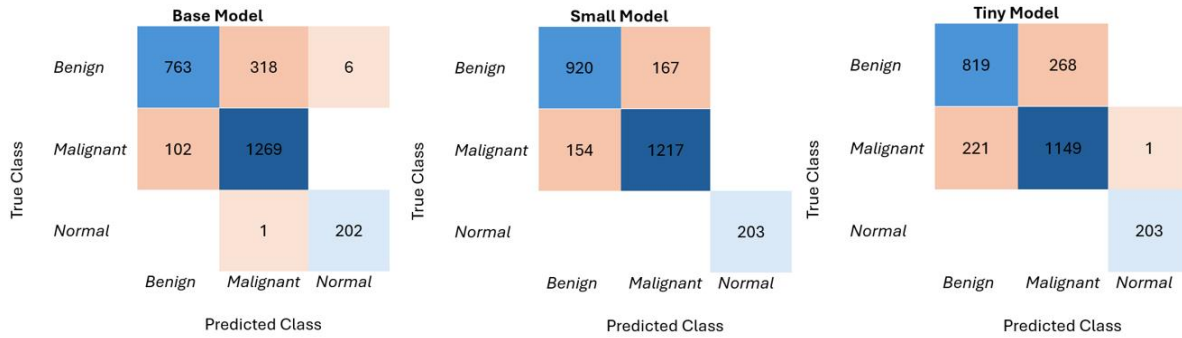
Figure 6. Confusion matrixes obtained for Base, Small and Tiny Models.

Figure 7 illustrates the Area Under the Curve (AUC) graphics for the three models. In the figure, the classes 1, 2 and 3 represents Bening Malignant and Normal classes respectively.
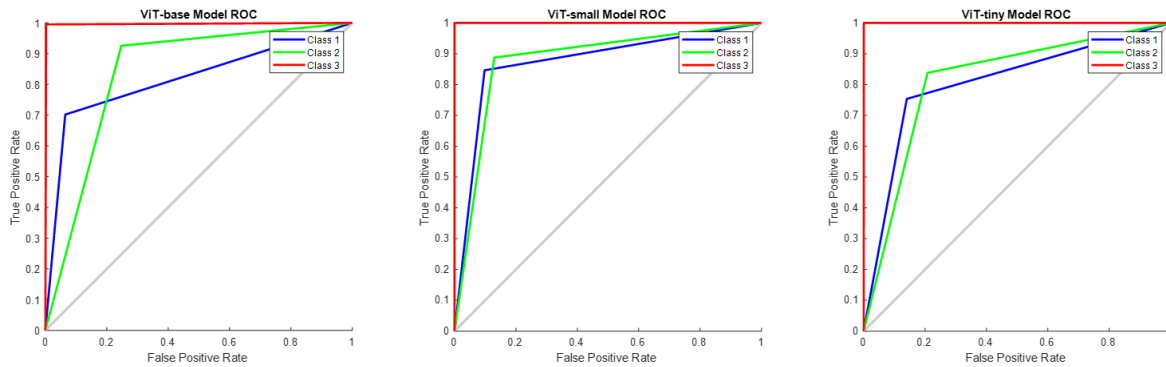
Figure 7. AUC graphics obtained for Base, Small and Tiny Models.

For the base model, the performance values were calculated as, Benign: 0.8186, Malignant: 0.8392, and Normal: 0.9963. For the small model, performance values are found as Benign: 0.8743, Malignant: 0.8791 and Normal: 1.0 and for the tiny model, the performance is found as Benign: 0.8065, Malignant: 0.8152 and Normal: 0.9998.

Figure 8 shows the progress of accuracy and loss during the ViTs Base model. As shown in Figure 4, the validation performance of the training process for the base model of the ViT network was 51.56%. This indicates that, during the validation phase, the model was able to correctly classify 51.56% of the samples, reflecting its ability to generalize from the training data to unseen data. While the performance might suggest room for improvement, it provides

valuable insight into the network's capabilities, and further optimizations or fine-tuning could lead to enhanced accuracy in future iterations.
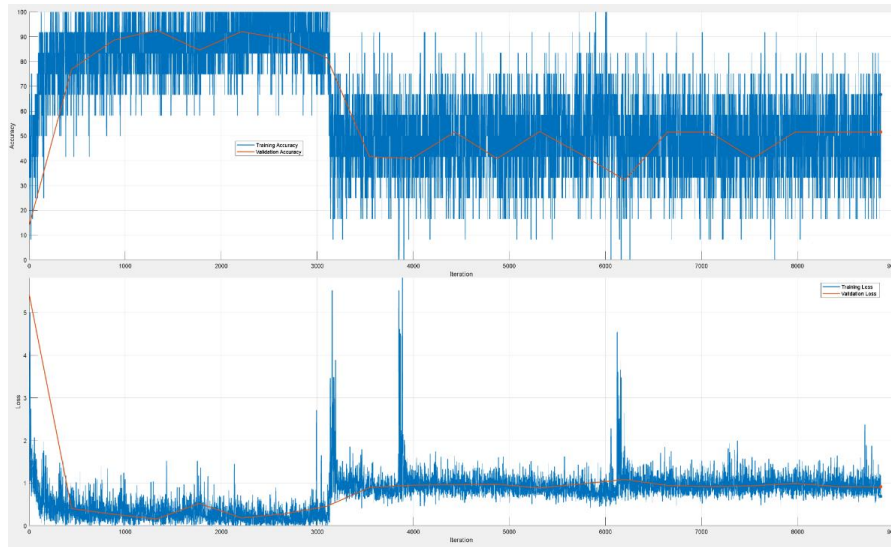
Figure 8. Accuracy and Loss values obtained for the base model.

Similarly, figure 9 is for the progress of accuracy and loss obtained for the small model of ViTs. According to the Small model, the validation performance of the training process was 88.00%. This high validation accuracy suggests that the model has effectively learned the features necessary for distinguishing between the classes in the dataset. The improved performance of the Small model compared to the base model demonstrates the advantages of using a more compact architecture, which may offer better generalization and efficiency in training. Further analysis could be conducted to understand the specific factors contributing to this improvement, such as the choice of hyperparameters or the model's ability to capture intricate patterns in the data.
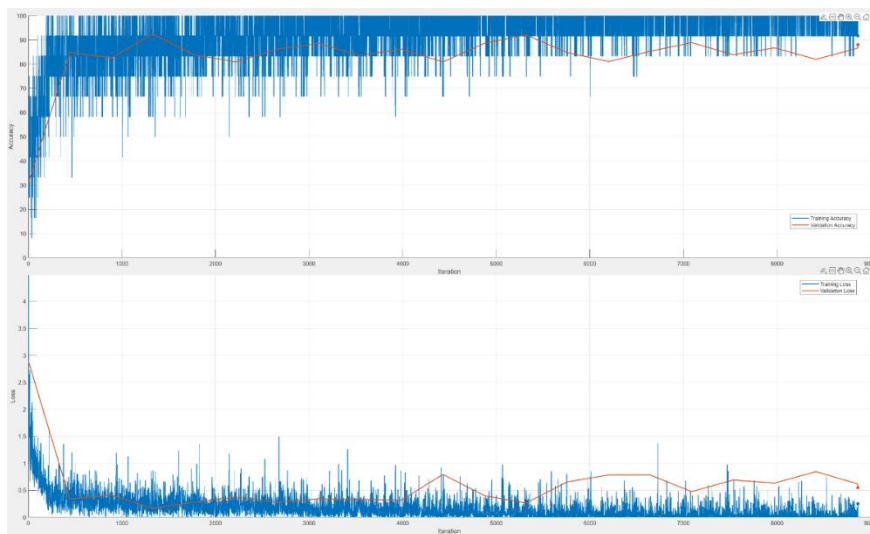
Figure 9. Accuracy and Loss values obtained for the small model.

Finally, figure 10 presents the progress of accuracy and loss values obtained for the tiny model.
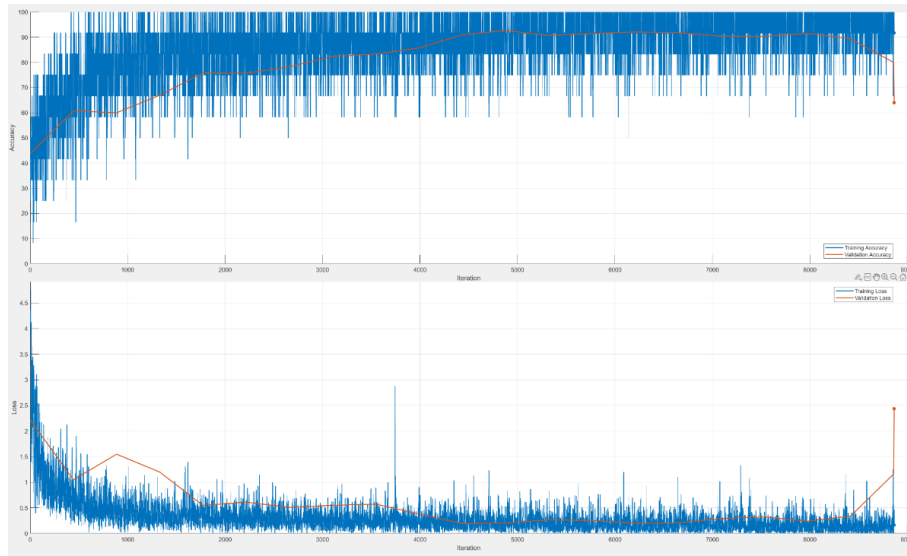
Figure 10. Accuracy and Loss values obtained for the tiny model.

According to the Tiny model, the validation success of the training process was 63.93%. This result indicates the model's performance in classifying images it had not seen during training, both during the intermediate validation tests and after the final training completion. These validation tests used unseen images, which are crucial for assessing the model's generalization ability. While the Tiny model shows a moderate level of validation accuracy, it suggests there may be potential for improvement, possibly through further tuning or more sophisticated techniques for feature extraction and model optimization. The test success for the Tiny model is also detailed in the confusion matrix in figure 3, which provides a deeper insight into the misclassifications and the overall model performance.

For all three models, table 5 provides a comprehensive overview of the training iteration progress, including the duration of each iteration, training and test performance, and calculation data from both the beginning and the end of the training process:

Table 5. Training iteration progress.

Iteration	Epoch	Base Time Elapsed	Base Training Accuracy	Base Validation Accuracy	Small Time Elapsed	Small Training Accuracy	Small Validation Accuracy	Tiny Time Elapsed	Tiny Training Accuracy	Tiny Validation Accuracy
0	0	00:01:28		13.652	00:00:41		30.951	00:00:27		43.738
1	1	00:01:29	25		00:00:41	25		00:00:27	50	
50	1	00:08:32	50		00:01:42	75		00:01:00	41.667	
100	1	00:17:28	66.667		00:02:40	91.667		00:01:36	33.333	
150	1	00:26:23	50		00:03:39	75		00:02:11	58.333	
200	1	00:34:57	83.333		00:04:37	58.333		00:02:43	41.667	
250	1	00:43:23	91.667		00:05:36	83.333		00:03:16	50	
300	1	00:51:47	58.333		00:06:35	75		00:03:50	58.333	
350	1	01:00:12	91.667		00:07:32	100		00:04:28	66.667	
400	1	01:08:39	91.667		00:08:30	75		00:05:07	58.333	
443	1	01:17:09	83.333	76.909	00:09:50	91.667	84.806	00:06:08	91.667	60.7
…										
8417	5	30:15:06	41.667	51.561	03:01:06	100	81.986	01:40:30	91.667	89.357
8450	5	30:23:41	75		03:01:51	100		01:40:54	91.667	
8500	5	30:36:30	50		03:02:58	100		01:41:29	91.667	
8550	5	30:49:25	58.333		03:04:05	100		01:42:05	100	
8600	5	31:02:18	66.667		03:05:11	100		01:42:41	91.667	
8650	5	31:15:14	66.667		03:06:18	100		01:43:16	100	
8700	5	31:28:08	33.333		03:07:25	100		01:43:52	100	
8750	5	31:41:03	50		03:08:32	100		01:44:28	100	
8800	5	31:53:59	50		03:09:39	91.667		01:45:02	91.667	
8850	5	32:06:55	25		03:10:46	100		01:45:39	91.667	
8860	5	32:23:00	50	51.561	03:11:35	100	86.574	01:46:10	100	79.955
8865	5	32:37:17	66.667	51.561	03:12:18	91.667	88.003	01:46:38	91.667	63.934

The training performances of the network models used, including their success rates, error rates, parameter sizes, and training times, are summarized in table 6. This table provides an overview of the performance of each model, helping to compare their relative effectiveness in terms of classification accuracy, model complexity (parameter size), and the time taken to complete the training process. The models demonstrate different strengths, with the Small model achieving the highest accuracy, while the Tiny model offers a more compact architecture with moderate performance. The Base model, although achieving lower accuracy, can still serve as a useful baseline for comparison against more optimized configurations.

Table 6. Performance metrics of the training and test process.

Model	Accuracy Train (%)	Accuracy Validation (%)	Accuracy Test (%)	Training Loss	Validation Loss	Parameters	Training Time
ViT-Base	66.667%	51.561%	83.9534%	0.69153	0.91771	86.8 million	32:37:40
ViT-Small	91.667%	88.003%	87.9369%	0.25361	0.54841	22.1 million	03:12:39
ViT-Tiny	91.667%	63.934%	81.5859%	0.16297	2.4384	5.7 million	01:47:01

When interpreting Table 6, it is evident that the Small model of the Vision Transformer (ViT) networks achieves the highest accuracy, with a performance difference of 3.99% compared to the Base model, despite having approximately 4 times fewer parameters. This highlights the effectiveness of the Small model in terms of both performance and computational efficiency.

Although the Tiny model has about 15 times fewer parameters than the Base model and approximately 4 times fewer parameters than the Small model, its performance remains close to that of the other models. Notably, the Tiny model achieves this level of success in significantly less time, which makes it a viable option for scenarios where computational speed is critical.

While the Base model ranks second in terms of accuracy, it is worth considering for certain applications where a balance between performance and computational time is required. Therefore, the choice of model depends heavily on the specific needs of the research or application, whether that is achieving the highest accuracy, minimizing computational time, or balancing both factors.

The ViT base model consists of 86.8 million parameters. Given the complexity of such a large model, processing images involves an extensive number of computations, leading to a significant demand for computational resources at maximum capacity. As a result, obtaining outcomes takes considerably longer compared to the small and tiny models. Although the ViT base model's validation performance during training appears significantly lower than that of the other two models, its test performance was found to be very close to theirs. Ultimately, when analyzing test performance, the results indicate that the accuracy rates across all three models are relatively close and fall within an acceptable range.

5   RESULTS AND DISCUSSION

Breast cancer remains one of the leading causes of mortality among women worldwide, with early detection playing a crucial role in improving treatment outcomes. One of the most important diagnostic tools in this context is mammography, which allows for the detection of breast masses, a key indicator of potential malignancy. In recent years, advancements in deep learning have demonstrated promising results in improving the accuracy and efficiency of medical image analysis, particularly through the use of Vision Transformers (ViTs). ViTs have gained significant attention for their ability to model long-range dependencies in images and leverage self-attention mechanisms, making them ideal candidates for complex medical imaging tasks. This study evaluates the performance of three different Vision Transformer models—base-16, small-16, and tiny-16—on a dataset of breast mammography images containing masses. These models were specifically chosen to assess how different configurations of ViTs, with varying sizes and parameter counts, perform on the task of classifying mammographic images into categories such as benign, malignant, and normal. The ViTs' self-attention mechanism helps address challenges posed by the inherent complexity of mammographic textures and the low contrast that is often seen in medical imaging, which can make traditional image classification techniques less effective. Through comparative analysis, this study highlights the strengths and limitations of each ViT model. The findings provide valuable insights into the performance of these models in terms of accuracy, training time, and computational efficiency. By evaluating their effectiveness in breast mass classification tasks, this research aims to contribute to the broader understanding of how transformer-based architectures can enhance diagnostic accuracy in medical imaging. The results serve as a benchmark for future research, paving the way for further exploration of ViTs and other transformer-based models in medical image classification and diagnosis. This study underscores the potential of Vision Transformers in advancing the field of medical image analysis, particularly for early breast cancer detection, and supports their future application in clinical settings.

This paper provides a thorough examination of the classification architecture of Vision Transformers (ViTs) in the context of breast mammography image classification. Specifically, it investigates three sub-models within the ViTs framework: the base-16, small-16, and tiny-16 models. Each of these sub-models has been individually evaluated for their performance in classifying mammographic images, which are crucial for early breast cancer detection. The study aims to provide an in-depth understanding of how these different ViT configurations, with

varying model sizes and complexities, contribute to the classification task. A comprehensive analysis is conducted to highlight the strengths, weaknesses, and performance characteristics of each sub-model in the ViT architecture. The base-16 model, with its larger parameter size, is assessed for its ability to capture complex patterns in mammographic images, while the small-16 and tiny-16 models, with fewer parameters, are evaluated for their efficiency and speed, particularly in clinical settings where computational resources may be limited. By discussing the specific advantages and limitations of each model, this paper offers valuable insights into the trade-offs between accuracy, computational cost, and training time. This analysis also explores the role of the self-attention mechanism inherent in ViTs, which enables the models to effectively focus on relevant features within the mammographic images, addressing challenges such as low contrast and intricate textures commonly found in medical imaging. The study emphasizes how the selection of the appropriate ViT sub-model can be tailored to different research or clinical needs, depending on the available computational resources and the required diagnostic accuracy.

The study primarily focuses on a theoretical and computational comparison of ViT models for breast cancer detection in mammographic imaging. By evaluating the Base-16, Small-16, and Tiny-16 ViT configurations on a standardized dataset, we provide a benchmark analysis that highlights their strengths and limitations in terms of accuracy, training time, and computational efficiency. However, we acknowledge that clinical validation and real-world testing with physicians would enhance the applicability of our findings. Future research directions could involve collaboration with radiologists to assess model performance in real clinical settings, integrating physician feedback to improve interpretability and usability. Additionally, testing the models on diverse, real-world datasets with varying imaging conditions and patient demographics could further validate their robustness and reliability. Such efforts would bridge the gap between theoretical performance and practical deployment, making these models more applicable for clinical decision-making.

The primary objective of this research is to evaluate the outputs of ViT models on the same dataset in order to draw conclusions about their strengths, weaknesses, benefits, and disadvantages. This will be accomplished by using the default parameters of the models. If we had begun out with the intention of surpassing the existing performance of the dataset in the literature by utilizing a single ViT model, our primary focus would have been on further improving the dataset through the application of image processing techniques.

Overall, this paper serves as a detailed guide for understanding the application of ViTs in medical image classification, particularly for breast cancer detection, and it lays the groundwork for further research into optimizing and refining transformer-based models for use in medical diagnostics.

Conflict of Interest Statement

There is no conflict of interest between the authors.

Statement of Research and Publication Ethics

The study is complied with research and publication ethics.

Artificial Intelligence (AI) Contribution Statement

This manuscript was composed, revised, analyzed, and prepared without the aid of any artificial intelligence techniques. All content, encompassing text, data analysis, and figures, was exclusively produced by the authors.

Contributions of the Authors

Uğur DEMİROĞLU formulated the theoretical framework, conducted the analytical computations, and executed the numerical simulations. Bilal ŞENOL took the lead in writing the manuscript. Both authors Uğur DEMİROĞLU and Bilal ŞENOL contributed to the final version of the work. Bilal ŞENOL supervised the project.

REFERENCES

[1]   M. Arnold *et al.*, "Current and future burden of breast cancer: Global statistics for 2020 and 2040," *The Breast*, vol. 66, pp. 15-23, 2022.

[2]   C. I. Lee and J. G. Elmore, "Beyond survival: a closer look at lead-time bias and disease-free intervals in mammography screening," *JNCI: Journal of the National Cancer Institute*, vol. 116, no. 3, pp. 343-344, 2024.

[3]   L. N. Fuzzell *et al.*, "Cervical cancer screening in the United States: Challenges and potential solutions for underscreened groups," *Preventive Medicine*, vol. 144, p. 106400, 2021.

[4]   G. Savarese *et al.*, "Global burden of heart failure: a comprehensive and updated review of epidemiology," *Cardiovascular Research*, vol. 118, no. 17, pp. 3272-3287, 2022.

[5]   S. Sriussadaporn *et al.*, "Ultrasonography increases sensitivity of mammography for diagnosis of multifocal, multicentric breast cancer using 356 whole breast histopathology as a gold standard," *Surgical Practice*, vol. 26, no. 3, pp. 181-186, 2022.

[6]   N. Pashayan *et al.*, "Personalized early detection and prevention of breast cancer: ENVISION consensus statement," *Nature Reviews Clinical Oncology*, vol. 17, no. 11, pp. 687-705, 2020.

[7]   L. Nicosia *et al.*, "History of mammography: analysis of breast imaging diagnostic achievements over the last century," *Healthcare*, vol. 11, no. 11, p. 1596, 2023.

[8]   C. Poggi, "The Evolution of the Radiographer's Educational Path: EBP and Communication Skills in the Mammography Room," in *Breast Imaging Techniques for Radiographers*, Springer Nature Switzerland, 2024, pp. 259-276.

[9]   H. O. Kolade-Yunusa and U. D. Itanyi, "Outcome of mammography examination in asymptomatic women," *Annals of African Medicine*, vol. 20, no. 1, pp. 52-58, 2021.

[10]   L. Abdelrahman *et al.*, "Convolutional neural networks for breast cancer detection in mammography: A survey," *Computers in Biology and Medicine*, vol. 131, p. 104248, 2021.

[11]   D. Barba *et al.*, "Breast cancer, screening and diagnostic tools: All you need to know," *Critical Reviews in Oncology/Hematology*, vol. 157, p. 103174, 2021.

[12]   W. Y. Sung *et al.*, "Experiences of women who refuse recall for further investigation of abnormal screening mammography: A qualitative study," *International Journal of Environmental Research and Public Health*, vol. 19, no. 3, p. 1041, 2022.

[13]   H. J. Han *et al.*, "Characteristics of breast cancers detected by screening mammography in Taiwan: a single institute's experience," *BMC Women's Health*, vol. 23, no. 1, p. 330, 2023.

[14]   A. Aleissaee *et al.*, "Transformers in remote sensing: A survey," *Remote Sensing*, vol. 15, no. 7, p. 1860, 2023.

[15]   Y. Liu *et al.*, "A survey of visual transformers," *IEEE Transactions on Neural Networks and Learning Systems*, 2023.

[16]   A. Khan *et al.*, "A survey of the recent architectures of deep convolutional neural networks," *Artificial Intelligence Review*, vol. 53, pp. 5455-5516, 2020.

[17]   A. Agarwal and N. Ratha, "Deep Learning in Computer Vision Progress and Threats," in *Applications of Artificial Intelligence, Big Data and Internet of Things in Sustainable Development*, vol. 23, 2022.

[18]   A. Dosovitskiy *et al.*, "An Image is Worth 16x16 Words: Transformers for Image Recognition at Scale," *arXiv:2010.11929*, 2020.

[19]   Y. Yuan *et al.*, "Tokens-to-Token ViT: Training Vision Transformers from Scratch on ImageNet," in *Proc. ECCV*, 2021, pp. 558–576.

[20]   A. Steiner *et al.*, "How to train your vit? data, augmentation, and regularization in vision transformers," *arXiv preprint arXiv:2106.10270*, 2021.

[21]   X. Wu *et al.*, "CTransCNN: Combining transformer and CNN in multilabel medical image classification," *Knowledge-Based Systems*, vol. 281, p. 111030, 2023.

[22]   M. Hayat *et al.*, "Hybrid Deep Learning EfficientNetV2 and Vision Transformer (EffNetV2-ViT) Model for Breast Cancer Histopathological Image Classification," *IEEE Access*, 2024.

[23]   G. Ayana and S. W. Choe, "Vision transformers-based transfer learning for breast mass classification from multiple diagnostic modalities," *Journal of Electrical Engineering & Technology*, vol. 19, no. 5, pp. 3391-3410, 2024.

[24]   M. L. Abimouloud *et al.*, "Advancing breast cancer diagnosis: token vision transformers for faster and accurate classification of histopathology images," *Visual Computing for Industry, Biomedicine, and Art*, vol. 8, no. 1, p. 1, 2025.

[25]   "NHS to launch world's biggest trial of AI breast cancer diagnosis," *The Guardian*, Feb. 4, 2025. [Online]. Available: https://www.theguardian.com/society/2025/feb/04/nhs-to-launch-worlds-biggest-trial-of-ai-breast-cancer-diagnosis.

[26]   Kaggle, "Mammography Dataset from INbreast, MIAS and DDSM," accessed Nov. 4, 2024. [Online]. Available: https://www.kaggle.com/datasets/emiliovenegas1/mammography-dataset-from-inbreast-mias-and-ddsm.

[27]   M. A. Al-Antari *et al.*, "Evaluation of deep learning detection and classification towards computer-aided diagnosis of breast lesions in digital X-ray mammograms," *Computer Methods and Programs in Biomedicine*, vol. 196, p. 105584, 2020.

[28]   X. Li *et al.*, "Multiparametric magnetic resonance imaging for predicting pathological response after the first cycle of neoadjuvant chemotherapy in breast cancer," *Investigative Radiology*, vol. 50, no. 4, pp. 195-204, 2015.

[29]   L. G. Falconí *et al.*, "Transfer learning in breast mammogram abnormalities classification with mobilenet and nasnet," in *2019 International Conference on Systems, Signals and Image Processing (IWSSIP)*, 2019, pp. 109-114.

[30]   W. Hu *et al.*, "A state-of-the-art survey of artificial neural networks for whole-slide image analysis: from popular convolutional neural networks to potential visual transformers," *Computers in Biology and Medicine*, vol. 161, p. 107034, 2023.

[31]   S. K. Hamed *et al.*, "Enhanced Feature Representation for Multimodal Fake News Detection Using Localized Fine-Tuning of Improved BERT and VGG-19 Models," *Arabian Journal for Science and Engineering*, pp. 1-17, 2024.

[32]   Y. Fang *et al.*, "You only look at one sequence: Rethinking transformer in vision through object detection," *Advances in Neural Information Processing Systems*, vol. 34, pp. 26183-26197, 2021.

[33]   Z. Zeng *et al.*, "You only sample (almost) once: Linear cost self-attention via Bernoulli sampling," in *International Conference on Machine Learning*, PMLR, 2021, pp. 12321-12332.

[34]   A. Rehman, "Transformers in Computer Vision: Recent Advances and Applications," *International Journal of Advanced Engineering Technologies and Innovations*, vol. 1, no. 1, 2022.

[35]   M. Hassanin *et al.*, "Visual attention methods in deep learning: An in-depth survey," *Information Fusion*, vol. 108, p. 102417, 2024.

[36]   M. Li *et al.*, "SACNN: Self-attention convolutional neural network for low-dose CT denoising with self-supervised perceptual loss network," *IEEE Transactions on Medical Imaging*, vol. 39, no. 7, pp. 2289-2301, 2020.

[37]   M. H. Guo *et al.*, "Beyond self-attention: External attention using two linear layers for visual tasks," *IEEE Transactions on Pattern Analysis and Machine Intelligence*, vol. 45, no. 5, pp. 5436-5447, 2022.

[38]   R. Divya and J. Prabhakar, "Vision Transformer-based Model for Human Action Recognition in Still Images," *Journal of Computational Analysis and Applications*, vol. 33, no. 08, pp. 522-531, 2024.

[39]   E. Şahin *et al.*, "Multi-objective optimization of ViT architecture for efficient brain tumor classification," *Biomedical Signal Processing and Control*, vol. 91, p. 105938, 2024.

[40]   Marqo, "Introduction to Vision Transformers," accessed Nov. 4, 2024. [Online]. Available: https://www.marqo.ai/course/introduction-to-vision-transformers.

[41]   A. Sriwastawa and J. A. Arul Jothi, "Vision transformer and its variants for image classification in digital breast cancer histopathology: A comparative study," *Multimedia Tools and Applications*, vol. 83, no. 13, pp. 39731-39753, 2024.

[42]   V. Jain *et al.*, "Transformers are adaptable task planners," in *Conference on Robot Learning*, PMLR, 2023, pp. 1011-1037.

[43]   S. Wang *et al.*, "When transformer meets robotic grasping: Exploits context for efficient grasp detection," *IEEE Robotics and Automation Letters*, vol. 7, no. 3, pp. 8170-8177, 2022.

[44]   L. Xu *et al.*, "Mctformer+: Multi-class token transformer for weakly supervised semantic segmentation," *IEEE Transactions on Pattern Analysis and Machine Intelligence*, 2024.

[45]   A. Deihim *et al.*, "STTRE: A Spatio-Temporal Transformer with Relative Embeddings for multivariate time series forecasting," *Neural Networks*, vol. 168, pp. 549-559, 2023.

[46]   W. Wang *et al.*, "Semi-supervised vision transformer with adaptive token sampling for breast cancer classification," *Frontiers in Pharmacology*, vol. 13, p. 929755, 2022.

[47]   H. E. Kim *et al.*, "Transfer learning for medical image classification: A literature review," *BMC Medical Imaging*, vol. 22, no. 1, p. 69, 2022.

[48]   L. Xu *et al.*, "Multi-class token transformer for weakly supervised semantic segmentation," in *Proceedings of the IEEE/CVF Conference on Computer Vision and Pattern Recognition*, 2022, pp. 4310-4319.

[49]   O. S. Khedr *et al.*, "The classification of bladder cancer based on Vision Transformers (ViT)," *Scientific Reports*, vol. 13, no. 1, p. 20639, 2023.

ON PERFORMANCE OF ABC, FPA, BBO AND MVO ALGORITHMS IN ANFIS TRAINING FOR SHORT-TERM FORECASTING OF CRUDE OIL PRICE

Ebubekir KAYA[1,2] , Ahmet KAYA[3] , Eyüp SIRAMKAYA[1] ,

Ceren BAŞTEMUR KAYA[4]*

[1] *Nevsehir Hacı Bektaş Veli University, Department of Computer Engineering, Nevşehir, Türkiye*

[2] *CEKA Software R&D Co. Ltd., Cappadocia Technopark, Nevşehir, Türkiye*

[3] *Nevsehir Hacı Bektaş Veli University, Department of Mathematics, Nevşehir, Türkiye*

[4] *Nevsehir Hacı Bektaş Veli University, Department of Computer Technologies, Nevşehir, Türkiye*

*** *Corresponding Author:* ceren@nevsehir.edu.tr

ABSTRACT

Crude oil is one of the most important assets that are used in the production of many industrial products in a wide variety of areas. The importance of crude oil has made it important to predict its future price. Therefore, it is possible to come across many studies in the literature in which the price of crude oil is estimated in the short or long term. In this study, innovative adaptive neuro-fuzzy inference systems (ANFIS) based approaches are proposed to estimate the daily minimum and maximum prices of crude oil. The used data was taken from the period between January 3, 2022, and December 29, 2023. A total of 516 different days of data were collected to create the dataset for analysis. For daily forecasting, time series data were transformed into a data set consisting of two inputs and one output. Moth-flame optimization algorithm (MFO), flower pollination algorithm (FPA), biogeography-based optimization (BBO) and artificial bee colony (ABC) were used in training ANFIS. The results obtained in the training and testing processes were compared. When the results obtained were compared, it was shown that the relevant algorithms were effective in the daily estimation of crude oil. It has been observed that effective results are also achieved at low evaluation numbers, especially thanks to the fast convergence feature of the MFO and BBO algorithms.

Keywords: Artificial intelligence, ANFIS, Crude oil, Metaheuristic algorithms, Time series analysis.

1 INTRODUCTION

Crude oil is one of the most important and even most strategically critical assets that is used in the production of many industrial products in a wide variety of areas, including fertilizers, pesticides, solvents, and plastics [1]. Furthermore, it is a source of several products, such as paraffin, asphalt, different fuels, and LPG [2]. In addition, it plays a leading role in meeting global energy demands, providing approximately one-third of worldwide energy consumption [3].

Therefore, it has an enormous effect on the economies of both producing and consuming countries as well as the global financial system [4, 5]. This demonstrates how vital it is to create price predictions. However, it is quite difficult to make an accurate prediction because there are numerous variables and events that affect the price, and as a result, the price fluctuates seriously [6]. These fluctuations have an impact on countries' inflation rates, economic growth, and investment decisions [7].

2 LITERATURE REVIEW

Many scientific approaches have been created and used in research to forecast crude oil prices. For example, Gupta and Nigam [8] used artificial neural networks (ANN) to reliably capture the shifting trends in crude oil prices. They demonstrate that identifying optimum time lags is a useful strategy for short-term price prediction.

Wu et al. [6] aimed to create an innovative hybrid approach for predicting crude oil prices. They eliminated outliers with the Hampel descriptor and reduced noise with the ensemble empirical mode decomposition approach. They proposed a modified water cyce algorithm to cover the deficient points of the traditional water cycle algorithm (WCA) in some conditions and used it to optimize the echo state network parameters. Finally, the efficacy of the model was tested and evaluated for daily and weekly crude oil price forecasts.

Chiroma et al. [9] proposed a hybrid technique for predicting West Texas Intermediate Oil (WTI) crude oil prices called GA-NN, which is based on the fundamentals of genetic algorithms and neural networks. This paper introduces a GA strategy to optimize the weights, biases, and topology of neural networks.

Mirmirani and Cheng [5]employed a VAR-based technique to predict US oil prices based on lagged data on oil prices, supply, and consumption. Additionally, the genetic

algorithm-based ANN model makes predictions based on oil supply, energy use, and supply of cash.

Al-Qaness et al. [10] used the dendritic nerve regression (DNR) model, which is an artificial neural network that has excellent potential performance in time series forecasting due to its ability to deal with nonlinear characteristics found in historical data. Several metaheuristic algorithms like the whale optimization algorithm (WOA), particle swarm optimization algorithm (PSO), genetic algorithm (GA), sine-cosine algorithm (SCA), differential evolution (DE), and harmony search algorithm (HS) have been added to the estimation process in order to get around some restrictions associated with parameter configuration and training.

In their work, Sohrabi et al. [11] predict West Texas Intermediate Oil (WTI) prices using the whale optimization algorithm (WOA) and ANN; and compare the results with traditional ANN results.

In order to successfully predict the prices of crude oil futures, Hu et al. [12] employed three well-known neural network techniques: multilayer perceptron, Elman recurrent neural networks (ERNN), and recurrent fuzzy neural networks (RFNN).

Anshori et al. [2] applied the ANFIS technique to optimize the price of crude oil. This technique's initial settings are optimized using the Cuckoo Search approach.

Depending on the nature of the problem and how it will be solved, methods mentioned in this literature have different advantages or disadvantages. For example, GA, which is inspired by biological evolution methods, uses the solution population to reach the global optimum without being stuck in local optima. Without differentiation, it can be used for both continuous and discrete problems. It has the benefit of operating with its own rules without requiring the issue to be linearized, but it also has the drawback of defining the fitness function and calculating the parameters required for the algorithm. [13].

On the other hand, ANN works incredibly well with large and complex data. It can be effectively used to solve a variety of problems, including regression, classification, and time series forecasting. Despite these advantages, its primary disadvantage is the time-consuming training process and the need for large data. Additionally, insufficient data might lead to overfitting. [14].

ANFIS, which we applied in our study, is a technique that combines fuzzy logic structure and ANN. Thanks to this structure, it can be successfully applied to various subjects. Fuzzy logic principles make background processes easier to understand. The inability to properly set

fuzzy logic rules and parameters is its primary limitation. Additionally, this adjustment process can be challenging and time-consuming [15].

When the literature is examined, it is seen that ANFIS-based methods are used in the estimation of crude oil. The training process is important in order to make effective estimations with ANFIS. Therefore, the optimization algorithms used in the training of ANFIS directly affect the result. In this study, for the first time, ANFIS training was performed with FPA, BBO, ABC and MFO algorithms for the estimation of daily price values of crude oil and their performances were compared.

3   MATERIAL AND METHOD

3.1   Adaptive Neuro-Fuzzy Inference Systems (ANFIS)

The Neuro-Fuzzy is a unique architecture that combines neural networks and fuzzy systems, enabling supervised learning and the conversion of complex systems into if-then rules. Neuro-Fuzzy systems can be viewed as neural networks that embody distributed knowledge across their connection weights. Research has shown that Neuro-Fuzzy systems are effective in various applications, particularly in adapting knowledge expressed in fuzzy linguistic rules. An adaptive network is a key component of Neuro-Fuzzy systems, consisting of nodes and directed connections with modifiable parameters [16].

Although there are many Neuro-fuzzy models proposed in the literature, the most popular one is the ANFIS model [17]. ANFIS consists of two parts as seen in Figure 1. These sections are called premise and consequence. Both sections are connected to each other with the IF-THEN rule. The parameters in these sections are used in ANFIS training. An ANFIS model consists of five layers. Output values corresponding to inputs are calculated with the calculations performed in the layers [17, 18].
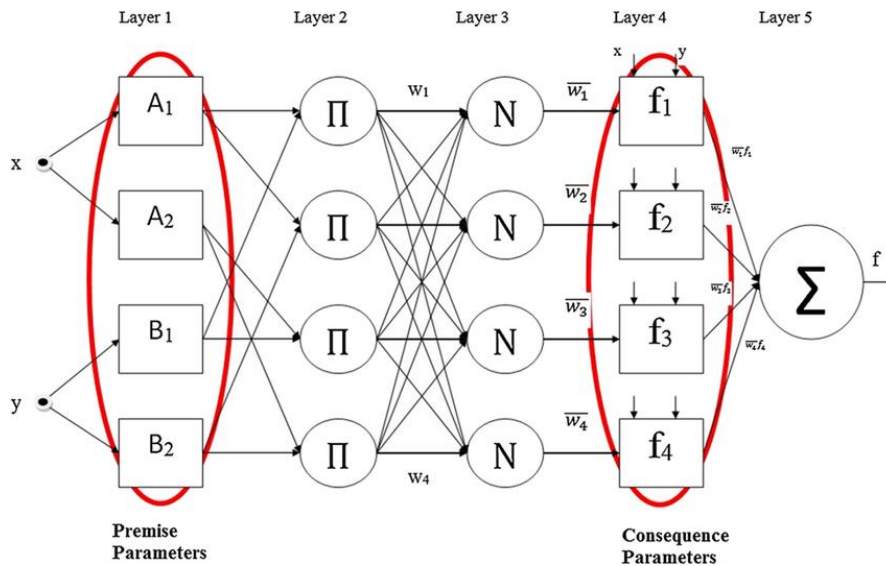
Figure 1. Display of parameters used in ANFIS training[18].

3.2   Moth-Flame Optimization Algorithm (MFO)

In nature, over 160,000 different species of moths have been documented, characterized by a two-stage life cycle consisting of a larval stage and a pupal stage, followed by the transformation into an adult moth [19]. One of the most intriguing aspects of moths' lives is their navigation method at night. They have evolved to fly at night using moonlight and employ a mechanism called transverse orientation to navigate. This mechanism enables the moth to maintain a constant angle with respect to the moon, allowing it to traverse long distances in a straight line [20]. Figure 2 illustrates a conceptual model of transverse orientation. Since the moon is far away from the moth, this mechanism guarantees flight in a straight line. Humans can also use this navigation method. For example, if a person wants to walk east and keeps the moon on their left side, they can move in a straight line.
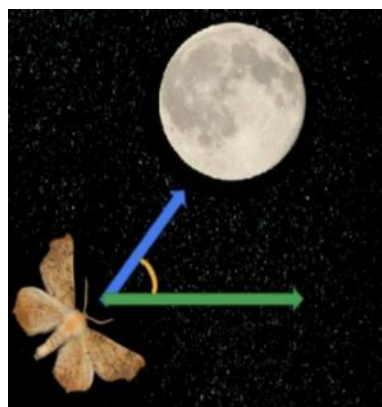
Figure 2. Moth's transverse orientation [21].

Figure 3 shows that moths do not follow a straightforward path, but instead fly in a spiral pattern around light sources. This is because the transverse orientation method is only effective when the light source is very far away (moonlight). In the case of artificial light sources, moths attempt to maintain the same angle with respect to the light source, resulting in spiral motion around the light.
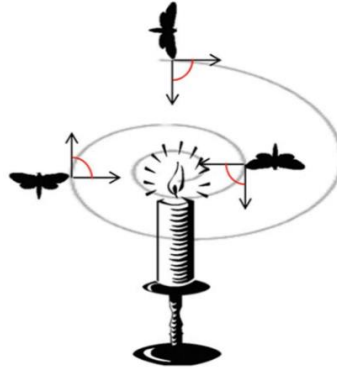
Figure 3. Moth's spiral flyingpath around a light source[21].

The Moth-Flame Optimization (MFO) algorithm was proposed by Mirjalili [22]. It is a population-based metaheuristic algorithm. MFO starts by generating a random population of moths in the solution space, followed by calculating the fitness value (i.e., position) of each moth and labeling the best position as a flame. Then, the moths' positions are updated using a spiral motion function to obtain better positions labeled by a flame, update the best individual positions, and repeat the previous steps until the termination criteria are met.

3.3 Flower Pollination Algorithm (FPA)

Prior to elucidating the intricacies of the Flower Pollination Algorithm (FPA), it is essential to delve into the fundamental principles governing the pollination behavior of plants. A dichotomy exists in the realm of pollination, as illustrated in Figure 4, which categorizes this phenomenon into two distinct forms.
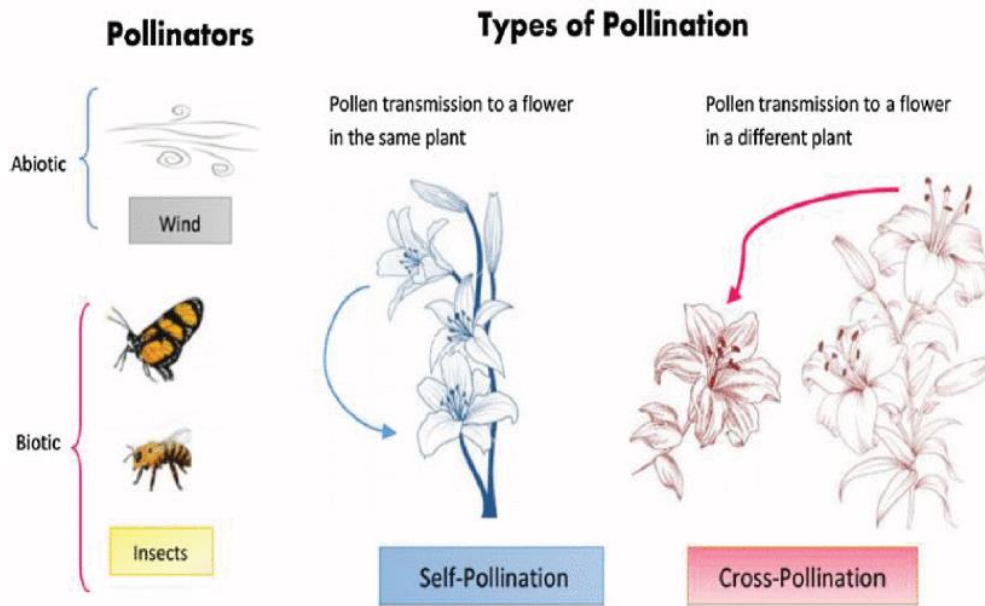
Figure4. The pollinators and pollination types[23].

Biotic or Cross-Pollination is precipitated by the agency of pollinators, including, but not limited to, avian and insect species. These pollinators traverse extensive distances, exhibiting varied velocities and speeds, thereby exemplifying a global pollination process characterized by Levy flight attributes [24-26]. Notably, a significant proportion of flowering plants (approximately 90%) on our planet conform to this pollination paradigm.

Abiotic or Self-Pollination occurs without the necessitation of external pollinators. A relatively smaller proportion of plants (approximately 10%) employ this pollination mechanism, wherein the distance traversed by pollinators, such as wind, is limited, resulting in a localized pollination process.

The flower pollination algorithm is shaped around four basic rules:

• Rule 1: Global Pollination Encompasses Biotic and Cross-Pollination via Levy Flight

Global pollination is characterized by the synergistic interplay between biotic and cross-pollination, mediated by pollinators exhibiting Levy flight patterns.

• Rule 2: Abiotic and Self-Pollination Induce Localized Pollination

Conversely, abiotic and self-pollination precipitate localized pollination, wherein the spatial scope of pollination is limited.

• Rule 3: Floral Similarity and Reproductive Probability

The similarity between two flowers is directly proportional to the probability of successful reproduction, a phenomenon referred to as flower constancy.

• Rule 4: Pollination Mode Selection via Switch Probability

The algorithm's pollination mode, whether local or global, can be modulated by adjusting the switch probability, a parameter bounded between 0 and 1.

3.4 Biogeography-Based Optimization (BBO)

Biogeography, a nebulous threshold beyond which a self-reinforcing paradigm of positive feedback is necessitated. This characteristic of biogeography bears a striking semblance to the principles of natural selection, wherein species, as they evolve to become increasingly adapted, augment their prospects for survival, thereby facilitating an enhanced capacity for dispersal and adaptation. Both natural selection and biogeography encompass this self-reinforcing attribute, wherein the iterative perpetuation of advantageous traits precipitates an incremental augmentation of fitness. However, the temporal scales at which these processes operate diverge significantly, with natural selection unfolding over an expansive timescale of millions and billions of years, whereas biogeography's timeframe is decidedly more compressed, spanning mere hundreds and thousands of years. This disparity in temporal scope suggests that, were we to invoke biogeography rather than natural selection as a motivating paradigm for an optimization algorithm (i.e., BBO as opposed to GAs), the prospect of achieving superior optimization outcomes is rendered more plausible. The supposition that biogeography optimizes habitats has, in turn, provided the impetus for the introduction of BBO as an optimization algorithm [27].

Biogeography-Based Optimization (BBO), developed by Dan Simon in 2008, is an evolutionary algorithm (EA) inspired by biogeography, the study of the distribution of biological species through time and space. Similar to other evolutionary algorithms, BBO aims to optimize a problem by maintaining a population of candidate solutions [27].

Each solution is comprised of a constellation of attributes or independent variables. A superior solution corresponds to a biological habitat that is optimally conducive to sustenance, whereas a suboptimal solution is tantamount to a habitat that is inimical to existence. Solutions with elevated degrees of fitness exhibit a propensity to share their attributes with other solutions; that is to say, attributes tend to migrate from solutions with high fitness to those with lower fitness, and vice versa. Conversely, solutions with diminished fitness exhibit a

predilection for accepting attributes shared by other solutions. Like other EAs, Biogeography-Based Optimization (BBO) encompasses two distinct phases: information sharing and mutation. In the context of BBO, information sharing is effectuated through the mechanism of migration.

3.5   Artificial Bee Colony (ABC)

In the year 2007, Karaboğa introduced the Artificial Bee Colony (ABC) algorithm, a novel optimization technique predicated on swarm intelligence, which simulates the intriguing foraging behavior exhibited by honey bees [28]. Within the hierarchical structure of a bee colony, the bees are delineated into three distinct species [29], each with their unique roles and responsibilities:

I.   Employed bees (forager bees): These diligent bees engage in an exhaustive search for sustenance sources, and upon their return to the hive, they disseminate pertinent information regarding the location of these sources to the onlooker bees, thereby facilitating a collective understanding of the environment.

II.   Onlooker bees (observer bees): These unemployed bees, awaiting their cue to initiate the search process, are informed by the employed bees about the locations of the sustenance sources, which they subsequently utilize as a starting point for their own exploration.

III.   Scout bees: These intrepid bees, tasked with the responsibility of abandoning depleted sources, embark upon an exploration of novel sustenance sources, conducting meticulous reconnaissance searches to identify potential alternatives.

In the ABC algorithm, the location of the source is metaphorically regarded as the solution to the problem at hand, while the quantity of source present is analogously considered as the fitness or quality of the solution. Each employed bee is assigned to a specific sustenance source, with the number of employed bees being commensurate with the number of solutions.

4   SIMULATIONS RESULTS AND DISCUSSION

In this study, ANFIS training was performed using ABC, FPA, BBO, and MFO metaheuristic optimization algorithms for short-term forecasting of crude oil. The data used is for the period between January 3, 2022, and December 29, 2023. Generally, the data excludes or does not account for weekends and public holidays. A total of 516 different days of data were collected to create the dataset for analysis.

Daily data is very important in modeling to understand sudden fluctuations or short-term trend changes. The point to be considered here is whether the data fluctuates significantly within the chosen time period. In our study, daily data for a two-year period was taken to obtain meaningful results and to ensure smooth operation of ANFIS. Normally, daily data is affected by seasonal factors and uncertainties such as short-term trends. Sometimes political events on a local or global scale affect the oil price. We took the data set for two years, allowing ANFIS to handle these impacts and learn the pattern. In addition, since we receive data for a long time, the system will be able to tolerate any deficiencies in the data. Taking the daily lowest and highest data is crucial to gain a better knowledge of the fluctuation in daily data and for ANFIS to understand and manage this pattern. In addition, these low and high values contain important information to determine the direction of the trend and the turning points.

The data set was created separately for the daily lowest and highest values. In other words, analyses were carried out to estimate the daily minimum and daily maximum values of crude oil. 80% of the dataset was used for the training process, while the rest was allocated to the testing process. Mean squared error (MSE) was utilized to calculate errors for both training and testing errors. For metaheuristic algorithms, the colony size was taken as 20. The maximum generation number was chosen as 2500.

The data obtained for the relevant prediction were transformed into data sets consisting of input and output in order to integrate it into the structure of ANFIS. In other words, time series data were transformed into a data set consisting of two inputs and one output. While the inputs represent the values of the previous two days, the output gives the value of the day to be estimated. The generalized Bell function (gbellf) was used in the structure of ANFIS. The network structure of ANFIS has a big impact on how well the algorithm performs. Therefore, the results were obtained by using 2, 3 and 4 membership functions for each input. In this way, the effect of the number of membership functions on performance was also analyzed.

Table 1 and Table 2 provides the mean error, best error, and standard deviation values for the training and test data acquired using these four metaheuristic methods for daily lowest and highest crude oil price respectively. BBO produced the most effective mean error and best error results, even though optimization algorithms for training data gave close results for the lowest price prediction. As is well known, a lower standard deviation denotes consistency between the results of different algorithm runs, while a higher standard deviation indicates greater variability. In the train phase, standard deviation values are around E-5, indicating that the optimization techniques provide consistent results across various runs. However, the FPA

method produced the best standard deviation value. Furthermore, the findings were better with 4 gbellf in the BBO algorithm, although it was usually found that different gbellf had no obvious impact on the results.

Table 1. Results found with ABC, FPA, BBO and MFO algorithms for daily lowest price prediction.

The Algorithm	The Number of MF	The Results					
		Train			Test		
		Mean	Best	Standard Deviation	Mean	Best	Standard Deviation
ABC	2	0.00154249	0.00140645	4.55721e-05	0.00132585	0.00125505	6.79725e-05
	3	0.00154616	0.00146477	3.29384e-05	0.00170155	0.00121331	0.00190897
	4	0.00153333	0.00148998	2.2437e-05	0.00132764	0.00116903	0.000134089
FPA	2	0.00153183	0.00150383	1.44265e-05	0.00131314	0.0011937	6.2601e-05
	3	0.00153748	0.00149388	2.15828e-05	0.00133359	0.00116378	0.000174327
	4	0.0015400	0.00148619	1.83605e-05	0.00134992	0.00122503	0.000104509
BBO	2	0.00147139	0.00140182	3.81338e-05	0.00135345	0.0012658	5.60871e-05
	3	0.00145527	0.00137498	3.81314e-05	0.00135535	0.00126513	5.35977e-05
	4	0.00143279	0.00132934	4.97694e-05	0.00138747	0.00127159	7.49651e-05
MFO	2	0.00150257	0.0014053	4.33461e-05	0.00134791	0.00128429	6.01915e-05
	3	0.0014741	0.0013621	5.28765e-05	0.00134216	0.0012741	6.08687e-05
	4	0.00146622	0.0013492	4.84771e-05	0.00135517	0.00125383	5.14631e-05

In the test phase for the lowest price prediction, the better and mean error values were found with the FPA algorithm. At this stage, the algorithms also returned results that were similar to each other. While the standard deviation statistics are consistent, the ABC algorithm's value for 3 gbellf is slightly higher.

In daily highest price prediction, the BBO algorithm outperformed others for a mean error value with 4 gbellf in the training phase. In addition, the best test error value was achieved as 0.00107589 with BBO. The other algorithms also performed well and provided results that were quite similar to BBO. In addition, consistent standard deviation values around E-5 were observed in both train and test phases.

Table 2. Results found with ABC, FPA, BBO and MFO algorithms for daily highest price prediction.

Algorithm	The Number of MF	The Results					
		Train			Test		
		Mean	Best	Standard Deviation	Mean	Best	Standard Deviation
ABC	2	0.00117105	0.00110336	4.61632e-05	0.00130587	0.00113348	8.39413e-05
	3	0.00115298	0.00110503	2.58662e-05	0.00126585	0.00112633	7.19967e-05
	4	0.00113414	0.00105515	2.4414e-05	0.00123768	0.0010982	7.02308e-05
FPA	2	0.00112432	0.00106925	1.41747e-05	0.00126797	0.00115898	5.6367e-05
	3	0.00114205	0.0011134	1.5816e-05	0.00129328	0.00114006	8.20375e-05
	4	0.00114664	0.00111429	1.58977e-05	0.00128786	0.00115503	8.81623e-05
BBO	2	0.00109202	0.000977377	3.54083e-05	0.00125036	0.00107589	5.69311e-05
	3	0.00107727	0.000885529	4.9627e-05	0.00125655	0.00117072	3.87653e-05
	4	0.00105926	0.000919088	5.70019e-05	0.0012569	0.001119	5.44527e-05
MFO	2	0.00111429	0.00094193	3.2932e-05	0.00127759	0.00122568	4.4203e-05
	3	0.0011035	0.00098341	2.93164e-05	0.00124368	0.00116902	2.94704e-05
	4	0.00108048	0.00097419	5.01938e-05	0.00125194	0.00118246	3.57427e-05

a)

b)

c)
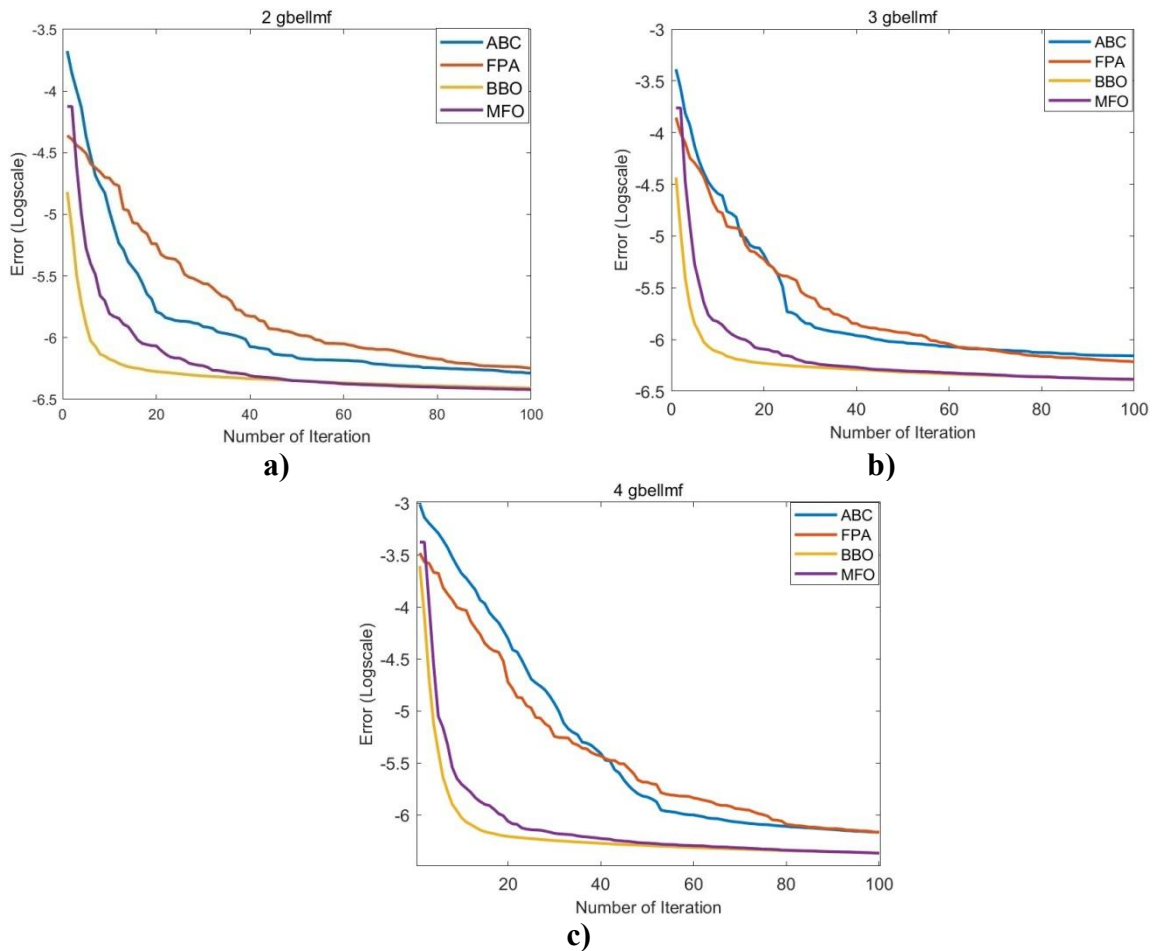
Figure 5. Comparison of convergence graphs of ABC, FPA, BBO and MFO algorithms for daily lowest price prediction when a) 2 gbellmf b) 3 gbellmf c) 4 gbellmf are used.

Figures 5 and 6 show that a similar scenario exists in both the test and training data. When the figures were analyzed for convergence to the intended value based on the number of iterations, we discovered that the BBO and MFO algorithms converged swiftly. However, the ABC and FPA algorithms converged at a slightly slower rate. After 100 iterations, BBO and MFO values converged to the same value, and ABC and FPA converged to a different value very close to this value, with BBO and MFO doing somewhat better.
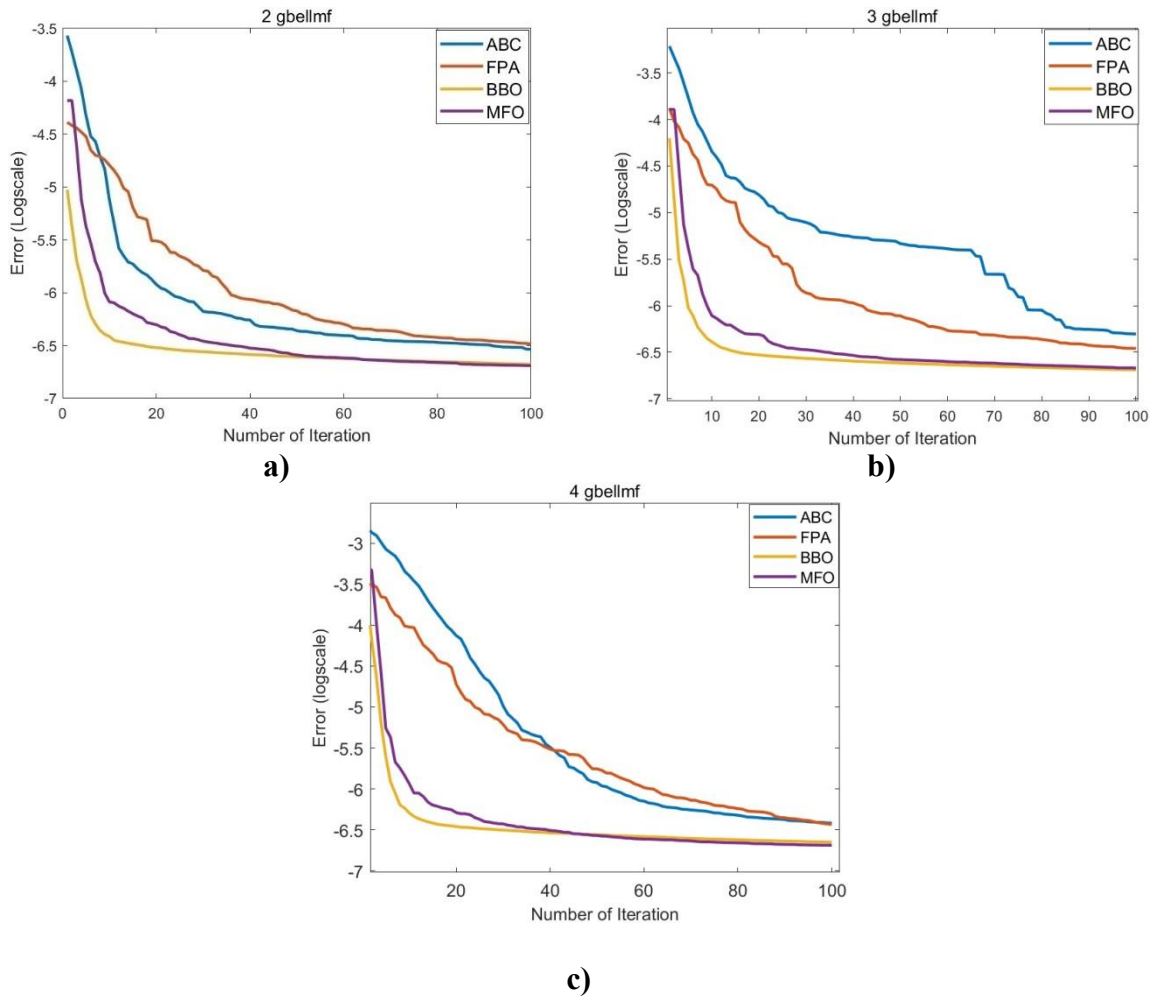
Figure 6. Comparison of convergence graphs of ABC, FPA, BBO and MFO algorithms for daily highest price prediction when a) 2 gbellmf b) 3 gbellmf c) 4 gbellmf are used.

It is seen that effective solutions are obtained with metaheuristic algorithms in solving the relevant problem. In both the estimation of the smallest value and the estimation of the largest value, all algorithms have reached e-03 level training and test error values. Namely, effective results were obtained in both the training and testing processes. Although the training algorithms started with random initial populations, they reached the most effective results they could find and supported them with low standard deviation values. It is important that the algorithms have the feature of repeating the same results. The training and testing performances

of the relevant algorithms are parallel to each other. In other words, they have shown the success in the both processes. Convergence is an important feature to examine the performance of training algorithms. Although the results of all algorithms are close to each other, we see that the convergence range to effective results is different. In other words, in cases where the maximum number of iterations is not important, all algorithms can be used in general. On the other hand, if it is necessary to reach a fast result, the algorithm with a high convergence speed is the reason for preference. When we look at this problem specifically, the convergence of BBO and MFO is better than other algorithms.

5   CONCLUSION

In this study, the performance of an ANFIS-based approach to estimate the daily minimum and maximum value of crude oil was investigated. The performances of ABC, FPA, BBO, and MFO algorithms were evaluated for the optimization of the parameters of ANFIS. In addition, the structure of ANFIS and the number of membership functions used directly affect the result. Therefore, the effect of different membership function numbers on the performance was also investigated. As a result of the study, the following general conclusions were reached:

• All algorithms performed well in daily crude oil prediction, as evidenced by their mean best error values.

• When doing a general evaluation, BBO often gives better results in the training process in general.

• While MFO and BBO have faster convergence in a small number of iterations, there is no meaningful difference between the algorithms in large numbers of iterations.

• The training and test outcomes of each algorithm were very similar in both the highest and lowest price data. This demonstrates that the learning process was carried out satisfactorily.

This study was developed for crude oil daily price prediction based on metaheuristic algorithm. It is a guiding study for future research to predict the prices of other goods with the same or different optimization algorithms.

There are some limitations in this study. Especially the population size and maximum generation number directly affect the result. It is possible to reach effective results by experimenting with different values of these control parameters. Another limitation is the number of inputs. In the scope of the study, time series data belonging to crude oil were

converted into a data set that ANFIS can understand. There are two inputs and one output in this data set. Changing the number of inputs can change the performance of the system. The results to be obtained for different input number can be analyzed. In addition, the performance of only four meta-heuristic algorithms was examined for the solution of the relevant problem. It is possible to evaluate the performance of different meta-heuristic algorithms.

Acknowledgment

Conflict of Interest Statement

There is no conflict of interest between the authors.

Statement of Research and Publication Ethics

The study is complied with research and publication ethics.

Artificial Intelligence (AI) Contribution Statement

This manuscript was entirely written, edited, analyzed, and prepared without the assistance of any artificial intelligence (AI) tools. All content, including text, data analysis, and figures, was solely generated by the authors.

Contributions of the Authors

Ebubekir Kaya: Conceptualization, methodology, validation, software, review and editing, original draft preparation, supervision; Ahmet Kaya: Methodology, software, data curation, original draft preparation; Eyüp Sıramkaya: Data curation, example analysis, original draft preparation; Ceren Baştemur Kaya: Data curation, example analysis, visualization.

REFERENCES

[1] Z. Cen and J. Wang, "Crude oil price prediction model with long short term memory deep learning based on prior knowledge data transfer," *Energy,* vol. 169, pp. 160-171, 2019.

[2] M. Y. Anshori, D. Rahmalia, T. Herlambang, and D. F. Karya, "Optimizing Adaptive Neuro Fuzzy Inference System (ANFIS) parameters using Cuckoo Search (Case study of world crude oil price estimation)," in *Journal of Physics: Conference Series*, 2021, vol. 1836, no. 1: IOP Publishing, p. 012041.

[3] S. Gao and Y. Lei, "A new approach for crude oil price prediction based on stream learning," *Geoscience Frontiers,* vol. 8, no. 1, pp. 183-187, 2017.

[4] M. Hamdi and C. Aloui, "Forecasting crude oil price using artificial neural networks: a literature survey," *Econ. Bull,* vol. 35, no. 2, pp. 1339-1359, 2015.

[5] S. Mirmirani and H. Cheng Li, "A comparison of VAR and neural networks with genetic algorithm in forecasting price of oil," in *Applications of artificial intelligence in finance and economics*: Emerald Group Publishing Limited, 2004, pp. 203-223.

[6] C. Wu, J. Wang, and Y. Hao, "Deterministic and uncertainty crude oil price forecasting based on outlier detection and modified multi-objective optimization algorithm," *Resources Policy,* vol. 77, p. 102780, 2022.

[7] T. Zhang, Z. Tang, J. Wu, X. Du, and K. Chen, "Multi-step-ahead crude oil price forecasting based on two-layer decomposition technique and extreme learning machine optimized by the particle swarm optimization algorithm," *Energy,* vol. 229, p. 120797, 2021.

[8] N. Gupta and S. Nigam, "Crude oil price prediction using artificial neural network," *Procedia Computer Science,* vol. 170, pp. 642-647, 2020.

[9] H. Chiroma, S. Abdulkareem, and T. Herawan, "Evolutionary Neural Network model for West Texas Intermediate crude oil price prediction," *Applied Energy,* vol. 142, pp. 266-273, 2015.

[10] M. A. Al-Qaness, A. A. Ewees, L. Abualigah, A. M. AlRassas, H. V. Thanh, and M. Abd Elaziz, "Evaluating the applications of dendritic neuron model with metaheuristic optimization algorithms for crude-oil-production forecasting," *Entropy,* vol. 24, no. 11, p. 1674, 2022.

[11] P. Sohrabi, H. Dehghani, and R. Rafie, "Forecasting of WTI crude oil using combined ANN-Whale optimization algorithm," *Energy Sources, Part B: Economics, Planning, and Policy,* vol. 17, no. 1, p. 2083728, 2022.

[12] J. W.-S. Hu, Y.-C. Hu, and R. R.-W. Lin, "Applying neural networks to prices prediction of crude oil futures," *Mathematical Problems in Engineering,* vol. 2012, no. 1, p. 959040, 2012.

[13] S. Sivanandam, S. Deepa, S. Sivanandam, and S. Deepa, *Genetic algorithms*. Springer, 2008.

[14] J. V. Tu, "Advantages and disadvantages of using artificial neural networks versus logistic regression for predicting medical outcomes," *Journal of clinical epidemiology,* vol. 49, no. 11, pp. 1225-1231, 1996.

[15] M. N. M. Salleh, N. Talpur, and K. Hussain, "Adaptive neuro-fuzzy inference system: Overview, strengths, limitations, and solutions," in *Data Mining and Big Data: Second International Conference, DMBD 2017, Fukuoka, Japan, July 27–August 1, 2017, Proceedings 2*, 2017: Springer, pp. 527-535.

[16] J.-S. Jang and C.-T. Sun, "Neuro-fuzzy modeling and control," *Proceedings of the IEEE,* vol. 83, no. 3, pp. 378-406, 1995.

[17] J.-S. Jang, "ANFIS: adaptive-network-based fuzzy inference system," *IEEE Transactions on Systems, Man, and Cybernetics,* vol. 23, no. 3, pp. 665-685, 1993.

[18] D. Karaboga and E. Kaya, "Adaptive network based fuzzy inference system (ANFIS) training approaches: a comprehensive survey," *Artificial Intelligence Review,* vol. 52, pp. 2263-2293, 2019.

[19] T. Smith and M. Villet, "Parasitoids associated with the diamondback moth, Plutella xylostella (L.), in the Eastern Cape, South Africa," 2004.

[20] K. J. Gaston, J. Bennie, T. W. Davies, and J. Hopkins, "The ecological impacts of nighttime light pollution: a mechanistic appraisal," *Biological Reviews,* vol. 88, no. 4, pp. 912-927, 2013.

[21]   M. Shehab, L. Abualigah, H. Al Hamad, H. Alabool, M. Alshinwan, and A. M. Khasawneh, "Moth–flame optimization algorithm: variants and applications," *Neural Computing and Applications,* vol. 32, no. 14, pp. 9859-9884, 2020.

[22]   S. Mirjalili, "Moth-flame optimization algorithm: A novel nature-inspired heuristic paradigm," *Knowledge-Based Systems,* vol. 89, pp. 228-249, 2015.

[23]   M. Abdel-Basset and L. A. Shawky, "Flower pollination algorithm: a comprehensive review," *Artificial Intelligence Review,* vol. 52, pp. 2533-2557, 2019.

[24]   S. Kalra and S. Arora, "Firefly algorithm hybridized with flower pollination algorithm for multimodal functions," in *Proceedings of the International Congress on Information and Communication Technology: ICICT 2015, Volume 1*, 2016: Springer, pp. 207-219.

[25]   I. Pavlyukevich, "Lévy flights, non-local search and simulated annealing," *journal of computational physics,* vol. 226, no. 2, pp. 1830-1844, 2007.

[26]   X.-S. Yang, "Flower pollination algorithm for global optimization," in *International conference on unconventional computing and natural computation*, 2012: Springer, pp. 240-249.

[27]   D. Simon, "Biogeography-based optimization," *IEEE Transactions on Evolutionary Computation,* vol. 12, no. 6, pp. 702-713, 2008.

[28]   D. Karaboga and B. Basturk, "A powerful and efficient algorithm for numerical function optimization: artificial bee colony (ABC) algorithm," *Journal of global optimization,* vol. 39, pp. 459-471, 2007.

[29]   D. Karaboga and B. Basturk, "On the performance of artificial bee colony (ABC) algorithm," *Applied Soft Computing,* vol. 8, no. 1, pp. 687-697, 2008.

INVERSE PREDICTION OF THE CALPHAD-MODELED PHYSICAL PROPERTIES OF SUPERALLOYS USING EXPLAINABLE ARTIFICIAL INTELLIGENCE AND ARTIFICIAL NEURAL NETWORKS

Yusuf UZUNOĞLU [1*] [iD], Yusuf ALACA [2] [iD]

[1] *Erciyes University, Materials Science and Engineering Department, Kayseri, Türkiye*

[2] *Hitit University, Computer Engineering Department, Çorum, Türkiye*

***Corresponding Author:** yusufuzunoglu11@gmail.com*

ABSTRACT

The CALPHAD methodology models the physical, mechanical, and thermodynamic properties of materials based on specified alloy compositions using phase equilibrium calculations and thermodynamic databases. With the CALPHAD approach, millions of material-property data can be obtained for each alloy composition over various temperature ranges. However, finding an alloy with the desired properties often requires lengthy trial-and-error processes that involve manually adjusting the composition. In this study, the goal is to inverse this approach using artificial intelligence to predict alloy compositions that yield the desired properties. Accordingly, in the JMatPro software based on the CALPHAD methodology, the physical properties (density, thermal conductivity, linear expansion, Young's modulus, bulk modulus, shear modulus, and Poisson's ratio) of 250 different Ni-Cr-Fe-based superalloys in the temperature range of 540–920 °C were modeled. A dataset with 5000 rows was created from the generated data, of which 80% was used to train the artificial intelligence model, while 20% was reserved for validation and testing. Through analyses using Explainable Artificial Intelligence (XAI) and Artificial Neural Networks (ANN), alloy compositions with the desired physical properties at a given temperature were predicted with a high accuracy rate of 98.03%. In conclusion, beyond obtaining material properties from alloy compositions through the CALPHAD approach, artificial intelligence techniques make it possible to accurately inverse predict alloy compositions that yield specified physical properties at a particular temperature.

Keywords: CALPHAD methodology, Explainable artificial intelligence, Artificial neural networks, Alloy design, Superalloy.

1   INTRODUCTION

The design and development of high-performance alloys, particularly superalloys, require precise control of their physical and mechanical properties at elevated temperatures. Traditional alloy design relies heavily on the CALPHAD (Calculation of Phase Diagrams) methodology, which utilizes phase equilibrium calculations and thermodynamic databases to model material properties based on specific alloy compositions [1]. By inputting alloy composition parameters, researchers can obtain extensive property data across temperature ranges, offering invaluable insights into alloy behavior under various conditions [2]. However, identifying compositions that achieve the target properties often necessitates labor-intensive adjustments and trial-and-error iterations, particularly for superalloys with complex requirements [3].

Artificial intelligence (AI) holds promise in material design because it can make rapid predictions from large datasets and perform inverse predictions of targeted properties [4] [5]. For instance, recent studies have demonstrated that Explainable Artificial Intelligence (XAI) and Artificial Neural Networks (ANNs) can effectively predict material properties and composition relationships, enhancing the efficiency of alloy design [6]. Unlike traditional methods, these AI-driven approaches leverage existing data to predict alloy compositions that satisfy specific mechanical and thermophysical requirements, thus reducing the experimental workload [7].

This study aims to address the limitations of the traditional CALPHAD approach by implementing an inverse prediction model. By using JMatPro software to model the physical properties of Ni-Cr-Fe-based superalloys within a targeted temperature range (540–920 °C), this work leverages AI to predict the alloy compositions necessary to achieve the desired properties. Our method expands on previous work by combining CALPHAD with artificial intelligence to improve prediction accuracy and the interpretability of results [8] [9]. This hybrid approach enables high-accuracy prediction of alloy compositions that exhibit specific physical characteristics, achieving a prediction accuracy of 98.03% in our experiments. Thus, our study provides a novel solution for inverse alloy design that complements existing computational tools in materials science [10].

2   MATERIALS AND METHODS

In this study, the JMatPro software, based on the CALPHAD methodology, was utilized to model the physical properties (density, thermal conductivity, linear expansion coefficient, Young's modulus, bulk modulus, shear modulus, and Poisson's ratio) of Ni-Cr-Fe-based superalloys (Inconel, Incoloy). A dataset of 5000 rows was generated from the obtained data, with 80% allocated to training the artificial intelligence (AI) model and 20% reserved for validation and testing. The AI model was developed using Explainable Artificial Intelligence (XAI) and Artificial Neural Networks (ANNs).

The proposed model (Figure 1) operates on a dataset containing 250 different compositions of Ni, Cr, Fe, Co, Mo, Si, Mn, Ti, Al, Nb, and Cu. The physical properties of these compositions (density, linear expansion, thermal conductivity, Young's modulus, bulk modulus, shear modulus, and Poisson's ratio) were calculated using the CALPHAD method. The obtained data were subjected to a normalization process before being used as input to the model. The normalized data were then fed into an artificial neural network (ANN) model, and the model outputs were analyzed using Explainable Artificial Intelligence (XAI) methods. This analysis process evaluated the effects of physical properties and temperature by classifying them into positive and negative impacts. The accuracy of the model results was validated through comparison with JMatPro software. Consequently, in contrast to the conventional approach of the CALPHAD methodology, which models the physical properties of materials based on their composition, this study successfully performed inverse modeling to determine the compositions corresponding to the desired physical properties.
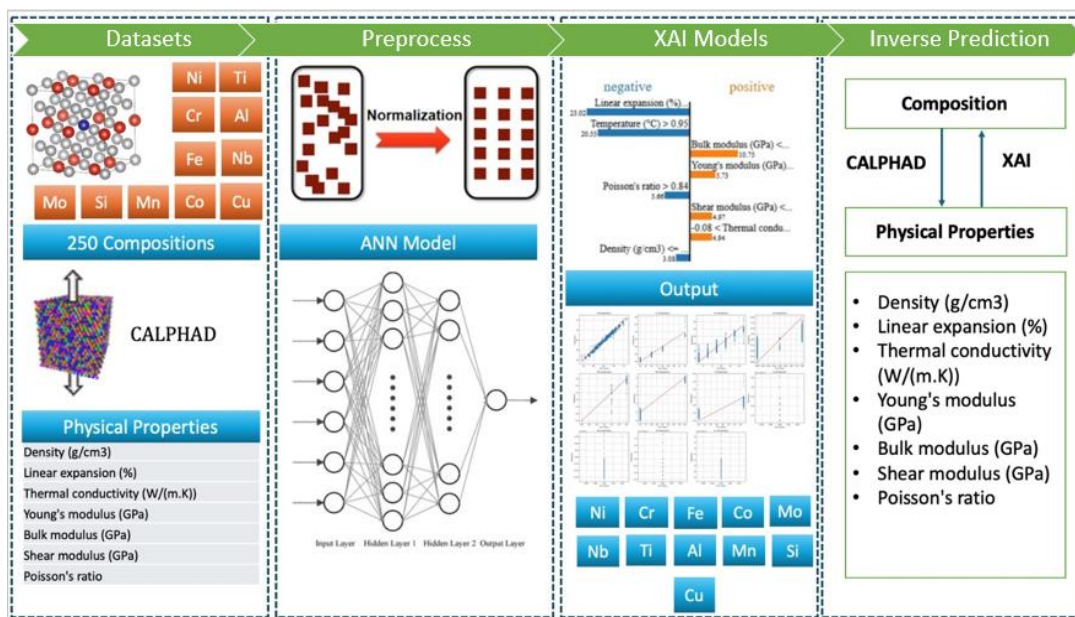
Figure 1. Proposed Model.

2.1 Dataset Generation

This study focuses on Ni-Cr-Fe (Inconel, Incoloy) alloys, which are among the most widely used superalloys in industry due to their high mechanical properties and ability to undergo precipitation hardening through solution treatment and aging. Ni-Cr-Fe (Inconel and Incoloy) alloys can be subjected to heat treatment processes, such as precipitation hardening, which helps stabilize the microstructure and maintain mechanical properties over prolonged periods at elevated temperatures. Precipitation hardening is a critical process that enhances the high-temperature strength of Inconel and Incoloy alloys [11].

The composition of JMatPro is based on the elements Ni, Cr, Fe, Co, and Mo, which constitute Ni-Cr-Fe alloys. Elements such as Nb, Ti, Al, Mn, Si, and Cu [12], which enable precipitation hardening and aging processes, are held constant at specific values across all alloys. This approach aims to discover a composition with superior mechanical properties due to precipitation hardening. The composition includes elements in the following weight percentages: Ni (50-75%), Cr (14-21%), Fe (5-15%), Co (1-2%), and Mo (2-3%), in various combinations. Additionally, the elements Nb (1 and 5%), Ti (1 and 2.5%), Al (0 and 0.5%), Mn (0.5 and 1%), Si (0.5%), and Cu (0.5%) were maintained at fixed values across all combinations. For each generated composition, Phase Fraction Diagrams and TTT diagrams were developed.

Table 1. Elemental Composition Ranges of Alloys in the Dataset (values represent wt.%).

Ni	Cr	Fe	Co	Mo	Nb	Ti	Al	Mn	Si	Cu
50-75	14-21	5-15	0-2	0-3	1, 5	1, 2.5	0, 0.5	0.5, 1	0.5	0.5

In the above table, 250 distinct compositions were generated from various combinations within the specified elemental ranges. For each composition, a total of 20 different temperature points were set in the range of 540–920 °C, with increments of 20 °C. For each temperature point, the density, thermal conductivity, linear expansion percentage, Young's modulus, bulk modulus, shear modulus, and Poisson's ratio were recorded in the dataset under the corresponding temperature entries. Consequently, physical properties corresponding to 20 temperature values were listed for each composition, resulting in a dataset comprising 5000 rows out of 250 compositions.

Table 2. The First Two Compositions (C1, C2) in the Dataset.

Composition	Alloying Elements (wt%)	Temperature (°C)	Density (g/cm3)	Linear expansion (%)	Thermal conductivity (W/(m. K))	Young's modulus (GPa)	Bulk modulus (GPa)	Shear modulus (GPa)	Poisson's ratio
C1	Ni: 67%	920.0	7.78093	1.71729	26.32702	137.58134	144.72433	51.27665	0.34156
	Cr: 22% Fe: 5%	900.0	7.79575	1.65069	25.87496	140.06745	146.50224	52.23848	0.34065
	Co: 0% Mo: 0%	880.0	7.80998	1.58694	25.45285	142.4019	148.15905	53.14259	0.33981
	Nb: 1%	⋮	⋮	⋮	⋮	⋮	⋮	⋮	⋮
	Ti: 2.5% Al: 0.5%	580.0	7.97686	0.8564	20.56181	169.22063	165.62852	63.63024	0.32972
	Mn: 1%	560.0	7.98607	0.81695	20.26687	170.75849	166.52779	64.23843	0.3291
	Si: 0.5% Cu: 0.5%	540.0	7.99514	0.77821	19.97256	172.27884	167.40553	64.84051	0.32848
C2	Ni: 66%	920.0	7.78113	1.71474	26.39128	138.42486	145.55014	51.59361	0.34149
	Cr: 22% Fe: 5%	900.0	7.79587	1.64846	25.94167	140.87727	147.30295	52.54247	0.3406
	Co: 1% Mo: 0%	880.0	7.81003	1.58504	25.52172	143.1844	148.93875	53.43608	0.33977
	Nb: 1%	⋮	⋮	⋮	⋮	⋮	⋮	⋮	⋮
	Ti: 2.5% Al: 0.5%	580.0	7.97642	0.85662	20.6351	169.93475	166.32878	63.8987	0.32972
	Mn: 1%	560.0	7.98564	0.81714	20.33941	171.47479	167.22758	64.50784	0.3291
	Si: 0.5% Cu: 0.5%	540.0	7.99472	0.77837	20.04428	172.99739	168.10489	65.11089	0.32848

As an example, the dataset created for only two alloy compositions is shown in the table above. For each composition, physical property values were recorded at 20 different temperatures ranging from 540 °C to 920 °C. In the second alloy (C2), unlike the first alloy (C1), an additional 1% Co was included. It was observed that the addition of 1% Co led to an increase in density, thermal conductivity, Young's modulus, bulk modulus, and shear modulus, while causing a decrease in linear expansion and Poisson's ratio. As demonstrated by these two examples, the physical property values for 250 different alloy combinations, modified within the ranges specified in Table 1, were added to the dataset under the corresponding temperature rows, resulting in a dataset of 5000 rows, as shown in Table 2.

Completing missing data is crucial to ensuring the integrity of the dataset. In this study, missing values were estimated using multiple linear regression based on the available data. Additionally, since the data obtained from JMatPro software were in different formats, they were converted to international SI units and standardized in terms of density (g/cm³), thermal conductivity (W/(m·K)), and expansion (%). To enable the artificial intelligence model to effectively learn the data, all physical properties were scaled between 0 and 1 using the Min-Max Normalization method and transformed into a tensor structure. Following these processes, data consistency was verified through statistical analyses by comparing with the original JMatPro values, ensuring the dataset's suitability for modeling.

2.2 Software Used for the CALPHAD Methodology

The datasets required to train the AI model were obtained using JMatPro software, which operates based on the CALPHAD methodology. In JMatPro, phase-fraction diagrams and TTT diagrams were generated by adding alloying elements to nickel at specified ratios. The diagrams created for each composition were analyzed to determine the appropriate heat treatment temperature that would yield the desired microstructure through precipitation hardening. The physical property values that the alloy would attain at this specified heat treatment temperature were then organized based on the temperature.

Each composition was simulated with appropriate heat treatment parameters to achieve the formation of the gamma, gamma prime, and gamma" phases. Phases such as delta, eta, laves, MC, M6C, and M3B2 were disregarded because they form only during long precipitation periods. Because the simulations were conducted under equilibrium conditions, the model prevented the formation of unwanted phases. The grain size of the matrix phase (gamma) was set to 100 microns. The grain sizes of the gamma prime and gamma" phases precipitating within the matrix phase were specified as 10 μm and 50 μm, respectively. For each composition, the heat treatment temperature and duration parameters were optimized to complete the precipitation of the gamma prime and gamma" phases within the matrix phase.

The JMatPro software performs Gibbs free-energy calculations, which are fundamental to the CALPHAD methodology. Gibbs free energy (G) provides information on a system's equilibrium state and phase formation.

$$G = H - TS \tag{1}$$

where:

H: Enthalpy (total heat content),

T: Absolute temperature,

S: Entropy (measure of disorder).

Enthalpy calculations are performed using standard formation enthalpies of pure elements and alloys. The enthalpy expression used in the CALPHAD model can be expanded to include the enthalpy changes of a phase as follows:

$$H = Href + \int_{Tref}^{T} Cp \, dT \tag{2}$$

where:

Href: Enthalpy at the reference temperature,

Cp: Heat capacity.

In the CALPHAD methodology, phase equilibria are determined by equalizing the chemical potentials of the components. The chemical potential (μi) for each component is calculated from the derivatives of the Gibbs free energy:

$$\mu i = \frac{\partial G}{\partial ni} \tag{3}$$

where *ni* represents the mole quantity of the component.

To determine phase equilibrium, the chemical potentials of each component must be equalized as follows:

$$\mu_i^{\alpha} = \mu_i^{\beta} \tag{4}$$

where α and β represent two different phases in equilibrium.

The heat capacity (*Cp*), which varies with temperature, is calculated and often expressed in polynomial form:

$$Cp = a + bT + cT^2 + dT^3 + \cdots \tag{5}$$

The coefficients (*a,b,c,d*) in this equation are determined based on experimental data or theoretical models.

JMatPro performs these calculations in the background to process the material data in its database. As a result of these processes, the phase structure of the input composition can be modeled and the thermodynamic, physical, or mechanical properties of this phase structure can be simulated with high accuracy.

In this study, JMatPro software was selected due to its superior features. One of the advantages of JMatPro over software like Thermo-Calc is its ability not only to perform thermodynamic calculations but also to predict mechanical and physical properties. JMatPro has the capacity to calculate properties of metal alloys such as phase transformations, elastic and plastic deformation characteristics, fatigue, and creep. In this regard, it offers a broader scope compared to Thermo-Calc, which mainly focuses on phase diagrams and equilibria [13].

Another significant advantage of JMatPro over Thermo-Calc is its ability to integrate engineering approaches into alloy development processes. This provides researchers with greater flexibility and accuracy in the design and optimization of new materials. Thus, it offers a solution that focuses not only on phase diagrams but also on the detailed prediction of mechanical properties [14].

With these superior features, JMatPro can create a model that approximates the mechanical properties of the generated composition. Consequently, in this project, the mechanical property data required to train artificial intelligence can be modeled in the software without the need for time-consuming experimental studies.

2.3 Development of the Artificial Intelligence Model

The artificial intelligence (AI) model developed in this study combines Explainable Artificial Intelligence (XAI) techniques with Artificial Neural Networks (ANNs) to facilitate the inverse prediction of physical properties in Ni-Cr-Fe-based superalloys. This model aims to overcome the limitations of traditional CALPHAD approaches by predicting alloy compositions with specified mechanical and thermal properties, thus optimizing the design process and reducing the reliance on trial and error.

2.3.1 Data Preparation and Model Architecture

A comprehensive training dataset was created, including data on density, thermal conductivity, linear expansion, Young's modulus, bulk modulus, shear modulus, and Poisson's ratio. The data were divided into training (80%) and validation/testing (20%) sets using a method widely applied to ensure robust model performance.[15].

ANNs were chosen for their capacity to model nonlinear, high-dimensional relationships, which are typical in complex alloy systems. Recent studies have demonstrated that ANNs can handle multivariable datasets and accurately model the dependencies in alloy properties when integrated with domain knowledge from materials science [16]. The model architecture includes several hidden layers optimized for neuron count and activation functions, enabling efficient learning of complex patterns while maintaining computational efficiency [17].

Ensuring the completeness of missing data is crucial for maintaining the integrity of the dataset. In this study, missing values were estimated using multiple linear regression based on

the available data. Additionally, since the data obtained from JMatPro software were provided in various formats, they were converted into international SI units and standardized into metrics such as density (g/cm³), thermal conductivity (W/(m·K)), and expansion (%). To allow the artificial intelligence model to effectively learn the data, all physical properties were scaled between 0 and 1 using the Min-Max Normalization method and then transformed into a tensor structure. Following these processes, data consistency was verified through statistical analyses by comparing the results with the original JMatPro values, ensuring the dataset's readiness for modeling.

2.3.2 Training and Optimization

The model was trained over 500 epochs, utilizing Mean Absolute Error (MAE) as the loss metric to minimize the error between the predicted and actual values. Figure 3(a) shows the rapid decrease in both training and validation losses in the initial epochs, followed by stabilization at epoch 100, indicating the model's learning plateau. This training approach, which is supported by backpropagation and gradient descent, is common in materials informatics applications where data complexity is high [18].

To enhance the model's generalizability and prevent overfitting, regularization techniques, such as dropout layers, were implemented. Studies have shown that such regularization methods are effective for improving the robustness of models in predictive material science, allowing models to generalize beyond the training dataset [19].

2.3.3 Explainable AI for Feature Analysis

To enhance interpretability, SHAP (SHapley Additive exPlanations) values were applied to assess feature importance in the ANN model. The XAI analysis revealed that linear expansion, temperature, and Poisson's ratio were the most influential predictors of alloy properties (Figure 2). The application of XAI techniques is essential in materials science, where understanding the relationship between compositional variables and property outcomes is critical for effective alloy design [20].

2.3.4 Model Performance Evaluation

The ANN model achieved an accuracy rate of 98.03%, closely approximating the JMatPro-generated values for key physical properties (Table 3). The high accuracy of the proposed model aligns with recent advancements in ANN-based alloy prediction models, which

demonstrate that machine learning models can provide reliable predictions that are comparable to traditional simulation methods [21]. This model's successful application validates the potential of integrating CALPHAD and AI approaches, paving the way for future AI-enhanced alloy design frameworks.

This work contributes to a growing body of research that uses machine learning to facilitate alloy design and property prediction, demonstrating the potential of AI to advance materials science beyond traditional methods [22] [23] [24].

3   RESULTS AND DISCUSSION

The artificial intelligence (AI) model developed for predicting the physical properties of Ni-Cr-Fe-based superalloys has demonstrated notable accuracy, achieving an overall prediction accuracy rate of 98.03%. This success is indicative of the model's potential to effectively aid alloy design by accurately predicting compositions that meet the target property requirements. The accuracy analysis shown in Table 3 reveals that the AI model's predictions closely align with the values obtained from JMatPro simulations, with minor deviations observed across different properties. This alignment underscores the reliability of the AI approach as a complementary tool to CALPHAD-based methodologies.

Table 3. Comparison of Desired Physical Properties with Values Obtained by Modeling the AI-Suggested Compositions in JMatPro and Their Accuracy Rates.

Composition Suggested by AI	Physical Properties at 920°C	Suggested Values of Composition to be Offered by AI	Values Obtained by Modeling the Composition Suggested by the AI Model in JMatPro	Accuracy (%)
Ni: 69.23 %	Density (g/cm3)	7.9	7.91415	99.820886
Cr: 15.05 %	Linear expansion (%)	1.59	1.65911	95.653459
Fe: 9.45 %	Thermal conductivity (W/(m. K)	27.7	28.34599	97.667906
Co: 1.33 %				
Mo: 0.54 %	Young's modulus (GPa)	146	142.92744	97.895506
Nb: 0.39 %	Bulk modulus (GPa)	157.5	153.9451	97.742920
Ti: 1.46 %	Shear modulus (GPa)	54.4	53.1225	97.651654
Al: 0.51 %	Poisson's ratio	0.346	0.34526	99.786127
Mn: 1.02 %				
Si: 0.51 %			Overall Accuracy (%):	**98.03**
Cu: 0.51 %				

In Table 3, the comparison between the target values of the suggested composition and the actual values obtained via JMatPro modeling illustrates a high level of congruency across key properties such as density, linear expansion, thermal conductivity, Young's modulus, bulk modulus, shear modulus, and Poisson's ratio. Each of these properties was predicted with an accuracy rate close to or exceeding 97%, with density and Poisson's ratio achieving exceptionally high accuracy rates of 99.82% and 99.79%, respectively. This high accuracy rate reflects the AI model's proficiency in capturing the intricate relationships between elemental composition and physical properties at elevated temperatures, specifically at 920 °C.

To gain a deeper understanding of how different input features influence AI model predictions, we employed Explainable Artificial Intelligence (XAI) techniques. The XAI analysis, as illustrated in the feature importance graph, indicates that linear expansion, temperature, and Poisson's ratio are among the most influential factors affecting the AI model's predictions. The SHAP (SHapley Additive exPlanations) values highlight that a higher linear expansion and temperature exert a positive impact on the prediction output, whereas parameters like density, bulk modulus, Young's modulus, and shear modulus have a more negative influence.
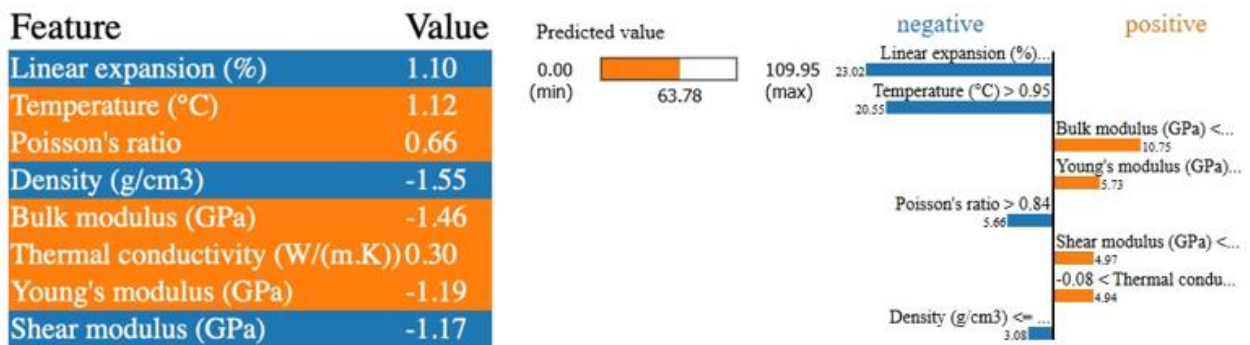
Figure 2. Effect of Physical Properties on Prediction.

Figure 2 presents the feature importance and impact analysis performed using SHAP (SHapley Additive exPlanations) values with Explainable Artificial Intelligence (XAI) techniques. Each feature's contribution to the model's prediction is shown on a scale ranging from negative to positive impact, with orange bars representing positive contributions and blue bars indicating negative contributions. The model's predicted value (63.78) falls within the possible range of 0–109.95.

Features such as linear expansion (%) and temperature (°C) exhibited positive impacts on the prediction outcome, with linear expansion contributing the highest positive value (23.20)

and temperature following closely (20.55). This suggests that an increase in these parameters tends to raise the predicted value, likely due to their direct relationship with the thermal behavior of alloys.

In contrast, features such as density (g/cm³), bulk modulus (GPa), shear modulus (GPa), Young's modulus (GPa), and thermal conductivity (W/(m. K)) exert negative influences. Among these, the bulk modulus has the most substantial negative effect (-10.75), followed by Young's modulus (-5.73). This negative impact indicates that higher values for these properties might correlate with a reduction in the model's target prediction, likely reflecting the mechanical rigidity of the alloy.

Poisson's ratio, while having a minor impact compared to the other features, shows a slightly negative influence, which is consistent with the mechanical and deformation behavior characteristics at various temperatures.

This insight into feature importance aligns with the underlying physics of Ni-Cr-Fe superalloys, where thermal expansion and mechanical stability at high temperatures are crucial factors in determining material performance. The model's ability to prioritize features that are inherently critical to alloy behavior demonstrates the model's interpretability and the potential of XAI to enhance trust in AI-driven alloy design.

The model's learning process over 500 epochs is visualized in the training and validation loss graphs, which show a significant decline in both training and validation losses as epochs progress. By the end of training, the losses converged, indicating that the model effectively minimized the errors without overfitting to the training data. Additionally, the Mean Absolute Error (MAE) graph reinforces this finding, as both the training and validation MAE values stabilize around low values, confirming the model's generalizability.
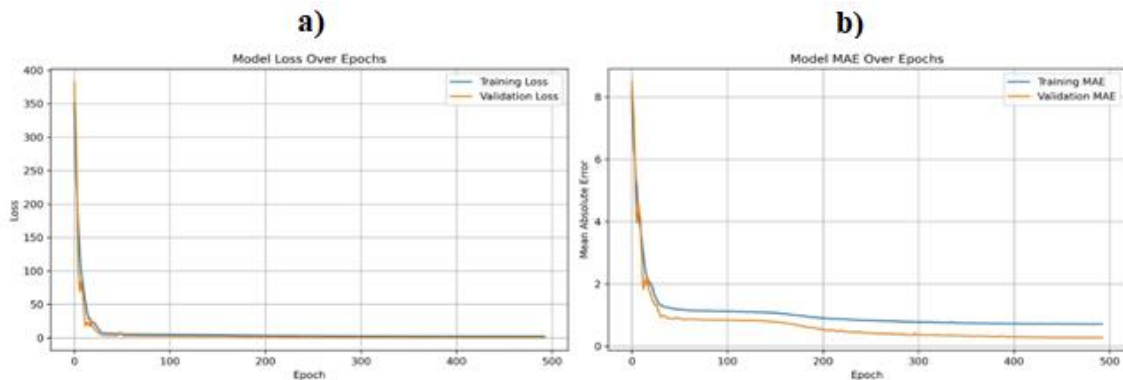
Figure 3. Model Loss and Mean Error Graphs Over Epochs: (a) Model Loss Graph, (b) Model Mean Absolute Error (MAE) Graph.

Figure 3(a) shows the loss of the machine learning model over 500 training epochs. The loss values for both the training and validation data decreased rapidly in the initial epochs and stabilized around epoch 100. This indicates that model performance has reached a plateau. Figure 3(b) shows the Mean Absolute Error (MAE) of the model for training and validation data over 500 epochs. The MAE values initially decreased rapidly and then stabilized, similar to the loss curve. The consistency between the training and validation MAEs indicates that the model achieves good generalizability without overfitting.
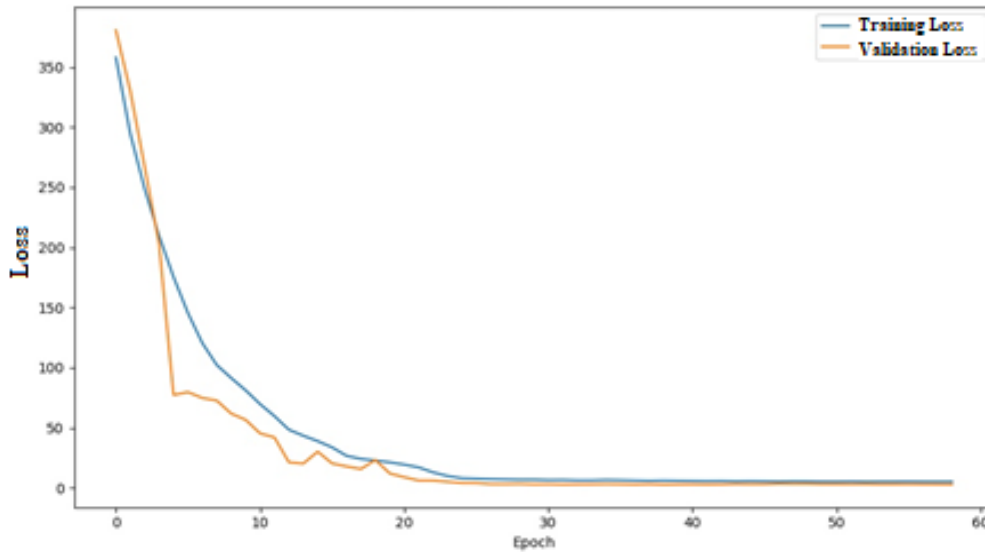
Figure 4. Training and Validation Loss Graph.

The rapid decrease in training and validation losses in early epochs (Figure 4) demonstrates the model's ability to quickly learn the relationships within the dataset. As training continued, the loss reduction became more gradual, suggesting that the model was fine-tuning its predictions. The convergence of training and validation losses at lower error rates reflects a balanced model that can maintain accuracy across unseen data.

Table 4 summarizes the error metrics used to evaluate the performance of the artificial neural network model. MSE (0.2245) and MAE (0.2742) numerically demonstrate the proximity of the model's predicted physical properties to the actual values. MSE is particularly important for understanding the magnitude of prediction errors, as it penalizes larger errors more heavily. The R^2 score (0.5504) indicates that the model can explain approximately 55% of the total variance. These results suggest that the model demonstrates reasonable performance but requires additional optimizations for improved outcomes.

Table 4. Evaluation of Model Performance Based on Error Metrics.

Error Metrics	Value	Description
Mean Squared Error (MSE)	0.2245	The mean of the squared differences between predicted and actual values. Larger errors are penalized more heavily.
Mean Absolute Error (MAE)	0.2742	The average of the absolute differences between predicted and actual values.
Coefficient of Determination (R²)	0.5504	A measure that indicates the proportion of the variance in the dependent variable explained by the model (%55 in this case).

The AI model's predictions were validated against the JMatPro outputs, which follow the CALPHAD methodology. As shown in the graphical and tabular data, the AI model consistently approximated JMatPro's physical property values with high accuracy. This demonstrates the potential of AI for efficient and reliable inverse alloy design. Unlike CALPHAD, which requires intensive calculations and adjustments, the AI model rapidly processes large datasets to deliver accurate predictions, offering a significant time-saving advantage.

Moreover, the use of Explainable AI provides a transparent view into the AI model's decision-making process, which is traditionally seen as a "black box" in neural network-based models. This transparency adds value by allowing researchers to understand the weight and impact of each feature, thus enhancing the model's applicability in real-world alloy design.

The results obtained from this study reveal that integrating CALPHAD-generated data with artificial intelligence, specifically with the support of XAI, offers a transformative approach to alloy design. This AI-driven framework not only enhances prediction accuracy and provides insights into the compositional dependencies of physical properties at high temperatures. This capability is especially valuable in designing high-performance superalloys for demanding applications such as aerospace and power generation, where precise control over properties like thermal conductivity, modulus, and expansion is crucial.

In conclusion, the AI model, validated using CALPHAD data, was found to be effective in predicting the physical properties of Ni-Cr-Fe-based superalloys with high accuracy. The use of XAI further strengthens the model's reliability and interpretability, making it a valuable tool for future alloy development. This study demonstrates a significant advancement in materials science, paving the way for more efficient and accurate alloy design processes driven by AI, which can be extended to other alloy systems in future research.

4   CONCLUSION AND SUGGESTIONS

In this study, a novel approach integrating the CALPHAD methodology with artificial intelligence, specifically Explainable Artificial Intelligence (XAI) and Artificial Neural Networks (ANN), was demonstrated to predict alloy compositions with desired physical properties for Ni-Cr-Fe-based superalloys. The AI model achieved a high prediction accuracy of 98.03%, thereby validating the efficacy of this inverse prediction approach in alloy design. By using JMatPro software to generate comprehensive datasets and applying XAI to interpret model outputs, this study provides a reliable and transparent method for optimizing superalloy compositions.

The results indicate that this AI-driven framework can significantly reduce the trial-and-error processes traditionally required for alloy design, thus saving time and resources. The integration of XAI also enhances the model's interpretability, allowing researchers to understand the influence of individual elements on alloy properties. This interpretability is crucial for practical applications because it helps identify optimal compositional ranges that meet specific mechanical and thermal requirements.

Suggestions for Future Work:

Expansion to Other Alloy Systems: Future research could extend this methodology to other alloy systems, such as Ti-based or Al-based alloys, to explore its generalizability and applicability across diverse materials.

Incorporation of Additional Properties: Including additional properties, such as creep resistance, fatigue strength, and corrosion resistance, could improve the model's relevance for specific industrial applications, particularly in aerospace and energy sectors where such properties are critical.

Real-World Validation: The experimental validation of AI-predicted compositions in real-world manufacturing and testing environments will provide further insights into the model's accuracy and practical feasibility.

Optimization of Model Architecture: Exploring different neural network architectures or hybrid machine learning models, such as ensemble learning techniques, may yield further improvements in prediction accuracy and computational efficiency.

Development of an Automated Alloy Design Platform: Combining CALPHAD and AI methods into an automated platform for alloy design could streamline the process for materials scientists, enabling rapid prototyping of alloys tailored to meet specific engineering requirements.

In conclusion, the integration of CALPHAD-generated data with advanced AI techniques represents a transformative approach to alloy design. This study demonstrates the potential of AI to complement traditional materials science methods, paving the way for efficient, data-driven alloy development. Future advancements in this field are expected to enhance the capabilities of AI in alloy design, enabling more sophisticated and customizable solutions in materials engineering.

Conflict of Interest Statement

There is no conflict of interest between the authors.

Statement of Research and Publication Ethics

The study is complied with research and publication ethics.

Artificial Intelligence (AI) Contribution Statement

This manuscript was entirely written, edited, analyzed, and prepared without the assistance of any artificial intelligence (AI) tools. All content, including text, data analysis, and figures, was solely generated by the authors.

Contributions of the Authors

Yusuf Uzunoğlu: Conceptualization, methodology, data curation, resources, and writing-original draft. Yusuf Alaca: Supervision, validation, visualization, formal analysis and writing-review & editing.

REFERENCES

[1] N. Saunders and A. P. Miodownik, *CALPHAD (Calculation of Phase Diagrams): A Comprehensive Guide*. Pergamon Press, 1998.

[2] H. L. Lukas, S. G. Fries, and B. Sundman, *Computational Thermodynamics: The Calphad Method*. Cambridge University Press, 2007.

[3] Y. Du, S. L. Chen, and B. Huang, "An Overview of CALPHAD Applications in Superalloy Design," *J. Alloys Compd.*, vol. 456, no. 1–2, pp. 18–29, 2008.

[4]   P. Raccuglia and others, "Machine-learning-assisted materials discovery using failed experiments," *Nature*, vol. 533, no. 7601, pp. 73–77, 2016.

[5]   T. Xie and J. C. Grossman, "Crystal Graph Convolutional Neural Networks for an Accurate and Interpretable Prediction of Material Properties," *Phys. Rev. Lett.*, vol. 120, no. 14, p. 145301, 2018.

[6]   K. T. Butler and others, "Machine learning for molecular and materials science," *Nature*, vol. 559, no. 7715, pp. 547–555, 2018.

[7]   L. Ward et al., "A general-purpose machine learning framework for predicting properties of inorganic materials," *npj Comput. Mater.*, vol. 2, no. 1, pp. 1–7, 2016.

[8]   D. Jha and others, "ElemNet: Deep Learning the Chemistry of Materials from Only Elemental Composition," *Sci. Rep.*, vol. 8, no. 1, pp. 1–13, 2018.

[9]   Y. Zhang and others, "Deep learning-based discovery of rare materials," *Nature*, vol. 569, no. 7754, pp. 368–373, 2019.

[10]   B. L. DeCost and others, "Scientific AI in materials science: A Pathway to Discovery and Insight," *MRS Bull.*, vol. 45, no. 8, pp. 614–623, 2020.

[11]   X. Zhang, "Heat treatment effects on Inconel alloys.," *J. Mater. Eng.*, 2019.

[12]   A. S. M. I. H. Committee and A. S. for M. H. T. Division, *Heat treating*, vol. 4. ASM international, 1991.

[13]   P. Palumbo, G., & Ferro, "Comparison of CALPHAD-based tools for materials science applications.," *J. Phase Equilibria Diffus.*, no. 34(5), pp. 398–405, 2013.

[14]   A. P. Zhao, J. C., Miodownik, "CALPHAD and its applications to materials science," *Prog. Mater. Sci.*, no. 51(3), pp. 241–312, 2006.

[15]   C. Chen, J. Zhao, and L. Li, "Machine Learning for Alloy Design: An Overview of Recent Advances," *Mater. Today*, vol. 48, pp. 15–27, 2021.

[16]   K. Tran et al., "Active Learning Across Intermetallics to Guide Alloy Design," *Nat. Commun.*, vol. 9, p. 4074, 2018.

[17]   A. Agrawal and A. Choudhary, "Deep Learning Applications and Challenges in Big Data Analytics for Manufacturing," *Manuf. Lett.*, vol. 15, pp. 12–19, 2019.

[18]   L. Ward and C. Wolverton, "A Machine Learning Approach for Predicting and Understanding the Properties of Multiprincipal Element Alloys," *npj Comput. Mater.*, vol. 4, p. 36, 2018.

[19]   J. Schmidt and others, "Recent Advances and Applications of Machine Learning in Solid-State Materials Science," *npj Comput. Mater.*, vol. 5, p. 83, 2019.

[20]   A. Karpatne and others, "Regularization Techniques for Neural Networks: An Overview and Applicability in Materials Science," *J. Appl. Phys.*, vol. 128, no. 14, p. 141501, 2020.

[21]   J. Ling, M. Hutchinson, and C. Wolverton, "Machine Learning for Multi-Property Predictions in Computational Materials," *Comput. Mater. Sci.*, vol. 138, pp. 140–152, 2017.

[22]   Y. Zuo and others, "Accelerated Discovery of Metallic Glasses Using Machine Learning," *Mater. Horizons*, vol. 6, no. 2, pp. 252–261, 2019.

[23]   Y. Xu, J. Luo, and W. Chen, "Artificial Neural Networks in Alloy Design: Development and Challenges," *Adv. Eng. Mater.*, vol. 22, no. 4, p. 1901206, 2020.

[24]   K. Kaufmann and K. S. Vecchio, "Artificial Intelligence in Materials Science: A New Frontier," *Mater. Sci. Eng. R Reports*, vol. 144, p. 100595, 2020.

ENHANCED EMOTION RECOGNITION THROUGH HYBRID DEEP LEARNING AND SVM INTEGRATION

Muhammed Kerem TÜRKEŞ [1] (iD), **Yıldız AYDIN** [1] * (iD)

[1] *Erzincan Binali Yıldırım University, Computer Engineering Department, Erzincan, Türkiye*

* Corresponding Author: yciltas@erzincan.edu.tr

ABSTRACT

The facial expression recognition system, which contributes to the processes to be more effective and faster in many fields such as medicine, education and security, plays an important role in various applications. For example, while emotional and psychological states can be monitored thanks to facial expression recognition in the health field, it can be used in critical applications such as lie detection in the security sector. In education, students' instant facial expressions are analyzed to contribute to the learning processes. The problem of emotion recognition from facial expressions, which is related to many fields, is of great importance in obtaining accurate and reliable results. Therefore, in order to increase the performance of emotion recognition from facial expressions, a hybrid approach combining deep learning and classical machine learning methods is considered in this study. In the proposed method, the ResNet50 model is used as a feature and Support Vector Machines (SVM) is used as a classifier. In this study, a hybrid approach consisting of the combination of ResNet50 and SVM methods is proposed-to increase the performance of emotion recognition from facial expressions. In order to analyze facial expressions, six basic emotions are classified as happiness, sadness, anger, fear, surprise and disgust using the CK+48 dataset. Experimental results show that the proposed hybrid approach has high accuracy in emotion recognition and outperforms traditional machine-learning algorithms.

Keywords: Hybrid model, ResNet50, Support vector machines (SVM), Deep learning.

1   INTRODUCTION

Facial identification is a well-established area in computer vision and artificial intelligence, which is widely applied to protection, user authentication and monitoring systems.

However, beyond identifying the identity, the analysis of facial expressions plays an important role in understanding emotions, psychological states and mutual communication. While traditional facial recognition is aimed at identifying individuals, facial expression recognition (FER) focuses on interpreting emotions based on subtle facial muscle movements.

Words, tone of voice and facial expressions are very important in face-to-face communication between people. It is observed that gestures and facial expressions have a significant impact on interpersonal relationships [1]. These facial expressions carry information about their emotional and psychological states as well as personality reflections [2]. The behaviors of people throughout their lives, a wide range of behavioral patterns from a simple issue to a difficult decision they take are generally referred to as emotional states [3], [4]. It is seen that 6 emotions (happiness, sadness, anger, fear, surprise, disgust), which are considered as basic emotions, are generally accepted and mutually used in every environment related to life and by people in these environments [5].

Emotion recognition from facial expressions facilitates various processes in many fields, especially in medicine, education and security [6]. It is seen that it will be used in platforms where various physical and mental diseases are detected in the field of health and direct or alternative suggestions are given for healthy life, in achieving success with the instant facial expressions and reactions of students in the field of education, in the field of security, in cases such as lie detection in investigations, etc. It is seen that it will contribute to increasing the success percentages in many sectors with these examples. [7], [8]. Therefore, within the scope of this study, a face recognition system with artificial intelligence, which is useful in many fields, has been studied.

Additionally, comprehensive experiments have been conducted to thoroughly evaluate the performance achieved by utilizing different features with various classifiers in the facial expression recognition problem. These experiments have been systematically categorized into three main groups: classical machine learning classifiers, which rely on handcrafted features, hybrid approaches that combine deep and traditional feature extraction techniques, and deep learning methods, which automatically learn hierarchical representations from data. This categorization allows for a detailed comparative analysis, highlighting the strengths and limitations of each approach in enhancing facial expression recognition accuracy. The general structure of the study is explained in the section Materials and Methods, where information about the features and classification methods is given. In Results and Discussion section,

information about the experimental results obtained within the scope of the study is given and in the last section, the study is concluded.

2   RELATED WORKS

Facial expression recognition applications consist of two basic steps: feature extraction and classification [9]. In many areas, high-performance values have been achieved by obtaining much stronger features by using hybrid features. There is a significant increase in classifier performance with the acquisition of strong features [10]. These studies are generally used in combination with feature extraction and classical machine learning methods or deep learning methods. In the study conducted by Li and Lima [11], to overcome the limitations such as the low generalization ability of network models and weak robustness of recognition systems, the features obtained using deep residual network ResNet-50 were combined with Convolutional Neural Networks (CNN). Experimental results show that the proposed method increases the success rates. In the study conducted by Bayrakdar et al. [12], The authors analyzed 4 different emotions (sadness, happiness, surprise, neutrality) of individuals through pre-created video files and reduced the number of image frames in these video files. They developed an advanced facial expression recognition system for video files thanks to threads in parallel with each other on a computer with high processing power and capacity. In the method proposed by Mukhopadhyay et al. [13], three different textural image features, namely Local Binary Pattern (LBP), Local Ternary Pattern (LTP) and Completed Local Binary Pattern (CLBP), which are sensitive to changes in facial expressions, were used. These features were used with the Convolutional Neural Network (CNN) model and more accurate results were obtained Sadeghi et al. [14] developed a new deep learning model, HistNet, for facial expression recognition. HistNet aims to increase accuracy by using histogram-based feature extraction instead of superficial information in the facial expression recognition task. In the study by Karnati et al. [15], feature extraction modules were applied regionally and structurally to detect distinctive features. Thanks to this method, they obtained a high-performance value for the dataset used. In Haq et al.'s study's study, convolutional neural networks (CNN) were used to analyze the universal emotional states of individuals in real-time [16]. As a result of this study, higher performance was obtained compared to the studies performed in real-time.

In order to contribute to the above-mentioned areas, this study aims to achieve a more successful classification performance by using robust features. To obtain robust features, some experiments were carried out on the dataset and classification was performed using feature

extraction and machine learning methods. In order to measure the performance values of the study, the CK+48 dataset was used as the dataset in this study. In this dataset, there are six class labels: happiness, sadness, anger, fear, surprise and disgust In this study, classical machine classifiers, deep learning methods and hybrid approaches were used. Thanks to the proposed methods, it is seen in line with the data obtained from the experimental results that the classification performance has increased.

3   MATERIALS AND METHODS

In this study, deep learning methods, classical machine classifiers and hybrid approaches are used to identify emotions from facial expressions. The hybrid approaches can be divided into two subcategories. In the first sub-category of hybrid approaches, classical features such as Scale-invariant feature transform (SIFT) and KAZE are used in the feature extraction step and deep learning methods are used in the classification step. In the second subcategory, features obtained from deep learning methods are used as features and classical machine classifiers are used as classifiers. This structure is given in Figure 1.

In the experiments, all machine learning and deep learning methods were used with their default hyperparameter settings as provided by the respective libraries. No manual tuning was performed for hyperparameter optimization. For instance, the Support Vector Machine (SVM) classifier was employed with the default radial basis function (RBF) kernel in the scikit-learn library. Similarly, other classifiers, including XGBoost, Random Forest, and Logistic Regression, were utilized with their standard parameters. Regarding deep learning-based feature extraction, the pre-trained ResNet50 models were applied without modifying their original configurations. This approach ensures that the results reflect the baseline performance of each method without additional optimization.
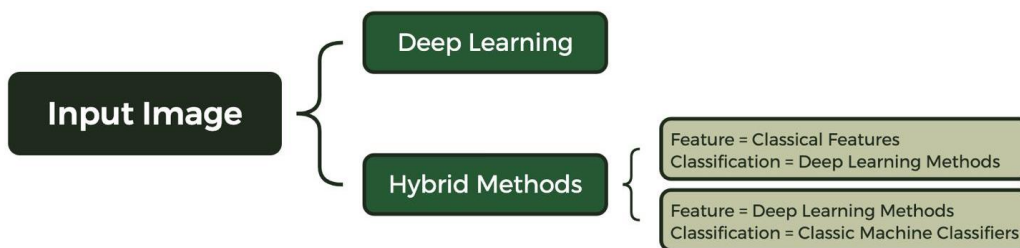
Figure 1. The general structure of the study.

In the designed system, Convolutional Neural Network (CNN), Scale-Invariant Feature Transform (SIFT), Visual Geometry Group 16 (VGG16), Residual Network 50 (ResNet50) and KAZE, methods are used for feature extraction, while Convolutional Neural Network (CNN),

Support Vector Machine (SVM), eXtreme Gradient Boosting (XGBoost), Radial Basis Function (RBF), and Logistic Regression (LR) methods are used in classification stages. With the input of the images in the data set, features are extracted and then the classifier is trained. After this process, the features extracted from the test data are classified with the test data. The methods used in the study are given in Figure 2. As a result of the experiments, the highest performance was obtained from the application in which the feature obtained with the Resnet50 deep learning method was used together with the SVM classifier. Data set, performance metrics, Resnet50 deep learning method and SVM classifier used in the proposed method are given in detail below.
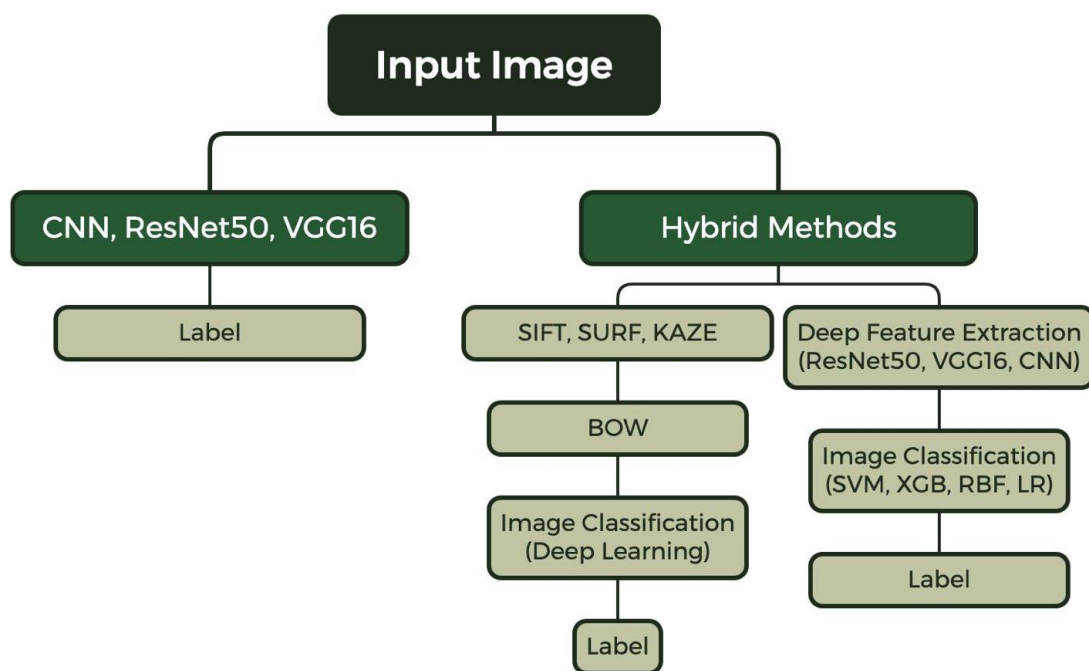
Figure 2. The methods used in the study.

3.1 Data Set

To analyze the emotion from facial expressions, the 'CK+48' dataset [17] was used in this study. This dataset was chosen because it is considered a well-organized and widely used standard in the field of facial expression recognition. Since it contains high-quality and clearly labeled facial expressions collected in a controlled environment, it allows for the accurate evaluation of the proposed method without the uncertainties that may be caused by environmental factors. The primary goal of this study is to evaluate the effectiveness of the proposed combined approach rather than addressing the difficulties related to spontaneous or natural expressions. Therefore, the CK+48 dataset is considered a suitable starting point to measure the basic performance of the method. Larger and more diverse datasets collected in

real-world scenarios, although they contain a wider range of facial expressions, bring with them additional challenges such as high computational costs, obstacles, and variability. Domain adaptation techniques, extensive data augmentation, or transfer learning strategies are usually required to increase generalizability. However, since this study mainly focuses on the development of the method, a widely used reference dataset, CK+48, was preferred for preliminary evaluation. In this dataset, there are images containing six human emotions (happiness, sadness, anger, fear, surprise, disgust). In the 'CK+48' dataset, there are '981' images. These images consist of 48x48 grey images. The images in the dataset are generally obtained from video frames and have not undergone much change [18]. Figure 4 shows sample images of the dataset.

Figure 3. Sample images of the CK+48 dataset.

3.2 Performance Metrics

In order to evaluate the performance of this study, recall, precision, and F1 scores were used. These metrics are determined according to the total number of true positives (TP), false positives (FP), false negatives (FN) and true negatives (TN). The equations of Accuracy, Recall (R), precision (P) and F1 score metrics are given in Equation 1-4.

$$Accuracy = \frac{TP + TN}{TP + TN + FP + FN} \tag{1}$$

$$Recall \ (rc) = \frac{TP}{TP + FN} \tag{2}$$

$$Precision\ (pr\ ) = \frac{TP}{TP + FP} \tag{3}$$

$$F1\ Score\ =\ 2 * \frac{Recall * Precision}{Recall + Precision} \tag{4}$$

3.3   Resnet50

When the layers of CNN architectures developed in the past are modified, the problem of gradient disappearance arises and the layers become non-scalable. As a result of this problem, the non-scalable layers will reach saturation with each layer added as a result of repeated operations and the performance will deteriorate. To solve this problem, ResNet architecture is built by combining blocks into layers. ResNet prevents the gradient vanishing by increasing the depth values of the network and preserving feature representations. In the ResNet architecture, jumping between connections can be done with a method called jumping or identification of connections. This method adds the input value of the layer behind to the output value of the layer ahead by skipping the other layers in between. With this method, the intermediate corrupted layers and the redundant convolutional layers are connected [19].

ResNet50 is obtained by replacing the 2-layer blocks in the network consisting of 34 layers with a 3-layer bottleneck block. This three-layer structure has dimensions of 1×1, 3×3 and 1×1. Layers with 1×1 dimensions change the values of the dimensions by increasing and decreasing. In the layer with 3×3 dimensions, it creates a small-sized bottleneck for input/output. In this way, the training speed of each layer is much faster.

Deep learning models can have higher generalization capacity when pre-trained on large datasets. However, since the data specific to a particular application is usually limited, the transfer learning method can yield more successful results by re-using a model trained on a large-scale dataset as a feature extractor [20]. In this study, the pre-trained ResNet-50 model is used for feature extraction, and then these features are processed with a traditional machine learning classifier, SVM.

3.4   Support Vector Machines (SVM)

Support vector machines (SVM) is a machine learning technique that is widely used in classification procedures, although it has been used in the literature for regression analysis and classification. This approach is based on a supervised learning model. While executing the algorithm, kernel functions can be used depending on the structure and type of the processed

data [21], [22]. Therefore, linear or non-linear classification processes can be performed by SVM. Support vector machines find the hyperplane that discriminates the data of the training with maximum margin and the samples are classified by means of the learned hyperplane. Structural risk minimization is the basis for the use of hyperplanes with maximum margins [23].

Example of linearly separable training for the primary optimization problem with fixed margins; $S = ((\overrightarrow{Xi}, y_1) \ldots, (.\overrightarrow{Xi}, y_i))$ and hyperplane $(\overrightarrow{W}, b)$, the solution of this problem is solved by the following equation 5. Minimum subtraction

$$y_1 \left[\overrightarrow{W}.\overrightarrow{Xi} + b \right] \geq 1, i = 1, \ldots, l \tag{5}$$

The lower plane of the edges is thus maximized.

Due to the primary optimization problem given above, the use of kernels becomes necessary and a high-dimensional feature space is used. The training examples are binary only as internal products and therefore do not need to be represented as feature vectors as long as training is in progress, nor do they need to be represented in the testing phase (Deisenroth, Faisal, & Ong, 2020).

Example of linearly separable training for the secondary optimization problem with fixed margins; $S = ((\overrightarrow{Xi}, y_1) \ldots, (.\overrightarrow{Xi}, y_i))$ and $\overrightarrow{a^*}$ If it is assumed to be, the solution of this specified problem is solved using the following equation 6. Maximum subtraction

$$W\left(\overrightarrow{a^*}\right) = \sum_{i=1}^{l} a_i - \frac{1}{2} \sum_{i,j=1}^{l} y_i, y_j, a_i, a_j, \overrightarrow{x_i}, \overrightarrow{x_j} \tag{6}$$

Then the weight vector $\overrightarrow{a^*} = \sum_{i=1}^{l}, y_i \, a_i * \overrightarrow{x_i}$ hyperplane with maximum margins is obtained.

4   RESULTS AND DISCUSSION

When the experimental results of the method proposed in this study are categorized, two main categories are formed. If these two categories are explained, the first category includes the experiments performed with deep learning methods, and the second category includes the experiments performed by combining deep learning methods and the methods used in classical machine classifiers.

CNN, VGG16 and ResNet50 methods, which are frequently used in the literature, are also used in this study to obtain performance data. Finally, inspired by the studies indicating that more successful results are obtained with the use of hybrid approaches in various fields [25], applications have been developed by using the methods in deep learning and classical machine classifiers as a hybrid. For this purpose, features were extracted using ResNet50, VGG16 and CNN deep learning methods. The obtained features were classified with SVM, XGB, LR and RF classifiers. In addition to these, the experimental results using SIFT, SURF and KAZE features in the feature extraction step and CNN deep learning method as the classification method are given in Table 1 and Figure 5.

Table 1. Performance results of the experiments performed on the CK+48 dataset.

Features	Classifier	Precision (%)	Recall (%)	F1 (%)	Accuracy (%)
CNN	SVM	3.63	14.29	5.78	25.38
	XGB	59.37	55.50	56.92	59.94
	RF	45.55	33.91	35.96	38.74
	LR	3.63	14.29	5.78	25.38
Resnet50	SVM	100.00	100.00	100.00	100.00
	XGB	95.66	93.76	94.62	95.62
	RF	96.44	94.19	95.16	95.51
	LR	97.57	97.95	97.74	98.17
VGG16	SVM	99.08	98.46	98.75	99.08
	XGB	98.48	97.94	98.17	98.47
	RF	98.72	97.14	97.87	98.37
	LR	99.43	99.03	99.22	99.49
CNN	CNN	91.91	93.92	92.81	94.58
ResNet50	ResNet50	64.35	62.40	62.32	71.86
VGG16	VGG16	94.32	95.70	94.80	95.25
SIFT	CNN	89.87	83.85	85.99	89.15
SURF	CNN	72.41	69.65	69.94	76.27
KAZE	CNN	87.54	78.60	80.86	86.78
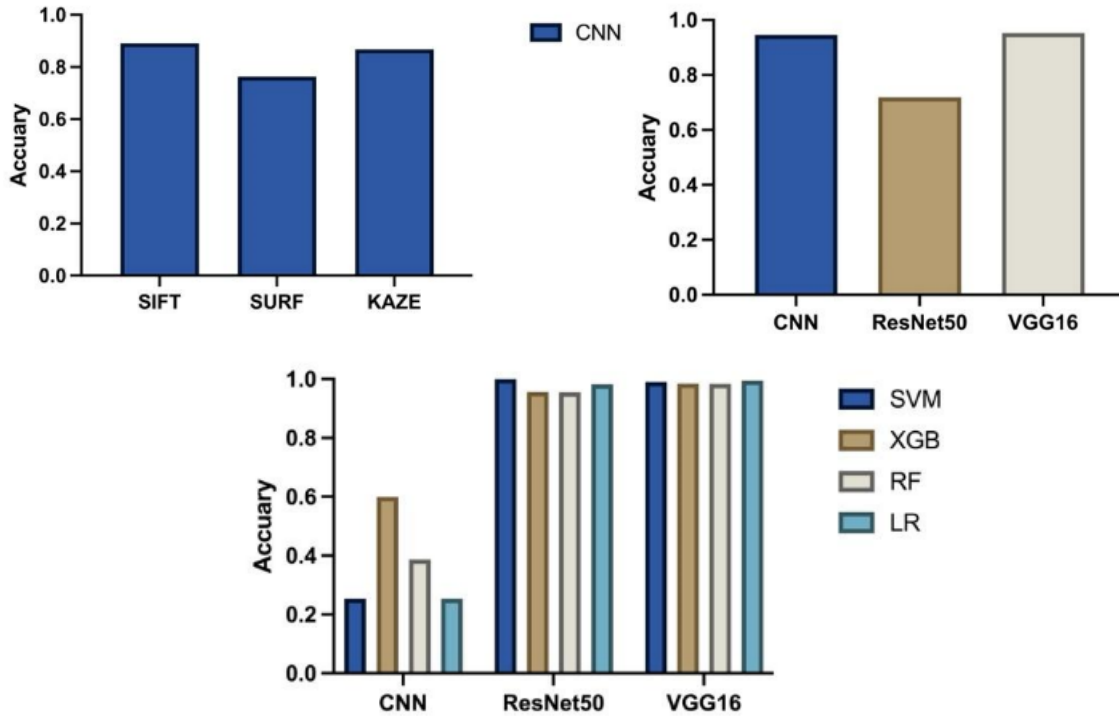
Figure 4. Graphs of experimental results.

As seen in Table 1 and Figure 5, the most successful method is the hybrid approach, which combines ResNet50 and SVM methods. Table 2 compares the proposed method's performance with studies developed using the CK+48 dataset in recent years.

Table 2. Performance results of the experiments performed on the CK+48 dataset.

Research	Methods	Accuracy (%)
Liu and Yue [26]	CNN-LSTM	84
Owusu and Wiafe [27]	Ada-AdaSVM	91.28
Syalomta et al. [28]	NNN-Net	98.63
Deepan et al. [29]	Gabor + CNN	99.43

As seen in Table 2, the proposed hybrid approach, which combines ResNet50 for feature extraction and SVM for classification, outperforms previously developed methods. While Deepan et al. [28] achieved an accuracy of 99.43% using a Gabor filter and CNN combination, our proposed method reached a perfect accuracy of 100%. This improvement can be attributed to the use of robust deep features extracted by ResNet50 and the high generalization capability of SVM. Unlike traditional CNN-based methods, our approach benefits from a more effective feature representation.

Although the proposed hybrid approach combining ResNet50 and SVM achieves high accuracy in emotion recognition, certain limitations are observed. One notable limitation is the use of the CK+48 dataset, which consists of well-posed and controlled facial expressions. This may lead to difficulties in generalizing the model to real-world scenarios where changes in lighting, occlusions, and spontaneous expressions are present. Additionally, the model may perform poorly in cases where facial expressions are ambiguous, which may lead to potential misclassifications. To partially address this limitation, the method was also evaluated on the JAFFE dataset, which includes more varied lighting conditions and facial expressions. The results obtained from the JAFFE dataset demonstrated an accuracy of 100%, indicating that the proposed approach maintains a reasonable level of performance even under less controlled conditions. Future work could focus on including more diverse datasets and integrating advanced augmentation techniques to improve robustness.

5   CONCLUSION

In this study, a new hybrid approach is used to analyze emotion from human facial expressions. While performing emotion detection from facial expressions, hybrid methods obtained by combining these two methods are used in order to obtain higher performance results compared to classical machine classifiers and deep learning methods. The CK+48 dataset and 981 images were used to test the application performed within the scope of the study. According to the results of the experiment, the recognition success of emotions was determined as 100% thanks to the method obtained by combining ResNet50 and SVM methods. Compared to existing methods (as shown in Table 2), our proposed hybrid approach achieves state-of-the-art performance, demonstrating the effectiveness of combining deep feature extraction with classical machine learning classifiers. In future studies, we aim to achieve higher performance with new methods developed on datasets containing different images and classes.

Acknowledgements

Conflict of Interest Statement

There is no conflict of interest between the authors.

Statement of Research and Publication Ethics

The study is complied with research and publication ethics.

Artificial Intelligence (AI) Contribution Statement

This manuscript was entirely written, edited, analyzed, and prepared without the assistance of any artificial intelligence (AI) tools. All content, including text, data analysis, and figures, was solely generated by the authors.

Contributions of the Authors

Muhammed Kerem Türkeş contributed to the experimental studies and preparation of the article.

Yıldız Aydın contributed to the experimental studies, interpretation of the data and management of the study.

REFERENCES

[1]   R. E. Riggio and J. Lee, "Emotional and interpersonal competencies and leader development," *Hum. Resour. Manag. Rev.*, vol. 17, no. 4, pp. 418–426, 2007, doi: 10.1016/j.hrmr.2007.08.008.

[2]   A. Petrovici and T. Dobrescu, "The Role of Emotional Intelligence in Building Interpersonal Communication Skills," *Procedia - Soc. Behav. Sci.*, vol. 116, pp. 1405–1410, 2014, doi: 10.1016/j.sbspro.2014.01.406.

[3]   A. G. Sanfey *et al.*, "The Neural Basis of Economic Decision-Making in the Ultimatum Game Published by: American Association for the Advancement of Science Stable URL: http://www.jstor.org/stable/3834595 The Neural Basis of Economic Decision-Making in the Ultimatum Game," *Science (80-.).*, vol. 300, no. 5626, pp. 1755–1758, 2003.

[4]   A. D. Angie, S. Connelly, E. P. Waples, and V. Kligyte, "The influence of discrete emotions on judgement and decision-making: A meta-analytic review," *Cogn. Emot.*, vol. 25, no. 8, pp. 1393–1422, 2011, doi: 10.1080/02699931.2010.550751.

[5]   A. Ortony, "Are All 'Basic Emotions' Emotions? A Problem for the (Basic) Emotions Construct," *Perspect. Psychol. Sci.*, vol. 17, no. 1, pp. 41–61, 2022, doi: 10.1177/1745691620985415.

[6]   F. Akar and İ. Akgül, "Derin Öğrenme Modeli ile Yüz İfadelerinden Duygu Tanıma," *Iğdır Üniversitesi Fen Bilim. Enstitüsü Derg.*, vol. 12, no. 1, pp. 69–79, 2022, doi: 10.21597/jist.976577.

[7]   D. Özdemir and S. Karaman, "Investigating interactions between students with mild mental retardation and humanoid robot in terms of feedback types," *Egit. ve Bilim*, vol. 42, no. 191, pp. 109–138, 2017, doi: 10.15390/EB.2017.6948.

[8]   D. Mehta, M. F. H. Siddiqui, and A. Y. Javaid, "Recognition of emotion intensities using machine learning algorithms: A comparative study," *Sensors (Switzerland)*, vol. 19, no. 8, pp. 1–24, 2019, doi: 10.3390/s19081897.

[9]   C. Turan and K. M. Lam, "Histogram-based local descriptors for facial expression recognition (FER): A comprehensive study," *J. Vis. Commun. Image Represent.*, vol. 55, no. January, pp. 331–341, 2018, doi: 10.1016/j.jvcir.2018.05.024.

[10]   Y. Aydin, "A Comparative Analysis of Skin Cancer Detection Applications Using Histogram-Based Local Descriptors," *Diagnostics*, vol. 13, no. 19, 2023, doi: 10.3390/diagnostics13193142.

[11]   B. Li and D. Lima, "Facial expression recognition via ResNet-50," *Int. J. Cogn. Comput. Eng.*, vol. 2, no. February, pp. 57–64, 2021, doi: 10.1016/j.ijcce.2021.02.002.

[12]   S. Bayrakdar, D. Akgün, and İ. Yücedağ, "An accelerated approach for facial expression analysis on video files," *Pamukkale Univ. J. Eng. Sci.*, vol. 23, no. 5, pp. 602–613, 2017, doi: 10.5505/pajes.2016.00908.

[13]   M. Mukhopadhyay, A. Dey, and S. Kahali, "A deep-learning-based facial expression recognition method using textural features," *Neural Comput. Appl.*, vol. 35, no. 9, pp. 6499–6514, 2023, doi: 10.1007/s00521-022-08005-7.

[14]   H. Sadeghi and A. A. Raie, "HistNet: Histogram-based convolutional neural network with Chi-squared deep metric learning for facial expression recognition," *Inf. Sci. (Ny).*, vol. 608, pp. 472–488, 2022, doi: 10.1016/j.ins.2022.06.092.

[15]   M. Karnati, A. Seal, S. Member, J. Jaworek-korjakowska, and O. Krejcar, "Facial Expression Recognition In-the-Wild Using," vol. 72, 2023.

[16]   H. B. U. Haq, W. Akram, M. N. Irshad, A. Kosar, and M. Abid, "Enhanced Real-Time Facial Expression Recognition Using Deep Learning," *Acadlore Trans. AI Mach. Learn.*, vol. 3, no. 1, pp. 24–35, 2024, doi: 10.56578/ataiml030103.

[17]   P. Lucey, J. F. Cohn, T. Kanade, J. Saragih, Z. Ambadar, and I. Matthews, "The extended Cohn-Kanade dataset (CK+): A complete dataset for action unit and emotion-specified expression," *2010 IEEE Comput. Soc. Conf. Comput. Vis. Pattern Recognit. - Work. CVPRW 2010*, no. July, pp. 94–101, 2010, doi: 10.1109/CVPRW.2010.5543262.

[18]   S. Li and W. Deng, "A Deeper Look at Facial Expression Dataset Bias," *IEEE Trans. Affect. Comput.*, vol. 13, no. 2, pp. 881–893, 2020, doi: 10.1109/TAFFC.2020.2973158.

[19]   K. He, X. Zhang, S. Ren, and J. Sun, "Deep residual learning for image recognition," *Proc. IEEE Comput. Soc. Conf. Comput. Vis. Pattern Recognit.*, vol. 2016-Decem, pp. 770–778, 2016, doi: 10.1109/CVPR.2016.90.

[20]   M. Hussain, J. J. Bird, and D. R. Faria, "A Study on CNN Transfer Learning for Image Classification," in *Advances in Computational Intelligence Systems*, 2019, pp. 191–202.

[21]   R. Gandhi, "Support Vector Machine Introduction to Machine Learning Algorithms," *Towar. Data Sci.*, vol. 7, no. 06, 2018, [Online]. Available: https://towardsdatascience.com/support-vector-machine-introduction-to-machine-learning-algorithms-934a444fca47.

[22]   S. Suthaharan, "Support Vector Machine," in *Machine Learning Models and Algorithms for Big Data Classification: Thinking with Examples for Effective Learning*, Springer, 2016, pp. 207–235.

[23]   S. Dutta and S. K. Bandyopadhyay, "Early Breast Cancer Prediction using Artificial Intelligence Methods," *J. Eng. Res. Reports*, vol. 13, no. 2, pp. 48–54, 2020, doi: 10.9734/jerr/2020/v13i217105.

[24]   M. P. Deisenroth, A. A. Faisal, and C. S. ONG, *Mathematics for*, no. c. Cambridge University Press., 2020.

[25]   Y. Aydın, "Automated identification of copy-move forgery using Hessian and patch feature," *J. Forensic Sci.*, vol. 69, no. 1, pp. 131–138, 2024.

[26]   A. Liu and H. Yue, "Facial Expression Recognition Based on CNN-LSTM," *Proc. 2023 7th Int. Conf. Electron. Inf. Technol. Comput. Eng.*, 2023, doi: 10.1145/3650400.3650480.

[27]   E. Owusu and I. Wiafe, "An advance ensemble classification for object recognition," *Neural Comput. Appl.*, vol. 33, no. 18, pp. 11661–11672, 2021, doi: 10.1007/s00521-021-05881-3.

[28]   N. Syalomta, N. Fasya Rahim, K. Usman, and N. K. Caecar Pratiwi, "Face Expressions Recognition Based on Image Processing using Convolutional Neural Network for Human Computer Interface," *SHS Web Conf.*, vol. 139, p. 03017, 2022, doi: 10.1051/shsconf/202213903017.

[29]   P. Deepan, R. Vidya, M. A. Reddy, N. Arul, J. Ravichandran, and S. Dhiravidaselvi, "A Hybrid Gabor Filter-Convolutional Neural Networks Model for Facial Emotion Recognition System," *Indian J. Sci. Technol.*, vol. 17, no. 35, pp. 3696–3703, 2024, doi: 10.17485/ijst/v17i35.1998.

MODELING MONKEYPOX: SPREAD OF OUTBREAK WITH SOCIAL DISTANCING, QUARANTINE AND VACCINATION

Mahir Demir [1] iD

[1] *Giresun University, Department of Mathematics, Giresun, Türkiye, mahir.demir@giresun.edu.tr*

ABSTRACT

In this paper, we introduced a novel mathematical model to simulate the spread of the zoonotic viral disease monkeypox, incorporating both human and rodent populations to capture the disease dynamics. Unlike previous models, we included a quarantine compartment for infected humans, a social distancing compartment for susceptible individuals, and vaccination with direct transmission to the recovered compartment, offering a more comprehensive framework for controlling the spread of monkeypox. We then compared the effectiveness of these three control measures in reducing disease transmission. To investigate the dynamics of the model, we first demonstrated that it has a unique, positive, and bounded solution. Next, we calculated the basic reproduction number, R_0 for the proposed model. A sensitivity analysis is then conducted to identify key parameters, followed by an assessment of their effects on R_0. Additionally, we analyzed the local stability of both the disease-free and endemic equilibrium points to identify the conditions under which the disease dies out or remains endemic. We first showed in stability analysis section that these three control parameters play important roles in stability of equlibrium points. After that our findings in sensitivity analysis indicated the critical role of recovery rates and incubation periods in shaping the outbreak trajectory. Besides them, our analysis of R_0 in 3-D plots showed that the human-to-human transmission (β_{hh}) has about 3 times greater impact than rodent-to-human transmission (β_{rh}) on R_0. Finally, we presented simulations to show single and combined effects of the control parameters: quarantine, social distancing and vaccination on the transmission of monkeypox virus.

Keywords: Mpox, Sensitivity analysis, Infectious disease, Basic reproduction number, Stability analysis.

1   INTRODUCTION

Monkeypox is a zoonotic viral disease caused by the monkeypox virus, a member of the Orthopoxvirus genus, which also includes the smallpox virus. First identified in 1958 in laboratory monkeys, the disease is primarily transmitted to humans through direct contact with infected animals, particularly rodents, or through respiratory droplets and contaminated objects from human-to-human contact [1]. Symptoms typically include fever, headache, muscle aches, and swollen lymph nodes, followed by a characteristic rash that often begins on the face and spreads to other body parts. The incubation period ranges from 5 to 21 days, and while the disease is generally less severe than smallpox, it can still lead to complications and, in rare cases, death, with mortality rates varying by geographic region and viral strain [2], [3].

Various mathematical models have been employed to investigate the transmission dynamics of monkeypox, focusing on interactions among different population groups. [4] introduced a SIQR-SEI model to analyze rodent-to-human transmission, highlighting the role of quarantine in controlling infection spread. Another study developed a deterministic model incorporating vaccination to explore monkeypox dynamics, revealing that epidemic outcomes depend heavily on vaccination efficacy (categorized as weak, medium, or strong) [5]. Additionally, a study by authors [6] emphasized quarantine and public awareness campaigns as essential strategies for reducing human-to-human transmission. However, these studies often excluded the exposed (E) compartment in their frameworks, which limits their application to diseases with significant latent periods.

Conversely, other studies have included the exposed compartment to capture more realistic transmission dynamics. [7] applied an SEIR model with low-infectious and high-infectious compartments alongside quarantine measures. [8] extended this by incorporating a quarantine compartment for infected individuals, improving insights into isolation's effectiveness. Similarly, [9] expanded the SEIR framework with a compartment for vaccinated individuals and [13] expanded with isolated individuals to model monkeypox transmission comprehensively. A recent study by [10] analyzed SEIR-based frameworks, highlighting their utility in understanding human-animal transmission interactions and guiding public health interventions. These contributions demonstrate the growing reliance on SEIR models to better reflect the disease's natural history and control strategies.

Unlike other studies on monkeypox modeling, we did not include a separate compartment for vaccinated individuals. Instead, vaccinated individuals were directly moved

to the recovered compartment, assuming immunity acquisition based on vaccine efficacy and vaccination rates among susceptible individuals. By grouping vaccinated and recovered individuals, we simplified the model, reflecting their shared immune status. Given monkeypox's primary transmission via direct contact with infected fluids or objects, we assumed negligible infection risk within the isolated (social distancing) compartment and focused on high-risk interactions. Our model incorporated vaccination, social distancing, and quarantine to analyze their combined effects on monkeypox virus transmission. Such control measures are well studied on COVID-19 virus [24-27]. For instance, the effects of social distancing, quarantine, and lockdown on COVID-19 dynamics were carefully analyzed in the study presented by [24].

The recent spread of monkeypox beyond its usual regions has shown the need for effective strategies to control its spread. Measures like vaccination, social distancing, and quarantine are known to work well individually, but their combined effects are less understood. It is important to study how these measures interact, especially since public compliance with social distancing and quarantine can impact the success of vaccination efforts. Understanding how to combine these strategies effectively can help manage monkeypox outbreaks and improve readiness for future pandemics, ensuring public health responses are both efficient and flexible.

In the following section, we first introduced the compartmental model, identified its equilibrium points, and calculated the basic reproduction number, R_0. We then analyzed the stability of these equilibrium points. A sensitivity analysis was conducted using parameter values derived from previous studies to understand how variations in key factors affect the spread of monkeypox outbreak. In the result section, we presented plots illustrating how R_0 changes in response to variations in critical parameters identified through sensitivity analysis. Finally, we discussed the individual and combined impacts of quarantine, social distancing, and vaccination on controlling disease spread.

2   MATERIAL AND METHOD

In this study, to model the spread of the monkeypox virus, the human population was divided into six compartments, and the rodent population was divided into four compartments. The SEIQPR model was used to represent the human population and the SEIR model was used to represent the rodent population. For the transmission diagram of the disease between compartments, see Figure 1, and for the definitions of the compartments, see Table 1. The total human population was expressed as $N_h = S_h + E_h + I_h + Q_h + P_h + R_h$ and the rodent

population was expressed as $N_r = S_r + E_r + I_r + R_r$. We assumed that a vaccinated human gains immunity to the monkeypox virus, allowing them to transition directly to the recovered class. Since monkeypox mainly transmits through direct contact with infected fluids or contaminated objects, we assume that the infection risk is negligible in the social distancing compartment (P_h) and exclude transmission in this group, focusing instead on higher-risk interactions.

2.1 Model Formulation

We proposed a compartmental model that incorporates both human and rodent populations to describe monkeypox transmission dynamics, represented by the following system of differential equations:

$$\frac{dS_h}{dt} = \Lambda_h - (\beta_{hh}I_h + \beta_{rh}I_r)S_h - (d_h + b + v)S_h$$

$$\frac{dE_h}{dt} = (\beta_h I_{hh} + \beta_{rh}I_r)S_h - (k_h + d_h)E_h$$

$$\frac{dI_h}{dt} = k_h E_h - (q + \mu_{h_1} + d_h + \gamma_{h_1})I_h$$

$$\frac{dQ_h}{dt} = qI_h - (\mu_{h_2} + d_h + \gamma_{h_2})Q_h$$

$$\frac{dP_h}{dt} = bS_h - (v + d_h)P_h$$

$$\frac{dR_h}{dt} = \gamma_{h_1}I_h + \gamma_{h_2}Q_h + v(S_h + P_h) - d_h R_h$$

$$\frac{dS_r}{dt} = \Lambda_r - (\beta_{rr}I_r + \beta_{hr}I_h)S_r - d_r S_r$$

$$\frac{dE_r}{dt} = (\beta_{rr}I_r + \beta_{hr}I_h)S_r - (k_r + d_r)E_r$$

$$\frac{dI_r}{dt} = k_r E_r - (\mu_r + d_r + \gamma_r)I_r$$

$$\frac{dR_r}{dt} = \gamma_r I_r - d_r R_r \tag{1}$$

where, $S_h(0) = S_{h,0}$, $E_h(0) = E_{h,0}$, $I_h(0) = I_{h,0}$, $Q_h(0) = Q_{h,0}$, $P_h(0) = P_{h,0}$, $R_h(0) = R_{h,0}$, $S_r(0) = S_{r,0}$, $E_r(0) = E_{r,0}$, $I_r(0) = I_{r,0}$ and $R_r(0) = R_{r,0}$ values represent the initial

conditions of the differential equation. That is, they express the number of individuals in each compartment at time $t = 0$. All these values are defined as non-negative real numbers with upper bounds. Similarly, all parameters defined in Table 2 are specified as positive real numbers with upper bounds. In the study, we mainly focused on the control parameters v (vaccination), b (social distancing), and q (quarantine) in the mitigation of monkeypox virus.
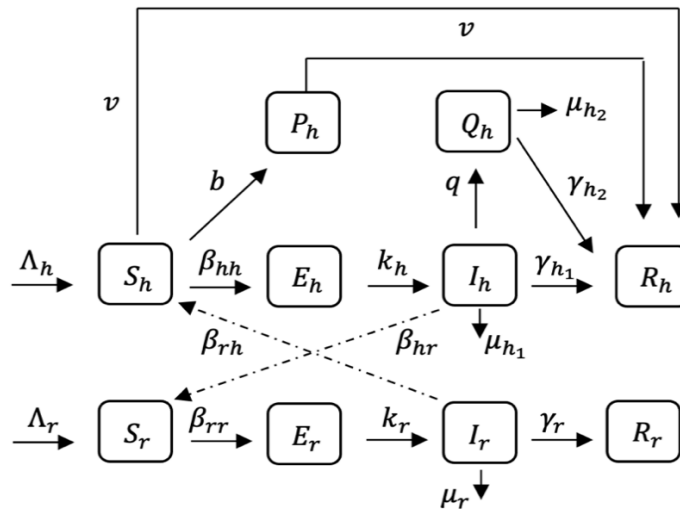
Figure 1. Flow diagram illustrating the disease transitions among the compartments.

Table 1. Population compartments and their descriptions.

Compartments	Descriptions	Initial densities of populations
S_r	Susceptible rodents	0.9990
E_r	Exposed rodents	0.0004
I_r	Infected rodents	0.0006
R_r	Recovered rodents	0.0000
S_h	Susceptible humans	0.9990
P_h	Social Distanced-Susceptible humans	0.0004
E_h	Exposed humans	0.0006
I_h	Infected humans	0.0000
Q_h	Quarantined-Infected humans	0.0000
R_h	Recovered humans	0.0000

Table 2. The model parameters, along with their descriptions and values in the time unit days. For the control parameters v, b, and q, we used a base value of 0.0001 and then varied them in result section to show their effects on the infected cases.

Parameters	Descriptions	Value ($\frac{1}{day}$)	Source
Λ_h	Recruitment rate of human population	-	-
d_h	Natural death rate of human population	-	-
β_{hh}	Disease transmission rate from humans to humans	0.3000	Assumed
β_{rh}	Disease transmission rate from rodents to humans	0.1500	Assumed
β_{rr}	Disease transmission rate from rodents to rodents	0.3000	Assumed
β_{hr}	Disease transmission rate from humans to rodents	0.1500	Assumed
v	(Vaccine efficacy rate) x (the percentage of vaccinated susceptible individuals)	0.0001	Assumed
b	Rate of transition to social distancing class from susceptible class	0.0001	Assumed
q	Rate of moving infected to quarantined-infected individuals	0.0001	Assumed
μ_{h_1}	Disease-induced death rate of human population in I_h	0.0033	[11]
μ_{h_2}	Disease-induced death rate of human population in Q_h	0.0555	[11]
k_h	Rate of exposed individuals becoming infected	0.0500	[12]
γ_{h_1}	Recovery rate due to natural immune response	0.0884	[11]
γ_{h_2}	Recovery rate due to hospitalization	0.0363	[11]
Λ_r	Recruitment rate of rodent population	-	-
d_r	Natural death rate of rodent population	-	-
k_r	Rate of exposed rodents becoming infected	0.3200	[12]
μ_r	Disease-induced death rate of rodent population	0.2814	[12]
γ_r	Recovery rate of rodents due to natural immune response	0.6000	[14]

Theorem 1. *Assuming that the initial conditions are defined in a region Ω, the system of differential equations given in (1) has a unique positive and bounded solution in the region Ω for each $t \in [0, T]$. Specifically,*

$$\Omega = \left\{ (S_h, E_h, I_h, Q_h, P_h, R_h, S_r, E_r, I_r, R_r) \subset \mathbb{R}_+^{10} : 0 < N_h \le \frac{\Lambda_h}{d_h}, 0 < N_r \le \frac{\Lambda_r}{d_r} \right\}.$$

Proof. Let's first show boundedness of solutions for model (1)

$$\frac{dN_h}{dt} = \frac{dS_h}{dt} + \frac{dE_h}{dt} + \frac{dI_h}{dt} + \frac{dQ_h}{dt} + \frac{dP_h}{dt} + \frac{dR_h}{dt}$$

$$= \Lambda_h - d_h(S_h + E_h + I_h + Q_h + P_h + R_h) - \mu_{h_1} I_h - \mu_{h_2} Q_h \quad (2)$$

$$\le \Lambda_h - d_h(S_h + E_h + I_h + Q_h + P_h + R_h)$$

$$\implies \frac{dN_h}{dt} \le \Lambda_h - d_h N_h$$

$$\implies \limsup_{t \to \infty} N_h \le \frac{\Lambda_h}{d_h}$$

If $\frac{dN_h}{dt}$ were positive, the solution would increase and go to infinity. Therefore, to prevent this increase, this derivative must take a maximum value of zero. In other words, if we want the solution to the differential equation system to remain within a boundary, the total number of individuals in the human population, $N_h(t)$, must either remain constant or decrease. Therefore, the derivative $\frac{dN_h}{dt}$ can be at most zero. Similarly, let us now demonstrate that the solution for the rodent population is also bounded:

$$\frac{dN_r}{dt} = \frac{dS_r}{dt} + \frac{dE_r}{dt} + \frac{dI_r}{dt} + \frac{dR_r}{dt}$$

$$= \Lambda_r - \mu_r I_r - d_r(S_r + E_r + I_r + R_r) \tag{3}$$

$$\leq \Lambda_r - d_r(S_r + E_r + I_r + R_r)$$

$$\implies \quad \frac{dN_r}{dt} \leq \Lambda_r - d_r N_r$$

$$\implies \quad \limsup_{t \to \infty} N_r \leq \frac{\Lambda_r}{\mu_r}.$$

Thus, $N_h \leq \frac{\Lambda_h}{d_h}$ and $N_r \leq \frac{\Lambda_r}{\mu_r}$. Now, we show the positivity of the solutions. by using Eq. 2, we get following since $-\mu_h Q_h \geq -\mu_h N_h$.

$$\frac{dN_h}{dt} = \Lambda_h - d_h(S_h + E_h + I_h + Q_h + P_h + R_h) - \mu_{h_1} I_h - \mu_{h_2} Q_h$$

$$\geq \Lambda_h - d_h N_h - \mu_h N_h = \Lambda_h - (d_h + \mu_{h_1} + \mu_{h_2}) N_h$$

By linearity of the differential equation, we can multiply the above inequality by the integral factor, $e^{\int_0^t (d_h + \mu_{h_1} + \mu_{h_2}) ds} = e^{(d_h + \mu_{h_1} + \mu_{h_2})t}$ and obtain the following for $s \in (0, t)$

$$N_h e^{(d_h + \mu_{h_1} + \mu_{h_2})t} = N_{h,0} + \Lambda_h \int_0^t e^{(d_h + \mu_{h_1} + \mu_{h_2})s} \, ds > 0.$$

Thus, we obtained $0 < N_h \leq \frac{\Lambda_h}{d_h}$. Similarly, by using Eq. 3, we got the following as

$$\frac{dN_r}{dt} = \Lambda_r - \mu_r I_r - d_r(S_r + E_r + I_r + R_r)$$

$$\geq \Lambda_r - (\mu_r + d_r) N_r$$

By linearity of the differential equation, we obtained

$$N_r e^{(\mu_r + d_r)t} \geq N_{r,0} + \Lambda_r \int_0^t e^{(\mu_r + d_r)s} \, ds > 0$$

Hence, $0 < N_h \leq \frac{\Lambda_h}{d_h}$ and $0 < N_r \leq \frac{\Lambda_r}{d_r}$.

2.2 Equilibrium Points of the Model

2.2.1 The disease-free equilibrium point and basic reproduction number (R_0)

The disease-free equilibrium is the state where no disease is present in the system ($I_r = I_h = 0$). Thus, the disease-free equilibrium of system (1) is given by

$$E_1 = (S_h^*, E_h^*, I_h^*, Q_h^*, P_h^*, R_h^*, S_r^*, E_r^*, I_r^*, R_r^*) = \left(\frac{\Lambda_h}{d_h}, 0,0,0,0,0, \frac{\Lambda_r}{d_r}, 0,0,0 \right).$$

Thus, this indicates that susceptible humans and rodents will stay at the maximum level when there is no disease since $0 < N_h \leq \frac{\Lambda_h}{d_h}$ and $0 < N_r \leq \frac{\Lambda_r}{d_r}$.

While determining the basic reproduction number (R_0), the Next Generation Matrix Method will be used [15]. This matrix is based on two main components: The new infections matrix (F): This matrix shows the rates at which new cases emerge in the epidemic. The transition matrix (V): This matrix represents the transitions of individuals among the classes: E_h, I_h, Q_h, E_r and I_r. We get these matrices in the order $(E_h, I_h, Q_h, E_r, I_r)$ as follow:

$$F = \begin{bmatrix} (\beta_{hh} I_h + \beta_{rh} I_r) S_h \\ 0 \\ 0 \\ (\beta_{rr} I_r + \beta_{hr} I_h) S_r \\ 0 \end{bmatrix} \quad \text{and} \quad V = \begin{bmatrix} (d_h + k_h) E_h \\ -k_h E_h + (q + \mu_{h_1} + d_h + \gamma_{h_1}) I_h \\ -q I_h + (\mu_{h_2} + d_h + \gamma_{h_2}) Q_h \\ (k_r + d_r) E_r \\ -k_r E_r + (\mu_r + d_r + \gamma_r) I_r \end{bmatrix}$$

$$\mathcal{F} = \begin{bmatrix} 0 & \beta_{hh} S_h & 0 & 0 & \beta_{rh} S_h \\ 0 & 0 & 0 & 0 & 0 \\ 0 & 0 & 0 & 0 & 0 \\ 0 & \beta_{hr} S_r & 0 & 0 & \beta_{rr} S_r \\ 0 & 0 & 0 & 0 & 0 \end{bmatrix} = \begin{bmatrix} 0 & \beta_{hh} \dfrac{\Lambda_h}{d_h} & 0 & 0 & \beta_{rh} \dfrac{\Lambda_h}{d_h} \\ 0 & 0 & 0 & 0 & 0 \\ 0 & 0 & 0 & 0 & 0 \\ 0 & \beta_{hr} \dfrac{\Lambda_r}{d_r} & 0 & 0 & \beta_{rr} \dfrac{\Lambda_r}{d_r} \\ 0 & 0 & 0 & 0 & 0 \end{bmatrix}_{E_1}$$

$$\mathcal{V} = \begin{bmatrix} k_h + d_h & 0 & 0 & 0 & 0 \\ -k_h & q + \mu_{h_1} + d_h + \gamma_{h_1} & 0 & 0 & 0 \\ 0 & -q & \mu_{h_2} + d_h + \gamma_{h_2} & 0 & 0 \\ 0 & 0 & 0 & k_r + d_r & 0 \\ 0 & 0 & 0 & -k_r & (\mu_r + d_r + \gamma_r) \end{bmatrix}_{E_1}$$

$$\mathcal{V}^{-1} = \begin{bmatrix} \frac{1}{k_h+d_h} & 0 & 0 & 0 & 0 \\ M_1 & \frac{1}{q+\mu_{h_1}+d_h+\gamma_{h_1}} & 0 & 0 & 0 \\ M_2 & \frac{q}{(q+\mu_{h_1}+d_h+\gamma_{h_1})(\mu_{h_2}+d_h+\gamma_{h_2})} & \frac{1}{\mu_{h_2}+d_h+\gamma_{h_2}} & 0 & 0 \\ 0 & 0 & 0 & \frac{1}{k_r+d_r} & 0 \\ 0 & 0 & 0 & \frac{k_r}{(k_r+d_r)(\mu_r+d_r+\gamma_r)} & \frac{1}{\mu_r+d_r+\gamma_r} \end{bmatrix}$$

where $M_1 = \frac{k_h}{(k_h+d_h)(q+\mu_{h_1}+d_h+\gamma_{h_1})}$ and $M_2 = \frac{qk_h}{(k_h+d_h)(q+\mu_{h_1}+d_h+\gamma_{h_1})(\mu_{h_2}+d_h+\gamma_{h_2})}$. By multiplying the matrices $\mathcal{F} \ and \ \mathcal{V}^{-1}$, we got the following

$$\mathcal{F}\mathcal{V}^{-1} =$$
$$\begin{bmatrix} \frac{\beta_{hh}\Lambda_h k_h}{d_h(k_h+d_h)(q+\mu_{h_1}+d_h+\gamma_{h_1})} & \frac{\beta_{hh}\Lambda_h}{d_h(q+\mu_{h_1}+d_h+\gamma_{h_1})} & 0 & \frac{\beta_{rh}\Lambda_h k_r}{d_h(k_r+d_r)(\mu_r+d_r+\gamma_r)} & \frac{\beta_{rh}\Lambda_h}{d_h(\mu_r+d_r+\gamma_r)} \\ 0 & 0 & 0 & 0 & 0 \\ 0 & 0 & 0 & 0 & 0 \\ \frac{\beta_{hr}\Lambda_r k_h}{d_r(k_h+d_h)(q+\mu_{h_1}+d_h+\gamma_{h_1})} & \frac{\beta_{hr}\Lambda_r}{d_r(q+\mu_{h_1}+d_h+\gamma_{h_1})} & 0 & \frac{\beta_{rr}\Lambda_r k_r}{d_r(k_r+d_r)(\mu_r+d_r+\gamma_r)} & \frac{\beta_{rr}\Lambda_r}{d_r(\mu_r+d_r+\gamma_r)} \\ 0 & 0 & 0 & 0 & 0 \end{bmatrix}$$

$$R_0^{hh} = \frac{\beta_{hh}\Lambda_h k_h}{d_h(k_h+d_h)(q+\mu_{h_1}+d_h+\gamma_{h_1})}, \quad R_0^{rh} = \frac{\beta_{rh}\Lambda_h k_r}{d_h(k_r+d_r)(\mu_r+d_r+\gamma_r)}$$

$$R_0^{hr} = \frac{\beta_{hr}\Lambda_r k_h}{d_r(k_h+d_h)(q+\mu_{h_1}+d_h+\gamma_{h_1})}, \quad R_0^{rr} = \frac{\beta_{rr}\Lambda_r k_r}{d_r(k_r+d_r)(\mu_r+d_r+\gamma_r)}$$

Here, R_0^{hh} and R_0^{rr} are the basic reproduction numbers for human-to-human, rodents-to-rodents transmission, while R_0^{hr} and R_0^{rh} are the basic reproduction numbers for the vectorial transmissions from human-to-rodent and rodent-to-human, respectively. Thus, the basic reproduction number for model (1) is a composition of the reproduction numbers as follows (see the studies for details: [16] and [17]). Shortly, when we arrange the characteristic polynomial of $\mathcal{F}\mathcal{V}^{-1}$ matrix and arrange it, we will get the following, which is the maximum eigenvalue of the matrix.

$$R_0 = \frac{1}{2}\left\{(R_0^{hh} + R_0^{rr}) + \sqrt{(R_0^{hh} + R_0^{rr})^2 - 4(R_0^{hh}R_0^{rr} - R_0^{hr}R_0^{rh})}\right\}$$

when we simplify the equation, we obtain

$$R_0 = \frac{1}{2}\left\{ (R_0^{hh} + R_0^{rr}) + \sqrt{(R_0^{hh} - R_0^{rr})^2 + 4R_0^{hr}R_0^{rh}} \right\} \tag{4}$$

Thus, any changes in these reproduction numbers affect the basic reproduction number, R_0.

2.2.2 Endemic equilibrium

This is the equilibrium where the disease stays in the system when $R_0 > 1$. See Theorem 4 for the existence of the endemic equilibrium point.

Theorem 2. *When $I_r > 0$, there is at least one endemic equilibrium point for the system given in equation (1).*

Proof. Suppose that $I_r > 0$. Setting $\frac{dI_r}{dt} = 0$ and $\frac{dR_r}{dt} = 0$, we obtained

$$E_r = \frac{\mu_r + d_r + \gamma_r}{k_r} I_r \tag{5}$$

$$R_r = \frac{\gamma_r}{d_r} I_r \tag{6}$$

when we set $\frac{dS_r}{dt} + \frac{dE_r}{dt} = 0$, we obtained

$$S_r = \frac{\Lambda_r - (k_r + d_r)E_r}{d_r} \tag{7}$$

Since $N_r = S_r + E_r + I_r + R_r$, $I_r = N_r - S_r - E_r - R_r$ and we got the following by using the equations (5-7)

$$I_r^* = \frac{\Lambda_r - d_r N_r}{\mu_r} \tag{8}$$

Hence,

$$S_r^* = \frac{\Lambda_r - (k_r + d_r)E_r}{d_r} = \frac{\Lambda_r}{d_r} - \frac{(k_r + d_r)(\mu_r + d_r + \gamma_r)}{d_r k_r} \frac{\Lambda_r - d_r N_r}{\mu_r} \tag{9}$$

$$E_r^* = \frac{\mu_r + d_r + \gamma_r}{k_r} \frac{\Lambda_r - d_r N_r}{\mu_r} \quad \text{and} \quad R_r^* = \frac{\gamma_r}{d_r} \frac{\Lambda_r - d_r N_r}{\mu_r} \tag{10}$$

Similarly, by setting $\frac{dI_h}{dt} = 0, \frac{dQ_h}{dt} = 0, \frac{dP_h}{dt} = 0$ and $\frac{dR_h}{dt} = 0$,

$$E_h = \frac{q + \mu_{h_1} + d_h + \gamma_{h_1}}{k_h} I_h, \qquad Q_h = \frac{q}{\mu_{h_2} + d_h + \gamma_{h_2}} I_h, \qquad S_h = \frac{v + d_h}{b} P_h \tag{11}$$

$$R_h = \frac{\gamma_{h_1} I_h + \gamma_{h_2} Q_h + v(S_h + P_h)}{d_h} = \frac{\gamma_{h_1} I_h}{d_h} + \frac{\gamma_{h_2} Q_h}{d_h} + \frac{v(d_h + b + v)}{v + d_h} S_h \tag{12}$$

As we set $\frac{dS_h}{dt} + \frac{dE_h}{dt} = 0$, then

$$S_h = \frac{\Lambda_h - (k_h + d_h)E_h}{d_h + b + v} = \frac{\Lambda_h - \frac{(k_h + d_h)(q + \mu_{h_1} + d_h + \gamma_{h_1})}{k_h}I_h}{d_h + b + v} \tag{13}$$

Since $N_h = S_h + E_h + I_h + Q_h + P_h + R_h$, $I_h = N_h - S_h - E_h - Q_h - P_h - R_h$ and we got the following by using the equations (11-13)

$$I_h^* = \frac{N_h - \frac{(v+1)\Lambda_h}{v + d_h}}{1 - \frac{(v+1)(k_h + d_h)(q + \mu_{h_1} + d_h + \gamma_{h_1})}{(v + d_h)k_h} + \frac{q + \mu_{h_1} + d_h + \gamma_{h_1}}{k_h} + \frac{\gamma_{h_1}}{d_h} + \frac{q(d_h + \gamma_{h_2})}{d_h(\mu_{h_2} + d_h + \gamma_{h_2})}} \tag{14}$$

Hence, the endemic equilibrium point, $E_2 = (S_h^*, E_h^*, I_h^*, Q_h^*, P_h^*, R_h^*, S_r^*, E_r^*, I_r^*, R_r^*)$ was obtained as

$$S_h^* = \frac{\Lambda_h - \frac{(k_h + d_h)(q + \mu_{h_1} + d_h + \gamma_{h_1})}{k_h}I_h^*}{d_h + b + v},$$

$$E_h^* = \frac{q + \mu_{h_1} + d_h + \gamma_{h_1}}{k_h}I_h^*,$$

$$I_h^* = \frac{N_h - \frac{(v+1)\Lambda_h}{v + d_h}}{1 - \frac{(v+1)(k_h + d_h)(q + \mu_{h_1} + d_h + \gamma_{h_1})}{(v + d_h)k_h} + \frac{q + \mu_{h_1} + d_h + \gamma_{h_1}}{k_h} + \frac{\gamma_{h_1}}{d_h} + \frac{q(d_h + \gamma_{h_2})}{d_h(\mu_{h_2} + d_h + \gamma_{h_2})}},$$

$$Q_h^* = \frac{q}{\mu_{h_2} + d_h + \gamma_{h_2}}I_h^*,$$

$$P_h^* = \frac{v + d_h}{b}S_h^* = \frac{v + d_h}{b}\frac{\Lambda_h - \frac{(k_h + d_h)(q + \mu_{h_1} + d_h + \gamma_{h_1})}{k_h}I_h^*}{d_h + b + v},$$

$$R_h^* = \frac{\gamma_{h_1}}{d_h}I_h^* + \frac{\gamma_{h_2}}{d_h}Q_h^* + \frac{v(d_h + b + v)}{v + d_h}S_h^* = \frac{v\Lambda_h}{v + d_h} + \left(\frac{\gamma_{h_1}}{d_h} + \frac{\gamma_{h_2}q}{d_h(\mu_{h_2} + d_h + \gamma_{h_2})} - \frac{v(k_h + d_h)(q + \mu_{h_1} + d_h + \gamma_{h_1})}{k_h(v + d_h)}\right)I_h^*,$$

$$S_r^* = \frac{\Lambda_r}{d_r} - \frac{(k_r + d_r)(\mu_r + d_r + \gamma_r)}{d_r k_r}\frac{\Lambda_r - d_r N_r}{\mu_r},$$

$$E_r^* = \frac{\mu_r + d_r + \gamma_r}{k_r}\frac{\Lambda_r - d_r N_r}{\mu_r},$$

$$I_r^* = \frac{\Lambda_r - d_r N_r}{\mu_r},$$

$$R_r^* = \frac{\gamma_r}{d_r}\frac{\Lambda_r - d_r N_r}{\mu_r}.$$

2.3 Stability Analysis of Equilibrium Points

In this section, we examined the stability analyses at the equilibrium points. In our model, once individuals reach the R_h or R_r class, they are no longer involved in the disease transmission process. They are assumed immune and do not contribute to future infections, meaning their behavior does not affect the ongoing dynamics of infection spread or disease stability. To reduce the complexity and calculation in stability analysis, we excluded these

classes. Thus, we calculated the Jacobian matrix of the differential equation system (1) in the order $(S_h, E_h, I_h, Q_h, P_h, S_r, E_r, I_r)$ as follows:

$$J = \begin{bmatrix} a_{11} & 0 & a_{13} & 0 & 0 & 0 & 0 & a_{18} \\ a_{21} & a_{22} & a_{23} & 0 & 0 & 0 & 0 & a_{28} \\ 0 & a_{32} & a_{33} & 0 & 0 & 0 & 0 & 0 \\ 0 & 0 & a_{43} & a_{44} & 0 & 0 & 0 & 0 \\ a_{51} & 0 & 0 & 0 & a_{55} & 0 & 0 & 0 \\ 0 & 0 & 0 & 0 & 0 & a_{66} & 0 & a_{68} \\ 0 & 0 & 0 & 0 & 0 & a_{76} & a_{77} & a_{78} \\ 0 & 0 & 0 & 0 & 0 & 0 & a_{87} & a_{88} \end{bmatrix}$$

where,

$a_{11} = -(\beta_{hh}I_h + \beta_{rh}I_r) - (d_h + b + v)$, $a_{13} = -\beta_{hh}S_h$, $a_{18} = -\beta_{rh}S_h$, $a_{21} = \beta_{hh}I_h + \beta_{rh}I_r$, $a_{22} = -(k_h + d_h)$, $a_{23} = \beta_{hh}S_h$, $a_{28} = \beta_{rh}S_h$, $a_{32} = k_h$, $a_{33} = -(q + \mu_{h_1} + d_h + \gamma_{h_1})$, $a_{43} = q$, $a_{44} = -(\mu_{h_2} + d_h + \gamma_{h_2})$, $a_{51} = b$, $a_{55} = -(v + d_h)$, $a_{66} = -\beta_{rr}I_r - d_r$, $a_{68} = -\beta_{rr}S_r$, $a_{76} = \beta_{rr}I_r$, $a_{77} = -(k_r + d_r)$, $a_{78} = \beta_{rr}S_r$, $a_{87} = k_r$, $a_{88} = -(\mu_r + d_r + \gamma_r)$.

Theorem 3. *The disease-free equilibrium point is asymptotically local stable if the conditions* $1 > R_0^{rr}$ *and* $1 > R_0^{hh}$ *are hold. Otherwise, it is unstable.*

Proof. The Jacobian matrix of the disease-free equilibrium point,

$$E_1 = (S_h^*, E_h^*, I_h^*, Q_h^*, P_h^*, S_r^*, E_r^*, I_r^*) = \left(\frac{\Lambda_h}{d_h}, 0, 0, 0, 0, \frac{\Lambda_r}{d_r}, 0, 0\right).$$

was calculated as

$$J_{E_1} = \begin{bmatrix} a_{11} - \lambda & 0 & a_{13} & 0 & 0 & 0 & 0 & a_{18} \\ 0 & a_{22} - \lambda & a_{23} & 0 & 0 & 0 & 0 & a_{28} \\ 0 & a_{32} & a_{33} - \lambda & 0 & 0 & 0 & 0 & 0 \\ 0 & 0 & a_{43} & a_{44} - \lambda & 0 & 0 & 0 & 0 \\ a_{51} & 0 & 0 & 0 & a_{55} - \lambda & 0 & 0 & 0 \\ 0 & 0 & 0 & 0 & 0 & a_{66} - \lambda & 0 & a_{68} \\ 0 & 0 & 0 & 0 & 0 & 0 & a_{77} - \lambda & a_{78} \\ 0 & 0 & 0 & 0 & 0 & 0 & a_{87} & a_{88} - \lambda \end{bmatrix}$$

and its characteristic polynomial was obtained from $|J_{E_1} - \lambda I_{8x8}| = 0$ as

$$(a_{66} - \lambda)[(a_{88} - \lambda)(a_{77} - \lambda) - a_{87}a_{78}]$$

$$(a_{55} - \lambda)(a_{44} - \lambda)(a_{11} - \lambda)[(a_{33} - \lambda)(a_{22} - \lambda) - a_{32}a_{23}] = 0$$

The eigenvalues, $\lambda_1 = a_{11} = -(\mu_{h_2} + d_h + \gamma_{h_2})$, $\lambda_2 = a_{44} = -(\mu_{h_2} + d_h + \gamma_{h_2})$, $\lambda_3 = a_{55} = -(v + d_h)$ and $\lambda_4 = a_{66} = -d_r$, are negative.

$$[(a_{88} - \lambda)(a_{77} - \lambda) - a_{87}a_{78}] = 0$$

$$\Leftrightarrow$$

$$\lambda^2 - (a_{77} + a_{88})\lambda + a_{77}a_{88} - a_{87}a_{78} = 0.$$

If $a_{77}a_{88} > a_{87}a_{78}$, then the eigenvalues are negative by Routh-Hurwitz Criteria (Routh, 1877; Hurwitz, 1895).

$$a_{77}a_{88} > a_{87}a_{78} \Leftrightarrow (k_r + d_r)(\mu_r + d_r + \gamma_r > k_r\beta_{rr} S_r$$

$$\Leftrightarrow 1 > \frac{\beta_{rr} \Lambda_r k_r}{d_r(k_r+d_r)(\mu_r+d_r+\gamma_r)} = R_0^{rr}$$

Similarly, for the following equation

$$[(a_{33} - \lambda)(a_{22} - \lambda) - a_{32}a_{23}] = 0$$

$$\Leftrightarrow$$

$$\lambda^2 - (a_{22} + a_{33})\lambda + a_{22}a_{33} - a_{32}a_{23} = 0$$

when $a_{22}a_{33} > a_{32}a_{23}$, the eigenvalues are negative by Routh-Hurwitz Criteria [18],[19].

$$a_{22}a_{33} > a_{32}a_{23} \Leftrightarrow (k_h + d_h)(q + \mu_{h_1} + d_h + \gamma_{h_1}) > k_h\beta_{hh}S_h$$

$$\Leftrightarrow 1 > \frac{\beta_{hh}\Lambda_h k_h}{d_h(k_h+d_h)(q+\mu_{h_1}+d_h+\gamma_{h_1})} = R_0^{hh}$$

Thus, under the following conditions, the disease-free equilibrium is stable.

$$1 > R_0^{rr} \tag{15}$$

$$1 > R_0^{hh} \tag{16}$$

Theorem 4. *Under conditions (17) and (18), the endemic equilibrium point is asymptotically local stable. Otherwise, it is unstable.*

Proof. Let's set the Jacobian matrix of the endemic equilibrium point in the form $|J_{E_2} - \lambda I_{8x8}| = 0$ as

$$J_{E_2} = \begin{bmatrix} a_{11} - \lambda & 0 & a_{13} & 0 & 0 & 0 & 0 & a_{18} \\ a_{21} & a_{22} - \lambda & a_{23} & 0 & 0 & 0 & 0 & a_{28} \\ 0 & a_{32} & a_{33} - \lambda & 0 & 0 & 0 & 0 & 0 \\ 0 & 0 & a_{43} & a_{44} - \lambda & 0 & 0 & 0 & 0 \\ a_{51} & 0 & 0 & 0 & a_{55} - \lambda & 0 & 0 & 0 \\ 0 & 0 & 0 & 0 & 0 & a_{66} - \lambda & 0 & a_{68} \\ 0 & 0 & 0 & 0 & 0 & a_{76} & a_{77} - \lambda & a_{78} \\ 0 & 0 & 0 & 0 & 0 & 0 & a_{87} & a_{88} - \lambda \end{bmatrix}$$

and then get the characteristic polynomial of the matrix,

$$[(a_{88} - \lambda)(a_{77} - \lambda)(a_{66} - \lambda) - a_{87}a_{78}(a_{66} - \lambda) + a_{87}a_{76}a_{68}](a_{55} - \lambda)(a_{44} - \lambda)$$

$$[(a_{33} - \lambda)(a_{22} - \lambda)(a_{11} - \lambda) - a_{32}a_{23}(a_{11} - \lambda) + a_{32}a_{21}a_{13}] = 0$$

The eigenvalues, $\lambda_1 = a_{44} = -\left(\mu_{h_2} + d_h + \gamma_{h_2}\right)$ and $\lambda_2 = a_{55} = -(v + d_h)$ are negative.

Now, we examine the other eigenvalues as

$$[(a_{88} - \lambda)(a_{77} - \lambda)(a_{66} - \lambda) - a_{87}a_{78}(a_{66} - \lambda) + a_{87}a_{76}a_{68}] = 0$$

$\Longleftrightarrow$

$$a_3\lambda^3 + a_2\lambda^2 + a_1\lambda + a_0 = 0$$

where, $a_3 = 1 > 0$, $a_2 = -(a_{66} + a_{77} + a_{88}) > 0$, $a_1 = -a_{87}a_{78} + a_{77}a_{88} + a_{66}(a_{77} + a_{88})$ and $a_0 = -a_{66}a_{77}a_{88} - a_{87}a_{76}a_{68} + a_{87}a_{78}a_{66}$. If $a_0, a_1 > 0$ and $a_2a_1 > a_3a_0$, then the eigenvalues are negative. Similarly, for the following equation

$$[(a_{33} - \lambda)(a_{22} - \lambda)(a_{11} - \lambda) - a_{32}a_{23}(a_{11} - \lambda) + a_{32}a_{21}a_{13}] = 0$$

$\Longleftrightarrow$

$$b_3\lambda^3 + b_2\lambda^2 + b_1\lambda + b_0 = 0$$

where, $b_3 = 1 > 0$, $b_2 = -(a_{11} + a_{22} + a_{33}) > 0$, $b_1 = -a_{32}a_{23} + a_{22}a_{33} + a_{11}(a_{22} + a_{33})$ and $b_0 = -a_{11}a_{22}a_{33} - a_{32}a_{21}a_{13} + a_{32}a_{23}a_{11}$. If $b_0, b_1 > 0$ and $b_2b_1 > b_3b_0$, then the eigenvalues are negative by Routh-Hurwitz Criteria. Thus, under the following conditions, the endemic equilibrium is stable.

$$a_0, \ a_1 > 0 \text{ and } a_2a_1 > a_3a_0 \tag{17}$$

$$b_0, \ b_1 > 0 \text{ and } b_2b_1 > b_3b_0 \tag{18}$$

3   RESULTS AND DISCUSSION

We presented and discussed model outputs in this section. It is important to emphasize that while we included the demographic parameters Λ_h, d_h, Λ_r and d_r in our analyses, they were not considered in the simulations. These parameters were utilized primarily to establish bounds on the model solutions in Section 2. Since these parameters pertain to the natural birth and death rates of specific populations and have no direct role in controlling infectious diseases, they are typically excluded in most infectious disease modeling frameworks [20], [21], [22].

This approach reflects the general practice of focusing on parameters directly influencing disease transmission and progression.

3.1 Stability Analysis

We investigate the stability of the disease-free equilibrium and endemic equilibrium points by using the parameter values given in Table 2. First, it is important to mention that since we are not including the demographic parameters, R_0 will be in the form:

$$R_0 = \frac{1}{2}\left\{(R_0^{hh} + R_0^{rr}) + \sqrt{(R_0^{hh} - R_0^{rr})^2 + 4R_0^{hr}R_0^{rh}}\right\} \tag{19}$$

where

$$R_0^{hh} = \frac{\beta_{hh}}{(q+\mu_{h_1}+d_h+\gamma_{h_1})}, \quad R_0^{rh} = \frac{\beta_{rh}}{(\mu_r+d_r+\gamma_r)} \tag{20}$$

$$R_0^{hr} = \frac{\beta_{hr}}{(q+\mu_{h_1}+d_h+\gamma_{h_1})}, \quad R_0^{rr} = \frac{\beta_{rr}}{(\mu_r+d_r+\gamma_r)} \tag{21}$$

and the disease-free equilibrium point will be in the form:

$$E_1 = (S_h^*, E_h^*, I_h^*, Q_h^*, P_h^*, R_h^*, S_r^*, E_r^*, I_r^*, R_r^*) = (1,0,0,0,0,0,1,0,0,0).$$

rather than

$$E_1 = (S_h^*, E_h^*, I_h^*, Q_h^*, P_h^*, R_h^*, S_r^*, E_r^*, I_r^*, R_r^*) = \left(\frac{\Lambda_h}{d_h},0,0,0,0,0,\frac{\Lambda_r}{d_r},0,0,0\right).$$

Depending on our calculation by using parameter values given in Table 2, $R_0^{hh} = 3.26 > 1$ and $R_0^{rr} = 0.34 < 1$. Having, $R_0^{hh} = 3.26 > 1$ violate the stability of the disease-free equilibrium point (see Theorem 3). Thus, the disease-free equilibrium point is unstable. This finding highlights the need for additional efforts to control the outbreak. Specifically, incorporating control parameters v, b, and q is essential to reducing R_0^{hh} and mitigating transmission rates. Similarly, when we investigated the endemic equilibrium point with the parameter values given in Table 2, we obtained followings

$$a_3 = 1 > 0$$
$$a_2 = 1.2014 + 0.3I_r > 0$$
$$a_1 = -0.096S_r + 0.36I_r + 0.28 > 0.$$
$$a_0 = 0.0846I_r > 0.$$

and so, the condition (17) in Theorem 4 holds

$$a_0, \ a_1 > 0 \text{ and } a_2a_1 > a_3a_0$$

since we obtained

$$a_2a_1 > a_3a_0$$

$$\Leftrightarrow \quad 0.3364 + 0.4325I_r - 0.1153S_r > 0.0846I_r$$

Even assuming $S_r \cong 1$ and $I_r \cong 0$, which are the extreme cases, the inequality still holds. Thus, the condition (17) in Theorem 4 holds. Now, let investigate the condition (18) in Theorem 4. If this condition holds, then endemic equilibrium point is stable otherwise unstable. We obtained the following

$$b_3 = 1 > 0$$

$$b_2 = 0.3I_h + 0.15I_r + 0.1427 + v + b + q > 0$$

$$b_1 = -0.015S_h + 0.05q + 0.0046 + (0.3I_h + 0.15I_r + b + v)(q + 0.1417)$$

$$b_0 = 0.05(0.3I_h + 0.15I_r + b + v)(q + 0.0917) + 0.015S_h(0.3I_h + 0.15I_r + b + v)$$

$$+0.015S_h(0.3I_h + 0.15I_r) > 0$$

It is challenging to determine whether the condition $b_2 b_1 > b_3 b_0$ holds with the given parameters in Table 2, as it also requires identifying the variables S_h, I_h, and I_r and the control parameters v, b, and q. While this could be investigated numerically, such an analysis falls outside the scope of this study. However, we emphasize that the control parameters (v, b, and q) play a crucial role in the stability of the endemic equilibrium point. In the following sections, we examine the effects of these control parameters to highlight their significance in mitigating monkeypox outbreaks.

3.2   Sensitivity Analysis

Several parameters significantly influence the behavior of the model (1). To identify the parameters most relevant to the infected cases ($I_h + Q_h$), we performed a sensitivity analysis. This analysis employed Latin Hypercube Sampling (LHS) combined with the Partial Rank Correlation Coefficients (PRCC) method, following the approach described by [23]. Using parameter ranges provided in Table 3, we generated samples from a uniform distribution and used these as inputs to simulate system (1) over 150 days. The final number of infected cases served as the output variable for this analysis. Table 3 presents the PRCC values, associated p-values, and the parameter ranges used.

The results highlight $v, b, q, \beta_{hh}, k_h, \gamma_{h_1}, \gamma_{h_2}, \mu_r$ and γ_r as statistically significant parameters based on their high PRCC values, suggesting they play a pivotal role in outbreak dynamics. Consequently, we further analyzed how varying v, b, q, and β_{hh} affects the infected cases while keeping all other parameters fixed as listed in Table 2 and maintaining the initial

conditions in Table 1. Figures 2a-2d illustrate these findings, showing how the cumulative cases at the end of the simulation period respond to changes in these key parameters.

This investigation demonstrated that the control parameters v (vaccination) and b (social distancing) have nearly identical impacts on controlling the outbreak (see Figures 2a and 2b). This similarity is expected, as both parameters serve to reduce the spread of the disease in similar implementation in our model. In the absence of vaccination, implementing and managing social distancing measures can play a crucial role in mitigating monkeypox outbreaks.

The analysis also revealed that the recovery rates in the model play a critical role in controlling the outbreak, as they are statistically significant parameters. Additionally, the incubation period parameter (k_h) was identified as influential. Therefore, to effectively manage monkeypox outbreaks, it is essential to carefully examine this parameter to gain a better understanding of the disease dynamics.

Table 3. Results of sensitivity analysis with partial rank correlation coefficient (PRCC), p-value, and the parameter ranges used for calculations of the PRCC and p-values.

Parameters	Descriptions	PRCC	*p*-value	Parameter Ranges
v	(Vaccine efficacy rate) x (the percentage of vaccinated susceptible individuals)	-0.65	$9.3e^{-16}$	0.0001-0.1
b	Rate of transition to social distancing class from susceptible class	-0.63	$2.6e^{-15}$	0.0001-0.1
q	Rate of moving infected to quarantined-infected individuals	-0.48	$5.1e^{-10}$	0.001-0.3
β_{hh}	Disease transmission rate from humans to humans	0.55	$1.7e^{-12}$	0.01-1
β_{rh}	Disease transmission rate from rodents to humans	0.20	0.05	0.01-1
β_{rr}	Disease transmission rate from rodents to rodents	0.17	0.08	0.01-1
β_{hr}	Disease transmission rate from humans to rodents	0.07	0.5	0.01-1
μ_{h_1}	Disease-induced death rate of human population in I_h	-0.20	0.05	0.0001-0.1
μ_{h_2}	Disease-induced death rate of human population in Q_h	-0.24	0.02	0.0001-0.1
k_h	Rate of exposed individuals becoming infected	-0.61	$1.9e^{-14}$	0.001-1
γ_{h_1}	Recovery rate due to natural immune response	-0.36	0.0002	0.001-0.5
γ_{h_2}	Recovery rate due to hospitalization	-0.66	$1.5e^{-16}$	0.001-0.5
k_r	Rate of exposed rodents becoming infected	0.04	0.7	0.01-1
μ_r	Disease-induced death rate of rodent population	-0.28	0.004	0.01-1
γ_r	Recovery rate of rodents due to natural immune response	-0.35	0.0003	0.01-2
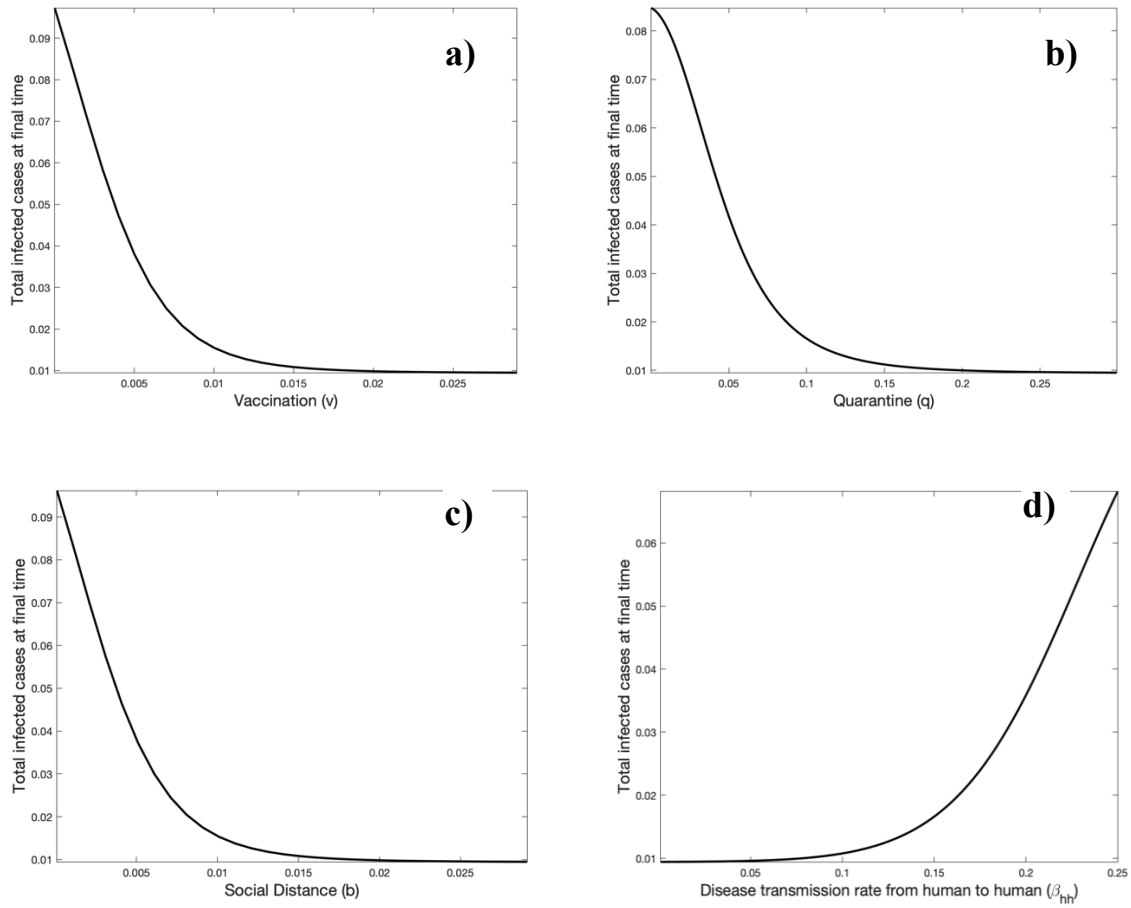
Figure 2. The total infected cases ($I_h + Q_h$) at the final time with respect to control parameters: vaccination (a), quarantine (b), social distance (c), and the disease transmission rate (d).

3.3 Analysis of Basic Reproduction Number, R_0

We investigated the changes on the basic reproduction number, R_0 depending on some of the important parameters presented by our sensitivity analysis in the previous subsection. We investigated the effect of the parameters $\gamma_{h_1}, q, \beta_{rh}$ and β_{hh} on R_0 while keeping all other parameters fixed as listed in Table 2. This investigation revealed that improving treatment quality to accelerate the recovery of infected individuals can significantly aid in mitigating the outbreak. Similarly, the rapid identification of infected individuals is equally crucial in controlling the spread of the disease (see Figure 3a).

a)

b)
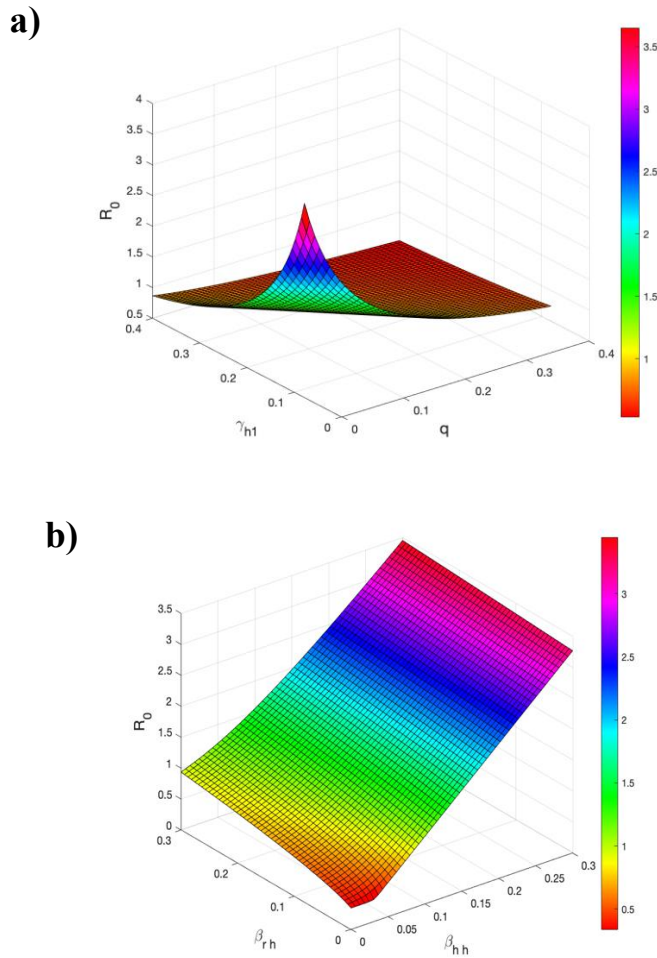
Figure 3. Surface plots of R_0. Plot a: showing the simultaneous impact of γ_{h_1} and q on R_0. Plot b: showing the simultaneous impact of β_{rh} and β_{hh} on R_0.

Our analysis also highlighted the significant influence of the parameter β_{hh} (human-to-human transmission) on the number of infected cases, compared to β_{rh} (rodent-to-human transmission). Notably, the human-to-human transmission was found to be nearly three times more impactful than the rodent-to-human transmission on the basic reproduction number (R_0) of the monkeypox virus (see Figure 3b).

3.4   Effects of Control Parameters on Infected Cases

As noted in the sensitivity analysis subsection (Figure 2), the control parameters v (vaccination) and b (social distancing) exhibit nearly identical effects on the number of infected cases. In Figure 4a, varying the parameters v or b between 0.0001 and 0.01 results in a similar reduction in infected cases, as indicated in the legend. However, applying both controls simultaneously leads to a substantially greater reduction in the infected cases, as demonstrated in Figure 4b.
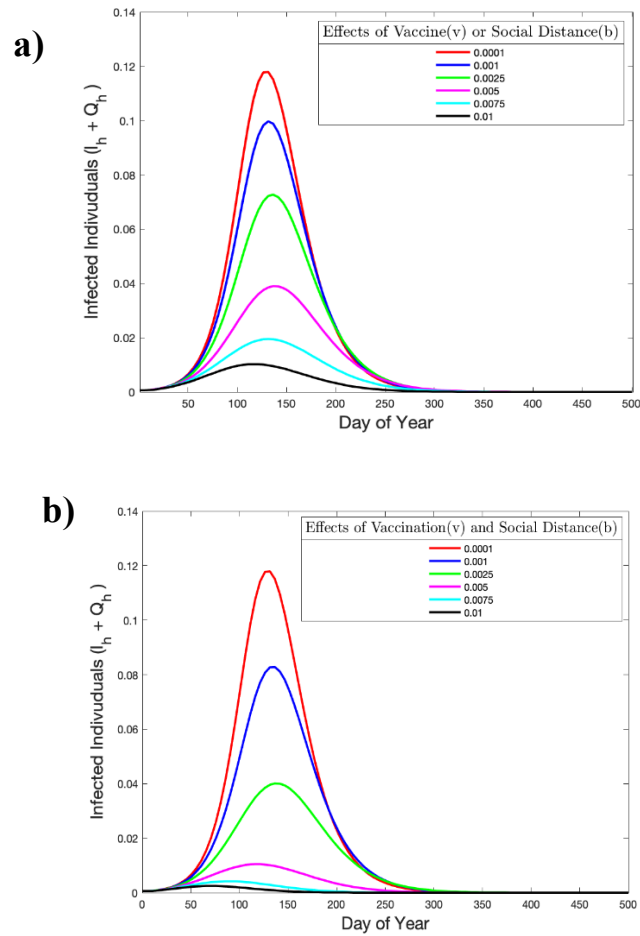
Figure 4. Effects of vaccination and /or social distancing on Infected cases. Plot a: the effect of vaccination or social distancing on the infected cases. Plot b: simultaneous effect of vaccination and social distancing on the infected cases.

When we applied only the quarantine parameter (q) to observe its effect on the infected cases, a noticeable shift in the peak of the infected cases curve emerged (see Figure 5a). This shift is influenced by the recovery rates: γ_{h_2}, which governs the transition from the quarantine compartment (Q_h) to the recovered compartment, and γ_{h_1}, which dictates recovery directly from the infected compartment to the recovered compartment. Since the recovery time is significantly longer in the quarantine compartment (Q_h), an increase in the number of individuals in Q_h leads to this observed shift.

When we simultaneously applied the three control parameters: v (vaccination), b (social distancing), and q (quarantine), we observed a significantly sharper reduction in the infected cases curve compared to when these controls were applied individually (see Figure 5b). The combined effect of these measures demonstrates the enhanced efficacy of a multi-faceted approach in the monkeypox outbreak mitigation. Specifically, when v and b are both greater

than 0.0025, and q exceeds 0.075, the number of infected cases is almost entirely eradicated. This finding underscores the importance of implementing these control measures together to achieve maximum suppression of disease transmission and highlights their combined impact on the control of monkeypox outbreaks.
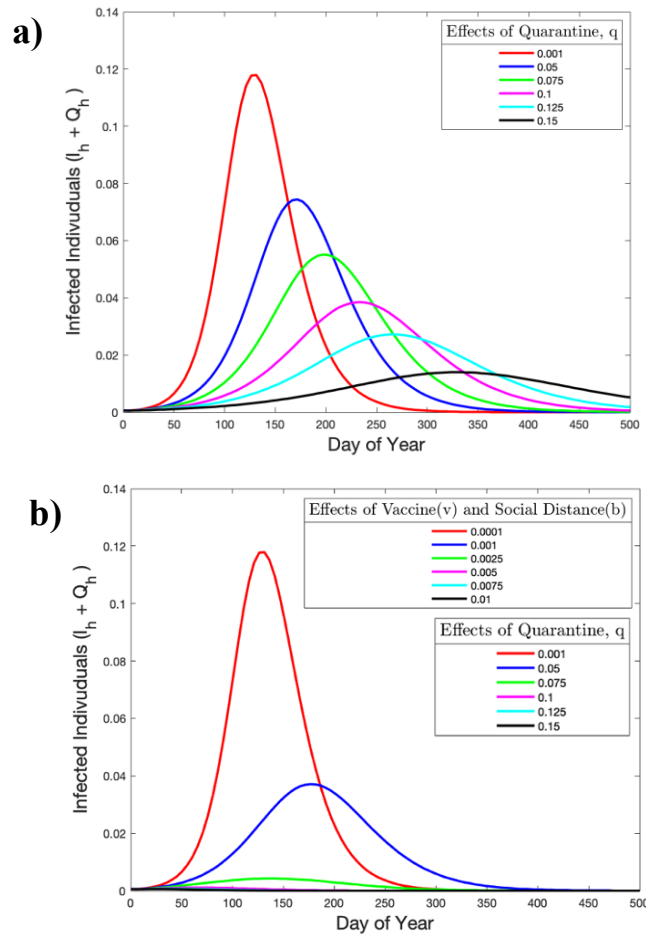
Figure 5. Plot a: the effect of quarantine on the infected cases. Plot b: the simultaneous combined effect of quarantine, vaccination and social distancing on the infected cases.

4   CONCLUSION AND SUGGESTIONS

In summary, our study provides a comprehensive analysis of the key parameters influencing the dynamics and control of the monkeypox outbreak, with a focus on stability analysis, sensitivity analysis, reproduction numbers, and the impact of control parameters. Stability analysis and Sensitivity analysis showed the importance of control parameters in the control of monkeypox outbreaks. Sensitivity analysis also revealed that parameters such as recovery rates and the incubation period play pivotal roles in shaping the outbreak trajectory. These findings highlight the importance of improving treatment quality and identifying infected

individuals quickly to mitigate disease spread effectively. Moreover, the significant role of human-to-human transmission (β_{hh}) compared to rodent-to-human transmission (β_{rh}) underscores the need for targeted interventions to disrupt transmission pathways most critical to the disease's basic reproduction number (R_0).

The investigation into the basic reproduction number further demonstrated that β_{hh} is nearly three times as influential as β_{rh} in determining R_0. This highlights the priority of focusing on human-to-human interactions when designing control strategies. Limiting direct transmission among individuals can have a far greater impact on reducing the overall spread than focusing on rodent-related transmission alone. Such insights are invaluable for allocating resources efficiently during an outbreak.

Finally, the analysis of control parameters v (vaccination), b (social distancing), and q (quarantine) emphasized their individual and combined effectiveness in reducing infected cases. While each parameter contributes meaningfully on its own, the simultaneous application of all three measures leads to a much sharper reduction in case numbers. Notably, when vaccination and social distancing parameters (v and b) exceed 0.0025, and the quarantine parameter (q) surpasses 0.075, the outbreak can be nearly eradicated. This demonstrates the power of a multifaceted approach, where integrating multiple control measures creates a synergistic effect, significantly enhancing outbreak mitigation.

In conclusion, our findings stress the necessity of a multifaced control strategy for the control of the monkeypox virus. By focusing on the most influential parameters and leveraging their combined effects, policymakers and health practitioners can design more effective interventions to manage and ultimately contain monkeypox disease outbreaks.

Conflict of Interest Statement

There is no conflict of interest between the authors.

Statement of Research and Publication Ethics

The study is complied with research and publication ethics.

Artificial Intelligence (AI) Contribution Statement

This manuscript was entirely written, analyzed, and prepared without the assistance of any artificial intelligence (AI) tools. All content, including text, data analysis, and figures, was solely generated by the author.

REFERENCES

[1]   P. R. Reed et al., "Monkeypox virus transmission and pathogenesis," *Journal of Infectious Diseases*, 2004.

[2]   Z. Jezek et al., "Human monkeypox," *American Journal of Tropical Medicine and Hygiene*, vol. 38, no. 2, pp. 3–13, 1988.

[3]   S. S. Bhullar et al., "Emerging zoonotic viral diseases: Insights into monkeypox and its management," *Medical Research Reviews*, 2022.

[4]   M. O. Sefiu, "Modeling the dynamics of rodent-human transmission of monkeypox using an SIQR-SEI framework," *Journal of Mathematical Epidemiology*, vol. 12, no. 3, pp. 256–271, 2024. *https://doi.org/10.38088/jise.1344860*

[5]   P. Emeka, M. Ounorah, F. Eguda, and B. Babangida, "Mathematical model for monkeypox virus transmission dynamics," *Epidemiology*, vol. 8, no. 3, p. 1000348, 2018, doi: 10.4172/2161-1165.1000348.

[6]   S. Somma, N. Akinwande, and U. Chado, "A mathematical model of monkeypox virus transmission dynamics," *Ife Journal of Science*, vol. 21, no. 1, pp. 195–204, 2019.

[7]   Q. Huang, Y. Sun, M. Jia, M. Jiang, Y. Xu, L. Feng, and W. Yang, "An effectiveness study of vaccination and quarantine combination strategies for containing mpox transmission on simulated college campuses," *Infectious Disease Modelling*, vol. 9, no. 3, pp. 805–815, 2024, doi: 10.1016/j.idm.2024.04.004.

[8]   M. S. Ullah and K. M. A. Kabir, "Behavioral game of quarantine during the monkeypox epidemic: Analysis of deterministic and fractional order approach," *Heliyon*, vol. 10, no. 5, p. e26998, 2024, doi: 10.1016/j.heliyon.2024.e26998.

[9]   R. Alharbi, R. Jan, S. Alyobi, Y. Altayeb, and Z. Khan, "Mathematical modeling and stability analysis of the dynamics of monkeypox via fractional-calculus," *Fractals*, vol. 30, Art. no. 2240266, 2022, doi: 10.1142/S0218348X22402666.

[10]   T. D. Frank, "Mathematical analysis of four SEIR-type models for monkeypox outbreaks: Human-animal interactions," *Mathematics*, vol. 12, no. 20, p. 3215, 2024, doi: 10.3390/math12203215.

[11]   O. J. Peter, F. A. Oguntolu, M. M. Ojo, O. Abdulmumin, A. O. Oyeniyi, R. Jan, and I. Khan, "Fractional order mathematical model of monkeypox transmission dynamics," *Physica Scripta*, vol. 97, no. 8, p. 084005, 2022, doi: 10.1088/1402-4896/ac7ebc.

[12]   O. I. Idisi, T. T. Yusuf, E. Adeniyi, A. A. Onifade, Y. T. Oyebo, A. T. Samuel, and L. A. Kareem, "A new compartmentalized epidemic model to analytically study the impact of awareness on the control and mitigation of the monkeypox disease," *Healthcare Analytics*, vol. 4, 2023, Art. no. 100267, doi: 10.1016/j.health.2023.100267.

[13]   P. O. J. Peter, S. Kumar, N. Kumari, F. A. Oguntolu, K. Oshinubi, and R. Musa, "Transmission dynamics of Monkeypox virus: a mathematical modelling approach," *Model Earth Syst Environ*, vol. 8, pp. 3423–3434, 2022, doi: 10.1007/s40808-021-01313-2.

[14]   R. Sah et al., "Monkeypox and its possible sexual transmission: Where are we now with its evidence?," *Pathogens*, vol. 11, no. 8, p. 924, 2022.

[15]   P. van den Driessche and J. Watmough, "Reproduction numbers and sub-threshold endemic equilibria for compartmental models of disease transmission," *Mathematical Biosciences*, vol. 180, pp. 29–48, 2002, doi: 10.1016/S0025-5564(02)00108-6.

[16]   O. Diekmann, J. A. P. Heesterbeek, and J. A. Metz, "On the definition and the computation of the basic reproduction ratio R₀ in models for infectious diseases in heterogeneous populations," *Journal of Mathematical Biology*, vol. 28, no. 4, pp. 365–382, 1990.

[17]   O. I. Idisi and T. T. Yusuf, "A mathematical model for Lassa fever transmission dynamics with impacts of control measures: Analysis and simulation," *European Journal of Mathematics and Statistics*, vol. 2, no. 2, pp. 19–28, 2021, doi: 10.24018/ejmath.2021.2.2.17.

[18]   E. J. Routh, *A Treatise on the Stability of a Given State of Motion, Particularly Steady Motion*. Cambridge, UK: Cambridge University Press, 1877.

[19]   A. Hurwitz, "Ueber die Bedingungen, unter welchen eine Gleichung nur Wurzeln mit negativen reellen Theilen besitzt," *Mathematische Annalen*, vol. 46, no. 2, pp. 273–284, 1895, doi: 10.1007/BF01446812.

[20]   G. Chowell, H. Nishiura, and L. M. A. Bettencourt, "Comparative estimation of the reproduction number for pandemic influenza from daily case notification data," *Journal of Theoretical Biology*, vol. 364, pp. 149–159, 2014, doi: 10.1016/j.jtbi.2014.08.004.

[21]   I. H. Aslan, M. Demir, M. M. Wise, and S. Lenhart, "Modeling COVID-19: Forecasting and analyzing the dynamics of the outbreak in Hubei and Turkey," *Mathematical Methods in the Applied Sciences*, vol. 45, no. 10, pp. 6481–6494, 2022, doi: 10.1002/mma.8181.

[22]   M. Demir, I. H. Aslan, and S. Lenhart, "Analyzing the effect of restrictions on the COVID-19 outbreak for some US states," *Theoretical Ecology*, vol. 16, pp. 117–129, 2023, doi: 10.1007/s12080-023-00557-1.

[23]   S. Marino, I. B. Hogue, C. J. Ray, and D. E. Kirschner, "A methodology for performing global uncertainty and sensitivity analysis in systems biology," *Journal of Theoretical Biology*, vol. 254, no. 1, pp. 178–196, 2008.

[24]   H. Joshi, M. Yavuz, S. Townley, and B. K. Jha. "Stability analysis of a non-singular fractional-order covid-19 model with nonlinear incidence and treatment rate". *Physica Scripta* 98.4 (2023): 045216.

[25]   H. Joshi. "Mechanistic insights of COVID-19 dynamics by considering the influence of neurodegeneration and memory trace", *Physica Scripta* 99.3 (2024): 035254

[26]   H. Joshi, and M. Yavuz. "Transition dynamics between a novel coinfection model of fractional-order for COVID-19 and tuberculosis via a treatment mechanism". *The European Physical Journal Plus* 138.5 (2023): 468.

[27]   H. Joshi, and B. K. Jha. Fractional reaction diffusion model for parkinson's disease, Proceedings of the International Conference on ISMAC in Computational Vision and Bio-Engineering 2018 (ISMAC-CVB). Springer International Publishing, 2019.

FLUOROQUINOLONE ANTIBIOTIC ADSORPTION ON THE FUNCTIONAL C$_{70}$ FULLERENES: A COMPUTATIONAL INSIGHT ON ADSORBENT APPLICATIONS

İskender MUZ [1] (iD)

[1]*Nevşehir Hacı Bektaş Veli University, Faculty of Art and Sciences, Department of Physics, Nevşehir, Türkiye,*
iskender023@gmail.com

ABSTRACT

Fluoroquinolone (FQ) adsorption on functional (Ca-, Fe-, Mg- and Zn-doped) C$_{70}$ fullerenes was investigated for the first time by density functional theory (DFT). Mg, Ca, Fe, and Zn doping were found to enhance sensitivity to FQ. The adsorption energies of functional C$_{70}$ fullerenes after FQ adsorption were found in the range of 23-37 kcal/mol. UV-Visible analysis reveals that the absorption maximum of the doped C$_{70}$ fullerenes shifts to a longer wavelength after the FQ adsorption. Moreover, the FQ adsorption significantly lowered the LUMOs in the Fe-doped C$_{70}$ fullerene. The Fe-doped C$_{70}$ fullerene also caused a notable decrease in band gap energy after FQ adsorption. Thus, Fe doping significantly increased the electrical conductivity, enabling the detection of FQ antibiotic on C$_{70}$ fullerene. The results revealed that Fe-doped C$_{70}$ fullerene may be a suitable adsorbent for FQ antibiotic.

Keywords: DFT, Fullerenes, Fluoroquinolone, Adsorbent.

1   INTRODUCTION

Fluoroquinolones (FQs) are a family of broad-spectrum antibiotics widely utilized to treat a various bacterial infections involving respiratory tract infections, urinary tract infections, gastrointestinal infections, and some skin infections [1], [2]. Through environmental factors such as agricultural runoff and wastewater irrigation, the FQs can penetrate and accumulate in the soil. Moreover, the FQs can persist for long periods of time after interaction with soil due to their low biodegradability. As a result, disruption of the soil microbiome can lead to various

environmental and health problems such as antibiotic resistance, plant uptake, and bioaccumulation in soil organisms [3], [4], [5], [6].

In recent decades, research has concentrated on examining the effectiveness of various adsorbent materials, such as activated carbon, clay minerals, ion exchange resins, and biochar, for removing fluoroquinolones [6], [7], [8]. However, most of these materials have some problems, such as high price and low adsorption ability [9], [10]. Therefore, there is a need for both low-cost and effective adsorbents to remove the FQs from contaminated environment.

Fullerenes are investigated for a variety of applications, including drug delivery, storage and adsorbents due to their unique structure and chemical stability. Furthermore, many studies shown that functional fullerenes can enhance their adsorption capacity and carrier properties [11], [12], [13], [14], [15], [16], [17], [18], [19], [20], [21], [22], [23]. N- and B-doped C_{70} fullerenes increase the sensitivity to mercaptopurine [24] and enhance the adsorption ability of pyrazinamide [25]. Al doping increases the adsorption ability of both C_{60} and C_{70} fullerenes, leading to stronger and more stable interactions with gemcitabine [26]. The Si- and Al-doped C_{70} fullerenes can effective materials for amphetamine detecting in various applications including drug monitoring and law enforcement [27]. This is due to changes in electronic properties that improve the binding interaction between drugs and functional C_{70} fullerenes. However, no study has specifically investigated the interaction between C_{70} fullerenes and the FQ antibiotic. Moreover, functional C_{70} fullerenes could be effective materials for detecting the FQ in various applications, including cancer therapy, drug administration and adsorbents. The purpose of study is to examine the possibility of the use of functional C_{70} fullerenes as an adsorbent to detect the FQ. The results including adsorption energies, HOMO – LUMO energy gaps, DOS, UV-visible absorption spectra and reactivity properties of pristine, Ca-, Fe-, Mg- and Zn-doped C_{70} fullerenes are examined by DFT/TD-DFT calculations [28].

2   COMPUTATIONAL DETAILS

Density functional calculations are carried out using Gaussian 09 software [29] on pristine, Ca-, Fe-, Mg- and Zn-doped C_{70} fullerenes, employing the B3LYP functional, 6-311G(d,p) basis set [30], and Grimme's three-parameter (GD3) empirical dispersion correction [31]. The density of spectra (DOS) are generated using GaussSum program [32]. Adsorption energies (E_{ad}) are generated by following equation:

$$E_{ad} = E\left(\frac{FQ}{Fullerenes}\right) - E(Fullerenes) - E(FQ) + E(BSSE) \qquad (1)$$

where BSSE is taken into consideration in the study because it produces accurate results in the calculation of weak interactions. Furthermore, the chemical hardness (η), chemical potential (μ), electrophilicity index (ω) and maximum amount of electronic charge index (ΔN_{tot}) are calculated from Koopman's theorem [33] using HOMO and LUMO energies as following: $\eta = (I - A)/2$, $\omega = \mu^2/2\eta$ and $\Delta N_{tot} = -\mu/\eta$. Multiwfn [34] and VMD [35] softwares used to calculate noncovalent interactions (NCI) and reduced density gradient (RDG). Additionally, TD-DFT calculations using the CAM-B3LYP functional [36] with the 6-311G(d,p) basis set are conducted to predict the UV-Vis absorption spectra.

3   RESULTS AND DISCUSSION

Figure 1 shows the electrostatic potential (ESP) patterns of the FQ and pristine C_{70} fullerene. The ESP is a quantity that reflects the potential energy stored in the field. Blue color show electro positivity, indicating that there is correlated with electron poor, while red color is presented for evaluation of electro negativity, indicating electron rich area (see Figure 1). The O and F atom of the FQ antibiotic is electron rich sites (in range of -0.02 – -0.03 a.u.). Since the O atom of FQ has a higher electronegativity than N, the electrostatic potential near O atom is stronger or more negative than near N atom. Moreover, the pristine C_{70} fullerene has a more neutral ESP pattern than FQ antibiotic.
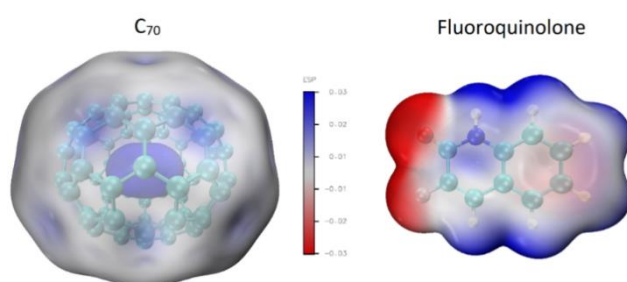
Figure 1. ESP patterns of pristine C_{70} fullerene (left) and FQ antibiotic (right).

The ESP patterns of functional C_{70} fullerene have been presented in Figure 2. The Ca, Fe, Mg and Zn doping to C_{70} fullerenes increases electronegativity by making the complex electron-rich, enhancing bonding capabilities. The functional C_{70} fullerenes with increased electronegativity may be more prone to interact with FQ. Therefore, functional C_{70} fullerenes result in stronger electron attraction of FQ antibiotic compared to pristine ones. In this study,

the results are investigated for electron transfers between functionalized C_{70} fullerenes and FQ which includes the electrons of red region (see Figure 2).
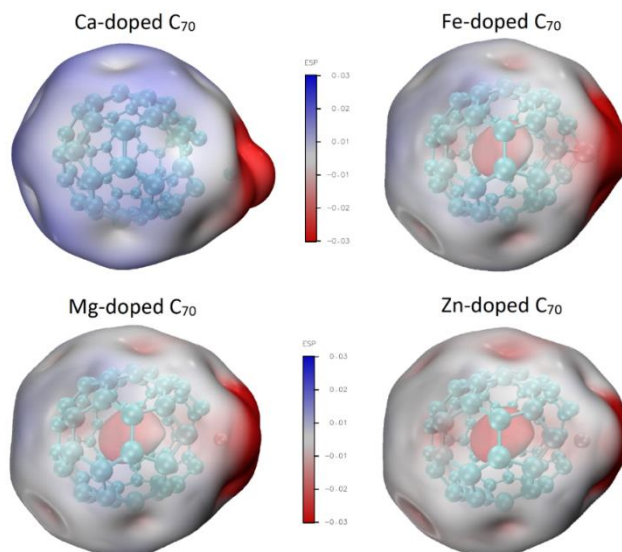
Figure 2. ESP patterns of functional C_{70} fullerenes.

Figure 3 shows the frontier molecular orbital analysis for FQ adsorption on pristine, Ca, Fe-, Mg- and Zn-doped C_{70} fullerenes.

Table 1. The calculated electronic parameters for pristine and functional C_{70} fullerenes before and after FQ adsorption.

Structure	E_g (eV)	LUMO (eV)	HOMO (eV)	ΔE_g	E_{ad} (kcal/mol)
C_{70}	2.68	-3.66	-6.34	-	-
C_{70}-FQ	2.69	-3.56	-6.25	0.37	-0.87
CaC_{70}	1.51	-4.00	-5.51	-	-
CaC_{70}-FQ	1.50	-3.47	-4.97	-0.66	-29.89
FeC_{70}	1.98	-3.88	-5.86	-	-
FeC_{70}-FQ	1.86	-3.40	-5.26	-6.06	-37.14
MgC_{70}	1.57	-4.33	-5.90	-	-
MgC_{70}-FQ	1.61	-3.64	-5.25	2.55	-34.42
ZnC_{70}	1.58	-4.49	-6.07	-	-
ZnC_{70}-FQ	1.65	-3.78	-5.43	4.43	-23.26

Frontier molecular orbital analysis helps to understand charge transfer processes by examining the interactions between the highest occupied molecular orbital (HOMO) of one molecule and the lowest unoccupied molecular orbital (LUMO) of another, which determines the ease and direction of electron transfer in a reaction. E_g values decreased in all the heterofullerenes after Ca and Fe, Mg and Zn doping was applied and electrical conductivity increased when compared to the pristine C_{70} fullerene results. The E_g values after Ca, Fe, Mg and Zn doping are found to be in the following decreasing order: pristine (2.68 eV) > Fe- (1.98

eV) > Zn- (1.58 eV) > Mg- (1.57 eV) > Ca- (1.51 eV). The E_g values of Ca- and Fe-doped C_{70} fullerenes before and after FQ adsorption are decreased, but Mg- and Zn-doped C_{70} fullerenes are increased (see Table 1). The percentage of difference of the HOMO-LUMO energy gap (ΔE_g) of complexes before and after FQ adsorption are shown in Figure 3. The ΔE_g values of Ca- and Fe-doped C_{70} fullerenes are slightly decreased in the range of 0.66 % and 6.06 %, but Mg- and Zn-doped C_{70} fullerenes are increased in the range of 2.55 % and 4.43 %. These results show that Ca and Fe doping and FQ adsorption increase electrical conductivity. Furthermore, Fe-doped C_{70} fullerene could be a suitable candidate for FQ adsorbents.
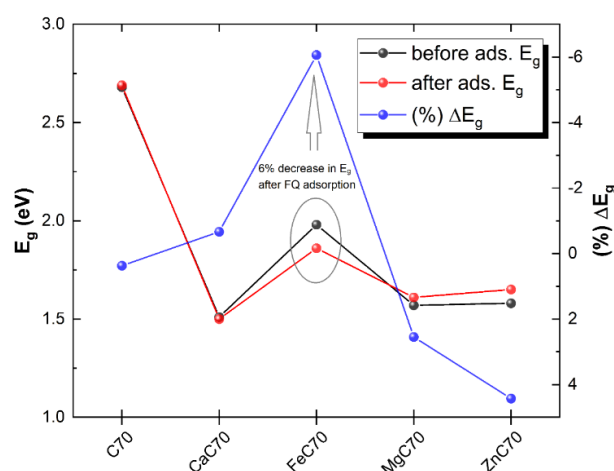
Figure 3. E_g and ΔE_g graphs before and after FQ adsorption.

Figure 4 shows the E_{ad} graph after FQ adsorption. Adsorption energy (E_{ad}) indicates to the energy change when a FQ antibiotic attaches to surface of a C_{70} fullerene. The E_{ad} values of pristine C_{70} fullerene is calculated to be -0.87 kcal mol^{-1}, indicating very low adsorption capacity. However, the E_{ad} drops sharply after Ca and Fe, Mg and Zn doping and it is calculated to be in the range of -29.89 and -37.14 kcal/mol.

Table 2. The calculated reactivity parameters for pristine and functional C_{70} fullerenes before and after FQ adsorption.

Structure	η (eV)	μ (eV)	ω (eV)	ΔN_{tot} (eV)
C_{70}	1.34	-5.00	9.33	3.73
C_{70}-FQ	1.35	-4.91	8.94	3.65
CaC_{70}	0.76	-4.76	14.97	6.30
CaC_{70}-FQ	0.75	-4.22	11.87	5.63
FeC_{70}	0.99	-4.87	11.98	4.92
FeC_{70}-FQ	0.93	-4.33	10.08	4.66
MgC_{70}	0.79	-5.12	16.66	6.52
MgC_{70}-FQ	0.81	-4.45	12.27	5.52
ZnC_{70}	0.79	-5.28	17.64	6.68
ZnC_{70}-FQ	0.83	-4.61	12.85	5.58
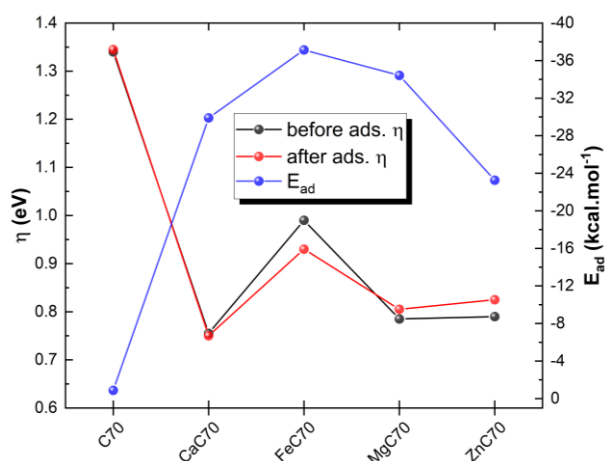
Figure 4. E_{ad} and η graphs for before and after FQ adsorption.

Table 2 lists quantum molecular descriptors, which are computational parameters derived from quantum chemical calculations that provide insights into a system's electronic structure, reactivity, stability, and interactions, helping predict chemical behavior and properties in various molecular systems. The chemical hardness (η) is described as a measure of a system's resistance to changes in its electron density. The η graph for before and after FQ is shown in Figure 4. After FQ adsorption, Fe-doped C_{70} fullerene has the highest hardness value (see Table 1). η value after both doping and adsorption is calculated to be in the following decreasing order: Fe- (0.93 eV) > Zn- (0.83 eV) > Mg- (0.81 eV) > Ca- (0.75 eV). This is followed by the fact that the electrophilic index (ω) and electronic charge index (ΔN_{tot}) seen in Table 2 have relatively lower values compared to the other doped (Ca, Mg and Zn) atoms. After FQ adsorption, Ca-doped C_{70} fullerene has the lowest hardness value. In other words, this is an indication that the complex is softer. Therefore, Ca-doped C_{70} fullerene is more reactive and can interact more strongly with the surfaces compared to the other dopant atoms. Comparing the graphs in Figure 4, after FQ adsorption, Fe-doped C_{70} fullerene has the highest hardness and adsorption energy. This may indicate that Fe-doped C_{70} fullerene binds to the FQ antibiotic by physical adsorption. In addition, Ca-doped C_{70} fullerene can bind to FQ antibiotic with stronger physical adsorption compared to Fe-doped C_{70} fullerene. For more detailed analysis of HOMO and LUMO changes of all complexes (CaC$_{70}$-FQ, FeC$_{70}$-FQ, MgC$_{70}$-FQ and ZnC$_{70}$-FQ) before and after FQ adsorption, DOS graphs were drawn and presented in Figures 5–6. HOMO and LUMO energies give insights into a molecule's electron-donating ability and electron-accepting ability, respectively. In addition, the energies of HOMO and LUMO are crucial in understanding the electronic character of complexes, reactivity, and its ability to absorb light.

Figure 5 shows the DOS plots of the doped (Ca, Fe, Mg and Zn) atoms compared to the pristine C_{70} fullerene in the range of -8.0-0.0 eV. The atoms doped to pristine C_{70} fullerene increase the HOMO value (see Table 1). Therefore, it is seen that the electron-donating tendency and electron-donating capacity of fullerenes increase after doping. The HOMO value of pristine C_{70} fullerene is calculated as -6.34 eV. The increase in HOMO values is found to be in the following decreasing order: Ca- (-5.51 eV) > Fe- (-5.86 eV) > Zn- (-5.90 eV) > Mg- (-6.07 eV). After doping, the HOMO value of Ca doped C_{70} fullerene is the highest and has increased from -6.34 to -5.51 eV compared to the pristine one. For this reason, the highest electron donation desire occurred with Ca doping and the lowest electron donation desire occurred with Mg doping. The LUMO value of pristine C_{70} fullerene is calculated as -3.66 eV. The decrease in LUMO values is found to be in the following increasing order: Ca- (-3.88 eV) < Ca- (-4.00 eV) < Mg- (-4.33 eV) < Zn- (-4.49 eV). After doping, the LUMO value of Ca doped C_{70} fullerene is the lowest and has decreased from -3.66 to -3.88 eV compared to the pristine one. Thus, the highest electron acceptance willingness has occurred with Fe doping.
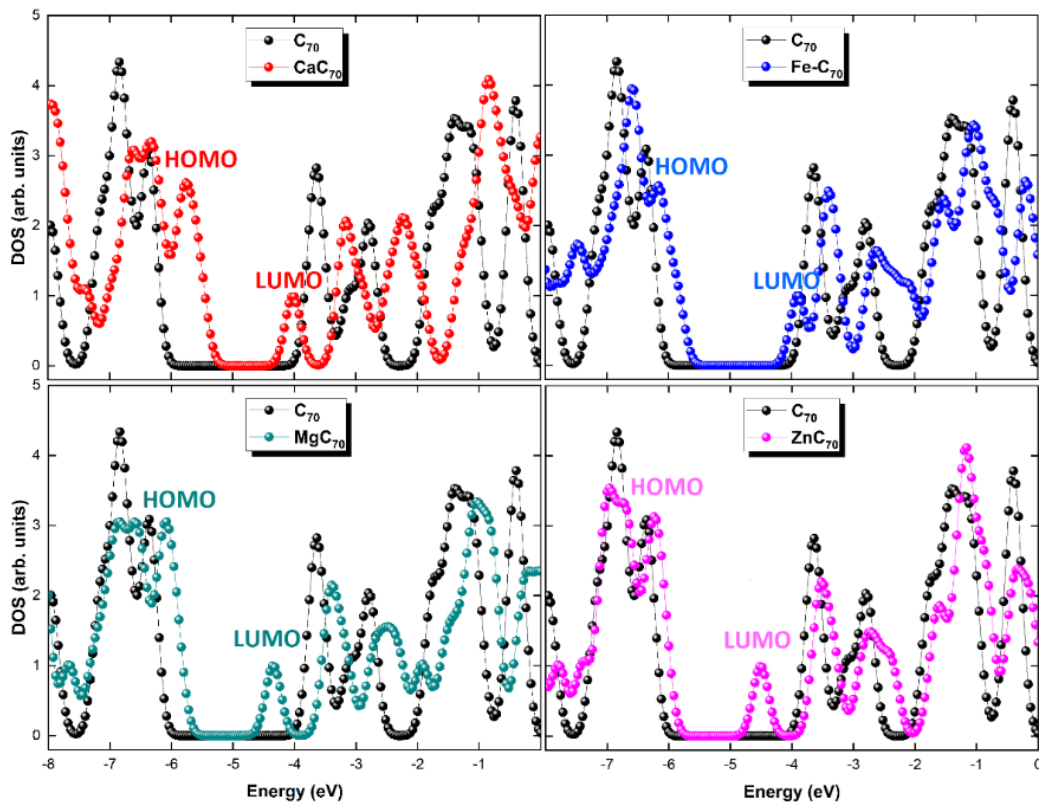
Figure 5. DOS of pristine and functionalized C_{70} fullerenes before FQ adsorption.
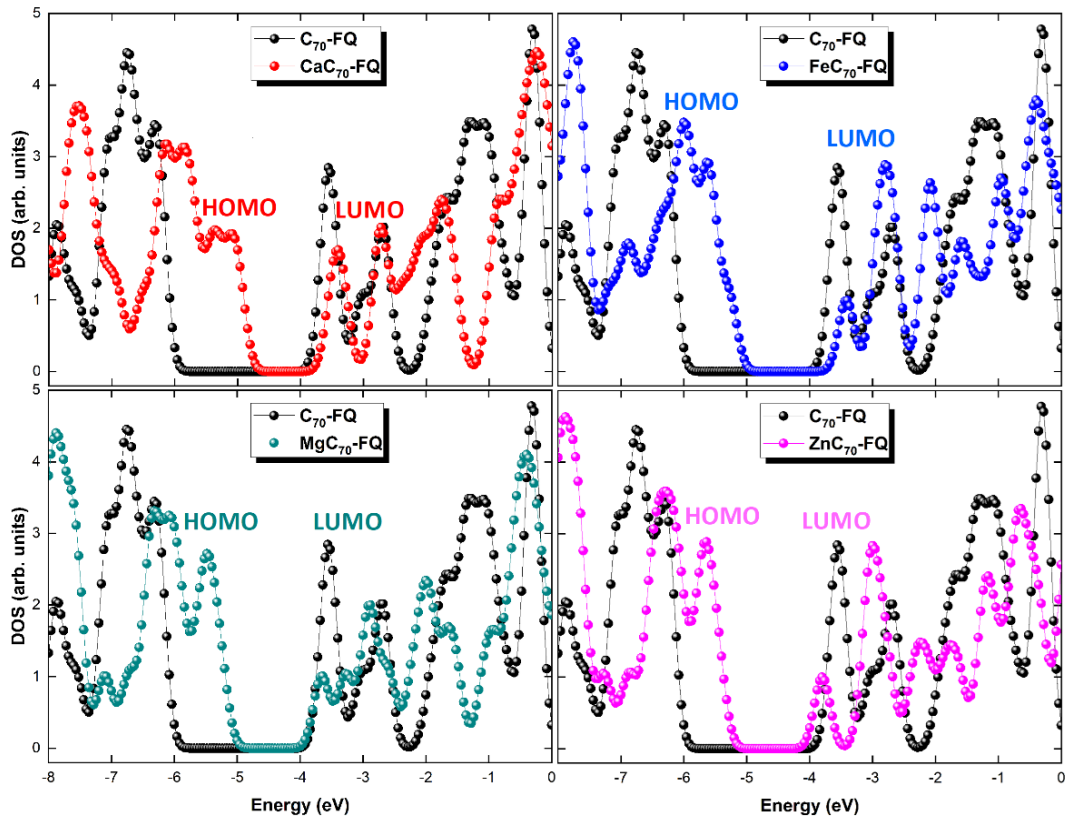
Figure 6. DOS of pristine and functionalized C₇₀ fullerenes after FQ adsorption.
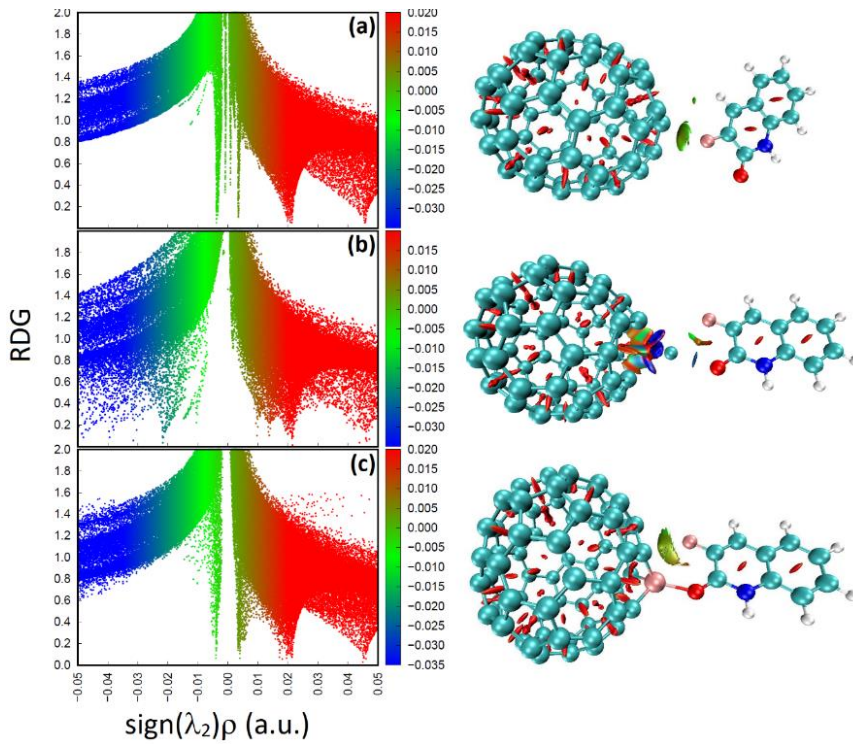
Figure 7. RDG plots and NCI isosurfaces of (a) pristine, (b) Ca- and (c) Fe-doped C₇₀ fullerenes after FQ adsorption.

Figure 6 shows the DOS graphs of CaC$_{70}$-FQ, FeC$_{70}$-FQ, MgC$_{70}$-FQ and ZnC$_{70}$-FQ complexes compared to pristine C$_{70}$ fullerene after FQ adsorption (C$_{70}$-FQ). HOMO values increase after doping and FQ adsorption (see Table 1). The HOMO value of C$_{70}$-FQ complex is calculated as -6.25 eV. The increase in HOMO values is found to be in the following decreasing order: Zn- (-5.43 eV) > Fe- (-5.26 eV) > Mg- (-5.25 eV) > Mg- (-4.97 eV). The decrease in LUMO values is calculated to be in the following decreasing order: Fe- (-3.40 eV) > Ca- (-3.47 eV) > Mg- (-3.64 eV) > Mg- (-3.78 eV). After FQ adsorption, the LUMO value of Fe doped C$_{70}$ fullerene is the lowest and has decreased from -3.56 to -3.40 eV compared to the pristine one (see Table 1). Thus, the highest electron acceptance willingness has occurred with both Fe doping and FQ adsorption.

When the E_g, ΔE_g and DOS values are examined, NCI and RDG analyses for two promising complexes (Ca- and Fe-doped C$_{70}$ fullerene) are presented in Figure 7. Low and high RDG values are represented by the blue color (electrostatic attraction) and red color (electrostatic repulsive), respectively. Furthermore, green color indicates regions with intermediate RDG values. These can represent places where noncovalent interactions are neither particularly strong nor weak. This could correspond to weak dipole-dipole interactions or Van der Waals forces. When RDG and NCI analyses are examined, it is seen that Ca-doped C$_{70}$ fullerene is in a stronger electrostatic attraction region to FQ antibiotic compared to Fe-doped C$_{70}$ fullerene. This supports that Ca-doped C$_{70}$ fullerene has a stronger physical adsorption compared to Fe-doped C$_{70}$ fullerene.
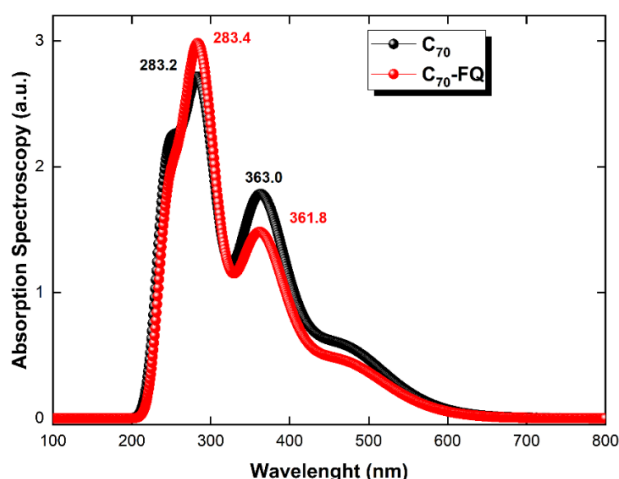
Figure 8. UV spectra of pristine C$_{70}$ fullerene before and after FQ adsorption.

Figures 8–9 show the UV–vis absorption spectra of pristine and functionalized C_{70} fullerenes before and after FQ adsorption, respectively. The UV–vis absorption spectra provide information about the light of absorption of the system in the ultraviolet (UV) and visible (vis) regions of the electromagnetic spectrum before and after FQ adsorption. The adsorption spectrum of pristine C_{70} fullerene shows a peak at 283.2 nm. After FQ adsorption, it showed a sharply peak at 283.4 nm with a very small shift (see Figure 8). Furthermore, it indicates that small changes occur in the pristine C_{70} fullerene environment without a major structural change or strong chemical reaction in the C_{70}-FQ complex. After FQ adsorption with Ca, Fe, Mg and Zn doping, the CaC_{70}-FQ, FeC_{70}-FQ, MgC_{70}-FQ and ZnC_{70}-FQ complexes show peaks at 283.6 nm, 290.4 nm, 281.6 nm and 276.8 nm, respectively (see Figure 9). In the Ca, Fe, Mg, and Zn-doped C_{70} complexes, the wavelength of the absorption maximum is shifted to a longer value after FQ adsorption. This serves as a clear indication of the alteration in the energy levels of the complex resulting from the interaction between FQ and doped C_{70} fullerenes. Furthermore, the shift of the maximum wavelength of Fe-doped C_{70} fullerene from 277.6 nm to 290.4 nm after FQ adsorption represents the largest shift compared to the others. It should also be noted that the strongest interaction may occur between Fe-doped C_{70} fullerene and FQ.
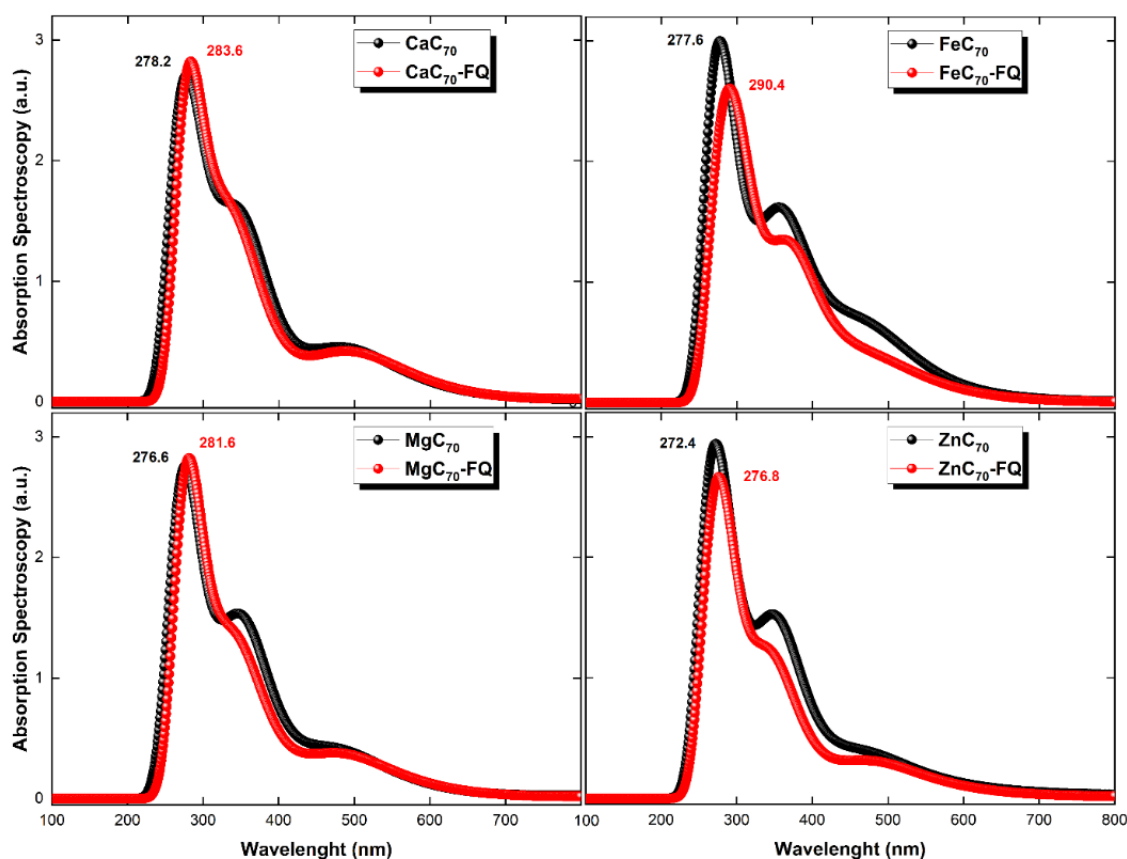
Figure 9. UV spectra of functionalized C_{70} fullerenes before and after FQ adsorption.

4 CONCLUSIONS

The adsorption of FQ antibiotic on the surface of four different functional C_{70} fullerenes has been examined using the DFT and TD-DFT methods. The FQ antibiotic is adsorbed onto the pristine C_{70} fullerene through its O-head, with an adsorption energy of around -0.87 kcal/mol. When the C atom of C_{70} is replaced by Ca, Fe, Mg and Zn atoms, adsorption energies increase and reach values between -23.26 and -37.14 kcal/mol. Time-dependent DFT calculations show that the absorption spectra of FQ/fullerene complexes shift toward higher wavelengths. The RDG and NCI analyses indicate that Ca-doped C_{70} fullerene exhibits a stronger region of electrostatic attraction to the FQ antibiotic compared to Fe-doped C_{70} fullerene. Ca, Fe, Mg and Zn doping causes small changes in HOMO and LUMO energies of functional C_{70} fullerenes. When the percentage values of the difference in band gap energies are compared, however, the electrical conductivity is significantly increased after FQ adsorption with Fe doping, which can enable the detection of FQ antibiotic on functional C_{70} fullerene. Fe-doped C_{70} fullerene causes a significant decrease in band gap energy after FQ adsorption. Thus, an increase in electrical conductivity occurs and an electrical signal can be generated. Furthermore, UV-Vis absorption spectra clearly indicate that the strongest interaction would be between Fe-doped C_{70} fullerene and FQ. The results of this study suggest that Fe-doped C_{70} fullerene may be a better adsorbent for FQ antibiotic.

Acknowledgment

Statement of Research and Publication Ethics

The study is complied with research and publication ethics.

Artificial Intelligence (AI) Contribution Statement

This manuscript was entirely written, edited, analyzed, and prepared without the assistance of any artificial intelligence (AI) tools. All content, including text, data analysis, and figures, was solely generated by the author.

REFERENCES

[1] Y. Xiang *et al.*, "Fabrication of sustainable manganese ferrite modified biochar from vinasse for enhanced adsorption of fluoroquinolone antibiotics: Effects and mechanisms," *Sci. Total Environ.*, vol. 709, p. 136079, Mar. 2020.

[2] S.-H. Chang, C.-C. Lu, C.-W. Lin, K.-S. Wang, M.-W. Lee, and S.-H. Liu, "Waste expanded polystyrene modified with H2SO4/biodegradable chelating agent for reuse: As a highly efficient adsorbent to remove fluoroquinolone antibiotic from water," *Chemosphere*, vol. 288, p. 132619, Feb. 2022.

[3] X. Liu, S. Lu, W. Guo, B. Xi, and W. Wang, "Antibiotics in the aquatic environments: A review of lakes, China," *Sci. Total Environ.*, vol. 627, pp. 1195–1208, Jun. 2018.

[4] X. Chi *et al.*, "Influent characteristics affect biodiesel production from waste sludge in biological wastewater treatment systems," *Int. Biodeterior. Biodegradation*, vol. 132, pp. 226–235, Aug. 2018.

[5] X. Van Doorslaer, J. Dewulf, H. Van Langenhove, and K. Demeestere, "Fluoroquinolone antibiotics: An emerging class of environmental micropollutants," *Sci. Total Environ.*, vol. 500–501, pp. 250–269, Dec. 2014.

[6] J. Kurasam, P. Sihag, P. K. Mandal, and S. Sarkar, "Presence of fluoroquinolone resistance with persistent occurrence of gyrA gene mutations in a municipal wastewater treatment plant in India," *Chemosphere*, vol. 211, pp. 817–825, Nov. 2018.

[7] S. A. C. Carabineiro, T. Thavorn-Amornsri, M. F. R. Pereira, and J. L. Figueiredo, "Adsorption of ciprofloxacin on surface-modified carbon materials," *Water Res.*, vol. 45, no. 15, pp. 4583–4591, 2011.

[8] Q. Wu, Z. Li, H. Hong, K. Yin, and L. Tie, "Adsorption and intercalation of ciprofloxacin on montmorillonite," *Appl. Clay Sci.*, vol. 50, no. 2, pp. 204–211, Oct. 2010.

[9] M. E. Peñafiel, J. M. Matesanz, E. Vanegas, D. Bermejo, R. Mosteo, and M. P. Ormad, "Comparative adsorption of ciprofloxacin on sugarcane bagasse from Ecuador and on commercial powdered activated carbon," *Sci. Total Environ.*, vol. 750, p. 141498, Jan. 2021.

[10] X. Peng, F. Hu, T. Zhang, F. Qiu, and H. Dai, "Amine-functionalized magnetic bamboo-based activated carbon adsorptive removal of ciprofloxacin and norfloxacin: A batch and fixed-bed column study," *Bioresour. Technol.*, vol. 249, pp. 924–934, Feb. 2018.

[11] E. S. Mirkamali, R. Ahmadi, K. Kalateh, and G. Zarei, "Adsorption of melphalan anticancer drug on the surface of fullerene (C-24): a comprehensive DFT study," *NANOMEDICINE J.*, vol. 6, no. 2, pp. 112–119, 2019.

[12] L. Zhang, Y.-L. Ye, X.-H. Li, J.-H. Chen, and W.-M. Sun, "On the potential of all-boron fullerene B40 as a carrier for anti-cancer drug nitrosourea," *J. Mol. Liq.*, vol. 342, p. 117533, Nov. 2021.

[13] C. Parlak and Ö. Alver, "A density functional theory investigation on amantadine drug interaction with pristine and B, Al, Si, Ga, Ge doped C60 fullerenes," *Chem. Phys. Lett.*, vol. 678, pp. 85–90, 2017.

[14] S. Bagheri Novir and M. R. Aram, "Quantum mechanical simulation of Chloroquine drug interaction with C60 fullerene for treatment of COVID-19," *Chem. Phys. Lett.*, vol. 757, p. 137869, Oct. 2020.

[15] F. Nattagh, S. Hosseini, and M. D. Esrafili, "Effects of B and N doping/codoping on the adsorption behavior of C60 fullerene towards aspirin: A DFT investigation," *J. Mol. Liq.*, vol. 342, p. 117459, Nov. 2021.

[16] İ. Muz, F. Göktaş, and M. Kurban, "A density functional theory study on favipiravir drug interaction with BN-doped C60 heterofullerene," *Phys. E Low-dimensional Syst. Nanostructures*, vol. 135, p. 114950, Jan. 2022.

[17] İ. Muz and M. Kurban, "A first-principles evaluation on the interaction of 1,3,4-oxadiazole with pristine and B-, Al-, Ga-doped C60 fullerenes," *J. Mol. Liq.*, vol. 335, p. 116181, 2021.

[18] İ. Muz, "Enhanced adsorption of fluoroquinolone antibiotic on the surface of the Mg-, Ca-, Fe- and Zn-doped C60 fullerenes: DFT and TD-DFT approach," *Mater. Today Commun.*, vol. 31, p. 103798, Jun. 2022.

[19] W. Li and T. Zhao, "Hydroxyurea anticancer drug adsorption on the pristine and doped C70 fullerene as potential carriers for drug delivery," *J. Mol. Liq.*, vol. 340, p. 117226, Oct. 2021.

[20]   S. Onsori and S. Montazeri, "Pyrazinamide Drug Adsorption on the Pristine and Doped C70 Fullerenes: A DFT/TDDFT Study," *J. Inorg. Organomet. Polym. Mater.*, vol. 31, no. 11, pp. 4222–4235, Nov. 2021.

[21]   A. S. Ghasemi, F. Ashrafi, S. A. Babanejad, and A. Elyasi, "Study of the Physicochemical Properties of Anti-Cancer Drug Gemcitabine on the Surface of Al Doped C60 and C70 Fullerenes: A DFT Computation," *J. Struct. Chem.*, vol. 60, no. 1, pp. 13–19, Jan. 2019.

[22]   W. Liu, J. Wei, and Y. Chen, "Electrospun poly(L-lactide) nanofibers loaded with paclitaxel and water-soluble fullerenes for drug delivery and bioimaging," *New J. Chem.*, vol. 38, no. 12, pp. 6223–6229, Nov. 2014.

[23]   M. K. Kiani, A. S. Ghasemi, and F. Ravari, "Theoretical study on carbonaceous materials as high efficient carriers for crizotinib drug in liquid water by density functional theory approach," *Struct. Chem.*, vol. 31, no. 4, pp. 1553–1561, Aug. 2020.

[24]   Y. Yang, A. Sun, and W. Gu, "Sensing behavior of pristine and doped C70 fullerenes to mercaptopurine drug: a DFT/TDDFT investigation," *Struct. Chem.*, vol. 32, no. 1, pp. 457–468, Feb. 2021.

[25]   S. Onsori and S. Montazeri, "Pyrazinamide Drug Adsorption on the Pristine and Doped C70 Fullerenes: A DFT/TDDFT Study," *J. Inorg. Organomet. Polym. Mater.*, vol. 31, no. 11, pp. 4222–4235, Nov. 2021.

[26]   A. S. Ghasemi, F. Ashrafi, S. A. Babanejad, and A. Elyasi, "Study of the Physicochemical Properties of Anti-Cancer Drug Gemcitabine on the Surface of Al Doped C60 and C70 Fullerenes: A DFT Computation," *J. Struct. Chem.*, vol. 60, no. 1, pp. 13–19, 2019.

[27]   E. Alipour, S. Maleki, N. Razavipour, N. Hajali, and S. Jahani, "Identification of amphetamine as a stimulant drug by pristine and doped C70 fullerenes: a DFT/TDDFT investigation," *J. Mol. Model.*, vol. 27, no. 6, p. 169, Jun. 2021.

[28]   M. Özcan, A. K. Havare, İ. Dervişoğlu, and Z. Yegingil, "DFT-based simulation for the semiconductor behavior of XGeCl3 (X=K, Rb) halide perovskites under hydrostatic pressure," *Phys. Scr.*, vol. 99, no. 10, p. 105914, Sep. 2024, doi: 10.1088/1402-4896/AD7243.

[29]   M. J. Frisch *et al.*, "Gaussian 09, Revision E.01," 2009.

[30]   A. D. Becke, "A new mixing of hatree-fock and local density functional theories," *J. Chem. Phys.*, vol. 98, no. 2, pp. 1372–1377, Jan. 1993.

[31]   S. Grimme, S. Ehrlich, and L. Goerigk, "Effect of the Damping Function in Dispersion Corrected Density Functional Theory," *J. Comput. Chem.*, vol. 32, no. 7, pp. 1456–1465, May 2011.

[32]   N. M. O'Boyle, A. L. Tenderholt, and K. M. Langner, "cclib: A library for package-independent computational chemistry algorithms," *J. Comput. Chem.*, vol. 29, no. 5, pp. 839–845, 2008.

[33]   T. Koopmans, "Über die Zuordnung von Wellenfunktionen und Eigenwerten zu den Einzelnen Elektronen Eines Atoms," *Physica*, vol. 1, no. 1–6, pp. 104–113, Jan. 1934.

[34]   T. Lu and F. Chen, "Multiwfn: A multifunctional wavefunction analyzer," *J. Comput. Chem.*, vol. 33, no. 5, pp. 580–592, 2012.

[35]   W. Humphrey, A. Dalke, and K. Schulten, "VMD: Visual molecular dynamics," *J. Mol. Graph.*, vol. 14, no. 1, pp. 33–38, 1996.

[36]   T. Yanai, D. P. Tew, and N. C. Handy, "A new hybrid exchange–correlation functional using the Coulomb-attenuating method (CAM-B3LYP)," *Chem. Phys. Lett.*, vol. 393, no. 1, pp. 51–57, 2004.

INVESTIGATION OF THE BEHAVIOR OF RC ELEVATED WATER TANKS ACCORDING TO TURKISH EARTHQUAKE CODES

Fatma ÜLKER PEKER [1*] iD

[1] *Malatya Turgut Özal University, Department of Civil Engineering, Malatya, Türkiye, fatma.peker@ozal.edu.tr*

ABSTRACT

Water tanks are critical structures that must be used without damage after an earthquake. Due to their vital importance, these structures are required to perform well under the influence of major earthquakes. In this study, the behavior of the RC elevated water tanks under earthquake effects was investigated. The water tank with a volume of 75 m^3, which is widely applied as a type project, was examined according to the calculation principles of the 1968, 1975, 1998, 2007, and 2018 earthquake codes. The analysis of the structure designed in the SAP2000 program was carried out according to the equivalent linear method. When the analysis results were compared according to the earthquake codes considered, it was concluded that the structure showed better behavior as the design criteria and calculation principles were improved from the 1968 earthquake code to the 2018 earthquake code. The comparative analysis results obtained from the study were evaluated specifically for an RC elevated water tank that was heavily damaged in the 6 February 2023 Kahramanmaraş earthquakes.

Keywords: Elevated water tanks, Earthquake code, Equivalent seismic load, Kahramanmaraş earthquakes.

1 INTRODUCTION

Earthquakes that occur as a result of sudden fractures in the earth's crust can have devastating effects on structures. Due to the significant losses and damages caused by major earthquakes, determining the behavior of structures against earthquakes is of great importance both in terms of ensuring the safety of life and property and in taking precautions against future earthquakes. Today, structures built using modern design and construction techniques generally

show good behavior against seismic effects, while old structures that do not receive the necessary engineering services are at risk [1-4].

On February 6, 2023, two major earthquakes occurred in the Pazarcık and Elbistan districts of Kahramanmaraş (MW= 7.7 and MW= 7.6). These earthquakes were devastating disasters that deeply affected 11 provinces and caused significant economic losses and deaths. As a result of these earthquakes, more than half a million buildings were damaged and collapsed. In addition to buildings, transportation networks, water storage and distribution systems, and energy transmission lines, which were of great importance after the earthquake, were also severely damaged. Due to the damage, there were problems in using these structures, also called lifelines, and therefore access to basic services was interrupted. As a result of these negativities, studies to determine the seismic safety of these structures, whose use should not be disrupted after the earthquake, have gained great importance [5-9].

Elevated water tanks are structures used primarily for drinking water storage and fire protection in a certain residential area. These structures are widely used in cities and industrial areas, and in recent years they have begun to be used in small settlements. After major earthquakes, it is desired that water tanks are not damaged, especially in large cities, both to fight fires and to prevent epidemics by providing clean water to the public. In this regard, it is vital to design water tanks to be earthquake resistant [10-12].

After major earthquakes affected many regions of the world, significant structural damage or collapses occurred in RC elevated water tanks (Figure 1). Water tanks are expected to remain functional after major earthquakes. It is very important to determine the seismic performance of these structures that need to be used immediately after the earthquake [13-16].

a)   b)   c)
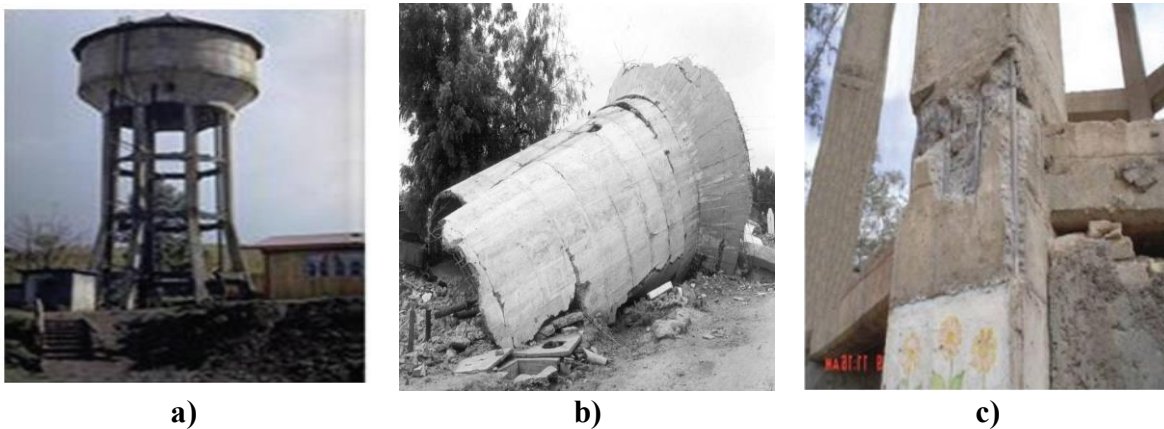
Figure 1. a-c) Examples of RC elevated water tanks damaged and collapsed in the earthquake [14, 15].

In the earthquake centered in Kahramanmaraş on February 6, 2023, it was observed that the structures in Türkiye were vulnerable to destructive earthquakes [17]. In recent times, our country has experienced major earthquakes, centered in Erzincan in 1992 (M_S=6.8), Dinar in 1995 (M_W=6.2), Adana-Ceyhan in 1998 (M_W=6.2), Kocaeli and Düzce in 1999 (M_W= 7.5 and M_W= 7.2), Van in 2011 (M_W=7.2), Elazığ in 2020 (M_W=6.8), and Kahramanmaraş in 2023 (M_W= 7.7 and M_W= 7.6). These earthquakes resulted in the loss of tens of thousands of lives and severe damage to thousands of structures. As a result of these earthquakes, earthquake-resistant structural design has become a current and important issue [17-19].

The Erzincan earthquake in 1939 caused heavy losses, and subsequently, the need to use earthquake codes to design earthquake resistant structures emerged. The earthquake codes have been continuously updated because of advancements in science and construction technologies. The current earthquake code (Turkish Building Earthquake Code-2018) was prepared much more comprehensively compared to previous codes. With this code, an AFAD-based earthquake calculation system was introduced in Türkiye. With this system, instead of regional calculations, precise earthquake data is obtained for each settlement. The Turkish Building Earthquake Code-2018 includes more precise seismic parameters compared to the previous earthquake code in terms of calculation principles and establishes a realistic and safe calculation method [18, 20, 21].

"Reinforced Concrete Elevated Water Tanks Type Projects" was published by the Ministry of Rural Affairs in 1971 as a reference for elevated water tanks. These types of projects have been continuously and widely implemented from the date of their publication up to the present day. The analysis and design of the existing water tank types were carried out according to the 1968 earthquake codes valid at the time of publication [11, 21-24].

There are few studies in the literature on the investigation of the dynamic behavior of elevated water tanks. Köksal et. al [25] examined the fluid-structure interactive behavior of a 1000 m³ volume RC elevated water tank under different seismic activities (Kocaeli, Van, Kahramanmaraş and Kobe earthquakes) using the Smoothed Particle Hydrodynamics (SPH) method with the Westergaard approach. The authors proved that considering the nonlinear behavior of the fluid during an earthquake with the SPH method provides consistency with the actual behavior of RC elevated water tanks and gives more realistic results than the traditional Westergaard approach. Gaikwad and Mangulkar [10] examined the dynamic response of RC elevated water tanks under static and dynamic loading, accounted for the hydrodynamic pressure effect of water. According to the detailed study and analysis results, it was found that

the response was significantly different with the equivalent static method and the dynamic method in the same region with the same capacity, the same geometry, the same height, the same importance factor and the response reduction factor. Demirören [11] explained the design rules of reinforced concrete elevated water tanks in detail and investigated their behavior under earthquake effects. In the study, the structural system of the water tank was considered as a type project, and the calculations were repeated for four different earthquake zones according to the 1998 earthquake code, and the relative storey drifts, rigidity irregularities and section effects of the columns were checked. Livaoğlu and Doğangün [16] investigated the effect of soil classes on the dynamic behavior of elevated water tanks with different structural systems. In the study, it was observed that the section effects occurring in the structural members of the elevated water tanks with two different load-bearing systems having the same tank volume were quite large by designing them according to the 1998 earthquake code and the 1st degree earthquake zone. Çelebioğlu [26] investigated the design of water tanks by taking into account the earthquake effect.

In this study, the seismic performance of critically important RC elevated water tanks that must be used immediately after an earthquake was investigated. Dynamic calculations of the structure were made separately according to the calculation principles of the 1968, 1975, 1997, 2007, and 2018 earthquake codes. The equivalent linear method based on period calculation, which started to be used with the 1968 earthquake code, was preferred as the calculation method. The reason why this method is preferred is that it is a common calculation method for all earthquake codes considered in this study. In this study, the RC elevated water tank type project with a volume of 75 m³, which is widely used in our country, was discussed. The tank was modeled and analyzed in the SAP2000 program in accordance with the type project. The analysis results were compared, and it was concluded that the design was safe for the structure according to the 2018 earthquake code. In order to show the effect of analysis results on the structure according to earthquake codes, an RC elevated water tank located in Malatya province and heavily damaged as a result of the 6 February Kahramanmaraş earthquakes was considered. The impact of earthquake codes on the damage status of this structure was examined.

The novelty of this study is to compare the design principles of the last five earthquake codes (1968, 1975, 1998, 2007, 2018) in the case of RC elevated water tank and to evaluate the seismic behavior of the water tanks under the influence of destructive earthquakes. After the Kahramanmaraş earthquakes, there were studies in the literature that evaluated seismic

behavior based on structural analysis, taking into account the damages occurring in different engineering structures. However, there are very few studies that include detailed structural analyses of water tanks and evaluate their seismic behavior after these earthquakes [25]. In this respect, the study will fill an important gap in the literature and make a significant contribution to earthquake engineering.

2 MATERIAL AND METHOD

2.1 Examination of Seismic Design Codes

In this section, the calculation principles in the last five earthquake codes starting from the 1968 earthquake code are explained in detail in order to determine the effect of the developments in the calculation methods in the earthquake codes on the dynamic behavior of the RC elevated water tank. When the calculation methods for these five codes are examined, it is noteworthy that the seismic calculation is made depending on the structure period based on empirical calculation, which is a common parameter in the codes.

As earthquake codes in Türkiye are updated, calculation methods have also been developed from simple to complex. Developments in the calculation method based on common parameters in earthquake codes are important in terms of seeing the change in the behavior of the structure and making correct comparisons. As a matter of fact, this comparison is decisive to see the effect of earthquake codes on the design of the structure.

In the literature, there are different studies examining the effects of changes in earthquake codes on structure design. Aksoylu and Arslan [27] compared the 2018 and 2007 earthquake codes in terms of calculation methods. For this purpose, they analyzed RC buildings with different storey heights and revealed the fundamental differences of the two codes in terms of seismic force calculation and control. Aksoylu et al [28] compared the 2007 and 2018 earthquake codes with the ASCE 7-16 earthquake code, taking into account parameters such as base shear force, top displacement, building period and relative-story displacement. Alyamaç and Erdoğan [29] examined the earthquake codes published from past to present in detail in terms of design and rules, and tried to determine how much the codes were complied with during the project and implementation stages. Işık [30] investigated the changes and innovations in the design principles according to the last five earthquake codes (1968, 1975, 1998, 2007 and 2018). In the study, the structural analysis of a 4-storey RC building was carried out and the analysis results were compared according to the calculation and design principles

of each code. The author revealed that the changes and renewals in the earthquake codes were a necessity and a gain. Karaca et al. [31] investigated the effect of the innovative approach in the 2018 earthquake code on building design. In the study, the authors analyzed the buildings designed according to the 2018 earthquake code according to the 2007 earthquake code and compared the design differences in the earthquake codes. Nemutlu et al. [32] designed and analyzed 4- and 9-storey RC structures separately to show the design differences in the 2007 and 2018 earthquake codes and examined the changes in base shear forces. Nemutlu et al. [33] investigated the changes in the calculation principles by considering the 2007 and 2018 earthquake codes. The differences between the acceleration spectra of Bingöl and Elazığ provinces were examined in the study. The authors proved that the acceleration values in the 2018 earthquake code were more economical and safer than the acceleration values in the 2007 earthquake code. Balun et al. [34] studied the effect of base shear force by considering simplified design rules for cast-in-place RC buildings according to the 2018 earthquake code. As a result of the analyses performed in the study, a comparison was made between the simplified seismic calculation and the standard seismic calculation. The authors determined the favorable or unfavorable situations of the simplified calculation in terms of the seismic design class, local soil class and the number of floors of the structure.

2.1.1 Regulation about the Buildings Constructed in the Disaster Regions-1968

The seismic force (shear force occurring at the base level of the structure) acting on the structures is calculated according to Equation 1 to withstand the seismic forces applied along the main axes perpendicular to each other.

$$F = C \times W \tag{1}$$

where W is the total structure weight ($\sum Wi$) and C is the seismic coefficient. C coefficient is obtained according to Equation 2.

$$C = C_O \times \alpha \times \beta \times \gamma \tag{2}$$

In this equation, C_O is the seismic zone coefficient, α is the seismic site coefficient, β is the structure importance coefficient, and γ represents the structure dynamic coefficient. The period of the structure is determined according to Equation 3, unless it is calculated based on experimental or reliable technical data.

$$T = 0.09H/\sqrt{D} \tag{3}$$

In this equation, H is the height of the structure from its base, and D is the width of the structure in the direction parallel to the horizontal forces affecting the structure. The floor weight to be considered in the calculation of the total seismic force is calculated according to Equation 4.

$$W_i = G_i + n_i \times P_i \tag{4}$$

In this equation, G_i is the total of the dead loads on the i-th floor, P_i is the total of the live loads on the i-th floor, and n_i is the live load coefficient on the i-th floor. n_i is taken as 1 in structures such as cinemas, theaters, schools, stadiums, and, warehouses. The seismic force acting on the structure is distributed throughout the height of the structure, according to Equation 5.

$$F = Fi * \frac{(W_i\, h_i)}{\sum W_i\, h_i} \tag{5}$$

In this equation, Fi is the horizontal force acting on the i-th floor, W_i is the weight of the i-th floor, and h_i is the height of the i-th floor from the base level.

2.1.2 Regulation about the Buildings Constructed in the Disaster Regions-1975

The sum of the static equivalent horizontal loads to be used in earthquake resistant sizing of structures is determined by Equation 6.

$$F = C \times W \tag{6}$$

In this equation, C is the seismic coefficient and is calculated according to Equation 7.

$$C = C_0 \times K \times S \times I \tag{7}$$

Where C_0 is the seismic zone coefficient, K is the structural type coefficient, S is the structural dynamic coefficient, and I is the structure importance coefficient, respectively. The structure dynamic coefficient is calculated according to Equation 8.

$$S = 1/|0.8 + T - T_0| \tag{8}$$

In this equation, T is the natural vibration period of the structure, and T_0 is the soil fundamental period. The natural vibration period of the structure is calculated according to

Equation 3. The total structure weight to be used in calculating the seismic force is calculated according to Equation 9.

$$W = \sum_{i=1}^{N} w_i \tag{9}$$

In this equation, w_i is the floor weight and is determined according to Equation 10.

$$w_i = g_i + nP_i \tag{10}$$

Where g_i is the total of the dead loads on the i-th floor, P_i is the total of the live loads on the i-th floor, and n is the live load coefficient, respectively. In structures such as warehouses, $n = 0.8$ is taken. The seismic load acting on the floors is determined according to Equation 11.

$$V_{t=}\Delta F_N + \sum_{i=1}^{N} F_i \tag{11}$$

For $H > 25$ m, the value of the additional equivalent seismic load ΔF_N acting on the N-th floor of the structure is determined depending on the fundamental vibration period (T_1). For $H < 25$ m, $\Delta F_N = 0$ is taken. The remaining part of the total equivalent seismic load, except ΔF_N, is distributed to all floors of the structure, including the N-th floor, with Equation 12.

$$F_i = (V_t - \Delta F_N)\left[\frac{w_i H_i}{\sum_{j=1}^{N} w_j H_j}\right] \tag{12}$$

2.1.3 Regulation about the Buildings Constructed in the Disaster Regions-1998

The total equivalent seismic load acting on the structure in the earthquake direction considered is determined by Equation 13.

$$V_t = \frac{WA(T_1)}{R_a(T_1)} \geq 0.10A_0IW \tag{13}$$

Where V_t is the equivalent seismic load (base shear), W is the weight of the structure, $A(T_1)$ is the spectral acceleration coefficient, A_0 is the local seismic acceleration, $R_a(T_1)$ is the seismic load reduction coefficient, T_1 is the first natural period of the structure, and I is the

structure importance coefficient, respectively. The first natural period of the structure is calculated according to Equation 14, unless a more precise calculation is made.

$$T_1 = 2\pi \left[\sum_{i=1}^{N} (m_i d_{fi}^2) \Big/ \sum_{i=1}^{N} (F_{fi} d_{fi}) \right]^{1/2} \tag{14}$$

The spectral acceleration coefficient is determined according to Equation 15, and the seismic load reduction coefficient is determined according to Equations 16-17.

$$A(T) = A_0 IS(T) \tag{15}$$

$$R_a(T) = 1.5 + (R - 1.5) T / T_A \rightarrow (0 \leq T \leq T_A) \tag{16}$$

$$R_a(T) = R \rightarrow (T > T_A) \tag{17}$$

The computation of the floor weight to be taken into account in the calculation of the seismic force in the structure is made according to the formulas defined in the 1975 earthquake code.

2.1.4 Regulation about the Buildings Constructed in the Earthquake Regions-2007

According to this code, the seismic calculation method is the same as the calculation method in the 1998 earthquake code. Based on scientific data, the 1998 earthquake code prepared seismic calculation methods more comprehensively than previous codes. In this respect, the code includes a more realistic and detailed calculation procedure.

2.1.5 Turkish Building Earthquake Code-2018

In the direction of the earthquake considered (X), the total equivalent seismic load acting on the entire structure, $V_{tE}(X)$, is determined by Equation 18.

$$V_{tE}^{(X)} = m_t S_{aR}(T_p^{(X)}) \geq 0.04 m_t IS_{DS} g \tag{18}$$

In this equation, m_t is the mass of the structure, and $S_{aR}(T_p^{(X)})$ is the reduced design spectral acceleration calculated by taking into account the predominant period of the structure $(T_p^{(X)})$ in the earthquake direction under consideration. I is the structure importance coefficient, S_{DS} is the design spectral acceleration coefficient defined for the short period, and g is the gravitational acceleration. The reduced design spectral acceleration of the structure is

calculated according to Equation 19. The predominant period of the structure is determined according to Equation 14 by taking into account the earthquake direction (X).

$$S_{aR}(T) = S_{ae}(T)/R_a(T) \qquad (19)$$

Where $S_{ae}(T)$ is the corner period of the horizontal elastic design acceleration spectrum, and $R_a(T)$ is the seismic load reduction coefficient. The calculation of the horizontal elastic design acceleration spectrum and the seismic load reduction coefficient is summarized by Equations 20–25.

$$S_{ae}(T) = \left(0.4 + 0.6\frac{T}{T_A}\right)S_{DS} \rightarrow (0 \le T \le T_A) \qquad (20)$$

$$S_{ae}(T) = S_{DS} \rightarrow (T_A \le T \le T_B) \qquad (21)$$

$$S_{ae}(T) = \frac{S_{D1}}{T} \rightarrow (T_B \le T \le T_L) \qquad (22)$$

$$S_{ae}(T) = \frac{S_{D1}T_L}{T^2} \rightarrow (T_L \le T) \qquad (23)$$

$$R_a(T) = \frac{R}{I} \rightarrow (T > T_B) \qquad (24)$$

$$R_a(T) = D + \left(\frac{R}{I} - D\right)\frac{T}{T_B} \rightarrow (T \le T_B) \qquad (25)$$

In these equations, T_A and T_B are the horizontal elastic design acceleration spectrum corner periods, T_L is the transition period to the constant displacement region, R is the structural system behavior coefficient, and D is the overstrength coefficient, respectively. S_{DS} and S_{D1} are calculated according to Equations 26-27.

$$S_{DS} = S_S F_S \qquad (26)$$

$$S_{D1} = S_1 F_1 \qquad (27)$$

In these equations, S_S is the map spectral acceleration coefficient for the period of 0.2 s, S_1 is the map spectral acceleration coefficient for the period of 1.0 s, F_S is the local soil effect coefficient for the period of 0.2 s, and F_1 is the local soil effect coefficient for the period of 1.0 s. The total equivalent seismic load is expressed as the sum of the equivalent seismic loads acting on the floors of the structure in Equation 28.

$$V_{tE}^{(X)} = \Delta F_{NE}^{(X)} + \sum_{i=1}^{N} F_{iE}^{(X)} \qquad (28)$$

The additional equivalent seismic load acting on the N-th floor (top) of the structure is determined according to Equation 29.

$$\Delta F_{NE}{}^{(X)} = 0.0075 N V_{tE}{}^{(X)} \tag{29}$$

The remaining part of the total equivalent seismic load, except $\Delta F_{NE}{}^{(X)}$, is distributed to the structure floors, including the N-th floor, in accordance with Equation 30.

$$F_{iE}{}^{(X)} = \left(V_{tE}{}^{(X)} - \Delta F_{NE}{}^{(X)}\right)\left[\frac{m_i H_i}{\sum_{j=1}^{N} m_j H_j}\right] \tag{30}$$

2.1.6 Comparison of Earthquake Codes

Before the 1998 earthquake code, the 1968 and 1975 earthquake codes used a rough calculation approach in seismic calculation methods. Since the 1998 earthquake code, the calculation method has been prepared in more detail based on scientific data. The calculation methods in this code form the basis of the 2007 and 2018 earthquake codes. The concept of an earthquake zone has started to be used with this code, and an earthquake hazard map has been prepared. Calculation methods have been improved with the current 2018 earthquake code. In this code, the concept of an earthquake zone has been eliminated, earthquake hazard maps have been developed, and site-specific design spectrums have begun to be used. Figure 2 shows the earthquake zone map and earthquake hazard map [21, 24, 35-39].

(a) **(b)**
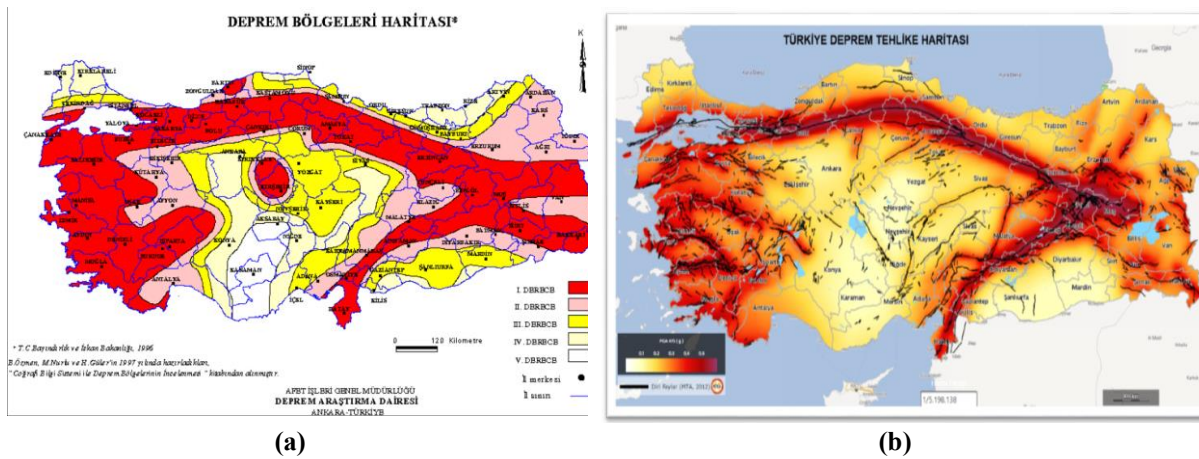
Figure 2. (a) 1996 Earthquake zone map, (b) 2018 Earthquake hazard map [38, 39].

2.2 Numerical Application

In this study, the RC elevated water tank type project with a volume of 75 m³ was discussed in the reference "Reinforced Concrete Elevated Water Tanks Type Projects" prepared

by the Ministry of Rural Affairs. The structure, which consists of six columns of 40x40 cm in size, is 25 m high, and there is a cylindrical water reservoir on the top floor. The design and analysis of the structure were performed using the SAP2000 program. The model of the structure created in the SAP2000 program is shown in Figure 3. While designing the structure, the columns and beams were modeled as frame elements and the tank as shell elements [40, 41].
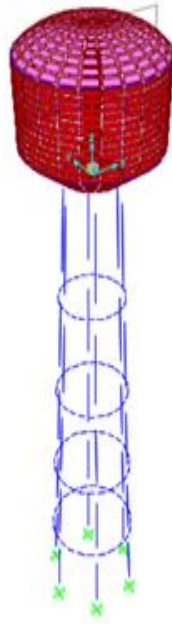
Figure 3. The SAP2000 model of the elevated water tank.

In order to determine the dynamic properties of the structure, modal analysis was first performed. The mode shapes, structural periods and mass participation ratios obtained as a result of the analysis were calculated. Modal analysis results are given in Table 1 and mode shapes are given in Figure 4.

According to the analysis results, high period values were obtained in the first two modes. The reason for this is that the stiffness and mass affecting the period of the structure are greatly affected by the height of the structure. The reason why the period and frequency values of the first two modes are the same is that the structure has symmetry in the x and y directions in terms of design features and the structural features are the same in both directions. When the mass participation ratios are examined, it is seen that the contribution of the first and second modes to the total response is about 89 percent. It is seen from the analysis results that torsion has no effect on the total response of the structure. In fact, it is understood from the plan of the structure that the floor masses are distributed uniformly in the building and coincide with the center of rigidity. In this case, only transverse displacement occurred in the structure; no

rotational displacement occurred since there was no torsional moment acting on the structure around the vertical axis.

Table 1. Modal analysis results.

Mode number	Direction	Period (s)	Frekans (Hz)	Participation factor (%)
1st	x	1.16	0.86	89.03
2nd	y	1.16	0.86	89.03
3rd	Torsion	0.87	1.15	0
4th	x	0.33	3.06	65.86
5th	y	0.33	3.06	65.86

Mode 1 (x)
T_1= 1.16 sec.

Mode 2 (y)
T_2= 1.16 sec.

Mode 3 (torsion)
T_1= 0.87 sec.
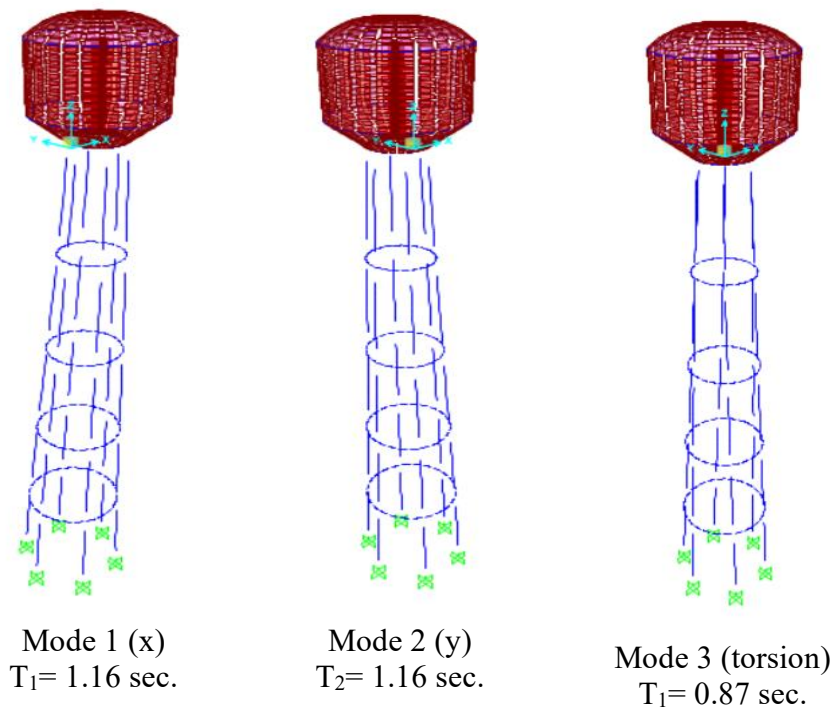
Figure 4. Mode shapes and period values of the structure.

During the dynamic analysis of the structure, the most critical stress concentrations were obtained for both directions of the earthquake by taking into account the loading conditions in the water tank. Stress values were calculated separately for the frame system carrying the reservoir and the reservoir. According to the analysis results, while there are no significant stress concentrations in the reservoir, it is seen that high compressive and tensile stresses occur in the column and beam supporting the reservoir in both directions of the earthquake (Figure 5). The stress values in the water tank are given in Table 2.

X direction   Y direction

(a)

X direction   Y direction

(b)
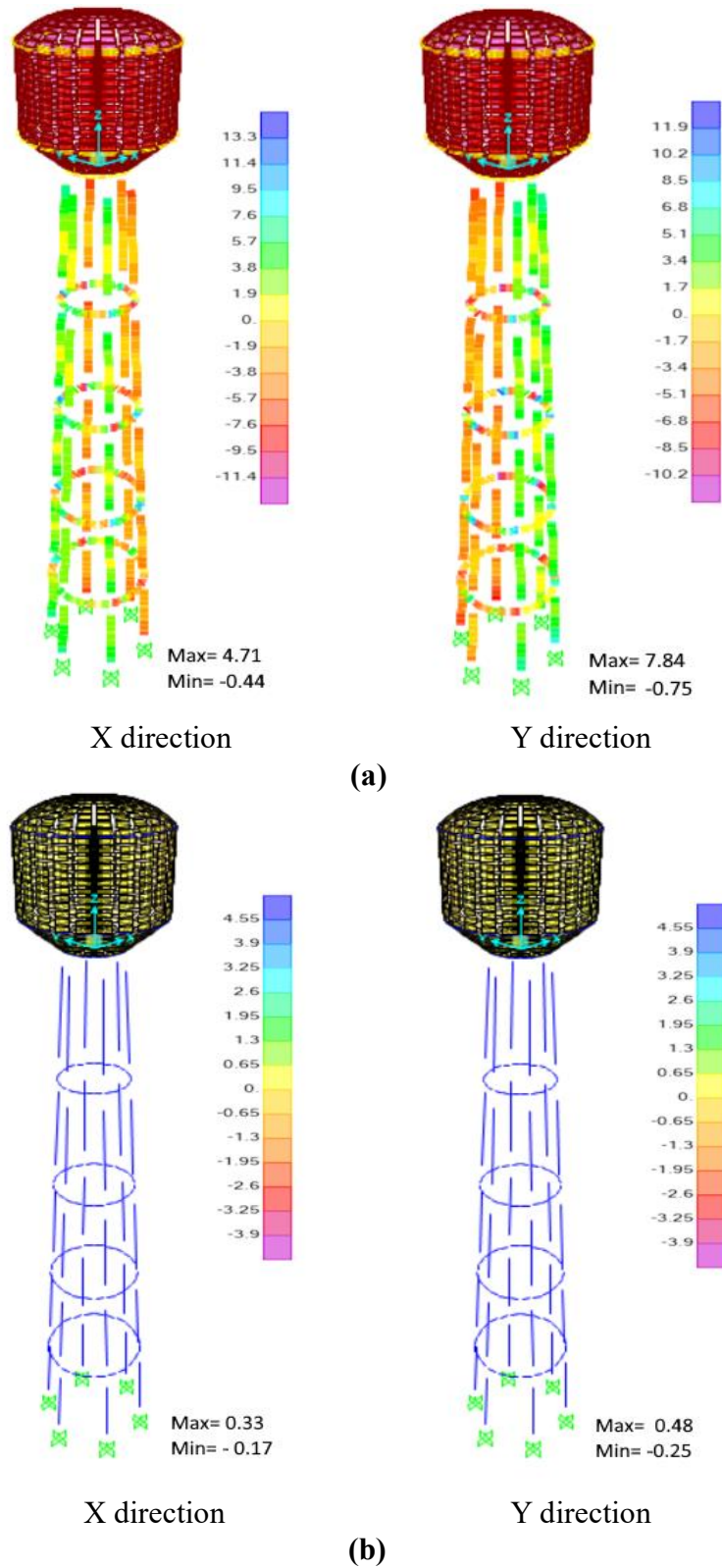
Figure 5. Stress concentration for water tank (MPa), (a) in the frame system (b) in the reservoir.

Table 2. Maximum stresses in the water tank.

Structural system	Compressive stresses (MPa)		Tensile stresses (MPa)	
Earthquake direction	x	y	x	y
Frame system	0.44	0.75	4.71	7.84
Reservoir	0.17	0.25	0.33	0.48

The dynamic calculation of the structure was carried out separately according to the principles of each earthquake code taken into account. The equivalent linear method was used as the dynamic calculation method. The seismic load calculated according to each earthquake code was defined separately in the SAP2000 program, and the dynamic analysis of the structure was carried out. According to this method, torsional moments of at least ±5% eccentricity at the geometric center of the structure, depending on the seismic forces acting on the floors, were included in the calculations. While performing dynamic calculations according to the 2018 earthquake code, dynamic parameters were obtained by assuming that the structure is located at a latitude of 38.38769° and a longitude of 38.16945° in Malatya Province. The self-weight of the structure, water load, hydrodynamic pressure effect of water, snow load, and wind load were used in the calculations as load effects. In the SAP2000 program, the weight of the structure under all these load effects was calculated as W = 1711.96 kN.

In the dynamic calculation of the structure according to 1968 earthquake codes, the C_O seismic zone coefficient was taken as 0.06, the seismic site coefficient as $\alpha = 1$, the structure importance coefficient as $\beta = 1$, the structure height as 29.7 m, and the structure width as 4.85 m, and the period of the structure was calculated as $T = 1.21$ s. Depending on the period of the structure, $\gamma = 0.41$ and the seismic coefficient $C = 0.025$ were determined. Thus, the seismic force was calculated as $F = 42.11$ kN. The floor weights calculated based on the seismic force are summarized in Table 3. The obtained forces were applied to the structure as equivalent seismic force in the SAP2000 program.

Table 3. Distribution of seismic force among floors according to the 1968 earthquake code.

Floor	W_i	H_i	$W_i \times H_i$	$F \times (W_i H_i)/\sum W_i H_i$
5	1143.41	25	28585.25	33.81
4	137.00	20	2740	3.24
3	140.41	15	2106.15	2.49
2	143.86	10	1438.6	1.70
1	147.28	5	736.4	0.87
Total	1711.96	-	35606.4	42.11

In the dynamic calculation of the structure according to 1975 earthquake codes, the seismic coefficient was taken as $C_0 = 0.10$, the structural dynamic coefficient was taken as $S = 1$, the structural type coefficient was taken as $K=3$, the structure importance coefficient was taken as $I = 1$, and the seismic coefficient C was calculated as 0.30. The seismic force was obtained as $F = 513.59$ kN. The floor weights calculated based on the seismic force are summarized in Table 4. The obtained forces were applied to the structure as equivalent seismic force in the SAP2000 program.

In the dynamic calculation of the structure according to 1998 earthquake codes, the first natural period was calculated as $T_1 = 0.64$ s. The local soil class was determined to be of type (B) according to the Z2 soil classification. The spectrum coefficient $S(T_1)$ was calculated to be 1.725. The seismic load reduction coefficient was taken as $R=4$ and the spectral acceleration coefficient was calculated as $A(T) = 0.69$. Thus, the total equivalent seismic load was calculated as $V_t = 295.30$ kN, and the additional equivalent seismic load acting on the N-th floor of the structure was calculated as $\Delta F_N = 13.15$ kN. The floor weights calculated based on the seismic force are summarized in Table 5. The obtained forces were applied to the structure as equivalent seismic force in the SAP2000 program.

Table 4. Distribution of seismic force among floors according to the 1975 earthquake code.

Floor	Wi	Hi	$W_i \times H_i$	$F \times (W_i H_i)/\sum W_i H_i)$
5	1143.41	25	28585.25	412.32
4	137.00	20	2740	39.52
3	140.41	15	2106.15	30.38
2	143.86	10	1438.6	20.75
1	147.28	5	736.4	10.62
Total	1711.96	-	35606.4	513.59

Table 5. Distribution of seismic force among floors according to the 1998 earthquake code.

Floor	Wi	Hi	$W_i \times H_i$	$F_i = (V_t - \Delta F_N)\left[\dfrac{w_i H_i}{\sum_{j=1}^{N} w_j H_j}\right]$	$F_i + \Delta F_N$
5	1143.41	25	28585.25	226.51	239.66
4	137.00	20	2740	21.71	21.71
3	140.41	15	2106.15	16.69	16.69
2	143.86	10	1438.6	11.40	11.40
1	147.28	5	736.4	5.84	5.84
Total	1711.96	-	35606.4	282.15	295.30

In the dynamic calculation of the structure according to 2007 earthquake codes, the first natural period of the structure as calculated as $T_1 = 0.51$ s. The local soil class was determined to be of type (B) according to the Z2 soil classification. The spectrum coefficient $S(T_1)$ was calculated to be 2.06. The seismic load reduction coefficient was taken as $R=4$ and the spectral acceleration coefficient was calculated as $A(T_1) = 0.824$. The total equivalent seismic load was calculated as $V_t = 352.66$ kN, and the additional equivalent seismic load acting on the N-th floor of the structure was calculated as $\Delta F_N = 13.22$ kN. The floor weights calculated based on the seismic force are summarized in Table 6. The obtained forces were applied to the structure as equivalent seismic force in the SAP2000 program.

Table 6. Distribution of seismic force among floors according to the 2007 earthquake code.

Floor	W_i	H_i	$W_i \times H_i$	$F_i = (V_t - \Delta F_N)\left[\dfrac{w_i H_i}{\sum_{j=1}^{N} w_j H_j}\right]$	$F_i + \Delta F_N$
5	1143.41	25	28585.25	272.51	285.73
4	137.00	20	2740	26.12	26.12
3	140.41	15	2106.15	20.08	20.08
2	143.86	10	1438.6	13.71	13.71
1	147.28	5	736.4	7.02	7.02
Total	1711.96	-	35606.4	282.15	352.66

In the dynamic calculation of the structure according to 2018 earthquake codes, the design spectrums were obtained from the Türkiye Earthquake Hazard Map Interactive Web Application [22]. In accordance with the ZC local soil class, the short period design spectral acceleration coefficient for 0.2 s (S_{DS}) was determined as 0.895 and the design spectral acceleration coefficient for the 1.0 s (S_{D1}) was determined as 0.317. Horizontal elastic design acceleration spectrum corner periods were calculated as $T_A = 0.071$ s and $T_B = 0.396$ s. In the horizontal elastic design spectrum, the transition period to the constant displacement region is $T_L = 6$ s. In the direction of the earthquake considered (X), the predominant period of the structure was calculated as $\left(T_p{}^{(X)}\right) = 0.51$ s.

The horizontal elastic design spectral acceleration value was obtained as $S_{ae}(T) = 0.622g$. Taking the structure importance coefficient $I = 1$, the seismic load reduction coefficient was determined as $R_a(T) = 8$. Depending on these parameters, the reduced design spectral acceleration value of the structure was $S_{aR}(T) = 0.078$. The total equivalent seismic load acting on the entire structure was calculated as $V_t = 133.53$, and the additional equivalent seismic load acting on the N-th floor of the structure was calculated as $\Delta F_N = 5$ kN. The floor

weights calculated based on the seismic force are summarized in Table 7. The obtained forces were applied to the structure as equivalent seismic force in the SAP2000 program.

Table 7. Distribution of seismic force among floors according to the 2018 earthquake code.

Floor	Wi	Hi	$W_i \times H_i$	$F_i = (V_t - \Delta F_N)\left[\dfrac{w_iH_i}{\sum_{j=1}^{N} w_jH_j}\right]$	$F_i + \Delta F_N$
5	1143.41	25	28585.25	103.20	108.20
4	137.00	20	2740	9.89	9.89
3	140.41	15	2106.15	7.60	7.6
2	143.86	10	1438.6	5.20	5.2
1	147.28	5	736.4	2.66	2.66
Total	1711.96	-	35606.4	128.55	133.53

The seismic force values calculated based on the equivalent linear method according to each earthquake code in the examined elevated water tank are summarized in Figure 6.
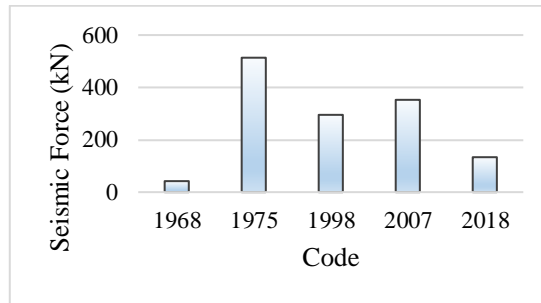
Figure 6. Comparison of seismic forces according to relevant codes.

The structural analysis results of the elevated water tank, which was analyzed in the SAP2000 program according to the relevant earthquake codes, are given in Table 8. The effects of compressive force and bending moment on the column members at the ground floor were taken into account. The maximum displacement in the structure occurred at the top point of the tank. When the analysis results in terms of base shear force, overturning moments, and displacement were examined, it was observed that the structural responses in the structure increase in proportion to the seismic forces.

Table 8. Comparative analysis results.

Codes	Structural effects				
	Max. displacement	Base shear force	Overturning moments	Compression force	Bending moment
1968	0.02	1360.7	37142.1	63.926	298.34
1975	0.26	16594.3	452959.5	779.615	3638.44
1998	0.15	9642	263231.9	342.36	2113.68
2007	0.18	11496.1	313842	408.86	2520.24
2018	0.06	4353.4	118845.5	521.78	3415.06

The displacement values obtained according to the relevant earthquake code are shown graphically in Figure 7. According to this, it is seen that the maximum value of peak displacement occurred in the 1975 earthquake code, while the minimum value occurred in the 1968 code.
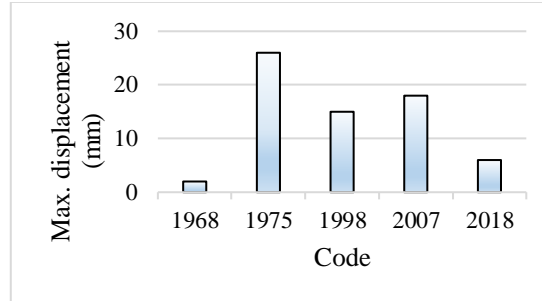
Figure 7. Change of displacement value in the structure according to the relevant codes.

According to the structural analysis results, the base shear force values obtained depending on the relevant earthquake code are shown graphically in Figure 8. It is seen that the maximum value of base shear force occurred in the 1975 earthquake code, while the minimum value occurred in the 1968 code.
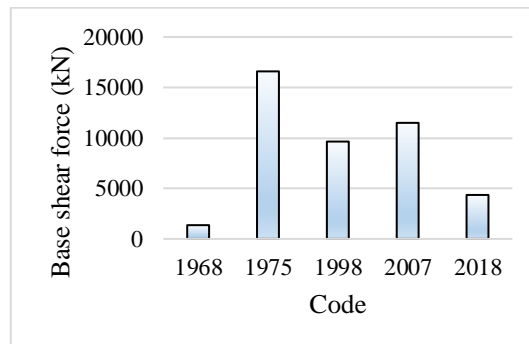
Figure 8. Change of base shear force value in the structure according to the relevant codes.

According to the structural analysis results, the overturning moment values obtained depending on the relevant earthquake code are shown graphically in Figure 9. It is seen that the maximum value of overturning moment occurred in the 1975 earthquake code, while the minimum value occurred in the 1968 code.
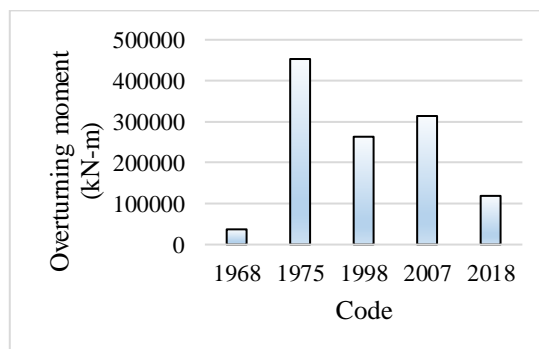
Figure 9. Change of overturning moment value in the structure according to relevant codes.

When the analysis results in Table 8 are examined, it is seen that the elevated water tanks are exposed to high forces and strained under the effect of the earthquake. Accordingly, the most reliable analysis results for the structure were obtained from the design according to the 2018 earthquake code. This is due to the advancement of calculation methods when earthquake code revisions and the improved adherence to the principle of ductility in design.

In the province of Malatya, which was affected by the Kahramanmaraş earthquakes, water tanks, like most engineering structures, were significantly damaged and became unusable. Figure 10 shows an RC elevated water tank located in the Yeşilyurt district that was heavily damaged as a result of the earthquakes in question. This water tank was constructed by selecting from the type project examples whose structural behavior was investigated in the study. As a result of the Kahramanmaraş earthquakes, major damage occurred to the columns and beams that form the load-bearing system of the elevated water tank.
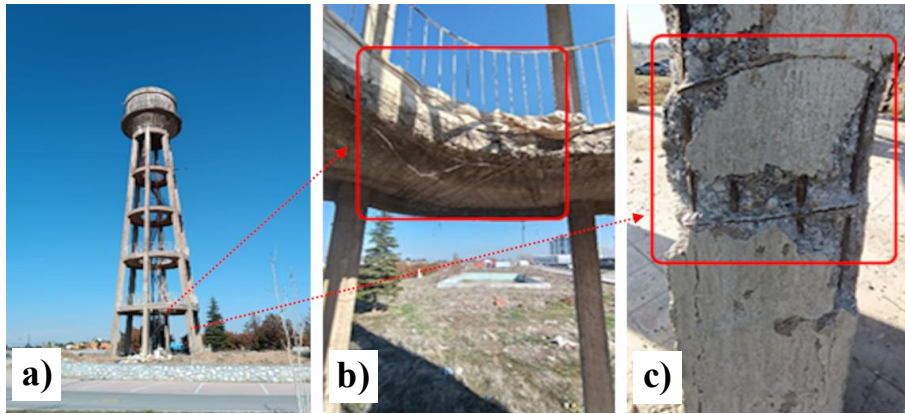
Figure 10. The RC elevated water tank damaged by the 6 February 2023 Kahramanmaraş earthquakes, a) general view, b) damaged ring beam, c) damaged column.

When the damage status of the structure was examined, it was observed that concrete failures, crushes, reinforcement buckling, and heavy reinforcement corrosion occurred in almost all of the beams and columns. As a result of these factors, it was determined that the structural members lost their carrying capacity and suffered severe damage. As seen in Figure 10, the main reasons for these damages in the structural members can be listed below.

- Aggregate granulometry is not suitable and therefore concrete quality is poor

- The reinforcement used has low strength

- All members have high stirrup spacing, and no stirrup densification was done

- Column sections are of inadequate size

As a result of all these deficiencies and defects, severe damage occurred to the structure in question. When the type project details of RC elevated water tanks, which are widely constructed in our country, are examined, a major deficiency in providing the necessary seismic performance of the structure is evident. The reason for this is the inadequacies in the structure design codes valid at the time when the type projects were prepared [21, 23, 24]. These inadequacies have manifested as deficiencies, including material classes, reinforcement ratios, and limitations on section ratios.

When the above analysis results are evaluated together with the damage state in the RC elevated water tank in Figure 10, it is concluded that the structure should be designed and constructed in accordance with the design conditions in the 2018 earthquake code to ensure its safety against earthquake effects.

3   RESULTS AND DISCUSSION

The use of lifeline structures after major earthquakes is of vital importance in ensuring social continuity. Water tanks are also one of the lifeline structures. These structures, which must be used uninterruptedly after major earthquakes, are expected to show good seismic behavior. However, after the Kahramanmaraş earthquakes, it was clearly seen that the necessary importance was not given in the design and construction processes of these structures. These structures received significant damage as a result of these earthquakes and their structural safety became critical. When the damage status was evaluated together with the design criteria in the current earthquake code, it was understood that the structure design was inadequate to ensure safety against earthquakes. As a result of this inadequacy, the effect of the design principles in the earthquake codes on the seismic behavior of the water tank was questioned.

In this study, the seismic behavior of the RC elevated water tank structure, which is of vital importance to be used undamaged after the earthquake, was investigated according to the earthquake codes of 1968, 1975, 1998, 2007, and 2018. An elevated water tank with a volume of 75 m³ was selected from the type project examples published by the Ministry of Rural Affairs, which is widely applied in our country, and its design was made in the SAP2000 program.

Modal analysis was performed to determine the dynamic properties of the structure. According to the analysis results, the same modal response results were obtained in both directions of the earthquake due to the design feature of the water tank. In the first two modes, the contribution of the structural mode to the total response is 89%. High period values were

obtained depending on the rigidity, mass properties, and height of the structure. It is also seen that torsion does not contribute to the dynamic response. Modal analysis results provide important information about the dynamic behavior of RC elevated water tanks.

Stress analysis was performed to better understand the behavior of the structure under seismic effects. In the water tank, stress values for the frame system and the reservoir were calculated separately. While no significant stress concentration occurred in the reservoir, very high compressive and tensile stresses occurred in the frame system. The most obvious reason for this is that the material properties and structural dimensions are inadequate against seismic effects in the structural members that statically support the weight of the reservoir. When the stress analysis results are evaluated specifically for the water tank in Figure 10, which was significantly affected by the Kahramanmaraş earthquakes, it is thought that the damages in the structure are due to being exposed to such high axial compressive and tensile stress cycles during the earthquakes.

In order to see the effect of design approaches in earthquake codes on the dynamic behavior of the water tank, the structural behavior of the tank was examined comparatively. For this purpose, seismic forces, displacements, base shear forces, and overturning moments in the structure were determined according to the calculation methods in all earthquake codes from the code valid on the date the type projects were published to the present day. The equivalent linear method was chosen as the dynamic calculation method.

Since the 1968 earthquake code, the equivalent linear method has been used in dynamic calculations of structures based on the structure period. This method continued to be developed and used in the 1975 earthquake code. In the 1998 earthquake code, the method was developed by including the effective ground acceleration coefficient depending on the earthquake zone and the spectrum coefficient depending on the local soil classes in the calculation formulations. In the 2007 earthquake code, the same calculation method continued to be applied, similar to the 1998 code, with some restrictions. The equivalent linear method with the 2018 earthquake code has been comprehensively developed based on the ductile design approach. According to this code, design acceleration spectra are obtained using Türkiye Earthquake Hazard Maps Interactive Web Application. Local ground effect calculations are made in more detail than in previous codes. With all these improved design principles, the most accurate results are obtained by making more realistic calculations according to the 2018 earthquake code.

When the dynamic analysis of the 75 m³ volume elevated water tank structure examined in this study is carried out separately according to the calculation principles of each earthquake code, it is seen that the most unfavorable results were obtained from the design according to the 1975 earthquake code. The reason for this is that there is a rough calculation method in this earthquake code, and the principle of ductility is not taken into consideration. With the 1998 earthquake code, calculation methods have been significantly improved, and the ductility requirement, which will contribute greatly to the seismic performance of structures, has begun to be taken into account in design. It was observed that the analysis results changed safely depending on the development of calculation methods from the 1975 earthquake code to the 2007 earthquake code. When the dynamic analysis of the structure was performed according to the current and valid 2018 earthquake code, more realistic and reliable analysis results were obtained.

4   CONCLUSION AND SUGGESTIONS

The water tank examined in this study is not an exceptional example. This example represents the general situation of RC elevated water tanks in Türkiye. In order for these structures to provide the necessary performance against future major earthquakes, the type projects used today need to be updated according to the 2018 earthquake code.

It was concluded that the structure showed better performance as the design criteria and calculation principles were improved from the 1968 earthquake code to the 2018 earthquake code. Obviously, structures in this situation are at risk. If structural repair and strengthening are not made by taking the necessary precautions, it is inevitable that a collapse will occur in the structure at any time.

In this study, the seismic behavior of RC elevated water tanks was investigated based on dynamic analysis. Apart from these structures, there are tank types with different materials and different design features. Similar studies can be conducted in the future to evaluate the seismic behavior of different tank types. This and similar studies will be a source for future studies.

Statement of Research and Publication Ethics

The study is complied with research and publication ethics.

Artificial Intelligence (AI) Contribution Statement

This manuscript was entirely written, edited, analyzed, and prepared without the assistance of any artificial intelligence (AI) tools. All content, including text, data analysis, and figures, was solely generated by the author.

REFERENCES

[1] Z. Celep, *Deprem Mühendisliğine Giriş ve Depreme Dayanıklı Yapı Tasarımı*. İstanbul: Beta Basım Yayım Dağıtım A.Ş., 2018.

[2] I. Onescu, A. Lo Monaco, N. Grillanda, M. Mosoarca, M. D'Amato, A. Formisano, G. Milani, F. Clementi, and M. Fofiu, "Simplified vulnerability assessment of historical churches in Banat seismic region, Romania," *International Journal of Architectural Heritage*, pp. 1–14, 2024, doi: https://doi.org/10.1080/15583058.2024.2341054.

[3] E. Arkan, E. Işık, E. Harirchian, M. Topçubaşı, and F. Avcil, "Architectural characteristics and determination seismic risk priorities of traditional masonry structures: A case study for Bitlis (Eastern Türkiye)," *Buildings*, vol. 13, no. 4, p. 1042, 2024, doi: https://doi.org/10.3390/buildings13041042.

[4] M. Leti and H. Bilgin, "Investigation of seismic performance of a premodern RC building typology after November 26, 2019 earthquake," *Structural Engineering and Mechanics*, vol. 89, no. 5, p. 491, 2024, doi: https://doi.org/10.12989/sem.2024.89.5.491.

[5] J. Yuzbasi, "Post-earthquake damage assessment: Field observations and recent developments with recommendations from the Kahramanmaraş earthquakes in Türkiye on February 6th, 2023 (Pazarcık M7.8 and Elbistan M7.6)," *Journal of Earthquake Engineering*, pp. 1–26, 2024, doi: https://doi.org/10.1080/13632469.2024.2353864.

[6] S. Avgın, M. M. Köse, and A. Özbek, "Damage assessment of structural and geotechnical damages in Kahramanmaraş during the February 6, 2023 earthquakes," *Engineering Science and Technology*, an International Journal, vol. 57, p. 101811, 2024, doi: https://doi.org/10.1016/j.jestch.2024.101811.

[7] F. Akar, E. Işık, F. Avcil, A. Büyüksaraç, E. Arkan, and R. İzol, "Geotechnical and structural damages caused by the 2023 Kahramanmaraş earthquakes in Gölbaşı (Adıyaman)," *Applied Sciences*, vol. 15, no. 5, p. 2165, 2024, doi: https://doi.org/10.3390/app14052165.

[8] C. Öser, S. Sargın, A. K. Yildirim, G. Korkmaz, E. Altinok, and M. K. Kelesoglu, "Geotechnical aspects and site investigations on Kahramanmaraş earthquakes, February 06, 2023," *Natural Hazards*, pp. 1–32, 2023, doi: https://doi.org/10.1007/s11069-024-07028-8.

[9] R. İzol, E. Işık, F. Avcil, M. H. Arslan, E. Arkan, and A. Büyüksaraç, "Seismic performance of masonry structures after 06 February 2023 earthquakes; site survey and FE modelling approach," *Soil Dynamics and Earthquake Engineering*, vol. 186, p. 108904, 2024, doi: https://doi.org/10.1016/j.soildyn.2024.108904.

[10] M. V. Gaikwad and M. N. Mangulkar, "Comparison between static and dynamic analysis of elevated water tank," *International Journal of Civil Engineering and Technology*, vol. 4, no. 3, pp. 12–29, 2013.

[11] R. Demirören, *Ayaklı betonarme su depolarının tasarım kuralları ve deprem etkisindeki davranışı*, M.S. thesis, Civil Engineering, Istanbul Technical University, İstanbul, Türkiye, 2005.

[12] G. W. Housner, "The dynamic behavior of water tanks," *Bulletin of the Seismological Society of America*, vol. 53, no. 2, pp. 381–387, 1963, doi: https://doi.org/10.1785/BSSA0530020381.

[13] N. D. Hadj-Djelloul, M. Djermane, N. Sharari, and S. Merabti, "Dynamic behavior of elevated water tanks under seismic excitation," *International Journal of Innovative Technology and Exploring Engineering,* vol. 9, no. 9, pp. 123–127, 2020.

[14] D. C. Rai, "Performance of elevated tanks in Mw 7.7 Bhuj earthquake of January 26th, 2001," *Journal of Earth System Science*, vol. 112, no. 3, pp. 421–429, 2003, doi: https://doi.org/10.1007/BF02709269.

[15]   S. Soroushnia, S. T. Tafreshi, F. Omidinasab, N. Beheshtian, and S. Soroushnia, "Seismic performance of RC elevated water tanks with frame staging and exhibition damage pattern," *Procedia Engineering*, vol. 14, pp. 3076–3087, 2011, doi: https://doi.org/10.1016/j.proeng.2011.07.387.

[16]   R. Livaoğlu and A. Doğangün, "Farklı taşıyıcı sisteme sahip ayaklı depoların zemin sınıflarına göre dinamik davranışlarının irdelenmesi," *Sakarya University Journal of Science*, vol. 7, no. 3, pp. 70–77, 2023.

[17]   U. Hancılar, K. Şeşetyan, E. Çaktı, E. Ş. N. Yenihayat, F. S. Malcıoğlu, K. Dönmez, T. Tetik, and H. Süleyman, *Strong ground motion and building damage estimations preliminary report,* Boğaziçi University, İstanbul, Türkiye, 2023.

[18]   M. T. Öztürk, *Eski deprem yönetmeliklerine göre boyutlandırılan betonarme binaların güncel yönetmeliğe göre deprem performansının belirlenmesi*, M.S. thesis, Civil Engineering, Istanbul Technical University, İstanbul, Türkiye, 2009.

[19]   E. Işık, F. Avcil, M. Hadzima-Nyarko, R. İzol, A. Büyüksaraç, E. Arkan, and Z. Özcan, "Seismic performance and failure mechanisms of reinforced concrete structures subject to the earthquakes in Türkiye," *Sustainability*, vol. 16, no. 15, p. 6473, 2024, doi: https://doi.org/10.3390/su16156473.

[20]   M. S. Döndüren, Ş. Hava, and A. S. Ecemiş, "Betonarme bir binanın eşdeğer deprem yükü yöntemi ile DBYBHY 2007 ve TBDY 2018 yönetmeliklerine göre analizi," *Konya Journal of Engineering Sciences*, vol. 9, no. 2, pp. 327–342, 2021, doi: https://doi.org/10.36306-konjes.867309-1529862.

[21]   TBEC, *Turkish Building Earthquake Code 2018*, Republic of Türkiye Ministry of Interior Disaster and Emergency Management Authority, Ankara, Türkiye, 2018.

[22]   DEMA, "Turkey earthquake risk map interactive web application," 2020. [Online]. Available: https://tdth.afad.gov.tr/TDTH/main.xhtml. Accessed: Nov. 23, 2024.

[23]   *T.C. Köy İşleri Bakanlığı, Betonarme Ayaklı Su Depoları Tip Projeleri*. Ankara, Türkiye, 1971..

[24]   ABYYHY-1968, *Regulation about the Buildings Constructed in the Disaster Regions – 1968*, Turkish Ministry of Construction and Settlement, Ankara, Türkiye, 1968.

[25]   O. Köksal, Z. Karaca, and E. Türkeli, "The effect of nonlinear sloshing response of water on seismic behavior of reinforced concrete elevated water tanks," *Periodica Polytechnica Civil Engineering*, vol. 68, no. 4, pp. 1328–1349, 2024, doi: https://doi.org/10.3311/PPci.23600.

[26]   M. F. Çelebioğlu, *Silindirik su deposu tasarımı*, M.S. thesis, Civil Engineering, Istanbul Technical University, İstanbul, Türkiye, 2004.

[27]   C. Aksoylu and M. H. Arslan, "2007 ve 2019 Deprem yönetmeliklerinde betonarme binalar için yer alan farklı deprem kuvveti hesaplama yöntemlerinin karşılaştırılması," *International Journal of Engineering Research and Development*, vol. 13, no. 2, pp. 359–374, 2021, doi: https://doi.org/10.29137/umagd.844186.

[28]   C. Aksoylu, A. Mobark, M. H. Arslan, and İ. H. Erkan, "A comparative study on ASCE 7-16, TBEC-2018 and TEC-2007 for reinforced concrete buildings," *Revista de la Construcción*, vol. 19, no. 2, pp. 282–305, 2020, doi: http://dx.doi.org/10.7764/rdlc.19.2.282.

[29]   K. Alyamaç and A. S. Erdoğan, "Geçmişten günümüze afet yönetmelikleri ve uygulamada karşılaşılan tasarım hataları," in *Deprem Sempozyumu*, Kocaeli, 2005.

[30]   E. Işık, "A comparative study on the structural performance of an RC building based on updated seismic design codes: Case of Turkey," *Challenge Journal of Structural Mechanics*, vol. 7, pp. 123–134, 2021, doi: https://doi.org/10.20528/cjsmec.2021.03.002.

[31]   H. Karaca, M. Oral, and M. Erbil, "Yapısal tasarım bağlamında 2007 ve 2018 deprem yönetmeliklerinin karşılaştırılması, Niğde örneği," *Niğde Ömer Halisdemir Üniversitesi Mühendislik Bilimleri Dergisi*, vol. 9, no. 2, pp. 898–903, 2020, doi: https://doi.org/10.28948/ngumuh.667365.

[32]   Ö. F. Nemutlu and A. Sarı, "Comparison of Turkish Earthquake Code in 2007 with Turkish Earthquake Code in 2018," *International Engineering and Natural Sciences Conference (IENSC 2018),* vol. 568, p. 76, 2018.

[33] Ö. F. Nemutlu, B. Balun, A. Benli, and A. Sarı, "Bingöl ve Elazığ illeri özelinde 2007 ve 2018 Türk deprem yönetmeliklerine göre ivme spektrumlarının değişiminin incelenmesi," *Dicle Üniversitesi Mühendislik Fakültesi Mühendislik Dergisi,* vol. 11, no. 3, pp. 1341–1356, 2020, doi: https://doi.org/10.24012/dumf.703138.

[34] B. Balun, Ö. F. Nemutlu, and A. Sarı, "TBDY 2018 basitleştirilmiş tasarım kurallarının taban kesme kuvvetine etkisinin incelenmesi," *Türk Doğa ve Fen Dergisi*, vol. 9, pp. 173–181, 2020, doi: https://doi.org/10.46810/tdfd.749257.

[35] ABYYHY-1975, *Regulation about the Buildings Constructed in the Disaster Regions – 1975*, Turkish Ministry of Public Works and Settlement, Ankara, Türkiye, 1975.

[36] ABYYHY-1998, *Regulation about the Buildings Constructed in the Disaster Regions – 1998*, Turkish Ministry of Public Works and Settlement, Ankara, Türkiye, 1998.

[37] DBYYHY-2007, *Regulation about the Buildings Constructed in the Earthquake Regions – 2007*, Turkish Ministry of Public Works and Settlement, General Directorate of Disaster Affairs Earthquake Research Department, Ankara, Türkiye, 2007.

[38] B. Özmen, M. Nurlu, and H. Güler, "Coğrafi bilgi sistemi ile deprem bölgelerinin incelenmesi," Turkish Ministry of Public Works and Settlement, General Directorate of Disaster Affairs, Ankara, 1997. [Online]. Available: https://gitrad.org.tr/wp-content/uploads/2022/02/cografibilgi.pdf. Accessed: Nov. 23, 2024.

[39] AFAD, *Türkiye Earthquake Hazard Map*, Disaster and Emergency Management Presidency, Ankara, Türkiye, 2018.

[40] TS500, *Design and Construction Rules of Reinforced Concrete Structures*, Turkish Standards Institute, Ankara, Türkiye, 2000.

[41] SAP2000 v22.1.0, *Structural Analysis Program*, Integrated Software for Structural Analysis and Design, Computers and Structures Inc., Berkeley, CA, USA, 2020.

GREEN SYNTHESIS OF SILVER NANOPARTICLES MEDIATED BY CINNAMON EXTRACT AND ITS POTENTIAL INSECTICIDAL EFFECT AGAINST *CALLOSOBRUCHUS MACULATUS* (F.) (COLEOPTERA: CHRYSOMELIDAE)

Fatma Nur ELMA [1] *, Masood HUSSAIN [2], Ahmet AVCI [3], Erol PEHLİVAN [4], Syed Tufail Hussain SHERAZI [5], Siraj UDDIN [6]

[1] *Selçuk University, Department of Plant Protection, Konya, Türkiye*
[2] *University of Sindh, National Center of Excellence in Analytical Chemistry, Jamshoro, Pakistan*
[3] *KTO Karatay University, Department of Mechatronics Engineering, Konya, Türkiye*
[4] *Konya Technical University, Department of Chemical Engineering, Konya, Türkiye*
[5] *University of Sindh, National Centre of Excellence in Analytical Chemistry, Jamshoro, Pakistan*
[6] *University of Karachi, HEJ Research Institute of Chemistry, International Center for Chemical and Biological Sciences, Karachi, Pakistan*
* Corresponding Author: fdundar@selcuk.edu.tr

ABSTRACT

Silver nanoparticles were successfully synthesized using cinnamon extract as a reducing agent. The synthesized nanoparticles, coated with cinnamon extract, were characterized through various optical and spectroscopic techniques. UV-visible spectroscopy confirmed the formation of cinnamon-extract-coated silver nanoparticles (Cinnamon-AgNPs) by optimizing parameters such as precursor salt concentration, pH, temperature and extract volume. The crystalline structure of the nanoparticles was examined using X-ray diffraction (XRD), while size distribution was analyzed through transmission electron microscopy (TEM). It was observed that cinnamon extract effectively stabilized silver nanoparticles and the average particle size was 23.3 nm, with a near-spherical shape. Advances in nanotechnology have recently offered novel approaches in plant protection strategies. The increasing resistance of stored-product pests like *Callosobruchus maculatus* to conventional insecticides necessitates the exploration of eco-friendly alternatives. In this study, the insecticidal activity of silver nanoparticles coated with cinnamon extract was evaluated against the adult stage of *Callosobruchus maculatus*. Additionally, the aqueous extract of cinnamon was also evaluated. Toxicity assays were conducted at varying concentrations of the nanoparticles and cinnamon extract, with exposure durations of 24, 48, and 72 hours. The results revealed that cinnamon-extract-coated silver nanoparticles exhibited the highest toxic effect at the highest concentration after 72 hours (60.72%). In contrast, the aqueous extract of cinnamon did not exhibit a significant toxic effect on *C. maculatus*. This significant difference highlights the synergistic insecticidal effect of the combination of silver nanoparticles and cinnamon extract. Overall, the findings highlight the significant potential of cinnamon-extract-mediated silver nanoparticles as an effective insecticidal agent against *Callosobruchus maculatus*.

Keywords: *Callosobruchus maculatus, Cinnamomum sp., Extract, Silver nanoparticles, Toxicitiy,* XRD.

1   INTRODUCTION

Nanomaterials research is a fascinating and distinctive field of science that plays an essential role in the advancement of modern technologies. The fabrication of metal nanoparticles offers exceptional properties by manipulating their size at the nanometer scale, which distinguishes them from their bulk materials. Metal nanoparticles have found applications in various domains, including agriculture [1], optical devices [2], photonics [3], biolabelling [4], biomedical [5], electrochemical analysis [6], biosensing [7], catalysis [8], information storage [9], and sensors [10]. Numerous synthesis methods have been reported in the literature, including, photochemical reduction [11], solvothermal [12], sonochemical [13], microwave-assisted [14], electrochemical [15], continuous-flow procedures [16], chemical reduction [17], physico-chemical [18], phytosynthesis [19], and thermal decomposition [20]. These traditional methods of metal nanoparticle synthesis often result in environmental contamination due to their reliance on hazardous chemicals and solvents.

In contrast, biosynthetic approaches to produce metal nanoparticles are considered environmentally friendly because they do not rely on harmful substances [21]. Recently, there has been a shift to bio-based nanoparticle synthesis, which is favored for its non-toxic and sustainable properties. Several plant extracts have been employed as both reducing and stabilizing agents in the synthesis of silver nanoparticles, including extracts from *Annona squamosa* peel extract, *Artocarpus heterophyllus*, *Curcuma longa* tuber, *Salvia fruticosa*, *Syzygium cumini*, *Cinnamomum zeylanicum* bark, *Hibiscus rosa-sinensis*, and other extracts. These extracts replace hazardous solvents by utilizing proteins, sugars, and flavonoid-based reducing agents [22], [23], [24].

The cowpea beetle, *Callosobruchus maculatus*, is a cosmopolitan insect pest. Its infestation often begins in the field when the mature pods dry, and once harvested and stored, the pest population rapidly increases, leading to destruction within 3-4 months [25], [26]. While chemical methods have effectively controlled these insects, continuous use has led to numerous negative side effects. As a result, alternative approaches to chemical insecticides have gained attention. Nanotechnology has emerged as a promising modern approach for insect pest management over the past two decades [27]. Recent studies in this field aim to increase pesticide effectiveness, reduce environmental pollution, and promote sustainable agricultural practices. For example, Dura *et al*. [28] reported that combining silver nanoparticles with plant extracts reduces the size of active substances in the plant content, allowing them to pass through

the cell walls of harmful microorganisms, thereby enhancing efficacy against pests. Plant-derived nano-formulations have been tested against various insect pests [29], [30], [31], [32], [33], but studies comparing the toxic effects of classical and nano-formulations synthesized from plants remain limited [34], [35], [36], [37]. Thus, the current study is the first to evaluate the toxic effects of silver nanoparticles (Ag NPs) synthesized with *Cinnamomum* extract, as well as the extract alone (prepared with water), against the adult stage of *Callosobruchus maculatus* (Coleoptera: Chrysomelidae).

2   MATERIAL AND METHOD

2.1   Chemicals and Reagents

During this study, high-purity chemicals and reagents were employed. NaOH (98%) and HCl (37%) were procured from Macron Fine Chemicals, while silver nitrate ($AgNO_3$, 97% pure) was sourced from Sigma-Aldrich. All reagents were directly used without any additional purification. Standards and solutions were prepared with deionized water, and all experimental procedures were performed at room temperature.

2.2   Fabrication and Characterization of plant extract protected AgNPs

The synthetic protocol involved the preparation of cinnamon root extract powder; this was achieved by grinding a sufficient quantity of cinnamon using a pestle and mortar. Fifteen grams of the powder were dissolved in 1000 mL of deionized water and left to sit for one day. After filtration, the extract was utilized to synthesize cinnamon-capped silver nanoparticles. For the one-step synthesis, 1.0 mL of 0.1 M $AgNO_3$ was mixed with 6.0 mL of deionized water in a beaker under magnetic stirring for 2 minutes. Subsequently, 3.0 mL of cinnamon root extract was added while stirring vigorously for 5 minutes. The mixture was left undisturbed to stabilize the nanoparticles.

A range of analytical techniques were employed to characterize the biosynthesized silver nanoparticles. An optimization study was conducted using a U-3900 spectrophotometer to refine reaction parameters. The crystalline structure of the extract-protected AgNPs was analyzed via X-ray diffraction (XRD) using a JES-FA/300 instrument. Morphological analysis was conducted using a high-resolution transmission electron microscope (HR-TEM, JEOLS).

2.3   Preparation of cinnamon extract

The preparation of cinnamon extract was conducted according to the method described by Velayutham *et al*. [38]. Fifty grams of powdered cinnamon samples were placed in Erlenmeyer flasks along with 500 mL of deionized water (previously boiled and cooled). The flasks were shaken using an electric shaker for 3 hours. The liquid phase was filtered through Whatman No. 1 filter paper. Deionized water was utilized for all dilutions prepared from the stock solution as well as for the control treatments.

2.4   Insect rearing

Adults of *Callosobruchus maculatus* were taken out from laboratory mass cultures reared in glass jars at $28 \pm 2°C$ and relative humidity of $60\pm10\%$ on cowpea. Newly emerged adults of *C. maculatus* (1-2 days old) from the laboratory culture were used for the experiments.

2.5   Toxic effect of cinnamon extract embedded AgNPs against Callosobruchus maculatus

During the laboratory trial, cinnamon extract and synthesized AgNPs were subjected to a dose–response bioassay for toxic effects on *Callosobruchus maculatus*. Different concentrations ranging from 5, 10, 20, 40 and 80 mg/l were prepared by diluting in sterile distilled water for synthesized AgNPs. Additionally, the extract of Cinnamon were prepared by diluting in sterile distilled water with 20, 40, 60, 80 and 100 mg/l concentrations. For each experimental treatment, 20 individuals were transferred to each of three Petri dishes. The aqueous cinnamon extract and synthesized AgNPs were topically applied to body surfaces by using a microsyringe as 2 µl for each concentration. Three replications were carried out for each concentration and control. Mortality was recorded every 24 hours for 3 days and the mortality data was corrected by using Abbot's formula [39].

3   RESULTS AND DISCUSSION

3.1   Synthesis and Characterization

UV-vis absorption of silver nanoparticles was confirmed in the spectra at 200-700 nm and analysis was carried out to optimize various reaction parameters. For this purpose, the optimization of concentration of salt was initially carried out and on the basis of more blue-shifted band in UV-vis spectra. Consequently, 0.3ml of 0.1M AgNO3 was optimized for further

study as depicted in Fig.1 (a). The observed plasma resonance peaked around at 435 nm, indicating the presence of silver nanoparticles in the solution [40], [41]. The inset photograph revealed that the initial solution was dark, and changes in concentration influenced the nanoparticle coloration. pH was identified as a critical factor in nanoparticle Based on peak shifts, pH 7 was chosen, as shown in Fig. 1(b), with corresponding color changes during the experiment also displayed in the inset.
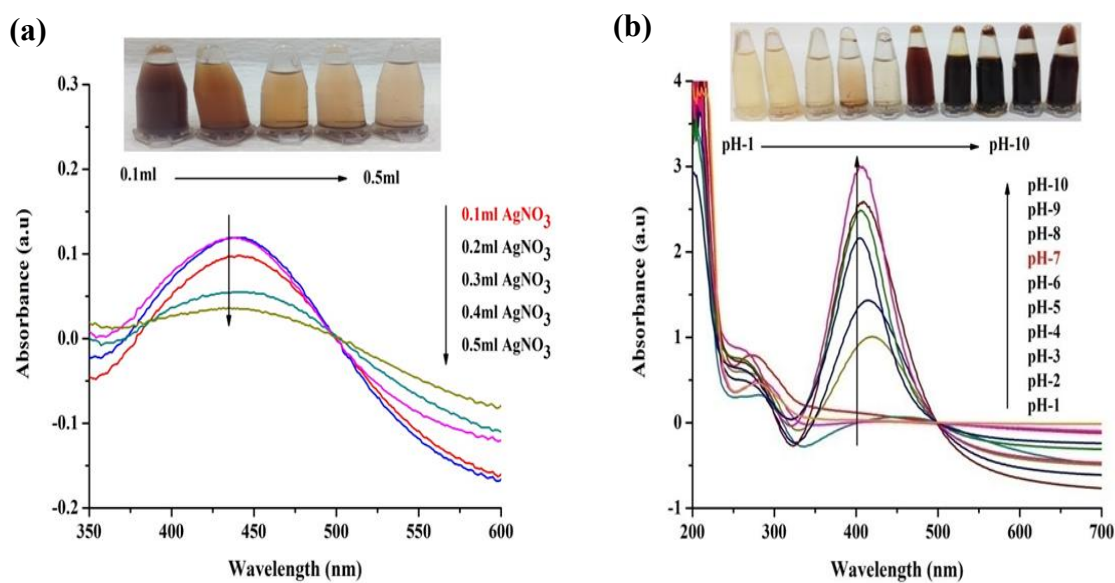
Figure 1. Optimization of 0.1M AgNO3 (a) and effect of pH on formation of cinnamon root extract capped AgNPs (b).

The optimization studies resulted in the production of small, narrowly distributed silver nanoparticles. The crystalline structure of the synthesized nanoparticles was confirmed using XRD analysis, with results presented in Fig. 2. The data indicated that the silver nanoparticles exhibited distinct crystalline peaks at 2Θ values of 38°, 44°, 63°, and 78°, corresponding to the (111), (200), (220), and (311) planes, respectively.
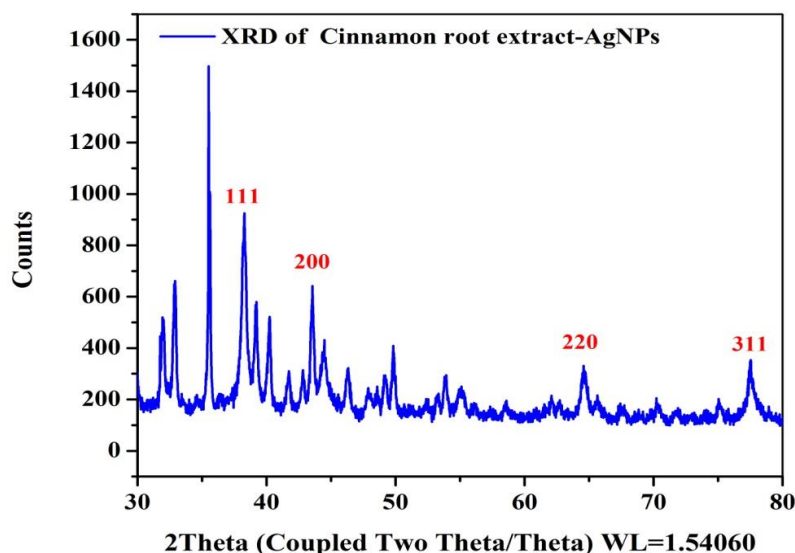
Figure 1. XRD pattern of Cinnamon root extract-protected silver nanoparticles.

Morphological analysis was conducted using a TEM instrument. The findings confirmed that the cinnamon extract effectively stabilized the silver nanoparticles, with an average particle size of 23.3 ± 2 nm, as depicted in Fig. 3(a) and (b). Furthermore, Fig. 3 highlighted the embedding of AgNPs within the cinnamon root extract matrix. The TEM images in Figure 3b show that the cinnamon-based nanoparticles are well-dispersed, round-shaped, and distinct from each other without aggregation.
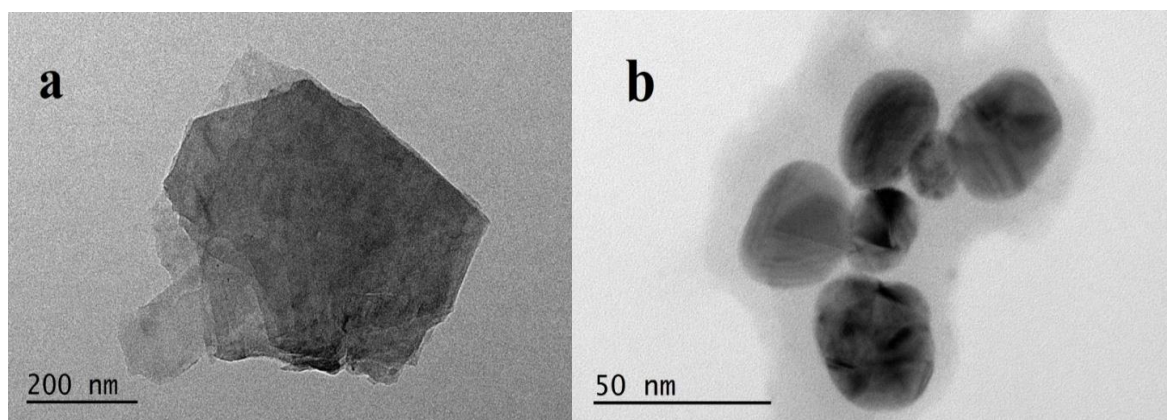
Figure 3. TEM images of a pure cinnamon root extract (a) and cinnamon root extract embedded AgNPs.

3.2   Toxic effects of Cinnamon embedded AgNPs against *Callosobruchus maculatus*

In this study, silver nanoparticles (AgNPs) were successfully synthesized using a green synthesis method with cinnamon extract. The insecticidal effect of the synthesized AgNPs was evaluated, and the results demonstrated that AgNPs coated with cinnamon extract exhibited

significant toxicity against *Callosobruchus maculatus*. The synthesized AgNPs showed higher mortality compared to the aqueous cinnamon extract, with a dose-dependent increase in effectiveness. The highest mortality rate (60.72%) was observed after 72 hours at the highest AgNP concentration. In contrast, the aqueous cinnamon extract alone exhibited a lower impact on *C. maculatus*, with mortality rates ranging from 12% to 33.33% at 48 and 72 hours (Table 1).

Table 2. Mortality of Callosobruchus maculatus adult at various concentrations of aqueous extract and synthesized AgNPs using Cinnamon.

Extract	Concentrations (mg/L)	24 h Mortality[a] %±SD	48 h Mortality[a] %± SD	72 h Mortality[a] % ± SD
Aqueous extract	20	3.34±1.20	12.06±1.67	14.04±1.02
	40	8.34±1.38	17.23±1.56	17.54±1.61
	60	10±1.24	24.13±1.26	28.07±1.89
	80	10±1.74	28.57±1.45	29.83±1.49
	100	11.66±0.96	30.35±1.58	33.3±1.69
Synthesized AgNPs	5	15±2.01	29.30±1.68	42.85±2.45
	10	23.3±1.98	34.48±2.86	48.21±2.05
	20	30±1.36	41.38±1.96	51.78±2.86
	40	35±2.28	51.72±2.35	57.14±2.78
	80	43.3±1.22	56.90±1.94	60.72±2.13

[a]The mortality was adjusted using Abbott formula

To our knowledge, no previous studies have investigated the insecticidal effects of cinnamon-derived silver nanoparticles (AgNPs) against *Callosobruchus maculatus*. While the toxicity of various nanoparticles towards *C. maculatus* and other insects (e.g., mosquitoes, rice weevils) has been reported [42], [38], [43], [44], [45], [33] research on the comparative insecticidal efficacy of plant-derived nano- and classical formulations remains limited [34],[35], [36], [37]. Balcı et al. [37] demonstrated that nano-formulations of *Melaleuca alternifolia* and *Azadirachta indica* extracts exhibited enhanced efficacy against *Tetranychus urticae* compared to their classical counterparts. Similarly, Al-Husseini et al. [39] reported that silver nanoparticles derived from *Punica granatum* displayed more significant greater toxicity against *Culex quinquefasciatus* than the corresponding ethanol extract. Our findings contribute to this limited body of knowledge by providing evidence of the insecticidal potential of cinnamon coated AgNPs against *C. maculatus*.

4   CONCLUSION AND SUGGESTIONS

A green and economical synthesis method was developed to create stable cinnamon-embedded silver nanoparticles (Ag NPs), using cinnamon as a dual protecting and reducing agent. This approach offers the advantages of simplicity, economic viability, environmental friendliness, ease of use, and high effectiveness. The resulting Ag NPs were characterized using advanced analytical techniques. Analysis revealed that the nanoparticles were uniformly small and highly stable.

Finally, the toxicity of the cinnamon-coated Ag NPs was assessed against adult *Callosobruchus maculatus* (Coleoptera: Chrysomelidae). Toxicity was evaluated over 24, 48, and 72-hour periods, using various concentrations of aqueous cinnamon extract (both with and without Ag NPs). The results demonstrated that the synthesized Ag NPs (at the highest concentration of 80 mg/L) exhibited maximal toxicity after 72 hours (60.72% mortality). In contrast, the cinnamon extract alone showed no significant effect on *C. maculatus*. However, the Ag NPs coated with cinnamon extract demonstrated a significant toxic effect on adult *C. maculatus*.

These findings, showing the significant toxicity of the cinnamon-coated Ag NPs, suggest their potential as botanical insecticides targeting *C. maculatus*. Further research is required to determine the precise mechanism of action and evaluate their efficacy under warehouse storage conditions. Future studies should also assess the effects on non-target organisms and consider the long-term environmental implications.

Conflict of Interest Statement

There is no conflict of interest between the authors.

Statement of Research and Publication Ethics

The study is complied with research and publication ethics.

Artificial Intelligence (AI) Contribution Statement

This manuscript was entirely written, edited, analyzed, and prepared without the assistance of any artificial intelligence (AI) tools. All content, including text, data analysis, and figures, was solely generated by the authors.

Contributions of the Authors

F. N. Elma contributed to the experimental studies, data interpretation, literature review and the preparation of the manuscript.

M. Hussain contributed to the experimental studies and the preparation of the manuscript.

A. Avcı contributed to the experimental studies, the preparation of the manuscript and editing.

E. Pehlivan contributed to the experimental studies.

S. T. H. Sherazi contributed to designing the study.

Sirajuddin contributed to designing the study.

REFERENCES

[1]   M. E. Demirbilek, "Tarım ve gıda nanoteknolojisi," *Gıda ve Yem Bilimi Teknolojisi Dergisi*, vol. 15, pp. 46–53, 2015.

[2]   P. Galletto, P. F. Brevet, H. H. Girault, R. Antoine, and M. Broyer, "Enhancement of the second harmonic response by adsorbates on gold colloids: The effect of aggregation," *J. Phys. Chem. B*, vol. 103, no. 41, pp. 8706–8710, 1999.

[3]   S. A. Maier, M. L. Brongersma, P. G. Kik, S. Meltzer, A. A. G. Requicha, and H. A. Atwater, "Plasmonics - A route to nanoscale optical devices," *Adv. Mater.*, vol. 13, no. 19, pp. 1501–1505, 2001.

[4]   S. R. Nicewarner-Pena et al., "Submicrometer metallic barcodes," *Science*, vol. 294, no. 5540, pp. 137–141, 2001.

[5]   C. A. Mirkin, R. L. Letsinger, R. C. Mucic, and J. J. Storhoff, "A DNA-based method for rationally assembling nanoparticles into macroscopic materials," in *Spherical Nucleic Acids*, Jenny Stanford Publishing, pp. 3–11, 2020.

[6]   C. M. Welch and R. G. Compton, "The use of nanoparticles in electroanalysis: A review," *Anal. Bioanal. Chem.*, vol. 384, no. 3, pp. 601–619, 2006.

[7]   M. Han, X. Gao, J. Z. Su, and S. Nie, "Quantum-dot-tagged microbeads for multiplexed optical coding of biomolecules," *Nat. Biotechnol.*, vol. 19, no. 7, pp. 631–635, 2001.

[8]   H. Tsunoyama, H. Sakurai, N. Ichikuni, Y. Negishi, and T. Tsukuda, "Colloidal gold nanoparticles as catalyst for carbon-carbon bond formation: Application to aerobic homocoupling of phenylboronic acid in water," *Langmuir*, vol. 20, no. 26, pp. 11293–11296, 2004.

[9]   S. Sun, C. B. Murray, D. Weller, L. Folks, and A. Moser, "Monodisperse FePt nanoparticles and ferromagnetic FePt nanocrystal superlattices," *Science*, vol. 287, no. 5460, pp. 1989–1992, 2000.

[10]   M. Hussain et al., "Cefuroxime derived copper nanoparticles and their application as a colorimetric sensor for trace level detection of picric acid," *RSC Adv.*, vol. 6, no. 86, pp. 82882–82889, 2016.

[11]   M. Harada, Y. Kimura, K. Saijo, T. Ogawa, and S. Isoda, "Photochemical synthesis of silver particles in Tween 20/water/ionic liquid microemulsions," *J. Colloid Interface Sci.*, vol. 339, no. 2, pp. 373–381, 2009.

[12]   M. J. Rosemary and T. Pradeep, "Solvothermal synthesis of silver nanoparticles from thiolates," *J. Colloid Interface Sci.*, vol. 268, no. 1, pp. 81–84, 2003.

[13] M. Darroudi, A. Khorsand Zak, M. R. Muhamad, N. M. Huang, and M. Hakimi, "Green synthesis of colloidal silver nanoparticles by sonochemical method," *Mater. Lett.*, vol. 66, no. 1, pp. 117–120, 2012.

[14] G. A. Kahrilas, L. M. Wally, S. J. Fredrick, M. Hiskey, A. L. Prieto, and J. E. Owens, "Microwave-assisted green synthesis of silver nanoparticles using orange peel extract," *ACS Sustain. Chem. Eng.*, vol. 2, no. 3, pp. 367–376, 2014.

[15] Y. Zhang et al., "Synthesis of silver nanoparticles via electrochemical reduction on compact zeolite film modified electrodes," *Chem. Commun. (Camb.)*, no. 23, pp. 2814–2815, 2002.

[16] J. Huang et al., "Continuous-flow biosynthesis of silver nanoparticles by lixivium of sundried *Cinnamomum camphora* leaf in tubular microreactors," *Ind. Eng. Chem. Res.*, vol. 47, no. 16, pp. 6081–6090, 2008.

[17] N. Xia, Y. Cai, T. Jiang, and J. Yao, "Green synthesis of silver nanoparticles by chemical reduction with hyaluronan," *Carbohydr. Polym.*, vol. 86, no. 2, pp. 956–961, 2011.

[18] N. Leopold and B. Lendl, "A new method for fast preparation of highly surface-enhanced Raman scattering (SERS) active silver colloids at room temperature by reduction of silver nitrate with hydroxylamine hydrochloride," *J. Phys. Chem. B*, vol. 107, no. 24, pp. 5723–5727, 2003.

[19] R. Arunachalam et al., "Phytosynthesis of silver nanoparticles using *Coccinia grandis* leaf extract and its application in the photocatalytic degradation," *Colloids Surf. B Biointerfaces*, vol. 94, pp. 226–230, 2012.

[20] S. Navaladian et al., "Thermal decomposition as route for silver nanoparticles," *Nanoscale Res. Lett.*, vol. 2, no. 1, pp. 44–48, 2006.

[21] S. Iravani, "Green synthesis of metal nanoparticles using plants," *Green Chem.*, vol. 13, no. 10, pp. 2638–2650, 2011.

[22] A. U. Khan, "Medicine at nanoscale: a new horizon," *Int. J. Nanomedicine*, vol. 7, pp. 2997–2998, 2012.

[23] P. Logeswari, S. Silambarasan, and J. Abraham, "Synthesis of silver nanoparticles using plants extract and analysis of their antimicrobial property," *J. Saudi Chem. Soc.*, vol. 19, no. 3, pp. 311–317, 2015.

[24] D. Erkakan, N. Y. Diker, M. Önal, and I. I. Çankaya, "Green synthesis of silver nanoparticles using *Salvia fruticosa* Mill. extract and the effect of synthesis parameters on their formation, antioxidant, and electrocatalytic activity," *Hacettepe J. Biol. Chem.*, vol. 50, no. 4, pp. 397–414, 2022.

[25] J. Huignard, B. Leroi, I. Alzouma, and J. F. Germain, "Oviposition and development of *Bruchidius atrolineatus* (Pic) and *Callosobrochus maculatus* (F.) in *Vigna unguiculata* cultures in Niger," *Int. J. Trop. Insect Sci.*, vol. 6, no. 6, pp. 691–699, 1985.

[26] A. Rahman and F. A. Talukder, "Bioefficacy of some plant derivatives that protect grain against the pulse beetle, *Callosobruchus maculatus*," *J. Insect Sci.*, vol. 6, no. 3, pp. 1–10, 2006.

[27] S. S. Ali et al., "Nanobiotechnological advancements in agriculture and food industry: Applications, nanotoxicity, and future perspectives," *Sci. Total Environ.*, vol. 792, Art. no. 148359, 2021.

[28] O. Dura, A. Tülek, İ. Sönmez, F. D. Erdoğuş, A. Yeşilayer, and İ. Kepenekci, "*Lantana camara* L. (Lamiales: Verbenaceae)'nın sulu ekstraktı kullanılarak hazırlanan gümüş nanopartikül (AgNPs) uygulamalarının Buğday gal nematodu [*Anguina tritici* Thorne, 1949 (Nematoda: Anguinidae)]'na etkileri," *Bitki Koruma Bülteni*, vol. 59, no. 2, pp. 49–53, 2019.

[29] G. Rajakumar and A. A. Rahuman, "Acaricidal activity of aqueous extract and synthesized silver nanoparticles from *Manilkara zapota* against *Rhipicephalus (Boophilus) microplus*," *Res. Vet. Sci.*, vol. 93, no. 1, pp. 303–309, 2012.

[30] S. M. Roopan et al., "Low-cost and eco-friendly phyto-synthesis of silver nanoparticles using *Cocos nucifera* coir extract and its larvicidal activity," *Ind. Crops Prod.*, vol. 43, pp. 631–635, 2013.

[31] S.-E. A. Araj, N. M. Salem, I. H. Ghabeish, and A. M. Awwad, "Toxicity of nanoparticles against *Drosophila melanogaster* (Diptera: Drosophilidae)," *J. Nanomater.*, vol. 2015, no. 1, pp. 1–9, 2015.

[32] F.-L. Yang, X.-G. Li, F. Zhu, and C.-L. Lei, "Structural characterization of nanoparticles loaded with garlic essential oil and their insecticidal activity against *Tribolium castaneum* (Herbst) (Coleoptera: Tenebrionidae)," *J. Agric. Food Chem.*, vol. 57, no. 21, pp. 10156–10162, 2009.

[33]   R. S. Esteves et al., "Insecticidal activity evaluation of *Persea venosa* Nees & Mart. essential oil and its nanoemulsion against the cotton stainer bug *Dysdercus peruvianus* (Hemiptera: Pyrrhocoridae) and pollinator bees," *Ind. Crops Prod.*, vol. 194, Art. no. 116348, 2023.

[34]   A. A. Zahir, A. Bagavan, C. Kamaraj, G. Elango, and A. A. Rahuman, "Efficacy of plant-mediated synthesized silver nanoparticles against *Sitophilus oryzae*," *J. Biopesticides*, vol. 5, 2012.

[35]   F. S. Jafer and M. R. Annon, "Larvicidal effect of pure and green-synthesized silver nanoparticles against *Tribolium castaneum* and *Callosobruchus maculatus*," *J. Global Pharma Technol.*, vol. 10, no. 3, pp. 448–454, 2018.

[36]   N. A. E. H. Hassanain, A. Z. Shehata, M. M. Mokhtar, R. M. Shaapan, M. A. E. H. Hassanain, and S. Zaky, "Comparison Between Insecticidal Activity of *Lantana camara* Extract and its Synthesized Nanoparticles Against Anopheline mosquitoes," *Pak. J. Biol. Sci.*, vol. 22, no. 7, pp. 327–334, 2019.

[37]   H. Balcı, F. Ersin, and E. Durmuşoğlu, "*Azadirachta indica* A. Juss (Meliaceae) ve *Melaleuca alternifolia* (Maiden & Betche) Cheel (Myrtaceae) ekstraktlarının klasik ve nano formülasyonlarının *Tetranychus urticae* Koch ve *Amblyseius swirskii* Athias-Henriot'ye etkilerinin belirlenmesi," *Türkiye Biyolojik Mücadele Dergisi*, vol. 11, no. 2, pp. 237–251, 2020.

[38]   K. Velayutham et al., "Larvicidal activity of green synthesized silver nanoparticles using bark aqueous extract of *Ficus racemosa* against *Culex quinquefasciatus* and *Culex gelidus*," *Asian Pac. J. Trop. Med.*, vol. 6, no. 2, pp. 95–101, 2013.

[39]   W. S. Abbott, "A method of computing the effectiveness of an insecticide," *J. Econ. Entomol.*, vol. 18, no. 2, pp. 265–267, 1925.

[40]   A. Ahmad, Z. Mushtaq, F. Saeed, M. Afzaal, and E. A. Jbawi, "Ultrasonic-assisted green synthesis of silver nanoparticles through cinnamon extract: biochemical, structural, and antimicrobial properties," *Int. J. Food Prop.*, vol. 26, no. 1, pp. 1984–1994, 2023.

[41]   D. K. Takci, S. Genc, and H. A. M. Takci, "Cinnamon-based rapid biosynthesis of silver nanoparticles; its characterization and antibacterial properties," *J. Cryst. Growth*, vol. 623, 2023.

[42]   M. T. Al-Husseini, H. R. Al-Mousawi, N. J. Kadhim, A. A.-R. Madhloom, D. Z. Aziz, and A. J. K. Muha, "Biological activity of *Punica granatum* silver nanoparticles against fourth larvae of *Culex quinquefasciatus* mosquito," *J. Phys.: Conf. Ser.*, vol. 1660, pp. 012–013, 2020.

[43]   J. T. da Costa et al., "Effects of different formulations of neem oil-based products on control *Zabrotes subfasciatus* (Boheman) on beans," *J. Stored Prod. Res.*, vol. 56, pp. 49–53, 2014.

[44]   A. M. M. Giongo, J. D. Vendramim, and M. R. Forim, "Evaluation of neem-based nanoformulations as alternative to control fall armyworm," *Ciênc. Agrotecnologia*, vol. 40, no. 1, pp. 26–36, 2016.

[45]   T. Stadler, M. Buteler, and D. K. Weaver, "Novel use of nanostructured alumina as an insecticide: Nanostructured alumina as insecticide," *Pest Manag. Sci.*, vol. 66, no. 6, pp. 577–579, 2010.

URBAN HEAT ISLAND EFFECT OF LARGE-SCALE RESIDENTIAL AREAS: A SPATIOTEMPORAL ANALYSIS OF ETIMESGUT DISTRICT IN ANKARA

Büşra Hilal KUTLU AYDIN [1] [*] , Burcu Halide ÖZÜDURU [1]

[1] *Gazi University, Department of City and Regional Planning, Ankara, Türkiye*

* Corresponding Author: hilalkutlu@gazi.edu.tr

ABSTRACT

Urban heat islands (UHI) disrupt the environmental balance in urban areas. The rate and impact of this formation are intensified by the increase in impervious surfaces, along with urban sprawl and land use changes. This increase reduces natural water absorption, causing heat retention and airflow restriction. Changes in land cover alter surface albedo, affecting energy interactions between the atmosphere and the surface, leading to local climate change. Remote detection methods are important tools for data gathering and assessing UHIs. This study uses a spatiotemporal analysis to examine the relationship between urban development and UHI change between 2005 and 2021, focusing on the Etimesgut district, located on the western development axis of Ankara, where land use changed from agricultural and public land to large-scale residential areas in the last three decades, in particular along with the development of mass housing by Housing Development Agency. Therefore, the district was under pressure for urban growth and mainly developed by transferring public property to private property. The analysis explains how urban sprawl increases land surface temperature (LST), contributing to the formation of UHIs. This study shows that in the Etimesgut district, where the built-up area has increased significantly between 2005 and 2021, from 9,040 ha to 12,934 ha, showing a 43.08% increase, there has been an increase in the LST by about four °C, rising from 43.33°C to 47.02°C in July. Satellite imagery-based findings indicate that the replacement of agricultural land by built-up areas accelerates the rise in temperatures in the region by weakening natural cooling mechanisms. This study intends to inform urban policy and policy development and offers an evidence-based approach using the Etimesgut district in Ankara as a case study. Urban development policies should cover climate-prone strategies and thermal governance to mitigate the UHI effects when barren or agricultural land is replaced with impervious surfaces of large-scale residential areas.

1   INTRODUCTION

Sustainable development is defined as "development that meets the needs of the present without compromising the ability of future generations to meet their own needs" (WCED, 1987), achieved through a balance among environmental, social, and economic factors. Its widespread adoption began with the Brundtland Report (1987). It was reinforced by subsequent initiatives such as the 1992 Earth Summit, Local Agenda 21 (LA21) publications, the European Commission's Green Papers, and the OECD's environmental policy reports for cities. These efforts aimed to address energy consumption, CO2 emissions, and waste management to mitigate the impacts of rising temperatures, sea-level rise, and extreme weather events [1]. The relationship between sustainable development and urban heat islands (UHIs) has emerged as a critical study area. UHIs result from urbanization-induced factors such as reduced vegetation, increased impervious surfaces, and anthropogenic heat emissions, which raise urban temperatures, degrade air quality, and pose significant public health risks. Reducing UHI effects through energy-efficient urban design, green infrastructure expansion, and climate adaptation strategies aligns directly with sustainable development goals. Thermal governance thus offers a strategic framework to enhance urban resilience, improve living conditions, and contribute to global efforts against climate change [2].

Urban areas are key to globalization and development models and show the evident transition to new land use types [3]. Research on UHIs has gained particular attention due to the impact of this transition on energy consumption in buildings, human comfort, air pollution, and urban ecology [4]. UHI forms when an urban area is warmer than the surrounding rural areas, with temperature differences observable on the surface or in the air, particularly near the ground. This phenomenon is influenced by surface energy and radiation balance accompanying urban development, as well as by natural factors, urban form and function, and time, which shows daily and seasonal variability [5]. The increase in air temperature leads to a decline in the quality of urban livability, thus giving rise to urban heat stress [4].

The UHI effect can impact local weather and climate by altering wind patterns and precipitation rates [6]. Impervious surfaces in cities, including building roofs, parking lots, roads, transportation infrastructure, tall buildings, and areas without vegetation (e.g., sandy or barren regions), primarily contribute to the UHI effect due to air trapping and airflow reduction [7]. The thermal balance in the built environment is defined as the sum of heat gains, heat storage, and heat losses. Since urban areas experience higher heat gains and lower heat losses

than surrounding rural or urban environments, the thermal balance in these areas is higher, leading to elevated ambient temperatures compared to rural regions. [8].

Residential areas typically consist of impervious surfaces, which act as barriers to water infiltration into the ground. The increase in impervious surface areas is the primary driver of hydrological and environmental changes linked to urban growth [9]. Changes in land use and land cover alter the surface albedo (reflectance or reflectivity), which enhances energy interactions between the atmosphere and the surface, leading to local climate impacts. Land use changes lead to alterations in LST [10]. Due to variations in land use and land cover (LULC) changes, the albedo, thermal conductivity, capacity, and retention of surfaces are affected [11].

Each city's LULC varies by its unique urban structure, the primary construction materials of the built environment, population density, shape, size, arrangement of buildings, planning strategies, and growth dynamics [12]. The increase in global warming is linked to LULC changes, with temperature fluctuations in urban centers being notably higher than in surrounding areas [13].

Population growth in cities and economic and functional expansion also alters urban morphology. This transformation necessitates the addition of physical structures such as housing, offices, industrial zones, commercial spaces, and transportation infrastructure to support urban activities [14]. Increasing population density, the expansion of residential areas, the rise in buildings and impervious surfaces, the type of construction materials used, greater vehicular traffic, excessive energy consumption, air pollution, and poor air circulation all contribute to changes in urban microclimates [15], [16]. To accommodate urban growth, cities expand beyond their urban boundaries, placing pressure on surrounding natural resources and replacing wetlands, vegetation, and agricultural land [17]. Economic development in cities often leads to new industrial zones, public infrastructure, open spaces, and residential developments. Urban sprawl, with the conversion of vegetative and barren lands near cities into urban areas, exacerbates the UHI effect [18] and causes changes in ecology, biodiversity, landscapes, and natural habitats [19]. The biophysical characteristics of urban spaces are key determinants of the local climate.

Remote sensing methods have proven to be valuable in understanding the LULC change. Earth observation data are widely used to assess the effects of UHI spatial distribution, urban vulnerabilities, and health-related risks [20]. Surface UHI is typically measured using

LST derived from thermal remote sensing, providing an opportunity to characterize UHI formation across various temporal scales (daily, seasonal, and annual) [4].

Various land cover indices have been developed to investigate the relationships between land cover changes and land surface temperature (LST). One such index is the Normalized Difference Vegetation Index (NDVI), which is utilized to assess vegetation density on a global scale, monitor drought events, track and predict agricultural productivity, identify fire-prone areas, and map desertification processes [21]. The correlation between NDVI and LST indicates that changes in vegetation cover can significantly influence surface temperatures. In particular, areas with dense vegetation are often associated with lower surface temperatures, highlighting the critical cooling effect of vegetation.

This study uses spatiotemporal analysis to examine the relationship between LULC change and the UHI. It focuses on the Etimesgut district in Ankara, a new development area, to identify how urban sprawl impacts local climate dynamics and contributes to the intensification of the UHI effect. This study investigates how land use changes from agriculture to large-scale residential areas between 2005 and 2021, influence the change in UHIs by increasing LST. The findings are evaluated in order to define how urban sprawl has an impact on a city, Ankara. Following the introduction, the second section explains the data and methods used. The third section presents the study's main findings, while the final section evaluates the results concerning urban policy and strategies.

2   STUDY AREA, DATA AND METHODOLOGY

2.1   Study Area

Ankara is the capital city of Turkiye, and it is experiencing a rapid population increase. The population, recorded at 4.466.756 in 2007, increased to 5,747,325 by 2021, representing a growth rate of 28,67% [22]. The growth of the city as a result of this increase has been influenced by various factors. These factors include the site selection of public institutions in the city center following the Jansen Plan, the first plan implemented, and the industrial and residential development zones designated after the Yücel-Uybadin Plan in 1957, the second plan implemented. Particularly, the increasing residential areas after the 1950s and the rise in informal housing (squatters) from the 1960s onwards contributed to Ankara's significant growth [41]. In the 1970s, particularly in the 1990s, the city expanded along its West, on the Istanbul and Eskisehir highways, with many public institutions and university campuses [23].

With the 1990 Master Plan, Ankara's previously monocentric and compact urban form transformed into a polycentric structure, where the population shifted towards newly developed residential areas and urban development occurred along various axes. The 1990 Master Plan developed the first strategies and planning decisions to overcome the city's geographic constraints, shaping Batikent, Sincan, and Cayyolu as large-scale residential areas located on the periphery, outside the central core [24]. In the 2023 Ankara Master Development Plan, residential development trends continue to expand along this corridor, reinforcing the decentralization policies of the 1990 Master Plan. The Etimesgut district is also designated as a large-scale residential area shaped by these plans. As a result of the LULC analysis conducted using Landsat satellite images, the built-up area in Ankara has increased from approximately 126,569 hectares in 2005 to approximately 162,586 hectares in 2021, reflecting a 28.46% increase.

In this context, the Etimesgut district was initially planned as part of the western development corridor, followed by the southwestern development corridor, emerging sequentially after the Batıkent-Sincan and Çayyolu satellite towns as a new growth area. The concentration of urban work zones in the district and the planning of large-scale residential areas after the 1980s have highlighted the residential regions. These planned developments were supported by social amenities and the strategic location of significant public buildings during this period. With the suburbanization process accelerating urban growth around the city, Etimesgut has undergone a transformation in housing typology, shifting from mass housing to luxury residential developments, making the district a significant hub in terms of housing, public structures, and infrastructure along with the urban development process accelerating urban growth around the district. The concentration of business zones and large-scale residential areas in the district after the 1980s has highlighted the significant change from agricultural to built-up land. Urban amenities supported these planned developments.

Neighborhoods within the Etimesgut district, such as Eryaman, Elvankent, Yapracık, and Bağlıca, have also become important residential areas following investments and urban growth after the 2000s. In particular, the large-scale residential developments in the district were significantly influenced by the mass housing projects initiated by the Housing Development Agency, which facilitated the transformation of land use from agricultural and public land to extensive residential areas over the last three decades. As a result, urban growth in Etimesgut was primarily driven by the transfer of public property to private property, placing the district under significant development pressure. The Etimesgut district was selected as the

study area due to the rapid population increase in Ankara following the declaration of the Republic and its designation as the capital, which accelerated the urbanization process and increased urban density. As urban density grew, new development corridors were planned, and growth along these corridors exceeded expectations. Therefore, the Etimesgut district is a key area for examining the impacts and consequences of urban development on the formation of UHIs. Figure 1 shows the district's location in Ankara and the location of neighborhoods in Etimesgut. This area was selected as the study site due to its rapid population increase and expansion, accelerating urbanization, and increasing urban density, contributing to urban sprawl. This study highlights the temperature source for the UHI effect, LULC, and NDVI parameters, focusing on changes between 2005 and 2021. A temperature change profile has been created.

Figure 1. Study Area: Etimesgut District Boundary and its Neighborhoods.

2.2   Data Sources

Landsat satellite images obtained from USGS (United States Geological Survey) for 2005 and 2021, including LST, land use, vegetation cover (NDVI), and data from Open Street Map (road network and building footprints), high-resolution Google Earth imagery digitization, and field survey data are utilized in this study. There are seven thermal band datasets. Among these, bands 1 to 5 and 7 have a spatial resolution of 30 meters, while the thermal band 6 has a resolution of either 120 meters (TM) or 60 meters (ETM+), depending on the sensor used.

2005 measurements were retrieved using the bands from Landsat 4-5 TM satellite images for each month of the year as follows:

- LST – (bands 3, 4, 6)

- NDVI – (bands 4, 3)

2021 measurements were retrieved using the bands from Landsat 8 TM satellite images for each month of the year as follows:

- LST – (bands 4, 5, 10)

- NDVI – (bands 4, 5)

July data were used following atmospheric and geometric corrections. Table 1 presents the dataset information for the satellite images for 2005 and 2021. According to Table 1, the cloud cover ratio was determined to be 0.02 for 2005 and 0.00 for 2021.

Table 1. Satellite image dates.

Year	Month	Day	Time	Sensor	Cloud Cover	Path	Row
2005	July	03.07.2005	08:14	Landsat 4-5 TM	0.02	177	32/33
2021	July	31.07.2021	08:27	Landsat 8 TIRS/ORS	0.00	177	32/33

Ground temperature data from meteorological stations provided by the Turkish State Meteorological Service are used to analyze the accuracy of the LST distribution obtained from satellite data. For 2005 and 2021 satellite data, only seven stations were operated by the Turkish State Meteorological Service in Ankara, and two were in Etimesgut (Table 2).

Table 2. Meteorological Station Locations in Ankara.

Station Number	Station Name	District	Latitude (Decimal)	Longitude (Decimal)	Elevation (m)
17127	Airport/Area	District	40.0788	32.5657	838
17128	Ankara Murtet Airport	Kazan	40.1240	32.9992	959
17129	Ankara Esenboga Airport	Cubuk	39.9558	32.6854	806
18250	Etimesgut Airport	Etimesgut	39.9725	32.8639	887
17131	Kecioren/9 (Ankara) Region	Kecioren	39.9343	32.7387	820
17134	Ankara Guvercinlik Airport	Etimesgut	39.8032	32.8434	1115
17137	Golbasi/Ufuk Danisment	Golbasi	39.7985	32.9716	1807

2.3   Method

The study method covers three stages. Following retrieving the indices through imagery acquisition, we perform some computations to prepare the data for analysis. NDVI, LST, LULC, Road Network and Built-up Areas, Meteorological, and Population Data have formed the base for analysis. Next, all indices are prepared using various computations (Figure 2). Following these computations, we analyzed the changes in 2005 and 2021. In this section, these stages are discussed in detail.

Figure 2. Flow Chart of Data Retrieval, Computation and Spatio-temporal Analysis Stages.

2.3.1 Data Retrieval and Computations

Normalized Difference Vegetation Index (NDVI)

Remote sensing technology can monitor vegetation cover. NDVI data is one of the most widely used tools for tracking vegetation. Using the near-infrared (NIR) and red (RED) wavelength bands of satellite imagery, NDVI assesses vegetation greenness, density, and changes in density. When vegetation is dense, reflectance in the red region decreases while reflectance in the near-infrared region increases. This variation is captured by NDVI data analysis [25], [40].

The NDVI value is calculated using the formula (NIR – RED) / (NIR + RED).

For Landsat 4 and 5, NDVI is calculated using two bands: Band 3 (RED) and Band 4 (NIR), while for Landsat 8, it is calculated using Band 4 (RED) and Band 5 (NIR).

NDVI ranges between -1 and +1, and areas covered with green vegetation always have a positive NDVI. Water bodies exhibit low reflectance in both spectral channels, resulting in a negative NDVI. The near-infrared (NIR) channel reflects more than the visible (RED) channel for soil. The soil's moisture content and the rainfall that impacts the vegetation in the study area also influence NDVI [38].

Land Surface Temperature (LST)

This study uses the classical method, which consists of six steps, for calculating LST. With advancements in remote sensing, LST obtained from satellites (such as Landsat, MODIS, and ASTER) is widely used to evaluate UHIs and analyze the effects of urban warming [26]. Satellite LST data vary depending on the period, resolution, accuracy, and availability. Using formulas from the USGS Landsat 8 handbook, the six-step process is followed to calculate LST from thermal bands (e.g., Landsat or MODIS satellite data). These stages are as follows: Conversion of Pixel Values (DN) to Spectral Radiance Values, Conversion of Spectral Radiance Values to Brightness Temperature Values, Determination of the NDVI, Determination of the Proportion of Vegetation (Pv), Determination of Emissivity (LSE) Values, Determination of LST Values [25].

Land Use-Land Cover (LULC)

LULC changes are closely associated with shifts in climatic conditions, which can be detected along with vegetation cover and soil moisture content [20], [27]. In urban areas, the change in LULC is directly related to urban growth and development [28]. Since the 1960s,

multispectral satellite imagery, such as WorldView2 and Landsat, has been a crucial data source for monitoring LULC changes [29]. The images were classified using the *Maximum Likelihood classification*, which helped obtain a LULC classification. The classification helped to categorize land cover into settlement areas, forest areas, vegetation, barren land, and water bodies.

Population Projection Calculation

To assess the impact of urban population density on temperature, population data for the central districts of the study area for the years 2007 and 2021 were obtained from the Turkish Statistical Institute [22]. The population of Etimesgut was 272,977 in 2007 and 606,472 in 2021. Due to the transition to address-based population registration in 2007, detailed data for the year 2005 was not available. Therefore, the population was projected for 2005, using 2007 data.

The *limited exponential growth method* was used for the population projection. This method assumes that population growth has an upper limit. Initially, the growth rates for each district, the corresponding populations, and the arithmetic average of the selected period (2007, 2013, 2021) growth rates are calculated [32]. The population growth rate (k) is calculated using Equation (1). The population in 2005 was 3,881,962 for Ankara and 272,977 for the Etimesgut District.

$$k = \begin{cases} k \leq 1 \; if \; k = 1 \\ 1 < k < 3 \; if \; k = \bar{k} \\ k \geq 3 \; if \; k = 3 \end{cases} \rightarrow \quad k = \left(\sqrt[t_s - t_i]{\frac{N_s}{N_i}} - 1 \right) \times 100 \qquad (1)$$

where;

t_s: Population based on the most recent census year,

t_i: Population based on the initial census year,

N_s: Population counted in the most recent census year,

N_i: Population counted in the initial census year.

The projected population is computed after calculating *k*, as shown in Equation (2).

$$N_p = N_s \times \left(1 + \frac{k}{100} \right)^{of \; years \; between \; ts \; and \; ti} \qquad (2)$$

where;

N_p: Projected Population,

N_s: Population counted in the most recent census.

2.3.2 Spatio-temporal Analysis

Following the data retrieval and computations, we analyzed the respective changes between 2005 and 2021. Thematic mapping has been useful for following the spatial change between these years. For both years, a crossectional display has been in effect. The data, corresponding to July for both years, highlight the differences reflected in the indices. The rise in temperatures is not solely dependent on the amount of vegetation but is also associated with climate change and other environmental factors [33].

3 RESULTS AND DISCUSSION

The findings reveal a significant increase in LST in the Etimesgut district between 2005 and 2021. This rise in LST is a clear indicator of the UHI effect.

NDVI: Using the bands from Landsat 4-5 and Landsat 8 satellite images for each month in 2005 and 2021 shows NDVI changes (Figure 3).

As illustrated in Figure 3 (a), the NDVI in 2005 varied between -0.90 and 0.73, while in Figure 3 (b) in 2021, the NDVI varied between -0.57 and 0.86. Positive NDVI indicates a high density of healthy vegetation. The highest NDVI in 2021 was 0.86, compared to 0.73 in 2005, with a %17.8 increase. When the NDVI value falls between 0 and -1, it indicates areas of bare soil, water bodies, or regions without vegetation. In 2005, the lowest NDVI value was -0.90; in 2021, this value increased to -0.57, suggesting a reduction in bare soil areas over the years.

This increase is valid for several neighborhoods; for example, in Eryaman, Alsancak, Ahi Mesut, and Elvankent, urban development created an overall increase in NDVI. Particularly for example, in Eryaman neighborhood (as shown in Figure 3(a) and 3(b)), the NDVI values varied between -0.006 and 0.51 in 2005 and between 0.049 and 0.66 in 2021; in the Alsancak neighborhood, the values ranged from -0.01 to 0.37 in 2005 and from 0.02 to 0.58 in 2021; and the Ahi Mesut neighborhood, the values varied between 0.05 and 0.42 in 2005 and between -0.23 and 0.69 in 2021; the Elvankent neighborhood, the values ranged from 0.05 to 0.42 in 2005 and from 0.02 to 0.67 in 2021. These neighborhoods experienced rapid development due to the development of large-scale residential areas. Along with this intensification, the increase in vegetation density in non-urbanized areas, the conversion of agricultural activities into active green spaces, and the implementation of green space designs within urbanized zones have

collectively contributed to a general increase in NDVI values. The relationship between NDVI and LST indicates that changes in vegetation can influence LST.
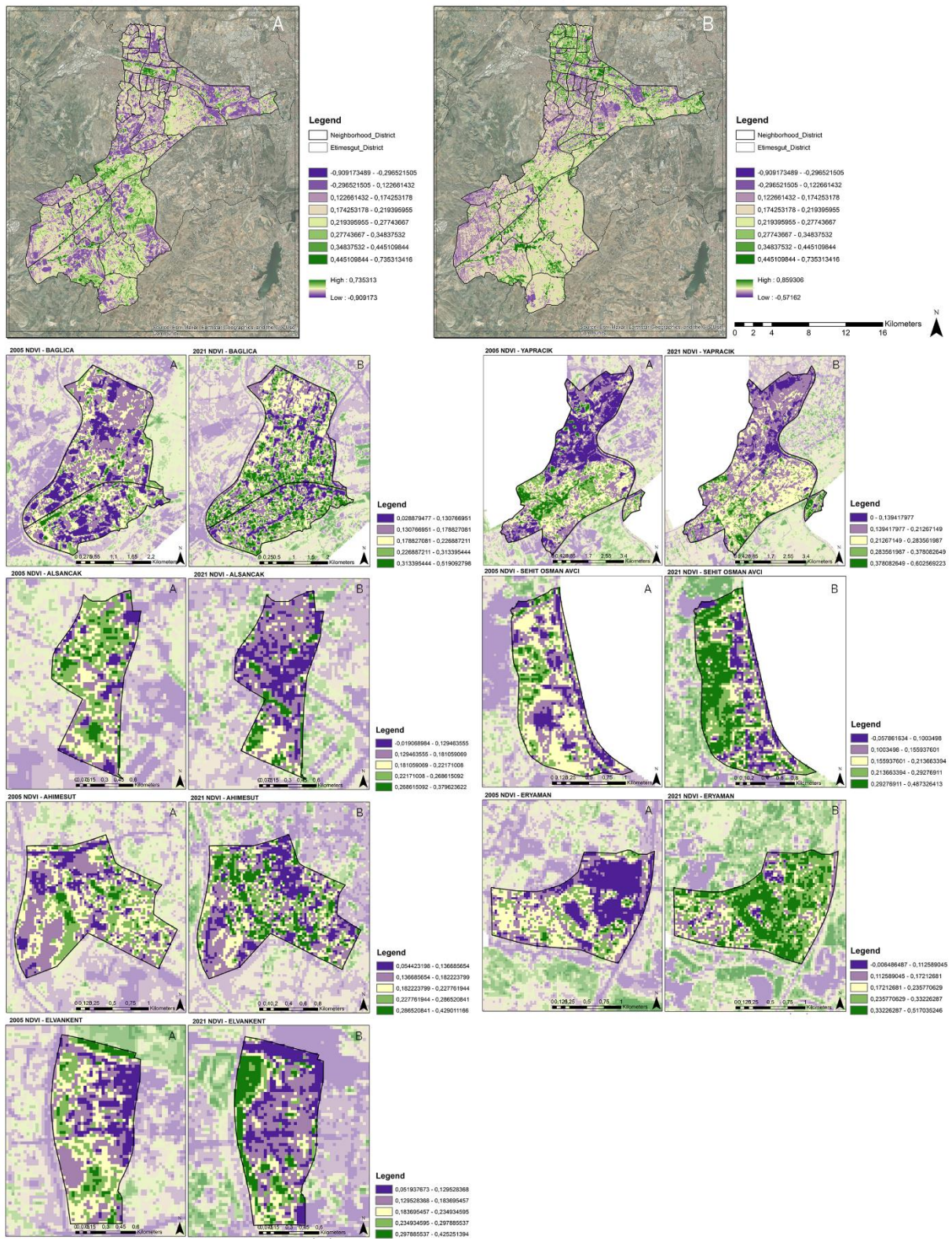

Figure 3. (a) NDVI of Etimesgut District (2005), (b) NDVI of Etimesgut District (2021).

The analysis shows that in 2005, the NDVI values for the Bağlıca, Yapracık, and Şehit Osman Avcı neighborhoods of Etimesgut were high, reflecting their rural character with agricultural land and large green spaces. In the Bağlıca neighborhood, the NDVI values varied between 0.02 and 0.51 in 2005 and between 0.02 and 0.67 in 2021; in the Yapracık neighborhood, the values ranged from 0.00 to 0.60 in 2005 and from -0.13 to 0.77 in 2021; and Şehit Osman Avcı neighborhood, the values varied between -0.05 and 0.48 in 2005 and between -0.30 and 0.67 in 2021. However, by 2021, urban development has significantly increased, particularly in Bağlıca and Yapracık. These areas experienced a sharp decline in NDVI values due to large-scale residential areas and social amenities, reducing green spaces. For example, Yapracık, in particular, was rapidly developed with large-scale residential projects of the Housing Development Agency, and the 2021 map shows low NDVI values, indicating the severe built-up area increase in the area.

According to the 2018 Urban Atlas Street Tree Layer data by Land Copernicus (Figure 4), the total area of street trees in Etimesgut is 11.01 km², which constitutes approximately 3.76% of the total surface area of 292.558528 km². This data indicates that the density of trees in the region is limited, and treeless grass areas predominantly characterize the landscape. The limited presence of broad-leaved trees and the predominance of treeless grasslands in Etimesgut are critical factors to consider in land surface temperature (LST) assessments, as the structure of the vegetation directly influences the distribution and intensity of surface temperatures.
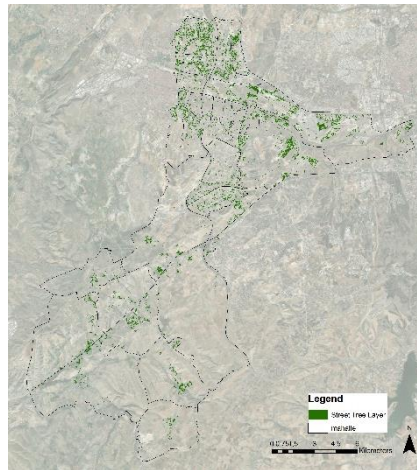

Figure 4. 2018 Urban Atlas Street Tree Layer of Etimesgut.

LST: LST thematic maps for the Etimesgut district were created using the thermal bands from Landsat 4-5 and 8 satellite images for each month in 2005 and 2021 (Figure 5a-5b).
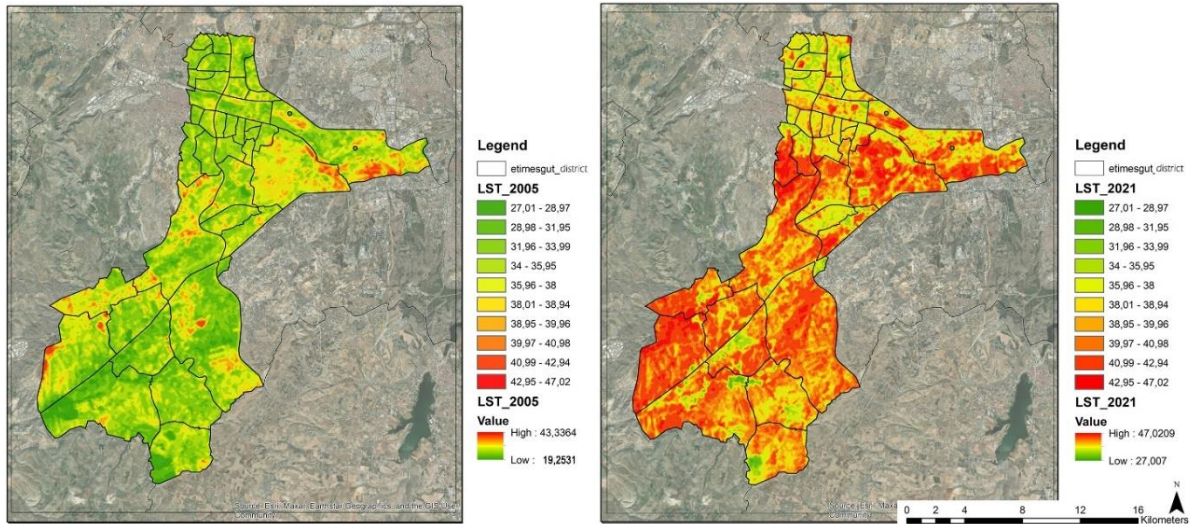
Figure 5. (a) LST of Etimesgut District (2005), (b) LST of Etimesgut District (2021).

The highest recorded temperature in July 2005 was 43.33°C; in July 2021, it reached 47.02°C (Figure 5a). This indicates that the hottest days in July 2021 were approximately 4°C warmer than in 2005. This temperature increase is a clear indicator of global warming and climate change, influenced by various factors such as extreme heat events, urbanization, deforestation, and rising greenhouse gas emissions.

In July 2005, the lowest recorded temperature was 19,25°C; in July 2021, it significantly increased to 27°C (Figure 5b). This change indicates a reduction in the difference between daytime and nighttime temperatures, showing that July 2021 was generally warmer than July 2005. Such a significant increase reflects a notable shift in local climate conditions and a general temperature rise. The rise in temperature, particularly at night, suggests milder nighttime conditions and a reduced cooling effect, highlighting the impact of impervious surfaces and other factors on local climate dynamics.

The 2005 NDVI analysis of the Eryaman and its surroundings—the Eryaman, Alsancak, Ahi Mesut, and Elvankent neighborhoods of Etimesgut—shows that due to the presence of green spaces and barren land, the LST values were generally lower and more moderate. However, by 2021, an increase in LST was observed in these neighborhoods. This indicates that the rise in built-up areas contributed to higher LST, again highlighting the impact of large-scale residential areas on local thermal conditions.

The changes in vegetation, assessed by NDVI, influence LST. However, the rise in temperatures is not solely dependent on the amount of vegetation but is also associated with climate change and other environmental factors. This highlights the complex interplay between

urban development, vegetation loss, and broader climatic and environmental changes, pointing to increasing LST values.

The Difference in LST Between 2005 and 2021: The LST values show a difference of -2 to 6 degrees between 2005 and 2021 (Figure 6).
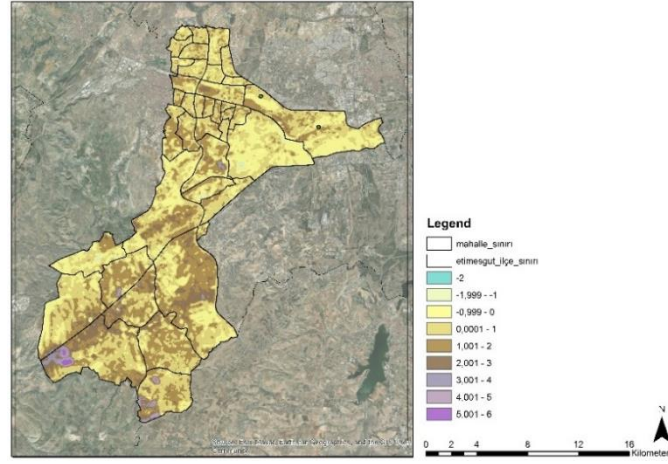

Figure 6. Difference in LST for Etimesgut District between 2005 and 2021.

When examining the LST differences, it is observed that temperatures have decreased in some areas and increased in others, indicating cooling in certain regions and warming in others. Areas where LST has dropped by up to -2°C may have experienced cooling due to environmental or microclimatic factors. These factors could include increased vegetation (which provides cooling through evapotranspiration), changing wind patterns, higher rainfall, or human-induced changes. In the recently developed neighborhoods of Bağlıca, Yapracık, Etiler, Yeşilova, Ballıkuyumcu, and Yukarı Yurtçu, the surface temperature (LST) differences range between 3°C and 6°C.

The LST difference across Etimesgut between 2005 and 2021 shows a notable increase, particularly in the Bağlıca and Yapracık neighborhoods. Rapid urban development, the reduction of vegetation, and increased urban density in these areas have led to a rise in LST. In contrast, the Eryaman, Alsancak, Ahi Mesut, and Elvankent neighborhoods show a smaller temperature difference. This may indicate that green spaces have been better preserved in these areas than Bağlıca and Yapracık neighborhoods and that urban development has been more limited, with growth occurring in a more balanced way.

LULC: LULC data for July 2005 and 2021 was obtained using satellite images through maximum likelihood classification, one of the supervised classification methods. As shown in

Figure 7, the LULC was categorized as settlement areas, forest areas, vegetation, barren land, and water bodies.
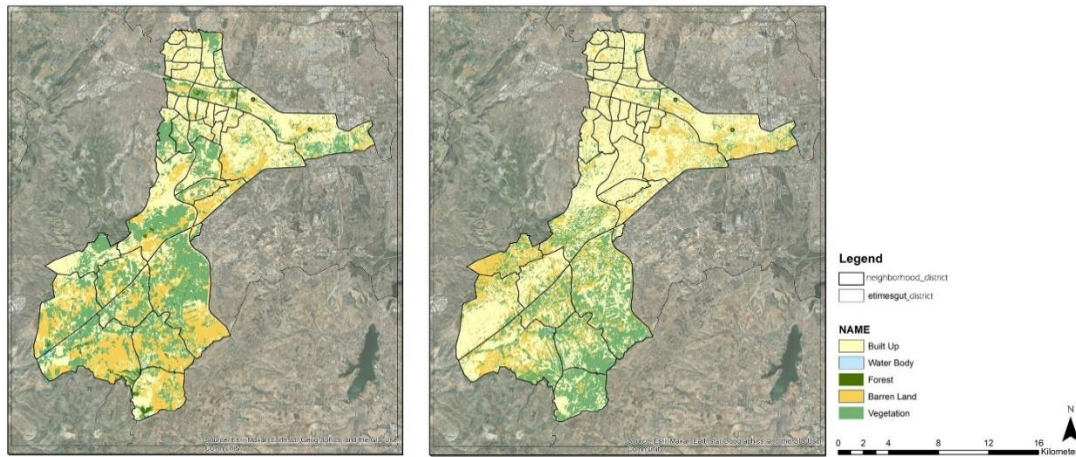

Figure 7. (a) LULC of Etimesgut District (2005), (b) LULC of Etimesgut District (2021).

As of 2005, the urbanized area in Etimesgut district covered approximately 9,040 hectares, while by 2021, this area had expanded to around 12,934 hectares, reflecting a 43.07% increase. In contrast, agricultural and forest land decreased from 7,697 hectares in 2005 to 5,347 hectares in 2021, marking a 30.53% decline. The land cover analysis indicates that from 2005 to 2021, forest and agricultural areas lost their characteristics, while built-up areas continued to expand partially.

The analysis shows that in 2005, the Eryaman, Alsancak, Ahi Mesut, and Elvankent neighborhoods had a high density of forests and vegetation, with relatively limited urban development. However, by 2021, these neighborhoods experienced fewer green spaces and more built-up areas. In contrast, also supported by the NDVI and LST analysis, the Bağlıca and Yapracık neighborhoods in 2005 had large areas of green and barren land with minimal development. By 2021, these areas underwent significant urban transformation, with urban areas expanding notably, particularly in Bağlıca and Yapracık, where green spaces were significantly reduced.

Road Network Analysis: The road network analysis reveals that the total road length increased from 1,107.56 km in 2005 to 1,773.08 km in 2021, representing an approximate increase of 60.08% (Figure 8 (a), (b)).
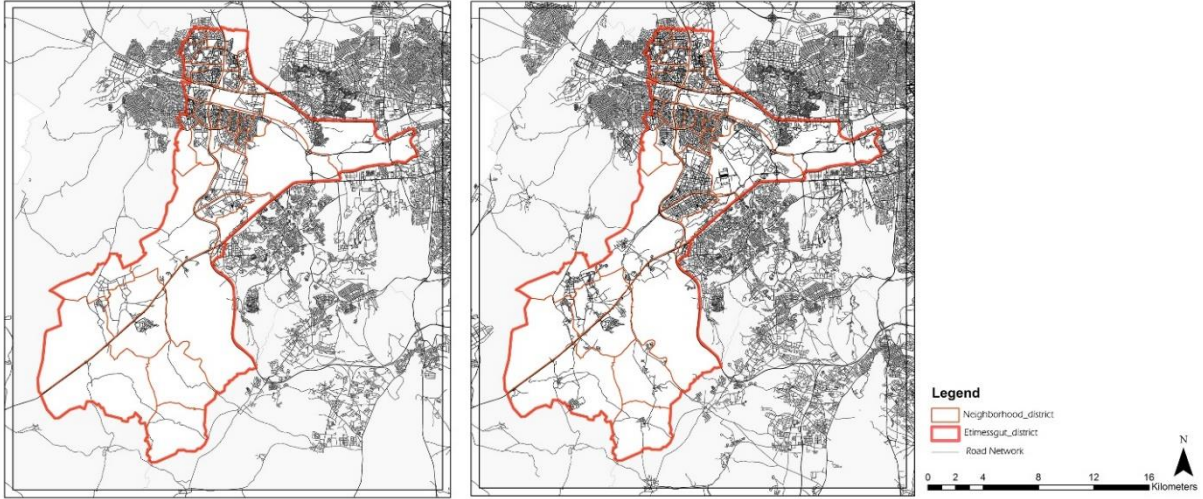
Figure 8. (a) Road Network Analysis of Etimesgut District (2005), (b) Road Network Analysis of Etimesgut District (2021).

The increase in road network length not only reflects economic growth and development but also serves as a significant indicator of urban expansion. An increasing population drives the need for more residential areas, business spaces, and services, leading to the expansion of cities and the construction of new roads. This process of urban growth, while addressing the demands of a growing population, contributes to rising surface temperatures due to the replacement of vegetated areas with impervious surfaces [39].

The analysis shows that in 2005, for example, the Eryaman, Alsancak, Ahi Mesut and Elvankent neighborhoods had a well-developed road network and established urban infrastructure, which is why there was little expansion in these areas by 2021. However, in the Bağlıca and Yapracık neighborhoods, the road network in 2005 was quite limited, with these areas predominantly rural and covered with green spaces. By 2021, the road network expanded significantly with the acceleration of large-scale residential development in the Bağlıca and Yapracık neighborhoods.

Building Footprint Analysis: When examining the changes between 2005 and 2021, the building footprint was calculated to be 6,625,205 m² in 2005 and 8,140,717 m² in 2021. The size of the building footprint increased by approximately 22.87% between 2005 and 2021 (Figure 9 (a), (b)).
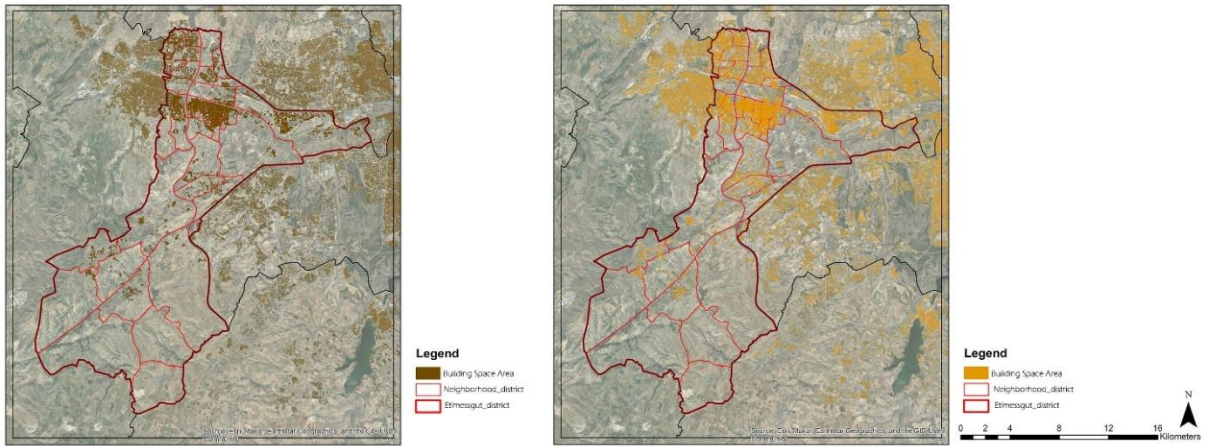
Figure 9. (a) Building Footprint Analysis of Etimesgut District (2005), (b) Building Footprint Analysis of Etimesgut District (2021).

This increase in the building footprint in the Etimesgut district is a clear indicator of urban development, which signifies the district's expansion with new large-scale residential areas and the intensification of the built-up areas, driven by population growth.

Denser built-up areas and the development of new housing projects typically progress in parallel with population growth, economic development, and infrastructure investments. In the case of Etimesgut, from 2005 to 2021, there was both physical expansion and an increase in building density. Between 2005 and 2021, significant urban development occurred across the district, with a notable increase in building footprint, particularly in the Bağlıca and Yapracık neighborhoods. In Bağlıca, the total building footprint area increased from 277,452 m² in 2005 to 439,468 m² in 2021, reflecting a growth of 58.39%. This expansion was accompanied by an increase in neighborhood density, which rose from 0.06 in 2005 to 0.1 in 2021, indicating a significant intensification of the built environment. In Yapracık, the total building footprint area grew from 213,832 m² to 218,161 m² during the same period, indicating a 2.02% increase.

In the Eryaman, Alsancak, Ahi Mesut, and Elvankent neighborhoods, where built-up areas are already high, there was a partial increase in density. In Elvankent neighborhood, the total building footprint increased from 226,285 m² in 2005 to 235,749 m² in 2021, reflecting a growth of 4.18%, in Alsancak neighborhood, increased from 137,884 m² to 201,753 m², showing a 46.31%, in Eryaman neighborhood, increased from 150,598 m² to 233,793 m², marking a 55.25% rise, and in Ahi Mesut neighborhood, increased from 93,433 m² to 209,135 m², achieving a notable increase of 123.81%. In Elvankent, this value rose from 0,17 m² to 0,18 m², in Alsancak from 0,12 m² to 0,18 m², in Eryaman from 0,06 m² to 0,1 m², and in Ahi Mesut

from 0,03 m² to 0,08 m². These changes indicate that larger-scale residential development is more intense in the Bağlıca and Yapracık neighborhoods of Etimesgut.

Perceived Air Temperature Spatial Interpolation Analysis (IDW): Spatial Interpolation Analysis is a function that represents the entire surface and predicts values at other points or sub-areas based on a set of discrete points or sub-areas given as spatial data [30]. Inverse distance weighing (IDW) performs a surface interpolation based on the weighted average of sample points, reducing the weight as the distance from the interpolated point increases [31]. The interpolation of average minimum and maximum temperatures across the district was calculated using the daily average minimum and maximum temperature values from the station data for 2005 and 2021 (Figures 10-11).
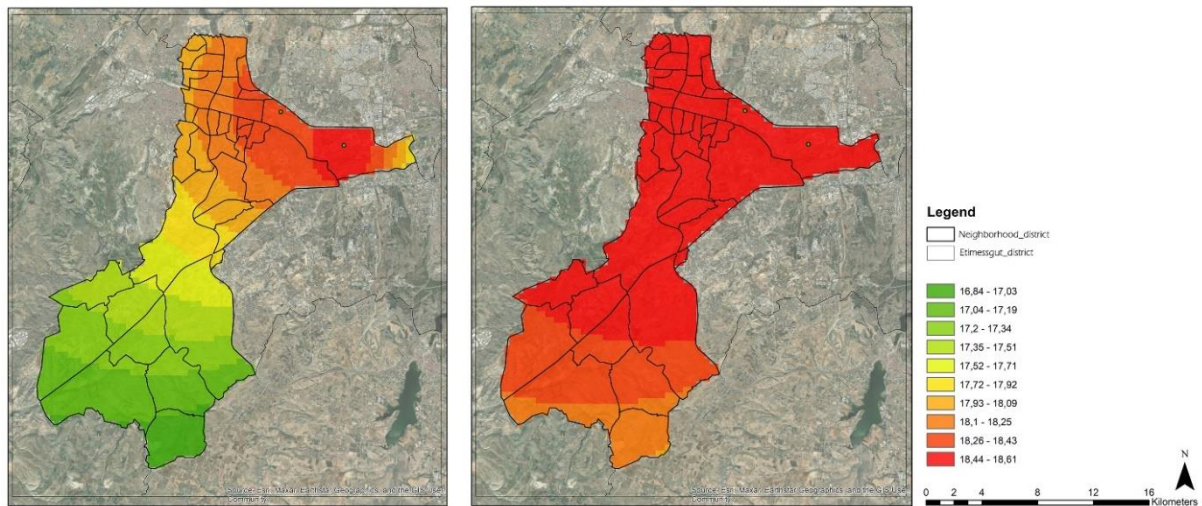

Figure 10. (a) Building Footprint Analysis of Etimesgut District (2005), (b) Building Footprint Analysis of Etimesgut District (2021).
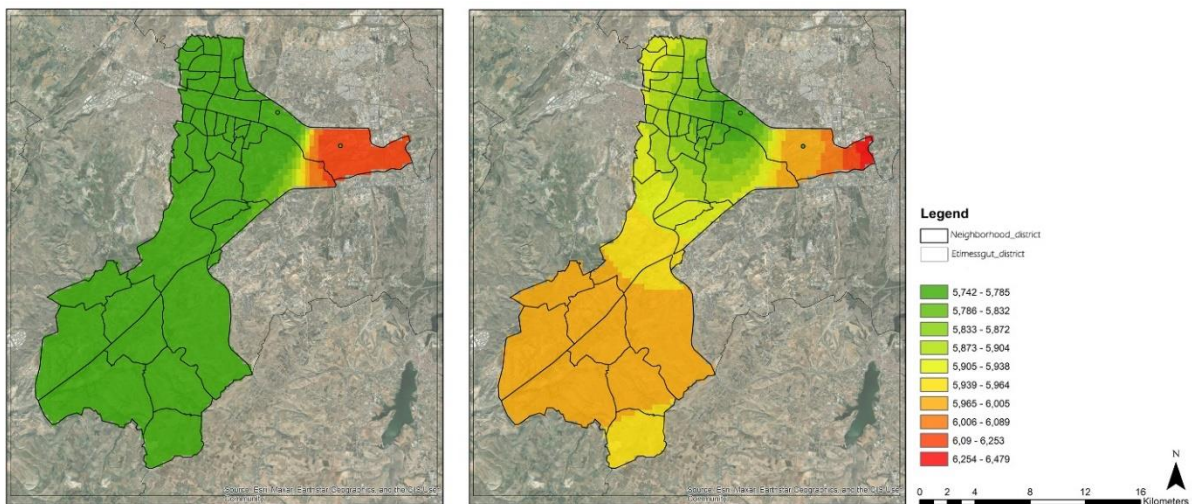

Figure 11. (a) Building Footprint Analysis of Etimesgut District (2005), (b) Building Footprint Analysis of Etimesgut District (2021).

In the temperature maps obtained through interpolation calculations, the average minimum and maximum temperature values show that in 2005, the average minimum temperature ranged between 5.52°C and 6.20°C (Figure 10 (a)), while the average maximum temperature ranged between 16.84°C and 18.61°C (Figure 11 (a)). In 2021, the average minimum temperature ranged between 5.74°C and 6.47°C (Figure 10 (b)), while the average maximum temperature ranged between 18.08°C and 19.30°C (Figure 11 (b)).

In Figure 12, the average hourly relative humidity (%) was calculated based on data from the Etimesgut Airport and Ankara Güvercinlik Airport stations in the Etimesgut district for 2005 and 2021. Accordingly, in 2005, the average hourly relative humidity at Etimesgut Airport was measured at 68.84%, while in 2021, this rate decreased to 61.19%. This indicates a decrease of approximately 7.65% in relative humidity between 2005 and 2021. For Ankara Güvercinlik Airport, data is not available for 2005, but it is recorded at 58.40% for 2021. We cannot assess the difference due to a lack of data at Ankara Güvercinlik Airport.
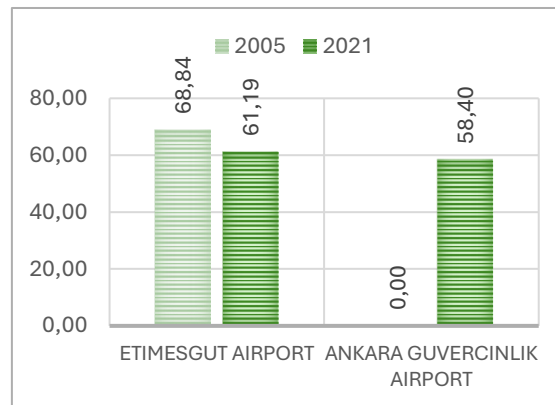
Figure 12. Average Hourly Relative Humidity (%).

In Figure 13, we compared the total precipitation in kilograms per square meter (mm = kg/m²) for 2005 and 2021, based on data from the Etimesgut Airport and Ankara Güvercinlik Airport stations. At Etimesgut Airport, the precipitation per square meter in 2005 was 1.10 kg; in 2021, this amount decreased by 5.45% to 1.04 kg. At Ankara Güvercinlik Airport, the precipitation in 2005 was measured at 1.08 kg, but by 2021, it had decreased by 21.30% to 0.85 kg. A reduction in precipitation is observed at both airports in 2021 compared to 2005; however, the decrease at Ankara Güvercinlik Airport is more significant than at Etimesgut Airport. This difference may be related to precipitation volume, as well as influenced by microclimatic effects, surface changes, urbanization differences, and airflows [42].
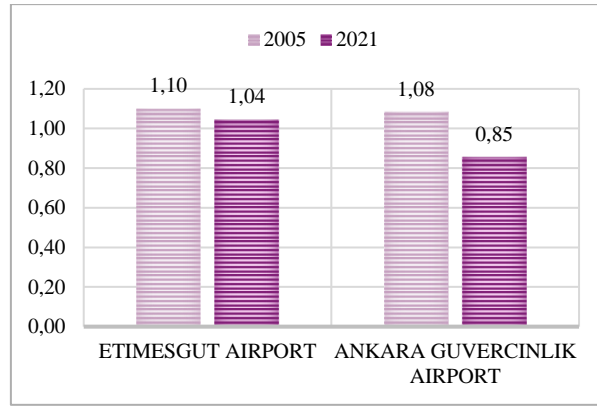
Figure 13. Total Precipitation (mm = kg/m²) – Kilograms of Precipitation per Square Meter.

Figure 14 presents the average wind speeds for 2005 and 2021 based on data from the Etimesgut Airport and Ankara Güvercinlik Airport stations. At Etimesgut Airport, the average wind speed was recorded at 1.45 m/s in 2005, which increased by 72.41% to 2.50 m/s in 2021. At Ankara Güvercinlik Airport, the average wind speed in 2005 was 0.34 m/s, and it rose dramatically by 552.94% to 2.22 m/s in 2021. Both airports experienced a significant increase in average wind speeds, with the rise at Ankara Güvercinlik Airport being much more significant.
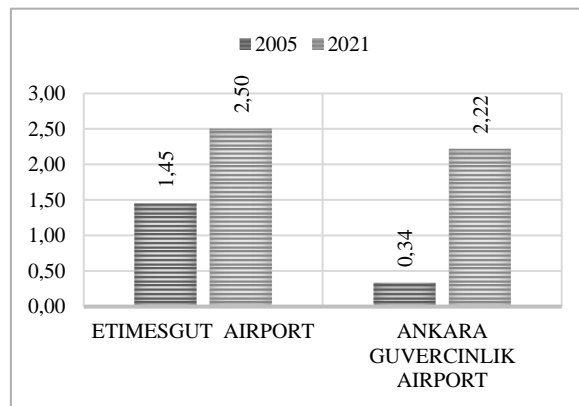
Figure 14. Average Wind Speed (m/s- meters per second).

In urban areas, relative humidity (%), precipitation, and wind speed influence changes in the average minimum and maximum temperature values. A wind speed interpolation was conducted across the central district using the average wind speed values from the measurement station data for 2005 and 2021. The results indicate that the change in wind speed shows similarities to the temperature interpolation results, with the observation that as wind speed increases, the measured temperature in the city decreases.

Population Projection Calculation: Figure 15 shows the population change in Etimesgut district for 2005 and 2021. The population of Etimesgut was 272,977 in 2005, and in 2021, it rose to 606,472, a 122% increase from 2005 to 2021. This indicates that the district has experienced significant population growth, which suggests that the development of new large-scale residential areas in Etimesgut has significantly influenced this growth process.
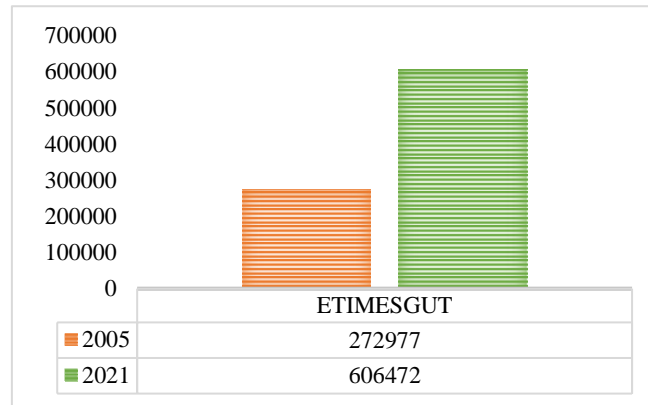
Figure 15. Total Population Change in Etimesgut District.

Profile Analysis: Analyzing the temperature variations along a profile line shows the LST profile change between points A and B in the Etimesgut district for 2005 and 2021 (Figure 16).
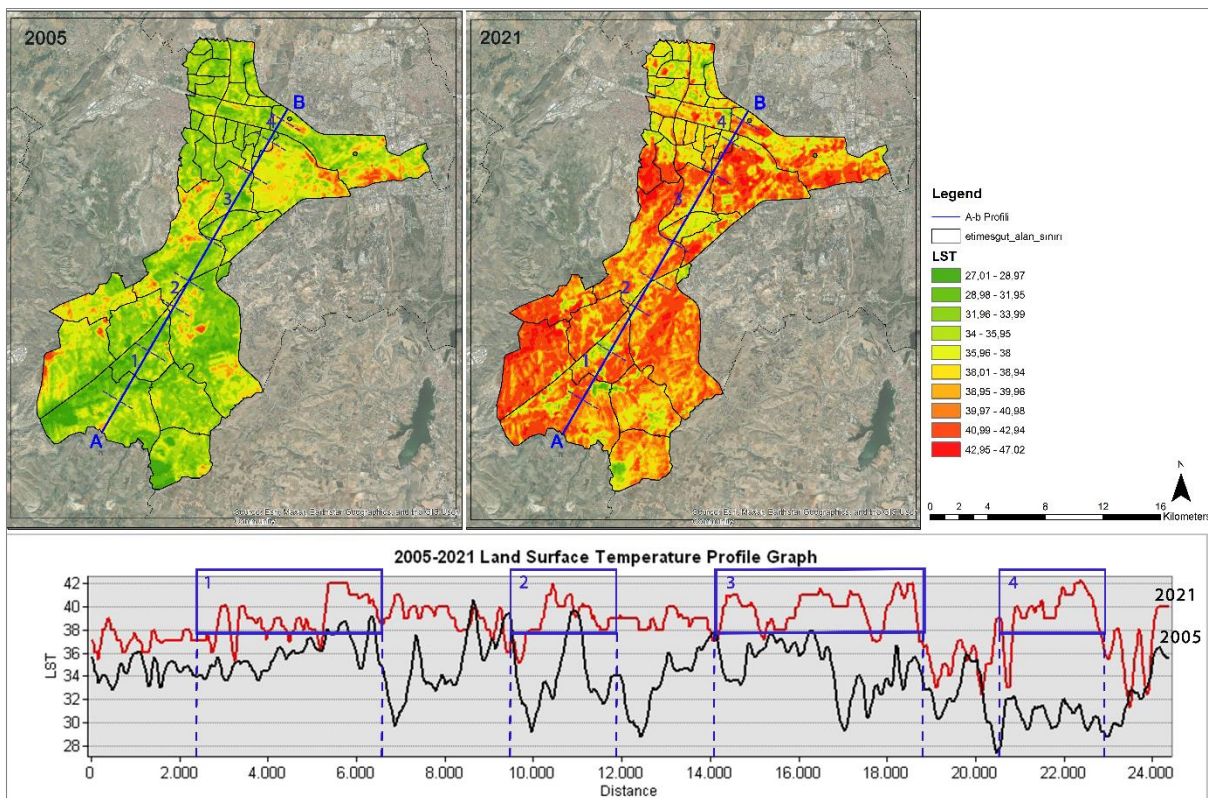
Figure 16. LST Profile Analysis of Etimesgut District (2005-2021).

On the map, green colors represent lower temperatures (27.01-28.97°C), while red and orange indicate higher temperatures (42.95-47.02°C). The temperatures from point A to point B in 2021 are generally higher compared to 2005. For example, within the 0-10 km range, temperatures ranged between 28-34°C in 2005, whereas in 2021, these values increased to a range between 36-40°C.

The UHI effect causes an increase in LST in areas with dense built-up increases. This effect results from buildings, asphalt roads, and other construction materials absorbing sunlight, releasing it slowly, and restricting airflow. The Etimesgut district has undergone an urbanization process since the 1990s, which accelerated in the 2000s. In particular, the neighborhoods of Eryaman, Elvankent, and Ahi Mesut began to develop in the 1990s, but rapid urbanization took place in the 2000s. In contrast, Bağlıca and Yapracık experienced a rapid construction boom after 2005. These neighborhoods previously exhibited more rural characteristics; however, after 2005, they gained an urban identity with increased housing projects. Between 2005 and 2021, a significant rise in LST was observed in the Etimesgut district. In 2005, particularly in the Bağlıca, Yapracık and Şehit Osman Avcı neighborhoods and the Eryaman, Alsancak, Ahi Mesut and Elvankent neighborhoods, lower LST and large green spaces were notable. However, by 2021, with the increase in built-up areas, LST in these neighborhoods rose to as high as 43°C. The UHI effect has intensified, especially in the Bağlıca and Yapracık neighborhoods, where urban spaces have replaced green spaces.

The profile graph illustrates the differences in temperature changes between points A and B. Significant spatial and temporal variations are observed. In Region 1, which consists of agricultural areas, surface temperatures were relatively lower in 2005; however, a noticeable increase is evident in 2021. This change can be attributed to the impact of agricultural activities, such as planting, harvesting, and soil processing, on surface temperature. Conversely, Regions 2, 3, and 4 exhibited lower temperatures in 2005 but experienced a significant increase in 2021. Increased urbanization, reduced surface permeability, and the intensification of the urban heat island (UHI) effect can explain this temperature rise.

4   CONCLUSION AND SUGGESTIONS

Since the 1950s, the city center, shaped by geomorphological thresholds, has concentrated in a basin, developing settlement areas with rapid population growth and new urban expansions. In recent years, debates on climate change and a general rise in temperatures have intensified. Research-based analyses have highlighted these effects, providing guidance

for urban policy and decision-making. This study demonstrates the increased spatiotemporal factors associated with the urban heat island (UHI) effect caused by built-up areas, particularly large-scale residential developments.

With the decentralization policies introduced by the 1990 Master Plan, the city's growth has expanded onto productive agricultural and public lands, primarily in the western region. With an economic emphasis on the construction sector, the residential development process has resulted in urban sprawl and population growth, particularly in the last three decades. This study examines the climate change impacts of this strategy through an analysis of the Etimesgut district in western Ankara. While the district includes other land use types, large-scale residential areas dominate.

Etimesgut, initially characterized by agricultural and public land, has experienced rapid urban development since the 1980s, with mass housing and large-scale residential developments by the Housing Development Agency. After the 1990s, rapid urbanization significantly transformed the district's built environment and natural surroundings. During this period, local and central administrations' planning policies promoted the creation of modern residential areas. However, this process often resulted in a fragmented and unsustainable urban fabric, particularly in areas with intensive housing development. Over time, Etimesgut, seen as a zone of mixed-use and transition, has evolved into an important satellite city of Ankara.

One significant impact of the development processes in Etimesgut is the prevalence of built-up areas with impervious surfaces, reduced barren land, and increased heat. Large asphalt roads, concrete multistorey structures, and other non-permeable surfaces built on agricultural land disrupt the natural water cycle by accumulating heat and surface water, leading to microclimate changes and intensifying the urban heat island (UHI) effect. Analysis of NDVI, LST, LULC, road networks, building footprints, and population changes reveals the extent of these impacts. Changes in climatic factors, such as relative humidity, total precipitation, and average wind speed, further support these findings. Profile analysis also highlights the overall LST changes across the district, providing strong evidence of the evolving UHI characteristics due to spatial development and zoning strategies, especially with converting agricultural land into large-scale residential areas.

Between 2005 and 2021, urban development and construction processes in Etimesgut significantly affected vegetation and surface temperatures, as evidenced by NDVI and LST data. The pronounced UHI effect in neighborhoods such as Bağlıca, Yapracık and Eryaman

underscores the critical need for preserving and expanding green spaces in urban planning. Although some neighborhoods saw improvements in plant cover by 2021, urbanization and global warming have led to significant surface temperature increases, highlighting these developments' environmental and climatic challenges.

This situation emphasizes the necessity of sustainable urban planning in Etimesgut. Preserving green and agricultural areas, carefully managing urban growth, and mitigating the UHI effect through sustainable strategies are vital for reducing environmental and climatic impacts.

The literature presents several studies at multiple scales; some focus on the UHI effect of recently built developments in a city [10], [11], while others, with a broader approach, analyze regions within a country [15], [34]. This study, conducted at the district level, highlights changes in selected neighborhoods where land use has recently shifted from agriculture to large-scale residential areas. This study is useful for identifying changes in UHI assessment factors and aims to inform urban policy-making by providing a pathway from research to actionable strategies. By exploring UHI assessment factors, we identified specific strategies and visualized them on maps to assist policymakers. Conducting similar analyses at smaller scales could further guide neighborhood development and regeneration policies, shaping urban design and planning.

The relationship between NDVI and LST reveals that changes in plant cover significantly influence surface temperatures. However, the rise in temperatures is not solely due to vegetation loss; climate change and other environmental factors also contribute. Despite some improvements in plant cover in 2021, surface temperature increases caused by global warming and local development remain evident. This highlights cities' need to align their plans with broader climate policies. In Etimesgut, a significant rise in surface temperatures was observed between 2005 and 2021, particularly in neighborhoods such as Bağlıca, Yapracık, and Eryaman, where intensive construction activity has occurred. This increase reflects the intensification of the UHI effect across the region.

The reduction of green spaces and intensive urban development have disrupted the environmental balance and elevated surface temperatures. Sustainable urban planning is critical in mitigating these impacts by increasing green spaces and addressing climate change. The preservation of natural areas is essential for the sustainable development of Etimesgut, requiring careful planning to integrate new green spaces and minimize the environmental impacts of

urbanization. Adopting sustainable urbanization principles is mandatory to combat climate change and promote eco-friendly urban growth. Balanced urbanization will improve the quality of life for residents while supporting environmental sustainability.

Studies on the urban heat island effect in Ankara address topics such as the impact of land use and cover changes caused by the increase in built-up areas on surface temperatures, the social, economic, environmental, institutional, and spatial dimensions of vulnerability to climate change, and the contributions of urban transformation practices to this effect [35], [36], [37]. As a unique example from Ankara, Turkey, this analysis in the Etimesgut district implies that both local and central governments should develop urban policies, programs, and strategies to mitigate the UHI effect as climate change has become more evident in recent years. For example, developing new zoning for integrating green spaces and less impervious surfaces into large-scale residential area developments and enforcing such regulations as development moratoriums of the construction companies can benefit both the inhabitants of the residential area and the city dwellers. In addition, adopting energy-friendly construction materials and limiting the height of the new developments in certain areas can be some of the policies that can be enhanced.

There is a growing concern in Turkey about developing a holistic urban planning and design framework for new residential developments. The aim is to integrate these developments into a compact urban form that fosters connections and promotes sustainability. The thermal governance approach focuses on engaging people in the public realm, enabling them to live, work, and socialize, thereby enhancing community ties. At the same time, this approach helps mitigate the UHI effect by promoting green infrastructure and facilitating sustainable commuting options, such as cycling and walking. Decision-makers should prioritize balancing built-up areas with green spaces and include natural cooling mechanisms in their plans. Such urban planning policies will improve the urban environment and reduce the climatic impacts of UHI formation, ultimately benefiting the community.

Land cover analysis reveals significant changes, including the loss of agricultural and forest lands and increased impervious surfaces. The reduction of green spaces and the dominance of non-permeable surfaces have contributed to rising surface temperatures, underscoring the urgent need to apply sustainability principles in city planning. To combat climate change, Etimesgut must invest in green infrastructure, including landscaped areas, wind corridors, and parks. These measures should also include increasing tree cover, implementing green and cool roofs, and integrating such features into buildings and public spaces. Combining

these initiatives with urban planning focused on environmental sustainability will mitigate urban thermal issues and support the realization of sustainable green policies.

Acknowledgment

This study is derived from the doctoral thesis " Fractal Analysis of the Impact of Urban Growth on Urban Heat Island Formation."

Conflict of Interest Statement

There is no conflict of interest between the authors.

Statement of Research and Publication Ethics

The study is complied with research and publication ethics

Artificial Intelligence (AI) Contribution Statement

This manuscript was entirely written, edited, analyzed, and prepared without the assistance of any artificial intelligence (AI) tools. All content, including text, data analysis, and figures, was solely generated by the authors.

Contributions of the Authors

All authors contributed equally.

REFERENCES

[1]   C. Altenburg, "Chapter 1 institutional and social capacities in lead cities in Europe and the United States: Success factors for urban sustainability?," in *Research in Urban Sociology*, Emerald Group Publishing Limited, 2012, pp. 3–28.

[2]   J.-H. Chang, "Thermal governance, urban metabolism and carbonised comfort: Air-conditioning and urbanisation in the Gulf and Doha," *Urban Stud.*, vol. 61, no. 15, pp. 2928–2944, 2024.

[3]   F. Musco, Ed., *Counteracting urban heat island effects in a global climate change scenario*. Cham: Springer International Publishing, 2016.

[4]   V. Costanzo, G. Evola, and L. Marletta, *Urban heat stress and mitigation solutions: An engineering perspective*. London, England: Taylor & Francis, 2021.

[5]   N. Badaro-Saliba, J. Adjizian-Gerard, R. Zaarour, and G. Najjar, "LCZ scheme for assessing Urban Heat Island intensity in a complex urban area (Beirut, Lebanon)," *Urban Clim.*, vol. 37, no. 100846, p. 100846, 2021.

[6]   P. Singh, N. Kikon, and P. Verma, "Impact of land use change and urbanization on urban heat island in Lucknow city, Central India. A remote sensing based estimate," Sustain. *Cities Soc.*, vol. 32, pp. 100–114, 2017.

[7]   U. Rajasekar and Q. Weng, "Urban heat island monitoring and analysis using a non-parametric model: A case study of Indianapolis," ISPRS J. Photogramm. *Remote Sens.*, vol. 64, no. 1, pp. 86–96, 2009.

[8]   R. Paolini and M. Santamouris, *Urban Climate Change and Heat Islands: Characterization, impacts, and mitigation*. Elsevier, 2022.

[9]   A. Ali and Z. Alam Nayyar, "A Modified Built-up Index (MBI) for automatic urban area extraction from Landsat 8 Imagery," *Infrared Phys. Technol.*, vol. 116, no. 103769, p. 103769, 2021.

[10]   R. Neog, "Analyzing dynamic behavior of land use and land surface temperature in the city of Imphal, India," *Acta Geophys.*, vol. 69, no. 6, pp. 2275–2290, 2021.

[11]   X. Zhou and H. Chen, "Impact of urbanization-related land use land cover changes and urban morphology changes on the urban heat island phenomenon," *Sci. Total Environ.*, vol. 635, pp. 1467–1476, 2018.

[12]   P. Mohammad, A. Goswami, S. Chauhan, and S. Nayak, "Machine learning algorithm based prediction of land use land cover and land surface temperature changes to characterize the surface urban heat island phenomena over Ahmedabad city, India," *Urban Clim.*, vol. 42, no. 101116, p. 101116, 2022.

[13]   O. A. Fashae, E. G. Adagbasa, A. O. Olusola, and R. O. Obateru, "Land use/land cover change and land surface temperature of Ibadan and environs, Nigeria," *Environ. Monit. Assess.*, vol. 192, no. 2, 2020.

[14]   A. Achmad, N. Fadhly, A. Deli, and I. Ramli, "Urban growth and its impact on land surface temperature in an industrial city in Aceh, Indonesia," *Lett. Spat. Resour. Sci.*, vol. 15, no. 1, pp. 39–58, 2022.

[15]   N. I. Molina-Gómez, L. M. Varon-Bravo, R. Sierra-Parada, and P. A. López-Jiménez, "Urban growth and heat islands: A case study in micro-territories for urban sustainability," *Urban Ecosyst.*, vol. 25, no. 5, pp. 1379–1397, 2022.

[16]   M. Carpio, Á. González, M. González, and K. Verichev, "Influence of pavements on the urban heat island phenomenon: A scientific evolution analysis," *Energy Build.*, vol. 226, no. 110379, p. 110379, 2020.

[17]   K. J. Gohain, P. Mohammad, and A. Goswami, "Assessing the impact of land use land cover changes on land surface temperature over Pune city, India*," Quat. Int.*, vol. 575–576, pp. 259–269, 2021.

[18]   A.-. A. Kafy, A.-A.- Faisal, A. Al Rakib, M. A. Fattah, Z. A. Rahaman, and G. S. Sattar, "Impact of vegetation cover loss on surface temperature and carbon emission in a fastest-growing city, Cumilla, Bangladesh," *Build. Environ.*, vol. 208, no. 108573, p. 108573, 2022.

[19]   R. J. Corner, A. M. Dewan, and S. Chakma, "Monitoring and prediction of land-use and land-cover (LULC) change," in *Dhaka Megacity*, Dordrecht: Springer Netherlands, 2014, pp. 75–97.

[20]   M. Waleed and M. Sajjad, "Warming cities in Pakistan: Evaluating spatial–temporal dynamics of urban thermal field variance index under rapid urbanization," in *Urban Sustainability*, Singapore: Springer Nature Singapore, 2023, pp. 67–82.

[21]   B. Ahmed, M. Kamruzzaman, X. Zhu, M. Rahman, and K. Choi, "Simulating land cover changes and their impacts on land surface temperature in Dhaka, Bangladesh," *Remote Sens. (Basel)*, vol. 5, no. 11, pp. 5969–5998, 2013.

[22]   "Nüfus İstatistikleri Portalı," Gov.tr. [Online]. Available: https://nip.tuik.gov.tr/. [Accessed: 04-Dec-2024].

[23]   "2023 Başkent Ankara Nazım İmar Planı," *Bel.tr*. [Online]. Available: https://www.ankara.bel.tr/ankara-buyuksehir-belediyesi-nazim-plan. [Accessed: 04-Dec-2024].

[24]   B. Günay, "Ankara çekirdek alanının oluşumu ve 1990 nazım planı hakkında bir değerlendirme," in Cumhuriyet'in Ankara'sı, T. Şenyapılı, Ed. Ankara, Türkiye: ODTÜ Geliştirme Vakfı Yayıncılık, 2005, pp. 60–118.

[25]   *Usgs.gov*. [Online]. Available: https://www.usgs.gov/landsat-missions/landsat-8-data-users-handbook. [Accessed: 04-Dec-2024].

[26] N. Nazarian and L. Norford, "Measuring and assessing thermal exposure," in *Urban Heat Stress and Mitigation Solutions*, London: Routledge, 2021, pp. 40–61.

[27] Y. Ghobadi, B. Pradhan, H. Z. M. Shafri, and K. Kabiri, "Assessment of spatial relationship between land surface temperature and landuse/cover retrieval from multi-temporal remote sensing data in South Karkheh Sub-basin, Iran," *Arab. J. Geosci.*, vol. 8, no. 1, pp. 525–537, 2015.

[28] Q. Weng, D. Lu, and J. Schubring, "Estimation of land surface temperature–vegetation abundance relationship for urban heat island studies," *Remote Sens. Environ.*, vol. 89, no. 4, pp. 467–483, 2004.

[29] *Academia.edu.* [Online]. Available: https://www.academia.edu/download/56616293/IJET-V4I1P4.pdf. [Accessed: 04-Dec-2024].

[30] N. S.-N. Lam, "Spatial interpolation methods: A review," *Am. Cartogr.*, vol. 10, no. 2, pp. 129–150, 1983.

[31] A. İlker, Ö. Terzi, and E. Şener, "Yağışın Alansal Dağılımının Haritalandırılmasında Enterpolasyon Yöntemlerinin Karşılaştırılması: Akdeniz Bölgesi Örneği," *Tek. Dergi*, vol. 30, no. 3, pp. 9213–9219, 2019.

[32] K. M. Çubukçu, *Planlamada Klasik Sayısal Yöntemler*. Ankara, Türkiye: ODTÜ Geliştirme Vakfı, 2008.

[33] M. E. Hereher, "Assessment of seasonal warming trends at the Nile Delta: a paradigm for human-induced climate change," *Environ. Monit. Assess.*, vol. 196, no. 1, 2024.

[34] *Researchgate.net.* [Online]. Available:

https://www.researchgate.net/publication/346534911_Effects_of_urban_growth_on_the_land_surface_t emperature_a_case_study_in_Taiyuan_China. [Accessed: 04-Dec-2024].

[35] *Org.tr.* [Online]. Available: https://dergipark.org.tr/en/pub/gazimmfd/issue/6678/88558. [Accessed: 04-Dec-2024].

[36] *Org.tr. [Online].* Available: https://dergipark.org.tr/en/pub/sdufenbed/article/221982. [Accessed: 04-Dec-2024].

[37] *Edu.tr. [Online].* Available: https://open.metu.edu.tr/handle/11511/58936. [Accessed: 04-Dec-2024].

[38] H. Yıldız, A. Mermer, E. Ünal, ve F. Akbaş, "Türkiye Bitki Örtüsünün NDVI Verileri ile Zamansal ve Mekansal Analizi", *Tarla Bitkileri Merkez Araştırma Enstitüsü Dergisi*, c. 21, sy. 2, ss. 50–56, 2012.

[39] I. D. Stewart and G. Mills, *The Urban Heat Island*. Elsevier, 2021.

[40] M. N. Rahman, M. R. H. Rony, F. A. Jannat, S. C. Pal, M. S. Islam, E. Alam, and A. R. M. T. Islam, "Impact of Urbanization on Urban Heat Island Intensity in Major Districts of Bangladesh Using Remote Sensing and Geo-Spatial Tools," *Climate*, vol.10, no.1, p.3, 2022.

[41] T. Şenyapılı, *Baraka'dan Gecekonduya*. İstanbul: İletişim Yayınları, 2004.

[42] L. Hao, G. Sun, X. Huang, R. Tang, K. Jin, Y. Lai, D. Chen, Y. Zhang, D. Zhou, Z.-L. Yang, L. Wang, G. Dong, and W. Li, "Urbanization alters atmospheric dryness through land evapotranspiration," *npj Climate and Atmospheric Science*, vol. 6, Art. no. 149, Sep. 2023. [Online]. Available: https://doi.org/10.1038/s41612-023-00429-x.

COMPARISON OF ESTIMATION METHODS FOR THE INVERTED EXPONENTIATED PARETO DISTRIBUTION

Kübra BAĞCI GENEL [1]

[1] *Van Yüzüncü Yil University, Department of Econometrics, Van, Türkiye, kubrabagci@yyu.edu.tr*

ABSTRACT

The inverted exponentiated exponential densities family is known for its flexibility and applicability in the field of reliability. This study evaluates the performance of different estimation methods for the inverted exponentiated Pareto (IEP) distribution, which is a special case of this family of distributions. In this study, the point and interval estimates of the parameters for the IEP distribution are obtained using Maximum Likelihood (ML), Maximum Product of Spacings (MPS), Cramer von Mises (CvM), and Anderson Darling (AD) methods. A Monte Carlo simulation is conducted to compare the efficiency of these estimation methods, while real data applications from different fields are utilized to demonstrate practical performance. The fitting performance of the methods is assessed using metrics such as root mean squared error, coefficient of determination, Anderson Darling, and the Kolmogorov-Smirnov test. Simulation results indicate that the MPS method generally outperforms the ML and CvM methods, whereas real data applications reveal that the CvM method provides the best parameter estimates, followed by MPS.

Keywords: AD, Inverted exponentiated Pareto, Inverted exponentiated, MPS, CVM, MLE.

1   INTRODUCTION

Numerous probability distributions with flexible characteristics have been extensively studied. Lifetime distributions are key in characterizing reliability and life characteristics in engineering and practical applications. Recently, Ghitany et al. [1] introduced the inverted exponentiated exponential distribution (IEED) family, which became a versatile option for analyzing various data. Distributions such as the inverted exponentiated exponential (IEE),

inverted exponentiated Rayleigh (IER), and inverted exponentiated Pareto (IEP) are part of this distribution family. The hazard rate function for this class is non-monotonic, allowing for flexibility in fitting different types of data. Previous studies examined this family and found it a promising alternative for modeling lifetime data, outperforming some commonly used distributions (see: [2,3]). The IEP distribution is one of the special cases of this family of distributions. The previous studies [4] highlighted the versatility of the IEP distribution, demonstrating its suitability for modeling diverse datasets that exhibit decreasing or non-monotone hazard rate behavior. The probability density function (pdf) and cumulative distribution function (cdf) for the IEP distribution are given as

$$f(x; \alpha, \beta) = \alpha \beta x^{-(\beta+1)} (1+x)^{-(\beta+1)} \left[1 - \left(\frac{1+x}{x} \right)^{(-\beta)} \right]^{\alpha-1}, \qquad x, \alpha, \beta > 0 \qquad (1)$$

and

$$F(x; \alpha, \beta) = 1 - \left[1 - \left(\frac{1+x}{x} \right)^{-\beta} \right]^{\alpha}, \qquad x, \alpha, \beta > 0 \qquad (2)$$

respectively. Here, α and β are model parameters. In Figure 1, in addition to cdf, different shapes for probability density and hazard rate functions are plotted for different values of parameters.
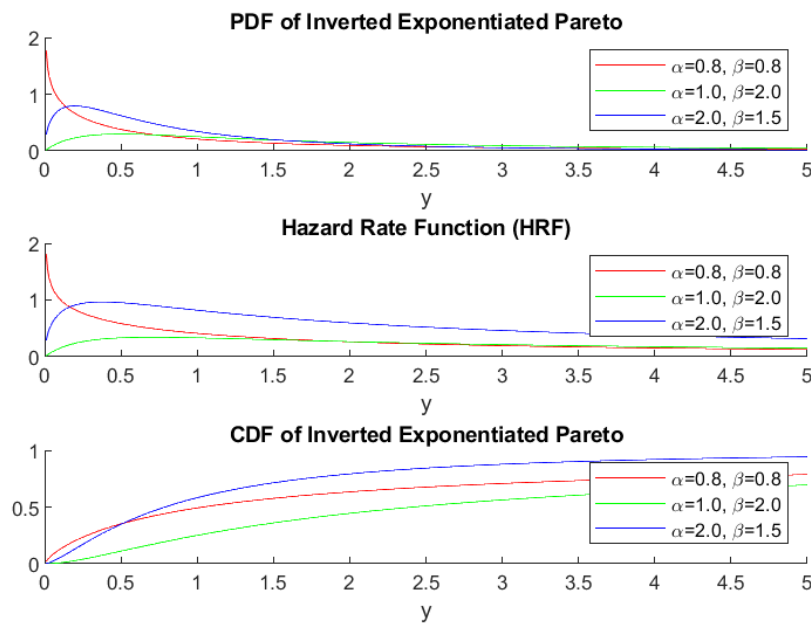

Figure 1. The pdf, hrf, and cdf of the IEP distribution chosen parameters.

Many studies have been conducted on the parameters, reliability, and hazard estimation of the IEED family. For example, system reliability was examined using classical and Bayesian approaches for the IEED family of distributions [5, 6]. Estimation for IER distribution was studied by Maurya et al. and Hashem et al. [7, 8] on censored data. In addition, the study by Rastogi [9] involves estimating the unknown parameters of an IER distribution under Type II progressive censoring, along with the estimation of reliability and hazard functions, using the Expectation–Maximization (EM) algorithm for maximum likelihood estimation (MLE). Similarly, Maurya et al. [4] obtained maximum likelihood (ML) estimates of an IEP distribution under progressive censoring. [10] estimated parameters for the inverse exponential distribution, using maximum likelihood and least squares methods. [8] proposed a pivotal inference approach for estimating the two parameters of the inverse exponentiated Rayleigh distribution using progressive censored data. According to their work, point and interval estimators are derived via the pivotal quantity method.[11] examined the impact of pressure on micro splat splashing diameters using stress-strength reliability analysis. They utilized ML and Bayesian estimators, along with confidence intervals for the IER distribution. [12] discusses confidence set estimation for the generalized inverted exponential distribution based on k-record values. Using pivotal quantities, exact balanced confidence intervals and regions are constructed, with criteria proposed to select the optimal candidates. [13] addressed parameter estimation for a competing risks model with latent failure times following a general family of inverted exponentiated exponential distributions using ML and Bayesian methods with generalized progressive hybrid censored data. Most recently, [14] conducted a study on the estimation of reliability in a multi-component system for the IEP distribution. On the parameter estimation side, as previously mentioned, MLE and Bayesian methods generally stand out in the related literature due to their widespread application and proven effectiveness for IEP distribution (see [4,14]).

Although the MLE method is the most effective under regularity conditions, in some cases, alternative methods can provide successful estimations, as the characteristics of the data can make certain methods more suitable than others. The minimum distance estimators are recognized for their robustness to unusual observations [15]. Also, the Maximum Product of Spacings (MPS) method is a viable alternative to MLE and can offer an improved performance in specific scenarios. This study employs the MPS, Cramér-von Mises (CvM), Anderson Darling (AD), and the MLE method in estimating the parameters of the IEP distribution. Moreover, while studies on the IEED family of distributions have primarily focused on

reliability estimation using data from its typical reliability applications, this work also considers a precipitation dataset for its application. To the extent of the author's knowledge, the CvM and AD estimations have not been utilized before for estimating unknown parameters of the IEP distribution previously. Here a Monte Carlo simulation study across different parameter values and sample sizes is conducted, and the observed Fisher information matrix is computed. Also, applications to real-world data from different fields are presented.

The structure of the study is outlined as follows: Section 2 describes the data used in this study and provides an overview of the estimation methods along with objective functions. Next, a Monte Carlo simulation study is carried out using the AD, CvM, MPS, and MLE methods. In the subsequent section, real data applications are presented, followed by concluding remarks summarizing the findings.

2 MATERIAL AND METHOD

2.1 Data

The first application involves a real dataset provided by [16], comprising thirty consecutive measurements of March precipitation (in inches) recorded in Minneapolis/St. Paul. The second dataset consists of 63 service times (measured in thousand hours) for aircraft windshields, as documented by [17].

First dataset :0.77, 1.74, 0.81, 1.20, 1.95, 1.20, 0.47, 1.43, 3.37, 2.20, 3.00, 3.09, 1.51, 2.10, 0.52, 1.62, 1.31, 0.32, 0.59, 0.81, 2.81, 1.87, 1.18, 1.35, 4.75, 2.48, 0.96, 1.89, 0.90, 2.05.

Second dataset: 0.046, 1.436, 2.592, 0.140, 1.492, 2.600, 0.150, 1.580, 2.670, 0.248, 1.719, 2.717, 0.280, 1.794, 2.819, 0.313, 1.915, 2.820, 0.389, 1.920, 2.878, 0.487, 1.963, 2.950, 0.622, 1.978, 3.003, 0.900, 2.053, 3.102, 0.952, 2.065, 3.304, 0.996, 2.117, 3.483, 1.003, 2.137, 3.500, 1.010, 2.141, 3.622, 1.085, 2.163, 3.665, 1.092, 2.183, 3.695, 1.152, 2.240, 4.015, 1.183, 2.341, 4.628, 1.244, 2.435, 4.806, 1.249, 2.464, 4.881, 1.262, 2.543, 5.140.

2.2 Methods

Let $X_1, X_2, \ldots, X_n$ be a random sample following the IEP distribution, and $X_{(1)}, X_{(2)}, \ldots, X_{(n)}$ are the ordered observations.

2.2.1 The ML Estimation

The MLEs of the parameters α and β, denoted as $\hat{\alpha}_{ML}$ and $\hat{\beta}_{ML}$ are obtained by $(\hat{\alpha}_{ML}, \hat{\beta}_{ML}) = \arg\max \log L\,(\alpha, \beta; x)$. As ML estimation has been previously detailed in earlier studies in the literature e.g. [4], the specific derivation is not repeated. Iterative methods are employed to estimate the parameters of the IEP distribution. The loglikelihood function for the IEP distribution is given in Eq.3.

$$\log L(\alpha, \beta; x) = \begin{aligned} & n\,\log(\alpha) + n\,\log(\beta) + (\beta - 1)\sum_{i=1}^{n}\log(x_i) - \\ & (\beta + 1)\sum_{i=1}^{n}\log(1 + x_i) + \\ & \sum_{i}^{n}(\alpha - 1)\log\left(1 - \left(\frac{(1 + x_i)}{x_i}\right)^{-\beta}\right) \end{aligned} \tag{3}$$

The asymptotic variance-covariance matrix for the MLEs of parameters α and β is represented by the information matrix (Eq.4.).

$$I(\alpha, \beta) = -E\left[\frac{\partial^2 LogL}{\partial\alpha\partial\beta}\right] \tag{4}$$

The use of the observed asymptotic variance-covariance matrix, rather than the exact expectations in the above expressions, is a typical implementation due to the difficulty of obtaining the expectations of the components of this matrix. Here the observed asymptotic variance-covariance matrix is used as well. The asymptotic variance-covariance matrix of the parameters can be obtained as

$$\begin{bmatrix} Var(\hat{\alpha}) & cov(\hat{\alpha}\hat{\beta}) \\ cov(\hat{\alpha}\hat{\beta}) & Var(\hat{\beta}) \end{bmatrix} = \begin{bmatrix} -\dfrac{\partial^2 logL}{\partial\alpha^2} & -\dfrac{\partial^2 logL}{\partial\alpha\partial\beta} \\ -\dfrac{\partial^2 logL}{\partial\alpha\partial\beta} & -\dfrac{\partial^2 logL}{\partial\beta^2} \end{bmatrix}^{-1} \tag{5}$$

Components of this matrix are,

$\frac{\partial^2 logL}{\partial\alpha^2} = -\frac{n}{a^2}$, $\frac{\partial^2 logL}{\partial\beta^2} = \frac{\sigma_1}{\left(\frac{x_i+1}{x_i}\right)^{\beta}\sigma_2} - \frac{n}{\beta^2} - \frac{\sigma_1}{\left(\frac{x_i+1}{x_i}\right)^{2\beta}\sigma_2^2}$ where $\sigma_1 = \log(\frac{x_i+1}{x_i})^2\,(a-1)$ and

$\sigma_2 = \frac{1}{\left(\frac{x_i+1}{x_i}\right)^{\beta}} - 1$ and $\frac{\partial^2 logL}{\partial\alpha\partial\beta} = -\frac{\log(\frac{x_i+1}{x_i})}{\left(\frac{x_i+1}{x_i}\right)^{\beta}\left(\frac{1}{\left(\frac{x_i+1}{x_i}\right)^{\beta}}-1\right)}$.

Under regularity conditions, the asymptotic properties of the MLE method promise that the asymptotic distribution of $\hat{\alpha}$ and $\hat{\beta}$ are normal (see Maurya et al., 2018). Consequently, using the asymptotic distribution of the MLEs, the approximate confidence intervals for unknown parameters can be obtained using $\hat{\alpha} \mp z_{\theta/2}\sqrt{V(\hat{\alpha})}$ and $\hat{\beta} \mp z_{\theta/2}\sqrt{V(\hat{\beta})}$ when $z_{\theta/2}$ is the $[100(1 - \theta/2)]^{th}$ percentile of standard normal distribution.

2.2.2 The CvM Estimation

The CvM estimation is a minimum distance estimation method that minimizes the Cramér–von Mises criterion to obtain parameter estimates by assessing the difference between the empirical and theoretical distribution functions. The CvM estimates of the parameters α and β, denoted as $\hat{\alpha}_{CvM}$ and $\hat{\beta}_{CvM}$ are obtained by $(\hat{\alpha}_{CvM}, \hat{\beta}_{CvM}) = \arg\min CvM\ (\alpha, \beta; \pmb{x})$ where

$$CvM(\alpha, \beta; x) = \sum_{i=1}^{n}\left[1 - \left(1 - \left(\frac{(1 + x_{(i)})}{x_{(i)}}\right)^{-\beta}\right)^{\alpha} - \frac{(2i - 1)}{(2n)}\right]^2 \tag{6}$$

The estimators of the parameters α and β can be obtained by solving the following nonlinear equations.

$$\frac{\partial CvM}{\partial \alpha} = 2\log\left(1 - \left(\frac{x_{(i)} + 1}{x_{(i)}}\right)^{-\beta}\right)\left(\left(1 - \left(\frac{x_{(i)} + 1}{x_{(i)}}\right)^{-\beta}\right)^{a}\right)$$

$$\left(\frac{2i - 1}{2n} + \left(1 - \left(\frac{x_{(i)} + 1}{x_{(i)}}\right)^{-\beta}\right)^{a} - 1\right) = 0 \tag{7}$$

$$\frac{\partial CvM}{\partial \beta} = 2a\log\left(\frac{x_{(i)} + 1}{x_{(i)}}\right)\left(\left(1 - \left(\frac{x_{(i)} + 1}{x_{(i)}}\right)^{-\beta}\right)\right)^{a-1} \frac{\left(\frac{2i - 1}{2n} + \left(\left(1 - \left(\frac{x_{(i)} + 1}{x_{(i)}}\right)^{-\beta}\right)\right)^{a} - 1\right)}{\left(\frac{x_{(i)} + 1}{x_{(i)}}\right)^{\beta}} = 0 \tag{8}$$

Since these derivations involve nonlinear equations, iterative methods are employed to estimate the parameters of the IEP distribution using the CvM method.

2.2.3 The MPS Estimation

The MPS estimation is a method that maximizes the product of the spacings between ordered sample points to obtain parameter estimates. The MPS estimators of the parameters α and β, denoted as $\hat{\alpha}_{MPS}$ and $\hat{\beta}_{MPS}$ are obtained by $(\hat{\alpha}_{MPS}, \hat{\beta}_{MPS}) = \arg\max D\,(\alpha, \beta; x)$ where The objective function for the MPS method is,

$$D = \sum_{i=0}^{n} log\big[F\big(X_{(i+1)}\big) - F\big(X_{(i)}\big)\big] \tag{9}$$

Here, $X(i)$ and $F(\cdot)$ are ordered observations, and the cdf is for the IEP distribution. The partial derivatives of the MPS objective function with respect to the parameters are

$$\frac{\partial MPS}{\partial \alpha} = \frac{\dfrac{a\,log\left(\dfrac{x_{(i)}+1}{x_{(i)}}\right)\sigma_4{}^{a-1}}{\left(\dfrac{x_{(i)}+1}{x_{(i)}}\right)^{\beta}} - \dfrac{a\,log\left(\dfrac{x_{(i+1)}+1}{x_{(i+1)}}\right)\sigma_3{}^{a-1}}{\left(\dfrac{x_{(i+1)}+1}{x_{(i+1)}}\right)^{\beta}}}{\sigma_4{}^{a} - \sigma_3{}^{a}} = 0 \tag{10}$$

and

$$\frac{\partial MPS}{\partial \beta} = \frac{\dfrac{a\,log\left(\dfrac{x_{(i)}+1}{x_{(i)}}\right)\sigma_4{}^{a-1}}{\left(\dfrac{x_{(i)}+1}{x_{(i)}}\right)^{\beta}} - \dfrac{a\,log\left(\dfrac{x_{(i+1)}+1}{x_{(i+1)}}\right)\sigma_3{}^{a-1}}{\left(\dfrac{x_{(i+1)}+1}{x_{(i+1)}}\right)^{\beta}}}{\sigma_4{}^{a} - \sigma_3{}^{a}} = 0\,, \tag{11}$$

where

$$\sigma_3 = 1 - \frac{1}{\left(\dfrac{x_{(i+1)}+1}{x_{(i+1)}}\right)^{\beta}} \text{ and } \sigma_4 = 1 - \frac{1}{\left(\dfrac{x_{(i)}+1}{x_{(i)}}\right)^{\beta}}\,.$$

Since these derivations involve nonlinear equations, iterative methods are employed to estimate the parameters of the IEP distribution using the MPS method.

2.2.4 The AD Estimation

The AD estimators of the parameters α and β, denoted as $\hat{\alpha}_{AD}$ and $\hat{\beta}_{AD}$, are obtained by $(\hat{\alpha}_{AD}, \hat{\beta}_{AD}) = \arg\min AD\,(\alpha, \beta; x)$ where

$$AD = -n - \frac{1}{n\sum_{i=1}^{n}(2i-1)\left\{logF\big(x_{(i)}\big) + log\big(1 - F\big(x_{(n+i-1)}\big)\big)\right\}} \tag{12}$$

Here, iterative methods are considered to estimate the parameters α and β.

2.3 Evaluating Criteria

The fitting performance is assessed through multiple metrics, including root mean squared error (RMSE), coefficient of determination (R²), and the Kolmogorov-Smirnov (KS) and Anderson Darling (AndDar) test statistic and p-values. Formulas of criteria used in evaluating results are given below.

$$RMSE = \left[\frac{1}{n}\sum_{i=1}^{n}\left(\hat{F}(X_{(i)}) - \frac{i}{n+1}\right)^2\right]^{\frac{1}{2}} \tag{13}$$

$$R^2 = 1 - \frac{\sum_{i=1}^{n}\left(\hat{F}(X_{(i)}) - \frac{i}{n+1}\right)^2}{\sum_{i=1}^{n}\left(\hat{F}(X_{(i)}) - \bar{\hat{F}}(X_{(i)})\right)^2} \tag{14}$$

$$KS = max\left|\hat{F}(X_{(i)}) - \frac{i}{n+1}\right| \tag{15}$$

$$AndDar^2 = -n - S_n, \tag{16}$$

where $S_n = \frac{2i-1}{n}(\log(F(x_i)) + \log(1 - F(x_{n+1-i})))$

Here, $\hat{F}(X_{(i)})$ is the estimated cdf, X(i) is the i-th order statistics, k is the number of the parameters, and n is the number of observations.

3 SIMULATION STUDY

This section focuses on a Monte Carlo simulation study conducted to evaluate the efficiency of estimation methods under various conditions. The study involves 1000 simulation runs, using sample sizes of *n*=10, 20, 50, 100, and 300. Parameter values are set as α=1, 0.5, and 3; β=1, 2, and 3. Estimates are obtained through the "genetic algorithm" function available in the Matlab R2021a optimization toolbox. The performance of the ML, MPS, CvM, and AD methods is assessed based on the well-known mean, variance, and Mean Squared Error (MSE) criteria.

Table 1. The Simulation Results for α and β=1.

Method	Mean	Variance	MSE	Mean	Variance	MSE
	n=10		$\hat{\alpha}$		$\hat{\beta}$	
MLE	1.14716891	0.11653618	0.13819487	1.14116204	0.11379887	0.13372560
CvM	1.09369312	0.13512124	0.14389964	1.09598416	0.13239732	0.14161028
MPS	0.89252066	0.11289056	0.12444237	0.87960376	0.11996129	0.13445655
AD	1.22845677	0.77304981	0.82524230	1.15532363	0.38391538	0.40804082
	n=20		$\hat{\alpha}$		$\hat{\beta}$	
MLE	1.1102750	0.08424498	0.09640557	1.09842024	0.07650079	0.08618734
CvM	1.1003792	0.0987992	0.1088752	1.0912126	0.0947396	0.1030593
MPS	0.9188027	0.0718207	0.0784137	0.90658045	0.07261128	0.08133849
AD	1.0926948	0.1835829	0.19217526	1.06753173	0.13072170	0.13528223
	n=50		$\hat{\alpha}$		$\hat{\beta}$	
MLE	1.05831	0.047419	0.050819	1.043302	0.040942	0.042817
CvM	1.06615	0.069658	0.074035	1.046368	0.06054	0.06269
MPS	0.94488	0.034942	0.037980	0.932457	0.033509	0.038071
AD	1.02769	0.049671	0.050439	1.014062	0.045379	0.045577
	n=100		$\hat{\alpha}$		$\hat{\beta}$	
MLE	1.03534	0.021187	0.022436	1.029194	0.018441	0.019293
CvM	1.03744	0.030809	0.032212	1.031819	0.027428	0.028441
MPS	0.96743	0.017637	0.018698	0.962811	0.016303	0.017686
AD	1.022734	0.022982	0.023499	1.018341	0.021035	0.021371
	n=300		$\hat{\alpha}$		$\hat{\beta}$	
MLE	1.01515	0.00601	0.00624	1.01274	0.006189	0.006351
CvM	1.00718	0.008712	0.008763	1.00477	0.008774	0.008797
MPS	0.98035	0.005649	0.006035	0.978706	0.005988	0.006441
AD	1.01006	0.007165	0.007267	1.007574	0.00731	0.007367

When Table 1 is examined, according to all of the sample sizes considered (except for β parameter for n=10 and n=300), the MPS estimations provided more efficient estimations for parameters of the IEP distribution according to the MSE criterion. The ML estimation for the β parameter performed better when n=10 and n=300 than the other estimation methods.

Table 2. The Simulation Results for α=0.5 and β=1.5.

Method	Mean	Variance	MSE	Mean	Variance	MSE
	n=10		$\hat{\alpha}$		$\hat{\beta}$	
MLE	0.577859	0.037183	0.043245	1.659585	0.145069	0.170536
CvM	0.556911	0.039066	0.042305	1.605075	0.172322	0.183362
MPS	0.491265	0.027559	0.027635	1.385413	0.165099	0.178229
AD	0.53109	0.034298	0.035265	1.522759	0.171612	0.17213
	n=20		$\hat{\alpha}$		$\hat{\beta}$	
MLE	0.547037	0.021364	0.023576	1.604913	0.138804	0.149811
CvM	0.531148	0.023325	0.024296	1.575843	0.151472	0.157225
MPS	0.485016	0.014875	0.0151	1.381182	0.137015	0.151132
AD	0.515455	0.019184	0.019423	1.52078	0.151043	0.151475
	n=50		$\hat{\alpha}$		$\hat{\beta}$	

Table 2 (Continued). The Simulation Results for α=0.5 and β=1.5.

Method	Mean	Variance	MSE	Mean	Variance	MSE
MLE	0.522472	0.008162	0.008667	1.583312	0.087704	0.094645
CvM	0.519148	0.0107	0.011066	1.566425	0.113044	0.117456
MPS	0.487298	0.006478	0.00664	1.424244	0.087126	0.092865
AD	0.509835	0.008639	0.008735	1.533871	0.103991	0.105139
	n=100		$\hat{\alpha}$			$\hat{\beta}$
MLE	0.511018	0.003376	0.003497	1.537007	0.049374	0.050743
CvM	0.509777	0.004268	0.004364	1.534701	0.068247	0.069452
MPS	0.490184	0.002895	0.002991	1.432924	0.045813	0.050313
AD	0.503828	0.003416	0.003431	1.507302	0.054463	0.054516
	n=300		$\hat{\alpha}$			$\hat{\beta}$
MLE	0.501821	0.001155	0.001158	1.508832	0.020478	0.020556
CvM	0.501935	0.001573	0.001577	1.508298	0.030791	0.03086
MPS	0.493891	0.001076	0.001113	1.465412	0.019429	0.020626
AD	0.499776	0.001288	0.001288	1.499337	0.023764	0.023764

According to Table 2, the MPS estimations provided more efficient estimations for parameters of the IEP distribution for nearly all of the cases according to the MSE criterion when α<β. When sample sizes were n=10 and n=300, the MLE method slightly performed better for the β parameter.

Table 3. The Simulation Results for α=3 and β=2.

Method	Mean	Variance	MSE	Mean	Variance	MSE
	n=10		$\hat{\alpha}$			$\hat{\beta}$
MLE	3.157901	0.199023	0.223956	2.109823	0.133131	0.145192
CvM	3.117907	0.205831	0.219733	2.092254	0.137451	0.145961
MPS	2.86754	0.161828	0.179373	1.957424	0.130235	0.132047
AD	3.023329	0.198482	0.199026	2.052693	0.133464	0.136241
	n=20		$\hat{\alpha}$			$\hat{\beta}$
MLE	3.176184	0.179092	0.210133	2.068628	0.094346	0.099056
CvM	3.13639	0.198528	0.21713	2.054232	0.095054	0.097995
MPS	2.874764	0.151692	0.167377	1.925536	0.088318	0.093863
AD	3.073496	0.187776	0.193177	2.027683	0.092983	0.093749
	n=50		$\hat{\alpha}$			$\hat{\beta}$
MLE	3.101851	0.14072	0.151093	2.029305	0.04506	0.045919
CvM	3.099932	0.15792	0.167906	2.022161	0.045969	0.04646
MPS	2.850305	0.139326	0.161735	1.918465	0.041734	0.048382
AD	3.042292	0.151618	0.153407	2.001181	0.043785	0.043787
	n=100		$\hat{\alpha}$			$\hat{\beta}$
MLE	3.045159	0.122246	0.124286	2.0097	0.02689	0.026984
CvM	3.032136	0.143489	0.144522	2.004854	0.032214	0.032237
MPS	2.861807	0.112669	0.131766	1.932097	0.025289	0.0299
AD	3.00291	0.133243	0.133251	1.992761	0.028761	0.028813
	n=300		$\hat{\alpha}$			$\hat{\beta}$

Table 3 (Continued). The Simulation Results for α=3 and β=2.

Method	Mean	Variance	MSE	Mean	Variance	MSE
MLE	3.044297	0.056834	0.058796	2.010898	0.012503	0.012621
CvM	3.048189	0.068014	0.070336	2.012961	0.01488	0.015048
MPS	2.949892	0.056863	0.059374	1.972669	0.012465	0.013212
AD	3.029772	0.059695	0.060581	2.005611	0.012985	0.013017

Finally, for α>β, all of the methods performed similarly for the cases considered. For smaller sample sizes, the MPS estimations are more efficient, and for larger sample sizes, the MLEs stand out more; also, the AD method is competitive when larger sample sizes are considered.

Overall, it can be said that the MSEs of all estimates decline with increasing sample size. This indicates that the examined estimation methods are potentially effective for data-fitting applications. In addition, the MPS estimations stand out for nearly all scenarios considered, and as expected, the ML estimations are improved when the sample size increases.

4   APPLICATION RESULTS AND DISCUSSION

This section presents modeling two different data from environmental and operational reliability areas with the IEP distribution using the ML, MPS, CvM, and AD methods. The fitting performances of the methods are examined through the criteria given in Section 2. In addition, fitted density, quantile-quantile (Q-Q), and probability–probability (P-P) plots are presented. Superior fit is indicated by smaller RMSE, AD, and KS statistics, alongside larger R^2 values and higher p-values from the KS test. In Table 4, estimated parameters and asymptotic confidence intervals (ACI) for the first data set are provided.

Table 4. Estimated Parameters and confidence intervals for the first data set.

Method	$\widehat{\alpha}$	$\widehat{\beta}$	ACI for $\widehat{\alpha}$	ACI for $\widehat{\beta}$
ML	7.093474	4.479320	(6.5912, 7.5958)	(4.2895, 4.6692)
MPS	7.593473	4.663268	(7.0912, 8.0958)	(4.4734, 4.8531)
CVM	6.593476	4.4767998	(6.0912, 7.0958)	(4.287, 4.6667)
AD	6.093473	4.0720337	(5.5912, 6.5958)	(3.8822, 4.2619)

According to Table 4, the ML and CvM methods yield relatively narrower intervals, suggesting stable estimation. The comparative results for the estimation methods are presented in Table 5 for precipitation data. Additionally, the fitted densities, Q-Q, and P-P plots for each method are illustrated in Figures 2 and 3. The analysis is carried out using Matlab R2021 and its built-in functions.

Table 5. Evaluating criteria for the first dataset.

Method	AndDar	R^2	RMSE	KS (p-value)
ML	0.160548	0.9896	0.0302	0.0757 (0.99026)
MPS	0.178832	0.9895	0.0307	0.0695 (0.99657)
CVM	0.171681	0.9916	0.0267	0.0663 (0.99819)
AD	0.236604	0.9825	0.0381	0.1068 (0.8480)

According to Table 5, the ML, MPS, AD, and CvM methods performed very closely for modeling precipitation data. However, the CvM method stands out for all criteria by providing the highest R^2 and p-values and the lowest AD, KS, and RMSE values.
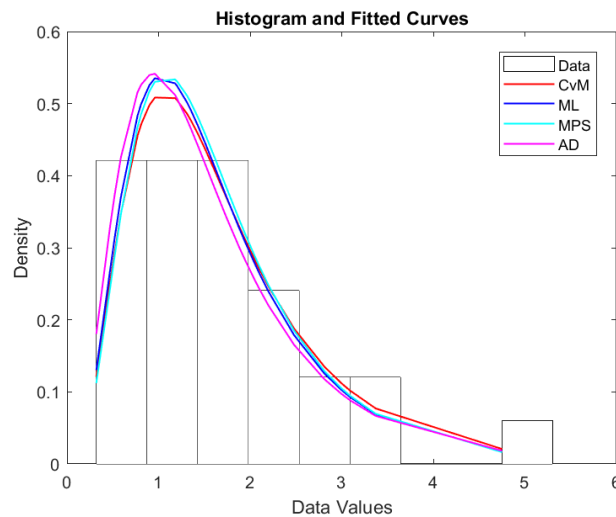

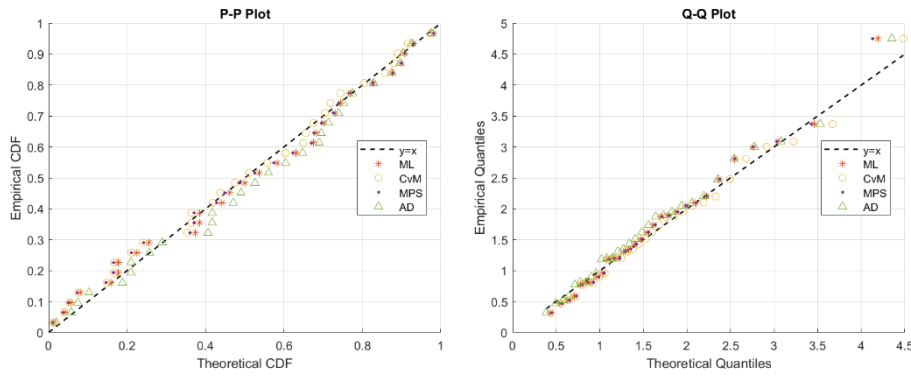*Figure 2. Fitting plots of estimation methods for the first dataset.*

Figure 3. Q--Q and P-P plots for the first data set.

It can be seen from Figure 2 that the CvM estimation method described the first dataset better than the other two methods. The ML, MPS, and AD methods are overfitted at the peak of the distribution compared to the CvM. Considering the sample size of this dataset (n=30), the CvM method seems to provide a more accurate estimation in this case. The Q-Q and P-P plots suggest that all four estimators perform similarly, with slight deviations in the upper quantiles suggesting underestimation at the tails.

In Table 6, estimated parameters and asymptotic confidence intervals for the second data set are provided.

Table 6. Estimated parameters and confidence intervals for the second data set.

Method	$\widehat{\alpha}$	$\widehat{\beta}$	ACI α	ACI β
ML	3.09890	3.25060	(2.8304, 3.3674)	(3.0608, 3.4405)
MPS	3.59890	3.7506	(3.3304, 3.8674)	(3.5607, 3.9405)
CVM	2.59893	3.30898	(2.3304, 2.8674)	(3.1192, 3.4989)
AD	2.0989	2.75060	(1.8304, 2.3674)	(2.5608, 2.9405)

According to Table 6, the ML, MPS, and CVM methods exhibited narrower confidence intervals, and the AD has the widest confidence intervals, implying greater variability. The comparative results for the estimation methods are presented in Table 7 for aircraft windshield data. Moreover, the fitted density, Q-Q, and P-P plots are provided for each method in Figures 4 and 5.

Table 7. Evaluating criteria for the second dataset.

Method	AndDar	R^2	RMSE	KS(p-value)
ML	2.7410	0.903899	0.08550	0.185989(0.022169)
MPS	2.2232	0.9486991	0.06403	0.152975(0.094129)
CVM	2.2841	0.944583	0.06114	0.129424(0.221862)
AD	2.5650	0.908621	0.075221	0.1372821 (0.1694)

Table 7 reveals that the MPS and CvM methods exhibit similar performance in modeling the aircraft windshield data and overweighing the ML and AD estimations. Among these, the MPS method achieved the highest R^2 while the CvM method presented the lowest KS and RMSE metrics.
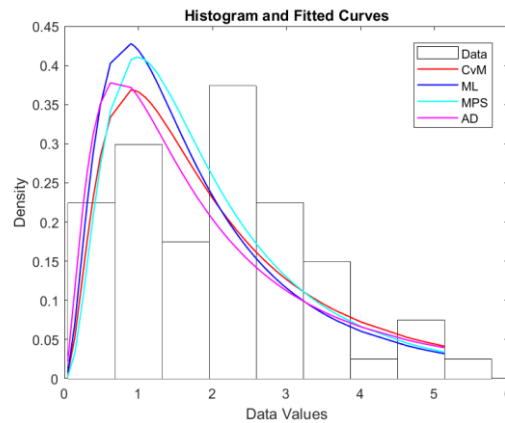
Figure 4. Fitting plots of estimation methods for the second dataset.
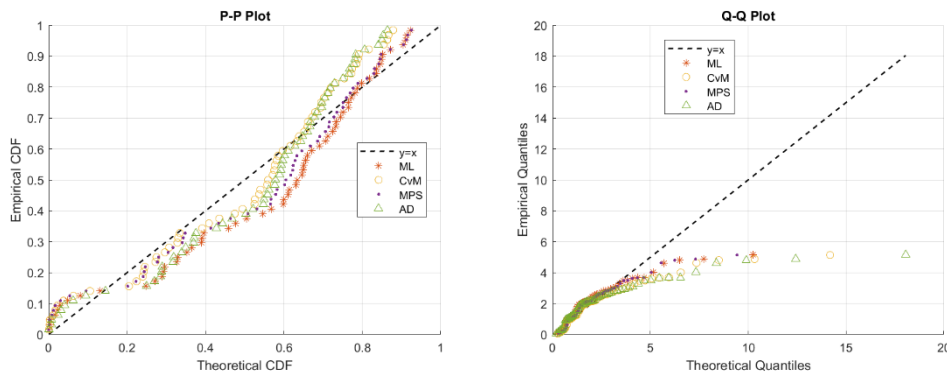
Figure 5. The Q-Q and P-P plots for the second data set.

According to Figure 4, although MPS described the distribution much better than the other methods, the ML method fitted data well in general but overfitted slightly at the peak. The CVM method is performed well in fitting the distribution as well. When the Q-Q and P-P plots are examined, it can be seen that similar outcomes are obtained as in fitted density plots. Since P-P plots emphasize deviations in distribution tails and Q-Q plots detect differences in

distribution shape, the Q-Q and P-P plots indicate that the CVM and MPS provide a closer fit to the theoretical distribution, and the ML and MPS reflect the tails of distribution much better.

In the applications, the MPS and CvM estimation methods demonstrated greater accuracy in estimating the parameters of the IEP distribution compared to the AD and ML methods for the data considered. For the first dataset, the CvM method proved to be the most effective. For the second dataset, both CvM and MPS outperformed ML and AD in fitting the parameters.

Although there is a growing body of research on the IEED family of distributions, studies remain limited and typically focus on maximum likelihood and Bayesian estimation. This work extends beyond traditional reliability studies by applying the approach to environmental data, highlighting the potential of the IEP distribution for modeling data across diverse fields. In addition, it is seen that considering the MPS method can lead to greater efficiency for considered data and simulations, even for small samples. Overall, the MPS and CVM methods can be strong alternatives to the ML method in estimating the parameters of the IEP distribution.

5   CONCLUSION AND SUGGESTIONS

Given its flexibility and applicability, the family of inverted exponentiated densities is frequently used as a reliable model for fitting a wide range of data. The IEP distribution is a special case of this family of distributions and is appreciated due to its flexibility. Here the ML, MPS, AD, and CvM methods are employed to estimate the parameters of the IEP distribution and evaluate their modeling performance through simulations and real data applications from different fields. The Monte Carlo simulation results reveal that the MPS method outperformed the AD, ML, and CvM for nearly all the cases considered. In real data applications, the CvM method emerges as the best method, with its closest competition being the MPS method. This study explores the application of MPS, AD, and CvM estimation methods for the IEP distribution, in addition to the traditional MLE approach, and demonstrates their effectiveness using two real data sets. These findings provide valuable insights into the practical use of different estimation techniques for IEP distribution.

Statement of Research and Publication Ethics

The study is complied with research and publication ethics.

Artificial Intelligence (AI) Contribution Statement

This manuscript was entirely written, edited, analyzed, and prepared without the assistance of any artificial intelligence (AI) tools. All content, including text, data analysis, and figures, was solely generated by the author.

REFERENCES

[1]   M. E. Ghitany, V. K. Tuan, and N. Balakrishnan, "Likelihood estimation for a general class of inverse exponentiated distributions based on complete and progressively censored data," *J Stat Comput Simul*, vol. 84, no. 1, pp. 96–106, Jan. 2014, doi: 10.1080/00949655.2012.696117.

[2]   H. Krishna and K. Kumar, "Reliability estimation in generalized inverted exponential distribution with progressively type II censored sample," *J Stat Comput Simul*, vol. 83, no. 6, pp. 1007–1019, Jun. 2013, doi: 10.1080/00949655.2011.647027.

[3]   M. Dube, H. Krishna, and R. Garg, "Generalized inverted exponential distribution under progressive first-failure censoring," *J Stat Comput Simul*, vol. 86, no. 6, pp. 1095–1114, Apr. 2016, doi: 10.1080/00949655.2015.1052440.

[4]   R. K. Maurya, Y. M. Tripathi, T. Sen, and M. K. Rastogi, "Inference for an Inverted Exponentiated Pareto Distribution Under Progressive Censoring," *J Stat Theory Pract*, vol. 13, no. 1, p. 2, 2018, doi: 10.1007/s42519-018-0002-y.

[5]   F. Kızılaslan, "Classical and Bayesian estimation of reliability in a multicomponent stress–strength model based on a general class of inverse exponentiated distributions," *Statistical Papers*, vol. 59, no. 3, pp. 1161–1192, 2018, doi: 10.1007/s00362-016-0810-7.

[6]   R. Kumari, Y. M. Tripathi, R. K. Sinha, and L. Wang, "Comparison of Estimation Methods for Reliability Function for Family of Inverse Exponentiated Distributions under New Loss Function," *Axioms*, vol. 12, no. 12, 2023, doi: 10.3390/axioms12121096.

[7]   R. K. Maurya, Y. M. Tripathi, T. Sen, and M. K. Rastogi, "On progressively censored inverted exponentiated Rayleigh distribution," *J Stat Comput Simul*, vol. 89, no. 3, pp. 492–518, Feb. 2019, doi: 10.1080/00949655.2018.1558225.

[8]   A. F. Hashem, S. A. Alyami, and M. M. Yousef, "Utilizing Empirical Bayes Estimation to Assess Reliability in Inverted Exponentiated Rayleigh Distribution with Progressive Hybrid Censored Medical Data," *Axioms*, vol. 12, no. 9, 2023, doi: 10.3390/axioms12090872.

[9]   M. K. Rastogi and Y. M. Tripathi, "Estimation for an inverted exponentiated Rayleigh distribution under type II progressive censoring," *J Appl Stat*, vol. 41, no. 11, pp. 2375–2405, Nov. 2014, doi: 10.1080/02664763.2014.910500.

[10]   F. Jamal, C. Chesneau, and M. Elgarhy, "Type II general inverse exponential family of distributions," *Journal of Statistics and Management Systems*, vol. 23, no. 3, pp. 617–641, Apr. 2020, doi: 10.1080/09720510.2019.1668159.

[11]   H. Panahi and S. Asadi, "Estimation of the micro splat splashing data using the inverted exponentiated Rayleigh stress-strength reliability model," *Journal of Statistics and Management Systems*, vol. 22, no. 8, pp. 1401–1416, Nov. 2019, doi: 10.1080/09720510.2019.1596594.

[12]   L. Wang, Y. M. Tripathi, S.-J. Wu, and M. Zhang, "Inference for confidence sets of the generalized inverted exponential distribution under k-record values," *J Comput Appl Math*, vol. 380, p. 112969, 2020, doi: https://doi.org/10.1016/j.cam.2020.112969.

[13]   C. Lodhi, Y. M. Tripathi, and L. Wang, "Inference for a general family of inverted exponentiated distributions with partially observed competing risks under generalized progressive hybrid censoring," *J Stat Comput Simul*, vol. 91, no. 12, pp. 2503–2526, Aug. 2021, doi: 10.1080/00949655.2021.1901290.

[14]   R. Kumari, Y. M. Tripathi, R. K. Sinha, and L. Wang, "Reliability estimation for the inverted exponentiated Pareto distribution," *Qual Technol Quant Manag*, vol. 20, no. 4, pp. 485–510, Jul. 2023, doi: 10.1080/16843703.2022.2125762.

[15]   D. L. Donoho and R. C. Liu, "The" automatic" robustness of minimum distance functionals," *The Annals of Statistics*, vol. 16, no. 2, pp. 552–586, 1988.

[16]   D. Hinkley, "On quick choice of power transformation," *J R Stat Soc Ser C Appl Stat*, vol. 26, no. 1, pp. 67–69, 1977.

[17]   D. N. P. Murthy, *Weibull models*. Wiley, 2004.

STUDY OF W+JET CROSS-SECTIONS AT NEXT-TO-LEADING ORDER AT FUTURE CIRCIULLAR COLLIDER AT √S=100 TEV

Gökhan HALİMOĞLU [1] * iD, Sehban KARTAL [1] iD

[1] İstanbul University, Department of Physics, İstanbul, Türkiye

* Corresponding Author: g.halimoglu@iku.edu.tr

ABSTRACT

This study provides a detailed investigation of $W + jets$ production in proton-proton collisions at $\sqrt{s} = 100 \ TeV$, focusing on the comparison of leading order and next-to-leading order cross-sections. By employing the UNLOPS algorithm, a unified framework was established to improve the accuracy and stability of theoretical predictions, particularly in the context of higher jet multiplicities. The k-factor, a critical metric for quantifying the impact of higher-order corrections, highlighted the substantial contributions of next-to-leading order processes compared to leading order, with a calculated value of 2.501. This value underscores the necessity of incorporating next-to-leading order corrections to achieve precise and reliable predictions in collider physics. The findings indicate that W^+ cross-sections are consistently higher than W^- cross-sections. Additionally, the differential cross-sections decrease as jet multiplicity increases, aligning with theoretical expectations.

This work emphasizes the importance of incorporating next-to-leading order corrections for future collider experiments, particularly for facilities like the future circular collider. The results provide a strong foundation for benchmarking theoretical predictions against experimental data and for guiding the optimization of next-generation colliders. Furthermore, the study highlights the versatility and robustness of the UNLOPS algorithm in addressing the challenges of high-energy jet dynamics, offering valuable insights into $W + jets$ processes and their role in advancing our understanding of Quantum Chromodynamics.

Keywords: FCC, WBoson, NLO, LO, Jets.

1   INTRODUCTION

The production of $W + jets$ has been a central focus in high-energy physics due to its importance in studying both the Standard Model (SM) and Beyond Standard Model (BSM) phenomena [1],[2]. Investigating the cross-sections of processes at leading order (LO) and next-to-leading order (NLO) provides essential insights, as NLO calculations significantly enhance the precision of theoretical predictions in high-energy physics [3][4]. Although many studies have been carried out at the Large Hadron Collider (LHC), exploring these processes for the future circular collider (FCC) remains highly significant [5].

To effectively explore $W + jets$ production at these energy scales, future collider facilities must be equipped with precise theoretical models. FCC is a next-generation collider project designed to push the frontiers of high-energy physics, with its first phase expected to be operational by 2035. The FCC is planned in multiple stages, including $FCC - ee$, an electron-positron collider for precision electroweak studies, followed by $FCC - hh$, a proton-proton collider aimed at exploring the highest energy regimes, and $FCC - eh$, an electron-proton collider for deep inelastic scattering investigations [5],[6].

Among these stages, $FCC - hh$ is particularly relevant to this study, as it is designed to operate at a center-of-mass energy of $\sqrt{s} = 100\,TeV$, providing an unprecedented environment for studying high-energy jet processes. In such high-energy environments, accurate theoretical frameworks are required to interpret experimental data reliably. Precise k-factor calculations, along with differential and total cross-section predictions, are essential for optimizing theoretical models in such colliders.

The ability to accurately model jet multiplicities and kinematic distributions at these energy scales ensures reliable comparisons between experimental data and theoretical expectations, ultimately contributing to new physics searches [7].

To achieve this level of accuracy, perturbative QCD calculations must be systematically improved through higher-order corrections. Theoretical calculations in particle physics are systematically expanded in perturbative orders. Leading order (LO) represents the first-order approximation, capturing the dominant contributions in a given process. Next-to-leading order (NLO), on the other hand, incorporates second-order corrections, including virtual loop effects and additional real emissions, improving the precision of theoretical predictions. These refinements reduce scale uncertainties and enhance agreement with experimental

measurements, making them crucial for reliable cross-section evaluations. In high-energy collisions, such as those at $FCC - hh$, precise theoretical modeling is essential, and the k-factor serves as a key indicator of the impact of NLO corrections, ensuring more accurate comparisons between theory and experimental data. The k-factor, which is mathematically defined as:

$$k = \sigma_{NLO}/\sigma_{LO} \tag{1}$$

serves as an indicator of the relative contribution of NLO corrections compared to LO predictions. When the k-factor is close to unity, it suggests that LO calculations are sufficient for describing the process. However, k-factors point to the necessity of NLO corrections for achieving greater accuracy in theoretical predictions [8],[9].

Beyond evaluating theoretical precision, the k-factor is also used to assess the agreement between calculations and experimental measurements [9],[10]. If significant higher-order corrections are required to align with experimental data, this highlights the importance of refining the theoretical framework.

This study employs the UNLOPS algorithm alongside MadGraph, a versatile simulation tool that calculates tree-level matrix elements, cross-sections, and generates event samples [11],[12]. The UNLOPS algorithm, specifically designed for jet processes, integrates perturbative corrections across multiple jet multiplicities, offering a unified theoretical framework. This method is particularly advantageous for incorporating NLO and next-to-next-to-leading order ($NNLO$) corrections, especially in cases where the number of final-state jets varies. By combining contributions from LO and NLO levels for different jet multiplicities, the UNLOPS algorithm provides a more accurate and stable prediction framework. This approach is critical for minimizing non-perturbative effects during hadronization and ensuring better alignment of theoretical predictions with experimental outcomes.

Compared to other merging schemes, UNLOPS offers significant advantages in smoothly integrating fixed-order and parton-shower contributions. UNLOPS was selected over alternative merging algorithms, including MEPS@NLO and Powheg, due to its ability to facilitate a smoother transition across varying jet multiplicities while preserving NLO precision. Unlike MEPS@NLO, which predominantly employs exclusive phase-space slicing, UNLOPS adopts a more comprehensive approach to incorporating additional jet emissions. In contrast to Powheg, UNLOPS enables a more seamless integration of fixed-order matrix elements with parton showers, resulting in enhanced stability in differential cross-section computations [13].

By leveraging these theoretical advancements, this research provides key theoretical benchmarks for future collider experiments. Through the use of these advanced methods, including parton shower matching and merging techniques within the UNLOPS framework, this study contributes to enhancing the precision of $W + jets$ cross-section predictions, offering valuable insights for future collider experiments, particularly at FCC energies.

2   CALCULATIONS

The calculations were performed using the MadGraph software package and Pythia8 [10][14],[15] for parton shower simulations, incorporating both LO and NLO contributions

The parameters employed for the formation of all processes have been compared in the tables below.

Table1. The parameters for calculating cross-sections at LO and NLO levels have been delineated.

Parameter	LO Parton Level Samples	NLO Parton Level Samples
Energy	$\sqrt{s} = 100\ TeV;\ QCD$	µF=mW
Scales	µR=µF=µES=mW	µF=mW
PDF	NNPDF23_lo_as_0130_qed	NNPDF23_nlo_as_0118_qed
Calculations	+0/1/2j @ LO and +0/1/2/3/4j @ LO	+0/1j @ NLO and +0/1/2j @ NLO
Parton Cuts	ptj > 0 GeV; |etaj| < 5.0; BWC=±15Γ	ptj > 10 GeV; BWC=±15Γ
Parton Shower	ickkw=0; xqcut=0.0; ptlund > 10 GeV	Pythia8; ickkw=4
Jet Clustering	Anti-kT; dR=0.4	Anti-kT; dR=0.4

The parameters used in this study are carefully chosen to ensure the accuracy and reliability of the simulated parton-level events at both LO and NLO. The center-of-mass energy ($\sqrt{s}$) is set to $100\ TeV$, representing a future collider scenario with high-energy QCD processes. The renormalization ($µR$) and factorization ($µF$) scales are dynamically defined using the W-boson mass (mW), minimizing theoretical uncertainties and improving the convergence of perturbative QCD predictions. For the parton distribution functions (PDFs), the NNPDF23_lo_as_0130_qed set is used for LO calculations, while NNPDF23_nlo_as_0118_qed is employed for NLO, providing a reliable description of parton momentum distributions within the proton.

The computational framework comprises two distinct configurations, namely Calculation I and Calculation II. This distinction allows for a systematic examination of jet activity across different perturbative orders, offering a clearer insight into the impact of higher-order corrections on differential cross-sections. Calculation I involve up to 2 jets at LO and 1 jet at NLO, whereas Calculation II extends the jet range to 4 jets at LO and 2 jets at NLO. To implement this framework, the simulation incorporates calculations covering a range of jet multiplicities, where LO samples account for processes with up to three additional jets (+0/1/2/3j/4j), while NLO samples include up to two additional jets (+0/1/2j).

The NLO samples are matched to parton showers using the $FxFx$ merging scheme [12], which ensures a smooth transition between fixed-order matrix element calculations and parton shower simulations, thus avoiding double counting and improving event generation fidelity [15].

Jet clustering is performed using the anti-kT algorithm [16] with a radius parameter of $dR = 0.4$, which is widely recognized for its efficiency and stability in collider physics. Cuts on jet transverse momentum P_T^{jet} and pseudorapidity $|\eta|$ are applied to define the phase space, with stricter cuts imposed on NLO samples to enhance numerical stability [15].

Specifically, NLO samples require $P_T^{jet} \geq 10\ GeV$, while LO samples use a looser threshold. The Born-level Weight Cut (BWC) is consistently set to 15 across all simulations [17].

The parton shower for NLO events is simulated using Pythia8, with the merging process controlled by the ickkw parameter, which facilitates the proper integration of matrix-element and parton-shower contributions. When set to 0, no merging is performed, which is the standard setting for LO events. In contrast, for NLO events, ickkw is assigned a value of 4, enabling $FxFx$ merging to establish a consistent connection between parton-level and shower-level emissions while preventing double counting errors. This configuration improves the precision and reliability of cross-section predictions, particularly in multi-jet processes, by ensuring an accurate representation of both hard scatterings and softer emissions, thereby capturing the intricate nature of QCD dynamics [18].

The comprehensive selection and implementation of these parameters are fundamental to achieving precise and reliable results, aligning with the goals of this study to provide a robust simulation framework for future collider experiments.

The aforementioned parameters and methods form the backbone of the simulations conducted in this study, ensuring consistency and precision in the cross-section calculations. The computational complexity involved in the multi-jet processes, particularly at *NLO*, necessitated significant computational resources. (*The simulations were performed on a high-performance workstation equipped with* 128 *GB of RAM and a 64-core 4 GHz processor*)

The entire process, which included matrix element computations, parton shower simulations, and merging, required approximately four weeks to complete. These resources underscore the computational demand of such detailed simulations, further emphasizing the importance of optimizing each parameter and method for accuracy and efficiency.

3   RESULTS AND DISCUSSION

The calculated cross-section values at both *LO* and *NLO* are systematically presented in the subsequent tables (Table 1, Table 2, and Table 3). These tables provide a comprehensive overview of the simulation results, highlighting the differences between *LO* and *NLO* predictions and their implications for the studied processes.

Table2. Leading order cross-sections.

Sub-Process	$\sigma(W^+ \to \ell^+\nu)$ [pb]	$\sigma(W^- \to \ell^-\nu)$ [pb]	Total Cross-section[pb]
$W^\pm(\to\ell^\pm\nu)+0j$	56253	51092	107340 ∓ 70.7
$W^\pm(\to\ell^\pm\nu)+1j$	49253	45520	94773 ∓ 111
$W^\pm(\to\ell^\pm\nu)+2j$	37351	34594	71946 ∓ 68
$W^\pm(\to\ell^\pm\nu)+3j$	25810	23745	49556 ∓ 99
$W^\pm(\to\ell^\pm\nu)+4j$	16217	14748	30965 ∓ 78

The cross-sections, expressed in picobarns (*pb*), calculated at leading order for various sub-processes are presented in Table 2. These calculations are based on a total of 100,000 generated events, ensuring statistical reliability in the results. These include processes with increasing jet multiplicities $(+0j, +1j, +2j, +3j, and +4j)$. For each sub-process, the individual cross-sections for W^+ and W^- production, along with their sum as the total cross-section, are provided.

As observed, the total cross-section decreases systematically with increasing jet multiplicity. For instance, the $W + 0j$ process exhibits the highest total cross-section of 107340 ±70.7 *pb*, whereas the $W + 4j$ process drops to 30965±78 *pb*. This trend aligns with

expectations, as higher jet multiplicities correspond to increasingly suppressed phase-space regions and more complex interactions, leading to reduced cross-section values.

Additionally, the cross-sections for W^+ production are consistently higher than those for W^- across all sub-processes listed in Table 2. This disparity reflects the underlying asymmetry in parton distribution functions ($PDFs$) within the proton, where u-quarks, which predominantly contribute to W^+ production, are more abundant than d-quarks.

The uncertainties reported for the total cross-sections are minimal, indicative of the accuracy of the calculations and the efficiency of the simulation framework.

These results provide a foundational understanding of the parton-level dynamics at LO, serving as a benchmark for comparisons with NLO calculations and experimental data.

Table3. Next-to-leading order cross-sections.

Sub-Process	σ(W+ → ℓ+v) [pb]	σ(W- → ℓ-v) [pb]	Total Cross-section[pb]
W±(→ℓ±v)+0j	146465	121959	268420 ∓ 1100
W±(→ℓ±v)+1j	95059	82654	177710 ∓ 1510
W±(→ℓ±v)+2j	60352	49900	110250 ∓ 2780

Table 3 showcases the cross-section results for processes with jet multiplicities ranging from $+0j$ to $+2j$ at NLO. These calculations are based on 50,000 generated events, ensuring statistical reliability in the results. As expected, the total cross-section decreases with increasing jet multiplicity, reflecting the growing complexity and phase-space restrictions associated with higher-order emissions. The total cross-section for $W + 0j$ is calculated as $268420 \pm 1100\ pb$, while the value drops to $110250 \pm 2780\ pb$ for $W + 2j$.

A consistent pattern of higher cross-section values for W^+ production compared to W^- production is observed, attributed to the asymmetry in parton distributions within the proton. The simulations are based on a uniform event count across all sub-processes, ensuring statistical comparability. The relatively low uncertainties associated with the total cross-sections indicate the stability and reliability of the NLO simulations.

Table4. UNLOPS cross-sections and k-factor.

	Inclusive cross-section [pb]	$k = σ\_nlo/σ\_lo$
LO	107345 ± 10734	2.501
NLO	268471 ± 13424	

Table 4 presents the inclusive cross-section values calculated at both *LO* and *NLO* using the UNLOPS merging scheme. The *NLO* cross-section 268471±13424 *pb* is significantly higher than the *LO* cross-section 107345±10734 *pb* , highlighting the enhanced precision and inclusion of higher-order corrections at the *NLO* level.

The k-factor, defined in Equation (1) as the ratio of the *NLO* cross-section to the *LO* cross-section, is calculated as 2.501. This value reflects the substantial contribution of *NLO* corrections to the overall cross-section and the importance of higher-order calculations in accurately modeling particle interactions.

These results demonstrate the robustness of the UNLOPS merging scheme in providing consistent and accurate predictions for inclusive cross-sections, which are crucial for both theoretical studies and experimental validations.
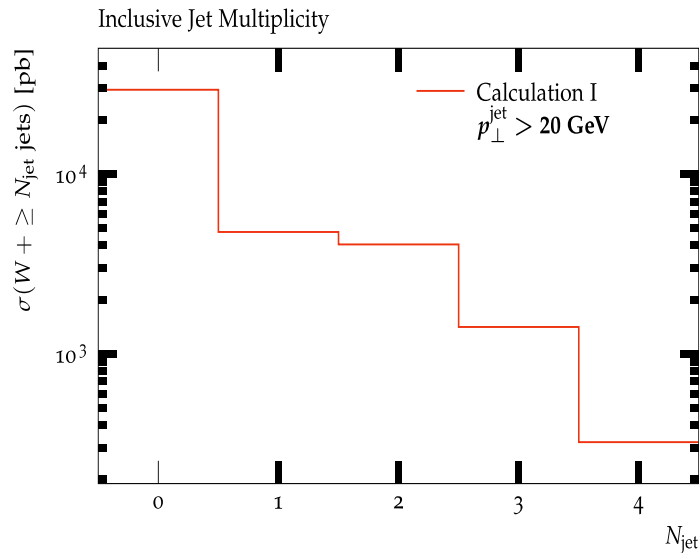

Figure1. Differential cross-sections are presented as a function of inclusive jet multiplicity ($P_T^{jet} > 20$ GeV) calculation I.
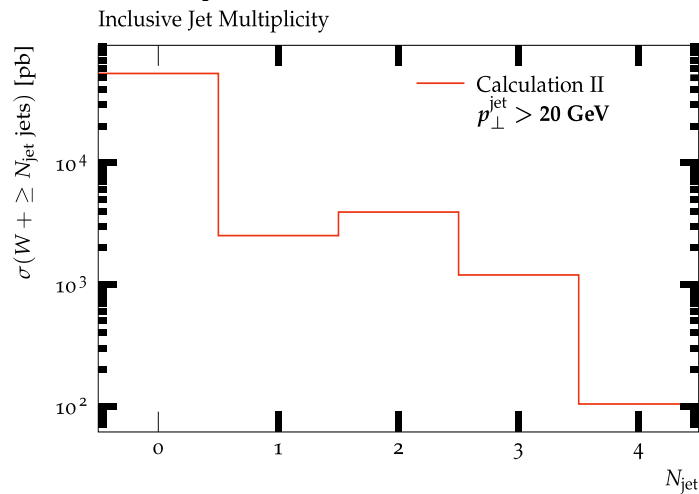

Figure2. Differential cross-sections are presented as a function of inclusive jet multiplicity ($P_T^{jet} > 20$ GeV) calculation II.

Figures 1 and 2 illustrate the differential cross-sections as a function of inclusive jet multiplicity N_{jet} for two distinct calculation methods, denoted as calculation I and calculation II. These plots provide a detailed comparison of the cross-section values for processes involving jets with $P_T^{jet} > 20\ GeV$. The stepwise decrease in cross-section with increasing N_{jet} is evident, reflecting the expected reduction in phase-space availability and the complexity of higher jet multiplicities.
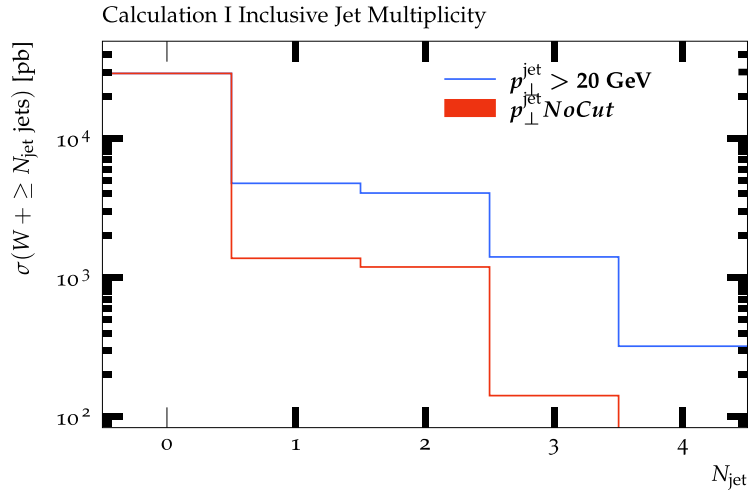
Figure3. Differential cross-sections as a function of inclusive jet multiplicity for Calculation I, comparing cases with and without a $p_\perp^{jet} > 20\ GeV$ cut.

Figure 3 focuses on calculation I and contrasts the cross-sections obtained with and without a transverse momentum cut $P_T^{jet} > 20\ GeV$. This comparison highlights the significant impact of applying such a cut, with noticeable differences in the inclusive cross-section values, particularly at higher jet multiplicities. This demonstrates the sensitivity of the results to jet kinematic cuts, which are crucial for aligning simulations with experimental conditions.

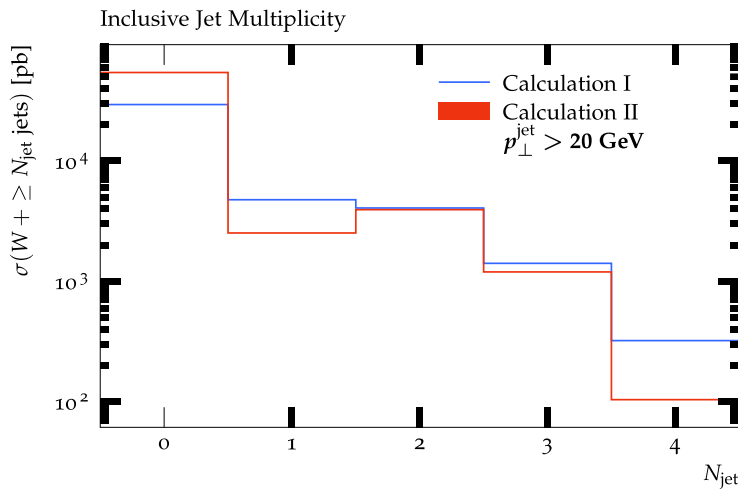**Figure4. The comparison of differential cross-sections is presented as a function of inclusive jet multiplicity for calculation I and calculation II.**

Finally, Figure 4 provides a direct comparison of calculation I and calculation II, emphasizing the differences in the predicted cross-sections for identical kinematic configurations. The overlapping trends observed in lower multiplicities $N_{jet} = 0.1$ gradually diverge at higher N_{jet}, indicating the distinct approaches used in the two calculation methods. This comparison is instrumental in evaluating the consistency and reliability of the methodologies employed.

Collectively, these plots offer an in-depth view of the inclusive jet multiplicity distributions and their dependence on calculation strategies and jet kinematic cuts. These insights are essential for benchmarking theoretical predictions against experimental data and refining the computational frameworks for high-energy collider physics.

The presented results, combining the detailed cross-section values from Tables 1 to 4 and the visual insights from Figures 1 to 4, provide a comprehensive understanding of the studied processes. The tabulated data systematically highlight the impact of increasing jet multiplicities, where a clear reduction in total cross-sections is observed due to the constraints imposed by phase-space availability and higher-order jet emissions. This trend is consistently reflected in the plotted differential cross-sections, emphasizing the consistency of the simulations.

Additionally, the comparison of *LO* and *NLO* cross-sections across different jet configurations underscores the significance of higher-order corrections in achieving more accurate predictions. The k-factor values derived from Table 4 demonstrate the substantial enhancement provided by *NLO* calculations, further validating their necessity for precise modeling in high-energy collisions. The visual comparison in Figure 4 complements this finding by revealing how different calculation methods diverge in their predictions, especially at higher jet multiplicities.

The agreement between tabulated and plotted results not only reinforces the reliability of the simulation framework but also highlights the importance of careful parameter selection and methodological rigor. These findings serve as a strong foundation for benchmarking theoretical predictions against experimental data and for further studies aimed at refining computational models in particle physics.

4   CONCLUSION AND SUGGESTIONS

This study presents a comprehensive analysis of $W + jets$ processes, focusing on both inclusive and differential cross-sections as functions of jet multiplicities at LO, NLO, and UNLOPS merging schemes. The results offer significant insights into the interplay between jet multiplicities, higher-order corrections, and theoretical predictions, which are essential for accurate modeling of collider experiments at future facilities like $FCC - hh$, where the high-energy proton-proton collisions provide an ideal environment for studying QCD-driven jet dynamics.

Our findings confirm that, across all configurations, W^+ boson cross-sections are consistently higher than W^- boson cross-sections. This asymmetry arises from the dominance of $u - quark$ contributions within the proton, directly impacting W^+ production rates. Furthermore, the total cross-sections at NLO were systematically larger than at LO, with a calculated k-factor of 2.501, highlighting the necessity of incorporating higher-order corrections for reliable predictions. These results are in strong agreement with theoretical expectations, reinforcing the validity of our computational framework.

In addition, differential cross-sections exhibit a systematic decline with increasing jet multiplicities, reflecting the phase space suppression and computational challenges associated with higher-order emissions. The comparison between LO and NLO calculations reveals that NLO not only enhances precision but also offers a more robust theoretical foundation, particularly for final states involving $1–2$ $jets$, where experimental uncertainties are critical. These findings emphasize the need for higher-order corrections to minimize theoretical uncertainties and align predictions with experimental observations.

A key aspect of this work is the implementation of the UNLOPS merging scheme, which enhances the reliability of theoretical predictions by ensuring a smooth transition between fixed-order matrix elements and parton showers. This merging strategy allows for a consistent treatment of high-energy and soft emissions, making it particularly valuable for inclusive jet multiplicity distributions at $FCC - hh$. Compared to other merging algorithms, UNLOPS provides improved stability in differential cross-section predictions, reinforcing its suitability for high-energy QCD studies.

To further refine these results, future studies should increase event statistics to 1 million, allowing for more precise evaluations of high-multiplicity jet events and reduced statistical uncertainties.

Beyond the scope of this study, exploring multi-boson production and heavy-flavor jet final states at $FCC - hh$ would offer deeper insights into $W + jets$ dynamics and new physics searches. These studies would not only aid in benchmarking theoretical frameworks but also support the development of experimental strategies for next-generation colliders.

Finally, to bridge the gap between theory and experiment, it is essential to incorporate experimental-level simulations, including detector effects and pile-up conditions. This would significantly enhance the applicability of our findings, ensuring that theoretical models are aligned with real collider data, ultimately contributing to the success of future $FCC - hh$ physics programs.

Conflict of Interest Statement

There is no conflict of interest between the authors.

Statement of Research and Publication Ethics

The study is complied with research and publication ethics.

Artificial Intelligence (AI) Contribution Statement

This manuscript was entirely written, edited, analyzed, and prepared without the assistance of any artificial intelligence (AI) tools. All content, including text, data analysis, and figures, was solely generated by the authors.

Contributions of the Authors

Gökhan Halimoğlu: Led the formulation of the research question and conducted the literature review. Actively participated in data collection and analysis, performing statistical evaluations of the results. Additionally, Gökhan Halimoğlu was responsible for drafting the initial manuscript and made substantial revisions to the entire text. Contributed significantly to the writing of the conclusions and the finalization of the manuscript.

Sehban Kartal: Provided overall guidance and conceptual direction for the study. Reviewed the manuscript drafted by Gökhan Halimoğlu, offering academic mentorship and feedback. Contributed to the data analysis and provided guidance on the methodology section. Played a key role in the final revision of the manuscript, ensuring its quality and correcting writing errors.

REFERENCES

[1] K. Öcalan, "Higher-order differential cross section calculation for the associated production of a W boson and jets in the electron decay channel at a center-of-mass energy of 13 TeV in proton-proton collisions," *Turk J Phys*, vol. 43, pp. 156–166, 2019.

[2] The ATLAS Collaboration, "Study of jets produced in association with a W boson in pp collisions at √s = 7 TeV with the ATLAS detector," Phys.Rev.D 85 (2012) 092002.

[3] J. M. Campbell, J. W. Huston, and W. J. Stirling, "Hard Interactions of Quarks and Gluons: a Primer for LHC Physics," Reports on Progress in Physics, vol. 70, no. 1, pp. 89–193, Jan. 2007. [Online]. Available: https://arxiv.org/abs/hep-ph/0611148

[4] [4K. Geiger and B. Müller, "QCD Evolution Equations for High Energy Partons in Nuclear Matter," Physical Review D, vol. 50, no. 1, pp. 337–357, Jul. 1994. [Online]. Available: https://doi.org/10.1103/PhysRevD.50.337

[5] M. Benedikt et al., "Future Circular Collider Study. Volume 3: The Hadron Collider (FCC-hh) Conceptual Design Report," *Eur. Phys. J. ST*, vol. 228, no. 4, pp. 755–1107, 2019.

[6] M. Benedikt and F. Zimmermann, Future Circular Collider Study. Volume 2: The Lepton Collider, CERN-ACC-2018-0057, CERN, Geneva, Switzerland, 2018. [Online]. Available: https://cds.cern.ch/record/2651299

[7] M. Mangano et al., Future Circular Collider Study. Volume 1: Physics Opportunities, CERN-ACC-2018-0056, CERN, Geneva, Switzerland, 2018. [Online]. Available: https://cds.cern.ch/record/2651305

[8] L. Lönnblad and S. Prestel, "Merging multi-leg NLO matrix elements with parton showers," Journal of High Energy Physics, vol. 2013, no. 3, p. 166, 2013.

[9] J. Alwalla, R. Frederix, S. Frixione, V. Hirschi, F. Maltoni, O. Mattelaer, H.-S. Shao, T. Stelzer, P. Torrielli, and M. Zaro, "The automated computation of tree-level and next-to-leading order differential cross sections, and their matching to parton shower simulations," JHEP, vol. 07, p. 079, 2014.

[10] T. Sjöstrand, S. Ask, J. R. Christiansen, R. Corke, N. Desai, P. Ilten, S. Mrenna, S. Prestel, C. O. Rasmussen, and P. Z. Skands, "An introduction to PYTHIA 8.2," *Computer Physics Communications*, vol. 191, pp. 159–177, 2015.

[11] R. Frederix and T. Moskalets, "Five-flavour scheme predictions for $t\bar{t}\,b\bar{b}$ at next-to-leading order accuracy," *European Physical Journal C*, vol. 84, no. 7, Article no. 763, Jul. 2024. Available: arXiv:2403.14419

[12] S. Hoeche, F. Krauss, M. Schonherr, and F. Siegert, "QCD matrix elements + parton showers: The NLO case," *Journal of High Energy Physics*, vol. 2013, no. 4, p. 27, 2013.

[13] K. Hamilton and P. Nason, "Improving NLO-parton shower matched simulations with higher order matrix elements," arXiv preprint arXiv:1004.1764, 2010. [Online]. Available: https://arxiv.org/abs/1004.1764

[14] S. Catani et al., "Matching matrix elements and parton showers in hadronic collisions: The k_T-factorization approach," *Journal of High Energy Physics*, vol. 2001, no. 5, p. 25, 2001.

[15] M. Rubin, G. P. Salam, and S. Sapeta, "Giant QCD K-factors beyond NLO," *Journal of High Energy Physics*, vol. 2010, no. 84, 2010.

[16] M. Cacciari, G. P. Salam, and G. Soyez, "The anti-kT jet clustering algorithm," *Journal of High Energy Physics*, vol. 2008, no. 4, p. 63, 2008.

[17] D. Kim, S. Lee, H. Jung, D. Kim, J. Kim, and J. Song, "A Panoramic Study of K-Factors for 111 Processes at the 14 TeV LHC," arXiv preprint, arXiv:2402.16276, Feb. 2024. [Online]. Available: https://doi.org/10.48550/arXiv.2402.16276

[18] J. Huston, "LO, NLO, LO* and jet algorithms," Proceedings of the Workshop on RadCor2009, arXiv:1001.2581, Oct. 2010. [Online]. Available: https://doi.org/10.48550/arXiv.1001.2581.

IDENTIFIABILITY ANALYSIS OF A MATHEMATICAL MODEL FOR THE FIRST WAVE OF COVID-19 IN TÜRKİYE

Tuğba AKMAN [1] (iD)

[1] *University of Turkish Aeronautical Association, Department of Computer Engineering, Ankara, Türkiye,*
takman@thk.edu.tr

ABSTRACT

In this work, a structurally identifiable mathematical model is developed to capture the first peak of COVID-19 in Türkiye. The daily numbers of COVID-19 cases, deaths, prevalence in the ICU, and prevalence on ventilation, obtained from the open-access TURCOVID-19 database, during the first peak, are used as observations. Structural identifiability analysis is performed using the open-source software Julia. For parameter estimation, some parameters are fixed based on the literature while the remaining parameters are estimated using the Data2Dynamics software. Our results align well with the observations. Then, a practical identifiability analysis based on the profile likelihood method is conducted to investigate uncertainties in the parameter values. It reveals that three of the model parameters, namely the progression rate of symptomatically infectious individuals to hospital and the transmission rates associated with exposed and symptomatically infectious individuals, are not practically identifiable. This means that the implementation of intervention strategies via this model must be performed carefully.

Keywords: Structural identifiability, Practical identifiability, COVID-19, Mathematical modeling, Türkiye.

1 INTRODUCTION

The novel coronavirus has changed the world in several ways, such as introducing new hygiene habits, emphasizing effective handwashing, skipping the handshake, working out at home, increasing reliance on online meetings, and raising awareness about vaccination or boosters. Once a novel virus began affecting the world, predicting the number of infectious

individuals, forecasting upcoming peaks, and determining the most suitable public interventions became crucial.

Researchers and scientists have paid attention to mathematical models in infectious disease modeling for decision-making. Intervention strategies and their impacts are compared using run charts, EWMA control charts, and p-control charts based on COVID-19 data from Türkiye [1]. An algorithm approximating the effect of nodes in complex networks has been developed under the susceptible-infectious-recovered (SIR) models [2]. We refer the reader to the studies for reviews on COVID-19 modeling (see, examples [3-5].). On the other hand, hypothetical models have gained importance in understanding the spread of the disease within communities. In particular, the potential use of face masks has been investigated in mathematical models; the importance of face masks together with non-pharmaceutical interventions is concluded [6]. As more data have been collected, models incorporating parameter estimation methods have revealed country-based differences driven by intervention strategies, human behavior, and technology. For example, differences have been observed in India, Mexico, Wuhan, Sweden, Canada, and Türkiye [7-12]. Vaccination programs have been examined through mathematical models, with findings suggesting that vaccination alone is not sufficient to control the spread [13]. The effects of awareness programs have also been studied, with results indicating that awareness and timely hospitalization are critical factors in eliminating the disease [14]. The impact of testing and isolation has been discussed, and authors have concluded that the timing of testing and the rate of testing are two key factors in developing effective control strategies [15]. Malik et al. have expressed the outbreak of COVID-19 as a fractional order system and considered an inverse problem to find the time-dependent parameters in the model for the data of India [16, 17].

The construction of a mathematical model consists of several steps [18, Figure. 1]. Model development is followed by structural identifiability analysis. This is necessary because two different parameter sets can sometimes lead to the same solution curves for a structurally nonidentifiable model. However, this can result in unrealistic model behavior. In fact, inefficient control strategies based on such models may cause the disease to spread even more. Therefore, it is crucial to analyze whether the model is structurally identifiable before proceeding with model calibration. Model calibration enables the determination of the parameter values in the model. While model parameters are structurally identifiable, they may not always be practically identifiable. Therefore, practical identifiability analysis is essential. If any parameter is found

to be practically nonidentifiable, then one must be careful in making predictions or adjustments in case of parameter perturbations.

Akman et al. constructed a mathematical model for COVID-19 in Türkiye [12], which captured the first peak using the data from the TURCOVID-19 database [19]. They also investigated the effect of underreporting [12]. In this work, we extend the model presented in the work [12] by splitting the symptomatically infectious subgroup into symptomatically infectious and hospitalized patients and adding a quarantine subgroup to model the first peak of the spread. Additionally, we investigate both the structural and practical identifiability of the model, which were not within the scope of the paper by Akman et al. [12]. From this current study, we have learned that caution is needed when making future predictions or planning interventions based on this model, as α_1, β_e, and β_s (the progression rate of symptomatically infectious individuals to hospital, and the transmission rates associated with exposed and symptomatically infectious individuals) are not practically identifiable. The rest of the paper is organized as follows: In Sec. 2, the mathematical model is developed and explained. Sec. 3 presents the structural identifiability analysis. Sec. 4 is devoted to model calibration, followed by the practical identifiability analysis in Sec. 5. Sensitivity analysis is discussed in Sec. 6. Simulation results are presented in Sec.7. This paper ends with a summary and conclusion.

2 MODEL DEVELOPMENT

We develop a mathematical model for the first wave of COVID-19 by splitting the total population of Türkiye at time t, denoted N(t), into nine mutually exclusive compartments of individuals for the period of March 11, 2020 - May 31, 2020. The variables in the model represent the number of individuals in each compartment: susceptible $S := S(t)$, exposed $E := E(t)$, asymptomatic and infectious but not tested $I_n := I_n(t)$, symptomatic and infectious $I_s := I_s(t)$, hospitalized and isolated $I_h := I_h(t)$, patients staying at ICU $I_{ICU} := I_{ICU}(t)$, ventilated $I_v := I_v(t)$, recovered $R := R(t)$ and quarantined $Q := Q(t)$ at time t. Therefore, the total population $N := N(t)$ is given by

$$N = S + E + I_n + I_s + I_h + I_{ICU} + I_v + R + Q.$$

We use the standard incidence and exclude isolated individuals, as motivated by the work [21], in the disease transmission state. Susceptible individuals (S) become infected because of the interactions with exposed individuals (E), asymptomatically infectious individuals (I_n), and symptomatically infectious individuals (I_s) at the rates of β_e, β_n, and β_s,

respectively. The exposed class (E) is affected by this interaction, and the exposed compartment decreases at the rate of k. A fraction ρ of exposed individuals show symptoms, while the rest move to the compartment of asymptomatically infectious individuals (I_n). Asymptomatically and symptomatically infectious individuals recover at the rates of γ_n and γ_s, respectively. Symptomatically infectious individuals may develop severe infections and get hospitalized at the rate of α_1. Hospitalized individuals die at the rate of μ_h and recover at the rate of γ_h. Hospitalized patients may be transferred to the ICU at the rate of α_2, and ICU patients may be ventilated (I_v) at the rate of α_3. Both ICU patients and ventilated patients recover at the rates of γ_{ICU} and γ_v, respectively, and pass away at the rates of μ_{ICU} and μ_v, respectively. During simulations, quarantine and isolation strategies are implemented, so susceptible individuals move to quarantine at the rate of c. We exclude quarantine of the subgroups of E, I_n and I_s, as quarantine is applied only when the number of infectious individuals becomes too high. Since we are modeling the early stages of the pandemic, we exclude the terms for natural death, births, and vaccination. Based on these assumptions, we develop the following model:

$$\frac{dS}{dt} = -(\beta_e E + \beta_n I_n + \beta_s I_s)\frac{S}{N - I_h - I_{ICU} - I_v - Q} - \eta S, \tag{1a}$$

$$\frac{dE}{dt} = (\beta_e E + \beta_n I_n + \beta_s I_s)\frac{S}{N - I_h - I_{ICU} - I_v - Q} - kE, \tag{1b}$$

$$\frac{dI_n}{dt} = (1 - \rho)kE - \gamma_n I_n, \tag{1c}$$

$$\frac{dI_s}{dt} = \rho kE - (\alpha_1 + \gamma_s)I_s, \tag{1d}$$

$$\frac{dI_h}{dt} = \alpha_1 I_s - (\alpha_2 + \gamma_h + \mu_h)I_h, \tag{1e}$$

$$\frac{dI_{ICU}}{dt} = \alpha_2 I_h - (\alpha_3 + \gamma_{ICU} + \mu_{ICU})I_{ICU}, \tag{1f}$$

$$\frac{dI_v}{dt} = \alpha_3 I_{ICU} - (\gamma_v + \mu_v)I_v, \tag{1g}$$

$$\frac{dR}{dt} = \gamma_n I_n + \gamma_s I_s + \gamma_h I_h + \gamma_{ICU} I_{ICU} + \gamma_v I_v, \tag{1h}$$

$$\frac{dQ}{dt} = \eta S, \tag{1i}$$

$S(0) = S_0, E(0) = E_0, I_n(0) = I_{n,0}, I_s(0) = I_{s,0}, I_h(0) = I_{h,0}, I_{ICU}(0) = I_{ICU,0}, I_v(0) = I_{v,0}, R(0) = R_{n,0}, Q(0) = Q_{n,0}.$ (1j)

We proceed with the proofs of existence and uniqueness, positivity and boundedness of the solution.

2.1 Model analysis

We observe that the right-hand side of model (1) is completely continuous and locally Lipschitzian. Therefore, its solution, namely S(t), E(t), I_n(t), I_s(t), I_h(t), I_{icu}(t), I_v(t), R(t), and Q(t), with non-negative initial conditions exists and is unique on the interval [0, t*], where 0 < t* < ∞ [22].

We first prove that the solution is positive. Consider t* = sup {t > 0: S(t), E(t), I_n(t), I_s(t), I_h(t), I_{icu}(t), I_v(t), R(t), Q(t) > 0 }. Then, by integration, Equation (1a) leads to

$$\frac{d}{dt}\left(S(t)\,exp(\eta t + \int_0^{t*} \frac{\beta_e E(u) + \beta_n I_n(u) + \beta_s I_s(u)}{N(u) - I_h(u) - I_{ICU}(u) - I_v(u) - Q(u)}\, du)\right) = 0.$$

Then, we obtain

$$S(t*)\,exp(\eta t* + \int_0^{t*} \frac{\beta_e E(u) + \beta_n I_n(u) + \beta_s I_s(u)}{N(u) - I_h(u) - I_{ICU}(u) - I_v(u) - Q(u)}\, du) - S(0) = 0.$$

We rewrite this equation to reach

$$S(t*) = S(0)\,exp(-\eta t* - \int_0^{t*} \frac{\beta_e E(u) + \beta_n I_n(u) + \beta_s I_s(u)}{N(u) - I_h(u) - I_{ICU}(u) - I_v(u) - Q(u)}\, du) \geq 0.$$

It means that the solution S(t) is non-negative. Similarly, we can follow the same approach to prove that all other solutions are non-negative.

We secondly prove that the model variables are bounded above. Therefore, we add all the equations up in model (1) to obtain

$$\frac{dN}{dt} = -\mu_h I_h - \mu_{icu} I_{icu} - \mu_v I_v \leq -min(\mu_h, \mu_{icu}, \mu_v)\, N = -\mu\, N,$$

where $min(\mu_h, \mu_{icu}, \mu_v) = \mu$. We observe that N is a decreasing function of time t and $N(t) = N(0)exp(-\mu t)$. Then, it means that all model variables are bounded above. We now proceed with the structural identifiability analysis.

3 STRUCTURAL IDENTIFIABILITY ANALYSIS

Identifiability analysis has been discussed in many studies (for example [23-27]). Here, we provide a summary based on these works.

A model parameter p_i is called identifiable if the confidence interval associated with p_i, denoted [$p+_i$, $p-_i$], is finite. There are two types of identifiability that can be investigated: structural and practical identifiability. The former is independent of the data and concerns the

structure of the mathematical model, while the latter considers the observations used for model fitting. Some mathematical models suffer from structural nonidentifiability, meaning that a unique parametrization of the model using the available observations cannot be achieved.

We, firstly, investigate the structural identifiability of model (1) by expressing it as

$$x'(t) = f(x, p), \qquad x(0) = x0, \tag{2}$$

where x and p denote the states and parameters of model (1), respectively. The data in this study comes from the open-access TURCOVID-19 database [28, 19]. The observations we have are the daily number of cases $y_1(t) = \rho k E$, the daily number of deaths $y_2(t) = \mu_h I_h + \mu_{ICU} I_{ICU} + \mu_v I_v$, ICU prevalence $y_3(t) = I_{ICU}$ and ventilation unit prevalence $y_4(t) = I_v$. We can write the observations as:

$$y(t) = g(x, p) . \tag{3}$$

The model given by Equation (2) is structurally identifiable if the vector p can be uniquely determined from the observations y(t) in Equation (3), assuming the observations are unlimited [23]. Otherwise, the model is considered unidentifiable. The formal definition is provided below [29].

Definition 1. Suppose that p and p̱ are two distinct parameter vectors. Model (1) is said to be globally (uniquely) structurally identifiable if

$$g(x, p) = g(x, p̱) \quad implies \quad p = p̱. \tag{4}$$

Definition 2. Model (1) is said to be locally structurally identifiable if for any p within an open neighborhood of p̱ in the parameter space,

$$g(x, p) = g(x, p̱) \quad implies \quad p = p̱. \tag{5}$$

Structural identifiability can be analyzed using various methods, such as the Taylor series method [30], Lie symmetries [31], generating power series approach [32], and differential algebra approach [33]. We prefer the differential algebra approach as the open-source software JULIA [33] and its structural identifiability package [25, 35] can perform this analysis and can capture both identifiable and nonidentifiable parameters. The differential algebra approach explains the structural identifiability as follows [36]:

Definition 3. Suppose that c($\mathbf{p}$) denotes the coefficients of the input-output equation corresponding to model (1). We say that model (1) is structurally identifiable from unlimited observations y(t) if and only if c($\mathbf{p}$) = c($\mathbf{\bar{p}}$) implies $\mathbf{p} = \mathbf{\bar{p}}$.

If a model is not structurally identifiable, reparametrization is required [37].

4 MODEL CALIBRATION

We proceed with parameter estimation for model (1) using the data obtained from the online database TURCOVID19 [19, 28]. The spread of the virus in the community changes over time due to public interventions. Therefore, we focus on the early dynamics of the spread, during which we can capture the first peak, specifically the period from March 11, 2020, to May 31, 2020, in Türkiye. We fit model (1) to the data, including the number of COVID-19 cases, the number of deaths, ICU prevalence, and ventilation prevalence. Let $\{t_i\}_{i=1}^{k_1}, \{t_i\}_{i=1}^{k_2}, \{t_i\}_{i=1}^{k_3}$ and $\{t_i\}_{i=1}^{k_4}$ represent the time points for each observation, respectively. The measurements contain some noise and can be expressed as

$$Y_1^i = y_1(t_i) + \epsilon_i, \quad i = 1,2,\cdots,k_1,$$

$$Y_2^i = y_2(t_i) + \epsilon_i, \quad i = 1,2,\cdots,k_2,$$

$$Y_3^i = y_3(t_i) + \epsilon_i, \quad i = 1,2,\cdots,k_3,$$

$$Y_4^i = y_4(t_i) + \epsilon_i, \quad i = 1,2,\cdots,k_4. \tag{6}$$

We estimate the parameters of model (1) by solving the following optimization problem:

$$\min p \left(\frac{1}{k_1} \sum_{i=1}^{k_1} \frac{|y_1(t_i)-Y_1^i|^2}{\tilde{Y}_1^2} + \frac{1}{k_2} \sum_{i=1}^{k_2} \frac{|y_2(t_i)-Y_2^i|^2}{\tilde{Y}_2^2} + \frac{1}{k_3} \sum_{i=1}^{k_3} \frac{|y_3(t_i)-Y_3^i|^2}{\tilde{Y}_3^2} + \right.$$

$$\left. + \frac{1}{k_4} \sum_{i=1}^{k_4} \frac{|y_4(t_i)-Y_4^i|^2}{\tilde{Y}_4^2} \right), \tag{7}$$

w. r. t. the constraint $p > 0$. $\tag{8}$

The terms $\tilde{Y}_t^i$ for t $\in \{1, 2, 3, 4\}$ are the average observations written as $\tilde{Y}_t^i = \frac{1}{k_t}\sum_{i=1}^{k_t} Y_t$.

After model calibration, practical identifiability is performed to investigate the confidence intervals of the model parameters.

5   PRACTICAL IDENTIFIABILITY ANALYSIS

We proceed with the practical identifiability analysis, as model (1) has been shown to be structurally identifiable. However, a structurally identifiable parameter may still be practically nonidentifiable. This often occurs when the observations or data used in model calibration are insufficient to compute a finite confidence interval [38]. It is defined as follows:

Definition 4. A parameter estimate p_i is practically nonidentifiable; despite the unique minimum of the likelihood for this parameter, the likelihood-based confidence region associated with the parameter is infinitely extended in increasing and/or decreasing direction of $\underline{p}_i$.

There are several methods to analyze parameter identifiability, including Bayesian sampling approaches [39, 40], bootstrap methods [41], and the Fisher information matrix [42]. Additionally, using the profile likelihood method [23, 24], we can determine the practically identifiable parameters with a 95% confidence interval, allowing us to assess parameter uncertainties in the model. We prefer this approach because it can be easily implemented using the d2d software after model calibration [43-45].

6   SENSITIVITY ANALYSIS

Global sensitivity analysis is performed for COVID-19 models to test the robustness of the model [12, 46]. In this work, the method of the partial rank correlation coefficient (PRCC) is used [47]. The aim is to measure the effect of each model parameter on a variable or observation to obtain a value between −1 and +1 and to determine the strength of this value. Computational details and simulation results are discussed in the next section.

7   SIMULATION RESULTS

After constructing the model and determining the type of data to use, we perform structural identifiability analysis. We use the open-source software JULIA [34] and its StructuralIdentifiability.jl package [25, 35] for the analysis.

However, we encountered a memory error in JULIA. This issue can be resolved by using linear first integrals, which speed up computations [46]. We apply a suitable transformation to the model (1) to eliminate one of the unknowns in the system. Details are provided in the appendix.

Based on the analysis performed in JULIA [33], we find that all variables and parameters of model (1) are globally identifiable. After confirming that the model is structurally identifiable, we proceed with parameter estimation using the d2d software [43-45]. We fix the values of some parameters related to the dynamics of COVID-19 based on the literature. The d2d software uses a deterministic optimisation algorithm, namely lsqnonlin, in the parameter estimation step [44]. In addition, the d2d software decides the most efficient ODE solver to find the numerical solution. The parameter interval is set as $p \in (10^{-6}, 10^5)$, with the upper bound for α_1 is fixed as 10^{11} and the lower bounds for β_e and β_s are set as 10^{-8}. The values of parameters and initial conditions are provided in Table 1.

Table 1. Parameter values.

Parameter	Value	Unit	Source
α_1	2.8×10^{10}	Day^{-1}	Calibrated
α_2	0.041	Day^{-1}	Calibrated
α_3	0.14	Day^{-1}	Calibrated
β_e	1.4×10^{-9}	Day^{-1}	Calibrated
β_n	1.7	Day^{-1}	Calibrated
β_s	6.3×10^{-6}	Day^{-1}	Calibrated
η	0.19	Day^{-1}	Calibrated
γ_h	0.1449	Day^{-1}	[47]
γ_{ICU}	0.231285	Day^{-1}	[47]
γ_n	0.3448	Day^{-1}	[47]
γ_s	0.1429	Day^{-1}	[47]
γ_v	0.239209	Day^{-1}	[47]
k	1/14	Day^{-1}	Estimated from [48]
μ_{ICU}	0.0605032	Day^{-1}	[12]
μ_h	0.000001	Day^{-1}	Adapted from [12]
μ_v	0.00029338	Day^{-1}	[12]
ρ	0.28	Day^{-1}	[12]
S_0	8×10^7	Individual	[12]
E_0	437	Individual	[12]
$I_{n,0}$	490	Individual	[12]
$I_{s,0}$	1	Individual	Data
$I_{h,0}, I_{ICU,0}, I_{hv,0}, R_{h,0}, Q_{h,0}$	0	Individual	Data

The optimization problem (7)-(8) is solved as a multi-start optimization problem with 500 iterations. Figure 1 shows that convergence is achieved, and the first-order optimality criterion is calculated as 3.82169×10^{-8}.
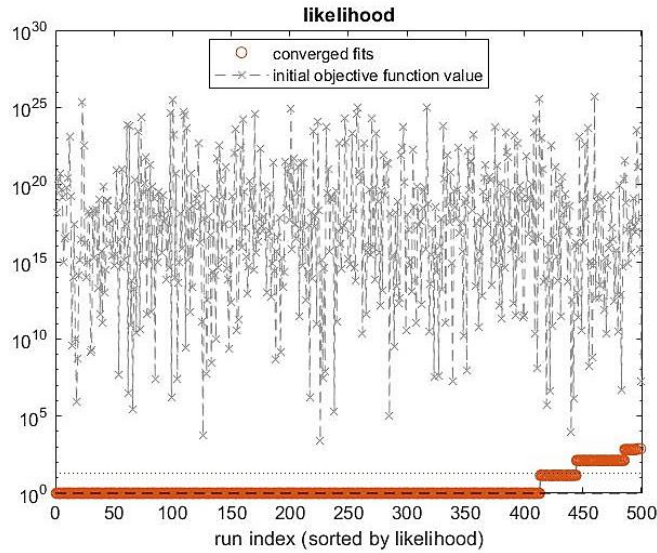
Figure 1. Overview about the multistart optimization.

We present the simulation results in Figure. 2-5. We observe that model (1) accurately predicts the dynamics, and the simulation results align well with the model observations.
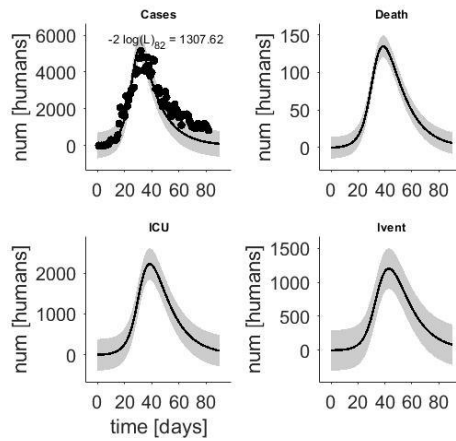

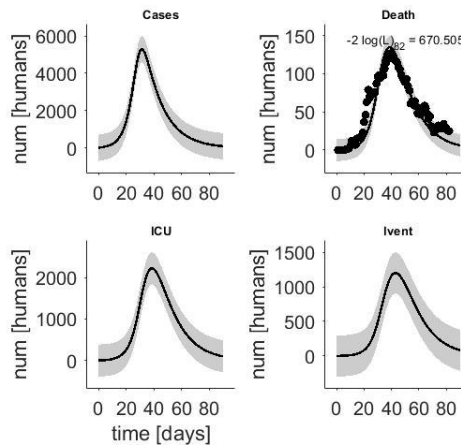*Figure 2. Simulation results for the number of cases.*

Figure 3. Simulation results for the number of deaths.

After model calibration, we proceed with the practical identifiability analysis using profile likelihood, which is performed by the d2d software.

We note that calibrated parameter values p_i's are displayed by gray stars, and thresholds for the confidence intervals are shown by the upper and lower dashed lines in Figure 6. We note that calibrated parameter values p_i's are displayed by gray stars, and thresholds for the confidence intervals are shown by the upper and lower dashed lines in Figure 4. We observe that the parameters α_1, β_e, and β_s are not practically identifiable, as a finite confidence interval for α_1 and β_e cannot be determined, and the confidence interval for β_s is very flat. The value of β_e is found at the left end of the parameter interval, indicating practical nonidentifiability. To overcome this, additional data sets should be incorporated during the model calibration step, such as data on the number of susceptible individuals. However, such data are difficult to collect, as it is not possible to test everyone in the population to determine whether they are infectious.
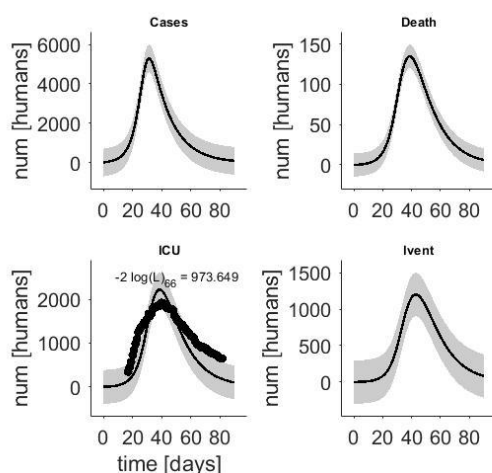

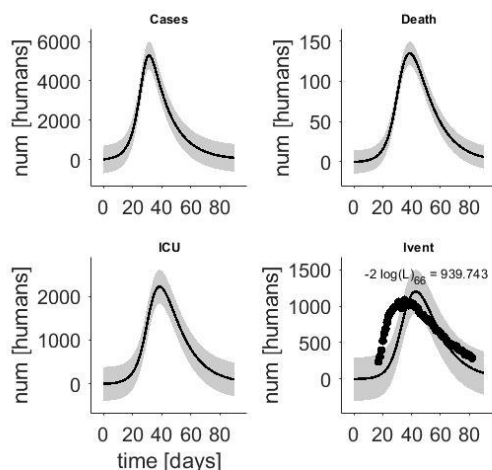*Figure 4. Simulation results for ICU prevalence.*

Figure 5. Simulation results for ventilation prevalence.

We proceed with sensitivity analysis. A MATLAB code developed by Lab has been modified for implementation of the method of PRCC [48]. Intervals for each parameter are set starting from half to twice the baseline value, and a uniformly distributed sample space with 1000 sample values is constructed.

We investigate the sensitivities of the number of cases and the number of deaths and present them in Figure. 7 and Figure. 8, respectively. We choose the days corresponding to the middle and the end of the simulation interval, namely days 40 and 80, respectively, for comparison purposes. We observe that the number of cases increases as the parameter β_n increases, while it decreases as the rate of quarantine, the rate of recovery for asymptomatically infectious.
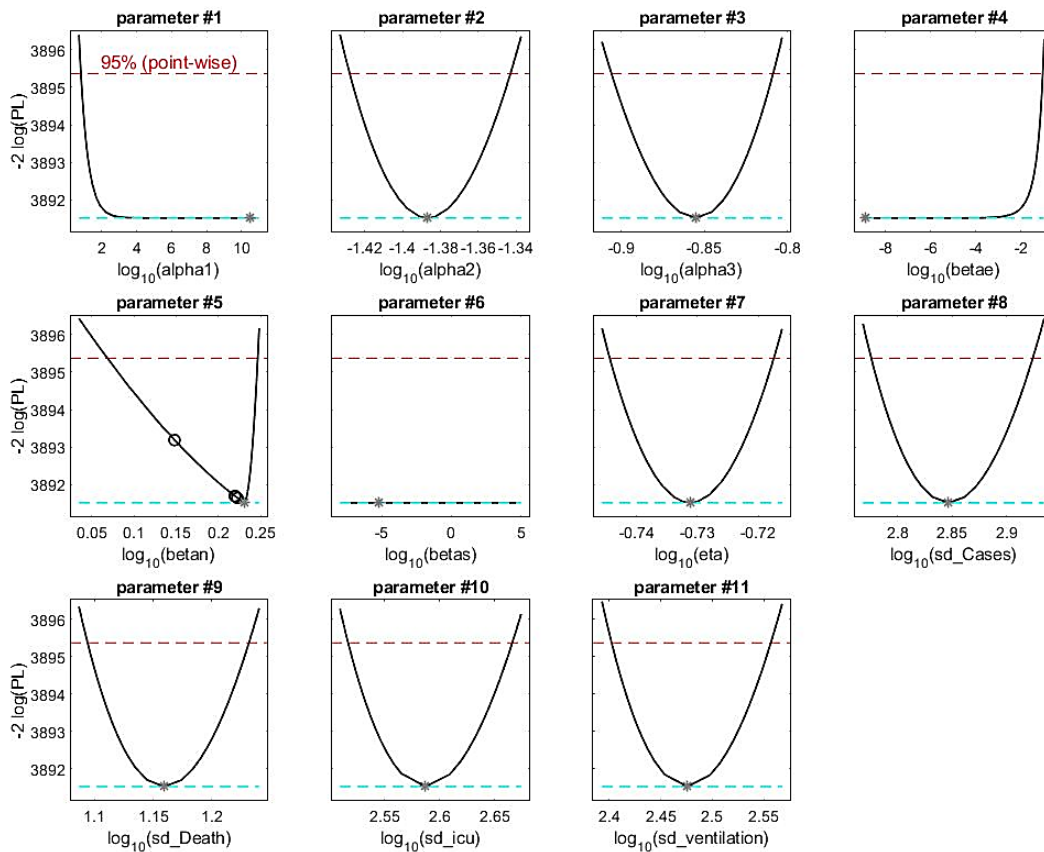
Figure 6. Profile likelihood curves.

For day 80, it is inversely proportional to the incubation period $1/k$. On the other hand, the number of deaths is proportional to the parameters β_n and α_2. It means that as the value of the transmission rate and the rate at which patients are transferred to ICU increases, the more people pass away. Negative, but the largest sensitivity in magnitude occurs for the parameter η meaning that as the rate of quarantine increases, more lives can be saved.
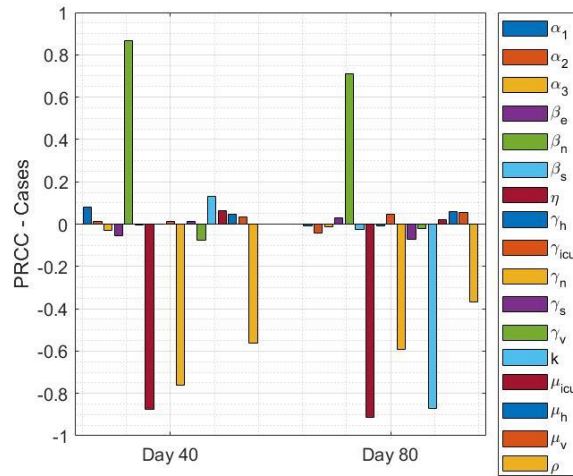
Figure 7. Sensitivity analysis for the number of cases.
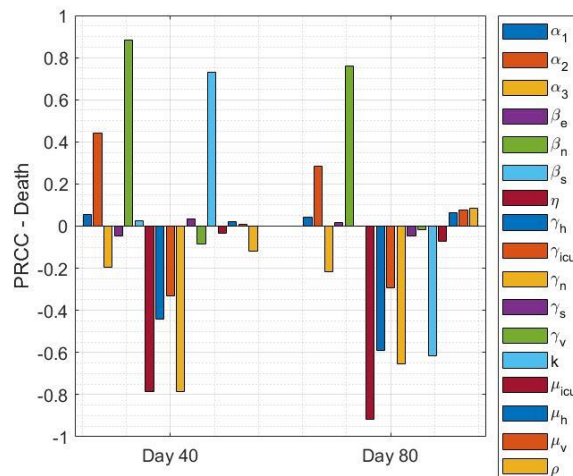
Figure 8. Sensitivity analysis for the number of deaths.

8   CONCLUSION AND SUGGESTIONS

We develop a model for disease transmission during the first peak of COVID-19 in Türkiye. We observe that our model is structurally identifiable when using the number of symptomatic cases, deaths, patients in the ICU, and ventilated patients as observations. Structural identifiability analysis is performed using the open-source software Julia and its structural identifiability package after simplifying the model based on linear first integrals. Model calibration is carried out as a multi-start optimization problem, and the simulation results align well with the data. Next, we investigate the variability of the parameters based on the profile likelihood method for parameter identifiability. We find that the parameters α_1, β_e, and β_s are not practically identifiable. It indicates that the implementation of intervention strategies

must be carried out with caution. In addition, we performed sensitivity analysis and determined the effect of the parameters on the observations, namely the number of cases and deaths. The disease transmission rate of asymptomatically infectious individuals and the rate of quarantine have the biggest impact on the observations. Indeed, the former is positively correlated, the latter is negatively correlated with the observations.

As future work, this model can be extended to model subsequent waves of the pandemic by incorporating delay terms, and the identifiability of the models developed for vaccination strategies can be investigated.

Acknowledgment

The author would like to thank the anonymous reviewers for the constructive feedback.

Statement of Research and Publication Ethics

The study is compiled with research and publication ethics.

Artificial Intelligence (AI) Contribution Statement

This manuscript was entirely written, edited, analyzed, and prepared without the assistance of any artificial intelligence (AI) tools. All content, including text, data analysis, and figures, was solely generated by the authors.

REFERENCES

[1]   E. Polat, "Using quality control charts for monitoring COVID-19 daily cases and deaths in Türkiye," *Bitlis Eren Üniversitesi Fen Bilimleri Dergisi*, vol. 13, no. 1, pp. 134–152.

[2]   A. Şimşek, "Estimating the expected influence capacities of nodes in complex networks under the susceptible-infectious-recovered model," *Bitlis Eren Üniversitesi Fen Bilimleri Dergisi*, vol. 13, no. 2, pp. 408–417.

[3]   R. Padmanabhan, H. S. Abed, N. Meskin, T. Khattab, M. Shraim, and M. A. Al-Hitmi, "A review of mathematical model-based scenario analysis and interventions for COVID-19," *Computer Methods and Programs in Biomedicine*, vol. 209, p. 106301, 2021.

[4]   I. Rahimi, F. Chen, and A. H. Gandomi, "A review on COVID-19 forecasting models," *Neural Computing and Applications*, vol. 35, no. 33, pp. 23671–23681, 2023.

[5]   Y. Xiang, Y. Jia, L. Chen, L. Guo, B. Shu, and E. Long, "COVID-19 epidemic prediction and the impact of public health interventions: A review of COVID-19 epidemic models," *Infectious Disease Modelling*, vol. 6, pp. 324–342, 2021.

[6]   S. E. Eikenberry, M. Mancuso, E. Iboi, T. Phan, K. Eikenberry, Y. Kuang, E. Kostelich, and A. B. Gumel, "To mask or not to mask: Modeling the potential for face mask use by the general public to curtail the COVID-19 pandemic," *Infectious Disease Modelling*, vol. 5, pp. 293–308, 2020.

[7]   S. K. Biswas, J. K. Ghosh, S. Sarkar, and U. Ghosh, "COVID-19 pandemic in India: a mathematical model study," *Nonlinear Dynamics*, vol. 102, pp. 537–553, 2020.

[8]   O. Torrealba-Rodriguez, R. Conde-Gutiérrez, and A. Hernández-Javier, "Modeling and prediction of COVID-19 in Mexico applying mathematical and computational models," *Chaos, Solitons & Fractals*, vol. 138, p. 109946, 2020.

[9]   A. J. Kucharski, T. W. Russell, C. Diamond, Y. Liu, J. Edmunds, S. Funk, R. M. Eggo, F. Sun, M. Jit, and J. D. Munday, "Early dynamics of transmission and control of COVID-19: a mathematical modelling study," *The Lancet Infectious Diseases*, vol. 20, no. 5, pp. 553–558, 2020.

[10]   M. Carlsson and C. Söderberg-Nauclér, "COVID-19 modeling outcome versus reality in Sweden," *Viruses*, vol. 14, no. 8, p. 1840, 2022.

[11]   A. R. Tuite, D. N. Fisman, and A. L. Greer, "Mathematical modelling of COVID-19 transmission and mitigation strategies in the population of Ontario, Canada," *CMAJ*, vol. 192, no. 19, pp. E497–E505, 2020.

[12]   T. Akman, E. Köse, and N. Tuncer, "Assessment of vaccination and underreporting on COVID-19 infections in based on effective reproduction number," *International Journal of Biomathematics*, pp. 2350102 – Online ready, 2024. [Online]. Available: https://doi.org/10.1142/S1793524523501024

[13]   S. Moore, E. M. Hill, M. J. Tildesley, L. Dyson, and M. J. Keeling, "Vaccination and non-pharmaceutical interventions for COVID-19: a mathematical modelling study," *The Lancet Infectious Diseases*, vol. 21, no. 6, pp. 793–802, 2021.

[14]   S. S. Musa, S. Qureshi, S. Zhao, A. Yusuf, U. T. Mustapha, and D. He, "Mathematical modeling of COVID-19 epidemic with effect of awareness programs," *Infectious Disease Modelling*, vol. 6, pp. 448–460, 2021.

[15]   S. Gao, P. Binod, C. W. Chukwu, T. Kwofie, S. Safdar, L. Newman, S. Choe, B. K. Datta, W. K. Attipoe, W. Zhang, and B. K. Datta, "A mathematical model to assess the impact of testing and isolation compliance on the transmission of COVID-19," *Infectious Disease Modelling*, vol. 8, no. 2, pp. 427–444, 2023.

[16]   A. Malik, N. Kumar, and K. Alam, "Estimation of parameter of fractional order COVID-19 SIQR epidemic model," *Materials Today: Proceedings*, vol. 49, pp. 3265–3269, 2022.

[17]   A. Malik, K. Alam, and N. Kumar, "Coefficient identification in SIQR model of inverse problem of COVID-19," *European Journal of Molecular and Clinical Medicine*, vol. 7, 2020.

[18]   L. Wanika, J. R. Egan, N. Swaminathan, C. A. Duran-Villalobos, J. Branke, S. Goldrick, and M. Chappell, "Structural and practical identifiability analysis in bioengineering: a beginner's guide," *Journal of Biological Engineering*, vol. 18, no. 1, p. 20, 2024.

[19]   U. Abdullah, Ş. Arslan, H. S. Manap, T. Gürkan, M. Çalışkan, A. Dayıoğlu, H. N. Efe, M. Yılmaz, A. Z. İbrahimoğlu, E. Gültekin, R. Durna, R. Başar, F. B. Osmanoğlu, and S. Ören, "Türkiye COVID-19 pandemi izleme ekranı," [Online]. Available: https://turcovid19.com/, August 2020.

[20]   N. Tuncer, A. Timsina, M. Nuno, G. Chowell, and M. Martcheva, "Parameter identifiability and optimal control of an SARS-CoV-2 model early in the pandemic," *Journal of Biological Dynamics*, vol. 16, no. 1, pp. 412–438, 2022.

[21]   A. Raue, C. Kreutz, T. Maiwald, J. Bachmann, M. Schilling, U. Klingmüller, and J. Timmer, "Structural and practical identifiability analysis of partially observed dynamical models by exploiting the profile likelihood," *Bioinformatics*, vol. 25, no. 15, pp. 1923–1929, 2009.

[22]   J. K. Hale, "Functional differential equations," in *Analytic Theory of Differential Equations: The Proceedings of the Conference at Western Michigan University, Kalamazoo, from 30 April to 2 May 1970*. Berlin, Heidelberg: Springer Berlin Heidelberg, Aug. 2006, pp. 9–22.

[23]   C. Kreutz, A. Raue, and J. Timmer, "Likelihood based observability analysis and confidence intervals for predictions of dynamic models," *BMC Systems Biology*, vol. 6, pp. 1–9, 2012.

[24]   R. Dong, C. Goodbrake, H. Harrington, and P. G., "Differential elimination for dynamical models via projections with applications to structural identifiability," *SIAM Journal on Applied Algebra and Geometry*, vol. 7, no. 1, pp. 194–235, 2023.

[25] G. Chowell, S. Dahal, Y. R. Liyanage, A. Tariq, and N. Tuncer, "Structural identifiability analysis of epidemic models based on differential equations: a tutorial-based primer," *Journal of Mathematical Biology*, vol. 87, no. 6, p. 79, 2023.

[26] E. Walter and L. Pronzato, *Identifiability of Parametric Models: From Experimental Data*. Springer, 1997.

[27] U. Abdullah, Ş. Arslan, H. S. Manap, T. Gürkan, M. Çalışkan, A. Dayıoğlu, H. N. Efe, M. Yılmaz, A. Z. İbrahimoğlu, E. Gültekin, R. Durna, R. Başar, F. B. Osmanoğlu, and S. Ören, "Türkiye'de COVID-19 pandemisinin monitorizasyonu için interaktif ve gerçek zamanlı bir web uygulaması: TURCOVID19 (An interactive web-based dashboard for COVID-19 pandemic in real-time monitorization in Türkiye: TURCOVID19)," *Anadolu Kliniği Tıp Bilimleri Dergisi*, vol. 25, no. Special Issue on COVID-19, pp. 154–155, 2020.

[28] N. Tuncer and T. T. Le, "Structural and practical identifiability analysis of outbreak models," *Mathematical Biosciences*, vol. 299, pp. 1–18, 2018.

[29] H. Pohjanpalo, "System identifiability based on the power series expansion of the solution," *Mathematical Biosciences*, vol. 41, no. 1–2, pp. 21–33, 1978.

[30] G. Massonis and A. F. Villaverde, "Finding and breaking Lie symmetries: implications for structural identifiability and observability in biological modelling," *Symmetry*, vol. 12, no. 3, p. 469, 2020.

[31] Y. Lecourtier, F. Lamnabhi-Lagarrigue, and E. Walter, "Volterra and generating power series approaches to identifiability testing," *Identifiability of Parametric Models*, pp. 50–66, 1987.

[32] L. Ljung and T. Glad, "On global identifiability for arbitrary model parametrizations," *Automatica*, vol. 30, no. 2, pp. 265–276, 1994.

[33] J. Bezanson, A. Edelman, S. Karpinski, and V. B. Shah, "Julia: A fresh approach to numerical computing," *SIAM Review*, vol. 59, no. 1, pp. 65–98, 2017.

[34] R. Dong, C. Goodbrake, H. A. Harrington, and G. Pogudin, "Differential elimination for dynamical models via projections with applications to structural identifiability," *SIAM Journal on Applied Algebra and Geometry*, vol. 7, no. 1, pp. 194–235, 2023.

[35] Y. R. Liyanage, N. Heitzman-Breen, N. Tuncer, and S. M. Ciupe, "Identifiability investigation of within-host models of acute virus infection," 2024. [Online]. Available: https://www.biorxiv.org/content/early/2024/05/10/2024.05.09.593464

[36] F.-G. Wieland, A. L. Hauber, M. Rosenblatt, C. Tönsing, and J. Timmer, "On structural and practical identifiability," *Current Opinion in Systems Biology*, vol. 25, pp. 60–69, 2021.

[37] A. Raue, J. Karlsson, M. P. Saccomani, M. Jirstrand, and J. Timmer, "Comparison of approaches for parameter identifiability analysis of biological systems," *Bioinformatics*, vol. 30, no. 10, pp. 1440–1447, 2014.

[38] I. Siekmann, J. Sneyd, and E. J. Crampin, "MCMC can detect nonidentifiable models," *Biophysical Journal*, vol. 103, no. 11, pp. 2275–2286, 2012.

[39] L. E. Eberly and B. P. Carlin, "Identifiability and convergence issues for Markov chain Monte Carlo fitting of spatial models," *Statistics in Medicine*, vol. 19, no. 17–18, pp. 2279–2294, 2000.

[40] M. Joshi, A. Seidel-Morgenstern, and A. Kremling, "Exploiting the bootstrap method for quantifying parameter confidence intervals in dynamical systems," *Metabolic Engineering*, vol. 8, no. 5, pp. 447–455, 2006.

[41] J. A. Jacquez and P. Greif, "Numerical parameter identifiability and estimability: Integrating identifiability, estimability, and optimal sampling design," *Mathematical Biosciences*, vol. 77, no. 1–2, pp. 201–227, 1985.

[42] "Data2Dynamics software," 2024. [Online]. Available: https://github.com/Data2Dynamics

[43] A. Raue, B. Steiert, M. Schelker, C. Kreutz, T. Maiwald, H. Hass, J. Vanlier, C. Tönsing, L. Adlung, R. Engesser, et al., "Data2Dynamics: a modeling environment tailored to parameter estimation in dynamical systems," *Bioinformatics*, vol. 31, no. 21, pp. 3558–3560, 2015.

[44]   A. Raue, M. Schilling, J. Bachmann, A. Matteson, M. Schelke, D. Kaschek, S. Hug, C. Kreutz, B. D. Harms, F. J. Theis, et al., "Lessons learned from quantitative dynamical modeling in systems biology," *PLOS ONE*, vol. 8, no. 9, p. e74335, 2013.

[45]   G. Pogudin, "Speeding things up via linear first integrals," 2024. [Online]. Available: https://github.com/SciML/StructuralIdentifiability.jl/issues/63

[46]   Soulaimani, A. Kaddar, and F. A. Rihan, "Stochastic stability and global dynamics of a mathematical model for drug use: Statistical sensitivity analysis via PRCC," *Partial Differential Equations in Applied Mathematics*, vol. 12, p. 100964, 2024.

[47]   S. Marino, I. B. Hogue, C. J. Ray, and D. E. Kirschner, "A methodology for performing global uncertainty and sensitivity analysis in systems biology," *Journal of Theoretical Biology*, vol. 254, no. 1, pp. 178–196, 2008.

[48]   K. Lab, "Our approach to uncertainty and sensitivity analysis (with R and MATLAB codes for use)," 2020. [Online]. Available: http://malthus.micro.med.umich.edu/lab/usanalysis.html

[49]   S. Zhang, J. Ponce, Z. Zhang, G. Lin, and G. Karniadakis, "An integrated framework for building trustworthy data-driven epidemiological models: Application to the COVID-19 outbreak in New York City," *PLOS Computational Biology*, vol. 17, no. 9, p. e1009334, 2021.

[50]   C. Elias, A. Sekri, P. Leblanc, M. Cucherat, and P. Vanhems, "The incubation period of COVID-19: A meta-analysis," *International Journal of Infectious Diseases*, vol. 104, pp. 708–710, 2021.

APPENDIX

We present the details of the transformation applied to model (1) to speed up the analysis in Julia, where the variable x1 t0 x9 represents the variables in model (1).

```
# Transformation #1

# Observe that: x1' + x2' + x9' +  y1 / rho = 0

# Therefore: x1 + x2 + x9 + int_y1 / rho = C1 for some constant C1

# We introduce new state int_y1' = 1/14 * rho * x2 and make it an output

# Then we can use x1 = C1 - x2 - x9 - int_y1 / rho to eliminate x1 from the system


# Transformation #2

# Observe that: x3' + x4' + x5' + x6' + x7' + x8' -  y1 / rho + y2 = 0

# Therefore: x3 + x4 + x5 + x6 + x7 + x8 - int_y1 / rho + int_y2 = C2 for some constant
C2

# We introduce new state int_y2' = muh*x5 + muICU*x6 + muv*x7 and make it an
output

# Then we can use x4 = C2 - x3 - x5 - x6 - x7 - x8 + int_y1 / rho - int_y2 to eliminate
x4 from the system
```

The code for structural identifiability analysis is given below:

```
ode = @ODEmodel(

    x2'(t) = (betae*x2(t) + betan*x3(t) + betas*(C2 - (x3(t)+x5(t)+x6(t)+x7(t)+x8(t)) +
int_y1(t) / rho - int_y2 ))*((C1 - x2(t) - x9(t) - int_y1(t) / rho)/((C1 - x2(t) - x9(t) - int_y1(t) /
rho)+x2(t)+x3(t)+(C2  -  (x3(t)+x5(t)+x6(t)+x7(t)+x8(t))  +  int_y1(t)  /  rho  -  int_y2
)+x8(t)+x9(t))) - (1/14)*x2(t),

    x3'(t) = (1-rho)*(1/14)*x2(t) - (gamman)*x3(t),
```

```
    x5'(t) = alpha1*(C2 - (x3(t)+x5(t)+x6(t)+x7(t)+x8(t)) + int_y1(t) / rho - int_y2 ) -
(alpha2+gammah + muh)*x5(t),

    x6'(t) = alpha2*x5(t) - (alpha3+gammaICU+muICU)*x6(t),

    x7'(t) = alpha3*x6(t) - (gammav + muv)*x7(t),

    x8'(t) = gamman*x3(t) + gammas*(C2 - (x3(t)+x5(t)+x6(t)+x7(t)+x8(t)) + int_y1(t)
/ rho - int_y2 ) + gammah*x5(t) + gammaICU*x6(t) + gammav*x7(t),

    x9'(t) = eta*(C1 - x2(t) - x9(t) - int_y1(t) / rho),

    int_y1'(t) = (1/14) * rho * x2(t),

    int_y2'(t) = muh*x5(t) + muICU*x6(t) + muv*x7(t),

    y1(t) = (1/14)*rho*x2(t),

    y2(t) = muh*x5(t) + muICU*x6(t) + muv*x7(t),

    y3(t) = x6(t),

    y4(t) = x7(t),

    y5(t) = int_y1(t),

    y6(t) = int_y2(t),

)


    println(assess_identifiability(ode, known_ic=[x2,x3,x5,x6,x7,x8,x9]))
```

THE EFFECT OF PISTACHIO VERA SHELL ASH (PSA) ON CONCRETE PERFORMANCE

Murat Doğruyol [1*] (iD), Mahmut Durmaz [1] (iD)

[1] Siirt University, Civil Engineering Department, Siirt, Türkiye

* Corresponding Author: mdogruyol@siirt.edu.tr

ABSTRACT

Cement production is a major contributor to global energy consumption and CO_2 emissions, prompting the need for sustainable alternatives in the construction industry. This study investigates the potential of Pistachio Vera Shell Ash (PSA), an agricultural waste, as a partial replacement for cement in concrete. PSA was substituted at 3%, 5%, and 10% by weight of CEM I 42.5 R cement in concrete mixtures, and its effects on the physical, mechanical, and microstructural properties of concrete were evaluated. The results indicate that as the PSA substitution rate increased, the water demand of the concrete mixtures rose, leading to reduced workability. At the 3% replacement level, the compressive strength of the concrete remained comparable to that of plain concrete and only a 10% reduction was observed at 28 days. However, higher substitution rates (5% and 10%) resulted in significant strength losses, with reductions of 21% and 42.7%, respectively. Despite its non-pozzolanic nature, PSA demonstrated potential as a supplementary cementitious material (SCM), particularly in regions with abundant pistachio production. The study concludes that PSA can contribute to sustainable construction practices by reducing the environmental impact of concrete production and promoting the recycling of agricultural waste. Further research is recommended to optimize PSA substitution levels and enhance its compatibility with concrete matrices.

Keywords: Supplementary cementitious materials (SCM)s, Pistachio vera shell ash (PSA), Concrete compressive strength, Sustainability, Biomass.

1   INTRODUCTION

Concrete is the world's most popular construction material [1,2]. Cement, the main material of concrete, uses a lot of energy during its production and causes significant CO_2 emissions [2,3]. It is estimated that 5 to 8 % of global CO_2 emissions are caused by the cement sector [4]. The development of sustainable materials that could reduce the financial and environmental costs associated with cement production is essential [5].

In recent years, the utilisation of agricultural and industrial wastes in the concrete industry has emerged as a promising approach both environmentally and economically. Agricultural wastes (e.g. rice husk ash, coconut husk, wheat straw) and industrial wastes (e.g. fly ash, blast furnace slag, silica fume, waste glass) can be used as cement or aggregate substitutes in concrete mixes, reducing natural resource consumption and alleviating waste management problems. These materials also offer an attractive option due to their generally low cost and abundant availability. The world has entered a rapid industrial development with the twenty-first century. Although this development provides great benefits in terms of civilization, considering the negative effects of industrial wastes on the environment, major problems arise [6–12]. The utilization of these waste materials with useful recycling mechanisms is important in terms of cost and at the same time in terms of improving environmental impacts. Reuse of waste materials reduces raw material procurement costs. The use of recycled materials also earns points in green building certifications such as BREEAM, LEED and DGNB [13]. Recycling of industrial and agricultural waste materials such as silica fume, fly ash [3,14], waste glass [15] and rice-husk ash [16], which is used in the construction sector, which is environmentally problematic, will contribute greatly to humanity in terms of both environmental aspects and improving the properties of concrete.

According to the 2019 data of the European Ready Mixed Concrete Association (ERMCO), the European Union (EU) produces approximately 0.60 m^3 of concrete per year, while this amount is 0.8 m^3 in Türkiye [17]. In this way, researches on increasing the performance and economizing of concrete are constantly ongoing [17].

There are many studies to increase the compressive strength and durability of concrete. The use of mineral additives in the concrete mixture is one of these methods. Mineral additives fly ash (FA), silica fume (SF), blast furnace slag (BFS) play an active role in increasing the mechanical properties and durability of concrete when used in appropriate proportions [18–21].

Recently, there are studies investigating the effect of agricultural wastes on concrete performance, rice husk ash is added to the concrete mixture and gives positive results [22,23]. The use of pistachio shell ash, which is a pozzolanic material, in cement and concrete provides advantages such as reducing the permeability of concrete, resistance to chemical effects, resistance to alkali-silica reaction, improvement in workability properties, and thus strength and durability of concrete [24]

According to TUIK data, Türkiye ranks third after Iran and the USA in pistachio production. The amount of pistachio produced in 21 countries in the world is 1.158.519 tons [25]. Pistachio production in Turkish cities including Gaziantep, Şanlıurfa, and Siirt is increasing due to growing demand. According to TUIK data, it has been stated that pistachio production has doubled in the last 15 years [25]. According to global statistical review data, world pistachios production (in shell basis) reached more than 638.000 tons in 2014 [18]. Burning rate of pistachio shell is 99 %. The rate of ash is 1.2 % [26–28]. Shell obtained from pistachio, one of the most important production resources of Siirt province, is used as fuel in furnaces, but the ash formed remains as waste.

In the study by Baran et al. (2020) [29] Hazelnut shell ash was substituted up to 30 wt. % in normal CEM I 42.5R ordinary Portland cement (OPC) mixtures. Compared to OPC, the addition of hazelnut shell ash reduced the setting time by 96% and increased the water requirement for standard consistency by 59%. As the ash content increased, the compressive strength results decreased significantly. The addition of more than 5% hazelnut shell ash resulted in an unsatisfactory 28-day compressive strength value.

In the study by Tekin et al. (2021) [24], the substitution of PSA up to 30 wt. % instead of OPC in cement mortars caused a significant increase in the water requirement of the mortar and a significant delay in the setting time of the cement due to the presence of carbon-based structures. PSA substitution up to 10% gave similar early strength development (2 days) to plain cement mortar. With longer curing times, the compressive strength values of plain cement mortars can be increased by up to 17% with the use of PSA (10%). A 30% PSA substitution significantly reduced the compressive strength value of cement mortars, which was significantly aided by higher porosity properties. Between 500 and 900 ° C, PSA has a higher specific surface area [30]. Using a variety of techniques, the possible synthesis of graphitic carbon structures from waste and bio-recycles has recently been reported [31]. The partial replacement of cement with biomass ash after incineration has been proposed as an important solution due to the possibility of hazardous heavy metal and substance contamination leaching

into the environment [32]. Furthermore, these carbon-based materials have recently gained popularity as a research topic for cement-based composites to improve their properties [33]. Therefore, the use of PSA as an SCM can bring significant economic and environmental benefits to the cement industry, particularly in countries with higher pistachio production [24].

This study aims to investigate the potential of PSA as a partial replacement for cement in concrete, focusing on its impact on workability, compressive strength, and microstructural properties. While previous studies have explored the use of other agricultural wastes in concrete, the unique chemical composition of PSA, characterized by high alkali content and low pozzolanic activity, presents both opportunities and challenges. By substituting PSA at 3%, 5%, and 10% by weight of cement, this research seeks to determine the optimal substitution level that balances environmental benefits with mechanical performance. Advanced microstructural analyses, including SEM, EDX, and XRD, were employed to understand the interaction between PSA and the concrete matrix.

The findings of this study are expected to contribute to the growing body of knowledge on sustainable construction materials, particularly in regions with high pistachio production, such as Türkiye. By recycling PSA, this research not only addresses waste management issues but also offers a viable solution to reduce the carbon footprint of concrete production. Furthermore, the study provides insights into the potential of PSA as a SCM, paving the way for future research on its long−term durability and performance in concrete applications.

2   MATERIAL AND METHOD

In this study, CEM I 42.5 R Portland cement and pistachio vera shell ash (PSA) obtained from the furnace flue filter of the pistachio shell burned at $300-350^{\circ}C$ in an industrial oven were used. Approximately 1.2 % of the burnt pistachio shell was obtained as ash. The sodium oxide (Na_2O), potassium oxide (K_2O), sulphite (SO_3), magnesium oxide (MgO) ratios in the structure of pistachio vera shell ash are higher than cement, while the amounts of calcium mono oxide (CaO) and silicon dioxide (SiO_2) are lower Table 1. While this has an effect on reducing the initial and final setting times, the low aluminum trioxide (Al_2O_3) and silicon dioxide (SiO_2) amount in pistachio vera shell ash has an effect on increasing the initial and final setting times. PSA is a cementitious waste material with a high specific surface area consisting of graphene, alumina, quartz and calcite-based structures [24]. According to ASTM C618 [34], for pozzolanic activity, the amount of silicon dioxide + aluminum trioxide + iron trioxide (SiO_2 + Al_2O_3 + Fe_2O_3) should be more than 70 % in natural pozzolan [35]. However, the sum of SiO_2

+ Al_2O_3 + Fe_2O_3 components in the structure of PSA is approximately 4 %. This shows that PSA is not pozzolanic. The results reported by Shakouri et al. [36] and Kamau et al. [37] are consistent with the possibility that the aggregation of particles is due to high K^+ content. Shakouri et al. [36] state that the K^+ content of crops is influenced by plant species and fertilizers applied. Therefore, since the total alkali content of PSA is high ($Na_2O_{eq} > 0.60$ %), it is important not to use it with aggregates containing reactive silica such as andesite, dacite, rhyolite, etc. in order not to cause alkali-silica reaction with PSA substitute [38]. Loss on ignition 18.33 % indicated that PSA was not fully calcined and should be burnt at higher temperatures. The fact that the Blaine value of PSA is similar to that of cement shows that it can be physically substituted for cement. In addition, the fact that the specific density value of PSA is lower than cement may enable the production of lightweight concrete (Table 1).

Natural stone in the range of 0–5 mm, 5–15 mm and 15–25 mm was used as aggregate. The density of sand consisting of fine aggregate is 2.62 g/cm^3, medium aggregate is 2.69 g/cm^3, and coarse aggregate is 2.72 g/cm^3. The sieve analysis of the aggregate mixture used in the experiment is given in Figure 3 according to the limit values. In addition, chryso delta brand superplasticizer was used. The density of the superplasticizer is 1153 kg / m^3.

Table 1. Physical and chemical values of PSA and Portland cement.

		Portland Cement	PSA
Components (%)	SiO_2	19.61	2.4
	Al_2O_3	4.92	0.65
	Fe_2O_3	3.15	0.77
	CaO	63.66	17.07
	MgO	2.19	5.92
	SO_3	2.54	12.96
	K_2O	0.75	33.77
	Na_2O	0.29	8.13
	Na_2Oeq	0.78	30.35
	Loss on ignition	2.89	18.33
	(S+A+F)	27.68	3.82
	Density (kg/m^3)	3130	2350
	Blaine (cm^2/g)	3274	3167
	Fineness (45 μ)	9.5	26.6

$Na_2Oeq^* = Na_2O + 0.658 K_2O$
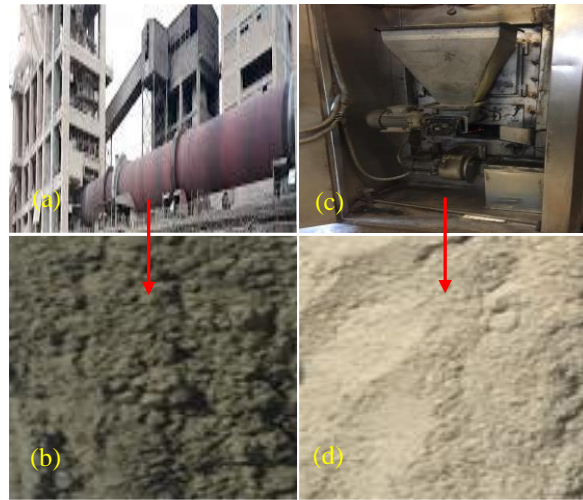
Figure 1. (a) Cement plant (b) macro images of Portland cement (c) Pistachio Shell Burning Industrial Furnace (d) macro images of PSA.
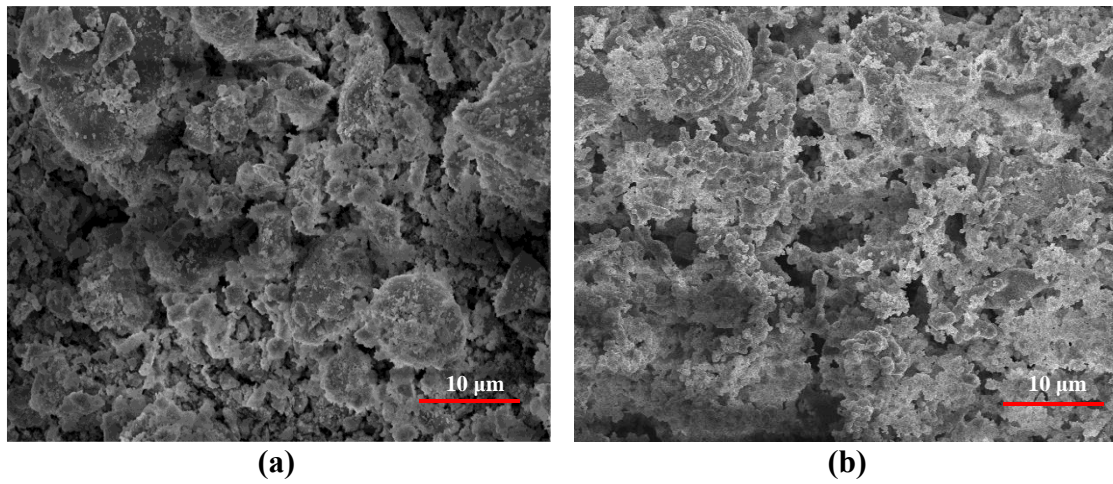
Figure 2. SEM images of (a) Portland cement (b) PSA.
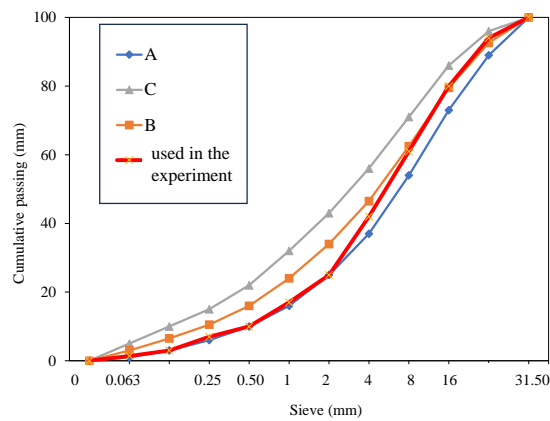
Figure 3. Sieve analysis.

In order for the materials in Figure 1, where macro images are presented, to be considered interchangeable, the chemical and physical properties presented in Table 1 must be similar. The close Blaine values of both materials are supported by the similar granules shown in the SEM images in Figure 2.

2.1 Method

In this study, mix proportions for 1m³ target concrete C25/30 design are given in Table 2 according to TS EN 196-1 [39]. In concrete production, 0, 3, 5 and 10 % by weight of PSA was substituted for Portland cement. The first mix was plain concrete (denoted by PL) and was used as the control group. PSA replaced cement at 3% (denoted by PSA3), 5% (denoted by PSA5) and 10% (denoted by PSA10) of the cement mass, respectively. In order to determine the 7-day and 28-day compressive strength of PSA-substituted concrete and plain concrete, 6 cube specimens of 150 mm × 150 mm × 150 mm³ were cast for each mix (see Figure 4). Specimens were demoulded after 24 hours and cured in saturated lime solution at 20 ± 2 ° C and R.H. ≈ 95% for 7, 28 days.

After determining the physical and mechanical properties of the concrete specimens, the specimens were pulverised and the hydration products were observed by scanning electron microscopy (SEM), energy dispersive spectrometry (EDS) and X-ray diffraction (XRD) analyses.


Figure 4. Sample preparation.

Table 2. Mix ratio of 1 m³ concrete and slump values.

Material	PL	PSA3	PSA5	PSA10
Portland cement, kg	300	291	285	270
PSA, kg	-	9	15	30
Water, kg	190	190	190	190
Admixture, kg	4.2	4.2	4.2	4.2
Fine aggregate 0-5mm, kg	983	981	981	978
Coarse aggregate 5-15 mm, kg	369	368	368	367
Coarse aggregate 15-25 mm,kg	404	403	403	402
Water/Binder	0.63	0.63	0.63	0.63
Unit weight, kg/m³	2250	2247	2245	2241

Cube specimens with dimensions of $150 \times 150 \times 150$ mm^3 was subjected to compressive tests in accordance with TS EN 12390-2 [40] after 28 days of curing in accordance with TS EN 12390-3 [41]. Compressive strength values were calculated by averaging three specimens from each design group after testing. The compressive strength was measured using a hydraulic concrete press machine with a load of 0.6 N/mm^2/sec.

For SEM, XRD analyses, samples were taken from the samples exposed to ambient and high temperature and brought into a form suitable for analysis. Firstly, the samples were made suitable for the SEM device. In order to take the images of the prepared samples, the surfaces to be imaged were made conductive with the help of Au coating device. The samples were placed in the chamber of the SEM device and then the process started. The surface morphologies of the samples were characterized at various scales by scanning electron microscopy (SEM, Hitachi SU3500).

XRD analyses were performed at a wavelength of 1.5406 (λ) between 10 and 90 ° at a step rate of 0.02 ° and a scan rate of 2 ° per minute.

3   RESULTS AND DISCUSSION

3.1   Slump values

Slump classification of the specimens was performed according to TS EN 206-1 [42] and EN 12350-2.

Figure 5. Slump values of (a) PL; (b) PSA10.

As the PSA substitution rate in the concrete increased, the water requirement of the specimens increased and workability decreased (see Figure 5). The slump value of plain concrete was 160 mm (slump class S4). Although the workability of the concrete did not change at 3% PSA substitution, the slump values decreased to 105 (slump class S3) and 80 mm (slump class S2) at 5% and 10% substitution, respectively (see Figure 6). The reason for the increase

in the need for water is thought to be the increase in surface area because of the small particle size of PSA. This increase in the amount of water resulted in an increase in the initial and final setting time.
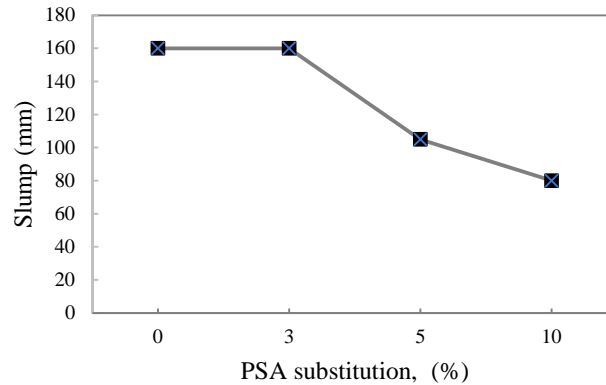

Figure 6. Slump values.

3.2   Compressive strength

This study examines the effects of agricultural waste PSA on the early and long-term compressive strength of concrete. According to the 7-day early strength results, the compressive strength of the PSA3 sample (27.4 MPa) is nearly identical to that of the reference concrete (PL) (27.5 MPa). This indicates that low substitution ratios of PSA do not significantly affect the early strength of concrete. However, it was observed that strength losses increased as the substitution ratio increased. In the 28-day strength values, compared to the reference concrete (34.40 MPa), the strength of PSA-containing concrete decreased with each increase in the substitution ratio. Particularly, the strength of the PSA10 sample dropped to 24.1 MPa, suggesting that high substitution ratios of PSA may negatively impact the mechanical properties of concrete Table 3. These results demonstrate that the use of agricultural waste PSA in concrete can be considered a sustainable solution, but the substitution ratio needs to be optimized. Additionally, investigating chemical or physical modifications to enhance the compatibility of PSA with the concrete matrix could be beneficial in minimizing strength losses.

Table 3. The effect of PSA substitution on the compressive strength values of concrete.

	Day 7			Day 28		
	Measured	σ^1	**Strength Effectiveness**[2]	**Measured**	σ^1	**Strength Effectiveness**[2]
	(MPa)		(%)	(MPa)		(%)
PL	27.5	1.20	-	34.4	1.05	-
PSA3	27.4	1.25	-0.1	31.2	1.15	-10.1
PSA5	25.8	1.30	-6.6	28.4	1.20	-21.1
PSA10	20.5	1.32	-34.1	24.1	1.35	-42.7

[1] standard deviation, [2]Strength-effectiveness$=\dfrac{PSA\ cs - PL\ cs}{PL\ cs} \times 100\%$
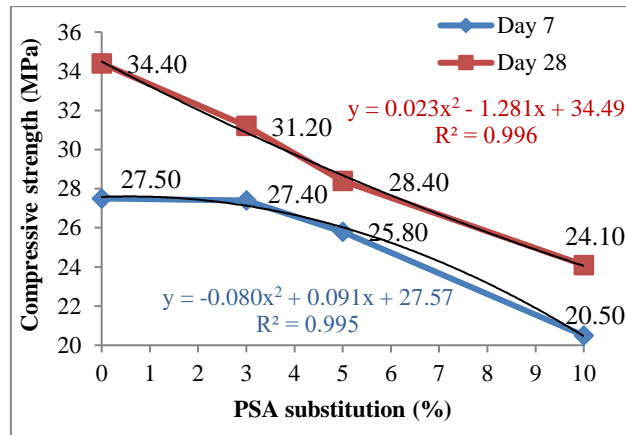
Figure 7. The effect compressive strength of PSA substitution.

Eq. (2) was obtained by applying regression analysis to the compressive strength value in Figure 7.

$$f'_{cf} \, (MPa) = \, f'_c + \, aV_s + \, bV_s^2 \tag{1}$$

$$f'_{cf} \, (MPa) = \, 34.49 - 1.281V_s + \, 0.023V_s^2 \tag{2}$$

Figure 7 was obtained by using the regression analysis and substituting f'c = 34.40 MPa in Equation. (1). Table 3 shows a favourable agreement between the test results and the compressive strength (day 28) predictions made using Equation. (2). Prediction errors are less than 1.07%.

3.3   Microstructure analyses

In this study, the interactions of PSA with the concrete matrix were investigated in detail using advanced microstructural analysis techniques such as SEM, EDX and XRD to better understand the mechanical effects.

Cement hydration products were observed with the SEM test of the 3 % of PSA-substituted sample. X-ray diffraction and energy dispersive spectrometry experiments show the interaction of calcium, chlorine and alkali ions in oxidised cement concrete with cement PSA, alite (Ca-Si-O), combeite (Na-Ca-Si) and wadeite (K-Si-O) compositions in cement.

The hydration products formed in concrete, portlandite (P), calcium hydroxide (Ca (OH)$_2$) crystals in the structure of calcium silicate hydrate gel (C-S-H) bind with pozzolans and form products with pozzolanic properties. Slab portlandite (P) crystals and ettringite structures (E) in the concrete sample were observed by scanning electron microscopy, Figure 8.
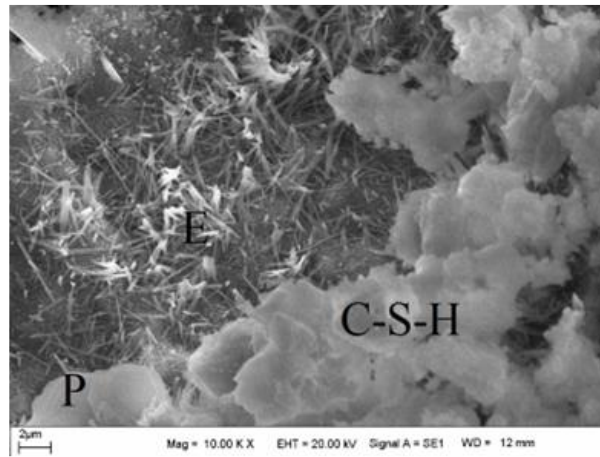
Figure 8. Hydration products of PSA3 P: portlandite (CH), E: ettringite ($C_6A\acute{S}_3H_{32}$), calcium silicate hydrate gel (C-S-H).

The high alkali content of PSA added in the cement paste caused the increase. The high alkali content of PSA caused the formation of calcium belit ($2CaSO_4.K_2SO_4$) in the cement paste. Thus, ettringite crystals in a needle-like shape, calcium alumina formation hydrates, and calcium monosulfoalumina hydrates are thought to reduce the viscosity of cement paste [29]. Additionally, ettringite crystals are quite stable and cause an enormous expansion in the cement paste, Figure 9.
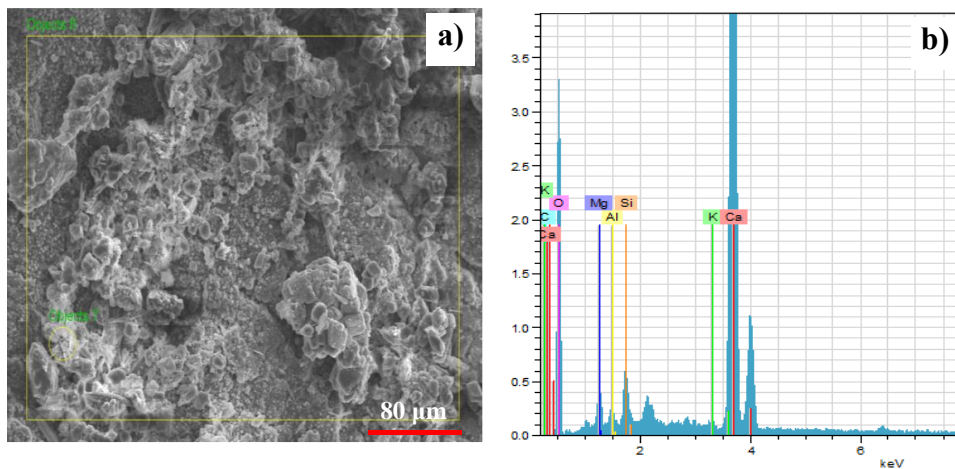
Figure 9. Analysis of PSA3 (a) SEM image; (b) EDS.

According to Figure 5, which shows the SEM-EDX analysis of 3% PSA-substituted concrete, calcium (Ca), silicon (Si), calcium (C) and oxide (O) ratios are high. Accordingly, the presence of calcium (Ca), silicon (Si) and oxide (O) is evidence of calcium silicate hydrate gel (C-S-H) formation. In addition, the presence of calcium (Ca) may have caused the formation of calcium carbonate (calcite).

According to Figure 10, Indicates the results of the XRD analysis of the concrete, The peak of quartz was observed at the position of 2 theta = 29.04 °. In addition, predominant mineral phases (calcite) at different Bragg angle positions (2 theta = 23.62 °, 31.02 °, 39.46 °)

stand out in XRD diffsubstitution patterns. It would be correct to say that higher calcite peaks occur in PSA-substituted concretes since shell ash is used. Portlandite (Ca (OH)$_2$) peaks can give us an idea for the strength product C-S-H in the amorphous structure. The similar intensity of the free-moving Ca (OH)$_2$ peaks in the two samples indicates that the samples have similar strength [43]. PSA substitution increased the amount of ettringite. The viscosity lowering effect of ettringite may be the reason for the decrease in slump analysis consistency in Figure 5 with increasing PSA substitution [44]. In addition, the volumetric expansion caused by the Ettringite needles can cause capillary cracks on the concrete surface due to internal forces and reduce the durability of the concrete [45,46].
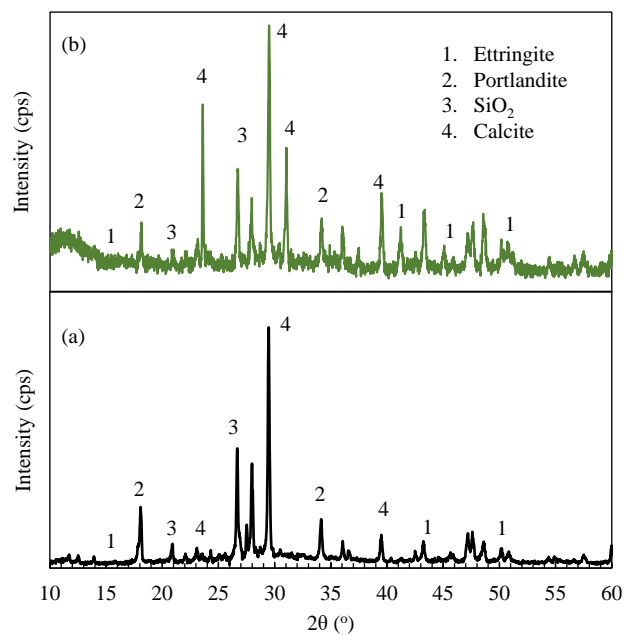
Figure 10. XRD analysis of (a) PL (b) PSA3.

4   CONCLUSIONS

This study highlights the importance of using agricultural waste as a cement substitute in concrete production from a sustainability perspective. Although pistachio shell ash (PSA), an agricultural waste, has no binding properties, it has significant potential to reduce the environmental impact of concrete and increase resource efficiency. The use of these wastes in concrete mixes helps to conserve natural resources, reduce the carbon footprint and alleviate waste management problems.

1- The workability of concrete showed an inverse relationship with PSA replacement rates. While a 3% PSA substitution maintained the original workability, a 10% substitution caused a 50% reduction in slump values. This high water demand resulting from the loss of

workability due to PSA can potentially promote crack formation and adversely affect the long-term durability of concrete.

2- The experimental results show that concrete with 3% PSA substitution achieved a compressive strength comparable to that of plain concrete at early age. However, there was a 10% decrease in compressive strength at 28 days. The decrease in compressive strength became more pronounced with higher substitution rates, showing strength reductions of 10%, 21% and 42% for 3%, 5% and 10% PSA substitutions, respectively, compared to the control mix.

3- SEM-EDX and XRD analyses revealed intense calcite peaks in the 3% PSA-substituted concrete specimen, which can be attributed to its agricultural waste origin. However, the observed intense ettringite formation is probably responsible for the decrease in both slump and compressive strength values.

4- Since the amount of silicon dioxide + aluminium trioxide + iron trioxide (SiO_2 + Al_2O_3 + Fe_2O_3) = 3.87 % < 70.00 % is low, it was that PSA is not a pozzolanic material. However, it is thought to have pozzolanic properties when used with cement.

5- This study demonstrates that incorporating PSA as a SCM —specifically at a 3% cement replacement level—delivers notable environmental and economic advantages by valorizing agricultural waste in alignment with global sustainability objectives. Beyond reducing reliance on conventional cement, the adoption of PSA contributes to natural resource conservation and mitigates CO_2 emissions inherent in cement manufacturing. This approach is particularly beneficial for regions with high pistachio cultivation, offering a dual solution for sustainable waste management and eco-conscious construction practices.

Acknowledgements

Conflict of Interest Statement

There is no conflict of interest between the authors.

Statement of Research and Publication Ethics

The study is complied with research and publication ethics.

Artificial Intelligence (AI) Contribution Statement

This manuscript was entirely written, edited, analyzed, and prepared without the assistance of any artificial intelligence (AI) tools. All content, including text, data analysis, and figures, was solely generated by the authors.

Contributions of the Authors

M.Doğruyol: Formal analysis, Investigation, Data curation, Conceptualization, Methodology, Resources, Writing - review & editing, Visualization. M.Durmaz: Conceptualization, Methodology, Formal analysis, Investigation, Writing - review & editing.

REFERENCES

[1] C. Zhang, H. Khorshidi, E. Najafi, and M. Ghasemi, "Fresh, mechanical and microstructural properties of alkali-activated composites incorporating nanomaterials: A comprehensive review," *Journal of Cleaner Production*, vol. 384, Art. no. 135390, 2023, doi: https://doi.org/10.1016/j.jclepro.2022.135390.

[2] B. Kanagaraj, N. Anand, U. J. Alengaram, S. Raj R, and G. Jayakumar, "Promulgation of engineering and sustainable performances of self-compacting geopolymer concrete," *Journal of Building Engineering*, vol. 68, Art. no. 106093, 2023, doi: https://doi.org/10.1016/j.jobe.2023.106093.

[3] A. Karaşin and M. Doğruyol, "An experimental study on strength and durability for utilization of fly ash in concrete mix," *Advances in Materials Science and Engineering*, vol. 2014, 2014, doi: https://doi.org/10.1155/2014/417514.

[4] A. M. Rashad, "A synopsis about the effect of basalt and natural fibers on geopolymer properties," *Natural Resources Conservation and Research*, vol. 1, 2018, doi: https://doi.org/10.24294/nrcr.v1i2.752.

[5] A. Gültekin, "Properties of basalt fiber-reinforced lightweight geopolymer mortars produced with expanded glass aggregate," *Bitlis Eren Üniversitesi Fen Bilimleri Dergisi*, vol. 13, pp. 205–215, 2024, doi: https://doi.org/10.17798/bitlisfen.1379342.

[6] Z. F. Uruk and A. K. Külünkoğlu İslamoğlu, "BREEAM, LEED ve DGNB yeşil bina sertifikasyon sistemlerinin standart bir konutta karşılaştırılması," *European Journal of Science and Technology*, pp. 143–154, 2019, doi: https://doi.org/10.31590/ejosat.512291.

[7] M. Doğruyol, "Diyarbakır bazaltının mineral katkıları ile kullanılmasının betonun dayanım ve dayanıklılığına etkisi," M.S. thesis, Dicle Üniversitesi, 2017.

[8] S. G. Gok and O. Sengul, "Mechanical properties of alkali-activated slag based SIFCON incorporating waste steel fibers and waste glass," *Construction and Building Materials*, vol. 408, Art. no. 133697, 2023, doi: https://doi.org/10.1016/j.conbuildmat.2023.133697.

[9] M. Doğruyol, "Characterization of historic mortars and the effect of rice husk ash (RHA) on quicklime," *Case Studies in Construction Materials*, vol. 21, 2024, doi: https://doi.org/10.1016/j.cscm.2024.e03542.

[10] P. K. Mehta, *Concrete: Structure, Properties and Materials*, 1986.

[11] V. M. Malhotra and P. K. Mehta, *High-Performance, High-Volume Fly Ash Concrete: Materials, Mixture Proportioning, Properties, Construction Practice, and Case Histories*, 2002.

[12]   A. Neville, "The confused world of sulfate attack on concrete," *Cement and Concrete Research*, vol. 34, pp. 1275–1296, 2004, doi: https://doi.org/10.1016/j.cemconres.2004.04.004.

[13]   S. G. Gok and O. Sengul, "The use of waste glass as an activator in alkali-activated slag mortars," *Proceedings of the Institution of Civil Engineers - Engineering Sustainability*, vol. 174, pp. 120–130, 2021, doi: https://doi.org/10.1680/jensu.19.00070.

[14]   M. Doğruyol, E. Ayhan, and A. Karaşin, "Effect of waste steel fiber use on concrete behavior at high temperature," *Case Studies in Construction Materials*, vol. 20, 2024, doi: https://doi.org/10.1016/j.cscm.2024.e03051.

[15]   S. G. Gök, I. Kılıç, and O. Sengul, "Properties of alkali-activated roller compacted concretes produced from waste aggregates," *Cement Wapno Beton*, vol. 26, pp. 352–363, 2021, doi: https://doi.org/10.32047/CWB.2021.26.4.7.

[16]   E. Ayhan, M. Doğruyol, F. Kıpçak, and A. Karaşin, "Atık taşıt lastik çelik lifinin beton davranışına etkisi," *DÜMF Mühendislik Dergisi*, 2024, doi: https://doi.org/10.24012/dumf.1468070.

[17]   Ready-mixed concrete industry statistic, ERMCO, 2019.

[18]   Global Statistical Review, *Nuts and Dried Fruits Global Statistical Review*, 2014–2015.

[19]   A. Karasin, M. Hadzima-Nyarko, E. Işık, M. Doğruyol, I. B. Karasin, and S. Czarnecki, "The effect of basalt aggregates and mineral admixtures on the mechanical properties of concrete exposed to sulphate attacks," *Materials*, vol. 15, 2022, doi: https://doi.org/10.3390/ma15041581.

[20]   L. Lam, Y. L. Wong, and C. S. Poon, "Effect of fly ash and silica fume on compressive and fracture behaviors of concrete," *Cement and Concrete Research*, vol. 28, no. 2, pp. 271–283.

[21]   F. Z. Çiçek, R. Pekgökgöz, S. B. Kazanasmaz, A. Sarıışık, and F. Avcil, "Effect of fly ash and metakaolin substituted forms on structural properties in light mortar with pumice aggregate," *Bitlis Eren Üniversitesi Fen Bilimleri Dergisi*, vol. 13, pp. 709–722, 2024, doi: https://doi.org/10.17798/bitlisfen.1479126.

[22]   R. Khan, A. Jabbar, I. Ahmad, W. Khan, A. Khan, and J. Mirza, "Reduction in environmental problems using rice-husk ash in concrete," *Construction and Building Materials*, vol. 30, pp. 360–365, 2012.

[23]   S. Yıldız, İ. Balaydın, and Z. Ç. Ulucan, "Pirinç kabuğu külünün beton dayanımına etkisi," *Fırat Üniversitesi Fen ve Mühendislik Bilimleri Dergisi*, vol. 19, no. 1, pp. 85–91, 2007.

[24]   İ. Tekin, İ. Dirikolu, and H. S. Gökçe, "A regional supplementary cementitious material for the cement industry: Pistachio shell ash," *Journal of Cleaner Production*, vol. 285, Art. no. 124810, 2021, doi: https://doi.org/10.1016/j.jclepro.2020.124810.

[25]   Turkish Statistical Institute (TUIK), *Pistachio Statistics (Vol. 2)*, 2018.

[26]   J. Parikh, S. A. Channiwala, and G. K. Ghosal, "A correlation for calculating HHV from proximate analysis of solid fuels," *Fuel*, vol. 84, no. 5, pp. 487–494, 2005.

[27]   R. Saidur, E. A. Abdelaziz, A. Demirbas, M. S. Hossain, and S. Mekhilef, "A review on biomass as a fuel for boilers," *Renewable and Sustainable Energy Reviews*, vol. 15, no. 5, pp. 2262–2289, 2011.

[28]   A. Taghizadeh-Alisaraei, H. A. Assar, B. Ghobadian, and A. Motevali, "Potential of biofuel production from pistachio waste in Iran," *Renewable and Sustainable Energy Reviews*, vol. 72, pp. 510–522, 2017.

[29]   Y. Baran, H. S. Gökçe, and M. Durmaz, "Physical and mechanical properties of cement containing regional hazelnut shell ash wastes," *Journal of Cleaner Production*, vol. 259, Art. no. 120965, 2020.

[30]   J. Hayashi, T. Horikawa, I. Takeda, K. Muroyama, and F. Nasir Ani, "Preparing activated carbon from various nutshells by chemical activation with K_2CO_3," *Carbon*, vol. 40, pp. 2381–2386, 2002, doi: https://doi.org/10.1016/S0008-6223(02)00118-5.

[31]   N. Raghavan, S. Thangavel, and G. Venugopal, "A short review on preparation of graphene from waste and bioprecursors," *Applied Materials Today*, vol. 7, pp. 246–254, 2017, doi: https://doi.org/10.1016/j.apmt.2017.04.005.

[32]   L. Tosti, A. van Zomeren, J. R. Pels, A. Damgaard, and R. N. J. Comans, "Life cycle assessment of the reuse of fly ash from biomass combustion as secondary cementitious material in cement products," *Journal of Cleaner Production*, vol. 245, Art. no. 118937, 2020, doi: https://doi.org/10.1016/j.jclepro.2019.118937.

[33]   M. Du, H. Jing, Y. Gao, H. Su, and H. Fang, "Carbon nanomaterials enhanced cement-based composites: Advances and challenges," *Nanotechnology Reviews*, vol. 9, pp. 115–135, 2020, doi: https://doi.org/10.1515/ntrev-2020-0011.

[34]   ASTM C618, *Standard Specification for Coal Fly Ash and Raw or Calcined Natural Pozzolan for Use in Concrete*, ASTM International, West Conshohocken, PA, USA, 2003.

[35]   Y. T. Erdoğan, *Materials of Construction*, M.E.T.U. Press, Ankara, 2002.

[36]   M. Shakouri, C. L. Exstrom, S. Ramanathan, and P. Suraneni, "Hydration, strength, and durability of cementitious materials incorporating untreated corn cob ash," *Construction and Building Materials*, vol. 243, 2020, doi: https://doi.org/10.1016/j.conbuildmat.2020.118171.

[37]   J. Kamau, A. Ahmed, P. Hirst, and J. Kangwa, "Suitability of corncob ash as a supplementary cementitious material," *International Journal of Materials Science and Engineering*, vol. 4, no. 4, pp. 215–228, n.d., doi: https://doi.org/10.17706/ijmse.2016.4.4.215-228.

[38]   M. Doğruyol, "Determination of ASR in concrete using characterization methods," *Buildings*, vol. 14, p. 657, 2024, doi: https://doi.org/10.3390/buildings14030657.

[39]   BS EN 196-1, *Methods of Testing Cement: Determination of Strength*, 2016.

[40]   12390-2-EQV, *Testing Hardened Concrete – Part 2: Making and Curing Specimens for Strength Tests*, 2019.

[41]   EN 12390-3, *Testing Hardened Concrete – Part 3: Compressive Strength of Test Specimens*, 2010.

[42]   TS EN 206+A2, *Beton – Özellik, Performans, İmalat ve Uygunluk*, 2021.

[43]   M. Doğruyol, "Characterisation of acrylic copolymer treated concretes and concretes of reinforced concrete buildings collapsed in the 6 February 2023 Mw = 7.8 Kahramanmaraş (Türkiye) earthquake," *Engineering Failure Analysis*, vol. 161, 2024, doi: https://doi.org/10.1016/j.engfailanal.2024.108249.

[44]   N. Thaulow, U. H. Jakobsen, and B. Clark, "Composition of alkali silica gel and ettringite in concrete railroad ties: SEM-EDX and X-ray diffraction analyses," 1996.

[45]   B. Baradan, H. Yazıcı, and H. Ün, *Betonarme Yapılarda Kalıcılık (Durabilite)*, DEÜ Mühendislik Fakültesi Yayınları, 2002.

[46]   M. Doğruyol and A. Karaşin, "Sülfatın beton ve betonarme elemanlara olumsuz etkisi," *Dicle Üniversitesi Mühendislik Fakültesi Mühendislik Dergisi*, vol. 2, no. 2, pp. 79–85, 2011.

THE CAUSALITY RELATIONSHIP BETWEEN BITCOIN AND DOLLAR, GOLD AND BIST100 INDEX

Hakan KAYA [1],* , Batuhan ÖZKAN [2]

[1] *Bitlis Eren University, Department of Economics, Bitlis, Türkiye*

[2] *Bitlis Eren University, Department of Statistics, Bitlis, Türkiye*

*** Corresponding Author:** hkaya@beu.edu.tr*

ABSTRACT

This study investigates the causal relationships between Bitcoin and the US Dollar (USD), Gold, and BIST100 Index as alternative investment instruments. Employing Hong's variance causality test, the research explores spillover effects in mean and volatility. Using daily data from September 17, 2014, to October 13, 2023, the study reveals a one-way average causality from Bitcoin to BIST100 and the USD. Variance test results show a two-way volatility spillover between Bitcoin and USD, Gold, and BIST100. Hacker-Hatemi-J symmetric causality test detects a one-way causality from Bitcoin to the USD, while Hatemi-J asymmetric test reveals a unidirectional causality from positive Bitcoin shocks to negative shocks of BIST100 and Gold, and bidirectional causality with USD's negative shocks. Additionally, a bidirectional causality exists from Bitcoin's negative shocks to Gold's positive shocks and a unidirectional causality to USD's negative shocks. Recognizing Bitcoin as a financial asset sheds light on its interaction with traditional markets, aiding investors in refining strategies. In summary, this study enhances comprehension of cryptocurrency's role by emphasizing the causal link between Bitcoin and the USD.

Keywords: Hong's causality test, Hatemi-J causality test, Bitcoin, USD, BIST100 index.

1   INTRODUCTION

Bitcoin (BTC) is the first virtual or cryptocurrency designed to operate on a distributed computer network, beyond the control of any individual, group, or entity, serving as both a currency and a means of payment [1,2]. Introduced by its creator Satoshi Nakamoto in 2008,

BTC's genesis involved the registration of the bitcoin.org domain in August 2008. In October of the same year, Nakamoto published the seminal paper titled "Bitcoin: A Peer-to-Peer Electronic Cash System," meticulously detailing the system required to create an "electronic system for transactions without relying on trust" [3,4]. The inaugural Bitcoin block, known as the genesis block (or block 0), was mined on January 3, 2009.

The primary goal behind the emergence of cryptocurrencies was to establish a unique digital payment system allowing unlimited financial transactions without the need for intermediaries such as banks or governments. This would eliminate the involvement of third parties in financial transactions. The distributed architecture provided by blockchain technology, coupled with cryptographic techniques, makes Bitcoin highly resistant to attacks and fraud [2]. Moreover, the transparency facilitated by blockchain technology ensures that transactions are recorded on the publicly accessible Bitcoin network, constituting one of Bitcoin's major advantages [5].

While digital currencies have recently gained prominence, the roots of blockchain technology trace back to 1982. Computer scientist, cryptographer, and inventor David Lee Chaum is recognized as the creator of digital currency. His 1982 thesis titled "Computer Systems Established, Maintained, and Trusted by Mutually Suspicious Groups" is the earliest known proposal for blockchain protocol [6,7].

Today, BTC stands undoubtedly as the most well-known and valuable digital currency. Initially traded for less than $1 in its early years (2010), it quickly soared to over $65,000 in a relatively short time (2021). With over 20,000 cryptocurrencies existing today, the emergence of new digital currencies is partly attributed to the fame of BTC. Furthermore, the proliferation of cryptocurrency exchanges and their increasing use for payments and transfers have transformed various digital currencies, including BTC, into significant investment instruments.

2   LITERATURE REVIEW

Sarker et al. [8] employed the nonlinear ARDL method and Granger causality test to investigate the impact of climate policy uncertainty and changes in energy prices on Bitcoin prices. Using data from October 1, 2013, to December 1, 2021, they analyzed monthly climate policy uncertainty (CPU), global energy price index (GPEI), and Bitcoin prices. Their findings showed that increases in climate policy uncertainty and decreases in the global energy price index positively affected Bitcoin in the short term. They highlighted those changes in climate

policy uncertainty and the global energy price index had significantly higher effects on Bitcoin in the long term. The Granger causality test revealed a bidirectional causality between Bitcoin and climate policy uncertainty, while a unidirectional causality from the global energy price index to Bitcoin was observed.

Fasanya et al. [9] explored the relationship between Bitcoin and gold markets in uncertainty caused by infectious diseases using jump and causality tests. Analyzing daily data from July 19, 2010, to May 26, 2020, encompassing Bitcoin, gold, and the Infectious Diseases Uncertainty (EMV-ID) index, their spillover tests suggested a low-level connection between the two markets. They emphasized that gold markets acted as a clear volatility transmitter, while Bitcoin markets acted as receivers of shocks. Moreover, during downward market movements, Bitcoin and gold markets were reported to be less correlated.

Tunçel et al. [10] investigated the causality relationship between Bitcoin prices and the BIST100 index. Using daily data from July 19, 2010, to January 10, 2020, they conducted Lee-Strazicich unit root tests, indicating that the Bitcoin variable stabilized at level I(0), while the BIST100 variable stabilized at level I(1). Employing the Toda-Yamamoto causality test, they identified a bidirectional causality relationship between the variables at a 5% significance level.

Kaymak and Koç [11] examined the causality relationship between Bitcoin and Borsa Istanbul based on transaction volumes. Covering the period from January 1, 2017, to December 1, 2021, they conducted ADF and PP unit root tests to ascertain the stationarity of the series. The results indicated stationarity after taking the first differences. Contrary to expectations, the Toda-Yamamoto causality test suggested no causality relationship between Bitcoin and Borsa Istanbul variables during the identified period.

Li et al. [12] investigated the causality relationship between Bitcoin and crude oil markets under extreme and non-extreme shocks such as terrorist attacks, political issues, or financial crises. Utilizing weekly closing prices for Bitcoin and crude oil, their findings suggested that the interaction between the variables varied over time, with stronger causal connections during periods of significant movements in oil returns. Asymmetric causal connections were identified during extreme shocks.

Özmerdivanlı [13] explored the relationship between Covid-19 pandemic indicators and various financial markets representing Turkey, including gold, BIST100, Bitcoin, and the US dollar. Using daily data from March 11, 2020, to July 31, 2021, they applied the Johansen cointegration test, revealing long-term cointegration among the variables. The VECM-based

causality test indicated long-term causality relationships in models where Bitcoin, interest rates, oil, and gold variables were dependent. In the short term, a unidirectional causality relationship was identified only between the US dollar and BIST100.

Kubar and Toprak [14] examined the relationship between Bitcoin and other top 10 cryptocurrencies (Ethereum, Tether, Ripple, etc.) during the period from August 21, 2020, to January 7, 2021. Employing Granger causality tests with daily closing prices in USD, they found a positive strong relationship between Bitcoin and all cryptocurrencies except Tether (USDT). Bidirectional causality was identified between Bitcoin and Ethereum, while unidirectional causality was observed between Bitcoin and other cryptocurrencies.

Soyaslan [15] investigated the short and long-term relationships and causality between Bitcoin and BIST100, BIST Banks, and BIST Technology variables. Using daily closing prices from April 21, 2011, to February 11, 2020, ADF and PP unit root tests indicated the removal of unit roots when first differences were taken. The Johansen cointegration test revealed a balanced relationship between Bitcoin and the BIST100 index, while no relationship was identified with BIST Banks and BIST Technology indices. Granger causality test results showed no causality relationship between Bitcoin and BIST100, BIST Banks, and BIST Technology indices in the short term.

3   MATERIAL AND METHOD

This study examines the causality relationship between Bitcoin (BTC) and the USD, Gold and BIST100 index using daily data between September 17, 2014 and October 13, 2023. Bitcoin and Gold prices are obtained from Yahoo Finance [16] database in US Dollars. The exchange rate is taken from the Central Bank of the Republic of Turkey (CBRT) [17] database as the USD/TL effective selling rate and BIST100 as the index value based on closing prices. Dates when the series are not traded are excluded from the analysis. All series subject to analysis are transformed into logarithmic return series $\left(log\, Y_{i,t} = log(X_{i,t}/X_{i,t-1})x100 \right)$.

In the study, firstly, the outlier values of the series converted into logarithmic return series were calculated and the outlier values were corrected by taking the average of 10 observations as suggested by Bodart and Candelon. After the correction of the outliers, the stationarity levels of the series were investigated with Augmented-Dickey Fuller and Phillips Perron unit root tests. After determining the stationarity levels of the series, the appropriate ARMA (p,q) models are examined within the framework of Akaike Information Criterion. After

determining the appropriate ARMA(p,q) models, the ARCH test was applied to the series to investigate whether there is an ARCH effect in the series. The ARCH effect is tested under the null hypothesis of no ARCH effect and the alternative hypothesis of an ARCH effect. The rejection of the null hypothesis of no ARCH effect at the 1%, 5% and 10% significance levels indicates that the series are suitable for Generalized Autoregressive Conditional Variance (GARCH) model structure. The series with the appropriate GARCH(p,q) model are estimated using GARCH, EGARCH, GJR-GARCH, IGARCH, APARCH, FIEGARCH and FIAPARCH models and the most appropriate GARCH(p,q) model is determined according to the model selection criteria.

In this study, the causality relationship between Bitcoin and USD, Gold and BIST100 index was estimated with the mean and variance causality tests developed by Hong [18] and calculated with the help of Generalized Autoregressive Conditional Variance with Variance (GARCH) models, and the cross-correlations between the squares of the standardized error terms obtained from the most appropriate GARCH model were calculated. Unlike classical causality tests (e.g. Granger [19]; Toda-Yamamoto [20]), the Hong [18] test for causality in variance proposes an asymptotic N (0,1) test procedure to measure volatility spillovers between two time series where the error terms are not constant variance and the two variables exhibit conditional variance and may have infinite conditional variance. This test procedure is based on the Cheung and Ng [21] test for causality in variance. Cheung and Ng [21] defined the condition for Y_t to be the cause of X_t in variance in two stationary and conditional variance series such as X_{t+1} and Y_t with information sets $I_t = \{X_{t-j}, J\} \geq 0$ and $J_t = \{X_{t-j}, Y_{t-j}, J\} \geq 0$, where $\mu_{x,t+1}$ is the conditional mean of X_{t+1} conditional on information set I_t through equation (1):

$$E\left\{\left(\left(X_{t+1} - \mu_{x,t+1}\right)^2 | I_t\right)\right\} \neq E\left\{\left(\left(X_{t+1} - \mu_{x,t+1}\right)^2 | J_t\right)\right\} \tag{1}$$

In order to test for causality in variance, the univariate GARCH (p,q) model must first be calculated. h_{it}^0 GARCH (p,q) equation is calculated from equation (2) to define the conditional variance calculated from the GARCH model:

$$h_{it}^0 = \omega_i^0 + \sum_{j=1}^{q} \alpha_{ij}^0 \varepsilon_{it-j}^2 + \sum_{j=1}^{p} \beta_{ij}^0 h_{it-j}^0 \tag{2}$$

For $i = 1,2$ in equation (2), it is defined as $\varepsilon_{it} = Y_{it} - \mu_{it}^0$ and $\varepsilon_{it} = Y_{it} - \mu_{it}^0$. Parameters $E(\varepsilon_{it}|I_{it-1}) = 0$ and $E(\varepsilon_{it}^2|I_{it-1}) = h_{it}^0$ represent the conditional variance of ε_{it}^2.

Under the assumption that parameters $\omega_i^0 > 0$; α_{ij}^0 and β_{ij}^0 ensure the strict positivity of h_{it}^0, the squared standardized errors for series X_t and Y_t are calculated with the help of the equations in equation (3):

$$\hat{u}_t = \left\{\frac{\left(Y_{it} - \mu_{it,Y}\right)^2}{\hat{h}_{it,Y}}\right\} \quad \text{and} \quad \hat{v}_t = \left\{\frac{\left(X_{it} - \mu_{it,X}\right)^2}{\hat{h}_{it,X}}\right\} \tag{3}$$

Following Chung and Ng [21], Hong [18] defines the cross-correlation formulation between $\hat{u}_t$ and $\hat{v}_t$ as the following equation, where T is the sample size, parameter $\hat{\rho}_{uv}(J)$ is the cross-correlations of $\hat{u}_t$ and $\hat{v}_t$ at lag J, and parameters $\hat{C}_{uu}(0)$ and $\hat{C}_{vv}(0)$ are the sample variances of $\hat{u}_t$ and $\hat{v}_t$:

$$\hat{\rho}_{uv}(J) = \left\{\hat{C}_{uu}(0)\hat{C}_{vv}(0)\right\}^{-\frac{1}{2}} C_{uv}(J) \tag{4}$$

Equation (4) imposes two conditions on the calculation of the cross-correlations of $\hat{u}_t$ and $\hat{v}_t$ at lag J. When $\hat{C}_{uu}(0) = T^{-1}\sum_{t=1}^{T}\hat{u}_t^2$ and $\hat{C}_{vv}(0) = T^{-1}\sum_{t=1}^{T}\hat{v}_t^2$, this condition is expressed by equation (5).

$$\hat{C}_{uv}(J) = \begin{cases} T^{-1}\sum_{t=j+1}^{T}\hat{u}_t\hat{v}_{t-j}, J \geq 0 \\ T^{-1}\sum_{t=-j+1}^{T}\hat{u}_{t+j}\hat{v}_t, J < 0 \end{cases} \tag{5}$$

Hong [18] improves the Chung and Ng [21] variance causality test and uses a weighting function of $k(\bullet)$ to calculate the variance causality relationship between X_t and Y_t, where M is a positive integer and the number of lags is defined. This weighted function is defined through kernel functions such as Bartlett, Daniell, Parzen and Tukey-Hanning [22]. In this context, based on $k(\bullet)$ weighting functions, the Hong [18] test for causality in variance is calculated through equation (6), which shows $C_T(k) = \sum_{J=1}^{T-1}(1 - \frac{J}{T})k^2(\frac{J}{M})$ mean equations and $D_T(k) = \sum_{J=1}^{T-1}(1 - \frac{J}{T})\left\{1 - \frac{(j+1)}{T}\right\}k^4(\frac{J}{M})$ variance equations:

$$Q = \frac{\left\{T\sum_{J=1}^{T-1}k^2(\frac{J}{M})\hat{\rho}_{uv}^2(J) - C_T(k)\right\}}{2D_T(k)^{\frac{1}{2}}} \tag{6}$$

In the study, the causality relationship between these variables is also investigated with the Hacker-Hatemi-J [23] and Hatemi-J [24] symmetric and asymmetric causality tests, which

allow the effects of positive and negative shocks on the series to be observed. Under the assumption that the causality relationship between the two series defined as y_{1t} and y_{2t} is investigated, the equations for series y_{1t} and y_{2t} will be formed as follows [25-27]:

$$y_{1t} = y_{1t-1} + \varepsilon_{1t} = y_{1,0} + \sum_{i=1}^{i} \varepsilon_{1i} \quad \text{and} \quad y_{2t} = y_{2t-1} + \varepsilon_{2t} = y_{2,0} + \sum_{i=1}^{i} \varepsilon_{2i} \tag{7}$$

$y_{1,0}$ and $y_{2,0}$ are the initial values, ε_{1i} and ε_{2i} are the error terms, and the positive and negative shocks in the error terms are the white noise error terms consisting of the sum of the positive and negative shocks of the error terms expressed as $\varepsilon_{1i}^+ = max(\varepsilon_{1i}, 0)$, $\varepsilon_{1i}^- = min(\varepsilon_{1i}, 0)$ and $\varepsilon_{2i}^+ = max(\varepsilon_{2i}, 0)$, $\varepsilon_{2i}^- = min(\varepsilon_{2i}, 0)$ $(\varepsilon_{1i} = \varepsilon_{1i}^+ + \varepsilon_{1i}^-, \varepsilon_{2i} = \varepsilon_{2i}^+ + \varepsilon_{2i}^-)$. In the Hatemi-J causality test, the positive and negative shocks in the variables with causality relationship are defined as $y_{1t}^+ = \sum_{i=1}^{t} \varepsilon_{1i}^+$, $y_{1t}^- = \sum_{i=1}^{t} \varepsilon_{1i}^-$, $y_{2t}^+ = \sum_{i=1}^{t} \varepsilon_{2i}^+$, $y_{2t}^- = \sum_{i=1}^{t} \varepsilon_{2i}^-$ in cumulative form. Under the assumption that the positive cumulative variable is equal to $(y_t^+ = (y_{1t}^+, y_{2t}^+))$ and the negative cumulative variable is equal to $(y_t^- = (y_{1t}^-, y_{2t}^-))$, the causality relationship is tested through the following model with the help of p. Lagged VAR(p) model:

$$y_t^+ = \alpha + A_1 y_{t-1}^+ + \cdots + A_p y_{t-1}^+ + u_t^+ \tag{8}$$

In equation (8), y_t^+ is the vector of variables, α is the fixed variable and u_t^+ is the error term vector. The Hacker-Hatemi-J [23] causality test allows estimating the causality relationship with boostrap simulation when the error terms are not normally distributed and there is an ARCH effect. In the application of Hacker-Hatemi-J [23] and Hatemi-J [24] causality tests, Akaike (AIC), Schwarz (SC) and Hannan-Quinn (HQ) information criteria can be used. However, in response to the fact that different results may emerge in models solved with SIC and HQ information criteria, Hatemi-J [24] developed the HJC information criterion based on the average of SIC and HQ information criteria. The HJC information criterion is defined as follows:

$$HJC = ln(|\hat{\Omega}_j|) + j\left(\frac{n^2 \ln T + 2n^2 \ln(\ln T)}{2T}\right) \tag{9}$$

$j = 0,1,\ldots,p$ In equation (9), parameter $\hat{\Omega}_j$ is the variance-covariance matrix of the error term of the VAR(p) model estimated at lag, n is the number of VAR model equations, and T is the number of observations [25,26]. After determining the appropriate lag length for the application of Hacker-Hatemi-j [23] and Hatemi-J [24] symmetric and asymmetric causality

tests, the null hypothesis H0: There is no Granger causality relationship between variables and the alternative hypothesis H1: There is a Granger causality relationship between variables are tested at 1%, 5% and 10% significance levels according to the calculated Wald test results. If the results obtained from the Wald test are greater than the critical values determined at the 1%, 5% and 10% significance levels, the null hypothesis is rejected and the causality relationship between the variables is accepted.

4   RESULTS AND DISCUSSION

The study first investigated the outlier values of the variables converted into return series. Accordingly, it is determined that there are 5 deviant observation values for BTC series, 36 for BIST100 series, 21 for USD series and 15 for Gold series. These deviant observation values were corrected by taking the average of 10 observations as suggested by Bodart and Candelon [28]. Graphs of the adjusted return series are presented in Figure 1. According to Figure 1, the years 2020 and 2022 indicate the periods with the highest volatility in the BIST100, USD and Gold series. When the said situation is evaluated daily BTC series, it is seen that the periods with the highest increase in volatility are 2017 and 2019.
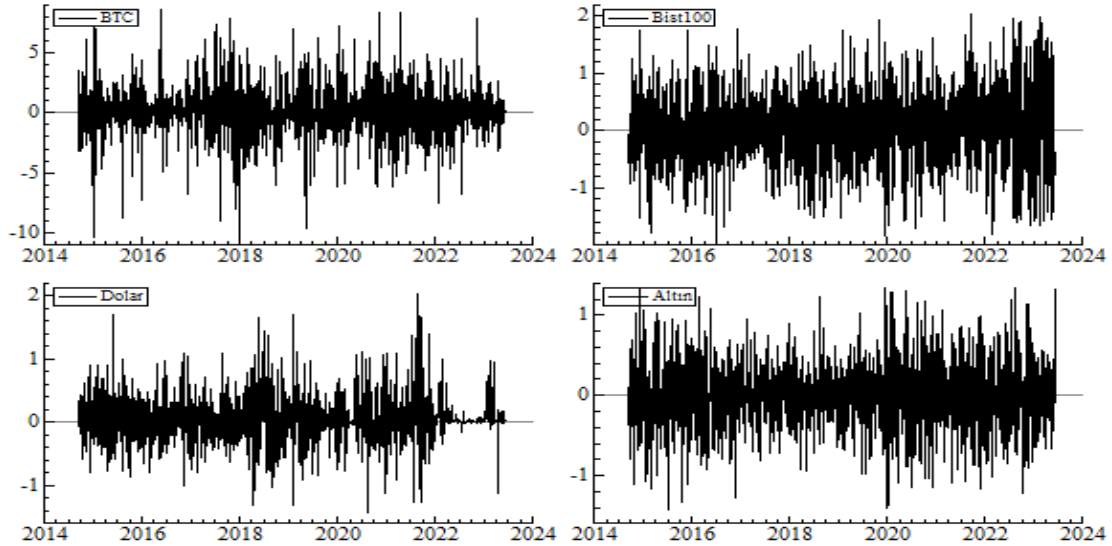
Figure 1. Adjusted series of BTC, BIST100, USD and Gold variables.

Table 1 presents descriptive statistics, ARCH(p,q) estimation results and Augmented-Dickey Fuller (ADF) and Phillips-Perron (PP) unit root test results. Table 1 shows that the mean of the BTC series is higher than the other series. The standard deviation value, which is a measure of volatility, is higher in the BTC series compared to other series. The standard deviation values of the BIST100 and USD series are higher than those of the Gold series. The

skewness coefficient indicates that the BTC, BIST100 and Gold series are left skewed while the USD series is right skewed. The kurtosis coefficient indicates that all series have a steep structure. Jarque-Bera test statistic results indicate that all series are not normally distributed. ARCH test results reveal that all series exhibit conditional variance characteristics. Box-Pierce autocorrelation test results daily series and their squares indicate the presence of ARCH effect. ADF and PP unit root test results indicate that all series are stationary at their level values.

Table 1. Descriptive statistics.

	BTC	BIST100	USD	GOLD
Average	0.0789	0.0588	0.0491	0.0084
Minimum	-10.368	-1.9616	-1.4153	-1.4320
Maximum	8.6277	2.0206	2.0402	1.3493
Std.Error	1.842	0.580	0.345	0.368
Kurtosis	7.320	3.766	6.606	4.366
Skewness	-0.2361	-0.0490	0.5669	-0.0422
J-Bera	1787.454 [0.000]	56.436 [0.000]	1352.375 [0.000]	177.477 [0.000]
ARCH(5)	16.617 [0.000]	10.880 [0.000]	110.48 [0.000]	6.8536 [0.000]
Q(50)	65.422 [0.0704]	71.2512 [0.025]	248.519 [0.097]	54.338 [0.312]
QS(50)	269.403 [0.000]	387.694 [0.000]	2333.84 [0.000]	220.494 [0.000]
ADF	-46.919***	-46.292***	-39.253***	-48.600***
PP	-46.945***	-46.417***	-41.350***	-48.600***
Number of Observation	2271	2271	2271	2271

Note: *, ** and *** denote stationarity at 10%, 5% and 1% significance levels, respectively. Values in parentheses are p probability values for rejecting the null hypothesis that the series are non-stationary at level values. ARCH(5) stands for LM conditional variance test. Q(50) and QS(50) are the Box-Pierce autocorrelation test results for the series and their squares, respectively. Q(p) values considered in the Box-Pierce autocorrelation test are determined as approximate integer values by taking the square root of the total number of observations i

After determining the stationarity levels of the series, the appropriate ARMA (p,q) models were determined within the framework of the Akaike Information Criterion. ARMA(2,2) model for BTC, ARMA (3,3) for BIST100, ARMA (2,3) for USD series and ARMA (2,2) for Gold series were determined as the most appropriate ARMA(p,q) models. After determining the appropriate ARMA(p,q) models, ARCH test was applied to the series and the null hypothesis of no ARCH effect was rejected at the 1%, 5% and 10% significance levels. This indicates that the series are suitable for the GARCH model structure. The conditional variance equations of the series with ARCH(p,q) model are analyzed with the help of GARCH models. Accordingly, FIEGARCH(2,2) for BTC series, GARCH(3,3) for BIST100 series,

FIEGARCH(2,3) for USD series and IGARCH(2,2) for Gold series are determined as the most appropriate models. Since the Jarque-Bera test results indicate that the series are not normally distributed, student-t distribution is used in GARCH model estimations. GARCH volatility estimation results for the series are presented in Table 2.

Table 2. Volatility model results.

Periods	ω	ν	α	β	d	θ_1	θ_2	Ø	t	Log(L)	Q(50)	$Q_S(50)$
BTC	0.068 [0.000]	2.026 [0.020]	-	0.750 [0.000]	0.667 [0.000]	0.053 [0.020]	0.317 [0.000]	-0.475 [0.013]	2.505 [0.000]	4178.218	71.059 [0.111]	30.851 [0.974]
BIST100	0.059 [0.000]	0.002 [0.204]	0.033 [0.002]	0.959 [0.000]					8.629 [0.000]	1901.555	46.567 [0.367]	36.917 [0.877]
USD	0.010 [0.000]	-2.138 [0.020]	-	-0.937 [0.000]	0.713 [0.000]	0.037 [0.346]	0.698 [0.000]	1.005 [0.000]	3.192 [0.000]	34.905	64.940 [0.057]	78.019 [0.903]
GOLD	0.009 [0.128]	0.000 [0.149]	0.0243 [0.003]	0.975 [-]	-	-	-	-	4.652 [0.000]	-847.171	43.756 [0.566]	37.3745 [0.865]

Note: Values in parentheses are probability values. ω is the constant term for the variance equation, v is the constant term for the mean equation, α and β are the ARCH-GARCH parameters denoting the asymmetric effect of shocks on volatility and persistence in the volatility set, respectively, and d is the long memory parameter for volatility. The parameters θ_1 and θ_2 denote the leverage effect. Ø is the ARCH parameter, t is the Student distribution parameter, Log(L) is the maximum likelihood, (50) and QS(50) are the Box-Pierce autocorrelation test results for the series and their squares, respectively. In the IGARCH (2,2) model calculated for the gold series, the β parameter is calculated by the (1- α) method. Therefore, the probability value is not observed.

According to the results presented in Table 2, the coefficient β, which expresses the persistence in volatility, is statistically significant at 1% significance level in the estimated BTC, BIST100 and USD models. This result indicates that the persistence of shocks in volatility is high. In the FIEGARCH models calculated for BTC and USD series, which include the leverage effect, the coefficients θ_1 and θ_2 are positive and statistically significant at 1% significance level. According to this result, good news in the market increases volatility more than bad news. In the models estimated for BTC and USD series, the d parameter, which indicates the presence of long memory in volatility, is positive and statistically significant at 1% significance level. The d > 0.5 condition of this parameter, which is defined as continuously stationary under the 0 < d < 0.5 condition, indicates that the persistence of shocks in volatility lasts longer, in other words, shocks in volatility are effective for a longer period of time.

Following the appropriate GARCH model estimations, the causality relationship between BTC, BIST100, USD and Gold series in the mean and variance were estimated using the squares of the standardized error terms obtained from the GARCH model estimations. According to the mean causality test results presented in Table 3, a unidirectional causality relationship was found from BTC to BIST100 at 5% and 1% significance levels, respectively, and from BTC to USD at 10% significance level.

Table 3. Causality test results at the mean.

Direction of Causality	M1	M2	M3	M4	M5
BIST100=>BTC	-0.080 [0.532]	-0.164 [0.565]	-0.323 [0.627]	-0.396 [0.654]	-0.621 [0.733]
BTC=>BIST100	-0.419 [0.662]	0.862 [0.194]	2.182** [0.015]	2.616*** [0.004]	2.916*** [0.002]
USD=>BTC	0.026 [0.490]	0.245 [0.403]	0.735 [0.231]	1.074 [0.142]	1.168 [0.121]
BTC=>USD	0.239 [0.405]	0.011 [0.496]	0.069 [0.473]	0.052 [0.479]	-0.042 [0.517]
GOLD=>BTC	-0.754 [0.774]	-0.712 [0.762]	-0.961 [0.832]	-0.879 [0.810]	-0.847 [0.801]
BTC=>GOLD	-0.463 [0.678]	0.563 [0.287]	1.346* [0.089]	1.575* [0.058]	1.643* [0.052]

Note: *, ** and *** denote 10%, 5% and 1% significance levels, respectively. Values in parentheses are p probability values. M is the maximum number of lags. Daniell Kernel function is used in the estimation of causality analysis.

Table 4 shows the variance causality test results between BTC, BIST100, USD and Gold series. In the light of the information presented in the Table, it is seen that there is a bidirectional causality relationship between BTC and BIST100, USD and Gold series at 1% significance level. This result also indicates that there is a strong volatility spillover between BTC and the BIST100, USD and Gold markets, which are defined as alternative investment instruments. This result shows that the BTC market has gained an important place in Turkey and that the development of financial technologies and information has led to a high level of pass-through among all the markets subject to the study. The high volatility spillovers observed in BTC and other alternative investment instruments not only increase the likelihood of unexpected losses for investors, but also point to the existence of excessive risk in the markets.

Following the tests for causality in the mean and variance, the symmetric and asymmetric causality relationship between BTC and the BIST100, USD and Gold series were analyzed. Table 5 presents the results of the Hacker-Hatemi-J causality test. As a result of VAR(p) model estimation, the appropriate lag length was determined as 2 according to the Akaike Information Criterion. Since all variables subject to the analysis were found to be stationary at their level values, no lag length was added and the model was tested with the HJC information criterion considering the appropriate lag length. The results of the causality test indicate that the null hypothesis of no causality from BTC to USD is rejected at the 10% significance level and there is a unidirectional causality relationship from BTC to USD when the variables are not divided into positive and negative shocks. Apart from the causality

relationship in question, no causality relationship was detected between the other variables subject to the study for all levels of significance.

Table 4. Causality test results for variance.

Direction of Causality	M1	M2	M3	M4	M5
BIST100=>BTC	3.484 [0.000]	6.062 [0.000]	8.153 [0.000]	10.013 [0.000]	11.143 [0.000]
BTC=>BIST100	4.957 [0.000]	7.501 [0.000]	9.923 [0.000]	11.928 [0.000]	12.225 [0.000]
USD=>BTC	24.865 [0.000]	25.899 [0.000]	25.744 [0.000]	25.659 [0.000]	24.732 [0.000]
BTC=>USD	4.307 [0.000]	5.831 [0.000]	7.034 [0.000]	8.257 [0.000]	8.249 [0.000]
GOLD=>BTC	9.535 [0.000]	9.929 [0.000]	9.580 [0.000]	9.812 [0.000]	10.638 [0.000]
BTC=>GOLD	7.212 [0.000]	9.673 [0.000]	12.151 [0.000]	13.638 [0.000]	14.433 [0.000]

Note: *, ** and *** denote 10%, 5% and 1% significance levels, respectively. Values in parentheses are p probability values. M is the maximum number of lags. Daniell Kernel function is used in the estimation of causality analysis.

Table 5. Hacker-Hatemi-J bootstrap causality test results.

Null Hypothesis (H_0)	W Test Statistics	1%	5%	10%
BTC≠>GOLD	0.921	6.704	3.740	2.237
GOLD≠>BTC	0.289	4.563	2.867	2.227
BTC≠>BIST100	0.066	5.305	3.226	2.552
BIST100≠>BTC	0.045	6.740	3.590	2.773
BTC≠>USD	3.448*	5.082	3.644	2.454
USD≠>BTC	1.779	6.206	4.832	3.778

Note: ***, ** and * indicate that the coefficient is significant at 1%, 5% and 10% significance levels, respectively. The optimal lag length is set as 1 based on k+dmax. HJC information criterion is chosen as the information criterion. Bootstrap number is taken as 1000.

The results of the Hatemi-J asymmetric causality test are presented in Table 6. According to the calculated Wald test results, there is a unidirectional Granger causality relationship from the positive shocks of BTC to the negative shocks of BIST100 and Gold, and a bidirectional Granger causality relationship to the negative shocks of USD. It is concluded

that there is a bidirectional Granger causality relationship from the negative shocks of BTC to the positive shocks of Gold and unidirectional Granger causality relationship towards the negative shocks of Gold, while there is a unidirectional Granger causality relationship from the negative shocks of BTC to the negative shocks of USD.

Table 6. Hatemi-J asymmetric causality test results.

Null Hypothesis (H_0)	W Test Statistics	1%	5%	10%
$BTC^+ \not\Rightarrow BIST100^+$	1.268	6.764	6.204	4.778
$BIST100^+ \not\Rightarrow BTC^+$	193.583***	16.367	5.511	4.891
$BIST100^- \not\Rightarrow BTC^-$	0.729	11.611	5.768	4.311
$BTC^- \not\Rightarrow BIST100^-$	208.500***	10.680	8.436	5.278
$BIST100^+ \not\Rightarrow BTC^-$	150.680 ***	10.901	6.739	4.687
$BTC^- \not\Rightarrow BIST100^+$	2.447	11.730	6.920	4.273
$BIST100^- \not\Rightarrow BTC^+$	0.812	7.916	6.030	4.471
$BTC^+ \not\Rightarrow BIST100^-$	141.333***	9.471	6.242	5.066
$GOLD^+ \not\Rightarrow BTC^+$	280.801***	10.670	5.845	4.367
$BTC^+ \not\Rightarrow GOLD^+$	2.411	10.172	7.286	6.064
$GOLD^- \not\Rightarrow BTC^-$	1.759	8.727	5.176	3.982
$BTC^- \not\Rightarrow GOLD^-$	253.702***	9.154	5.870	4.482
$GOLD^+ \not\Rightarrow BTC^-$	173.613***	7.482	6.084	5.264
$BTC^- \not\Rightarrow GOLD^+$	4.202*	10.617	5.255	4.068
$GOLD^- \not\Rightarrow BTC^+$	3.979	14.954	8.675	5.828
$BTC^+ \not\Rightarrow GOLD^-$	151.294***	13.743	8.355	6.690
$USD^+ \not\Rightarrow BTC^+$	189.302***	8.147	7.209	5.722
$BTC^+ \not\Rightarrow USD^+$	5.444	9.455	8.005	6.754
$USD^- \not\Rightarrow BTC^-$	1.266	7.178	5.389	4.565
$BTC^- \not\Rightarrow USD^-$	117.011***	11.073	7.413	5.687
$USD^+ \not\Rightarrow BTC^-$	357.211***	11.352	8.005	5.076
$BTC^- \not\Rightarrow USD^+$	0.011	9.446	5.485	4.708
$USD^- \not\Rightarrow BTC^+$	7.412*	12.654	8.478	6.410
$BTC^+ \not\Rightarrow USD^-$	382.851***	10.483	7.176	4.950

Note: ***, ** and * indicate that the coefficient is significant at 1%, 5% and 10% significance levels, respectively. The optimal lag length is set as 2 based on k+dmax. HJC information criterion is chosen as the information criterion. The number of bootstraps is taken as 1000. + sign indicates positive shocks and – sign indicates negative shocks.

5   CONCLUSION AND SUGGESTIONS

This study examines the causal relationships between Bitcoin (BTC), the BIST100 index, the US Dollar (USD), and gold using daily data spanning from September 17, 2014, to October 13, 2023. To analyze both symmetric and asymmetric causal interactions among these financial instruments, the study employs Hong's mean and variance causality tests [18], as well as the symmetric (Hacker-Hatemi-J [23]) and asymmetric (Hatemi-J [24]) causality tests.

The empirical findings reveal various causality relationships among the examined variables. The results from the mean causality test indicate a weak unidirectional causality from BTC to USD, whereas variance causality tests identify significant volatility spillover effects across all four financial instruments. The asymmetric causality test further detects a unidirectional causality from BTC's positive shocks to the negative shocks of the BIST100 and gold, along with a bidirectional causality between BTC's positive shocks and USD's negative shocks.

These results align with previous studies investigating the interactions among these financial assets. Prior research by Sarker et al. [8], Li et al. [12], and Fasanya et al. [9] highlights Bitcoin's heightened sensitivity to external shocks, such as economic uncertainty and commodity price fluctuations, corroborating our findings on volatility spillovers. Similarly, Özmerdivanlı [13] identifies a long-term relationship between Bitcoin and major financial indicators, reinforcing the strong connection observed between BTC and USD. The literature also indicates that Bitcoin interacts with traditional financial assets, particularly during periods of economic instability. However, some studies present divergent findings. For instance, Kaymak and Koç [11] assert that BTC does not exhibit significant causality with Borsa Istanbul transaction volumes, contradicting our findings on volatility spillovers with the BIST100. Additionally, studies by Bouri et al. [14] and Dyhrberg [15] suggest that Bitcoin operates largely independently of traditional financial assets, functioning primarily as a speculative asset rather than an integrated investment instrument. These perspectives indicate that Bitcoin's price dynamics may be structurally distinct from those of conventional financial markets.

The findings of this study underscore the interconnectedness of Bitcoin, the BIST100, the US dollar, and gold within financial markets. The observed volatility spillovers suggest that price movements in these assets can influence one another, emphasizing the need for investors to consider these interdependencies when constructing diversified portfolios. Furthermore, the growing prominence of Bitcoin and its increasing interactions with traditional financial

instruments necessitate enhanced regulatory oversight in the development of monetary policies and risk management strategies. Future research could extend this analysis by incorporating macroeconomic variables to further elucidate these relationships, as well as employing advanced econometric and machine learning methodologies to improve predictive accuracy. Comparative studies across various financial markets could provide additional insights into the differential impacts of these instruments. The significant volatility spillovers identified among BTC, USD, gold, and the BIST100 highlight the importance of further research on risk management strategies for cryptocurrency-inclusive portfolios.

Acknowledgement

Conflict of Interest Statement

There is no conflict of interest between the authors.

Statement of Research and Publication Ethics

The study is complied with research and publication ethics

Artificial Intelligence (AI) Contribution Statement

This manuscript was entirely written, edited, analyzed, and prepared without the assistance of any artificial intelligence (AI) tools. All content, including text, data analysis, and figures, was solely generated by the authors.

Contributions of the Authors

Hakan KAYA: Literature Review, Data Collection and Model Development, Data Analysis, Interpretation of the Results, Editing.

Batuhan ÖZKAN: Data Collection and Model Development, Methodology, Data Analysis, Interpretation of the Results, Manuscript Writing.

REFERENCES

[1]   J. Frankenfield, "What is bitcoin? How to mine, buy, and use it," *Investopedia*. [Online]. Available: https://www.investopedia.com/terms/b/bitcoin.asp. Accessed: Sept. 25, 2023.

[2]   Binance Academy, "Bitcoin," *Binance Academy*. [Online]. Available: https://academy.binance.com/en/glossary/bitcoin. Accessed: Sept. 25, 2023.

[3]   B. Wallace, "The rise and fall of Bitcoin," *Wired*, vol. 19, no. 12, 2011.

[4]   S. Nakamoto, *Bitcoin: A peer-to-peer electronic cash system*, unpublished manuscript, 2008.

[5]   James, "The history of Bitcoin: A complete timeline of the start of Web3," *History Cooperative*. [Online]. Available: https://historycooperative.org/the-history-of-bitcoin/. Accessed: Sept. 25, 2023.

[6]   D. L. Chaum, *Computer systems established, maintained and trusted by mutually suspicious groups*, Ph.D. dissertation, Univ. of California, Berkeley, 1982.

[7]   A. T. Sherman, F. Javani, H. Zhang, and E. Golaszewski, "On the origins and variations of blockchain technologies," *IEEE Security & Privacy*, vol. 17, no. 1, pp. 72–77, 2019.

[8]   P. K. Sarker, C. K. M. Lau, and A. K. Pradhan, "Asymmetric effects of climate policy uncertainty and energy prices on bitcoin prices," *Innovation and Green Development*, vol. 2, no. 2, Art. no. 100048, 2023.

[9]   I. O. Fasanya, O. J. Oyewole, and M. Dauda, "Uncertainty due to infectious diseases and bitcoin-gold nexus: Evidence from a non-parametric causality-in-quantiles approach," *Resources Policy*, vol. 82, Art. no. 103549, 2023.

[10]   M. B. Tunçel, Y. Alptürk, M. A. Altunay, and İ. Bekci, "Kripto paralar ile BIST100 endeksi arasındaki nedensellik ilişkisi: Bitcoin örneği," *Abant Sosyal Bilimler Dergisi*, vol. 22, no. 1, pp. 367–374, 2022.

[11]   O. Kaymak and S. Koç, "Examining the relationship between Borsa Istanbul trading volumes and Bitcoin trading volumes with the Toda Yamamoto approach 2017:01 – 2021:12," *Gazi İktisat ve İşletme Dergisi*, vol. 8, no. 3, 2022.

[12]   D. Li, Y. Hong, L. Wang, P. Xu, and Z. Pan, "Extreme risk transmission among bitcoin and crude oil markets," *Resources Policy*, vol. 77, Art. no. 102761, 2022.

[13]   A. Özmerdivanlı, "Covid-19 pandemisi ile çeşitli finansal göstergeler arasındaki nedensellik ilişkisi: Türkiye örneği," *Ekonomi, Politika & Finans Araştırmaları Dergisi*, vol. 6, IERFM Özel Sayısı, pp. 172–191, 2021.

[14]   Y. Kubar and Y. Toprak, "Bitcoin ve Altcoin'ler arasındaki ilişkinin Granger nedensellik testi ile analizi," *Journal of Emerging Economies and Policy*, vol. 6, no. 1, pp. 233–247, 2021.

[15]   E. Soyaslan, "Bitcoin fiyatları ile BİST 100, BİST Banka ve BİST Teknoloji Endeksi arasındaki ilişkinin analizi," *Fiscaoeconomia*, vol. 4, no. 3, pp. 628–640, 2020.

[16]   *Yahoo Finance Historical Dataset*. [Online]. Available: https://finance.yahoo.com/quote/GC=F/. Accessed: Oct. 13, 2023.

[17]   *Türkiye Cumhuriyet Merkez Bankası Elektronik Veri Dağıtım Sistemi (TCMB/EVDS)*. [Online]. Available: https://evds2.tcmb.gov.tr/index.php. Accessed: Oct. 13, 2023.

[18]   Y. Hong, "A test for volatility spillover with application to exchange rates," *Journal of Econometrics*, vol. 103, no. 1, pp. 183–224, 2001.

[19]   C. W. Granger, "Investigating causal relations by econometric models and cross-spectral methods," *Econometrica*, vol. 37, no. 3, pp. 424–438, 1969.

[20]   H. Y. Toda and T. Yamamoto, "Statistical inference in vector autoregressions with possibly integrated processes," *Journal of Econometrics*, vol. 66, no. 1–2, pp. 225–250, 1995.

[21]   Y.-W. Cheung and L. K. Ng, "A causality-in-variance test and its application to financial market prices," *Journal of Econometrics*, vol. 72, no. 1, pp. 33–48, 1996.

[22]   E. Çevik, Ç. H. Terzioğlu, and E. İ. Çevik, "Bitcoin ile önemli döviz kurları arasında nedensellik ilişkisi," *Iğdır Üniversitesi Sosyal Bilimler Dergisi*, ICOMEP Özel Sayısı, pp. 109–130, 2021.

[23]   R. S. Hacker and A. Hatemi-J, "Tests for causality between integrated variables using asymptotic and bootstrap distributions: Theory and application," *Applied Economics*, vol. 38, no. 13, pp. 1489–1500, 2006.

[24]   A. Hatemi-J, "Asymmetric causality tests with an application," *Empirical Economics*, vol. 43, no. 1, pp. 447–456, 2012.

[25]   U. K. Pata, "Türkiye'de enflasyon, tasarruf ve ekonomik büyüme arasındaki ilişkilerin simetrik ve asimetrik nedensellik testleri ile analizi," *Maliye Dergisi*, vol. 174, pp. 92–111, 2018.

[26]   M. Yetim and R. Yamak, "Türkiye'de döviz kurundan fiyatlara geçişkenlik etkisi: Hatemi-J asimetrik nedensellik testi," *Trakya Üniversitesi Sosyal Bilimler Dergisi*, vol. 21, no. 1, pp. 203–221, 2019.

[27]   H. Kaya, "Olağanüstü dönemlerde enflasyon olgusu ve çözüm önerileri," in *Türkiye Ekonomisinde Petrol Fiyatı ve Döviz Kuru Volatilitesinin Enflasyon Üzerine Etkisi: Covid-19 Dönemi Üzerine Bir İnceleme*, S. Koç and Y. U. Uzun, Eds. Bursa: Ekin Basım Yayın, 2022, pp. 39–59.

[28]   V. Bodart and B. Candelon, "Evidence of interdependence and contagion using a frequency domain framework," *Emerging Markets Review*, vol. 10, no. 2, pp. 140–150, 2009.

DEEPFAKE IMAGE DETECTION WITH TRANSFER LEARNING MODELS

Lutfi Emre DEMİR [1] (iD), **Yavuz CANBAY** [2,*] (iD)

[1]Kahramanmaraş Sütçü İmam University, Department of Information Systems, Kahramanmaraş, Türkiye

[2]Kahramanmaraş Sütçü İmam University, Department of Computer Engineering, Kahramanmaraş, Türkiye

* Corresponding Author: yavuzcanbay23@gmail.com

ABSTRACT

Deepfake is a technology that employs artificial intelligence to generate fake images and videos that closely mimic real ones. The rapid growth and dissemination of digital modifications generate considerable concern in the media, politics, and social networking. Among the concerns faced include the dissemination of misinformation, reputational damage, and threats to physical security. Given these concerns, prompt and reliable identification of Deepfakes is crucial for protecting information security and mitigating its negative impacts. Therefore, the development of effective technologies for Deepfake detection is essential to counter this increasing threat. This study aims to identify Deepfake images and examine the efficiency of transfer learning algorithms in Deepfake identification. This study employed the most commonly utilized transfer learning models, including InceptionV3, EfficientNet, NASNet, ResNet, DenseNet, Xception and ConvNeXt, to perform the detection task. An extensive public dataset of 190,000 images, including both real and artificially generated, was utilized in the study. The performance of each model was assessed by using the metrics of accuracy, precision, recall, and F1-score. DenseNet was the most successful model with a test accuracy of 93%. The obtained results have shown that transfer learning models can effectively detect the Deepfake images, providing a practical approach to the challenge with reasonable performance scores.

Keywords: Deepfake detection, Information security, Transfer learning

1   INTRODUCTION

Advancements in artificial intelligence and deep learning have made Deepfake technology possible, transforming the production of realistic synthetic media content. Deepfake

is a combination of "deep learning" and "fake," referring to the technology that processes visual and auditory data to generate impressively realistic imitation images and movies. Although Deepfake offers benefits in diverse domains like entertainment, advertising, and education, they also present significant risks. The utilization of Deepfakes, especially for the malicious aims of misinformation, privacy violation, cyberbullying, and fraud, has raised significant ethical and security issues. Once shared over social media, this type of content can be utilized to influence the community, damage faith in digital interactions, incur economic consequences, and potentially increase social unrest [1].

The rapid proliferation and growing complexity of Deepfake media necessitate the urgent development of reliable detection methods. The consequences of undercover and undetectable Deepfakes are severe, involving electoral manipulation, financial deception, and societal unrest. Consequently, there is an urgent demand for innovative technology capable of consistently and effectively identifying "fake" materials.

In the literature, there exist some studies considering detection of Deepfake media. For instance, Afcharve et al. [2] presents a deep learning method for detecting face forgeries produced by hyper-realistic fake video generation techniques such as Deepfake and Face2Face. For this purpose, two different low-layer and fast networks capable of extracting mesoscopic or medium-scale features of images were designed. The proposed networks provided successful results even in video formats where traditional image analysis techniques are inadequate due to the information degradation caused by data compression. The method was tested on an existing dataset and a custom dataset compiled from online videos. In the tests, over 98% detection success was achieved for Deepfake videos and over 95% for Face2Face videos. The CNN-based model used in the study achieved 98.40% accuracy on the FaceForensics++ dataset.

Prajapati et al. [3] aimed to develop deep learning-based generic models to detect Deepfakes, which are synthetic videos created by replacing the face in an original image with the face of another person. The paper proposed a new Generative Adversarial Network (GAN) based model, called MRI-GAN, which detects fake videos using perceptual differences in images. The proposed MRI-GAN model was tested on the Deepfake Detection Challenge dataset while evaluating perceptual differences with structural similarity index. Experimental results showed that the model based on flat frames achieves 91% test accuracy, while the MRI-GAN framework achieves 74% accuracy.

Miao et al. [4] presented a new method that improves the generalization ability and robustness in the field of face forgery detection to prevent the malicious use of face manipulation technology. The proposed model encodes the relationships between patches by extending the Transformer structure with a bag-of-local-feature approach, which allows the model to learn local forgery features without any explicit supervision. The effectiveness of the method had been extensively tested on the FaceForensics++, Celeb-DF and DeeperForensics-1.0 datasets. According to the test results, 87.86% accuracy was achieved on FaceForensics++ dataset, 82.52% AUC on Celeb-DF dataset and 97.01% accuracy on DeeperForensics-1.0 dataset.

Deepfake detection was considered as a fine discrimination-oriented classification problem instead of traditional binary classification to capture fine details in [5]. The proposed multi-attention network-based model combined both low-level textural and high-level semantic features using attentional mechanisms to highlight forgery traces. In order to improve the learning process of the model, regional loss of independence and an attention-guided data augmentation strategy were also added. In the test studies on various datasets, it outperformed other models with 97.60% accuracy on the FaceForensics++ dataset and 0.1679 loss value on the DFDC dataset.

Since there is a challenge between different types of GANs for detecting deepfake images, Kanwal et al. [6] proposed a general solutions. In their work, they aimed to detect deepfake images using Siamese Networks with triplet loss function. The experiments were performed in two different cases. In the first case, the training and test sets were chosen from the same dataset, which consisted of real images from the FFHQ dataset and fake images generated by StyleGAN. In the second case, the training and test sets were chosen from different datasets, in which case the model was trained on the FFHQ dataset and StyleGAN and tested on images generated by PGAN. The results showed that using contrast loss or triplet loss instead of cross-entropy or MSE improves the generalization ability of the model. An accuracy of 94.80% was achieved in the study

In a study by Rafique et al. [7], fake face detection was addressed using two machine learning algorithms based on features extracted by AlexNet and ShuffleNet models. A new image descriptor is also developed to improve the predictive power of the proposed network. The authors claimed that there are differences in compression levels between the original and fake images. In this context, the proposed approach evaluates the difference between the original image and its versions with 85% compression. This method is called Error Level

Analysis (ELA), which reveals the lost details due to the compression level. The images obtained by ELA are given to AlexNet and ShuffleNet models for feature extraction. The generated feature vector was passed to SVM and k-NN classifiers for classification as real or fake. In the experiments, on the Real and Fake Face Detection dataset, ShuffleNet achieved the highest accuracy with 88.2% when combined with k-NN classifier and 87.9% when combining with SVM classifier.

In another study, Nida et al. [8] aimed to detect real and fake face images using transfer learning. Since it is difficult to detect forgery by visual inspection alone, this research uses the "Real and Fake Face Detection" dataset created by the Computational Intelligence Photography Lab, in Yonsei University. In the proposed method, images are normalized as a first step and then preprocessed with Error Level Analysis. These normalized images are trained with various pre-trained deep learning models to classify fake and real faces. The VGG models showed the highest performance with fewer epochs than the other techniques; VGG-16 achieved 91.97% training accuracy and VGG-19 achieved 92.09% training accuracy. Model performances were evaluated by comparing with confusion matrix and existing methods.

Patel et al. [9] proposed an end-to-end method that combines features extracted by various CNN models to detect deepfake videos at frame level. Using the DFDC dataset, frames in videos are processed as individual images and features are extracted from these images. These features were then used for deepfake detection with a Random Forest classifier. Thanks to the features extracted with MobileNet CNN, 90.2% accuracy was achieved.

Joshi et al. [10] used the Xception model for the detection of deepfake images and videos. They used a dataset obtained from Kaggle, which contains 90,000 images of real and deepfake content. The model was trained by fine-tuned transfer learning. Data replication and regularization techniques were applied to increase the robustness of the model. With 93.01% accuracy on the test dataset, this method provided an effective solution against deepfake content spread on the internet and social media. The results showed that the Xception model provides a reliable deepfake detection method thanks to its strong classification capabilities.

Liao el al. [11] proposed a Transformer network that uses the self-attention mechanism to model long-range dependencies and global reception domains. A dual-branch feature extraction framework was developed and the extracted features are combined with transformer's encoder structure and the cross-attention mechanism to model them efficiently. The proposed method achieved 83.5%, 70.25% and 78.5% accuracy on Deepfake, Face2Face and NeuralTextures datasets respectively.

Table 1. Comparison of the studies in the literature

Study	Method	Success Rate
[2]	MesoNet	98.40%
[3]	MRI-GAN + SSIM and Simple Frame Model	91% (Simple Frame Model), 74% (MRI-GAN)
[4]	Transformer + Bag-of-Local-Feature	87.86% (FaceForensics++) 82.52% (Celeb-DF), 97.01% (DeeperForensics)
[5]	Multi-attentional Network	97.60%
[6]	Siamese Network	94.80%
[7]	AlexNet, ShuffleNet, ELA, k-NN, SVM	88.2% (ShuffleNet + k-NN) 87.9% (ShuffleNet + SVM)
[8]	VGG16 and VGG19	91.97% VGG16 92.02% VGG19
[9]	Frame-Based MobileNet + Random Forest Classifier	90.2%
[10]	Xception	93.01%
[11]	Transformer	83.5% (Deepfake) 70.25% (Face2Face) 78.5% (NeuralTextures)

The rest of this paper is organized as follows. The Materials and Methods section details the dataset, the computational environment and the transfer learning models employed in this paper. In particular, it also explains the performance metrics used for evaluation indicators. Experimental studies give the details about the experiments and provides a comparative analysis of the model performance in terms of the metrics of accuracy, precision, recall, and F1-score. It also discusses the strengths and weaknesses of each model, and demonstrate that DenseNet performs best among others in the detection of deepfake. Finally, the Conclusion summarizes the achievement of the study's results, presenting the effectiveness of DenseNet for such a real-world application and pointing to the directions of future work, i.e., the use of ensemble method, and video-oriented deepfake detection.

2 MATERIAL AND METHODS

In this section, the materials and methods used in the study are explained.

2.1 Dataset Description

This work used a dataset of 190,000 labeled images obtained from the reference [12], which includes real and GAN-generated deepfake images. The dataset used is a modified and

enhanced version of the OpenForensics dataset, utilizing various manipulation methods such as face swapping and reenactment. Each image was created in 256 x 256 JPG format. Some samples from real and fake image are shown in Figure1.

Figure 1. Real and fake image samples.

2.2   Transfer Learning Models

Transfer learning has become a promising method in machine learning, especially when training samples are small or computational power is limited. It is possible to repurpose a model pre-trained on a huge dataset (e.g., ImageNet) for a given task by means of transfer learning, which not only does this save the computational cost, but also to exploit the knowledge contained within pre-trained features. In the following sections, seven leading transfer learning model were briefly explained.

2.2.1 InceptionV3

InceptionV3 stands out among deep learning architectures with its multi-scale feature extraction capability. Thanks to Inception modules, it learns both fine details and general features by using kernel filters of different sizes simultaneously. This is particularly advantageous for detecting manipulations in fake content. Auxiliary classifiers minimize the problem of damped gradients and provide more stable learning during model training. InceptionV3 offers a strong balance between accuracy and computational efficiency when

working on large data sets, making it ideal for complex tasks such as deep fake detection [13]. InceptionV3 has the ability to learn features at different scales simultaneously, which is an important factor in deepfake detection. In this study, the purpose of using this model is that it can detect both the overall structure and small anomalies in face manipulations. Moreover, the ability to capture distortions at different frequencies in forged images with versatile convolution kernels makes the model a powerful option for deepfake analysis.

2.2.2 EfficientNet

EfficientNet is a model specifically designed for processing large datasets, and the EfficientNet variant used in this study is pre-trained on ImageNet, which is characterized by its computational efficiency in resource-limited environments [14]. EfficientNet is a model that can achieve high accuracy with less computational power thanks to its optimized balance of depth, width and resolution. It is preferred for large datasets used in deepfake image detection due to its fast-training process and low parameter requirement. It is also good at capturing small and subtle changes in manipulated facial images.

2.2.3 ResNet

ResNet achieves training of deep multilayer networks with damped gradient with the help of residual connections. Through these connections, the gradients can be returned more efficiently and models can be trained on deeper layers. ResNet architecture with layered scheme is capable of visualizing the complex visual damages in fake images. The ResNet model employed in the work performed well, maintaining an optimal trade-off between depth and computational cost. ResNet was tested on particularly large and diverse datasets [15]. ResNet offers high generalization capacity by learning from deep layers. In particular, it produces more stable results by minimizing feature loss in the detection of images containing a wide variety of manipulation techniques such as deepfakes. In this study, this model was employed since it can analyze fake images successfully by supporting multi-layer information flow.

2.2.4 DenseNet

DenseNet maximizes information flow by connecting the output of each layer to all subsequent layers. These dense connections allow the model to both avoid gradient loss and learn more effectively with fewer parameters. This feature of DenseNet yields powerful results, especially for large and diverse data sets [16]. Thanks to the strong information sharing between

layers, DenseNet can learn fine details in fake images more effectively. Its high accuracy in transfer learning provides an advantage in a task where fine details are critical, such as deepfake detection. In particular, we preferred to use this model since it is effective in determining the differences between real and fake faces by learning small manipulations better.

2.2.5 Xception

Xception is computationally efficient, since it uses less parameters than conventional convolutions. It uses depthwise separable convolutions. In this model, it is possible to learn channel-based as well as spatial features in separate steps, and thus the model is a versatile tool for the identification of low-level as well as high-level manipulations. By its optimized design, Xception can achieve accuracy on difficult problems, including deep fake detection [17]. Xception is a particularly computationally efficient model. Its ability to achieve high accuracy using fewer parameters in the transfer learning process is a critical advantage in the classification of deepfake images. In this study, it is especially preferred because of its ability to detect facial manipulations and fine details. Its ability to better analyze deep forgery traces used in forged content increases its effectiveness in deepfake detection.

2.2.6 NasNet

The main benefits of NasNet include the possibility of finding an automated architecture that is best suited to a given task, along with high resistance to different manipulations. The purpose of this model is to find the best architecture for individual tasks without direct human supervision. Nevertheless, the model applied in the study did not achieve a good performance because other models performed much better. This indicates that the model needs to be fine-tuned for certain tasks e.g., detection of deep fakes [18]. In this paper, since the deepfake problem involves complex and dynamic data, NasNet was used for better performance thanks to its large model search space. Another advantage is that it reduces manual hyperparameter tuning in transfer learning processes and can be easily adapted to different datasets.

2.2.7 ConvNeXt

ConvNeXt integrates some architectural developments proposed in recent years as image transformers into a ResNet-type hierarchical backbone of low, medium and high levels, instead of a traditional CNN-conceptual model. The large kernel size and the application of Layer Normalization help this approach to generalize well in terms of both computational and

representation learning performance. It serves as a backbone for computer vision tasks as we are able to efficiently capture local and global spatial features in the model. With an optimized structure, ConvNeXt achieves high performance in challenging areas such as object detection and image classification [19]. In this study, ConvNeXt, one of the latest versions of modern CNN architectures, was chosen for its fast adaptation in transfer learning processes, deep feature learning capability and superior performance on large datasets. The ability to capture subtle textural differences in deepfake images gives this model an advantage in detection processes.

2.3   Model Implementation

This study employed transfer learning with fine-tuning to optimize efficiency and accuracy. Rather than training models from scratch, we utilized pre-trained deep networks to preserve general feature representations while fine-tuning the deeper layers for enhanced adaption to deepfake-specific characteristics. This methodology enabled us to decrease computing cost, prevent overfitting, and enhance classification precision on our dataset. Our findings validate its efficiency, with DenseNet having 93% accuracy, illustrating the benefits of integrating transfer learning with fine-tuning for deepfake detection. While there exist many variations of CNNs, we preferred to use mostly used transfer learning techniques such as InceptionV3, EfficientNet, NasNet, ResNet, DenseNet, Xception and ConvNeXt in our study.
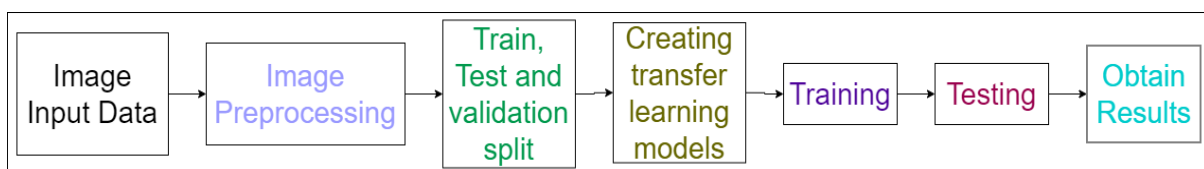

Figure 2. *The workflow of the model implementation.*

Figure 2 presents the workflow of the experimental implementations. In the workflow of the model implementation, firstly, the image dataset was loaded for the processing purpose. Every image was labelled as "fake" or "real" and the dataset was structured taking these labels into account. Data loaded was formatted according to the desired format for each model layer. Then in preprocessing, the size of each image was standardized to 224x224. The aim of resizing image is making the model run fast, stable and effectively. The dataset was divided into 75% training, 20% validation and 5% test. During this process, the balanced structure of the dataset, with 50% fake and 50% real images, was maintained, meaning the number of images in each class was kept equal. Subsequently, transfer learning models were developed and fine-tuned

using the training dataset, followed by validation with the validation dataset. The models' performances through the trained model were evaluated using the test dataset. Accuracy, precision, recall and F1-score were used as performance indicators. Those metrics allowed to account for the goodness of the model and its performance by class. The results were then presented in tables and confusion matrix in the following subsections.

Sigmoid activation function was used due to its application in binary classification and that the output of the network gets transformed into a value between 0 and 1. In addition, the Adam optimization algorithm was used for weight optimization of the learned model. Binary Cross-Entropy was chosen as loss function as it is normally applied in the case of binary classification problems. Each model was trained during the learning phase for 10 epochs. Batch size was determined as 32. The learning rate was left at its default value.

3   EXPERIMENTAL RESULTS AND DISCUSSION

Accurate detection and classification of Deepfake images is crucial. In this section, the performances of seven transfer learning methods were obtained and then compared. A 190,000 labelled image dataset was used in the experiments. Accuracy, precision, recall and F1-Score metrics were employed for evaluations [20-23].

According to the obtained results, DenseNet achieved the highest test accuracy demonstrating its ability to accurately differentiate real and manipulated content. InceptionV3 and Xception followed closely with test accuracies of 92.60% and 92.15%, respectively. The performance metrics obtained in the experimental studies are presented in Table 2.

Table 2. Performance results of the transfer learning algorithms.

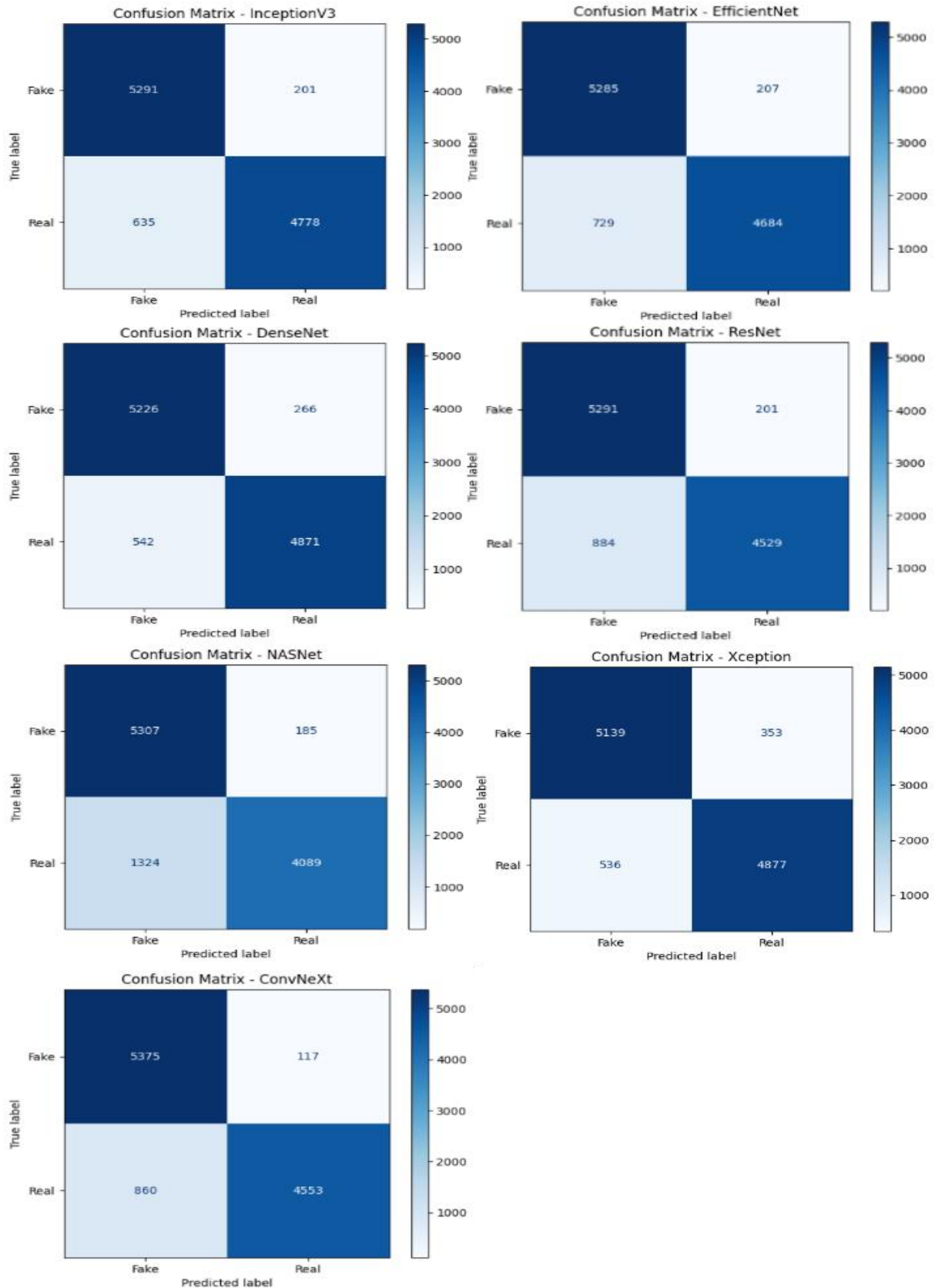| Model	Train Accuracy (%)	Test Accuracy (%)	Precision (%)	Recall (%)	F1-Score (%)
InceptionV3	99.17	92.60	93	92	92
EfficientNet	99.31	91.67	92	91	91
ResNet	99.12	90.54	91	90	90
DenseNet	98.90	93.00	93	93	93
Xception	99.33	92.15	92	92	92
NasNet	99.30	86.16	88	86	86
ConvNeXt	99.33	91.36	92	91	91

Figure 3. The confusion matrices of the transfer learning models.

For a more detailed analysis of model performances, the confusion matrix of all the models were given in Figure 3. These matrices summarize true positives, false positives, true negatives, and false negatives, providing a more nuanced picture of the classification behavior of each of the models. As can be seen from Table 2, the best test accuracy is obtained by DenseNet across all the categories with scarce misclassifications. Conversely, NasNet provides generally worse detection test results.

According to the results provided in Figure 3, InceptionV3 presented 635 FP and 201 FN, EfficientNet had 729 FP and 207 FN, DenseNet resulted 542 FP and 266 FN, ResNet presented 884 FP and 201 FN, NasNet produced 1324 FP and 185 FN, Xception had 536 FP and 353 FN and finally ConvNeXt resulted in 860 FP and 117 FN. These results show that DenseNet is the most successful model in terms of total number of FP and FN.

The dataset employed in this work, which contains 190,000 GAN-generated images, is one of the largest studied in the deepfake detection tasks. This extensive and multimodal dataset offered a valuable chance to evaluate the models' generalization across different kinds of manipulations. Within these conditions, DenseNet performed well and resulted in the best performance.

DenseNet architecture has the merit of feature reuse, and thus has been effective as its datasets are large and training data is heterogeneous. The dense connectivity between layers allowed the model to efficiently capture complex patterns and subtle inconsistencies in deepfake manipulations. InceptionV3 and Xception also performed well because of their ability to capture multi-scale features. These models accounted for the variety of distortions in the dataset, however, because of their slightly lower F1 scores as compared with DenseNet, there is still potential to be fully exploited in the context of also dealing with subtle artifacts. ConvNeXt presented the highest training accuracy of 99.33%, highlighting its capability to adapt to the training data, followed by EfficientNet with 99.31% accuracy. But, test accuracy of ConvNeXt (91.36%) is a little overfitting, highlighting the needs for methods including regularization, and advanced data augmentation to promote generalization. In the ConvNeXt model, performance metrics show 91% test accuracy and an F1-score of 91%. ResNet and NasNet have the worse testing performances. While ResNet's deep architecture provided some benefits, it may not have fully leveraged the dataset's diversity, leading to less effective generalization. That reliance on automated architecture design of NasNet might have made it less able to retain the complex features necessary for this task. The large dataset played a crucial role in evaluating the models' robustness. Models like DenseNet are resistant to these

conditions, while others like NasNet failed to generalize effectively. However, the variety of manipulations in the dataset probably uncovered weaknesses in architectures that are not well-suited for fine-grained pattern recognition. The strong performance of DenseNet shows that it is suitable for real-world deployment, which is especially important for applications where understanding the situation's accuracy and recall is crucial. The capacity to process large amounts of data quickly makes it a good candidate for real application deepfake detection systems.

4   CONCLUSION

This study evaluated seven transfer learning models InceptionV3, EfficientNet, ResNet, DenseNet, Xception, NasNet and ConvNeXt for the task of deepfake detection using a dataset of 190,000 images including both real and fake images. The main objective was to compare these architectures in terms of performance in the detection of manipulation in terms of accuracy, precision, recall and F1-score.

DenseNet was obtained as the best-performing model, achieving the highest test accuracy among all evaluated architectures. Its densely connected layers and feature reuse capability allowed it to excel in identifying subtle manipulations present in deepfake images. This robust performance, underlines its usefulness for real-world applications.

The dataset played an important role in shaping the outcomes of the models. Containing many kinds of manipulations, it offered an evaluation not only of model robustness, but also of model generalization power. The large number of samples in the dataset also validated the comparative analysis, providing a stable used as a benchmark. However, while DenseNet demonstrated superior performance, other models like InceptionV3, Xception and ConvNeXt also achieved commendable results, with high accuracy, indicating their capability to handle such tasks effectively.

Future studies will investigate ensemble methodologies to enhance robustness through a combination of different models. Furthermore, we plan to expand our methodology to encompass video-based deepfake detection, and using more advanced models to detect deepfake images.

Conflict of Interest Statement

There is no conflict of interest between the authors.

Statement of Research and Publication Ethics

The study is complied with research and publication ethics.

Artificial Intelligence (AI) Contribution Statement

This manuscript was entirely written, edited, analyzed, and prepared without the assistance of any artificial intelligence (AI) tools. All content, including text, data analysis, and figures, was solely generated by the authors.

Contributions of the Authors

L.E. Demir: Methodology, formal analysis, visualization, data curation, writing & editing.

Y. Canbay: Conceptualization, methodology, writing, visualization, supervision.

REFERENCES

[1]   M. S. Rana, M. N. Nobi, B. Murali, and A. H. Sung, "Deepfake detection: A Systematic Literature Review," *IEEE Access,* vol. 10, pp. 25494-25513, 2022.

[2]   D. Afchar, V. Nozick, J. Yamagishi, and I. Echizen, "Mesonet: A Compact Facial Video Forgery Detection Network," in *2018 IEEE International Workshop on Information Forensics and Security (WIFS)*, 2018: IEEE, pp. 1-7.

[3]   P. Prajapati and C. Pollett, "Mri-gan: A Generalized Approach to Detect Deepfakes Using Perceptual Image Assessment," *arXiv preprint arXiv:2203.00108,* 2022.

[4]   C. Miao, Q. Chu, W. Li, T. Gong, W. Zhuang, and N. Yu, "Towards Generalizable and Robust Face Manipulation Detection via Bag-Of-Local-Feature," *arXiv preprint arXiv:2103.07915,* 2021.

[5]   H. Zhao, W. Zhou, D. Chen, T. Wei, W. Zhang, and N. Yu, "Multi-attentional Deepfake Detection," in *Proceedings of the IEEE/CVF Conference on Computer Vision and Pattern Recognition*, 2021, pp. 2185-2194.

[6]   S. Kanwal, S. Tehsin, and S. Saif, "Exposing AI Generated Deepfake Images Using Siamese Network With Triplet Loss," *Computing and Informatics,* vol. 41, no. 6, pp. 1541–1562, 2022.

[7]   R. Rafique, M. Nawaz, H. Kibriya, and M. Masood, "Deepfake Detection Using Error Level Analysis and Deep Learning," in *2021 4th International Conference on Computing & Information Sciences (ICCIS)*, 2021: IEEE, pp. 1-4.

[8]   N. Nida, A. Irtaza, and N. Ilyas, "Forged Face Detection Using ELA and Deep Learning Techniques," in *2021 International Bhurban Conference on Applied Sciences and Technologies (IBCAST)*, 2021: IEEE, pp. 271-275.

[9] M. Patel, A. Gupta, S. Tanwar, and M. Obaidat, "Trans-DF: A Transfer Learning-Based End-To-End Deepfake Detector," in *2020 IEEE 5th International Conference on Computing Communication And Automation (ICCCA)*, 2020: IEEE, pp. 796-801.

[10] P. Joshi and V. Nivethitha, "Deep Fake Image Detection using Xception Architecture," in *2024 5th International Conference on Recent Trends in Computer Science and Technology (ICRTCST)*, 2024: IEEE, pp. 533-537.

[11] M. Liao and M. Chen, "A New Deepfake Detection Method by Vision Transformers," in *International Conference on Algorithms, High Performance Computing, and Artificial Intelligence (AHPCAI 2024)*, 2024, vol. 13403: SPIE, pp. 953-957.

[12] M. Karki. *deepfake and real images*: https://www.kaggle.com/datasets/manjilkarki/deepfake-and-real-images, (23.12.2024).

[13] C. Szegedy, V. Vanhoucke, S. Ioffe, J. Shlens, and Z. Wojna, "Rethinking the Inception Architecture for Computer Vision," in *Proceedings of the IEEE Conference on Computer Vision and Pattern Recognition*, 2016, pp. 2818-2826.

[14] M. Tan and Q. Le, "Efficientnet: Rethinking Model Scaling for Convolutional Neural Networks," in *International Conference on Machine Learning*, 2019: PMLR, pp. 6105-6114.

[15] K. He, X. Zhang, S. Ren, and J. Sun, "Deep Residual Learning For Image Recognition," in *Proceedings of the IEEE Conference on Computer Vision and Pattern Recognition*, 2016, pp. 770-778.

[16] G. Huang, Z. Liu, L. Van Der Maaten, and K. Q. Weinberger, "Densely Connected Convolutional Networks," in *Proceedings of The IEEE Conference on Computer Vision and Pattern Recognition*, 2017, pp. 4700-4708.

[17] F. Chollet, "Xception: Deep Learning with Depthwise Separable Convolutions," in *Proceedings of The IEEE Conference on Computer Vision and Pattern Recognition*, 2017, pp. 1251-1258.

[18] B. Zoph, V. Vasudevan, J. Shlens, and Q. V. Le, "Learning Transferable Architectures for Scalable Image Recognition," in *Proceedings of the IEEE Conference on Computer Vision and Pattern Recognition*, 2018, pp. 8697-8710.

[19] Z. Liu, H. Mao, C.-Y. Wu, C. Feichtenhofer, T. Darrell, and S. Xie, "A Convnet for the 2020s," in *Proceedings of the Ieee/Cvf Conference On Computer Vision and Pattern Recognition*, 2022, pp. 11976-11986.

[20] D. M. Powers, "Evaluation: From Precision, Recall and F-Measure to Roc, Informedness, Markedness and Correlation," *Arxiv Preprint Arxiv:2010.16061,* 2020.

[21] A. Utku, Z. Ayaz, D. Çiftçi, and M. A. Akcayol, "Deep Learning Based Classification for Hoverflies (Diptera: Syrphidae)," *Journal of the Entomological Research Society,* Vol. 25, No. 3, Pp. 529-544, 2023.

[22] Y. Canbay, S. Adsiz, and P. Canbay, "Privacy-Preserving Transfer Learning Framework for Kidney Disease Detection," *Applied Sciences,* Vol. 14, No. 19, P. 8629, 2024.

[23] Y. Kaya, Z. Yiner, M. Kaya, and F. Kuncan, "A New Approach to Covid-19 Detection from X-Ray Images Using Angle Transformation with Googlenet and Lstm," *Measurement Science and Technology,* Vol. 33, No. 12, P. 124011, 2022.

PREDICTING BITCOIN MINING ENERGY CONSUMPTION USING MACHINE LEARNING: A CASE FOR K-NEAREST NEIGHBORS REGRESSION

Nazmiye ELİGÜZEL [1] , **Sena AYDOĞAN** [2] *

[1] *Gaziantep İslam, Science and Technology University, Department of Industrial Engineering, Gaziantep, Türkiye*

[2] *Gazi University, Department of Industrial Engineering, Ankara, Türkiye*

* Corresponding Author: senaaydogan@gazi.edu.tr

ABSTRACT

The energy consumption of Bitcoin mining has emerged as a critical topic in cryptocurrency research, influenced by the significant environmental and economic impacts of blockchain activities. This study examines the energy consumption of Bitcoin mining with a dataset that includes essential blockchain variables such as overall hash rate, network difficulty, daily confirmed transactions, mempool size, average block size, and daily Bitcoin output. A new energy consumption indicator is proposed to contribute to the research domain. The proposed indicator better accurately reflects the dynamics of blockchain energy utilization. Various machine learning models, such as Random Forest, Gradient Boosting, Support Vector Regression, and Multi-layer Perceptron, are evaluated, with particular emphasis on k-Nearest Neighbors Regression (k-NNR). The k-NNR model surpassed all other models, with a $R2$ value of 0.80427 and a Mean Squared Error (MSE) of 0.00441, indicating its high prediction accuracy. Analysis of feature importance indicated that daily Bitcoin production and block size are significant determinants of energy use. The findings underscore the efficacy of k-NNR in energy modeling, offering insights into Bitcoin's energy dynamics and establishing a foundation for more energy-efficient blockchain systems.

Keywords: Bitcoin, Energy consumption, Hash rate, k-Nearest neighbor regression, Machine learning.

1 INTRODUCTION

Blockchain is a disruptive form of distributed ledgers, developed by Satoshi Nakamoto [1] in 2008. A blockchain is a distributed, decentralized, and securely maintained peer-to-peer

network that facilitates the management of information and trust among users without requiring a trusted third party [2]. This could diminish the influence of central authorities within financial ecosystems, consequently lessening the necessity for intermediaries like banks or government agencies to maintain trust. Blockchain technology, as a distributed database, facilitates the sharing of digital events among all members in the blockchain. The information included in each block is encrypted with a "hash" value. Every block in a blockchain encompasses the hash value of the preceding block [2], [3]. This approach can diminish fraud attempts by enhancing transparency, thereby significantly reducing the likelihood of data manipulation. The cryptocurrency market has experienced substantial growth in recent years [4]. This growth could require the implementation of new regulations within financial markets. Since 2009, various cryptocurrencies have developed, beginning with Bitcoin, the initial prominent implementation of Satoshi Nakamoto's blockchain technology announced in 2008 [5]. Bitcoin, as articulated by Satoshi Nakamoto, is a decentralized peer-to-peer electronic cash system that employs a consensus protocol to avoid double spending across different nodes [5].

Bitcoin mining is a decentralized computing procedure in which transactions are authenticated and included into the public ledger, referred to as the blockchain. The procedure for generating bitcoins is termed mining, and the individuals involved are referred to as miners. All transactions are executed and recorded on a decentralized ledger: the blockchain [6]. This may result in heightened individual engagement within the financial system, motivating users to actively participate in the blockchain, thereby assisting in the mitigation of fraud and data manipulation. The energy consumption of cryptocurrencies has emerged as a prominent topic of discourse in recent years [6]. An increased electricity cost per bitcoin mining indicates increased consumption of energy [7]. Substantial discrepancies exist in the calculations of bitcoin's energy usage because to numerous uncertainties in the process, including the type of hardware utilized in mining and its operational duration. Estimating future energy consumption for Bitcoin mining is challenging, as Bitcoin values directly influence mining activities and, consequently, energy usage [6]. A significant number of recent studies have been released, all of which anonymously emphasize the escalating energy issue associated with bitcoin mining [4], [6], [8]–[10]. Several significant studies in the literature examine bitcoin mining and energy consumption, which we addressed in our research.

Maiti [7] examined the non-linear correlation between Bitcoin prices and energy consumption from 2010 to 2021 with a Threshold Regression model. It delineates six regimes of price fluctuations influenced by energy consumption thresholds, revealing substantial effects

just in high consumption regimes, hence highlighting the disparate impact of energy on Bitcoin price dynamics. Sapra and Shaikh [4] examined the influence of market indices and Ethereum prices on Bitcoin energy use, employing Autoregressive Distributed Lag modeling with data from 2018 to 2023. The study indicates that rising Ethereum prices and cryptocurrency indices lead to increased Bitcoin energy consumption and emissions, implying the necessity for green investments in cryptocurrencies that employ alternatives to proof-of-work (PoW) techniques. Kevser [11] analyzed the correlation of geopolitical dangers, global economic policy uncertainty, and Bitcoin energy use. Analysis of data from 2011 to 2022, employing Hatemi-J causality tests, indicates that global concerns elevate Bitcoin demand and energy consumption, positioning Bitcoin as a safeguard in times of uncertainty while exacerbating its environmental consequences. Tissaoui et al. [12] utilized the Quantile Nonlinear Autoregressive Distributed Lags (QNARDL) model and Extreme Gradient Boosting (XGBoost) to evaluate the influence of Bitcoin prices on energy consumption. Short-term price increases result in rapid energy surges, however long-term impacts diminish energy consumption, with XGBoost surpassing conventional forecasting techniques. Sapra et al. [13] analyzed the causal relationships among Bitcoin's energy use, pricing, and market volatility. The study concludes that Bitcoin prices Granger-cause energy use, whereas the reverse is not true, positioning price as a net contributor and consumption as a recipient in market dynamics. Syzdykova [14] analyzed the energy requirements of Bitcoin mining, emphasizing its substantial contribution to world electricity usage, amounting to 204.5 Terawatt hours (TWh) per year by 2022. The research highlights the shortcomings of the PoW process and promotes the incorporation of renewable energy in mining operations. Kohli et al. [5] compared the energy usage of cryptocurrencies with centralized systems such as Visa, highlighting Bitcoin's environmental impact comparable to that of national energy usage. The research commends Ethereum 2.0's shift to proof-of-stake as a significant achievement in sustainability. Zaghdoudi et al. [15]employed machine learning methods, including XGBoost, to forecast energy usage affected by uncertainty indices. The results underscore economic policy uncertainty and geopolitical risks as major predictors, illustrating the effectiveness of sophisticated modeling tools. Bublyk et al. [16] projected Bitcoin's energy consumption would attain 142 TWh by 2026, incurring substantial environmental consequences. It advocates for the association of mining activities with renewable energy sources to reduce their environmental impact. Adewuyi et al. [17] conducted an investigation into Bitcoin's energy consumption employing structural break and non-linear analytics. It recognizes bubbles associated with market activities and advocates for sustainable investments and policies to mitigate the environmental impact of cryptocurrency mining.

Table 1 indicates summary of literature on Bitcoin energy consumption.

Table 1. Literature on Bitcoin Energy Consumption.

Study	Objective	Methodology	Variables	Time Period (Frequency)	Key Findings	Contribution
Maiti [7]	Investigate the non-linear relationship between Bitcoin prices and energy consumption.	Threshold Regression Model	Bitcoin price	November 2010 - October 2021 (Monthly)	Bitcoin prices are significantly influenced by energy consumption only in high-consumption regimes, highlighting uneven impacts.	Explores complex price-energy dynamics and identifies energy-related thresholds in price fluctuations.
Sapra & Shaikh [4]	Assess the impact of crypto indices and Ethereum prices on Bitcoin energy usage.	Autoregressive Distributed Lag (ARDL)	CBECI, Average Block size, Hash rate, No of transactions, Cix200, Etherium price	December 2018 - January 2023 (Monthly)	Rising Ethereum prices and crypto indices drive Bitcoin energy consumption and emissions. Suggests green investment in non-PoW mechanisms.	Advocates for environmentally sustainable crypto practices through alternative technologies.
Kevser [11]	Analyze the link between geopolitical risks, global policy uncertainty, and Bitcoin energy use.	Hatemi-J Causality Test	Global economic political uncertainty, geopolitical risk	May 2011 - February 2022 (Monthly)	Global uncertainties increase Bitcoin demand and energy consumption, positioning Bitcoin as a hedge but exacerbating environmental concerns.	Highlights Bitcoin's dual role as a financial hedge and an environmental burden in uncertain scenarios.
Tissaoui et al. [12]	Evaluate Bitcoin price effects on energy consumption.	QNARDL Model, XGBoost	Bitcoin price	1 July 2010 - 1 December 2022 (Daily)	Short-term price increases lead to energy surges, but long-term effects reduce consumption. XGBoost excels in prediction.	Demonstrates XGBoost's predictive accuracy in energy modeling.
Sapra et al. [13]	Explore causal relationships between Bitcoin energy use, prices, and market volatility.	Vector Auto Regression based Granger Causality, Diebold-Yilmaz Connectedness Analysis	CBECI, Crypto volatility index, bitcoin closing price	31 March 2019 - 30 March 2023 (Daily)	Bitcoin prices Granger-cause energy use; prices act as net contributors, while energy use is a recipient in market dynamics.	Provides insights into Bitcoin's market energy feedback loops.
Syzdykova [14]	Examine Bitcoin's energy consumption and mining inefficiencies.	Literature Review	-	-	Bitcoin's annual electricity usage reached 204.5 TWh by 2022. Advocates for renewable energy in mining.	Emphasizes PoW inefficiencies and recommends renewable energy adoption.
Kohli et al. [5]	Compare cryptocurrency energy use with centralized systems like Visa.	Comparative Analysis	-	-	Bitcoin's energy use is equivalent to that of some nations. Ethereum 2.0's shift to proof-of-stake is highlighted as a sustainability milestone.	Stresses the need for transitions to proof-of-stake and energy-efficient practices.
Zaghdoudi et al. [15]	Predict CBECI influenced by uncertainty indices using machine learning.	Machine Learning (XGBoost, Support Vector Regression, CatBoost)	CBECI, Economic policy uncertainty index, geopolitical risk index, energy uncertainty index	1 July 2010 - 1 December 2022 (Quarterly)	Economic and geopolitical risks are significant predictors of Bitcoin energy use. XGBoost outperforms other models.	Demonstrates the utility of advanced machine learning tools for energy prediction.

Table 1 (Continued). Literature on Bitcoin Energy Consumption.

Study	Objective	Methodology	Variables	Time Period (Frequency)	Key Findings	Contribution
Bublyk et al. [16]	Forecast spending on digital transformation technologies and services worldwide	Regression Analysis	Total cryptocurrency market cap, bitcoin energy consumption, etherium energy consumption	2017 – 2022 (Quarterly)	Bitcoin energy consumption projected to reach 142 TWh by 2026; recommends linking mining to renewable energy sources.	Proposes renewable energy integration in mining operations.
Adewuyi et al. [17]	Investigate Bitcoin's energy use and carbon footprint, focusing on bubbles and structural breaks.	Structural Break and Non-Linear Analytics	Maximum and optimal electricity consumption, maximum and optimal average emissions, global economic policy index, no of transactions, the level of credit risk, VIX index, google trend, geopolitical risk, volatility, volume, bitcoin energy consumption, bitcoin carbon footprint	7 July 2010 – 4 December 2021 (Daily)	Identifies market-driven energy bubbles and advocates for sustainable investments and policies to reduce the environmental impact of mining.	Calls for regulatory and investment measures to mitigate crypto mining's ecological footprint.

Research gaps identified in literature and our contributions are as follows:

- Many studies utilize restricted factors such as price, market indices, or geopolitical threats, yet fail to comprehensively incorporate blockchain data (e.g., hash rate, network difficulty, mempool size). We employ various blockchain parameters, including hash rate, network difficulty, mempool size, block size, and daily confirmed transactions, to enhance our analysis of energy consumption.

- Current research frequently employs long-term aggregate data (monthly, yearly), but short-term, granular analyses (daily data) are infrequently conducted. We concentrate on detailed, short-term blockchain data (61 days), providing new insights into daily energy consumption trends.

- Limited studies emphasis on developing supplementary measures for energy consumption related to particular blockchain activities. We introduce an extra indicator for energy consumption, facilitating improved analysis of blockchain energy dynamics. The estimated energy consumption indicator, which is based on daily total hash rate and daily electricity usage, reflects the energy requirements of systems in a more dynamic

and realistic way. This approach not only refines energy estimations but also provides valuable insights for policymakers and researchers studying sustainable blockchain operations.

- Our study is distinguished by its comparative investigation of various machine learning techniques to model and forecast Bitcoin's energy consumption. We assess the efficacy of multiple algorithms, including prevalent methods such as Random Forest, Gradient Boosting, Support Vector Regression, and Multi-layer Perceptron. We concentrate on the k-Nearest Neighbors Regression (k-NNR), which remains inadequately examined in the current literature.

This paper is organized as follows: after the introduction, the Material and Method section elucidates the data collection and preprocessing procedures, the feature selection process, the development of an additional energy consumption metric, and detailed analysis of k-NNR. The Results and Discussion section delineates the findings from the model comparisons, underscores the preeminence of k-NNR, and elucidates the ramifications of the results within the framework of blockchain energy dynamics. Conclusion encapsulates the principal contributions of the study, delineates its limits, and proposes avenues for further research.

2   MATERIAL AND METHOD

This section outlines the processes of data collection and preprocessing, the feature selection stage, the calculation of an additional metric energy consumption, data normalization, k-NNR, and model evaluation. The stages applied in this section is summarized in Figure 1.

The dataset used in this study was obtained from publicly available blockchain data [18], including metrics such as total hash rate, network difficulty, daily confirmed transactions, mempool size, average block size, and daily Bitcoin output. The dataset was cleaned by removing any unnecessary spaces in column names and filtering out rows with missing data. The hash rate, an indicator of the processing power allocated to protecting a blockchain via proof-of-work consensus, is essential for thwarting various attacks [19]. In Bitcoin mining, difficulty quantifies the challenge miners face in locating a valid block, which is standardized across the whole network and is recalibrated every 2016 blocks [20]. Daily confirmed transactions indicates the daily volume of processed confirmed transactions. The mempool effectively illustrates the increase in transactions pending confirmation, serving as a leading

signal of prospective cash flows that may influence bitcoin's trading volumes and market prices [21]. Block size denotes the quantity of transactions contained within the block [22]. Namely, the Bitcoin block size denotes the maximum data capacity of an individual block within the Bitcoin blockchain. Each block encompasses transaction data, and its size dictates the number of transactions that can be incorporated within a single block. Daily Bitcoin output denotes the total quantity of Bitcoin processed each day. Data for the specified entries was gathered from blockchain.com [18] over a period of 61 days, from October 4 to December 5. Bitcoin mining and energy consumption are influenced by variables such as market volatility, mining difficulty, and transaction volume. A 61-day dataset provides a sufficient time frame to analyze changes in these variables. In the literature, datasets spanning 30 to 90 days are frequently used for short- and medium-term forecasts [23], [24]. A 61-day period strikes a suitable balance for effective model training and testing in short-term predictions. These entries were recognized as essential for comprehending energy consumption within the blockchain network. Table 2 presents the sample data from our investigation, encompassing a duration of 14 days.
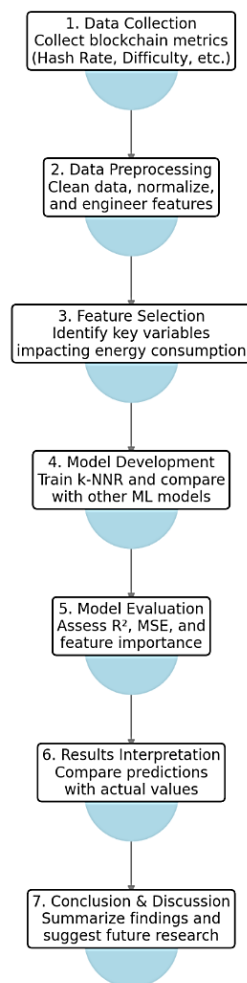

Figure 1. Methodological stages of the study.

Table 2. Sample Data from Bitcoin Mining Dataset.

Date	Total hash rate (TH/s)	Network difficulty	Daily confirmed transactions	Mempool size	Average block size (MB)	Daily Bitcoin output
5 November 2024	702351988.692	101646843652784	501641	111112.224	1.740	1268937.223
6 November 2024	773092476.762	101646843652784	553047	109742.375	1.670	902154.559
7 November 2024	788251152.777	101646843652784	497146	117335.380	1.700	953404.938
8 November 2024	717510664.707	101646843652784	577146	133364.323	1.630	551065.648
9 November 2024	702351988.692	101646843652784	558278	137806.078	1.550	808961.400
10 November 2024	747828016.737	101646843652784	462458	141248.557	1.640	1204667.966
11 November 2024	687193312.677	101646843652784	503677	143844.458	1.630	1383872.631
12 November 2024	737722232.727	101646843652784	570979	169088.875	1.610	1222908.306
13 November 2024	697299096.687	101646843652784	503566	186026.771	1.560	1058121.422
14 November 2024	641717284.633	101646843652784	562223	186044.266	1.570	928123.081
15 November 2024	757933800.747	101646843652784	602655	168264.260	1.610	524803.198
16 November 2024	793304044.782	101646843652784	598496	157410.719	1.670	444772.304
17 November 2024	757933800.747	101646843652784	673308	179352.193	1.710	888920.856
18 November 2024	789177471.480	101766294632436	810805	190610.734	1.600	943414.474

The supplied data delineates daily indicators pertaining to the Bitcoin network from November 5 to November 18, 2024. In previous studies (see Table 1), the major indicators - the total hash rate, network difficulty, daily confirmed transactions, mempool size, and daily Bitcoin output – have been used extensively to evaluate the energy consumption of the Bitcoin network. This dataset offers an overview of the Bitcoin network's performance and activity, emphasizing the relationship among hash rate, difficulty, transaction volume, and mining rewards over time. In this study, we add another indicator, namely energy consumption, which measures the energy needs of systems by looking at the daily total hash rate and daily power usage. This gives a more accurate and updated picture of energy use.

2.1 Energy Consumption Analysis of Bitcoin Mining

The energy usage of Bitcoin mining is closely associated with the processing power necessary for its PoW method. The energy requirement can be assessed by integrating the

network's hash rate with the energy efficiency of mining equipment [6]. There are considerable differences in the calculations of bitcoin's energy consumption because to numerous uncertainties in the process, including the type of device utilized in mining and the duration of its operation [6].

We utilized data from the Cambridge Bitcoin Electricity Consumption Index (CBECI) [25]. CBECI offers current estimates of Bitcoin's daily energy requirements and an annualized electricity consumption prediction. Due to the decentralized structure of the network, the exact power demand cannot be ascertained; therefore, numerous assumptions were made, including hypothetical lower-bound and upper-bound estimates. These two borders represent an informed estimate, providing a more precise representation of the real power demand. The lower-bound estimate represents the potential minimum overall power requirement predicated on the optimal scenario that all miners consistently utilize the most energy-efficient equipment. The upper-bound estimate represents the theoretical maximum total power requirement predicated on the worst-case scenario wherein all miners consistently utilize the least energy-efficient hardware, provided that operating the equipment stays economically viable concerning electricity expenses. The estimate is predicated on the more plausible premise that miners utilize a blend of profitable hardware [25]. The data obtained from the CBECI on December 27, 2024, is as follows: Theoretical Lower Bound: an annual consumption of 92.610 TWh, Estimated Consumption: with an annual consumption of 180.970 TWh, Theoretical Upper Bound: with an annual consumption of 417.520 TWh. TWh refers terawatt-hour. The formula for daily electricity consumption is presented in Equation 1.

$$Daily\ electricity\ consumption\ (TWh) = \frac{Annualised\ consumption\ (TWh)}{365} \qquad (1)$$

This study assessed daily electricity usage by utilizing estimated electrical consumption data in accordance with Equation 1.

$$Daily\ electricity\ consumption\ (TWh) = \frac{180.970}{365} = 0.496$$

The rationale for utilizing estimated energy consumption data is its enhanced realism. Daily energy consumption is determined by multiplying the daily total hash rate by the daily electricity usage, as specified in Equation 2.

$$Energy\ consumption =$$
$$Total\ hash\ rate\ (TWh) * daily\ electricity\ consumption (TWh) \qquad (2)$$

The determined energy consumption factor will serve as the dependent variable in the proposed study.

The purpose of this study's proposed extra indicator is to improve the precision of estimates regarding the energy usage of Bitcoin mining. This metric incorporates essential blockchain metrics that impact energy consumption, such as hash rate, block size, and transaction volume. This indication offers a more dynamic approach to energy estimation by reflecting fluctuations in network conditions, as opposed to traditional methods that focus exclusively on mining difficulty or electricity costs.

2.2   k- Nearest Neighbors Regression (k-NNR)

k-NNR is one of the most ancient and straightforward regression techniques [26]. k-NNR is a form of supervised learning technique. Supervised learning deduces a function (learner) from a dataset, which comprises a collection of training instances referred to as samples. Each sample consists of a pair including an input vector (instance) and the corresponding output value. Upon completing the training set, the learner aims to accurately ascertain the output for novel situations. [27]. k-NNR generates estimates by analyzing the results of the k nearest neighbors to the specified position. Consequently, to facilitate predictions using k-NNR, a metric for assessing the distance between the query point and instances from the sample cases is required [28]. The method calculates the distance between a query point and all data points in the training set to make a prediction. The Euclidean distance is one of the most prevalent methods for measuring this distance. Therefore, Euclidean distance is utilized in this study. The algorithm determines the k nearest neighbors to the query point utilizing the selected distance measure. In regression, the predictions are the mean of the outcomes of the k nearest neighbors [28]. Equation 3 is the formula for generating predictions.

$$y = \frac{1}{k} \sum_{i=1}^{k} y_i \tag{3}$$

where y is the predicted value, k is the number of neighbors, y_i is the energy consumption value at index i.

First, all features are normalized to a range of 0 to 1 using Min-Max scaling in order to guarantee comparability across variables of different scales. This action enhanced the results' interpretability and lessened bias in the regression models. Network difficulty, daily confirmed transactions, mempool size, average block size, and daily Bitcoin output are utilized as input

variables to predict the energy consumption. Using equations 1 and 2, the dependent variable, energy consumption, is calculated by multiplying the daily electricity usage by the overall hash rate. To assess model performance, the dataset is split into subsets for testing (20%) and training (80%). k-NNR is utilized as the modeling technique because of its interpretability and efficacy in analyzing linear relationships. Through trial and error, we determine that the number of neighbors, k, is 8. Figure 2 demonstrates the impact of varying the number of neighbors (k) on the test R² score k-NNR across different training set sizes (85, 80, and 75).
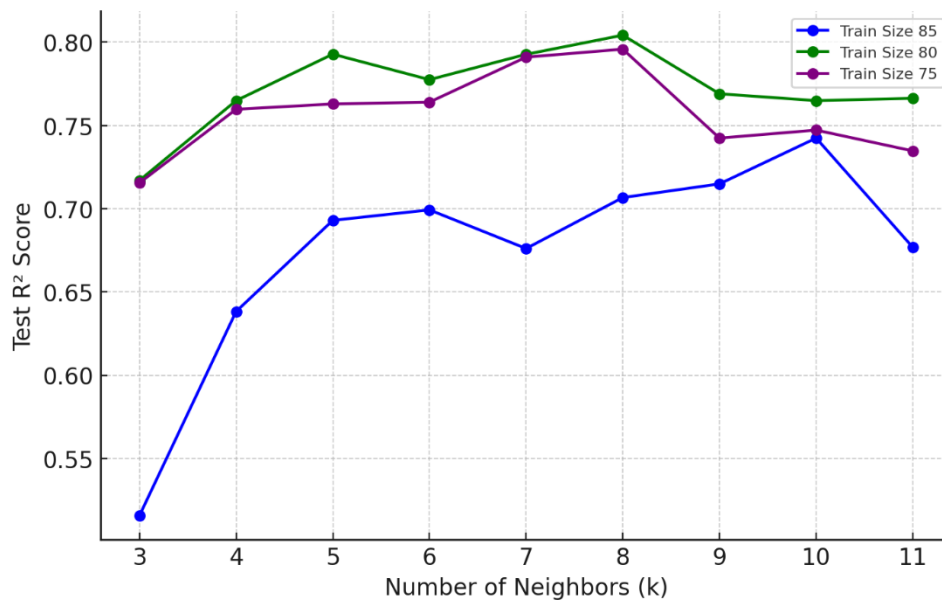
Figure 2. Test R2 score vs. number of neighbors(k) for k-NNR.

This analysis highlights that the optimal number of neighbors for k-NNR lies around k = 7 to 9, depending on the training set size. Based on this trend, we selected k=8 as the optimal value, as it provides a strong balance between generalization and performance across different training sizes.

To ensure the reproducibility of our study, we use a fixed random seed (42) for train-test splits and model training. Features are normalized using Min-Max scaling, and energy cost per transaction is calculated. Python programming software is utilized for analysis. Experiments are performed on a system with an 11th Gen Intel Core i7-11370H processor (3.30GHz) and 16GB RAM.

3   RESULTS AND DISCUSSION

This section delineates the outcomes of the k-NNR model employed to forecast energy consumption in Bitcoin mining. The k-NNR model produced a R^2 (coefficient of determination) value of 0.804, signifying that the model accounts for 80% of the variance in energy consumption. This elevated R^2 indicates the efficacy of the k-NNR model in elucidating the correlation between the chosen features network difficulty, daily confirmed transactions, mempool size, average block size, and daily Bitcoin output and the goal variable, energy consumption. The Mean Squared Error (MSE), which quantifies the average squared deviation between anticipated and actual values, is determined as 0.004. The little error underscores the model's accuracy in predictions and its capacity to generalize effectively to novel inputs. The conjunction of a high R^2 and low MSE substantiates the dependability and precision of the k-NNR model in evaluating energy consumption within blockchain networks. These results confirm the significance of preprocessing operations, including normalization and feature selection, which assured the model efficiently utilized the input data.

The results are corroborated by feature importance analysis and comparisons of anticipated and actual performance. These visuals and data elucidate the model's efficacy and the significance of each feature. Figure 3 depicts the simulated feature importance for the k-NNR model, highlighting the relative contributions of input variables to energy consumption prediction.
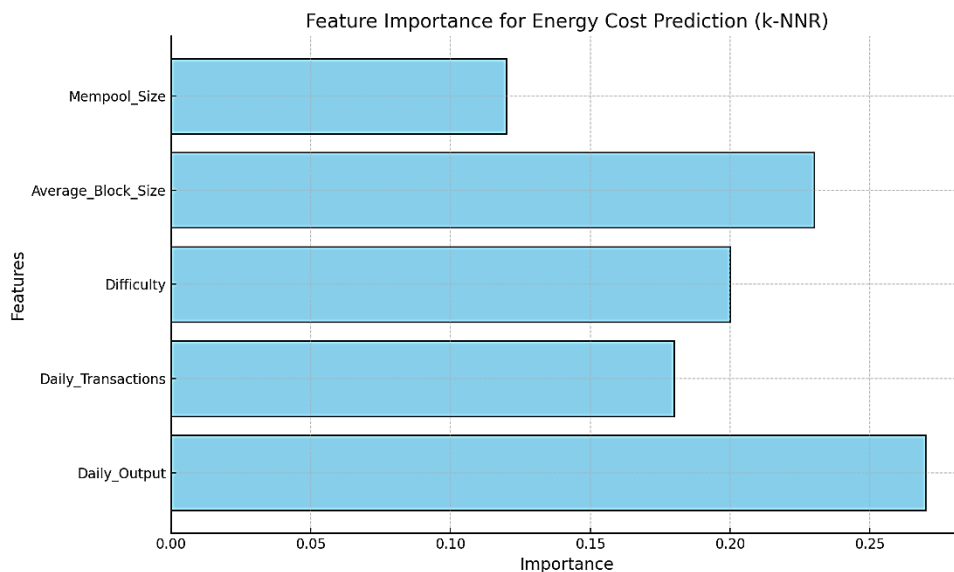

Figure 3. Feature Importance for Energy Consumption Prediction.

Daily Bitcoin output proves to be the most significant variable, underscoring its essential function in influencing energy usage. Average block size and Network difficulty demonstrates substantial contributions, highlighting their influence on mining operations and energy consumption. Daily confirmed transactions and mempool size exhibites moderate significance, indicating their relevance to network activity while demonstrating a lesser direct impact on energy use. Figure 4 displays the scatter plot comparing estimated energy consumption with actual values for the test dataset. The red dashed line denotes the optimal fit where forecasts align precisely with the actual values.
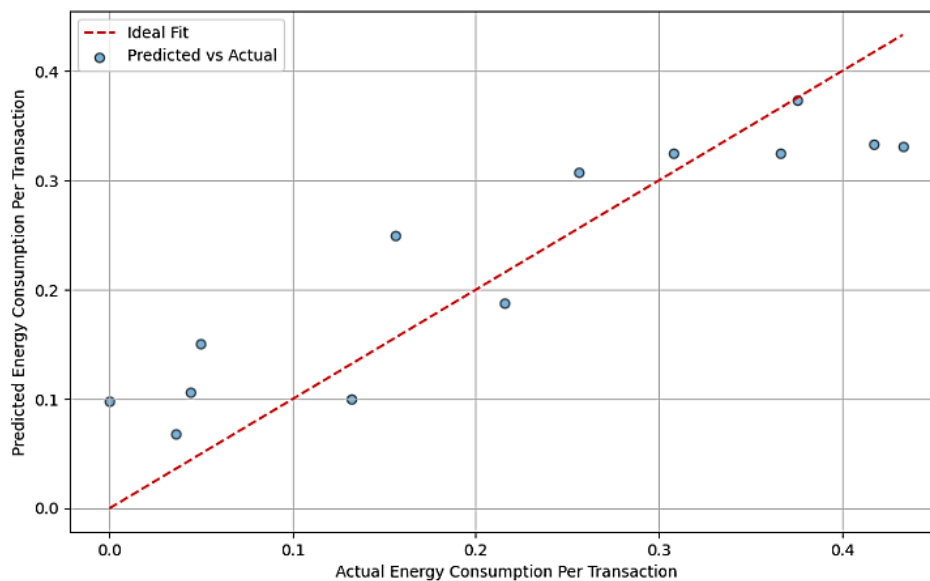

Figure 4. Predicted vs. Actual Energy Consumption (TWh) Per Transaction.

The majority of points are concentrated near the optimal fit line, signifying high prediction accuracy of the model. The R^2 value of 0.804 indicates the model's robust predictive performance, accounting for 80% of the variance in energy consumption. This performance confirms the efficacy of k-NNR regression in examining blockchain data.

3.1　Comparison of various machine learning methods

This study evaluated and contrasted various machine learning algorithms according to their efficacy in regression tasks. Figure 5-8 present a comparative analysis of multiple machine learning models based on their training R², test R², training MSE, and test MSE across different training sizes.
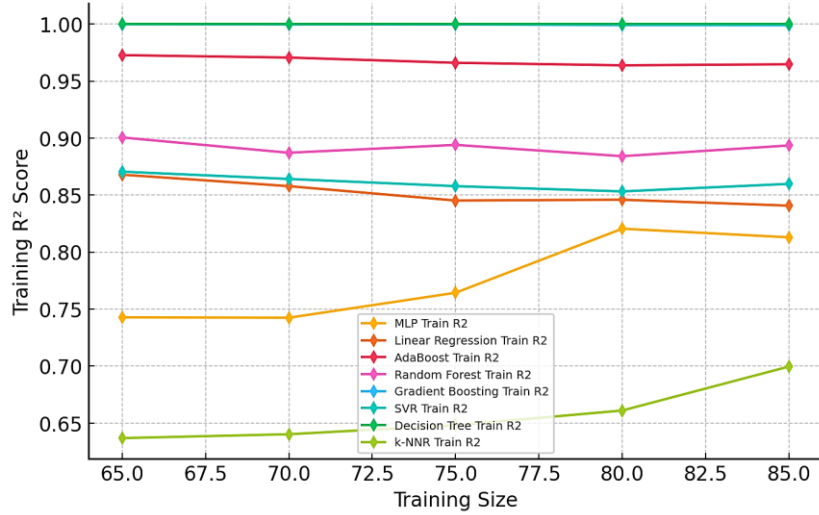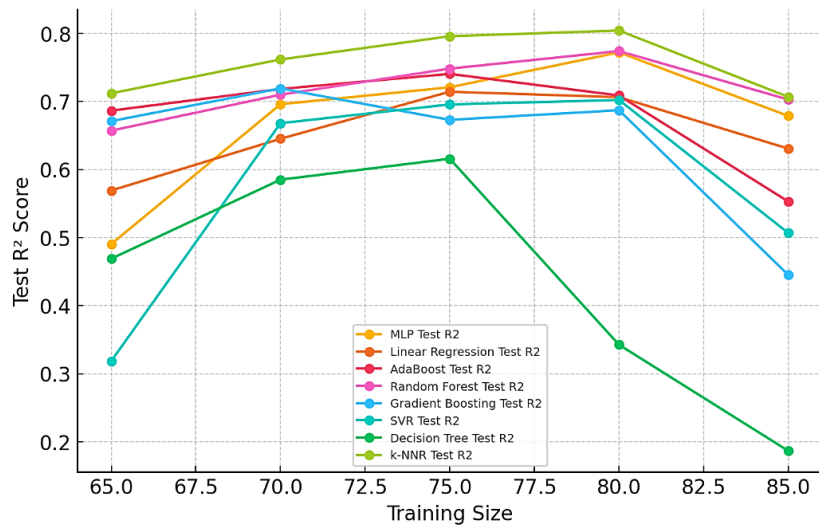
Figure 5. Training R² score vs. training size.
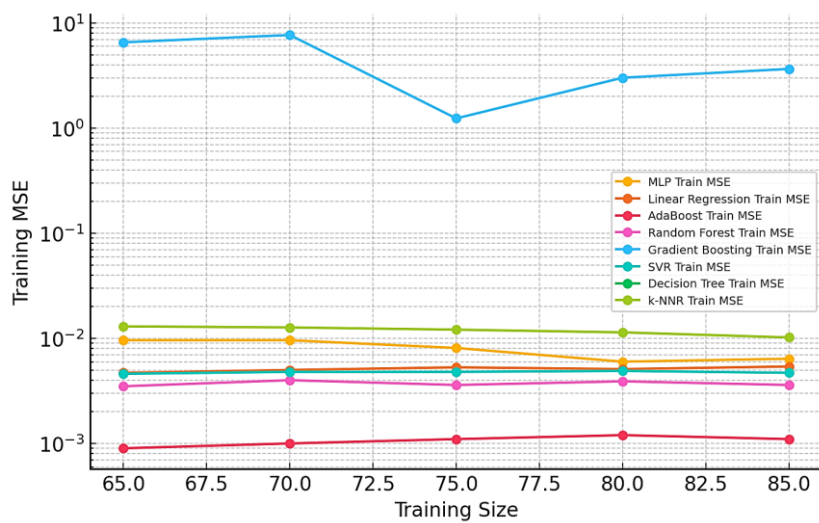

Figure 6. Test R² vs. training size.

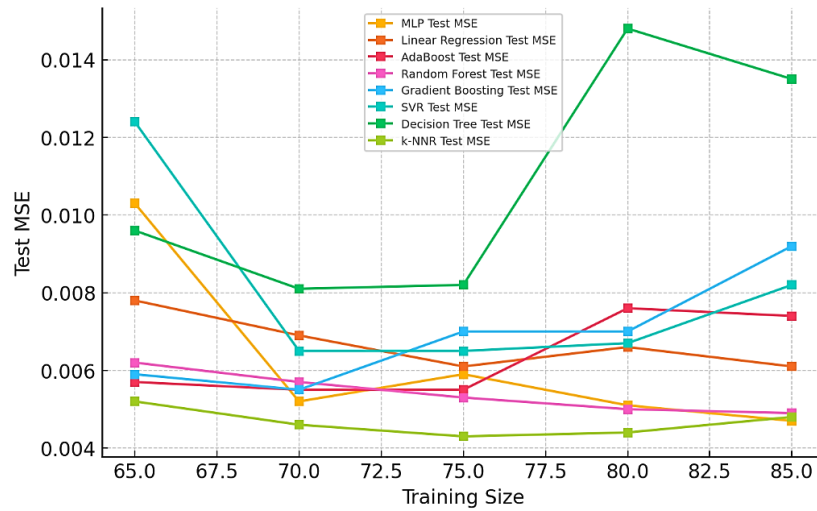*Figure 7. Training MSE vs. training size.*

Figure 8. Test MSE vs. training size.

The Decision Tree Regression model attains a R² value approaching 1, indicating a significant likelihood of overfitting. This indicates that the model retains training data instead of generalizing patterns. Gradient Boosting Regression shows a large gap between training and test MSE. Gradient Boosting appears to exhibit somewhat elevated test errors across all training sizes, indicating a potential failure to adequately capture the complexity of the data, resulting in under fitting. It appears that Support Vector Regression is unable to adequately capture data variance. Regardless of training amount, k-NNR consistently maintains one of the lowest test MSE values. According to the stability of its test MSE, k-NNR is not severely over fitted or under fitted. k-NNR has a more moderate training R^2 value than Decision Tree, which has an R^2 near 1, indicating overfitting. This indicates that k-NNR is not memorizing the training data, implying it is probably generalizing effectively to novel data. k-NNR constantly ranks among the foremost models regarding test R² performance.

The outcomes are presented in Table 3 below, whereby the algorithms are evaluated based on two principal metrics: R^2 and MSE. Elevated R^2 values represent enhanced predictive accuracy, and diminished MSE values indicate reduced prediction mistakes.

Table 3. Comparison of various machine learning algorithms.

Methods	Training Size	Test Size	Training R^2	Test R^2	Training MSE	Test MSE
Multi-layer Perceptron Regression	85	15	0.8129	0.6787	0.0064	0.0047
	80	20	0.8205	0.7721	0.0060	0.0051
	75	25	0.7643	0.7208	0.0081	0.0059
	70	30	0.7424	0.6959	0.0096	0.0052
	65	35	0.7427	0.4904	0.0096	0.0103
Linear Regression	85	15	0.8407	0.6307	0.0054	0.0061
	80	20	0.8459	0.7062	0.0051	0.0066
	75	25	0.8452	0.7143	0.0053	0.0061
	70	30	0.8578	0.6451	0.0050	0.0069
	65	35	0.8679	0.5691	0.0047	0.0078
AdaBoost Regression	85	15	0.9647	0.5529	0.0011	0.0074
	80	20	0.9638	0.7087	0.0012	0.0076
	75	25	0.9660	0.7405	0.0011	0.0055
	70	30	0.9706	0.7183	0.0010	0.0055
	65	35	0.9727	0.6865	0.0009	0.0057
Random Forest Regression	85	15	0.8935	0.7028	0.0036	0.0049
	80	20	0.8841	0.7740	0.0039	0.0050
	75	25	0.8940	0.7482	0.0036	0.0053
	70	30	0.8871	0.7099	0.0040	0.0057
	65	35	0.9005	0.6571	0.0035	0.0062
Gradient Boosting Regression	85	15	0.9989	0.4450	3.6616	0.0092
	80	20	0.9991	0.6871	3.0207	0.0070
	75	25	0.9996	0.6729	1.2383	0.0070
	70	30	0.9997	0.7191	7.7044	0.0055
	65	35	0.9998	0.6711	6.5582	0.0059
Support Vector Regression	85	15	0.8598	0.5067	0.0047	0.0082
	80	20	0.8532	0.7021	0.0049	0.0067
	75	25	0.8578	0.6956	0.0048	0.0065
	70	30	0.8641	0.6680	0.0048	0.0065
	65	35	0.8705	0.3185	0.0046	0.0124
Decision Tree Regression	85	15	1.0	0.1865	0	0.0135
	80	20	1.0	0.3424	0	0.0148
	75	25	1.0	0.6158	0	0.0082
	70	30	1.0	0.5850	0	0.0081
	65	35	1.0	0.4689	0	0.0096
k-NNR	85	15	0.6996	0.7067	0.0102	0.0048
	80	20	0.6610	**0.8042**	0.0114	0.0044
	75	25	0.6481	0.7958	0.0121	0.0043
	70	30	0.6402	0.7617	0.0127	0.0046
	65	35	0.6368	0.7119	0.013	0.0052

Among the assessed approaches, the k-NNR proved to be the most efficient model, attaining the greatest R^2 value of 0.804 and the lowest MSE of 0.004. The results reveal that the k-NNR exhibited enhanced predicted accuracy and reduced error relative to other models, establishing it as the ideal selection for this investigation.

The performance of ensemble models, including Random Forest Regression and AdaBoost Regression, is commendable; yet, their findings are somewhat inferior to those of the k-NNR. Linear Regression, Support Vector Regression, and Multi-layer Perceptron Regression exhibit satisfactory performance but do not attain equivalent accuracy levels. The Gradient Boosting Regression and Decision Tree Regression exhibit inferior performance, with the former demonstrating a comparatively lower R^2 and a larger MSE, while the latter is the least effective of all models. The restricted application of the k-NNR technique in forecasting Bitcoin mining energy usage can be ascribed to various factors. The majority of research in the domain supports tree-based methodologies (Random Forest, Gradient Boosting) and Support Vector Regression because of their capacity to manage intricate nonlinear interactions. This study's findings indicate that k-NNR surpasses previous models, exhibiting a high R^2 of 0.804 and a low MSE of 0.004, thereby establishing it as a formidable alternative. Its efficacy is rooted in its capacity to identify local patterns in energy use, adeptly represent short-term variances, and sustain a robust equilibrium between training and testing performance, hence avoiding the overfitting observed in models such as Decision Tree Regression. Due to its simplicity, interpretability, and robust generalization capabilities, k-NNR offers a largely overlooked but highly effective method for blockchain energy modeling. In conclusion, the comparison analysis identifies the k-NNR as the most effective method for the specified regression problem.

This study's findings highlight numerous innovative additions to Bitcoin energy consumption modeling. This study presents a novel energy consumption indicator that offers a more accurate and dynamic depiction of blockchain energy usage, in contrast to prior research that predominantly depends on economic indicators or long-term aggregated data. The suggested indicator integrates critical blockchain variables—namely hash rate, network difficulty, mempool size, block size, and daily confirmed transactions—to provide a more thorough comprehension of energy consumption trends in Bitcoin mining. This innovative method improves the precision of energy assessments and offers a significant metric for researchers and policymakers seeking to boost energy efficiency in blockchain systems.

Our study presents key innovations and differences relative to current research on k-nearest neighbors (KNN) in bitcoin prediction applications. The following is existing research on KNN in blockchain:

Table 4. Existing research on KNN in bitcoin applications.

Authors	Application	Methods Used	Approach	Key Findings
Chevallier et al. [29]	Bitcoin Price Forecasting	KNN, ANN, SVM, Random Forest, AdaBoost, Ridge Regression	Segmentation of Bitcoin with Alternative Assets	Random Forest and AdaBoost Performed Best
Gu et al. [30]	Investment Model	KNN, ANN, Grey Prediction, LSTM	Comparison of Various Prediction Models	LSTM was Found Superior
Cortez et al. [31]	Crypto vs. Fiat Market Liquidity	KNN, ARMA, GARCH	Bid-Ask Spread Prediction	KNN Performed Better for Short-Term Predictions
Da Silva et al. [32]	Bitcoin Price Forecasting	KNN, SVR, ANN, GLM, Cubist	VMD-STACK Framework for Multi-Step Forecasting	Ensemble Learning Improved Prediction
Mayo & Elgazzar [33]	Cryptocurrency Price Prediction	KNN, ANN, SVM, Naïve Bayes, Random Forest	Analyzing Supply-Side Factors for Prediction	ANN and Random Forest Performed Best
Freeda et al. [34]	Bitcoin Price Forecasting	KNN, Random Forest, Gaussian Naïve Bayes, SVM, RNN	Comparison with Deep Learning Models	RNN Outperformed KNN
Ahmed et al. [35]	Bitcoin Price Prediction	KNN, XGBoost, Gradient Boosting, Random Forest, Linear Regression, SVM	Performance Evaluation Across Models	Gradient Boosting Achieved Highest Accuracy
Benjamin et al. [36]	Crypto Investment Strategy	KNN, Random Forest, Linear Regression	Financial Market Prediction	Random Forest Was More Effective
Jenifel et al. [37]	Bitcoin Price Forecasting	KNN, Linear Regression, Ridge Regression, Decision Tree, Random Forest, SVM, Neural Networks	Performance Analysis of Various ML Models	KNN Was Tested but Not Best Performing
Kawli et al. [38]	Cryptocurrency Price Prediction	KNN, LSTM, Bayesian Regression, SVM, Random Forest	Multi-Asset Price Forecasting	Random Forest and LSTM Achieved Best Results
Akyildirim et al. [39]	Bitcoin Futures Price Prediction	KNN, Logistic Regression, Naïve Bayes, Random Forest, SVM, Extreme Gradient Boosting	High-frequency Intraday Data Analysis	SVM Outperformed KNN in Prediction Accuracy
Li et al. [40]	Stock and Bitcoin Price Forecasting	Mask-LSTM, Mask-BiLSTM, Mask-GRU, KNN	Feature Fusion for Time-Series Prediction	Hybrid Model Outperformed Individual Models

The proposed study differs significantly from existing research by focusing on Bitcoin mining energy consumption rather than price prediction, fraud detection, or transaction classification. Unlike previous studies that rely on market indicators or macroeconomic factors, we incorporate direct blockchain metrics such as hash rate, network difficulty, mempool size, and daily Bitcoin output to develop a more precise energy consumption model. Additionally, while k-NNR has been underutilized in blockchain energy research, our study demonstrates its superior performance over Random Forest, Gradient Boosting, and Support Vector Regression, achieving the highest predictive accuracy ($R^2 = 0.804$, MSE = 0.004).

4 CONCLUSION AND SUGGESTIONS

This research employed the k-NNR model to forecast energy usage in Bitcoin mining, using essential parameters such network difficulty, daily confirmed transactions, mempool size, average block size, and daily Bitcoin output. The findings indicated that the k-NNR model attained robust predictive efficacy, evidenced by a R^2 value of 0.80 and a MSE of 0.004. These results underscore the model's reliability and precision in elucidating the intricate links between input features and energy consumption. The results emphasize the importance of daily Bitcoin production and average block size as key determinants of energy usage, highlighting the relevance of these parameters in mining activities. The study offers significant insights into Bitcoin's energy dynamics, although certain limits should be recognized. The investigation was confined to a 61-day dataset, which, although providing precise short-term insights, may not reflect longer-term trends or anomalies in blockchain activity. Although the 61 days dataset provides sufficient insights for short-term trend analysis, longer datasets may be required to capture seasonal and long-term fluctuations in Bitcoin mining energy consumption. The analysis presupposes that mining equipment and energy efficiency are constant, perhaps failing to capture real-world fluctuations. Further study can address these shortcomings by augmenting the dataset with longitudinal data, integrating fluctuations in mining hardware efficiency, and evaluating supplementary machine learning techniques. This study's findings establish a robust foundation for formulating energy-efficient solutions in bitcoin mining and directing sustainable blockchain operations.

Future research could enhance forecast accuracy by merging real-time blockchain indicators with external economic and environmental variables. Subsequent research could investigate the effects of alternate consensus processes, such as proof-of-stake, on energy efficiency. Enhancing the comparison study with deep learning models could provide more profound insights into energy use trends.

Acknowledgements

Conflict of Interest Statement

There is no conflict of interest between the authors.

Statement of Research and Publication Ethics

The study is complied with research and publication ethics.

Artificial Intelligence (AI) Contribution Statement

This manuscript was entirely written, edited, analyzed, and prepared without the assistance of any artificial intelligence (AI) tools. All content, including text, data analysis, and figures, was solely generated by the authors.

Contributions of the Authors

Nazmiye Eligüzel: Performed the computations, developed the model, wrote the manuscript.

Sena Aydoğan: Collected the data, reviewed the literature, revised the manuscript.

REFERENCES

[1]   S. Nakamato, "Bitcoin: A peer-to-peer electronic cash system," *Decentralized Bus. Rev.*, 2008.

[2]   H. Alshahrani *et al.*, "Sustainability in Blockchain: A Systematic Literature Review on Scalability and Power Consumption Issues," *Energies*, vol. 16, no. 3, 2023, doi: 10.3390/en16031510.

[3]   N. Eligüzel, "An analysis of the integration of sustainability concepts into blockchain technology," *Int. J. Appl. Methods Electron. Comput.*, vol. 11, no. 3, pp. 158–164, 2023, doi: 10.58190/ijamec.2023.43.

[4]   N. Sapra and I. Shaikh, "Impact of Bitcoin mining and crypto market determinants on Bitcoin-based energy consumption," *Manag. Financ.*, vol. 49, no. 11, pp. 1828–1846, 2023, doi: 10.1108/MF-03-2023-0179.

[5]   V. Kohli, S. Chakravarty, V. Chamola, K. S. Sangwan, and S. Zeadally, "An analysis of energy consumption and carbon footprints of cryptocurrencies and possible solutions," *Digit. Commun. Networks*, vol. 9, no. 1, pp. 79–89, 2023, doi: 10.1016/j.dcan.2022.06.017.

[6]   S. Küfeoğlu and M. Özkuran, "Energy Consumption oF Bitcoin Mining," in *Cambridge Working Papers in Economics: 1948*, .

[7]   M. Maiti, "Dynamics of bitcoin prices and energy consumption," *Chaos, Solitons Fractals X*, vol. 9, p. 100086, 2022, doi: 10.1016/j.csfx.2022.100086.

[8]   A. de Vries, "Bitcoin's energy consumption is underestimated: A market dynamics approach," *Energy Res. Soc. Sci.*, vol. 70, no. August, p. 101721, 2020, doi: 10.1016/j.erss.2020.101721.

[9]   D. Das and A. Dutta, "Bitcoin's energy consumption: Is it the Achilles heel to miner's revenue?," *Econ. Lett.*, vol. 186, p. 108530, 2020, doi: 10.1016/j.econlet.2019.108530.

[10]   J. Li, N. Li, J. Peng, H. Cui, and Z. Wu, "Energy consumption of cryptocurrency mining: A study of electricity consumption in mining cryptocurrencies," *Energy*, vol. 168, pp. 160–168, 2019, doi: 10.1016/j.energy.2018.11.046.

[11]   M. Kevser, "Bitcoin as an Alternative Financial Asset: Relations Between Geopolitical Risk, Global Economic Political Uncertainty, and Energy Consumption," *PAMUKKALE J. EURASIAN Socioecon. Stud.*, vol. 9, no. 2, pp. 117–131, 2022.

[12]   K. Tissaoui, T. Zaghdoudi, S. Boubaker, B. Hkiri, and M. Talbi, "Testing the Nonlinear Long- and Short-Run Distributional Asymmetries Effects of Bitcoin Prices on Bitcoin Energy Consumption: New Insights

through the QNARDL Model and XGBoost Machine-Learning Tool," *Energies*, vol. 17, no. 2810, 2024.

[13] N. Sapra, I. Shaikh, D. Roubaud, M. Asadi, and O. Grebinevych, "Uncovering Bitcoin's electricity consumption relationships with volatility and price: Environmental Repercussions," *J. Environ. Manage.*, vol. 356, no. January, p. 120528, 2024, doi: 10.1016/j.jenvman.2024.120528.

[14] A. Syzdykova, "Bitcoin Mining and Energy Consumption of Bitcoin," *J. Econ. Soc. Res.*, vol. 10, no. 19, pp. 1–15, 2023.

[15] T. Zaghdoudi, K. Tissaoui, M. Maâloul, Y. Bahou, and N. Kammoun, "Can Economic, Geopolitical and Energy Uncertainty Indices Predict Bitcoin Energy Consumption? New Evidence from a Machine Learning Approach," *Energies*, vol. 12, no. 3245, 2024.

[16] Y. Bublyk, O. Borzenko, and A. Hlazova, "Cryptocurrency energy consumption: Analysis, global trends and interaction," *Environ. Econ.*, vol. 14, no. 2, pp. 49–59, 2023, doi: 10.21511/ee.14(2).2023.04.

[17] A. O. Adewuyi, B. A. Wahab, A. K. Tiwari, and H. X. Do, "Do bitcoin electricity consumption and carbon footprint exhibit random walk and bubbles? Analysis with policy implications," *J. Environ. Manage.*, vol. 367, no. August, p. 121958, 2024, doi: 10.1016/j.jenvman.2024.121958.

[18] "Blockchain.com," 2024. https://www.blockchain.com/explorer/charts (accessed Dec. 14, 2024).

[19] D. Kim, D. Ryu, and R. I. Webb, "Does a higher hashrate strengthen Bitcoin network security?," *Financ. Innov.*, vol. 10, no. 1, 2024, doi: 10.1186/s40854-023-00599-8.

[20] X. Zhang, R. Qin, Y. Yuan, and F. Y. Wang, "An Analysis of Blockchain-based Bitcoin Mining Difficulty: Techniques and Principles," *Proc. 2018 Chinese Autom. Congr. CAC 2018*, pp. 1184–1189, 2018, doi: 10.1109/CAC.2018.8623140.

[21] A. Mikhaylov, H. Dinçer, S. Yüksel, G. Pinter, and Z. A. Shaikh, "Bitcoin mempool growth and trading volumes: Integrated approach based on QROF Multi-SWARA and aggregation operators," *J. Innov. Knowl.*, vol. 8, no. 3, 2023, doi: 10.1016/j.jik.2023.100378.

[22] B. Aygün and H. Arslan, "Block size optimization for PoW consensus algorithm based blockchain applications by using whale optimization algorithm," *Turkish J. Electr. Eng. Comput. Sci.*, vol. 30, pp. 406–419, 2022, doi: 10.3906/elk-2105-217.

[23] M. Karimuzzaman, S. Afroz, M. M. Hossain, and A. Rahman, "Modelling COVID-19 cases and deaths with climate variables using statistical and data science methods," *Soft Comput.*, vol. 28, no. 21, pp. 12561–12574, 2024, doi: 10.1007/s00500-024-10352-7.

[24] A. Vij, K. Saxena, and A. Rana, "Prediction in Stock Price Using of Python and Machine Learning," *2021 9th Int. Conf. Reliab. Infocom Technol. Optim. (Trends Futur. Dir. ICRITO 2021*, pp. 1–4, 2021, doi: 10.1109/ICRITO51393.2021.9596513.

[25] "Cambridge Bitcoin Electricity Consumption Index," *University of Cambridge*, 2024. https://ccaf.io/cbnsi/cbeci (accessed Dec. 27, 2024).

[26] B. Nguyen, C. Morell, and B. De Baets, "Large-scale distance metric learning for k-nearest neighbors regression," *Neurocomputing*, vol. 214, pp. 805–814, 2016, doi: 10.1016/j.neucom.2016.07.005.

[27] Y. Song, J. Liang, J. Lu, and X. Zhao, "An efficient instance selection algorithm for k nearest neighbor regression," *Neurocomputing*, vol. 251, pp. 26–34, 2017, doi: 10.1016/j.neucom.2017.04.018.

[28] J. Tanuwijaya and S. Hansun, "LQ45 stock index prediction using k-nearest neighbors regression," *Int. J. Recent Technol. Eng.*, vol. 8, no. 3, pp. 2388–2391, 2019, doi: 10.35940/ijrte.C4663.098319.

[29] J. Chevallier, D. Guégan, and S. Goutte, "Is It Possible to Forecast the Price of Bitcoin?," *Forecasting*, vol. 3, no. 2, pp. 377–420, 2021, doi: 10.3390/forecast3020024.

[30] A. Gu *et al.*, "Empirical Research for Investment Model Based on VMD-LSTM," *Math. Probl. Eng.*, vol. 2022, 2022, doi: 10.1155/2022/4185974.

[31] K. Cortez, M. D. P. Rodríguez-García, and S. Mongrut, "Exchange market liquidity prediction with the k-nearest neighbor approach: Crypto vs. fiat currencies," *Mathematics*, vol. 9, no. 1, pp. 1–15, 2021, doi: 10.3390/math9010056.

[32] R. G. Da Silva, M. H. Dal Molin Ribeiro, N. Fraccanabbia, V. C. Mariani, and L. Dos Santos Coelho, "Multi-step ahead Bitcoin Price Forecasting Based on VMD and Ensemble Learning Methods," *Proc. Int. Jt. Conf. Neural Networks*, 2020, doi: 10.1109/IJCNN48605.2020.9207152.

[33]   D. Mayo and H. Elgazzar, "Predicting Cryptocurrency Price Change Direction from Supply-Side Factors via Machine Learning Methods," *2022 IEEE World AI IoT Congr. AIIoT 2022*, pp. 330–336, 2022, doi: 10.1109/AIIoT54504.2022.9817249.

[34]   S. E. Freeda, T. C. E. Selvan, and I. G. Hemanandhini, "Prediction of Bitcoin Price using Deep Learning Model," *Proc. 5th Int. Conf. Electron. Commun. Aerosp. Technol. ICECA 2021*, no. Iceca, pp. 1702–1706, 2021, doi: 10.1109/ICECA52323.2021.9676048.

[35]   F. U. Ahmed, M. Ahmed, F. H. Mahi, S. H. Abdullah, and S. A. Suha, "A Comparative Performance Evaluation of Bitcoin Price Prediction Using Machine Learning Techniques," *2023 Int. Conf. Inf. Commun. Technol. Sustain. Dev. ICICT4SD 2023 - Proc.*, pp. 194–198, 2023, doi: 10.1109/ICICT4SD59951.2023.10303490.

[36]   J. J. Benjamin, R. Surendran, and T. Sampath, "A professional strategy for Bitcoin and Ethereum using Machine Learning for Investors," *4th Int. Conf. Inven. Res. Comput. Appl. ICIRCA 2022 - Proc.*, no. Icirca, pp. 798–804, 2022, doi: 10.1109/ICIRCA54612.2022.9985532.

[37]   M. Geetha Jenifel, R. Anita Jasmine, and D. Umanandhini, "Bitcoin Price Predictive Dynamics Using Machine Learning Models," *2024 15th Int. Conf. Comput. Commun. Netw. Technol. ICCCNT 2024*, pp. 1–6, 2024, doi: 10.1109/ICCCNT61001.2024.10725542.

[38]   D. Kawli, A. Chaudhari, P. Ingale, G. Telange, and A. Banik, "Crypto-Visionary Price Forecasting System," *Proc. 5th Int. Conf. Smart Electron. Commun. ICOSEC 2024*, no. Icosec, pp. 1645–1650, 2024, doi: 10.1109/ICOSEC61587.2024.10722487.

[39]   E. Akyildirim, O. Cepni, S. Corbet, and G. S. Uddin, "Forecasting mid-price movement of Bitcoin futures using machine learning," *Ann. Oper. Res.*, vol. 330, no. 1–2, pp. 553–584, 2023, doi: 10.1007/s10479-021-04205-x.

[40]   Y. Li *et al.*, "MLBGK: A Novel Feature Fusion Model for Forecasting Stocks Prices: MLBGK: A Novel Feature Fusion Model…: Y. Li et al.," *Comput. Econ.*, no. 0123456789, 2024, doi: 10.1007/s10614-024-10796-x.

OPTICAL FARADAY MANIPULATING LONGITUDINAL COMPONENT OF OPTICAL VORTEX BEAMS

Fatma TAMBAĞ [1, *] (iD), Koray KÖKSAL[1, 2] (iD)

[1] *Bitlis Eren University, Department of Physics, Bitlis, Türkiye*

[2] *Gaziantep Islamic Science and Technology University Faculty of Engineering and Natural Sciences, Gaziantep, Türkiye*

* Corresponding Author: ftambag@gmail.com

ABSTRACT

In this study, we aim to investigate the novel application of the Optical Faraday effect in manipulating the longitudinal component of optical vortex beams, which are characterized by their unique orbital angular momentum and helical phase structure. The Optical Faraday effect, induced by the interaction of a magnetic field with a specific optical crystal, results in a rotation of the polarization plane of light. This phenomenon is harnessed to exert precise control over the longitudinal component of optical vortex beams, a feature not typically present in conventional light beams. Our theoretical analysis explores the modulation of the longitudinal component, revealing a significant influence on the beam's polarization characteristics, intensity distribution, and phase characteristics. This manipulation breaks new grounds for increasing the precision of optical systems, with potential applications in advanced optical communication, high-density data storage, and quantum information processing. The findings show that by finely tuning the magnetic field and material properties, it is possible to achieve a new kind of control mechanism over the propagation and interaction of optical vortex beams. This work paves the way for further exploration into the dynamic control of structured light, offering promising prospects for future photonic technologies.

Keywords: Faraday effect, OAM, Longitudinal component, Optical vortex.

1   INTRODUCTION

The manipulation and control of light's properties are fundamental in the progression of optical sciences and the development of innovative technologies [1-4]. Among the various types

of light beams, optical vortex beams have emerged as a particularly fascinating subject due to their unique capability of carrying orbital angular momentum (OAM) [5,6] This property can be described as a direct result of their helical phase front, which imparts a characteristic 'twist' to the wavefront, resulting in a doughnut-shaped intensity profile with a central null point [7-9]. The potential applications of optical vortex beams are extensive, spanning from advanced optical communication [10,11] systems to quantum information processing [12,13] and high-resolution imaging [14-16].

Optical vortex beams offer a unique avenue for encoding information within the phase structure of the light beam itself [17,18]. This feature can be harnessed to significantly enhance data transmission capacities by using OAM states as an additional degree of freedom for multiplexing [10,11]. Such an approach is crucial in optical communication systems. Furthermore, the distinctive phase and intensity profile of these beams can improve resolution and contrast in imaging applications, which is critical for detailed observations in biological research and materials science [14-16].

One of the key challenges in fully exploiting the potential of optical vortex beams lies in the precise control of their properties, particularly the longitudinal component of the electric field. In traditional light beams, the longitudinal component is typically minimal; however, in optical vortex beams, this component can be substantial due to the complex phase structure and because of reducible beam waist parameters. Controlling this longitudinal component allows for more meaningful and useful manipulation of the beam's phase and intensity, which is essential for applications requiring precise beam shaping, such as optical trapping and laser machining [19-22].

The Optical Faraday effect offers a compelling theoretical framework for manipulating the properties of light, including the longitudinal component of optical vortex beams. This magneto-optical phenomenon, first observed by Michael Faraday, involves the rotation of the polarization plane of light as it passes through a material under the influence of a magnetic field aligned with the direction of propagation. The degree of rotation, known as the Faraday rotation, depends on the Verdet constant of the material, the strength of the magnetic field, and the wavelength of the light. The ability to control these parameters allows for precise modulation of the light's polarization and, consequently, its intensity and phase characteristics [23-26].

In this theoretical exploration, we aim to develop a comprehensive understanding of how the Optical Faraday effect can be utilized to manipulate the longitudinal component of optical vortex beams. We will explore the mathematical foundations underlying the interaction

between optical vortex beams and the magnetic field-induced birefringence. This involves analyzing the propagation dynamics of the beams passing through a magneto-optical material under varying magnetic fields and assessing how these interactions alter the beam's polarization, intensity, and longitudinal component. Theoretical models have been developed to predict the outcomes of these interactions, focusing on identifying the conditions under which the longitudinal component can be most effectively controlled.

The theoretical investigation leads also to the implications of this control for practical applications. In optical communication, for instance, manipulating the longitudinal component could allow for more sophisticated modulation schemes, potentially increasing data throughput. In quantum information processing, precise control over the optical beam's properties is crucial for the manipulation and measurement of quantum states. Additionally, in the realm of optical sensing and metrology, the ability to finely tune the beam's properties could enhance the sensitivity and accuracy of measurements.

By providing a theoretical framework for the manipulation of the longitudinal component of optical vortex beams using the Optical Faraday effect, this study aims to bridge the gap between fundamental optical theory and potential practical applications. The insights gained from this research will not only contribute to the broader understanding of light-matter interactions but also suggest new pathways for technological advancements in fields as diverse as telecommunications, materials science, and quantum computing.

Therefore, the application of the Optical Faraday effect to optical vortex beams represents a promising new frontier in photonics. By leveraging this phenomenon to manipulate the longitudinal component of these beams, we open up new possibilities for their use in a variety of advanced optical systems. This theoretical study lays the groundwork for future experimental validation and technological innovation, positioning optical vortex beams at the forefront of next-generation optical technologies.

Now, we will present the theoretical framework employed to analyze the interaction of an optical vortex beam with a magneto-optic crystal under the influence of an external magnetic field. The analysis begins with the description of polarization modes using the Poincaré sphere, a powerful tool for visualizing and understanding the state of polarization in terms of spherical coordinates. By mapping the polarization states onto this sphere, we can effectively describe the dynamic behavior of the light as it propagates through the crystal.

Next, we introduce the optical vortex structure of the light, characterized by its Laguerre-Gaussian (LG) mode, which features a helical phase front and a doughnut-shaped intensity profile. The optical vortex beam exhibits vector polarization, where the electric field is structured as a superposition of two circularly polarized components with opposite winding numbers. These components, representing right-hand and left-hand circular polarizations, are critical in defining the unique phase and intensity characteristics of the vortex beam.

2 MATERIAL AND METHOD

The electric field of the light after passing through the magneto-optic crystal is mathematically expressed as the combination of these two oppositely polarized components. Importantly, the magneto-optic effect causes the refractive indices of the crystal for the right-hand and left-hand circular polarizations to differ, leading to a phase shift between them. This differential phase shift, induced by the external magnetic field, is crucial in understanding the resultant electric field distribution and the modifications in the polarization state.

Through this theoretical framework, we calculate the resultant electric field by considering the refractive index changes due to the magneto-optic effect, which encompasses the influence of the magnetic field on the crystal. These calculations are pivotal in predicting the behavior of the optical vortex beam as it interacts with the magneto-optic medium, providing insights that align with the experimental observations.

A polarized electric field vector can be effectively described using the polarization modes on the Poincaré sphere. The expression for the polarization state is given by

$$\hat{\epsilon}_l = e^{il\phi}(\hat{x} - i\hat{y})u_P + e^{-il\phi}(\hat{x} + i\hat{y})\mathcal{V}_P \tag{1}$$

where u_P and $\mathcal{V}_P$ are defined as

$$u_P = \frac{1}{\sqrt{2}}\sin\left(\frac{\Theta_P}{2}\right)e^{\frac{-i\Phi_P}{2}} \; ; \; \mathcal{V}_P = \frac{1}{\sqrt{2}}\cos\left(\frac{\Theta_P}{2}\right)e^{\frac{i\Phi_P}{2}} \tag{2}$$

where $\boldsymbol{\Theta_P}$ and $\boldsymbol{\Phi_P}$ parameters are angular variables on Poincar'e sphere. These parameters determine the orientation and ellipticity of the polarization state. The electric field components can be expressed as

$$F_{l,p}^{(1)}(r) = u_P e^{il\phi}\tilde{F}_{l,p}(\rho); \; F_{l,p}^{(2)}(r) = \mathcal{V}_P e^{-il\phi}\tilde{F}_{l,p}(\rho) \tag{3}$$

where $\widetilde{F}_{l,p}(\boldsymbol{\rho})$ is the vector potential amplitude function, described by the Laguerre-Gaussian mode as

$$\tilde{F}_{l,p}(\rho) = A_0 \sqrt{\frac{p!}{(p+|l|)!}}\, e^{-\frac{\rho^2}{\omega_0^2}} \left(\frac{\sqrt{2}\rho}{\omega_0}\right)^{|l|} L_p^{|l|}\left(\frac{2\rho^2}{\omega_0^2}\right) \tag{4}$$

where ρ is the radial coordinate, A_0 is the normalization constant. This function depends solely on the radial distance ρ and the electric field $\boldsymbol{E}$ can be explicitly written as

$$E = (\hat{x} - i\hat{y})F^{(1)}e^{in_-k_z z} - \hat{z}c\left\{\frac{\partial F^{(1)}}{\partial x} - i\frac{\partial F^{(1)}}{\partial y}\right\}e^{in_-k_z z} + (\hat{x} + i\hat{y})F^{(2)}e^{in_+k_z z}$$
$$-\hat{z}c\left\{\frac{\partial F^{(2)}}{\partial x} + i\frac{\partial F^{(2)}}{\partial y}\right\}e^{in_+k_z z} \tag{5}$$

where n_- and n_+ represent the refractive indices of the magneto-optic material for left- and right-circularly polarized light, respectively. In vacuum $\boldsymbol{n}^{(+)} = \boldsymbol{n}^{(-)} = 1$. For the magneto-optic crystal, it is possible to observe the difference between the n_- and n_+ refractive indices due to the change in Faraday angle such that [23]

$$n^{(-)} - n^{(+)} = \gamma\Theta \tag{6}$$

where Θ is the rotation angle given by the standard expression

$$\Theta = VBL \tag{7}$$

where V, B and L are the Verdet constant of the material, applied axial magnetic field and the thickness of the medium, respectively. And the parameter $\gamma = 2\,c/\omega L$ indicates the relationship between the refractive index difference and Faraday angle. The left-hand circular polarisation and the right hand one produce equal but opposite change (in sign) of the rotation angle suggesting the following forms

$$n^{(-)} = n_0 + \left(\frac{\gamma\Theta}{2}\right); \quad n^{(+)} = n_0 - \left(\frac{\gamma\Theta}{2}\right) \tag{8}$$

where n_0 is the refractive index in the absence of the magnetic field.

The z-component in the equation refers to the longitudinal electric field component, indicating that the electric field is polarized in all three spatial dimensions:

x, y and z. It is important to note that the longitudinal component of the wave becomes negligible when the beam waist ω_0 is significantly larger than the wavelength λ, i.e. $\omega_0 \gg \lambda$.

However, recent studies have shown that the longitudinal electric field can contribute significantly to the total electric field when the beam waist is small, even while adhering to the optical diffraction limit (approximately for $\omega_0 > 0.7\lambda$).

In our previous study [25], we observed the effect of an external magnetic field applied along the light propagation direction on the polarization of light possessing only a transverse electric component as it traversed through a magneto-optic crystal. Notably, no significant changes were observed in the radial profile of the light. However, in our current investigation, it has become evident that the external magnetic field indeed influences the presence and orientation of the longitudinal electric component. This finding underscores the complex interplay between the magnetic field and the electric field components of light within the magneto-optic medium, suggesting a more nuanced mechanism that governs the light-matter interaction in such environments. This discovery challenges the conventional understanding and opens new avenues for exploring the manipulation of light in advanced photonic applications.

It is not possible to produce an explicit form of the Equation 5. But, we can revise the equation for specific values of $\boldsymbol{E}$

$$E(\rho,\phi,L) = \frac{u(\rho)}{\sqrt{2}}\left\{\begin{matrix}\hat{x}\left[e^{(ikLn_0-i\Theta+il\phi)} + e^{(ikLn_0+i\Theta-il\phi)}\right] - \\ i\hat{y}\left[e^{(ikLn_0-i\Theta+il\phi)} - e^{(ikLn_0+i\Theta-il\phi)}\right]\end{matrix}\right\} \tag{9}$$

The Figure 1 presented elucidates the influence of an external magnetic field on the propagation of light through a magneto-optic crystal, particularly focusing on the interplay between the longitudinal and transverse electric field components. In our earlier research, we primarily investigated the impact of an external magnetic field on light possessing only a transverse electric component, noting that while the polarization of the light was affected, there were no observable changes in the radial profile. This suggested that the transverse electric field's interaction with the magnetic field was relatively straightforward and did not invoke significant alterations in the spatial distribution of the light intensity.

However, the current figure delves deeper into the situation by incorporating the presence of a longitudinal electric component, which is subjected to the same external magnetic field. Each subplot in the figure corresponds to a specific Faraday angle, $\boldsymbol{\theta}$, which represents different magnitudes of the applied magnetic field. The color maps and overlaid contour lines provide a detailed visualization of how the electric field distribution evolves under varying conditions.
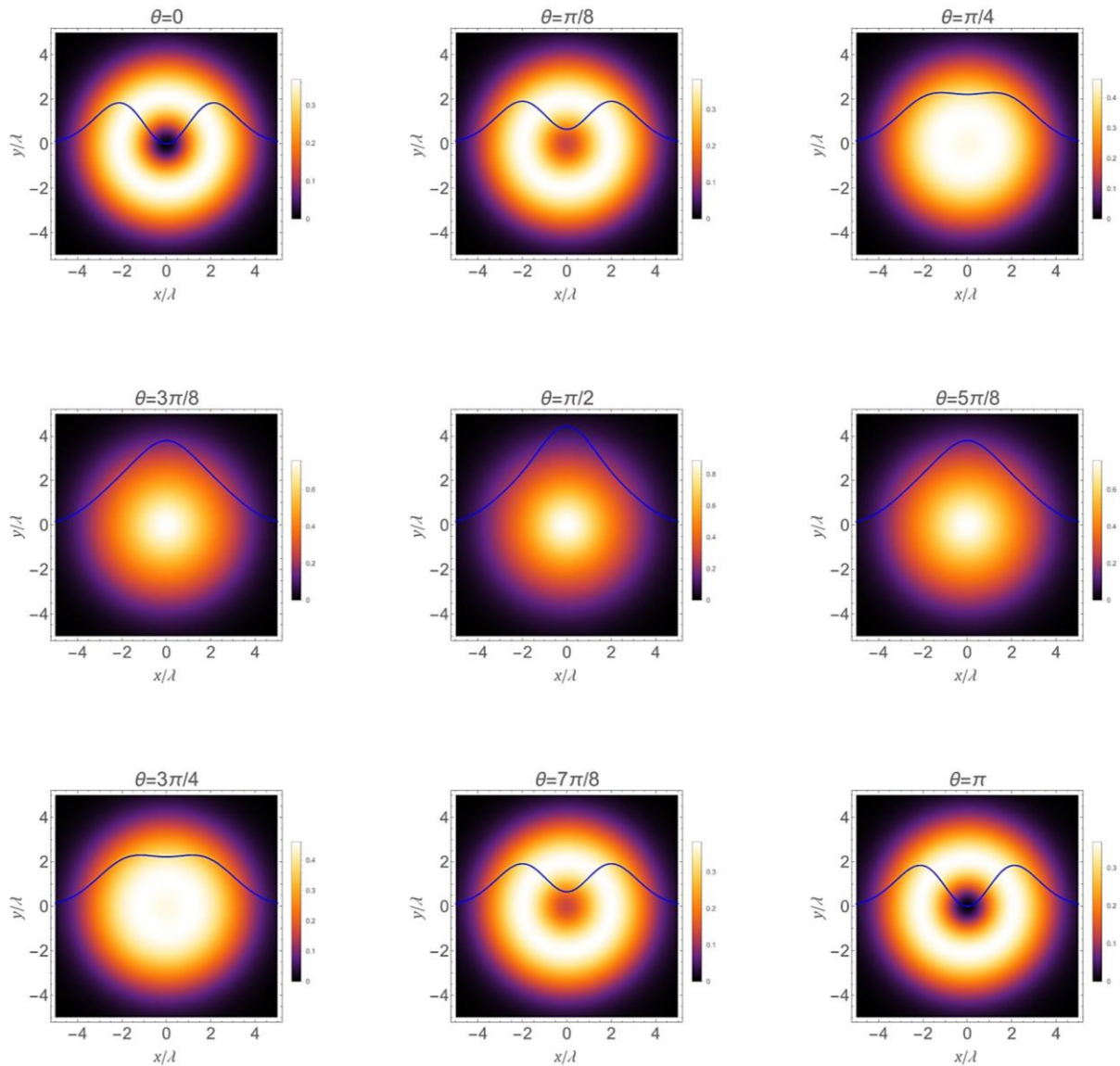
Figure 1. Density profile changes according to Faraday angle for values
$\theta_p = \pi/2, \varphi_p = \pi/2, l = 1, p = 0$. *The value $\varphi_p = \pi$ corresponds to the azimuthal polarization on the Poincar'e sphere. The impact of an external magnetic field on the electric field distribution within a magneto-optic crystal, as visualized for various Faraday angles (θ) which depends on the magnetic field. Each subplot represents the evolution of the electric field, with both longitudinal and transverse components, as θ increases from 0 to π. The color maps indicate the intensity distribution, while the overlaid contour lines highlight the ρ dependent modulation of the electric field. The figure demonstrates the significant influence of the magnetic field on the longitudinal electric component, revealing complex interactions and symmetry breaking as the field orientation changes.*

At $\boldsymbol{\theta} = \mathbf{0}$, the electric field distribution exhibits a certain symmetry, with the transverse component predominantly determining the overall pattern. As the angle $\boldsymbol{\theta}$ increases, representing a change in the magnetic field's strength, there is a noticeable alteration in the electric field distribution. This is especially pronounced in the longitudinal component, which begins to exhibit more complex patterns and deviations from the initial symmetry.

When $\boldsymbol{\theta}$ reaches π/2, the longitudinal component's influence becomes most apparent, as evidenced by the significant changes in the electric field distribution. The figure suggests that the external magnetic field strongly affects the longitudinal component, causing it to vary in a manner that is not observed when only the transverse component is present. As $\boldsymbol{\theta}$ continues to increase, the patterns evolve further, indicating that the longitudinal component's response to the magnetic field is highly sensitive to the field's magnitude.

This comprehensive analysis of the electric field distribution as a function of the Faraday angle meaning of the applied magnetic field highlights the intricate dynamics at play within the magneto-optic medium. The findings depicted in this figure underscore the complex relationship between the external applied magnetic field and the electric field components of the light, particularly emphasizing the critical role of the longitudinal component, which had been previously underappreciated.

We can perform another analysis by investigating the Figure 1 which shows how the magnetic field, that is, the Faraday angle, affects the $\boldsymbol{\theta_p}$ polarization and therefore the total electric field radial profile distribution. In the first place, we assume that the light that will pass through the magneto-optic crystal in the z direction without any external magnetic field is azimuthally polarized ($\boldsymbol{\varphi_p} = \boldsymbol{\pi}$). For the $\boldsymbol{l} = \mathbf{1}$ case, as shown in the figure, to better illustrate the ring-shaped intensity distribution in the x-y plane, a radial distribution graph was obtained with the blue line. Due to the radial symmetry, the intensity distribution and the graph represented by the blue line are independent of the azimuthal angle $\boldsymbol{\phi}$ and represent the singularity. The dark region located in the middle of the ring with radial symmetry and representing the singularity changes with the increase in the value of the Faraday angle, which depends on the magnetic field. The main reason for this

$$I = \frac{2E_0^2 e^{-\frac{2\rho^2}{\omega_0^2}} (4c^2 \sin^2 \theta \, (\omega_0^2 - \rho^2)^2 + \rho^2 \omega_0^4 \omega^2)}{\omega_0^6} \tag{10}$$

is that the resulting radial profile consists of two parts. The first part, the expression $4c^2 \sin^2 \theta \, (\omega_0^2 - \rho^2)^2$, shows the longitudinal wave component. This component contributes

to the result according to the θ angle. For $\theta = \pi$ case, the light has azimuthal polarization, and the direction of rotation of the azimuthal polarization vectors for this position (For $\theta = \pi$) is opposite to the For $\theta = 0$ case. Here we come across an interesting fact. Before, we were placing a linear polarizer behind the magneto-optic crystal to understand the change in radial polarization. However, with the contribution of the longitudinal wave component, the need for a linear polarizer is eliminated. Equation 5 that we obtained for the electric field gives us the orientation of the polarization vectors and their change depending on the Faraday angle.

The graph presented in Figure 1 is crucial in advancing our understanding of how an external magnetic field, characterized by the Faraday angle θ, influences the propagation of light through a magneto-optic crystal. This research focuses on the interaction between the longitudinal and transverse components of the electric field within this medium. The figure's significance lies in its detailed visualization of the electric field distribution as the magnetic field strength, and consequently the Faraday angle, increases. The evolution of these patterns, especially the longitudinal component's response, highlights a complex interplay that was previously underestimated. At different Faraday angles, the radial symmetry and the resulting singularities change, providing insights into how the longitudinal component can alter the light's behavior within the magneto-optic crystal.

The practical implications of this study are vast. The ability to manipulate the longitudinal electric field without the need for external linear polarizers, as suggested by the results, opens up new possibilities in photonic applications, such as the design of advanced optical devices that rely on precise control of light polarization. The observed changes in the radial profile due to the Faraday effect can be leveraged to develop highly sensitive sensors or modulators that operate based on the external magnetic field's influence on light.

Moreover, these findings provide a foundational understanding that can support future research. By illustrating how the Faraday angle affects both the radial distribution and the polarization states, this study offers a framework that other researchers can build upon to explore new methods of light manipulation in magneto-optic materials. This could lead to the development of novel technologies in fields ranging from telecommunications to quantum computing, where precise control over light's properties is essential. The figure demonstrates that by carefully controlling the magnetic field, we can achieve significant modulation of light's electric field components, leading to new applications and furthering our understanding of light-matter interactions in magneto-optic environments.

This research provides a comprehensive exploration of the intricate dynamics involved in the polarization of light as it propagates through a magneto-optic crystal under the influence of an external magnetic field. By methodically varying the Faraday angle, we have revealed significant alterations in the spatial distribution and orientation of polarization vectors, which undergo a remarkable evolution from azimuthal to radial configurations. This study not only sheds light on the previously underappreciated role of the longitudinal electric field component but also highlights its critical importance in influencing the overall polarization profile, especially in the presence of strong magnetic fields.

3   RESULTS AND DISCUSSION

Initially, when no external magnetic field is applied, the polarization vectors of the light are arranged in a symmetrical azimuthal mode around the axis of the beam. This alignment serves as a baseline, clearly demonstrating the light's initial polarization state before any magnetic influence is introduced. As the magnetic field strength increases, leading to a corresponding increase in the Faraday angle, the behavior of these polarization vectors begins to change noticeably. At a relatively low Faraday angle, the symmetry of the azimuthal polarization starts to break down, especially near the center of the beam, where new and stronger polarization vectors emerge, deviating towards the longitudinal (z) direction. This deviation indicates a significant transition in the polarization state, one that traditional models based on the Poincaré sphere cannot fully explain, as these models typically assume polarization within a plane perpendicular to the light's direction of travel.

As the Faraday angle increases further, reaching a midpoint value, the transformation of the polarization state becomes more pronounced. The electric field vectors, which initially exhibited a predominantly azimuthal orientation, gradually realign themselves into a radial configuration. This transition is particularly significant because it underscores the external magnetic field's ability to induce a fundamental shift in the light's polarization state, moving from azimuthal to radial polarization. This change is accompanied by a strong orientation of the electric field vectors in the z-direction, especially near the center of the beam, where the influence of the longitudinal component becomes increasingly dominant.

When the Faraday angle reaches higher values, approaching three-quarters of its maximum, the study reveals a reemergence of helical polarization patterns, this time with a counterclockwise orientation. Interestingly, despite the strong z-directional component observed at this stage, its overall intensity diminishes as the magnetic field continues to

strengthen. This suggests a complex interplay between the transverse and longitudinal components of the electric field, where the dominance of one over the other is highly sensitive to the precise configuration of the magnetic field. Furthermore, the gradual transition from azimuthal to radial polarization modes, driven by the varying magnetic field, highlights the versatility of magneto-optic materials in enabling precise control over light's polarization state.

At the peak Faraday angle, the study shows a complete reversal of the polarization vectors compared to their initial state. The azimuthal polarization reappears, but with a critical twist: the vectors are now oriented in the opposite direction to their original alignment. This reversal not only completes the cycle of polarization transformation but also demonstrates the magnetic field's capability to control the polarization vectors' direction and intensity with remarkable precision. The fact that the radial profile of the light remains consistent, regardless of this reversal, underscores the robust nature of the polarization state changes induced by the magnetic field.

4   CONCLUSION AND SUGGESTIONS

The findings from this study have significant implications for both fundamental research and practical applications. The ability to manipulate polarization states without the need for external polarizing elements, such as linear polarizers, represents a major advancement in the field of photonics. This capability could lead to the development of new optical devices, such as switches, sensors, and modulators, that rely on the precise control of light polarization in three dimensions. Additionally, the insights gained into the behavior of the longitudinal electric field component offer a deeper understanding of magneto-optic interactions, which could inform the design of future experiments and theoretical models in the field.

Moreover, the results suggest that by carefully adjusting the external magnetic field, a wide range of polarization states can be achieved, each with unique properties that could be exploited for specific technological applications. For instance, in the field of optical communications, the ability to switch between different polarization modes could enhance both the speed and security of data transmission. In sensing technologies, the sensitivity of the polarization state to the external magnetic field could be used to develop highly accurate magnetic field sensors with broad industrial and scientific applications.

The study also paves the way for further research in related fields, such as quantum optics and nanophotonics, where the ability to control light at very small scales is crucial. The

techniques demonstrated here for manipulating light polarization could have significant implications for quantum information processing, where precise control over photon states is essential. Additionally, the ability to tailor light polarization in magneto-optic materials could lead to the development of new materials with engineered optical properties, opening up new avenues in material science and photonics.

In conclusion, this research not only advances our understanding of light-matter interactions in magneto-optic materials but also establishes a foundation for future technological developments in photonics. The demonstrated ability to precisely control light polarization through external magnetic fields represents a significant step forward, with far-reaching implications for both fundamental science and practical applications in a wide range of fields.

Acknowledgements

Conflict of Interest Statement

There is no conflict of interest between the authors.

Statement of Research and Publication Ethics

The study is complied with research and publication ethics.

Artificial Intelligence (AI) Contribution Statement

This manuscript was entirely written, edited, analyzed, and prepared without the assistance of any artificial intelligence (AI) tools. All content, including text, data analysis, and figures, was solely generated by the authors.

Contributions of the Authors

Fatma Tambağ: Writing, Investigation, Data Curation

Koray Köksal: Review, Editing, Formal Analysis, Methodology, Validation

REFERENCES

[1] M. De Oliveira and M. R. Dennis, "Vortex knots in light," *Nature Photonics*, vol. 15, pp. 253–256, 2021.

[2] O. V. Angelsky, A. Y. Bekshaev, S. G. Hanson, C. Y. Zenkova, I. I. Mokhun, and J. Zheng, "The spin–orbit interactions of structured light," *Frontiers in Physics*, vol. 8, p. 114, 2020.

[3] H. Rubinsztein-Dunlop, A. Forbes, M. V. Berry, M. R. Dennis, D. L. Andrews, M. Mansuripur, C. Denz, C. Alpmann, P. Banzer, T. Bauer, *et al.*, "Roadmap on structured light," *Journal of Optics*, vol. 19, no. 1, p. 013001, 2016.

[4] M. Babiker, V. Lembessis, K. Köksal, and J. Yuan, "Orbital angular momentum of light in optical communication," in *Structured Light for Optical Communication*, Elsevier, 2021, pp. 37–76.

[5] D. L. Andrews and M. Babiker, *The Angular Momentum of Light*. Cambridge: Cambridge University Press, 2012.

[6] A. M. Yao and M. J. Padgett, "Orbital angular momentum: origins, behavior and applications," *Advances in Optics and Photonics*, vol. 3, no. 2, pp. 161–204, 2011.

[7] Y. S. Kivshar and E. A. Ostrovskaya, "Optical vortices: new tools for scientific and engineering applications," *Optics and Photonics News*, vol. 12, p. 11, 2001.

[8] J. E. Curtis and D. G. Grier, "Structure of optical vortices," *Physical Review Letters*, vol. 90, p. 133901, 2003.

[9] G. Indebetouw, "Optical vortices and their propagation," *Journal of Modern Optics*, vol. 40, no. 1, pp. 73–87, 1993.

[10] J. Wang, "Advances in communications using optical vortices," *Photonics Research*, vol. 4, no. B14, 2016.

[11] W. Shao, S. Huang, X. Liu, and M. Chen, "Tightly focused optical vortex beam shaping," *Optics Communications*, vol. 427, pp. 545–550, 2018.

[12] Ş. Suciu, G. A. Bulzan, T. A. Isdrailă, A. M. Pălici, S. Ataman, C. Kusko, and R. Ionicioiu, "High-dimensional quantum gates using vortex beams," *Physical Review A*, vol. 108, no. 5, p. 052612, 2023.

[13] D. Bacco, D. Cozzolino, B. Da Lio, Y. Ding, K. Rottwitt, and L. K. Oxenløwe, "Multiplexing quantum and classical signals in a single fiber," in *Proc. 22nd Int. Conf. Transparent Optical Networks (ICTON)*, IEEE, 2020, pp. 1–4.

[14] Y. Shen, X. Wang, Z. Xie, C. Min, X. Fu, Q. Liu, M. Gong, and X. Yuan, "Optical vortices 30 years on: OAM manipulation from topological charge to multiple singularities," *Light: Science & Applications*, vol. 8, p. 90, 2019.

[15] G. Sun, F. Zhang, K. Zhao, and S. Pan, "High-capacity optical data storage using vortex beams," *Journal of Lightwave Technology*, vol. 42, pp. 1894–1902, 2024.

[16] M. Liu, Y. Lei, L. Yu, X. Fang, Y. Ma, L. Liu, J. Zheng, and P. Gao, "On-chip generation and multiplexing of optical vortices using metasurfaces," *Nanophotonics*, vol. 11, pp. 3395–3405, 2022.

[17] J. Wu, H. Li, and Y. Li, "Generation of optical vortices using spatial light modulators," *Optical Engineering*, vol. 46, no. 1, p. 019701, 2007.

[18] Z. Long, H. Hu, X. Ma, Y. Tai, and X. Li, "Chiral light–matter interaction in plasmonic vortex devices," *Journal of Physics D: Applied Physics*, vol. 55, no. 43, p. 435105, 2022.

[19] G. F. Q. Rosen, "Measurement of orbital angular momentum states using interference," *JOSA B*, vol. 40, p. C73, 2023.

[20] K. A. Forbes and G. A. Jones, "Quantum coherence of light with orbital angular momentum," *Physical Review A*, vol. 103, no. 5, p. 053515, 2021.

[21] K. Koksal, M. Babiker, V. Lembessis, and J. Yuan, "Twisted photon transport in inhomogeneous media," *Optics Communications*, vol. 490, p. 126907, 2021.

[22] M. Babiker, J. Yuan, K. Koksal, and V. Lembessis, "Spin and orbital angular momentum coupling in non-paraxial optical fields," *Optics Communications*, vol. 554, p. 130185, 2024.

[23]   P. Berman, "Angular momentum and the Einstein–de Haas effect," *American Journal of Physics*, vol. 78, no. 3, pp. 270–276, 2010.

[24]   K. J. Carothers, R. A. Norwood, and J. Pyun, "Organic photonics: materials and applications," *Chemistry of Materials*, vol. 34, pp. 2531–2542, 2022.

[25]   F. Tambag, K. Koksal, F. Yildiz, and M. Babiker, "Orbital angular momentum interaction with atomic systems," *Optics Communications*, vol. 545, p. 129649, 2023.

[26]   I. Crassee, J. Levallois, A. L. Walter, M. Ostler, A. Bostwick, E. Rotenberg, T. Seyller, D. Van Der Marel, and A. B. Kuzmenko, "Giant Faraday rotation in single- and multilayer graphene," *Nature Physics*, vol. 7, pp. 48–51, 2011.

CLASSIFICATION OF MALICIOUS NETWORK DATASET WITH RESIDUAL CNN

Mücahit KARADUMAN [1] (iD), **Sercan YALÇIN** [2, *] (iD), Muhammed YILDIRIM [3] (iD)

[1] *Malatya Turgut Özal University, Computer Engineering Department, Malatya, Türkiye*

[2] *Adıyaman Eren University, Mechanical Engineering Department, Adıyaman, Türkiye*

[3] *Malatya Turgut Özal University University, Mechanical Engineering Department, Malatya, Türkiye*

*** Corresponding Author:** svancin@adiyaman.edu.tr*

ABSTRACT

This paper proposes a Residual Convolutional Neural Network (CNN) based model for malicious traffic detection. Network security is becoming increasingly important every day as the digital world develops. It aims to classify the data labeled as benign and malicious in the ready dataset. In the proposed model, first of all, all the information in the dataset is digitized. Then, it is normalized to the range of 0-1 and made ready as an input to the proposed architecture. It is aimed to classify the information in this two-class dataset with the proposed Residual Convolutional Neural Network (CNN) architecture. The accuracy rate obtained after the training and testing stages of the model is 94.9%. This accuracy rate shows that the proposed model successfully results in the detection of malicious packets in network attacks and can be used for network security.

Keywords: Network security, Residual CNN, Malicious packet detection, Classification.

1   INTRODUCTION

The development of Internet networks brings many problems along with the increasing communication methods provided over these networks. Security threats for individuals, institutions, and states are reaching serious dimensions with the increasing digitalization. The basic problems of computer networks include secure transfer, data protection, and performance.

Computer networks contain many communication devices. The most basic of these devices are routers [1], switches [2], and personal use devices. The most undesirable situation is for attackers to connect to computer networks and launch attacks.

Information security is important for individuals' privacy, protection of their private information and feeling safe, while it is of great importance for states in terms of national security, strategic information and protection of critical infrastructures. Ensuring data security is based on confidentiality, integrity and accessibility. Confidentiality is possible only by guaranteeing access to authorized persons. Data integrity is possible by guaranteeing its originality and proving that it has not been changed by unauthorized persons. Ensuring access at the desired time and speed is also among the important elements. Violation of these rules can cause great material and moral losses and security gaps. The development, expansion and widespread use of networks bring about an increase in attacks. These attacks are carried out for reasons such as stopping system operations, stealing information and preventing communication. The types of attacks are given in Table 1. Distributed Denial of Service (DDoS) attacks are attacks carried out to render networks inoperable by creating high network traffic [3]. Man-in-the-Middle (MitM) attacks are attacks carried out to secretly capture, monitor or change the communication of two parties in communication [4]. Phishing Attacks are attacks that are created by sharing misleading information and documents to deceive people and steal their personal information [5]. In attacks made with SQL Injections, the attacker adds unauthorized and malicious SQL query codes to the codes and attacks are made to access the database [6]. The aim is to seize the system and obtain information.

Table 1. Network attack types and characteristics.

Attack Types	Features
DDoS	It sends high traffic to the network from many sources, making services unavailable.
MitM	It is a way of intercepting the communication between two parties and monitoring and changing the information.
Phishing Attacks	It means obtaining personal information by misleading users.
SQL Injections	It is done to gain unauthorized access to the database with malicious SQL codes.

Data packets on the network are the primary targets for attackers. In case of a security breach, attacks such as packet sniffing, packet forwarding, packet replay and packet poisoning are carried out. These attacks generally monitor network traffic, collect sensitive information,

unencrypted information is easily captured, network traffic is directed to the wrong place, data packets can be sent repeatedly to deceive the system and malicious network packets can be added to manipulate the system and disrupt its operation. All these attacks reveal the importance of network security. Detection of attacks is possible both by conscious users and by developing intelligent systems. When the studies on computer networks and attack types and their detection are examined, it is seen that many detection studies have been carried out with machine learning methods. When the detection studies for DDoS attacks are examined, it is seen that while Support Vector Machines (SVM) architecture is used for detection [3], [7], [8], [9], deep learning architectures are used for detection in CNN models [10], [11], [12], [13], [14]. Again, in the detection studies conducted for MitM attacks, it is seen that SVM [15], K-Nearest Neighbors (KNN) [16] and CNN [17] models are used and successful results are obtained. There are many studies in the literature on phishing attack detection and when these studies are examined, there are studies with different models of SVM [18], KNN [19] and CNN [20], [21] architectures. It is seen that machine learning methods are used in SQL injection attacks [6], [22], [23], [24], [25], [26]. It is seen that these studies have intensified in recent years and successful results are obtained. In this study, a study is made on determining whether the packets transmitted during communication in a network traffic are secure.

There are studies on the subject in the literature. Shombot et al., in their study to predict phishing attacks, created a graphical user interface to detect whether websites are phishing or not. They conducted experiments with different machine learning methods in the study. After the preprocessing steps, the highest accuracy of 84% was achieved in the polynomial SVM classifier [18].

Irsan et al. used a dataset consisting of 10,000 data for phishing detection. In this study, they compared KNN and decision trees. Data preprocessing was first done in the study, and then models were trained and tested. They stated that the KNN classifier (accuracy %95) was more successful than decision trees (accuracy %93) in the dataset used for phishing detection [19].

Bezkorovalnyi et al. stated that they analyzed modern methods to detect phishing emails. The study highlighted that deep learning models can extract valuable features without applying a preprocessing step to the data. In this study, the advantages and disadvantages of different methods are included [20].

Gupta et al. stated that information security and privacy caused by phishing attacks pose a serious risk. In the relevant study, they used the Cuckoo Search algorithm to adjust the

hyperparameters of the proposed CNN model. The accuracy value obtained in this study was 90%. In this paper, hyperparameter optimization comes to the fore [21].

Kocyigit et al. used genetic algorithms and classifiers for phishing detection. The selection of important features was performed using genetic algorithms. Different ablation results were included in the study. When the features selected using genetic algorithms were classified in the classifiers, the highest success was achieved with 92.93% in the Random Forest classifier [27].

Mankar et al. emphasized that malicious URLs cause significant financial losses. Four different models were used in the study. At the end of the study, they stated that decision trees and random forest models achieved an accuracy rate of 91%. This study obtained lower accuracy values in KNN and Naive Bayes models [28].

A deep learning based model is proposed in the study. The proposed deep learning model is a model with residual connections and is a new approach to classifying packets in the network. The formalization processes performed from the dataset also include innovation in digitizing the data received in the network. The digitization and normalization of both the texts in the data and the information in all other columns, including IP addresses, ensures that all parameters in the network are taken into account in the classification phase.

In this study, the details of the dataset used are given in section 2. In addition, the details about the proposed method and all the success metrics used are included in this section. In section 3, examples from the units in the used dataset are given, and then the confusion metric and performance metrics showing the results of the proposed model are given. In the last section, the evaluations and results are interpreted, and suggestions for the future are made.

2   SYSTEM THEORY

2.1   Dataset

Data packets in computer networks can be modified by attackers and made harmful. Distinguishing and filtering these malicious and normal packets from each other is of great importance in terms of information and network security. In the dataset prepared for this purpose by Saadoon and Behadili (2024) [29], the transmitted data packets are recorded in two classes as benign and malicious. 9 features are kept for each packet in the dataset. These features are Protocol(P), remote_ip(Ri), remote_port(Rp), local_ip(Li), local_port(Lp), md5_hash(Mh), sha512_hash(Sh), Length(L) and data_hex(Dh). Malicious network dataset features are given

in Figure 1. In order to obtain these features, they collected the packets using the honey trap method placed with Honeytrap in the system they created.

The features used for the dataset are protocols used in network communication such as Protocol Hyper-Text Transfer Protocol (HTTP), File Transfer Protocol (FTP) or Secure Shell (SSH). remote_ip is the IP address of the system from which the remote connection is initiated (attacker) and remote_port is the port number of the same system. local_ip is the IP address of the local system and the port of this system is called local_port. md5_hash is the payload hash used to both identify and compare files and data. sha512_hash is the SHA-512 hash obtained for the payload and is kept as a secure identification for the file and data. Length represents the length of the payload in bytes. data_hex is the hexadecimal representation of the raw payload.
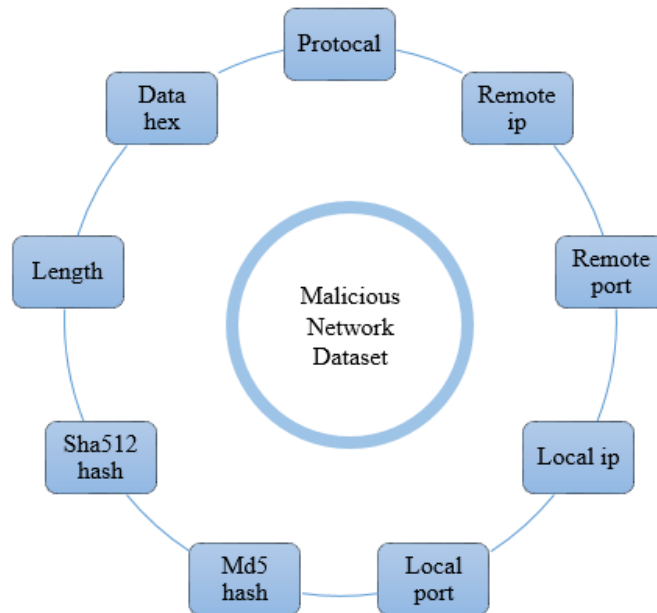
Figure1. Malicious network dataset features.

2.2   The proposed method

The use of artificial intelligence methods to detect attacks on computer networks is important in terms of ensuring the security and automation of systems. Residual networks allow deeper networks to be trained efficiently by reducing the vanishing gradient problem encountered in the training of deep neural networks. While traditional deep networks may experience a learning process hindered by the vanishing gradients as the network gets deeper, skip connections alleviate this problem and facilitate the gradient flow during backpropagation. This structure improves training by accelerating learning and allowing deep networks to generalize better. Residual blocks preserve parameter efficiency and increase accuracy rates

without increasing the depth of the model using identity mapping. The general structure of the residual CNN-based model developed for the classification of data in the dataset is given in Figure 2. In the proposed model, a ready-made dataset is used first. Transformation and normalization processes are applied to bring the features in this dataset to a usable format in the deep learning model.
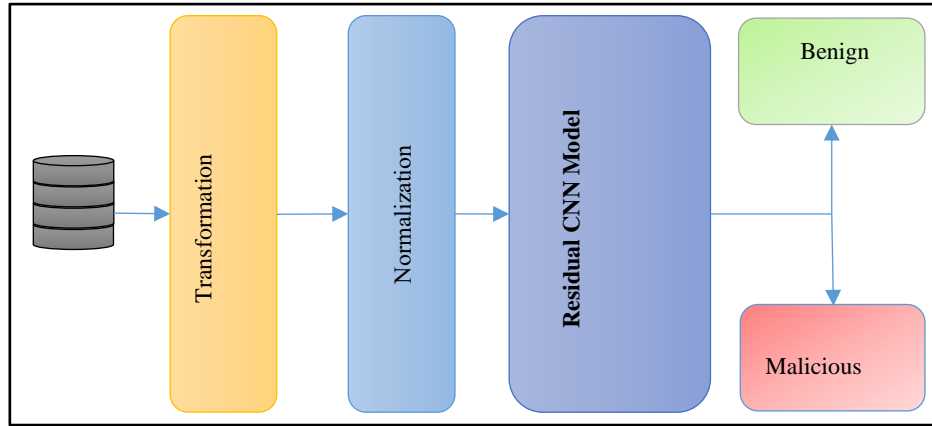

Figure 2. The proposed method.

In the transformation step, firstly the hash and hex properties are analyzed. The formulas used for these analyses are given in Equations 1, 2, and 3.

$$Total_{hash} = \begin{cases} \sum_{i=1}^{n} ord(c_i), & if\ x\ is\ a\ string \\ 0, & otherwise \end{cases} \tag{1}$$

In Equation 1, x represents a hash string, n represents the length of the string, c_i represents the ith character of the string, and ord calculates the ASCII value of the given character.

$$Total_{hex} = \begin{cases} \sum_{i=1}^{n} int(x[i:i+2], 16), & if\ x\ is\ a\ string \\ 0, & otherwise \end{cases} \tag{2}$$

In Equation 3, x represents a hex string, n represents the total number of binary in the hexadecimal string, $i:i+2$ represents the ith 2-character group of the string, $int(x[2i-2:2i],16)$ calculates the decimal equivalent of the 16 data.

$$Mean_{hex} = \begin{cases} \dfrac{\sum_{i=1}^{n} int(x[i:i+2], 16)}{n}, & if\ x\ is\ a\ string\ and\ n > 0 \\ 0, & otherwise \end{cases} \tag{3}$$

Equation 4 is used to convert IP addresses into numerical form.

$$Num_{IP} = (o_1 \cdot 256^3) + (o_2 \cdot 256^2) + (o_3 \cdot 256^1) + (o_4 \cdot 256^0) \qquad (4)$$

The Equation 4 calculates the numerical equivalent of the IP address and represents each octet of those values. Then, the normalization step is started. In the normalization step, the values are normalized to the range of 0-1 using Equation 5.

$$x' = \frac{x - x_{min}}{x_{max} - x_{min}} \qquad (5)$$

In Equation 5, x is the data point to be normalized, x_{min} is the smallest value of the dataset, x_{max} is the largest value of the dataset, and x' is the normalized value. After this stage, the data is divided and given as input to the residual CNN model. The normalized dataset is divided into two parts as training and testing. While 80% of the data is separated for training, 20% of the data is separated for testing.

The residual CNN architecture is created and the data classification step is passed. In this step, first the architecture is designed in a way that the One-dimensional Convolution Layer (Conv1D) process will be applied. Then the maxpooling step is performed and then the residual connection is added in the dropout step. With this connection, a shortcut is created and the dropout and Conv1D steps are combined. This step is usually added to accelerate learning and reduce gradient loss problems. The Residual CNN architecture created for the proposed model is given in Figure 3. The model parameters were determined as learning rate 0.001, epoch number was used as 100 and batch size was used as 32. Adam was also preferred as the optimization algorithm.
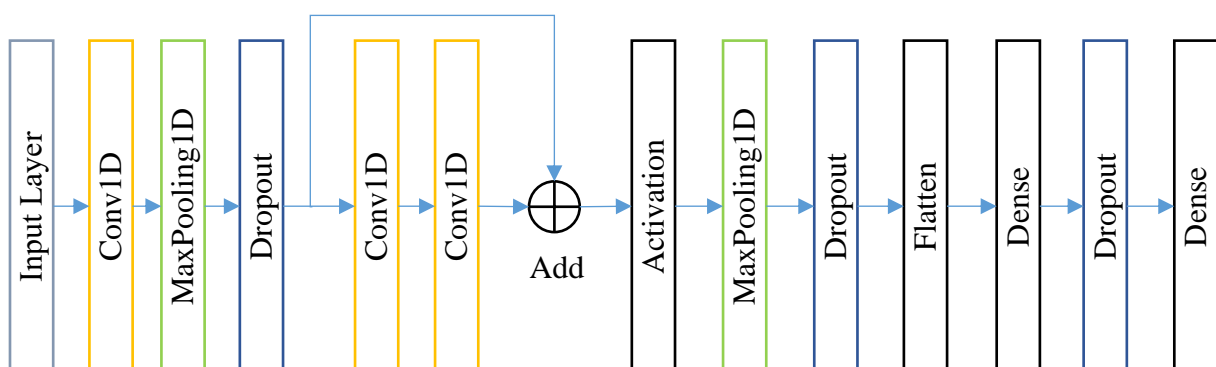

Figure3. Structure of the Residual CNN model.

Table 2. Performance metrics.

Performance Metric	Formula
Accuracy	$\dfrac{TP + TN}{TP + TN + FP + FN}$
Precision	$\dfrac{TP}{TP + FP}$
Recall	$\dfrac{TP}{TP + FN}$
Specificity	$\dfrac{TN}{TN + FP}$
F1-Score	$2 \cdot \dfrac{(Precission \cdot Recall)}{(Precission + Recall)}$
MCC	$\dfrac{(TP \cdot TN) - (FP \cdot FN)}{\sqrt{(TP + FP)(TP + FN)(TN + FP)(TN + FN)}}$
Balanced Accuracy	$\dfrac{Recall(Sensitivity) + Specificity}{2}$

The success of the studies is possible with the analysis of the classification results. With these analyses, performance metrics are calculated, and the rate of correct predictions of the model, the rates of incorrect and missing classifications are determined. Thus, the working accuracies for different classes can be determined. Performance metrics are calculated with the values of TP (True Positive), TN (True Negative), FP (False Positive), FN (False Negative). In addition to the basic criteria Accuracy, Precision and Recall, the imbalance between classes is determined with Specificity. In addition, criteria such as Balanced Accuracy and MCC (Matthews Correlation Coefficient) are used in performance analysis. The calculation methods of these performance metrics are given in Table 2.

3   EXPERIMENTAL RESULTS

The malicious network dataset consists of a total of 27978 records. Half of these records contain malicious data and the other half contain benign data. Some records in the dataset are given in Table 3.

The data in the table first passes through the transformation step and all the data is calculated as numerical values. Sums and averages are calculated for Hash and Hex values. Digitization operations are performed for IP addresses. After the digitization step is completed, the normalization step is passed and all digitized data is normalized to the 0-1 range. After this step, the preprocessed data were classified using four different classifiers accepted in the literature to compare the proposed model's performance. These models are KNN, SVM, Naive

Bayes (NB) [30], and Logistic Regression (LR) [31]. In the confusion matrix, 0 represents Benign data, while 1 represents Malicious data. The confusion matrices obtained from these classifiers are presented in Figure 4

Table 3. Some data from dataset.

| P	Ri	Rp	Li	Lp	Mh	Sh	L	Dh	Class
tcp	80.75.212.9	42196	165.227.180.71	8697	f7f3a1b1a76482b3d2e3b5b5b06f072a	82e7da3fa6cbd0cbc51670637a99b8701a974c9723515fb146c36acd05cca8527e7019a2030426cfcc150a6b50de92753efa159fb978e29ca570a25fecc23586	105	434f4e4e454354207777772e676f6f676c652e636f6d3a34343320485454502f312e310d0a486f73743a207777772e676f6f676c652e636f6d0d0a557365722d4167656e743a204d6f7a696c6c612f352e300d0a436f6e6e656374696f6e3a20636c6f73650d0a0d0a	benign
tcp	192.155.90.220	62806	165.227.180.71	8098	4643f0885b733a87ca7674674d4bfed5	a1893f0d5155e3e6e5dbda0c0afa2cb20666d0fb147913e927b50b75c4af9ab74db54d05083f5a89023a93868f87a8f1721c16838044382003f0792da9f08a2a	239	16030100ea010000e60303c11726e29b15ca160dc139358664ae3a462be91f05a769ed31afb2284195033f20d34616321b8909d6bc0043975afee318ba161c33c3d63b1ae9f4f23d5289c1790026c02bc02fc02cc030cca9cca8c009c013c00ac014009c009d002f0035c012000a13011302130301000077000500050100000000000a000a0008001d001700180019000b0002010000d001a00180804040308070805080604010501060105030603020102035ff0100010000120000002b000504030403030033002600240011d0020de063782f7afd56a605fceb4c3f52f82af9ee40d9af817ee15ed5b700c6f4c22	malicious
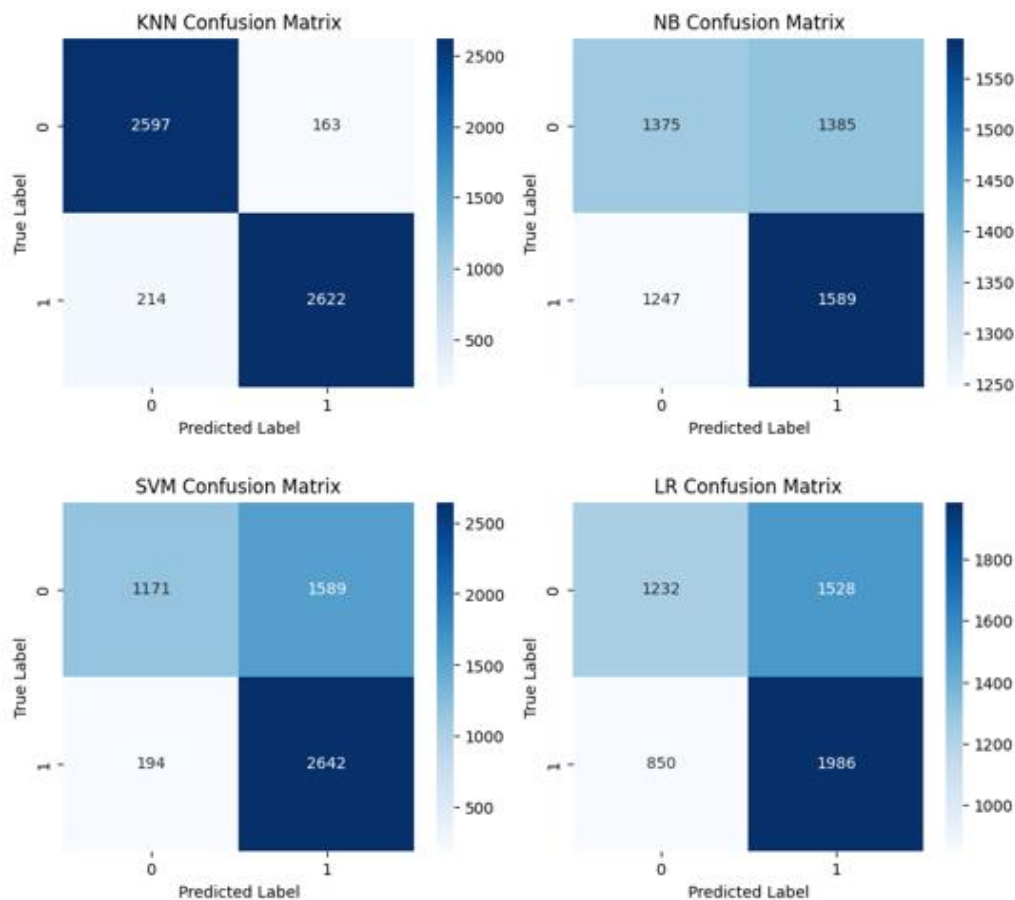
Figure 4. Confusion matrix of Classifiers.

When the confusion matrices presented in Figure 4 are examined, it is seen that the most successful classifier is KNN. The values that the KNN classifier incorrectly predicted are close to each other. The KNN classifier predicted 163 images belonging to the benign class as malicious. It predicted 214 images belonging to the malicious class as benign. It is undesirable for false negative values to be high. Because the model predicts the malicious data as benign.

After this step, the model is trained for classification by entering 100 epochs and 32 batch size values with the Residual CNN model. 80% of the dataset is used for training. The training accuracy obtained after the training of the model is 94.57%. Then, the test step of the model is performed with the test data. The remaining 20% of the data is used at this stage. The test accuracy is calculated as 94.9%.

The confusion matrix of the proposed model is given in Figure 5. In the confusion matrix, 0 represents Benign data, while 1 represents Malicious data. When the values in the confusion matrix are examined, it is seen that the Benign correct detection rate TN is recognized with a high value of 2592 and the FP with a relatively low value of 168. Similarly, while the Malicious correct prediction TP has a high value of 2717, it is seen that the FN has a low value of 119. When the confusion matrices of the classifiers accepted in the literature are examined in Figure 5, it is seen that the FN value is 214 in the KNN classifier, 1247 in NB, 194 in SVM, and 850 in LR. In the proposed model, this value is 119. The FN value in the proposed model is much lower than that of others.
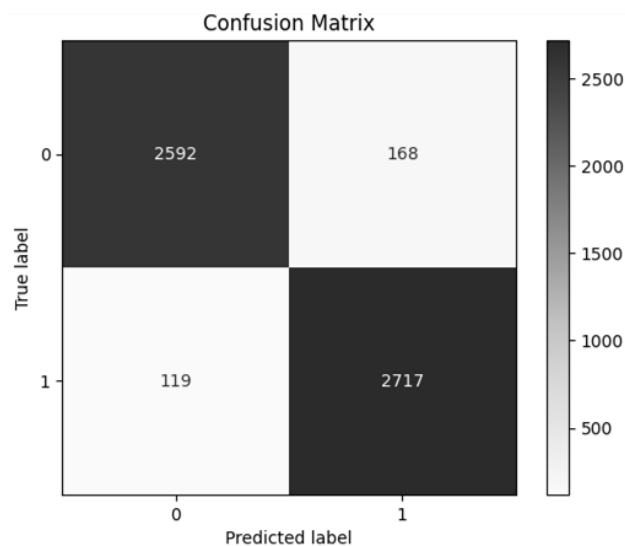

Figure 5. Confusion matrix of Proposed Model

As a result of all these evaluations, it is seen that the proposed model has a high rate of correct prediction in both classes and exhibits a good performance. While the FP and FN rates support the good performance of the model in the low probability, it also increases the general

accuracy of the model and the Balanced Accuracy and Specificity values, which are the balance indicators between the classes, by increasing the indicators such as Precision and Recall. Table 4 provides the performance metrics of the models used to obtain the application results in the study.

Table 4. Performance metrics of models (%).

	Accuracy	Precision	Recall	Specificity	F1	MCC	Balanced Accuracy
KNN	93.26	93.27	93.26	94.09	93.26	0.86	93.27
NB	52.97	52.94	52.97	49.82	52.92	0.06	52.92
SVM	68.14	73.96	68.14	42.43	65.90	0.41	67.79
LR	57.51	57.83	57.51	44.64	56.80	0.15	57.33
Proposed Model	94.90	94.20	95.80	93.90	95.00	0.90	94.90

When Table 4 is examined, it is seen that the highest accuracy value of 94.90% is obtained in our proposed Residual CNN model. This is predicted by KNN, SVM, LR, and NB classifiers, respectively.

4   CONCLUSION

Thanks to the spread of internet networks and digitalization, information security and privacy issues have come to the forefront, and attacks to seize or damage this information are increasing daily. Detection and prevention of these attacks will prevent possible material and moral losses. For this purpose, classification was performed with a ready-made dataset belonging to the MitM attack type in this study. The data was first transformed and digitized in the study, and normalization was applied. After these processes, the developed Residual CNN architecture performed the classification process. It is seen that the packets were correctly classified with a 94.9% accuracy rate in the classification step. This study reveals that the Residual CNN architecture, which is a deep learning method in the detecting network attacks, detects malicious packets with a high accuracy rate and can be used for network security. In this way, it is seen that good points will be reached in terms of protecting network security and data integrity by utilizing deep learning architectures to prevent data loss, material losses, and personal information theft.

Conflict of Interest Statement

There is no conflict of interest between the authors.

Statement of Research and Publication Ethics

The study is complied with research and publication ethics.

Artificial Intelligence (AI) Contribution Statement

This manuscript was entirely written, edited, analyzed, and prepared without the assistance of any artificial intelligence (AI) tools. All content, including text, data analysis, and figures, was solely generated by the authors.

Contributions of the Authors

Mücahit Karaduman contributed to the experimental studies, data interpretation, and the preparation of the manuscript. Sercan Yalçın contributed to the experimental studies and the preparation of the manuscript. Muhammed Yıldırım contributed to the experimental studies.

REFERENCES

[1]   Aweya J. IP router architectures: an overview. Int. J. Commun. Syst. 2001; 14(5); 447–475.

[2]   Femenias G, Lassoued N, Riera-Palou F. Access point switch ON/OFF strategies for green cell-free massive MIMO networking. IEEE access 2020; 8: 21788–21803.

[3]   Mirkovic J, Reiher P. A taxonomy of DDoS attack and DDoS defense mechanisms. ACM SIGCOMM Comput. Commun. Rev. 2004, 34(2): 39–53.

[4]   Pingle B, Mairaj A, Javaid A Y. Real-world man-in-the-middle (MITM) attack implementation using open source tools for instructional use. in 2018 IEEE International Conference on Electro/Information Technology (EIT), 2018, pp. 192–197.

[5]   S. Gupta, A. Singhal, and A. Kapoor, "A literature survey on social engineering attacks: Phishing attack," in *2016 international conference on computing, communication and automation (ICCCA)*, 2016, pp. 537–540.

[6]   R. Rawat and S. K. Shrivastav, "SQL injection attack detection using SVM," *Int. J. Comput. Appl.*, vol. 42, no. 13, pp. 1–4, 2012.

[7]   K. Lee, J. Kim, K. H. Kwon, Y. Han, and S. Kim, "DDoS attack detection method using cluster analysis," *Expert Syst. Appl.*, vol. 34, no. 3, pp. 1659–1665, 2008.

[8]   J. Ye, X. Cheng, J. Zhu, L. Feng, and L. Song, "A DDoS attack detection method based on SVM in software defined network," *Secur. Commun. Networks*, vol. 2018, no. 1, p. 9804061, 2018.

[9]   U. Ince and G. Karaduman, "Classification of Distributed Denial of Service Attacks Using Machine Learning Methods," *NATURENGS*, vol. 5, no. 1, pp. 15–20, 2024.

[10]   M. A. Al-Shareeda, S. Manickam, and M. A. Saare, "DDoS attacks detection using machine learning and deep learning techniques: Analysis and comparison," *Bull. Electr. Eng. Informatics*, vol. 12, no. 2, pp. 930–939, 2023.

[11]   A. R. Shaaban, E. Abd-Elwanis, and M. Hussein, "DDoS attack detection and classification via Convolutional Neural Network (CNN)," in *2019 Ninth International Conference on Intelligent Computing and Information Systems (ICICIS)*, 2019, pp. 233–238.

[12]   A. A. Najar, M. N. Sugali, F. R. Lone, and A. Nazir, "A novel CNN-based approach for detection and classification of DDoS attacks," *Concurr. Comput. Pract. Exp.*, vol. 36, no. 19, p. e8157, 2024.

[13]   A. A. Najar and S. M. Naik, "Cyber-secure SDN: A CNN-based approach for efficient detection and mitigation of DDoS attacks," *Comput. \& Secur.*, vol. 139, p. 103716, 2024.

[14]   C. Padmavathy *et al.*, "1D CNN Based Model for Detection of DDoS Attack," in *2024 2nd International Conference on Device Intelligence, Computing and Communication Technologies (DICCT)*, 2024, pp. 1–6.

[15]   A. Kumar, I. Sharma, S. Mittal, and others, "Enhancing Security through a Machine Learning Approach to Mitigate Man-in-the-Middle Attacks," in *2024 IEEE 9th International Conference for Convergence in Technology (I2CT)*, 2024, pp. 1–6.

[16]   K. V. Rao, B. R. Akshaya, G. G. Satvik, B. Rohith, and G. C. B. Lahari, "Machine Learning based Man-in-the-Middle Attack Prediction," in *2024 3rd International Conference on Applied Artificial Intelligence and Computing (ICAAIC)*, 2024, pp. 1393–1399.

[17]   M. Iddrisu, K. Takyi, R.-M. O. M. Gyening, K. O. Peasah, L. A. Banning, and K. Owusu-Agyemang, "An improved man-in-the-middle (MITM) attack detections using convolutional neural networks," *Multidiscip. Sci. J.*, vol. 7, no. 3, p. 2025129, 2025.

[18]   E. S. Shombot, G. Dusserre, R. Bestak, and N. B. Ahmed, "An application for predicting phishing attacks: A case of implementing a support vector machine learning model," *Cyber Secur. Appl.*, vol. 2, p. 100036, 2024.

[19]   M. Irsan, F. Febriana, H. H. Nuha, and H. R. P. Sailellah, "Phishing Detection on URL Data Using K-Nearest Neighbors Method," in *2024 International Conference on Innovation and Intelligence for Informatics, Computing, and Technologies (3ICT)*, 2024, pp. 792–797.

[20]   P. R. Uyyala, "Phishing email detection using CNN," *J. Eng. Technol. Manag.*, vol. 72, pp. 1046–1051, 2024.

[21]   B. B. Gupta, A. Gaurav, R. W. Attar, and V. Arya, "A Novel Cuckoo Search-Based Optimized Deep CNN Model for Phishing Attack Detection in IoT Environment," 2024.

[22]   R. D. N. Shakya, D. N. S. Dharmaratne, and M. Sandirigama, "Detection of SQL Injection Attacks Using Machine Learning Techniques," in *2024 International Conference on Electrical, Communication and Computer Engineering (ICECCE)*, 2024, pp. 1–6.

[23]   H. C. Altunay, "Detection of SQL Injection Attacks Using Machine Learning Algorithms Based on NLP-Based Feature Extraction," in *2024 9th International Conference on Computer Science and Engineering (UBMK)*, 2024, pp. 468–472.

[24]   M. Thilakraj, S. Anupriya, M. M. Cibi, and A. Divya, "Detection of SQL Injection Attacks," in *2024 International Conference on Inventive Computation Technologies (ICICT)*, 2024, pp. 1515–1520.

[25]   W. Zhao, J. You, and Q. Chen, "SQL Injection Attack Detection Based on Text-CNN," in *Proceedings of the 2024 International Conference on Generative Artificial Intelligence and Information Security*, 2024, pp. 292–296.

[26]   M. Shahbaz, G. Mumtaz, S. Zubair, and M. Rehman, "Evaluating CNN Effectiveness in SQL Injection Attack Detection," *J. Comput. \& Biomed. Informatics*, vol. 7, no. 02, 2024.

[27]   Kocyigit, E., Korkmaz, M., Sahingoz, O. K., & Diri, B. (2024). Enhanced feature selection using genetic algorithm for machine-learning-based phishing URL detection. Applied sciences, 14(14), 6081.

[28]   Mankar, N. P., Sakunde, P. E., Zurange, S., Date, A., Borate, V., & Mali, Y. K. (2024, April). Comparative Evaluation of Machine Learning Models for Malicious URL Detection. In 2024 MIT Art, Design and Technology School of Computing International Conference (MITADTSoCiCon) (pp. 1-7). IEEE.

[29]   M. S. Saadoon and S. F. Behadili, "Malicious network dataset," 2024, *Zenodo*. doi: 10.5281/ZENODO.14559922.

[30]   Kohavi, R. (1996, August). Scaling up the accuracy of naive-bayes classifiers: A decision-tree hybrid. In Kdd (Vol. 96, pp. 202-207).

[31]   Hosmer Jr, D. W., Lemeshow, S., & Sturdivant, R. X. (2013). Applied logistic regression. John Wiley & Sons.

SEISMIC PERFORMANCE OF THE KAHRAMANMARAŞ EARTHQUAKES: GROUND MOTION PREDICTION MODELS AND THE ROLE OF VERTICAL COMPONENTS

Ömer Faruk Nemutlu [1] *, Ali Sarı [2]

1 Bingöl University, Civil Engineering Department, Bingöl, Türkiye

2 İstanbul Teknik University, Civil Engineering Department, İstanbul, Türkiye

* Corresponding Author: ofnemutlu@bingol.edu.tr

ABSTRACT

On February 6, 2023, two very large earthquakes occurred in Türkiye. These earthquakes occurred on the Eastern Anatolian Fault, one of the most active fault zones in Türkiye. After two earthquakes occurred 9 hours apart, with Pazarcık (7.7 Mw) and Elbistan (7.6 Mw) epicenters, 11 cities of the country were directly affected by the earthquake. In addition to a significant number of casualties, structural damage caused by the earthquake occurred. Ground motion prediction equations (GMPEs), in short, are used to estimate the impact/value that the acceleration/velocity/spectral parameters etc. of a wave moving from an earthquake source can create in a study area. With the help of these attenuation relations, various earthquake parameters can be estimated depending on distance. In this study, the peak ground acceleration (PGA) values obtained from the stations taking measurements during the Kahramanmaraş earthquakes were examined using 6 different attenuation relations valid for Türkiye. In the study, data from 105 different stations measured during the Kahramanmaraş earthquake were used. In addition, the vertical earthquake effect caused by the earthquake was evaluated in terms of Turkish seismic code conditions. Looking at the study results; The approach of ground classifications, the fact that the acceleration values of the Kahramanmaraş earthquake remained above the curves of the attenuation relations and the failure to consider different earthquake characteristics have shown that the current attenuation relations are weaknesses. It has been observed that earthquake data deviate in a certain distance region in all attenuation relations. The GMPEs generally did not show high agreement with the Kahramanmaraş earthquake data. For this reason, the situations that should be taken into consideration when preparing a new decay relationship are examined. Finally, it was concluded that the higher-than-expected vertical earthquake effects were not assessed correctly in the code and therefore the vertical acceleration spectra given in the code should be updated.

Keywords: GMPEs, Kahramanmaras earthquakes, Seismic codes, Vertical earthquake effect.

1   INTRODUCTION

There are 3 main stages to assess earthquakes. These are before the earthquake, during the earthquake and after the earthquake. Before an earthquake occurs, precautions are taken to minimize the damage that earthquakes will cause. During an earthquake, personal protection is required and afterward, it is necessary to move away from the structures with minimum impact. In the post-earthquake stage, there are search and rescue activities, damage assessment and debris removal and finally reconstruction processes. Among these processes, if the earthquake that occurs after the earthquake is a destructive earthquake, the damage assessment stage is an important stage in terms of precautions to be taken for subsequent earthquakes.

There are many studies in the literature on the structural damages that occurred after the February 6, 2023 Kahramanmaraş earthquakes and the causes of these damages. The studies conducted are on the assessment of seismic hazard, examination of earthquake characteristics, structural and non-structural damages, types of damage in reinforced concrete structures, examination of damage in masonry structures, damages in industrial structures, and assessment of losses.

The February 6, 2023 Kahramanmaraş earthquake caused severe damage to masonry buildings in Adıyaman. The collapse mechanisms of these buildings were examined, spectral acceleration values were analyzed, and reinforcement recommendations were presented [1]. The February 6, 2023 Kahramanmaraş earthquake caused serious damage to industrial structures; various structural damages were observed in liquid storage tanks, grain silos, prefabricated reinforced concrete structures and steel industrial structures[2]. In another study, the causes of damage to reinforced concrete buildings in Adıyaman were evaluated in terms of material quality, design errors and reinforcement details [3]. After the Kahramanmaraş earthquake, seismic analysis of historical masonry buildings was evaluated with field observations and advanced calculations. Nonlinear finite element analyses performed on a historical building in Hatay confirmed the observed damage mechanisms and reinforcement recommendations were presented [4]. The February 6, 2023 Kahramanmaraş earthquake caused major structural damage in Hatay. In the study, the causes of damage to reinforced concrete and steel structures were examined, construction defects and design errors were evaluated and recommendations based on TSC-2018 were presented [5]. High PGA values were measured in Kahramanmaraş earthquakes. When Disaster and Emergency Management Affair (DEMA) stations were examined, the highest PGA was seen in the east-west component of station 4614

for the Pazarcık epicenter earthquake. The value measured as 2.006g exceeds the design spectrum with a return period of 2475 years specified in the Turkish Seismic Code 2018[6]. Other stations with high PGA values are 3135, 3129, 3125 and 3126, respectively [7].

One of the most important areas of earthquake science is seismic hazard analysis. With seismic hazard analysis, the data of past earthquakes and the effects of expected future earthquakes can be predicted. In seismic hazard analysis, there are two approaches as probabilistic and deterministic seismic hazard analysis.

In deterministic hazard analysis, analysis is carried out for the largest earthquake and the most unfavorable single earthquake at the shortest distance [8]. In probabilistic seismic hazard analysis, analysis is carried out with a probabilistic approach, thinking about every magnitude and every earthquake distance that is likely to occur within the study area. Seismic hazard analysis consists of 4 stages in the most general sense (Figure 1). These stages are as follows:

● Modeling of seismic sources

●Magnitude-Recurrance relationships

●Attenuation models

●Probabilistic acquisition of probabilistic probabilities of exceeding an earthquake parameter (obtaining Earthquake Hazard Maps)

These stages are followed sequentially, and seismic hazard analysis are carried out and the effects of earthquakes (e.g. S_a, PGA, PGV, etc.) are predicted. One of the most important steps in making these predictions correctly is the correct selection of the attenuation relations to be used. The attenuation model should reflect the earthquake, fault characteristics, earthquake magnitude, distance of the earthquake to the study area, and specific earthquake characteristics caused by the earthquake well and accurately. For this reason, when performing seismic hazard analyzes in a region, the most appropriate GMPE should be determined for the region or new GMPEs should be created and used for that region [9].
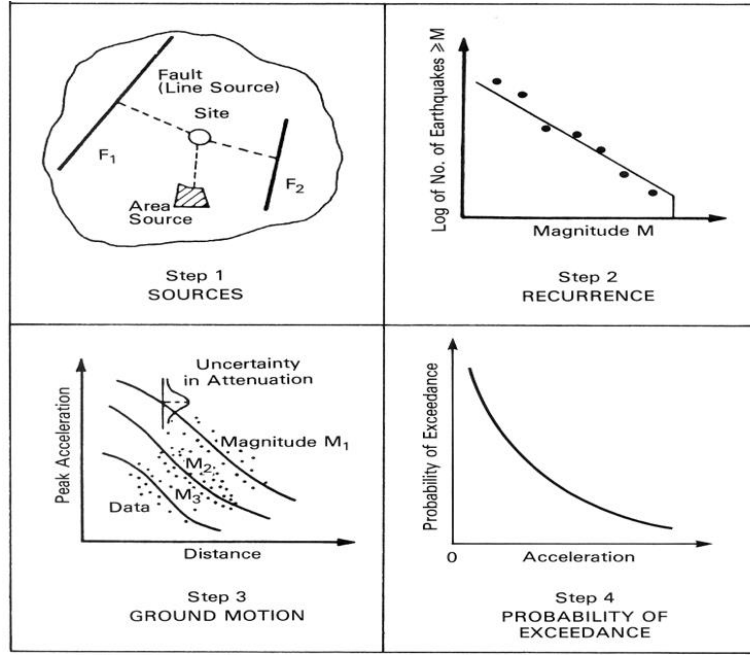
Figure 1. Stages of seismic hazard analysis[8].

Seismic hazard analyses for cities in Türkiye are available in the literature [10]. Seismic hazard analyses were performed for Sakarya province, and peak ground acceleration and spectral acceleration maps were produced according to different exceedance probabilities. In addition, possible fault distances and earthquake magnitudes were determined, and comparisons were made with the seismic code. It was observed that the accelerations obtained after the hazard analysis had values above the hazard maps [11]. The seismic hazard of Kahramanmaraş and its surroundings was assessed by the probabilistic method, and the East Anatolian Fault and Bitlis Thrust Belt were determined as the riskiest regions. The calculated acceleration values were compared with the Türkiye Earthquake Zones Map and regional harmony was analyzed [12]. Probabilistic seismic hazard analysis was performed for Van province and maximum acceleration values were determined for different exceedance probabilities. The obtained results were compared with the components of the 2011 Van earthquakes and the spectrum curves recommended in the Turkish Earthquake Code. Simulated earthquake records were obtained to be used for performance analysis of buildings in Van province [13]. According to the probabilistic seismic hazard analysis results for Bingöl province, the peak ground acceleration values with a probability of being exceeded within 50 years of 2%, 10% and 50% in Bingöl province were determined as 1.03 g, 0.58 g and 0.24 g, respectively, and the recurrence periods were calculated as 42, 105, 266 and 670 years for earthquakes of magnitude 6.0, 6.5, 7.0 and 7.5, respectively. The results obtained reveal that the region is under high seismic hazard and the earthquake effect must be taken into consideration in the design of structures [9].

Attenuation relations are mathematical equations that model the interaction between ground and structures during an earthquake and predict the effects of ground motion on structures. These relations are used primarily in engineering applications to calculate the magnitude and propagation of ground motion based on factors such as soil class, distance, and local ground conditions. Using accurate attenuation relations plays a critical role in improving the safety and durability of buildings and other structural systems. In addition, these relations help optimize earthquake engineering designs and more accurately assess the effects of local fault zones and structural weaknesses. Therefore, the development and proper application of attenuation relations are of great importance in risk analysis and damage estimation.

During recent seismic events, it has been observed that the vertical component of ground motion surpasses the horizontal component. This is contrary to the assumption in current codes that the vertical motion is 1/2 to 2/3 of the horizontal component. Immediately after destructive earthquakes, engineers report that structural damage such as buckling in large columns or fractures in large reinforced concrete columns used in highway and building structures are caused by strong vertical ground motion. These findings indicate that seismic designs that ignore the vertical ground motion component pose serious safety risks, especially for structures constructed near active fault lines, and may increase the risk of collapse [14]. The general view of code engineers is that the vertical component of ground motion is lower than the horizontal component and the V/H ratio remains less than 1. Many codes recommend scaling a single spectrum obtained for the horizontal component using an average V/H ratio of 2/3. However, in this approach, it is assumed that all components of the vertical motion have the same frequency content. However, studies in nearby fault areas prove that the V/H ratio may be below 2/3 [15].

In this study, the compatibility with Kahramanmaraş earthquake data was evaluated by using various GMPEs used in Türkiye and the world. The aim of this study is to observe how the existing GMPEs converge with an up-to-date earthquake data. Thus, by revealing the weaknesses and strengths of these attenuation relations, it will be seen which situations should be assessed when creating a new GMPE for this region. In addition, an evaluation of the horizontal and vertical acceleration values obtained from the stations that took records in the Kahramanmaraş earthquakes was also made in the study. This evaluation was compared over the spectra in the Turkish seismic code. In the following sections of the review, the results obtained are examined with their justifications.

2   MATERIAL AND METHOD

2.1   06 February 2023 Earthquakes and Seismicity of the Region

The East Anatolian Fault Zone (EAFZ) is one of the active fault zones that has produced significant earthquakes throughout history. It has come to the fore especially with the 2020 Sivrice, Elazig and 2023 Kahramanmaraş earthquakes that have occurred in recent years and has been the center of attention of researchers [16], [17], [18]. This fault zone, which starts from the Karlıova district of Bingöl and extends to Hatay, fully meets the characteristics of lateral slip faults. Figure 2; It shows important active fault zones and plates in Türkiye [19], [20].
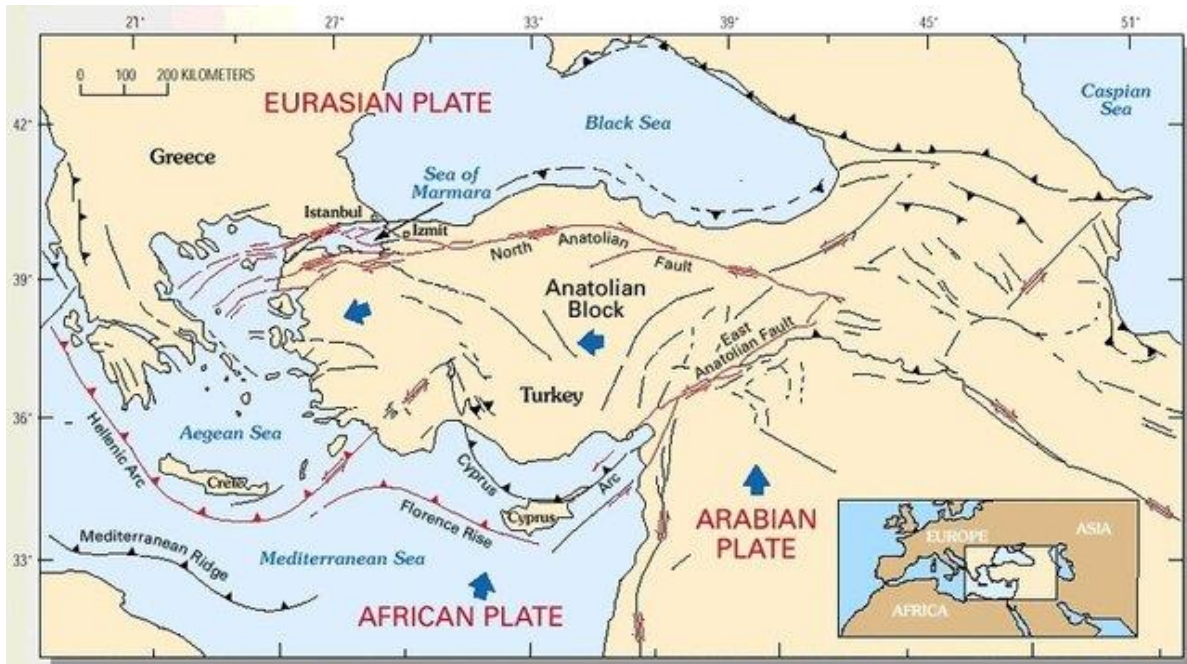
Figure 2. Important active fault zones in Türkiye [20].

This fault line (EAFZ), located at the junction of the Arabian plate and the Anatolian plate, produced 2 major earthquakes on February 6, 2023, 9 hours apart [21]. Some views suggest that the first earthquake (Pazarcık M_w 7.7) that occurred on February 6, 2023 did not start directly on the East Anatolian Fault, but instead occurred on the previously unmapped Narlı Fault. However, other studies argue that the earthquake started directly on the East Anatolian Fault. Therefore, there are different scientific approaches to the earthquake's starting point and the rupture mechanism on the fault plane [22] [23]. The epicenter of the first earthquake was Pazarcik, with a magnitude of 7.7 M_w [24]. The surface deformation on this earthquake-induced fault is about 300 km [25]. The second earthquake occurred at noon on the same day with a magnitude of 7.6 M_w centered in Elbistan [24]. These two earthquakes caused significant structural damage and loss of life. 11 provinces in Türkiye were affected by the

earthquake [26]. The earthquake was also felt in Syria and caused casualties. According to official data, the loss of life in 11 provinces caused by the 2023 Kahramanmaraş earthquakes is over 50000. The provinces affected after the earthquake are larger than many countries in Europe in terms of surface area. The map showing the epicenter of the earthquake and aftershock activity is given in Figure 3.
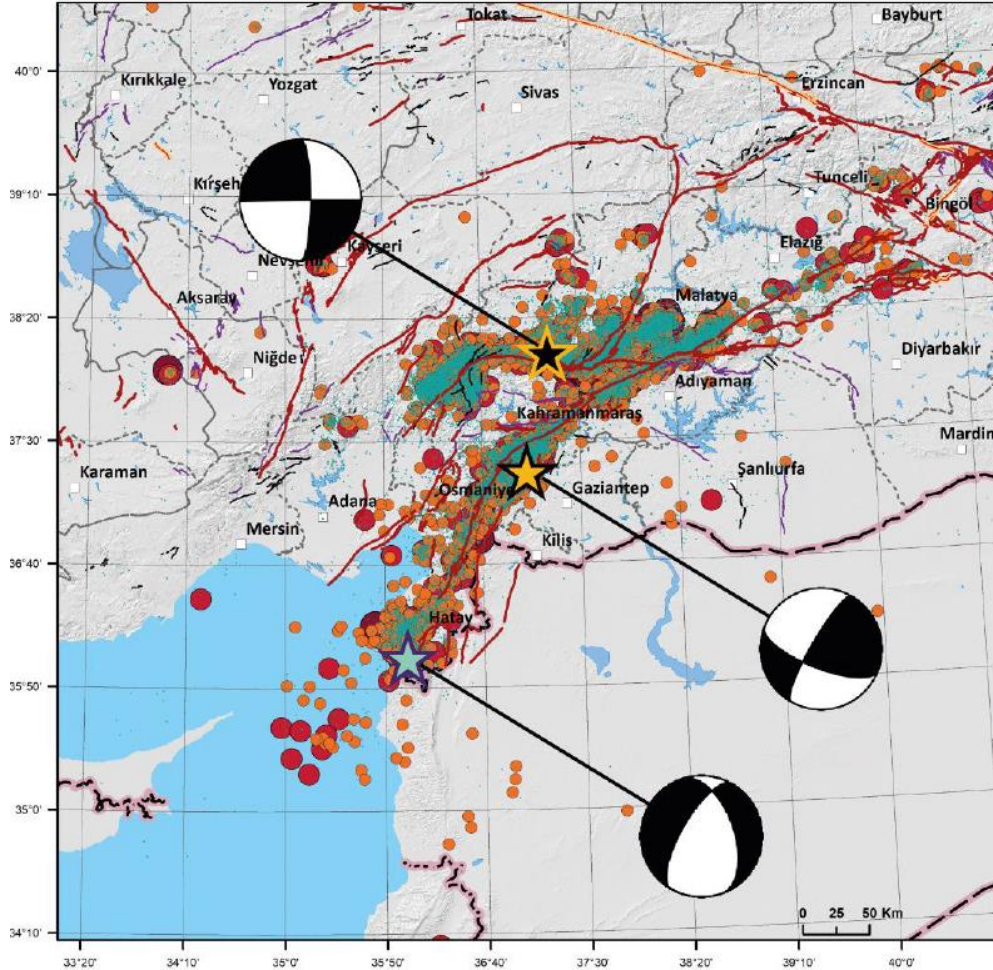

Figure 3. Epicenters of the earthquake, mainshock and aftershock activities [24].

After such a big earthquake, many researchers have carried out studies in the field and continue their research [5], [16], [27]. Having very important data in this field is seen as an advantage. Because it has benefited from significant advancements in earthquake science after every major earthquake.

2.2   Selection of Earthquake Records

To make a comparison with the attenuation relations, the stations that took records in the 2023 Kahramanmaraş earthquakes andT the data of these stations were used. The stations used in

the study are the stations belonging to Disaster and Emergency Management Affair (DEMA). Figure 4 below shows the distribution of the stations that take records.

The records used in the study were filtered by considering the distance class evaluated by the attenuation relations. The records used in this study include records of stations at 200 km or less from the epicenter. Table 1 provides information about the stations used in the study. The horizontal and vertical components of the greatest ground acceleration are the R_{JB}, R_{rup}, R_{epi} and R_{hyp} distances, Vs_{30} values and the soil classification made according to Eurocode8 [28] (according to Eurocode8 Table 3.1) is the information given in Table 1. R_{epi} is the distance from the epicenter, i.e. the point on the ground where the earthquake occurred, to the study area. R_{hyp} is defined as the distance between the focus of the earthquake and the study area. R_{rup} is defined as the distance between the fracture caused by the earthquake and the study area, while the Joyner-Boore distance, i.e. the distance between the fracture projection on the plane and the study area. In another definition, the Joyner-Boore distance is defined as the shortest distance to the fault surface. In general, when the studies are examined, the R_{rup} and R_{JB} values are accepted as equal [29]. In the examination, stations with unknown Vs_{30} value were considered in the study as D ground class. Its acceptance as D ground class was determined by making an acceptance as in the report published by Boğaziçi University. In the Bogazici earthquake report, ZC ground class was accepted for stations whose ground class was unknown [21].

Table 1. Codes of 105 stations belonging to the DEMA observation network used in the study.

| Station Codes							
0118	2712	3147	4620	0210	3134	4409	5807
0119	2718	3301	4621	0213	3135	4410	5809
0120	3112	3303	4624	0214	3136	4412	5810
0122	3115	3305	4625	2107	3137	4413	6203
0123	3116	3802	4628	2309	3138	4414	6302
0124	3123	3803	4629	2310	3139	4611	6303
0125	3124	3804	4630	2409	3140	4612	6304
0127	3125	3805	4631	2703	3141	4613	6305
0128	3126	4404	4632	2704	3142	4615	6306
0129	3129	4405	4701	2707	3143	4616	7901
0130	3131	4406	5102	2708	3144	4617	8002
0201	3132	4407	5103	2709	3145	4618	8003
0208	3133	4408	5805	2711	3146	4619	8004
		NAR			Note: The stations used are the stations belonging to the DEMA observation network.		
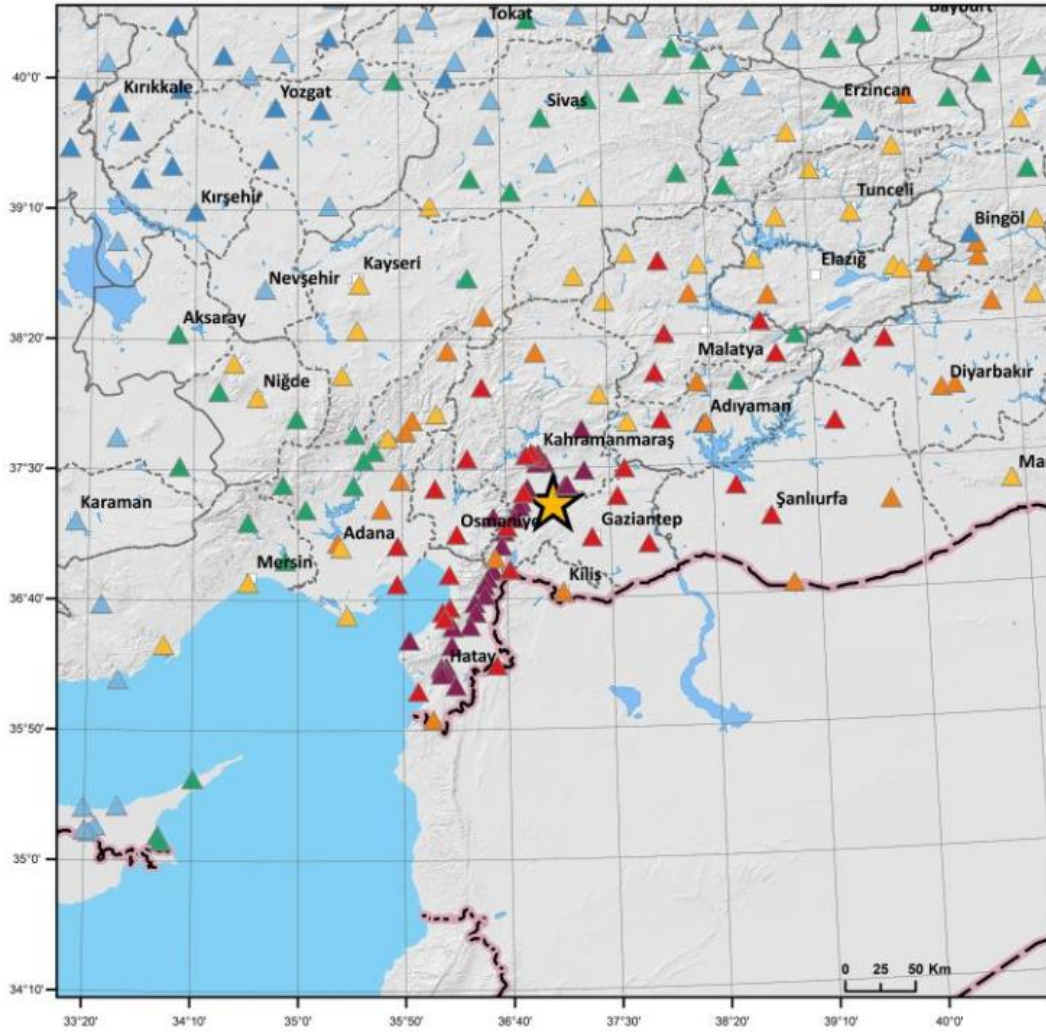
Figure 4. Distribution of record stations[24].

Records of a total of 105 stations were used in the study. The distribution of these records according to different soil classes is given in Table 2.

Table 2. Distribution of records used according to soil classes [28].

Soil Classes	Number of Records
A	11
B	56
C	12
D	26
Total	105

2.3   Ground Motion Prediction Equations (GMPEs)

In this study, a total of 6 GMPEs were used [30], [31], [32], [33], [34], [35]. All these relations are attenuation relations that have been developed for Türkiye and its surroundings or are suitable for use in Türkiye. GMPEs are usually prepared according to a specific region,

country or faults with similar characteristics. In the studies carried out, the suitability of the GMPE to the regions belonging to which characteristics are specified. This situation was evaluated when selecting GMPEs [31]. From the attenuation relations, Abrahamson et al. (2014)[30] are the attenuation relations, It is a GMPE prepared for the NGAWest2[36], [37] project and has applicability in many regions of the world. The names of the attenuation relations and the information about these attenuation relations are given in the Table 3 below.

When the parameters in the equations given in Table 3 are examined, expressions such as a, b, a1, b1 define the regression coefficients. M represents the relevant earthquake magnitude (generally the moment magnitude), R represents the distance to the study area, G_1, G_2, F_N, F_R, S_A, S_B are constant coefficients reflecting the ground properties, and r represents the hypotenuse of the distance between the study area and the fault focal point.

Table 3. Information on the 6 GMPEs Used.

GMPE publication	Equation	Explanation
Energy Considerations in Ground Motion Attenuation and Probabilistic Seismic Hazard Studies [34]	$log\ (Y_{ij})\ = a + b(M_i - 6) + c(M_i - 6)^2 + dlog\sqrt{R_{ij}^2 + h^2} + eG_1 + fG_2$	It was developed for the Northwest Marmara Region.
Site-Dependent Spectra Derived from Ground Motion Records in Türkiye[33]	$ln\ Y\ = b_1 + b_2(M - 6) + b_3(M - 6)^2 + b_5\ ln\ ln\ r\ + b_v ln\ (V_S/V_A)\ \ r = (r_{cl}^2 + h^2)^{\frac{1}{2}}$	It has been developed for the whole of Türkiye.
A Local Ground-Motion Predictive Model for Türkiye, and Its Comparison with Other Regional and Global Ground-Motion Models[31]	$M \leq c_1$ $ln\ (Y) = a_1 + a_2(M - c_1) + a_4(8.5 - M)^2 + [a_5 + a_6(M - c_1)]\ ln\ \sqrt{R_{jb}^2 + a_7^2} + a_8 F_N + a_9 F_R$ $M \geq c_1$ $ln\ (Y) = a_1 + a_3(M - c_1) + a_4(8.5 - M)^2\ [a_5 + a_6(M - c_1)]\ ln\ \sqrt{R_{jb}^2 + a_7^2} + a_8 F_N + a_9 F_R$	It was developed for Türkiye using data sets belonging to Italy and Türkiye.
An attenuation based on Turkish strong motion data and iso-acceleration map of Türkiye[35]	$PGA = 2.18^{0.0218(33.3M_W - R_e + 7.8427S_A + 18.9282S}$	It is a GMPE developed for Türkiye. The equation is formed in an exponential simple form. The way the equation is formed is different from the general form.

Table 3 (Continued). Information on the 6 GMPEs Used.

GMPE publication	Equation	Explanation
Empirical Equations for the Prediction of PGA , PGV, and Spectral Accelerations in Europe, the Mediterranean Region, and the Middle East[32]	$log\ (PSA)\ = b_1 + b_2 M + b_3 M^2 + (b_4 + b_5 M) log \sqrt{R_{jb}^2 + b_6^2} + b_7 S_S + b_8 S_A + b_9 F_N + b_{10} F_R + \epsilon \sigma$	It has been developed for the Mediterranean, European and Middle Eastern regions.
Summary of the ASK14 Ground Motion Relation for Active Crustal Regions[30]	$= a_1 + a_5 (M - M_1) + a_8 (8.5 - M)^2 + [a_2 + a_3 (M - M_1)] \ln(R) + a_{17} R_{RUP}$ M>M$_1$ $= a_1 + a_4 (M - M_1) + a_8 (8.5 - M)^2 + [a_2 + a_3 (M - M_1)] \ln(R) + a_{17} R_{RUP}$ M$_2$<M<M$_1$	It was developed for different regions on Earth as part of the NGAWest project.

3   RESULTS AND DISCUSSION

3.1   Evaluation of GMPEs

Within the scope of the study, 6 different GMPEs compatible with Türkiye were used from the attenuation relations in the literature. In the evaluation, a comparison was made with the PGA parameters obtained from the stations after the Kahramanmaraş earthquake. When making the comparison, the Magnitude value in the attenuation relations was taken as the M value of 7.7 M_w given by the earthquake [21]. In addition, curves were obtained by considering the standard deviation values specified in the attenuation relations, considering the + and - standard deviation values. In the study, soil properties were classified as A, B, C and D soils according to the Vs_{30} value specified in the records of the stations and the soil classification specified in [9]. The soil classification differs in the GMPEs used. For each GMPE, the records were analyzed according to the different ground grouping procedure. In attenuation relations, the way in which the size, distance and soil properties to be used are evaluated differs. Since it is an examination made after the earthquake, the magnitudes examined are clear. These quantities were used in Mw. The distances to the epicenter of the earthquake were evaluated based on the distance of the stations to the epicenter. Here, Joyner-Boore (R_{JB}) distances are used, which are consistent with the attenuation relations used [38]. Soil classifications were carried out because of coefficients or shear wave velocity values compatible with the definitions of each attenuation relation. Ground classification was made with the Vs_{30} values obtained from the information of the stations, and the curves of the attenuation relations were grouped.

All the GMPEs used in the study were obtained according to the PGA value. The obtained curves are intended to be compared with the PGA values measured by the stations. The graphs from Figure 5 to Figure 10 show the curves of the GMPEs and the PGA values obtained from the station. While the darker of the curves gives the main curve of the attenuation relation, the gray curves above and below this curve show the curves obtained if the standard deviation is regarded. The point values in red show the distribution of the PGA values of the stations divided into different soil classes.

The curves of the Sarı's GMPE used are given in Figure 5. The soil classification of the GMPE is given according to Vs_{30} values. In the GMPE, A and B soil classification were evaluated together. Since the coefficients used in the soil classification in the GMPE are the same on the A and B coefficents, they are given on the same curve. When the standard deviations are deemed, it is seen that the curves of the GMPE and the PGA values obtained from the stations are generally compatible. However, low compliance is observed at values between 50 and 100 km.
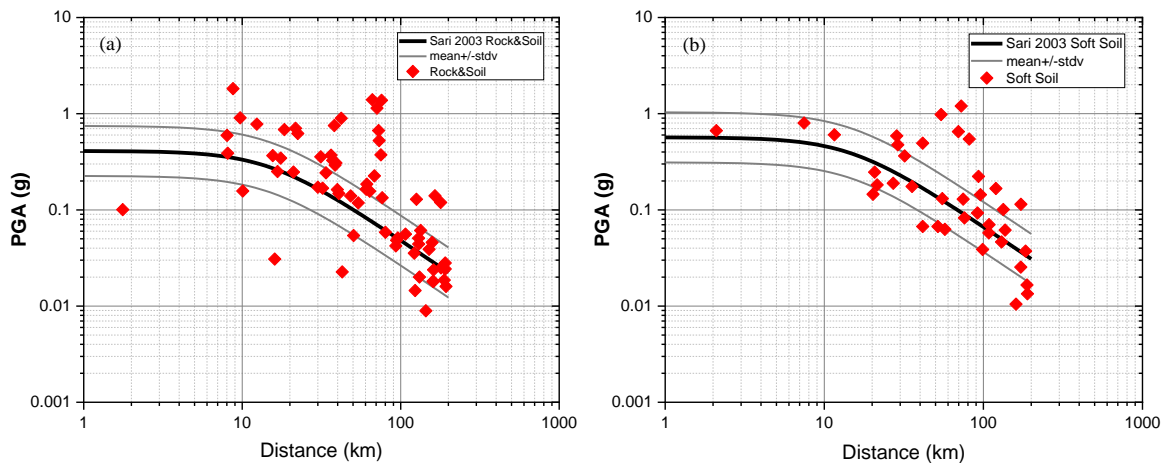
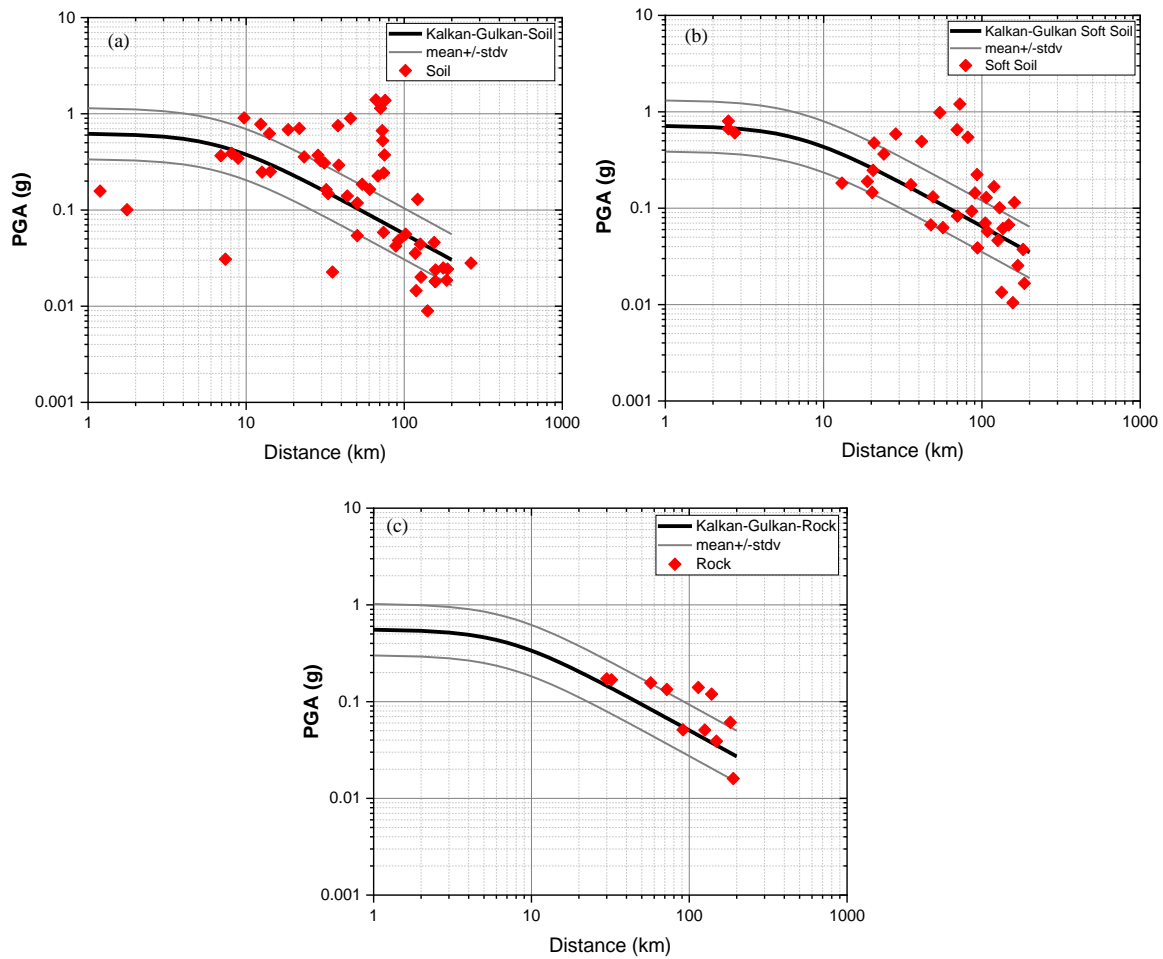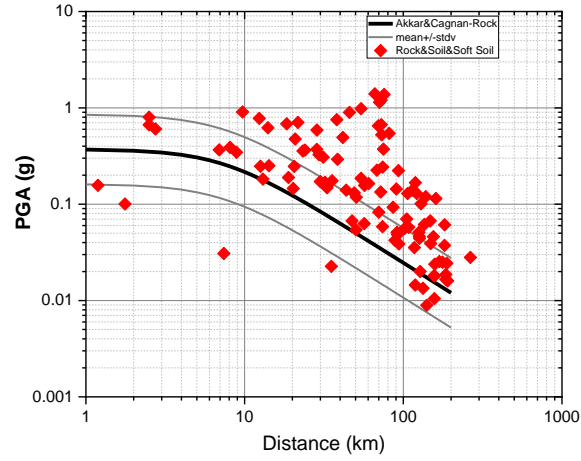***Figure 5. Comparison of Sari's model prediction of pga with observed data from Kahramanmaras earthquake for all soil classes (a) Rock&Soil (b) Soft Soil.***

Three different soil classes are defined according to the GMPEs used. This soil classification is divided into three groups. As the ground classes decrease, the harmony between them decreases. The soil classification in this GMPE was made according to Vs_{30} values. Elaboration of the soil classification in attenuation relations will increase the harmony in attenuation relations. In Figure 6, the curves of the GMPE are given. Although the harmony of the curve obtained for soils with high shear wave value (>700 m/sec) seems high, the low number of records makes it difficult to make a clear interpretation on this issue.

Akkar&Çağnan study[31], all the records used in this study were compared over a single curve of the GMPE. All records evaluated due to the assessment for the single soil class are marked on the curve. Significant deviations were observed in records between 10 and 100 km. This is because attenuation relations are given for a single ground. It is predicted that these deviations will take lower values if the classification of different soil classes is possible. The curve of the GMPE is given in Figure 7.

As shown in Table 3, the GMPE proposed by Ulusay et al. [35] was developed using a different approach compared to the general GMPE formulation. Although an equation in exponential form is typically expected to exhibit low compatibility, it demonstrates a behavior relatively similar to other attenuation relationships. Again, deviations are seen in similar distance regions in this GMPE. As with other GMPEs, Kahramanmaraş earthquake data are generally concentrated on the upper side of the curve. The curves of the GMPE are given in Figure 8 according to different soil classes.

Figure 6. Comparison of Kalkan and Gülkan's model prediction of pga with observed data from Kahramanmaras earthquake for all soil classes (a) Soil (b) Soft Soil (c) Rock.

Figure 7. Comparison of Akkar&Çağnan's model prediction of pga with observed data from Kahramanmaras earthquake for all soil classes.
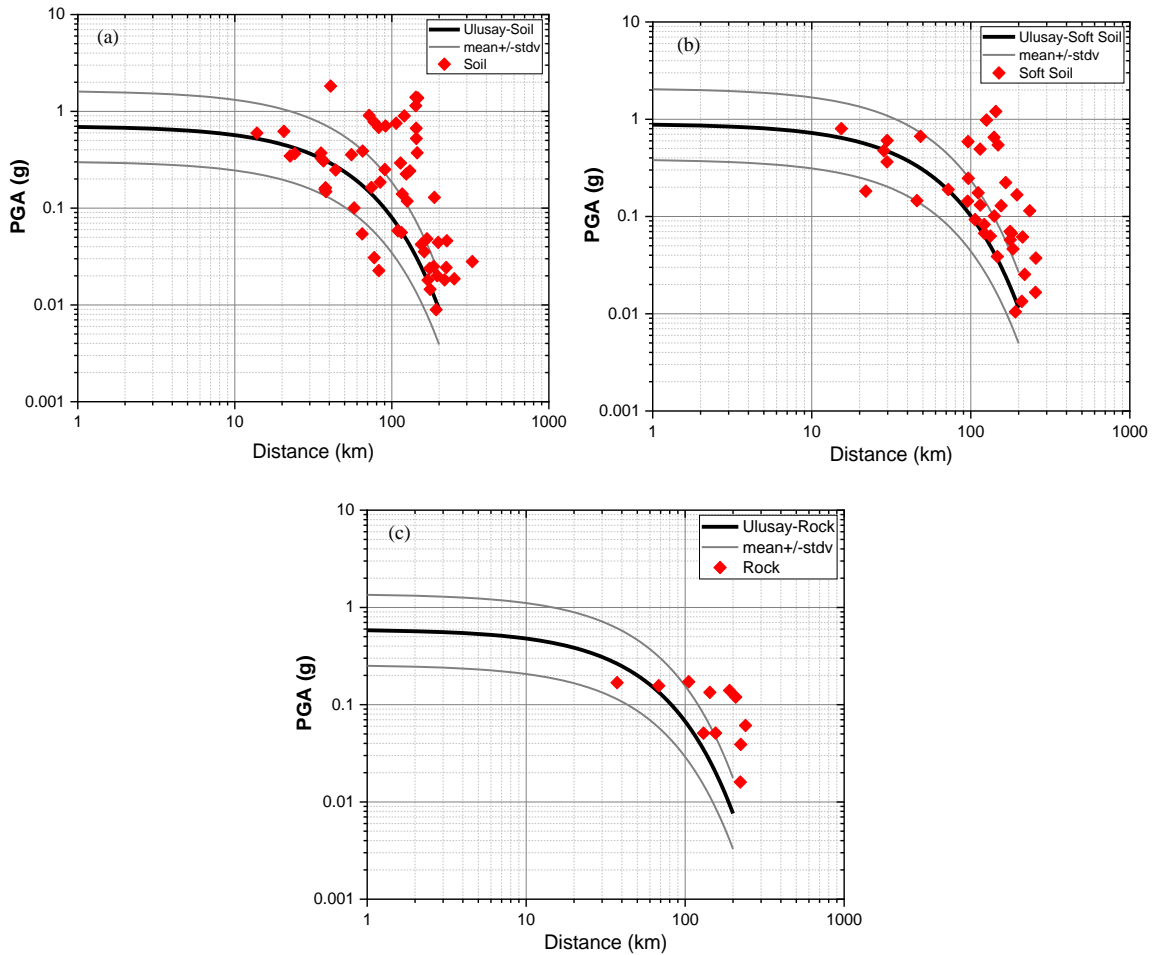

Figure 8. Comparison of Ulusay's model prediction of pga with observed data from Kahramanmaras earthquake for all soil classes (a) Soil (b) Soft Soil (c) Rock.

In this attenuation relation, two different curves of soil classification were obtained. The curve and earthquake data of the GMPE take values close to the curve on soft soils. However, the same deviations are present in similar distance zones. This situation is seen in all attenuation relations. These deviations may be related to the characteristics of the records. In addition, it may be due to the low reflectivity of the attenuation relations. The fact that the attenuation relations do not consider different earthquake characteristics (near fault effect, super-shear effect, orientation effects, etc.) and that the ground classifications make assumptions over the coefficients negatively affect the correct reflection. The curves of the GMPE are given in Figure 9. Abrahamson et al. [30], a GMPE prepared for different regions of the world, is given in Figure 10 for two different soil classifications. This GMPE proposes different equations by accepting a given Vs_{30} value and magnitude value as the threshold value. In Table 3, different GMPE equations of the study are given.
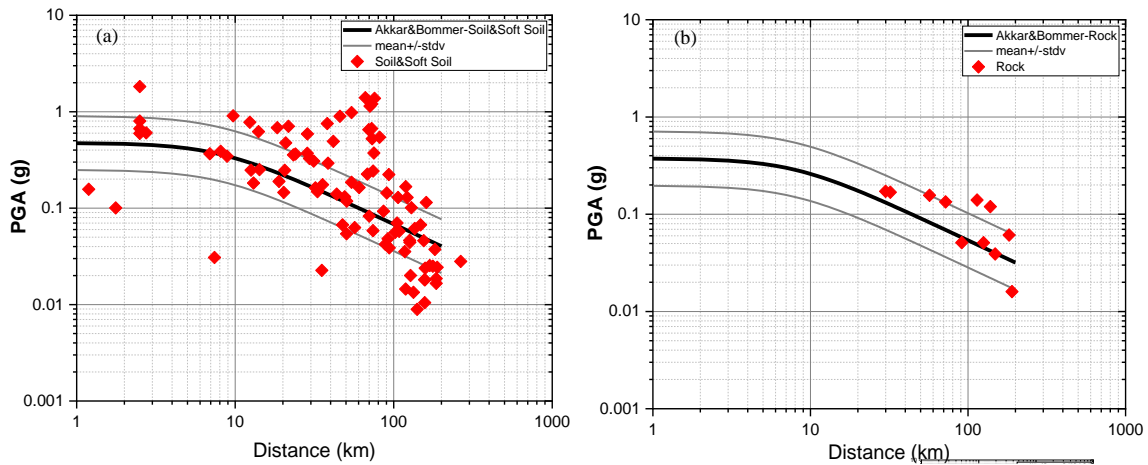

Figure 9. *Comparison of Akkar&Bommer's model prediction of pga with observed data from Kahramanmaras earthquake for all soil classes (a) Soil-Soft Soil (b) Rock.*
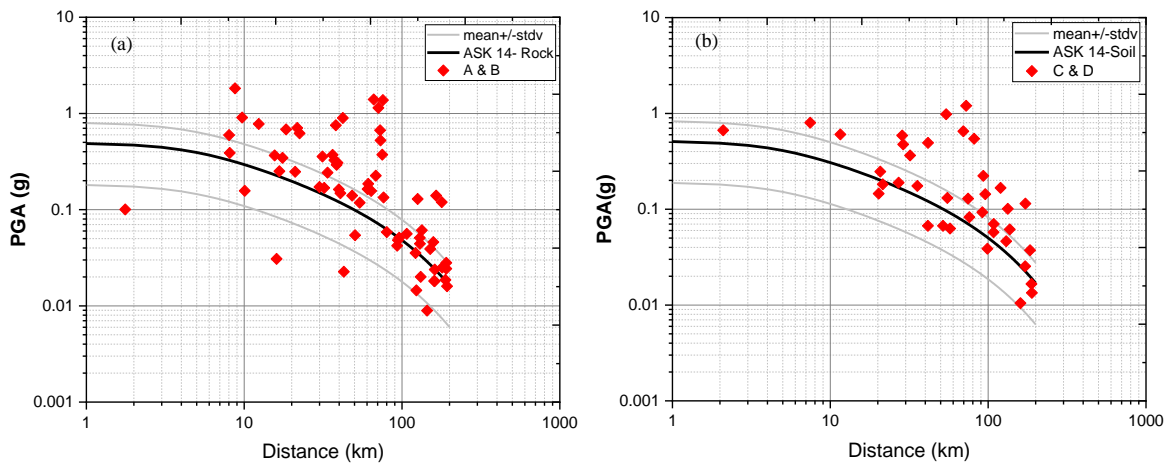

Figure 10. *Comparison of ASK14's model prediction of pga with observed data from Kahramanmaras earthquake for all soil classes (a) A&B (b) C&D.*

When we look at the agreement of the PGA values measured by the attenuation relations in the study, the agreement with the curves increases as the distance increases. As the ground class improves, the concordance of the attenuation relations and PGA values seems to be high, but the number of stations with good ground is low. Therefore, it becomes difficult to say that there is a connection between direct soil classification and PGA parameters. Since the characteristics of the earthquake under consideration are assessed differently in each GMPE, the power to predict the PGA parameters differs. For this reason, the different earthquake behaviors that occurred in the Kahramanmaraş earthquake make it difficult to comply with the PGA parameter of Altunsu et al. [5]. In the literature on the Kahramanmaraş earthquake, super-shear, near fault effect, basin effect, liquefaction and different ground behaviors do not coincide with the currently used GMPEs. This situation shows that there is a need for a new GMPE after the Kahramanmaraş earthquakes.

3.2   General assessment of GMPEs

The 6 different GMPEs used below, and the earthquake records used in the study of the Kahramanmaraş earthquake are given together. Although the agreement between PGA and GMPEs increases as we move away from the epicenter, it shows that it does not fully reflect the behavior of earthquake parameters. Different earthquake characteristics need to be taken into account and updated in GMPEs [39]. When the curves of the attenuation relations and the PGA values of the earthquake records are examined; it is seen that the earthquake records of the Kahramanmaraş earthquake take values above the attenuation relations. Although the standard deviation is examined for the + and – states for each attenuation relation, the standard deviation is positively dominant. In general, all the GMPEs reviewed remain under the Kahramanmaraş earthquake records. This situation reveals that the data sets need to be updated to predict high PGA values in the new GMPEs to be created.

Ground motion prediction equations (GMPEs) should account for significant earthquake characteristics such as near-fault effects, basin effects, and high vertical ground motion. Incorporating these factors into the equations will enhance the predictive accuracy of GMPEs. Although researchers like Somerville have conducted studies on integrating near-fault effects into attenuation relationships, these effects are not yet fully incorporated into contemporary approaches. Neglecting these factors may lead to an incomplete or inaccurate representation of the actual earthquake behavior.
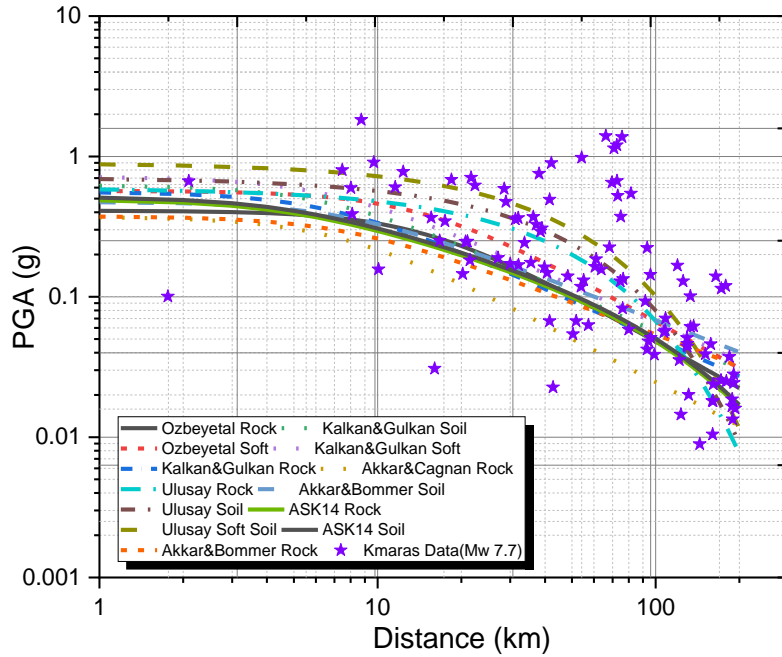
Figure 11. Comparison of the GMPEs.

4 EVALUATION OF HORIZONTAL AND VERTICAL EARTHQUAKE EFFECT

Kahramanmaraş earthquakes have shown us that the vertical earthquake effect is also a very important parameter. When the stations that take records are examined, very high vertical component values of the Kahramanmaraş earthquake are seen. Following the Kahramanmaraş earthquakes, it has been observed that the high vertical ground motion component contributed to increased structural damage levels. Figure 12 illustrates the damage caused by the high vertical ground motion effects during the Kahramanmaraş earthquakes. An analysis of earthquake records from the affected regions reveals the presence of high vertical ground motion components. Figure 13 presents the horizontal and vertical acceleration records from selected stations during the Kahramanmaraş earthquakes.

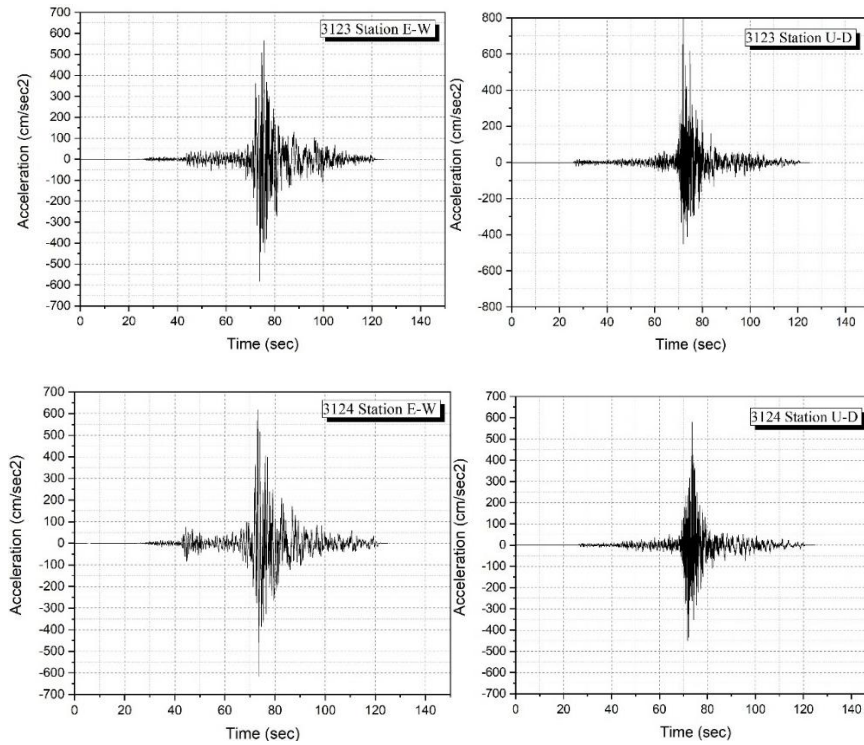*Figure 12. Damage caused by the high vertical earthquake effect.*

Figure 13. Horizontal and vertical acceleration time history for Kahramanmaraş Earthquake.

In this study, the ratios of the acceleration values of the largest component and the vertical direction from the horizontal components of the stations that took measurements in Kahramanmaraş earthquakes were obtained. The variation of these values with respect to R_{JB} distances is given in Figure 14. When Figure 14 is examined, the distribution of the change of the ratio of the vertical acceleration value to the horizontal acceleration value according to the distance is given. In this graph, a value of 0.8 is considered as the threshold value. The reason for this can be explained by the ratio between the spectra in the Turkish Seismic Code 2018[6].
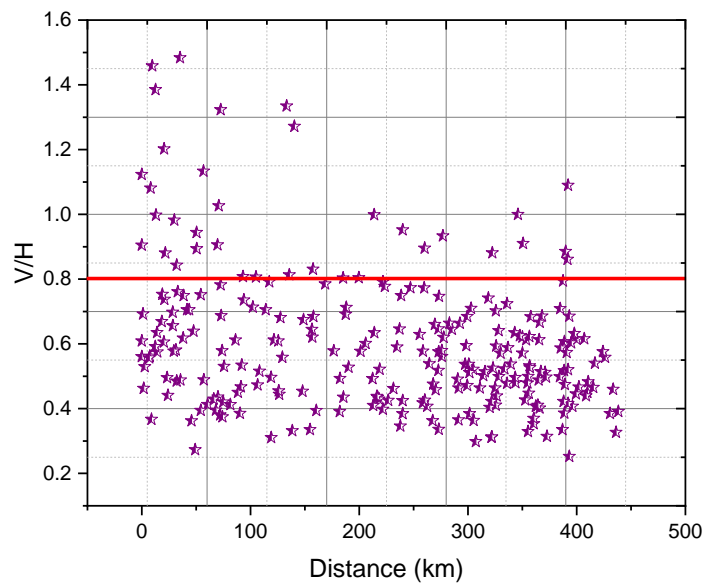

Figure 14. Variation of horizontal and vertical earthquake rates by stations[29].

Figure 15 shows the horizontal and vertical elastic spectra included in the Turkish Seismic Code 2018 (TSC 2018). When these spectra are examined, the minimum and maximum values of the spectral acceleration values of the spectrum are expressed with different values. There is a change of 0.8 between the values of the horizontal elastic spectrum and the vertical elastic spectrum. This situation means that; the earthquake code accepts that the ratio of horizontal and vertical earthquake effects to each other does not exceed 0.8. However, as can be seen in the figure above, there are many acceleration records in which the ratio of vertical and horizontal earthquake accelerations of Kahramanmaraş earthquakes exceeds 0.8. This situation shows that the vertical earthquake effect is a high effect in the Kahramanmaraş earthquake, and this effect should be considered in a different way in new studies and seismic codes. It has been observed that different characteristics of the earthquake, such as the vertical earthquake effect, should be analyzed correctly when considering the effects of the earthquake.
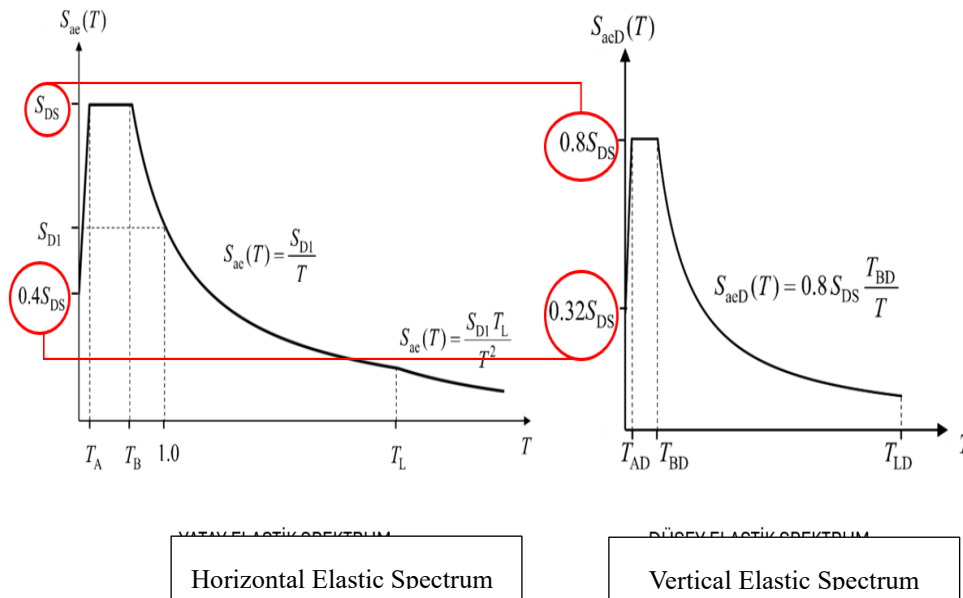

Figure 15. Comparison of horizontal and vertical spectra according to the TSC 2018.

When Figure 14 is examined, it is seen that the V/H ratio exceeds 0.8 in many records. This situation shows the lack of an approach to considering vertical earthquakes in seismic codes. The importance of vertical earthquake effects has emerged once again after the Kahramanmaraş earthquake. In addition, the records given in Figure 14 were obtained without any ground classification. By classifying according to ground classification, near fault conditions, basin effect, super shear effect, etc., the situations that increase the amplitude of the vertical earthquake component can be determined.

5   CONCLUSION AND SUGGESTIONS

After the Kahramanmaraş earthquakes, earthquake science will be updated at a significant level. In this study, attenuation relations, which are an indispensable approach in seismic hazard assessment, which is a special field in the field of earthquake engineering, were evaluated. These equations, which are used to predict the earthquake effect of a possible earthquake before the earthquake occurs, were tested with this study using the acceleration values of the Kahramanmaraş earthquake. In the study, the compatibility of 6 different GMPEs in the literature applicable to Türkiye with Kahramanmaraş earthquake data was examined. In addition, in the study, the change of the vertical earthquake effect with the horizontal earthquake effect was examined by examining the Kahramanmaraş earthquake data. The findings obtained because of this study were evaluated and the following results were obtained:

• With this study, some parts that are missing in a new GMPE to be prepared were evaluated. After these evaluations, it is expected to give an idea of how to consider the change of ground conditions, vertical earthquake effect and distance conditions that should be considered in a new GMPE.

• Deviations between earthquake records and curves are observed in a certain distance region. This is due to the different characteristics of the earthquake records and the lack of elaboration of the soil classifications.

• In general, the curves are below the actual earthquake data in the GMPEs examined in the study. This suggests that PGA values are indeed underestimated. Taking this situation into account in a new GMPE to be prepared for Türkiye, data sets should be updated.

• The necessity of different soil classification approaches was seen in this study. It is insufficient that soil classifications are generally limited to a single parameter or to affect the attenuation relations with a coefficient.

• Earthquakes have some special characteristics. These characteristics such as directivity effect, super shear effect, high vertical earthquake component, and ground behavior should be integrated into attenuation relations.

•If the vertical earthquake component is higher than expected, it shows the weakness of the seismic codes. In this context, it should be ensured that the vertical elastic spectra of the seismic codes are updated, and the vertical earthquake effect is accurately reflected.

• Evaluating the outcomes, it becomes clear that the attenuation relations should be updated with a more detailed, realistic approach and new data sets, or a new GMPE should be prepared for Türkiye.

Conflict of Interest Statement

There is no conflict of interest between the authors.

Statement of Research and Publication Ethics

The study is complied with research and publication ethics.

Artificial Intelligence (AI) Contribution Statement

This manuscript was composed, revised, analyzed, and prepared without the aid of any artificial intelligence techniques. All content, encompassing text, data analysis, and figures, was exclusively produced by the authors.

Contributions of the Authors

Writing - review & editing, Ö.F.N.; Formal analysis,Ö.F.N.; Investigation,Ö.F.N.; Data curation, Ö.F.N. and A.S.; Conceptualization, A.S. and Ö.F.N.; Methodology, A.S. and Ö.F.N.; Validation, A.S. and Ö.F.N.

REFERENCES

[1]   E. Işık *vd.*, "Structural damages in masonry buildings in Adıyaman during the Kahramanmaraş (Turkiye) earthquakes (Mw 7.7 and Mw 7.6) on 06 February 2023", *Engineering Failure Analysis*, c. 151, sy May, 2023, doi: 10.1016/j.engfailanal.2023.107405.

[2]   S. Öztürk, E. Altunsu, O. Güneş, ve A. Sarı, "Investigation of industrial structure performances in the Hatay and Gaziantep provinces during the Türkiye earthquakes on February 6, 2023", *Soil Dynamics and Earthquake Engineering*, c. 179, s. 108569, Nis. 2024, doi: 10.1016/j.soildyn.2024.108569.

[3]   O. İnce, "Structural damage assessment of reinforced concrete buildings in Adıyaman after Kahramanmaraş (Türkiye) Earthquakes on 6 February 2023", *Engineering Failure Analysis*, c. 156, s. 107799, Şub. 2024, doi: 10.1016/j.engfailanal.2023.107799.

[4]   V. Kahya *vd.*, "Evaluation of earthquake-related damages on masonry structures due to the 6 February 2023 Kahramanmaraş-Türkiye earthquakes: A case study for Hatay Governorship Building", *Engineering Failure Analysis*, c. 156, s. 107855, Şub. 2024, doi: 10.1016/j.engfailanal.2023.107855.

[5]   E. Altunsu, O. Güneş, S. Öztürk, S. Sorosh, A. Sarı, ve S. T. Beeson, "Investigating the structural damage in Hatay province after Kahramanmaraş-Türkiye earthquake sequences", *Engineering Failure Analysis*, c. 157, s. 107857, 2024, doi: https://doi.org/10.1016/j.engfailanal.2023.107857.

[6]   AFAD, *Türkiye Bina Deprem Yönetmeliği-2018(TBDY-2018)*. 2018.

[7] E. Damcı, R. Temür, Z. Kanbir, Ç. Şekerci, ve E. Öztorun Köroğlu, "Comprehensive investigation of damage due to 2023 Kahramanmaraş Earthquakes in Türkiye: Causes, consequences, and mitigation", *Journal of Building Engineering*, c. 99, s. 111420, Nis. 2025, doi: 10.1016/j.jobe.2024.111420.

[8] M. Kutanis, "Sismik Tehlike Analizi", Sakarya Üniversitesi, 2003.

[9] B. Balun, O. F. Nemutlu, A. Benli, ve A. Sari, "Estimation of probabilistic hazard for Bingol province, Turkey", *Earthquakes and Structures*, c. 18, sy 2, ss. 223-231, Şub. 2020, doi: 10.12989/EAS.2020.18.2.223.

[10] E. Işık, "Bitlis İlinin Depremselliği", *Erciyes Üniversitesi Fen Bilimleri Enstitüsü Dergisi*, c. 29, sy 3, ss. 267-273, 2013.

[11] E. Harman ve H. S. Küyük, "Sakarya ili için olasılığa dayalı sismik tehlike analizi Probabilistic seismic hazard analysis for the city of Sakarya", 2016.

[12] Y. İnce, "Kahramanmaraş ve çevresinin Olasılıksal Sismik Tehlike Analizi", Master's, Sakarya Universitesi (Turkey), Turkey, 2016. [Çevrimiçi]. Erişim adresi: https://www.proquest.com/dissertations-theses/kahramanmaraş-ve-çevresinin-olasılıksal-sismik/docview/2700777760/se-2?accountid=62760

[13] H. Ulutaş, "Van İli Sismik Tehlike Analizi", Master's, Sakarya Universitesi (Turkey), Turkey, 2012. [Çevrimiçi]. Erişim adresi: https://www.proquest.com/dissertations-theses/van-ili-sismik-tehlike-analizi/docview/2689296158/se-2?accountid=62760

[14] B. Shrestha, "Vertical Ground Motions and Its Effect on Engineering Structures: A State of the Art Review", program adı: International Seminar on Hazard Management for Sustainable Development, Katmandu,Nepal, 2009, ss. 190-202.

[15] N. Newmark ve W. Hall, "Earthquake Spectra and Design", *EERI Monographs*. 1982.

[16] F. Avcil *vd.*, "Effects of the February 6, 2023, Kahramanmaraş earthquake on structures in Kahramanmaraş city", *Nat Hazards*, c. 120, sy 3, ss. 2953-2991, Şub. 2024, doi: 10.1007/s11069-023-06314-1.

[17] Ö. F. Nemutlu, B. Balun, ve A. Sari, "Damage assessment of buildings after 24 January 2020 Elazig-Sivrice earthquake", *Earthquakes and Structures*, c. 20, sy 3, ss. 325-335, Mar. 2021, doi: 10.12989/EAS.2021.20.3.325.

[18] E. Sayın *vd.*, "24 January 2020 Sivrice-Elazığ, Turkey earthquake: geotechnical evaluation and performance of structures", *Bulletin of Earthquake Engineering*, c. 19, sy 2, ss. 657-684, 2021, doi: 10.1007/s10518-020-01018-4.

[19] "Türkiye'deki depremler listesi", *Vikipedi*. 08 Kasım 2024. Erişim: 20 Kasım 2024. [Çevrimiçi]. Erişim adresi: https://tr.wikipedia.org/w/index.php?title=T%C3%BCrkiye%27deki_depremler_listesi&oldid=34181847

[20] K. Gökkaya, "Geographic analysis of earthquake damage in Turkey between 1900 and 2012", *Geomatics, Natural Hazards and Risk*, c. 7, Nis. 2016, doi: 10.1080/19475705.2016.1171259.

[21] U. Hancılar *vd.*, "Strong Ground Motion and Building Damage Estimations Preliminary Report (v6)", c. 2023, sy February. 2023.

[22] M. Abdelmeguid, C. Zhao, E. Yalcinkaya, G. Gazetas, A. Elbanna, ve A. Rosakis, "Dynamics of episodic supershear in the 2023 M7.8 Kahramanmaraş/Pazarcik earthquake, revealed by near-field records and computational modeling", *Commun Earth Environ*, c. 4, sy 1, s. 456, Ara. 2023, doi: 10.1038/s43247-023-01131-7.

[23] Z. Wang, W. Zhang, T. Taymaz, Z. He, T. Xu, ve Z. Zhang, "Dynamic Rupture Process of the 2023 *Mw* 7.8 Kahramanmaraş Earthquake (SE Türkiye): Variable Rupture Speed and Implications for Seismic Hazard", *Geophysical Research Letters*, c. 50, sy 15, s. e2023GL104787, Ağu. 2023, doi: 10.1029/2023GL104787.

[24] AFAD, "06 Şubat 2023 Pazarcık-Elbistan (Kahramanmaraş) Mw: 7.7 – Mw: 7.6 Depremleri Raporu", AFAD, 2023.

[25] E. Hussain, S. Kalaycıoğlu, C. W. Milliner, ve Z. Çakir, "Preconditioning the 2023 Kahramanmaraş (Türkiye) earthquake disaster", *Nature Reviews Earth & Environment*, c. 4, sy 5, ss. 287-289, 2023.

[26]   Ö. F. Nemutlu, A. Sari, ve B. Balun, "06 Şubat 2023 Kahramanmaraş Depremlerinde (Mw 7.7-Mw 7.6) Meydana Gelen Gerçek Can Kayıpları Ve Yapısal Hasar Değerlerinin Tahmin Edilen Değerler İle Karşılaştırılması", *Afyon Kocatepe University Journal of Sciences and Engineering*, c. 23, sy 5, ss. 1222-1234, Eki. 2023, doi: 10.35414/akufemubid.1302254.

[27]   F. Akar, E. Işık, F. Avcil, A. Büyüksaraç, E. Arkan, ve R. İzol, "Geotechnical and Structural Damages Caused by the 2023 Kahramanmaraş Earthquakes in Gölbaşı (Adıyaman)", *Applied Sciences*, c. 14, sy 5, s. 2165, Mar. 2024, doi: 10.3390/app14052165.

[28]   Eurocode 8, *Eurocode 8: Design of structures for earthquake resistance*, 2005.

[29]   Ö. F. Nemutlu, "R Değerleri ile PGA Değerleri Arasındaki Uyumun İncelenmesi: 6 Şubat 2023 Kahramanmaraş Depremleri", program adı: Cumhuriyet 11th International Conference on Applied Sciences, Ankara: Academy Global Publishing House, Nis. 2024, ss. 19-28.

[30]   N. A. Abrahamson, W. J. Silva, ve R. Kamai, "Summary of the ASK14 ground motion relation for active crustal regions", *Earthquake Spectra*, c. 30, sy 3, ss. 1025-1055, 2014, doi: 10.1193/070913EQS198M.

[31]   S. Akkar ve Z. Çağnan, "A local ground-motion predictive model for Turkey, and its comparison with other regional and global ground-motion models", *Bulletin of the Seismological Society of America*, c. 100, sy 6, ss. 2978-2995, 2010, doi: 10.1785/0120090367.

[32]   S. Akkar ve J. J. Bommer, "Empirical equations for the prediction of PGA, PGV, and spectral accelerations in Europe, the mediterranean region, and the Middle East", *Seismological Research Letters*, c. 81, sy 2, ss. 195-206, 2010, doi: 10.1785/gssrl.81.2.195.

[33]   E. Kalkan ve P. Gülkan, "Site-dependent spectra derived from ground motion records in Turkey", *Earthquake Spectra*, c. 20, sy 4, ss. 1111-1138, 2004, doi: 10.1193/1.1812555.

[34]   A. Sarı, "Energy Considerations in Ground Motion Attenuation and Probabilistic Seismic Hazard Studies", 2003.

[35]   R. Ulusay, E. Tuncay, H. Sonmez, ve C. Gokceoglu, "An attenuation relationship based on Turkish strong motion data and iso-acceleration map of Turkey", *Engineering Geology*, c. 74, sy 3-4, ss. 265-291, 2004, doi: 10.1016/j.enggeo.2004.04.002.

[36]   N. Gregor *vd.*, "Comparison of NGA-West2 GMPEs", *Earthquake Spectra*, c. 30, sy 3, ss. 1179-1197, 2014, doi: 10.1193/070113EQS186M.

[37]   PEER, "Pacific Engineering Research Center Strong Ground Motion Database". 2021. [Çevrimiçi]. Erişim adresi: http://ngawest2.berkeley.edu

[38]   W. B. Joyner ve D. M. Boore, "Peak horizontal acceleration and velocity from strong-motion records including records from the 1979 Imperial Valley, California, earthquake", *Bulletin of the seismological Society of America*, c. 71, sy 6, ss. 2011-2038, 1981.

[39]   Ö. F. Nemutlu ve B. Balun, "Evaluation of November 23, 2022, Duzce Earthquake data with Ground Motion Prediction Equations", *Bitlis Eren Üniversitesi Fen Bilimleri Dergisi*, c. 12, sy 4, ss. 1248-1260, Ara. 2023, doi: 10.17798/bitlisfen.1376430.

CAFFEINE COATED IRON OXIDE CRUSTACEAN FOR AMMONIA BORANE DEHYDROGENATION DEVELOPMENT OF MAGNETIC NICKEL NANOPARTICLES

Erhan ONAT [1] (iD)

[1] *Bitlis Eren University, Department of Electricity and Energy, Bitlis, Türkiye, eonat@beu.edu.tr*

ABSTRACT

The aim of this study was to develop nickel (Ni) nanoclusters with caffeine-coated magnetic iron oxide (Fe_3O_4) center shells for the catalytic hydrolysis of ammonia borane (AB). In the study, magnetic iron oxide (MIO) clusters were obtained by hydrothermal treatment. These clusters were first coated with caffeine according to the reflux method at 150 $^{\circ}$C for 12 hours, and then Ni was decorated on these clusters by impregnation method. Magnetic Ni catalyst ($Ni@C/Fe_3O_4$) was synthesized by dropping 10 M 20 mL sodium borohydride ($NaBH_4$-SBH) into the Ni-C/ Fe_3O_4 magnetic nanoclusters in solution as a result of the loading processes carried out at room conditions. After filtration, washing and drying in nitrogen atmosphere, the crumbled catalyst was identified by advanced identification techniques (FT-IR, BET, SEM, EDX, XPS) and used in AB hydrolysis.

The solvate medium, catalyst amount, AB concentration, temperature and repeated use parameters were investigated for AB catalytic hydrolysis. As a result of the optimization at 303 K, the best hydrogen production was determined as 7873 mL/g.min using 2.5 % NaOH, 30 mg catalyst and 300 mM AB. The catalyst cycle frequency (TOF) was measured as 1447 s^{-1}. As a result of reaction kinetics investigations, it was determined that the reaction was 1st order and the reaction activation energy was 35.07 kJ/mol.

Keywords: Ammonia borane, Dehydrogenation, Fe_3O_4, Hydrolysis, Catalyst, $Ni@C/Fe_3O_4$.

1   INTRODUCTION

Renewable energy sources are the solution to reduce the negative impact of greenhouse gases caused by fossil fuels on the world. When alternative energy sources are examined in general, it will be seen that solar energy, wind energy, biomass energy, tidal energy, geothermal

energy and hydrogen energy are used as alternative energy sources. These alternative energy sources are preferred at different levels according to country conditions. Renewable energy source technology is currently being used and continues its development in parallel with the studies carried out by researchers. Hydrogen energy technology, which enables energy production at different values at regional and seasonal levels due to its various limitations, is an energy technology with many advantages [1] – [3].

Hydrogen is one of the best alternative energy carriers to meet the demand for efficient and clean energy in terms of being obtained from many sources, high energy density and not having a harmful effect on the environment [4].

Hydrogen is a colorless, odorless gas that makes up 75% of the mass of the universe. Hydrogen, which is converted into energy in fuel units, is expected to be used as fuel in vehicles and airplanes in the near future. Hydrogen is a non-toxic, inexhaustible and renewable source of clean energy. Hydrogen is a gas that can be stored, transported, converted into other forms of energy, and energy can be obtained with high efficiency. An important feature of hydrogen is that it cannot be used as a primary energy source. Hydrogen is converted into energy in fuel cells [5], [6].

Hydrogen converted into energy in fuel cells is currently used as a gas. Since hydrogen is a gas that takes up a lot of volume, storing and transporting it as a gas causes safety risks and cost losses. This problem is largely overcome by storing hydrogen in different ways. The most important storage technique is the solid storage of hydrogen in boron-based compounds. When the compounds used in hydrogen storage are examined, it is seen that ammonia borane takes the lead. Ammonia borane offers many advantages such as high hydrogen storage (19.6% by mass), stability up to high temperatures, non-toxicity, and the possibility of hydrogen production from water in addition to hydrogen in its own structure as a result of hydrolysis [7] – [9].

As with other compounds in which hydrogen is chemically stored, hydrogen production (dehydrogenation) from ammonia borane is realized by catalytic reactions under catalyst control. The hydrolysis reaction for the catalytic reaction of ammonia borane is given in Equation 1.

$$NH_3BH_3 + 2H_2O \rightarrow NH_4BO_2 + 3H_2 \tag{1}$$
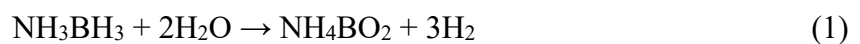
The fact that the reaction is catalyst-controlled and makes it possible to produce hydrogen from water makes the use of ammonia borane as a hydrogen storage source more important [10], [11].

The re-release of hydrogen from boron compounds is realized by catalytic processes using catalysts. Catalysts are generally defined as substances that increase the reaction rate. Catalysts, which are not among the substances that react or are formed, are involved in increasing the reaction rate by reducing the activation energy of the reaction. In systems where catalysts are used, energy loss is prevented and time is saved. Catalyst structures are highly preferred thanks to their advantages such as ensuring product control in the catalytic process, preventing loss of time, and reducing energy costs to low levels [12] – [14]

Features such as repeated use of catalysts, recovery and production from environmentally friendly materials make the material from which the catalyst is developed important. These properties are largely present in magnetic nanoparticles. Magnetic nanoparticles are a type of particle with a very wide range of applications. Therefore, there are many production methods. Depending on technological developments, magnetic nanoparticle production continues its development [15] – [17].

Today, magnetic nanoparticle production methods are co-precipitation, microemulsion, thermal decomposition, solvothermal (hydrothermal) synthesis, chemical reduction, sonochemical reactions, microwave method, chemical vapor deposition, arc discharge, laser pyrolysis, combustion synthesis, annealing methods [18].

Magnetic material is used in many fields such as superparamagnetism, high sensitivity, biocompatibility, separation technology, protein immobilization, catalysis, adsorption, drug/gene delivery, biosensors, magnetic resonance imaging, contrast enhancement, biophotonics, detection of cancer cells and tissue engineering. Among these areas of use, adsorption and catalytic processes are the most widely used areas of magnetic nanoparticles [19] – [23].

In this study, environmentally friendly magnetic nanoparticles were synthesized by hydrotemal method and the synthesized nanoparticles were used as support material for the catalyst structure obtained from nickel metal. In the presence of synthesized nickel-based magnetic nanoparticle catalyst structures, the parameters of hydrogen production (dehydrogenation) by hydrolysis from ammonia borane were investigated.

2 MATERIAL AND METHOD

Among the chemicals used in the study; Ammonia borane (AB), Sodium borhydride (SBH-NaBH$_4$) Sodium hydroxide (NaOH), Nickelchloride hexahydrate (NiCl$_2$×6H$_2$O), Iron (II) chloride tetrahydrate (FeCl$_2$×4H$_2$O), Iron (III) chloride hexahydrate (FeCl$_3$×6H$_2$O) were obtained from Sigma Aldrich and ammonia (NH$_3$) was obtained from TEKKİM. Ultrapure water was used in synthesis and hydrolysis processes. The devices used in the study were an oven, magnetic stirrer with heater, precision balance and gas collection unit. The oven was used in drying processes, the magnetic stirrer in reduction and metal loading processes, the precision balance in weighing processes, and the gas collection unit in time-dependent hydrogen production processes.

In the study, MIO was produced by hydrothermal method according to Equation 2 by taking the amount of material. In this process, metal salts containing Fe^{2+} and Fe^{3+} ions were taken into autoclave with pure water (50 mL of pure water and 10 mL of ammonia) by adding ammonia so that the pH was around 11.

$$Fe^{2+} + Fe^{3+} + 8\,OH^- \rightarrow Fe_3O_4 + 4\,H_2O \qquad (2)$$

The autoclave was kept at 180 °C for 8 hours and then the autoclave was allowed to come to room temperature. The obtained MIO was magnetically washed 7-8 times and Fe$_3$O$_4$ was obtained by vacuum filtration. Then, the magnetic material was allowed to dry at 60 °C for 16 hours in nitrogen atmosphere. The dried MIO and caffeine were taken in a 1:1 ratio and refluxed in distilled water at 150 °C for 12 hours. Then, after magnetic washing and drying in nitrogen atmosphere, nickel plating of the magnetic material to be used as support material was performed by impregnation method. For this process, Ni salt dissolved in pure water was dripped at 750 rpm under room conditions on the support material, which was also well dispersed in pure water. After 2-3 hours of dripping, the sample was stirred in a magnetic stirrer in pure water for 24 hours under room conditions. After Ni decoration, 10 M 20 mL SBH solution was dripped onto the mixture to reduce Ni metal atoms on the support surface. After the dropping process, the mixture was kept for about 2 hours and it was observed that the bubbles stopped coming out. Then, the catalyst separated from the filtrate by vacuum filtration was kept at 70 °C in the presence of nitrogen gas for 12 hours to dry [24] – [26]. The dried magnetic material coated caffeine nickel catalyst (Ni@C/Fe$_3$O$_4$) was crumbled and its structure was investigated. FT-IR, BET, SEM, EDX, XPS, SEM, EDX and XPS analyses were performed to elucidate the material structure. After structure elucidation, AB catalytic hydrolysis reactions

were carried out. Hydrolysis reactions were interpreted according to the formation of H_2 amount. For this process, water-gas displacement was utilized and the amount of H_2 released over time was recorded with the help of a stopwatch. The best hydrogen production values were determined as a result of parameter investigations such as support loading, solution medium and catalyst amount.

3   RESULTS AND DISCUSSION

The magnetic properties of the materials synthesized within the scope of the study were tested in solution and solid media. Images of these test processes are given in Figure 1.
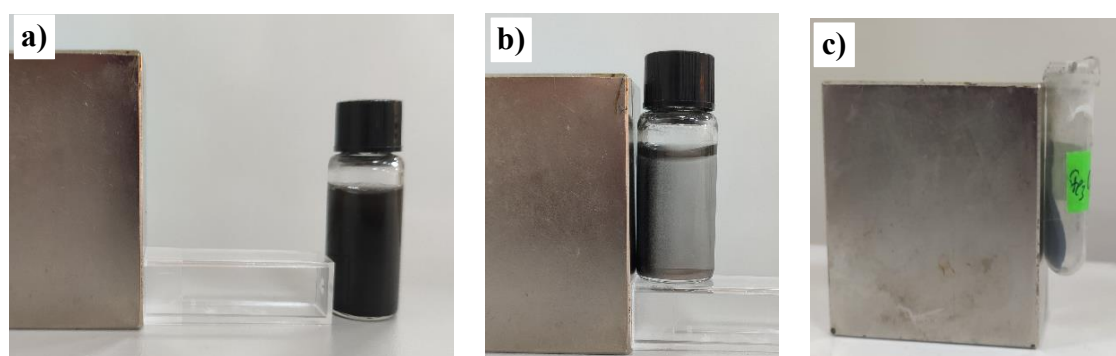

Figure 1. Behavior of magnetic Ni@C/Fe₃O₄ in magnetic field (a) Before magnetic field (b) In water in magnetic field (c) In solid state in magnetic field.

3.1   Characterization of Fe₃O₄ and Ni@C/Fe₃O₄

FT-IR, EDX, SEM and BET analyses were performed to characterize the structure of the samples that were found to have magnetic properties. When FT-IR given in Figure 2 is analyzed, it is seen that there is no significant shift in the outlines. This means that the coated material does not disturb the magnetic structure. When only the peaks of Fe_3O_4 are analyzed, it is seen that the prominent Fe_3O_4 peaks between 980-1200 cm^{-1} disappear completely after caffeine and Ni coating. This means that the coating and decoration were successfully realized. The caffeine-induced C-C and C-N peaks in the 800-950 cm^{-1} range also confirm this data [27] – [29].
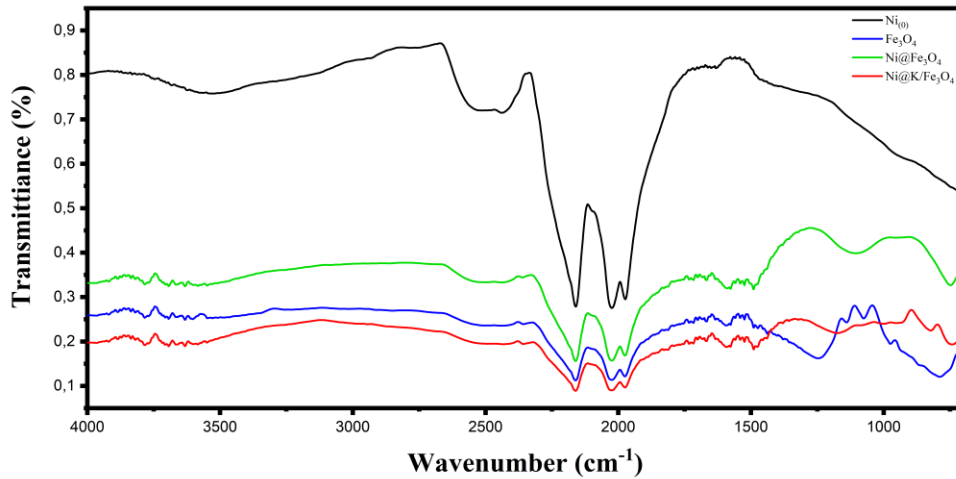
Figure 2. FT-IR image of Ni(0), Fe₃O₄, Ni@Fe₃O₄, Ni@C/Fe₃O₄ synthesized in this study.

EDX data given in Figures 3 and 4 confirm that Fe_3O_4 and $Ni@C/Fe_3O_4$ were successfully synthesized within the scope of the study. SEM analysis of the material consisting only of Fe_3O_4 magnetic material is given in Figure 3. In the figure, it is seen that a magnetic material in the form of a ball rod with a weight in the form of a rod is obtained. It is understood from the SEM images that the average particle diameter of the material in question is 51 nm. SEM analysis of $Ni@C/Fe_3O_4$ magnetic nanoparticles obtained after loading Fe_3O_4 with caffeine and Ni is given in Figure 4. As seen in the figure, it is seen that the particles, which are predominantly rod-shaped as a result of caffeine and Ni loading, have a spherical structure. It is understood from Figure 4 that $Ni@C/Fe_3O_4$ magnetic nanoparticles with a diameter of 24.6 nm instead of the average 51 nm formed only by magnetic iron oxides. BET analysis also confirms this situation. Because while Fe_3O_4 BET surface analysis is 13.7167 m^2/g, $Ni@C/Fe_3O_4$ BET surface analysis is 47.5764 m^2/g. This means that the effective catalytic surface is more [30].

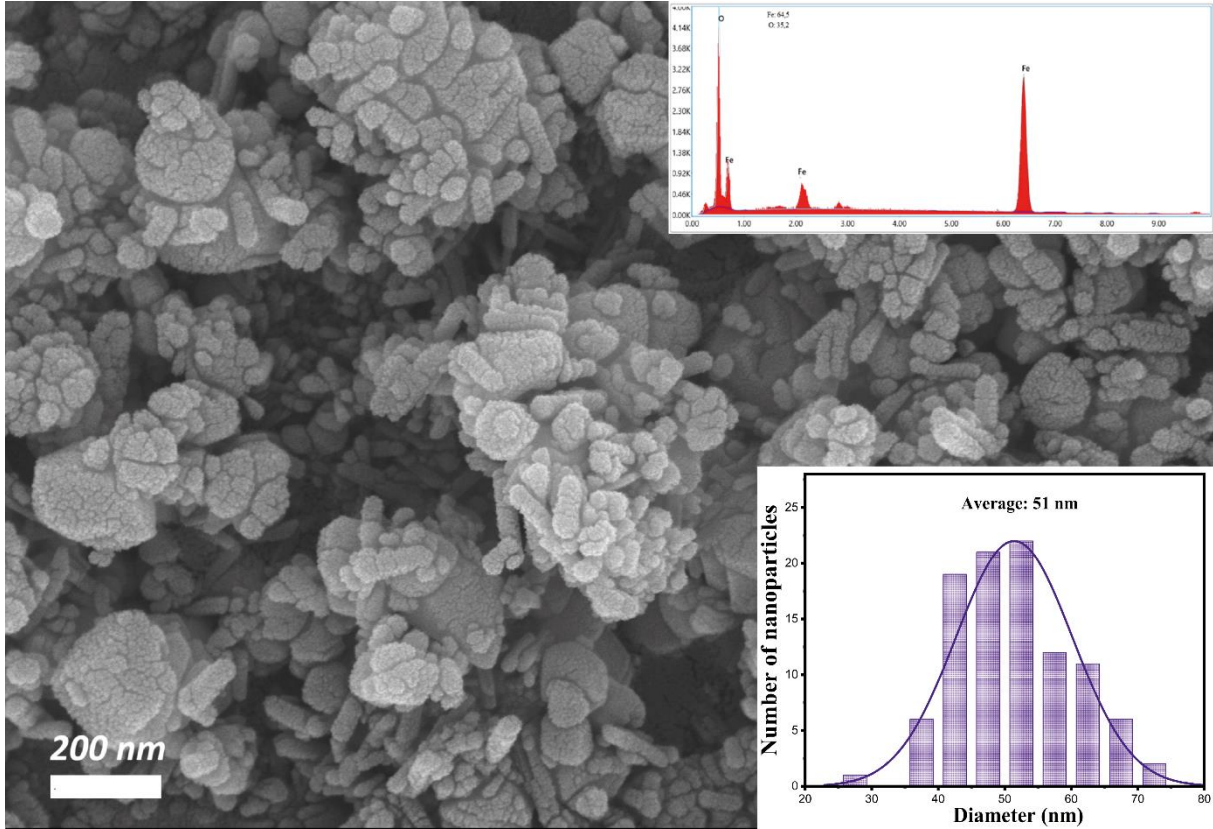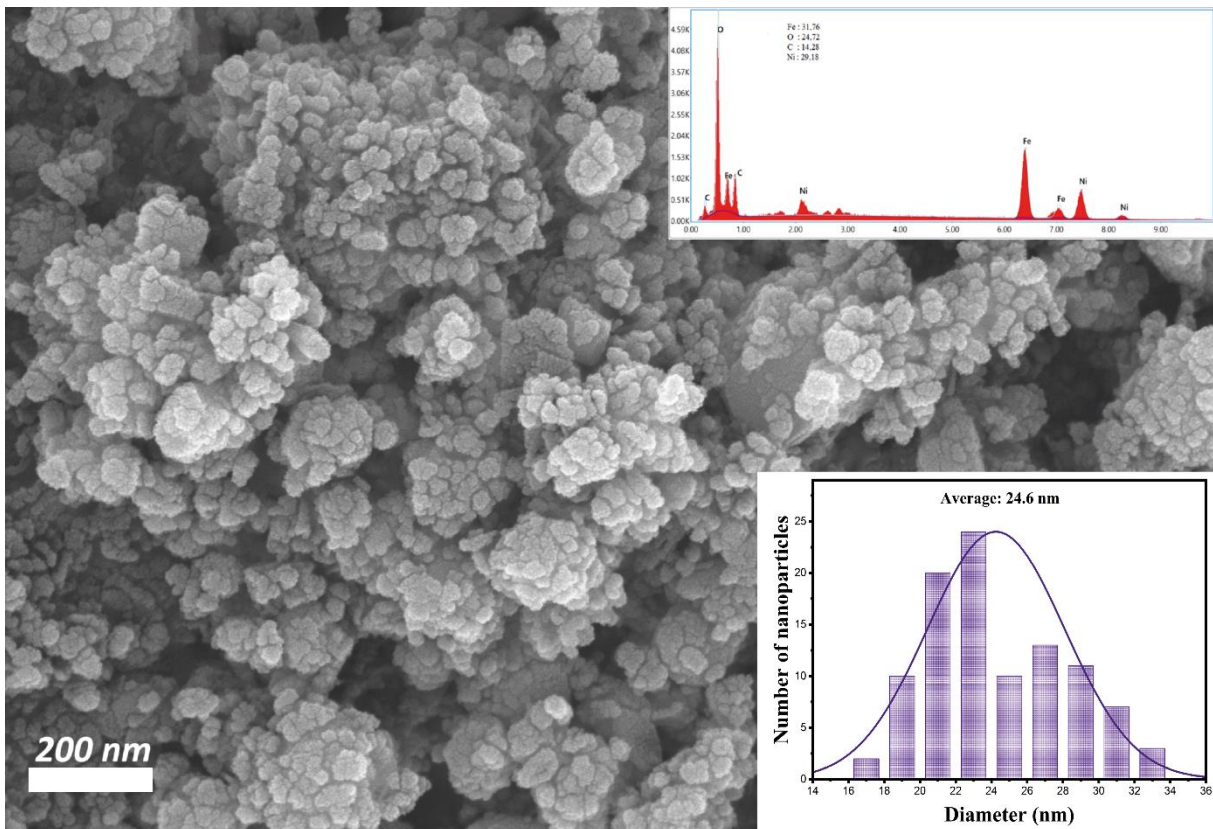*Figure 3. SEM, EDX analysis and average particle diameters of Fe₃O₄.*

Figure 4. SEM, EDX analysis and average particle diameters of Ni@C/Fe₃O₄.

XPS analyses performed to determine the behavior of the electrons in the Ni metal atom clusters successfully attached to the $Fe_3O_4@C$ surface as a result of reduction under SBH are given in Figure 5. In the XPS analysis of magnetic Ni nanoparticles, which were determined to have a high catalytic effect within the scope of the study, significant peaks of 858 eV for $Nip_{3/2}$, 864 eV for $Nis_{1/2}$ and 533 eV for O1s were detected [26], [31]. These XPS analyzes are given in Figure 5.

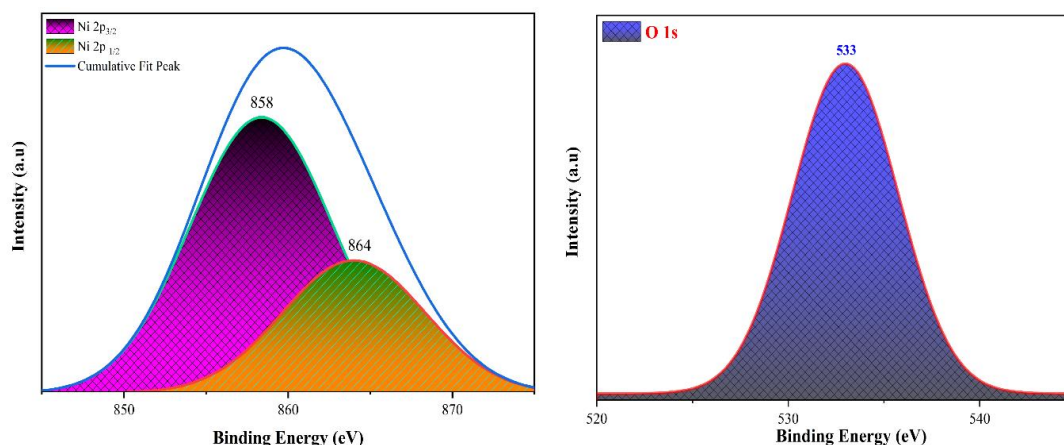*Figure 5. XPS analysis of Ni@C/Fe₃O₄.*

3.2   Dehydrogenation

After the determination of the material structure, the dehydrogenation parameter investigation of the study was carried out. These processes are given respectively. First of all, the parameters of $Ni_{(0)}$ for nickel loading, nickel loading on magnetic material and caffeine and then nickel loading on magnetic material were investigated. As a result of the hydrolysis process for three different structures, the degradation values of ammonia borane over time due to hydrogen formation are shown in Figure 6 a. It is clearly seen that the caffeine coated magnetic material shows high catalytic effect. After the determination of the support loading pattern, it is understood from Figure 6 b that the best H_2 production from hydrolysis reactions carried out at different NaOH concentrations is at 2.5 % NaOH. It is evaluated that hydrogen yield decreases at concentrations above 2.5% because metaborate screens the catalyst surface. As a result of the catalytic hydrolysis reactions carried out with different catalyst amounts in the continuation of the study, it is seen in Figure 6 c that the reaction time shortens with increasing catalyst amount. In the calculations for the best H_2 production per catalyst, it was determined that the highest H_2 yield was 4978 mL/g.min at 30 mg catalyst. This can be attributed to the best combination concentration of catalyst and hydrogen source. Hydrolysis data obtained as a result

of dehydrogenation processes carried out at different AB concentrations are given in Figure 6 d. As seen in the figure, H_2 production increases with increasing AB concentration. 7873 mL/g.min H_2 yield was obtained as a result of catalytic dehydrogenation with 300 mM AB. This value is quite high for Ni metal AB dehydrogenation [10].

As a result of optimization procedures with Ni@C/Fe$_3$O$_4$ for H_2 production, 2.5 % NaOH, 30 mg catalyst usage and 300 mM AB concentration were determined for the best hydrolysis data at 303 K. H_2 production at these values is 7873 mL/g.min per catalyst amount.
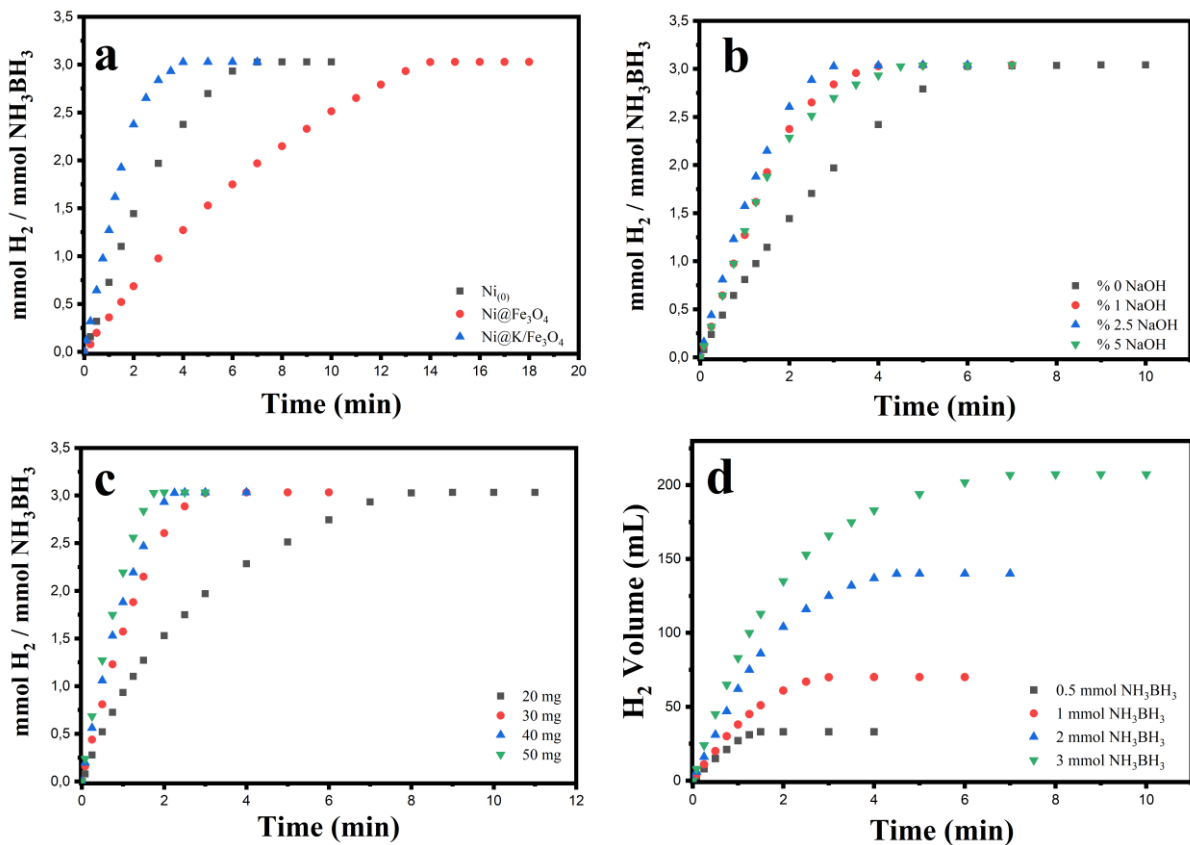

Figure 6. Ni@C/Fe$_3$O$_4$ catalytic dehydrogenation data; a) support loading, b) NaOH effect, c) catalyst amount, d) AB concentration.

After the completion of H_2 optimization, hydrolysis reactions at different temperatures were carried out for the kinetic data analysis of equation 1 catalyzed by Ni@C/Fe$_3$O$_4$ catalyst. The data for these reactions are given in Figure 7 a. As seen in the figure, the reaction accelerates in parallel with increasing temperature. As a result of the 0th, 1st and nth reaction equation correlations of the catalytic hydrolysis data performed at 30, 40, 50 and 60 $^{\circ}$C, it was determined that the AB hydrolysis reaction catalyzed by Ni@C/Fe$_3$O$_4$ catalyst was 1st order. Based on the 1st order reaction data, when the graph of ln k versus 1/T is plotted, we see a graph as shown

in Figure 7 b. When the relevant data were substituted in the Arrhenius equation (Equation 3), the activation energy (Ea) of the reaction was determined as 35.07 kJ/mol [32].

$$lnk = lnA-Ea / RT \tag{3}$$

Six consecutive hydrolysis reactions were carried out for repeated use of the catalyst. After each use, 90% of the solution was decanted into a different container and a new hydrogen source was added and 100% product yield was achieved in all repeated uses (Figure 7 c). The slight decrease in catalytic activity due to repeated use can be attributed to the deformation of the catalyst active surface. It is considered that the main factor in this deformation is due to the adhesion of sodium hydroxide and metaborate to the catalyst surface [33], [34].
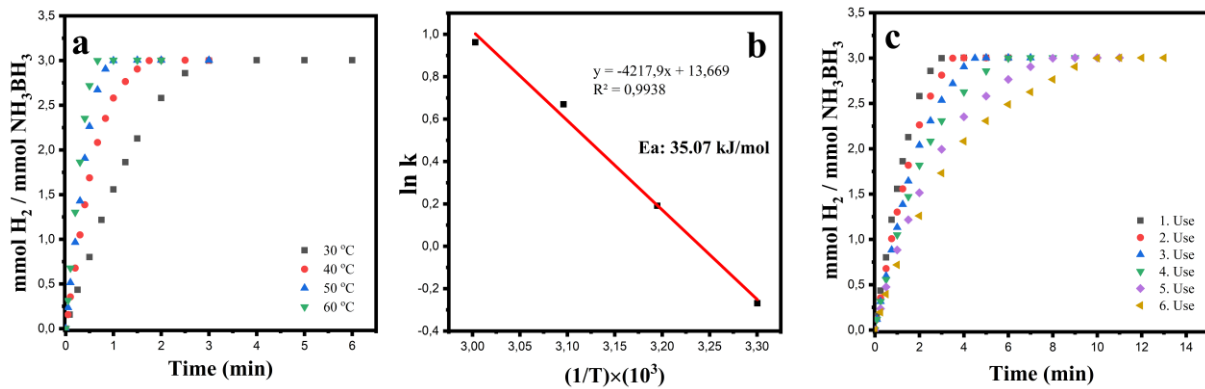

***Figure 7.** Ni@C/Fe₃O₄ catalytic dehydrogenation data; a) Temperature effect, b) Arrhenius equation data, c) Catalyst repeated use.*

Another key parameter measured to determine catalyst efficiency is the catalytic efficiency cycle frequency (TOF) value. Hydrogen is formed as a product at the end of ammonia borane decomposition. In this study, the cycle frequency was measured in terms of the number of moles of hydrogen (product) formed depending on the number of moles of magnetic nickel catalyst according to the following equation (Equation 4).

$$\text{TOF} = \frac{Mole\ Amount\ of\ the\ Product}{Mole\ Amount\ of\ catalyst\imath\ \times\ Time} \tag{4}$$

The TOF value was determined as 1447 s⁻¹ in the calculations made at the highest value measured for hydrogen velocity within the scope of the study.

4   CONCLUSION AND SUGGESTIONS

Within the scope of the study, magnetic material synthesis was successfully realized by hydrothermal method. As a result of the analysis for structure identification, it was determined that the magnetic nanomaterial was synthesized as targeted at the beginning of the study. It was understood from the decomposition data of the ammonia borane reaction that the catalytic effect of the synthesized magnetic nickel nanoparticles was high. When the studies in which nickel metal catalyzed the decomposition of ammonia borane as a catalyst were examined (Table 1), it was understood that the catalyst structure was synthesized at low activation energy and high hydrogen production rate.

Table 1. Some studies in which ammonia borane was catalyzed in the presence of nickel catalyst.

Catalyst	Ea (k.J.mol^{-1})	HGR (mL/g.min)	TOF (s^{-1})	Temperature (^{o} C)	Reference
Ni/C	31.6	834	-	25	[35]
Pt$_x$-Ni$_{-1-x}$	39	4784.7	-	30	[36]
Pt-Ni	46.8	1299.2	751	25	[37]
Ni$_{0.33}$@Pt$_{0.67}$/C	33	5469	-	30	[38]
Ni/SiO$_2$	34	-	132	25	[39]
Ni@C/Fe$_3$O$_4$	35.07	7873	1447	30	**This study**

In this study in which ammonia borane degradation data were investigated in the presence of magnetic nickel nanoparticles; it was determined that 2.5 % NaOH was used as the best solvent medium, 30 mg of catalyst was used as the best catalyst amount and hydrogen production rate increased in parallel with increasing ammonia borane concentration. It was determined that 7873 mL/g.min hydrogen production rate was achieved as a result of catalytic decomposition with 300 nM ammonia borane at 30 ^{o}C under the best conditions. The catalytic activity cycle frequency (TOF) at the best hydrogen production rate was measured as 1447 s^{-1}. As a result of the analysis and calculations for the reaction kinetics of the catalytic process, it was determined that the reaction was 1st order. The activation energy (Ea) of the reaction was determined as 35.07 kJ/mol. This shows that Ni@C/Fe$_3$O$_4$ catalyst reduces the reaction activation energy to very low values. It is evaluated that both the magnetic nanoparticle to be used in hydrogen production and other catalytic processes, decorating the magnetic material with active metal after caffeine coating will create a high catalytic effect.

Statement of Research and Publication Ethics

The study is complied with research and publication ethics.

Artificial Intelligence (AI) Contribution Statement

This manuscript was entirely written, edited, analyzed, and prepared without the assistance of any artificial intelligence (AI) tools. All content, including text, data analysis, and figures, was solely generated by the author.

REFERENCES

[1]   P. J. Megía, A. J. Vizcaíno, J. A. Calles, and A. Carrero, "Hydrogen production technologies: From fossil fuels toward renewable sources. A mini review," *Energy Fuels*, vol. 35, no. 20, pp. 16403–16415, 2021.

[2]   A. Pareek, R. Dom, J. Gupta, J. Chandran, V. Adepu, and P. H. Borse, "Insights into renewable hydrogen energy: Recent advances and prospects," *Mater. Sci. Energy Technol.*, vol. 3, pp. 319–327, 2020.

[3]   E. Onat, F. A. Celik, E. Karabulut, and M. S. Izgi, "High availability and outstanding catalytic activity in sodium borohydride hydrolytic dehydrogenation of CQD/GO@Co catalyst by green synthesis: Experimental and computational perspective," *Int. J. Hydrogen Energy*, vol. 83, pp. 903–915, 2024.

[4]   A. Midilli and I. Dincer, "Hydrogen as a renewable and sustainable solution in reducing global fossil fuel consumption," *Int. J. Hydrogen Energy*, vol. 33, no. 16, pp. 4209–4222, 2008.

[5]   M. A. Rosen and S. Koohi-Fayegh, "The prospects for hydrogen as an energy carrier: an overview of hydrogen energy and hydrogen energy systems," *Energy Ecol. Environ.*, vol. 1, no. 1, pp. 10–29, 2016.

[6]   E. L. V. Eriksson and E. M. Gray, "Optimization and integration of hybrid renewable energy hydrogen fuel cell energy systems—A critical review," *Appl. Energy*, vol. 202, pp. 348–364, 2017.

[7]   W. Jiao et al., "Magnetic Ni and Ni/Pt hollow nanospheres and their catalytic activities for hydrolysis of ammonia borane," *J. Mater. Chem. A Mater. Energy Sustain.*, vol. 2, no. 43, pp. 18171–18176, 2014.

[8]   E. Onat, F. A. Çelik, Ö. Şahin, E. Karabulut, and M. S. İzgi, "H2 production from ammonia borane hydrolysis with catalyst effect of titriplex® III carbon quantum dots supported by ruthenium under different reactant conditions: Experimental study and predictions with molecular modelling," *Int. J. Hydrogen Energy*, 2024.

[9]   U. B. Demirci, "Ammonia borane, a material with exceptional properties for chemical hydrogen storage," *Int. J. Hydrogen Energy*, vol. 42, no. 15, pp. 9978–10013, 2017.

[10]   W.-W. Zhan, Q.-L. Zhu, and Q. Xu, "Dehydrogenation of ammonia borane by metal nanoparticle catalysts," *ACS Catal.*, vol. 6, no. 10, pp. 6892–6905, 2016.

[11]   R. P. Shrestha, H. V. K. Diyabalanage, T. A. Semelsberger, K. C. Ott, and A. K. Burrell, "Catalytic dehydrogenation of ammonia borane in non-aqueous medium," *Int. J. Hydrogen Energy*, vol. 34, no. 6, pp. 2616–2621, 2009.

[12]   A. K. Figen, "Dehydrogenation characteristics of ammonia borane via boron-based catalysts (Co–B, Ni–B, Cu–B) under different hydrolysis conditions," *Int. J. Hydrogen Energy*, vol. 38, no. 22, pp. 9186–9197, 2013.

[13]   M. S. İzgi, Ö. Şahin, E. Onat, and S. Horoz, "Metanolde sentezlenen Co-B katalizörün sodyum hidrolizi üzerine etkisi," *J. Inst. Sci. Technol.*, vol. 7, no. 4, pp. 151–160, 2017.

[14]   N. C. Smythe and J. C. Gordon, "Ammonia borane as a hydrogen carrier: Dehydrogenation and regeneration," *Eur. J. Inorg. Chem.*, vol. 2010, no. 4, pp. 509–521, 2010.

[15] H. Cui, Y. Liu, and W. Ren, "Structure switch between α-Fe$_2$O$_3$, γ-Fe$_2$O$_3$ and Fe$_3$O$_4$ during the large scale and low temperature sol–gel synthesis of nearly monodispersed iron oxide nanoparticles," *Adv. Powder Technol.*, vol. 24, no. 1, pp. 93–97, 2013.

[16] M. Seehra, *Magnetic Spinels: Synthesis, Properties and Applications*, Bod–Books on Demand, 2017.

[17] M. S. İzgi, M. Ş. Ece, H. Ç. Kazici, Ö. Şahin, and E. Onat, "Hydrogen production by using Ru nanoparticle decorated with Fe$_3$O$_4$@SiO$_2$-NH$_2$ core-shell microspheres," *Int. J. Hydrogen Energy*, vol. 45, no. 55, pp. 30415–30430, 2020.

[18] Y. Hao and A. S. Teja, "Continuous hydrothermal crystallization of α–Fe$_2$O$_3$ and Co$_3$O$_4$ nanoparticles," *J. Mater. Res.*, vol. 18, no. 2, pp. 415–422, 2003.

[19] S. Gil, C. R. Correia, and J. F. Mano, "Magnetically labeled cells with surface-modified Fe$_3$O$_4$ spherical and rod-shaped magnetic nanoparticles for tissue engineering applications," *Adv. Healthcare Mater.*, vol. 4, no. 6, pp. 883–891, 2015.

[20] S. Shabestari Khiabani, M. Farshbaf, A. Akbarzadeh, and S. Davaran, "Magnetic nanoparticles: preparation methods, applications in cancer diagnosis and cancer therapy," *Artif. Cells Nanomed. Biotechnol.*, vol. 45, no. 1, pp. 6–17, 2017.

[21] D. V. Voronin et al., "In vitro and in vivo visualization and trapping of fluorescent magnetic microcapsules in a bloodstream," *ACS Appl. Mater. Interfaces*, vol. 9, no. 8, pp. 6885–6893, 2017.

[22] L. Xu, M.-J. Kim, K.-D. Kim, Y.-H. Choa, and H.-T. Kim, "Surface modified Fe$_3$O$_4$ nanoparticles as a protein delivery vehicle," *Colloids Surf. A Physicochem. Eng. Asp.*, vol. 350, no. 1–3, pp. 8–12, 2009.

[23] S. Liu, H. Chen, X. Lu, C. Deng, X. Zhang, and P. Yang, "Facile synthesis of copper (II) immobilized on magnetic mesoporous silica microspheres for selective enrichment of peptides for mass spectrometry analysis," *Angew. Chem. Int. Ed.*, vol. 41, no. 49, pp. 7557–7561, 2010.

[24] E. Onat, "Synthesis of a cobalt catalyst supported by graphene oxide modified perlite and its application on the hydrolysis of sodium borohydride," *Synth. Met.*, vol. 306, 2024.

[25] E. Onat and S. Ekinci, "A new material fabricated by the combination of natural mineral perlite and graphene oxide: Synthesis, characterization, and methylene blue removal," *Diam. Relat. Mater.*, vol. 143, 110848, 2024.

[26] Ö. Şahin, S. Ekinci, M. S. İzgi, and E. Onat, "Effect of different solvents on hydrogen production from hydrolysis of potassium borohydride with a new and active Ni-based catalyst synthesized by green synthesis," *Int. J. Hydrogen Energy*, 2024.

[27] P. Panneerselvam, N. Morad, and K. A. Tan, "Magnetic nanoparticle (Fe$_3$O$_4$) impregnated onto tea waste for the removal of nickel (II) from aqueous solution," *J. Hazard. Mater.*, vol. 186, no. 1, pp. 160–168, 2011.

[28] A. Mulyasuryani, R. Tjahjanto, and R. Andawiyah, "Simultaneous voltammetric detection of acetaminophen and caffeine base on cassava starch–Fe$_3$O$_4$ nanoparticles modified glassy carbon electrode," *Chemosensors*, vol. 7, no. 4, p. 49, 2019.

[29] H. İ. Ulusoy, E. Yılmaz, and M. Soylak, "Magnetic solid phase extraction of trace paracetamol and caffeine in synthetic urine and wastewater samples by a using core-shell hybrid material consisting of graphene oxide/multiwalled carbon nanotube/Fe$_3$O$_4$/SiO$_2$," *Microchem. J.*, vol. 145, pp. 843–851, 2019.

[30] H. W. Di, Y. L. Luo, F. Xu, Y. S. Chen, and Y. F. Nan, "Fabrication and caffeine release from Fe$_3$O$_4$/P(MAA-co-NVP) magnetic microspheres with controllable core-shell architecture," *J. Biomater. Sci.*, vol. 22, no. 4–6, pp. 557–576, 2011.

[31] E. Onat, M. S. İzgi, Ö. Şahin, and C. Saka, "Nickel/nickel oxide nanocomposite particles dispersed on carbon quantum dot from caffeine for hydrogen release by sodium borohydride hydrolysis: Performance and mechanism," *Diam. Relat. Mater.*, 2024.

[32] E. Onat and S. Ekinci, "Study of the sodium borohydride hydrolysis reaction's performance via a kaolin-supported Co–Cr bimetallic catalyst," *Afyon Kocatepe Univ. J. Sci. Eng.*, vol. 24, pp. 1061–1070, 2024.

[33] S. Ekinci and E. Onat, "Activated carbon assisted cobalt catalyst for hydrogen production: Synthesis and characterization," *Balıkesir Univ. J. Inst. Sci.*, vol. 26, no. 2, pp. 455–471, 2024.

[34]   E. Onat, S. Ekinci, Ö. Şahin, and M. S. İzgi, "Effective and environmentally friendly Co nanocatalyst on sodium borohydride hydrolysis in different solvents," *Int. J. Hydrogen Energy*, 2025.

[35]   L. Zhou, T. Zhang, Z. Tao, and J. Chen, "Ni nanoparticles supported on carbon as efficient catalysts for the hydrolysis of ammonia borane," Nano Res., vol. 7, no. 5, pp. 774–781, 2014.

[36]   X. Yang, F. Cheng, J. Liang, Z. Tao, and J. Chen, "PtxNi$_{1-x}$ nanoparticles as catalysts for hydrogen generation from hydrolysis of ammonia borane," Int. J. Hydrogen Energy, vol. 34, no. 21, pp. 8785–8791, 2009.

[37]   J. Zhang, X. Zheng, W. Yu, X. Feng, and Y. Qin, "Unravelling the synergy in platinum-nickel bimetal catalysts designed by atomic layer deposition for efficient hydrolytic dehydrogenation of ammonia borane," Appl. Catal. B, vol. 306, 121116, 2022.

[38]   X. Yang, F. Cheng, J. Liang, Z. Tao, and J. Chen, "Carbon-supported Ni$_{1-x}$@Ptx (x = 0.32, 0.43, 0.60, 0.67, and 0.80) core-shell nanoparticles as catalysts for hydrogen generation from hydrolysis of ammonia borane," Int. J. Hydrogen Energy, vol. 36, no. 3, pp. 1984–1990, 2011.

[39]   Ö. Metin, S. Özkar, and S. Sun, "Monodisperse nickel nanoparticles supported on SiO$_2$ as an effective catalyst for the hydrolysis of ammonia–borane," Nano Res., vol. 3, no. 9, pp. 676–684, 2010.